CODEN: JASMAN

The Journal of the Acoustical Society of America

ISSN: 0001-4966

Vol. 110, No. 2 August 2001

(Continued)

THE JOURNAL OF THE ACOUSTICAL SOCIETY OF AMERICA VOL. 110, NO. 2, AUGUST 2001

CONTENTS—*Continued from preceding page*

(Continued)

THE JOURNAL OF THE ACOUSTICAL SOCIETY OF AMERICA VOL. 110, NO. 2, AUGUST 2001

CONTENTS—*Continued from preceding page*

(Continued)

THE JOURNAL OF THE ACOUSTICAL SOCIETY OF AMERICA VOL. 110, NO. 2, AUGUST 2001

CONTENTS—*Continued from preceding page*

ACOUSTICAL NEWS—USA

Elaine Moran
Acoustical Society of America, Suite 1NO1, 2 Huntington Quadrangle, Melville, NY 11747-4502

Editor's Note: *Readers of this Journal are encouraged to submit news items on awards, appointments, and other activities about themselves or their colleagues. Deadline dates for news items and notices are 2 months prior to publication.*

New Fellow of the Acoustical Society of America

Emily A. Tobey—For contributions to understanding speech and language development in cochlear implant users.

Results of the ASA Election

The following candidates were elected Officers and Members of the Executive Council in the 2001 Society election:

Richard Stern, *President-Elect*
William A. Yost, *Vice President-Elect*
Whitlow W. L. Au, *Member of the Executive Council*
Winifred Strange, *Member of the Executive Council*

CHARLES E. SCHMID
Executive Director

Regional Chapter News
North Carolina Regional Chapter Celebrates 35 Years—Tours New Concert Hall with Larry Kirkegaard, and Honors Larry Royster

The North Carolina Regional Chapter celebrated its 35th Anniversary 20 April at the Raleigh Convention and Conference Center. About 85 members and guests attended. The technical highlight was a tour and discussions of the new Meymandi Concert Hall and Fletcher Opera Theater. Our special guests were project acousticians Larry Kirkegaard and Ed Dugger of Kirkegaard Associates, and the project architect Irv Pearce. Meymandi is a 1650-seat shoebox design with variable reverberation for both symphonic and pops music. It has received high praise, especially considering the tight budget.

The technical program also featured demonstrations of animal vocalizations by Elizabeth von Muggenthaler of Fauna Communications Institute, and discussions of instrumentation developments by Rich Peppin of Scantek, Will Kinard of Bruel & Kjaer, and Bill Wright of Endevco. Nine commercial vendors and consultants supported the meeting with exhibits and displays. Several members brought instruments from the 1960's to display the technology available when the chapter was founded.

The meeting concluded with a social following a review of chapter history and recognition of chapter founders and leaders. Three of the ten original organizers were present: Larry Royster, Mack Preslar, and Guy Rudisill. The meeting was especially memorable for the attendance of many past chapter leaders. This included some who had left acoustics and moved away, but who came back for a special reunion. Former members came from as far as Alabama, Florida, and even Oregon. Attendees included six of the eight Honorary Life Members of the chapter, 21 of the 29 people who have served as chapter chair, and 6 of the 14 others who have held officer positions (see Fig. 1).

Chapter founder Larry Royster was recognized for his 35 years of service, including contributions to over half the chapter meetings, and more than 30 years service on the chapter board. Noting his impending retirement, the chapter made Dr. Royster an Honorary Life Member of the chapter.

FIG. 1. Twenty-one of the 29 past chapter chairs pictured above attended the meeting.

 0001-4966/2001/110(2)/643/2/$18.00

USA Meetings Calendar

Listed below is a summary of meetings related to acoustics to be held in the U.S. in the near future.

2001

15–19 August — ClarinetFest 2001, New Orleans, LA [Dr. Keith Koons, ICA Research Presentation Committee Chair, Music Dept., Univ. of Central Florida, P.O. Box 161354, Orlando, FL 32816-1354; Tel.: 407-823-5116; E-mail: kkoons@pegasus.cc.ucf.edu].

19–24 August — Asilomar Conference on Implantable Auditory Prostheses, Pacific Grove, CA [Michael Dorman, Dept. of Speech and Hearing Science, Arizona State Univ., Tempe, AZ 85287-0102; Tel.: 480-965-3345; Fax: 480-965-0965; E-mail: mdorman@asu.edu].

4–6 October — Ninth Annual Conference on the Management of the Tinnitus Patient, Iowa City, IA [Rich Tyler, Tel.: 319-356-2471; E-mail: rich-tyler@uiowa.edu; WWW: www.medicine.uiowa.edu/otolaryngology/news/news].

7–10 October — 2001 IEEE International Ultrasonics Symposium Joint with World Congress on Ultrasonics, Atlanta, GA [W. O'Brien, Electrical and Computer Engineering, Univ. of Illinois, 405 N. Mathews, Urbana, IL 61801; Fax: 217-244-0105; WWW: www.ieee-uffc.org/2001].

29–31 October — NOISE-CON 01, The 2001 National Conference and Exposition on Noise Control Engineering, Portland, ME [Institute of Noise Control Engineering, P.O. Box 3206 Arlington Branch, Poughkeepsie, NY 12603; Tel.: 914-462-4006; Fax: 914-462-4006; E-mail: omd@ince.org; WWW: users.aol.com/inceusa/ince.html].

15–18 November — American Speech Language Hearing Association Convention, New Orleans, LA [American Speech-Language-Hearing Association, 10801 Rockville Pike, Rockville, MD 20852; Tel.: 888-321-ASHA; E-mail: convention@asha.org; WWW: professional.asha.org/convention/abstracts/welcome.asp].

3–7 December — 142nd Meeting of the Acoustical Society of America, Ft. Lauderdale, FL [Acoustical Society of America, Suite 1NO1, 2 Huntington Quadrangle, Melville, NY 11747-4502; Tel.: 516-576-2360; Fax: 516-576-2377; E-mail: asa@aip.org; WWW: asa.aip.org]. Deadline for submission of abstracts: 3 August 2001.

2002

21–23 February — National Hearing Conservation Association Annual Conference, Dallas, TX [NHCA, 9101 E. Kenyon Ave., Ste. 3000, Denver, CO 80237; Tel.: 303-224-9022; Fax: 303-770-1812; E-mail: nhca@gwami.com; WWW: www.hearingconservation.org/index.html].

10–13 March — Annual Meeting of American Institute of Ultrasound in Medicine, Nashville, TN [American Institute of Ultrasound in Medicine, 14750 Sweitzer Lane, Suite 100, Laurel, MD 20707-5906; Tel.: 301-498-4100 or 800-638-5352; Fax: 301-498-4450; E-mail: conv_edu@aium.org; WWW: www.aium.org].

3–7 June — 143rd Meeting of the Acoustical Society of America, Pittsburgh, PA [Acoustical Society of America, Suite 1NO1, 2 Huntington Quadrangle, Melville, NY 11747-4502; Tel.: 516-576-2360; Fax: 516-576-2377; E-mail: asa@aip.org; WWW: asa.aip.org].

2–6 December — Joint Meeting: 144th Meeting of the Acoustical Society of America, 3rd Iberoamerican Congress of Acoustics and 9th Mexican Congress on Acoustics, Cancun, Mexico [Acoustical Society of America, Suite 1NO1, 2 Huntington Quadrangle, Melville, NY 11747-4502; Tel.: 516-576-2360; Fax: 516-576-2377; E-mail: asa@aip.org; WWW: asa.aip.org/cancun.html].

Cumulative Indexes to the *Journal of the Acoustical Society of America*

Ordering information: Orders must be paid by check or money order in U.S. funds drawn on a U.S. bank or by Mastercard, Visa, or American Express credit cards. Send orders to Circulation and Fulfillment Division, American Institute of Physics, Suite 1NO1, 2 Huntington Quadrangle, Melville, NY 11747-4502; Tel.: 516-576-2270. Non-U.S. orders add $11 per index.

Some indexes are out of print as noted below.

Volumes 1–10, 1929–1938: JASA, and Contemporary Literature, 1937–1939. Classified by subject and indexed by author. Pp. 131. Price: ASA members $5; Nonmembers $10.

Volumes 11–20, 1939–1948: JASA, Contemporary Literature, and Patents. Classified by subject and indexed by author and inventor. Pp. 395. Out of Print.

Volumes 21–30, 1949–1958: JASA, Contemporary Literature, and Patents. Classified by subject and indexed by author and inventor. Pp. 952. Price: ASA members $20; Nonmembers $75.

Volumes 31–35, 1959–1963: JASA, Contemporary Literature, and Patents. Classified by subject and indexed by author and inventor. Pp. 1140. Price: ASA members $20; Nonmembers $90.

Volumes 36–44, 1964–1968: JASA and Patents. Classified by subject and indexed by author and inventor. Pp. 485. Out of Print.

Volumes 36–44, 1964–1968: Contemporary Literature. Classified by subject and indexed by author. Pp. 1060. Out of Print.

Volumes 45–54, 1969–1973: JASA and Patents. Classified by subject and indexed by author and inventor. Pp. 540. Price: $20 (paperbound); ASA members $25 (clothbound); Nonmembers $60 (clothbound).

Volumes 55–64, 1974–1978: JASA and Patents. Classified by subject and indexed by author and inventor. Pp. 816. Price: $20 (paperbound); ASA members $25 (clothbound); Nonmembers $60 (clothbound).

Volumes 65–74, 1979–1983: JASA and Patents. Classified by subject and indexed by author and inventor. Pp. 624. Price: ASA members $25 (paperbound); Nonmembers $75 (clothbound).

Volumes 75–84, 1984–1988: JASA and Patents. Classified by subject and indexed by author and inventor. Pp. 625. Price: ASA members $30 (paperbound); Nonmembers $80 (clothbound).

Volumes 85–94, 1989–1993: JASA and Patents. Classified by subject and indexed by author and inventor. Pp. 736. Price: ASA members $30 (paperbound); Nonmembers $80 (clothbound).

Volumes 95–104, 1994–1998: JASA and Patents. Classified by subject and indexed by author and inventor. Pp. Price: ASA members $40 (paperbound); Nonmembers $90 (clothbound).

ACOUSTICAL NEWS—INTERNATIONAL

Walter G. Mayer
Physics Department, Georgetown University, Washington, DC 20057

Australia to host 2003 Western Pacific Acoustics Conference

WESTPRAC 7, which was held in Japan in October 2000, was attended by about 500 delegates from 17 countries, according to a report in *Acoustics Australia*. It was also announced that the name of the Conference, Western Pacific Regional Acoustics Conference, will no longer contain the word Regional and the next conference will be WESPAC 8. It will be held in Melbourne in April 2003. Preliminary information is available from charlesd@iprimus.com.au

Papers published in *Acoustical Science and Technology*

A listing of Regular Papers appearing in the latest issue of the English language version of the Journal of the Acoustical Society of Japan, *Acoustical Science and Technology*, was published for the first time in the January 1995 issue of the Journal. This listing is continued below.

The May 2001 issue, Vol. 22, No. 3, contains the following contributions:

Yoram Meron and Keikichi Hirose, ''Automatic alignment of musical score to perform music''
Tomoyasu Taguti and Yoshimasa (Kakuryo) Tohnai, ''Acoustical analysis on the sawari tone of Chikuzen biwa''
Kenshi Kishi, Hitoshi Maeda, and Masanori Sugai, ''A new percussion instrument 'hokyo' made of Sanukite''
Yasuhiro Goto, ''Implicit memory for rhythmic tone sequence: A pilot study on perceptual priming for short temporal pattern''
Akira Nishimura, Mitsumi Kato, and Yoshinori Ando, ''The relationship between the fluctuations of harmonics and the subjective quality of flute tone''
Tamotsu Shirado and Masuzo Yanagida, ''Relationship between off-scale perception and the perception of simultaneity of two pure tones presented almost simultaneously''
Masashi Yamada and Shiro Yonera, ''Temporal control mechanism of repetitive tapping with simple rhythmic patterns.''

The Japanese Acoustical Society has an excellent home page which lists titles, abstracts, and texts of tutorials, papers, and letters appearing in current and previous issues of *Acoustical Science and Technology*. The Web site is http://wwwsoc.nacsis.ac.jp/index-e.html. Since this information is readily available from that Web site *The Journal* will discontinue printing ''Papers published in *Acoustical Science and Technology*.''

International Commission for Acoustics (ICA)—New Web site

The International Commission for Acoustics, ICA, has changed its Web site address to http://www.icacommission.org. The home page contains current news about the commission, its activities, member organizations or societies, its purpose and constitution, a meeting calendar, as well as other information of interest to the worldwide community of acousticians.

International Meetings Calendar

Below are announcements of meetings to be held abroad. Entries preceded by an * are new or updated listings with full contact addresses given in parentheses. *Month/year* listings following other entries refer to meeting announcements, with full contact addresses, which were published in previous issues of the *Journal*.

August 2001

9–11 **Meeting of the Society for Music Perception and Cognition (SMPC2001)**, Kingston, Ontario, Canada. (Fax: +1 613 533 2499; Web: psyc.queensu.ca/~smpc/) *6/01*

28–30 **INTER-NOISE 2001**, The Hague. (Web: internoise2001.tudelft.nl) *6/99*

September 2001

2–7 **17th International Congress on Acoustics (ICA)**, Rome. (Fax: +39 6 4976 6932; Web: www.ica2001.it) *10/98*

3–7 ***7th International Conference on Speech Communication and Technology (Eurospeech 2001)**, Aalborg, Denmark. [P. Dalsgaard, Center for PersonKommunikation (CPK), Aalborg University, Denmark. E-mail: pd@cpk.auc.dk; Web: eurospeech2001.org]

10–14 **International Symposium on Musical Acoustics (ISMA 2001)**, Perugia. (Fax: 39 75 577 2255; Web: www.cini.ve.cnr.it/ISMA2001) *10/99*

30–5 **Conference on Microgravity Transport Processes in Fluid, Thermal, Materials, and Biological Sciences**, Banff. (Fax: +1 212 591 7441; Web: www.engfnd.org/engfnd/lay.html) *4/01*

October 2001

1–3 **Acoustics Conference in Canada 2001**, Nottawasaga Resort, Ontario (Fax: +1 905 660 4110; Web: www.caa2001.com) *6/01*

17–19 **32nd Meeting of the Spanish Acoustical Society**, La Rioja, Spain. (Fax: +34 91 411 76 51; Web: www.ia.csic.es/sea/index.html) *10/99*

25–26 **Fall Meeting of the Swiss Acoustical Society, Walllis/Valais**. (Web: www.sga-ssa.ch) *02/01*

November 2001

14–15 **Institute of Acoustics Autumn Conference**, Stratford-upon-Avon, U.K. (Fax: +44 172 785 0553; Web: www.ioa.org.uk) *6/01*

16–18 **Reproduced Sound 17**, Stratford-upon-Avon, U.K. (Fax: +44 172 785 0553; Web: www.ioa.org.uk) *6/01*

19–23 **Russian Acoustical Society Meeting**, Moscow. (Fax: +7 095 126 8411; Web: www.akin.ru/e_rao.htm) *6/01*

21–23 **Australian Acoustical Society Annual Meeting**, Canberra. (E-mail: m.burgess@adfa.edu.au; Web: www.users.bigpond.com/Acoustics) *02/01*

March 2002

4–8 **German Acoustical Society Meeting (DAGA 2002)**, Bochum. (Web: www.ika.ruhr-uni-bochum.de) *10/00*

April 2002

8–11 ***6th Congress of the French Acoustical Society, joint with the Belgian Acoustical Society**, Lille, France. (Société Française d'Acoustique, 23 av. Brunetière, 75017 Paris, France. Web: www.isen.fr/cfa2002)

May 2002

27–30 **Joint Meeting: Russian Acoustical Society and Conference on Ocean Acoustics**, Moscow. (Fax: +7 095 124 5983; Web: rav.sio.rssi.ru/Ixconf.html) *6/01*

 0001-4966/2001/110(2)/645/2/$18.00

June 2002

4–6 **6th International Symposium on Transport Noise and Vibration**, St. Petersburg, Russia. (Fax: +7 812 127 9323; E-mail: noise@mail.rcom.ru) *02/01*

10–14 **Acoustics in Fisheries and Aquatic Ecology**, Montpellier, France. (Web: www.ices.dk/symposia/) *12/00*

August 2002

19–23 **16th International Symposium on Nonlinear Acoustics (ISNA16)**, Moscow. (Fax: +7 095 126 8411; Web: acs366b.phys.msu.su/isna) *12/00*

26–28 ***2nd Biot Conference on Poromechanics**, Grenoble, France. (J.-L. Auriault, Laboratoire 3S, Domaine Universitaire, BP53, 38041 Grenoble, France. Fax: +33 4 76 82 70 43; Web: geo.hmg.inpg.fr/biot2001)

September 2002

16–21 **Forum Acusticum 2002 (Joint EAA-SEA-ASJ Meeting)**, Sevilla, Spain. (Fax: +34 91 411 7651; Web: www.cica.es/aliens/forum2002) *2/00*

December 2002

2–6 **Joint Meeting: 9th Mexican Congress on Acoustics, 144th Meeting of the Acoustical Society of America, and 3rd Iberoamerican Congress on Acoustics**, Cancún. (E-mail: sberista@maya.esimez.ipn.mx; Web: asa.aip.org) *10/00*

June 2003

8–13 ***XVII International Evoked Response Audiometry Study Group Symposium**, Puerto de la Cruz, Tenerife, Canary Islands, Spain. (Fax: +34 922 27 03 64; Web: www.ierasg-2003.org)

September 2003

1–4 ***Eurospeech 2003**, Geneva, Switzerland. (SYMPORG SA, Avenue Krieg 7, 1208 Geneva, Switzerland; Fax: +41 22 839 8485; Web: www.symporg.ch/eurospeech2003)

April 2004

5–9 **18th International Congress on Acoustics (ICA2004)**, Kyoto, Japan. (Web: ica2004.or.jp) *4/01*

OBITUARIES

John E. Cole III • 1942–1999

John E. (Jack) Cole III, died on 13 February 1999, at age 56, of a prolonged illness associated with a spinal cord injury he suffered in 1995 while bicycling to work. He is survived by his wife Judith, sons Alexander and Stephen, and sister Carolyn Cochrane. Jack was born in Upper Darby, PA. After receiving a B.S. in Mechanical Engineering from Drexel University in 1965, he attended Brown University, earning a M.Sc. in Mechanical Engineering in 1967 and a Ph.D. in 1970. His thesis topic was ''The Propagation of Sound Through Atmospheric Fog.'' Upon graduation, Dr. Cole joined the faculty of Tufts University as an Assistant Professor of Mechanical Engineering (1970–1977). During this period, he was also a Summer Faculty Fellow with Stanford University and with NASA Ames Research Center (1971–1972). He joined Cambridge Acoustical Associates, Inc. (CAA) in 1978 as a Scientist, rising to Senior Scientist, Principal Scientist, and eventually President of this acoustical consulting firm in 1994. Dr. Cole's interests while he was at CAA covered a broad spectrum of acoustical research, and his numerous accomplishments led to publications in the *Journal of Atmospheric Sciences*, *Journal of Sound and Vibration*, the *Shock and Vibration Bulletin*, *AIAA Journal*, and the *Journal of Computers and Structures*, as well as the *Journal of the Acoustical Society of America (JASA)*. While at CAA he worked closely with Dr. Miguel C. Junger on a number of projects, resulting, for example, in the co-authoring of papers in JASA on nonuniform structural wave guides (1979) and on bubble swarm acoustics (1980). Consulting work for the NASA–Marshall Space Flight Center led to Jack's co-authoring *The Handbook of the Acoustical Characteristics of Turbomachinery Cavities*, with Michael J. Lucas *et al.* (ASME, 1997). Dr. Cole was a Registered Professional Engineer in Massachusetts, a member of the American Society of Mechanical Engineers, and a Fellow of the ASA.

David E. Weston • 1929–2001

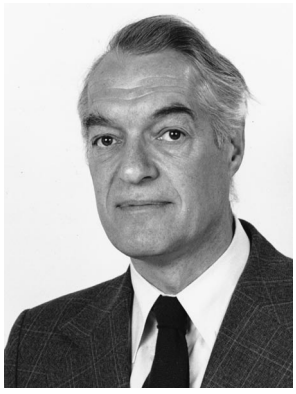

David E. Weston, a Fellow of the Acoustical Society of America, died suddenly of heart failure at his home on 19 January 2001. Dr. Weston, who was born 16 November 1929, graduated from Imperial College (University of London) in 1950 and obtained his M.Sc. in 1952, also from Imperial College, under the guidance of R. W. B. Stephens. His M.Sc. project, on the propagation of sound waves in tubes, resulted in a paper which was published in 1953 in the Proceedings of the Physical Society and which is still amongst his most frequently cited publications. He joined the Admiralty Research Laboratory (now the Admiralty Research Establishment) in 1951 and stayed with this organization until his retirement in 1989, his title then being Individual Merit Deputy Chief Scientific Officer. Dr. Weston is perhaps best known for his pioneering fixed range experiments at Perranporth in the Bristol Channel in the 1960s. These resulted in a number of publications on shallow water propagation and on the acoustic effects of bladdered fish. In addition to this experimental work, he subsequently laid the foundations for the currently accepted theory of scattering and absorption of sound by fish.

During his early years Weston worked with A. B. Wood, and by the age of 32 he had published a total of nine articles, letters, and notes in journals, on subjects as diverse as MoirT fringes, explosive sources, flux propagation theory, horizontal refraction, and the theory of ray invariants that now bears his name. During this period, he had a productive exchange visit to the Hudson Laboratories (Columbia University) in 1964–1965. In 1970 he received a D.Sc. degree from London University and was awarded the Rayleigh Silver Medal by the British Acoustical Society (now Institute of Acoustics). During a second visit to the USA, this one taking place in 1978–1979 and at the Applied Research Laboratories (University of Texas), he worked with C. T. Tindle on the theoretical relationships between ray and mode properties in wave guide propagation, one of the most fruitful collaborations of his long career.

After his retirement in 1989, David worked as a consultant to BAeSEMA Ltd. (now BAE Systems) in London, and his advice continued to be sought after by scientists throughout the world, resulting in many invited lectures and visits to research labs. He was well known for his in-depth knowledge across many different aspects of underwater sound, from generation mechanisms to the detection process, through propagation, scattering and absorption (most notably, but by no means exclusively, by fish), and ambient noise. His leadership in the British acoustics community is exemplified by his service as President of the UK Institute of Acoustics (1982–1984). The Acoustical Society of America recognized his extensive achievements with its Helmholtz–Rayleigh Medal in 1998, the award being titled the Helmholtz–Rayleigh Interdisciplinary Silver Medal in Acoustical Oceanography and Underwater Acoustics. The citation was for ''seminal work on the physics of explosive sources, scattering, and the horizontal refraction of sound.''

Over his lifetime, Dr. Weston published at least 67 papers in 11 different journals (including 32 in JASA alone), along with several encyclopedia articles and many reports. He continued to publish papers drawing on the results of the experiments in the Bristol Channel for more than 20 years after the experiments were carried out. This was made possible by his meticulous record keeping and a painstaking attention to detail. A striking example with regard to the latter is an incident that occurred during a project meeting: he was describing the subtle but sometimes important effects caused by departures from sphericity of a fish bladder. He was asked what shape a typical bladder might have, a question which many would have either side stepped or at best answered by quoting statistics of aspect ratios of representative oblate spheroids. But David astonished all present by putting his hand in his jacket pocket and pulling out a perfect specimen of what turned out to be a gurnard swim bladder. Its shape was a spheroidal main cavity with two adjoining tubular side pods, one on each side like handlebars.

David will long be remembered as the leading figure in underwater acoustics in the United Kingdom during the second half of the 20th Century, just as A. B. Wood will be remembered in regard to the first half. He is survived by his widow Joyce (nee Nicholls), his daughter Anna, and his son Peter.

MICHAEL A. AINSLIE

Auyuab Mohammed • 1928–2001

Auyuab Mohammed, a Fellow of the Acoustical Society of America, passed away in Halifax, Nova Scotia, on 9 April 2001 at the age of 73 after a lengthy battle with cancer. He was born in San Fernando, Trinidad, and moved to Canada in 1949, where he received his B.Sc. and M.Sc. from the University of Manitoba. His Ph.D. was subsequently received from the University of British Columbia. All of his degrees were in electrical engineering. He joined the Canadian Department of National Defence's Naval Research Establishment (later called the Defence Research Establishment Atlantic, DREA) in Dartmouth in 1954. There, he worked as a defense scientist in various positions in acoustics, signal processing, and applied mathematics. He later managed the Applied Mathematics Section of DREA and was also responsible for its central computer facilities. He became a member of the Acoustical Society of America in 1964, and was elected a Fellow of the Society in 1971 for theoretical studies on transducer arrays, reverberation, and signal processing. He retired from DREA in 1988.

BOOK REVIEWS

P. L. Marston
Physics Department, Washington State University, Pullman, Washington 99164

These reviews of books and other forms of information express the opinions of the individual reviewers and are not necessarily endorsed by the Editorial Board of this Journal.

Editorial Policy: *If there is a negative review, the author of the book will be given a chance to respond to the review in this section of the Journal and the reviewer will be allowed to respond to the author's comments. [See "Book Reviews Editor's Note," J. Acoust. Soc. Am.* ***81****, 1651 (May 1987).]*

Marine Mammals and Low-frequency Sound: Progress Since 1994

National Research Council

National Academy Press, Washington, DC, 2000.
Price: $35.00 (paperback) ISBN: 0-309-06886-X.

The National Research Council's (NRC's) report *Marine Mammals and Low-frequency Sound: Progress Since 1994* is a book that all users of underwater sound should read, as the topic is a critical one. But when reading it, the reader should realize that in addition to much good information and analysis, this report also contains some serious flaws. This review looks at the positive aspects of the report first, and then turns to the flaws, in the hope that this ordering will persuade the reader to eventually look at this report, despite its blemishes.

The report begins with an Executive Summary and Recommendations, so that ''power readers'' (sic) can cut to the conclusions, and make important policy decisions without bothering too much with the detailed facts that led up to them. That personally irksome ordering aside, two excellent recommendations are immediately made to Congress: (1) to re-define ''type B harassment'' of marine mammals in terms of significant disruption of behaviors critical to survival and reproduction and (2) to acknowledge the relative significance of different sources of sound in the ocean, insofar as this is known, and provide new means to bring *all* commercial sources of sound into the MMPA's (Marine Mammals Protection Act) legal and regulatory framework. These two recommendations are almost worth the price of the report. The first recommendation would negate the senseless concept that ''taking'' of a marine mammal (i.e., producing a noticeable behavioral change) is to be strictly avoided, and replace it with a much saner ''real harm'' criterion. The second recommendation supports a ''uniform standard of justice'' for marine mammal regulations, something that ocean acoustics scientists and the Navy have desired for at least a decade. Both ocean scientists and the Navy are held to rather strict sound emission regulations, whereas the oil industry has seen somewhat more relaxed regulations. But the biggest ocean noise polluter, the shipping industry, goes entirely unregulated, and this second NRC report recommendation addresses that inequity.

There are further recommendations made for NMFS (the National Marine Fisheries Service) and also for various marine mammal research sponsors, and these are rather well thought out. However, these latter recommendations also point to NMFS and the Navy leading the charge and paying the way for the marine mammal research and monitoring that needs to be done, and here I must disagree with the report. Oil exploration and shipping activities contribute the lions' share to the noise pollution in the ocean, and the report should ask them to pay a fair and proportional share for the research needed for mitigation. Instead, the report just says they ''should contribute,'' a rather timid recommendation, given the much bolder ones made to Congress.

After the executive summary, the report embarks on a brief introduction to sound propagation in the sea, on the ATOC (Acoustic Thermometry of Ocean Climate) project's history, objectives, and structure, and finally on the overlap of the ATOC source's bandwidth with marine vertebrate hearing ranges. This section is generally well done, with one exception to be discussed later. By the way, the assessment of the ATOC project and the associated MMRP (Marine Mammal Research Project) were the *primary* charters of this NRC report, though it is not at all obvious from the title of the report.

The second chapter describes the MMRP's results, and this chapter is probably the meatiest and most scientifically intriguing of the entire book. Dan Costa's California elephant seal translation results seem to indicate no impact to seals that dove quite near the ATOC source, whereas Calambokidis' aerial survey seemed to show some slight avoidance of the ATOC source by humpback whales and Risso's dolphins. The Hawaii playback experiments also produced some marginal results. When the dust clears, the report concludes that the observable effects of the ATOC sources are small to nonexistent, but that more work needs to be done, both to tighten the data analyses already initiated and to take more data. The MMRP investigators are also given a rather resounding hand slap for not publishing their results quickly enough, and are criticized over points of experimental design that disagree with the panel's vision. These latter two points reveal, more than anything else, some of the friction that existed between the panel and the MMRP investigators.

The third chapter of the report, ''Assessment of Continuing Research Needs,'' also has good technical meat, in that it is the biologist's ''wish list'' for future research into the topic. Aside from a few more jibes at the MMRP scientists for their ''sins of omission,'' this chapter is fairly noncontroversial, and presents some interesting glimpses into the possible future of marine mammal acoustics.

Chapter four of the book brings up an issue that is universally important to anyone putting a sound source into the ocean, whether purposely or incidentally—that of regulation. Two main issues are discussed in this chapter: (1) the definitions of the two types of harassment, Level A and Level B, and (2) the scientific and incidental harassment permitting process. Concerning the first topic, the report suggests only minor adjustments to the Level A, injurious impact rules, which are tied to the fairly reasonable concept of ''temporary threshold shift (TTS).'' However, the Level B acoustic harassment rules, which regulate ''taking'' animals (where a ''take'' is defined as using an acoustic stimulus that produces a measurable change in an animals' behavior), come under well-deserved fire from the report. The report suggests that level B harassment be redefined as follows:

> ''Level B—has the potential to disturb a marine mammal or marine mammal stock in the wild by causing meaningful disruption of biologically significant activities, including but not limited to, migration, breeding, care of young, predator avoidance or defense, and feeding.''

To this reviewer, this was one of the highlights of the report. Another highlight is the report's criticism of the gross inconsistencies in the permitting process. The following passage, which spotlights some of the inconsistencies, was particularly biting (and depending on your viewpoint, entertaining):

> ''For example, a biologist proposing to study how a whale responds to vessel noise would have to apply for a scientific research permit, whereas an oceanographer planning to transit such a habitat would not be subject to any regulation, and an acoustician using a similar level of sound for studies unrelated to marine mammals might need to obtain an incidental harassment authorization. It seems illogical to regulate the artificially induced acoustic stimuli more intensely than vessel-induced sound, which adds the risk of actually striking the whale.''

The final regular chapter of the report, Chap. 5, ''Findings and Rec-

 0001-4966/2001/110(2)/649/2/$18.00

ommendations,'' gives the NRC committee's views on what should have been done by the MMRP, what should be done in the future to regulate ATOC and ATOC type experiments, and what future research needs to be addressed. I could go into much detail here, but perhaps a brief synopsis will suffice. From the point of view of the biologists, the numerous recommendations made on how the MMRP could have been improved, what future regulations there should be on sound sources (especially fixed, ATOC type emitters), and what future research should be done in marine mammal biology studies might look quite reasonable. To the acousticians and physical oceanographers using sound sources for their research, these same recommendations might look rather excessive and self-serving by the biologists. What the viewpoint of the regulatory agencies might be toward these recommendations, I cannot even guess. Let me just leave this issue with the hope that reasonable and rational solutions will eventually be reached.

The report concludes with several useful and interesting appendices, which include committee biographies, a summary of the 1994 NRC report (the precursor to this report), relevant U.S. regulations for marine mammals, OSHA regulations, a glossary of acronyms, and a list of species discussed in the report (a helpful little Latin to English glossary).

Having discussed the highlights of the report, I now turn to some of the defects of the report. I would again remind the reader that my judgments here are not of strictly quantitative matters, and so have a degree of subjectivity in them.

As mentioned, the first obvious flaw in the report is its title, which is a misnomer. The report is a review of ATOC and the MMRP, but not a review of the entirety of marine mammal research since 1994. Though mention is necessarily made of other research, it is not at all the main focus.

Another flaw in the NRC report, to this reviewers mind, is the underrepresentation of ocean acousticians on the panel, especially since the report deals with the effects of ocean acoustic instrumentation. Though the NRC generally strives hard to have its panels fairly represented by discipline, one can argue that this did not happen in this case. A deficiency in ocean acoustics expertise shows up through a number of small, but basic, errors in acoustics, which should have been avoided in such a high-profile report, and detract significantly from it.

Moreover, most ocean acousticians and MMRP investigators I talked to also felt that there was a distinct negative bias in the overall viewpoint of the report towards ATOC and the MMRP. In that allegations of bias are both serious and generally impossible to prove or disprove, I will shy away from the considerable effort needed to plead the case from either side. However, I *will* give my own personal opinion here, and agree with the ATOC and MMRP investigators that there does seem to be a disapproving attitude toward their work in the report, above and beyond the strictly scientific and technical criticisms made.

The next two ''defects'' I would mention reflect my thoughts on what important points the report omitted. First, one never gets ''the big picture'' of where ATOC fits in as a possible hazard to marine mammals. Is ATOC on a par with shipping, fishing, whaling, oil exploration, and other threats to marine mammals? And thus, by implication, does the report address a major or minor environmental issue? It would be nice for the report to place the problem it addresses in the ''threat continuum,'' but this never happens. And finally, it would have been nice for the report to advocate a more equitable distribution of the responsibility for marine noise pollution. However, that again begs the ''big picture'' question, which is not addressed.

To conclude, despite its flaws, this NRC report should be read. Its topic is just too important for any user of sound in the ocean to ignore. However, it is also hoped that in the near future, this report will be supplemented by one that really does address the full issue of ''Marine Mammals and Low Frequency Sound: Progress Since 1994.''

JAMES F. LYNCH
Woods Hole Oceanographic Institution
Woods Hole, Massachusetts 02543

REVIEWS OF ACOUSTICAL PATENTS

Lloyd Rice
11222 Flatiron Drive, Lafayette, Colorado 80026

The purpose of these acoustical patent reviews is to provide enough information for a Journal reader to decide whether to seek more information from the patent itself. Any opinions expressed here are those of reviewers as individuals and are not legal opinions. Printed copies of United States Patents may be ordered at $3.00 each from the Commissioner of Patents and Trademarks, Washington, DC 20231. Patents are available via the Internet at http://www.uspto.gov.

Reviewers for this issue:

GEORGE L. AUGSPURGER, *Perception, Incorporated, Box 39536, Los Angeles, California 90039*
IBRAHIM M. HALLAJ, *Wolf Greenfield & Sacks P.C., 600 Atlantic Avenue, Boston, Massachusetts 02210*
DAVID PREVES, *Songbird Hearing, Inc., 5 Cedar Brook Drive, Cranbury, New Jersey 08512*
KEVIN P. SHEPHERD, *M. S. 463, NASA Langley Research Center, Hampton, Virginia 23681*
WILLIAM THOMPSON, JR., *601 Glenn Road, State College, Pennsylvania 16803*
ERIC E. UNGAR, *Acentech, Incorporated, 33 Moulton Street, Cambridge, Massachusetts 02138*

6,163,503

43.30.Sf SYSTEM, APPARATUS, AND METHOD FOR GEOGRAPHIC POSITIONING OF MARINE FAUNA

Sigmar Gudbjornsson, Seltjarnarnes, Iceland
19 December 2000 (Class 367/6); filed in Iceland 23 February 1998

A system, apparatus, and method are described for determining the positions of underwater animals. The procedure involves placing an acoustic transponder on the animal and then establishing communications with another transponder carried by a surface vessel whose position is determined via a GPS satellite.—WT

5,978,316

43.30.Xm MARINE SEISMIC SOURCE

Loran D. Ambs and John J. Sallas, assignors to Western Atlas International, Incorporated
2 November 1999 (Class 367/134); filed 29 September 1997

A seismic acoustic source consists of a surface marine vehicle **12** whose hull **30** has bottom **31** in contact with a body of water. The vehicle **12** may be towed by a ship, airship, or helicopter via tow-cable **18**. The hull **30** houses some kind of vibratory acoustic source **36** which may be driven hydraulically, pneumatically, electromechanically, electrostatically, chemically, or simply mechanically. The nature of umbilical line **24** therefore depends upon the type of source. The source illustrated in this figure is a

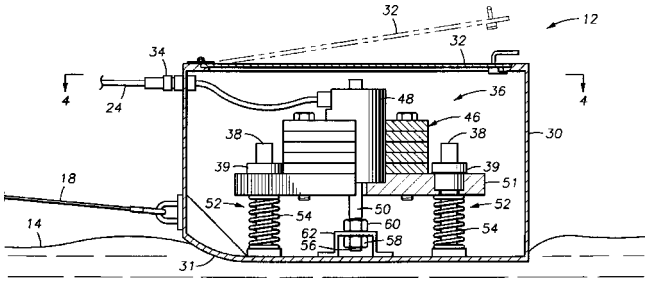

hydraulic vibrator **48** supported on base plate **51**, with additional reaction masses **46**, all of which are resiliently mounted from the hull by a number of springs **54**. Piston rod **50** is securely attached to bracket or rib **62**, which is fastened to bottom **31**, by means of nuts **58** and **60**. Piston rod **50** is caused to vibrate along its axis thereby causing bottom **31** to vibrate and radiate sound into the body of water.—WT

5,889,730

43.30.Yj UNDERWATER AUDIO COMMUNICATION SYSTEM USING BONE CONDUCTED SOUND

David F. May, assignor to Trigger Scuba, Incorporated
30 March 1999 (Class 367/132); filed 5 January 1998

An underwater communication system for relaying audio signals to a diver consists of a conventional swimmer's mask with head strap to which is connected a transceiver unit and at least one water-proofed bone conduction transducer, electrically connected to the transceiver, and held in place against the mastoid bone behind the ear by the head strap.—WT

6,138,515

43.35.Zc APPARATUS FOR THE ACOUSTIC DETECTION OF DEFECTS IN A MOVING STRIP

Jean-Pierre Moufle and Philippe Piquemal, assignors to Sollac
31 October 2000 (Class 73/639); filed in France 8 March 1996

One or more Lamb-wave transducers are housed in a sensor wheel that is made of a flexible material and filled with an acoustic coupling fluid. The axle of this sensor wheel is held stationary by a bridge arrangement as the circumference of the wheel rolls along the top of the moving metal strip in which defects are to be detected. A delivery system ahead of the wheel drops coupling fluid on the strip's surface and a roller spreads this fluid uniformly to ensure continuous and efficient coupling. The bridge presses the sensor wheel against the test strip and can move the wheel along the width of the strip.—EEU

6,125,706

43.38.Dv HIGH TEMPERATURE ELECTROMAGNETIC ACOUSTIC TRANSDUCER

Jonathan D. Buttram, Bedford, Virginia and John H. Flora, Lynchburg, Virginia
3 October 2000 (Class 73/643); filed 25 July 1997

This ultrasonic transducer, intended for inspection of materials at high temperatures, provides cooling of the coils, magnets and onboard circuitry by forced gas flows via a cooling system that is configured so that it does not interfere with the magnetic fields. The transducer is designed so that its electronic subcomponents (coil and PC cards) can be removed easily for repair.—EEU

 0001-4966/2001/110(2)/651/9/$18.00

5,889,873

43.38.Fx PIEZOELECTRIC ACOUSTIC TRANSDUCER

Yoshifumi Sasaki, assignor to TDK Corporation
30 March 1999 (Class 381/190); filed in Japan 11 March 1996

Rather than making solder connections to a piezoelectric element in an apparatus such as a buzzer, the electrical connections are accomplished by simple mechanical contact of an electrical lead with a spring loaded contact that bears against both the piezoelectric element and the electrical lead.—WT

6,147,932

43.38.Fx ACOUSTIC TRANSDUCER

Douglas S. Drumheller, assignor to Sandia Corporation
14 November 2000 (Class 367/165); filed 6 May 1999

This patent pertains to a transducer for use in down-hole applications, claimed to permit wider machining tolerances and easier assembly than a similar transducer described in an earlier patent. A sandwich-style piezoelectric crystal, constructed of two half-cylindrical parts, is mounted around a cylindrical mandrel and compressed between a shoulder on that mandrel and an anvil. The entire assembly is threaded into a cylindrical housing.—EEU

6,150,752

43.38.Fx ACOUSTIC TRANSDUCER WITH LIQUID-IMMERSED, PRE-STRESSED PIEZOELECTRIC ACTUATOR IN ACOUSTIC IMPEDANCE MATCHED TRANSDUCER HOUSING

Richard P. Bishop, assignor to Face International Corporation
21 November 2000 (Class 310/328); filed 17 April 1998

This patent actually pertains to a vibratory tool for finishing exposed surfaces of a work medium, such as plastic concrete. Blades in the shape of a disc or plate are immersed in a liquid that is located in a housing. Each blade is made to execute ''wing flapping'' motions by an electrically actuated piezoelectric element connected to the blade's center, so that vibratory energy is transmitted via the oil to the base of the housing, and from there to the work medium. The blades are claimed to be impedance matched to the oil, as is the top surface of the housing base, and the impedance of the bottom of that base is claimed to be matched to that of the work medium for maximum efficiency.—EEU

6,105,430

43.38.Hz INSPECTION OF CONCRETE STRUCTURES USING SONIC TOMOGRAPHY

William F. Kepler and Leonard J. Bond, assignors to the United States of America as represented by the Secretary of the Interior
22 August 2000 (Class 73/594); filed 2 July 1998

This patent pertains to means for detecting defects in large concrete structures, such as dams. A plurality of sensors is placed along the dam and measured impacts are applied sequentially at a number of locations. The resulting signals are stored and used to determine the travel times from the various impact points to the sensor locations. The propagation velocities along the different paths are then determined from the known impact and sensor positions. A tomography program running on a general-purpose computer is used for these calculations and to produce a graphical representation of the detected anomalies.—EEU

6,128,958

43.38.Hz PHASED ARRAY SYSTEM ARCHITECTURE

Charles A. Cain, assignor to The Regents of the University of Michigan
10 October 2000 (Class 73/626); filed 11 September 1997

A driving and switching system is described for driving phased arrays of many elements. By using multiplexers and properly switching between a plurality of driving signals having distinct phases, the array may be driven with a limited number of amplifiers being fewer than the number of individual array elements.—IMH

6,148,088

43.38.Ja SPEAKER SYSTEM

Seiki Suzuki and Noboru Kyouno, assignors to Mitsubishi Denki Kabushiki Kaisha
14 November 2000 (Class 381/345); filed in Japan 11 November 1997

An impedance-compensated loudspeaker, invented by Watkins in the 1970s, has two voice coils **21** and **22**. Coil **22** is fed through an L-C network **10** having a minimum impedance at the loudspeaker's frequency of resonance. It seems obvious that if several such loudspeakers are connected in

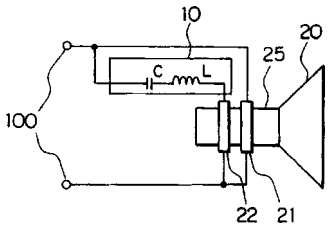

parallel, only one network is required. However, the patent document requires seven pages filled with mathematical formulas to demonstrate that such is the case.—GLA

6,151,402

43.38.Ja VIBRATION TRANSDUCERS

Henry Azima *et al.*, assignors to New Transducers Limited
21 November 2000 (Class 381/396); filed in the United Kingdom 2 September 1995

This patent relates to transducers for loudspeakers comprising panel-form acoustic radiating elements. Such a transducer is intended to be mounted on a member so as to apply a localized couple and thus to produce bending waves. A typical transducer consists of a tubular magnetic member that is rigidly attached to the loudspeaker panel. A secondary tubular member surrounds the first and is attached to it via resilient elements. This member also supports motor coils, which are configured to induce rotation of the magnetic member about its axis.—EEU

6,154,557

43.38.Ja ACOUSTIC TRANSDUCER WITH SELECTIVE DRIVING FORCE DISTRIBUTION

Michael Montour and David Alexander Todd, assignors to Sonigistix Corporation
28 November 2000 (Class 381/431); filed 21 May 1998

The object of this patent is reduction in the number and volume of magnets required to drive planar magnetic loudspeakers so as to obtain smooth frequency responses. According to this patent, magnets are arranged asymmetrically with respect to the loudspeaker membrane's frame, and voice coils that are shaped to interact with these magnets are imbedded in the membrane. The geometries are selected to couple energy preferably into

those membrane modes that result in smoother frequency response characteristics.—EEU

6,148,089

43.38.Kb UNIDIRECTIONAL MICROPHONE

Hiroshi Akino, assignor to Kabushiki Kaisha Audio Technica
14 November 2000 (Class 381/356); filed in Japan 10 July 1998

Relatively small, self-contained boundary microphones are commonly used for voice pickup in situations where microphones must be inconspicuous. This invention goes one step farther. It is a clever method for flush-mounting a tiny microphone, yet maintaining a unidirectional pickup pattern.—GLA

6,167,139

43.38.Lc APPARATUS AND METHOD FOR CONTROLLING SOUND FOR AUDIO/VIDEO APPLIANCE

Mun Seob Kim, assignor to LG Electronics, Incorporated
26 December 2000 (Class 381/102); filed in Republic of Korea 11 December 1996

This patent describes a control system for adjusting the volume and tone controls of an audio sound system. Although not specifically so stated, the intended application would be for audio and television remote controls. The novel aspect of this system is that the tone control is automatically compensated according to the volume control setting. If the tone control is changed, then that new tone setting will track across various volume levels to obtain an approximately uniform perception of the tone balance.—DLR

6,137,883

43.38.Si TELEPHONE SET HAVING A MICROPHONE FOR RECEIVING AN ACOUSTIC SIGNAL VIA KEYPAD

Kevin D. Kaschke and David L. Bond, assignors to Motorola, Incorporated
24 October 2000 (Class 379/433); filed 30 May 1998

A retractable-extendable acoustical element **18** is built into the housing **12** of a telephone set. The acoustical element retracts into the keypad housing when not in use. This feature allows the apparatus to have a smaller overall size than conventional telephones when the acoustical element (e.g., microphone) is retracted.—IMH

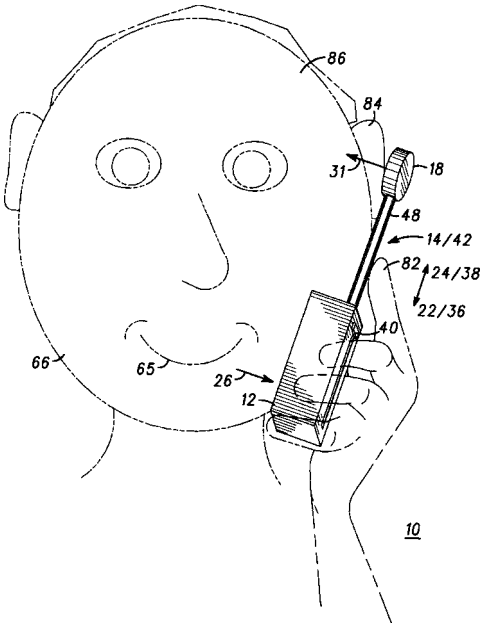

6,138,512

43.40.Le METHOD AND APPARATUS FOR DETERMINING SOURCE LOCATION OF ENERGY CARRIED IN THE FORM OF PROPAGATING WAVES THROUGH A CONDUCTING MEDIUM

Ronald A. Roberts *et al.*, assignors to Iowa State University Research Foundation, Incorporated
31 October 2000 (Class 73/570); filed 29 July 1998

The method discussed in this patent is stated to be particularly applicable to the location of acoustic emission sources in one-dimensional and two-dimensional dispersive acoustic media. The signal resulting from a source is sensed at a number of points simultaneously and recorded. Modes of propagation are isolated by spatial and temporal Fourier transformation of the recorded signals. Generalized cross correlation is applied to these signals to locate the source.—EEU

5,939,179

43.40.Tm CONSTRAINT TYPE VIBRATION DAMPING MATERIAL

Kunihiko Yano *et al.*, assignors to Nichias Corporation
17 August 1999 (Class 428/212); filed in Japan 29 March 1995

Constrained-layer viscoelastic damping configurations, particularly for use as shims in brakes in order to prevent brake squeal, are made by coating a rubber layer on a metal base plate and depositing a hard thermosetting plastic atop the rubber layer. Constrained-layer damping has been well known for at least four decades, but the technology described in this patent is claimed to be inexpensive and effective.—EEU

5,983,722

43.40.Yq PIEZOBLOC ACCELEROMETER

Thomas Berther *et al.*, assignors to K. K. Holding AG
16 November 1999 (Class 73/514.34); filed 12 November 1997

A piezoceramic bender element **4** is housed within two solid ceramic blocks **2** and **3**. The bender is clamped at its left-hand end in this figure. A gap of indicated clearance dimension **7** has been machined out of blocks **2** and **3**. Dimension **7** is chosen to prevent breakage of the bender by snubbing its motion should the unit experience harsh shock excitation. Signal wires **9** are connected to the two piezoceramic bender plates either by solder or conductive epoxy. The slot **8**, within which the electrical connections are made, is subsequently filled with a castable sealing material. This unit is designed to be responsive to vibratory inputs oriented along the *Z* direction of the figure. The units may be rotated relative to one another and stacked in such a manner as to produce a composite structure which is responsive to vibratory inputs along three mutually orthogonal directions.—WT

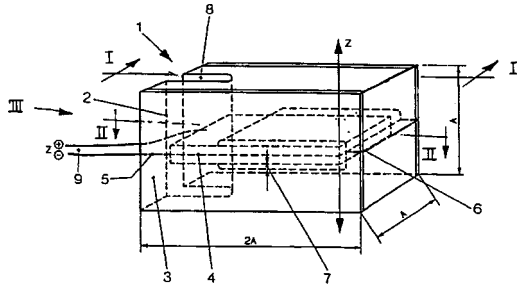

6,155,224

43.50.Gf NOISE SILENCER FOR VEHICLE ENGINE INTAKE SYSTEM

Hiroki Akihisa *et al.*, assignors to Denso Corporation
5 December 2000 (Class 123/184.57); filed in Japan 18 August 1998

An intake silencer for an automobile engine is described which consists of two resonators. Low frequency noise, below about 200 Hz, is attenuated by resonator **17**, which has a valve **20** at its entrance. Positive sound pressure opens the valve, thus enabling the operation of the resonator which is connected to ambient pressure via pipe **18**. This valve arrangement

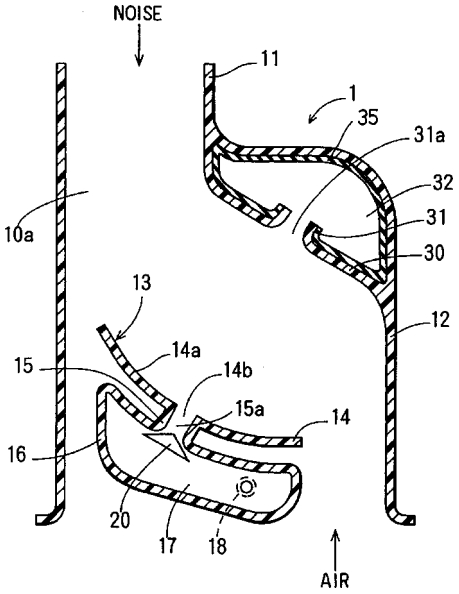

is said to provide greater bandwidth of attenuation than a conventional Helmholtz resonator. The face of this resonator, **14**, has a parabolic shape, the focus of which is at the entrance to the second resonator, **32**, which is designed to attenuate high frequency noise above about 200 Hz.—KPS

6,155,225

43.50.Gf VEHICLE ENGINE INTAKE MUFFLER

Takehiro Suzuki, assignor to Suzuki Motor Corporation
5 December 2000 (Class 123/184.57); filed in Japan 8 October 1998

The patent describes an arrangement of resonators for use in automobile engine inlet systems. In contrast to conventional designs having two resonators, a third resonator is introduced which is designed to attenuate sounds at intermediate frequencies. This additional resonator is designed to fit within the front wheel fender of the vehicle and, for that reason, has a ''bent back'' shape. Details of manufacture and construction are provided which are aimed at ease of assembly.—KPS

6,160,892

43.50.Gf ACTIVE MUFFLER

Istvan L. Ver, assignor to BBN Corporation
12 December 2000 (Class 381/71.5); filed 30 December 1993

An active noise control system designed for use in jet engine test cell exhaust silencers (''hush houses'') is aimed at attenuating the low frequencies which are ineffectively treated by conventional, passive means. Loudspeakers, **45**, are mounted around the circumference of exhaust duct **17**, and are behind an acoustically resistive layer **31**. The resistance of this layer is substantially less than the characteristic acoustic impedance of the gas in the

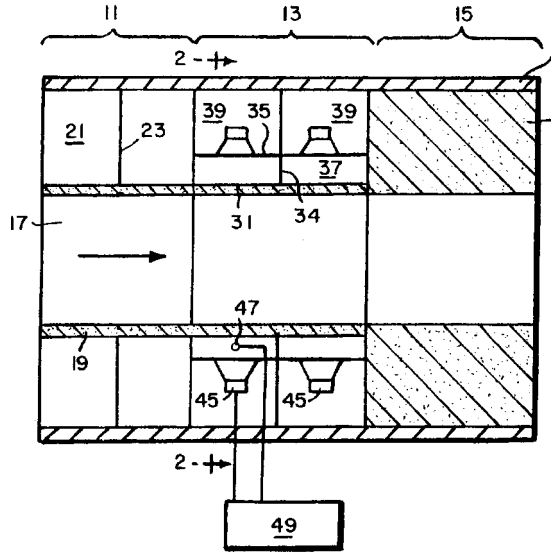

duct (e.g., 0.2 ρc). Microphones, **47**, are placed in front of the loudspeakers, and provide signals to a feedback control system which seeks to minimize the sound pressures at the microphones. This reduces the impedance of the volume in front of the loudspeakers, thus increasing the effectiveness of the resistive layer.—KPS

6,164,058

43.50.Gf ARRANGEMENT FOR DAMPING COMBUSTION-CHAMBER OSCILLATIONS

Klaus Dobbeling *et al.*, assignors to ABB Research Limited
26 December 2000 (Class 60/39.36); filed in European Patent Office 15 July 1997

A method to suppress thermoacoustic oscillations in the annular combustion chamber of a gas turbine is described. The air cooling ducts are tuned to the fundamental resonance frequency of the combustion chamber by careful selection of their lengths. In contrast to using Helmholtz resonators, these half-wavelength resonators will also suppress higher order modes. Geometrical details are provided.—KPS

6,170,265

43.50.Gf METHOD AND DEVICE FOR MINIMIZING THERMOACOUSTIC VIBRATIONS IN GAS-TURBINE COMBUSTION CHAMBERS

Wolfgang Polifke *et al.*, assignors to ABB Search Limited
9 January 2001 (Class 60/725); filed in European Patent Office 15 July 1997

A method to suppress thermoacoustic oscillations in the combustion chamber of a gas turbine is described. The fuel enters at **14** and is mixed with air in chamber **12** before combustion occurs in chamber **16**. Lengths $\mathbf{L_{mix}}$ and $\mathbf{L_{BK}}$ are selected such that fluctuations in the gas velocity at the

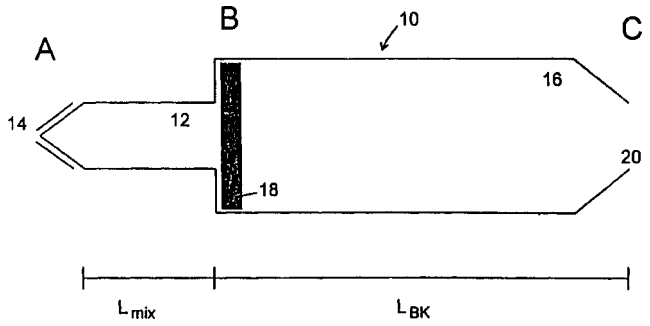

location of the fuel injection induce pressure fluctuations at the combustion chamber outlet **20** which are out of phase with pressure fluctuations occurring in the combustion chamber. Design guidance on the selection of values of the key parameters are provided along with numerical examples.—KPS

6,151,954

43.50.Lj DEVICE FOR DETECTING KNOCKING IN AN INTERNAL COMBUSTION ENGINE

Keiichiro Aoki and Yoichi Kurebayashi, assignors to Toyota Jidosha Kabushiki Kaisha; Denso Corporation
28 November 2000 (Class 73/35.08); filed in Japan 3 September 1996

This patent describes a scheme for detecting knocking in an internal combustion engine which relies on measurement of ions generated during the combustion process. An ionic current detection unit is connected to the ignition coil, in parallel with the spark plugs. The circuitry of this detection unit is designed to isolate knocking from other noise components.—KPS

6,132,005

43.50.Yw DETECTING SEAM BOUNDARY USING PICK SOUND

John Gordon Mazlin *et al.*, assignors to Tangential Technologies PTY
17 October 2000 (Class 299/1.1); filed in Australia 14 November 1995

This patent relates to a means for distinguishing a boundary between layers of different materials encountered in mining. As picks (cutting elements shaped somewhat like canine teeth) on mining machines scrape along surfaces to dislodge chunks of material, these generate noise, claimed to occur primarily at resonance frequencies of the picks. A system according to this patent uses a microphone near the cutting head to sense the airborne noise generated during cutting, determines the corresponding spectra, and compares them to predetermined spectra.—EEU

6,134,968

43.58.Bh PORTABLE ACOUSTIC IMPEDANCE MEASUREMENT SYSTEM

Robert K. Kunze, Jr. *et al.*, assignors to The Boeing Company
24 October 2000 (Class 73/589); filed 19 July 1999

A cylindrical wave guide tube has a compression driver attached to one end and a second end that is open. The open end can be placed against the surface whose impedance is to be measured and is provided with an annular gasket to ensure an adequate seal. A fitting in the side of the tube has access ports through which microphones can be inserted. An end cap can be mounted on the open end of the tube for calibration purposes.—EEU

6,172,940

43.58.Fm TWO GEOPHONE UNDERWATER ACOUSTIC INTENSITY PROBE

James A. McConnell *et al.*, assignors to the United States of America as represented by the Secretary of the Navy
9 January 2001 (Class 367/178); filed 27 January 1999

An acoustic intensity probe comprises two identical, collinear geophones supported by means of springs, which are stiff in the radial direction to keep the geophones aligned. The springs are quite compliant in the axial direction to allow motion in that direction within an acoustically transparent and neutrally buoyant housing. Because the geophones have inherently low electrical impedance outputs, they can be connected to the associated signal analyzing electronics via relatively long cables without the need for intervening preamplifiers. While each geophone individually provides a measurement of the acoustic particle velocity, the spatial gradient of the velocity between the two separated geophones is a measure of the acoustic pressure. This is in contrast to most intensity probes wherein two pressure sensors are used and the spatial gradient of the pressure is a measure of the particle velocity.—WT

6,170,333

43.58.Kr APPARATUS FOR DETECTING ABNORMAL SOUND AND METHOD FOR JUDGING WRONG IN MACHINE

Michihiro Jinnai *et al.*, assignors to Entropy Software Laboratory, Incorporated
9 January 2001 (Class 73/570); filed in Japan 14 March 1997

This device listens to a machine and compares the sound with past emissions to determine whether the machine is operating properly. A coarse spectrum analysis is performed using, perhaps, 6 or 7 channels. Second- and third-order statistics are computed for the band amplitude values. These vectors of spectral statistics are compared to stored reference patterns collected during proper machine operation.—DLR

6,173,074

43.58.Kr ACOUSTIC SIGNATURE RECOGNITION AND IDENTIFICATION

Anthony Peter Russo, assignor to Lucent Technologies, Incorporated
9 January 2001 (Class 382/190); filed 30 September 1997

This spectrum analysis device processes the audio signature from a piece of machinery in order to determine what state the machine is in, whether it is operating correctly, and, in some cases, to determine what type of machine is running. Operating on a Fourier transform (FFT) of the audio signal, the device performs a feature analysis, primarily intended to track any detectable harmonic structure. Correlations are detected along any of eight directions in the time/frequency plane. A ''blob coloring'' algorithm is then used to mark groups of adjacent active pixels.—DLR

6,161,434

43.60.Rw METHOD AND DEVICE FOR DETECTING AND LOCATING A REFLECTING SOUND SOURCE

Mathias Fink, Meudon, France and Jacques Lewiner, Saint-Cloud, France
19 December 2000 (Class 73/587); filed in France 13 June 1996

The subject of this patent is applicable to detection and localization of acoustic emissions in solid objects and to finding the locations of reflective underwater targets. It is claimed to be suitable for detection of a sound source in a noisy medium and/or of one exhibiting reflections and multiple refractions that defeat other methods. Electrical signals obtained from an array of receiving transducers are stored, time-reversed, and amplified to produce excitation signals. The latter are applied to emission transducers that have substantially the same locations as the receiving transducers. The signals received when the emission transducers are actuated are again stored and processed to detect the possible presence of a source.—EEU

6,169,813

43.66.Ts FREQUENCY TRANSPOSITIONAL HEARING AID WITH SINGLE SIDEBAND MODULATION

Charles S. Richardson and Arnold S. Lippa, assignors to Hearing Innovations, Incorporated
2 January 2001 (Class 381/312); filed 16 March 1994

An audio frequency signal amplitude modulates an ultrasonic carrier and the resultant is used for bone conduction transmission to the human sensory system. Single sideband modulation is said to be used to achieve better performance than the double sideband modulation technique described in previous implementations.—DAP

6,173,063

43.66.Ts OUTPUT REGULATOR FOR FEEDBACK REDUCTION IN HEARING AIDS

John Laurence Melanson, assignor to GN ReSound as
9 January 2001 (Class 381/318); filed 6 October 1998

A regulator stabilizes the supply voltage for the output stage of a hearing aid containing a feedback canceling mechanism. The voltage regulator helps keep the gain of the output stage constant in the presence of

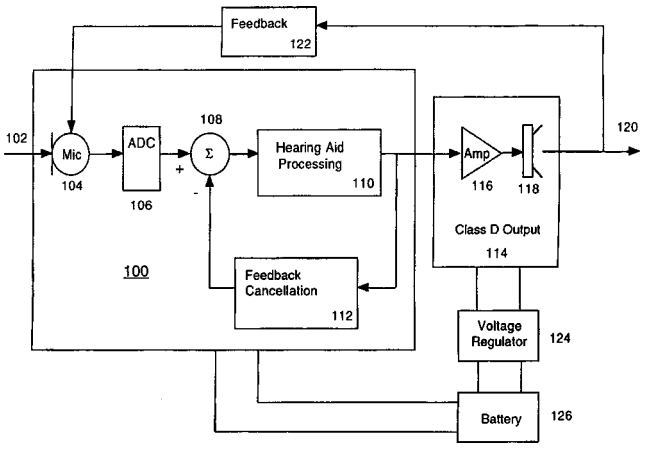

battery voltage variation, thus allowing the feedback path to be modeled more accurately by the feedback cancellation algorithm.—DAP

6,167,373

43.72.Ar LINEAR PREDICTION COEFFICIENT ANALYZING APPARATUS FOR THE AUTOCORRELATION FUNCTION OF A DIGITAL SPEECH SIGNAL

Toshiyuki Morii, assignor to Matsushita Electric Industrial Company, Limited
26 December 2000 (Class 704/219); filed in Japan 19 December 1994

This patent covers a variety of speech analysis techniques applicable to speech coding, such as would be used in a cell phone. The main two of these techniques are the use of multiple analyzer methods and a short windowing technique which reduces the delay in recovering speech spectral data. The different analyzer methods generally all fall within the realm of code-excited

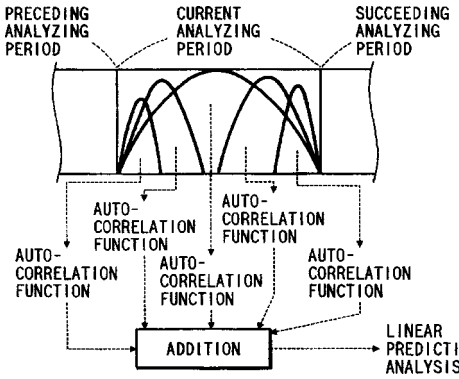

LPC, but use different tradeoffs in the selection of subframe and codebook structures and differing assignment of bits to various parts of the signal. In the short window technique, a kind of weighted autocorrelation correction is applied to partial windows, as shown in the figure, to produce quick estimates of the LPC spectral data, such as during affricate consonants.—DLR

6,167,374

43.72.Gy SIGNAL PROCESSING METHOD AND SYSTEM UTILIZING LOGICAL SPEECH BOUNDARIES

Shmuel Shaffer *et al.*, assignors to Siemens Information and Communication Networks, Incorporated
26 December 2000 (Class 704/227); filed 13 February 1997

This speech encoding system attempts to separate the input speech stream into logical units, in most cases, words. Each logical unit is transmitted as a single packet, said to allow better recovery in the case of transmission errors. The argument is that if an entire word is lost, rather than word fragments, the person at the receiving end is more likely to be aware of the reception problem and ask for clarification, if necessary, thus decreasing the chance of a misunderstood message.—DLR

6,173,250

43.72.Gy APPARATUS AND METHOD FOR SPEECH–TEXT–TRANSMIT COMMUNICATION OVER DATA NETWORKS

Kenneth Jong, assignor to AT&T Corporation
9 January 2001 (Class 704/3); filed 3 June 1998

This patent appears to be little more than an attempt to cover a large domain of previously well-known technologies. Voice communication in a network chat room situation would be provided by using a recognizer, transmitting the text, and optionally using a synthesizer at the receiving end. Overlapping a number of patents covering the ''phoneme vocoder'' techniques, the patent presents nothing new.—DLR

6,173,256

43.72.Gy METHOD AND APPARATUS FOR AUDIO REPRESENTATION OF SPEECH THAT HAS BEEN ENCODED ACCORDING TO THE LPC PRINCIPLE, THROUGH ADDING NOISE TO CONSTITUENT SIGNALS THEREIN

Ercan F. Gigi, assignor to U.S. Philips Corporation
9 January 2001 (Class 704/219); filed in European Patent Office 31 October 1997

This speech vocoder represents an attempt to revive the methods of basic linear predictive coding by addressing the issue of buzziness in the speech output. The method consists of adding more noise into the output to

mask the buzz. In the initial analysis, voiced and unvoiced regions are treated separately with respect to both the filter coefficients and the gain value. Formant peak and valley amplitudes and the measured pitch are used in various ways to compute four separate measures of noise, called the ''noise scaling'' factors. Scaled noise is reintroduced into the voiced regions using any of several methods.—DLR

6,172,641

43.72.Ja NAVIGATION SYSTEM WITH AUDIBLE ROUTE GUIDANCE INSTRUCTIONS

Jeffrey Alan Millington, assignor to Magellan DIS, Incorporated
9 January 2001 (Class 342/357.13); filed 9 April 1998

This vehicle navigation system is tied into the loudspeakers of the car's radio or CD player to provide audible announcements of the selected route and the general status of the journey. For maximum effect, the system assumes a four-speaker arrangement. Rather than a true HRTF-based three-dimensional sound field, the system merely controls the volume to the individual speakers to simulate various positions of the announcer. The patent is

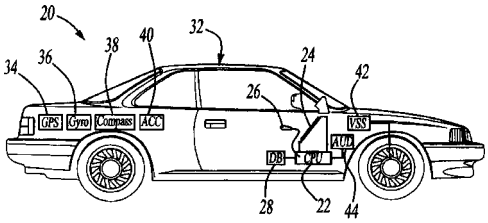

not entirely clear on what situations would be most effectively presented by changing the apparent sound direction, but one can imagine an upcoming turn being announced with increasing loudness in the right front, and then as you miss the turn, the announcement slowly fades out in the right rear.—DLR

6,167,371

43.72.Kb SPEECH FILTER FOR DIGITAL ELECTRONIC COMMUNICATIONS

Gilles Miet and Daniela Parayre-Mitzova, assignors to U.S. Philips Corporation
26 December 2000 (Class 704/205); filed in France 22 September 1998

The idea of enhancing the intelligibility of a speech signal by reducing the bandwidths of the poles is an old one, going back at least to the 1970s. This system adds to that the idea of inserting zeroes in between adjacent poles. Zero positions are computed as weighted averages of the pairs of

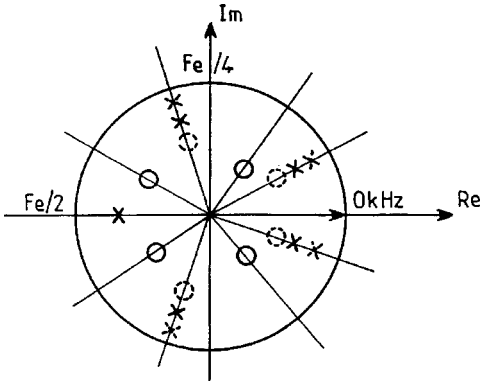

neighboring poles, however, there is no detailed treatment of what the values of the weights should be. One embodiment of the device involves the use of LPC parameters, pole positions in particular, extracted from the input during the normal operation of a standard cell phone coding system.—DLR

6,169,555

43.72.Kb SYSTEM AND METHODS FOR COMMUNICATING THROUGH COMPUTER ANIMATED IMAGES

Minoru Yamamoto, assignor to Image Link Company, Limited
2 January 2001 (Class 345/473); filed 23 April 1996

This patent describes a system for controlling the display of an animated puppet in real-time response to speech input, typically from a remote-location. The animation would be able to wave from side to side, wiggle its ears, tap its toes, and various other such contortions, in the interest of con-

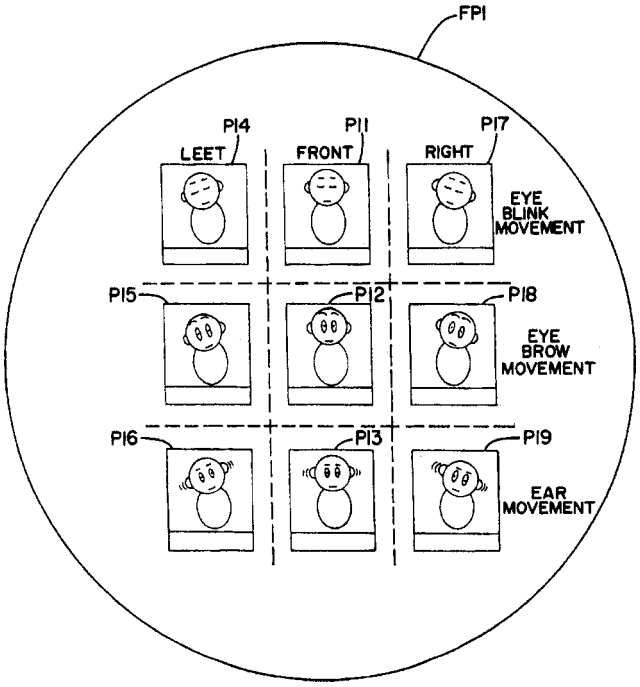

veying certain states of mind of the talker. And meanwhile, the puppet would also talk, displaying lip and jaw movements appropriate for the speech signal.—DLR

6,167,117

43.72.Ne VOICE-DIALING SYSTEM USING MODEL OF CALLING BEHAVIOR

Craig A. Will, assignor to Nortel Networks Limited
26 December 2000 (Class 379/88.03); filed 7 October 1996

Previous patents covering voice dialing have described the use of statistics about the calling party to help in the recognition of the name of the party to be called. Such information usually includes calling patterns, such as the time of day, the day of the week, duration of the call, and whether the call was answered. This patent covers the use of a neural network to do the actual computation. The usefulness of the system as a personal directory assistant is also described.—DLR

6,167,376

43.72.Ne COMPUTER SYSTEM WITH INTEGRATED TELEPHONY, HANDWRITING AND SPEECH RECOGNITION FEATURES

Richard Joseph Ditzik, Bonita, California
26 December 2000 (Class 704/235); filed 21 December 1998

This personal computer assistant includes a number of human interface capabilities, including speech and handwriting recognition, which can run simultaneously and interactively. The speech recognizer includes both a speaker dependent mode, tuned to the user, and a speaker independent mode, for incoming speech, such as by telephone. The pen may be used online to correct recognition errors in real time. The pen controls are designed so as to anticipate possible poor performance of the recognition of live telephone speech.—DLR

6,167,377

43.72.Ne SPEECH RECOGNITION LANGUAGE MODELS

Laurence S. Gillick *et al.*, assignors to Dragon Systems, Incorporated
26 December 2000 (Class 704/240); filed 28 March 1997

This is a method to be used by a speech recognition system to take advantage of the best of recognition results obtained with a variety of language models. Various recognizers may use models based on *n*-gram statistics, categories, topics, or most recent utterances. In the method described here, word candidates are found by using several such models. The lists of such candidates are combined by applying a weighting for each model. A special case for the topic model allows the user to specify lists of new words which should be included in the model.—DLR

6,173,076

43.72.Ne SPEECH RECOGNITION PATTERN ADAPTATION SYSTEM USING TREE SCHEME

Koichi Shinoda, assignor to NEC Corporation
9 January 2001 (Class 382/226); filed in Japan 2 March 1995

This speech recognition system is based on a typical application of hidden Markov models (HMMs) to store the reference patterns. Each HMM state is a mixture of Gaussian distributions, in the usual manner. In addition, a tree structure is produced which represents the history or makeup of the

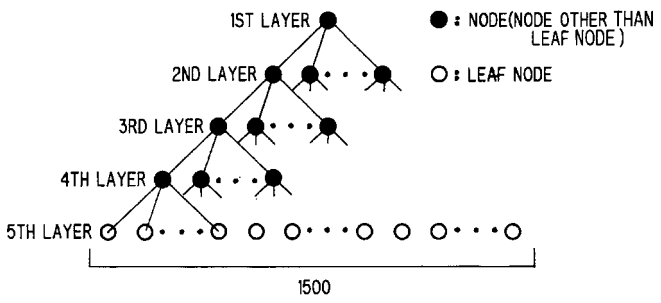

Gaussian means of each HMM state, including the number of training examples used for each distribution. Using the tree structure to decide how much to adapt each of the mean values, it is possible to perform a high-quality adaptation to a new speaker based on a relatively small sample of speech from that person.—DLR

6,173,192

43.72.Ne INTERACTIVE VOICE RESPONSIVE RADIO TUNING SYSTEM

Larry K. Clark, assignor to Honeywell International, Incorporated
9 January 2001 (Class 455/563); filed 1 October 1996

In this application, a speech recognition system would be used by a pilot to state the name of a radio contact point, for example, to change the radio frequency to that of a different control tower. Upon recognizing the name of a radio contact center, the device would verbally request a confirmation, and then directly change the radio channel setting. Stored data about nearby contact points would be used to weight the recognition candidates, reducing confusion between similar sounding location names.—DLR

6,173,251

43.72.Ne KEYWORD EXTRACTION APPARATUS, KEYWORD EXTRACTION METHOD, AND COMPUTER READABLE RECORDING MEDIUM STORING KEYWORD EXTRACTION PROGRAM

Takahiro Ito *et al.*, assignors to Mitsubishi Denki Kabushiki Kaisha
9 January 2001 (Class 704/7); filed in Japan 5 August 1997

This keyword spotting system stores a variety of technically equivalent expressions for each desired keyword. Occurrences in the target speech of any of the stored expressions are detected and related to the meaning of the corresponding keyword set. Although described in terms of Japanese char-

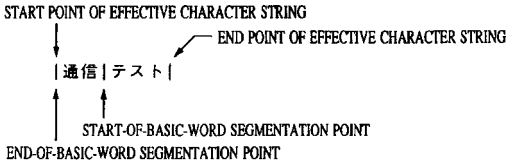

acters, some of the claims seem to present the ideas in a language-independent manner. However, since these claims use the term ''character,'' it is not clear to what extent such language independence is actually achieved.—DLR

6,173,258

43.72.Ne METHOD FOR REDUCING NOISE DISTORTIONS IN A SPEECH RECOGNITION SYSTEM

Xavier Menendez-Pidal *et al.*, assignors to Sony Corporation; Sony Electronics, Incorporated
9 January 2001 (Class 704/233); filed 9 September 1998

This speech recognizer uses a type of cepstral normalization to reduce the effect of noise in the input signal on recognition performance. An FFT spectrum is processed to produce controls for a spectral subtractor. The spectrally subtracted speech is then passed to a filter bank, a log compressor, a normalizer, to two cosine transforms, and finally to the recognizer system.

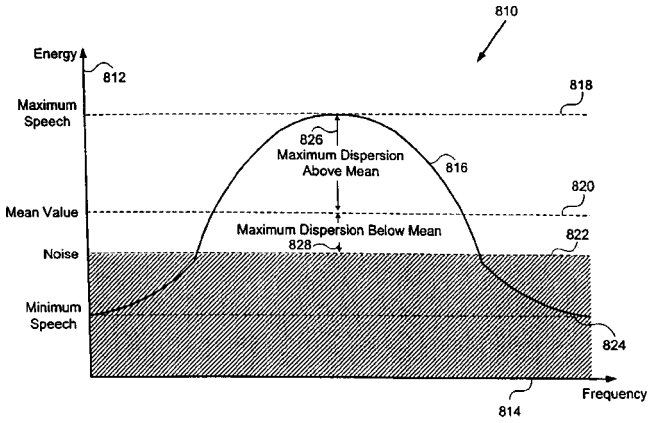

The normalizer operates on delta and delta features using mean values and left and right variances. These features are included with the acoustic vectors in the recognizer inputs.—DLR

5,977,866

43.80.Nd BIRD DISPERSING SYSTEM

John Barthell Joseph, Jr., Greenville, Mississippi and Q. Martin Schoenheiter, Jr., Salt Lake City, Utah

2 November 1999 (Class 340/384.1); filed 29 January 1998

A system for dispersing birds away from an airfield consists of a central computer unit, an antenna system, a hand held transmitter, and a number of remotely located gas cannons, each connected to a single control unit. Upon command, each cannon produces a loud explosion fueled by gas from a pressurized storage tank housed on the cannon unit. Each cannon unit also houses all-weather loudspeakers which radiate, upon command, an endless recording of loud noises such as barking dogs or sirens. All time sequencing of the sounds is regulated by the computer unit which can be controlled either locally or remotely via the hand held transmitter.—WT

Finite-element method to study harmonic aeroacoustics problems

C. Peyret[a] and G. Élias
ONERA/DSNA, B.P. 72, 92320 Châtillon, France

(Received 22 September 1999; revised 17 March 2001; accepted 12 April 2001)

The analysis of aeroacoustics propagation is required to solve many practical problems. As an alternative to Euler's linearized equations, an equation was established by Galbrun in 1931. It assumes the flow verifies Euler's equations and the perturbation is small and adiabatic. It is a linear second-order vectorial equation based on the displacement. Galbrun's equation derives from a Lagrangian density and provides conservative expressions of the aeroacoustics intensity and energy density. A (CAA) method dealing with the numerical resolution of Galbrun's equation using the finite-element method (FEM) is presented. The exact solution for the propagation of acoustic modes inside an axisymmetric straight-lined duct in the presence of a shear flow is known and compared with the FEM solution. Comparisons are found to be in good agreement and validate a first step in the development of a CAA method based on the FEM and Galbrun's equation. The FEM is then applied to an axisymmetric duct including a varying cross section and a nonuniform flow with respect to both the axial and the radial coordinates. The expression of the aeroacoustics intensity implemented in the FEM provides an accurate in-duct power balance. © *2001 Acoustical Society of America.* [DOI: 10.1121/1.1378355]

PACS numbers: 43.20.Bi, 43.20.Mv, 43.28.Py [LCS]

LIST OF SYMBOLS

a_0	celerity of sound
$\boldsymbol{b}(\boldsymbol{\xi})$	connecting vector
$\boldsymbol{G}(\boldsymbol{\xi})$	Galbrun's equation
$\boldsymbol{i}$	acoustic intensity ($\mathrm{W\,m^{-2}}$)
k	wave number
k_z	longitudinal wave number
Λ	Galbrun's equation Lagrangian density
M	Mach number
$\boldsymbol{n}$	normal vector
p_0	static pressure
p	acoustic pressure
$\boldsymbol{v}_0$	flow velocity
$\boldsymbol{v}$	acoustic velocity
R	duct radius
r	radial axis
z	longitudinal axis
Z	locally reacting reduced impedance
δ	boundary layer thickness
$\boldsymbol{\xi}$	acoustic displacement vector
$\boldsymbol{\eta}$	vectorial test function
$\overline{\boldsymbol{\eta}}$	complex conjugate of $\boldsymbol{\eta}$
${}^{\mathrm{T}}\boldsymbol{\xi}$	transposed acoustic displacement vector
Π	acoustic power ($\mathrm{J\,m^{-2}}$)
ρ_0	static density
ρ	acoustic density
ω	pulsation
$\boldsymbol{\nabla}\cdot$	divergence operator
$\boldsymbol{\nabla}$	gradient operator
$\boldsymbol{\nabla}\times$	curl operator

I. INTRODUCTION

Many aeroacoustics problems, such as diffraction, jet noise, duct acoustics, liner design, etc., require the prediction of sound propagation in a nonuniform flow. From a theoretical point of view, one difficulty arises from the unsuccessful attempt to establish a general propagation equation governing the pressure field, or some scalar parameter related to it. In particular, if the mean flow is rotational, the decomposition of the perturbations in terms of independent acoustic, rotational, and entropic modes, as initiated by Chu and Kovasznay[1] in the late 1950s in the uniform flow case, is no longer valid. In the early 1970s, a third-order partial differential equation for the pressure was established by Lilley[2] and others, assuming a parallel sheared flow and a uniform static pressure. Because the attempts to relax these assumptions have failed, present studies in CAA are orientated to the resolution of the full Euler's linearized equations. This task can be achieved solving the system as it stands. However, an alternative is presented here using the displacement as a unique parameter. In the early 1930s, assuming small adiabatic perturbations and Eulerian flows, Galbrun[3] established a reformulation of Euler's linearized equations based on the displacement. Galbrun's equation is a second-order linear partial differential equation (see, also, Ref. 4).

The finite-element method[5–8] and Galbrun's equation may be an attractive alternative to the finite-difference method and Euler's linearized equations.[9–11] Galbrun's equation is based on displacement. Although displacement is an appropriate variable to represent both acoustics and rotational modes and to deal with the boundary conditions in the

[a]Electronic mail: peyret@onera.fr

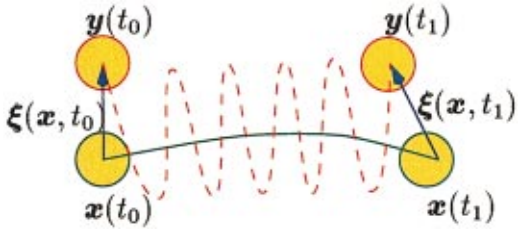

FIG. 1. Displacement vector, $\boldsymbol{x}(t)$ is solid line and $\boldsymbol{y}(t)$ is dashed line.

presence of flow (at any interface, the continuity of the pressure and the normal component of the displacement is required), only a few works deal with Galbrun's equation. The likely reason is that displacement is not a usual variable for the acoustics community. In 1985, Poiré[12] used Galbrun's equation and detailed a so-called mixed representation based on Eulerian and Lagrangian perturbations of the flow for linear and nonlinear problems. More recently, Godin[13] took into account structure displacement to express the boundary condition at the interface of free, rigid, and absorbing surfaces for hydroacoustics problems with displacement vectors. Ben Tahar and Goy[14] also proposed a variational formulation based on the displacement and Galbrun's equation to solve vibroacoustic problems in the presence of flow, with appropriate boundary conditions at the interfaces. Also, Galbrun's equation is associated with Lagrangian density. As an immediate consequence, conservative expressions of aeroacoustics energy density and intensity were established for Eulerian stationary flows.

Our main objective is to demonstrate the interest and capabilities of the finite-element method (FEM) and Galbrun's equation. A first application for analyzing in-duct sound propagation[15] here is realized. The theoretical background of Galbrun's equation, weak formulation, and Lagrangian density are summarized in Sec. II. Section III describes the implementation of the FEM. Comparisons between Galbrun and Lilley's solutions for the propagation in a lined straight duct are given in Sec. IV. Finally, the application of the FEM to a lined duct with a varying cross section, in the presence of parallel shear flow, is considered in Sec. V.

II. PROBLEM FORMULATION

This section briefly presents the theoretical formulation of Galbrun's equation. The main results involved in the FEM implementation are discussed. It first recalls the definition of the displacement vector and gives Galbrun's equation expression, a weak formulation, a Lagrangian density, and aeroacoustics intensity expressed with the displacement. This section can help the reader not familiar with this formulation, but does not aim at providing demonstrations of the algebraic formula. More details can be found in Refs. 1, 3, 12, and 13.

A. Acoustic displacement

Consider an infinitesimal fluid element inside a flow: between times t_0 and t_1, the element follows the path $\boldsymbol{x}(t)$ resulting from the flow convection (solid line in Fig. 1). Now, reconsider the fluid element, inside the flow at the same time and suppose the presence of a disturbance: the element follows path $\boldsymbol{y}(t)$ resulting from flow convection and displacement caused by the disturbance (dashed line in Fig. 1). The displacement vector is defined as

$$\boldsymbol{\xi}(\boldsymbol{x},t)=\boldsymbol{y}(t)-\boldsymbol{x}(t).$$

The so-called mixed representation of aeroacoustics, developed by Poirée[12] in 1985, uses the displacement vector to distinguish the aeroacoustics perturbation (acoustic mode: $\boldsymbol{\nabla}\cdot\boldsymbol{\xi}$ plus rotational mode: $\boldsymbol{\nabla}\times\boldsymbol{\xi}$) inside the aerodynamic airflow. By separating perturbation and aerodynamics, one can describe two different phenomena (flow and aeroacoustics propagation).

B. Galbrun's equation

Usually, the flow $(p_0,\rho_0,\boldsymbol{v}_0)$ and the perturbation $(p,\rho,\boldsymbol{v})$ are described with Euler's variables. In the case of a small adiabatic perturbation ($p\ll p_0$, $\rho\ll\rho_0$, and $v\ll a_0$), Poirée shows that the usual Eulerian variables, namely, the acoustic pressure, density, and velocity, are related to the displacement:

$$p=-\rho_0 a_0\,\boldsymbol{\nabla}\cdot\boldsymbol{\xi}-\boldsymbol{\xi}\cdot\boldsymbol{\nabla}p_0,\quad \rho=-\rho_0\,\boldsymbol{\nabla}\cdot\boldsymbol{\xi}-\boldsymbol{\xi}\cdot\boldsymbol{\nabla}\rho_0,$$
$$\boldsymbol{v}=\frac{d\boldsymbol{\xi}}{dt}-\boldsymbol{\xi}\cdot\boldsymbol{\nabla}\boldsymbol{v}_0, \tag{2.1}$$

where $dU/dt=\partial U/\partial t+(\boldsymbol{v}_0\cdot\boldsymbol{\nabla})U$ is the total time derivative referred to the unperturbed flow $\boldsymbol{v}_0$. In practice, these relations show that when computing the displacement field, it is possible to return to the standard Eulerian pressure, velocity, or density. Starting from Euler's linearized equations, using the Lagrangian displacement and assuming acoustic propagation is isentropic (i.e., $ds=0$ in the Lagrangian system), the reformulation of Euler's linearized equations leads to Galbrun's equation:

$$\boldsymbol{G}(\boldsymbol{\xi})=\rho_0\frac{d^2\boldsymbol{\xi}}{dt^2}-\boldsymbol{\nabla}(\rho_0 a_0^2\boldsymbol{\nabla}\cdot\boldsymbol{\xi})+(\boldsymbol{\nabla}\cdot\boldsymbol{\xi})\boldsymbol{\nabla}p_0-{}^{\mathrm{T}}\boldsymbol{\nabla}\boldsymbol{\xi}\cdot\boldsymbol{\nabla}p_0=\mathbf{0}. \tag{2.2}$$

Galbrun's equation is an aeroacoustic propagation equation, based on the single displacement variable. As mentioned by Poirée,[16] using both the relations, Eq. (2.1), and Galbrun's equation, Eq. (2.2), some works attempted[17,18] here to establish a wave equation based on a single variable $(p,\rho,\boldsymbol{v})$, but the authors failed because algebraic expressions are too complex. Obviously, assuming an homogeneous medium, the Helmholtz equation is directly retrieved.

C. Weak formulation

Consider a three-dimensional finite-volume V_0 whose envelope is S_0 and $\boldsymbol{n}$ is the outside normal vector to S_0. There is no acoustic source inside the fluid so $\boldsymbol{G}(\boldsymbol{\xi})=\mathbf{0}$ and we are searching $\boldsymbol{\xi}\in\mathbf{H}(\mathrm{grad};V_0)$, so that

$$\left\{\forall\,\boldsymbol{\eta}\in\mathbf{H}(\mathrm{grad};V_0);\quad \int_{-\infty}^{\infty}\int_{V_0}\boldsymbol{G}(\boldsymbol{\xi})\cdot\boldsymbol{\eta}\,dV dt=0\right\},$$

where the functional space $\mathbf{H}(\mathrm{grad};V_0)$ is defined in Sec. III A. Integrating by parts gives

$$\Big\{\forall\,\eta\in\mathbf{H}(\mathrm{grad};V_0);$$

$$\int_{-\infty}^{\infty}\left(\int_{V_0}B_V(\boldsymbol{\xi},\boldsymbol{\eta})dV+\oint_{S_0}\boldsymbol{b}(\boldsymbol{\xi})\cdot\boldsymbol{\eta}\,dS\right)dt=0. \tag{2.3}$$

The bilinear form $B_V(\boldsymbol{\xi},\boldsymbol{\eta})$ reads

$$B_V(\boldsymbol{\xi},\boldsymbol{\eta})=\rho_0\frac{d\boldsymbol{\xi}}{dt}\cdot\frac{d\boldsymbol{\eta}}{dt}-\rho_0a_0^2\boldsymbol{\nabla}\cdot\boldsymbol{\xi}\,\boldsymbol{\nabla}\cdot\boldsymbol{\eta}-(\boldsymbol{\xi}\cdot\boldsymbol{\nabla}p_0)\boldsymbol{\nabla}\cdot\boldsymbol{\eta}$$
$$-(\boldsymbol{\eta}\cdot\boldsymbol{\nabla}p_0)\boldsymbol{\nabla}\cdot\boldsymbol{\xi}-\tfrac{1}{2}\,{}^{\mathrm{T}}\boldsymbol{\xi}\boldsymbol{\nabla}^2p_0\boldsymbol{\eta}-\tfrac{1}{2}\,{}^{\mathrm{T}}\boldsymbol{\eta}\boldsymbol{\nabla}^2p_0\boldsymbol{\xi}, \tag{2.4}$$

with $\boldsymbol{\nabla}^2p_0=\{\partial^2p_0/\partial x_i\partial x_j\}$ and

$$\boldsymbol{b}(\boldsymbol{\xi})=\rho_0(\boldsymbol{v}_0\cdot\boldsymbol{n})\frac{d\boldsymbol{\xi}}{dt}-\rho_0a_0^2\boldsymbol{\nabla}\cdot\boldsymbol{\xi}\,\boldsymbol{n}. \tag{2.5}$$

D. Lagrangian density

$B_V(\boldsymbol{\xi},\boldsymbol{\eta})$ is a bilinear symmetric form so that the associated quadratic form is a Lagrangian density associated with Galbrun's equation:

$$\Lambda(\boldsymbol{x},t,\boldsymbol{\xi}_{,t},\boldsymbol{\xi}_{,x})=\frac{1}{2}\rho_0\frac{d\boldsymbol{\xi}^2}{dt}-\frac{1}{2}\rho_0\,a_0^2\boldsymbol{\nabla}\cdot\boldsymbol{\xi}^2-(\boldsymbol{\xi}\cdot\boldsymbol{\nabla}p_0)\boldsymbol{\nabla}$$
$$\cdot\boldsymbol{\xi}-\tfrac{1}{2}\,{}^{\mathrm{T}}\boldsymbol{\xi}\boldsymbol{\nabla}^2p_0\boldsymbol{\xi}, \tag{2.6}$$

where $\boldsymbol{\xi}_{,t}=(\partial\boldsymbol{\xi}/\partial t)$ and $\boldsymbol{\xi}_{,x}=(\partial\boldsymbol{\xi}/\partial\boldsymbol{x})$. In the case of a stationary Eulerian flow, the Lagrangian density does not depend on time. For such flows, conservative expressions of aeroacoustics energy density Π and intensity $\boldsymbol{i}$ are established by using the time invariance of the Lagrangian density.[19,20] The expressions read:

$$\Pi=\frac{\rho_0}{2}\frac{d\boldsymbol{\xi}}{dt}\cdot\frac{d\boldsymbol{\xi}}{dt}-\rho_0\frac{d\boldsymbol{\xi}}{dt}\cdot(\boldsymbol{v}_0\cdot\boldsymbol{\nabla})\boldsymbol{\xi}+\frac{1}{2\rho_0a_0^2}$$
$$\times[p^2-(\boldsymbol{\xi}\cdot\boldsymbol{\nabla}p_0)^2], \tag{2.7}$$

and

$$\boldsymbol{i}=\rho_0\left(\frac{\partial\boldsymbol{\xi}}{\partial t}\cdot\frac{d\boldsymbol{\xi}}{dt}\right)\boldsymbol{v}_0+p\frac{\partial\boldsymbol{\xi}}{\partial t}, \tag{2.8}$$

and verify

$$\frac{\partial\Pi}{\partial t}+\boldsymbol{\nabla}\cdot\boldsymbol{i}=0. \tag{2.9}$$

The same expressions were also established by Godin[13] with a different approach. In contrast with usual formulations based on Eulerian variables, these expressions are conservative. However, in Sec. II C, the integration by parts of Galbrun's equation could be done differently (for the terms depending on p_0). There are several weak formulations leading to a Lagrangian density. This means the expressions of aeroacoustics energy density and intensity do not have a unique definition and there might be several other definitions of the potential energy linking aerodynamic flow, static pressure, and acoustic perturbation. Choosing one Lagrangian density is physically equivalent to choosing one definition for energy.

E. Harmonic weak formulation

For harmonic solutions, with pulsation ω, we set

$$\boldsymbol{\xi}(\boldsymbol{x},t)=\boldsymbol{\xi}(\boldsymbol{x})e^{j\omega t}\quad\text{and}\quad\boldsymbol{\eta}(\boldsymbol{x},t)=\boldsymbol{\eta}(\boldsymbol{x})e^{j\omega t}.$$

The weak formulation is transformed into the frequency domain and Eq. (2.3) becomes

$$\Big\{\forall\,\eta\in\mathbf{H}(\mathrm{grad};V_0);$$

$$\int_{V_0}B_V(\boldsymbol{\xi},\overline{\boldsymbol{\eta}})dV+\oint_{S_0}\boldsymbol{b}(\boldsymbol{\xi})\cdot\overline{\boldsymbol{\eta}}\,dS=0\Big\}, \tag{2.10}$$

where

$$B_V(\boldsymbol{\xi},\overline{\boldsymbol{\eta}})=\rho_0\omega^2\boldsymbol{\xi}\cdot\overline{\boldsymbol{\eta}}-\rho_0a_0^2\boldsymbol{\nabla}\cdot\boldsymbol{\xi}\,\boldsymbol{\nabla}\cdot\overline{\boldsymbol{\eta}}+\rho_0(\boldsymbol{v}_0\cdot\boldsymbol{\nabla})$$
$$\times\boldsymbol{\xi}\cdot(\boldsymbol{v}_0\cdot\boldsymbol{\nabla})\overline{\boldsymbol{\eta}}+j\rho_0\omega\boldsymbol{\xi}\cdot(\boldsymbol{v}_0\cdot\boldsymbol{\nabla})\overline{\boldsymbol{\eta}}$$
$$-j\rho_0\omega\overline{\boldsymbol{\eta}}\cdot(\boldsymbol{v}_0\cdot\boldsymbol{\nabla})\boldsymbol{\xi}, \tag{2.11}$$

if static pressure p_0 is assumed constant (such an assumption is not correct for aeroacoustics problems, however, our purpose is to solve Galbrun's equation with the FEM and terms with p_0 do not present a major interest from the numerical point of view). Also, in Eq. (2.11), we use the conjugate of $\boldsymbol{\eta}$ because $(\boldsymbol{\xi},\boldsymbol{\eta})\in\mathbb{C}^2$ and $B_V(\boldsymbol{\xi},\overline{\boldsymbol{\eta}})\in\mathbb{R}$.

III. FINITE-ELEMENT METHOD

A. Functional spaces

In general, the analytical resolution of Galbrun's equation is not possible because the displacement fields, solutions of Galbrun's equation, belong to infinite-dimension functional spaces and cannot be expressed with known functions. The solutions are searched for with the finite-element method, by approaching functional spaces, with the finite-dimension ones. The required properties of these spaces depend on the equation being solved. Our method uses $\mathbf{H}(\mathrm{grad};V_0)$ elements and may compute Galbrun's solutions in the presence of nonuniform flow. By definition, $\mathbf{H}(\mathrm{grad};V_0)$ is the Sobolev space[7,8] defined as

$$\mathbf{H}(\mathrm{grad};V_0)=\{\boldsymbol{u}\in\mathbf{L}^2(V_0)\quad\text{and}\quad\boldsymbol{\nabla}\boldsymbol{u}\in\mathbf{L}^2(V_0)\},$$

where

$$\mathbf{L}^2(V_0)=\left\{\boldsymbol{u},\int_{V_0}\boldsymbol{u}(\boldsymbol{x})\cdot\overline{\boldsymbol{u}}(\boldsymbol{x})d\boldsymbol{x}<\infty\right\}.$$

Any vectorial function in $\mathbf{L}^2(V_0)$, whose gradient is also in $\mathbf{L}^2(V_0)$ belongs to $\mathbf{H}(\mathrm{grad};V_0)$. Conforming $\mathbf{H}(\mathrm{grad};V_0)$ elements may be used in computations with nonuniform flow. However, from the mathematical point of view, the problem is not well posed because of the $(\boldsymbol{v}_0\cdot\boldsymbol{\nabla})$ operators included in d/dt, and thereby the method is not robust enough to handle industrial computations. More studies on the mathematical properties of Galbrun's equation are in progress. The present method is a first step of a work that should lead to a CAA method based on the FEM.

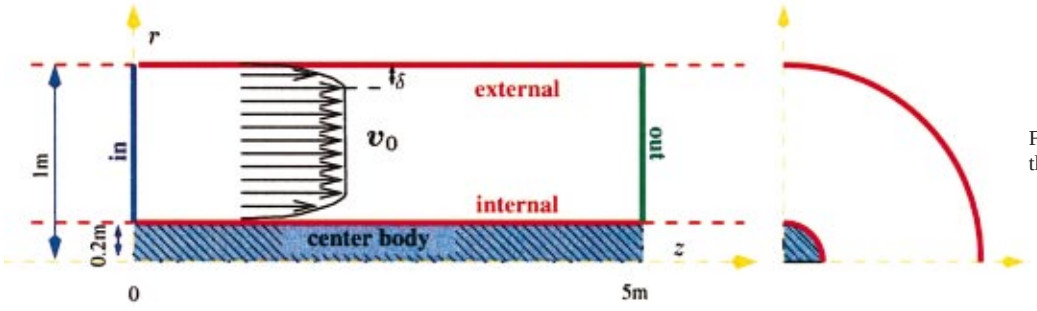

FIG. 2. Axisymmetric lined duct in the presence of a shear flow.

B. Discretization

The section describes the implementation of the FEM in solving Galbrun's equation for a two-dimensional (2D) AXI geometry. Introducing the cylindrical coordinates, and azimuthal order m, we set

$$\boldsymbol{\xi}(r,\theta,z)=\boldsymbol{\xi}(r,z)e^{-jm\theta} \quad \text{and} \quad \overline{\boldsymbol{\eta}}(r,\theta,z)=\overline{\boldsymbol{\eta}}(r,z)e^{+jm\theta}.$$

By definition, a finite element is composed of

(1) a geometric element of V_0,
(2) a set of degrees of freedom (or connectors), and
(3) a finite-dimension subspace of the chosen functional space.

The fluid inside the bounded volume V_0 is meshed with triangles using Delaunay's technique. Volume V_0 is subdivided with n_v triangles e_i where $i=1\cdots n_v$ and envelope S_0 with n_s segments s_i. If $V(e_i)$ is the volume of finite element e_i and $S(s_i)$ the length of segment s_i, we approximate V_0 and S_0 with, respectively,

$$\sum_{i=1}^{n_v} V(e_i) \quad \text{and} \quad \sum_{i=1}^{n_s} S(s_i),$$

and Eq. (2.10) is approximated with

$$\left\{ \forall \eta \in \mathbf{H}(\text{grad};V_0), \quad \sum_{i=1}^{n_v} \int_{V(e_i)} B_V(\boldsymbol{\xi},\overline{\boldsymbol{\eta}})dV + \sum_{i=1}^{n_s} \oint_{S(s_i)} \boldsymbol{b}(\boldsymbol{\xi})\cdot\overline{\boldsymbol{\eta}}dS=0 \right\}. \tag{3.1}$$

Consider the geometric element e_i whose contribution is

$$\forall \boldsymbol{\eta} \in \mathbf{H}[\text{grad};V(e_i)], \quad \int_{V(e_i)} B_V(\boldsymbol{\xi},\overline{\boldsymbol{\eta}})dV.$$

The geometric triangular element e_i with nodal values of displacement $\{\boldsymbol{\xi}_1,\boldsymbol{\xi}_2,\boldsymbol{\xi}_3\}$ as connectors and functions, expressed in barycentric coordinates with $(u,v)\in[0,1]$ and $v\in[0,1-u]$,

$$a_1(u,v)=(1-u-v), \quad a_2(u,v)=u, \quad a_3(u,v)=v, \tag{3.2}$$

is conform with $\mathbf{H}[\text{grad};V(e_i)]$. This is the kind of element used in the method.

IV. PROPAGATION IN A STRAIGHT LINED DUCT

A configuration is defined in Fig. 2 to handle comparisons between Galbrun's and Lilley's solutions. An axisymmetric duct of radius 1 m, including a center body of radius 0.2 m, is considered. A locally reacting absorbing material of

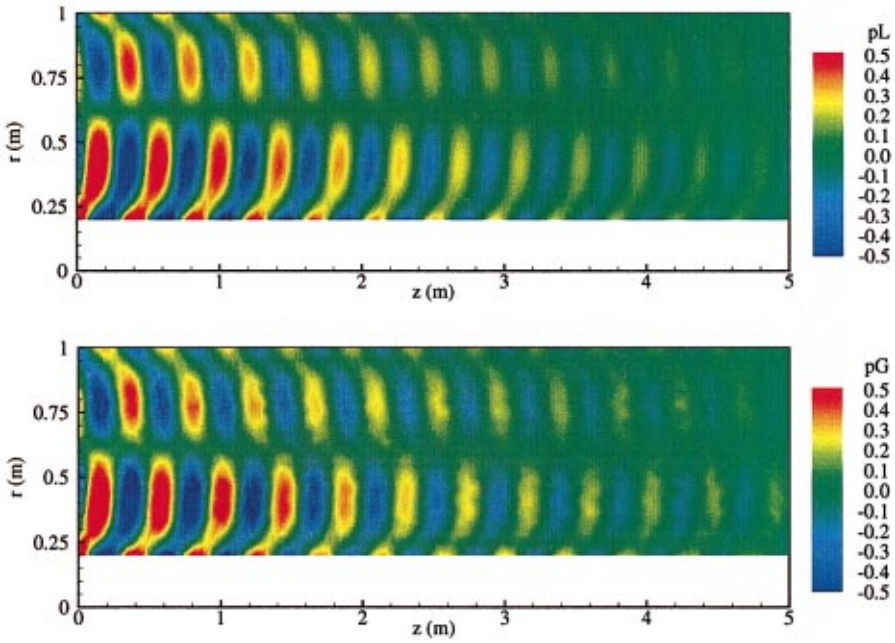

FIG. 3. $\text{Re}[p_{2,2}(r,z)]$ at frequency 1350 Hz computed with Lilley's equation on the upper plot and Galbrun's equation on the lower plot. $M_0=+0.5$, $\delta=0.15$ m, $Z=1-j$.

5 m length is applied on both the duct wall and the center body. The reduced impedance Z of the liner is equal to $1-j$ (the choice of that value is arbitrary and more realistic impedance values could be taken into account by the same method). The in-duct flow is similar to the one used by Eversman[21] for duct acoustics studies. Even if the flow does not strictly verify Euler's equation, we suppose the effect will not be too penalizing. The temperature and the static pressure are constant. The velocity profile of the flow $\boldsymbol{v}_0(r)$, including a boundary layer of thickness δ close to the duct walls and the center body, is defined as follows:

- In the presence of a center body, the radial Mach number $M(r)$ is

$$M(r)=M_0\sin\left(\frac{\pi}{2\delta}r\right), \quad \text{if } 0\leqslant r\leqslant\delta,$$
$$M(r)=M_0, \quad \text{if } \delta\leqslant r\leqslant R-\delta, \tag{4.1a}$$
$$M(r)=M_0\sin\left[\frac{\pi}{2\delta}(R-r)\right], \quad \text{if } R-\delta\leqslant r\leqslant R.$$

- Otherwise,

$$M(r)=M_0, \quad \text{if } 0\leqslant r\leqslant R-\delta,$$
$$M(r)=M_0\sin\left[\frac{\pi}{2\delta}(R-r)\right] \quad \text{if } R-\delta\leqslant r\leqslant R. \tag{4.1b}$$

A. Lilley's solution

During the 1970s a number of studies[21–23] were developed to solve Lilley's equation using the modal approach. In the present paper, the Mungur and Gladwell method[24] is applied to determine the modal structure of the in-duct pressure. Let m and n designate the azimuthal and the radial mode orders. For nonuniform flow, the modal solution is obtained with a classical Runge–Kutta integration[25] of Lilley's equation.[2] To properly select a given mode (m,n), the integration starts with the eigensolutions for an infinite annular duct with a uniform flow, based on the mth-order Bessel functions of the first and second kind. The acoustic pressure field in the annular duct is given in cylindrical coordinates by

$$p(r,\theta,z,t)=\sum_{m,n} p_{m,n}(r)e^{j(\omega t-m\theta-k_z z)}.$$

Mungur and Gladwell's method provides $p_{m,n}(r)$ together with the axial wave number $k_z(m,n)$. A specific code has been developed to compute the in-duct pressure with the modal approach.

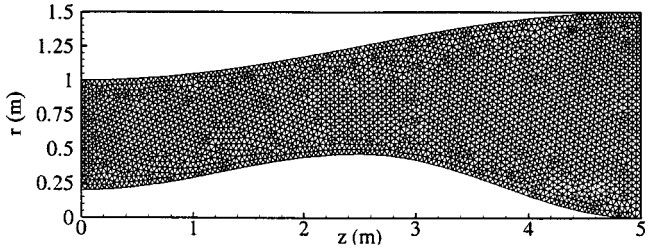

FIG. 4. Meshing of the duct.

B. Galbrun's solution

For the FEM computation, the inner region between the center body and the wall duct is meshed with linear elements. At frequency $f=1350$ Hz ($kR\approx 25$), with the typical size of the elements about $\lambda/6$ (where λ is the total wavelength), about 5000 elements are needed to compute the displacement field.

The FEM is based on the displacement vector, so that the problem above, expressed with the Euler's pressure variable, has to be formulated with the displacement variable. This can be directly achieved using Eqs. (2.4) and (2.5), especially for the boundary conditions imposed at the source, on the lined walls, and at the duct exit.

1. Expressions of the boundary conditions

At the duct entrance ($z=0$), the acoustic pressure $p_{m,n}(r)$ computed with the modal approach is considered as the acoustical boundary condition. Corresponding values of displacement are established with

$$\boldsymbol{\xi}=\begin{bmatrix}\xi_r\\ \xi_\theta\\ \xi_z\end{bmatrix}=\frac{1}{\rho_0 a_0^2(k-k_z M_0)^2}\begin{bmatrix}(\partial p/\partial r)\\ -j\dfrac{m}{r}p\\ -jk_z p\end{bmatrix},$$

and directly introduced into the global system.

On the duct wall and on the center body a local acoustic reduced impedance[26] Z is applied, so that

$$p=\rho_0 a_0 Z\frac{\partial\boldsymbol{\xi}}{\partial t}\cdot\boldsymbol{n},$$

using the third equation of Eq (2.1), and as $\boldsymbol{v}_0\cdot\boldsymbol{n}=\boldsymbol{0}$ on the linings, the equation reads

$$p=j\rho_0 a_0 Z\omega(\boldsymbol{\xi}\cdot\boldsymbol{n}).$$

As the normal component of the flow speed on the linings is zero, $\boldsymbol{b}(\boldsymbol{\xi})=p\boldsymbol{n}$, so that

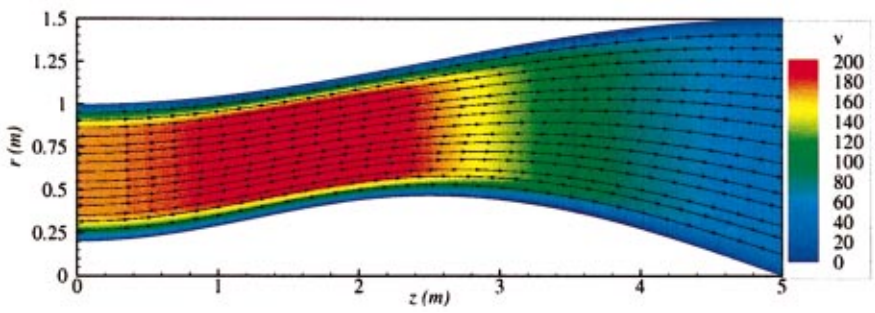

FIG. 5. Flow velocity and streamlines.

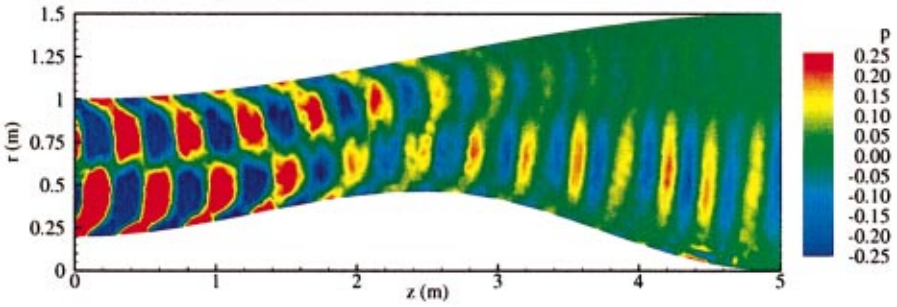

FIG. 6. Re$[p_{2,2}(r,z)]$ at frequency 1350 Hz computed with Galbrun's equation. $M_0=0.5$, $\delta=0.15$ m, $Z=1-j$.

$$\boldsymbol{b}(\boldsymbol{\xi})\cdot\overline{\boldsymbol{\eta}}=j\rho_0 a_0 Z\,\omega(\boldsymbol{\xi}\cdot\boldsymbol{n})(\overline{\boldsymbol{\eta}}\cdot\boldsymbol{n}). \tag{4.2}$$

In the cross-section $z=5$ m, a nonreflective condition is required to properly simulate the one-way propagation in the positive z direction. Using Euler's variables, one usually imposes on the cross section an anechoic termination based on the wave impedance (i.e., the ratio of the pressure and the normal acoustic velocity). A similar condition is applied with the displacement variable

$$\boldsymbol{b}(\boldsymbol{\xi})=j\rho_0(\omega-k_z v_0)\begin{bmatrix} v_0 & & \\ & v_0 & \\ & & \omega/kz \end{bmatrix}\boldsymbol{\xi}=\mathcal{Z}\boldsymbol{\xi}.$$

The matrix $\mathcal{Z}$ depends on the acoustic mode and can be considered as an impedance matrix. The expression of $B_S(\boldsymbol{\xi},\boldsymbol{\eta})$ for a modal nonreflective condition reads

$$\boldsymbol{b}(\boldsymbol{\xi})\cdot\overline{\boldsymbol{\eta}}=\overline{\boldsymbol{\eta}}\cdot\mathcal{Z}\boldsymbol{\xi}. \tag{4.3}$$

C. Results

From among the many test computations used to validate the FEM, the results obtained for the case of sound propagation of the mode (2,2) at frequency $f=1350$ Hz, for upstream propagation, is proposed. The flow is defined by the Mach number M_0 and a boundary layer of thickness $\delta=0.15$ m, according to Eqs. (4.1a) and (4.1b).

The real part of Euler's acoustic pressure in Pa is plotted in Fig. 3 for both computed solutions. As the displacement field is computed with the FEM, the corresponding acoustics pressure values are first returned using Eq. (2.1) in the case of a uniform static pressure:

$$p=-\rho_0 a_0\nabla\cdot\boldsymbol{\xi}.$$

Obviously, the solutions are in good agreement and validate the weak formulation and the FEM implementation. We can observe that, due to the liner attenuation, the pressure strongly decreases with respect to the axial coordinate and goes nearly to zero at the duct end. As the sound pressure level is strongly reduced by the liner absorption, the boundary condition at the duct exit does not significantly modify Galbrun's solution.

V. PROPAGATION IN A LINED DUCT WITH A VARYING CROSS SECTION

This section presents an application of the FEM to propagation in a lined duct with a varying cross section. The fluid inside the duct is assumed to have a constant flow rate, so that the radial velocity profile varies along the center line. For this configuration, Lilley's equation is no longer valid due to the flow variations with respect to the axial coordinate. Moreover, as shown below, the radial structure of the mode imposed at the duct entrance is not conserved and the modal approach is not appropriate anymore. In addition to the in-duct pressure field computation, the power balance performed with the expression, Eq. (2.8), of the acoustic intensity and the usual Cantrell and Hart expression,[27] Eq. (5.2), are compared.

A. In-duct pressure field

The flow velocity model remains similar to the one used in the previous test cases. It is characterized by the Mach number M_0 and a constant boundary layer of thickness $\delta=0.15$ m. The flow velocity and the streamlines are plotted in Fig. 4. At $z=2$ m, where the cross-section nozzle is minimum, the Mach number reaches about 0.6.

Figure 5 represents the mesh of the fluid used for the FEM computations. The mesh is generated with nonstructured linear elements. Again, to obtain an accurate solution, the size of the elements is chosen as less than $\lambda/6$. For this application, the boundary conditions are similar to those used in the test cases. A locally reacting liner with a normalized impedance $Z=1-j$ is applied on the walls. At the source location, $z=0$, a mode (2,2) at the frequency 1350 Hz is introduced. An impedance condition $Z=\rho_0 a_0$ is also applied at the duct end, $z=5$ m. The real part of the pressure field computed with the FEM is plotted in Fig. 6. In addition to the attenuation of the sound due to the liner absorption, the pressure field clearly exhibits a change in the radial slice with a maximum level towards the center body. This conversion is generated by the flow variations together with the varying cross section. In practice, such a redistribution can significantly modify radiation in the far field.

TABLE I. Acoustic energy check up with Cantrell and Hart (5.2) and expression (2.8).

Border	Cantrell and Hart, Eq. (5.2)	Eq. (2.8)
Π_s (duct entrance)	100.00%	100.00%
Π_r (center body)	−51.99%	−42.26%
Π_R (duct wall)	−63.06%	−51.45%
Π_e (duct exit)	−4.72%	−3.88%
Σ	−19.77%	2.41%

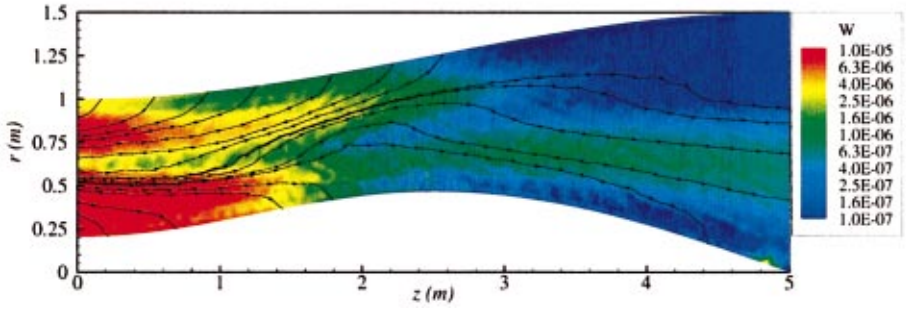

FIG. 7. Acoustic energy and intensity streamlines.

B. Aeroacoustics intensity

Conservative expressions of aeroacoustics energy density and intensity were established in Sec. II D. Comparisons with more usual expressions (Cantrell and Hart's expressions[27]) are proposed. We recall that these expressions read

$$\Pi^* = \frac{1}{2}\left(\rho_0 \boldsymbol{v}^2 + \frac{p^2}{\rho_0 a_0^2}\right) + \frac{p}{\rho_0}\boldsymbol{v}\cdot\boldsymbol{v}_0, \tag{5.1}$$

$$\boldsymbol{i}^* = (p + \rho_0 \boldsymbol{v}\cdot\boldsymbol{v}_0)\left(\boldsymbol{v} + \frac{p}{\rho_0 a_0^2}\boldsymbol{v}_0\right). \tag{5.2}$$

The energy conservation law in the harmonic regime states that the intensity (i.e., the acoustic energy flux or acoustic power) integrated over a closed surface is zero. For the simulations, a closed surface corresponding to the four boundaries of the inner fluid is defined. The cross sections at the source and the duct exit, the center body, and the duct wall allow the computation of the acoustic powers Π_s, Π_e, Π_r, and Π_R, respectively. Theoretically, the balance power in the duct is $\Pi_s = \Pi_r + \Pi_R + \Pi_e$. This can also be expressed as

$$\Pi_r/\Pi_s + \Pi_R/\Pi_s + \Pi_e/\Pi_s = 100\%,$$

with Π_s as a reference. The powers in the duct are evaluated using the expression of the intensity Eq. (2.8). For comparison purpose, the standard Cantrell and Hart expression of the intensity is also computed. In this latter case, to obtain the Eulerian pressure, p and velocity $\boldsymbol{v}$ are first derived from the displacement field $\boldsymbol{\xi}$ using system (2.1).

Table I shows the distribution of the power computed with expressions (2.8) and (5.2). First, the power radiated through the duct exit is only 4% due to the strong absorption caused by the liners applied on the center body and the duct walls. It is also observed that the power balance is retrieved with a relative error of 2% with expression (2.8), while the error reaches 20% using the Cantrell and Hart definition. Such a result demonstrates the accuracy of expression (2.8) and confirms that the use of expression (5.2) is not appropriate in this situation, including high subsonic flow and low frequency. Notice that even if the intensity flux (Π_r and Π_R) integrated upon the walls gives the same figures with both expressions (because the flow speed is zero), the relative powers Π_r/Π_s and Π_R/Π_s are not equal, because the expressions lead to different values of Π_s.

Finally, Fig. 7 presents the energy density and the intensity streamlines computed with Eqs. (2.7) and (2.8). The streamlines indicate the acoustic power spreading in the duct. In particular, they show that most of the energy bends towards the center body, in agreement with the pressure field in Fig. 6.

VI. CONCLUSION

The finite-element method and Galbrun's equation may be an attractive alternative to the finite-difference method and Euler's linearized equations for predicting aeroacoustics propagation. The first results obtained with the FEM for the case of propagation in a lined duct in the presence of a shear parallel flow are in good agreement with known solutions given by the modal approach. An application to a duct with a varying cross section also shows the capabilities of the FEM Galbrun model to handle more realistic configurations. The expression of the aeroacoustics intensity based on the displacement vector has been implemented in the FEM. In the low-frequency range, the energy is conserved with an error of about 3%. These first results confirm the accuracy of the FEM computations and demonstrates the interest in the Galbrun formalism. Future studies will deal with the implementation of other finite elements and comparisons between the different formulations.

ACKNOWLEDGMENTS

The research presented in this paper was sponsored by DSA/SPA/ST/STA (26, boulevard Victor 00460 ARMES—FRANCE) and monitored by Bernard Poire.

[1] B. T. Chu and Kovasznay, "Nonlinear interactions in a viscous heat conducting compressible gas," J. Fluid Mech. **3**, 494–514 (1958).
[2] G. M. Lilley, "Theory of turbulence generated jet noise, noise radiation from upstream sources, and combination of noise," Technical Report No. AFAPL-TR-72-53, Lockheed Georgia Company (1972) (unpublished).
[3] H. Galbrun, *Propagation d'Une Onde Sonore dans l'Atmosphère et Theorie des Zones de Silence* (Gauthier-Villars, Paris, 1931).
[4] J. P. Bosquet, "L'étude par approximations successives des mouvements varieś des mileux continus," in *Comptes Rendus II*, Bruxelles, 19–23 juin, II^e Congrès national des Sciences (1935), pp. 1437–1447.
[5] O. C. Zienkiewicz and R. L. Taylor, *Finite Element Method—Basic Formulation and Linear Problems* (McGraw-Hill, New York, 1989), Vol. 1.
[6] G. Dhatt and G. Touzot, in *Une Présentation de la Méthode des éléments Finis*, 2nd ed., edited by S. A. Maloine (Paris, 1984).
[7] P.-A. Raviart and J.-M. Thomas *Introduction l'Analyse Numérique des Équations aux Dérivées Partielles* (Masson, Paris, 1992).
[8] P. G. Ciarlet and J. L. Lions. *Handbook of Numerical Analysis*, 1st ed. (North-Holland, Amsterdam, 1996), Vol. 4.
[9] T. Colonius, S. K. Lele, and P. Moin, "Direct computation of the sound generated by a two-dimensional shear layer," 15th AIAA Aeroacoustics Conference, Paper No. 93-4328 (1993).

[10] S. Mu and S. Mahalingam, ''Direct numerical simulation of acoustic shear flow interaction in two-dimensional ducts,'' AIAA Pap. **34**, 237–243 (1996).
[11] C. W. Tam and J. C. Webb, ''Dispersion-relation-preserving finite-difference schemes for computational acoustics,'' J. Comput. Phys. **107**, 262–281 (1993).
[12] B. Poirée, ''Les équations de l'acoustique linéaire et nonlinéaire dans un écoulement de fluide parfait,'' Acustica **57**, 5–25 (1985).
[13] O. A. Godin, ''Reciprocity relations and energy conservation for waves in the system: Inhomogeneous fluid flow-anisotropic solid body,'' Acoust. Phys. **43**, 688–693 (1996).
[14] M. Ben Tahar and E. Goy, ''Resolution of a vibroacoustic problem in the presence of a nonuniform mean flow,'' Fourth AIAA Joint Aeroacoustics Conference, Paper No. 98-2215 (1998).
[15] C. J. Peyret, ''Acoustic propagation in presence of an arbitrary flow,'' J. Acoust. Soc. Am. **103**, 2840 (1998).
[16] B. Poirée, ''Représentation lagrangienne et eulérienne de l'acoustique linéaire et nonlinéaire,'' J. Phys. **40**, C48-C52 (1979).
[17] J. L. Kerrebrock, ''Waves and wakes in turbomachine annuli with swirl,'' AIAA Paper No. 74–87 (1974).
[18] J. L. Kerrebrock, ''Small disturbances in turbomachine annuli with swirl,'' AIAA J. **15**, 794–803 (1977).
[19] L. Landau and E. Lifchitz, *Physique Théorique—Mécanique*, 4th ed. (Mir, Moscow, 1982).
[20] L. Landau and E. Lifchitz, *Physique Théorique—Théorie des Champs*, 4th ed. (Mir, Moscow, 1989).
[21] W. Eversman, ''Effect of boundary layer on the transmission and attenuation of sound in an acoustically treated circular duct,'' J. Acoust. Soc. Am. **49**, 1372–1380 (1971).
[22] W. Eversman and R. J. Beckemeyer, ''The transmission of sound in ducts with thin shear layers—convergence to the uniform flow case,'' J. Acoust. Soc. Am. **52**, 216–220 (1972).
[23] M. N. Mikhail and A. N. Abdelhamid, '' Transmission and far-field radiation of sound waves in and from lined ducts containing shear flow,'' AIAA Pap. **73**, 1013 (1973).
[24] P. Mungur and G. M. L. Gladwell, ''Acoustic wave propagation in a sheared fluid contained in a duct,'' J. Sound Vib. **9**, 28–48 (1969).
[25] W. H. Press, S. A. Teukolsky, W. T. Vetterling, and B. P. Flannery, *Numerical Recipes in Fortran, the Art of Scientific Computing*, 2nd ed. (Cambridge University, Cambridge, 1992).
[26] U. Ingard, ''Influence of fluid motion past a plane boundary on sound reflection, absorption, and transmission,'' J. Acoust. Soc. Am. **31**, 1035–1036 (1959).
[27] R. H. Cantrell and R. W. Hart, ''Interaction between sound and flow in acoustic cavities: Mass, momentum, and energy considerations,'' J. Acoust. Soc. Am. **36**, 697–706 (1964).

The reflected and transmitted acoustic field excited by a supersonic source in a two media configuration

B. J. Kooij[a)]
Laboratory of Electromagnetic Research, Centre for Technical Geoscience, Delft University of Technology, P.O. Box 5031, 2600 GA Delft, The Netherlands

C. Kooij
Laboratory of Electromagnetic Theory, Eindhoven University of Technology, P.O. Box 513, 5600 MB Eindhoven, The Netherlands

(Received 28 November 2000; accepted for publication 27 April 2001)

The acoustic wave field due to a supersonic motion of a rigid object over a half-space is investigated. The analysis presented leads to closed form expressions for the reflected and transmitted conical waves as separate contributions. The linearized acoustic field equations are applied to obtain representations for the fields in a combined Laplace–Fourier transform domain. To these representations, which are mapped into the proper form, we apply the Cagniard–de Hoop technique in order to find closed form time–domain solutions for the reflected and transmitted acoustic fields. Attention is focused on supersonic effects, so the analysis concentrates on application of the Cagniard–de Hoop technique to obtain closed form space–time domain expressions from the contributions of poles, appearing in the transform domain representation for the reflected and transmitted acoustic wave field. It turns out that these pole contributions, next to wave solutions of the conical type also can give rise to headwaves, associated with the reflected conical wave. Numerical results for the reflected as well as the transmitted conical wave field are presented for an air–sea configuration with supersonic source velocities up to MACH 5. © *2001 Acoustical Society of America.* [DOI: 10.1121/1.1381020]

PACS numbers: 43.20.Px [ANN]

I. INTRODUCTION

In this paper the acoustic wave phenomena associated with an object in horizontal supersonic motion over the surface of a half-space (sea or land) are investigated mathematically. The soil of the land is modeled as a fluid, assuming the shear stresses are neglectable. Hence, we will not encounter surface waves (Scholte waves) along the air–soil interface; see de Hoop and van der Hijden.[1] In the analysis that follows the media in the half-spaces of the configuration are acoustically represented as homogeneous, isotropic fluids in which the basic acoustic field equations are applied in linearized form. However, the method outlined here in principle is also applicable to the more general problem of an elastodynamic soil in which Scholte waves can occur along the air–soil interface. The method presented is based on the Cagniard–de Hoop technique; see de Hoop and Frankena.[2] This method is the more attractive one when we have a layered media configuration, having the advantage of leading, in principle, to the formulation of the acoustic field in closed form directly in the space–time domain by inspection of the suitably parametrized, spatially inverse transformed, field expressions.

The Cagniard–de Hoop method has been applied in the elastodynamic case, Gakenheimer and Miklowitz,[3] Kennedy and Herrmann,[4,5] Bakker *et al.*[6] Even nonuniform motion of a traveling line source was studied in elastodynamics by Freund[7] and extended by Watanabe[8] to the three-dimensional case of an acoustic half-space with a point source performing a circular motion. For the electromagnetic case of a moving source in an unbounded medium Kooij[9] applied the Cagniard–de Hoop method leading to an elegant solution in the supersonic state for the conical waves, which are in electromagnetics known as the Cerenkov waves; see Jones.[10] The procedure of Bakker *et al.*[6] can be applied to solve the comparable moving source problem in our acoustic two-media configuration, however in this method the conical wave phenomena do not show up mathematically as a separate partial solution, resulting exclusively from pole contributions, which makes it impossible to study their reflection and transmission properties. The procedure presented by Kooij[9] leads to a representation in which the conical waves indeed show up mathematically as separate phenomena, it is however restricted to an unbounded homogeneous medium.

In the present paper it is shown that the problem of a moving acoustic source in a two-media configuration can be represented in a form in which the conical wave contributions show up mathematically as separate terms when in the Cagniard–de Hoop method the adequate set of Fourier transform variables, associated with the coordinates along the interface, are chosen. In the final stage conical wave solutions, consistent with the results presented by Kooij,[9] appear as contributions of complex conjugate poles in the analysis. As the average intrinsic acoustic wave speed in sea or soil is several times higher than in air also head waves, associated with the various parts of the reflected field, among which conical precursive parts, will occur along the interface, thus complicating the overall picture of the acoustic wave propagation near the surface of the half-space.

[a)]Electronic mail: b.j.kooij@its.tudelft.nl

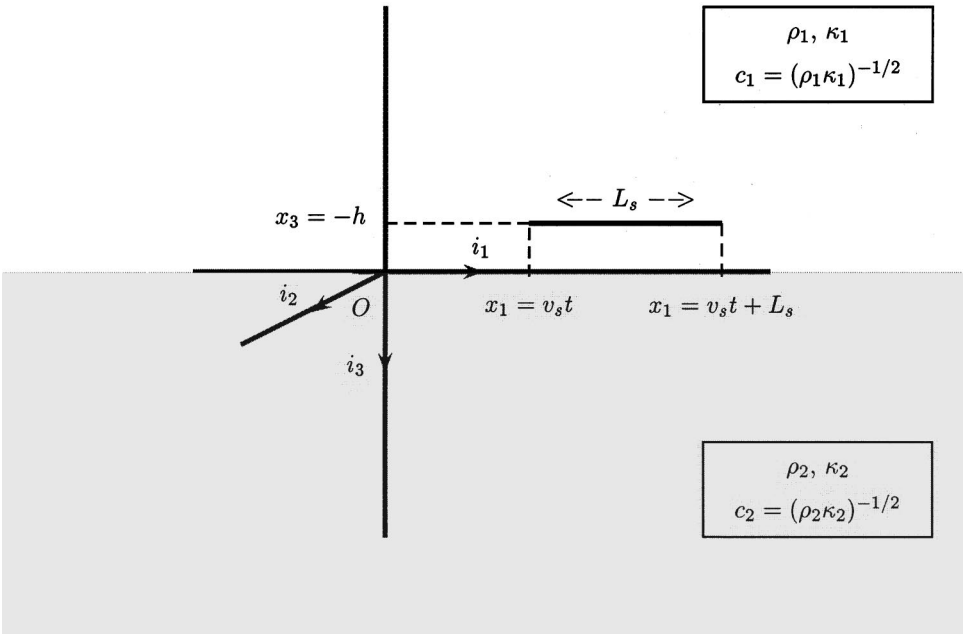

FIG. 1. The two-media configuration with a supersonic object with a length L_s moving with velocity v_s and located at a level $x_3 = -h$.

II. DESCRIPTION OF THE CONFIGURATION

To specify the position in the two-media configuration we employ the coordinates (x_1,x_2,x_3) with respect to a fixed, orthogonal Cartesian reference frame with origin $\mathcal{O}$ and three mutually perpendicular base vectors $\mathbf{i}_1,\mathbf{i}_2,\mathbf{i}_3$ of unit length. In the indicated order the three base vectors form a right-handed system. In accordance with the convention in seismology $\mathbf{i}_3$ points downwards. The interface between the media coincides with the plane $x_3=0$. The object is modeled as a rigid material circular cylinder with length L_s and a radius that is supposed to be vanishing small. Prior to the instant of time $t=0$ the object is supposed to be at rest. The object with the endpoints located at the coordinates $(0,0,-h)$ and $(L_s,0,-h)$ starts to move and act as an acoustic source of the dipole type with the nonzero extend L_s along the line of motion only, at $t=0$, with uniform velocity:

$$\mathbf{v}_s = v_s \mathbf{i}_1 . \tag{1}$$

In the entire domain $\mathbb{R}^3$ we distinguish the sub-domains $\mathcal{D}_0$, $\mathcal{D}_1$, and $\mathcal{D}_2$ as follows:

$$\mathcal{D}_0 \overset{\text{def}}{=} \{(x_1,x_2) \in \mathbb{R}^2; -\infty < x_3 < -h\}, \tag{2}$$

$$\mathcal{D}_1 \overset{\text{def}}{=} \{(x_1,x_2) \in \mathbb{R}^2; -h < x_3 < 0\}, \tag{3}$$

$$\mathcal{D}_2 \overset{\text{def}}{=} \{(x_1,x_2) \in \mathbb{R}^2; 0 < x_3 < \infty\}. \tag{4}$$

We denote the mass density ρ and the compressibility κ in $\mathcal{D}_0 \cup \mathcal{D}_1$ as ρ_1 and κ_1, and in $\mathcal{D}_2$ as ρ_2 and κ_2, respectively. Then their accompanying intrinsic acoustic wave-speeds are defined as

$$c_{1,2} \overset{\text{def}}{=} (\rho_{1,2}\kappa_{1,2})^{-1/2}, \tag{5}$$

respectively (see Fig. 1).

In the sections that follow we assume $c_2 > c_1$ and that the acoustic source is in a supersonic motion with respect to the wave velocity in the upper half-space $(c_1 < v_s < c_2)$ or in both half-spaces $(c_1 < c_2 < v_s)$.

III. BASIC EQUATIONS AND BOUNDARY CONDITIONS

With the acoustic field quantities supposed continuously differentiable, the medium pressure $p(\mathbf{x},t)$ and the acoustic field velocity $\mathbf{v}(\mathbf{x},t)$ due to a moving dipole-type source with density $f(\mathbf{x},t)$ are locally related according to the following equations:

$$\nabla p + \rho\ \partial_t \mathbf{v} = f \mathbf{i}_1 , \tag{6}$$

$$\nabla \cdot \mathbf{v} + \kappa\ \partial_t p = 0, \tag{7}$$

in which $\rho = \rho_1$, $\kappa = \kappa_1$ when $x_3 < 0$ and $\rho = \rho_2$, $\kappa = \kappa_2$ when $x_3 > 0$. In Eqs. (6)–(7) the acoustic wave velocity is defined as $\mathbf{v} \overset{\text{def}}{=} v_1 i_1 + v_2 i_2 + v_3 i_3$. The one-dimensional distributed moving source with length L_s, defined in the previous section, can be formulated as

$$f(\mathbf{x},t) = F L_s^{-1} \delta(x_2)\,\delta(x_3+h)[H(x_1 - v_s t) - H(x_1 - L_s - v_s t)]H(t), \tag{8}$$

in which the function H denotes the Heaviside unit step function and F denotes some amplitude function. Across the interface of the two media, i.e., at the plane $x_3 = 0$, the boundary conditions,

$$\lim_{x_3 \uparrow 0} p = \lim_{x_3 \downarrow 0} p, \tag{9}$$

$$\lim_{x_3 \uparrow 0} v_3 = \lim_{x_3 \downarrow 0} v_3, \tag{10}$$

hold. The linearity of the basic equations (6)–(7) ensures that the acoustic wave field due to the source in the upper medium $(x_3 < 0)$ can be understood as the superposition of the incident wave field, which is the wave field that would be

present if the medium around the source is extended to infinity, and the reflected wave field which accounts for the presence of the interface at $x_3=0$. The wave field that is present in the lower medium ($x_3>0$) is denoted as the transmitted wave field.

IV. REPRESENTATIONS FOR THE ACOUSTIC FIELD IN THE LAPLACE–FOURIER TRANSFORM DOMAIN

To carry out our analysis efficiently we subject the basic acoustic equations (6)–(7) together with the boundary conditions (9) and (10) to a Laplace transformation with respect to time according to

$$\hat{p}(\mathbf{x},s)\overset{\text{def}}{=}\int_{\tau=0}^{\infty} p(\mathbf{x},\tau)\exp(-s\tau)d\tau, \quad \text{with } s\in\mathbb{R}^+ \tag{11}$$

and a spatial Fourier transformation with respect to x_1 and x_2 according to

$$\tilde{p}(\alpha_1,\alpha_2,x_3,s)\overset{\text{def}}{=}\int_{-\infty}^{\infty}dx_2\int_{-\infty}^{\infty}\hat{p}(\mathbf{x},s)\exp[s(\alpha_1x_1+\alpha_2x_2)]dx_1, \quad \text{with } \alpha_1,\alpha_2\in\mathcal{I}, \tag{12}$$

where $\mathcal{I}$ denotes the imaginary axis in the complex α_1-plane and α_2-plane. Application of the boundary conditions (9) and (10) then yields the Laplace–Fourier transform domain expression for the reflected and transmitted acoustic fields. These transformed pressure fields appear as the difference of two terms of identical form related to the source endpoints $l=L_s$ and $l=0$, i.e., $\tilde{p}(\alpha_1,\alpha_2,x_3,s)=\tilde{p}(\alpha_1,\alpha_2,x_3,s;l=L_s)-\tilde{p}(\alpha_1,\alpha_2,x_3,s;l=0)$. The spatial counterpart of the fields are obtained via the inverse spatial Fourier transform as defined by

$$\hat{p}(\mathbf{x},s)\overset{\text{def}}{=}\left(\frac{s}{2\pi i}\right)^2\int_{-i\infty}^{i\infty}d\alpha_2\int_{-i\infty}^{i\infty}\tilde{p}(\alpha_1,\alpha_2,x_3,s)\times\exp[-s(\alpha_1x_1+\alpha_2x_2)]d\alpha_1. \tag{13}$$

The application of Eq. (13) leads to a representation of the field in the space–domain in which we have integration contours in the complex α_1 and α_2 plane. To arrive at a representation in one complex plane only, we introduce the following transformation:

$$\alpha_1=w\cos\theta-iq\sin\theta, \quad \alpha_2=w\sin\theta+iq\cos\theta, \tag{14}$$

with $-\infty<q<\infty$ and in which θ follows from the polar representation:

$$x_1-l=r\cos\theta, \quad \text{with } l=0,L_s, \qquad x_2=r\sin\theta. \tag{15}$$

In the inverse spatial Fourier transform of Eq. (13), now written in terms of the integration variables w, q, the odd part of the integrand with respect to q can be discarded. The integration with respect to q can subsequently be reduced to the range $0\leqslant q<\infty$. Now, upon the introduction of the transformation $(w,q)\rightarrow(w,\beta)$ according to

$$(c_1^{-2}-w^2+q^2)^{1/2}=\beta(c_1^{-2}-w^2)^{1/2}, \quad \text{with } 0\leqslant q<\infty,\ 1\leqslant\beta<\infty \text{ and } w\in\mathcal{I}, \tag{16}$$

we make the connection with a transformation used in a similar free-space problem (Kooij[9]). Employing Eq. (16) in the expression for the acoustic pressure in the space–domain leads to the representation in the Laplace-transform domain which serves as our basis for the application of the Cagniard–de Hoop technique. This yields for the incident field $\hat{p}^{\text{inc}}$ with $x_3<0$, the reflected field $\hat{p}^{\text{refl}}$ with $x_3<0$ and the transmitted field $\hat{p}^{\text{trans}}$ with $x_3>0$,

$$\begin{bmatrix}\hat{p}^{\text{inc}}(\mathbf{x},s;l)\\ \hat{p}^{\text{refl}}(\mathbf{x},s;l)\\ \hat{p}^{\text{trans}}(\mathbf{x},s;l)\end{bmatrix} = \frac{iF}{4\pi^2v_sL_s}\int_1^{\infty}\frac{d\beta}{\sqrt{\beta^2-1}}\int_{-i\infty}^{i\infty}\begin{bmatrix}\exp(-s|x_3+h|\gamma_1)\\ \tilde{R}\exp(-s|x_3-h|\gamma_1)\\ \tilde{T}\exp[-s(x_3\gamma_2+h\gamma_1)]\end{bmatrix} \times\frac{w\cos\theta-v_s^{-1}}{[(w\cos\theta-v_s^{-1})^2+(\beta^2-1)(c_1^{-2}-w^2)\sin^2\theta]} \times\exp(-srw)dw, \tag{17}$$

in which

$$\tilde{R}=\frac{\rho_2\gamma_1-\rho_1\gamma_2}{\rho_2\gamma_1+\rho_1\gamma_2}; \quad \tilde{T}=\frac{2\rho_2\gamma_1}{\rho_2\gamma_1+\rho_1\gamma_2}, \tag{18}$$

where

$$\gamma_1=\gamma_1(\beta)=\beta(c_1^{-2}-w^2)^{1/2}, \tag{19}$$

$$\gamma_2=\gamma_2(\beta)=[\beta^2(c_1^{-2}-w^2)-(c_1^{-2}-c_2^{-2})]^{1/2}. \tag{20}$$

The accompanying Laplace-transformed acoustic pressure field is obtained from Eq. (17) through

$$\hat{p}(\mathbf{x},s)=\hat{p}(\mathbf{x},s;l=L_s)-\hat{p}(\mathbf{x},s;l=0). \tag{21}$$

In the following sections we investigate the reflected and transmitted field on the basis of Eq. (17). The incident field can also be solved with the representation in Eq. (17) as a starting point, however the methods described by Kooij[9] for traveling sources in infinite homogeneous media are more straightforward.

V. THE REFLECTED ACOUSTIC FIELD IN SPACE–TIME DOMAIN

In this section the reflected acoustic field expressions are transformed back to the space–time domain by means of the Cagniard–de Hoop method. In the analysis we distinguish two contributions, i.e., the body-wave and the conical-wave. Both field contributions can under certain conditions give rise to separate head-wave contributions. In the next two subsections we will deal with these two contributions separately. In the first subsection we will transform the body-wave part of the reflected acoustic wave-field together with its associated head-wave part back to the space–time do-

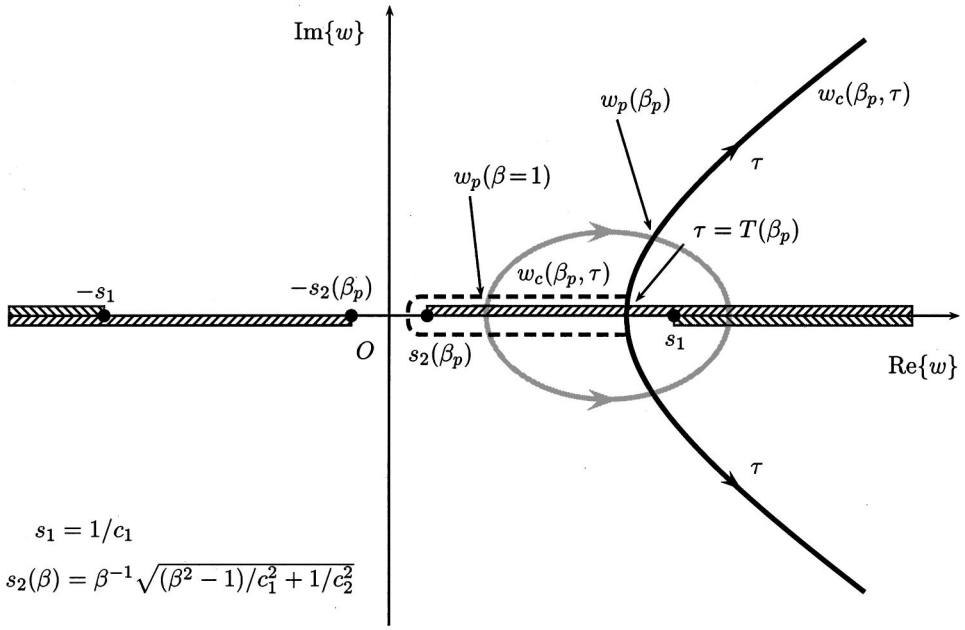

FIG. 2. The Cagniard contour w_c together with the pole path w_p in the complex w-plane, when $c_1 < v_s < c_2$.

main, while in the second subsection we will transform the conical-wave part of the reflected acoustic wave-field together with its associated head-wave part back to the space–time domain.

A. The reflected body-wave and the associated head-wave

In the transformation back to the space–time domain using the Cagniard–de Hoop method we start from Eq. (17) by deforming the path of integration in the complex w-plane along a path such that

$$r(w + a\beta\sqrt{c_1^{-2} - w^2}) = \tau, \quad \text{with } \tau \text{ real and positive,} \tag{22}$$

in which $a = |x_3 - h|/r$ with $x_3 < 0$. The solution to Eq. (22) is obtained as

$$w_c(\tau,\beta) = \frac{\tau}{r(1+a^2\beta^2)} - \frac{a\beta}{r(1+a^2\beta^2)}\sqrt{T^2(\beta) - \tau^2}, \quad \text{when } \tau \leqslant T(\beta), \tag{23}$$

$$w_c(\tau,\beta) = \frac{\tau}{r(1+a^2\beta^2)} \pm i\frac{a\beta}{r(1+a^2\beta^2)}\sqrt{\tau^2 - T^2(\beta)}, \quad \text{when } \tau > T(\beta), \tag{24}$$

in which

$$T(\beta) = rc_1^{-1}\sqrt{1+a^2\beta^2}. \tag{25}$$

The integral along the arcs at infinity vanish by virtue of Jordan's lemma. We obtain with Eq. (24) for w the parametric representation $\mathcal{W}_c = \{w \in \mathcal{C}; w = w_c(\tau,\beta)\}$ which represents a hyperbola located on the right half of the complex

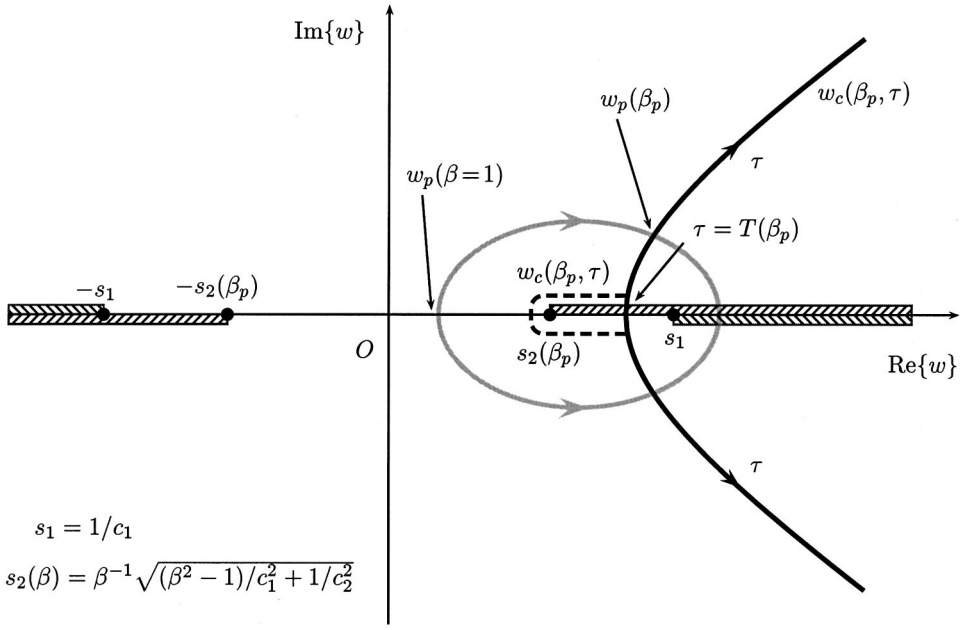

FIG. 3. The Cagniard contour w_c together with the pole path w_p in the complex w-plane, when $c_1 < c_2 < v_s$ and $|\theta| < \Psi$.

w-plane. In the right half of the complex w-plane we have a branch point located at $w=1/c_1$ from which the accompanying branch cut starts along the real axis towards infinity such that $\mathrm{Re}(\gamma_1)\geqslant 0$. Further, we have a branch point located at $w=\beta^{-1}\sqrt{(\beta^2-1)c_1^{-2}+c_2^{-2}}$ from which the accompanying branch cut starts along the real axis towards infinity such that $\mathrm{Re}(\gamma_2(\beta))\geqslant 0$. To circumvent that for certain values of β the Cagniard contour intersects the branch cut that corresponds to the branch point of γ_2 we have to supplement the Cagniard contour with a loop around this branch cut. This loop around the branch cut of γ_2 represents the head-wave contribution. In the process of deformation of the integration contour in the complex w-plane we can encounter for a fixed β two complex conjugated poles that are the zeroes of the denominator of the integrand in Eq. (17). These pole contributions represent the reflected conical wave part which is analyzed in the next subsection. In Fig. 2 and Fig. 3 we have plotted the Cagniard contour w_c, together with the pole path (a collection of poles as a function of β), in the complex w-plane.

By applying the parametrization of Eq. (24) in Eq. (17) we obtain an expression in which an integration with respect to τ and an integration with respect to β occurs according to

$$\hat{p}_b^{\mathrm{refl}}(\mathbf{x},s;l)$$

$$=\frac{iF}{2\pi^2 v_s L_s}\int_{\beta=1}^{\infty}\frac{i\,d\beta}{\sqrt{\beta^2-1}}\mathrm{Re}\int_{\tau=T(\beta)}^{\infty}\frac{\exp(-s\tau)}{\sqrt{\tau^2-T^2(\beta)}}$$

$$\times\frac{(w_c\cos\theta-v_s^{-1})\sqrt{c_1^{-2}-w_c^2}\tilde{R}}{(w_c\cos\theta-v_s^{-1})^2+(\beta^2-1)(c_1^{-2}-w_c^2)\sin^2\theta}d\tau,$$

$$\text{with}\quad l=0,L_s. \tag{26}$$

By interchanging the order of integration we get an expression for the reflected acoustic body-wave from which we obtain the space–time domain counterpart by inspection according to

$$p_b^{\mathrm{refl}}(\mathbf{x},t;l)$$

$$=-\frac{FH(t-T(1))}{2\pi^2 v_s L_s}\mathrm{Re}\int_{\beta=1}^{\beta=B(t)}\frac{d\beta}{\sqrt{\beta^2-1}\sqrt{t^2-T^2(\beta)}}$$

$$\times\frac{(w_c\cos\theta-v_s^{-1})\sqrt{c_1^{-2}-w_c^2}\tilde{R}}{(w_c\cos\theta-v_s^{-1})^2+(\beta^2-1)(c_1^{-2}-w_c^2)\sin^2\theta},$$

$$\text{with}\quad l=0,L_s, \tag{27}$$

in which

$$B(t)=\frac{1}{a}\sqrt{\left(\frac{c_1 t}{r}\right)^2-1}. \tag{28}$$

In Eq. (27) w_c denotes $w_c(\tau,\beta)$ according to Eq. (24) with the upper sign. The head-wave associated with the reflected body-wave exists for β-values,

$$1<\beta<\beta^{\max}(a)$$

$$=\sqrt{\frac{1}{2}\left[\left(1-\frac{c_1^2}{c_2^2}\right)+\sqrt{\left(1-\frac{c_1^2}{c_2^2}\right)^2+\frac{4}{a^2}\left(1-\frac{c_1^2}{c_2^2}\right)}\right]}, \tag{29}$$

and since $\beta^{\max}(a)\geqslant 1$ we obtain from Eq. (29) the condition

$$a\leqslant\sqrt{c_2^2/c_1^2-1}. \tag{30}$$

Employing the appropriate parametrization along the real w-axis, see Eq. (23), we find for the integral along the loop around the branch cut of γ_2 in terms of τ

$$\hat{p}_{hb}^{\mathrm{refl}}(\mathbf{x},s;l)$$

$$=-\frac{F}{2\pi^2 v_s L_s}\int_{\beta=1}^{\beta=\beta^{\max}(a)}\frac{d\beta}{\sqrt{\beta^2-1}}\int_{\tau=\tau^{\min}(\beta)}^{T(\beta)}\Xi(\tau,\beta)$$

$$\times\exp(-s\tau)d\tau,\quad\text{with}\quad l=0,L_s, \tag{31}$$

in which

$$\tau^{\min}(\beta)=r\beta^{-1}\sqrt{c_2^{-2}+(\beta^2-1)c_1^{-2}}+ra\sqrt{c_1^{-2}-c_2^{-2}}, \tag{32}$$

$$\Xi(\tau,\beta)=\mathrm{Im}\left[\frac{(w_c\cos\theta-v_s^{-1})\sqrt{c_1^{-2}-w_c^2}\tilde{R}}{[(w_c\cos\theta-v_s^{-1})^2+(\beta^2-1)(c_1^{-2}-w_c^2)\sin^2\theta]\sqrt{T^2(\beta)-\tau^2}}\right]. \tag{33}$$

Then after interchanging the order of integration we find by inspection the following expression for the head-wave associated with the body wave in the space–time domain:

$$p_{hb}^{\mathrm{refl}}(\mathbf{x},t;l)=-\frac{F}{2\pi^2 v_s L_s}\left\{\int_{\beta=1}^{\beta=\beta_u(t)}\frac{d\beta}{\sqrt{\beta^2-1}}\Xi(t,\beta)[H(t-\tau^{\min}(1))-H(t-T(1))]\right.$$
$$\left.+\int_{\beta=B(t)}^{\beta=\beta_u(t)}\frac{d\beta}{\sqrt{\beta^2-1}}\Xi(t,\beta)[H(t-T(1))-H(t-\tau^{\max})]\right\},\quad \text{with } l=0,L_s, \tag{34}$$

in which

$$\tau^{\max}=rc_1^{-1}\sqrt{1+\frac{a^2}{2}\left[(1-c_1^2c_2^{-2})+\sqrt{(1-c_1^2c_2^{-2})^2+\frac{4}{a^2}(1-c_1^2c_2^{-2})}\right]}, \tag{35}$$

$$\beta_u(t)=\frac{r\sqrt{c_1^{-2}-c_2^{-2}}}{\sqrt{r^2c_1^{-2}-(t-ra\sqrt{c_1^{-2}-c_2^{-2}})^2}}. \tag{36}$$

The instantaneous head-wave front follows directly from $t=\tau^{\min}(1)$. The trailing edge of the head-wave follows from $t=\tau^{\max}$ as part of the parabola $r^2=c_1^2t^2-c_1t\sqrt{1-c_1^2c_2^{-2}}|x_3-h|$. This parabola crosses the body-wave front in the plane of the mirrored source and also there where the head-wave front touches the body-wave front. We note that the location of the head-wave front and the trailing edge are not dependent on θ. Concluding this section we also note that for $\theta=0$ the complex conjugate poles in Eq. (27) reduce to one pole on the real w-axis at $w_p=v_s^{-1}$ which may be encountered when we integrate along the branch cut of the branch point $w=c_2^{-1}$. In this case the integrals occurring in Eq. (34) must be interpreted as principal value integrals.

B. The reflected conical wave and the associated head-wave

From the basic expression Eq. (17) it is seen that the integrand has two complex conjugated poles in the complex w-plane which coincide on the real axis in the case $\theta=0$. In the process of contour deformation these poles could be encountered and their contributions should be taken into account. It turns out that these pole contributions represent the reflected conical wave contribution. In order to find these pole contributions we have to study the locations of the poles in the w-plane as a function of β and determine which poles have been encountered in the process of deformation of the Cagniard contour in the complex w-plane.

When $\theta\neq 0$ and

$$v_s^{-1}/\cos\,\theta<w_c(\beta=1,T)=c_1^{-1}/\sqrt{1+a^2}, \tag{37}$$

the complex conjugate poles w_p and w_p^* for increasing values of β move away from $w_p(\beta=1)=v_s^{-1}/\cos\theta$ towards the Cagniard–de Hoop path of Eq. (24). For a certain value $\beta=\beta_p$ the poles and the Cagniard path meet. This means that all the poles $w_p(\beta)$ and $w_p^*(\beta)$ with $1\leqslant\beta\leqslant\beta_p$ have to be taken into account since these poles are encountered in the process of contour deformation. The inequality of Eq. (37) in fact defines a conical part of space centered around the axis of motion $(x_1,0,h)$ of the mirrored source, with an apex at $(0,0,h)$ and the boundary surface $d_\perp/(x_1-l)=\sqrt{v_s^2c_1^{-2}-1}$ in which $d_\perp=r\sqrt{a^2+\sin^2\theta}$. Within this part of space, pole contributions from Eq. (17) can be expected. However, as part of the reflected field, only the pole results from points located in the upper half-space $(x_3<0)$ in this conical domain are physically significant. The poles that are encountered by the contour $w_c(\beta_p,\tau)$ between $\beta=1$ and $\beta=\beta_p$ are obtained from the denominator in Eq. (17) as

$$w_p(\beta)=\frac{\cos\theta}{v_s(1-\beta^2\sin^2\theta)}\pm i\frac{\sin^2\theta\sqrt{(\beta^2-1)[(v_s^2-c_1^2)v_s^{-2}\sin^{-2}\theta-\beta^2]}}{c_1(1-\beta^2\sin^2\theta)}$$
$$\text{with } 1\leqslant\beta\leqslant\beta_p\leqslant v_s^{-1}|\sin\theta|^{-1}\sqrt{v_s^2-c_1^2}. \tag{38}$$

By setting the denominator in Eq. (17) equal to zero for $w=w_p$ and solving for β^2-1 we find β in terms of w_p. In fact we find

$$\beta^2-1=-\frac{(w_p\,\cos\,\theta-v_s^{-1})^2}{\sin^2\,\theta(c_1^{-2}-w_p^2)}. \tag{39}$$

Using this result in the expressions for $\gamma_{1,2}(\beta)$ yields $\gamma_{1,2}(w_p)$ which no longer contains β. The contribution of the two conjugated poles in the complex w-plane is now found from Eq. (17) as

$$\hat{p}_c^{\mathrm{refl}}(\mathbf{x},s;l)=\frac{F}{2\pi v_s L_s}\int_0^{\sqrt{\beta_p^2-1}}\frac{du}{\sqrt{1+u^2}[\cos^2\,\theta-u^2\sin^2\,\theta]}\left[\frac{(w_p\,\cos\,\theta-v_s^{-1})\tilde{R}\exp[-sr(w_p+a\,\gamma_1(w_p))]}{2i\,\mathrm{Im}(w_p)}\right.$$
$$\left.+\frac{(w_p^*\,\cos\,\theta-v_s^{-1})\tilde{R}^*\exp[-sr(w_p^*+a\,\gamma_1(w_p^*))]}{2i\,\mathrm{Im}(w_p^*)}\right],\quad \text{with } l=0,L_s, \tag{40}$$

where $u=\sqrt{\beta^2-1}$ has been introduced for convenience. With the change of variable,

$$\overline{w}_p=(w_p-\cos\ \theta/v_s)/|\sin\ \theta|, \tag{41}$$

the vertical slownesses $\gamma_{1,2}(w_p)$ attain the canonical form

$$\gamma_{1,2}(\overline{w}_p)=\sqrt{c_{1,2}^{-2}-v_s^{-2}-\overline{w}_p^2}. \tag{42}$$

Consequently, after expressing Eq. (40) in terms of $\overline{w}_p$, we now can seek again a parametrization of $\overline{w}_p$ along a contour in the complex $\overline{w}_p$-plane in terms of some real and positive variable τ such that

$$r[\overline{w}_p|\sin\ \theta|+a\gamma_1(\overline{w}_p)]=\tau-\frac{r\ \cos\ \theta}{v_s}=\tau', \tag{43}$$

and strive to reshape Eq. (40) into the Laplace transform integral of Eq. (11). Solving Eq. (43) for $\overline{w}_p$ in terms of τ' yields

$$\overline{w}_{cp}(\tau')=\frac{|\sin\ \theta|}{r(\sin^2\ \theta+a^2)}\tau'-\frac{a}{r(\sin^2\ \theta+a^2)}\times\sqrt{(T_p')^2-(\tau')^2},\quad \text{when}\quad \tau'\leqslant T_p', \tag{44}$$

$$\overline{w}_{cp}(\tau')=\frac{|\sin\ \theta|}{r(\sin^2\ \theta+a^2)}\tau'\pm i\frac{a}{r(\sin^2\ \theta+a^2)}\times\sqrt{(\tau')^2-(T_p')^2},\quad \text{when}\quad \tau'>T_p', \tag{45}$$

in which

$$T_p'=r\sqrt{(a^2+\sin^2\ \theta)(c_1^{-2}-v_s^{-2})}. \tag{46}$$

From Eq. (39) we find, consistent with Eq. (45),

$$\sqrt{\beta^2-1}=\mp i\left[\frac{\overline{w}_{cp}\ \cos\ \theta-v_s^{-1}|\sin\ \theta|}{\sqrt{c_1^{-2}-(\overline{w}_{cp}|\sin\ \theta|+v_s^{-1}\ \cos\ \theta)^2}}\right],\quad \text{with}\ \ \mathrm{Re}\sqrt{\beta^2-1}\geqslant 0. \tag{47}$$

The Cagniard contour $\overline{w}_{cp}$ that results from the deformation of the pole path $\overline{w}_p$ is depicted in the $\overline{w}_p$-plane in Fig. 4 and Fig. 5.

The original and deformed pole paths are located on the right half of the complex $\overline{w}_p$-plane and both the end points of the original and deformed pole paths coincide. It appears that the horizontal closing paths of the deformed pole paths together only contribute for the part where the branchcut of $\gamma_2(\overline{w}_p)$ is present between $\overline{w}_p(1)$ and $\overline{w}_{cp}(T_p')$, see Fig. 4. This contribution represents the head-wave part of the reflected conical wave. In the case $c_1<v_s<c_2$ (Fig. 4) the pole $\overline{w}_p(1)$ is always located on the branchcut of $\gamma_2(\overline{w}_{cp})$, hence the horizontal closing paths in between $\overline{w}_p(1)$ and $\overline{w}_{cp}(T_p')$ contribute. In the case $c_1<c_2<v_s$ (Fig. 5) however, the pole $\overline{w}_p(1)$ may be located to the left or to the right of the branchpoint of $\gamma_2(\overline{w}_{cp})$ on the real $\overline{w}_p$-axis. When

$$\overline{w}_p(1)<s_2, \tag{48}$$

only the parts in between the branchpoint s_2 and $\overline{w}_{cp}(T_p')$ contribute, which implies that in this case,

$$s_2=\overline{w}_{cp}(\tau'_{\min}). \tag{49}$$

On the other hand when

$$s_2<\overline{w}_p(1)<\overline{w}_{cp}(T_p'), \tag{50}$$

the horizontal paths contribute in the complete range in between $\overline{w}_p(1)$ and $\overline{w}_{cp}(T_p')$, so now

$$\overline{w}_p(1)=\overline{w}_{cp}(\tau'_{\min}). \tag{51}$$

Consequently, in the case $c_1<c_2<v_s$ the separation of the sub-domains of space adhering to the cases Eq. (48) and Eq. (50) is found from

$$\overline{w}_p(1)=s_2 \tag{52}$$

We obtain from Eq. (52),

$$|\theta|=\arctan\sqrt{v_s^2c_2^{-2}-1}\overset{\text{def}}{=}\Psi. \tag{53}$$

The fronts of the head-waves associated with the reflected conical waves as defined in Eq. (49) and Eq. (51) can be expected to have different forms in the sub-domains $|\theta|<\Psi$ and $|\theta|>\Psi$, respectively.

The complementary hyperbolic part of the deformed pole paths in Figs. 4 and 5 represent the body-wave part of the reflected conical wave. The expression for $\tau'_{\max}$ can be found from the substitution of $\overline{w}_{cp}(\tau')$ in Eq. (39) and using the fact that $\overline{w}_p(\beta_{\max})$ does not take part in the process of deformation, so β is real there. Employing the appropriate parametrization of Eq. (45) or Eq. (44) in Eq. (40) using Eq. (47), we can rewrite the head-wave part and the body-wave part of the reflected conical pressure field as separate integrals with integration variable τ'. By inspection we then find for the reflected conical pressure $p_c^{\text{refl}}(\mathbf{x},t';l)$ with $t'=t-r\ \cos\ \theta/v_s$ and $l=0,L_s$, which is decomposed into a head wave part and a body wave part, respectively, according to $p_c^{\text{refl}}(\mathbf{x},t';l)=p_{hc}^{\text{refl}}(\mathbf{x},t';l)+p_{bc}^{\text{refl}}(\mathbf{x},t';l)$,

$$p_{hc}^{\text{refl}}(\mathbf{x},t';l)=\frac{F}{2\pi v_sL_s}\mathrm{Im}\left[\frac{\tilde{R}(\overline{w}_{cp})\Pi(\overline{w}_{cp})}{\sqrt{(T_p')^2-t'^2)}}\right]\times[H(t'-t'_{\min})-H(t'-T_p')], \tag{54}$$

$$p_{bc}^{\text{refl}}(\mathbf{x},t';l)=\frac{F}{2\pi v_sL_s}\mathrm{Re}\left[\frac{\tilde{R}(\overline{w}_{cp})\Pi(\overline{w}_{cp})}{\sqrt{t'^2-(T_p')^2)}}\right]\times[H(t'-T_p')-H(t'-t'_{\max})], \tag{55}$$

in which

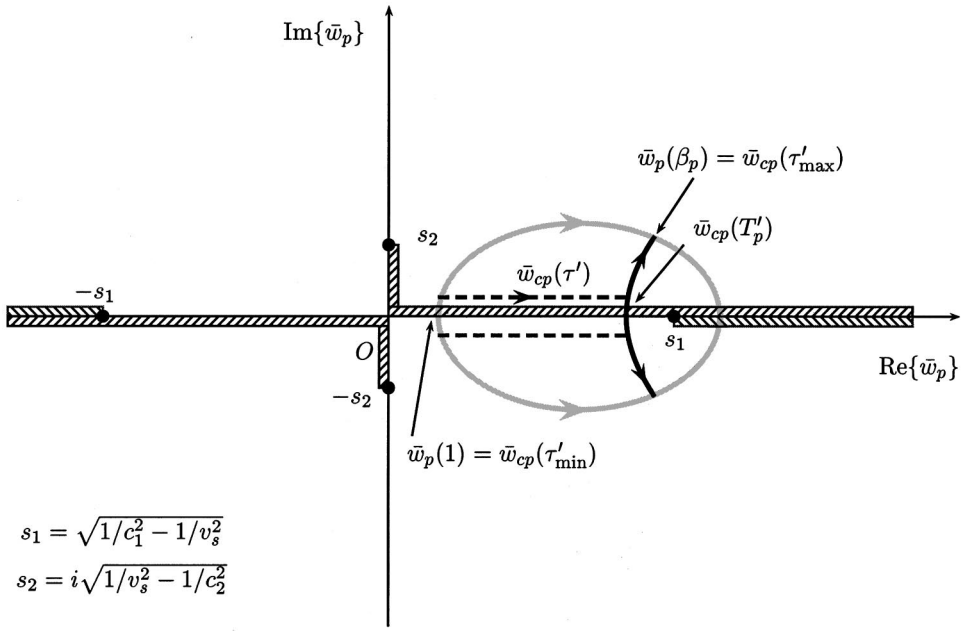

FIG. 4. The part of the pole path $\bar{w}_p(\beta)$ (plotted in gray) from $\beta=1$ to $\beta=\beta_p$ which is deformed into the plotted Cagniard contour $\bar{w}_{cp}$ in the complex $\bar{w}_p$-plane, when $c_1<v_s<c_2$.

$$\Pi(\bar{w}_{cp}) = \frac{(\bar{w}_{cp} - |\tan\theta|/v_s)[\gamma_1^2(\bar{w}_{cp}) + \bar{w}_{cp}(\bar{w}_{cp} - |\tan\theta|/v_s)]}{[\bar{w}_{cp} - t'|\sin\theta| r^{-1}(a^2+\sin^2\theta)^{-1}][\gamma_1^2(\bar{w}_{cp}) + (\bar{w}_{cp} - |\tan\theta|/v_s)^2]}, \tag{56}$$

with

$$t_{\max} = t'_{\max} + \frac{r\cos\theta}{v_s} = \frac{v_s r\cos\theta}{c_1^2}. \tag{57}$$

The minimum arrival time $t_{\min}$ when $c_1<v_s<c_2$ is obtained as

$$t_{\min} = t'_{\min} + \frac{r\cos\theta}{v_s} = \frac{r}{v_s\cos\theta} + ar\sqrt{c_1^{-2} - (v_s\cos\theta)^{-2}}, \tag{58}$$

and when $c_1<c_2<v_s$ obtained as

$$t_{\min} = t'_{\min} + \frac{r\cos\theta}{v_s} = r|\sin\theta|\sqrt{c_2^{-2} - v_s^{-2}} + ar\sqrt{c_1^{-2} - c_2^{-2}} + \frac{r\cos\theta}{v_s}, \quad \text{when } |\theta|<\Psi, \tag{59}$$

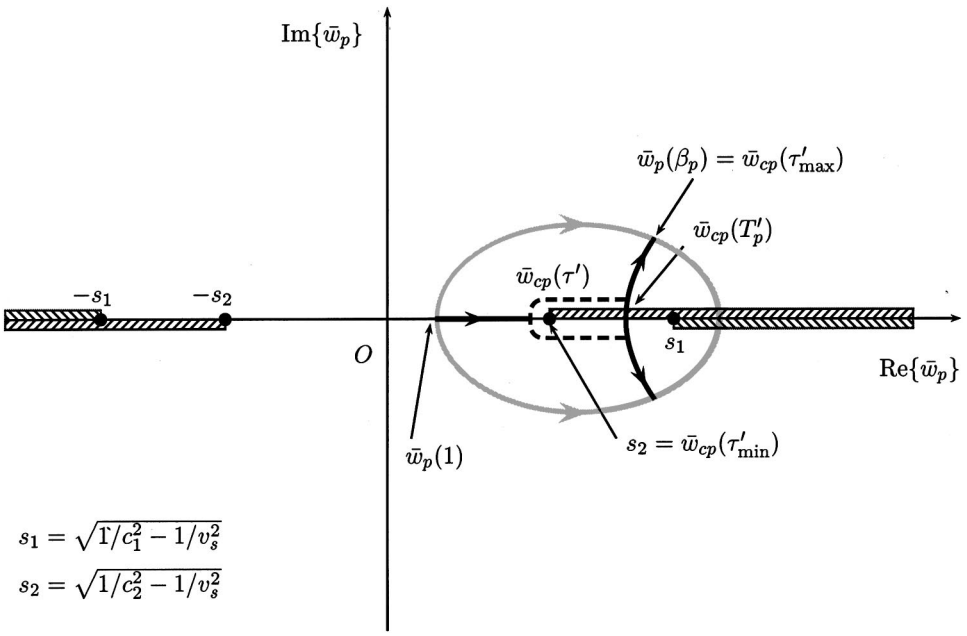

FIG. 5. The part of the pole path $\bar{w}_p(\beta)$ (plotted in gray) from $\beta=1$ to $\beta=\beta_p$ which is deformed into the plotted Cagniard contour $\bar{w}_{cp}$ in the complex $\bar{w}_p$-plane, when $c_1<c_2<v_s$ and $|\theta|<\Psi$.

$$t_{\min}=t'_{\min}+\frac{r\cos\theta}{v_s}$$

$$=\frac{r}{v_s\cos\theta}$$

$$+ar\sqrt{c_1^{-2}-(v_s\cos\theta)^{-2}},\quad \text{when } |\theta|>\Psi. \quad (60)$$

The symbol $\overline{w}_{cp}$ is defined by Eq. (44) in Eq. (54) and by Eq. (45) with the upper sign in Eq. (55), where τ' is replaced by t'. In the case $c_1<v_s<c_2$ the domain of space where the head-wave $p_{hc}^{\text{refl}}(\mathbf{x},t)$ can be encountered is determined by the condition

$$\overline{w}_p(1)<\overline{w}_{cp}(T'_p), \quad (61)$$

from which the following domain for θ is found:

$$0<|\theta|<\arctan\left(\sqrt{\frac{v_s^2}{c_1^2(1+a^2)}-1}\right), \quad (62)$$

pertaining to Eq. (58). In the case $c_1<c_2<v_s$ two subdomains can be defined where a headwave $p_{hc}^{\text{refl}}(x,t)$can be encountered. They follow from the following conditions:

$$\overline{w}_{cp}(T'_p)>\sqrt{c_2^{-2}-v_s^{-2}},\quad \text{when } |\theta|<\Psi, \quad (63)$$

$$\overline{w}_p(1)<\overline{w}_{cp}(T'_p),\quad \text{when } |\theta|>\Psi. \quad (64)$$

We obtain the domains

$$\arctan\left(\frac{a\sqrt{c_2^{-2}-v_s^{-2}}}{\sqrt{c_1^{-2}-c_2^{-2}-a^2(c_2^{-2}-v_s^{-2})}}\right)<|\theta|<\Psi, \quad (65)$$

pertaining to Eq. (59) and

$$\Psi<|\theta|<\arctan\left(\sqrt{\frac{v_s^2}{c_1^2(1+a^2)}-1}\right), \quad (66)$$

pertaining to Eq. (60), respectively. It appears that all boundaries in Eqs. (65)–(66) coincide when $a=\sqrt{c_2^2c_1^{-2}-1}$, so this value is the upper boundary for a. Obviously, to define the domain of the existence of the head-waves we have to add the inequality

$$\frac{h}{r}\leqslant a<\sqrt{c_2^2c_1^{-2}-1}, \quad (67)$$

as the interface $x_3=0$ determines the lower boundary of a.

VI. THE TRANSMITTED ACOUSTIC FIELD IN SPACE–TIME DOMAIN

In a similar way we can find space–time domain expressions for the transmitted acoustic pressure field. The analysis can be carried out along the same lines, however the Cagniard contours that occur in the complex w-plane and $\overline{w}_p$-plane are no longer hyperbola's but follow from a quartic equation. This quartic equation can be solved according to Kooij[9] with the aid of Cardano's formula. The corresponding contour has such a form that it can never intersect the branch cuts that occur along the real axis in the complex w-plane. Consequently, no head-waves are present in the transmitted field.

A. The transmitted body-wave

In the transformation back to the space–time domain we follow the same procedure as for the reflected body-wave. The Cagniard–de Hoop path in the complex w-plane now follows from the quartic equation:

$$\tau=rw+h\gamma_1(\beta)+x_3\gamma_2(\beta), \quad (68)$$

which is solved using Cardano's formula. Substitution of the parametrization of Eq. (68) in the expression for the transmitted field in Eq. (17) yields after interchanging the order of integration the space–time domain counterpart by inspection according to

$$p_b^{\text{trans}}(\mathbf{x},\tau;l)$$

$$=-\frac{FH(t-T_t(1))}{2\pi^2v_sL_s}\text{Im}\int_{\beta=1}^{\beta=Q(\tau)}\frac{d\beta}{\sqrt{\beta^2-1}}$$

$$\times\frac{\tilde{T}(w_c\cos\theta-v_s^{-1})\partial_\tau w_c}{(w_c\cos\theta-v_s^{-1})^2+(\beta^2-1)(c_1^{-2}-w_c^2)\sin^2\theta},$$

$$\text{with } l=0,L_s, \quad (69)$$

in which w_c is the solution of the parametrization in Eq. (68). The point $w=w_0$ on the real w-axis in between 0 and the nearest branchpoint is the point where the Cagniard contour leaves the real w-axis. This point is found by differentiating Eq. (68) with respect to w which yields

$$r-w\left[\frac{h}{\gamma_1(\beta)}+\frac{x_3}{\gamma_2(\beta)}\right]=0,\quad \text{at } w=w_0. \quad (70)$$

From the numerically obtained function $w_0(\beta)$ the corresponding parametrized time $T_t(\beta)$ is found via Eq. (68) as $T_t(\beta)=rw_0+h\gamma_1(\beta,w_0)+x_3\gamma_2(\beta,w_0)$. The function $Q(\tau)$ is found by solving $\tau=T_t(\beta)$ for β, numerically.

B. The transmitted conical wave

In a similar way as for the reflected field the poles that are present in the denominator of the expression for the transmitted body-wave can be encountered in the process of contour deformation in the complex w-plane. In the transonic situation ($c_1<v_s<c_2$) the poles that are encountered represent a certain pole path from $\beta=\beta_{\min}$ to $\beta=\beta_{\max}$ in the complex w_p-plane. With increasing depth x_3 below the interface $x_3=0$ this range of β reduces to zero. Hence, pole contributions in the transmitted field in this case will only be present within an upper part of the lower medium. We note moreover that in this case the pole contributions are drowned in the transmitted spherical body wave. In the supersonic situation ($c_1<c_2<v_s$) the poles encountered represent a pole path from $\beta=1$ to $\beta=\beta_{\max}$ and represent a transmitted conical wave that is precursive to the transmitted spherical

body-wave. This pole path is again transformed to a Cagniard–de Hoop path in the complex $\overline{w}_p$-plane which satisfies the relation

$$\tau' = \tau - \frac{r\cos\theta}{v_s} = r|\sin\theta|\overline{w}_p + h\sqrt{c_1^{-2} - v_s^{-2} - \overline{w}_p^2} + x_3\sqrt{c_2^{-2} - v_s^{-2} - \overline{w}_p^2}, \tag{71}$$

where τ' is real and positive. The end points $\overline{w}_p(\beta_{\min})$ and $\overline{w}_p(\beta_{\max})$ of the pole path are found numerically and do not take part in the process of deformation. They remain fixed as these points satisfy Eq. (68). The τ' values $\tau'_{\min}$ and $\tau'_{\max}$ that are associated with these endpoints are found then numerically using the fact that $\beta(\tau')$ is real at $\tau' = \tau'_{\min}$ and $\tau' = \tau'_{\max}$. Carrying out the parametrization of Eq. (71) in the complex $\overline{w}_p$-plane we obtain the following space–time domain expression for the transmitted conical field by inspection, with $t' = t - r\cos\theta/v_s$,

$$p_{bc}^{\text{trans}}(\mathbf{x},t';l) = -\frac{F[H(t'-t'_{\min}) - H(t'-t'_{\max})]}{2\pi v_s L_s}\,\text{Re}\left\{\frac{(\overline{w}_{cp} - |\tan\theta|v_s^{-1})[\gamma_1^2 + \overline{w}_{cp}(\overline{w}_{cp} - |\tan\theta|v_s^{-1})]\tilde{T}\partial_t\overline{w}_{cp}}{\text{Im}(\overline{w}_{cp})[(\overline{w}_{cp} - |\tan\theta|v_s^{-1})^2 + \gamma_1^2]\gamma_1}\right\},$$
$$\text{with } l = 0, L_s, \tag{72}$$

where $\overline{w}_{cp}$ is the numerical solution of Eq. (71) with τ' replaced by t'. Further, we have in Eq. (72) $t'_{\min} = t_{\min} - r\cos\theta/v_s$ and $t'_{\max} = t_{\max} - r\cos\theta/v_s$.

VII. NUMERICAL RESULTS

The numerical example we present in this section is an air/water interface according to Fig. 1 in which $\rho_1 = 1.3$ kg/m^3, $c_1 = 328$ m/s and $\rho_2 = 1000$ kg/m^3, $c_2 = 1500$ m/s. In this numerical example we assume that the source, which is an object of length $L_s = 30$ m and zero thickness, travels at $h = 8000$ m above the interface with a supersonic constant speed $v_s = 400$ m/s. The traveling speed v_s is in this case in between the wavespeeds of the two media, i.e., $c_1 < v_s < c_2$, and will be referred to as a transonic state. In this transonic state we will have a conical wave in the air that will be reflected and transmitted at the interface at $x_3 = 0$. In Fig. 6 we present a snapshot at $t = 480$ s of the reflected conical acoustic pressure field at 2 m above the air/water interface, observed in the first quadrant of the horizontal x_1-, x_2-plane covering an area of 160 km by 160 km. In this area the field is calculated in a 200 by 200 grid of equally spaced datapoints.

The amplitudes of the pressure field in Fig. 6 have been limited to values of $\pm 10^{-6}$ Pa since the amplitude at the time of arrival of the wave front has infinite amplitude due to the root singularity in the expression for the reflected conical pressure field. In Fig. 7 we have limited the amplitude of the acoustic pressure even more in order to observe the lower field amplitudes, wave front and trailing edge more clearly.

The gray bow shaped area in Figs. 6 and 7 represents the head-wave part of the reflected conical wave. Further, it is observed from Fig. 6 and Fig. 7 that the head-wave part has an amplitude that is much smaller than the bodywave part of the reflected conical pressure field. In Fig. 8 we have depicted the transmitted conical pressure field at 2 m below the interface.

The shapes of the wave fronts and the trailing edges in Fig. 8 seem to be different from the reflected conical wave,

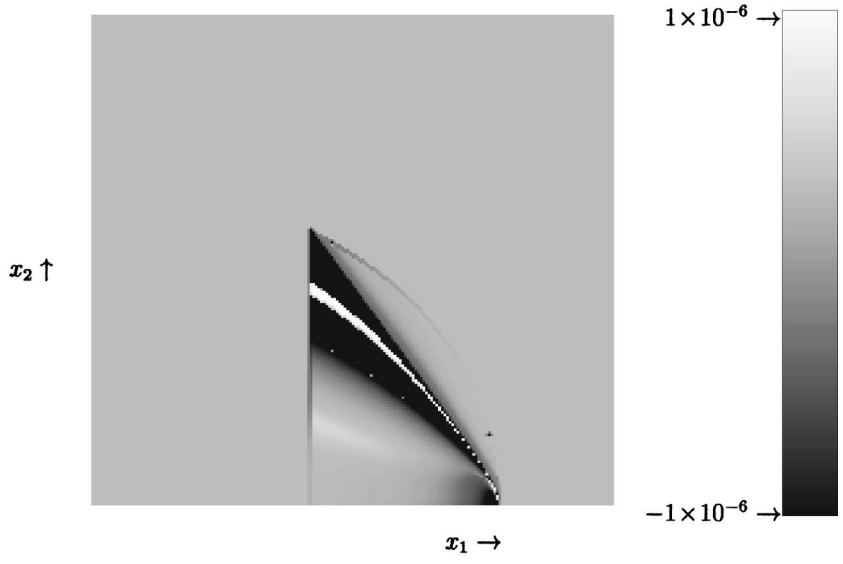

FIG. 6. Snapshot in a horizontal x_1-, x_2-plane of the reflected conical pressure field with $v_s = 400$ m/s, recorded at $x_3 = -2$ m, $t = 480$ s and the pressure field limited to $\pm 10^{-6}$ Pa.

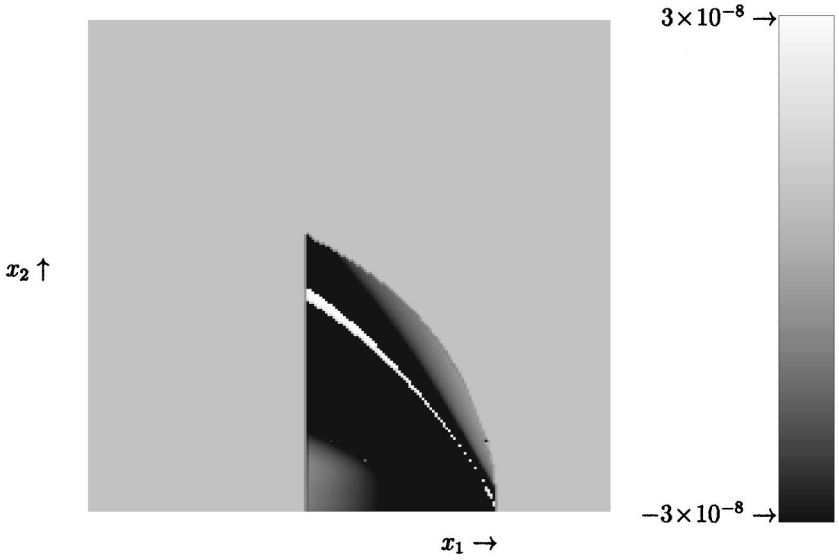

FIG. 7. Snapshot in a horizontal x_1-, x_2-plane of the reflected conical pressure field with $v_s=400$ m/s, recorded at $x_3=-2$ m, $t=480$ s and the pressure field limited to $\pm3\times10^{-8}$ Pa.

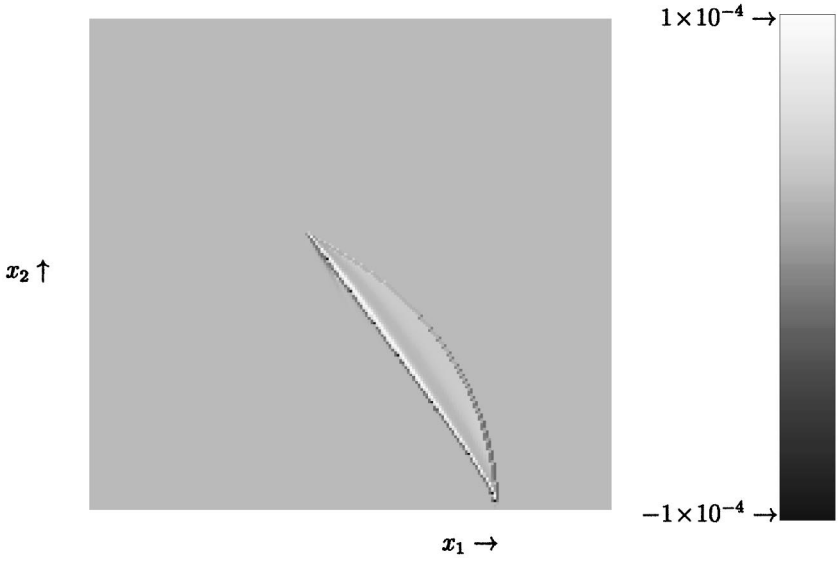

FIG. 8. Snapshot in a horizontal x_1-, x_2-plane of the transmitted conical pressure field with $v_s=400$ m/s, recorded at $x_3=2$ m, $t=480$ s and the pressure field limited to $\pm10^{-4}$ Pa.

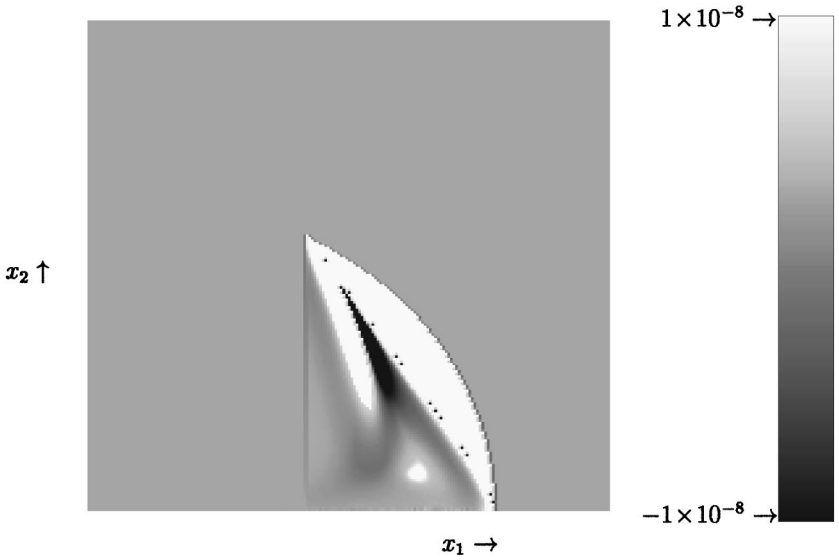

FIG. 9. Snapshot in a horizontal x_1-, x_2-plane of the transmitted conical pressure field with $v_s=400$ m/s, recorded at $x_3=2$ m, $t=480$ s and the pressure field limited to $\pm10^{-8}$ Pa.

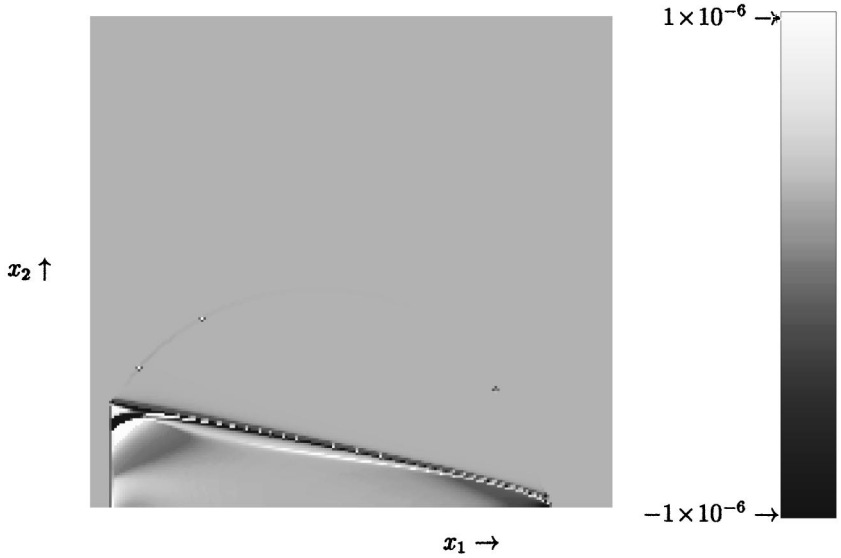

FIG. 10. Snapshot in a horizontal x_1-, x_2-plane of the reflected conical pressure field with $v_s=1640$ m/s, recorded at $x_3=-2$ m, $t=110$ s and the pressure field limited to $\pm10^{-6}$ Pa.

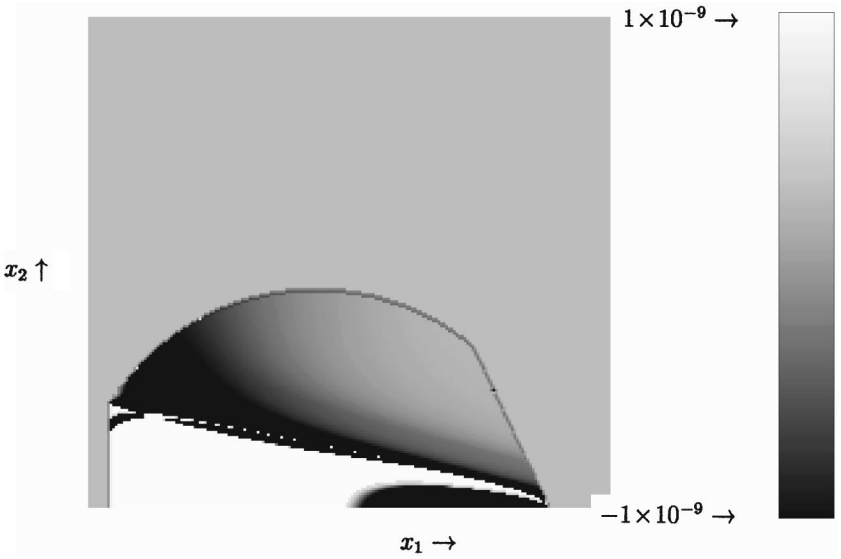

FIG. 11. Snapshot in a horizontal x_1-, x_2-plane of the reflected conical pressure field with $v_s=1640$ m/s, recorded at $x_3=-2$ m, $t=110$ s and the pressure field limited to $\pm10^{-9}$ Pa.

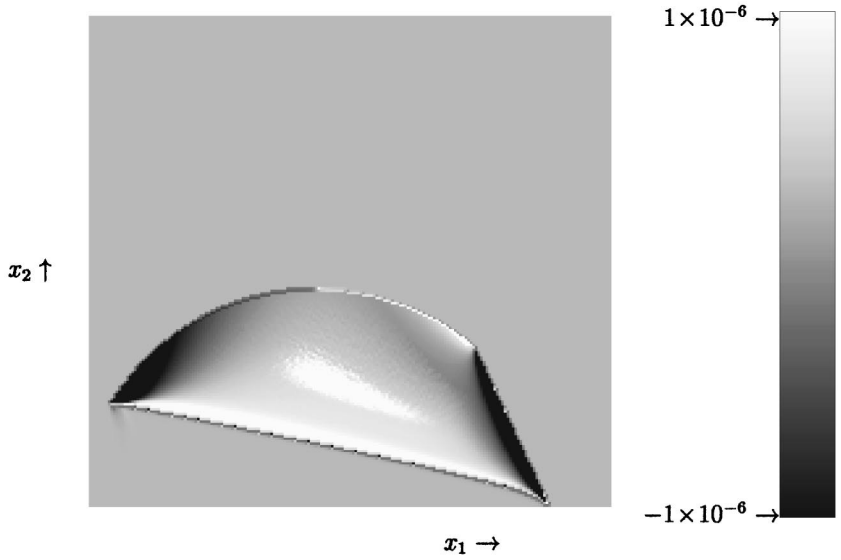

FIG. 12. Snapshot in a horizontal x_1-, x_2-plane of the transmitted conical pressure field with $v_s=1640$ m/s, recorded at $x_3=2$ m, $t=110$ s and the pressure field limited to $\pm10^{-6}$ Pa.

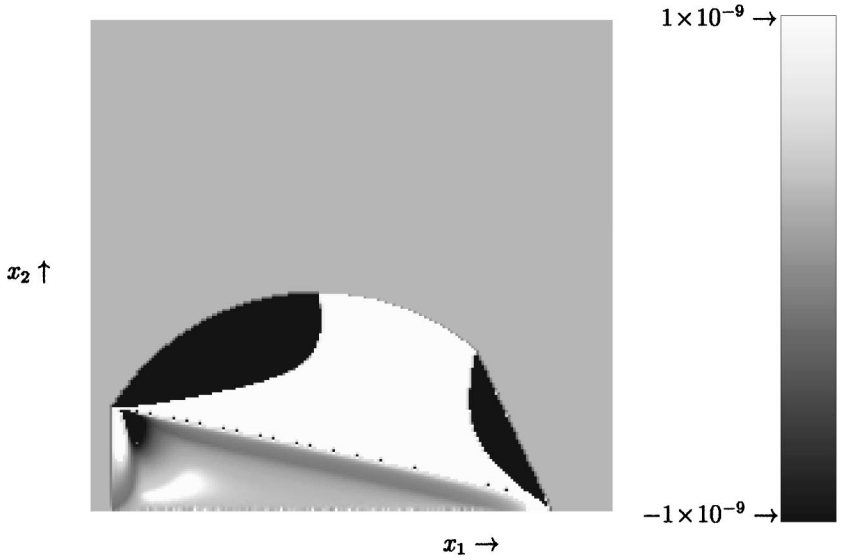

FIG. 13. Snapshot in a horizontal x_1-, x_2-plane of the transmitted conical pressure field with $v_s=1640$ m/s, recorded at $x_3=2$ m, $t=110$ s and the pressure field limited to $\pm10^{-9}$ Pa.

however if we limit the amplitude of the field to $\pm10^{-8}$ Pa we see in Fig. 9 that the wave front and trailing edge have the same shape.

In contrast with Figs. 6 and 7 the amplitude of the bow shaped part, which is here part of the transmitted conical body-wave, is now much larger than the amplitude of the complementary part. It must be remarked again that this transmitted conical field is not precursive; in fact it is drowned in the transmitted body-wave field.

In the next numerical example we assume that the source, which is an object of length $L_s=30$ m and zero thickness, travels at $h=8000$ m above the interface with a supersonic constant speed $v_s=1640$ m/s (MACH 5). The traveling speed v_s is in this case larger then the wavespeeds of the two media, i.e., $c_1<c_2<v_s$, and will be referred to as a supersonic state. In this supersonic state we will have a conical wave in the air that will be reflected and transmitted at the interface at $x_3=0$. In Fig. 10 we present a snapshot at $t=110$ s of the reflected conical acoustic pressure field at 2 m above the air/water interface, observed in the first quadrant of the horizontal x_1-, x_2-plane covering an area of 160 km by 160 km. In this area the field is calculated in a 200 by 200 grid of equally spaced datapoints.

As before, Figs. 10 and 11 show the situation for two different levels of limitation of the pressure field.

The area inside the deformed bow represents the head-wave part of the reflected conical wave. The right-hand side of the head-wave front is shaped as a wedge. This is the situation described in Sec. IV in connection with Eqs. (52) and (53). The transition point between the bow shaped and wedge shaped part correspond with $\theta=\Psi$, while the wedge shape and the bow shape of the head-wave front follow from Eqs. (59) and (60), respectively. Further, it is observed from Fig. 10 and Fig. 11 that the head-wave part has an amplitude that is much smaller than the body-wave part of the reflected conical pressure field. In Figs. 12 and 13 we have depicted the transmitted conical pressure field at 2 m below the interface for two different limitations of the amplitude level.

The amplitude of the deformed bow shaped part, which is now part of the transmitted conical body-wave, is now much larger than the amplitude of the complementary part.

[1] A. T. de Hoop and J. H. M. T. van der Hijden, ''Generation of acoustic waves by an impulsive point source in a fluid/solid configuration with a plane boundary,'' J. Acoust. Soc. Am. **75**, 1709–1715 (1984).
[2] A. T. de Hoop and H. J. Frankena, ''Radiation of pulses generated by a vertical dipole above a plane non-conducting Earth,'' Appl. Sci. Res., Sect. B **8**, 369–377 (1960).
[3] D. C. Gakenheimer and J. Miklowitz, ''Transient excitation of an elastic half-space by a point load traveling on the surface,'' J. Appl. Mech. **36**, 505 (1969).
[4] T. C. Kennedy and G. Herrmann, ''Moving load on a fluid-solid interface: Supersonic region,'' J. Appl. Mech. **40**, 137–142 (1973).
[5] T. C. Kennedy and G. Herrmann, ''The response of a fluid–solid interface to a moving disturbance,'' J. Appl. Mech. **41**, 287–288 (1974).
[6] M. C. M. Bakker, M. D. Verweij, B. J. Kooij, and H. A. Dieterman, ''The traveling point load revisited,'' Wave Motion **29**, 119–135 (1999).
[7] L. B. Freund, ''The response of an elastic solid to nonuniformly moving surface loads,'' J. Appl. Mech. **40**, 699 (1973).
[8] K. Watanabe, ''Transient response of an acoustic half-space to a rotating point load,'' Quarterly Appl. Math. **36**, 39 (1978).
[9] B. J. Kooij, ''Analysis of transient electromagnetic fields in an electrical utility substation environment,'' Ph.D. thesis, Delft University, Delft, The Netherlands, 1994.
[10] D. S. Jones, *The Theory of Electromagnetism* (Pergamon, Oxford, 1964).

Theory of frequency dependent acoustics in patchy-saturated porous media

David Linton Johnson[a)]
Schlumberger-Doll Research, Old Quarry Road, Ridgefield, Connecticut 06877-4108

(Received 5 December 2000; revised 15 April 2001; accepted 23 April 2001)

The theory of the dynamic bulk modulus, $\tilde{K}(\omega)$, of a porous rock, whose saturation occurs in patches of 100% saturation each of two different fluids, is developed within the context of the quasi-static Biot theory. The theory describes the crossover from the Biot–Gassmann–Woods result at low frequencies to the Biot–Gassmann–Hill result at high. Exact results for the approach to the low and the high frequency limits are derived. A simple closed-form analytic model based on these exact results, as well as on the properties of $\tilde{K}(\omega)$ extended to the complex ω-plane, is presented. Comparison against the exact solution in simple geometries for the case of a gas and water saturated rock demonstrates that the analytic theory is extremely accurate over the entire frequency range. Aside from the usual parameters of the Biot theory, the model has two geometrical parameters, one of which is the specific surface area, S/V, of the patches. In the special case that one of the fluids is a gas, the second parameter is a different, but also simple, measure of the patch size of the stiff fluid. The theory, in conjunction with relevant experiments, would allow one to deduce information about the sizes and shapes of the patches or, conversely, to make an accurate sonic-to-seismic conversion if the size and saturation values are approximately known. © *2001 Acoustical Society of America.* [DOI: 10.1121/1.1381021]

PACS numbers: 43.20.Jr [DEC]

I. INTRODUCTION

The Biot theory is the appropriate starting point for the analysis of acoustics in fluid-saturated porous and permeable media, although many real materials, such as sedimentary rocks, certainly do have other, additional operative mechanisms. The theory does, however, work well in the sense that it is usually able to predict the speeds of sound of a saturated sample if the dry speeds are measured and the fluid properties are known. A possible exception occurs when a sample is partially saturated with two very different fluids, such as a gas and a liquid which shall be called ''water'' here. On the one hand, the argument is that the effective modulus of the pore fluid is given by Wood's law, K_W, which is exact for the static compressibility of a two-fluid mixture. The use of K_W in the Biot–Gassmann equations then makes a prediction about the saturation dependence of both compressional and shear speeds. This was most convincingly demonstrated by Murphy (1984) and subsequently by Mavko and Mukerji (1998). On the other hand, if one of the two fluids is a gas this Biot–Gassmann–Woods (BGW) theory predicts that there is a very abrupt change in the compressional modulus when only a very small gas saturation is introduced; essentially the compressional modulus is either the dry value or the fully saturated value and it is very unlikely to lie in between the two limits. This feature is seriously questioned by the acoustic logging data of Brie *et al.* (1995) who showed that there is a continuum of measured speeds ranging from the dry to the saturated values.

A possible way out had been suggested by White (1975) and White *et al.* (1976) who showed that if the acoustic sample is 100% saturated with water in some regions (''patches''), and 100% saturated with gas in others, then the BGW limit holds only if the frequency is so low that the pore pressure has time to equilibrate between the two phases. [In point of fact, this last low frequency limiting feature was pointed out by Dutta and Odé (1979a, b) and Dutta and Seriff (1979c) who corrected several mistakes in the original White papers.] This equilibration process is governed by the so-called Biot acoustic slow wave, a diffusive phenomenon in which the diffusivity depends upon the permeability of the sample, the viscosity of the fluid, etc. Norris (1993) pointed out that the high frequency limit of this process is a situation in which the shear modulus is globally constant and the bulk modulus is piecewise constant within each patch. Thus within each patch the bulk modulus is given by the Biot–Gassmann equation evaluated with respect to the saturating fluid within that patch. Within the context of ordinary elasticity theory, when the shear modulus is everywhere constant, Hill's theorem [Hill (1963, 1964)] gives the exact result for the resulting effective modulus for the composite. This Biot–Gassmann–Hill (BGH) result for the effective bulk modulus is much more smoothly varying as a function of gas saturation than is the BGW theory. Dvorkin *et al.* (1999) showed, in fact, that BGH, considered as a function of saturation, is numerically very similar to the empirical formula proposed by Brie *et al.* (1995). Finally, a number of authors have shown experimentally that it is possible to see either BGW or BGH behavior, depending upon the saturation protocol and the measurement frequency [Mavko and Nolen-Hoeksema (1994); Knight *et al.* (1998); Cadoret *et al.* (1995, 1998); Mavko and Mukerji (1998)]. To be sure, not all of these authors give the same interpretation to the underlying physical phenomenon as I do here, although all of them do

a)Electronic mail: thesound@ridgefield.sdr.slb.com

 0001-4966/2001/110(2)/682/13/$18.00

see a dramatic difference in acoustic properties, depending upon saturation technique and/or frequency.

The crossover frequency between BGW and BGH scales roughly as $\omega_c \sim D/L^2$, where D is the slow wave diffusivity [cf. Eq. (9) (below)] in the region with the ''harder'' fluid (water), and L is the ''size'' of the patch for that fluid. The goal of this article is to present a simple theory of the frequency dependence of that crossover, which depends upon only two parameters reflective of the patch geometry. It is presumed that the frequency is always low compared to two different crossover frequencies, ω_B, the Biot frequency, and ω_x, the frequency at which the wavelengths become comparable to the size of the patches.

One of the parameters in the theory is simply the specific area of the boundary surface between the two patches (the ratio of the surface area to the sample volume). Therefore, one could in principle determine the sizes of the patches by means of the observed frequency dependence of the acoustic speeds and attenuations. These two parameters appear in the exact results for the approach to the aforementioned high and low frequency limits, which are discussed in the next section. The general features of the crossover behavior, including the low and high frequency limits, are illustrated with two simple, specific geometries, the concentric spheres and the periodic slab geometries, in Sec. III. The simple model for $\tilde{K}(\omega)$ respects these low and high frequency limits as well as other, general properties of the exact result, considered as a function of complex-valued frequency. It is described in Sec. IV.

In Sec. V the model is used in conjunction with the Pochhammer–Cree equation to investigate the dispersion and attenuation of extensional modes in a fully saturated cylinder. Comparison is made against calculations done with the full Biot theory in that geometry. This allows one to validate the use of the theory in the frequency range around ω_c as well as to see its breakdown as one crosses ω_x and ω_B. The paper is summarized in Sec. VI where it is indicated how one might use this model in a practical sense to extract information about the size and shape of the patches. As far as I am aware, there is no other existing technique for doing so except, perhaps, in the case that a gas patch is so large it may be detected as a ''bright spot'' in seismic reflections.

It is understood that other mechanisms, such as the microscopic ''squirt'' mechanisms [Mavko and Nur (1979); Murphy *et al.* (1986)], may well dominate the effects considered here. It is known that the squirt mechanism in sandstone is greatly reduced if there is a nominal confining stress on the sample which closes all the cracks. It is also known that acoustic speeds in carbonate rocks are generally less sensitive to applied pressure [Anselmetti and Eberli (1993); Winkler and Liu (1996)], which implies that carbonate rocks have fewer ''cracks'' to close than do sandstones. Therefore, the dominant mechanism for *in situ*, partially saturated rocks may well be the patchy saturation effect. In any event, this is the exclusive focus of the present manuscript. Even within the context of patchy saturation, it may well be the case that the wetting fluid preferentially saturates regions of small pores, because of capillary effects [Goertz and Knight (1998)]. This effect is also not considered in the present manuscript. Rather, the porous medium is assumed to be everywhere homogeneous, except for the saturating fluid.

II. THEORY

A. General considerations

Consider, then, a porous and permeable solid, which we presume to be describable by the Biot equations. It is saturated with two different Newtonian fluids, having saturations S_1 and $S_2 = 1 - S_1$; at any point in the sample it is saturated 100% either with the one fluid or the other. Within the context of the Biot theory we consider the response of the sample to a uniform compressive stress, applied at a finite frequency. We presume that this frequency is low enough that throughout the sample the Biot theory is everywhere in its low frequency limit. Thus the fast compressional and shear waves are nondispersive and nonattenuating whereas the slow compressional wave is diffusive in character. The starting equations are essentially those of Biot (1956):

$$0 = \nabla \cdot \boldsymbol{\tau}, \tag{1}$$

$$\phi\left(\frac{\partial \mathbf{U}}{\partial t} - \frac{\partial \mathbf{u}}{\partial t}\right) = -\frac{k}{\eta}\nabla p_f. \tag{2}$$

Here, the tensor $\boldsymbol{\tau}$ represents the total stress (solid plus fluid phases), p_f is the pore pressure, $\mathbf{u}(\mathbf{U})$ is the displacement of the solid (fluid) phase, ϕ is the porosity, k is the permeability, and η is the fluid viscosity. $\boldsymbol{\tau}$ and p_f are related to the strains in the fluid, E_{ij}, and solid, ϵ_{ij}, phases in the usual manner [Biot (1956)]:

$$\boldsymbol{\tau} = [(P+Q-2N)\epsilon_{ll} + (R+Q)E_{ll}]\delta_{ij} + 2N\epsilon_{ij}, \tag{3}$$

$$p_f = -\frac{1}{\phi}[RE_{ll} + Q\epsilon_{ll}]. \tag{4}$$

Explicit expressions for P, Q, and R in terms of K_s, the bulk modulus of the solid phase, K_b, the bulk modulus of the porous skeleton, and K_f the bulk modulus of the pore fluid, are given by Biot and Willis (1957) in somewhat awkward form; they are also given in Johnson (1986):

$$P = \frac{(1-\phi)[1-\phi-K_b/K_s]K_s + \phi(K_s/K_f)K_b}{1-\phi-K_b/K_s+\phi K_s/K_f} + \frac{4}{3}N,$$

$$Q = \frac{(1-\phi-K_b/K_s)\phi K_s}{1-\phi-K_b/K_s+\phi K_s/K_f}, \tag{5}$$

$$R = \frac{\phi^2 K_s}{1-\phi-K_b/K_s+\phi K_s/K_f}.$$

N is the shear modulus of the skeleton frame. Written in this way, continuity of $\boldsymbol{\tau}\cdot\hat{\mathbf{n}}$, p_f, $\mathbf{u}$, and $\mathbf{U}\cdot\hat{\mathbf{n}}$ are guaranteed by Eqs. (1) and (2) even if the fluid properties are discontinuous across a surface whose outward normal is $\hat{\mathbf{n}}$.

Equations (1) and (2) follow from the full Biot equations simply by setting to zero all inertial terms and by taking the dynamic permeability, $\tilde{k}(\omega)$, equal to its dc value, k; this is essentially the approach employed by Norris (1993). Dutta and Odé (1979a, b) also explicitly showed that this approach gives the same results as the full Biot theory as long as the

frequency is low enough. The requirement is $\omega \ll \omega_B$ where the Biot crossover frequency is expressible in terms of the fluid density, ρ_f, and the tortuosity of the pore space, α_∞ as

$$\omega_B = \frac{\eta\phi}{k\rho_f\alpha_\infty}, \tag{6}$$

using the notation of Johnson *et al.* (1994).

In a homogeneously saturated medium the ''normal mode'' solutions of Eqs. (1) and (2) are as follows: (a) There are solutions in which the fluid and solid are locked together, $\mathbf{u}=\mathbf{U}$, and the total stress is related to their (mutually equal) strain by the usual equations of isotropic elasticity: $\tau_{ij} = K_{\mathrm{BG}}\epsilon_{ll}\delta_{ij} + 2N(\epsilon_{ij} - (1/3)\epsilon_{ll}\delta_{ij})$. Here, N is the shear modulus of the porous skeleton and $K_{\mathrm{BG}} \equiv P + 2Q + R - (4/3)N$ is the Biot–Gassmann result for the compressive modulus:

$$K_{\mathrm{BG}}(K_f) = \frac{K_s + [\phi(K_s/K_f) - \phi - 1]K_b}{1 - \phi - (K_b/K_s) + \phi(K_s/K_f)}. \tag{7}$$

The dependence of K_{BG} on K_f is emphasized for later use.

(b) There are also solutions to Eqs. (1) and (2) in which the fluid and solid are not locked together and all relevant quantities obey a diffusion equation with a diffusivity given by:

$$D(K_f) = \frac{k}{\eta\phi^2}\frac{PR - Q^2}{P + 2Q + R}, \tag{8}$$

where an explicit expression for D and limiting behaviors thereof are given in Chandler and Johnson (1981):

$$D(K_f) = \frac{kK_f}{\eta\phi}\left(1 + \frac{K_f}{\phi(K_b + (4/3)N)}\left\{1 + \frac{1}{K_s}\left[\frac{4}{3}N\left(1 - \frac{K_b}{K_s}\right) - K_b - \phi\left(K_b + \frac{4}{3}N\right)\right]\right\}\right)^{-1}. \tag{9}$$

Were the medium to be homogeneously saturated with a single fluid, these equations, taken literally, imply that compressional and shear waves should propagate unattenuated with speeds given by

$$V_p = \sqrt{[K_{\mathrm{BG}} + (4/3)N]/\rho} \tag{10}$$

and

$$V_{\mathrm{sh}} = \sqrt{N/\rho}, \tag{11}$$

respectively. (ρ is the total density.) The neglected terms in the full Biot equations predict, among other things, that the compressional and shear modes are dispersive and possess attenuation; these effects are explicitly neglected in this article as compared against those induced by patchy saturation.

If saturation of the sample occurs in patches, however, in which two different fluids occupy different regions then, at any instance of time, the wave-induced pore pressure in the one fluid will be different from that in the other. The pressures will try to equilibrate via the diffusive mechanism mentioned above. All relevant quantities will vary continuously from point to point. There is a crossover frequency which is determined by the time it takes a pressure wave to diffuse across a characteristic patch size. This claim can be made more precise, as follows.

It is assumed that although the saturation occurs in patches, there is a size scale, large compared to the patches, but small compared to a relevant acoustic wavelength, over which the sample is statistically homogeneous from one such region to the next. What are the elastic properties of such a region? Consider a characteristic volume element and imagine *either* that it is periodically repeated throughout space *or* that the external boundary is sealed against flow. In either case, the condition

$$\int [\mathbf{u} - \mathbf{U}]\cdot\hat{\mathbf{n}}\, dS = 0 \tag{12}$$

holds true on the bounding surface. The sample is subjected to an oscillatory external normal stress, $\boldsymbol{\tau}\cdot\hat{\mathbf{n}} = -P_e\hat{\mathbf{n}}e^{-i\omega t}$, which is spatially uniform over the bounding surface and this induces an oscillatory change in the sample volume, $\delta V e^{-i\omega t}$. The relevant question is: What is the effective bulk modulus, $\tilde{K}(\omega) = -V(P_e/\delta V)$, of the sample? In general, the answer to this question depends upon the spatial distribution of the two fluids, but there are simple, exact results which apply to the high and low frequency limits.

This question makes sense only if the frequency is low enough that the wavelengths of the fast compressional and shear waves are large compared to the dimensions of the patches. That is, in addition to $\omega \ll \omega_B$ as discussed above, the condition $\omega \ll \omega_x$ should hold where

$$\omega_x \sim V_{\mathrm{sh}}/L. \tag{13}$$

V_{sh} is the speed of the slower shear wave in the two patches and L is a characteristic patch dimension. The theory presented here presupposes, then, that $\omega_c \ll (\omega_B, \omega_x)$ so that one can investigate the crossover region from $\omega \ll \omega_c$ to $\omega \gg \omega_c$ while maintaining the validity of the two quasistatic assumptions $\omega \ll (\omega_B, \omega_x)$. Let us, therefore, consider the low frequency and high frequency limits of Eqs. (1) and (2) with the understanding that the frequency is never so high as to violate the quasistatic assumption. Depending on the values of the parameters in the problem, of course, it is possible that there may be no window of validity for this quasi-static approximation. In Sec. III I will discuss a specific example of a geometry in which ω_c, ω_x, and ω_B are readily apparent. To the extent that the physics can accurately be described by Eqs. (1) and (2) it is clear that $\tilde{K}(\omega)$ is a scaled function of the combination $\omega L^2/k$, where L is an overall size factor [Dutta and Odé (1979a, b)]. Thus the results presented in this article can be rescaled for different permeabilities and different overall sizes.

B. Low frequency limit

If the frequency is low enough, then during each half cycle of oscillation the fluid in the pore space is able to equilibrate at a common value. The effective modulus of the pore fluid is given by Wood's law, K_W, which is exact for the static modulus of two liquids:

$$\frac{1}{K_W} = \frac{S_1}{K_{f1}} + \frac{S_2}{K_{f2}}, \tag{14}$$

TABLE I. Values of input parameters for the calculation of patchy saturation effects.

ϕ	0.284
K_s	35 GPa
K_b	2.637 GPa
N	1.740 GPa
k	$10^{-13}\,\mathrm{m}^2$
K_f (water)	2.25 GPa
η (water)	10^{-3} Pa s
K_f (gas)	10^5 Pa
η (gas)	10^{-5} Pa s

where S_j and K_{fj} are the saturation and modulus, respectively, of the j-th fluid. From Eqs. (1) and (2) it is an exact result, independent of the spatial distribution of the fluids, that the static modulus is given by the Biot–Gassmann expression for a fictitious fluid whose modulus is K_W: $\tilde{K}(\omega=0)=K_{\mathrm{BG}}(K_W)\overset{\mathrm{def}}{=}K_{\mathrm{BGW}}$, which makes physical sense. This is proven directly from Eqs. (1) and (2) in Appendix A; Dutta and Odé (1979b) had proved this explicitly for the spherical shells model but it is true for any patch geometry. From Eq. (14) it is clear that when the fluids, gas and water, say, have moduli which differ by orders of magnitude, as in Table I, then K_{BGW} is dominated by the properties of the more compressive fluid, unless the saturation is nearly 100% that of the other fluid.

One can do better, however, by developing a perturbation theory in which the solution is expanded in powers of ω, viz:

$$\mathbf{u}(\mathbf{r};\omega)=\mathbf{u}^{(0)}(\mathbf{r})-i\omega\mathbf{u}^{(1)}(\mathbf{r})+(-i\omega)^2\mathbf{u}^{(2)}(\mathbf{r})+\cdots, \tag{15}$$

and similarly for the other variables. Equations (1) and (2) must hold order by order, and so the solution at zeroth order becomes a source term for the first order, etc. For example, the first order contribution to the pore pressure satisfies

$$\nabla\cdot\left\{\frac{1}{\eta(\mathbf{r})}\nabla p_f^{(1)}\right\}=-\frac{\phi}{k}[E_{ll}^{(0)}-\epsilon_{ll}^{(0)}]. \tag{16}$$

The idea is that the macroscopic expression for the energy dissipation per cycle, which can be expressed in terms of $\tilde{K}(\omega)$, is equal to the same quantity expressed as a volume integral of the appropriate combination of microscopically varying field variables. This equality must hold order by order, in powers of ω. The macroscopic expression for the power dissipation averaged over one cycle is

$$\overline{P}=\frac{1}{2}\mathrm{Real}\int\frac{\partial\mathbf{u}^*}{\partial t}\cdot\boldsymbol{\tau}\cdot\hat{\mathbf{n}}\,dS\equiv-\frac{1}{2}\mathrm{Real}\left[i\omega V\frac{|P_e|^2}{\overline{K}(\omega)}\right], \tag{17}$$

where the integral is taken over the bounding surface of the sample. The microscopic expression is

$$\overline{P}=-\frac{1}{2}\mathrm{Real}\int\phi\left(\frac{\partial\mathbf{U}^*}{\partial t}-\frac{\partial\mathbf{u}^*}{\partial t}\right)\cdot\nabla p_f\,dV. \tag{18}$$

From Eq. (18) it is simple to see that the lowest order nonzero contribution to $\overline{P}$ is proportional to ω^2 and it involves $p_f^{(1)}$, $\mathbf{u}^{(0)}$, and $\mathbf{U}^{(0)}$ (because $p_f^{(0)}$ is spatially uniform). Therefore, from Eq. (17), $\tilde{K}(\omega)$ must have an expansion of the form

$$\lim_{\omega\to0}\tilde{K}(\omega)=K_{\mathrm{BGW}}[1-i\omega T+O(i\omega)^2], \tag{19}$$

where the real-valued parameter $T>0$ is defined in terms of the solution to an auxiliary problem which follows directly from Eq. (16). Let

$$g(\mathbf{r})=\frac{(1-K_b/K_s)(1/K_W-1/K_f(\mathbf{r}))}{(1-K_b/K_s-\phi K_b/K_s+\phi K_b/K_W)} \tag{20}$$

and let $\Phi(\mathbf{r})$ be the solution to

$$\nabla\cdot\left[\frac{-1}{\eta(\mathbf{r})}\nabla\Phi(\mathbf{r})\right]=g(\mathbf{r}). \tag{21}$$

The result for T, after a lot of algebra, is

$$T=\frac{\phi^2}{k}\frac{K_{\mathrm{BGW}}}{V}\int g(\mathbf{r})\Phi(\mathbf{r})dV. \tag{22}$$

Equation (21) is mathematically equivalent to an electrical conductivity problem in which there is a position dependent conductivity, $1/\eta(\mathbf{r})$, and a distributed current source, $g(\mathbf{r})$, for which electrical neutrality, $\int g(\mathbf{r})dV\equiv0$, is guaranteed by Eq. (14). The function $\Phi(\mathbf{r})$ plays the role of the electrostatic potential. Consequently, the parameter T depends on the geometry of the patches in a complicated and nonlocal way, which can be solved only in certain simplifying geometries, as is done later in this section.

The physical significance of the parameter T can be more easily understood in the simple extreme in which one phase "gas" is much more compressible and much less viscous than the other "fluid" phase: $K_g\ll K_f$ and $\eta_g\ll\eta_f$, i.e., as if the gas phase is a simple vacuum. Define the auxiliary function $\tilde{\Phi}$, defined on the space occupied by the fluid, V_f, by

$$\nabla^2\tilde{\Phi}=-1\quad\mathbf{r}\in V_f, \tag{23}$$

subject to the boundary condition

$$\tilde{\Phi}\equiv0 \tag{24}$$

on the interface with the vacuum phase, as well as the usual no net-flow boundary condition on the external surface of the sample. The relevant "size" of the fluid phase, l_f, may be defined by integrating $\tilde{\Phi}$ over the space occupied by the fluid:

$$l_f^2\overset{\mathrm{def}}{=}\frac{1}{V_f}\int_{V_f}\tilde{\Phi}\,d^3\mathbf{r}. \tag{25}$$

This kind of definition of an effective size occurs in other contexts involving diffusion [Torquato (1991); Eqs. (19)–(21) of Wilkinson *et al.* (1991); Bug *et al.* (1992)]. For the special case of a sphere of radius R, $l_f=R/\sqrt{15}$. Also, let us define a diffusion coefficient:

$$D_T \overset{\text{def}}{=} \frac{kK_b}{S_f \eta_f \left(1-\frac{K_b}{K_s}\right)^2}. \tag{26}$$

D_T is reminiscent of, though distinct from, the diffusivity of a deformable skeletal frame in an incompressible, viscous fluid [cf. Eq. (2.11) of Johnson (1982)]. Then, in this limit that the one phase is a vacuum, the parameter T is the mean lifetime for diffusion across the fluid patch:

$$\lim_{(\eta_g, K_g)\to 0} T \equiv l_f^2/D_T. \tag{27}$$

Note that, in this limit, T is independent of the modulus K_f.

Note also that the parameter T is always inversely proportional to permeability. It is worth recalling that the neglected terms in the full Biot theory also predict a low frequency dependence analogous to Eq. (19) but with a coefficient which is proportional to k [Johnson *et al.* (1994)]. Therefore, there is a critical value of the permeability such that if the sample permeability is higher than this value, the neglected terms in the full Biot theory are more important than the patchy saturation mechanism considered here. In such cases, the full Biot theory must be used, rather than the quasi-static limit of Eqs. (1) and (2). The situation is similar to that which may occur in the extensional modes of a permeable cylinder [Johnson and Kostek (1995)]. To oversimplify somewhat, one may say that in these situations $\omega_B < \omega_c$, thus invalidating one of the key assumptions for this kind of theory.

C. High frequency limit

If the frequency is high enough the pore pressures in the two phases do not have enough time to equilibrate within one half cycle. Consequently, to a first approximation the pore pressure is constant within each phase, and there is a discontinuous jump in pore pressure across the boundary between phases. The situation is that the shear modulus is everywhere constant, having value N, whereas the bulk modulus has the value $K_1 = K_{\rm BG}(K_{f1})$ in region 1 and similarly for region 2. In such a situation Hill's theorem [Hill (1963, 1964)] is an exact result for the effective bulk modulus of the composite, which shall be denoted $K_{\rm BGH}$:

$$\frac{1}{K_{\rm BGH}+(4/3)N} = \frac{S_1}{K_1+(4/3)N} + \frac{S_2}{K_2+(4/3)N}. \tag{28}$$

The composite is always elastically isotropic whether or not the geometry is isotropic. Thus the high frequency limit of $\tilde{K}(\omega)$ is $K_{\rm BGH}$, as Norris (1993) more or less has observed. Hill's theorem was originally proved for the case of two constituents but the obvious extension of Eq. (28) to the case of arbitrarily varying $K(\mathbf{r})$ is also true [Milton (2001)].

To this point, on the surface which separates region 1 from region 2 the total stress is continuous, the displacements of the fluid and of the solid (which are locked together) are continuous, but the pore pressure is discontinuous, having a value $p_f^{(1)}$ in region 1 and similarly for region 2. ($p_f^{(j)}$ has a different meaning than it did in the previous subsection.) In reality, continuity of pore pressure is achieved by the generation of a slow compressional wave which propagates/diffuses away from the interface. In the immediate vicinity of the interface the pore pressure is, therefore,

$$p_f(\mathbf{r}) = \begin{cases} p_f^{(1)} + A\exp(-iq_1 x) & x<0 \\ p_f^{(2)} + B\exp(iq_2 x) & x>0 \end{cases}, \tag{29}$$

where x is a local coordinate normal to the interface and

$$q_j = \sqrt{i\omega/D_j} \tag{30}$$

is the wave vector of the slow wave in region $j=1,2$ in terms of the diffusion coefficient given by Eq. (8). It is understood that the frequency is high enough that $|q_j^{-1}|$ is everywhere small compared with the local radius of curvature on the surface so that locally the interface is flat. Amplitudes A, B are determined by the requirement that the pore pressure, $p_f(\mathbf{r})$, and the fluid flux, $\phi[\mathbf{u}-\mathbf{U}]\cdot\hat{\mathbf{n}}$, be continuous:

$$A = -\frac{\eta_1\sqrt{D_1}[p_f^{(1)}-p_f^{(2)}]}{\eta_1\sqrt{D_1}+\eta_2\sqrt{D_2}}, \tag{31}$$

$$B = \frac{\eta_2\sqrt{D_2}[p_f^{(1)}-p_f^{(2)}]}{\eta_1\sqrt{D_1}+\eta_2\sqrt{D_2}}. \tag{32}$$

By setting the macroscopic dissipation implied by $\tilde{K}(\omega)$, Eq. (17), equal to the volume integral of the microscopic dissipation engendered by this slow wave mechanism, Eq. (18), one can derive an expression for the imaginary part of $\tilde{K}(\omega)$ in this high frequency limit, valid for real-valued ω. Recognizing that $\tilde{K}(-\omega^*) = \tilde{K}^*(\omega)$ when ω is extended to the complex plane allows one to deduce an analytic expression for the approach to the high frequency limit:

$$\lim_{\omega\to\infty} \tilde{K}(\omega) = K_{\rm BGH}[1-G(-i\omega)^{-1/2}+\cdots], \tag{33}$$

where the real-valued coefficient G is

$$G = \frac{kK_{\rm BGH}}{\eta_1\sqrt{D_1}+\eta_2\sqrt{D_2}} \frac{\int|\Delta p_f|^2\, dS}{|P_e|^2 V}, \tag{34}$$

and $\Delta p_f = p_f^{(1)} - p_f^{(2)}$ is the would-be discontinuity in pore pressure across the interface, S, between the two regions.

Although the pore pressure and the relative flux are now continuous, the total stress and the individual displacements are now slightly discontinuous. However, the amplitudes of these discontinuities are of order $O(\omega^{-1/2})$ and they extend a distance from the interface which is also of order $O(\omega^{-1/2})$. Therefore, corrections to Eq. (33) are of order $O(\omega^{-1/2}) \times O(\omega^{-1/2}) = O(\omega^{-1})$. These corrections, therefore, do not affect the validity of Eq. (33).

It is a remarkable feature of Hill's theorem that the volumetric component of the strain, ϵ_{ll}, is spatially uniform within each region and the theorem specifies how this constant value relates to the applied compressive stress, P_e, as well as to the elastic constants of the two phases: cf. Eqs. (4.12) of Hill (1963):

$$\epsilon_{ll}^{(j)} = -\frac{[K_{3-j}+(4/3)N]P_e}{K_1K_2+(4/3)N(S_1K_1+S_2K_2)}, \tag{35}$$

where $j=1,2$ labels the region in question. This result holds independent of the shape of the patch and is true even if the patch is not contiguous. Since the pore pressure in each phase, far from the interface, is given by $p_f^{(j)}=-(1/\phi)(R_j+Q_j)\epsilon_{ll}^{(j)}$ from Eq. (4) for the j-th region, we have the result that the would-be discontinuity is constant along the interface between the two regions and may therefore be factored outside the integral in Eq. (34). The final result may be succinctly written as:

$$\lim_{\omega\to\infty}\tilde{K}(\omega)=K_{\mathrm{BGH}}\left[1-\left|\frac{\Delta p_f}{P_e}\right|^2\frac{S}{V}\frac{i}{q^*}+\cdots\right], \tag{36}$$

where $\Delta p_f/P_e$ is the would-be discontinuity in pore pressure, relative to the applied external stress, and is given exactly as:

$$\frac{\Delta p_f}{P_e}=\frac{(R_2+Q_2)[K_1+(4/3)N]-(R_1+Q_1)[K_2+(4/3)N]}{\phi S_1K_1[K_2+(4/3)N]+\phi S_2K_2[K_1+(4/3)N]}. \tag{37}$$

The effective wave vector, q^*, is a property of the two phases adjoining the interface:

$$q^*=\sqrt{i\omega/D^*}, \tag{38}$$

where the effective diffusivity is

$$D^*=\left[\frac{k\,K_{\mathrm{BGH}}}{\eta_1\sqrt{D_1}+\eta_2\sqrt{D_2}}\right]^2. \tag{39}$$

S/V is the ratio of the boundary area between the two phases, S, to the sample volume, V. In Eq. (36) it is the only quantity which is reflective of the patch geometry; K_{BGH}, D^*, and Δp_f depend only upon the saturation values.

III. EXAMPLES: SLAB AND CONCENTRIC SPHERES GEOMETRIES

To illustrate these high and low frequency limits as well as the general frequency dependence of this crossover phenomenon, it is straightforward to consider two simple geometries: (a) The concentric spheres geometry whereby region 1 is a sphere of radius R_a surrounded by region 2 of outer radius R_b. By imposing the no-flow boundary condition on the outer surface White (1975) and Dutta and Odè (1979a, b) have used this geometry as a model for a periodic array of spherical inclusions. One has $S_1=(R_a/R_b)^3$, $S/V=3R_a^2/R_b^3$, and Eq. (21) can be solved in closed form to get the following expression for T:

$$\begin{aligned}T=\frac{K_{\mathrm{BGW}}\phi^2}{30kR_0^3}\{&[3\eta_2g_2^2+5(\eta_1-\eta_2)g_1g_2-3\eta_1g_1^2]R_a^5\\&-15\eta_2g_2(g_2-g_1)R_a^3R_b^2+5g_2[3\eta_2g_2\\&-(2\eta_2+\eta_1)g_1]R_a^2R_b^3-3\eta_2g_2^2R_b^5\}.\end{aligned} \tag{40}$$

(b) The periodic slab geometry whereby region 1 is a layer of thickness L_1 and region 2 is a layer of thickness L_2, periodically repeated as in White *et al.* (1976) and Norris (1993). Here, $S_1=L_1/(L_1+L_2)$, $S/V=2/(L_1+L_2)$, and, again, T can be evaluated in closed form:

$$\begin{aligned}T=-\frac{K_{\mathrm{BGW}}\phi^2}{6k(L_1+L_2)}\{&\eta_1g_1^2L_1^3+3\eta_1g_1g_2L_1^2L_2\\&+3\eta_2g_1g_2L_1L_2^2+\eta_2g_2^2L_2^3\}.\end{aligned} \tag{41}$$

Equations (1) and (2) can be solved numerically exactly using techniques analogous to those of, e.g., Dutta and Odè (1979a, b), for the concentric spheres, and Norris (1993), for the slab geometries. The method of solution is described in Appendix B. The patchy effect is maximized when the frame modulus is relatively weak (so that the overall stiffness is sensitive to the type of fluid saturation), one fluid is gas and the other is a liquid such as water (so that the two fluids are quite different), and the gas saturation is relatively small (so that BGW and BGH have very different values). The parameter set in Table I was chosen with these conditions in mind. The results are shown in Fig. 1 for three geometries, all at the same gas saturation, $S_g=10\%$. The left column is the real part of $\tilde{K}(\omega)$, whereas the right column is the specific attenuation, $1/Q_K=-\mathrm{Imag}\,\tilde{K}(\omega)/\mathrm{Real}\,\tilde{K}(\omega)$. The first and second rows are for the concentric spheres geometry. In the top row the gas occupies the inner sphere, whereas in the second row water occupies the inner sphere. The third row is the slab geometry. The results are plotted over a wide frequency range simply to emphasize the approach to the limiting results, Eqs. (19) and (33). In reality, the frequency $\omega_x/(2\pi)$, Eq. (13), is approximately 8 kHz. The Biot crossover frequency, Eq. (6), is $\omega_B/(2\pi)=128$ kHz.

The solid lines are the results of numerical calculations. The values for K_{BGW} and K_{BGH} are indicated as horizontal dashed lines ($K_{\mathrm{BGW}}<K_{\mathrm{BGH}}$). The high and low frequency asymptotes, Eqs. (19) and (36), are indicated as dotted lines; the real part of Eq. (19) is simply K_{BGW}. The dashed line is the theoretical model, to be discussed in the next section. It is immediately apparent that the shapes of the curves for $\tilde{K}(\omega)$ are quite different in the three cases even though the values of K_{BGW} and K_{BGH} are the same (because the values for the saturations are the same). Moreover, the shapes do *not* change if one simply rescales the relative sizes in the geometry while keeping the saturations fixed. This resizing simply rescales the frequency axis, leaving the shapes unaffected, as was discussed earlier in this section. An understanding of these different shapes is provided by the theoretical model, as follows.

IV. THEORETICAL MODEL FOR $\tilde{K}(\omega)$

Any closed-form expression for $\tilde{K}(\omega)$ with claims to be accurate is constrained, not only by Eqs. (19) and (36), but also by fairly general considerations based on causality. Since the relaxation mechanism is diffusive in character, any singularities of $\tilde{K}(\omega)$ as well as those of $1/\tilde{K}(\omega)$ must occur for ω on the negative imaginary axis. Moreover, because $\tilde{K}(\omega)$ is the Fourier transform of a real-valued response function, one has the reflection symmetry

$$\tilde{K}(-\omega^*)=\tilde{K}^*(\omega). \tag{42}$$

These properties are proven in Appendix C. Although there must be an infinitude of such analytic functions that satisfy

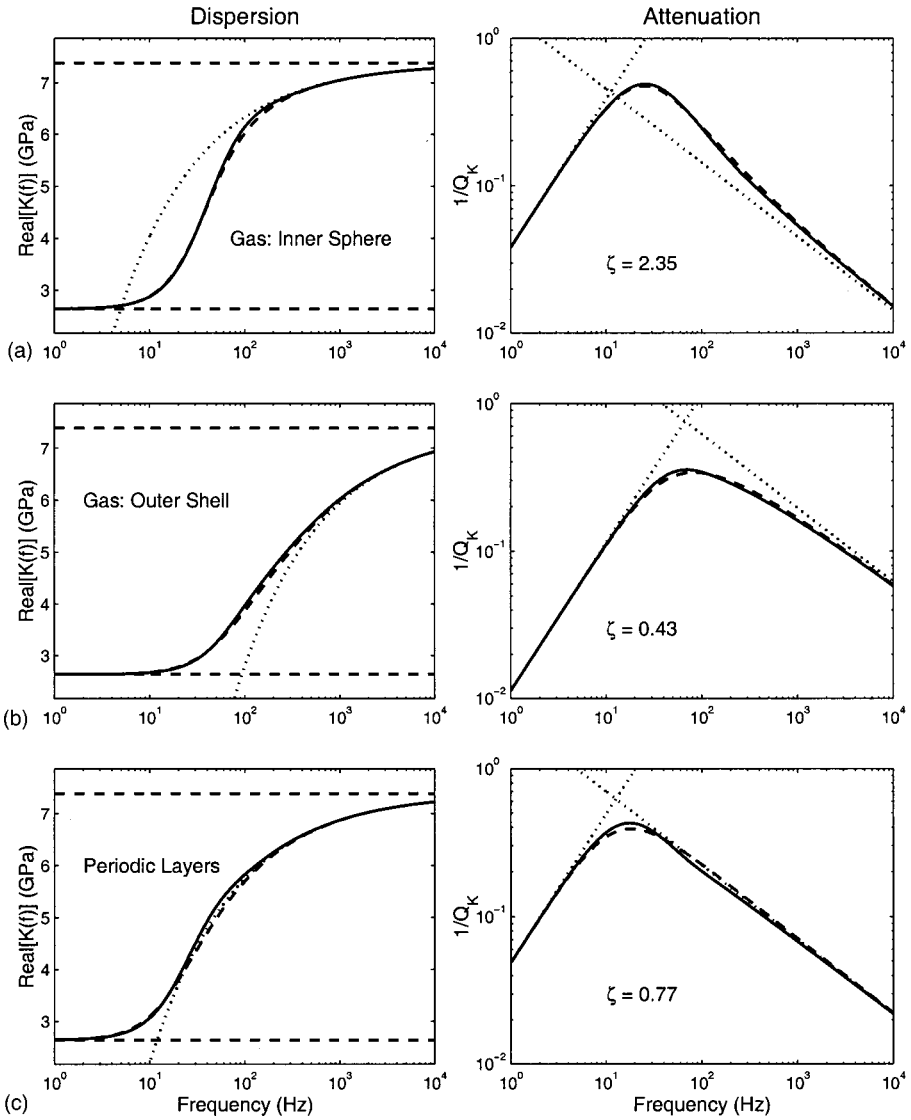

FIG. 1. Dispersion (Real $[\tilde{K}(\omega)]$) and attenuation $[1/Q_K = -\text{Imag}\,\tilde{K}(\omega)/\text{Real}\,\tilde{K}(\omega)]$ due to the patchy saturation effect for a gas/water combination, $S_g = 10\%$, in three different situations. Solid lines are numerically exact solutions, dotted lines are the high and low frequency limiting expressions, Eqs. (36) and (19), and dashed lines represent the analytic expression, Eq. (43). (a) Top row: The gas is located in an inner sphere, $R_a = 4.642$ cm, surrounded by a shell of water, $R_b = 10$ cm. (b) Middle row: The roles are reversed, $R_a = 9.655$ cm, $R_b = 10$ cm. (c) Bottom Row: A periodic slab geometry, $L_g = 2$ cm, $L_w = 18$ cm. The other material parameters are listed in Table I. The values of ζ, Eq. (45), are shown.

these exact relations, it is likely that any two of them differ very little from each other, or from the exact solution, for values of ω on the real axis. What might such an analytic function look like? In order for Eq. (33) to be satisfied, it must have either a branch point somewhere on the negative imaginary axis, or an infinite sequence of poles on the negative imaginary axis. It must also obey Eq. (19). The very simplest imaginable such function is, perhaps, that suggested by Pride *et al.* (1993) in an analogous context:

$$\tilde{K}(\omega) = K_{\text{BGH}} - \frac{K_{\text{BGH}} - K_{\text{BGW}}}{1 - \zeta + \zeta\sqrt{1 - i\omega\tau/\zeta^2}}, \tag{43}$$

where consistency with Eqs. (19) and (33) requires

$$\tau = \left[\frac{K_{\text{BGH}} - K_{\text{BGW}}}{K_{\text{BGH}} G}\right]^2 \tag{44}$$

and

$$\zeta = \frac{(K_{\text{BGH}} - K_{\text{BGW}})^3}{2K_{\text{BGW}} K_{\text{BGH}}^2 T G^2} = \frac{(K_{\text{BGH}} - K_{\text{BGW}})}{2K_{\text{BGW}}} \frac{\tau}{T}. \tag{45}$$

In Eq. (43) the branch cut in the definition of the square root function, $\sqrt{Z}$, is taken to be along the negative real Z-axis. With this convention, it is straightforward to demonstrate that all poles, zeroes, and branchcuts of Eq. (43) lie on the negative imaginary ω-axis. There is a simple pole if and only if $\zeta > 1$. This function, for real values of ω, is plotted in Fig. 1 as dashed lines. It is clear that it is an excellent approximation to the exact solution in all cases. Note that the parameters ζ and τ are *not* fitting parameters, but are calculated from S/V and T separately, as indicated above, so that Eq. (43) has the correct, exact limiting behaviors. Moreover, the validity of the comparison has been checked over the range of saturations $S_g = 1\%$ to $S_g = 99\%$. There is no need to consider different values of the permeability or of the overall size scale since they simply change the scale of the frequency axis. The examples used here are for a relatively compressible rock, using gas and water. If a more rigid rock were used, or if the two fluids were more similar, then the patchy saturation effect is diminished, but Eq. (43) is able to accurately describe the physics.

To the extent that Eq. (43) accurately describes $\tilde{K}(\omega)$, it is obvious that the parameter ζ, given by Eq. (45), is a shape parameter, whereas τ sets the frequency scale. When $\zeta < 1$, the crossover region is quite broad, whereas when $\zeta > 1$,

the crossover region is quite narrow, as seen in the examples of Fig. 1. When $\zeta > 1$, Eq. (43) has a simple pole at $\omega = -i(2\zeta - 1)/\tau$. It is this pole which causes the specific attenuation, $1/Q_K$, to overshoot the high frequency asymptote in the first row of Fig. 1. There is no pole anywhere in the complex ω-plane when $\zeta < 1$. It bears emphasizing, however, that the numerically exact solution does *not* have the same singularities as does the model, Eq. (43). Rather, the former possesses a countably infinite sequence of simple poles on the negative imaginary axis and no branch points. Fortunately for the success of this model, acoustic measurements are done with real values for the frequency.

Finally, the results of this section allow one to make a more careful definition of the crossover frequency. A reasonable choice would be that frequency where the high and low frequency asymptotes for $1/Q_K$ intersect, as is seen in the right half of Fig. 1. From Eqs. (19), (36)–(39), and (45) this frequency may be written as

$$\omega_c = D^* \left[\frac{2K_{\mathrm{BGW}}^2 K_{\mathrm{BGH}}^4 \zeta^2}{(K_{\mathrm{BGW}} - K_{\mathrm{BGH}})^6} \right]^{1/3} \left(\frac{\Delta p_f}{P_e} \right)^4 \left[\frac{S}{V} \right]^2 . \tag{46}$$

As was indicated in the Introduction, the crossover frequency is of the form $\omega_c = D/L^2$, but to the extent that $\zeta \approx 1$, it would appear that the relevant diffusivity is D^*; the relevant patch size is V/S, modified by the prefactors as indicated. These prefactors, however, depend only upon the numerical value of the saturations and not on the patch geometry. There may very well be better ways of rewriting Eq. (46).

V. MODES IN A FULLY SATURATED POROUS CYLINDER

The previous sections dealt with situations in which the two conditions, $\omega \ll \omega_B$ and $\omega \ll \omega_x$, were presumed to be valid even though the frequency may be large or small compared to ω_c. In this section I describe a simple geometry in which all three crossover frequencies are readily apparent and for which the quasi-static limit is well-described by the effective bulk modulus given by Eq. (43).

Consider a porous and permeable cylindrical rod, of radius a, which is fully saturated with a Newtonian fluid. Let us assume the pore space is "open" to the surrounding air, which can successfully be approximated as a vacuum. The question is: What are the axially symmetric normal modes of propagation in such a system? Here, a normal mode is one for which the axial and temporal variations of the displacements and stresses are given by $\exp[i(k_z(\omega)z - \omega t)]$. It may seem that this problem is unrelated to the topic of this article inasmuch as the pores are now open, not sealed, but I will demonstrate not only that the patchy saturation model, Eq. (43), is relevant but also that this problem can clearly demonstrate the various crossover frequencies.

If the rod were simply an elastic material, the dispersion of the normal modes, $k_z(\omega)$, would be given in terms of the solution to the classical Pochhammer–Cree equation, which naturally follows from the requirement that the relevant stress components vanish on the surface of the rod. See, for example, Eq. (6.131) of Achenbach (1973). The inputs to this equation are the density, ρ, the bulk modulus, K, the shear modulus, N, and the radius, a, of the rod.

For the case at hand in which the rod is porous and permeable, the Biot theory must, in general, be used. The validity of using the Biot theory to describe extensional modes in open-pore rods was established experimentally by Mörig and Burkhardt (1989). The method of calculation is analogous to that of the Pochhammer–Cree equation but because there are fast and slow compressional components to the modes, as well as a shear component, there needs to be an additional boundary condition for which there is no analog in ordinary elasticity theory. If the pore space of the rod is open to the surrounding air, the additional boundary condition is taken to be that the pore pressure vanishes on the surface of the rod: $p_f(r=a) = 0$. Of course the total stress also vanishes on the surface: $\boldsymbol{\tau}(r=a) \cdot \hat{\mathbf{n}} = 0$. Results of such numerical calculations are described by Dunn (1986) and by Johnson and Kostek (1995). The desired complex-valued wave vector, $k_z(\omega)$, is given as a root of a specific determinantal equation. The results of such calculations using the parameter set of Table I are presented in Fig. 2. In order to use the full Biot theory it was assumed that $\rho_f = 1000\,\mathrm{kg/m^3}$, $\rho_s = 2650\,\mathrm{kg/m^3}$, and $\alpha_\infty = 3.52$ in the notation of Johnson and Kostek (1995). The radius of the cylinder is $a = 10\,\mathrm{cm}$. The phase velocity, V_E, and the specific attenuation, $1/Q_E$, for these extensional modes are related to $k_z(\omega)$ by

$$k_z(\omega) = \frac{\omega}{V_E(\omega)} \left[1 + \frac{i}{2Q_E(\omega)} \right]. \tag{47}$$

There are three distinct features in these plots which will be discussed momentarily.

First, however, suppose for a moment that the rod is saturated in an inner cylinder of radius $b < a$. If the pore space in the region $b < r < a$ is "saturated" by vacuum then $p_f(r) \equiv 0$ in the region $b < r < a$. In this case, it really does not matter if the outer radius is sealed or open. Therefore the low frequency acoustics of this system may be accurately described by the model $\tilde{K}(\omega)$, Eq. (43). Since $K_g \equiv 0$, one has $K_W = 0$ and $K_{\mathrm{BGW}} = K_b$ regardless the value of b. This is still true in the limit $b \to a$, i.e., if the porous cylinder is fully saturated and the open-pore boundary condition holds. In Eq. (43) one has $S_f \to 1$, $K_{\mathrm{BGH}} \to K_{\mathrm{BG}}(K_f)$, and $S/V \to 2/a$. The diffusion length l_f, Eq. (25), is $l_f \to a/\sqrt{8}$ [Wilkinson *et al.* (1991)]. It is simple enough to use $\tilde{K}(\omega)$, Eq. (43), in the Pochhammer–Cree equation and repeat the mode search in order to determine the dispersion and attenuation of extensional modes. These results are also plotted in Fig. 2.

Three observations are noted: (1) The structure that is centered in the region 10–100 Hz is precisely the patchy saturation effect about which this article is concerned. The model $\tilde{K}(\omega)$ does an excellent job of accurately describing the acoustic properties in this region, as it was intended to do. (2) The dispersion centered at 4 kHz is due to the fact that the wavelengths are becoming comparable to the radius of the cylinder. This feature is essentially identical to that calculated from the Pochhammer–Cree equation using a fre-

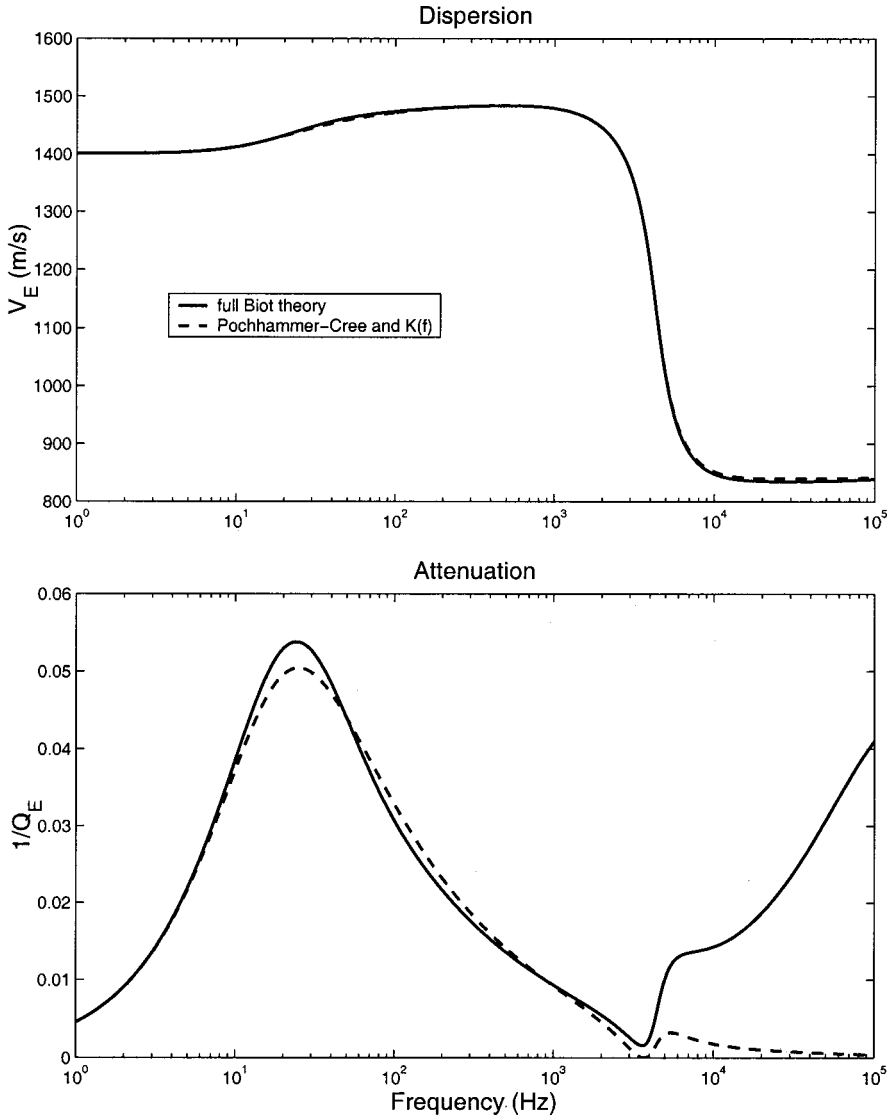

FIG. 2. Dispersion and attenuation of axissymmetric modes in a fully saturated porous cylinder of radius $a = 10$ cm using the full Biot theory and using the patchy saturation model, $\tilde{K}(\omega)$, in the Pochhammer–Cree equation. The parameter set is as in Table I (water). It was also assumed that $\rho_f = 1000$ kg/m^3, $\rho_s = 2650$ kg/m^3, and $\alpha_\infty = 3.52$.

quency independent modulus given by $K_{\mathrm{BG}}(K_f)$. Strictly speaking, this is now outside the intended range of validity of the patchy saturation model, Eq. (43), because the patch size is also equal to a. Thus the crossover frequency, Eq. (13), for this problem is $\omega_x/(2\pi) = 4$ kHz. (3) The onset of additional attenuation at high frequencies predicted by the full Biot theory is not at all captured by the patchy saturation model because this represents the onset of the crossover region within the Biot theory itself. From Eq. (6) one has $\omega_B/(2\pi) = 128$ kHz. All three crossover frequencies, ω_c, ω_x, and ω_B, are thus clearly manifested in Fig. 2.

The rather large value of the rod radius, $a = 10$ cm, was chosen so that the three crossover frequencies would be well separated. If the radius was chosen to be a factor of 10 larger still, then ω_c would be reduced by a factor of 100, ω_x would be reduced by a factor of 10, and ω_B would be unaffected. Conversely, if the radius were much smaller than 10 cm, the three crossover effects would tend to overlap. Similarly, if the permeability were decreased by a factor of 10, then ω_c would be reduced by a factor of 10, ω_x would be unaffected, and ω_B would be increased by a factor of 10.

For the problem of extensional modes in a fully saturated cylindrical rod, Gardner (1962) developed a well-known low frequency approximation to the full Biot theory, his Eq. (3.6), which may be written as

$$(k_z)^2 = \left(\frac{\omega}{V_{\mathrm{sh}}}\right)^2 \times \left\{\frac{(V_{\mathrm{sh}}^2 - V_p^2)(PR - Q^2) + V_{\mathrm{sh}}^2(R+Q)^2\Theta(qa)}{(4V_{\mathrm{sh}}^2 - 3V_p^2)(PR - Q^2) + 4V_{\mathrm{sh}}^2(R+Q)^2\Theta(qa)}\right\}, \tag{48}$$

where

$$\Theta(x) = \frac{2J_1(x)}{xJ_0(x)}. \tag{49}$$

V_p is the speed of the fast compressional wave, Eq. (10), and q is the wave vector of the slow wave, Eq. (30). A plot of the dispersion and attenuation predicted by Eq. (48) is virtually indistinguishable from that of the full Biot theory for frequencies below 1 kHz in Fig. 2; this kind of comparison is analyzed in Johnson and Kostek (1995). Similarly, the low frequency limit of the Pochhammer–Cree equation can be simplified to yield

$$(k_z)^2=\omega^2\frac{\rho}{\tilde{Y}(\omega)}, \tag{50}$$

where the effective Young's modulus is

$$\tilde{Y}(\omega)=\frac{3N\tilde{K}(\omega)}{\tilde{K}(\omega)+N/3}. \tag{51}$$

Below 1 kHz, Eq. (50) is virtually indistinguishable from the results of the mode search using the Pochhammer–Cree equation and $\tilde{K}(\omega)$. Equations (48) and (50) certainly seem different but it is the central theme of this article that they can predict very similar acoustic results.

It is not always the case that Eqs. (48) and/or (50) are accurate descriptors of the low frequency acoustics of a porous fluid-saturated cylinder. If the permeability is so high that $\omega_x \ll \omega_c$ then there is no frequency range over which either of these low frequency approximations accurately describe the attenuation. This point is the subject of the article by Johnson and Kostek (1995).

VI. CONCLUSIONS

In summary, a simple analytic model for the frequency dependence of the bulk modulus due to the diffusive equilibration of two different pore fluids has been presented in Eq. (43). The model presumes the frequency is low compared to ω_B, Eq. (6), and compared to ω_x, Eq. (13). The model introduces only two parameters characteristic of the geometry of the saturation patches. These parameters are T, given by Eqs. (20)–(22), and S/V, the ratio of the surface area of a patch to the sample volume; they enter into the exact expressions for the high and low frequency limits. In the special case that the "gas" phase may be approximated as a vacuum, T is the diffusion time for equilibrating stress in the porous skeleton over the size, l_f, of the fluid patch, where l_f is defined by Eq. (25). The model agrees very well with the numerical results for simple geometries. It is asserted that the model will also work well in other, not so simple geometries but in order to check one must do detailed numerical calculations. The usefulness of the result is that the model can be used to predict seismic-sonic drift, to analyze 4D seismic studies, and it can be used to determine the approximate sizes of the patches, presuming, of course, that one is confident that one is dealing with a situation in which this mechanism is the dominant one. In a practical sense, ζ and τ may be taken as the two parameters, determined by a fit to acoustic data, and S/V and T (or l_f) deduced therefrom. In short, the wave vector of the slow wave, $q(\omega)$, may be used as a yardstick for measuring patch characteristics.

ACKNOWLEDGMENTS

I am grateful to J. G. Berryman, B. A. Tichelaar, and K. Winkler for making several critical suggestions concerning the content of the manuscript. I am especially grateful to C. M. Sayers for providing me with unpublished results of his which spurred my initial interest in this problem.

APPENDIX A: STATIC LIMIT

In this Appendix it is shown that the Biot–Gassmann–Woods result (BGW) holds true in the static limit, regardless of the geometry of the patches. Consider the relations which are the inverse to those of Eqs. (3) and (4):

$$\epsilon_{ij}=\frac{1}{3K_b}\left[\frac{1}{3}\tau_{ll}+\alpha p_f\right]\delta_{ij}+\frac{1}{2N}\left[\tau_{ij}-\frac{1}{3}\tau_{ll}\delta_{ij}\right] \tag{A1}$$

and

$$E_{ll}=d\,\tau_{ll}+f p_f, \tag{A2}$$

where

$$\alpha=1-\frac{K_b}{K_s}, \tag{A3}$$

$$d=\frac{1}{3\phi}\left[\frac{1}{K_s}-\frac{1-\phi}{K_b}\right], \tag{A4}$$

and

$$f(K_f)=\frac{1}{\phi}\left[\frac{1}{K_s}-\frac{1-\phi}{K_b}-\frac{\phi}{K_f}\right]. \tag{A5}$$

Equation (A1) and the coefficient α are discussed by Nur and Byerlee (1971). As far as I know, Eq. (A2) appears here for the first time. In Eqs. (A1)–(A5), since it is assumed that the porous rock is homogeneous, only the coefficient f depends upon the saturating fluid and, therefore, it is the only coefficient which is position dependent. From Eq. (4) it is clear that p_f is spatially constant in the static limit. In this limit, then, the solutions may be taken to have the property that τ_{ij} and ϵ_{ij} are global constants whereas E_{ll} is constant within each patch. There are two such types of static solution:

(a) Pure shear: In this case $\tau_{ll}\equiv 0$, $p_f\equiv 0$, $E_{ll}\equiv 0$, and $\epsilon_{ij}=(1/2N)\tau_{ij}$, as one would expect intuitively.

(b) Pure compression: Here the stress is spatially constant, with a value given by the external stress $\tau_{ij}=-P_e\delta_{ij}$. The volumetric strain of the solid phase is globally constant with a value

$$\epsilon_{ll}=-\frac{1}{K_b}[P_e-\alpha p_f], \tag{A6}$$

and the volumetric strain in the fluid phase is constant within each patch:

$$E_{ll}^{(j)}=-3dP_e+f^{(j)}p_f, \tag{A7}$$

where $f^{(j)}=f(K_f^{(j)})$ is the value appropriate to the jth region. From the assumed boundary condition on the external surface, either periodic or sealed pore, we have:

$$\begin{aligned}0&=\int[\mathbf{u}-\mathbf{U}]\cdot\hat{\mathbf{n}}\,dS\\&=\int[\nabla\cdot\mathbf{u}-\nabla\cdot\mathbf{U}]dV\\&=\int[\epsilon_{ll}-E_{ll}]dV\\&=V[\epsilon_{ll}-S_1E_{ll}^{(1)}-S_2E_{ll}^{(2)}].\end{aligned} \tag{A8}$$

Therefore,

$$\epsilon_{ll} = S_1 E_{ll}^{(1)} + S_2 E_{ll}^{(2)} = -3\, dP_e + (S_1 f^{(1)} + S_2 f^{(2)}) p_f = -3\, dP_e + f(K_W) p_f, \tag{A9}$$

where K_W is the Wood's law modulus, Eq. (14). The pore pressure, p_f, can be eliminated between Eqs. (A6) and (A9) with the result that

$$\epsilon_{ll} = -\frac{1}{K_{\mathrm{BG}}(K_W)} P_e, \tag{A10}$$

and the theorem is proved. Combining the results for shear and compression, the static limit for the deformation in a patchy-saturated porous medium, subject to the no-net-flow boundary condition, may be written

$$\epsilon_{ij} = \frac{\tau_{ll}}{9K_{\mathrm{BGW}}}\delta_{ij} + \frac{1}{2N}\left[\tau_{ij} - \frac{1}{3}\tau_{ll}\delta_{ij}\right]. \tag{A11}$$

APPENDIX B: METHOD OF NUMERICAL SOLUTION FOR SLAB AND CONCENTRIC SPHERES GEOMETRIES

It is relatively simple to solve Eqs. (1) and (2) numerically if the geometry of the patches is either the periodic slab or the concentric sphere geometry. The method of solution is sketched out here in this Appendix.

Periodic slab geometry

Here it is assumed that region 1 is a layer of thickness L_1 and region 2 is a layer of thickness L_2, periodically repeated along the z-axis as in White *et al.* (1976) and Norris (1993). Here, $S_1 = L_1/(L_1+L_2)$. We consider a problem in which the two displacements **u**, **U** point in the z-direction. Moreover, all variables depend only upon the z-coordinate. By the symmetry of this problem the solution to Eqs. (1) and (2) has the property that there is no relative flow at the midpoint of each slab so, in effect, this geometry may be considered either as a periodic structure or as a sealed boundary unit.

From Eq. (1) it is clear that τ_{33} is constant everywhere. Equation (3) simplifies to:

$$(P+Q)\frac{du}{dz} + (R+Q)\frac{dU}{dz} = \tau_{33} = \text{constant}. \tag{B1}$$

Equations (2) and (4) can be combined as

$$-i\omega\phi(U-u) = \frac{k}{\eta\phi}\left[R\frac{d^2U}{dz^2} + Q\frac{d^2u}{dz^2}\right]. \tag{B2}$$

In Eqs. (B1) and (B2), the material constants η, P, Q, and R have different values within the two different regions.

There are two different kinds of solutions to Eqs. (B1) and (B2): (1) The first kind is one for which $u(z) \equiv U(z)$. Here one has $d^2u/dz^2 \equiv 0$ from Eq. (B2). Therefore, for this kind of solution

$$u(z) = U(z) = \frac{\tau_{33}}{K_{\mathrm{BG}} + (4/3)N}(z - z_0), \tag{B3}$$

where z_0 is an arbitrary constant and $K_{\mathrm{BG}}(K_f)$ is given by Eq. (7). (2) The second kind of solution is one for which $(P+Q)u(z) + (R+Q)U(z) \equiv 0$. For this kind of solution $\tau_{33} = 0$; u and U vary as $\exp(\pm iqz)$ where $q(\omega)$ is given by Eq. (30) for region 1 or 2. (q is different in the two regions.)

Within each region the general solution is a linear combination of the various solutions described above:

$$u(z) = \frac{\tau_{33}}{K_{\mathrm{BG}} + (4/3)N}(z - z_0) - (R+Q) \times [A\sin(qz) + B\cos(qz)],$$

$$U(z) = \frac{\tau_{33}}{K_{\mathrm{BG}} + (4/3)N}(z - z_0) + (P+Q) \times [A\sin(qz) + B\cos(qz)], \tag{B4}$$

$$p_f(z) = -\frac{1}{\phi}\left\{\frac{(R+Q)\tau_{33}}{K_{\mathrm{BG}} + (4/3)N} + q(RP - Q^2) \times [A\cos(qz) - B\sin(qz)]\right\}.$$

There are six unknown constants, (z_0, A, B) in each of the two regions, which are determined by the requirement that the particular solution must satisfy certain boundary conditions. Without loss of generality one may set $z_0 \equiv 0$ in one of the regions because a departure from this assumption merely represents an additional overall translation of the entire geometry. The remaining five parameters are determined by the five boundary conditions: continuity of u, U, and p_f on the boundary between the two slabs and equality of u and U on each of the midpoints of the two slabs. The five equations in five unknowns can be inverted using a commercial linear equation solver with the result that each z_0, A, or B is linearly related to τ_{33}. Inasmuch as the problem has been defined in terms of a uniaxial strain deformation, the resulting effective bulk modulus, $\tilde{K}(\omega)$, can be deduced from the solution via

$$\tau_{33} = \left[\tilde{K}(\omega) + \frac{4}{3}N\right]\left[\frac{u(z+L_1+L_2) - u(z)}{L_1+L_2}\right]. \tag{B5}$$

Note that this solution for $\tilde{K}(\omega)$ is independent of z and independent of the value of τ_{33}.

Concentric spheres geometry

Here region 1 is a sphere of radius R_a surrounded by region 2 of outer radius R_b: $S_1 = (R_a/R_b)^3$. The outer surface is presumed to be sealed: $u(R_b) = U(R_b)$. The method of solution is analogous to that of the slab geometry, above. Here, the spherically symmetric solutions to Eqs. (1) and (2) obey the following equations:

$$\frac{d}{dr}\left[(P+Q)\left(\frac{du}{dr} + \frac{2u}{r}\right) + (R+Q)\left(\frac{dU}{dr} + \frac{2U}{r}\right)\right] = 0, \tag{B6}$$

and

$$-i\omega\phi(U-u)=\frac{k}{\eta\phi}\frac{d}{dr}\left[Q\left(\frac{du}{dr}+\frac{2u}{r}\right)+R\left(\frac{dU}{dr}+\frac{2U}{r}\right)\right]. \tag{B7}$$

The solutions for which $u(r)\equiv U(r)$ are linear combinations of r and r^{-2}. The solutions for which $(P+Q)u(r)+(R+Q)U(r)\equiv 0$ are linear combinations of spherical Bessel functions, $j_1(qr)$ and $n_1(qr)$, where q is given by Eq. (30). The general solution in each region may therefore be written as

$$\begin{aligned}
u(r)&=Ar+Br^{-2}+(R+Q)[Fj_1(qr)+Gn_1(qr)],\\
U(r)&=Ar+Br^{-2}-(P+Q)[Fj_1(qr)+Gn_1(qr)],\\
p_f(r)&=-\frac{3}{\phi}(R+Q)A+\frac{RP-Q^2}{\phi}\\
&\quad\times q[Fj_0(qr)+Gn_0(qr)],\\
\tau_{rr}(r)&=3K_{\mathrm{BG}}A-4Nr^{-3}B-4N(R+Q)\\
&\quad\times r^{-1}[Fj_1(qr)+Gn_1(qr)].
\end{aligned} \tag{B8}$$

The quantities η, P, Q, R, K_{BG}, and $q(\omega)$ have different values in the two different regions.

There are eight unknown amplitudes: A, B, F, G in each of the two regions. The requirement that the particular solution be finite at $r=0$ implies $B=0$ and $G=0$ in region 1. The remaining six boundary conditions are: continuity of u, U, p_f, and τ_{rr} at $r=R_b$, the sealed pore boundary condition $u(R_b)=U(R_b)$, and $\tau_{rr}(R_b)=-P_e$ where P_e is the externally applied pressure. Again, a linear equation solver allows one to invert for the numerical value of each of the six remaining constants, and the field variables are determined uniquely everywhere. The bulk modulus, $\tilde{K}(\omega)$, can be deduced from this solution via its definition: $\tilde{K}(\omega)=-V(P_e/\delta V)$ where $V=(4/3)\pi R_b^3$ and $\delta V=4\pi R_b^2 u(R_b)$:

$$\tilde{K}(\omega)=-\frac{R_bP_e}{3u(R_b)}=-\frac{R_b^3P_e}{3[A_2R_b^3+B_2]}, \tag{B9}$$

where A_2, B_2 refer to the coefficients A and B in region 2.

APPENDIX C: ANALYTIC STRUCTURE OF $\tilde{K}(\omega)$

The frequency dependent bulk modulus is the Fourier transform of a real-valued causal response function [pp. 247–262, Landau and Lifshitz (1960)]:

$$\tilde{K}(\omega)=\int_0^\infty \hat{K}(t)\exp(i\omega t)dt. \tag{C1}$$

Equation (C1) allows for the analytic continuation of the definition to include complex values of ω. We see by inspection that

$$\tilde{K}(-\omega^*)=\tilde{K}^*(\omega), \tag{C2}$$

where the asterisk connotes complex conjugation. We also see by inspection that $\tilde{K}(\omega)$ is analytic everywhere in the upper-half complex ω-plane. Any singularities of $\tilde{K}(\omega)$ must lie in the lower half-plane. For the problem at hand, we now show that all singularities lie on the negative imaginary axis.

First, a preliminary identity will be derived. Consider a specific eigenvalue problem in which all quantities vary as $\mathbf{u}(\mathbf{r})\exp(-i\omega_n t)$, etc., where ω_n is the complex-valued eigenvalue. The fields obey the equations of motion (1) and (2), the no-net-flow boundary condition, Eq. (12), and they also obey the following imposed condition on the bounding surface:

$$\int \mathbf{u}\cdot\boldsymbol{\tau}^*\cdot\hat{\mathbf{n}}\,dS=0. \tag{C3}$$

The quantities appearing in Eq. (C3) are understood to be the position dependent parts, only. Consider the following identity applied to any one of the eigenmodes:

$$\begin{aligned}
\{u_i\tau_{ij}^*\}_{,j}&=u_{i,j}\tau_{ij}^*=\epsilon_{ij}\tau_{ij}^*\\
&=\left[\frac{1}{3K_b}\left(\frac{1}{3}\tau_{ll}+\alpha p_f\right)\delta_{ij}+\frac{1}{2N}D_{ij}\right]\tau_{ij}^*\\
&=\frac{1}{3K_b}\left(\frac{1}{3}\tau_{ll}+\alpha p_f\right)\tau_{ii}^*+\frac{1}{2N}D_{ij}D_{ij}^*,
\end{aligned} \tag{C4}$$

where $D_{ij}=\tau_{ij}-(1/3)\tau_{ll}\delta_{ij}$ is the deviatoric part of the stress tensor. The first equality follows from Eq. (1), the second follows because τ is symmetric, and the third follows from Eq. (A1). The integral of the LHS of Eq. (C4) over the volume of the sample vanishes because of Eq. (C3). Therefore, the desired identity is derived:

$$\int p_f\tau_{ll}^*\,dV=-\int\left[\frac{1}{3\alpha}|\tau_{ll}|^2+\frac{3K_b}{2N\alpha}(\mathbf{DD}^*)_{ll}\right]dV. \tag{C5}$$

This integral is, therefore, real-valued for any eigenmode.

Next, consider Eq. (2), rewritten slightly:

$$i\omega_n\frac{\eta\phi}{k}[U_i-u_i]=p_{f,i}. \tag{C6}$$

Take the dot product of Eq. (C6) with $\mathbf{U}^*-\mathbf{u}^*$ and integrate over the sample volume:

$$\begin{aligned}
&i\omega_n\int\frac{\eta\phi}{k}|U_i-u_i|^2\,dV\\
&\quad=\int(U_i^*-u_i^*)p_{f,i}\,dV\\
&\quad=\int p_f(\mathbf{U}^*-\mathbf{u}^*)\cdot\hat{\mathbf{n}}\,dS-\int(E_{ll}^*-\epsilon_{ll}^*)p_f\,dV.
\end{aligned} \tag{C7}$$

The surface integral vanishes, either because the surface is sealed or because of the periodic boundary conditions. The strain elements can be eliminated by use of Eqs. (A1) and (A2). The cross term can be eliminated by means of Eq. (C5). Therefore,

$$
\begin{aligned}
i\omega_n \int \frac{\eta\phi}{k} |U_i - u_i|^2 \, dV \\
&= \int \left(d - \frac{1}{3K_b} \right) \left[\frac{1}{3\alpha} |\tau_{ll}|^2 + \frac{3K_b}{2N\alpha} (\mathbf{DD}^*)_{ll} \right] dV \\
&\quad + \int \left(\frac{\alpha}{K_b} - f \right) |p_f|^2 \, dV. \qquad \text{(C8)}
\end{aligned}
$$

Inasmuch as all integrals in Eq. (C8) are patently real-valued, the eigenvalue frequencies, $\{\omega_n\}$, are all imaginary.

So imagine that $\tilde{\omega}_p$ is either a pole of order N or an essential singularity of $\tilde{K}(\omega)$. The corresponding field variables have the property that P_e is finite but $\delta V = \int \mathbf{u}\cdot\hat{\mathbf{n}}\, dS$ is zero. Therefore, the field variables for this solution satisfy Eq. (C3); the corresponding field variables constitute an eigenmode, in the sense just discussed. Therefore, $\tilde{\omega}_p$ lies on the imaginary axis, and it must be on the negative imaginary axis because $\tilde{K}(\omega)$ is analytic in the upper half-plane.

Consider possible branch points. Imagine that ω_a and ω_b lie just on opposite sides of a branch cut. The corresponding solutions, $\mathbf{u_a}$ and $\mathbf{u_b}$, etc., are distinct, but may be taken to correspond to the same value of P_e. The difference between the two solutions, $\delta\mathbf{u} = \mathbf{u_a} - \mathbf{u_b}$, is also a solution having frequency $\omega_a = \omega_b$. This solution, $\delta\mathbf{u}$, satisfies Eq. (C3), because $P_e = 0$. Therefore, the branch cut must lie entirely on the negative imaginary axis.

The compressibility, $\tilde{C}(\omega) = 1/\tilde{K}(\omega)$, is also a relevant causal response function. All the arguments given above can be shown to also apply to $\tilde{C}$. Therefore, all zeroes, singularities, and branchpoints of $\tilde{K}(\omega)$ and of $\tilde{C}(\omega)$ lie on the negative imaginary ω-axis.

Achenbach, J. D. (**1973**). *Wave Propagation in Elastic Solids* (North-Holland/Elsevier, New York).

Anselmetti, F. S., and Eberli, G. P. (**1993**). ''Controls on sonic velocities in carbonates,'' PAGEOPH **141**, 287–323.

Biot, M. A. (**1956**). ''Theory of propagation of elastic waves in a fluid saturated porous solid. I. Low frequency range,'' J. Acoust. Soc. Am. **28**, 168–178.

Biot, M. A., and Willis, D. G. (**1957**). ''The elastic coefficients of the theory of consolidation,'' J. Appl. Mech. **24**, 594–601.

Brie, A., Pampuri, F., Marsala, A. F., and Meazza, O. (**1995**). ''Shear sonic interpretation in gas-bearing sands,'' SPE Paper 30595, pp. 701–710.

Bug, A. L. R., Grossman, E. L., Morgan, D. D., and Berne, B. J. (**1992**). ''Diffusion-limited reactions in spherical cavities,'' J. Chem. Phys. **96**, 8840–8852.

Cadoret, T., Marion, D., and Zinszner, B. (**1995**). ''Influence of frequency and fluid distribution on elastic wave velocities in partially saturated limestones,'' J. Geophys. Res. **100**, 9789–9803.

Cadoret, T., Mavko, G., and Zinszner, B. (**1998**). ''Fluid distribution effect on sonic attenuation in partially saturated limestones,'' Geophysics **63**, 154–160.

Chandler, R. N., and Johnson, D. L. (**1981**). ''The equivalence of quasistatic flow in fluid-saturated porous media and Biot's slow wave in the limit of zero frequency,'' J. Appl. Phys. **52**, 3391–3395.

Dunn, K.-J. (**1986**). ''Acoustic attenuation in fluid-saturated porous cylinders at low frequencies,'' J. Acoust. Soc. Am. **79**, 1709–1721.

Dutta, N. C., and Odé, H. (**1979a**). ''Attenuation and dispersion of compressional waves in fluid-filled porous rocks with partial gas saturation (White model)—Part I: Biot theory,'' Geophysics **44**, 1777–1788.

Dutta, N. C., and Odé, H. (**1979b**). ''Attenuation and dispersion of compressional waves in fluid-filled porous rocks with partial gas saturation (White model)—Part II: Results,'' Geophysics **44**, 1789–1805.

Dutta, N. C., and Seriff, A. J. (**1979c**). ''On White's model of attenuation in rocks with partial gas saturation,'' Geophysics **44**, 1806–1812.

Dvorkin, J., Moos, D., Packwood, J. L., and Nur, A. M. (**1999**). ''Identifying patchy saturation from well logs,'' Geophysics **64**, 1756–1759.

Gardner, G. H. F. (**1962**). ''Extensional waves in fluid-saturated porous cylinders,'' J. Acoust. Soc. Am. **34**, 36–40.

Goertz, D., and Knight, R. (**1998**). ''Elastic wave velocities during evaporative drying,'' Geophysics **63**, 171–183.

Hill, R. (**1963**). ''Elastic properties of reinforced solids: Some theoretical principles,'' J. Mech. Phys. Solids **11**, 357–372.

Hill, R. (**1964**). ''Theory of mechanical properties of fibre-strengthened materials: I. Elastic behavior,'' J. Mech. Phys. Solids **12**, 199–212.

Johnson, D. L. (**1982**). ''Elastodynamics of gels,'' J. Chem. Phys. **77**, 1531–1539.

Johnson, D. L. (**1986**). ''Recent developments in the acoustic properties of porous media,'' in *Frontiers in Physical Acoustics XCIII*, edited by D. Sette (North Holland Elsevier, New York), pp. 255–290.

Johnson, D. L., Plona, T. J., and Kojima, H. (**1994**). ''Probing porous media with first and second sound II. Acoustic properties of water-saturated porous media,'' J. Appl. Phys. **76**, 115–125.

Johnson, D. L., and Kostek, S. (**1995**). ''A limitation of the Biot–Gardner theory of extensional waves in fluid-saturated cylinders,'' J. Acoust. Soc. Am. **97**, 741–744.

Knight, R., Dvorkin, J., and Nur, A. (**1998**). ''Acoustic signatures of partial saturation,'' Geophysics **63**, 132–138.

Landau, L. D., and Lifshitz, E. M. (**1960**). *Electrodynamics of Continuous Media* (Addison-Wesley, New York).

Mavko, G., and Mukerji, T. (**1998**). ''Bounds on low-frequency seismic velocities in partially saturated rocks,'' Geophysics **63**, 918–924.

Mavko, G., and Nolen-Hoeksema, R. (**1994**). ''Estimating seismic velocities in partially saturated rocks,'' Geophysics **59**, 252–258.

Mavko, G. M., and Nur, A. (**1979**). ''Wave attenuation in partially saturated rocks,'' Geophysics **44**, 161–178.

Milton, G. (**2001**). (to be published) *The Theory of Composites* (Cambridge University Press, Cambridge).

Mörig, R., and Burkhardt, H. (**1989**). ''Experimental evidence for the Biot–Gardner theory,'' Geophysics **54**, 524–527.

Murphy, W. F. (**1984**). ''Acoustic measures of partial gas saturation in tight sandstones,'' J. Geophys. Res. **89**, 11549–11559.

Murphy, W. A., Winkler, K. W., and Kleinberg, R. A. (**1986**). ''Acoustic relaxation in sedimentary rocks: Dependence on grain contacts and fluid saturation,'' Geophysics **51**, 757–766.

Norris, A. N. (**1993**). ''Low-frequency dispersion and attenuation in partially saturated rocks,'' J. Acoust. Soc. Am. **94**, 359–370.

Nur, A., and Byerlee, J. D. (**1971**). ''An exact effective stress law for elastic deformation of rock with fluids,'' J. Geophys. Res. **76**, 6414–6419.

Pride, S. R., Morgan, F. D., and Gangi, A. F. (**1993**). ''Drag forces of porous-medium acoustics,'' Phys. Rev. B **47**, 4964–4978.

Torquato, S. (**1991**). ''Diffusion and reaction among traps: Some theoretical and simulation results,'' J. Stat. Phys. **65**, 1173–1206.

White, J. E. (**1975**). ''Computed seismic speeds and attenuation in rocks with partial gas saturation,'' Geophysics **40**, 224–232.

White, J. E., Mikhaylova, N. G., and Lyakhovitskiy, F. M. (**1976**). ''Low-frequency seismic waves in fluid-saturated layered rocks,'' Izv., Acad. Sci., USSR, Phys. Solid Earth **11**, 549–654.

Wilkinson, D. J., Johnson, D. L., and Schwartz, L. M. (**1991**). ''Nuclear magnetic relaxation in porous media: The role of the mean lifetime $\tau(\rho, D)$,'' Phys. Rev. B **44**, 4960–4973.

Winkler, K. W., and Liu, X. (**1996**). ''Measurement of third-order elastic constants in rocks,'' J. Acoust. Soc. Am. **100**, 1392–1398.

Comparison of *in situ* and laboratory acoustic measurements on Lough Hyne marine sediments

Angus I. Best,[a] Quentin J. Huggett,[b] and Andrew J. K. Harris
Southampton Oceanography Center, European Way, Southampton SO14 3ZH, United Kingdom

(Received 2 June 1999; revised 8 December 2000; accepted 27 April 2001)

Compressional wave velocity and attenuation were measured at frequencies of 200–1500 Hz on seafloor sediments at Lough Hyne, Ireland, using a mini-boomer source and hydrophone array. Velocity and attenuation were also measured in the laboratory at 200–800 kHz on a 1 m long sediment core taken from the site. The *in situ* results indicate an average sediment phase velocity of about 1600 m/s and sediment quality factor of 10–20. The laboratory core measurements give an average phase velocity of 1793 ± 26 m/s and quality factor of 16 ± 5. The poorly sorted, Lough Hyne sediments are highly attenuating and highly dispersive when compared to values published in the literature for well-sorted, marine sediments such as clean sands and marine clays. The results are consistent with the few published data for poorly sorted sediments, and indicate that intrinsic attenuation is highest when the mass ratio of mud (clay+silt) to sand grade particles is close to unity. It is proposed that compliance heterogeneities are most abundant when mud and sand grade particles are present in roughly equal proportions, and that the observations support local viscous fluid flow as the most likely loss mechanism. © *2001 Acoustical Society of America.*
[DOI: 10.1121/1.1382616]

PACS numbers: 43.20.Jr, 43.20.Ye, 43.30.Ma, 43.30.Xm [DLB]

I. INTRODUCTION

A detailed understanding of acoustic wave propagation in marine sediments will ultimately lead to improved geoacoustic models and better geotechnical predictions from high resolution acoustic datasets (e.g., Chirp reflection profiles). Accurate and reliable measurements of both velocity dispersion and attenuation over a broad frequency range are key to advancing our knowledge in this area, given that different sediment types will exhibit different spectral signatures. Whether measured on laboratory samples or on the seafloor, the spectral signature (or ''spectral fingerprint'') of a volume of sediment will depend on the intrinsic physical properties of the sediment and on extraneous, experimental constraints, such as geometric effects and the coupling of the source and receiver to the sediment. The challenge is to design experiments that will enable the latter effects to be minimized, or corrected, so that the true intrinsic properties of the sediment can be measured.

The sediment acoustics literature reveals that, for a wide range of sediment types (fully saturated with seawater), and to first order, attenuation varies according to the first power of measurement frequency and that velocity dispersion is very small, if not negligible, over the frequency range 1 Hz–1 MHz.[1–3] However, more complex frequency dependencies of velocity and attenuation are predicted by the Biot model[4,5] and its derivatives,[6–9] and there is experimental evidence to support this.[10] Biot's original model predicts energy loss and velocity dispersion due to global, viscous fluid flow in the pores of a sediment; experimental evidence has been provided by several authors[11–13] for Biot global flow in artificial sands and sandstones with high porosities and permeabilities. For poorly sorted marine sediments with significant proportions of clay, silt, and sand grains, global flow becomes less important because of their low permeability. Indeed, significant attenuation has been observed in marine sediments with magnitudes much higher than can be predicted by the Biot theory alone (e.g., experimental data of Shumway;[14] see Sec. III).

It is now generally accepted that local viscous fluid flow (or squirt flow) is the dominant loss mechanism in sedimentary rocks, caused by compliance heterogeneities in the sediment. While theoretical models have been developed that relate squirt flow to microcracks or grain contacts in rocks,[15,16] there are no existing models that predict the comprehensive effects of squirt flow due to clay minerals in sedimentary rocks, although an increasing amount of experimental evidence points to clay squirt flow as the dominant loss mechanism.[17,18] Given the similar mineral assemblages of sedimentary rocks (sandstones, siltstones, claystones) and unconsolidated marine sediments (sands, silts, and clays), it would be surprising if clay squirt flow does not turn out to be an important mechanism in marine sediments.

To further understand wave propagation mechanisms in marine sediments, both velocity and attenuation must be measured accurately and reliably over the bandwidth of interest for practical applications (i.e., 1 Hz–1 MHz). This is because the principle of causality dictates that velocity dispersion and attenuation are intimately linked, and hence, the nature of the frequency dependence will give clues to the precise loss mechanism in different sediments. There are very few published datasets of velocity and attenuation spectra over any significant bandwidth for marine sediments. Wingham[1] presented data for a well-sorted, medium grained sand consistent with attenuation varying as the first power of

[a]Electronic mail: aib@soc.soton.ac.uk
[b]Also at Geotek Limited, Nene House, Drayton Fields, Daventry, Northamptonshire NN11 5EA, United Kingdom.

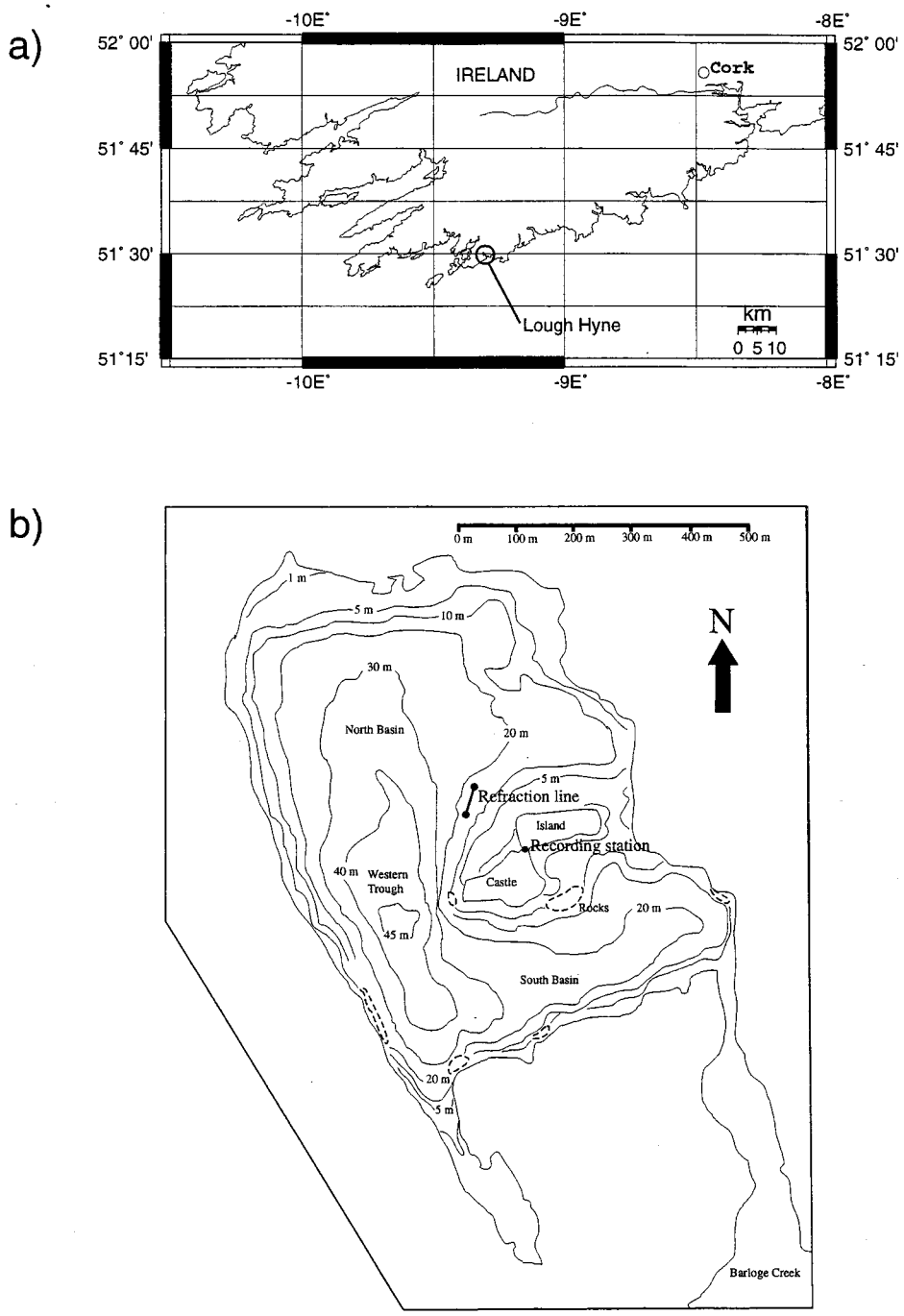

FIG. 1. (a) The location of Lough Hyne. (b) Bathymetry and position of refraction line and recording station.

frequency and very small velocity dispersion (<1%) over the frequency range 50–350 kHz. A literature search reveals no complete datasets for poorly sorted (highly attenuating) marine sediments such as those described below. Poorly sorted sediments comprising various proportions of sand, silt, and clay are commonly found in seafloor environments around the world and yet they are the least well understood in terms of wave propagation mechanisms, certainly when compared to their well-sorted cousins (clean sand of various grades, clean silts, pure marine clays).

In this paper, broadband compressional wave measurements on seafloor sediments in Lough Hyne, Ireland, are compared to broadband measurements on a 1 m long push core from the same site. The experiments were conducted as part of an ongoing study into the validity of marine sediment core measurements, given that sample disturbance can be significant. Our purpose in this paper is to present new experimental data and to discuss the results in terms of the wave propagation mechanisms.

II. *IN SITU* MEASUREMENTS

A. Method

In situ measurements were carried out in August 1995 at Lough Hyne, southwest Ireland [see Fig. 1(a)]. The sheltered location and shallow water of this sea lough, connected to

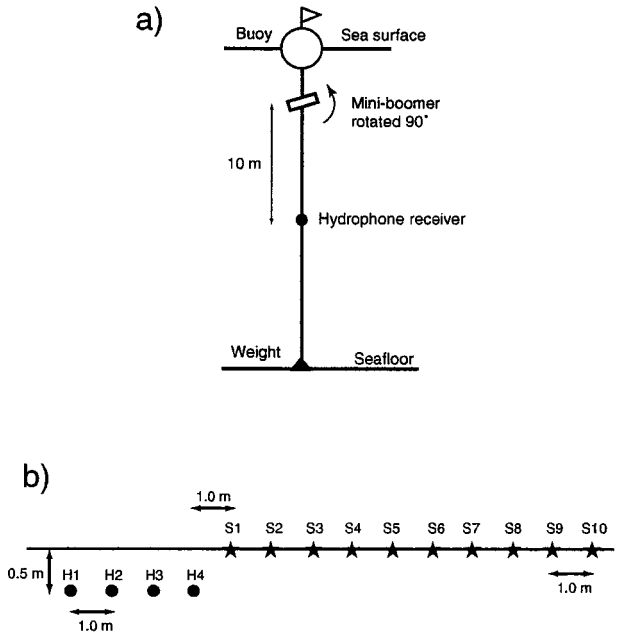

FIG. 2. Geometry of (a) water column experiment; (b) refraction line.

the Atlantic Ocean by the narrow Barloge Creek [see Fig. 1(b)], provided excellent conditions for performing controlled seafloor experiments with the assistance of SCUBA divers.

A mini-boomer acoustic source, specially designed for these experiments, used a high-voltage inverter to drive a magnetopropulsive plate of diameter 20 cm. Water column tests of the source radiation pattern were carried out by suspending the boomer and a hydrophone receiver on a rope from a small boat in about 20 m of water; the weighted end of the rope rested on the seafloor while a surface buoy ensured that the rope was kept taught and as near vertical as possible [see Fig. 2(a)]. Rotating the face of the boomer plate relative to the hydrophone receiver did not produce any significant amplitude variations, indicating a repeatable source with a spherical radiation pattern [see Fig. 3(a)]. The waterborne pulse had a spectral content between 0–11 kHz (−36 dB points) with a notch at about 2.5 kHz, as shown in Fig. 3(b). The hydrophone receiver was omnidirectional with a flat frequency response up to 10 kHz. The source level is estimated to be 215 dB *re* 1 μPa @1 m, producing maximum strains in the sediment of $\sim 10^{-5}$, and suggests that nonlinear effects can be neglected.

A seafloor refraction line was shot in about 15 m of water, parallel to the bathymetric contours [see Figs. 1(b) and 2(b)], using a linear receiver array comprising four hydrophones identical to the one mentioned above. The four hydrophones were taped to a length of white rope at 1 m intervals together with their junction boxes, the amplifier box, and the array cables. This arrangement enabled the SCUBA divers to align the array on the seafloor with the correct receiver spacing. The rope, marked at 1 m intervals, was extended about 15 m beyond the array so that it could be used to correctly position the mini-boomer firing points. The divers then detached the hydrophones from the rope (although still attached electrically) and pushed each one into the soft sediment to a depth of 0.5 m using a specially made steel rod with a depth mark. A diver then positioned the mini-boomer face down on the seabed at successive firing points at 1 m increments at distances 1–13 m from the last hydrophone [H4 in Fig. 2(b)]. The face-down position was found to give the best coupling of sound energy into the sediments after preliminary experiments on the beach; lead weights were placed on top of the mini-boomer to further improve the coupling.

The mini-boomer firing and recording station was positioned on Castle Island [see Fig. 1(b)] and connected to the seabed instruments via about 200 m of screened cables. A four channel, digital storage oscilloscope was used to record the signals on 3.5 in. floppy diskettes. The firing and recording process was coordinated from the beach via two-way radio. A person in a small boat on a station above the array was able to prompt the diver to move the mini-boomer to the next shot point by means of a surface marker buoy connected to the diver by a light rope.

The source and receivers in a traditional refraction line are usually placed at the surface, and not buried like the array described here. The reason for burying the hydrophones was simply to reduce water-borne noise.

The common receiver gather for receiver H1 is shown in Fig. 4; both direct arrivals and sea surface reflections can be identified.

B. Data processing

Spectral analysis was carried out on the common receiver gathers for receivers H1 and H2 in Fig. 2(b) (the records were incomplete for H3 due to disk storage problems, and those for H4 could not be used because of an electrical fault during acquisition). The quality factor (Q) was calculated using three methods: log-spectral ratios, direct computation of spectral components, and the filter correlation method of Courtney and Mayer.[19]

The log-spectral ratios method assumes that the attenuation coefficient, α, is a linear function of frequency, f, over the observation frequency band (i.e., $\alpha = kf$; k is a constant) and that any geometric effects, such as spherical spreading, are independent of frequency. For example, the log-spectral ratio (or LSR) of the signals received at $H1$ from shot points S1 and S2 in Fig. 2(b) is given by the equation

$$\ln\left(\frac{A_2(f)}{A_1(f)}\right) = -k\cdot\Delta x\cdot f - \ln\left(\frac{G_1}{G_2}\right), \tag{1}$$

where $A_1(f)$ and $A_2(f)$ are the spectral amplitudes of the signals from shots S1 and S2, respectively; Δx is the difference in source–receiver distances; and G_1 and G_2 represent the unknown geometric losses, assumed to be independent of frequency. The gradient $(k\cdot\Delta x)$ of the least squares regression line fitted to the graph of LSR versus frequency enables quality factor, Q, to be computed from

$$Q = \frac{\pi\cdot\Delta x}{(k\cdot\Delta x)\cdot U}, \tag{2}$$

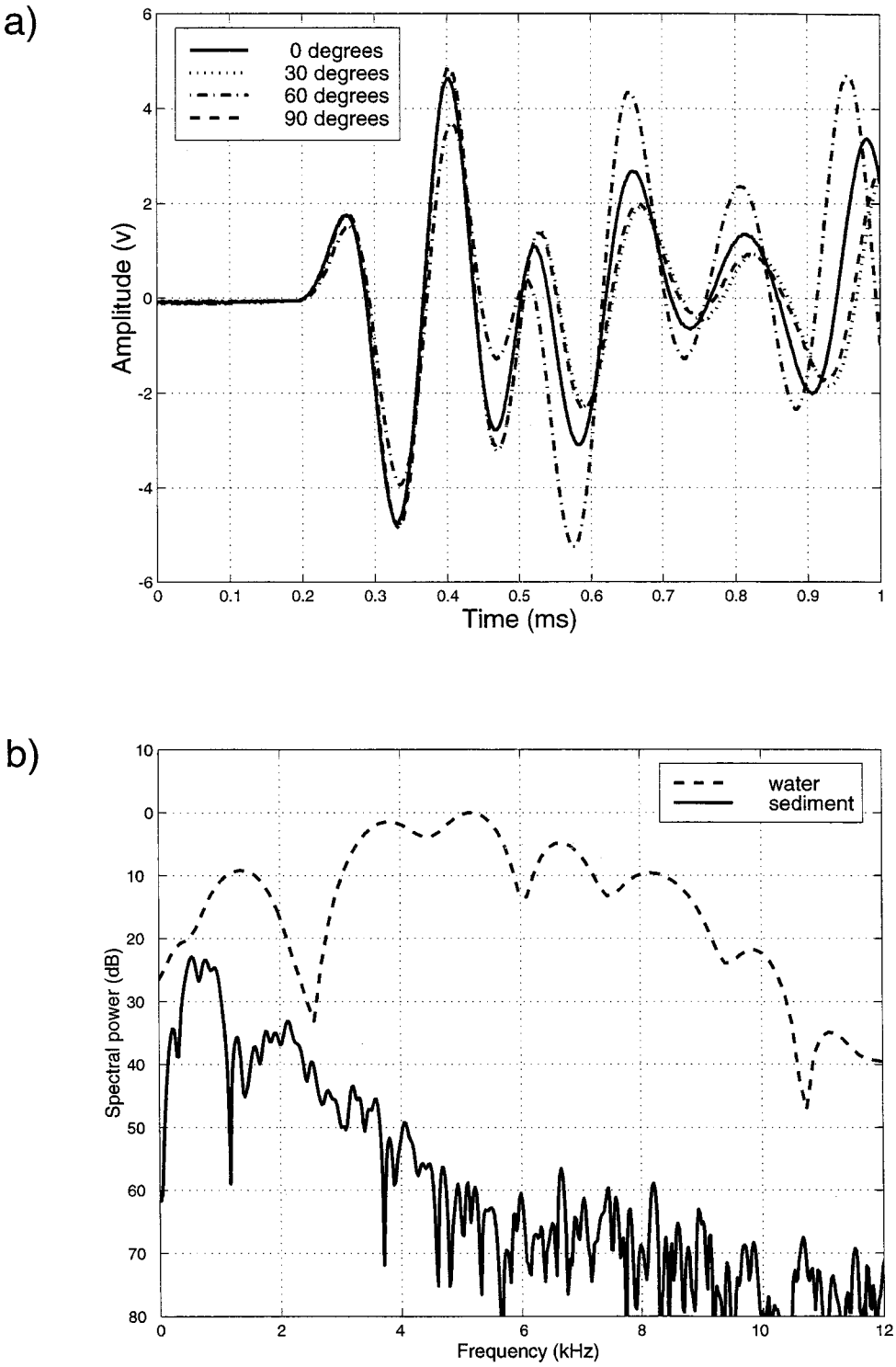

FIG. 3. (a) Water column recordings for mini-boomer at various orientations to the hydrophone receiver. (b) A comparison of spectral power (relative to maximum water column shot power) for the water column and sediment shots, both at a 10 m source–receiver distance.

where, U is the group velocity. Hence, a single Q value is computed for the entire frequency range of the recorded pulse.

The direct computation and filter correlation methods, unlike the LSR method, require some assumptions to be made about geometric losses for the experimental geometry used at Lough Hyne. If these assumptions are valid then the results should indicate the frequency dependence of Q over the range of observation frequencies. Given the results of the water column tests, a spherical spreading law is a reasonable assumption. Hence, the attenuation coefficient is given by

$$\alpha(f)=\frac{1}{\Delta x}\ln\left(\frac{A_2(f)\cdot r_2}{A_1(f)\cdot r_1}\right), \tag{3}$$

where, r_1 and r_2 are the source–receiver distances for S1 and S2, respectively. The quality factor is computed from

$$Q(f)=\frac{\pi\cdot f}{\alpha(f)\cdot c(f)}, \tag{4}$$

where, $c(f)$ is the phase velocity given by

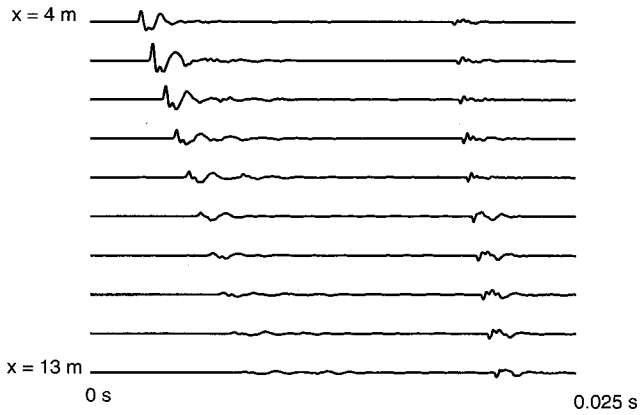

FIG. 4. A common receiver gather for hydrophone H1 (CRG H1).

$$c(f)=\frac{\Delta x}{\left((t_2-t_1)-\dfrac{[\phi_2(f)-\phi_1(f)]}{2\cdot\pi\cdot f}\right)}. \tag{5}$$

t_1 and t_2 are the window start times, and $-\phi_1(f)$ and $-\phi_2(f)$ are the phase delays of the signals for S1 and S2, respectively.

The filter correlation technique can potentially give more stable results than the other methods, especially when small time windows must be used because the signal of interest is close to other arrivals. The first arrivals in Fig. 4 show signs of interference by the slightly later, direct water arrival that are impossible to separate by time gating (windowing); see Fig. 5 for a clearer picture of the waveforms.

The filter correlation method used here was adapted from that described by Courtney and Mayer;[19] a brief description follows. First, the bandwidth of the received signals was determined and divided into equal, narrow bands of 200–300 Hz, 300–400 Hz, 400–500 Hz, and so on up to 4900–5000 Hz. The signals received for each source–receiver distance were windowed to remove the sea surface reflections (noting the window start times to enable the correct computation of phase velocity) and filtered according to the passbands indicated above using a causal, Butterworth filter like the one described in Kanasewich.[20] Each filtered time series was then cross-correlated with a similarly filtered reference time series; the magnitude of the resultant cross-correlation function is a maximum when the two filtered time series align. The signal at a source–receiver distance of 5 m was used as the reference instead of that at 4 m, the closest offset, as the signal amplitude at 4 m is actually smaller than that at 5 m (see Sec. II C). The time shift corresponding to the cross-correlation maximum can be used to calculate the delay time (including that due to velocity dispersion) in the sediment. The attenuation coefficient, $\alpha(f)$, for each passband was calculated according to Eq. (3) with $A_1(f)$ and $A_2(f)$ equal to the root-mean-square energy of the reference and signal time series, respectively. The phase velocity and attenuation coefficient calculated for each passband were assigned to the passband central frequency.

C. Results

The results for common receiver gather H1 are discussed below (common receiver gather H2 gave similar results). One area of concern particularly relevant to attenuation measurements is the repeatability of the coupling between the mini-boomer source and the seafloor. Figure 6 shows two comparisons of first arrivals that were repeated during the experiment; the agreement is excellent in both cases, which suggests that unrepeatable coupling is not a significant source of experimental error.

The graph (not shown) of the first break arrival time versus source–receiver distance can be closely approximated by a straight line giving a group velocity of 1716 ± 10 m/s using least squares regression. There are no slope breaks, which suggests a weak velocity gradient in the upper few meters below the seafloor. For the purpose of the spectral analysis, where signals from shot point pairs are compared, it is assumed that the rays have travelled horizontally through

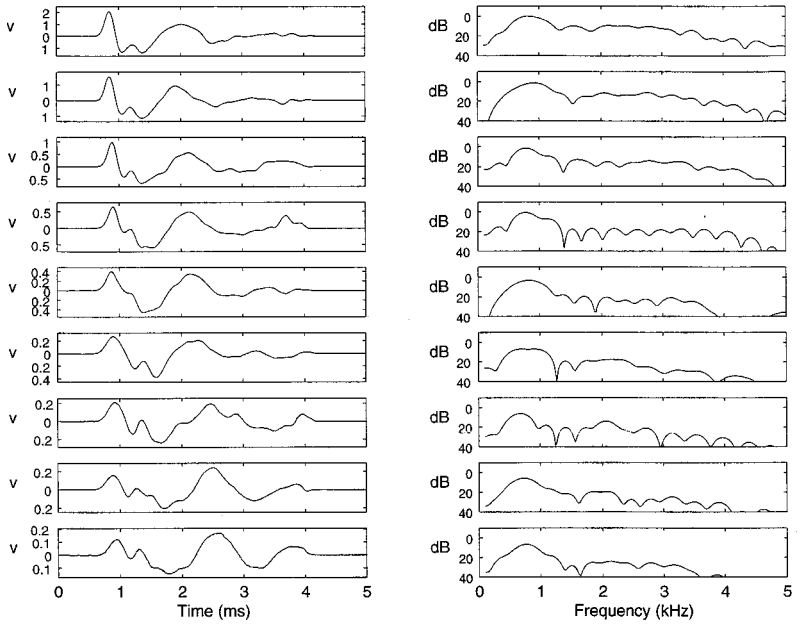

FIG. 5. Windowed signals and their corresponding power spectra for CRG H1, offsets 5–13 m.

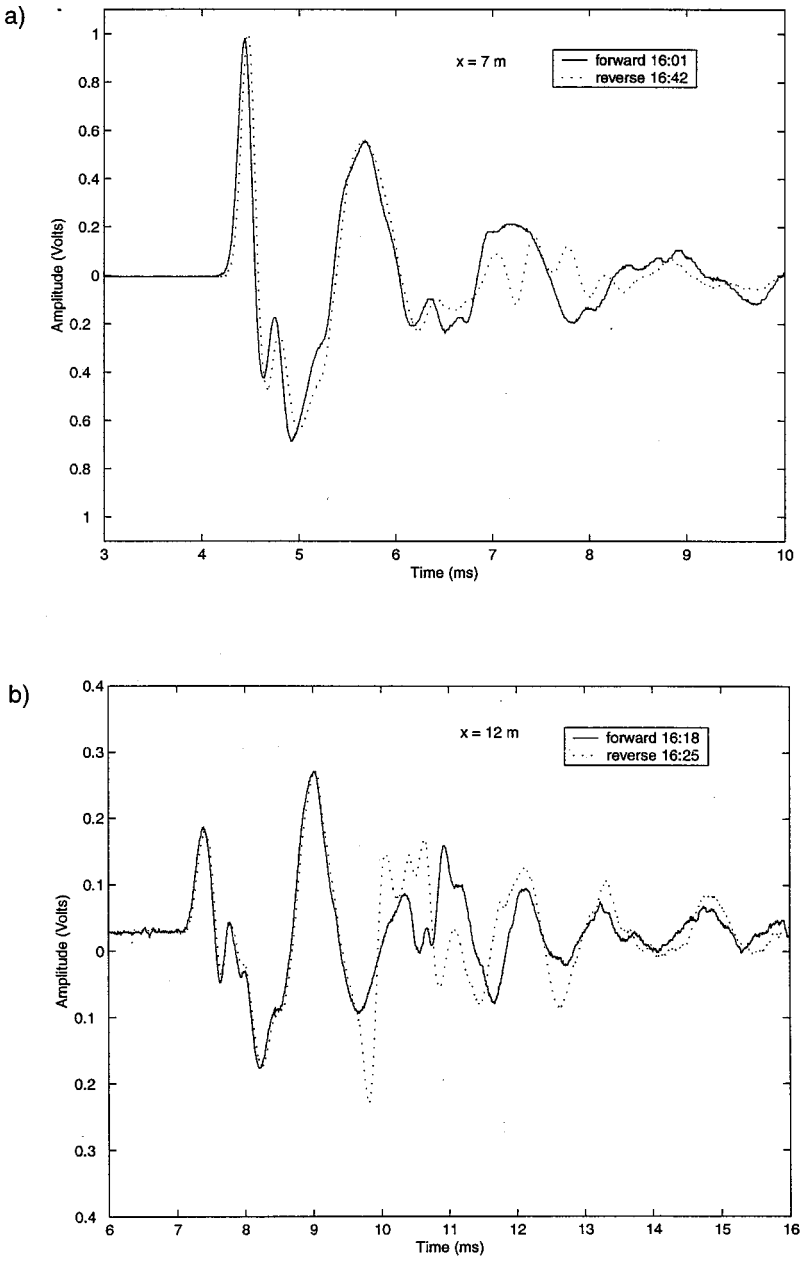

FIG. 6. A comparison of mini-boomer seafloor refraction line shots at different times (indicated) at offsets of (a) 7 m and (b) 12 m. The mini-boomer was removed from the seafloor between each shot.

the sediment along the same paths except for the difference in pathlength.

The LSR results for source–receiver distances of 6 and 13 m relative to the reference signal at 5 m are shown in Fig. 7. The slope, which should be negative according to Eq. (1), of the linear least squares fit to the data between 200–1500 Hz is so small for distances 6–8 m that Eq. (2) gives negative Q values; the other distances result in a mean Q of 19.5 ± 10.8. The amplitude spectra seem to be "well behaved" only below 1500 Hz, corresponding to the first spectral peak in Fig. 3.

The spectral analysis using Eqs. (3)–(5) for the direct computation method gave unstable results that depended on the window length. However, they were broadly similar to the filter correlation results and so only the latter are discussed here. Figure 8 shows the average of the filter correlation results for shot–receiver distances 6–13 m in the bandwidth 200–5000 Hz with 95% confidence intervals. Although there is significant instability in the results at certain frequencies (large confidence limits), the magnitudes of the computed values seem reasonable. Overall, phase velocity increases from about 1500 m/s at 200 Hz to about 1650 m/s at frequencies above 800 Hz; attenuation coefficient shows a broadly linear increase with frequency between 200–2400 Hz, except for a spectral peak at about 1500 Hz that is possibly associated with the spectral notch at 1500 Hz seen in Fig. 3; quality factor varies between about 5–20 below 2500 Hz.

The question is whether these results represent the true intrinsic acoustic properties of the seafloor sediment (assumed here to be one homogeneous layer) or whether they are a consequence of wave propagation effects such as reflection, refraction, scattering, interface waves, and so on. The limited core data available (see below) means that it is

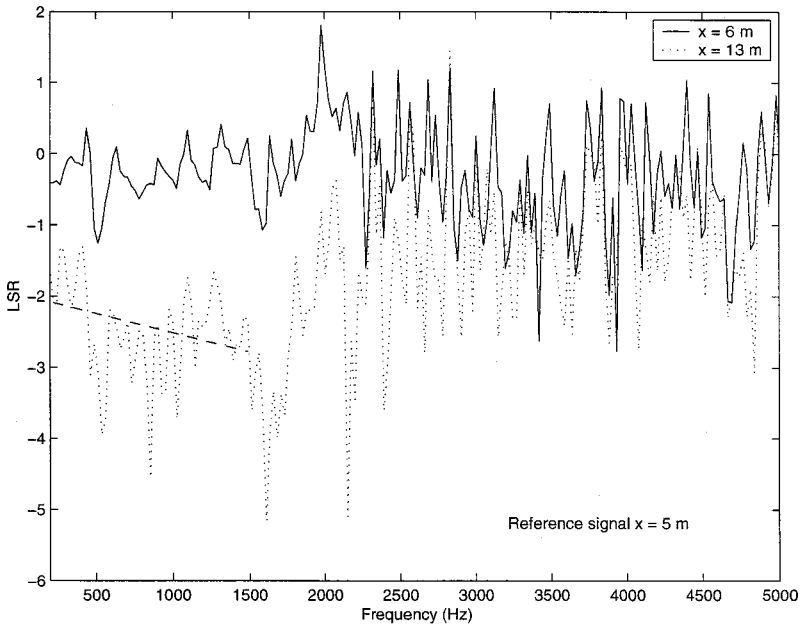

FIG. 7. Log-spectral ratios (LSR) plot for CRG H1 offsets 6 and 13 m. The reference signal was at an offset of 5 m.

impossible to provide a definitive answer; however, some insight can be gained by generating synthetic acoustic records using the forward reflectivity model of Fuchs and Müller.[21]

Figure 9 shows the synthetic acoustic records computed using the layer model in Table I with parameters derived from core measurements (see Sec. III C). The synthetic records show some of the features seen in the Lough Hyne data, such as the rapidly attenuating first arrival, the low-frequency, direct water path arrival with a large positive amplitude, and the increase in amplitude between 4–5 m offsets. At short offsets the two arrivals merge while they are clearly separated at larger offsets. Destructive interference between these two arrivals may explain the spectral notch at 1500 Hz in Fig. 3, that might be expected at a frequency equivalent to about half the dominant wavelet period, here equal to 0.68 ms, giving destructive interference at 1470 Hz. Using the same model with a spike source pulse instead of the Ricker wavelet used in Fig. 9 demonstrates that the refracted ''arrival'' is a combination of closely spaced, refracted arrivals from the model layers. Surprisingly, while the direct water path arrival in the model ($Qp=1000$) has virtually no decrease in amplitude, this arrival on the *in situ* data closely follows the amplitude decay of the sediment-borne arrivals; the most logical explanation is that the water near the seabed is actually quite highly attenuating. This could be related in some way to the peak spawning times of invertebrates in Lough Hyne from July to September[22] and to the rough seabed; underwater photographs reveal an abundance of mounds on the seafloor, created by burrowing animals, and very cloudy water due to suspended organic matter.

The velocity and attenuation calculations do not distinguish between the refracted and water-borne arrivals, but

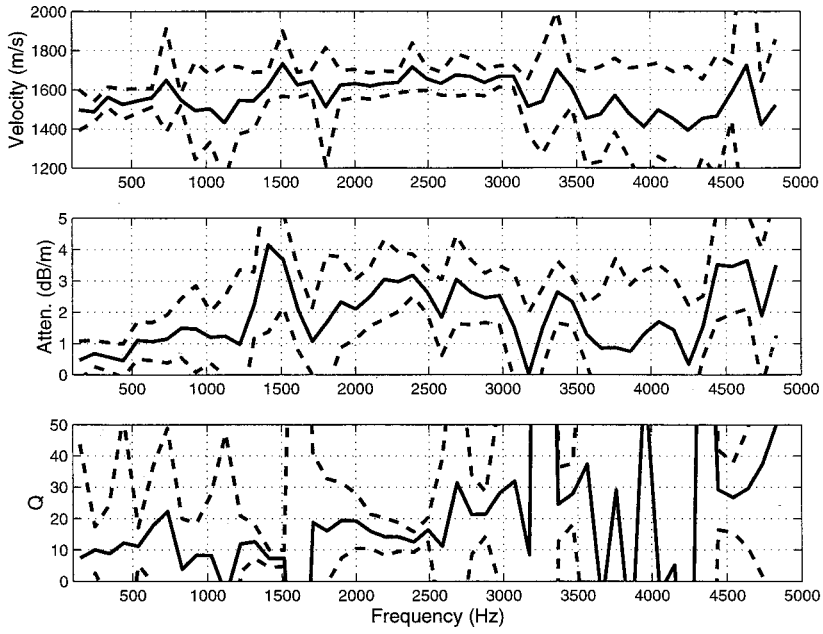

FIG. 8. Average compressional wave velocity, attenuation coefficient, and quality factor spectra for CRG H1 for offsets 5–13 m. The 95% confidence limits are indicated.

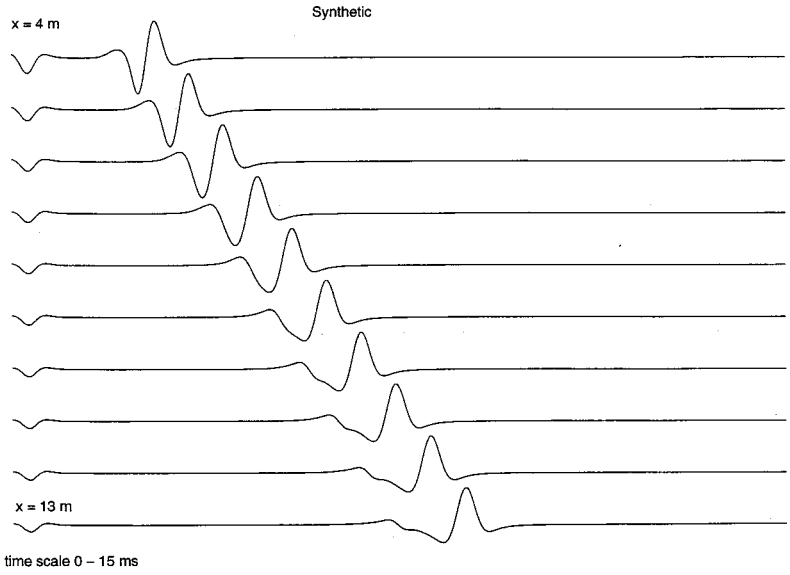

FIG. 9. Synthetic acoustic records for the reflectivity model in Table I.

simply compute the values for each passband frequency. The *in situ* data in Figs. 4 and 5 seem to show that the waterborne pulse is of a much lower-frequency content than the refracted sediment arrivals, therefore, it is probably safe to assume that the apparent velocity dispersion in Fig. 8 is due to the difference in velocity of water and sediment. The results suggest that the near-seafloor water has a similar attenuation to the sediments with a quality factor between 10–20.

Linear least-squares regression of the first break arrival times gives a velocity of 1716 ± 10 m/s for the *in situ* data, and 2211 ± 50 m/s for the synthetic data; the simple, unweighted, average velocity of the model layers is 1782 ± 37 m/s. On this basis, it would appear that the *in situ* velocities of the sediment layers at 200–1500 Hz are significantly lower than those measured in the laboratory at 342 kHz, and lower than the first break velocity; the phase velocity of about 1600 m/s above 800 Hz in Fig. 8 seems a reasonable estimate.

Realistic quality factors vary between 5–20 for 200–1500 Hz in Fig. 8 and compare well with the LSR result above. The various assumptions of constant Q and frequency-independent spherical spreading seem to be self-consistent here. The instability of the data make it very difficult to derive any more detail on the frequency dependence of the quality factor. Changing the Qp values to 100 for each of the layers in the reflectivity model in Table I has the predicted effect on the refracted arrivals; hence, the assumption seems valid that the high attenuation of the refracted arrivals is directly related to the low Q of the sediment layers. Some doubts may stem from the nature of the shell layer at 22–37 cm depth, the acoustic properties of which could not be measured on the sediment core because of signal scattering (see Sec. II C). However, scattering from individual shells (1–2 cm long) is not thought to be a problem at the wavelengths of the *in situ* experiment (>1 m). The core density measurements (reliable) and subsequent prediction of *P*-wave velocity in the shell layer indicate an intermediate velocity to the adjacent layers, and not a large velocity contrast.

III. LABORATORY MEASUREMENTS

A. Method

A 1 m push core was taken at the refraction line site for laboratory analysis. The core was split longitudinally and logged for *P*-wave velocity (500 kHz), bulk density (gamma ray attenuation method), and magnetic susceptibility at 1 cm intervals using an automated system (a multisensor core logger, or MSCL).[23] The core was also described and subsampled for grain size analysis. The mean logged core temperature was 14 °C.

Velocity and quality factor measurements were also made on the core using broadband transducers in the transmission mode, placed manually in contact with the core in a similar manner to the automated core logging system [see Fig. 10(a)] and coupled using water (the core temperature was also about 14 °C). The measurement locations were se-

TABLE I. Horizontal layer parameters for input to the reflectivity model of Fuchs and Müller (Ref. 21).

Layer No.	Depth (m)	*Vp* (m/s)	*Qp*	*Vs* (m/s)	*Qs*	Density (kg/m^3)
0	0.0–15.0	1500	1000	0	1000	1024
1	15.0–15.23	1745	10	50	10	1784
2	15.23–15.37	1765	10	50	10	1838
3	15.37–15.56	1830	10	50	10	1896
4	15.56–16.00	1770	10	50	10	1809
5	16.00–25.00	1800	10	50	10	1800

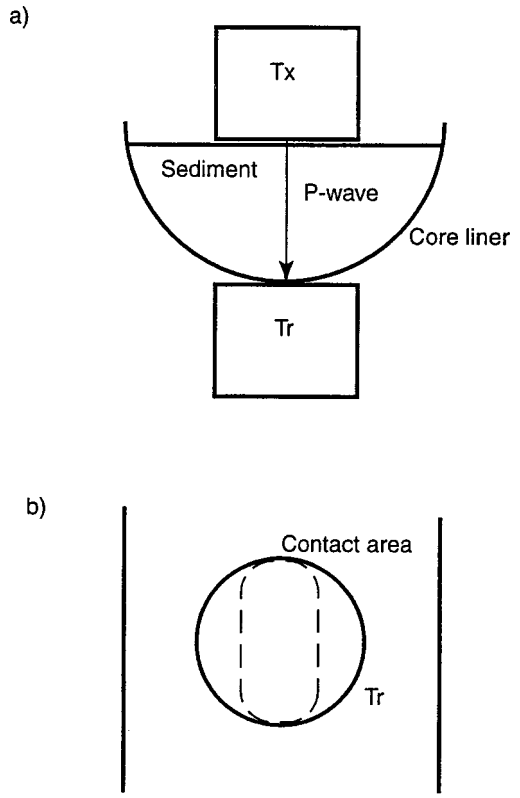

FIG. 10. (a) Experimental setup for acoustic core measurements. (b) Plan view of transducer/core liner contact area.

lected according to the MSCL results to give velocities and attenuations representative of the Lough Hyne sediments for a comparison with the *in situ* results.

The curvature of the core liner means that the contact area of the receiving transducer [Tr in Fig. 10(b)] is not circular, making it difficult to predict the geometric effects on signal amplitude and phase. However, geometric effects can be mostly eliminated by comparing travel times and amplitudes measured through sediment- and water-filled liners, knowing the acoustic properties of water (see below).

B. Data processing

A direct computation and the filter correlation methods were used to process the broadband core data. Equation (5), with subscripts 1 and 2 referring to the water- and sediment-filled liner, respectively, could not be used because the small differences in core thickness gave unstable results. The following equation was used to compute phase velocity, $c(f)$, instead (for the filter correlation method):

$$c(f)=\frac{(x_2-x_l)}{(|t_2-t_1|+t_w+\delta t)}, \tag{6}$$

where x_2 is the total core thickness, x_l is the linear thickness; t_1 and t_2 are the start times of the windowed sediment and water signals, respectively; δt is the time shift computed using the filter correlation method, as described in Sec. II B; and $t_w=x_w/C_w$, where x_w is 0.0251 m and V_w is taken as 1500 m/s. In essence, Eq. (6) corrects the measured travel time through the water-filled liner for any geometric effects and adds to this the time delay, including dispersion. In this case, the time delay due to dispersion in the sediment is computed, assuming that there is no dispersion in the water (i.e., t_w is constant for all frequencies), unlike in Eq. (5), where no such assumption is made because the known spectral differences are considered there. Since the water temperature at 15 m depth in Lough Hyne falls in the range 12 °C–16 °C during the summer,[22] no temperature corrections were applied to either the core logger or the broadband velocity measurements.

The attenuation coefficient was calculated using

$$\alpha(f)=\frac{1}{(x-x_l)}\ln\left(\frac{A_w(f)}{A(f)}\right)+\alpha_w f^2(x_w-x_l), \tag{7}$$

where $A(f)$ and $A_w(f)$ are the signal rms energies through the sediment- and water-filled liner, respectively (geometric effects cancel out); x_w is the measured thickness of the water-filled liner; and α_w is the attenuation in distilled water (36×10^{-15} N m^{-1} Hz^{-2} at 10 °C).[24] The quality factor was calculated using $\alpha(f)$ in Eq. (4). The filter correlation passbands were 200–300 kHz; 300–400 kHz; 400–500 kHz, etc., up to 800–900 kHz.

C. Results

The core logs in Fig. 11 show that the Lough Hyne sediments are quite variable in their physical properties, even over such a short depth range of 1 m, and these variations correspond to several layers recognized by visual inspection. The most obvious layers are the shell bed between 23–37 cm subbottom depth, which comprises whole and broken gastropod shells up to 2 cm long; and the mud layer between 56–61 cm depth.

The MSCL velocities were highly spurious and are not shown. Instead, the broadband velocities at 342 kHz are plotted as open circles in Fig. 11, together with velocities predicted using the Gassmann model[25] based on the MSCL density that seems reliable. The main unknowns in the model are the frame bulk and shear moduli that must be estimated by fitting the model velocity to the measured velocity; arbitrary, constant frame moduli were used in Fig. 11. In reality, the frame moduli will depend also on the porosity of the sediment, as this is directly related to the grain size distribution and, hence, sediment fabric. However, the model results give some estimate of the velocity variability in the core due to porosity variations. The results predict a slight increase in velocity in the shell and mud layers, but no dramatic changes. This information was used in the reflectivity model of the *in situ* data (see Sec. II C and Table I).

Core drying is a possible cause for concern as the broadband results were obtained 1 year after the MSCL measurements, which in turn were made 1 year after the core was collected, although the core was stored at 4 °C in a dark room during this time. It is known that coarse sediments (e.g., sands and gravels) are more susceptible to drying than muds, although all the sediments have appreciable mud contents (see below), and there were no visual signs of the core drying out. If the surface (<1 mm) of the silty sediments had been only partially saturated then there would have been a loss in coupling between the upper transducer face and the

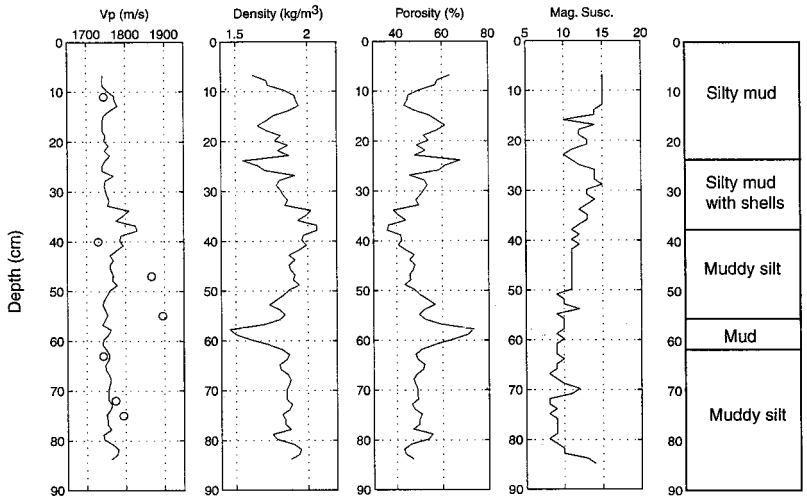

FIG. 11. Multisensor core logger results for the 1 m long Lough Hyne core with lithological description. The continuous velocity curve was derived from the density data using Gassmann's model; the open circles represent the laboratory broadband velocity measurements (342 kHz) at selected depths.

sediment, as all measurements were made with the protective plastic film (impermeable to water; approximately 0.1 mm thick) in place. The broadband transducers were carefully placed to avoid visible shells to minimize scattering problems, although scattering was still a problem for the measurements in the shell layer (depths 22, 26, 33 cm; not plotted as they seem spurious at 2342, 4098, and 3335 m/s at 342 kHz, respectively).

Bulk density varies between 1400–2100 kg/m^3, while porosity varies between 36%–60%. Porosity, ϕ, was computed using the relationship

$$\phi = \frac{(\rho_g - \rho)}{(\rho_g - \rho_w)}, \tag{8}$$

where ρ is the measured sediment density, ρ_g is the grain density (taken here as 2.65 g/cm^3, the value for quartz), and ρ_w is the density of seawater (1.024 g/cm^3).

Table II lists the results of the grain size analysis for sediment subsamples taken from core depths corresponding to the broadband measurement locations. Mean grain diameter (Mz), sorting (σ_1) and skewness (SK_1) were calculated according to the methods described by McManus.[26] It can be seen that the Lough Hyne sediments range from moderately sorted ($0.7 < \sigma_1 < 1$), through poorly sorted ($1.0 < \sigma_1 < 2.0$), to very poorly sorted ($2.0 < \sigma_1 < 4.0$), and the mean grain diameter ranges from 2.9ϕ (fine sand) to 5.5ϕ (coarse silt). The grain size distribution is symmetrical ($-0.1 < SK_1 < 0.1$) to positively skewed ($0.1 < SK_1 < 0.3$). The recorded broadband signals and their power spectra are shown in Fig. 12; the two uppermost plots are for the water-filled liner used as the reference signal in the filter-correlation method. The core depths 22, 26, and 33 cm, corresponding to the shelly layer, have a low signal-to-noise ratio and have significant spectral power more than 36 dB down on the maximum power of the water-filled liner spectrum; the other signals are generally greater than -36 dB up to about 600 kHz.

The results from the direct computation and filter correlation methods were very similar, and so only the filter correlation results are presented (there were no interfering pulses). The phase velocity, attenuation coefficient, and quality factor spectra for all core depths measured, shown in Fig. 13, show a range of magnitudes and similar frequency trends. The exceptions are the attenuation coefficient spectra for depths 22, 26, and 33 cm (corresponding to the shell layer) that show broad maxima while the other core depths show steadily increasing attenuation over the observation bandwidth (<700 kHz). Even though the signal-to-noise ratio is approaching the experimental resolution for these three core depths, the similarity in the spectra give some confi-

TABLE II. Porosity, bulk density, and grain size analysis data for the Lough Hyne core subsamples. Mean grain diameter (Mz), sorting (σ_1), and skewness (SK_1) were calculated according to McManus (Ref. 26).

Depth (cm)	Porosity (%)	Bulk density (g/cm^3)	Sand fraction (%)	Silt+clay fraction (%)	(silt+clay)/ sand ratio	Mean diameter (Mz)	Sorting (σ_1)	Skewness (SK_1)
11.0	45.2	1.91	44.9	55.3	1.2	3.9	1.8	0.1
22.0	52.7	1.79	62.4	37.6	0.6	3.8	0.9	−0.1
26.0	58.4	1.7	50.3	49.6	1.0	4.1	0.8	0.0
33.0	49.6	1.84	17.9	82.2	4.6	5.5	1.4	0.0
40.0	42.3	1.96	68.6	31.8	0.5	2.9	1.7	0.2
47.0	46.1	1.91	21.8	78.6	3.6	5.1	1.3	0.0
55.0	49.8	1.84	74.0	26.0	0.4	3.4	1.0	0.0
63.0	48.2	1.87	57.6	42.4	0.7	3.2	2.2	0.1
72.0	49.2	1.85	56.2	43.8	0.8	3.4	2.2	0.1
75.0	50.9	1.82	64.1	35.8	0.6	3.0	1.8	0.2

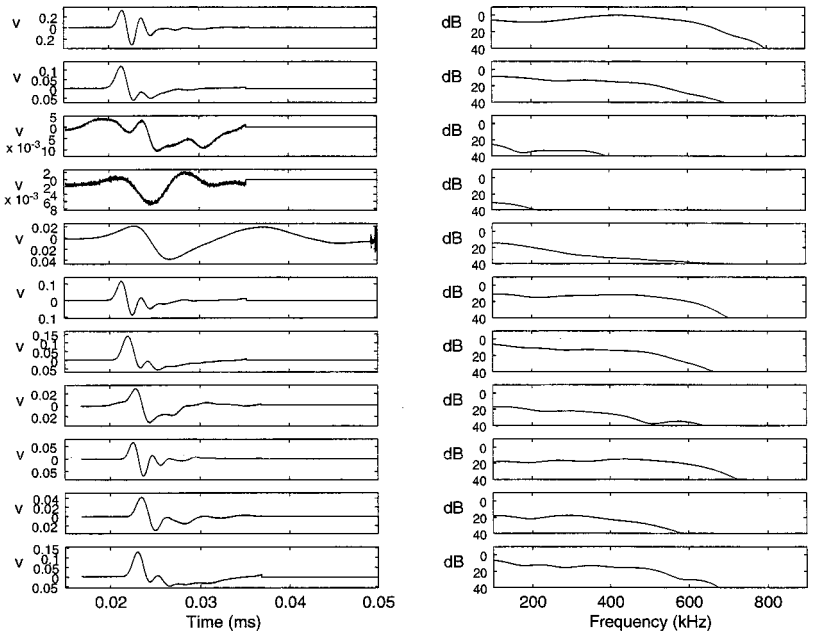

FIG. 12. Windowed, broadband acoustic signals for the Lough Hyne core with their corresponding power spectra. The uppermost plots are for the water-filled liner, the rest are for core depths 11 cm (top), 22, 26, 33, 40, 47, 55, 63, 72, and 75 cm (bottom).

dence that these are not random results. There is no evidence for Rayleigh scattering (f^4 dependence of the attenuation coefficient).

As our main purpose in this paper is to compare the *in situ* and laboratory properties of the Lough Hyne sediments, a simple average of the results was taken (shell layer results omitted) and plotted in Fig. 14. Phase velocity stays fairly constant at about 1800 ± 50 m/s between 200–700 kHz. The attenuation coefficient shows a linear frequency dependence while the quality factor is in the 10–20 range and shows a slight increase with frequency.

IV. DISCUSSION

A. Frequency dependence of velocity and attenuation

Since researchers began to collate sediment acoustic data from different observation frequencies, the most common trend to emerge has been a linear dependence of attenuation coefficient on frequency, equivalent to a constant Q (quality factor) or to a constant Q^{-1} (dissipation factor). It is generally accepted that constant Q is a good first-order approximation to wave propagation in marine sediments.[2,27] Also, many of the published data indicate marine sediments have relatively high Q (50–100) and insignificant velocity dispersion (<1%), e.g., Wingham.[1] However, the laboratory data presented by Shumway,[14,28] supported by *in situ* attenuation measurements by McCann and McCann[29] show that constant Q does not describe detailed observations over part of the frequency spectrum (20–30 kHz), and that Q in this part of the spectrum is low (<50) and velocity dispersion is significant (>1%). It would be surprising if clean, well-sorted sands, such as those used in Wingham's experiments, behaved in the same manner as well-sorted marine clays, or as poorly sorted sediments comprising a mixture of clay, silt, and sand grains.

The Lough Hyne attenuation coefficients and velocities (the average values from Figs. 8 and 14) have been plotted against measurement frequency in Figs. 15 and 16 together with published data. Sample descriptions indicating mixed sediments (clay/silt/sand) in Table I of Bowles' paper[27] (a compilation of many authors' results) seemed most appropriate for a comparison with the Lough Hyne results, and are taken here to represent well-sorted marine sediments over the whole frequency range of interest (a few Hz to 1 MHz). Although Bowles did not provide any geotechnical data, the last statement can be justified on the basis of the laboratory results of McCann and McCann (who did provide geotechnical data: porosity, grain size information, carbonate content, etc.) that are included in the Bowles dataset and indicate porosities greater than 60%, commonly associated with well-sorted, fine grained marine sediments. The data from Table 1a of Shumway's paper[14] represent mixed sediments of both low porosity (36%–50%) and high porosity (50%–75%) in shallow water (<50 m).

There are several interesting features worthy of comment.

(1) The Lough Hyne *in situ* velocities at 200–1500 Hz fall within the range of Shumway's velocities at 20–30 kHz, and are lower than the Lough Hyne core velocities at 200–800 kHz. Shumway's velocity data (none provided by Bowles) show a bimodal distribution at 20–30 kHz: poorly sorted, low porosity sediments (refer to Table 1a in Shumway's paper[14]) cluster around 1700 m/s, while well-sorted, high porosity sediments cluster around 1500–1550 m/s.

(2) The magnitudes of the Lough Hyne attenuation measurements are significantly higher than those for the Bowles data in both observation bandwidths. Shumway's attenuation data range between those of Bowles at 20–30 kHz and significantly higher values.

(3) Fitting trend lines to log–log plots of attenuation coefficient versus frequency f gives dependencies of $f^{0.63 \pm 0.33}$ ($R^2 = 0.68$) for the *in situ* results and $f^{0.88 \pm 0.10}$ ($R^2 = 0.98$) for the laboratory results. The data diverge significantly from the linear frequency depen-

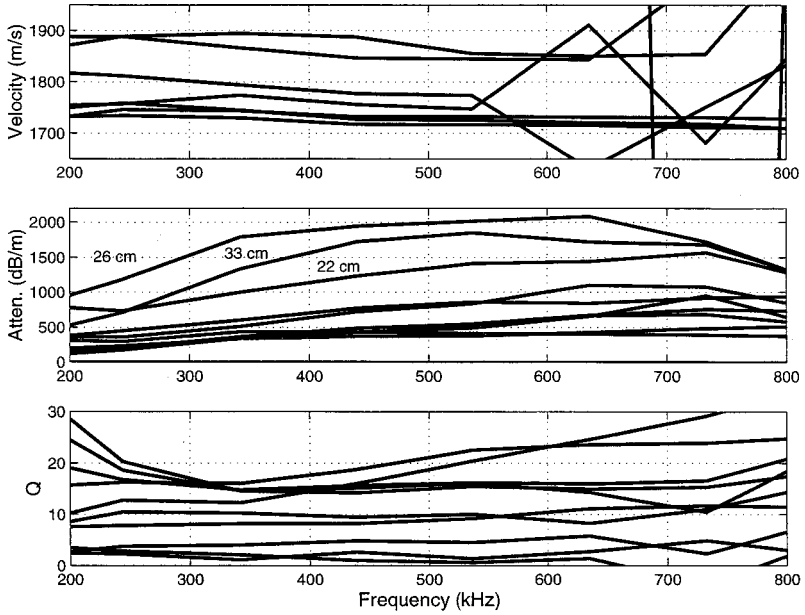

FIG. 13. Laboratory compressional wave velocity, attenuation coefficient, and quality factor spectra for the Lough Hyne core. Core depths 22, 26, and 33 cm are labeled.

dencies often quoted in the literature, and show different dependencies in the two observation bandwidths.

(4) The observed velocity dispersion between the *in situ* and laboratory central frequencies is 12.5% (taken here as 1600 m/s at 800 Hz, and 1800 m/s at 342 kHz, respectively).

Although there are uncertainties associated with both datasets (discussed in Secs. II C and III C), it is difficult to attribute such a large difference in velocity to experimental error alone. Is it only coincidence that Shumway's velocities for similar sediments at 20–30 kHz fall within the range of the Lough Hyne observations? Is it only a coincidence that a constant Q model[30] with $Q=15$ predicts a velocity dispersion of 12.8% for the same frequency range (800 Hz to 342 kHz)?

B. Attenuation mechanisms

Taken at face value, these results provide evidence of significant velocity dispersion between *in situ* and laboratory frequencies in highly attenuating marine sediments. Given the impermeable nature of these sediments, it is no surprise that Biot's global fluid flow model[4,5] greatly underestimates the magnitudes of attenuation and velocity dispersion observed in the Lough Hyne sediments, as indicated Figs. 15 and 16. Note that the unknown frame moduli were adjusted to give a Biot velocity of about 1550 m/s, but they could have been set to give a velocity of 1800 m/s. In either case, the predicted velocity dispersion and attenuation are negligible. Stoll's model[8] and Leurer's adaptation[9] were not used here because they rely on empirical knowledge of the shear modulus and damping that were unavailable in this case.

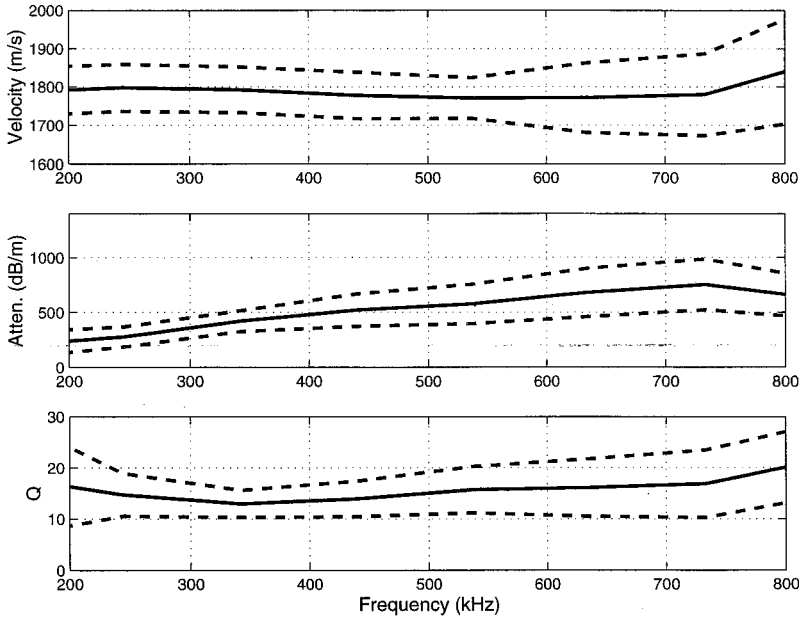

FIG. 14. Average laboratory compressional wave velocity, attenuation coefficient, and quality factor spectra for the Lough Hyne core.

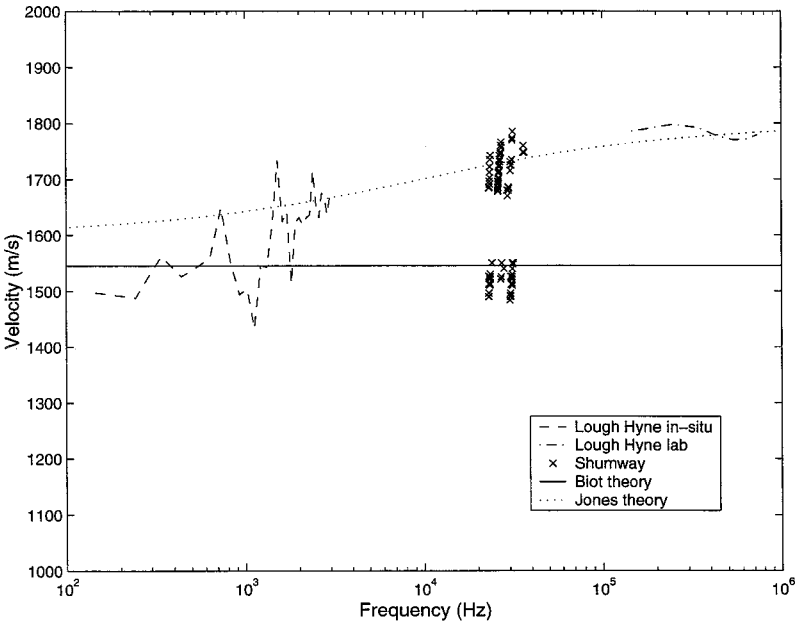

FIG. 15. A comparison of Lough Hyne *in situ* and laboratory velocity data with the published data of Bowles (Ref. 27) and Shumway (Ref. 14), and with the theoretical models of Biot (Refs. 4 and 5) and Jones (Ref. 33). Note the log-frequency scale.

However, the idea that the dominant intrinsic loss mechanism can be modeled using complex elastic moduli is valuable.

Solid friction between mineral grains was once mooted as an important attenuation mechanism in sediments and sedimentary rocks. This has largely been discounted as a significant loss mechanism in sedimentary rocks at the small strains associated with acoustic waves.[31] Instead, an increasing volume of literature suggests that attenuation in sedimentary rocks is largely caused by local viscous fluid flow (or squirt flow) due to compliance heterogeneities such as grain contacts or microcracks,[15,32] or even clay minerals.[18] In the absence of a complete squirt flow model based solely on measurable geotechnical input parameters (i.e., one that allows the derivation of the frequency-dependent, complex frame elastic moduli from purely geotechnical considerations), the Lough Hyne data were compared to the phenomenological model of Jones[33] using a bulk modulus of 4.9 GPa, a pore fluid viscosity of 1.52×10^{-3} Pa s, and a compliance heterogeneity aspect ratio of 1.5×10^{-3}. By arbitrarily adjusting the model parameter governing the width of the central relaxation peak (Cole–Cole distribution), it was possible to approximate the magnitude and frequency dependence of velocity and attenuation coefficient in Figs. 15 and 16. It was impossible to get an exact fit to both the velocity and the attenuation curves, although it was possible to fit one or the other curve using the model. This suggests the data do not conform precisely to the viscoelastic model, which may be due either to the experimental errors already outlined, or to another loss mechanism.

It is easy to imagine how, in a poorly sorted sediment, compliance heterogeneities with aspect ratios of the order 10^{-3} could exist due to the irregular morphology of clay mineral flocs and floc-grain contacts. Figure 17 is a log–log

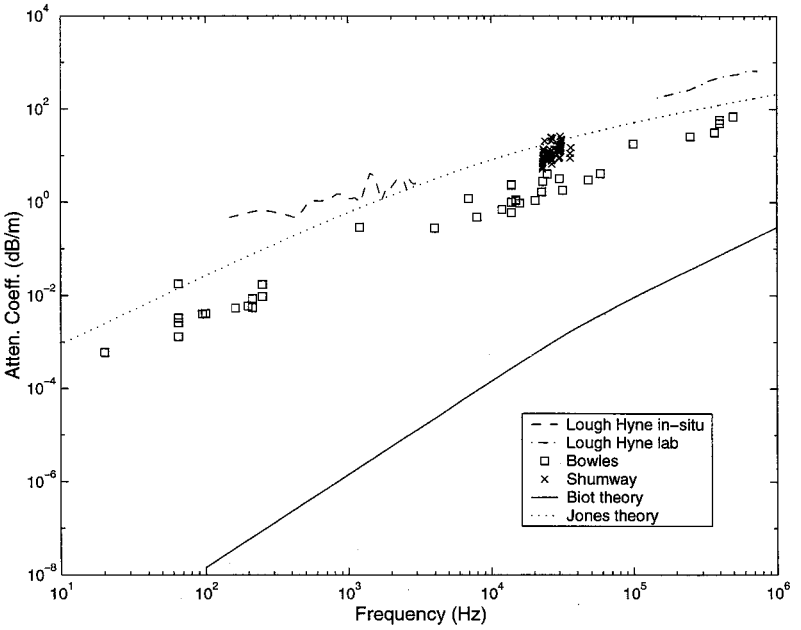

FIG. 16. A comparison of Lough Hyne *in situ* and laboratory attenuation data with the published data of Bowles (Ref. 27) and Shumway (Ref. 14), and with the theoretical models of Biot (Refs. 4 and 5) and Jones (Ref. 33). Note the log–log scale.

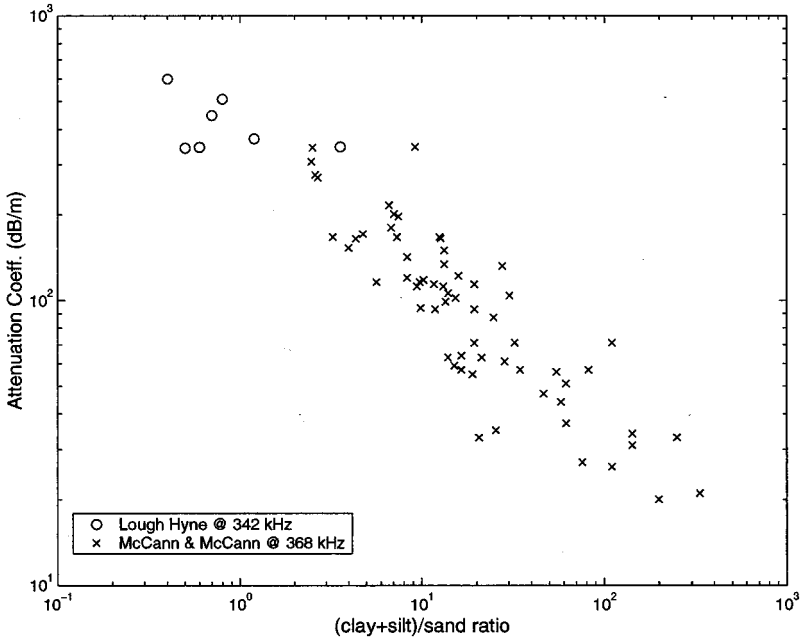

FIG. 17. A plot of Lough Hyne laboratory attenuation results at 342 kHz, and those of McCann and McCann (Ref. 29) at 368 kHz, against the mass ratio of mud (total clay and silt) to sand. Note log–log scale.

plot of the attenuation coefficient at 342 kHz against the mass ratio of total clay and silt to sand in the low porosity (36%–60%) Lough Hyne sediments. Also plotted for comparison are the 368 kHz data of McCann and McCann[29] for high porosity (>60%) silty clays. The original intention was to plot the ratio of clay to total sand and silt (i.e., the ratio of compliant to noncompliant minerals), but the limited grain size data dictated the grouping of clay and silt. Despite this, there appears to be a strong correlation between attenuation and (clay+silt)/sand ratio, and the two independent datasets follow the same trend (note the log–log scale). ''Clay squirt flow'' is a strong candidate for the dominant loss mechanism in poorly sorted marine sediments. The contacts between compliant, irregularly shaped clay flocs and stiff silt/sand grains could provide the necessary compliant, water saturated, pores necessary for squirt flow.

It is interesting to note that there was no evidence of free gas, either in the Lough Hyne sediment core or observed by the divers on the seafloor, which is often quoted as being responsible for high attenuation in marine sediments.

Despite these problems, a clear pattern emerges of high attenuation and significant velocity dispersion in the Lough Hyne sediments. The observed magnitudes and frequency dependencies of compressional wave velocity and attenuation can be described by a phenomenological local viscous (squirt) flow model. One explanation is that the compliance heterogeneities necessary for squirt flow are most abundant, and, hence, lead to the greatest losses, in poorly sorted sediments when mud (clay+silt) and sand are present in nearly equal proportions; the surface interactions of irregularly shaped clay flocs, silt, and sand grains provide the compliant pores necessary for squirt flow.

Perhaps the most significant finding of this study is the highly attenuating nature of the Lough Hyne sediments and their correspondence to laboratory data for similar, poorly sorted, marine sediments reported by other authors. It is surprising that these important and ubiquitous sediments have merited relatively few studies in the literature when compared to their well-sorted cousins (clean sands or marine clays).

V. CONCLUSIONS

The high-resolution data presented here give an indication of what can be achieved using broadband measurement techniques that allow frequency-dependent velocity and attenuation to be measured. The quality of the *in situ* and laboratory acoustic data is excellent, although the study would have benefitted from more core samples and early core analysis. The interpretation of the *in situ* data would have benefitted from a more accurate forward reflectivity model in both the depth below seafloor and the horizontal extent of the sedimentary layers identified (i.e., deeper and more core samples needed). Also, larger samples would have allowed the laboratory resonant column method to be used that could have provided unambiguous compressional wave results in the 10–30 kHz range, and shear modulus data.

ACKNOWLEDGMENTS

This work was funded variously by the Natural Environment Research Council, United Kingdom (UK), the Defense and Evaluation Research Agency UK, and the European Commission under Contract No. MAS3-CT95-0038. Special thanks go to the Irish National Parks and Wildlife Service for granting permission to use Lough Hyne and to the following people for contributing to the success of the fieldwork program: Mike Somers, Peter Schultheiss, Sally Marine, Graham Lake, Bryony Chapman, Becky Case, and Sam Marks. Thanks also to Dave Gunn for core logging, to Emma Gould for grain size analysis, and to Tim Minshull for advice on reflectivity modeling.

[1] D. J. Wingham, J. Acoust. Soc. Am. **78**, 1757–1760 (1985).
[2] A. C. Kibblewhite, J. Acoust. Soc. Am. **86**, 716–738 (1989).
[3] M. J. Buckingham, J. Acoust. Soc. Am. **102**, 2579–2596 (1998).
[4] M. A. Biot, J. Acoust. Soc. Am. **28**, 168–178 (1956).
[5] M. A. Biot, J. Acoust. Soc. Am. **28**, 179–191 (1956).
[6] R. D. Stoll, Geophysics **42**, 715–725 (1977).
[7] R. D. Stoll, J. Acoust. Soc. Am. **68**, 1341–1350 (1980).
[8] R. D. Stoll, *Sediment Acoustics* (Springer-Verlag, Berlin, 1989), Vol. 26.
[9] K. C. Leurer, Geophysics **62**, 1465–1479 (1997).
[10] R. D. Stoll, J. Acoust. Soc. Am. **77**, 1789–1799 (1985).
[11] J. M. Hovem and G. D. Ingram, J. Acoust. Soc. Am. **66**, 1807–1812 (1979).
[12] D. L. Johnson and T. J. Plona, J. Acoust. Soc. Am. **72**, 556–565 (1982).
[13] T. Klimentos and C. McCann, Geophysics **53**, 1605–1609 (1988).
[14] G. Shumway, Geophysics **25**, 451–467 (1960).
[15] G. Mavko and D. Jizba, Geophysics **56**, 1940–1949 (1991).
[16] J. Dvorkin, G. Mavko, and A. Nur, Geophysics **60**, 97–107 (1995).
[17] T. Klimentos and C. McCann, Geophysics **55**, 998–1014 (1990).
[18] A. I. Best and C. McCann, Geophysics **60**, 1386–1397 (1995).
[19] R. C. Courtney and L. A. Mayer, J. Acoust. Soc. Am. **93**, 1145–1154 (1993).
[20] E. R. Kanasewich, *Time Series Analysis in Geophysics*, 3rd ed. (University of Alberta Press, Edmonton, Canada, 1981).
[21] K. Fuchs and G. Müller, Geophys. J. R. Astron. Soc. **23**, 417–433 (1971).
[22] D. Minchin, Invertebrate Reproduction and Development **22**, 229–238 (1992).
[23] D. E. Gunn and A. I. Best, Geo-Mar. Lett. **18**, 70–77 (1998).
[24] G. W. C. Kaye and T. H. Laby, *Tables of Physical and Chemical Constants*, 16th ed. (Longman, City, 1995).
[25] F. Gassmann, Geophysics **16**, 673–685 (1951).
[26] J. McManus, in *Techniques in Sedimentology*, edited by M. Tucker (Blackwell Scientific Publications, Oxford, 1991), pp. 63–85.
[27] F. A. Bowles, J. Acoust. Soc. Am. **101**, 3385–3397 (1997).
[28] G. Shumway, Geophysics **25**, 659–682 (1960).
[29] C. McCann and D. M. McCann, Geophysics **34**, 882–892 (1969).
[30] E. Kjartansson, J. Geophys. Res. **84**, 4737–4748 (1979).
[31] K. W. Winkler and A. Nur, Geophysics **47**, 1–15 (1982).
[32] W. F. Murphy, K. W. Winkler, and R. L. Kleinberg, Geophysics **51**, 757–766 (1986).
[33] T. D. Jones, Geophysics **51**, 1939–1953 (1986).

Frequency analysis of the acoustic signal transmitted through a one-dimensional chain of metallic spheres

Michel de Billy[a)]
LED, Case Courrier 7087, Université Paris 7, Tour 33, 2, Place Jussieu, 75251 Paris Cedex 05, France

(Received 5 November 2000; accepted for publication 14 May 2001)

This work investigates the propagation of acoustic pulses through a chain of elastic spheres embedded in air. This study is an extension of the works realized on individual sphere by several authors for measuring elastic constant and internal friction with a monofrequential acoustic excitation. The frequency analysis of the experimental transmitted train waves exhibit maxima which were correlated to different types of free vibration modes: the Rayleigh modes (R_{nl}), the torsional modes (T_{nl}), and the spheroidal modes (S_{nl}). These resonances may be generated separately according to the polarization of the excitation pulse. © *2001 Acoustical Society of America.* [DOI: 10.1121/1.1385179]

PACS numbers: 43.20.Ks [DEC]

I. INTRODUCTION

In a previous paper, the propagation of acoustic pulses in a one-dimensional chain of elastic spherical beads embedded in air was studied in the time domain for two different polarizations of excitation.[1] The present study is concerned with the same experimental problem but the results are preferentially analyzed in the frequency domain and more specifically we explore the high frequency component of the transmitted signals. The frequency spectra of the experimental acoustic signals exhibit maxima which are interpreted as free vibration modes of elastic spheres in air. It is clearly demonstrated that the generation of these types of resonances—which is justified by the existence of guided waves—depends on the polarization of the transmitters. The Rayleigh waves family is generated only when the polarization of the incident wave is longitudinal[2,3] whereas torsional and spheroidal modes[4–7]—which were first studied by Lamb[8]—are observed only when a shear polarization is used for the excitation of the emitter. The physical justification of these experimental observations is based on the fact that the surface waves verify the phase condition standing surface waves such that the distance traveled by the wave around the target equals an integer or half integer numbers of wavelength. It is important also to notice that, for spheres embedded in air, we obtained similar Regge trajectories to the ones observed for samples immersed in water. For the identification of the resonances, we used the notation (n,l) according to the formalism of the classical resonance theory of nuclear reactions previously applied for the interpretation of acoustic scattering from submerged elastic spheres and cylinders.[9–16] The evolution of the frequency spectra as a function of the number of spheres in the chain is also performed. This analysis lets us compare our results with those published earlier in the geophysics field for one sphere.

II. EXPERIMENTAL SETUP AND PROCEDURE

The objective of this work is to achieve a frequency analysis of acoustic signals traveling through a one-dimensional chain of identical beads or an individual sphere. For this purpose, compressional and shear contact broadband acoustic transducers are used. The experimental technique—described in detail in Ref. 1—is an association of the NdB method[17] and the ''resonant sphere technique,'' which was developed to measure the elastic properties of rocks and spheres of different materials.[18] The local excitation on the sample is realized with short ultrasonic pulses which presents major advantages for a frequency analysis. No fluid coupling is used for the contact between the front face of the transducers and the balls as well as between two adjacent spheres. In addition to the harmonic excitation of the piezoelectric material of the transducers, a constant static force F_0 is applied along the axis of the chain. The frequency analysis of the acoustic train waves is realized by calculating the fast Fourier transform (FFT) of the acoustic signal selected on the screen of an oscilloscope (Lecroy 9200) before being plotted. When free vibrations of the specimen are excited, peaks are observed in the frequency spectrum.

Two typical examples of recorded signals are given in Fig. 1. The first one [Fig. 1(a)] is characteristic of a longitudinal excitation and reception; it was obtained with a chain made up with six balls of 8 mm in diameter. The second train wave [Fig. 1(b)] was recorded with a chain made up of two balls of 8 mm in diameter and is characteristic of a shear excitation. The two signals which both present a high-frequency component are differentiated by the existence of a low-frequency component in the case of a transversal excitation. In the following, we focus our investigation on the high-frequency component and we shall distinguish two frequency analysis according to the polarization of the transmitters (longitudinal or transversal).

III. FREQUENCY ANALYSIS OF THE ACOUSTIC SIGNALS (CASE OF LONGITUDINAL EXCITATION AND RECEPTION)

The frequency analysis of acoustic wave trains such as the one represented in Fig. 1(a) are shown in Fig. 2 for two different values of the static force [Fig. 2(a), $F_0 = 15N$; Fig. 2(b), $F_0 = 30N$]. Similar data are reported in Fig. 3, which

a)Electronic mail: mdebilly@ccr.jussieu.fr

 0001-4966/2001/110(2)/710/7/$18.00

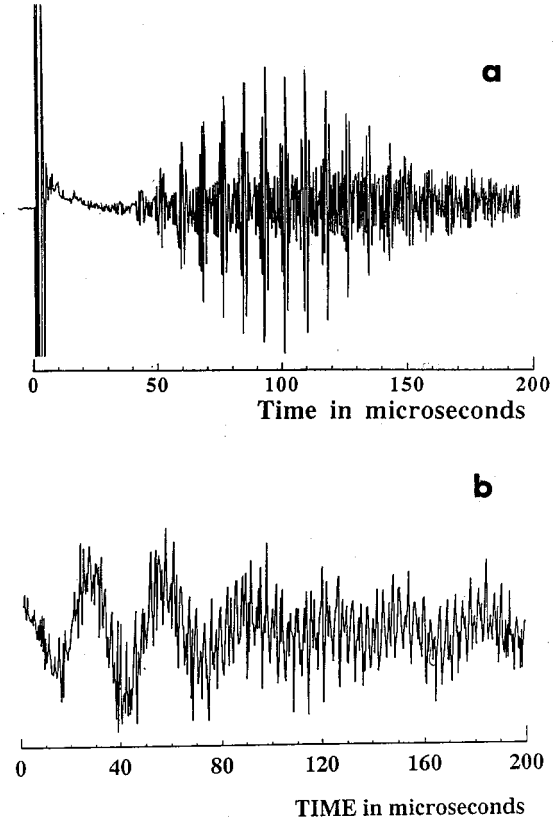

FIG. 1. Typical examples of the acoustical signals transmitted through a chain of elastic spheres submitted to an axial pressure: (a) the polarization of the excitation pulse is longitudinal; (b) the polarization of the excitation pulse is transversal.

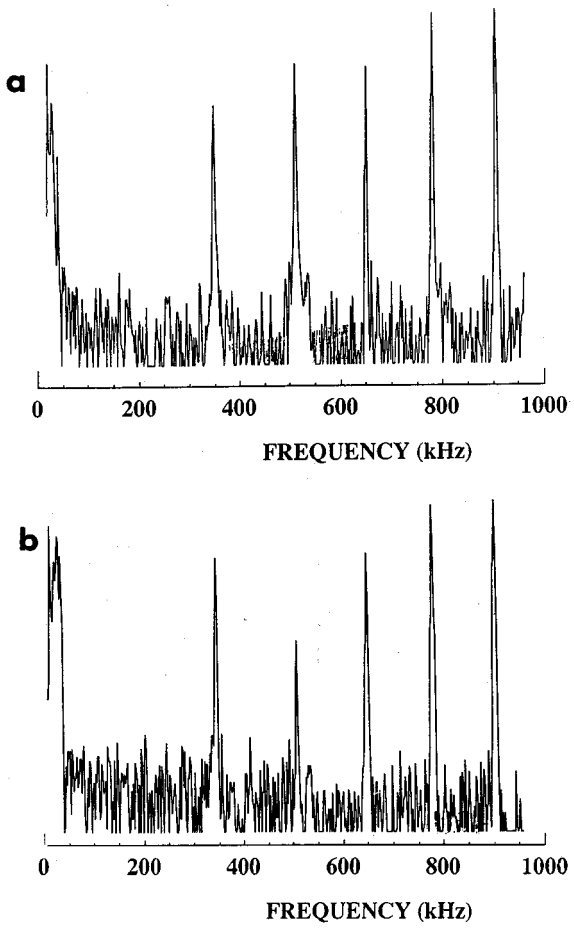

FIG. 2. Examples of calculated frequency spectra for two values of the static force (a) $F_0=15N$ and (b) $F_0=30N$.

shows a part of a wave train and its associated frequency spectrum; the data are obtained with a chain made up of 9 steel beads of 5 mm in diameter and the value of the static force is constant ($F_0=30N$). The purpose of the following analysis is to argue for elucidating the origin of the quasi-regularly spaced peaks observed in the frequency spectra.

A. Sound velocity measurement in air: Normalization

Usually most of the experimental data obtained with an immersed specimen are presented as a function of the normalized frequency: k_1a where k_1 is the modulus of the wave vector calculated in water. In the following some experimental data will be plotted versus the nondimensional frequency: k_0a where k_0 designates the wave number measured in air (a is the radius of the specimen). The sound velocity was measured and its value was estimated to 341 ± 3 m/s.

B. General considerations on the experimental frequency spectra

Let us designate by ${}^aF_i^j$ the frequency position of the ith peak (or apparition order in the spectrum) of the jth experiment. The left superior index gives the diameter of the investigated target. In the first three columns of Table I are given, for different experimental conditions, the frequency positions of the peaks expressed in kHz. For the definition of ${}^aF_i^j$ let us write the following symbols:

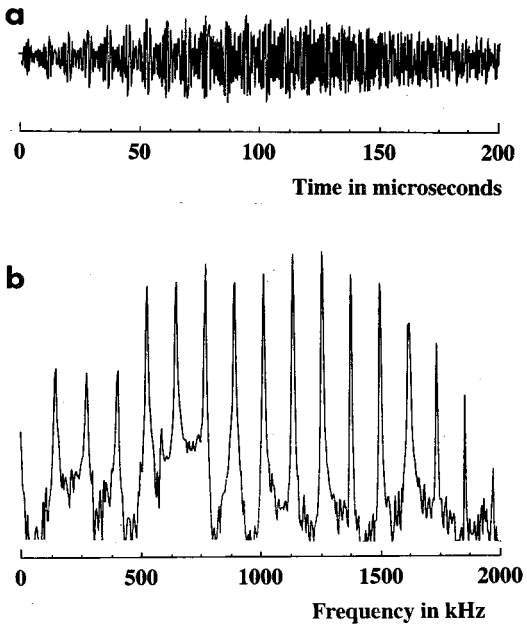

FIG. 3. Part of the acoustic signal (a) and its associated frequency spectrum (b). The time shift from the origin is 430 μs and the chain is made up of 9 steel beads of 8 mm in diameter ($F_0=30N$).

TABLE I. Data obtained in the case of a longitudinal excitation and detection (steel beads of 8 mm in diameter): Experimental values of the resonant frequency positions; nondimensional frequency values for comparison with results of Table II; identification of the Rayleigh modes; experimental values of the phase velocity of the modes and of the normalized phase velocity with respect to the Rayleigh wave velocity (C_R).

${}^8F_i^1$ (kHz)	${}^8F_i^2$ (kHz)	${}^8F_i^3$ (kHz)	$\langle k_{0,i}\rangle a$	Mode (n,l)	V_{ph} (m/s)	V_{ph}/C_R
340	340	338	24.8	(2,1)	3413	1.13
504	504	502	37.2	(3,1)	3614	1.20
646	644	642	47.3	(4,1)	3603	1.20
776	776	776	57.0	(5,1)	3541	1.18
906	904	904	66.6	(6,1)	3498	1.16
1030	1032		75.8	(7,1)	3447	1.14
1154	1152		84.8	(8,1)	3407	1.13
1276			93.9	(9,1)	3371	1.12
1400			103.0	(10,1)	3346	1.11
1520			111.9	(11,1)	3317	1.10
1640			120.7	(12,1)	3293	1.09
1760			129.6	(13,1)	3272	1.09
1880			138.4	(14,1)	3252	1.08
2000			147.2	(15,1)	3238	1.07
2124			156.3	(16,1)	3231	1.07
2240			164.9	(17,1)	3212	1.07
2360			173.8	(18,1)	3202	1.06
2476			182.2	(19,1)	3187	1.06
2600			191.4	(20,1)	3183	1.06
2716			199.9	(21,1)	3170	1.05
2838			208.9	(22,1)	3168	1.05

(a) ${}^8F_i^1$: three steel beads of 8 mm in diameter and $F_0 = 20N$;
(b) ${}^8F_i^2$: six steel beads of 8 mm in diameter and $F_0 = 10N$;
(c) ${}^8F_i^3$: six steel beads of 8 mm in diameter and $F_0 = 30N$.

In the first two columns of Table II are given the data obtained for two chains made up with spheres of 5 mm in diameter:

TABLE II. Data obtained in the case of a longitudinal excitation and detection; steel beads of 5 mm in diameter: Experimental values of the resonant frequency positions; nondimensional frequency values for comparison with results of Table I; identification of the Rayleigh modes; experimental values of the phase velocity of the modes and normalized phase velocity (C_R is the Rayleigh wave velocity).

${}^5F_i^1$ (kHz)	${}^5F_i^2$ (kHz)	$\langle k_{0,i}\rangle a$	Mode (n,l)	V_{ph} (m/s)	V_{ph}/C_R
540		24.8	(2,1)	3391	1.13
800		36.8	(3,1)	3588	1.19
1028	1032	47.3	(4,1)	3586	1.19
1236	1240	56.9	(5,1)	3528	1.17
1440	1444	66.2	(6,1)	3478	1.15
1640	1644	75.4	(7,1)	3433	1.14
1836	1840	84.5	(8,1)	3398	1.13
	2032	93.5	(9,1)	3358	1.11
	2224	102.3	(10,1)	3325	1.10
	2424	111.5	(11,1)	3309	1.10
	2612	120.2	(12,1)	3280	1.09
	2804	129.0	(13,1)	3261	1.08
	2992	137.7	(14,1)	3239	1.07

(a) ${}^5F_i^1$: fifteen steel beads of 5 mm in diameter and $F_0 = 30N$;
(b) ${}^5F_i^2$: thirty steel beads of 5 mm in diameter and $F_0 = 30N$.

An analysis of the experimental data reported in Tables I and II confirms the following.

(1) For a given value of the radius of the ball, the position of the frequency ${}^aF_i^j$ does not vary versus the static force F_0.
(2) The ${}^aF_i^j$ values are not affected by the number of the beads which make up the chain.
(3) If we designate by $\langle k_{0,i}\rangle$ the mean value of the modulus of the wave vector of the ith peak calculated over the j experiments, it is verified that the product $\langle k_{0,i}\rangle a$ is the same for a constant value of i (the order of apparition of the peak in the spectrum). This is illustrated by comparing columns 4 and 3 of Tables I and II, respectively.
(4) Similar results are obtained with an individual spherical bead.

C. Analysis of the frequency spectra in terms of "resonance"

Previous experiments realized in air on free chains with contact broadband transducers pointed out in the wave train a periodic structure the origin of which was identified as resulting from spherical Rayleigh-type surface waves circumnavigating in phase around the spheres.[1] According to the formalism of the classical resonance theory of nuclear radiation and usually adopted in the literature in the case of cylindrical and spherical targets immersed in water,[2,3,9–16] the different peaks observed in the recorded experimental frequency spectra were designated by an index pair (n,l) where n designates the mode order (or the number of circumferential nodes on the surface) and l the order of resonance within each mode n. The family of resonances $l=1$ was identified as the "Rayleigh family." The breathing mode (0, 1) and the mode (1, 1) do not exist in this family. The families labeled by $l \geqslant 2$ were called "whispering gallery" modes.

The identification of the peaks is given in Tables I and II for the two types of spheres. Twenty one modes were identified in the case of the target consisting of steel beads of 8 mm in diameter; thirteen modes were observed in the case of a chain made up with steel beads of 5 mm in diameter.

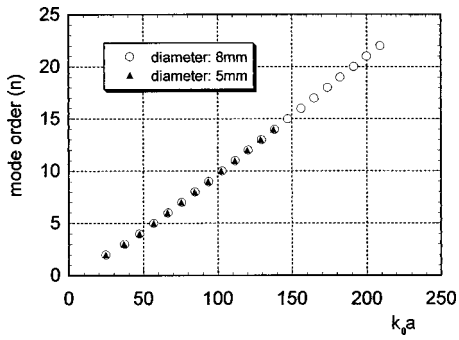

FIG. 4. Discrete variations of the mode order (n) as a function of the normalized frequency (discrete first Regge trajectory).

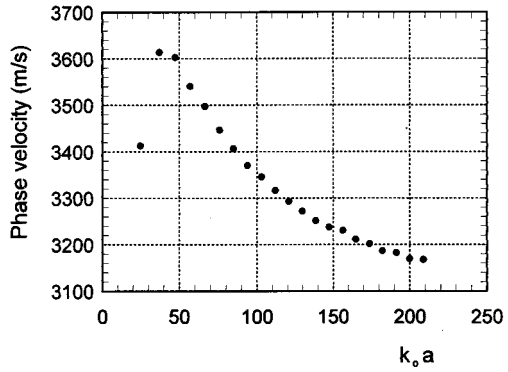

FIG. 5. Experimental variations of the phase velocity vs the normalized frequency k_0a.

These results are consistent (within less than 4%) with the results published by Williams *et al.*,[19] who studied the transient response of spheres submitted to an acoustic wave incident along the axis. As expected the curve $n(k_0a)$, which represents the first Regge trajectory,[9,13] should reveal data aligned for a large range of the product k_0a: this is very well verified in Fig. 4 for the two types of spheres.

For each mode n, the phase velocity V_{ph} may be calculated by the classical relationship:

$$V_{\mathrm{ph}}(n)=2\pi a\,\langle F_i\rangle\,\frac{1}{(n+1/2)}, \tag{1}$$

where $\langle F_i\rangle$ designates the value of the resonant frequency averaged over the different experiments realized on spheres of the same radius. The term $\frac{1}{2}$ is due to the phase jump when the surface wave goes through the focal point.[15] The experimental values of the phase velocity calculated from Eq. (1) are given in Tables I and II for the two types of spheres. The variations of V_{ph} versus the adimensional frequency (k_0a) are plotted in Fig. 5. We note that the curve points out a maximum and has an asymptotic value close to the Rayleigh wave velocity propagating on semi-infinite unbounded medium ($C_R=3005$ m/s) as it is suggested by the values of the ratio V_{ph}/C_R given in the last columns of Tables I and II. These curves offer a very similar behavior to the plots obtained in air for the aluminum cylinder (Fig. 6 of Ref. 14 and Fig. 11 of Ref. 16).

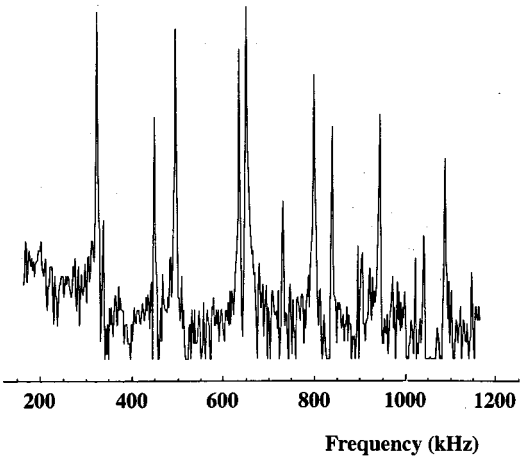

FIG. 7. Experimental frequency spectrum obtained in air with an individual steel sphere of 8 mm in diameter.

To sum up, we have demonstrated that a dilatational excitation of a chain of spherical beads immersed in air gives rise to free vibrations of the target which are limited to the so-called Rayleigh-type modes. The frequency positions of these resonances are well identified and many modes of this family may be detected.

IV. FREQUENCY ANALYSIS OF THE ACOUSTIC SIGNALS (CASE OF SHEAR EXCITATION AND RECEPTION)

Experiments were also achieved on individual spheres and chains of spherical beads located between two shear broadband contact transmitters and submitted to a static loading. The transmitter was again excited with short pulses and a part of the transmitted wave train was gated to calculate the Fourier integral.

In the case of individual spheres, the frequency response of the samples points out a succession of narrow peaks; this is illustrated in Figs. 6 and 7 where are plotted the frequency spectrum obtained with an elastic steel sphere of 7 and 8 mm in diameter, respectively. The existence of such maxima was already mentioned by several authors,[7,20–22] who have identified these peaks as torsional and spheroidal vibration modes. These two kinds of vibration were first studied by Lamb[8] and more recently by Satô and Usami,[6] who calcu-

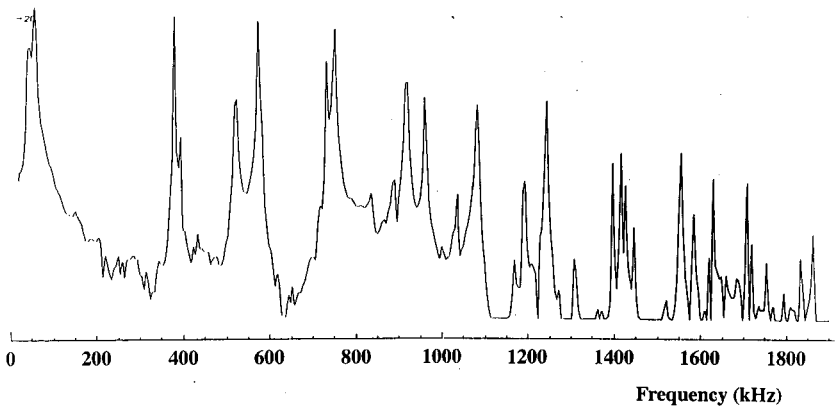

FIG. 6. Experimental frequency spectrum obtained in air with an individual steel sphere of 7 mm in diameter.

TABLE III. Comparison between the mean values of the product fa (in MHz mm) of torsional modes ($T_{n,i-1}$) and spheroidal modes ($S_{n,l-1}$) modes measured in this experiment for different experimental conditions and the values calculated by Sâto and Usami (Ref. 6). (1) One sphere of 7 mm in diameter. (2) One sphere of 8 mm in diameter. (3) One sphere of 5 mm in diameter. (4) Two spheres of 8 mm in diameter. (5) Four spheres of 8 mm in diameter. (6) Nineteen spheres of 8 mm in diameter. (7) Fifteen spheres of 5 mm in diameter.

fa (Ref. 6)	Modes		Frequency times radius (MHz mm) (1)	(2)	(3)	(4)	(5)	(6)	(7)
1.27	T_{20}		1.28	1.29	1.29	1.28	1.28	1.29	1.28
1.33		S_{20}	1.33	⋯	1.33	⋯	⋯	⋯	⋯
1.74		S_{11}	1.78	1.80	1.79	1.80	1.78	⋯	⋯
1.96	T_{30}		1.96	1.98	1.97	1.98	1.98	1.97	1.97
2.54		S_{40}	2.52	2.56	2.54	2.54	2.55	⋯	⋯
2.59	T_{40}		2.59	2.60	2.60	2.60	2.61	2.60	2.59
2.93	T_{11}		2.88	2.93	2.91	⋯	⋯	⋯	⋯
3.07		S_{50}	3.07	3.10	⋯	⋯	⋯	⋯	⋯
3.18	T_{50}		3.17	3.20	3.20	3.20	3.20	3.20	3.19
3.28		S_{31}	3.32	3.36	3.35	3.36	3.36	⋯	⋯
3.58		S_{60}	3.59	3.60	⋯	⋯	⋯	⋯	3.59
3.63	T_{21}		⋯	3.64	⋯	⋯	⋯	⋯	⋯
3.77	T_{60}		3.75	3.76	3.77	3.78	3.78	3.78	3.77
4.07		S_{70}	4.06	⋯	⋯	⋯	⋯	⋯	⋯
4.10		S_{41}	4.14	⋯	⋯	⋯	⋯	⋯	⋯
4.23		S_{22}	⋯	4.18	⋯	⋯	⋯	⋯	⋯
4.33	T_{70}		4.32	4.36	4.35	4.35	4.35	4.35	4.33
4.56		S_{80}	4.55	4.60	⋯				
4.89	T_{80}	S_{51}	4.86	4.92	⋯				
4.93		S_{32}	4.93	4.96	⋯				
4.94	T_{41}		4.97	5.02	⋯				
5.03		S_{90}	5.04	5.08	⋯				
5.35	T_{22}		5.30	⋯	⋯				
5.44	T_{90}		5.42	5.48	⋯				
5.52		$S_{10,0}$	5.53	5.58	⋯				
5.61	T_{51}		5.65	⋯	⋯				
5.68		S_{61}	5.69	5.74	⋯				
6.00	$T_{10,0}$	or $S_{11,0}$	5.97	⋯	⋯				
6.04	T_{32}		6.00	6.02	⋯				
6.19	T_{61}		6.12	⋯	⋯				
6.54	$T_{11,0}$		⋯	6.58	⋯				
7.09	$T_{12,0}$		⋯	7.12	⋯				

lated the numerical solutions of the characteristic equation for the two types of modes. The notation used for the identification of the torsional modes (pure shear mode) and the spheroidal modes (mixed shear and longitudinal modes) is $T_{n,l-1}$ and $S_{n,l-1}$, respectively, where l designates the l_{th} mode of the nth harmonic with $n=1,2,3,...$ and $l=1,2,3,...$. The fundamental torsional mode T_{10} does not exist.

The identification of the peaks observed in our experimental frequency spectra was obtained from the comparison between the experimental frequency positions of the peaks and the frequency positions of the vibration modes calculated by Satô and Usami.[6] Columns 4–6 of Table III give the experimental values of the product *fa* (frequency times the radius of the sphere) expressed in MHz mm, in the case of three individual steel spheres of 7, 8, and 5 mm in diameter, respectively, for which a peak is observed. These values were first compared with each other and then with the values of the same quantity calculated from the tables given in Ref. 6 and reported in the first column of Table III. This double comparison shows a very good agreement between the three

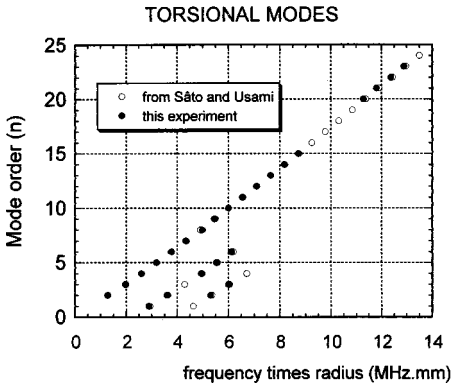

FIG. 8. Mode order versus frequency times radius for the torsional waves family (discrete Regge trajectories).

experimental determinations and a very good correspondence between the experimental and the theoretical values of the resonant frequencies for each free vibration. Most of the fundamental and low harmonics of the torsional and spheroidal modes were identified without ambiguity (see columns 2 and 3 in Table III). To confirm the validity of the identification, we have plotted in Figs. 8 and 9 the theoretical and experimental discrete Regge's trajectories $n(fa)$. The agreement is very good and validates identification of the modes up to the mode order 23 for the torsional modes and up to the mode order 12 for the spheroidal modes.

In conclusion, it was experimentally verified that in the case of an individual sphere submitted to a transversal excitation, torsional and spheroidal modes are excited and that the frequency positions of the two kinds of modes are not affected by the variations of the axial pressure. Now the question is: What about a chain made up of several identical metallic spheres in contact?

Some experimental frequency spectra obtained with chains of different composition and submitted to a shear excitation are given in Figs. 10, 11(b), and 12(a). The frequency spectrum plotted in Fig. 10 was obtained with a sample formed with two steel beads of 8 mm diameter; the frequency spectrum of the train wave represented in Fig. 11(a) is redrawn in Fig. 11(b). It was measured with a chain made up with fifteen steel beads of 5 mm diameter and the last spectrum [Fig. 12(a)] illustrates the case of a chain made

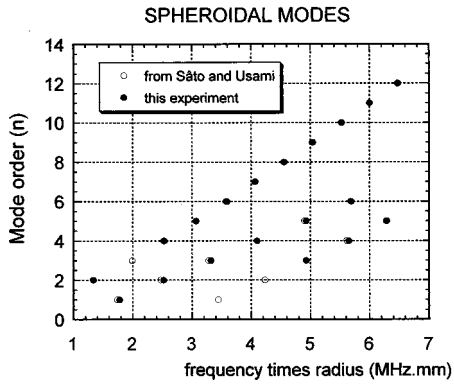

FIG. 9. Mode order versus frequency times radius for the spheroidal waves family (discrete Regge trajectories).

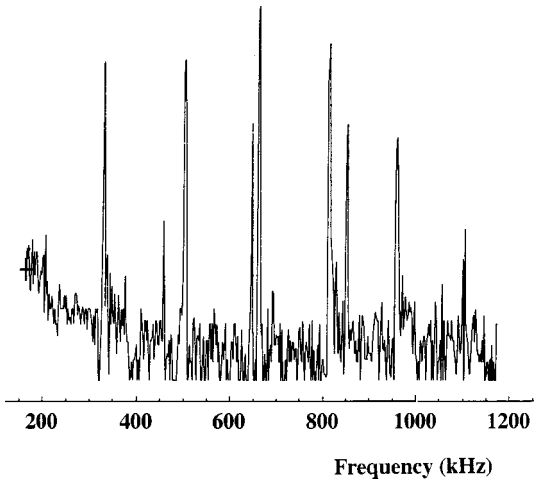

FIG. 10. Experimental frequency spectrum obtained in air with two steel spheres of 8 mm in diameter.

up of nineteen steel balls of 8 mm diameter. These spectra represent the FFT of a ''gated'' received train wave which is the part of the signal visualized on the screen of the oscilloscope (Lecroy 9200); the ''gate'' may be shifted by translating the signal on the screen of the oscilloscope.

As in the case of individual spheres, the frequency spectra reveal the presence of peaks the positions of which agree very well (within less than 0.5%) with those observed with one bead of the same material (steel) and of the same diameter. This is confirmed in columns 7–10 in Table III. So, we concluded that, again, torsional and spheroidal modes are excited and propagate in the chain as the Rayleigh surface

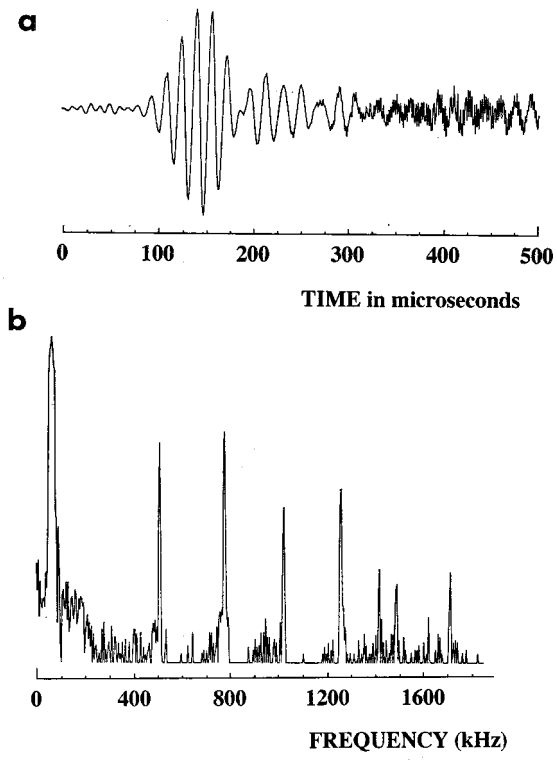

FIG. 11. ''Gated'' train wave obtained with 19 steel spheres in contact (a) and its frequency spectrum associated (b). The diameter of the spherical beads is 8 mm and the polarization of the acoustic excitation is transversal.

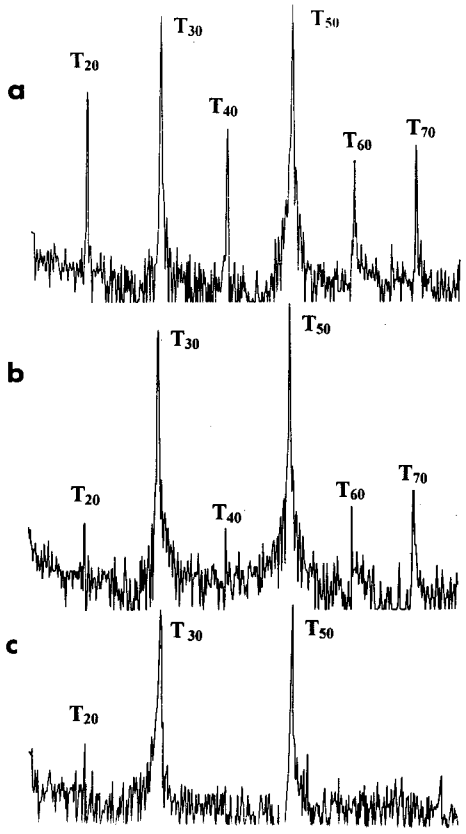

FIG. 12. Evolution of the ''gated'' train wave as a function of the position of the gate in the high frequency component of the signal.

waves do when a longitudinal polarization is used for the excitation of the chain.

It was also experimentally observed that the peak distribution in the frequency spectrum changes when the length of the chain increases or when the ''gated'' signal is shifted from the beginning to the end of the received time signal. The first observation is confirmed by the analysis of columns 7 and 9 of Table III: For a long chain (column 9) all the modes other than the torsional modes T_{n0}—which correspond to the first modes ($l=1$) of all harmonics (n)—disappear inducing that they are more attenuated during the propagation than the modes T_{n0}. The second observation is illustrated in Figs. 12(b) and 12(c).

V. CONCLUSION

In the present paper it was carried out that it is possible to generate and propagate in air two kinds of eigenvibration modes for individual spherical resonator and for chains made up with elastic spherical bead(s) with stress-free boundary conditions according to the polarization of the excitation pulses: The ''Rayleigh wave family'' which is excited with longitudinal pulses and torsional and spheroidal modes which are generated with a transversal excitation. The results should contribute to a better apprehension of the free eigenvibration modes and could be considered as a complementary analysis of the resonance excitation mechanism observed in water. The agreement between the experimental and theoretical resonance frequencies is very good. The ex-

perimental observations of the evolution of the frequency spectra with the length of the chain as well as the position of the temporal gate indicate that information on the attenuation of the modes may be obtained. So it was verified that the torsional modes are much less attenuated than the spheroidal modes during the propagation in chains. As the experimental method based on the pulse resonant technique is easy to realize and works very well for measurements in air, it could be used for testing the sphericity and homogeneity of the spheres.

[1] M. de Billy, ''Experimental study of sound propagation in a chain of spherical beads,'' J. Acoust. Soc. Am. **108**, 1486–1495 (2000).
[2] W. G. Neubauer, *Acoustic Reflection from Surfaces and Shapes* (Naval Research Laboratory, Washington, D.C.).
[3] V. Vogt and W. G. Neubauer, ''Relationship between acoustic reflection and vibrational modes of elastic spheres,'' J. Acoust. Soc. Am. **60**, 15–22 (1976).
[4] T. R. Meeker and A. H. Meitzler, in *Physical Acoustics*, edited by W. P. Mason (Academic, New York, 1972), Vol. I, Part A, pp. 111–167.
[5] B. A. Auld, *Acoustic Fields and Waves in Solids* (Wiley, New York, 1973), Vol. II.
[6] Y. Sâto and T. Usami, ''Basic study on the oscillation of a homogeneous elastic sphere,'' Geophys. Mag. **31**, 15–24 (1962).
[7] F. Birch, ''Velocity and attenuation from resonant vibrations of spheres of rock, glass and steel,'' J. Geophys. Res. **80**, 756–764 (1975).
[8] H. Lamb, ''On the vibrations of an elastic spheres,'' Proc. London Math. Soc. **13**, 189–212 (1882).
[9] L. Flax, L. R. Dragonette, and H. Überall, ''Theory of elastic resonance excitation by sound scattering,'' J. Acoust. Soc. Am. **63**, 723–731 (1978).
[10] H. Überall, L. R. Dragonette, and L. Flax, ''Relation between creeping waves and normal modes of vibration of curves body,'' J. Acoust. Soc. Am. **61**, 711–715 (1977).
[11] R. D. Doolittle, H. Überall, and P. Ugincius, ''Sound scattering by elastic cylinders,'' J. Acoust. Soc. Am. **43**, 1–14 (1968).
[12] S. K. Numrich, W. E. Howell, J. V. Subrahmanyam, and H. Überall, ''Acoustic ringing response of the individual resonances of an elastic cylinder,'' J. Acoust. Soc. Am. **80**, 1161–1169 (1986).
[13] G. Maze, J. L. Izbicki, and J. Ripoche, ''Resonances of plates and cylinders: Guided waves,'' J. Acoust. Soc. Am. **77**, 1352–1357 (1985).
[14] G. V. Frisk, J. W. Dickey, and H. Überall, ''Surface wave modes on elastic cylinders,'' J. Acoust. Soc. Am. **58**, 996–1008 (1975).
[15] G. Maze, F. Lecroq, D. Decultot, J. Ripoche, S. K. Numrich, and H. Überall, ''Acoustic scattering from finite cylindrical elastic objects,'' J. Acoust. Soc. Am. **90**, 3271–3278 (1991).
[16] N. D. Veksler, ''Transverse whispering gallery waves in scattering by elastic cylinders,'' Ultrasonics **28**, 67–76 (1990).
[17] S. K Numrich and H. Überall, in *Physical Acoustics*, edited by A. D. Pierce and R. N. Thurston (Academic, New York, 1992), Vol. XXI, p. 276.
[18] D. B. Fraser and R. C. Lecraw, ''Novel method of measuring elastic and anelastic properties of solids,'' Rev. Sci. Instrum. **35**, 1113–1115 (1964).
[19] K. L. Williams, G. S. Sammelmann, D. H. Trivet, and R. H. Kackman, ''Transient response of an elastic spheroidal surface waves and quasicylindrical modes,'' J. Acoust. Soc. Am. **85**, 2372–2377 (1989).
[20] A. Tverdokhlebov, ''Resonant cylinder for internal friction measurement,'' J. Acoust. Soc. Am. **80**, 217–224 (1986).
[21] W. P. Mason, K. J. Marfurt, D. N. Beshers, and J. T. Kuo, ''Internal friction of metal spheres showing the effect of the anisotropy of the component metals,'' J. Acoust. Soc. Am. **62**, 1206–1212 (1977).
[22] N. Soga and O. L. Anderson, ''Elastic properties of tektites measured by resonant sphere technique,'' J. Geophys. Res. **72**, 1733–1739 (1967).

Measuring second-order time-average pressure

B. L. Smith and G. W. Swift
Condensed Matter and Thermal Physics Group, Los Alamos National Laboratory, Los Alamos, New Mexico 87545

(Received 21 February 2001; accepted for publication 2 May 2001)

Measurements of the spatial distribution of the time-averaged second-order pressure in a plane standing wave in atmospheric air are reported. Several measurement pitfalls are identified, and solutions are described. These include accounting for slight nonlinearity of the piezoresistive transducer and careful mounting of the transducer. Streaming causes extra complication when a capillary-connected manometer is used. With the proper technique and instrumentation, results are in good agreement with theory. © *2001 Acoustical Society of America.*
[DOI: 10.1121/1.1382615]

PACS numbers: 43.25.Qp, 43.25.Zx, 43.25.Gf [MFH]

I. INTRODUCTION

In thermoacoustic engines and refrigerators, streaming can transport a significant amount of heat. One initial attempt[1] to diagnose such streaming by measuring the second-order time-average pressure differences accompanying it was qualitatively reasonable but did not inspire high confidence in quantitative accuracy. Hence, we undertook the simpler measurements described here to learn how to measure second-order time-average pressure differences accurately and routinely.

For our purposes, a nonlinear periodic pressure wave can be described by

$$p(x,y,z,t)=p_m+\mathrm{Re}[p_1(x,y,z)e^{i\omega t}]+p_{2,0}(x,y,z)+\mathrm{Re}[p_{2,2}(x,y,z)e^{i2\omega t}]+\cdots. \quad (1)$$

The Eulerian pressure p, which is the pressure at a given location x,y,z as a function of time t, is written as the sum of several terms. The mean pressure p_m is the steady pressure that exists in the absence of any acoustic oscillation. It is usually independent of x,y,z, because body forces such as gravity are usually negligible. The fundamental acoustic oscillation at angular frequency $\omega=2\pi f$ is accounted for with the complex function $p_1(x,y,z)$, whose magnitude gives the amplitude of the fundamental pressure oscillation and whose phase gives the temporal phase of the oscillation. In the absence of nonlinear effects these p_m and p_1 terms might suffice. However, nonlinear effects, such as that described by the $(\mathbf{v}\cdot\nabla)\mathbf{v}$ term in the momentum equation (where $\mathbf{v}$ is the velocity), generate both harmonics such as $p_{2,2}$ and time-averaged phenomena such as streaming and the time-averaged second-order pressure denoted here by $p_{2,0}$. In our notation, the first subscript, 2, indicates that the magnitude of this term is second order in the acoustic amplitude, and the second subscript, 0, indicates the temporal frequency of the term. Measurement of $p_{2,0}$ is challenging because it is much smaller than both p_m and $|p_1|$.

The nature and magnitude of $p_{2,0}$ have generated activity and controversy in the acoustics literature. Twenty years ago, much of this activity was inspired by the desire to understand the radiation pressure on an acoustically levitated sphere. Decades earlier, the interest focused on the radiation pressure exerted by an ultrasonic beam on a flat plate. This body of work is reviewed by Lee and Wang,[2,3] who rightly point out that the confusion and controversy arise because radiation pressure is a small, subtle nonlinear effect, and in particular that extreme care must be taken to pose questions clearly. It is widely accepted[2–4] that

$$p_{2,0}=\frac{|p_1|^2}{4\rho_m a^2}-\frac{\rho_m|\mathbf{v}_1|^2}{4}+C, \quad (2)$$

if viscous and thermal effects can be neglected, where ρ_m is the mean density, a is the speed of sound, and C is a constant that is independent of space and time. For the plane standing wave of interest to us below, whose pressure amplitude is P_1 (a positive real number) at the pressure antinode $x=0$, the fundamental wave is described by

$$p_1(x)=P_1\cos kx, \quad (3)$$

and

$$|\mathbf{v}_1(x)|=(P_1/\rho_m a)|\sin kx|, \quad (4)$$

yielding

$$p_{2,0}=-\frac{P_1^2}{2\rho_m a^2}\sin^2 kx+C'. \quad (5)$$

Much of the historic controversy about radiation pressure has arisen from C (or C'), whose value depends on constraints external to the wave itself. For example, C depends on whether a resonator is vented to atmospheric pressure p_m at a particular location or is sealed with p_m trapped in the resonator before it is insonified. To avoid this confusion, we will consider only the difference between $p_{2,0}$'s measured at two different locations, so that the location-independent constant C is irrelevant. (The acoustic-levitation literature avoids this issue as well, because the net radiation force on a body completely enveloped by a sound wave is independent of C.) Our apparatus, described in Sec. II, had many pressure-sensor ports disposed along the standing wave, essentially allowing $p_{2,0}$ differences to be measured between ports. The experimental results, described in Sec. III, are in good agreement with Eq. (5).

However, to achieve these experimental results we had to avoid the many subtle pitfalls discussed in Sec. IV, only some of which we had anticipated. Some pitfalls depend on the hydrodynamics and acoustics of the wave and the wave-to-transducer fluid interface; others are characteristic of the particular transducer we used. The main purpose of this paper is to explain these pitfalls, so that other researchers can avoid them.

II. APPARATUS

The apparatus used in this study is shown schematically in Fig. 1. All measurements are made with 80-kPa air (atmospheric pressure at Los Alamos) inside of a 0.91-m-long aluminum pipe having an inner diameter of 10.2 cm. The top end of the pipe is closed by a plate that enforces a velocity node at this location. The flow entering the pipe at the lower, ''open'' end passes through a honeycomb flow straightener (10-cm-long, 4-mm-diameter tubes, with nearest neighbors separated by 0.25-mm-thick web) to ensure that no large turbulent structures enter the pipe and that the velocity profile is uniform. Pressure measurements are made at nine equally spaced locations (including the closed end) that extend down the entire pipe. The measurement ports are staggered azimuthally to prevent any disturbance created at one port from affecting another. The clean geometry is designed to create a plane standing wave as described by Eqs. (3) and (4) with $x=0$ at the closed end, and therefore a known distribution of p_1 and $p_{2,0}$.

The wave is generated by a driver system consisting of eight JBL 2206H loudspeakers. The speakers are arranged in four parallel sets of two speakers in series. This arrangement is capable of providing sufficient displacements and larger pressure amplitudes than are possible with all eight speakers in parallel. In order to allow for operation outside of the manufacturer's specifications for electrical power and frequency without thermal damage to the voice coil, the passive cooling system provided in each speaker by the manufacturer is replaced by the active system sketched in Fig. 1(b). The cooling flow loop is closed to ensure that no air is added or removed from the apparatus. Air driven by a blower is cooled by a heat exchanger before entering eight parallel paths, one to each speaker. The air enters the speaker through the center of the magnet, and is forced though the gap between the magnet and the voice coil. It then exits through the three ports in the magnet which originally provided passive cooling. These ports are connected to the inlet side of the blower, thus completing the cooling loop.

The fundamental resonance of the system is found to be $f=70$ Hz, with almost a quarter wavelength in the 0.91-m-long pipe. At this frequency, pressure amplitudes of 14 kPa (174 dB *re* 20 μPa rms) are easily achievable at the closed end. For the next resonance, at $f=210$ Hz, almost three-quarter wavelengths are in the pipe and a pressure amplitude of 7 kPa can be produced. The complicated geometry of the speakers' enclosure plus the pipe suppresses harmonic generation,[5] so shock waves do not occur even at these high amplitudes.

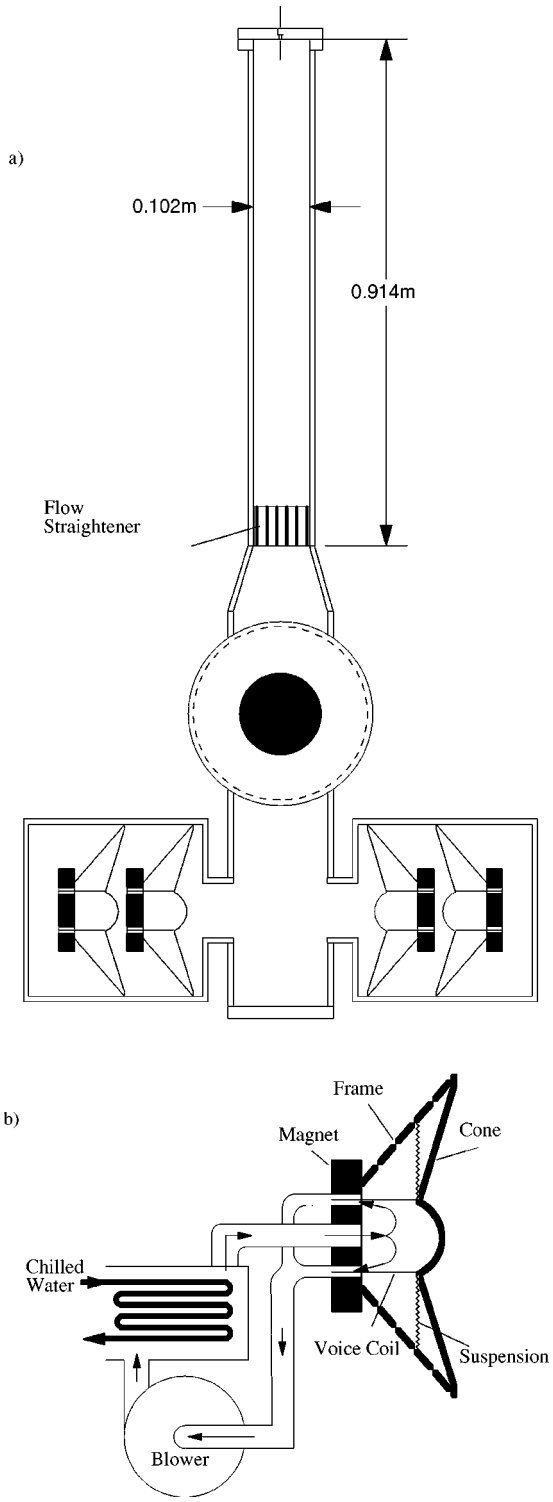

FIG. 1. Schematics of apparatus. (a) Pipe and driver system. Cross sections of four of the eight speakers are visible in the lowest part of the drawing; the other four have the same arrangement, but displaced upward along the apparatus and rotated 90° with respect to the long axis of the apparatus. (b) Detail of cooling-air loop for one speaker. The blower and chilled-water heat exchanger are shared among all eight speakers.

III. MEASUREMENTS OF $p_{2,0}$

All of the measurements reported in this section are made using differential piezoresistive pressure transducers (Endevco 8510B) referenced to atmospheric pressure. Each sensor is mounted by the manufacturer inside the tip of a

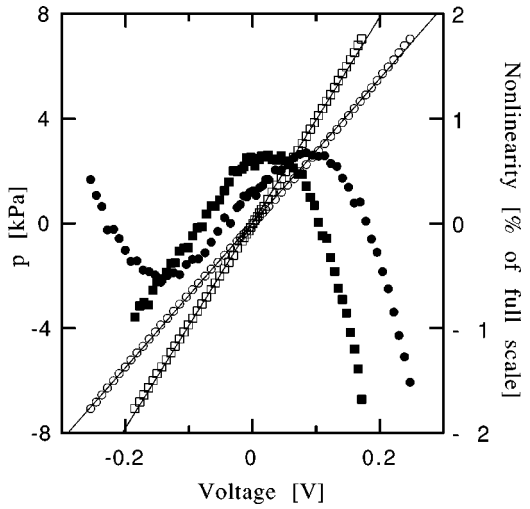

FIG. 2. Calibration data for two 1-psi pressure sensors. The raw data indicated by the open symbols and the linear fits to them are associated with the left axis. The filled symbols, associated with the right axis, show differences between the linear fits and the data.

3.86-mm-o.d. threaded tube. The threads begin above the sensor in an effort to reduce any strain on the sensor element when the transducer is torqued down. The transducer is sealed to the apparatus by an O-ring. Although these transducers are nominally linear (the manufacturer specifies less than 1% of full scale nonlinearity for the 1- and 2-psi transducers used here), their nonlinearity is significant for accurate measurements of $p_{2,0}$, so we account for it by in-house calibration of the transducers. The transducers are calibrated statically against a Bourdon-tube gauge (Wallace and Tiernan model FA 145, checked against a NIST traceable standard) with ticks of 27 Pa. The specified accuracy for this gauge is 33 Pa. The dial was read and recorded to an estimated accuracy of 13 Pa. The calibration data are shown in Fig. 2 for two 1-psi transducers (open symbols) along with linear fits to the data. The errors that would be incurred by using the linear fits are also plotted (closed symbols). Rather than the linear fit, we use a third-order polynomial to convert voltage to pressure. The differences between the data and the polynomial appear random with an rms value of 6 Pa, much smaller that the accuracy of the Bourdon-tube gauge. As will be shown in Sec. IV, failure to account for the nonlinearity of the pressure transducer would result in a substantial error in the time-averaged pressure result. The manufacturer's specifications for the piezoresistive pressure transducers give hysteresis and nonrepeatability errors that are each 0.2% of full scale. The rms sum of these two uncertainties plus the accuracy specification of the Bourdon-tube gauge is 0.6%, which will be assumed to be the uncertainty of the measurements.

For measurement of the time-dependent signals, data are acquired phase locked to the forcing signal by a 100-K sample/s 12-bit A-D acquisition system and stored on a laboratory computer. All results are averaged over at least 100 cycles. For each measurement, one transducer is placed in the closed end, while the second is successively moved along the other eight measurement ports. The voltage signals from the pressure transducers are converted to pressure $p(t)$ using the calibration curves described above before averaging. The

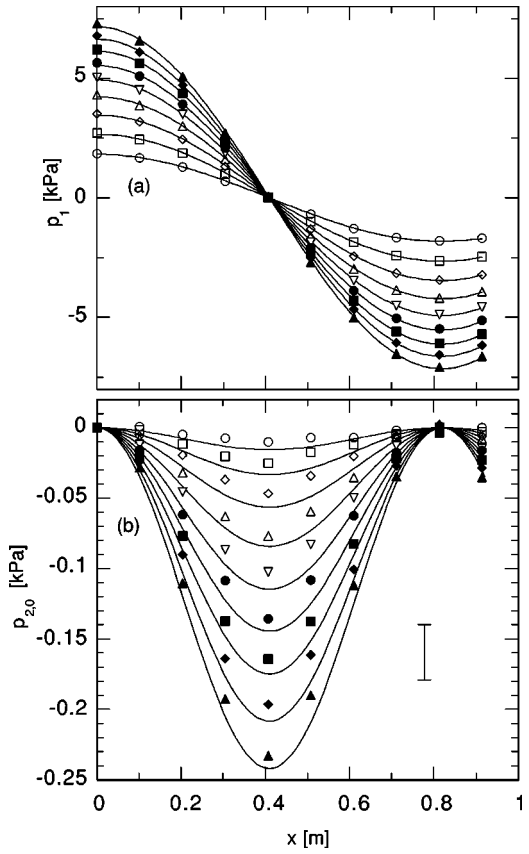

FIG. 3. Symbols show measured distributions of (a) $p_1(x)$ and (b) $p_{2,0}(x)$ for 210-Hz waves of nine different amplitudes in the pipe. In (a), the lines represent Eq. (3) with P_1 adjusted to fit the data. In (b), the lines represent Eq. (5) with no adjustable parameters, with P_1 obtained from the fits in (a), and with $C'=0$. A representative error bar is also shown.

fundamental pressure amplitude p_1 is calculated using a Fourier transform of $p(t)$, and the time average is also computed.

Two cases are studied: 210 Hz, for which two pressure antinodes exist within the measurement domain, and 70 Hz, which allows larger amplitudes. The 1-psi full-scale transducers are used for the 210-Hz case, while the 2-psi transducers are used for the 70-Hz case. In both cases, the largest amplitude studied is nominally the full scale of the transducer. Data are acquired as fast as the data acquisition system allows, resulting in 220 samples/cycle for the 210-Hz case and 700 samples/cycle for the 70-Hz case. The distribution of $p_1(x)$ and $p_{2,0}(x)$ are shown for these two cases in Figs. 3 and 4. In each case, data were acquired for several closed-end amplitudes P_1, and each amplitude is given a unique symbol. For each of the $p_1(x)$ distributions, the data are fitted to $P_1 \cos kx$, where P_1 is a fit parameter and $k = 2\pi f/a$. Recall from Sec. I that the theoretical distribution of $p_{2,0}$ contains a spatially independent constant that may vary with pressure amplitude. Since we are not interested in the absolute time-average pressure, but rather how this pressure varies in space, we ignore this constant by subtracting the time-averaged pressure at the closed end from each distribution. The results are shown in Figs. 3(b) and 4(b), along with curves generated using Eq. (5) and the P_1 values from

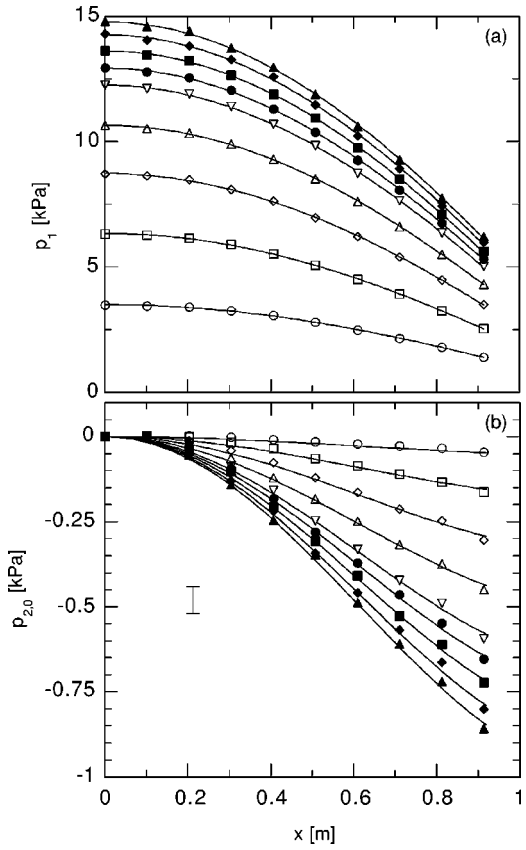

FIG. 4. Symbols show measured distributions of (a) $p_1(x)$ and (b) $p_{2,0}(x)$ for 70-Hz waves of nine different amplitudes in the pipe. In (a), the lines represent Eq. (3) with P_1 adjusted to fit the data. In (b), the lines represent Eq. (5) with no adjustable parameters, with P_1 obtained from the fits in (a), and with $C'=0$. A representative error bar is also shown.

the first-order curve fits. The $p_{2,0}$ distributions for 210 Hz shown in Fig. 3(b) match the theoretical distributions well, with differences everywhere less than the measurement accuracy. The agreement of the measurement with Eq. (5) is very good. A more accurate result can be obtained at higher amplitudes, such as the 70-Hz case shown in Fig. 4(b).

The writings of the theoretical leaders of a previous generation, such as Morse and Ingard[6] and Westervelt,[7] suggest that the truth of Eqs. (2) and (5) was once so well known that citation or publication of experimental validation was unnecessary. This attitude seems surprising, given the controversy in the literature mentioned above in Sec. I. Nevertheless, we have found only one previously published experimental $p_{2,0}$ result for a plane standing wave, similar to our Fig. 3: Van Doren's master's thesis.[8] His experiment is based on Morse and Ingard's suggestion to measure $p_{2,0}$ in a horizontal standing wave in air by observing spatial variations in the depth of a thin layer of water below the standing wave. Van Doren's results agree with the accepted theory to better than a factor of 2, but perhaps not as well as one would expect.

IV. PITFALLS

These results belie many possible pitfalls with the measurement of second-order time-average pressure, some of which have already been discussed briefly. In this section, the pitfalls that we have identified and therefore avoided will be discussed in detail.

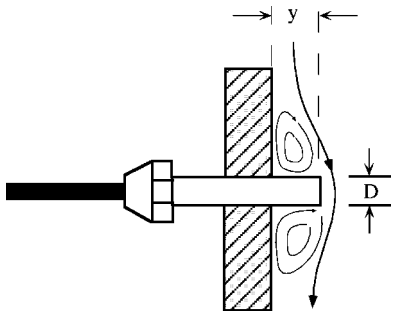

FIG. 5. Arrangement used to study the impact of pressure-sensor misalignment.

For steady flow, it is well known that a pressure sensor in the presence of fluid motion must be mounted flush to a wall that is parallel to the flow direction in order to provide an accurate measurement of Eulerian (static) pressure,[9] and that the pressure gradient normal to the wall is negligible.[10] However, the error incurred due to misalignment in an oscillatory flow is not known. For this reason, an additional pressure port was added to the apparatus at $x=0.864$ m that allowed the pressure sensor to be extended into the flow. The arrangement is shown schematically in Fig. 5. The sensor is traversed through the domain -1.3 mm$<y<1.3$ mm, where y is the extension of the sensor from the wall, by incrementally rotating the threaded transducer 1/6th of a turn resulting in increments of 0.13 mm in y. We estimate that y is known to within ± 0.13 mm. The maximum difference in alignment between the center of the sensor and its edges due to the curvature of the pipe wall is less than half of this estimated error. The speakers are driven at 70 Hz and the local velocity magnitude is estimated using Eq. (4) and the measured values of P_1 at the closed end. Data for five local velocities are shown in Fig. 6. In general, extending the sensor into the flow results in a negative pressure error that scales with $\rho|\mathbf{v}|^2$. The extension of the sensor from the wall is normalized by the sensor diameter D since we conjecture that three-

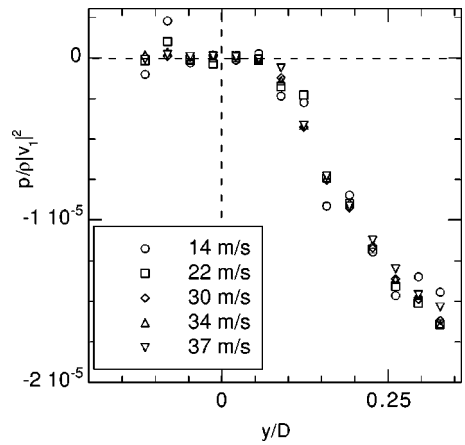

FIG. 6. Error in time-average static pressure measurement as a function of the sensor–wall alignment. Positive y values indicate that the sensor extends into the flow. Inset shows values of $|\mathbf{v}_1|$. Note that the normalization by $|\mathbf{v}_1|^2$ increases the scatter of the low-velocity data.

dimensional effects will begin to dominate as this value approaches 1, and the behavior may depart from $\rho|\mathbf{v}|^2$. The static pressure measurement error is caused by the pressure gradient associated with the streamline curvature induced by the obstacle (sensor) as shown in Fig. 5. No effect is seen until $y>0.05D$, which is not surprising given that the viscous penetration depth ($\delta_\nu=\sqrt{2\nu/\omega}$, where ν is the kinematic viscosity) for these conditions is $0.078D$. Interestingly, however, retracting the sensor inside of the pipe wall has no effect, at least up to $y=-1.27$ mm. With these results in mind, all measurements discussed in Sec. III were made with the pressure sensors recessed slightly from the inside wall of the pipe.

Although the results in Sec. III speak to the utility of the piezoresistive pressure transducer for simultaneous measurement of pressure amplitude and time average, other more sensitive devices for time-average measurements are available at a lower price. For example, a capacitance manometer with an uncertainty of 0.3% of the reading can easily be found. Furthermore, since the time-average pressure values are so small compared to the oscillation amplitudes, it is reasonable to expect that a great advantage in accuracy of the $p_{2,0}$ measurement could be obtained by utilization of a sensitive manometer. Even a simple water manometer, observed through a cathetometer, can easily resolve pressure differences of 0.1-mm $H_2O=1$ Pa. However, such devices are much less compact than their piezoresistive counterparts, and thus cannot be easily embedded directly in the wall of the apparatus. Typically, such devices are connected to a small ''tap'' in the wall of the apparatus via a flexible hose. It was anticipated that the acoustic impedance of the tap would need to be large to prevent the large acoustic pressure oscillations from causing large oscillatory velocity through the tap and therefore perhaps altering the reading. Despite our use of small-diameter taps, early results using this method indicated problems, so it was abandoned in favor of the piezoresistive transducers as described above. With confidence in the piezoresistive results, they now provide a baseline for comparison to illustrate problems encountered with the tap/remote manometer method.

In some measurements 6 years ago at Los Alamos, a 440-Hz standing wave in helium was used, with mean pressures ranging from 0.3 to 3 MPa and with two tap capillaries of 0.1-mm diameter and 1-m length extending from a differential manometer to two different places in the standing wave. Results bore little resemblance to Eq. (5). We have now identified two possible causes of error in this method: streaming in the capillary, and jetting at the capillary entrance.

Streaming occurs in the capillary because acoustic power $\mathrm{Re}[p_1\tilde{U}_1]/2$, where U_1 is the complex volume-velocity amplitude, must flow into and along the capillary to maintain viscous acoustic dissipation in it, and hence a term $\mathrm{Re}[\rho_1\tilde{U}_1]/2$ in the second-order time-averaged mass flux, with $\rho_1=\rho_m p_1/p_m$, must flow in as well. If the manometer has no leaks, no net mass can flow into the capillary, so $\rho_m U_{2,0}=-\mathrm{Re}[\rho_1\tilde{U}_1]/2$ must flow out of the capillary. Then, the second-order Navier–Stokes equation indicates that

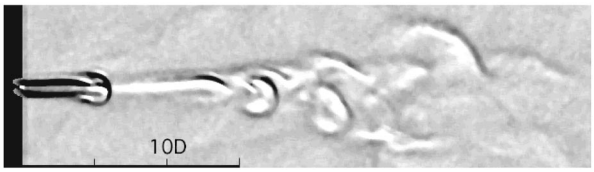

FIG. 7. Schlieren image of the flow induced when a pressure tap ($D=1.8$ mm) is exposed to an oscillating pressure. Pressure amplitude at the tap location is 0.51 kPa and $f=70$ Hz.

$\Delta p_{2,0}$ must exist in the capillary, in order to overcome viscous forces acting on $U_{2,0}$. The calculation of this $\Delta p_{2,0}$ is simple for a short capillary, treated as a lumped flow resistance R_ν, connected to an infinitely compliant manometer. In this case, $U_1=p_{1,e}/R_\nu$, where $p_{1,e}$ is the complex pressure amplitude at the capillary entrance. Then, $p_1(x)$ varies linearly along the length l of the capillary, from $p_{1,e}$ at the entrance to 0 at the manometer. Hence, $U_{2,0}$ is also linear, varying from $|p_{1,e}|^2/2p_mR_\nu$ at the entrance to 0 at the manometer. Integrating $\nabla p_{2,0}=\Delta p_{2,0}/\Delta x=U_{2,0}R_\nu/l$ along the length of the capillary yields

$$\Delta p_{2,0}=|p_{1,e}|^2/4p_m \tag{6}$$

for the pressure drop along the length of the capillary. Because $p_m=\rho_m a^2/\gamma$, where γ is the ratio of isobaric to isochoric specific heats, the error indicated by Eq. (6) is the same order of magnitude as the effect given in Eq. (5) that we are trying to measure. Remarkably, repeating this calculation for an infinite-length acoustic transmission line comprised of resistance per unit length and compliance per unit length gives exactly the same result. Including the effects of inertance and thermal relaxation present in a capillary whose diameter is not much smaller than the viscous and thermal penetration depths would presumably change the result. We have not verified Eq. (6) experimentally, but there seems to be no way to avoid such an effect if a capillary is used in an attempt to ''time average'' the pressure hydrodynamically.

Even if Eq. (6) (or its equivalent with inertance and thermal relaxation included) is accepted as true and is applied as a correction to measured results, jetting at the capillary entrance can sometimes add yet another second-order time-averaged pressure difference to the measurement. At Reynolds numbers much greater than unity, oscillating flow at the entrance to a tube is very asymmetric, with outflow creating a long jet (often with vortex rings) and inflow more broadly distributed in angle. This asymmetry of flow pattern causes asymmetry in the oscillating pressure drop across the entrance, so that the time-average pressure drop is nonzero. The magnitude of this pressure drop depends on details of the entrance edges, but its order of magnitude is $\rho|\mathbf{v}|^2$.

Details of one such jet are shown in the schlieren image taken in the vicinity of a pressure tap exposed to an oscillating pressure of amplitude 0.51 kPa shown in Fig. 7. A 1.8-mm-diameter 35-mm-long tap is used, and is connected to a 3.2-mm-i.d., 3.8-m-long hose. The pressure oscillations force air in and out of the pressure tap. The exiting air rolls into a vortex ring which propagates away under its self-induced velocity. The image clearly shows the roll-up of a nascent vortex ring and the starting jet behind the ring, which is

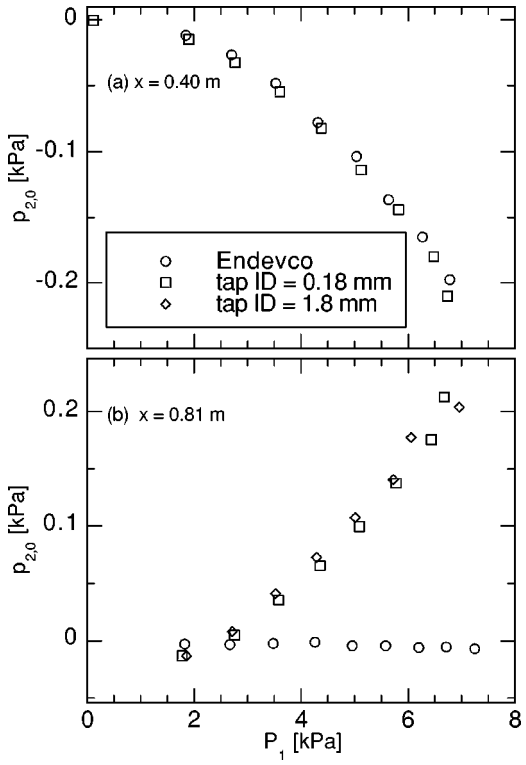

FIG. 8. Time-averaged pressure measurements made at 210 Hz using a capacitance manometer attached to a wall tap, compared with "correct" results using a piezoresistive transducer for both time average and amplitude. (a) Measurement at pressure node. (b) Measurement at pressure antinode.

indicative of a stroke length $2|\mathbf{v}_1|/\omega$ much larger than the orifice diameter. The remnants of rings from several previous cycles are also visible farther down stream. This type of flow is referred to as a synthetic jet, and it has been shown[11] that the pressure near the orifice of a synthetic jet is altered. Jetting is likely also occurring on the opposite side of the tap (into the flexible hose), resulting in a situation so complex that no resulting pressure measurement should be surprising or believed. Images were also acquired at higher frequencies and higher amplitudes and are not shown. In general, larger amplitude results in a longer stroke length and therefore a longer starting jet column. Increased frequency will reduce the stroke length and decrease the spacing between vortices. Note that the pressure amplitude used in Fig. 7 is very small compared with those used elsewhere in this study.

To assess the impact of this flow on pressure measurements, we used a capacitance manometer connected via the same hose to a 35-mm-long tap. Two tap diameters were used: 0.18 and 1.8 mm. As indicated above, we anticipated that this method would suffer most in regions of large pressure amplitude. For this reason, the speakers were driven at 210 Hz, and measurements were made at both the pressure node ($x=0.40$ m) and an antinode ($x=0.81$ m) and are plotted versus the closed-end pressure amplitude in Fig. 8. As expected, the pressure tap results are in good agreement with the piezoresistive transducer results at the pressure node [Fig. 8(a)]. However, where the pressure amplitude is large, at the pressure antinode [Fig. 8(b)], use of a pressure tap results in large errors that increase with pressure amplitude. It is also remarkable that the tap diameter seems to have little effect.

Other sources of error in the time-averaged measurement are due to effects within the transducer and how its output is interpreted. Although not of concern for these measurements, it is crucial to sample the signals rapidly enough to capture any short-duration features[1] that might contribute to $p_{2,0}$. Furthermore, if the transducer is nonlinear, measurement of its average voltage does not give the average pressure directly. Suppose that the transducer is exposed to pressure

$$p(t)=p_m+|p_1|\cos\ \omega t+p_{2,0}, \tag{7}$$

and that the transducer voltage depends on pressure via

$$V=V_m+A(p-p_m)+B(p-p_m)^2, \tag{8}$$

with B a small coefficient of nonlinearity. Substituting Eq. (7) into Eq. (8), taking the time average, and neglecting the very small term $Bp_{2,0}^2$ yields

$$V_{\text{avg}}=V_m+Ap_{2,0}+B|p_1|^2/2, \tag{9}$$

so that a naive measurement of average voltage would suggest that the average pressure is $p_m+p_{2,0}+B|p_1|^2/2A$ instead of the true value, $p_m+p_{2,0}$. For our calibrations of these transducers, B/A is found to be of the order of 0.005 kPa^{-1}.

In addition, it was found that for the more sensitive transducers used, the zero value was altered significantly each time the transducer was moved to a new port and torqued down. In fact, even though an effort was made to reproduce the same torque each time, the zero value of the transducer varied with a standard deviation of 0.03 kPa over the entire data set. For this reason, at each location, data were taken with the speakers off to obtain a correct zero value.

V. CONCLUSIONS

Accurate measurements of the second-order time-averaged pressure in a standing wave in atmospheric air have been made at two frequencies and at pressure amplitudes as large as 17.5% of p_m using piezoresistive pressure transducers built into the resonator walls. Several possible error sources are identified including sensor–wall alignment and transducer nonlinearity. It is found that the former error source can be eliminated simply by ensuring that the sensor is either flush or slightly recessed. Nonlinearity errors are removed by full calibration of the transducers, and the use of polynomial fits to the calibration data. It has also been shown that the use of capillary taps can lead to very erroneous results.

ACKNOWLEDGMENTS

The authors would like to thank C. Espinoza for his expert assistance in the construction of the driver system used in this work, M. Hamilton and S. Putterman for useful conversations, J. Olson for trying such measurements at Los Alamos 6 years ago, and the Office of Basic Energy Sciences in the U.S. DOE for financial support.

[1] S. Backhaus and G. W. Swift, ''A thermoacoustic-Stirling heat engine: Detailed study,'' J. Acoust. Soc. Am. **107**, 3148–3166 (2000).
[2] T. G. Wang and C. P. Lee, ''Radiation pressure and acoustic levitation,'' in *Nonlinear Acoustics*, edited by M. F. Hamilton and D. T. Blackstock (Academic, New York, 1998), pp. 177–205.
[3] C. P. Lee and T. G. Wang, ''Acoustic radiation pressure,'' J. Acoust. Soc. Am. **94**, 1099–1109 (1993).
[4] L. D. and E. M. Lifshitz, *Fluid Mechanics* (Pergamon, New York, 1982), Sec. 64.
[5] C. C. Lawrenson, B. Lipkens, T. S. Lucas, D. K. Perkins, and T. W. Van Doren, ''Measurements of macrosonic standing waves in oscillating closed cavities,'' J. Acoust. Soc. Am. **104**, 623–636 (1998).
[6] P. M. Morse and K. U. Ingard, *Theoretical Acoustics* (McGraw-Hill, New York, 1968), p. 869.
[7] P. J. Westervelt, ''The mean pressure and velocity in a plane acoustic wave in a gas,'' J. Acoust. Soc. Am. **22**, 319–327 (1950).
[8] T. W. Van Doren, ''Scattering of sound by sound in a waveguide, and d.c. pressure generation in a standing wave field,'' Master's thesis, The University of Texas at Austin (1990).
[9] F. M. White, *Fluid Mechanics* (McGraw-Hill, New York, 1986), p. 89.
[10] H. Schlichting, *Boundary-Layer Theory* (McGraw-Hill, New York, 1968).
[11] B. L. Smith and A. Glezer, ''The formation and evolution of synthetic jets,'' Phys. Fluids **10**, 2281–2297 (1998).

On the theory of acoustic flow measurement

J. C. Wendoloski[a)]
CSIRO, Telecommunications and Industrial Physics, P.O. Box 218, Lindfield NSW 2070, Australia

(Received 27 January 2000; revised 25 January 2001; accepted 1 March 2001)

The motivation for this paper arises from problems frequently encountered in acoustic flow measurement. Of primary concern is that acoustic flow meters, rather than directly measuring the volume flow rate, measure some biased average of fluid velocity in a duct. That is, the average is usually not equal to the volume flow rate divided by the duct cross-sectional area, and is influenced by alterations in the flow profile. In this paper perturbation analysis is used to characterize nontrivial situations under which a sound field may be convected to first order by the unbiased cross-sectionally averaged flow. Perturbation analysis previous to this paper has considered only the plane-wave approach to the problem. This paper will examine the use of higher-order duct modes. It will be shown that under certain circumstances these modes are less prone to distortion by the flow field than the plane wave, and will still average the flow to an approximation which improves with mode order. The study is restricted to the consideration of rectangular section ducts and cylindrical ducts with axisymmetric flow fields. As an aside, the two-dimensional viscous convective wave equation by Mungur and Gladwell [J. Sound Vib. **9**, 28–48 (1969)], has been extended to three dimensions in this paper. In deriving this form it was noticed that an error existed in the original equation. This error has been corrected in the present three-dimensional version of the equation. [DOI: 10.1121/1.1369103]

PACS numbers: 43.28.Gq [DEC]

I. INTRODUCTION

Fluid flow measurement by acoustic, or more particularly ultrasonic, techniques has become a problem of considerable practical interest. The primary advantages of such a technique are noninvasion of the flow and high dynamic range (see von Jena *et al.*[1] and Lynnworth[2] for applications).

The motivation for this paper arises from problems frequently encountered in the design of ultrasonic fluid flow meters. Foremost among these is that ultrasonic flow meters, rather than directly measuring the volume flow rate, by their nature measure the fluid velocity, or more accurately, some weighted average of fluid velocity in a conduit. Except in the simplest cases (i.e., low-frequency plane waves, see Robertson,[3,4] or where ray theory is valid and multiple paths are used, see Lynnworth[2]); this average is not equal to the volume flow rate divided by the duct cross-sectional area, and is influenced by alterations in the flow profile (see, for instance, Håkansson and Delsing[5] and Heritage[6]).

In this paper, perturbation analysis is used to characterize nontrivial situations under which a sound field may be convected to first order by the mean flow. That is, in a manner which is insensitive to the cross-sectional flow profile in the duct (assuming the profile is axially invariant). Perturbation theory is often valid at first order in flow metering applications, as the Mach number is often sufficiently small to warrant this. It should be pointed out that perturbation analysis has previously been used in the study of sound convection in ducts (see Robertson[3] and Shankar[7]). We restrict ourselves to the consideration of rectangular section ducts, and cylindrical ducts with axisymmetric flow fields, as these are the most commonly considered cases.

The majority of approaches to the analysis of ultrasonic flow measurement seem to have relied on numerical and physical experiments, and ray-type approximations (see von Jena *et al.*,[1] Kroemer *et al.*,[8] Lynnworth,[9] Lynnworth,[2] Sanderson[10]). Correspondingly, many loose prescriptions for design arise such as: ''uniform insonification of the conduit.'' Although this statement does contain some truth, refraction can play a significant role at the frequencies commonly used. Consequentially, entities such as plane waves and pencil beams, as they are generally used, can become invalid approximations. [Generally, if the required flow resolution is to be improved (all other things being equal), the component of the ray path in the direction of the flow must be increased. In a medium where the flow profile is nonuniform, this increase in path length will increase the refractive effects on beams approximated as rays. Some current flow-meter designs in fact incorporate reflections down the conduit which increase the path length (see von Jena *et al.* [1]). Under these circumstances it would appear to be profitable to examine guided waves themselves, which have axially invariant profiles.]

The papers by Robertson[3,4] are an exception to this in that they do provide rigorous treatment of the subject within certain approximations. They present the conclusion that low-frequency plane waves in ducts convect in a fashion insensitive to velocity and temperature profile variations. However, there is no indication in their work as to whether there are other ways to achieve the same result. Indeed, the conclusion that low-frequency plane waves average profile inhomogeneities is expected. It is well known from scattering theory that the scattered field is insensitive to details of a scatterer which are small compared with a wavelength. It will be shown in this paper that increasing the order of the acoustic duct mode can, in certain circumstances, reduce

a)Electronic mail: johncw@tip.csiro.au

 0001-4966/2001/110(2)/724/14/$18.00

flow-induced modal distortion, that is shape change (to which the plane wave mode is most prone), and that the bias error also decreases with increasing mode order.

We note at this stage the papers by Lechner.[11,12] These papers make claim to having developed approximate analytical solutions for modes in a flow duct. Furthermore, they suggest certain modal combinations which convect in a manner supposedly insensitive to flow profile. Some doubt exists in this work owing to the use of an incorrect governing equation [Eq. (8) of Lechner[12]].

A great deal of theoretical and numerical work has been done in the general area of flow ducts.[3,4,7,13–65] It seems to the author, however, that this vein of literature is somewhat divorced from the large body of literature concerned with ultrasonic flow measurement. The focus of the former is usually on low frequencies and high Mach numbers, such as is appropriate to high-speed gas applications, as opposed to the low speed, high frequency applications considered in this paper. The basic governing equations developed in this area (flow ducts) are the same as those used in this work. This paper does, however, make a small extension and a small correction to a very general form of these equations.

In particular, the two-dimensional viscous convective wave equation by Mungur and Gladwell[13] has been extended to three dimensions in this paper (although perturbation analysis is only performed for the inviscid case). This is a rather straightforward extension. However, in deriving this form it was noticed that an error existed in the original equation. This error does not appear to be a simple misprint, as it is followed through several equations. It has been corrected in the present three-dimensional version of the equation. Mungur and Gladwell[13] is a canonical reference to the literature cited above; hence, it was thought worthwhile to include this work.

II. CIRCULAR SECTION WAVEGUIDES

In this section a perturbative approach is employed to examine a rigid-walled circular section waveguide, carrying a low Mach number steady flow of arbitrary profile. It is true that fully developed profiles, in the absence of external fields, take a fixed shape depending on the shape of the duct section. However, flow around obstacles may produce developing profiles (particularly in the case of high-speed laminar flow) which develop slowly over a length of several duct diameters (and many wavelengths, at ultrasonic frequencies). The shape of the profiles depends upon the perturbing object. The aim of this work is to describe sound fields which convect with the duct mean flow velocity no matter what the profile shape. As a first approximation to this end, we make the assumption that the profiles are invariant along the duct axis. This condition will be discussed at greater length in Sec. III.

Assume a polar coordinate system for the duct with r as the radial coordinate (going from 0 to R, the pipe radius), θ the polar angle, and z the axial coordinate. Let K represent the axial wave number component divided by the free-space wave number (k), and m be an integer (representing the number of circumferential nodes). The flow field is assumed to be axisymmetric; hence, the pressure field may be written as $p(r)e^{i(kKz+m\theta)}$ (where the time dependence is harmonic and has been suppressed). The equation for $p(r)$ is then

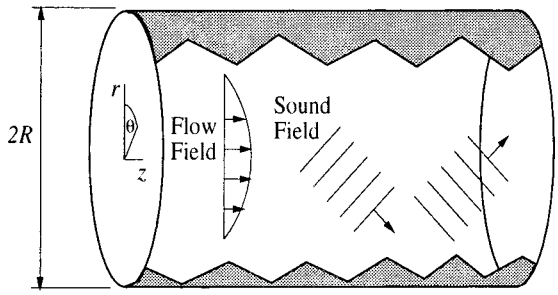

FIG. 1. Cutaway of a circular duct carrying a shear flow and being interrogated by a sound field (the flow field is assumed axisymmetric).

$$p''(r)+\left(\frac{1}{r}+\frac{2K}{1-M(r)K}M'(r)\right)p'(r)+k^2\left[(1-M(r)K)^2-K^2-\frac{m^2}{k^2r^2}\right]p(r)=0, \tag{1}$$

where $M(r)$ is the Mach number profile (see Agarwal and Bull[14]). Positive M implies the flow is in the positive z direction. A diagram of this configuration is given in Fig. 1. In linearized equations of this general type, the particle velocities associated with the sound wave are considered to be small with respect to the steady flow velocities. A further discussion of the approximations made in equations of this type is given in Sec. III.

A. A perturbative formalism

Consider a rearrangement of Eq. (1) such that the explicitly flow-dependent terms are taken to the right as a source term. The resulting equation is

$$p''(r)+\left(\frac{1}{r}\right)p'(r)+\left(k^2(1-K^2)-\frac{m^2}{r^2}\right)p(r)=-4\pi\rho(r), \tag{2}$$

where

$$\rho(r)=\frac{1}{4\pi}\left[\left(\frac{2K}{1-M(r)K}\right)M'(r)p'(r)-k^2(2KM(r)-M(r)^2K^2)p(r)\right]. \tag{3}$$

Now consider a homogeneous version of Eq. (2). This defines the unperturbed radial factors of the transverse eigenfunctions of the waveguide which are Bessel functions, but are written here symbolically as ψ_{mn}. They are equal to $J_m(j_{mn}r/R)$, where $J'_m(j_{mn})=0$. The equation is

$$\frac{1}{r}\frac{d}{dr}\left(r\frac{d\psi_{mn}}{dr}\right)+\left(k_{mn}^2-\frac{m^2}{r^2}\right)\psi_{mn}=0, \tag{4}$$

where $k_{mn}^2=k^2(1-K_{mn}^2)$ represents the transverse wave number component of the (m,n)th acoustic mode.

First-order perturbation formulas for the flow-perturbed modes and wave numbers may be developed by applying the perturbation procedure found in Morse and Feshbach.[66] In our case, the resultant formula for $k_t^2(=k^2(1-K^2))$ is im-

plicit even at first order, since $\rho(r)$ is a function of K and hence k_t. The first-order results of interest are

$$(k_t^{(1)})^2 = k_{pq}^2 + U_{pqpq} \tag{5}$$

and

$$p_{pq}^{(1)}(r) = \psi_{pq}(r) + \sum_{(m,n)\neq(p,q)}^{\infty} \psi_{mn}(r)\frac{U_{pqmn}}{(k_{pq}^2 - k_{mn}^2)}, \tag{6}$$

where

$$U_{pqmn} = \frac{2K^{(1)}}{\sqrt{\Delta_{pq}\Delta_{mn}}}\int_0^R r\,dr\,\psi_{mn}(r)\left[\left(1-\frac{1}{2}M(r)K^{(1)}\right)\right.$$
$$\left.\times k^2 M(r)\psi_{pq}(r) - \left(\frac{M'(r)}{1-M(r)K^{(1)}}\right)\psi'_{pq}(r)\right]. \tag{7}$$

The normalization factor Δ_{pq} is equal to $\int_0^R r\,dr\,\psi_{pq}^2(r)$. A further approximation will now be made by omitting terms involving $M^2(r)$ or $M(r)M'(r)$, since $M(r)$ and $M'(r)$ are presumed to be small quantities. This results in a simplified expression for U_{pqmn} given by

$$U_{pqmn}^{(l)} = \frac{2K^{(1)}}{\sqrt{\Delta_{pq}\Delta_{mn}}}\int_0^R r\,dr\,\psi_{mn}(r)$$
$$\times[k^2 M(r)\psi_{pq}(r) - M'(r)\psi'_{pq}(r)]. \tag{8}$$

Now, from our definition of k_t we have $(k_t^{(1)})^2 = k^2(1-(K^{(1)})^2)$. Similarly, we have that $k_{pq}^2 = k^2(1-K_{pq}^2)$. It follows then that

$$K_{pq}^2 - (K^{(1)})^2 = 2K^{(1)}I_{pqpq}, \tag{9}$$

where $I_{pqmn} = U_{pqmn}^{(l)}/(2K^{(1)}k^2)$. The following identities are also defined:

$$I_1^{(pq)} = \frac{1}{\Delta_{pq}}\int_0^R \psi_{pq}^2(r)M(r)r\,dr, \tag{10}$$

$$I_2^{(pq)} = \frac{R^2}{\Delta_{pq}}\int_0^R \psi'_{pq}(r)\psi_{pq}(r)M'(r)r\,dr. \tag{11}$$

These imply that

$$K_{pq}^2 - (K^{(1)})^2 = 2K^{(1)}\left(I_1^{(pq)} - \frac{I_2^{(pq)}}{k^2R^2}\right). \tag{12}$$

The assumption is now made that

$$(K^{(1)})^2 \gg 2K^{(1)}\left(I_1^{(pq)} - \frac{I_2^{(pq)}}{k^2R^2}\right). \tag{13}$$

Equation (13) will be valid for first-order perturbations except for frequencies near the modal cutoff frequencies. As the frequency approaches cutoff, the normalized axial wave number (K) tends to zero for the upstream wave and is of $O(M)$ for the downstream wave. The plane wave is exempted from this, however, since for small Mach numbers $K\sim 1$. Equations (12) and (13) imply

$$K^{(1)} = K_{pq} - \left(I_1^{(pq)} - \frac{I_2^{(pq)}}{k^2R^2}\right), \tag{14}$$

which we will evaluate for various mode sets and radial dependences of the Mach number.

B. Perturbation integrals

The first case we will consider is for the plane-wave mode. In this case $\psi_{00}=1$, $\psi'_{00}=0$, and $\Delta_{00}=R^2/2$. This implies that

$$I_1^{(00)} = \frac{2}{R^2}\int_0^R M(r)r\,dr, \tag{15}$$

$$I_2^{(00)} = 0. \tag{16}$$

Hence,

$$K^{(1)} = 1 - M_{av}, \tag{17}$$

which confirms that the axial wavenumber of the plane wave is perturbed by the *average* Mach number M_{av}, as expected. A case which is of special interest is that of a Mach number profile which depends on the square of the radius, as well as a constant term. This case is interesting for two reasons. First, the exact solution of the Navier–Stokes equations for *Poiseuille* flow, happens to render a flow profile of the said form. Second the integrals in Eqs. (10) and (11) are exactly tractable when $M(r)$ is of the said form. The results for $M(r)=r^2/R^2$ are

$$I_1^{(0q)} = \tfrac{1}{3} \quad q>0, \tag{18}$$

$$I_2^{(0q)} = 0 \quad q>0. \tag{19}$$

These results may be obtained by using Eq. (3) in Sec. 2.12.32 of Prudnikoff *et al.*,[67] and Eqs. (42) and (114) in Sec. 7.14.2 of Prudnikoff *et al.*[68] Equation (3) of Ref. 67 gives results for the definite integrals $I_1^{(0q)}$ and $I_2^{(0q)}$ in terms of generalized hypergeometric functions, and Eqs. (42) and (114) of Ref. 68 allow simplification of the hypergeometrics. Equations (18) and (19) imply that for a profile of the form $M(r)=M_c(1+Ar^2/R^2)$, we have for $q>0$

$$K^{(1)} = K_{0q} - M_c(1+A/3) \tag{20}$$

$$= K_{0q} - M_{av}(1+A/3)/(1+A/2), \tag{21}$$

which for the case of a fully developed laminar profile ($A=-1$) renders

$$K^{(1)} = K_{0q} - M_c(2/3) \tag{22}$$

$$= K_{0q} - M_{av}(4/3). \tag{23}$$

Hence, for the common case of laminar flow, the plane-wave mode convects with the mean flow and *all* the symmetric higher modes convect with 4/3 of the mean flow. A curious result, but one which may shed some light on complicated calibration curves encountered by ultrasonic flow meter designers with nonideal transducers (i.e., ones that should act like ''pistons'' but do not). This result has been verified by the author, using Taylor expansions.

Obviously, the Mach number profile in the integrands of Eqs. (10) and (11) is in unknown form. To make general progress, we consider limiting asymptotic (large argument) forms of the modal functions in the integrand of Eqs. (10) and (11), in order to demonstrate conditions under which

Eqs. (10) and (11) may become independent of the Mach number profile. This is done as follows. First, we have that

$$I_1^{(pq)}=\frac{2M_{av}}{J_p^2(j_{pq})(1-p^2/(j_{pq})^2)}\int_0^1 J_p^2(j_{pq}\mu)P(\mu)\mu\,d\mu, \quad (24)$$

and

$$I_2^{(pq)}=\frac{2M_{av}j_{pq}}{J_p^2(j_{pq})(1-p^2/(j_{pq})^2)}\int_0^1 J_p'(j_{pq}\mu)J_p(j_{pq}\mu) \times P'(\mu)\mu\,d\mu, \quad (25)$$

where

$$P(r/R)=M(r)/M_{av}. \quad (26)$$

(The prime on the functions above denotes differentiation with respect to the argument not necessarily μ.)

Now, consider the case when p is fixed, $q\gg p$, and $q\gg 1$, so that

$$J_p(j_{pq}\mu)\sim\sqrt{2/(\pi j_{pq}\mu)}\cos(j_{pq}\mu-p\pi/2-\pi/4). \quad (27)$$

We will substitute this form into Eqs. (24) and (25) and integrate the resulting lowest-order asymptotic expressions. Obviously Eq. (27) will not be valid for sufficiently small μ, but assuming that the integrand is piecewise continuous on [0, 1], the error caused by the asymptotic expression vanishes in the asymptotic limit as $q\to\infty$ since $j_{pq}\to\infty$ and so the invalid portion of the integral tends to zero. Substituting Eq. (27) into Eqs. (24) and (25), and using some standard double-angle trigonometric identities, we have

$$\begin{aligned}I_1^{(pq)}-I_2^{(pq)}/(k^2R^2) &= M_{av}\int_0^1 P(\mu)d\mu+M_{av}(-1)^p f_q \\ &\times\int_0^1\sin((2q+p-1)\pi\mu)\cos(\pi\mu/2)P(\mu)d\mu \\ &+M_{av}(-1)^p f_q\int_0^1\cos((2q+p-1)\pi\mu) \\ &\times\sin(\pi\mu/2)P(\mu)d\mu, \end{aligned} \quad (28)$$

where $f_q=1-2(\pi q/kR)^2$. [We have also used $J_p^2(j_{pq})\sim 2/(\pi j_{pq})$ and $j_{pq}\sim\pi(q+p/2-3/4)$ which hold for fixed p and $q\gg p$.] For any piecewise continuous function representing the profile $P(\mu)$, the last two terms must tend to zero by virtue of the completeness of the trigonometric series $\sin(n\pi\mu),\cos(n\pi\mu)$. The first term then gives a direct integral over the Mach number profile. *This average, however, isn't the correct one for mean flow*. It should, of course, be $\int_0^1 P(\mu)\mu\,d\mu$. The average contains a bias, ostensibly introduced by the shape of the duct. This result can be generalized to other duct shapes which have sections with rigid boundaries and which lie on coordinate lines in systems in which the unperturbed Helmholtz equation separates. However, this is beyond the scope of the present work.

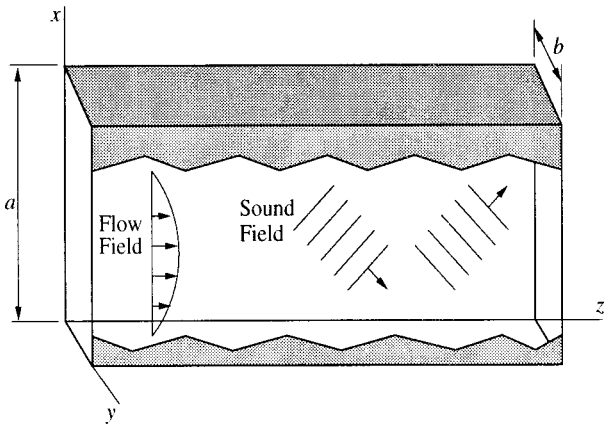

FIG. 2. Cutaway of a rectangular duct carrying a shear flow and being interrogated by a sound field.

III. RECTANGULAR CROSS SECTIONS

In this section a general three-dimensional version of the flow problem is solved. It will be demonstrated that in a rectangular duct it is possible to generate a single higher-order mode that will convect with a flow average which tends toward becoming unbiased as the mode number is increased.

A partial derivation of a three-dimensional version of the convective wave equation of Mungur and Gladwell[13] is given in this section. This has been done for the reasons given in the Introduction as well as to demonstrate the applicability of such equations to practical ultrasonic cases.

A. The convective wave equation in rectangular coordinates

The Navier–Stokes equations for continuity of momentum density in a fluid may be written in a Cartesian coordinate system, in tensor form as

$$\rho\frac{\partial u_i}{\partial t}+\rho u_j\frac{\partial u_i}{\partial x_j}=\rho F_i-\frac{\partial p}{\partial x_i}+\frac{\partial}{\partial x_j}2\mu \times\left[\frac{1}{2}\left(\frac{\partial u_j}{\partial x_i}+\frac{\partial u_i}{\partial x_j}\right)-\frac{1}{3}\frac{\partial u_k}{\partial x_k}\delta_{ij}\right], \quad (29)$$

where u_j represents the fluid velocity, p represents the pressure, μ represents the shear viscosity, and ρ represents the density. The symbol F_i represents the resultant external force on the fluid. It should be noted that implied summation over like indices in a term has been assumed in Eq. (29).

To derive the linearized wave equation it is necessary to assume that the above variables may be written as the sum of large steady terms and small fluctuating terms, the latter being associated with the acoustic field. Furthermore, we assume that the steady velocity field varies only in the x, y directions, being constant, as with the other variables, in the z direction. A diagram of the present configuration is given in Fig. 2.

The latter assumption will not of course be true in most realistic cases, since flows are seldom fully developed. The purpose of this paper, however, is to find fields which are insensitive to shear profiles. In this regard it is hoped that such results will also remain insensitive to shear profiles

which depend weakly on z. Obviously, this analysis is approximate in nature. If changes of the steady parameters with z are significant over a wavelength, then it seems likely that the eigenfunction analysis will be useless. In ultrasonic work, however, one may expect wavelengths to be of a scale much smaller than that characteristic of steady velocity changes in a slowly developing flow (note we also ignore cross flows). One might make these statements quantitative by assuming the modal amplitudes to be slowly varying functions of displacement and perhaps time (see Nayfeh *et al.*,[40] Sec. II B), but this extension is beyond the scope of the present paper.

The assumption that the acoustic particle velocities are small with respect to mean flow velocities will break down at sufficiently low flow velocities. Take for instance a water flow of 1 liter per minute in a 50-mm pipe. The average velocity v of this flow is

$$v = 1\,\mathrm{l\,min^{-1}}/(\pi \times 0.025^2\,\mathrm{m^2}) = 0.0085\,\mathrm{m\,s^{-1}}. \tag{30}$$

The characteristic impedance of water (ρc) is approximately

$$1000\,\mathrm{kg\,m^{-3}} \times 1500\,\mathrm{m\,s^{-1}} = 1.5 \times 10^6\,\mathrm{N\,s\,m^{-3}}. \tag{31}$$

Now, consider a disturbance which may be approximated as a linear plane wave where $p = \rho c u$ (where p is the acoustic pressure amplitude and u is the amplitude of the particle velocity). In order to have u equal to less that one-tenth v, we require $u = (0.0085/10)\,\mathrm{m\,s^{-1}}$. In this case, the acoustic pressure amplitude would be: $p = 1.5 \times 10^6 \times 0.000\,85 = 1.3\,\mathrm{kPa}$. That is, $\sim$1% of an atmosphere. This condition may easily be violated in common ultrasonic applications. Care must therefore be taken in the application of the present work to practical cases.

Assuming acoustic fluctuations in density are approximately equal to acoustic pressure fluctuations divided by the speed of sound squared, it can be seen that even at 10 kPa the density fluctuations are only about 4×10^{-4}% of the mean density of water. For the purposes of the following derivation it will also be assumed that the viscosity fluctuations are small compared with the mean viscosity. (In the final analysis it will be assumed that the fluid is inviscid: a far cruder assumption.)

We therefore write our variables as

$$\begin{aligned} &p = p' + P_0, \quad u_j = u_j' + U_0 \delta_{j,3}, \\ &\rho = \rho' + \rho_0, \quad \mu = \mu' + \mu_0, \end{aligned} \tag{32}$$

where the fluctuating components are primed (and lower case) and the steady components are subscripted with zero (and are both lower and upper case). As we are interested in a homogeneous wave equation, we shall assume that the resultant external force F_i is steady. This force is often negligible, but could be included in this analysis to allow us to rigorously consider fully developed profiles other than the standard types.

A full derivation of the three-dimensional version of the convective wave equation of Mungur and Gladwell,[13] for an ideal gas, is given in the Appendix. A brief description of the derivation is given here. One result from this derivation is also included to show the error in the original work of Mungur and Gladwell. This result is given in Eq. (33). Up to this result, the fluid is not assumed to be a gas as the fluctuating viscosity remains in the equation. The description follows.

The forms in Eq. (32) are substituted into Eq. (29), whereupon the time average of this equation is subtracted, and the products of fluctuating terms are neglected. This results in three linearized equations representing continuity of momentum density, for the x, y, and z directions, respectively. In addition to these equations, a time-filtered linearized conservation of mass equation is required, as well as a good many rearrangements and differentiations. These result in

$$\begin{aligned} \frac{\partial^2 \rho'}{\partial t^2} = {} & \nabla^2 p' - 2U_0 \frac{\partial^2 \rho'}{\partial z\,\partial t} - U_0^2 \frac{\partial^2 \rho'}{\partial z^2} \\ & + 2\rho_0 \left[\frac{\partial u_x'}{\partial z}\frac{\partial U_0}{\partial x} + \frac{\partial u_y'}{\partial z}\frac{\partial U_0}{\partial y} \right] + \frac{4}{3}\frac{\mu_0}{\rho_0}\left[\frac{\partial}{\partial t}\nabla^2 \rho' \right. \\ & + U_0 \frac{\partial}{\partial z}\nabla^2 \rho' + 2\left(\frac{\partial U_0}{\partial x}\frac{\partial^2 \rho'}{\partial z\,\partial x} + \frac{\partial U_0}{\partial y}\frac{\partial^2 \rho'}{\partial z\,\partial y} \right) \\ & \left. + \frac{\partial \rho'}{\partial z}\left(\frac{\partial^2 U_0}{\partial x^2} + \frac{\partial^2 U_0}{\partial y^2} \right) \right] - \mathbf{2}\frac{\partial \mu'}{\partial z}\left[\frac{\partial^2 U_0}{\partial x^2} + \frac{\partial^2 U_0}{\partial y^2} \right] \\ & - 2\left[\frac{\partial^2 \mu'}{\partial z\,\partial x}\frac{\partial U_0}{\partial x} + \frac{\partial^2 \mu'}{\partial z\,\partial y}\frac{\partial U_0}{\partial y} \right]. \end{aligned} \tag{33}$$

The factor of 2 in boldface does not appear in the corresponding two-dimensional expressions in Mungur and Gladwell[13] [see Eq. (13) of their paper]. This error has been followed in their work and appears to arise from the neglect of one part of a product rule differentiation. This factor does not affect Eq. (34) or (39) below, and therefore is not important to the remainder of this paper. The final version of the three-dimensional Mungur and Gladwell equation requires a little more work and, as mentioned above, has been relegated to the Appendix.

When the viscosity is neglected this governing equation becomes

$$\begin{aligned} \frac{1}{c^2}\frac{\partial^2 p'}{\partial t^2} = {} & \nabla^2 p' - M^2 \frac{\partial^2 p'}{\partial z^2} + 2\rho_0 c \left[\frac{\partial u_x'}{\partial z}\frac{\partial M}{\partial x} + \frac{\partial u_y'}{\partial z}\frac{\partial M}{\partial y} \right] \\ & - \frac{2M}{c}\frac{\partial^2 p'}{\partial z\,\partial t}, \end{aligned} \tag{34}$$

where $M(x,y) = U_0(x,y)/c$. [See the Appendix, and set τ_1, τ_2, and δ to zero in Eq. (A11). Note M is positive when the flow is in the positive z direction.] We now drop the primes and subscripts on the variables and search for separable solutions of the form

$$p = F(x,y) f(z,t), \tag{35}$$

$$u_x = G(x,y) f(z,t), \tag{36}$$

$$u_y = H(x,y) f(z,t), \tag{37}$$

where

$$f(z,t) = e^{-\beta_a z} e^{i(\omega t - k_z z)}, \tag{38}$$

β_a is the attenuation constant, and k_z is the z component of the wave vector. Substituting these expressions into Eq. (34), and using Eqs. (A1) and (A2) when $\mu=0$, we finally arrive at

$$\frac{\partial^2 F}{\partial x^2}+\frac{\partial^2 F}{\partial y^2}+\left(\frac{2K}{1-MK}\right)\left[\frac{\partial F}{\partial x}\frac{\partial M}{\partial x}+\frac{\partial F}{\partial y}\frac{\partial M}{\partial y}\right] +k^2[1-K^2(1-M^2)-2MK]F=0, \tag{39}$$

where

$$K=\frac{\beta_a+ik_z}{ik}, \tag{40}$$

and $k=\omega/c$. Equations (34) and (39) already exist in the literature, being derived directly from the linearized inviscid equations of flow [see Kapur and Mungur,[29] who actually derive equations slightly more general than (34) and (39)]. Our main purpose for including the preceding derivation is to extend (to three dimensions) and correct the equations of Mungur and Gladwell.

A couple of points should be noted about Eq. (39). First, it cannot in general be reduced further to ordinary differential equations by separation of variables. We might consider a two-dimensional version of this equation, but even that does not represent a standard *Sturm Liouville* problem. This implies that we cannot prove that the eigenfunction solutions to this equation are complete or orthogonal. Indeed, they do not in general appear to be orthogonal, although numerical studies suggest they are complete, at least in some cases (see Shankar[45]). If eigenfunctions of the form shown in Eqs. (35)–(37) do not form a complete set, then clearly other types of solution exist and may be excited by some source distributions.

These points will not be expounded upon as we are considering only single modes in this paper. The subject of completeness is, however, of concern in general, as one may wish to place finite aperture transducers in duct walls to generate particular solutions of Eq. (39).

B. Perturbation theory for the rectangular duct

In this section we are concerned with rectangular geometries. For this purpose consider a rectangular section duct of width a in the x direction and b in the y direction (the axial direction being the z direction). Again, the diagram of this configuration is given in Fig. 2. Application of the perturbation theory described in Sec. II A to Eq. (39) leads to

$$K_{pq}^2-(K^{(1)})^2=2K^{(1)}I_{pqpq}, \tag{41}$$

where

$$K_{pq}=\sqrt{1-k_{pq}^2/k^2}, \tag{42}$$

with

$$k_{pq}^2=(\pi p/a)^2+(\pi q/b)^2, \tag{43}$$

and

$$I_{pqmn}=\frac{1}{\sqrt{\Delta_{pq}\Delta_{mn}}}\int_0^a\int_0^b dx\,dy \times\left[M\psi_{pq}-\frac{1}{k^2}(\boldsymbol{\nabla}_{xy}M\cdot\boldsymbol{\nabla}_{xy}\psi_{pq})\right]\psi_{mn}. \tag{44}$$

The symbol $\boldsymbol{\nabla}_{xy}$ is the two-dimensional Laplacian in the xy plane. As before, terms of $O(M^2)$ have been neglected. Furthermore, the attenuation constant β_a is set equal to zero. For rigid boundary conditions, we have that

$$\psi_{mn}=\sqrt{\frac{\epsilon_m\epsilon_n}{ab}}\cos(\pi mx/a)\cos(\pi ny/b), \tag{45}$$

where the Neumann factor ϵ_m is defined by

$$\epsilon_m=\begin{cases}1 & m=0,\\ 2 & m>0,\end{cases} \tag{46}$$

and the normalization factor Δ_{pq} is equal to unity, since orthonormal eigenfunctions have been used.

Placing these results in the form of Eq. (14), we have that

$$K^{(1)}=K_{pq}-\left(I_1^{(pq)}-\frac{I_2^{(pq)}}{k^2a^2}-\frac{I_3^{(pq)}}{k^2b^2}\right), \tag{47}$$

where

$$I_1^{(pq)}=\frac{\epsilon_p\epsilon_q}{ab}\int_0^a\int_0^b dx\,dy\,M(x,y)\cos^2(\pi px/a)\cos^2(\pi qy/b), \tag{48}$$

and

$$I_2^{(pq)}=-(\pi pa)\frac{\epsilon_p\epsilon_q}{ab}\int_0^a\int_0^b dx\,dy\,\frac{\partial M(x,y)}{\partial x}\sin(\pi px/a) \times\cos(\pi px/a)\cos^2(\pi qy/b), \tag{49}$$

$$I_3^{(pq)}=-(\pi qb)\frac{\epsilon_p\epsilon_q}{ab}\int_0^a\int_0^b dx\,dy\,\frac{\partial M(x,y)}{\partial y} \times\cos^2(\pi px/a)\sin(\pi qy/b)\cos(\pi qy/b). \tag{50}$$

Note that in writing the above expressions we have imposed a condition analogous to Eq. (13) for the circular case. This is

$$(K^{(1)})^2\gg 2K^{(1)}\left(I_1^{(pq)}-\frac{I_2^{(pq)}}{k^2a^2}-\frac{I_3^{(pq)}}{k^2b^2}\right). \tag{51}$$

It would be simpler to have perturbation integrals which only depend on M and not its gradient. This may be achieved for rigid ducts by re-expressing Eq. (44) using Green's theorem as

$$I_{pqmn}=\int_0^a\int_0^b dx\,dy\,M\left[\psi_{pq}\psi_{mn}+\frac{1}{k^2}\boldsymbol{\nabla}_{xy}\cdot(\psi_{mn}\boldsymbol{\nabla}_{xy}\psi_{pq})\right] \tag{52}$$

$$-\frac{1}{k^2}\oint_S M\psi_{mn}\boldsymbol{\nabla}\psi_{pq}\cdot d\mathbf{S}, \tag{53}$$

where the surface integral is over the boundary of the duct and the surface element $d\mathbf{S}$ points away from the interior of

the duct. Of course, for rigid wall conditions the surface term is zero. The volume integral may be reduced to Fourier cosine-type integrals when $pq=mn$ (i.e., as occurs in a first-order perturbation expression). The latter is achieved using well-known double-angle trigonometric identities, and the result is

$$I_{pqpq}=\frac{\epsilon_p\epsilon_q}{4ab}\left\{\int_0^a\int_0^b dx\,dy\,M(x,y)+\frac{1}{2}(1+K_{p0}^2)\right.$$
$$+\int_0^a\int_0^b dx\,dy\,M(x,y)\cos(2\pi px/a)+\frac{1}{2}(1+K_{0q}^2)$$
$$+\int_0^a\int_0^b dx\,dy\,M(x,y)\cos(2\pi qy/b)+\frac{1}{2}(1+K_{pq}^2)$$
$$\left.+\int_0^a\int_0^b dx\,dy\,M(x,y)\cos(2\pi px/a)\cos(2\pi qy/b)\right\}. \tag{54}$$

Again, we write this result in the form of equation (14)

$$K^{(1)}=K_{pq}-I_{pqpq}. \tag{55}$$

Equations (54) and (55) govern the first-order convection of the acoustic field. The first and foremost property of interest arises from the first term in Eq. (54). This integral (together with its normalization factor) is the definition of average flow. It contributes a convection term in Eq. (55) which is equal to the profile-averaged Mach number. Furthermore, the other terms contribute correctly to this average as p and q are set to zero. The Neumann factors adjust correctly for the inclusion of the extra terms. This of course must be the case since all that is then being said is that a plane wave correctly averages any flow profile, when first-order perturbation theory is valid (this was mentioned in the Introduction and seen before in the case of the circular duct). When p or q or both are not equal to zero, error terms exist in Eq. (54).

The task at hand appears to be choosing the mode numbers so as to simultaneously minimize the above (bias) error terms as well as excursions from the first-order theory. Numerical experiments in the literature (see Shankar[45] and Agarwal and Bull[14]) have shown that plane waves are generally the most prone to flow-induced shape change and that the change decreases with increasing mode order. This effect will be derived later in this paper using perturbation theory. Significant modal shape changes of course invalidate first-order perturbation theory, which assumes no shape change in the mode field. We will, therefore, consider methods which encompass higher-order modes for eliminating bias errors.

The first integral in Eq. (54) contributes an unbiased average of the flow. The other three integrals are basically Fourier cosine integrals, with arguments double the corresponding modal arguments. It seems then that a method of minimizing the last three integrals would be to choose a mode so that the cosine factors in Eq. (54) are approximately orthogonal to the flow profile. This is obviously difficult to arrange in practice, and if one knew for certain what the flow profile was, this theory would be redundant.

If $M(x,y)$ is a piecewise continuous function, the cosine integrals must tend to zero as p and q tend to infinity. This occurs by virtue of the completeness of the Fourier cosine basis functions $\cos p\pi x/a$ and $\cos q\pi y/b$ (as in the case of the circular duct). Therefore, an obvious way of minimizing bias error is to use higher-order duct modes. To put this in practical terms, if the flow profile may be approximated by a low-order polynomial, then the use of a large-order mode in one coordinate direction (say, perhaps, $p\sim 20$ and $q=0$) may provide a sufficiently unbiased average for many applications.

Some other observations can be made along the lines of symmetry arguments. Profiles comprised of a constant term plus terms which are antisymmetric about the center of the duct will be averaged correctly, due to the fact that the cosine functions appearing in Eq. (54) are all even, about $(a/2,b/2)$.

C. Modal shape change

The above arguments for eliminating bias errors are really only useful if the first-order perturbation theory becomes a superior approximation as the mode number increases. This may easily be shown for the case of a cylindrical duct with an axisymmetric flow field or the nondegenerate case of a two-dimensional duct. For three-dimensional rectangular ducts the situation becomes somewhat problematic (again, except where the effective dimensionality can be reduced). Strictly degenerate cases are dealt with by assuming that the unperturbed state is a specific linear combination of the degenerate modes. This linear combination, of course, depends upon the nature of the perturbation (in our case this would include the flow profile), which is a rather undesirable state of affairs. In nearly degenerate cases, some perturbed modes will demonstrate high sensitivity to the perturbation. Minute variations in the aspect ratio of the duct can change the first-order correction for the perturbed mode by an order of magnitude, or simply invalidate the first order theory (see Fig. 3 in what follows).

For the above reasons it is desirable for us to limit the aspect ratio so as to eliminate problems associated with degeneracy. In the next section a first-order expression for the shape change in the flow perturbed modes will be introduced and a ''perturbation parameter'' depending on the shape of the flow profile and the frequency will be extracted from this expression. This parameter will in effect be an upper bound for the flow-dependent terms in the first-order expression. Section III E will then examine problems associated with modal degeneracy, which also arise from the first-order expression for the shape change in the flow. Section III F will summarize these results into a simple expression, which will be valid for most practical cases.

D. A perturbation parameter

The perturbed mode may be written as

$$\psi_{pq}^{(1)}(x,y)=\psi_{pq}(x,y)+\sum_{(m,n)\neq(p,q)}\frac{U_{pqmn}}{(k_{pq}^2-k_{mn}^2)}\psi_{mn}(x,y), \tag{56}$$

where $U_{pqmn}=2K^{(1)}k^2I_{pqmn}$. The mean square difference in mode shape can therefore be written as

$$s_{pq}=\int_0^a\int_0^b\|\psi_{pq}^{(1)}(x,y)-\psi_{pq}(x,y)\|^2dx\,dy$$
$$=\sum_{(m,n)\neq(p,q)}\frac{\|U_{pqmn}\|^2}{(k_{pq}^2-k_{mn}^2)^2}$$
$$=\frac{a^4}{\pi^4}\sum_{(m,n)\neq(p,q)}\frac{\|U_{pqmn}\|^2}{[p^2+(qa/b)^2-m^2-(na/b)^2]^2}. \quad (57)$$

The numerators of this series, i.e., the $\|U_{pqmn}\|$ terms, contain the flow-dependent information in the series. Replacing them with an upper bound will allow us to more easily estimate the magnitude of the series, and provide information on how the series depends on the shape of the flow profile and frequency.

To do this, it will be easiest to use the perturbation integrals in the form of Eq. (44). Using the result that $\psi_{ij}(x,y)$ and its partial derivatives (with respect to x and y) form complete trigonometric series over $[a\times b]$, we have that

$$\frac{a^2}{\pi^2}\|U_{pqmn}\|\leqslant(\epsilon_n\epsilon_m\epsilon_p\epsilon_q)^{1/2}\Lambda_{k,pq}, \quad (58)$$

where

$$\Lambda_{k,pq}=\frac{2K^{(1)}(ka)^2}{\pi^2}\left\{\langle M-M_{av}\rangle_{\rm rms}+\frac{\pi p}{ka}\left\langle\frac{\partial M}{\partial X}\right\rangle_{\rm rms}+\frac{\pi q}{kb}\left\langle\frac{\partial M}{\partial Y}\right\rangle_{\rm rms}\right\}, \quad (59)$$

and

$$\langle f(x,y)\rangle_{\rm rms}=\left(\frac{1}{ab}\int_0^a\int_0^b\|f(x,y)\|^2dx\,dy\right)^{1/2}, \quad (60)$$

$$X=kx, \quad (61)$$

$$Y=ky. \quad (62)$$

It is implied in this derivation that M and its partial derivatives are piecewise continuous functions over $[a\times b]$. The term $\Lambda_{k,pq}$ may be interpreted as a perturbation parameter based on the standard deviation of the flow profile from its mean, and the rms. magnitude of the flow shear in the x and y directions. The term $\langle M-M_{av}\rangle_{\rm rms}$ will be referred to later as σ_M: the standard deviation in the Mach number profile. Note that there is no implication of ''randomness'' intended by use of the term ''standard deviation.'' It is used simply as a mathematical formula for measuring shape deviations from the mean in the flow profile.

The assumption of piecewise continuity of the partial derivatives of M breaks down for the classical expressions used for fully developed turbulent profiles. The profiles of Nikuradse and Prandtl (see Blevins,[69] page 41) indicate a logarithmic dependence on the radial coordinate for circular ducts. This dependence, however, has been derived from the wall condition alone and is therefore thought to be independent of the shape of the duct.

In reality, of course, a viscous sublayer exists near the wall so that the gradients at the wall are not infinite as predicted by the logarithmic dependence (see Blevins,[69] page 41). Nevertheless, for high Reynolds number flows the logarithmic dependence can be a good enough approximation to make the derivative terms in Eq. (59) dominant. In fact, they become excessively large upper bounds in this case, since the integrands of the integrals upon which they are based contain $\sin(\pi px/a)$ and $\sin(\pi qy/b)$ terms which go to zero at the boundaries [these terms can be seen in Eqs. (49) and (50)]. Actually, they do so at the same rate that the classical profile gradient becomes singular. For these reasons a more precise (but also more cumbersome) version of Eq. (59) is given. It renders an appropriate upper bound for turbulent profiles with large wall gradients

$$\Lambda_{k,pq}=\frac{2K^{(1)}(ka)^2}{\pi^2}\left\{\langle M-M_{av}\rangle_{\rm rms}+\frac{\pi p}{ka}\left\langle\frac{\partial M}{\partial X}\sin(\pi px/a)\right\rangle_{\rm rms}+\frac{\pi q}{kb}\left\langle\frac{\partial M}{\partial Y}\sin(\pi qy/b)\right\rangle_{\rm rms}\right\}. \quad (63)$$

Equation (63) is a rather awkward-looking expression; however, it and Eq. (59) will be referred to in Sec. III F and both simplified into one expression which will cover virtually all cases of practical interest.

E. Degeneracy

Now, with regard to our discussion on degeneracy and aspect ratio in Sec. III C, we shall examine the perturbation of the $q=0$ modes only. The $\|U_{mnp0}\|^2$ term in the numerator of the sum in Eq. (57) will be replaced by an upper bound of the type shown in Eq. (58). The sum may then be broken up as follows to take into account the Neumann factors, and to demonstrate the limit to the two-dimensional case. The mean square difference in mode shape is thus subject to the following inequality:

$$s_{p0}\leqslant\Lambda_{k,p0}^2\left[2\epsilon_p\sum_{n=1}^{\infty}\left\{\frac{1}{[(na/b)^2-p^2]^2}+2\sum_{m=1}^{\infty}\frac{1}{[m^2+(na/b)^2-p^2]^2}\right\}+2\epsilon_p\sum_{\substack{m>0\\ m\neq p}}\frac{1}{[m^2-p^2]^2}+\begin{cases}0 & p=0\\ 2/p^4 & p>0\end{cases}\right]. \quad (64)$$

Now, for the purposes of removing problems associated with modal degeneracy, we shall limit the aspect ratio so that

$$a/b\geqslant\begin{cases}1 & p=0,\\ \sqrt{2}p & p>0.\end{cases} \quad (65)$$

(Note that we deal here only with ducts of aspect ratio greater than unity to avoid redundancy.) The factor of $\sqrt{2}$ in the preceding equation was chosen for analytical convenience to some extent. Suffice it to say that this factor must

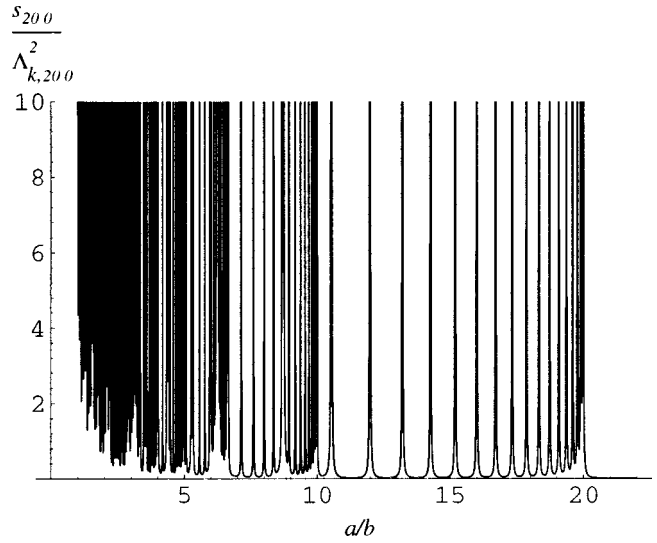

FIG. 3. $s_{20\,0}/\Lambda^2_{k,20\,0}$ versus aspect ratio a/b [for mode number (20, 0)].

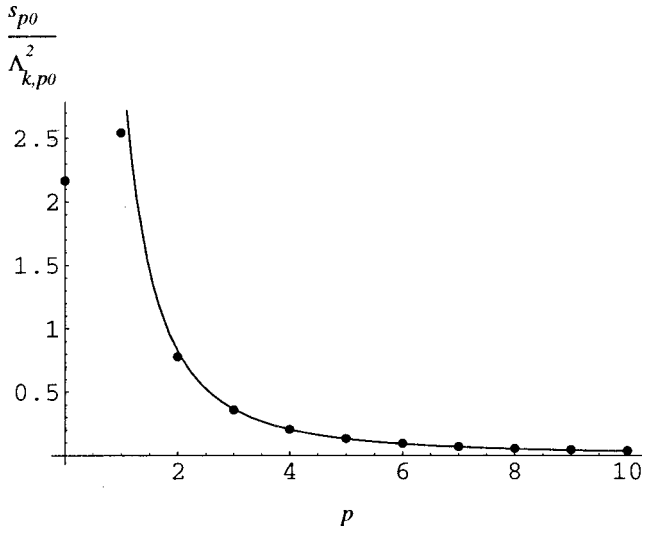

FIG. 4. $s_{p0}/\Lambda^2_{k,p0}$ versus mode number p, for aspect ratio $a/b=10\sqrt{2}$, is shown as dots. Asymptotic two-dimensional limit $\pi^2/3p^2$ is shown as a solid curve.

be somewhat larger than unity to remove problems associated with near degeneracy [examine the first term of Eq. (64) for a quantitative description of the singularity at $a/b=p$]. Using result 25 in section 5.1.25 of Prudnikov *et al.*,[70] Eq. (64) may be reduced to

$$s_{p0}\leqslant\Lambda^2_{k,p0}\left[2\epsilon_p\sum_{n=1}^{\infty}\left\{\frac{\pi}{4\alpha^3}\coth\pi\alpha+\frac{\pi^2}{4\alpha^2}\operatorname{cosech}^2\pi\alpha\right\}+\begin{cases}\pi^4/45 & p=0\\ \dfrac{\pi^2}{3p^2}-\dfrac{3}{4p^4} & p>0\end{cases}\right], \tag{66}$$

where $\alpha^2=(na/b)^2-p^2$ (note that this formula is valid for imaginary α). The expression inside the square brackets in Eq. (66) has been plotted in Fig. 3 for $a/b\geqslant 1$ and $p=20$. The spikes occurring in the figure are poles of the summation. These occur at aspect ratios where two or more modes are exactly degenerate. The present first-order theory is obviously no longer valid for these aspect ratios. The positions of the poles are given by a simple expression

$$a/b=\frac{1}{n}\sqrt{p^2-l^2}, \tag{67}$$

where $l=0,1,2,...,p$. The density of the poles increases on average as n becomes large (and a/b becomes small) since a small percentage change in n (i.e., n changing by 1) then gives rise to a new series of poles.

We now return to the cases governed by Eq. (65). By limiting the aspect ratio as per Eq. (65), we may neglect the $\operatorname{cosech}^2\pi\alpha$ term in Eq. (66) (with less than 3% error in the worst case). Furthermore, $\coth\pi\alpha$ may be approximated by unity (with less than 0.5% error). Therefore, the sum over n in Eq. (66) is to a good approximation

$$\frac{\pi}{4}\sum_{n=1}^{\infty}\frac{1}{((na/b)^2-p^2)^{3/2}}=\begin{cases}\dfrac{\pi}{4}\left(\dfrac{b}{a}\right)^3\displaystyle\sum_{n=1}^{\infty}\frac{1}{n^3} & p=0,\\ \dfrac{\pi}{4}\dfrac{1}{\beta^3p^3}\displaystyle\sum_{n=1}^{\infty}\frac{1}{(n^2-1/\beta^2)^{3/2}} & p>0,\end{cases} \tag{68}$$

where $\beta=a/(bp)$ and is greater than or equal to $\sqrt{2}$ in accordance with Eq. (65). The sums in Eq. (68) may be evaluated numerically. (This first sum has a well-known numerical value. In the case of the second sum an upper bound may be given corresponding to $\beta=\sqrt{2}$. This is trivially evaluated by direct summation.) Hence, we may write

$$s_{p0}\leqslant\Lambda^2_{k,p0}\begin{cases}\dfrac{\pi^4}{45}+\dfrac{\pi}{2}\left(\dfrac{b}{a}\right)^3\times 1.2020... & p=0,\\ \dfrac{\pi^2}{3p^2}+\dfrac{\pi}{\beta^3p^3}\times 3.0627...-\dfrac{3}{4p^4} & p>0.\end{cases} \tag{69}$$

Of course, the product βp, in the $p>0$ branch of the preceding equation is simply the aspect ratio of the duct (a/b). It has been written in this fashion so that when one uses Eq. (65), which fixes a range for β by relating aspect ratio to mode number, it can be seen that the term in question goes as $1/p^3$. The upper bounds are not excessive, having been carefully evaluated, and therefore ought to give reasonable indications of the relative sizes of the various modal shape perturbations in worst-case scenarios.

Let us examine the case where ten modes are excited in turn in a duct (i.e., ψ_{p0} with $p\leqslant 10$). So that the expressions are true for all modes and the same duct is used for all modes, we will set $a/b=10\times\sqrt{2}$. Figure 4 shows the results. It is apparent from this graph that modal shape change in worst-case scenarios may be minimized by using higher-order modes.

Further, it may be seen that in the asymptotic limit for large p, $s_{p0}/\Lambda_{k,p0}^2 \sim \pi/3p^2$ [again, assuming that the aspect ratio is allowed to increase with the highest mode number according to Eq. (65)]. Figure 4 superimposes this asymptotic limit on the preceding example and the difference is small in this case for $p \geqslant 2$. In the case of an idealized two-dimensional waveguide, Eq. (69) reduces to

$$s_{p0} \leqslant \Lambda_{k,p0}^2 \begin{cases} \dfrac{\pi^4}{45} & p=0, \\ \dfrac{\pi^2}{3p^2} - \dfrac{3}{4p^4} & p>0. \end{cases} \tag{70}$$

The minimization of modal shape change by the use of higher-order modes is suggested very clearly by this expression.

F. Summary of results on modal shape change

In the previous section, we showed that in certain cases higher-order modes are less prone to shape perturbation. The cases we considered in this regard are where the $(p,0)$ modes are used and $a/b \geqslant \sqrt{2}p$. In the limit as $a/b \to \infty$ this becomes the case of a two-dimensional duct.

Now consider Eq. (59). What we desire is to simplify this expression [and/or Eq. (63)] by showing that the shear terms may be neglected or replaced by an upper bound which is constant (of order unity) times the standard deviation term.

It may often be the case that for shear flows, changes in $M(x,y)/\sigma_M$, on the scale of a wavelength, are on rms average (over the cross section of the duct) of order unity or less. This is true for laminar profiles, which do not contain sharp variations over the scale of the duct width a. In this case, provided the profile is interrogated with a mode well above its cutoff frequency, the shear terms in Eq. (59) may be of similar magnitude to the standard deviation term, or smaller, depending on the wavelength.

A common case where the flow shear is much larger than the profile standard deviation is fully developed turbulent flow. In this case sharp gradients exist near the wall. This was addressed before in Sec. III D. In this case, Eq. (63) should be used to estimate the size of the modal perturbations.

In order to examine this case we consider a Mach number profile with a constant standard deviation σ_M. This can be written as follows:

$$M(x,y) = \sigma_M \mathcal{P}(x,y)/\sigma_{\mathcal{P}}. \tag{71}$$

To estimate the size of the derivative terms for the $q=0$ modes, assume the profile $\mathcal{P}(x,y)$ in Eq. (71) to be of the form

$$\mathcal{P}(x,y) = f(x)g(y), \tag{72}$$

where

$$f(x) = \begin{cases} \log_{10}(2x/a) + c_1 & x \leqslant a/2 \\ \log_{10}(2-2x/a) + c_1 & x > a/2, \end{cases} \tag{73}$$

where c_1 is an arbitrary real constant. The function $g(y)$ is left unspecified for the moment, but will be addressed shortly. The form in Eq. (72) is by no means all encompassing, but should be general enough to demonstrate the removal of the gradient singularity in Eq. (73).

According to Eq. (63), the derivative term should contribute a value of

$$T_{\text{deriv}} = \frac{\pi p}{k^2 a} \sigma_M \langle f'(x) g(y) \sin(\pi p x/a) \rangle_{\text{rms}} / \sigma_{\mathcal{P}}, \tag{74}$$

where

$$f'(x) = \begin{cases} 1/(x \ln 10) & x \leqslant a/2 \\ 1/((x-a)\ln 10) & x > a/2. \end{cases} \tag{75}$$

For fixed σ_M, Eq. (74) becomes large when $\sigma_{\mathcal{P}} \to 0$ [i.e., when $\mathcal{P}(x,y) \to 1$]. Since $f(x)$ and $g(y)$ are functions of independent coordinates, in this example, we set $g(y)=1$ to maximize its contribution to T_{deriv}. [Note that for practical situations which give rise to fully developed turbulent flows, setting $g(y)=1$ is likely to be a good approximation in the limit of high Reynolds number, as $g'(y)$ does not enter into Eq. (74).] By evaluating the integrals in Eq. (74), we have that

$$T_{\text{deriv}} \leqslant \sigma_M \frac{\pi^2 p \sqrt{p}}{(ka)^2} \tag{76}$$

for all values of c_1.

Now, the conditions in Eqs. (13) and (51) imply that $K^{(1)}$ is of order unity (say for practical purposes larger than 1/2). This also implies $ka > \pi p$. Taking all these things together and further approximating $s_{p0}/\Lambda_{k,p0}^2$ by its asymptotic limit (i.e., $\pi^2/3p^2$) we have that first-order rms perturbations in mode shape $s_{p,0}^{1/2}$ are governed by a number

$$W = \begin{cases} (ka)^2 \sigma_M & p=0, \\ (ka)^2 \sigma_M / p & p>0. \end{cases} \tag{77}$$

This number indicates the dependences on ka, σ_M, and mode number, of first-order modal perturbations, in two-dimensional and extreme aspect ratio cases. It should be valid for many practical acoustic flow measurement applications; that is, those where changes in the profile over a wavelength are small or of the order of the standard deviation of the profile, except for the possibility of turbulent wall shear, which is also allowed. The full expression in Eq. (69) can of course be used where one wishes to consider strong flow gradients other than turbulent wall shear.

The number W governs first-order shape changes. Higher-order perturbation expansions of shape change contain higher powers of $(k_{pq}^2 - k_{mn}^2)$ in their denominators. It may then prove to be true that worst-case higher-order shape perturbations are killed off faster than $1/p$ [shown in Eq. (77)].

IV. A NUMERICAL STUDY

For the purposes of illustrating the results of the perturbation theory, a numerical example has been calculated for a two-dimensional rigid-walled duct with a shear flow profile shown in Fig. 5. The profile is assumed to exist in approxi-

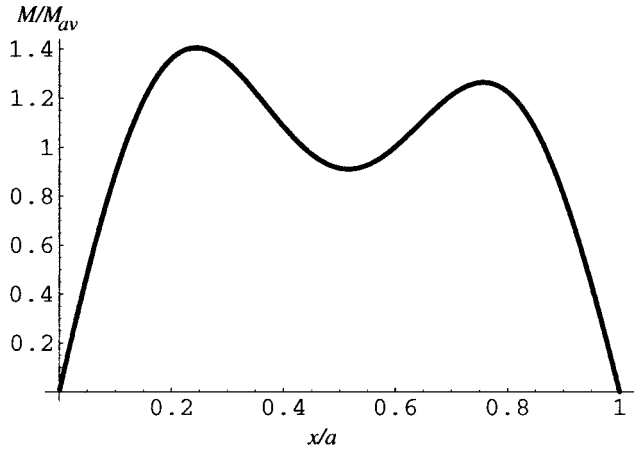

FIG. 5. Normalized Mach number profile (M/M_{av} vs x/a), for the two-dimensional example problem.

mately the same form for several duct diameters and many wavelengths in accordance with the assumptions given in Sec. III A.

The profile is given as a worst case and was picked on the basis of its lack of ''specialness,'' that is, lack of symmetry and flatness. It also has a nominal similarity to an actual profile produced by experimental work at the laboratory where this paper was written (see the author's address). Other profiles were studied and similar results were obtained. In general, laminar-type wall conditions [$\sim(1-r^2)$ as $r \rightarrow 1$] produced more modal distortion for a given wavelength and mean flow rate. Hence, the chosen profile contains these.

Figure 6 shows the modal shape perturbations at $ka = 100$. Although numerical values are not given here, it is

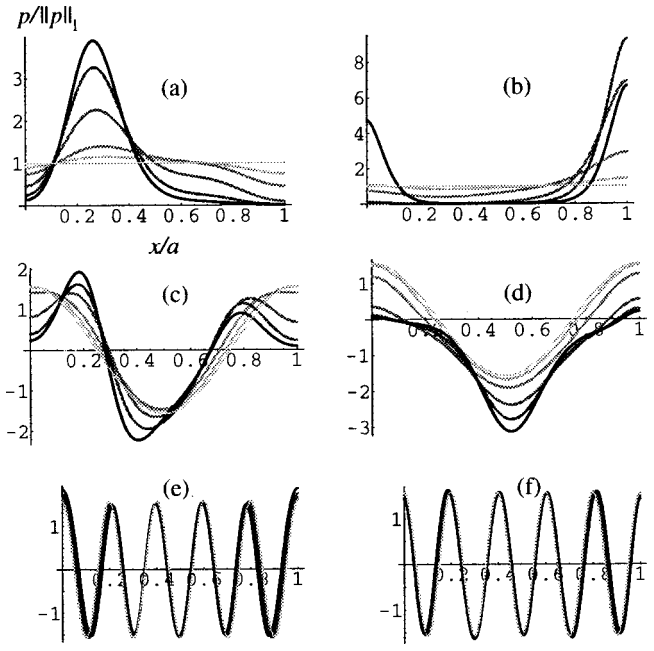

FIG. 6. Normalized mode functions ($p/\|p\|_1$ vs x/a, where $\|p\|_1$ is the L_1 norm of p) at various Mach numbers for the two-dimensional example. Here, $ka = 100$. (a) mode 0 (fundamental) upstream; (b) mode 0 downstream; (c) mode 2 upstream; (d) mode 2 downstream; (e) mode 10 upstream; (f) mode 10 downstream. The curves are for the Mach numbers: 0, 0.001, 0.003, 0.01, 0.02, 0.03, corresponding to shades from light gray to black, respectively.

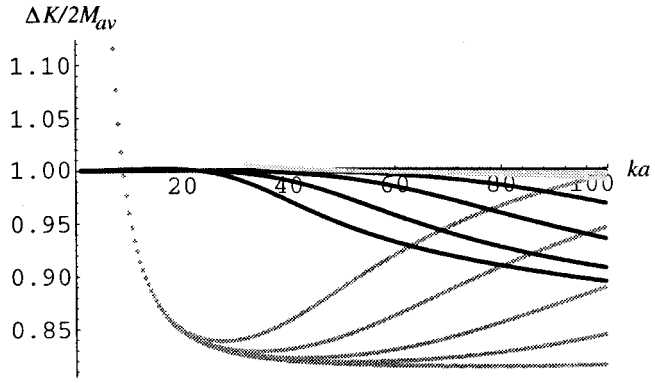

FIG. 7. Normalized upstream–downstream axial wave number differential $\Delta K/2M_{av}$ vs ka at several Mach numbers. Mode 0 (fundamental), mode 2, and mode 10 are shown in different shades ranging from black to light gray, respectively. The curves for each mode (shade) represent the Mach numbers 0.001, 0.004, 0.0075, 0.0015, 0.03. These lie respectively *below* each other for mode 0 and mode 10, and, respectively, *above* each other for mode 2. Note that the mode 10 curves lie nearly on top of the ka axis as well as each other in this figure. The first order perturbation prediction for the wave number differentials are 1, 0.81, and 0.995 for modes 0, 2, and 10, respectively.

clear that the first-order theory qualitatively predicts the trend, with the flow-induced shape perturbation in the mode decreasing with mode order.

Figure 7 demonstrates the effect of frequency, mode number, and Mach number on flow averaging. A normalized upstream–downstream axial wave number differential $\Delta K/2M_{av}$ is plotted against ka at several Mach numbers.

The quantity $\Delta K/2M_{av}$ should be equal to unity for an unbiased acoustic average of the flow at small Mach numbers. [The exact expression for $M_{av}<1$ is $\Delta K(1-M_{av}^2)/2M_{av}$; however, for the Mach numbers used in this example the difference is negligible.]

According to Eq. (77) the first-order theory should become more accurate as ka and the Mach number profile standard deviation are decreased (W is minimized). In the present example the Mach number profile standard deviation increases with Mach number. Equation (77) also predicts the first-order theory should become more accurate as the mode number increases (again, W is minimized).

In Fig. 7 we see that, sufficiently far from the cutoff frequencies, and at combinations of ka, σ_M, and mode number where W is minimized, the wave number differential approaches the first-order perturbation prediction. The first-order error is the difference of this prediction from unity and has been denoted a ''bias error'' in Sec. III B. The first-order perturbation predictions are given in the caption of Fig. 7.

Departures from the first-order theory are pronounced for mode 0 and mode 2, whereas for mode 10, the departures are relatively small. Even though mode 0 has a zero bias error, the departure from the first-order theory is enough to produce a maximum total averaging error of $\sim$10% for this mode. Mode 2 has a 19% bias error, and the total error is highly dependent on Mach number and ka. Mode 10 has both small bias error and total averaging error, for the ranges of Mach number and ka shown. These results are consistent with the perturbation analysis.

V. CONCLUSIONS

In Secs. II and III we have employed perturbation theory to examine the convection of higher-order modes in rigid flow ducts. It has been shown that for rigid circular waveguides, only the plane-wave mode convects with the mean flow. The higher modes in this case convect with an incorrect flow average. The problem with using a plane wave appears to be that it is the most sensitive to flow-induced distortion. Modal distortion (shape change) has been shown to increase for all modes with the rms shear and the standard deviation of the flow profile, as well as the square of the frequency.

It has been noted before in the literature that flow-induced modal distortion decreases with increasing mode number. A rigorous result has been obtained in this paper for the case of rigid rectangular waveguides which approximate one-dimensional systems [in the sense of Eq. (65)]. The result is that, in the first-order limit, the worst-case modal shape change goes as $1/p$ (where p is the mode number). This result cannot be easily generalized to rigid rectangular waveguides with arbitrary aspect ratio owing to a problem with modal degeneracy.

Concerning convection, a result has been obtained for rigid rectangular waveguides (of any aspect ratio) and a fixed piecewise continuous flow profile. First-order perturbation theory predicts that in the worst case, increasing the mode number will decrease the convection bias. That is, the higher the mode order, the closer it will be to being convected by the average Mach number. A two-dimensional example is given in Sec. IV, which bears out this conclusion as well as that of the modal shape change decreasing with mode number.

Putting these results together, we find that in flow metering applications where distortion of the plane wave is a problem, higher-order modes may be used to improve the average of the flow. The caveats are that the duct must be acoustically rigid and rectangular, and must approximate a one-dimensional system in the sense of Eq. (65).

APPENDIX: THE CONVECTIVE WAVE EQUATION

Following from the text in Sec. III A, we substitute the forms in Eq. (32) into Eq. (29), whereupon the time average of this equation is subtracted from itself, and the products of fluctuating terms are neglected. This results in three linearized equations

$$\rho_0\frac{\partial u_x'}{\partial t}+\rho_0 U_0\frac{\partial u_x'}{\partial z}=-\frac{\partial p'}{\partial x}+\mu_0\nabla^2 u_x'+\frac{1}{3}\mu_0\frac{\partial}{\partial x}\operatorname{div}\mathbf{u}'+\frac{\partial\mu'}{\partial z}\frac{\partial U_0}{\partial x}, \tag{A1}$$

$$\rho_0\frac{\partial u_y'}{\partial t}+\rho_0 U_0\frac{\partial u_y'}{\partial z}=-\frac{\partial p'}{\partial y}+\mu_0\nabla^2 u_y'+\frac{1}{3}\mu_0\frac{\partial}{\partial y}\operatorname{div}\mathbf{u}'+\frac{\partial\mu'}{\partial z}\frac{\partial U_0}{\partial y}, \tag{A2}$$

$$\rho_0\frac{\partial u_z'}{\partial t}+\rho_0\left(u_x'\frac{\partial U_0}{\partial x}+u_y'\frac{\partial U_0}{\partial y}\right)+\rho_0 U_0\frac{\partial u_z'}{\partial z}=-\frac{\partial p'}{\partial z}+\mu_0\nabla^2 u_z'+\mu'\left(\frac{\partial^2 U_0}{\partial x^2}+\frac{\partial^2 U_0}{\partial y^2}\right)+\frac{1}{3}\mu_0\frac{\partial}{\partial z}\operatorname{div}\mathbf{u}'+\frac{\partial\mu'}{\partial x}\frac{\partial U_0}{\partial x}+\frac{\partial\mu'}{\partial y}\frac{\partial U_0}{\partial y}, \tag{A3}$$

for the x, y, and z directions, respectively. In addition to these equations, we require the time-filtered linearized conservation of mass equation, which reduces to

$$\frac{\partial\rho'}{\partial t}+U_0\frac{\partial\rho'}{\partial z}+\rho_0\operatorname{div}\mathbf{u}'=0. \tag{A4}$$

Combining these equations, with a good many rearrangements and differentiations, one arrives at [compare with Mungur and Gladwell,[13] Eq. (13)]

$$\begin{aligned}\frac{\partial^2\rho'}{\partial t^2}=&\nabla^2 p'-2U_0\frac{\partial^2\rho'}{\partial z\,\partial t}-U_0^2\frac{\partial^2\rho'}{\partial z^2}\\&+2\rho_0\left[\frac{\partial u_x'}{\partial z}\frac{\partial U_0}{\partial x}+\frac{\partial u_y'}{\partial z}\frac{\partial U_0}{\partial y}\right]+\frac{4}{3}\frac{\mu_0}{\rho_0}\left[\frac{\partial}{\partial t}\nabla^2\rho'\right.\\&\left.+U_0\frac{\partial}{\partial z}\nabla^2\rho'+2\left(\frac{\partial U_0}{\partial x}\frac{\partial^2\rho'}{\partial z\,\partial x}+\frac{\partial U_0}{\partial y}\frac{\partial^2\rho'}{\partial z\,\partial y}\right)\right.\\&\left.+\frac{\partial\rho'}{\partial z}\left(\frac{\partial^2 U_0}{\partial x^2}+\frac{\partial^2 U_0}{\partial y^2}\right)\right]-2\frac{\partial\mu'}{\partial z}\left[\frac{\partial^2 U_0}{\partial x^2}+\frac{\partial^2 U_0}{\partial y^2}\right]\\&-2\left[\frac{\partial^2\mu'}{\partial z\,\partial x}\frac{\partial U_0}{\partial x}+\frac{\partial^2\mu'}{\partial z\,\partial y}\frac{\partial U_0}{\partial y}\right].\end{aligned} \tag{A5}$$

This is the same as Eq. (33) of Sec. III A. The next stage in obtaining the required equation involves expressing ρ' and μ' in terms of p'. Mungur and Gladwell state that in an inviscid fluid with no thermal conductivity, propagation may be considered to take place adiabatically and isentropically. In this case, we have

$$\rho'=\frac{p'}{c^2}, \tag{A6}$$

where c is the velocity of sound. In viscous fluids energy dissipation by viscosity gives rise to a change in entropy of the system. Thermal, entropic, and viscous waves are the result. Mungur and Gladwell take these effects into account by deriving the following approximate relations, which now assume the fluid is an ideal gas:

$$\rho'=\frac{p'+\delta}{c^2}, \tag{A7}$$

where

$$\delta=-(\gamma-1)\frac{\epsilon}{i\omega(1-MK)}. \tag{A8}$$

The ϵ term is extended to three dimensions here and is given by

$$\epsilon = 2\mu_0\left[\frac{\partial U_0}{\partial y}\left(\frac{\partial u_z'}{\partial y}+\frac{\partial u_y'}{\partial z}\right)+\frac{\partial U_0}{\partial x}\left(\frac{\partial u_z'}{\partial x}+\frac{\partial u_x'}{\partial z}\right)\right]$$
$$-\frac{u_z'}{U_0}\mu_0\nabla_{xy}U_0\cdot\nabla_{xy}U_0+(\eta-1)\mu_0\frac{p'}{P_0}\nabla_{xy}U_0\cdot\nabla_{xy}U_0$$
$$-\eta\mu_0\frac{\rho'}{\rho_0}\nabla_{xy}U_0\cdot\nabla_{xy}U_0+\kappa_0\left[\frac{1}{P_0}\nabla^2p'-\frac{1}{\rho_0}\nabla^2\rho'\right]. \tag{A9}$$

The symbol ∇_{xy} is the two-dimensional Laplacian in the xy plane, M is the Mach number (U_0/c), and K represents the normalized z component of the complex wave vector. The symbol η is the index relating viscosity and temperature, and is approximately 0.72 to 0.75 for gases (according to Mungur and Gladwell), γ is the ratio of the principal specific heats, and κ_0 is the steady thermal conductivity of the gas. The term δ in Eq. (A8) will transform our wave equation from second order to fourth order. Presumably, some simplifications can be made for gases in which the viscosity plays only a small part in determining the acoustic fields.

In order to obtain our final wave equation, we note that Mungur and Gladwell have also given an expression relating the fluctuating viscosity to p' and δ. This is

$$\mu' = \tau_2[(\gamma-1)p'-\delta], \tag{A10}$$

where $\tau_2=\eta\mu_0/(\rho_0c^2)$. Mungur and Gladwell further define $\tau_1=4\mu_0/(3\rho_0c^2)$ as the viscous relaxation time. By substituting all these relations into Eq. (A5) and by rewriting U_0/c as M, we obtain

$$\frac{1}{c^2}\frac{\partial^2(p'+\delta)}{\partial t^2}=\nabla^2(p'+\delta)-\nabla^2\delta-\frac{2M}{c}\frac{\partial^2(p'+\delta)}{\partial z\,\partial t}-M^2\frac{\partial^2(p'+\delta)}{\partial z^2}+2\rho_0c\left[\frac{\partial u_x'}{\partial z}\frac{\partial M}{\partial x}+\frac{\partial u_y'}{\partial z}\frac{\partial M}{\partial y}\right]$$
$$+\tau_1c\left[\frac{1}{c}\frac{\partial}{\partial t}\nabla^2(p'+\delta)+M\frac{\partial}{\partial z}\nabla^2(p'+\delta)+2\left(\frac{\partial M}{\partial x}\frac{\partial^2(p'+\delta)}{\partial z\,\partial x}+\frac{\partial M}{\partial y}\frac{\partial^2(p'+\delta)}{\partial z\,\partial y}\right)\right.$$
$$\left.+\frac{\partial(p'+\delta)}{\partial z}\left(\frac{\partial^2M}{\partial x^2}+\frac{\partial^2M}{\partial y^2}\right)\right]-\mathbf{2}\tau_2c\left((\gamma-1)\frac{\partial(p'+\delta)}{\partial z}-\gamma\frac{\partial\delta}{\partial z}\right)\left[\frac{\partial^2M}{\partial x^2}+\frac{\partial^2M}{\partial y^2}\right]$$
$$-2\tau_2c\left[\left((\gamma-1)\frac{\partial^2(p'+\delta)}{\partial z\,\partial x}-\gamma\frac{\partial^2\delta}{\partial z\,\partial x}\right)\frac{\partial M}{\partial x}+\left((\gamma-1)\frac{\partial^2(p'+\delta)}{\partial z\,\partial y}-\gamma\frac{\partial^2\delta}{\partial z\,\partial y}\right)\frac{\partial M}{\partial y}\right]. \tag{A11}$$

Compare this with Eq. (19) of Mungur and Gladwell,[13] noting the extra factor of 2 present in boldface, as for Eq. (33) in this paper.

[1] A. von Jena, V. Mágori, and W. Russwurm, "Ultrasound gas-flow meter for household application," Sens. Actuators A **37–38**, 135–140 (1993).
[2] L. C. Lynnworth, *Physical Acoustics XIV* (Academic, New York, 1979), pp. 487–503.
[3] B. Robertson, "Effect of arbitrary temperature and flow profiles on the speed of sound in a pipe," J. Acoust. Soc. Am. **62**, 813–818 (1977).
[4] B. Robertson, "Flow and temperature profile independence of flow measurements using long acoustic waves," Trans. ASME **106**, 18–20 (1984).
[5] E. Håkansson and J. Delsing, "Effects of flow disturbance on an ultrasonic gas flowmeter," Flow Meas. Instrum. **3**, 227–233 (1992).
[6] J. E. Heritage, "The performance of transit time ultrasonic flowmeters under good and disturbed flow conditions," Flow Meas. Instrum. **1**, 24–30 (1989).
[7] P. N. Shankar, "On acoustic refraction by duct shear layers," J. Fluid Mech. **47**, 81–91 (1971).
[8] N. Kroemer, A. von Jena, and T. Vontz, "Ultraschall-durchflußmesser für industrielle Andwendungen," Tech. Mess. **64**, 180–189 (1997).
[9] L. C. Lynnworth, "Ultrasonic flowmeters," Trans. Inst. Meas. Control (London) **4**, 2–24 (1982).
[10] M. L. Sanderson and J. Hemp, "Ultrasonic flowmeters—a review of the state of the art," in International Conference on Advances in Flow Measurement Techniques, number 3, pp. 157–178, 1981.
[11] H. Lechner, "Ultrasonic flow metering based on transit time differentials which are insensitive to flow profile," J. Acoust. Soc. Am. **74**, 955–959 (1983).
[12] H. Lechner, "Ultrasonic measurement of volume flow independent of velocity distribution," in *Proceedings of the 9th IMEKO Congress of the International Measurement Confederation held from the 24th to the 28th May 1982 Berlin–West*, edited by Prof. Striker (North-Holland, Amsterdam, 1983), Vol. 2, pp. 279–288.
[13] P. Mungur and G. M. L. Gladwell, "Acoustic wave propagation in a sheared fluid contained in a duct," J. Sound Vib. **9**, 28–48 (1969).
[14] N. K. Agarwal and M. K. Bull, "Acoustic wave propagation in a pipe with fully developed turbulent flow," J. Sound Vib. **132**, 275–298 (1989).
[15] R. J. Astley, "A finite element, wave envelope formulation for acoustical radiation in moving flows," J. Sound Vib. **103**, 471–485 (1985).
[16] N. Atalla and S. Glegg, "A geometrical acoustics approach for calculating the effects of flow on acoustics scattering," J. Sound Vib. **171**, 681–694 (1994).
[17] D. Blokhintzev, "The propagation of sound in an inhomogeneous and moving medium I," J. Acoust. Soc. Am. **18**, 322–334 (1946).
[18] J. R. Breton and D. Middleton, "General theory of acoustic propagation through arbitrary fluid media I. Propagation equations, conditions of the medium, and general dynamical solutions," J. Acoust. Soc. Am. **69**, 1245–1260 (1981).
[19] D. C. Pridmore-Brown, "Sound propagation in a fluid flowing through an attenuating duct," J. Fluid Mech. **4**, 393–406 (1958).
[20] P. O. A. L. Davies, "Realistic models for predicting sound propagation in flow duct systems," Noise Control Eng. **40**, 135–141 (1993).
[21] W. Eversman, "Representation of a 1/*N* power law boundary layer in the sheared flow acoustic transmission problem," J. Sound Vib. **24**, 459–469 (1972).
[22] W. Eversman, "Approximation for thin boundary layers in the sheared flow duct transmission problem," J. Acoust. Soc. Am. **53**, 1346–1350 (1973).
[23] G. R. Gogate and M. L. Munjal, "Analytical solution of sound propagation in lined or unlined circular ducts with laminar mean flow," J. Sound Vib. **160**, 465–484 (1993).
[24] G. R. Gogate and M. L. Munjal, "Sound propagation in ducts with bulk reacting lining in the presence of laminar mean flow," J. Acoust. Soc. Am. **99**, 1779–1782 (1996).
[25] M. Goldstein and E. Rice, "Effect of shear on duct wall impedance," J. Sound Vib. **30**, 79–84 (1973).
[26] A. S. Hersh and I. Catton, "Effect of shear flow on sound propagation in rectangular ducts," J. Acoust. Soc. Am. **50**, 992–1003 (1971).

[27] U. Ingard, ''Influence of fluid motion past a plane boundary on sound reflection, absorption, and transmission,'' J. Acoust. Soc. Am. **31**, 1035–1036 (1959).
[28] Z. L. Ji, Q. Ma, and Z. H. Zhang, ''A boundary element scheme for evaluation of four-pole parameters of ducts and mufflers with low Mach number nonuniform flow,'' J. Sound Vib. **185**, 107–117 (1995).
[29] A. Kapur and P. Mungur, ''On the propagation of sound in a rectangular duct with gradients of mean flow and temperature in both transverse directions,'' J. Sound Vib. **23**, 401–404 (1972).
[30] S.-H. Ko, ''Sound attenuation in lined rectangular ducts with flow and its application to the reduction of aircraft engine noise,'' J. Acoust. Soc. Am. **50**, 1418–1432 (1971).
[31] S.-H. Ko, ''Sound attenuation in acoustically lined circular ducts in the presence of uniform flow and shear flow,'' J. Sound Vib. **22**, 193–210 (1972).
[32] S.-H. Ko, ''Theoretical prediction of sound attenuation in acoustically lined annular ducts in the presence of uniform flow and shear flow,'' J. Acoust. Soc. Am. **54**, 1592–1606 (1973).
[33] M. N. Mikhail and A. N. Abdelhamid, ''Transmission and far field radiation of sound waves in and from lined ducts containing shear flow,'' AIAA Paper No. 73–1013 (1973).
[34] R. Mani, ''Sound propagation in parallel sheared flows in ducts: The mode estimation problem,'' Proc. R. Soc. London, Ser. A **371**, 393–412 (1980).
[35] S. Mariano, ''Effect of wall shear layers on the sound attenuation in acoustically lined rectangular ducts,'' J. Sound Vib. **19**, 261–275 (1971).
[36] E. Meyer, F. Mechel, and G. Kurtze, ''Experiments on the influence of flow on sound attenuation in absorbing ducts,'' J. Acoust. Soc. Am. **30**, 165–174 (1958).
[37] W. Möhring, ''Energy flux in duct flow,'' J. Sound Vib. **18**, 101–109 (1971).
[38] W. Möhring, ''On energy, group velocity and small damping of sound waves in ducts with shear flow,'' J. Sound Vib. **29**, 93–101 (1973).
[39] W. Möhring, E. A. Müller, and F. Obermeier, ''Problems in flow acoustics,'' Rev. Mod. Phys. **55**, 707–724 (1983).
[40] A. H. Nayfeh, J. E. Kaiser, and D. P. Telionis, ''Acoustics of aircraft engine-duct systems,'' AIAA J. **13**, 130–153 (1975).
[41] W. Neise, W. Frommhold, F. P. Mechel, and F. Holste, ''Sound power determination in rectangular flow ducts,'' J. Sound Vib. **174**, 201–237 (1993).
[42] J.-G. Ih, C.-M. Park, and H.-J. Kim, ''A model for sound propagation in capillary ducts with mean flow,'' J. Sound Vib. **190**, 163–175 (1996).
[43] K. S. Peat, ''A first approximation to the effects of mean flow on sound propagation through cylindrical capillary tubes,'' J. Sound Vib. **175**, 475–489 (1994).
[44] J. Rebel and D. Ronneberger, ''The effect of shear stress on the propagation and scattering of sound in flow ducts,'' J. Sound Vib. **158**, 469–496 (1992).
[45] P. N. Shankar, ''Sound propagation in duct shear layers,'' J. Sound Vib. **22**, 221–232 (1972).
[46] P. N. Shankar, ''Acoustic refraction and attenuation in cylindrical and annular ducts,'' J. Sound Vib. **22**, 233–246 (1972).
[47] S. D. Savkar, ''Propagation of sound in ducts with shear flow,'' J. Sound Vib. **19**, 355–372 (1971).
[48] M. A. Swinbanks, ''The sound field generated by a source distribution in a long duct carrying sheared flow,'' J. Sound Vib. **40**, 51–76 (1975).
[49] D. H. Tack and R. F. Lambert, ''Influence of shear flow on sound attenuation in a lined duct,'' J. Acoust. Soc. Am. **38**, 655–666 (1965).
[50] B. J. Tester, ''Some aspects of sound attenuation in lined ducts containing inviscid mean flows with boundary layers,'' J. Sound Vib. **28**, 217–245 (1973).
[51] B. J. Tester, ''Acoustic energy flow in lined ducts containing uniform or plug flow,'' J. Sound Vib. **28**, 205–215 (1973).
[52] B. J. Tester, ''The propagation and attenuation of sound in lined ducts containing uniform or plug flow,'' J. Sound Vib. **28**, 151–203 (1973).
[53] J. Z. Wu, H. Y. Ma, and J. M. Wu, ''Viscous sound-vortex interaction in a duct shear flow,'' J. Sound Vib. **172**, 103–126 (1994).
[54] T. W. Wu and L. Lee, ''A direct boundary integral formulation for acoustic radiation in a subsonic uniform flow,'' J. Sound Vib. **175**, 51–63 (1994).
[55] S. Ishii and T. Kakutani, ''Acoustic waves in parallel shear flows in a duct,'' J. Sound Vib. **113**, 127–139 (1987).
[56] K. S. Peat, ''Convected acoustic wave motion along a capillary duct with an axial temperature gradient,'' J. Sound Vib. **203**, 855–866 (1997).
[57] K.-W. Jeong and J.-G. Ih, ''A numerical study on the propagation of sound through capillary tubes with mean flow,'' J. Sound Vib. **198**, 67–79 (1996).
[58] R. J. Astley and W. Eversman, ''A finite element formulation in the eigenvalue problem in lined ducts with flow,'' J. Sound Vib. **65**, 61–74 (1979).
[59] D. C. Pridmore-Brown, ''Sound propagation in a temperature- and wind-stratified medium,'' J. Acoust. Soc. Am. **34**, 438–443 (1962).
[60] G. R. Gogate and M. L. Munjal, ''Analytical solution of the laminar mean flow wave equation in a lined or unlined two-dimensional rectangular duct,'' J. Acoust. Soc. Am. **92**, 2915–2923 (1992).
[61] R. J. Astley and J. G. Bain, ''A three-dimensional boundary element scheme for acoustic radiation in low Mach number flows,'' J. Sound Vib. **109**, 445–465 (1986).
[62] A. H. Nayfeh, J. E. Kaiser, and B. S. Shaker, ''Effect of mean-velocity profile shapes on sound transmission through two-dimensional ducts,'' J. Sound Vib. **34**, 413–423 (1974).
[63] J. F. Unruh and W. Eversman, ''The transmission of sound in an acoustically treated rectangular duct with boundary layer,'' J. Sound Vib. **25**, 371–382 (1972).
[64] A. H. Nayfeh and J. Sun, ''Effect of transverse velocity and temperature gradients on sound attenuation in two-dimensional ducts,'' J. Sound Vib. **34**, 505–517 (1974).
[65] L. Nijs and C. P. A. Wapenaar, ''The influence of wind and temperature gradients on sound propagation, calculated with the two-way wave equation,'' J. Acoust. Soc. Am. **87**, 1987–1998 (1990).
[66] P. M. Morse and H. Feshbach, *Methods of Theoretical Physics* (McGraw-Hill, New York, 1953).
[67] A. P. Prudnikov, Y. A. Brychkov, and O. I. Marichev, *Integrals and Series. Volume 2: Special Functions* (Gordon and Breach, New York, 1986).
[68] A. P. Prudnikov, Y. A. Brychkov, and O. I. Marichev, *Integrals and Series. Volume 3: More Special Functions* (Gordon and Breach, New York, 1990).
[69] R. D. Blevins, *Applied Fluid Dynamics Handbook*, 1st ed. (Krieger Malabar, FL, 1992).
[70] A. P. Prudnikov, Y. A. Brychkov, and O. I. Marichev, *Integrals and Series. Volume 1: Elementary Functions* (Gordon and Breach, New York, 1986).

Matched-field source tracking by ambiguity surface averaging

Laurie T. Fialkowski, John S. Perkins, Michael D. Collins, and Michael Nicholas
Naval Research Laboratory, Washington, D.C. 20375

John A. Fawcett
Defence Research Establishment Atlantic, Dartmouth, Nova Scotia B2Y 3Z7, Canada

W. A. Kuperman
Marine Physical Laboratory, Scripps Institute of Oceanography, University of California, San Diego, La Jolla, California 92152

(Received 22 December 1999; revised 23 March 2001; accepted 28 March 2001)

The method of matched-field source tracking by ambiguity surface averaging is demonstrated using low-frequency shallow-water acoustic data recorded on a vertical array. In this method, source motion is taken into account by averaging values from individual, short time-average matched-field ambiguity functions; each resulting average value corresponds to a trial source track. The result is a new ambiguity function which depends on six parameters: the three-dimensional coordinates of the initial and final source positions. A simplification to four parameters is made by assuming the source remains at a constant depth. Only mild restrictions are made on trial tracks considered, and the resulting ambiguity surfaces can be plotted as a function of final coordinates by holding the initial coordinates fixed at the optimal position. When applied to experimental data, the number of high sidelobes present in individual matched-field ambiguity surfaces is greatly reduced. Also, the technique appears robust to uncertainties in replica computation (due to various mismatch problems) and periods when the signal-to-noise ratio is low. [DOI: 10.1121/1.1385897]

PACS numbers: 43.30.Wi [SACB]

I. INTRODUCTION

Matched-field tracking (MFT) is a generalization of traditional matched-field processing (MFP) where source motion is included in the parameter landscape, thereby extending the MFP result of localization into one of localization and tracking. In its simplest and most widely used form, MFP is a detection and localization technique that correlates measured hydrophone data with simulated acoustic fields, or replicas, which correspond to trial source locations.[1–3] Matched-field tracking incorporates source motion into the parameter landscape by averaging traditional MFP results along candidate tracks through a time sequence of MFP ambiguity functions. In general, a resulting MFT ambiguity function depends upon several source variables: initial position, speed, and direction.

The specific MFT applications presented in this paper reduce the parameter landscape to the source's initial and final position by assuming a constant speed and a constant direction for each segment of a track. This is a reasonable limitation for short periods of time. By iteratively applying MFT over time to consecutive track segments, with each iteration allowing for a different constant speed and direction, a history of MFT ambiguities can follow a source without serious limitations on the movement of the source.

The MFT applications presented here are of experimental data using a vertical line array (VLA), although the method is not limited to vertical array applications. A range-dependent propagation model is used to precompute the replicas over the analysis area, where the complexity of the range-dependent environment is relied upon to break the azimuthal symmetry of the VLA; this is referred to as ''environmental symmetry breaking.''[4,5] Tracking based on variations in received level due to environmental complexity has also been proposed.[6]

The MFT results presented show ambiguity functions which maintain many of the same robust characteristics of the constituent MFP ambiguity surfaces, while additionally suppressing many of the MFP ambiguous peaks. This ambiguity suppression characteristic is a result of the averaging technique applied, as well as of the environmental complexity of the particular analysis area. As the source moves, ambiguous MFP peaks will eventually fade, while the peak corresponding to the source, even when not a global peak, moves in a more consistent fashion, providing a higher average value along the corresponding MFT track (even in the case of data ''drop outs'').

The idea of searching for tracks in a sequence of ambiguity functions is not new. The historically more common approach is to identify peaks within individual MFP ambiguity surfaces, and determine tracks through these peaks.[7,8] However, determining what defines a peak is a common difficulty, especially at higher frequencies where propagation patterns dictate a more complicated MFP ambiguity function with many ambiguous peaks. Other authors have proposed surface summation techniques which ignore the determination of peaks.[9–12] For example, in 1994 Bucker proposed a matched-field tracking method using a sum over time and frequency.[12] Due to the computationally intensive nature of his method, constraints were placed on the endpoints of the track. Maranda and Fawcett proposed an algorithm in 1991 that also ignores peak determination.[9] Similar to the MFP

ambiguity surface averaging technique presented in this paper, Maranda and Fawcett implement a sum of frequency-azimuth (FRAZ) spectra which implicitly has high values along tracks with more peaks. One of the main attractions of this method is that the algorithm is able to ''ride out'' fades, and associate a reappearing peak with one that existed several measurements prior to the fade. This idea was further improved in 1992, when Fawcett and Maranda implemented a Newton's maximization algorithm and used a coarser grid to improve computational efficiency.[10] The same authors extend the work further to incorporate passive MFP into their methods by including propagation information.[11]

The method presented here differs from already-published efforts in several ways. The tracking is performed in a horizontal plane, with very mild restrictions on the source's position, speed, and direction. The method does not involve the identification nor tabulation of peaks among individual MFP ambiguity surfaces, which in turn reduces computational overhead. It should also be noted that a full range-dependent propagation model is used, and replicas are precomputed to lessen the computational burden. Although the method presented in this paper is demonstrated for a single frequency, the extension to multiple frequencies is straightforward by the application of either coherent or incoherent multifrequency matched-field methods.[13–15] The technique presented in this paper is successfully applied to experimental data, showing its viability in real-world scenarios.

One problem that must be addressed in any MFP application is the nonstationarity of a source. For MFP, a stable cross-spectral density (CSD) matrix of the data is necessary.[2] This is especially critical with high-resolution or adaptive techniques requiring inverses or eigenvalue decompositions. For a stationary source, a stable CSD matrix is simply obtained by a long average over time in the spectral domain. However, if a source is moving, then the amount of time that can be averaged without violating the stationarity assumption is limited. Song has researched this very issue extensively and provided general rules for limits on averaging time.[16] Tran and Hodgkiss[17] found that low speeds do not degrade standard processing results significantly. In the case of high speeds, many methods have been suggested to overcome this difficulty, ranging from more sophisticated replica generation[3,18,19] to more sophisticated matched-field processors.[20] In the data analyzed for this paper, the source is moving slowly and therefore obtaining enough averages for a stable CSD matrix is not a problem. However, this issue needs to be addressed in the future for the more general MFT problem.

In the next section, the formulation of the MFT technique is presented. The section following contains a brief description of the experimental data set processed. In the fourth section, results of MFT applied to experimental data are presented. In the final section, results are summarized.

II. MATCHED-FIELD TRACKING

Matched-field tracking (MFT) is a technique based on the average of individual matched-field processing (MFP) ambiguity surfaces. In conventional MFP at a single frequency, a vector of replica fields is matched to a single-frequency time-averaged data covariance matrix. For example, the Bartlett processor is defined by

$$b_n(\mathbf{x}) = \hat{\mathbf{p}}(\mathbf{x})^* \hat{K}_n \hat{\mathbf{p}}(\mathbf{x}), \tag{1}$$

where

$$\hat{K}_n = \frac{\langle \mathbf{d}_n^* \mathbf{d}_n \rangle}{|\langle \mathbf{d}_n^* \mathbf{d}_n \rangle|} = \frac{\Sigma_{i=n}^{n+M} \mathbf{d}(t_i)^* \mathbf{d}(t_i)}{|\Sigma_{i=n}^{n+M} \mathbf{d}(t_i)^* \mathbf{d}(t_i)|}. \tag{2}$$

Here, $\hat{K}_n$ is the normalized cross-spectral density (CSD) matrix averaged over M time realizations, $\mathbf{d}_n$ is the acoustic pressure data vector measured at time t_n, $\hat{\mathbf{p}}(\mathbf{x})$ is the normalized time-invariant phone pressure replica vector for a source at the physical location $\mathbf{x}$, and* denotes complex conjugation. Although the replica vector is sometimes provided by a database of measured data,[21] it is more commonly provided by one of several numerical simulation models. For the results presented in this paper, $\hat{\mathbf{p}}(\mathbf{x})$ is provided by an adiabatic normal mode calculation,[22] and a short time-averaged CSD data matrix is used to avoid violating the assumption of the source's stationarity. The Bartlett processor is chosen for its robustness, rather than a high-resolution processor which would require a longer CSD matrix average time.

In general, an MFP ambiguity is a function of three spatial coordinates, which is often reduced to two by either assuming the target maintains a constant depth, or a constant azimuth. For the implementations presented in this paper, the dimensional simplification of $\mathbf{x}$=(lat, lon) at a constant depth is made, or simply $\mathbf{x}=(x,y)$. Searching for a target in the parameter space of $\mathbf{x}=(x,y)$ is chosen over the more common parameter search space of $\mathbf{x}$=(range, depth) because, in most applications, an unknown source does not travel at a constant azimuth to the receiver array.

One MFT ambiguity function is defined by

$$B_J(x_i, y_i; x_f, y_f) = \frac{1}{N} \sum_{n=0}^{N-1} 10 \cdot \log(b_{n+J}(x_n, y_n)), \tag{3}$$

where

$$x_n = x_i + (n-1)\frac{x_f - x_i}{N-1}, \tag{4}$$

$$y_n = y_i + (n-1)\frac{y_f - y_i}{N-1}. \tag{5}$$

Here, (x_i, y_i) and (x_f, y_f) are the initial and final coordinates, respectively, which define a track of constant speed and direction in two dimensions. The integer N corresponds to the number of individual MFP ambiguity surfaces in the sum, and J indicates the time of the first CSD matrix of the track, $\hat{K}_J$ [see Eq. (1)]. The assumption that a source maintains a constant speed and direction for the duration of the track is the only constraint on how many elements (N) can be included in the average; the amount of time represented by the average should not be so long as to make this assumption too restrictive or unrealistic. The average in Eq. (3) is done in logarithmic units because Makris[23] has shown that matched filtering with logarithmic units is an optimal approach to pattern recognition in a wide variety of problems.

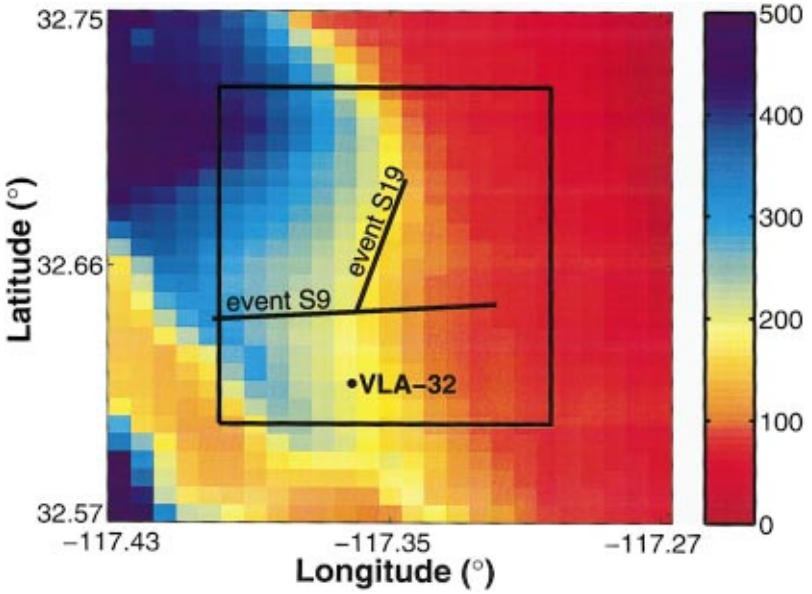

FIG. 1. Bathymetry for SWellEx-96 region. Overlay depicts analysis area for matched-field tracking and the two source tracks analyzed in this paper, event S9 and event S19.

For the results in this paper, each MFP ambiguity is normalized to its peak prior to incorporation into an MFT average. That is,

$$B_J(x_i,y_i;x_f,y_f)=\frac{1}{N}\sum_{n=0}^{N-1}10\cdot\log(\hat{b}_{n+J}(x_n,y_n)), \tag{6}$$

where

$$\hat{b}_{J+n}(x_n,y_n)=\frac{b_{J+n}(x_n,y_n)}{\max(b_{J+n}(x_n,y_n))}. \tag{7}$$

This normalization scheme results in an ambiguity function B_J that is a measure of the relative degradation of each point along the track. It is also appropriate to average the MFP ambiguity surfaces without prior normalization, so that the MFP results are relative to each other over time. In doing so, the value of B_J gives the average degradation for the whole track. The resulting ambiguity function B_J in either normalization scheme has the same structure and dynamic range; there is simply a constant shift equal to the average of the MFP ambiguity function peaks

$$\frac{1}{N}\sum_{n=0}^{N-1}10\cdot\log(\max(b_{J+n}(x_n,y_n))).$$

For the general case of MFT of a source with constant speed and direction, the resulting ambiguity is a function of six parameters: the three initial spatial coordinates of the track, and the three final spatial coordinates of the track. The (lat, lon) dimensional simplification implemented here results in a four-dimensional parameter space for B_J. Four dimensions is still beyond simple visualization capabilities, and therefore the ambiguity B_J is plotted as a function of the two final coordinates, (x_f,y_f). The two initial coordinates, (x_i,y_i), are held fixed at those which produce the overall highest value for B_J. That is, if

$$B_J(x_I,y_I;x_F,y_F)=\max_{(x_i,y_i;x_f,y_f)}B_J(x_i,y_i;x_f,y_f), \tag{8}$$

then

$$B_{J\text{plot}}(x_f,y_f)=B_J(x_I,y_I;x_fy_f). \tag{9}$$

This is a convenient way of displaying the results because a sequence of MFT ambiguity functions clearly depicts the movement of the source in a horizontal plane.

If the parameter space for (x_i,y_i) and (x_f,y_f) is large, the computation time required to compute each B_J can be significant, although not necessarily prohibitive. In the interest of computational time savings, a two-step iterative

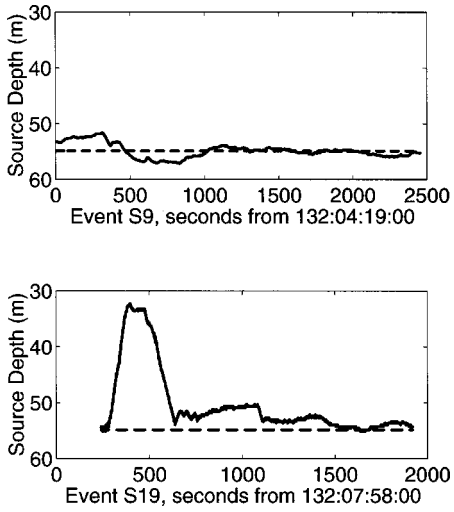

FIG. 2. Experimentally recorded source depth during events S9 and S19.

TABLE I. Sediment parameters used for replica computations in analysis area. These were obtained from archival sources.

	Sediment layer 1	Sediment layer 2	Basement
Thickness (m)	30	800	
C_p top (m/s)	1572.4	1881	5200
C_p bottom (m/s)	1593.0	3245	
ρ (g/cm^3)	1.76	2.06	2.66
α (dB/λ)	0.3	0.09	0.03

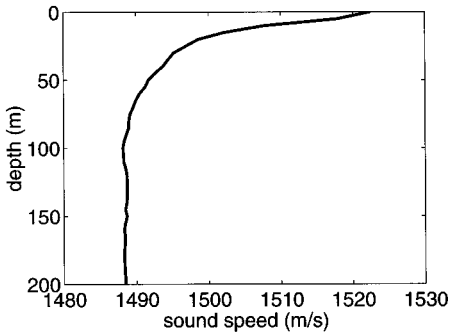

FIG. 3. Experimentally obtained sound-speed profile for SWellEx-96; used for replica computations.

scheme is employed for the tracking in this paper. For the first iteration, the parameter space for (x_i, y_i) and (x_f, y_f) is coarsely gridded. The initial coordinates which produce the overall highest value for B_J over this coarsely gridded space are chosen as the candidate global optimum initial coordinates, $(\hat{x}_I, \hat{y}_I)$. The tracking is then repeated with a much finer grid for the parameter space for all spatial coordinates, with the parameter space of (x_i, y_i) constrained to be "close" to $(\hat{x}_I, \hat{y}_I)$. The optimum initial coordinates for this constrained region $(\hat{\hat{x}}_I, \hat{\hat{y}}_I)$ are chosen to represent the global (x_I, y_I). How coarsely the initial replica grid should be sampled depends on the processing frequency and the environmental complexity of the region of interest.

Further computational time savings is achieved for the results in this paper when examining a *sequence* of overlapping MFT tracks. The iterative grid refining process described in the previous paragraph is only applied to the first segment of the track sequence. In subsequent segments, the parameter space of (x_i, y_i) is constrained to be close to $(\hat{\hat{x}}_I, \hat{\hat{y}}_I)$ of the previous segment. This specific MFT application assumes that the first MFT ambiguity has successfully located and tracked a source $[B_J(\hat{\hat{x}}_I, \hat{\hat{y}}_I; x_F, y_F)]$, and that subsequent MFT results will follow the path of the same source. Such an approximation is especially useful in a scenario where a source is localizable for a short period of time, but difficult to follow thereafter.

MFT works on the principle that, on average, each ambiguity surface b_{J+n} in the summation [Eq. (3)] has a high value at the source's true location, even if it is not the peak of each individual MFP ambiguity surface. False tracks are not as likely to have high average values, since false-alarm peaks within each MFP ambiguity function fade in time, thereby degrading the average value.

The robustness of MFT is due in part to the added information of more data in one result. However, a balance must be struck between allowing a track to be long enough to reap the added benefits of MFT over MFP, but not so long as to unrealistically constrain the target's movement, since each individual MFT track assumes a constant speed and constant direction. The appropriate constraints on track parameters (time and physical length) depend on the problem and should be applied on an individual basis. The constraints applied for

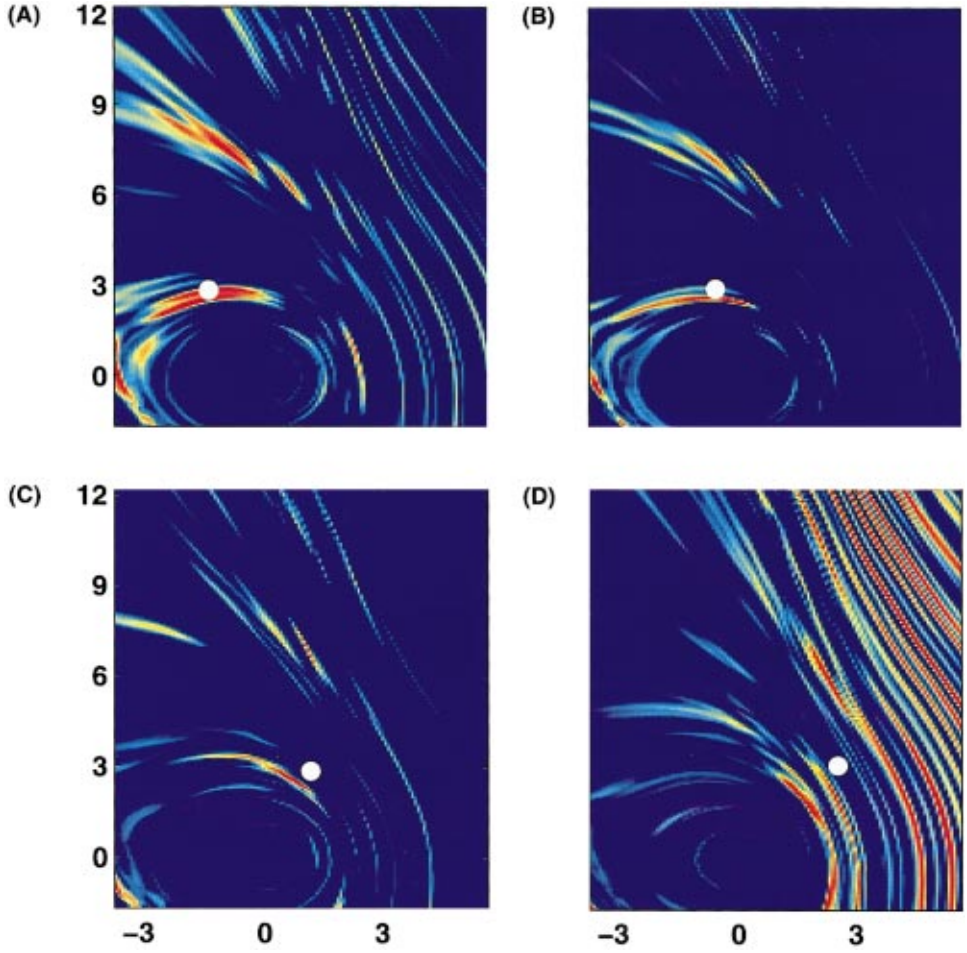

FIG. 4. Four typical Bartlett processor MFP results for event S9. The dynamic range of each plot is 6 dB, with red representing lowest degradation and blue representing highest degradation. The true source location, as determined by GPS, is denoted by the white circle, and is at the following distances from the VLA-32: (A) 3.19 km; (B) 2.99 km; (C) 3.09 km; (D) 3.99 km. The VLA-32 is at (0,0).

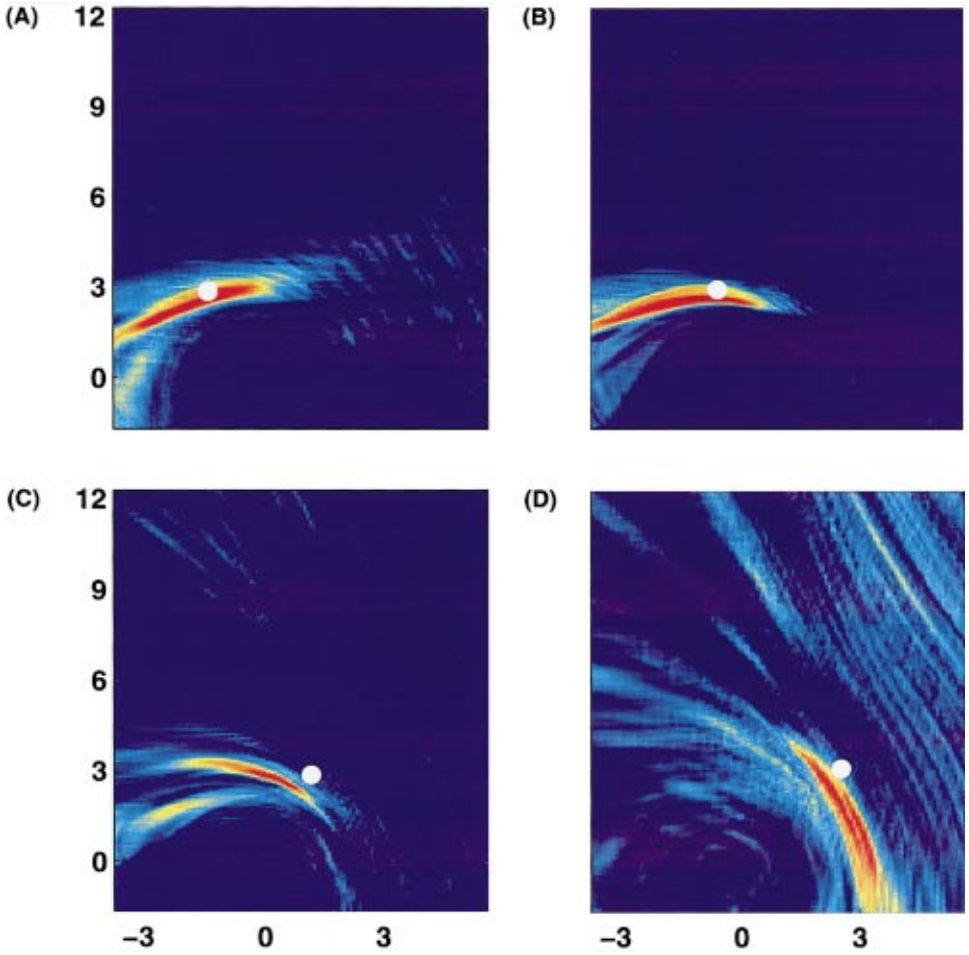

FIG. 5. Four typical tracking results for event S9. The dynamic range of each plot is 6 dB, with red representing lowest degradation and blue representing highest degradation. Each tracking result is a function of four parameters $(x_i, y_i; x_f, y_f)$. The ambiguity surfaces shown result from holding (x_i, y_i) fixed at the optimal initial position. The true final source position for each tracking result is denoted by a white circle, and is at the following distances from the VLA-32: (A) 3.19 km; (B) 2.99 km; (C) 3.09 km; (D) 3.99 km. The VLA-32 is at (0,0).

the data set analyzed in this paper are described in detail in Sec. IV, where the MFT results are presented.

III. SWellEX-96

The data analyzed in this paper were collected during SWellEX-96, a field experiment carried out as a joint effort between Space and Naval Warfare Systems Command, Marine Physical Laboratory-Scripps Institution of Oceanography, and the Naval Research Laboratory.[24]

All results presented are from data recorded on a 32-element vertical line array (VLA-32) located in approximately 200 m of water near latitude 32° 37′ North and longitude 117° 22′ West. The hydrophones are separated by 5 m, with the deepest 6.4 m from the bottom, and the shallowest 161.4 m from the bottom. Figure 1 is a schematic depicting the VLA-32 location and two experimental source tracks overlying the bathymetry. The analysis area chosen for results presented in this paper is approximately 15 by 20 km, and is also depicted in Fig. 1. The analysis of the two source tracks depicted, event S9 and event S19, is presented in this paper. Event S9 is an east–west track across bathymetric contours, while event S19 is a northward track along a bathymetric contour.

The data in both events are recorded from a J-15-3 towed source, which emitted taper signals.[24] The frequency processed here is 148 Hz, for which the J-15-3 source level was 156 dB. The nominal source tow speed is 5 kn (about 2.6 m/s), and was taken into account when determining the appropriate amount of averaging necessary to achieve a stable cross-spectral density (CSD) matrix of the data without violating the stationarity assumption.[16]

The nominal source tow depth is 54.86 m. Figure 2 displays the actual source tow depth for the events processed as

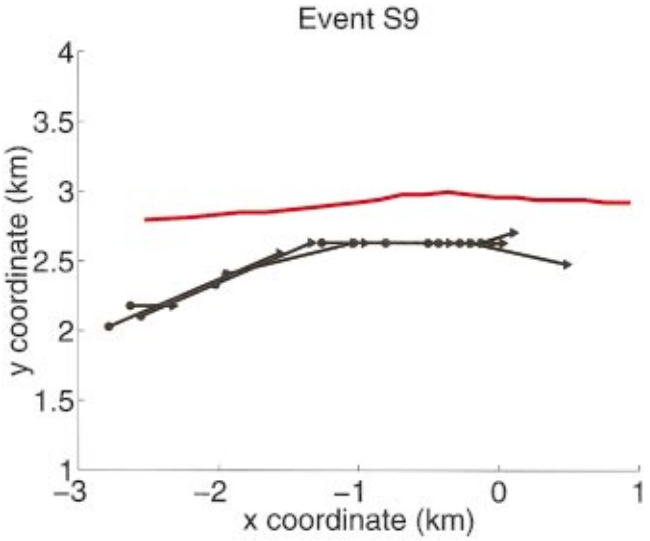

FIG. 6. Summary of all MFT results for event S9. Red line is source's true track as measured by ship's GPS. Black lines represent the peaks of consecutive MFT ambiguity functions.

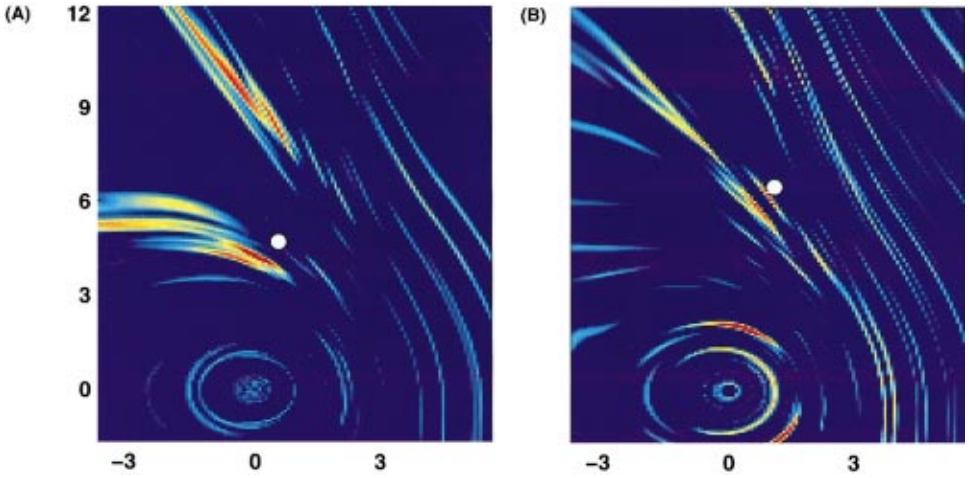

FIG. 7. Two typical Bartlett processor MFP results for event S19. The dynamic range of each plot is 6 dB, with red representing lowest degradation and blue representing highest degradation. The true source location, as determined by GPS, is denoted by the white circle, and is at the following distances from the VLA-32: (A) 4.7 km; (B) 6.6 km. The VLA-32 is at (0,0).

determined by the depth sensor on the source. The depth variations of the source are expected to cause some degradation in the horizontal plane MFP results because these results are based on the assumption that the source remains at a constant depth. However, these degraded MFP results are appropriate for showing MFT's robustness to periodic misplacement of the peak due to imprecise modeling in the replicas (in this case, the violation of the constant depth assumption).

IV. MFT RESULTS

In this section results of MFT applied to SWellEx-96 experimental data are presented. All replicas $[\mathbf{p}(\mathbf{x})]$ are computed using the WRAP model,[25] in conjunction with the KRAKEN model for computing the required adiabatic normal modes.[26] The environmental parameters used for the modal computations are from a combination of archival and experimental sources. The bathymetry and sediment parameters are archival,[27] while the water column sound-speed profiles were recorded during the experiment.[24] The bathymetry is displayed in Fig. 1. Table I contains a summary of the sediment parameters, and Fig. 3 displays the sound-speed profile used. The replicas were computed using the nominal source depth of 55 m over the entire 15- by 20-km region.

All CSD matrices represent a spectral domain average of 15 consecutive snapshots in time, each computed using a 2-s FFT of the time series. Therefore, each CSD matrix represents 30 s of time, during which the source moves approximately 78 m.

The first track presented, event S9, is an east–west track that traverses across bathymetric contour lines. Processing for this event was started at 132:04:19:28 Z, which corresponds to a time when the source was well within the boundaries of the analysis area. Figure 4 shows four typical 148-Hz MFP ambiguity functions from event S9, at 5, 10, 20, and 30 min into the track. The *x*- and *y*-axis on these plots are distance in kilometers from the VLA, and the VLA is located at (0,0). These ambiguity surfaces clearly display how the environment breaks the east–west symmetry in the MFP output; without environmental asymmetry, the MFP ambiguity function for a vertical array has circular ambiguity rings. Although the peaks of most of the surfaces in Fig. 4 are close to the source's true location (denoted by a white circle), there are also ambiguous peaks far from the source location. This is especially true in the case of Fig. 4(D), where the source is in much shallower water ($\approx$100 m), and may be due to the inability of adiabatic normal modes to properly model steep downslope propagation. Figure 5 depicts MFT results where the final source location of each MFT track is the same as the source locations from the MFP results in Fig. 4. In other words, the last ambiguity surface in each sum corresponds to the CSD matrix at 5, 10, 20, and 30 min into the track. For

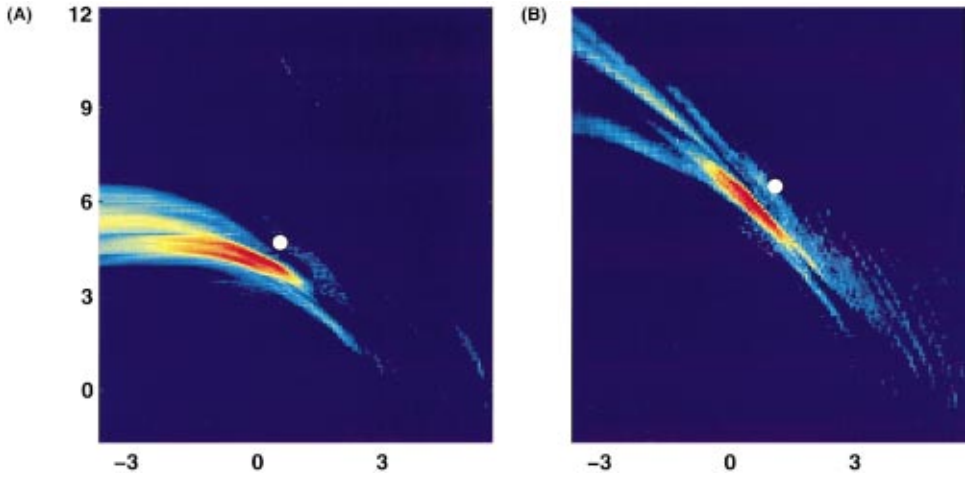

FIG. 8. Two typical tracking results for event S19. The dynamic range of each plot is 6 dB, with red representing lowest degradation and blue representing highest degradation. Each tracking result is a function of four parameters $(x_i, y_i; x_f, y_f)$. The ambiguity surfaces shown here result from holding (x_i, y_i) fixed at the optimal initial position. The true final source position for each tracking result is denoted by a white circle, and is at the following distances from the VLA-32: (A) 4.7 km; (B) 6.6 km. The VLA-32 is at (0,0).

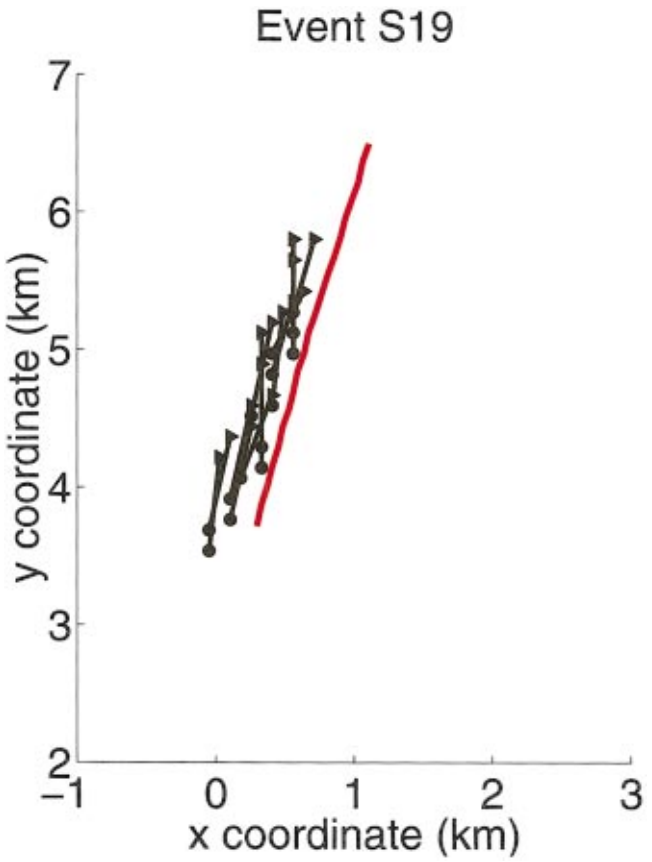

FIG. 9. Summary of all MFT results for event S19. Red line is source's true track as measured by ship's GPS. Black lines represent the peaks of consecutive MFT ambiguity functions.

each plot in Fig. 5, ten MFP ambiguity functions were included in the average, creating tracks corresponding to 300 s. In all cases, when compared to the corresponding MFP output, the main peak is broadened while the high ambiguities are suppressed. Figure 6 is a visual summary of the MFT results along the whole track of event S9. The red line is the source's true track, as recorded by GPS. Each of the short black lines is the peak track from each overlapping MFT segment along the portion of event S9 analyzed; the circle denotes the optimum initial position (x_I^*, y_I^*), and the triangle denotes the optimum final position (x_F, y_F). The first optimum track is the result of the two-step iterative scheme described in Sec. II. The first step involves a full search of the analysis area for all four parameters using a coarse grid (550-m resolution) in order to identify the candidate global optimum initial coordinates $(x_{\hat{I}}, y_{\hat{I}})$. The second step involves a finer grid (110-m resolution) with a search for the optimum initial coordinates (x_I^*, y_I^*) constrained to be within 1.1 km of $(x_{\hat{I}}, y_{\hat{I}})$, and a full search for the optimum final coordinates. The rest of the optimum tracks depicted in Fig. 6 were found using the finer grid (110 m) with the initial coordinates constrained to be within 2.2 km of the previous initial coordinates, and the final coordinates only constrained by the grid resolution (110 m) over the entire analysis area.

The other experimental track analyzed, event S19, is a north–south track which runs along the 200-m bathymetric contour line. The path between source and receiver is practically range independent, and therefore the MFP results show clearer localization than those of event S9. The environmental range dependence to either side of the source track provides more azimuthal variations than in the case of event S9, so the environmental symmetry breaking of the MFP ambiguity surface is enhanced. MFT tracking on event S19 was started at 132:08:10:46 Z, which is a time shortly beyond the rapid change in depth seen in Fig. 2(B). Figure 7 shows two typical 148-Hz MFP ambiguity functions from event S19; the first is 5 min into the track, and the second is 20 min into the track. Although the peaks of both of these surfaces are close to the source's true location (denoted by a white circle), there are also ambiguous peaks far from the true source location. Figure 8 depicts MFT results where the final source location of each MFT track is the same as the source locations from the MFP results in Fig. 7. As with the previous example, the main peak is broadened around the correct source position, while the high ambiguous peaks from the corresponding MFP ambiguity surfaces are suppressed. Similar to Fig. 6, Fig. 9 is a visual summary of event S19. The red line is the source's true track, as recorded by GPS. Each of the short black lines is the peak track from each overlapping MFT segment from the portion of event S19 processed; the circle denotes the optimum initial position (x_I^*, y_I^*), and the triangle denotes the optimum final position (x_F, y_F). All of the constraint parameters are the same as for event S9.

V. SUMMARY

A matched-field tracking technique is presented which expands on traditional MFP techniques by incorporating source motion into the parameter landscape. With the source moving, the number of snapshots for each source position is limited, so results presented combine a short time-average CSD matrix with the Bartlett processor. The high sidelobes often present in MFP results are successfully reduced by the tracking algorithm.

MFT is applied to experimental data obtained during SWellEX-96. For the applications presented, the source is assumed to maintain a constant depth, speed, and direction for each 5-min segment of data. This assumption reduces the number of parameters of each ambiguity function to four: the initial and final (x,y) locations of the source. Plots of the MFT ambiguity as a function of final position for successive track segments show the movement of the source. In addition to successfully tracking a source, the method reduced the problem of high sidelobes and was robust to periodic misplacement of the peak in the individual MFP ambiguity functions.

ACKNOWLEDGMENTS

This work was supported in part by the Office of Naval Research.

[1] H. P. Bucker, "Use of calculated sound fields and matched field detection to locate sound sources in shallow water," J. Acoust. Soc. Am. **59**, 368–373 (1976).
[2] A. B. Baggeroer, W. A. Kuperman, and P. N. Mikhalevsky, "An overview of matched field methods in ocean acoustics," IEEE J. Ocean Eng. **18**(4), 401–424 (1993).

[3] A. Tolstoy, *Matched Field Processing for Underwater Acoustics* (World Scientific, Singapore, 1993).
[4] J. A. Fawcett, M. L. Yeremy, and N. R. Chapman, ''Matched-field localization in a range-dependent environment,'' J. Acoust. Soc. Am. **99**, 272–282 (1996).
[5] J. S. Perkins and W. A. Kuperman, ''Environmental signal processing: Three-dimensional matched-field processing with a vertical array,'' J. Acoust. Soc. Am. **87**, 1553–1556 (1990).
[6] M. D. Collins, L. T. Fialkowski, W. A. Kuperman, and J. S. Perkins, ''Environmental source tracking,'' J. Acoust. Soc. Am. **94**, 3335–3341 (1993).
[7] M. J. Wilmut, J. M. Ozard, and P. Brouwer, ''Evaluation of two efficient target tracking algorithms for matched-field processing with horizontal arrays,'' J. Comput. Acoust. **3**, 311–326 (1995).
[8] M. J. Wilmut, J. M. Ozard, and B. Woods, ''An efficient target tracking algorithm for matched field processing,'' OCEANS'93 Proceedings **3**, 81–85 (1993).
[9] B. H. Maranda and J. A. Fawcett, ''Detection and localization of weak targets by space-time integration,'' IEEE J. Ocean Eng. **16**, 189–194 (1991).
[10] J. A. Fawcett and B. H. Maranda, ''Localization by maximizing long-time integrated spectral power,'' IEEE Trans. Signal Process. **40**, 460–464 (1992).
[11] J. A. Fawcett and B. H. Maranda, ''A hybrid target motion analysis/matched-field processing localization method,'' J. Acoust. Soc. Am. **94**, 1363–1371 (1993).
[12] H. Bucker, ''Matched-field tracking in shallow water,'' J. Acoust. Soc. Am. **96**, 3809–3811 (1994).
[13] N. O. Booth, P. A. Baxley, P. W. Schey, W. S. Hodgkiss, G. L. D'Spain, and J. J. Murray, ''Source localization with broad-band matched-field processing in shallow water,'' IEEE J. Ocean Eng. **21**, 402–412 (1996).
[14] G. J. Orris, M. Nicholas, and J. S. Perkins, ''The matched-phase coherent multifrequency matched-field processor,'' J. Acoust. Soc. Am. **107**, 2563–2575 (2000).
[15] P. W. Schey and N. O. Booth, ''Multitone Matched-Field Processing in SWellEx-1,'' Technical Document 2720, Naval Command, Control and Ocean Surveillance Center, San Diego, CA (1994).
[16] H. C. Song, ''Performance bounds on the passive localization of a moving source for ocean acoustics,'' Ph.D. thesis, MIT, 1990.
[17] J.-M. Q. D. Tran and W. S. Hodgkiss, ''Matched-field processing of 200-Hz continuous wave (cw) signals,'' J. Acoust. Soc. Am. **89**, 745–755 (1991).
[18] H. C. Song, ''Performance bounds for passively locating a moving source of a known frequency in oceanic wave-guide using a vertical array,'' IEEE J. Ocean Eng. **18**, 189–198 (1993).
[19] C. A. Zala and J. M. Ozard, ''Matched-field processing for a moving source,'' J. Acoust. Soc. Am. **92**, 403–417 (1992).
[20] J. R. Daugherty and J. F. Lynch, ''Surface wave, internal wave, and source motion effects on matched field processing in a shallow water waveguide,'' J. Acoust. Soc. Am. **87**, 2503–2526 (1990).
[21] L. T. Fialkowski, M. D. Collins, W. A. Kuperman, J. S. Perkins, L. J. Kelly, A. Larsson, J. A. Fawcett, and L. H. Hall, ''Matched-field processing using measured replica fields,'' J. Acoust. Soc. Am. **107**, 739–746 (2000).
[22] A. D. Pierce, ''Extension of the method of normal modes to sound propagation in an almost-stratified medium,'' J. Acoust. Soc. Am. **37**, 19–27 (1965).
[23] Nicholas C. Makris, ''A foundation for logarithmic measures of fluctuating intensity in pattern recognition,'' Opt. Lett. **20**, 2012–2014 (1995).
[24] N. O. Booth, J. S. Perkins, G. Dorrance, D. Carlton, and C. Janes, ''SWellEX-96 Preliminary Data Report,'' unpublished report, Naval Command, Control and Ocean Surveillance Center, San Diego, CA (1996).
[25] W. A. Kuperman, M. B. Porter, J. S. Perkins, and R. B. Evans, ''Rapid computation of acoustic fields in three-dimensional ocean environments,'' J. Acoust. Soc. Am. **89**, 125–133 (1991).
[26] M. B. Porter, ''The KRAKEN Normal Mode Program,'' SACLANT Undersea Research Centre Memorandum SM-245, 1991.
[27] R. T. Bachman, P. W. Schey, N. O. Booth, and F. J. Ryan, ''Geoacoustic databases for matched-field processing: Preliminary results in shallow water off San Diego, California,'' J. Acoust. Soc. Am. **99**, 2077–2085 (1996).

Low-frequency long-range propagation and reverberation in the central Arctic: Analysis of experimental results

Greg Duckworth, Kevin LePage,[a] and Ted Farrell[b]
BBN Technologies, an operating unit of Verizon Communications, Inc., 70 Fawcett Street, Cambridge, Massachusetts 02138

(Received 8 April 1997; revised 30 August 2000; accepted 15 December 2000)

BBN and the ASW Environmental Acoustic Support program office of ONR conducted a low-frequency reverberation and transmission loss experiment in the central Arctic during the spring of 1992. In this article we report analysis of these data which extracts the controlling propagation and reverberation characteristics. The recorded source levels are combined with the received levels recorded at range to estimate the dependence of the scattering strength of the ice canopy on incident and backscattered grazing angle in frequency bands between 10 and 70 Hz. Results show that the monostatic backscattering strength is roughly proportional to frequency and angle squared, with a nominal value of −47 dB at 40 Hz and 8.5° grazing. © *2001 Acoustical Society of America.* [DOI: 10.1121/1.1371543]

PACS numbers: 43.30.Hw, 43.30.Ma [DLB]

I. INTRODUCTION

Propagation and reverberation under the Arctic ice canopy has long been of interest to the underwater acoustics community. In the spring of 1992, BBN and the ASW Environmental Acoustic Support program office of ONR conducted a reverberation experiment as a part of AREA-92 which was directed toward measuring low-frequency propagation and reverberation characteristics in the central Arctic.[1] The experimental parameters were ideal for generating data suitable for a propagation and scattering strength analysis. A large aperture vertical line array and horizontal line array were deployed in the upwardly refracting low-speed upper duct in the central Arctic, and large sources were deployed in this duct both in a quasimonostatic geometry to evaluate reverberation and also at large ranges (between 30 and 200 km) from the receiving arrays to evaluate transmission loss. The goal was to understand and characterize the angular and frequency characteristics of reverberation in the central Arctic and incident signal characteristics.

Examination of the reverberation time series obtained from this experiment showed peaks in received energy at late times on all beams that seemed to be associated with convergence zone propagation to and from the ice cover by deeper diving rays. These periodic arrivals were observed to be superimposed on a more uniform background of reverberation that arrived at shallower angles. The relative amplitude of the energy in the shallow angles was also observed to be diminished at late time. These distinguishing characteristics of the received time series motivated the use of the multipath arrival times to separate signals which had scattered from the ice at different grazing angles.

Propagation in the Arctic, while quite stable in terms of low water column variability, has been the subject of extensive study over the years as researchers have tried to understand a loss mechanism that is anomalously high. Recent advances in wave theory modeling of the acoustic–elastic interaction of acoustic energy with the ice canopy have improved the ability to estimate this propagation loss at the lower frequencies (under 70 Hz) of interest in this experiment. Using the new theoretical loss parameters in combination with a standard normal mode propagation code, an improved capability for the prediction of the propagation characteristics in the Arctic is obtained. This capability in turn offers new opportunities for interpreting and understanding Arctic reverberation time series. The ability to predict forward propagation offers the potential to eliminate propagation effects from the backscattered time series to expose the underlying backscattering properties of the ice canopy. A particularly powerful approach is to pursue a model-based inversion for these parameters. This paper presents a model-based inversion for the unknown ice canopy scattering strength parameters using a partially coherent forward model (where groups of modes interact coherently with themselves and incoherently with other groups of modes), and a two-parameter model for ice canopy scattering strength. The results obtained from this inversion agree well with ice canopy scattering strengths predicted by theory. The results show that there is much promise in model-based inversion of reverberation time series for scattering strength parameters in environments where the forward propagation has been sufficiently well characterized, and where propagation effects conspire to reveal angular information about the scattering process.

II. EXPERIMENTAL SCENARIO

The low-frequency active component of the AREA-92 experiment was conducted over a period of 10 days beginning on 18 March 1992.[1] The source shots and the receiving arrays were located at the ZIRCON base camp, situated at approximately 87.5 °N and 10 °W in the eastern central Arctic. The camp geometry is illustrated in Fig. 1. The

[a]Present address: Saclant Undersea Research Centre, VI. S. Bartolomeo 400, 19138 La Spezia, Italy; electronic mail: lepage@saclantc.nato.int
[b]Present address: Ortho-Clinical Diagnostics, Johnson & Johnson Co., 100 Indigo Creek Dr., Rochester, NY 14626.

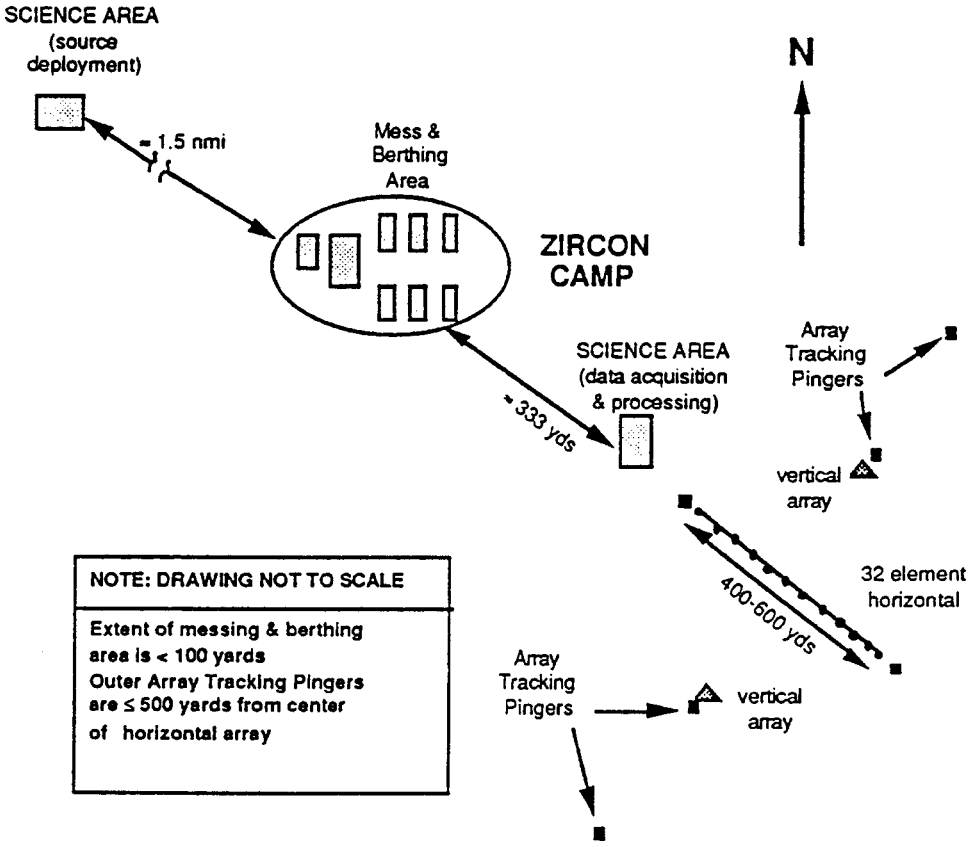

FIG. 1. ZIRCON ice camp layout and reverberation experiment geometry.

JACKPOT camp at 86.5 °N and 27 °W provided additional recording of the incident field at range and a retransmissions at known equivalent scatter strength for calibration. During the experiment approximately 55 Gbytes of time series data were recorded at a sample frequency of 752 Hz from the horizontal line array (HLA) and the vertical line array (VLA) located at the base camp. The HLA was composed of 32 individual ''staves,'' each of which was a vertical line array composed of eight omnidirectional hydrophones. The aperture of the staves was 60 m, with the upper element deployed at a depth of 62 m. The staves were used to obtain gain against local bottom reverberation and nearby ice noise. The responses from the eight elements in each stave were summed to form a single ''element'' in the HLA and were recorded. In addition the response from the top hydrophone of each stave was also recorded. The horizontal aperture of the HLA was 480 m, or approximately 13 acoustic wavelengths at 40 Hz. The HLA was deployed 1.5 km from the source drop hole in a quasimonostatic configuration. The array geometry is illustrated in Fig. 2.

The large aperture 32-element VLA was also deployed approximately 1.5 km from the drop hole. This array had an aperture of 217 m with the uppermost element deployed at a depth of 62 m. In addition to recording the 32 summed stave outputs and the 32 top hydrophones of the HLA, and the 32 hydrophones of the VLA, 64 other channels were also recorded, including 5 desensitized hydrophones deployed at various depths approximately 100 m from the sources, and 5 geophone channels from the ice canopy. The source monitoring hydrophones made it possible to directly measure the wave form and energy source level of the shots in the monostatic geometry for quality assurance and for comparison to the source model. All the hydrophones were calibrated to 1 dB rms.

For quasimonostatic experiments, explosive charges of 38-lb TNT equivalent were deployed through the drop hole indicated in Fig. 1. The charges were detonated at a depth of 95 m and the resulting quasimonostatic reverberation time series were recorded on the HLA and VLA. To calibrate the acoustic propagation, several bistatic experiments (called transects) were also carried out. During these experiments sources were deployed at 95 m depth at significant ranges from the receiving array. These remote sites were accessed

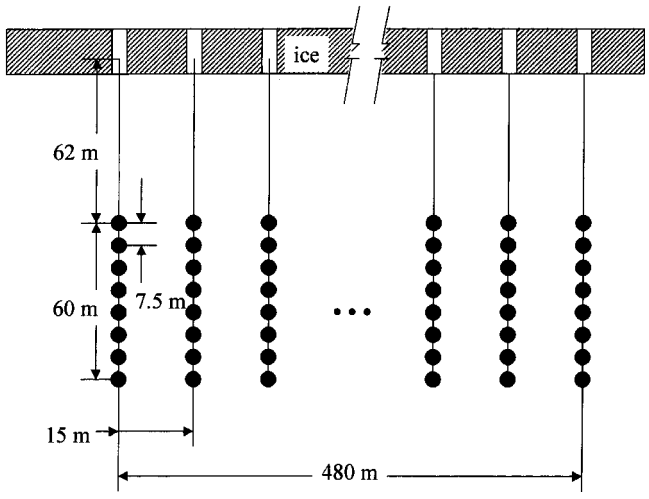

FIG. 2. HLA geometry, showing the small vertical line array elements which were used to obtain array gain against high-angle reverberation.

by helicopter. By analyzing the arrivals of these remote detonations on the VLA and HLA at the ZIRCON camp, the characteristics of the incident sound could be quantified as a function of range from the source.

Collection and on-site analysis of the data was facilitated by a real time data processing suite designed and implemented for the experiment by members of the BBN team.[1] The Arctic Processing and Display System displayed the received level in each of two selectable frequency bands as a function of time in a pseudocolor geo display (reverberation time series converted to color display as a function of range and azimuth) and in *A*-scan form (time series displayed in a stacked format) for each of 32 beams. It also provided a data retrieval and analysis capability for quick look analysis of the data. The system also archived all 128 channels of raw 16-bit sensor data continuously.

The collected data sets were of high dynamic range and signal-to-noise ratio (SNR). The ambient noise was below 80 dB $re\ \mu\text{Pa}/\sqrt{\text{Hz}}$ at 40 Hz. The time series of the shots themselves were highly repeatable and inspection of the source monitoring hydrophones showed that their signature corresponded well to the Wakeley explosive source model[2] for the 95-m source depth and the 38 lb of explosives used. About 300 s of data, corresponding to roughly 200 km of range from the ZIRCON camp, was analyzed from a single stave for the purposes of the reverberation analysis. This azimuthally omnidirectional receiver served to average the reverberation data over a large annular scattering area at each time analyzed, giving statistical stability to the resulting scattering strengths. It also obviated the need for the beam-shape corrections to the received data that would have been required if beam output data had been used. Future analysis of these data should include individual beam analysis to characterize the range and azimuth variation of the scattering strength due to inhomogeneity of the ice surface. Cursory inspection of the 32 beam outputs of the HLA beamformer showed that the azimuthal distribution of reverberation at times before the interaction with the bathymetry was quite uniform.

At times beyond 300 s, significant interaction with bathymetry in the vicinity of Greenland and the Morris Jesup Plateau was observed. Even at these ranges, the reverberation power level from the ice surface was above the noise floor of the experiment. However, contamination of the surface scattered data with bottom backscatter caused us to discontinue use of the data beyond this range.

The sound speed profile was measured *in situ* using both winched CTD and XSV/XBT systems. In addition local measurements of the under-ice profiles[1] were used to provide inputs to the propagation loss model. The measured roughness standard deviation measured in the vicinity of the array was 2.2 m, with a correlation length scale of 22 m and a fractal dimension[3] of 2.5. In most respects, other than the lack of information on the basin-wide distribution of under-ice roughness, the environment was very well characterized.

III. SEMICOHERENT MODEL FOR FORWARD PROPAGATION TO SCATTERING PATCHES

The stability and range independence of the forward propagation, the unique upper duct of the sound channel, and the vertical partitioning of the source energy caused by the interference between the source and its image, provide an opportunity to divide the forward propagation to the scattering patches on the ice canopy into three naturally distinct propagation groups. The first of these groups, ''group 1,'' corresponds to the low grazing angle first (and at higher frequencies, second) acoustic modes. In the Arctic these modes suffer very high propagation loss due to significant interaction with the ice cover, and mode 1 in particular is trapped in a lower-speed upper duct at all but the lowest frequencies. This mode also has a significantly slower group speed than all the other modes. For these reasons this mode is the only component of group 1 up to 40 Hz. At frequencies above 40 Hz, mode 2 also becomes trapped in the upper duct and is therefore included in group 1. The sparse modal population in group 1 contrasts with the second and third groups; ''group 2'' is a bundle of modes representing a mid-depth refracted surface-reflected (RSR) ray, and ''group 3'' is a bundle of modes representing the deepest diving RSR ray. At low frequencies group 2 is composed of modes 2 through 15. These modes combine together coherently into a raylike propagator that is launched at the first angle of maximum constructive interference between the source and its image, and interacts with the ice canopy approximately every 30 km. (The first Lloyd mirror angle of maximum constructive interference occurs at a grazing angle of approximately 10.9° at 40 Hz for a source depth of 95 m, assuming a uniform sound speed of 1436 m/s.) Group 3 is launched at the second Lloyd mirror angle, which assuming isovelocity is 22.2° (it is actually closer to 17.5° for the actual profile; this is determined by the third maximum of the mode shape function at the source depth corresponding to a mode with this grazing angle). Modes in group 3 interact with the ice canopy every 50 km or so. The characteristics of the three groups are summarized in Tables I and II for the 30- and 40-Hz frequency bands.

Due to the convergence-zone-like nature of the group 2

TABLE I. Group characteristics for the 30-Hz band as determined by KRAKENC.

Propagation groups at 30 Hz				
Group	Grazing angle at surface (deg)	Normal modes included	Group speed (m/s)	Turning depth (m)
1 = upper duct	7.9	1	1439	170
2 = mid-depth	12.5 ± 1.30	2–13	1457 ± 2.0	1514 ± 545
3 = deep RSR	17.5 ± 0.63	14–30	1465 ± 1.3	3935 ± 327

TABLE II. Group characteristics for the 40-Hz band as determined by KRAKENC. Comparison with Table I shows that the propagation group characteristics are quite stable in adjacent frequency bands.

Propagation groups at 40 Hz				
Group	Grazing angle at surface (deg)	Normal modes included	Group speed (m/s)	Turning depth (m)
1 = upper duct	8.4 ± 2	1–2	1442	210 ± 100
2 = mid-depth	12.5 ± 1.30	3–17	1457 ± 1.5	1527 ± 506
3 = deep RSR	17.5 ± 0.63	20–40	1465 ± 1.4	3937 ± 327

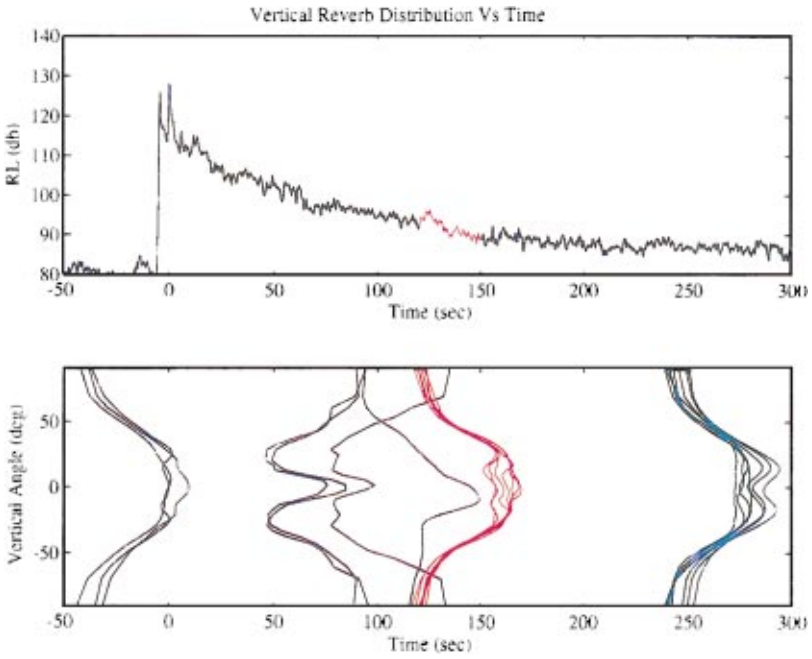

FIG. 3. The angular distribution of reverberation as a function of time in the 40-Hz band. At early time (shown in violet) the energy was observed to arrive from the bottom and the near surface. At later times (shown in red), after the bottom interacting modes died out, the reverberation energy was uniformly distributed in arrival angle. However at late times (shown in green), corresponding to two-way travel times to ranges greater than 150 km, propagation losses suffered by the first acoustic mode lead to reduced reverberation at low angles, leaving a distinct time-angle distribution of backscattered consistent with periodic boundary interactions of the deeper diving RSR rays.

and group 3 propagation, the reverberation signatures of these groups are fairly isolated in time. These modes interact most strongly with the ice canopy at the interference distance of their mode sets and lead to reverberation features in the received level that are periodic in time. The periods are set by the convergence zone separation and the average group speeds of the modes in the groups. Energy propagating to and from a scattering patch via group 1 gives a more continuous received level (RL) that attenuates slowly with time.

At long range, the reverberation caused by group 1 becomes less important, as energy is stripped out of mode 1 sooner than out of the higher-order modes. This is a unique feature of Arctic propagation and is caused by the higher derivative of the mode shape function of mode 1 at the ice boundary.[4] The effect of the high mode 1 attenuation is that the reverberation has a distinctly evolving structure in energy distribution as a function of grazing angle and time. At early times (sufficiently late to allow for the decay of the high-angle bottom multiples), the reverberation is evenly distributed across grazing angles, but at times corresponding to scatterer ranges greater than 150 km, mode 1 is attenuated to the point where most of the reverberation arrives at the steeper RSR angles. The resulting temporal characteristics of the RL time series are illustrated in Fig. 3, where the beamformed time response of the vertical line array is shown. The colors on the angular spectrum in the lower plot correspond to the colored part of the reverberation time series in the upper plot from which the angular spectra were obtained. The green result (corresponding to times around 250 s after the shot) at the right-hand side of the lower plot shows a dimple in the angular distribution of energy at low grazing angles that is absent from the red curve of the angular distribution taken 130 s after the shot.

It is worthwhile to point out here that although the mode 1 attenuation is higher than for the other modes, there are favorable characteristics to this propagation path that can be exploited for sonar operations. First, since the mode 1 path is continuously ensonifying the upper reaches of the ocean, there is continuous coverage in range. Second, the (back) scattering strength associated with this mode is lower than for all the higher angle modes, despite the fact that the cumulative losses suffered by this mode are higher than for the other modes. Third, even though mode 1 suffers unfavorably high transmission loss, this has only a second-order effect on sonar operations in a reverberation-dominated environment like the Arctic. The most important implication is that the range beyond which the detection becomes impossible due to the ambient noise floor is shorter than for the higher-order modes. However, the results shown in this paper indicate that this range is not restrictively short, so the advantages outlined previously can be exploited over reasonable distances.

Given the characteristics of the propagation in the Arctic, it is possible to pose an inverse problem where an assumed spatially homogeneous scattering strength for the ice canopy may be determined for three grazing angles corresponding to the three distinct groups of modes. The inverse uses the ''semicoherent'' mode model outlined previously, where the three groups of modes interfere coherently among themselves in order to yield the well-defined convergence zone behavior of groups 2 and 3, but where the groups themselves interact incoherently at the receiver due to raylike behavior of the groups sampling independent ice surface patches. Thus, we use coherent propagation of the modes in the groups to get the required transmission losses, but may analyze the total received reverberation by separating the contributions of each group in the reverberation level (power) domain. This model of the reverberation is motivated by (1) the natural distribution of incident energy into the three groups caused by the analysis bands and the source deployment depth, (2) the different group velocities of the three groups, which implies that independent ice scattering patches are interrogated by each group at late times, and (3) the character of the observed reverberation, which shows reverberation features that seem to be associated with the three

different groups as defined, with relatively little azimuthal fluctuation from beam to beam.

Critical to the success of an inversion of ice canopy scattering strength is the ability to model the amplitude of the signal incident on the ice canopy in an accurate way. In Sec. IV we discuss the forward model used to estimate the one-way TL, and compare the model predictions to the data obtained during the bistatic experiments. Following this the inverse problem is formally defined and results for the ice canopy scattering cross section are obtained.

IV. DETERMINATION OF THE PROPAGATION CHARACTERISTICS OF THE SEMICOHERENT FORWARD MODEL

Recent advances in modeling acoustic interactions with the ice canopy have enabled improved forward modeling of acoustic propagation in the Arctic. A hybrid technique that combines reflection coefficients from a perturbation theory for rough elastic ice[5] with KRAKENC[6] has proven to yield good agreement between predictions and historical observations.[4] The complex version of KRAKENC is required when using this approach because the complex reflection coefficients used to define the upper boundary condition yields a complex characteristic equation for the modal eigenvalues. This hybrid modeling technique is able to predict the historically measured attenuation coefficient for the Arctic, and was used with good success to predict received energy levels for the combined Russian–American TransArctic Acoustic Propagation experiment conducted in April 1994.[7] Reference 4 gives a detailed discussion of the theory, along with comparisons of theoretical modal attenuations to historical observations of attenuation, but the technique's requirements and sensitivities are discussed here in reference to modeling the data under consideration.

The insertion of complex rough surface reflection coefficients into KRAKENC involves no approximation. However, the determination of the reflection coefficient for the Arctic ice is the subject of a substantial body of research.[8–10] Recently it has been shown[4] that when the elasticity of the ice canopy is accounted for properly, first-order perturbation theory can return estimates of the reflection coefficient with the correct order of magnitude and frequency dependence. The elastic perturbation theory takes as arguments the incident angle and the rough surface power spectrum of the ice cover, the mechanical properties of the ice, the ice thickness, and the sound speed of the water directly under the ice. It returns a reflection coefficient that is good to second order in the roughness itself and the scattered field. When inserted into KRAKENC this reflection coefficient yields complex modal eigenvalues that are in general agreement with experimental observations for overall empirical loss. Because of the unique propagation characteristics of the Arctic, it is found that mode 1 always suffers the highest propagation loss in the frequency range of interest, because this mode interacts most strongly with the ice cover. Put another way, the dependence of the mode shape for mode 1 at the ice–water interface is much stronger than for the other modes, and consequently small changes in the under-ice profile cause large changes to the incident field. The result is a significant amount of forward scatter of energy of spatially uncorrelated phase, resulting in a higher than usual accumulated loss along the propagation path for this mode. However, due to the very low grazing angle, backscatter remains low for this mode.

It is important to point out that at the grazing angles corresponding to the propagating modes for the frequency range of interest in this study, the perturbation approximation is valid. For instance, at 40 Hz a roughness excursion of 33 m would cause the expansion parameter $k_z \eta$, where η is the local ice excursion in meters, to equal one for mode 1. For this reason there is cause to be confident that the first-order perturbation solution is the first term in a rapidly convergent series and is therefore appropriate for modeling low-frequency Arctic ice canopy scattering from most features.

As mentioned in Sec. II, ice roughness parameters were measured *in situ* during the experiment. Spectral estimates of the under-ice profiles in the limited area in the immediate vicinity of the ZIRCON camp yielded a correlation length scale of 22 m, and rms roughness of 2.2 m, and a fractal dimension of 2.5[1] (for a definition of fractal dimension see for instance Goff *et al.*[3]). These measured values are in close agreement with the ice roughness measurements cited by DiNapoli and Mellen,[8] so we expected the empirical attenuation over all paths measured during the experiment to closely conform to their empirical value of 0.04 dB/km at 40 Hz. However, a simple fit to the forward propagation loss measurements from the experiment indicated an empirical attenuation value of 0.078 dB/km best fit the 40-Hz data. Scaling the roughness of the ice canopy to a rms value of 3 m was required in order to obtain good agreement between the theoretical predictions and the data.

It is interesting to note that the 3-m rms ice roughness value required for proper modeling agrees with the roughness found in the LeSchack ice roughness standard deviation database in ICECAP[11] at the location of the experiment. This database also indicates an increase of the standard deviation with decreasing latitude, as the ice pack compresses in the vicinity of the Lincoln Sea and over the Morris Jesup Plateau. In these regions the database shows the roughness increasing to a value between 3.5 and 4 m rms. An opposite trend is observed in the database for ice north of the experimental location, with values slightly greater than 2.5 m found over the north pole. These numbers are all substantially higher than the 2.2 m measured *in situ*. For these reasons, along with the higher than normal observed propagation loss, we conclude that the local measurement may under-represent the global value of ice roughness present during the experiment.

Therefore, for the purposes of this study, a loss model similar to scenario D in Ref. 4 was implemented, using a roughness standard deviation of 3 m instead of the measured value of 2.2 m, while retaining the ice roughness correlation scale of 22 m, and the ice roughness fractal dimension of 2.5 determined from the power spectral estimates of the under-ice profiles. The compressional and shear velocities in the model corresponded with those estimated by Miller *et al.*,[12] and an ice thickness of 3 m was chosen, as this corresponded to thicknesses observed during drilling operations. The mag-

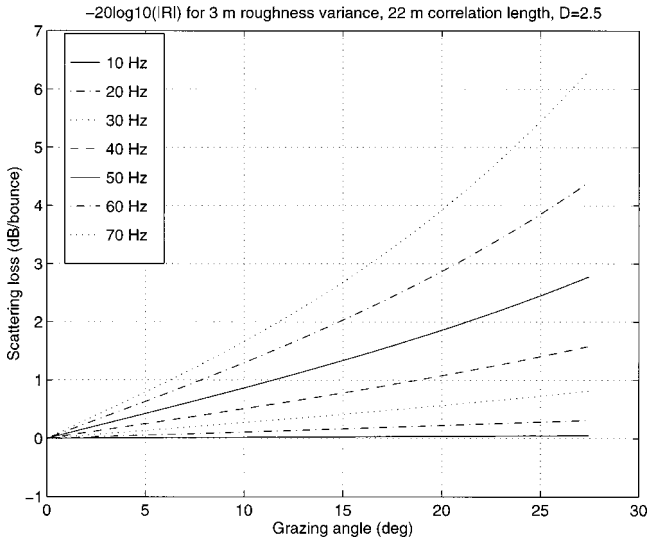

FIG. 4. Reflection coefficient as a function of grazing angle and frequency for the rough elastic ice model. The correlation length of the ice cover is taken to be 22 m, the rms roughness is assumed to be 3 m, and the fractal dimension D of the ice roughness is assumed to be 2.5. The correlation length scale and the fractal dimension were determined by *in situ* measurements, but the 3-m rms roughness assumed was substantially rougher than the measured value of 2.2 m. This roughness was used in order to obtain agreement with the measured propagation loss, which was twice as high as historical measurements predict.

nitude of the reflection coefficient for the ice estimated by the theory using these parameters is illustrated in Fig. 4. The sound speed profile measured by CTD cast during the experiment is illustrated in Fig. 5. The modal attenuations corresponding to the propagating modes obtained using this rough surface reflection coefficient and this sound speed profile are illustrated in Fig. 6, where it can be seen that the modal attenuation at 40 Hz varies between 0.08 dB/km for mode 1 and 0.02 dB/km for the higher-order modes.

Comparison between modeled and observed propagation characteristics. Using the source monitoring hydrophone, which was unaffected by the surface reflection over a sufficiently long duration to capture the bubble pulses, the

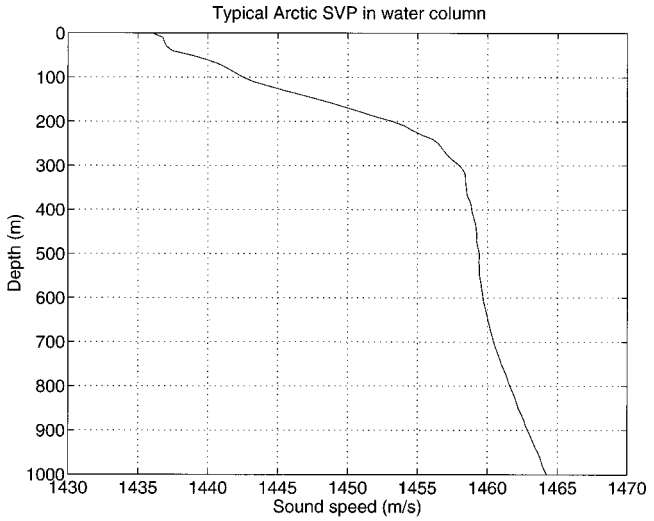

FIG. 5. Central Arctic sound speed profile obtained from CTD measurement taken at the ZIRCON camp.

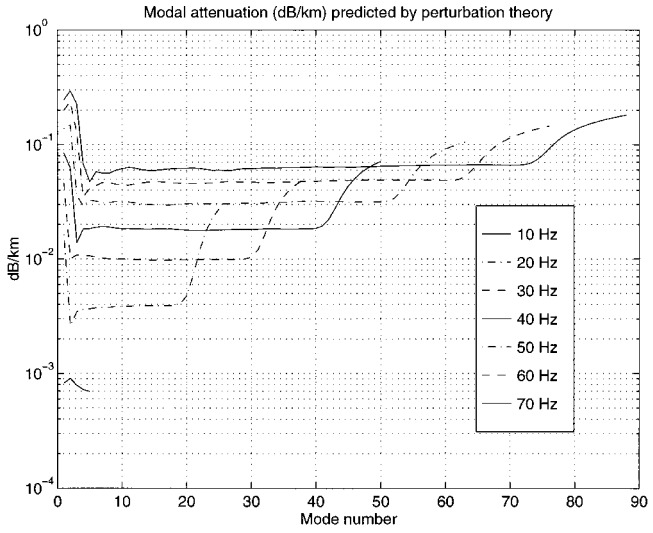

FIG. 6. Modal attenuations for forward scatter from ice with roughness parameters roughness variance $(H^2)=9\ \mathrm{m}^2$, correlation length $(l)=22$ m, fractal dimension $(D)=2.5$.

complex source spectrum of one of the shots was estimated. This spectrum was used along with the KRAKENC model discussed previously to synthesize the total received time series over the 5- to 75-Hz band at ranges measured during the bistatic transects. Comparisons between the actual recorded time series in Fig. 7 and the predictions in Fig. 8 show that excellent agreement was obtained by using the 3-m rms roughness value. The agreement shows that the propagation characteristics of the Arctic sound channel can be modeled to very high fidelity, given the data to tune the model. This highlights the importance of obtaining direct measurements of propagation loss during reverberation experiments, especially when pursuing a model-based inversion, in order to ensure modeling the forward propagation with sufficient accuracy.

During the experimental period, helicopter transects were flown to drop sources for bistatic scattering experiments. These drops also served as spot-checks for transmission loss as a function of range, but due to their sparsity, could not be used directly to construct propagation loss curves. The time domain comparison shown in Figs. 7 and 8, and similar frequency domain comparisons with the empirical models derived from the KRAKENC modeling mentioned previously, were used to validate the forward propagation losses needed for the inversions. The excellent amplitude and kinematic matching of the model and data goes far to reduce our initial discomfort with using a historically supported roughness of 3 m rms, rather than the 2.2 m rms measured over a limited region.

V. REVERBERATION MODEL

In Sec. III we characterized the reverberation in the central Arctic as the incoherent sum of three coherent modal groups, identified with surface, mid-depth, and RSR paths. Since the mean grazing angle and group delays of these three paths are distinct and quite tightly grouped about the mean, it is reasonable to hypothesize a model of the reverberation that assumes that at any given time the reverberation is received

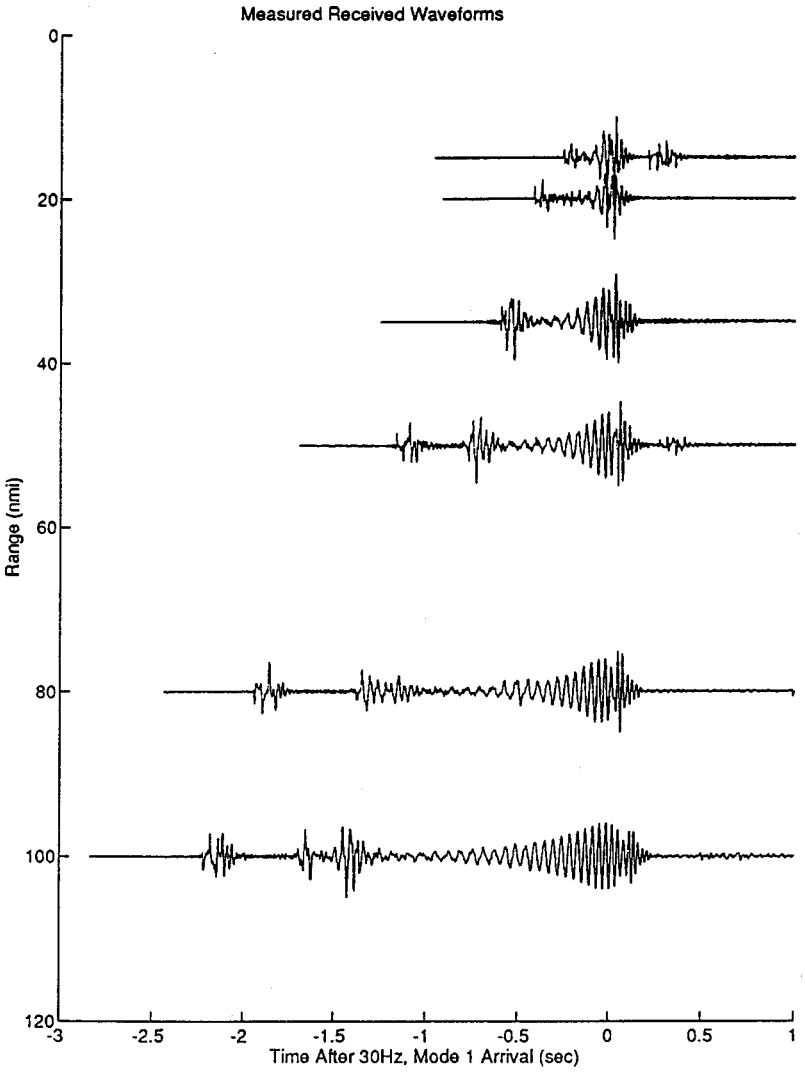

FIG. 7. The time series received at various distances from the source during the bistatic transect experiments. The range at which the experiment was conducted is indicated on the vertical axis.

from a total of nine scattering patches. Each of these patches is associated with a different pair of the three possible incoming and outgoing propagation paths. The reverberation as a function of time may therefore be viewed as the incoherent superposition of nine time series, each of which is caused by the same homogeneous scattering strength interrogated at different sets of incident and scattered angles and at different ranges, and hence independent realizations (in the case of patches associated with different incoming and outgoing groups, there are two possible ways for energy to come in and leave, corresponding to the *nm* and *mn* pairs: these are also assumed to be incoherently additive although strictly they are not).

Proceeding accordingly, we propose the following model for the time-dependent received reverberation plus noise power level, rl, centered about frequency ω_0 that is parametrized on a range independent, narrow-band scattering kernel $\sigma(\theta_n,\theta_m|\omega_0)$. Suppressing the explicit dependence on frequency the model has the form

$$\mathrm{esl}\sum_n \sum_m \mathrm{tg}_n^+(r_{nm}(t))A_{nm}(t,\tau)\sigma(\theta_n,\theta_m)\mathrm{tg}_m^-(r_{nm}(t))+\mathrm{nl} \simeq \mathrm{rl}(t,\tau), \tag{1}$$

where θ_n and θ_m are the average incident and scattered angles of the energy in groups *n* and *m*, the integration time τ is equal to the reciprocal bandwidth, 0.1 s in our analysis, and esl and nl are the energy source level and the ambient noise power in the analysis band. The propagation gain tg_n^+ on the group trajectory *n* from the point source to the scattering patch A_{nm} is corrected to include the incident field only. The backscattered propagation gain tg_n^- from the scattering patch back to the receiver is similarly corrected to include the scattered field only. The means of determining the incident and scattered modal amplitudes, ϕ^+ and ϕ^-, is based on the Wentzel–Kramers–Brillouin decomposition of the modes into up-going and down-going plane waves. The approach and its limitations are discussed in Appendix A.

In Eq. (1) the range r_{nm} to the center of the scattering patch is defined by

$$r_{nm}(t)=\frac{t}{S_n+S_m}, \tag{2}$$

where $S_{n,m}$ are the modal group slownesses

$$\left.\frac{\partial k_{n,m}}{\partial\omega}\right|_{\omega=\omega_0}.$$

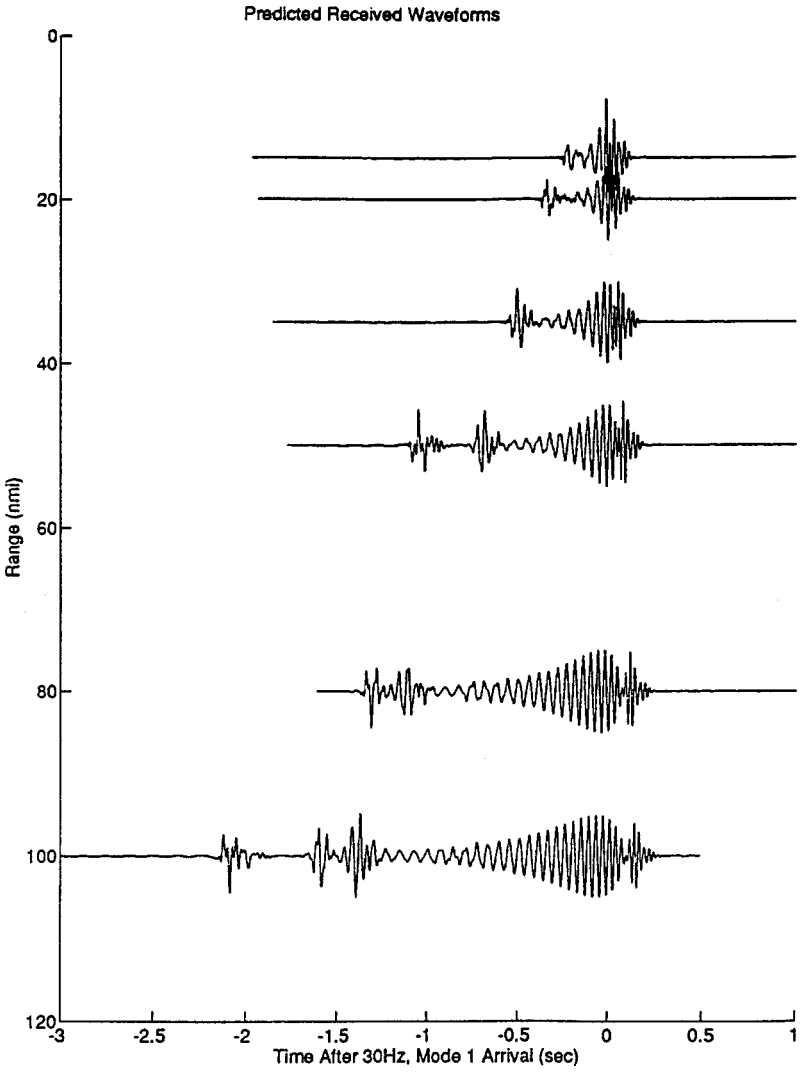

FIG. 8. The synthetic time series computed for the ranges recorded in Fig. 6. The good agreement gives confidence that the forward propagation modeling necessary for the scattering strength inverse has captured the proper magnitude and interference structure of the actual propagation channel.

This is found by taking the stationary phase approximation to the round-trip propagator of the modes

$$e^{i(\omega_0 t-(k_n+k_m)r)}\int_{\omega_B} e^{i\omega(t-(S_n+S_m)r)}d\omega,$$

where ω_B is the band of interest centered about ω_0.

The ensonified area A_{nm} observed over the pulse duration time τ is defined as half the pulse duration multiplied by the average group velocity, the range and the horizontal directivity of the receiver

$$A_{nm}(t,\tau)=\tau\frac{C_g^n+C_g^m}{4}r_{nm}(t)\Delta\Theta, \tag{3}$$

where the modal group velocity C_g^n is equal to the inverse of the modal slowness S_n. The additive noise level term nl in Eq. (1) is included for generality and plays an important role in the robustness of the inversion for the scattering strength, for without it scattering strength estimates would be biased upwards by ambient noise at late time.

The ''transmission gains'' (always less than one and expressed as power ratios, not dB, and hence distinct from TL) for the various groups are determined by summing the corrected modal amplitudes over the contributing modes

$$\mathrm{tg}_n^+(r)=\frac{2\pi}{\rho^2(z_s)r}\left|\sum_{j\in n}\phi_j(z_s)\phi_j^+(0)\frac{e^{-ik_jr}}{\sqrt{k_j}}\right|^2 \tag{4}$$

and

$$\mathrm{tg}_m^-(r)=\frac{2\pi}{\rho^2(z_r)r}\left|\sum_{j\in m}\phi_j(z_r)\phi_j^-(0)\frac{e^{-ik_jr}}{\sqrt{k_j}}\right|^2, \tag{5}$$

where z_s and z_r are the source and receiver depths, respectively, and k_j are the complex modal eigenvalues obtained from KRAKENC using the rough surface reflection coefficient obtained from elastic perturbation theory, as explained in Sec. IV.

Our goal is to obtain robust estimates of the scattering kernel (assumed homogeneous, or spatially invariant and isotropic) with the model outlined previously. For this reason we evaluate the reverberation from all azimuthal angles simultaneously to increase the degrees of freedom available in the data. This is consistent with the uniformity of the reverberation observed over the 32 beams of the HLA. Integrating the reverberation over all azimuths, we select $\Delta\Theta=2\pi$. In addition we restrict the degrees of freedom available for fitting the data by parametrizing the scattering kernel according to a grazing angle power law

$$\hat{\sigma}(\theta_n,\theta_m)=\alpha\{\sin\theta_n \sin\theta_m\}^{\gamma}, \tag{6}$$

where α is defined to be the scattering strength in dB.

Aside from ensuring the overconstraint of the inversion equations, the parametrization in Eq. (6) is also useful in that it can model at least two of the canonical scattering laws from commonly used scattering theory. For instance Lambert's law, which indicates that the scattered power is dependent on the projected scattered area, is obtained with $\gamma=1$ and $10\log 10(\alpha)=-27$, while the perturbative expressions for homogeneous boundary scattering strengths are well approximated by $\gamma=2$. The latter result is discussed in more detail in Appendix B.

On the left-hand side of Eq. (1) only the scattering strength average and noise level over the observation are unknown. As pointed out earlier, the source energy levels esl are known from the analysis of the source monitoring hydrophones, and corresponded closely to those predicted using the Wakeley source model[2] directly to estimate the time series. The transmission gains are determined numerically according to the techniques outlined in Sec. IV and in Eqs. (4) and (5). As discussed in Sec. IV, the good agreement between the transect data in Fig. 7 and the broadband transect predictions in Fig. 8 indicates that the calculated transmission gains will accurately represent the energy incident on the ice as a function of range and time. It is worthwhile to reiterate that high-quality transmission gains are required if estimates of the scattering strength are to remain unbiased by late time reverberation levels, where inconsistencies in overall propagation loss levels can introduce significant biases into the inversion results. The coherent structure of the transmission gains is also of primary importance for successful scattering strength inversion, as the propagation model must be able to predict the temporal structure observed in the reverberation time series.

VI. INVERSION OF REVERBERATION TIME SERIES FOR SCATTERING STRENGTH

The known environmental parameters: transmission gains versus incident and scattered angles and range, energy source level, and ensonified area are determined through the evaluations of Eqs. (2)–(5). It remains to solve Eq. (1) for the parameters of scattering amplitude, α, noise level, nl, and power law, γ. Inversion for the first two parameters forms a linear inverse problem. However, the reverberation level is a nonlinear function of the scattering strength power law. Since there are few parameters and the forward problem is very inexpensive to compute, we conceptually solve the linear inverse problem over a range of assumed power law exponents γ and then choose the result with the smallest rms fitting error

$$e_{\mathrm{rms}}(\gamma)=\sqrt{\frac{1}{T}\int_0^T\{\mathrm{rl}(t)-\widehat{\mathrm{rl}}(t,\gamma)\}^2dt}. \tag{7}$$

However, due to the large decrease in rl over time, late time data are ignored by the metric in Eq. (7). In order to place more equal emphasis on the late reverberation arrivals, the received power levels are therefore multiplied by the inverse of the cylindrical spreading term (r or alternatively time, t) before inversion. This still emphasizes high SNR early reverberation slightly because we do not try to compensate for attenuation effects in this equalization. We then choose as our error metric the rms fitting error between the equalized received and modeled power level

$$\epsilon_{\mathrm{rms}}(\alpha,\gamma,nl)=\sqrt{\frac{1}{N}\sum_{n=0}^{N-1}t_n\{\mathrm{rl}(t_n,\tau)-\widehat{\mathrm{rl}}(t_n,\tau|\alpha,\gamma,\mathrm{nl})\}^2}, \tag{8}$$

where $T\equiv N\Delta t$ is the total time over which the error is evaluated, $t_n=n\Delta t$, and Δt is the sampling interval of the smoothed reverberation time series, 0.1 s. These are approximately independent samples for a smoothing interval of 0.1 s with 10-Hz resolution. The predicted received level $\widehat{\mathrm{rl}}$ that was subtracted from the data to form the error is computed at the center frequency of each analysis band, and is a function of the scattering power, α, the angular dependence parameter, γ and the noise level, nl.

To minimize the error metric in Eq. (8) we compute a linear inverse for each trial value of γ by the method of least squares. The linear combination of the three propagation group outgoing transmission gains tg_n^+ with the three incoming transmission gains tg_m^- leads to a total of nine two-way transmission gains, which are all modulated by the unknown common scattering amplitude α. For each fixed value of the angular dependence parameter, γ, all the angular dependence of these nine different scattering paths may be calculated in advance.

The inverse is found in the following way. The nine two-way transmission gains are multiplied by the scattering area and precomputed angular dependence kernel and summed as in Eq. (1). This vector of received level structure elements, denoted $\widehat{\mathrm{rl}}_0$ to indicate that they represent the received level for unity scattering strength for the assumed angular dependence parameter γ, are used to define the overconstrained system of equations

$$\underbrace{\begin{Bmatrix} t_0\widehat{rl}_0(t_0,\omega|\gamma) & t_0 \\ t_1\widehat{rl}_0(t_1,\omega|\gamma) & t_1 \\ t_2\widehat{rl}_0(t_2,\omega|\gamma) & t_2 \\ \vdots & \vdots \\ t_{N-1}\widehat{rl}_0(t_{N-1},\omega|\gamma) & t_{N-1} \end{Bmatrix}}_{\hat{\mathbf{A}}} \underbrace{\begin{bmatrix} \alpha(\omega) \\ nl(\omega) \end{bmatrix}}_{\mathbf{s}} = \underbrace{\begin{Bmatrix} t_0 rl(t_0,\omega) \\ t_1 rl(t_1,\omega) \\ t_2 rl(t_2,\omega) \\ \vdots \\ t_{N-1} rl(t_{N-1},\omega) \end{Bmatrix}}_{\mathbf{a}}. \tag{9}$$

In condensed notation, we wish to minimize

$$\{\mathbf{e}^{\dagger}\mathbf{e}\}=[\{\hat{\mathbf{A}}\mathbf{s}-\mathbf{a}\}^{\dagger}\{\hat{\mathbf{A}}\mathbf{s}-\mathbf{a}\}],$$

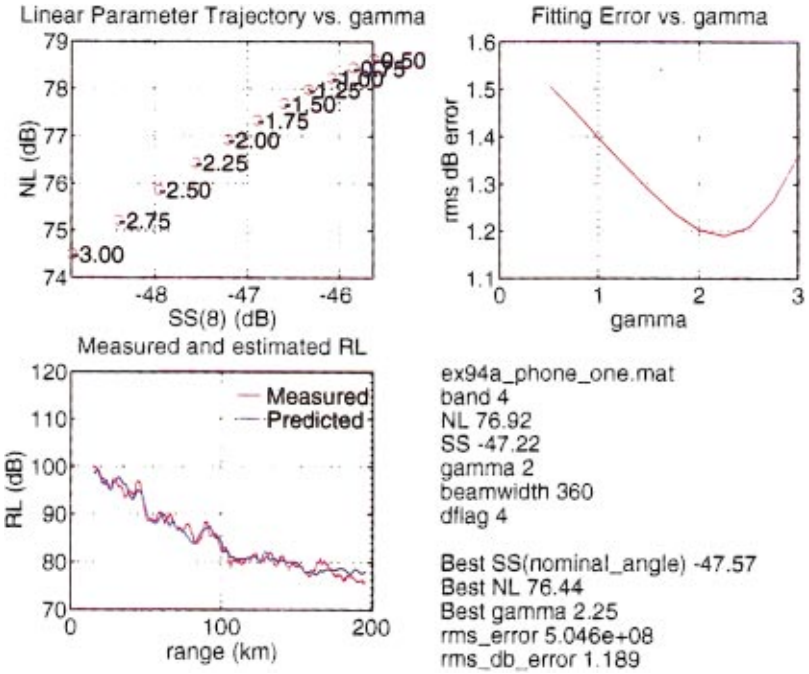

FIG. 9. Summary of scattering strength inversion for the 35- to 45-Hz frequency band. For $\gamma=2$, the scattering strength is estimated at -47.2 dB *re* m^2 at 8° grazing incident and reflected. Good agreement between the predicted and measured reverberation levels, indicated in the lower-left panel, is obtained by combining the constituent propagation groups together to yield the observed structure.

where $\mathbf{e}^\dagger$ indicates the transpose of **e**. It is well known that this minimization is obtained by setting

$$\mathbf{s}=\{\hat{\mathbf{A}}^\dagger\hat{\mathbf{A}}\}^{-1}\hat{\mathbf{A}}^\dagger\mathbf{a}, \tag{10}$$

the Moore–Penrose or generalized inverse.[13] The solution for **s** is obtained over the range of relevant angular power laws γ, and then the $\epsilon_{\rm rms}$ from Eq. (8) is plotted as a function of γ to determine the combination of α, nl, and γ that best represents the observations.

VII. SCATTERING STRENGTH RESULTS

The solution of the overconstrained system of Eq. (10) using band-limited reverberation data over trial angular power laws $0.5\leqslant\gamma\leqslant3.0$ yielded scattering strength estimates for each frequency band. An example of the power law scan for the 10-Hz band centered at 40 Hz is given in Fig. 9. The upper-left plot indicates the average noise level and scattering strength $10\log10(\alpha(\sin\theta_m\sin\theta_n)^\gamma)$ (evaluated for group 1 at $\theta_n=\theta_m=8°$) achieving the best fit as a function of the angular dependence exponent γ. The required noise level ranges from 78.5 dB *re* μPa/$\sqrt{\rm Hz}$ at $\gamma=0.5$ to 74.5 dB *re* μPa/$\sqrt{\rm Hz}$ at $\gamma=3.0$. These values compare favorably to typical omni phone noise levels during the experiment. The minimum rms error between the measured rl and the estimate $\hat{\rm rl}$, shown in the upper-right plot, is achieved at a value of $\gamma=2.25$. For this angular dependence the inversion yields a scattering strength estimate of -47.6 dB *re* m^2 at 8° grazing. At this value of γ, the measured and predicted received re-

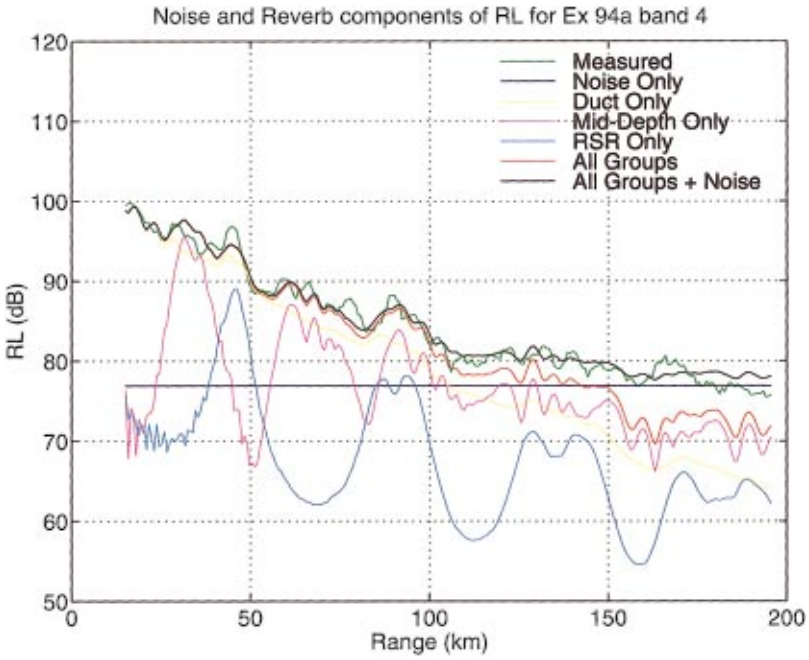

FIG. 10. Components of scattering strength inversion for the 35- to 45-Hz frequency band. Reverberation model contributions from the lower sound speed upper duct path are shown in yellow, while the mid-depth and RSR contributions are shown in magenta and blue, respectively. The sum of all the propagation paths without additive noise are shown in red. The constant additive noise level is shown in purple. The total modeled reverberation level, which includes the noise term, is shown in black. Comparison with the measured reverberation level, which is shown in green, indicates good agreement and shows the importance of modeling coherent multipath effects in the propagation.

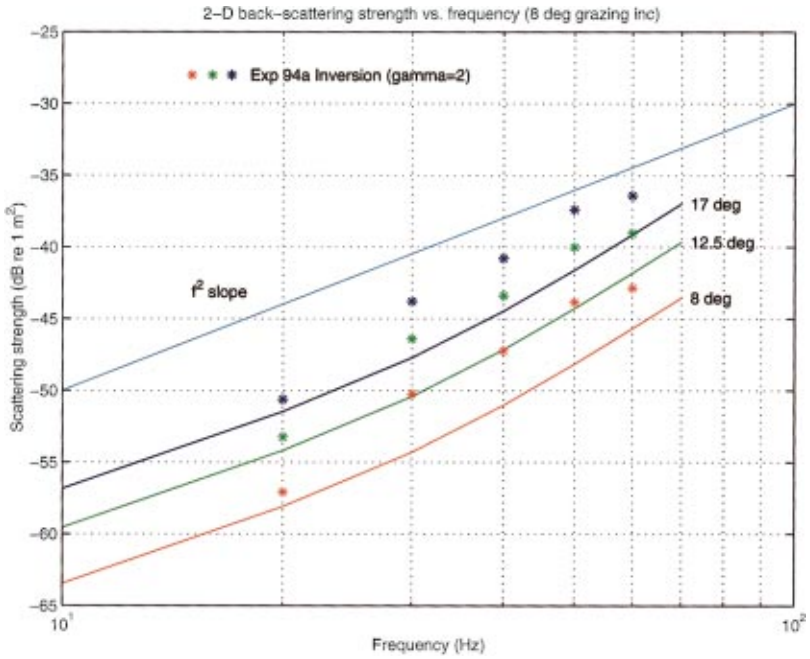

FIG. 11. Predictions of scattering strength from 2D elastic perturbation theory and experimental results from the linear inversion of reverberation level. Here the inversion has been constrained to adopt the power law dependence of perturbation theory, i.e., $\gamma=2$.

verberation power are indicated in the lower-left plot. This figure shows the general overall agreement, including the ability of the model to estimate propagation structure related effects at the first and second convergence zones for the RSR paths. For $\gamma=2$, the scattering strength is estimated at -47.2 dB, not significantly different. In fact, the estimated group 1 scattering strength is quite robust to assumptions of the power law and noise level, varying only $\pm$ 1 dB over the range of reasonable power law exponents between $\gamma=1$ and $\gamma=3$. Because the reverberation from the higher modes is more sensitive to the assumed values of γ, the uncertainty in the scattering strength for group 2 (12.5° grazing) varied over a range from 2.5 dB lower to 1 dB higher than the estimate at $\gamma=2$, and for group 3 (17.5° grazing) the uncertainty varied between 5 dB lower and 3 dB higher for suboptimal power laws γ.

These results also make clear that although the RL data have a large number of degrees of freedom in them and thus low statistical fluctuation, the residual fitting error over γ is prevented from going much below 1 dB rms by bias errors introduced by the modeling assumptions, such as use of the semicoherent, range independent model, and the assumption of range independence of the scattering strength. While we feel that the fact that the estimates for gamma cluster around 2 for all frequency bands analyzed is significant, this model parameter is not well resolved using our current solution to the inverse problem. The ''flatness'' of the error curve in the upper-right panel of Fig. 9 is an indicator of this. The dominant reason for our poor resolution is that, as shown in Fig. 10, the reverberation data are highly dominated by the mode 1 (group 1, or duct) return that ensonifies the surface at 8°. The 12° group 2 (mid-depth) return is approximately equal to

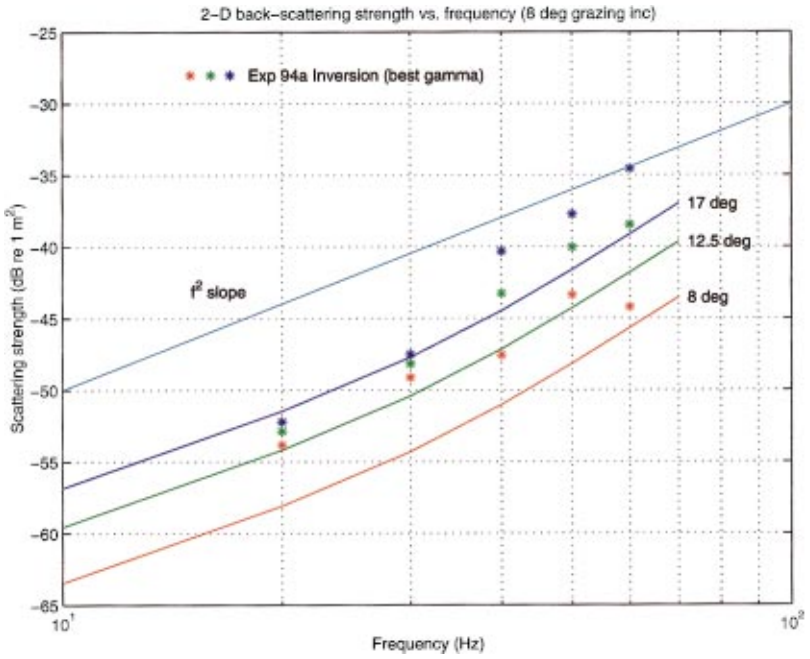

FIG. 12. Predictions of scattering strength from 2D elastic perturbation theory and experimental results from the linear inversion of reverberation level. Here the value of the angular power law is unconstrained and allowed to adopt the best value. Angular dependence of the scattering strength estimated by the inversion procedure increases with frequency, with γ equaling two at 40 Hz and three at 60 Hz.

the duct return at a few discrete ranges less than 100 km, and does dominate beyond 100 km, however the data importance are diminished by our geometric-only range emphasis to the data. The 17° group 3 (RSR) return is well below the duct level at all ranges considered. Thus, errors in the power law are not strongly penalized because the predominance of the data are at a single angle.

Figure 10 provides insight into how the constituent scattering paths combine to yield the total predicted reverberation level. In Fig. 10, the measured reverberation level is plotted in green. In black the best prediction is plotted, showing good overall agreement between the observed reverberation and the model using the best choice of parameters. The total estimate is the incoherent sum of the nine scattering paths discussed earlier. In this plot all the energy backscattered into the three groups from energy incident in the lower sound speed upper duct is indicated in yellow. At short range the lower sound speed upper duct contains the most energy, so the largest contribution to reverberation out to ranges of about 120 km is from the lower sound speed upper duct energy. Beyond this range mid-depth energy, indicated in magenta, tends to excite more reverberation as the lower sound speed upper duct energy has been stripped by surface losses. However for shorter ranges, the confluence of mid-depth modes at ranges of 30, 60, and 90 km can spike up to provide levels of reverberation equivalent to, or greater than, those contributed by lower sound speed upper duct paths. Similarly the RSR paths shown in blue also provide an observable contribution to the reverberation level at convergence zone ranges of 45, 90, and 135 km. As pointed out previously, it is precisely the presence of these modes that provides the inversion scheme with information regarding the angular power law γ of the scattering strength.

VIII. COMPARISON OF ESTIMATED SCATTERING STRENGTHS TO THEORETICAL PREDICTIONS

Constraining the angular power law of the scattering strength to the $\gamma=2$ value predicted by perturbation theory, inversions for the scattering strength of the Arctic ice canopy as a function of frequency were obtained and compared to theoretical estimates obtained with two-dimensional elastic perturbation theory. The derivations of the two-dimensional perturbation theory scattering strength is discussed in Appendix B. The two-dimensional scattering model assumes that scattering patches are azimuthally uncorrelated. In Fig. 11 the results are shown for the first column of the scattering matrix, i.e., those elements where the incident angle corresponds to the lower sound speed upper duct and the scattered angles correspond to the three propagation paths. The scattering strength estimated for a 3-m rms roughness, consistent with the value used for the forward scattering loss analysis, is shown by the solid curves, and the inversion results are shown by the asterisks at 20, 30, 40, 50, and 60 Hz with γ constrained to a value of 2.

We see that by constraining the angular power law of the scattering strength inversion to agree with the asymptotic form of perturbation theory, the resulting estimates of reverberation level in the Arctic underestimate the data by about 3–5 dB. Due to the constraint on the angular dependence of the inversion, at the higher backscattered angles the agreement is similar. The overall frequency dependence of the scattering strength inversions seems to be best fit by an f^2 power law indicated by the dashed line, as does the frequency dependence of the elastic perturbation scattering strength predictions. It is useful to note that the frequency dependence of the scattering loss predicted by the elastic perturbation obeys this relationship.[4] As scattered energy reduces the coherent reflection coefficient, this similarity in power law between backscattered power and forward loss is natural.

In Fig. 12 the results of the inversions using the angular power law that minimized the ϵ given in Eq. (8) are superimposed on the perturbation predictions. Here we see a trend in the data, where for low frequencies the best γ is found to be quite close to one, and at high frequencies approaches $\gamma=3$. The result is that at low frequencies the scattering strength is virtually identical into all backscattered angles, whereas at the higher frequencies a greater angular dependence to the scattered energy is detected. At this time, we do not understand the reason for the frequency trend in our best fit gamma estimate. This may be a result of incorrectly, or unmodeled, scattering phenomenology that requires further analysis, or a result of inadequacies in our dataset. Our recommendation for use of these results in practical sonar equation modeling is to use the theoretically supported gamma $=2$ value, and the scattering parameter, α, that results from it. As mentioned before, the power law parameter was not particularly well resolved by our dataset. Revisiting the upper-right panel in Fig. 9 we see that the rms dB fitting error only varies by about 25% over the entire parameter range of γ, from 1.2 to 1.4 dB rms. This is consistent with the fact that the peaks in the reverberation associated with groups 2 and 3 are rather confined in time, so that matching them correctly only decreases the rms error obtained over the whole reverberation sequence by a small factor. As before, the inversions seem to indicate a scattering strength frequency dependence proportional to f^2 or perhaps $f^{5/2}$.

IX. CONCLUSIONS

In summary, the scattering strength of the Arctic ice was found to roughly obey a frequency squared law, with backscattering strengths for the lower sound speed upper duct with 8° grazing angle varying from approximately -57 dB *re* m^2 at 20 Hz to -47 dB *re* m^2 at 40 Hz and -43 dB *re* m^2 at 60 Hz. The data at 40 Hz are best fit with an angular dependence of the Arctic ice canopy scattering strength with close to a square law dependence of the form

$$\sigma(\theta_i,\theta_s)=0.14(\sin\theta_i \sin\theta_s)^{2.25},$$

quite consistent with perturbation theory, although a trend from lower angular dependence at low frequency to higher angular dependence at high frequency was found. Little support was found for the first power Lambert law angular dependence often cited in bottom scattering strength results, except at the lowest frequencies. The overall magnitudes of the observed scattering strengths were found to agree to within 3–5 dB with the values predicted by two-dimensional perturbation theory, when the elastic properties of the ice

were used in conjunction with the measured power spectrum of the ice canopy, and the LeSchack value of 3-m rms ice roughness was used. This 3-m rms roughness was also required to model the higher than average propagation loss values measured during the experiment, and we have reached the conclusion that the 2.2-m rms value measured in the immediate vicinity of the ZIRCON ice camp was not representative.

The scattering strength parameters obtained from this analysis are theoretically reasonable results that are useful for the practical prediction of Arctic reverberation at low frequencies. We have high confidence in the scattering values for the mode 1 contained in the surface duct, which is the most useful mode for active sonar in the Arctic because of its favorable depth and range coverage and its lower scattering strength. The fact that the predominance of our data are due to mode 1 is not a coincidence—the hypothesis of the Central Arctic LFA Feasibility Experiment[1] was that the design of an Arctic low-frequency active sonar should exploit mode 1 to minimize reverberation, despite its larger TL. Our measurement of scattering strength at 12° is also reasonably robust ($-3/+1$ dB) to our uncertainty in the angular dependence power law, γ. However our confidence in γ itself, and hence extrapolation of scattering strength to other angles, stems more from theory than the measurements reported here. Our results are further dependent on theory to the extent that theoretical predictions were used for the source and propagation models. In this case the quality of the forward model was ensured by the availability of measured TL from transects data, and the source model was verified through favorable comparison to the data collected on the source monitoring hydrophones. The value of the theoretical modeling of the propagation loss is that it helps to illuminate the physics behind the unique propagation characteristics of the Arctic. The model is also required to construct the semicoherent model in a rigorous way. The reasonable consistency between the data and model results for the propagation suggest that elastic perturbation theory is capable of modeling forward propagation loss at low frequencies in the Arctic. However, the underestimation of the scattering strength by 3–5 dB suggests that the first-order perturbation approach is not entirely capable of modeling the measured backscatter, implying that large slope/height features must account for this deficit.

ACKNOWLEDGMENTS

The authors would like to thank the AEAS program managers at ONR, Robert Feden and Barry Blumenthal, for the opportunity to collect and analyze this data set. We also would like to thank the reviewers for their helpful and insightful comments which helped to sharpen the focus of the paper during the review process.

APPENDIX A: SURFACE CORRECTION

Although the transmission gains of the total field may be determined to excellent precision by KRAKENC, Eq. (1) requires that we correct the transmission gains to the incident and scattered transmission gains at the surface. The correction is required in order to estimate the scattering strength as defined by theory, which is the normalized ratio of the scattered intensity $\langle s^2 \rangle$ at some range r to the incident intensity p^2 on the scattering aperture L,

$$\sigma(\theta_n, \theta_m) = \frac{\langle s^2(\mathbf{r}) \rangle |\mathbf{r}|}{p^2(\theta_n) L},$$

where $\mathbf{r} = r(\cos\theta_m e_r + \sin\theta_m e_z)$ and the scattered field is observed in a halfspace with uniform sound speed.

Since for the geometries of ice canopy scattering the incident and scattered transmission gains are related to the up- and down-going component of the total field at the surface, we must appeal to a ray theoretical description of the mode field to separate the amplitudes of either of these components from the total field. For general mode shapes found by finite differences the distinction between up- and down-going wave components is lost. However for WKBJ modes, which are obtained under an eikonal approximation from the depth separated wave equation, the following expressions for the up- and down-going wave components in terms of the mode shapes and their derivatives can be derived from their approximate forms:[14]

$$\phi_n^+(z) = -\frac{i}{2k_{nz}(z)} \left. \frac{\partial \phi(z')}{\partial z'} \right|_{z'=z} + \left[\frac{1}{2} - \frac{i \partial k_{nz}(z')/\partial z'|_{n'=z}}{4k_z(z)^2} \right] \phi_n(z), \tag{A1}$$

$$\phi_n^-(z) = \frac{i}{2k_{nz}(z)} \left. \frac{\partial \phi(z')}{\partial z'} \right|_{z'=z} + \left[\frac{1}{2} + \frac{i \partial k_{nz}(z')/\partial z'|_{z'=z}}{4k_z(z)^2} \right] \phi_n(z). \tag{A2}$$

In Eqs. (A1) and (A2), k_{nz} is the vertical wave number of the nth mode at the specified depth. At a free surface, where the total field is identically equal to zero, these equations specify that the magnitude of the up- and down-going components of the field are each equal to half of the maximum value of the mode shape for the case of constant sound speed. Since at low frequencies the Arctic ice canopy appears acoustically to be very close to a free surface, this correction gives incident and scattered field transmission gains that are approximately one half of the maximum value of the transmission gains (e.g., the value at the mode shape maximum) at any given range. Thus measured scattering strengths obtained using maximum transmission gains could be corrected by adding 12 dB, since each transmission gain is too large by a factor of 4 (corresponding to 6 dB too little TL). However it is clear that using uncorrected transmission gains to the surface will result in extremely large estimates of scattering strength since the total field near the surface becomes quite small.

In practice the approximate relations in Eqs. (A1) and (A2) are only good for depths shallower than the depth below which the WKBJ modes are cut off and become evanescent in the water column. We evaluate these equations at the surface so this difficulty is avoided. Since the nonunity gain elastic perturbation reflection coefficients were used as boundary conditions when KRAKENC solved for the modes

shapes, a small contribution to the up- and down-going field amplitudes was obtained through evaluation of the second term in Eqs. (A1) and (A2). However the bulk of the correction was provided by the derivative of the mode shape in the first term, which was determined through postprocessing of the mode shapes using a finite difference scheme.

APPENDIX B: SCATTERING STRENGTH

The perturbation theory scattering kernels such as those that appear in LePage *et al.*[4] can be useful representations of the scattered field. One attraction to the spectral integral formulation is that the solutions for the scattered field are obtained in the frequency wave number domain. Thorsos[15] has derived the transformations from spectral densities to scattering cross section for the ensemble average of the two-dimensional scattering kernel

$$\sigma_{2\mathrm{D}}(\mathbf{q},\mathbf{k}) = q_z^2 \langle \tilde{\mathbf{s}}(\mathbf{q}|\mathbf{k}) \rangle^2 2 - D, \tag{B1}$$

where σ is the scattering cross section, $\tilde{\mathbf{s}}$ is the two-dimensional scattering kernel for unity plane-wave excitation, $\mathbf{k}$ is the two-dimensional horizontal wave number vector of the incident field, $\mathbf{q}$ is the scattered horizontal wave number vector, and q_z represents the vertical wave number of the scattered field in the acoustic half-space. Here it is useful to include the explicit equation for the ensemble average of the square of the $2-D$ scattering kernel for unit amplitude plane wave excitation

$$\langle \tilde{\mathbf{s}}(\mathbf{q}|\mathbf{k}) \rangle^2 = P(\mathbf{q}-\mathbf{k}) \times \left| \tilde{\mathbf{B}}^{-1}(\mathbf{q}) \left(\frac{\partial \tilde{\mathbf{B}}(\mathbf{k})}{\partial z} - i(\mathbf{q}-\mathbf{k}) \circ \tilde{\mathbf{b}}(\mathbf{k}) \right) \tilde{\overline{\chi}}_0(\mathbf{k}) \right|^2, \tag{B2}$$

where $\overline{\chi}_0$ is the unperturbed response of the ice sheet to a unity amplitude incident plane wave. Equation (B2) is the magnitude square of the scattering kernel Eq. (2) in LePage *et al.* for acoustic-elastic scattering. The matrices $\tilde{\mathbf{B}}$ enforce the boundary conditions at the ice–water and ice–air interface. The matrix $\mathbf{b}$ accounts for backscatter caused by the rotation of the boundary conditions under a small slope hypothesis. For scattering from halfspaces, it has been verified that Eq. (B2) together with Eq. (B1) gives scattering strengths which are in agreement with the perturbation part of the rough surface scattering strength from Mourad *et al.*[16] Here the scattering is from an elastic ice sheet of 3 m thickness. For the appropriate choice of the boundary operator and the unperturbed field amplitude $\tilde{\chi}_0$ for this ice sheet, the scattered field vector $\tilde{\mathbf{s}}$ contains as its first element the downward scattered pressure amplitude at wave number $\mathbf{q}$.

Goff *et al.* have shown that an isotropic rough surface of fractal dimension D obeys a power law asymptotic to $k^{-8+2\mathrm{D}}$,

$$P(\mathbf{k}) = \frac{4\pi(3-D)H^2(k_r)^{-2}}{(k^2/k_r^2+1)^{4-D}}. \tag{B3}$$

In this case, for a simple boundary interaction, such as with a free surface, Eq. (B2) is proportional to

$$\langle \tilde{\mathbf{s}}_{i,i+1}(\mathbf{q}|\mathbf{k}) \rangle^2 \propto \frac{k_0^2 \sin^2 \theta_i}{(k_0^2 l^2+1)^{4-D}}.$$

For the fractal dimension $D=2.5$ and the correlation length scale of $l=22$ m used in this study this is proportional to

$$\langle \tilde{\mathbf{s}}_{i,i+1}(\mathbf{q}|\mathbf{k}) \rangle^2 \propto \frac{\sin^2 \theta_i}{k_0}$$

over the upper end of the frequency range of interest. As discussed in the following the scattering mechanics of the ice canopy actually modify this frequency dependence. For free surface scattering the two-dimensional scattering strength may then be expressed in the angular domain as

$$\sigma_{2\mathrm{D}}(\theta_s, \theta_i) \propto k_0 \sin^2 \theta_s \sin^2 \theta_i. \tag{B4}$$

From Eq. (B4) it is observed that the scattering strength goes to zero quadratically in the incident and scattered angles θ_i and θ_s, and that for a given wave number spectrum the two-dimensional cross section grows linearly with frequency. The results obtained for elastic perturbation grow more quickly as a function of frequency, due to the effect of the subsonic flexural wave which is excited in the ice sheet by the scattering process. The spectrum of this mode away from resonance effects low-angle scattering in the propagating regime.

[1] G. L. Duckworth, T. Farrell, K. LePage, and C. Atkinson, "Central Arctic LFA Feasibility Experiment," J. Underwater Acoust. **48**, 157–176 (1998).
[2] J. Wakeley, Jr., "Pressure-signature model for an underwater explosive charge," J. Underwater Acoust. **27**, 445–449 (1977).
[3] J. Goff and T. Jordan, "Stochastic modeling of seafloor morphology: Inversion of Sea Beam data for second order statistics," J. Geophys. Res. B **93**, 13589–13608 (1988).
[4] K. LePage and H. Schmidt, "Modeling of low frequency transmission loss in the central Arctic," J. Acoust. Soc. Am. **96**, 1783–1795 (1994).
[5] W. Kuperman and H. Schmidt, "Self-consistent perturbation approach to rough surface scattering in stratified elastic media," J. Acoust. Soc. Am. **86**, 1511–1522 (1989).
[6] M. B. Porter, "The KRAKEN Normal Mode Program (DRAFT)," SACLANT ASW Research Centre, La Spezia, Italy (1991).
[7] P. N. Mikhalevsky, A. B. Baggeroer, A. Gavrilov, and M. Slavinsky, "Continuous wave and M-sequence transmissions across the Arctic," J. Acoust. Soc. Am. **96**, 3235–3236 (1994).
[8] F. DiNapoli and R. Mellen, "Low frequency attenuation in the Arctic ocean," in *Ocean Seismo-Acoustics*, edited by T. Akal and J. M. Berkson (Plenum, New York, 1986), pp. 387–395.
[9] J. Robert Fricke, "Acoustic scattering from elemental ice features: Numerical modeling results," J. Acoust. Soc. Am. **93**, 1784–1796 (1993).
[10] O. I. Diachok, "Effects of sea-ice ridges on sound propagation in the Arctic ocean," J. Acoust. Soc. Am. **59**, 1110–1120 (1976).
[11] R. E. Keenan, "PC ICECAP: Physics Documentation," AEAS Arctic Program Report No. 91-006, Stennis Space Center, MS, 1991.
[12] B. E. Miller and H. Schmidt, "Observation and inversion of seismo-acoustic waves in a complex Arctic ice environment," J. Acoust. Soc. Am. **89**, 1668–1685 (1991).
[13] W. Menke, *Geophysical Data Analysis: Discrete Inverse Theory* (Academic, New York, 1984).
[14] K. J. McCann, M. E. Ladd, and C. S. Hayek, "Upward and downward propagating mode for a normal mode treatment of reverberation," John Hopkins University APL Tech. Mem. No. STS-90-046, 1990.
[15] E. I. Thorsos and D. R. Jackson, "The validity of the perturbation approximation for rough surface scattering using a Gaussian roughness spectrum," J. Acoust. Soc. Am. **86**, 261–277 (1989).
[16] P. D. Mourad and D. R. Jackson, "High frequency sonar equation models for bottom backscatter and forward loss," in *Proceedings of Oceans '89* (IEEE, New York, 1989), pp. 1168–1175.

Low-frequency sound generation by an individual open-ocean breaking wave

Steven L. Means[a] and Richard M. Heitmeyer
Naval Research Laboratory, Code 7121, Washington, DC 20375

(Received 13 April 1999; revised 4 August 2000; accepted 20 April 2001)

Bubble cloud resonances have been proposed as an explanation of the low-frequency acoustic radiation produced by breaking waves. A previous model [H. N. Ogũz, J. Acoust. Soc. Am. **95**, 1895–1912 (1994)] considered excitation of the bubble cloud by a rigid piston at the base of a hemispherical bubble cloud. The present model considers excitation of the cloud by individual point sources within the cloud. A Green's function is obtained for a point source displaced from the origin of a hemispherical bubble cloud beneath a pressure release surface. The method of images and superposition allow one to obtain the field generated by a distribution of point sources within the bubble cloud. The frequency-dependent radiation pattern for two distributions of point sources within the cloud is obtained. Distributing the point sources within the forward sector of the bubble cloud generates spectral characteristics consistent with measured open-ocean breaking wave spectra. [DOI: 10.1121/1.1379729]

PACS numbers: 43.30.Nb [SAC-B]

I. INTRODUCTION

Ambient noise in the open ocean has long been correlated with wind speed.[1,2] More recent work[3–7] has shown that upper frequencies (more than ~1 kHz) of the noise spectrum are well correlated with oscillations of individual bubbles entrained during wave breaking and has been modeled theoretically.[8] Due to the absence of significant populations of large bubbles observed beneath breaking waves,[9] it is unlikely that acoustic radiation from individual large bubbles can explain the low-frequency portion (less than ~1 kHz) of the observed ambient noise spectra.

Collective oscillations of bubble clouds were suggested as a low-frequency sound generation mechanism of breaking waves as early as 1985.[10,11] Although a number of other candidate mechanisms have been proposed,[12] recent laboratory studies[13–15] have provided evidence of sound generation through collective oscillations of bubble clouds. Additionally, simultaneous at-sea observations of breaking waves and acoustic signatures[16,17] have shown a correlation between the presence of bubble clouds and low-frequency acoustic radiation in the open ocean.

A number of papers[18,19] have reported on theoretical mechanisms governing the oscillation and radiation of bubble clouds; however, few comprehensive models have been developed. In developing a comprehensive model for the generation of low-frequency sound by collective oscillations of bubble cloud entrained via wave breaking, one must consider the mechanism by which the bubble cloud is excited. A number of mechanisms have been proposed; however, concurrence of opinion is that newly entrained bubble oscillations are the principal source of sound generation by breaking waves.[8] Therefore, it is reasonable to consider the entrainment of bubbles as the dominant excitation mechanism of the bubble cloud.

II. PREVIOUS MODEL

In 1994, H. N. Ogũz[20] proposed a model to predict low-frequency sound levels generated by a distribution of individual breaking waves. The model was based on a simplified model for low-frequency sound generation from a single breaking wave. Although this model was somewhat successful in explaining the noise field due to a distribution of breaking waves, it did not predict spectra from individual breaking waves that are consistent with experimental observations. Ogũz's model for a single breaking wave considers the excitation of the bubble cloud by an effective pressure due to a distribution of newly formed bubbles at the air–bubble cloud interface. This is equivalent to forcing the bubble cloud into oscillation with a rigid disk as illustrated in Fig. 1. In his model development, he assumes a number of characteristics of the composition,[4,5,7,9,21–29] size,[30] and growth rate[31] of the bubble cloud, and strength[4] of excitation based on observations reported by other researchers. He derives the following expression for the far-field acoustic pressure,

$$p(\bar{r}') = \frac{1}{kr}\sum_{n=0}^{\infty} c_n i^{2n+1} e^{-ikr} P_{2n+1}(\cos\theta) \tag{1}$$

where

$$c_n = \frac{(4n+3)\Sigma_{m=0}^{\infty} A_{mn}\left(j_{2n+1}(k_c a) j'_{2m}(k_c a) - j'_{2n+1}(k_c a) j_{2m}(k_c a)\right)}{(k/k_c) h'_{2n+1}(ka) j_{2n+1}(k_c a) - h_{2n+1}(ka) j'_{2n+1}(k_c a)},$$

[a]Electronic mail: means@wave.nrl.navy.mil

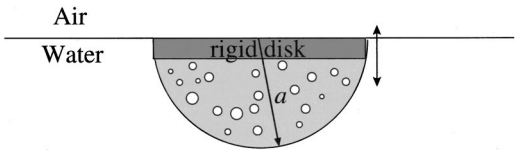

FIG. 1. Diagram of equivalent excitation mechanism as used in the Ogũz model. The bubble cloud is excited by the effective pressure of a number of newly entrained bubbles near the cloud–air interface.

$$A_{mn}=\frac{(-1)^{n+2m}(4m+1)(2m-1)!!(2n+1)!!}{(2n+1-2m)(n+m+1)2^m m!2^{n+1}n!}.$$

The function $P_n(x)$ is the Legendre polynomial of order n, and $j(x)$ and $h(x)$ are the spherical Bessel and Hankel functions, respectively. The bubble cloud is of radius a and the interior and exterior wave numbers are given by k and k_c, respectively. The primes indicate a derivative with respect to the argument.

An angle-frequency surface of the pressure field intensity, based on Eq. (1), is shown in Fig. 2. This surface shows the angular radiation pattern as a function of frequency (along the radial coordinate) in the central plane of the bubble cloud's cross section at a fixed distance from the cloud. The parameter values used to produce Fig. 2 are given in Table I. The cloud radius and void fraction were chosen such that the fundamental cloud resonance would be in agreement with the resonance peak observed experimentally, which appears below. However, these values are still well within the large range of observed values reported in existing literature. The remaining parameters are those used by Ogũz in his analysis. The dominant feature of this angle-frequency surface is the strong harmonic line set. These lines are produced by the resonances of the bubble cloud and can be predicted from the bubble cloud size and the effective frequency-dependent sound speed within the cloud.

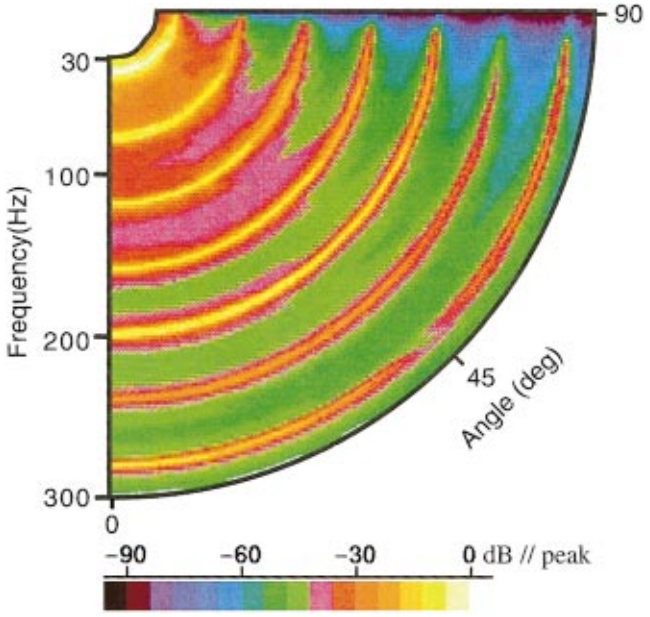

FIG. 2. Angle-frequency surface of the field predicted by the Ogũz model calculated via Eq. (1). A strong harmonic line set is predicted with each line being related to a mode of oscillation of the bubble cloud. The resonance frequencies can be predicted from the cloud size and the effective sound speed within the cloud, which is dependent on the composition of the cloud.

TABLE I. Parameter values used in Eq. (1) to characterize the size and composition of the hemispherical bubble cloud. The cloud radius and void fraction were chosen so that the fundamental resonance would agree with an experimental measurement. The remaining values were those chosen in Ogũz's analysis. All of the parameter values are within the range of experimental observations.

Parameter	Description	Value
a	bubble cloud radius	0.75 m
$r_{\text{bub}-\min}$	minimum bubble radius	5.0×10^{-5} m
$r_{\text{bub}-\max}$	maximum bubble radius	2.0×10^{-3} m
$f(r_{\text{bub}})$	bubble radii distribution: r_{bub}^{-n}	$n=4.3$
β	void fraction	0.03

III. EXPERIMENTAL MEASUREMENTS

In the spring of 1995, time coincident measurements of acoustic signatures and the occurrence, locations, and sizes of individual breaking waves were obtained.[17] The Naval Research Laboratory, in conjunction with the Marine Physics Laboratory, conducted the experiment from onboard the RP FLIP moored approximately 2 nm west of San Clemente Island. The acoustic signatures were obtained from the end-fire beam of a vertical array deployed at the end of a 23-m face boom mounted on the lower deck of the FLIP. The element spacing and the depth of the array were selected to interrogate a 34-m-diam disk on the ocean surface at a fre-

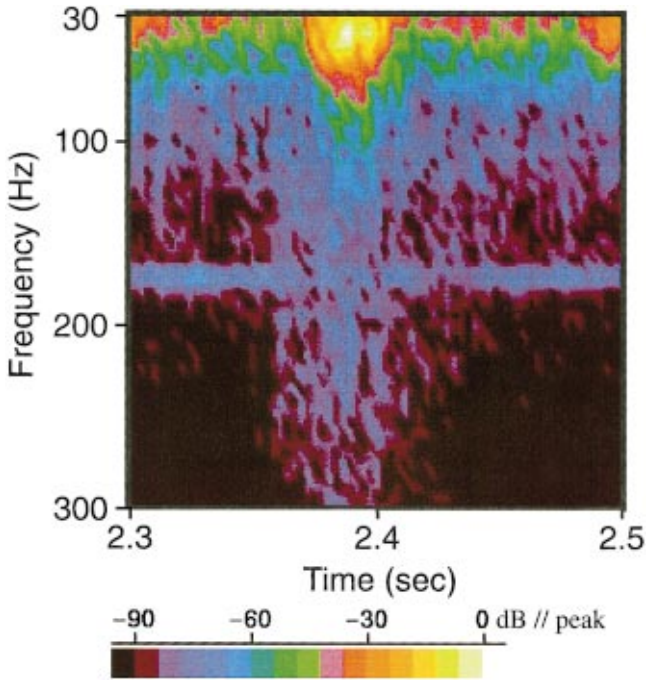

FIG. 3. Time-frequency surface obtained experimentally in at-sea measurements on the end-fire beam of an array deployed from aboard RP FLIP northeast of San Clemente Island. A single low-frequency peak in the spectra appears at ~40 Hz. Similar low-frequency peaks were observed in roughly $\frac{1}{3}$ of 221 analyzed spectra. The spectral line at 180 Hz is pump noise from the research vessel.

quency of 400 Hz. A video camera mounted on the upper deck of the FLIP recorded the breaking wave surface properties.

Figure 3 shows a time-frequency signature of a single breaking wave that was observed in the field of view of the video camera during 12 m/s winds. The video recording indicated that the active portion of the breaking wave had a duration of 3.5 s and an equivalent radius of about 7.4 m. As such, it was one of the largest waves observed during the 30-min observation period. The wave itself was a spilling breaker that was composed of three distinct crests over its 3.5-s lifetime. All of the breaking waves observed during the period were spilling rather than plunging.

A prominent feature is the single low-frequency peak near 40 Hz. The line at 180 Hz is due to pump noise from the research platform. Roughly one-third of the 221 acoustic signatures observed in the video recordings contained a peak in the 40 to 60 Hz range. The remaining signatures consisted of broadband bursts with significant energy at the lower frequencies without an obvious resonance peak. The strong harmonic line set, as predicted by the Ogũz model, was not evident in any of the measured signatures. Previous at-sea[16] and laboratory[15] measurements indicate similar spectra. The at-sea measurements did not show discernible resonance peaks; however, ambient shipping levels precluded observations below 75 Hz during most of the reported times. The laboratory measurements did, however, show individual spectral peaks below 150 Hz that were shown to be associated with bubble cloud oscillations.

IV. POINT SOURCE EXCITATION MODEL

In an attempt to develop a more physically realistic bubble cloud excitation model without the inherent resonance structure of the previous model, one considers the field produced by a distribution of point sources (newly formed bubbles) within an effectively homogeneous hemispherical bubble cloud. The field produced by a single point source within a hemispherical bubble cloud beneath a pressure-release surface is equivalent, via the method of images, to a pair of oppositely phased point sources within a spherical cloud. The total field due to a distribution of sources may then be found by summing incoherently the fields generated by the individual point sources and their images.

The field for an individual point source within a spherical cloud is found by solving for the Green's function, G, in the inhomogeneous Helmholtz equation,

$$(\nabla^2+k^2)\mathrm{G}=-\frac{4\pi\delta(r-r')\delta(\theta-\theta')\delta(\phi-\phi')}{r^2\sin\theta}. \quad (2)$$

This function must satisfy the boundary conditions, continuity of pressure and normal velocity, at the surface of the bubble cloud. The coordinate system used in this development is shown in Fig. 4 and is oriented such that the positive z direction is beneath the surface. Here the primed variables indicate source location. The Green's function may be expressed as a summation of the solutions of the particular and interior and exterior homogeneous equations,

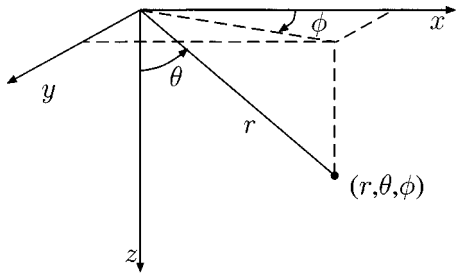

FIG. 4. Coordinate system chosen for the point source excitation model development.

$$(\nabla^2+k_c^2)\mathrm{G}_p=-\frac{4\pi\delta(r-r')\delta(\theta-\theta')\delta(\phi-\phi')}{r^2\sin\theta}, \quad (3a)$$

$$(\nabla^2+k_c^2)\mathrm{G}_{\mathrm{int}}=0 \quad \text{for } r\leqslant a, \quad (3b)$$

$$(\nabla^2+k^2)\mathrm{G}_{\mathrm{ext}}=0 \quad \text{for } r\geqslant a, \quad (3c)$$

where k_c is the effective wave number, as discussed below, within the bubble cloud.

The particular Green's function, G_p, may be derived by following a procedure similar to that found in a paper by Luk *et al.*[32] It is also presented in the text of Morse and Ingard[33] without derivation as

$$\mathrm{G}_p=ik_c\sum_{n=0}^{\infty}(2n+1)\sum_{m=0}^{n}\epsilon_m\frac{(n-m)!}{(n+m)!}\cos(m(\phi-\phi'))\times P_n^m(\cos\theta')P_n^m(\cos\theta)\times\begin{cases}j_n(k_cr')h_n(k_cr), & \text{if } r>r',\\ j_n(k_cr)h_n(k_cr'), & \text{if } r<r',\end{cases} \quad (4)$$

where

$$\epsilon_m=\begin{cases}1, & \text{if } m=0,\\ 2, & \text{if } m>0.\end{cases}$$

The homogeneous solutions may be expressed, based on the geometry of the problem, in terms of Legendre polynomials, spherical Bessel or Hankel functions, and undetermined constants as

$$\mathrm{G}_{\mathrm{int}}=\sum_{n=0}^{\infty}\sum_{m=-n}^{n}a_{nm}e^{im\phi}P_n^m(\cos\theta)j_n(k_cr), \quad (5a)$$

$$\mathrm{G}_{\mathrm{ext}}=\sum_{n=0}^{\infty}\sum_{m=-n}^{n}b_{nm}e^{im\phi}P_n^m(\cos\theta)h_n(kr). \quad (5b)$$

The boundary conditions at the bubble cloud–water interface are used to solve for a_{nm} and b_{nm} yielding an exterior solution $(r>a)$ of

$$G(\mathbf{r}',\mathbf{r},k)$$
$$=\sum_{n=0}^{\infty}\sum_{m=-n}^{n} ik_c(2n+1)\frac{(n-m)!}{(n+m)!}$$
$$\times e^{-im\phi'}P_n^m(\cos\theta')j_n(k_c r')$$
$$\times\frac{(h_n(k_c a)j_n'(k_c a)-h_n'(k_c a)j_n(k_c a))}{((\rho/\rho_c)h_n(ka)j_n'(k_c a)-(k/k_c)h_n'(ka)j_n(k_c a))}$$
$$\times e^{im\phi}P_n^m(\cos\theta)h_n(kr). \tag{6}$$

A simple check, necessary although not sufficient, may be performed by allowing $k_c \to k$ and $\rho_c \to \rho$, i.e., removing the bubble cloud–water discontinuity. In doing this, Eq. (6) reduces to Eq. (4) as expected.

As postulated earlier, the bubble clouds that form beneath breaking waves may be modeled as a homogeneous media at low frequencies; i.e., frequencies lower than the natural frequency of the largest bubbles. The work of Commander and Prosperetti,[34] based on linearization of a nonlinear model of pressure wave propagation within a bubbly liquid, yields an expression for the effective wave number within the bubble cloud as

$$k_c^2=\omega^2/c^2+4\pi\omega^2\overline{n}\int_0^{\infty}\frac{r_{\text{bub}}f(r_{\text{bub}})dr_{\text{bub}}}{\omega_o^2-\omega^2+2ib\omega}, \tag{7}$$

where ω_o and b are the frequency dependent natural frequency and damping factor of individual bubbles, $\overline{n}$ is the number of bubbles per unit volume, and $f(r_{\text{bub}})$ is the normalized bubble radii distribution function. See the work of Commander and Prosperetti[34] for a detailed derivation of these parameters. The above expressions, Eqs. (6) and (7), may be used to predict the far-field pressure due to a distribution of point sources (excited bubbles) by incoherently summing the field for each source and its image.

V. EXCITATION MECHANISM

Individual bubbles entrained within the process of wave breaking may be excited via a number of possible mechanisms. Once excited they radiate acoustic energy. A number of excitation mechanisms have been proposed,[35] such as radial and asymmetric flows and turbulence. The results of the present analysis are relatively independent of the excitation mechanism chosen. Therefore, a simple model will be used to make the analysis tractable. Hollet and Heitmeyer[36] proposed that a bubble is excited into oscillation by a sudden pressure change when it is instantly entrained into the water at a depth. A more detailed explanation may be found in the text by Leighton.[35] The pressure difference at the bubble surface would be that of the liquid pressure plus surface tension,[3]

$$P_o=\rho g z'+\frac{2\sigma}{r_{\text{bub}}}. \tag{8}$$

The pressure field radiated by an excited bubble is that of a damped sinusoid.[4] Therefore, the pressure at the bubbles surface can be expressed as

$$p_s(t)=P_o e^{-bt}\cos(\omega_o t+\psi). \tag{9}$$

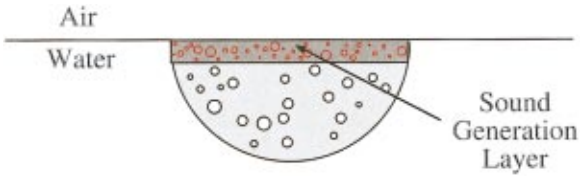

FIG. 5. Distribution of point sources (newly entrained bubbles) used for comparing the point source excitation model with the disklike excitation of Ogüz model. Points sources are randomly distributed within a thin layer (7.05×10^{-3} m) just beneath the air–sea interface.

The monopole amplitude[37] or source strength as a function of time would then be given by

$$S(t)=r_{\text{bub}}e^{-ikr_{\text{bub}}}p_s(t). \tag{10}$$

Since the bubble is considered to be entrained instantaneously at a depth, ψ will be considered to be zero. The source strength spectrum, $S(\omega)$, of an individual bubble is obtained via the Fourier transform of Eq. (10) and is expressed as

$$S(\omega)=\frac{r_{\text{bub}}e^{-ikr_{\text{bub}}}P_o(b-i\omega)}{\sqrt{2\pi}(b^2-2ib\omega-\omega^2+\omega_o^2)}. \tag{11}$$

Therefore, for some large distance exterior of the bubble cloud, the pressure spectrum, due to one point source, is determined by the product of the source strength spectrum and the exterior Green's function. The power spectrum from a distribution of point sources and their images is then determined by

$$P(\omega,\overline{r'})=\sum_{n=1}^{N}|S_n(\omega)|^2|G_n(\mathbf{r},\mathbf{r}_n')-G_n(\mathbf{r},\mathbf{r}'_{\text{image }n})|^2, \tag{12}$$

where N is the total number of active bubbles.

VI. MODEL COMPARISON

A comparison between the proposed and existing models is made by allowing the point source distribution of the proposed model to be analogous to the piston excitation of the Ogüz model. This is done by randomly distributing the sources within a thin layer just beneath the water's surface (see Fig. 5). The angle-frequency intensity field shown in Fig. 6 is due to 1000 active bubbles distributed within a layer extending 7.05×10^{-3} m beneath the surface. The parameters contained in Table I were used here for comparison purposes. The bubble radii distribution of the active bubbles is the same as that of the bubbles composing the bubble cloud. In comparing Figs. 2 and 6, one sees the same basic harmonic structure. The point source excitation model predicts broader resonance peaks and a steeper decrease in peak levels with increasing frequency. However, the basic structures are similar and both exhibit characteristics not seen in experimental measurements.

VII. NEW SOURCE DISTRIBUTION

In an effort to explain the difference between the models' predictions and experimental measurements one may note several postulates of the models. First, the models are

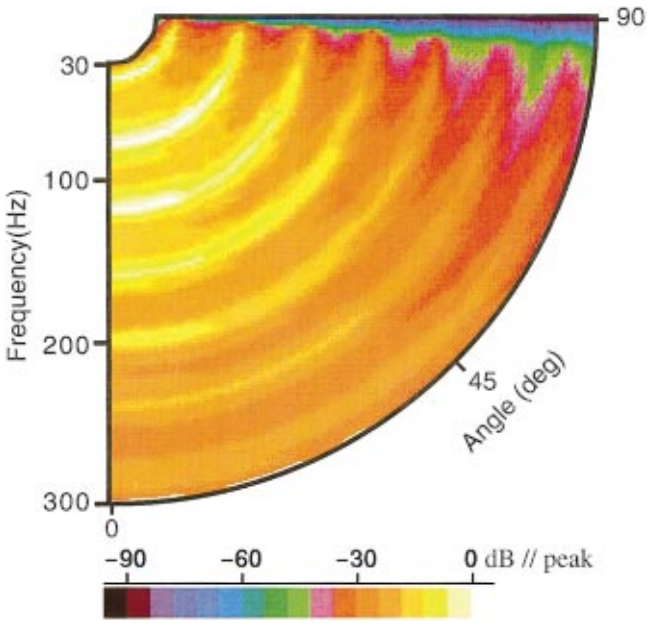

FIG. 6. Angle-frequency surface of the field predicted by the point source excitation model with the layerlike source distribution as illustrated above. The field characteristics are similar to those predicted by the Ogũz model. The same harmonic structure is apparent, although the resonance peaks are broader. As in the case of the Ogũz model, these characteristics are not evident in experimental measurements.

based on a perfectly spherical bubble cloud geometry which is obviously an abstraction of entrained clouds under open-ocean breaking waves. Second, the models consider a well-defined interface between the edge of the cloud and surrounding water. Since the predicted resonances of the cloud are associated with the higher modes of the cloud volume, one may *a priori* assume that these postulates could contribute to the disparity with experimental measurements. However, any shape of an entrained bubble cloud will have higher order modes of vibrations that would necessarily give rise to resonances similar to those predicted by the spherical geometry. In studying the images of entrained bubble clouds reported by Lamarre and Melville[38] (wave tank) and by Deane[39] (surf), one comes to the conclusion that there does in fact appear to be a relatively distinct boundary between the cloud and surrounding water. At the frequencies of interest here, the length scale of the boundaries would be on the order of 0.2 m, or roughly a quarter of the bubble cloud's modeled radius, before being on the same order of a wavelength. This does not appear to be the case in these images. Therefore, neither of these two postulates would appear to give rise to the observed discrepancies.

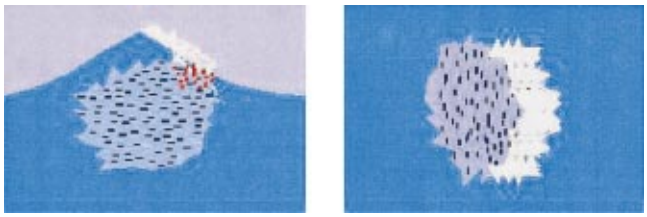

FIG. 7. Illustration of entrainment region during the breaking of a wave (side view and top view). Newly formed bubbles are entrained at the leading edge of the breaker as it propagates to the right.

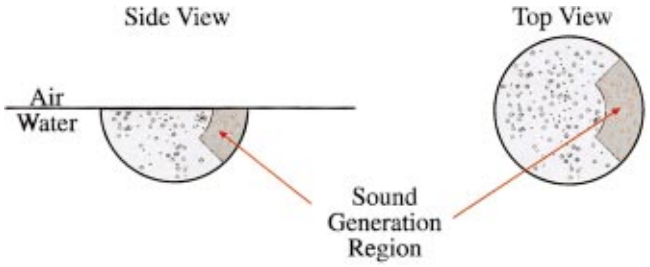

FIG. 8. Distribution of point sources modeling a hypothetical entrainment of bubbles during the breaking of a wave. The active bubbles are randomly distributed in the outer portion of a volumetric sector.

The main advantage of the point source excitation model is that sources can be distributed within the bubble cloud based on the physical mechanisms occurring during wave breaking. To date, no conclusive study has been carried out to determine the characteristics of the entrainment and how they vary for wave parameters and breaker type. However, one may proceed by making assumptions based on observations made in the existing literature. Kolaini and Crum[40] observed that during the breaking of a wave bubbles are entrained at its leading edge. This has also been proposed in theoretical work by Longuet-Higgins and Turner.[41] The shape and relative dimensions of the entrainment region may be drawn from observations[42] and photographs[38] in the works of Lamarre and Melville. An attempt to illustrate these properties within a breaking wave is shown in Fig. 7. The actual entrainment region used in this study is shown in Fig. 8. The active bubbles are randomly distributed within the boundaries: $a/2 \leqslant r' \leqslant a$, $-\pi/4 \leqslant \phi' \leqslant \pi/4$, and $\pi/4 \leqslant \theta' \leqslant \pi/2$.

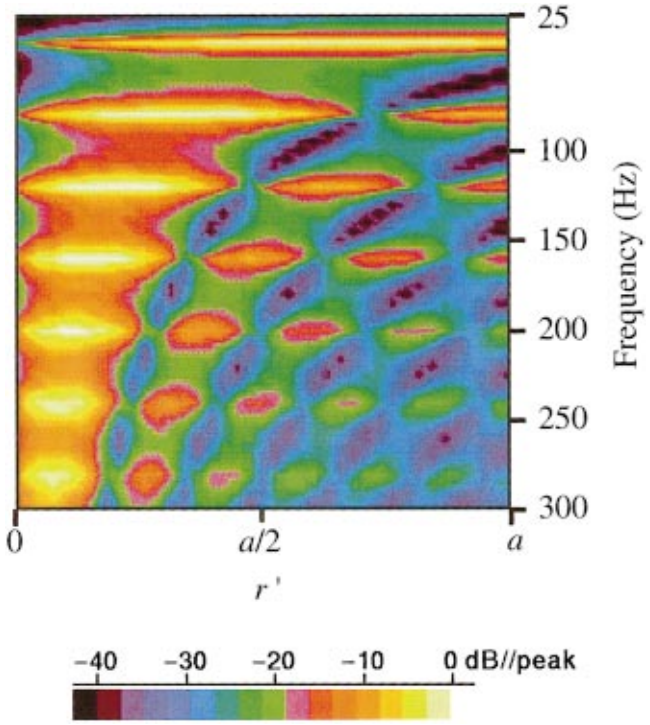

FIG. 9. Axial spectrum generated by moving the point source from the origin toward the perimeter of the bubble cloud along $\theta' = 3\pi/8$. This shows that the fundamental mode is predominant when the point source is in the outer portion of the cloud.

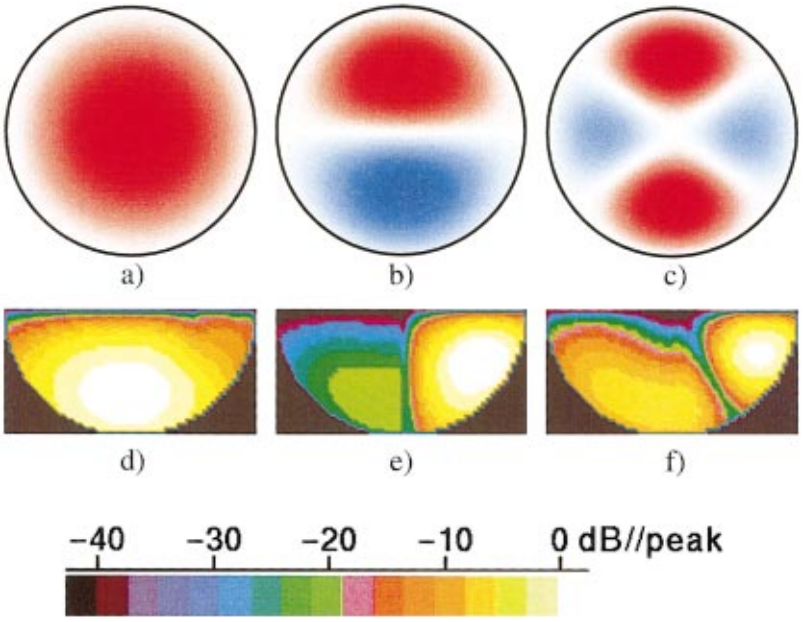

FIG. 10. Parts (a), (b), and (c) represent the instantaneous internal pressure field for the first three modes of oscillation for the given cloud composition and geometry. The resonances of the complete sphere, as prescribed by the method of images, are of interest here. They have resonant frequencies of 38, 56, and 72 Hz, respectively. The remaining parts, (d), (e), and (f), represent the interior acoustic intensity within the hemispherical cloud excited by the random distribution of active bubbles, as described in the text, at frequencies of excitation corresponding to first three modes.

One may investigate the effect of the source locations by obtaining the response of the cloud by a single source in different locations. Figure 9 shows the far-field axial ($\theta=0$) pressure intensity as a function of frequency as a single point source is moved from the origin of the hemispherical cloud to the outer edge along the $\theta'=3\pi/8$ radial. It is evident that as the source is moved away from the origin most of the energy is contained within the fundamental mode. At positions near the origin most of the energy exists in higher order modes.

This phenomenon may be explained by considering the modes of the spherical cloud. It is the modes of the full sphere, as prescribed by the method of images, which are of interest here. Figures 10(a), (b), and (c) show the interior pressure field within the spherical cloud for the first three modes of vibration: 38, 56, and 72 Hz, respectively. Pressure nodes within the spherical cloud can be seen for the higher-order modes. Therefore, when an active bubble is near a node it is less effective at exciting the cloud into oscillation or more effective if it is near an anti node. Since higher

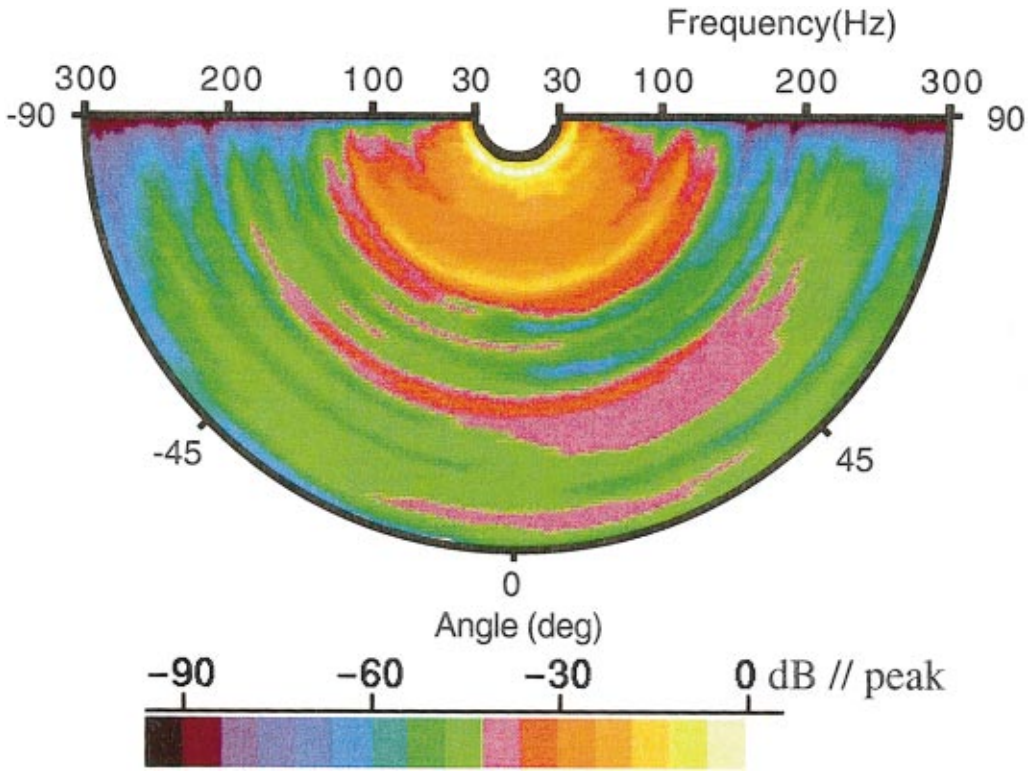

FIG. 11. Angle-frequency surface of the field predicted by the point source excitation model with the sectorlike source distribution as illustrated above. The spectra is dominated by a low-frequency peak similar to that of at-sea measurements. Harmonics are still noticeable, although they are greatly reduced in level. The third and fifth harmonics are at least 16 and 32 dB lower, respectively, than the fundamental peak.

modes have more nodes within the sphere they are less likely to be excited by a distribution of active bubbles.

Figures 10(d), (e), and (f) are the interior acoustic energy when the cloud is excited by the sectorlike distribution of active bubbles at frequencies corresponding to the first three modes of vibration of the spherical cloud. The node at the upper surface is from the pressure release boundary condition. Since the orientation is chosen arbitrarily for Figs. 10(b) and (c), the nodal pattern for the two higher modes appears to be rotated in Figs. 10(e) and (f). The larger excited volume evident in the fundamental mode will correspond to higher far-field radiation levels, as will be seen in the next figure.

The angle-frequency surface in Fig. 11 shows the sound field generated by the sector like distribution of active bubbles. The harmonics of the fundamental mode of resonance of the bubble cloud are greatly reduced. The odd harmonics are more prominent than those of the even harmonics. However, the third and fifth harmonics are at least 16 and 32 dB lower, respectively, than the fundamental. The radiation pattern is slightly asymmetric, which is expected at the low frequencies of interest.

The fundamental peak of the bubble cloud resonance still coincides with the single low-frequency peak of the experimental signature. However, the smooth rolloff from the single peak is not successfully predicted by the new model. Several mechanisms or a combination of mechanisms could account for this discrepancy. One may also be able to vary properties of the sound generation region to tailor the model's predictions. To that end, exhaustive measurements of the mechanisms governing the entrainment of air within oceanic breaking waves would be needed to aid in that development.

VIII. CONCLUSIONS

In this article we have shown discrepancies between the spectra predicted by an existing theoretical model which considers sound generation from an individual breaking wave and that of at-sea experimental measurements. We have proposed an alternative model which allows more flexibility in implementing cloud excitation mechanisms accurately. Due to the lack of a complete study of the bubble entrainment mechanisms of breaking waves, we have proposed a hypothetical distribution of sources within the bubble cloud. Spectra obtained by the new model with the more realistic distribution of sources have spectral structure that is more in agreement with at-sea observations. This new model provides a means of implementing physically realistic cloud excitation mechanisms and suggests the need for more in-depth studies of the entrainment and excitation of individual bubbles which occur in open-ocean breaking waves.

ACKNOWLEDGMENTS

The authors would like to thank Dr. Ralph Goodman and Dr. Ali Kolaini for helpful discussions during the development of this work. This work has been supported by The Office of Naval Research base funding at The Naval Research Laboratory.

[1] V. O. Knudsen, R. S. Alford, and J. W. Emling, "Underwater ambient noise," J. Mar. Res. **7**, 410–429 (1948).
[2] G. M. Wenz and M. P. Bradley, "Acoustic ambient noise in the ocean: Spectra and sources," J. Acoust. Soc. Am. **34**, 1936–1956 (1962).
[3] P. A. Crowther, "Bubble noise creation mechanisms," in *Sea Surface Sound*, edited by B. R. Kerman (Kluwer Academic, Dordrecht, The Netherlands, 1988), pp. 131–150.
[4] H. Medwin and M. M. Beaky, "Bubble sources of the Knudsen sea noise spectra," J. Acoust. Soc. Am. **86**, 1124–1130 (1989).
[5] H. Medwin and A. C. Daniel, Jr., "Acoustical measurements of bubble production by spilling breakers," J. Acoust. Soc. Am. **88**, 408–412 (1990).
[6] H. C. Pumphrey and J. E. Ffowcs Williams, "Bubbles as Sources of Ambient Noise," IEEE J. Ocean Eng. **15**, 268–274 (1990).
[7] G. E. Updegraff and V. C. Anderson, "Bubble noise and wavelet spill recorded 1 m below the ocean surface," J. Acoust. Soc. Am. **89**, 2264–2279 (1991).
[8] M. R. Loewen and W. K. Melville, "A model of the sound generated by breaking waves," J. Acoust. Soc. Am. **90**, 2075–2080 (1991).
[9] J. Wu, "Bubble populations and spectra in near-surface ocean: summary and review of field measurements," J. Geophys. Res. **86**, 457–463 (1981).
[10] W. M. Carey and M. P. Bradley, "Low-frequency ocean surface noise sources," J. Acoust. Soc. Am. **78**, S1–S2 (1985).
[11] A. Prosperetti, "Bubble-related ambient noise in the ocean," J. Acoust. Soc. Am. **78**, S2 (1985).
[12] D. J. Kewley, D. G. Browning, and W. M. Carey, "Low-frequency wind-generated ambient noise source levels," J. Acoust. Soc. Am. **88**, 1894–1902 (1990).
[13] S. W. Yoon, L. A. Crum, A. Prosperetti, and N. Q. Lu, "An investigation of the collective oscillations of a bubble cloud," J. Acoust. Soc. Am. **89**(2), 700–706 (1991).
[14] A. Kolaini, R. A. Roy, and L. A. Crum, "An investigation of the acoustic emissions from a bubble plume," J. Acoust. Soc. Am. **89**, 2452–2455 (1991).
[15] M. R. Loewen and W. K. Melville, "An experimental investigation of the collective oscillations of bubble plumes entrained by breaking waves," J. Acoust. Soc. Am. **95**, 1329–1343 (1994).
[16] R. D. Hollett, "Observations of underwater sound at frequencies below 1500 Hz from breaking waves at sea," J. Acoust. Soc. Am. **95**, 165–170 (1994).
[17] J. A. Schindall and R. M. Heitmeyer, "Breaking wave noise measurements at frequencies below 400 Hz," J. Acoust. Soc. Am. **100**, 2732 (1996).
[18] A. Prosperetti, "Bubble-related ambient noise in the ocean," J. Acoust. Soc. Am. **84**, 1042–1054 (1988).
[19] W. M. Carey, J. W. Fitzgerald, and D. G. Browning, "Low Frequency Noise from Breaking Waves," in *Natural Physical Source of Underwater Sound*, edited by B. R. Kerman (Kluwer Academic, Boston, 1993), pp. 277–304.
[20] H. N. Ogũz, "A theoretical study of low-frequency oceanic ambient noise," J. Acoust. Soc. Am. **95**, 1895–1912 (1994).
[21] H. Medwin, "*In situ* acoustic measurements of bubble population in coastal ocean waters," J. Geophys. Res. **88**, 599–611 (1970).
[22] P. A. Kolovayev, "Investigation of the concentration and statistical size distribution of wind-produced bubbles in the near-surface ocean layer," Oceanology **15**, 659–661 (1976).
[23] H. Medwin, "Acoustical determinations of bubble-size spectra," J. Acoust. Soc. Am. **62**, 1041–1044 (1977).
[24] H. Medwin, "Counting bubbles acoustically: a review," Ultrasonics **15**, 7–13 (1977).
[25] H. Medwin, "*In situ* acoustic measurements of microbubbles at sea," J. Geophys. Res. **82**, 971–976 (1977).
[26] B. D. Johnson and R. C. Cooke, "Bubble populations and spectra in coastal waters: a photographic approach," J. Geophys. Res. **84**, 3761–3766 (1979).
[27] G. B. Crawford and D. M. Farmer, "On the spatial distribution of ocean bubbles," J. Geophys. Res. **92**, 8231–8243 (1987).
[28] H. Medwin and N. D. Breitz, "Ambient and transient bubble spectral densities in quiescent seas and under spilling breakers," J. Geophys. Res. **94**, 12751–12759 (1989).
[29] S. Vagle and D. M. Farmer, "The measurement of bubble-size distributions by acoustical backscatter," J. Atmos. Ocean. Technol. **9**, 630–644 (1992).

[30] J. Wu, ''Individual characteristics of whitecaps and volumetric description of bubbles,'' IEEE J. Ocean Eng. **17**, 150–158 (1992).
[31] E. C. Monahan and M. Lu, ''Acoustically relevant bubble assemblages and their dependence on meterological parameters,'' IEEE J. Ocean Eng. **15**, 340–349 (1990).
[32] K. M. Luk, K. W. Leung, K. Y. A. Lai, and D. Lin, ''Analysis of hemispherical dielectric resonator antenna,'' Radio Sci. **28**, 1211–1218 (1993).
[33] P. M. Morse and K. U. Ingard, *Theoretical Acoustics* (Princeton U. P., Princeton, NJ, 1968), p. 352.
[34] K. W. Commander and A. Prosperetti, ''Linear pressure waves in bubbly liquids: Comparison between theory and experiments,'' J. Acoust. Soc. Am. **85**, 732–746 (1989).
[35] T. G. Leighton, *The Acoustic Bubble* (Academic, London, 1994), p. 234.
[36] R. D. Hollett and R. M. Heitmeyer, ''Noise generation by bubbles formed in breaking waves,'' in *Sea Surface Sound*, edited by B. R. Kerman (Kluwer Academic, Dordrecht, The Netherlands, 1988), pp. 449–461.
[37] A. D. Pierce, *Acoustics: An Introduction to its Physical Principles and Applications* (Acoustical Society of America, Woodbury, NY, 1989), pp. 159–165.
[38] E. Lamarre and W. K. Melville, ''Instrumentation for the Measurement of Void-Fraction in Breaking Waves: Laboratory and Field Results,'' IEEE J. Ocean Eng. **17**, 204–215 (1992).
[39] G. B. Deane, ''Sound generation and air entrainment by breaking waves in the surf zone,'' J. Acoust. Soc. Am. **102**, 2671–2689 (1997).
[40] A. Kolaini and L. A. Crum, ''Observations of underwater sound from laboratory breaking waves and the implications concerning ambient noise in the ocean,'' J. Acoust. Soc. Am. **96**, 1755–1765 (1994).
[41] M. S. Longuet-Higgins and J. S. Turner, ''An 'entraining plume' model of a spilling breaker,'' J. Fluid Mech. **63**, 1–20 (1974).
[42] E. Lamarre and W. K. Melville, ''Void-fraction measurements and sound-speed fields in bubble plumes generated by breaking waves,'' J. Acoust. Soc. Am. **95**, 1317–1328 (1994).

Experimental study of geo-acoustic inversion uncertainty due to ocean sound-speed fluctuations

Martin Siderius, Peter L. Nielsen, and Jürgen Sellschopp
SACLANT Undersea Research Centre, Viale San Bartolomeo 400, 19138 La Spezia, Italy

Mirjam Snellen and Dick Simons
TNO Physics and Electronics Laboratory, Underwater Acoustics Group, Oude Waalsdorperweg 63, 2509 JG The Hague, The Netherlands

(Received 28 June 2000; revised 12 March 2001; accepted 27 April 2001)

Acoustic data measured in the ocean fluctuate due to the complex time-varying properties of the channel. When measured data are used for model-based, geo-acoustic inversion, how do acoustic fluctuations impact estimates for the seabed properties? In May 1999 SACLANT Undersea Research Center and TNO-Physics and Electronics Laboratory (FEL), conducted a shallow-water experiment on the Adventure Bank off the southwest coast of Sicily, Italy to assess the effects of a time-varying ocean on acoustic propagation and geo-acoustic inversion. A favorable area for acoustic propagation was identified which had slight internal wave activity and a weakly range-dependent bathymetry with sand-like bottom properties. Oceanographic and acoustic measurements were performed continuously over a 3-day period. Broadband (0.2–3.8 kHz) acoustic signals from a bottom-moored source were transmitted over fixed paths and received on a moored vertical hydrophone array. During the transmissions extensive environmental measurements (e.g., sound speed, current, sea-surface waveheight, etc.) were made to correlate the time-varying environmental and acoustic data. Modeled acoustic data show time variability which agrees with the measurements. Results illustrate severe problems when modeling shallow-water acoustic propagation at ranges beyond a few kilometers in the frequency band considered. Further, the acoustic fluctuations in time caused erroneous time variability in inverted seabed properties. [DOI: 10.1121/1.1385898]

PACS numbers: 43.30.Zk, 43.30.Re, 43.30.Pc, 43.30.Ma [DLB]

I. INTRODUCTION

Prediction of sound propagation in the ocean is generally performed by assuming time invariance for the short period of an experiment. This assumption has been shown to be sufficient for certain shallow-water regions as numerical modeling of received energy levels[1] and received time series[2,3] has been performed successfully by using ''frozen'' environmental inputs. However, other experiments conducted in particular shallow-water regions show significant variability in acoustic data caused by changes in the oceanographic conditions with time.[4,5] Anomalies in acoustic energy levels in a certain frequency band were detected during the Yellow Sea summer experiment,[6] and decorrelation times as low as a few minutes were observed in time series acquired during the 1995 SWARM experiment.[7] The fluctuations in the acoustic data from these experiments are most likely due to a strong internal wave activity.[8,9] The appearance of strong internal waves was known *a priori* to those experiments, and the objective of the experiments was to investigate how this time-dependent oceanography affects the acoustic propagation. Accurate predictions of sound propagation in these regions cannot be achieved unless a good estimate of the time- and range-varying environment is included in the modeling. Therefore, a successful propagation prediction depends on the amount of environmental information available and the degree of postprocessing desired from the raw acoustic signals (e.g., averaged transmission loss or complete time series).

To address the issue of modeling acoustic propagation in time-dependent shallow-water environments, SACLANT Undersea Research Center and TNO-FEL conducted the Advent'99 experiments. These took place in May 1999 on the Adventure Bank off the southwest coast of Sicily. Broadband linear-frequency-modulated (LFM) and multitone (MT) acoustic signals were transmitted every minute for up to 18 h, and the signals were received on a moored 64-element vertical line array (VLA) at three fixed ranges of 2, 5, and 10 km. This experimental setup allows, to some extent, isolation of the channel's time- and range-dependence. The experimental area was carefully chosen to have weakly range-dependent bathymetry and bottom properties, and relatively low time variability in the water column (i.e., absence of strong tidal-induced internal waves, which is typical for the Mediterranean Sea). In contrast to the Yellow Sea and the 1995 SWARM experiments, the region for the Advent'99 experiment shows favorable (i.e., easy to model) conditions for acoustic propagation modeling. The reason for choosing this site was to assess the degree of time variability of received acoustic data in a benign shallow-water area and to further understand the limitations of propagation modeling in a time-varying ocean. Only oceanographic data taken from the measurements were used in the propagation modeling (i.e., no synthetic environments were generated using ocean modeling).

Matched-field processing (MFP) geo-acoustic inversion is a technique that uses measured acoustic signals to deter-

mine seabed properties.[10–13] For MFP inversion, a propagation model is used to determine the acoustic response using various combinations of seabed input parameters. Efficient search algorithms are applied to determine the parameter set giving the optimal match between modeled and measured data (for a given cost function). The assumption being the best fit to the measured data occurs when the correct seabed parameters are used. Using measured data, the MFP-based geo-acoustic inversion method has been demonstrated to be a useful technique for estimating shallow-water seabed parameters.[14,15] Variations in seabed parameter predictions can result when MFP geo-acoustic inversion is applied to different time realizations of measured acoustic data. This undesirable outcome can be caused both by the numerical methodology and by fluctuations in the environment. Methodological variability occurs in cases where unknown parameters have little sensitivity and therefore the fitness between modeled and measured fields does not depend on the value of a particular parameter. In a related article, a detailed analysis of the numerical methodology of MFP, geo-acoustic inversion has been considered.[16] Using a subset of the data considered here (multitones at 2-km source–receiver separation), the article shows that with a more complex description of the seabed (than that used here) several of the parameters are unstable due primarily to the numerical method. Here, a simple parametrization is chosen and that provides numerical stability, whereby slight perturbations to the acoustic data result in only slight perturbations to the predicted parameter values.

The other contribution to the variability in MFP geo-acoustic parameter estimates is due to the fluctuations in the measured acoustic fields. The purpose of this paper is to determine how acoustic time fluctuations impact geo-acoustic inversion. There has been much effort toward improving the numerical methods of MFP inversion; however, there may be limitations due to the environment. It is known that acoustic fields measured in the ocean will fluctuate with time due to a dynamic rough sea surface and random sound-speed fluctuations in the water column. When used for geo-acoustic inversion, model parameters will adjust and try to compensate for the fluctuations. The complicated ocean sound-speed structure causing the true acoustic fluctuations are typically not taken into account in the computation. How do the acoustic fluctuations impact geo-acoustic inversion? Acoustic fluctuations may translate into harmless shifts in apparent (predicted) source or receiver positions. Or, these fluctuations may translate into not-so-harmless shifts in predicted seabed properties (e.g., sediment sound speed). For frequencies below 1 kHz, the seabed properties do not change during the time of an acoustic experiment. However, if the geo-acoustic inversion modeling compensates for acoustic fluctuation by adjusting seabed properties, then an erroneous time variability will appear in the inverted seabed properties. One application for estimating seabed properties over a large area is using an MFP, geo-acoustic survey with a towed sound source and moored array of hydrophones.[17] If seabed property estimates depend on ocean variability it may be difficult, or impossible, with such a towed system, to distinguish between true sediment spatial variability and that caused by ocean fluctuations (unless all the time variability of the ocean is included in the acoustic propagation modeling). Such a system would require placing a limitation on acoustic frequency and source–receiver range separation that depends on the oceanography.

An overall description of the Advent'99 experiment is given in Sec. II, followed by analyses of oceanographic and acoustic data collected. Correlations between oceanographic and acoustic variability are established, and correlation time scales for the acoustic data are presented as a function of acoustic frequency and propagation range. In Sec. III MFP, geo-acoustic inversion is performed by searching for bottom properties and source–receiver geometry to obtain the best estimate of seabed properties (and best agreement between modeled and measured data). Environmental parameters found for subsequent received signals indicate the impact of the time-varying ocean on parameter estimates. Also in Sec. III, a simulated acoustic data set is generated using measured bathymetry and two-dimensional sound-speed profiles, which is subsequently used for geo-acoustic inversion. These simulations produce inverted seabed properties with a variability that closely resembles those found using the measured data. In this way, the variability in the inversion results are attributed primarily to the ocean sound-speed profiles.

II. THE ADVENT'99 EXPERIMENTS

A schematic of the experimental setup for the Advent'99 experiment is shown in Fig. 1. Broadband acoustic LFM and MT signals covering a frequency band from 200 Hz to 1.6 kHz were transmitted every minute for up to 18 h. The acoustic source was mounted 4 m off the bottom in a moored tower at a water depth of 76 m (source depth $z_s = 72$ m). The signals were received on a moored 62-m, 64-element VLA at three fixed ranges of 2, 5, and 10 km. The signals were transmitted for around 5 h along the 2- and 5-km track and 18 h along the 10-km track. In addition, LFM signals in the frequency band from 2.0 to 3.8 kHz were transmitted for around 4 h along the 5-km track. The replica signal was measured for each transmission (except for the 2.0–3.8-kHz transmissions) using a reference hydrophone near the source. Each of these replicas was used to eliminate time-varying properties of the source when estimating the transfer function of the waveguide.

The sound-speed profile in the water column was measured by a 49-element conductivity–temperature–depth (CTD) chain towed by ITNS CICLOPE with a data sampling every 2 s. The CTD chain spanned around 80% of the water column, and the chain was towed continuously between the acoustic source and the VLA (10-km track) during all the acoustic transmissions (except for the 2.0–3.8-kHz transmissions). The tows resulted in sound-speed profile sections every hour along the 10-km propagation track, indicating both time- and range-variability. Details are provided in Sec. II B.

Oceanographic equipment was moored along the acoustic propagation track in order to correlate changes in the received acoustic signals with changes in the environment. Measurements of the sea surface height was performed by a wave rider moored between the source and the VLA for the 2-km acoustic track (sampling every 0.4 s). Two bottom-

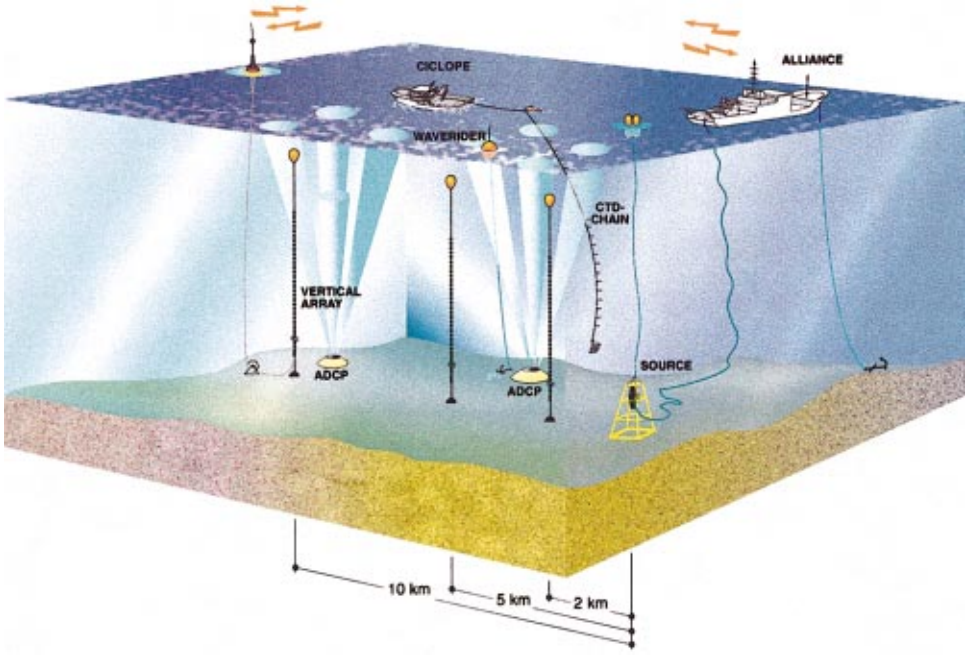

FIG. 1. Advent'99 experimental region on Adventure Bank. Acoustic transmissions were made from a source moored 4 m off the bottom, and the signals were received on a 64-element bottom-moored VLA at three ranges from the source.

moored acoustic-Doppler-current-profiler (ADCP) systems were recording the current over almost the entire water column. A 600-kHz ADCP (Barnacle) system was moored close to the source with a data sampling every 5 min, and a 300-kHz system (Sentinel) was positioned at the VLA for the 10-km acoustic track, acquiring data every 6 min. Besides the bottom-moored ADCP systems, the current was measured by the ship-born ADCP system on the NRV ALLIANCE. Details concerning the collected wave rider and ADCP data are included in the Appendix.

The meteorological condition (e.g., wind speed and direction, temperature) was determined continuously by the onboard (NRV ALLIANCE) meteo system, and satellite images of the sea-surface temperature were provided every day. Seismic surveys were performed along the propagation tracks to estimate the bottom-layering structure and the sound speeds in the layers.

A. Acoustic data

The similarity between the received signals across the VLA is determined by applying a correlator similar to the normalized Bartlett power. This correlator is often used in geo-acoustic inversion as a measure of the mismatch between modeled and experimental data.[13] Here, the modeled data are substituted by one of the received signals (reference signal), which is correlated with the subsequent received signals during the fixed path experiment (matched-field correlation). The normalized Bartlett power between the reference signal and any of the other received signals is defined as follows:

$$B = \frac{|\Sigma_{i=1}^{N_D} p_i q_i^*|}{\sqrt{\Sigma_{i=1}^{N_D}|p_i|^2 \Sigma_{i=1}^{N_D}|q_i|^2}}, \tag{1}$$

where N_D is the number of hydrophones. The complex pressure vectors p_i and q_i are obtained by a Fourier transform of the time series, and (*) denotes the complex conjugate operation. The measure in Eq. (1) corresponds to the generalized beamformer, and it has a value of 1 for two identical signals and 0 for completely uncorrelated signals. The correlation of the chosen reference signal with the subsequent received signals is shown in Fig. 2. Only the first 4.5 h of the correlation is shown for comparison between the three ranges.

In general the correlation time decreases as the frequency and propagation range increases: the acoustic signal is more sensitive to changes in the environment at higher frequencies, and the signal propagates through more of these changes at longer ranges. At the 2-km range the similarities of the signals are high within the 4.5 h, but at higher frequencies the correlation decreases smoothly as the geo-time progresses. This decrease in correlation is clearly seen for the 5- and 10-km ranges, where the value of the correlation changes abruptly at frequencies between 600 and 700 Hz. For the 2.0–3.8-kHz transmissions along the 5-km track, the received signals rapidly decorrelate (within a few minutes). The very low correlation for certain geo-times and all frequencies is due to missing acoustic data, or due to the high noise level from ITNS CICLOPE towing the CTD chain as it approaches the VLA. During the broadband (200–800-Hz) propagation modeling and geo-acoustic inversion (Sec. III), a maximum value of the Bartlett power in Eq. (1) between the data and model was determined as 0.85 and 0.65 for the 2- and 10-km track, respectively. Using these optimized values of the correlator as a threshold, the maximum time of propagation is several hours for the 2-km track and less than an hour for the 10-km track. After that time, the changes in the environment affect the acoustic propagation significantly.

B. Oceanographic data

The ITNS CICLOPE towed the CTD chain along the track between the moored source and the VLA during the three fixed propagation path experiments. Sections of time- and

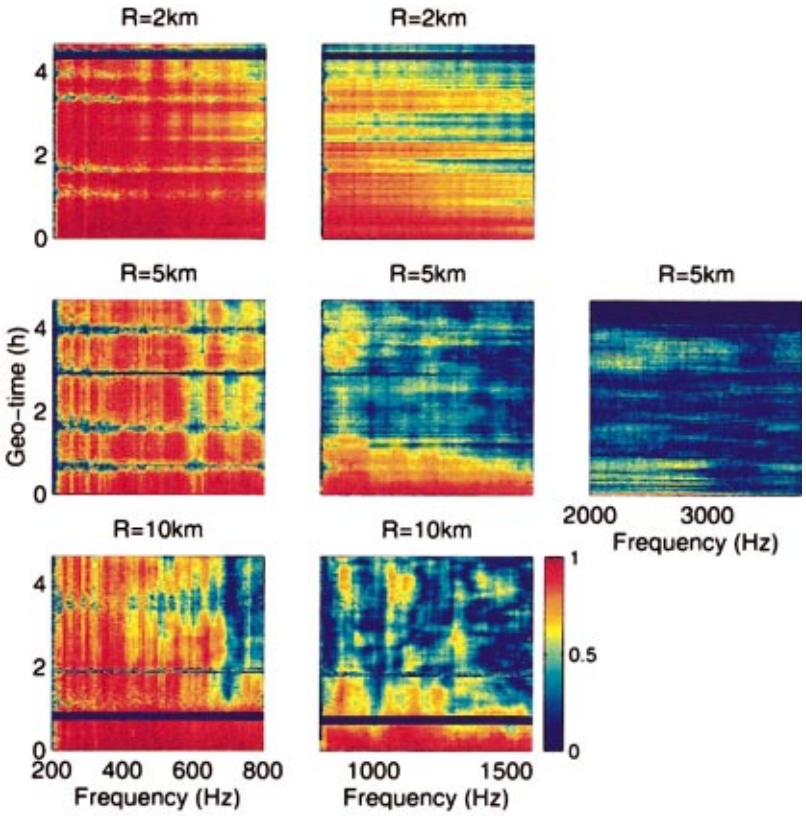

FIG. 2. Matched-field correlation of the received acoustic signals as a function of frequency and geo-time (up to 4.5 h) for the three fixed propagation paths.

range-dependent sound-speed profiles were acquired every hour along the 10-km propagation track (the CTD-chain track was kept constant over the three experiments even though the VLA was moved). Sound-speed profiles were subsampled every minute from these sections, which corresponds to a range separation of 140 m between the profiles. Each CTD sensor was positioned around 1.5 m apart in depth with the first sensor at a depth of 2.5 m. The time- and range sections are not fully ''synoptic'' representations of the water column due to the time of 1 h required to complete one tow section. Examples of the sound-speed structure at four different times along the 10-km track are shown in Fig. 3. The source and VLA positions (for that day), and the bathymetry along the propagation path are also indicated.

All the profiles from the CTD tow show a weak time- and range dependency that divides the 10-km track into a

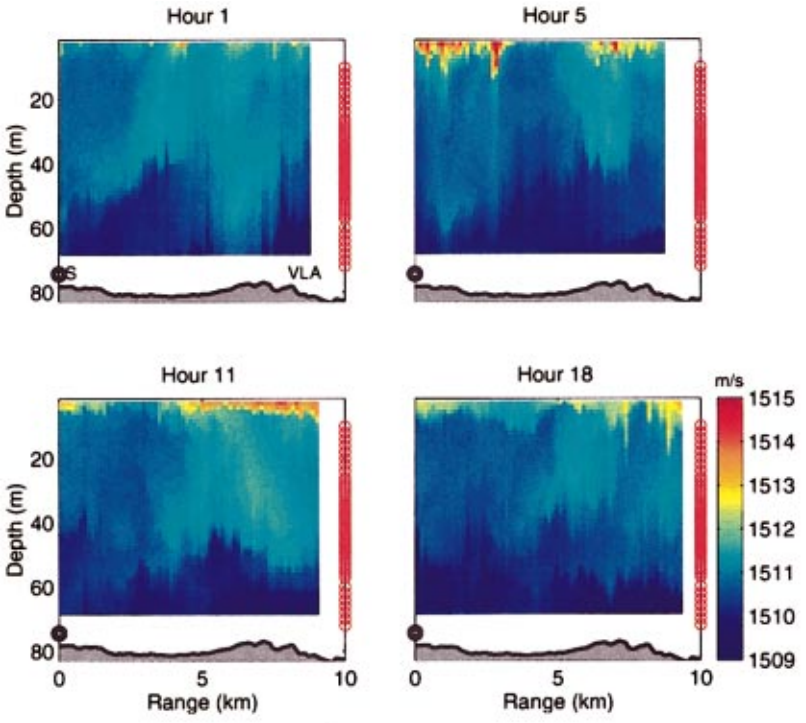

FIG. 3. Sound-speed profiles from the towed CTD chain along the 10-km acoustic track. The source (S) was moored 4 m above the bottom, and the VLA had 64 hydrophones in a nested configuration. The bathymetry is very weakly range dependent.

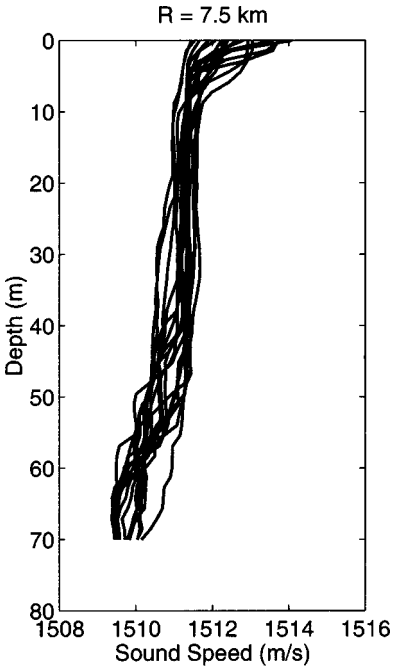

FIG. 4. Measured sound-speed profiles from the CTD chain taken in approximately the same location over 18 h.

relatively low- and high-sound-speed region, indicating the presence of a weak dynamic frontal feature. The profiles along the shorter tracks are almost range independent. The water column is also close to being isovelocity, and the fluctuations of the sound speed at a particular position along the track does not exceed a few m/s during the acoustic transmissions. This is illustrated in Fig. 4, where 18 individual profiles from the CTD chain are shown at range a of 7.5 km from the source. Because of the isovelocity profiles the acoustic signal will have strong interaction with the sea surface. The sea-surface conditions during the acoustic transmissions are documented in the Appendix.

The absence of a strong thermocline causes only small fluctuations in the sound-speed profiles (mainly at the shallow thermocline) and indicates a low internal wave energy for this particular time and location. Internal waves are also created by interaction of the ocean current with irregularities of the bottom topography. There is some evidence of that here, but it is also weak as the bathymetry has low variability with only a few meters change in water depth over 10 km (Figs. 3 and 4). The make-up of the bottom was determined qualitatively by seismic survey techniques (using a Uniboom source and 10-element towed array). Along the track the survey images indicate a bottom consisting of a sandy sediment layer overlying a harder sub-bottom.

III. MATCHED-FIELD INVERSION RESULTS

Geo-acoustic inversion by MFP requires choices to be made about how to parametrize the seabed for implementation in a forward acoustic propagation code. Here, a simple parametrization is used consisting of a homogeneous sediment layer over an infinite half-space. This simple model was chosen after sensitivity tests showed added complexity did not significantly improve the fit between measured and modeled data. Further, the simple geo-acoustic model adds robustness, as a complicated model may result in some parameter estimates having instability purely due to the numerical procedure.[16] Five seabed parameters were altered through the search for the optimal environment: sediment sound speed (constant with depth), sediment thickness, sub-bottom sound speed (constant with depth), attenuation, and density. Attenuation and density were assumed constant through the sediment and sub-bottom. A schematic of the synthetic environment used as input to the propagation model is shown in Fig. 5.

Two forward models were used: for the LFM signals, the layered normal-mode code PROSIM[18] was used (over the band 220–780 Hz in 4-Hz increments) and for the MT signals (200–700 Hz in 100-Hz increments) the normal-mode code SNAP[19] was used. The kernel of the PROSIM model is based on the ORCA[20] normal-mode model. The measured acoustic field was extracted every hour for each source–receiver range of 2, 5, and 10 km for the MFP inversion. A real axis search for eigenvalues was used with both SNAP and PROSIM, since including the entire complex plane showed minor differences in the predicted acoustic field for source–

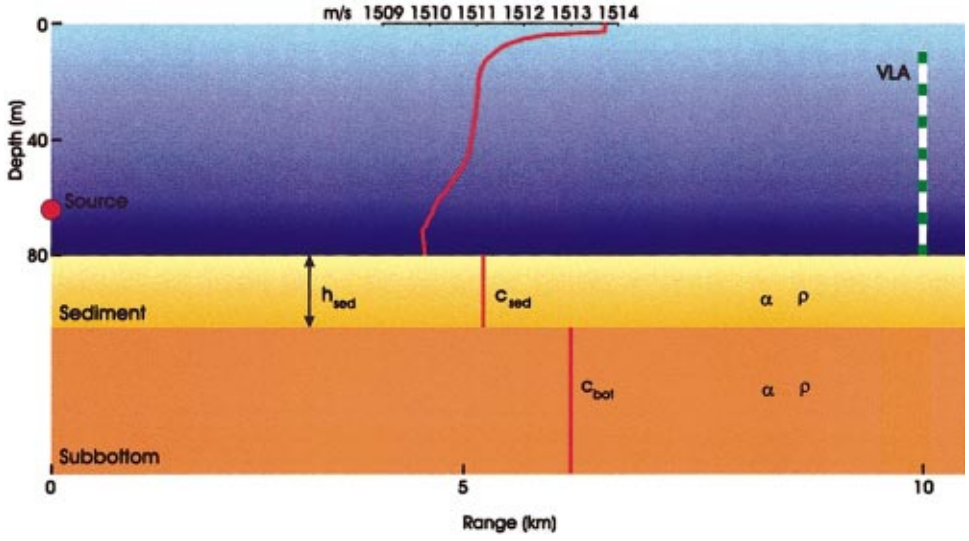

FIG. 5. Synthetic environment used as input to the numerical model for propagation modeling (geo-acoustic inversion).

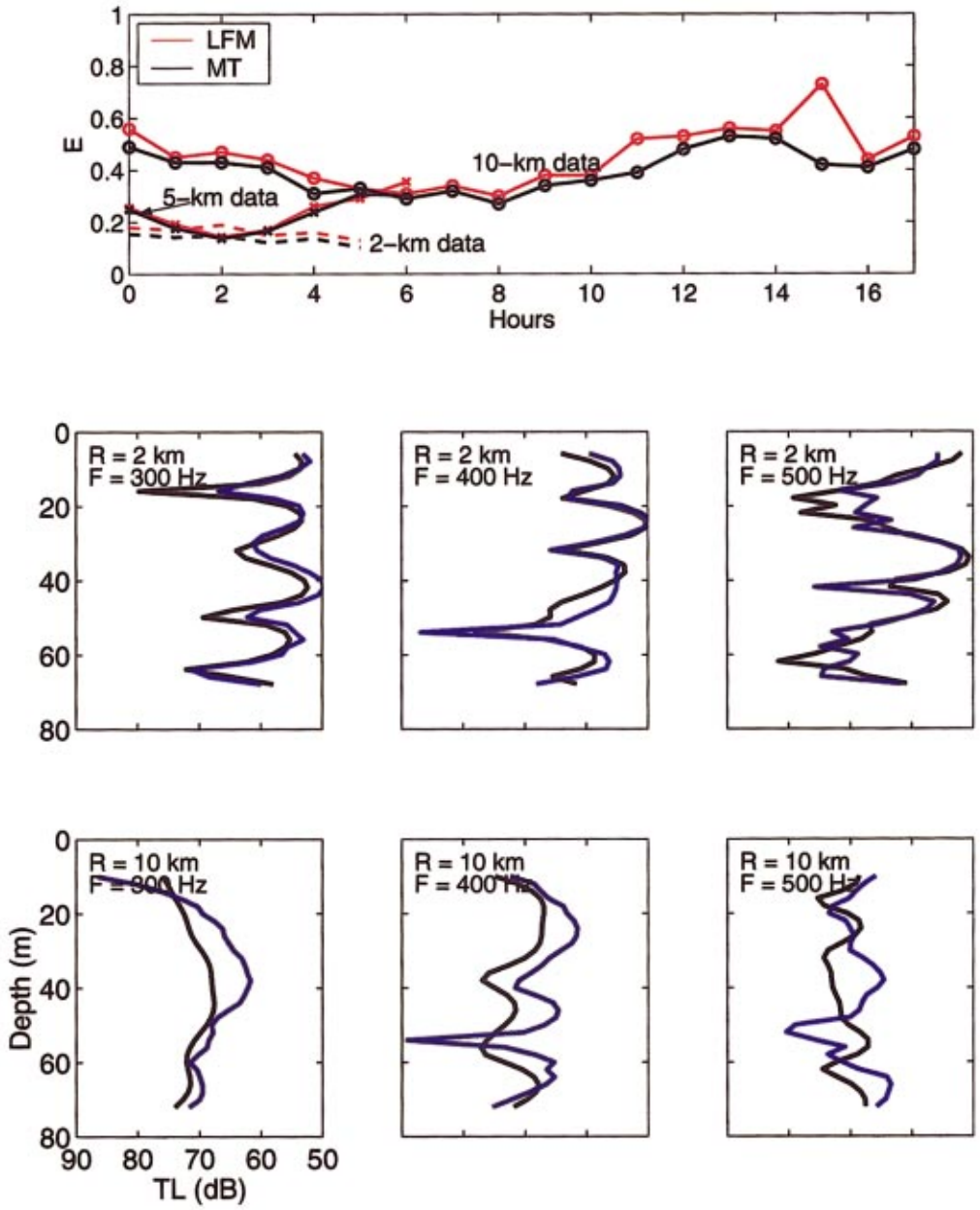

FIG. 6. Top panel shows the optimum value of E for 2-, 5-, and 10-km data sets. The LFM signals are shown as red lines and the MT in black (2 km—dashed lines, 5 km-× symbol on lines and 10 km ○ symbol on lines). In the lower panels, the measured (black) and modeled (blue) MT transmission loss is shown.

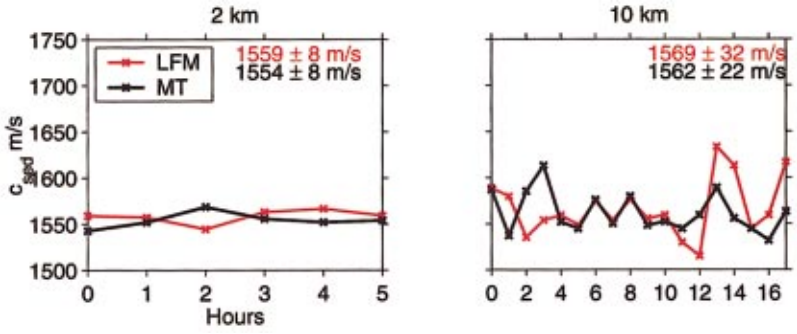

FIG. 7. Results for sediment sound speed. Left panel is for 2 km and right for 10 km.

receiver ranges considered here. Seabed attenuation was included by adding a small perturbation to the real eigenvalues.[21] Taking the expected attenuation values for the experimental site, the perturbation approach appeared a reasonable approximation.

The water sound speed was taken from the towed CTD-chain data. For each model environment, the sound speed along the track at the time closest to the acoustic transmission was averaged over range. These averaged profiles were used in the range-independent propagation modeling (6 profiles for 2-km data, 4 for 5 km, and 18 for 10 km). A correlation function, E, quantifies the agreement between the simulated, q, and measured, p, acoustic fields. The data considered here is taken over N_D hydrophones (here, 32 with 2-m spacing) in depth along the VLA and over N_F frequencies (6 for MT data and 141 for LFM). The correlation function is based on the incoherent multifrequency Bartlett processor similar to Eq. (1)

$$E = 1 - \frac{1}{N_F} \sum_{j=1}^{N_F} \frac{|\Sigma_{i=1}^{N_D} p_{ij} q_{ij}^*|}{\sqrt{\Sigma_{i=1}^{N_D} |p_{ij}|^2 \Sigma_{i=1}^{N_D} |q_{ij}|^2}}. \quad (2)$$

This correlation function is normalized and always produces $0 \leqslant E \leqslant 1$ (where a perfect match yields $E = 0$). The optimum set of environmental parameters corresponding to the minimum of Eq. (2) is determined using a genetic algorithm in the SAGA inversion package.[22] The search has been performed on the measured data taken every hour using 2000 iterations for each of 30 populations (60 000 forward models for each time realization), alternating between optimum geometry and bottom properties search[23] to obtain maximum stability in the search algorithm.

The final values for E are shown in the upper panel of Fig. 6 for the LFM and MT signals at 2-, 5-, and 10-km source–receiver separations. The agreement between the final E value for the LFM and MT signals provides confidence in the optimum (final) results. The consistent, lower value of E for the 2-km data indicates that a better match between model and measured data is achieved for this range. All the measured data considered here were selected for at least 10-dB signal-to-noise ratio. Therefore, the higher E value for the 10-km data is primarily attributed to the range-dependent channel. At 5 km the value of E is sometimes as low as for the 2-km data (at hour 2) but also has increased values exceeding some of the 10-km values (at hour 6). The resulting transmission loss (TL) which corresponds to the lowest value of E for the MT transmissions at both 2- and 10-km is also shown in Fig. 6.

The following subsections separately present and discuss the optimized parameter results for the geo-acoustic properties and the source and receiver positions.

A. Optimization for geo-acoustic parameters

The inverted properties for the sediment sound speed as a function of time at 2- and 10-km are shown in Fig. 7. The 5-km results are summarized along with all the inverted geo-acoustic properties in Table I. Much greater variability is seen for the inverted sediment sound speed taken from the 10-km propagation (32 m/s) in comparison with 2 km (8 m/s). Since the 2-km propagation contained only 5 h of data, for comparison, the most stable 5 h of the 10-km data set (between the 5th and 10th hour) had a standard deviation of 11–15 m/s. From all the 2-km data the spread between the highest and lowest sound speeds is 26 m/s and for 10 km it was 120 m/s. Taking only the most stable 5 h of the 10-km data produced a spread of 35 m/s.

Results using MT signals are also shown in Fig. 7 (for comparison with the LFM results). The purpose for including two signal types using different propagation models is to test the inversion algorithm for consistency. Because the LFM and MT acoustic fields are not identical and different propagation models were used, the search algorithm took distinct paths leading to seabed parameter estimates for both data types. The agreement between inverted seabed properties for the LFM and MT signals is an indication that the algorithm and numerical method is stable. Although the LFM and MT signal types produced inverted values which sometimes differ, the time variability is similar for both. In cases where the cost function is low, the LFM and MT signals have good agreement in the inverted seabed properties. The MT signals have higher signal-to-noise ratio, but the LFM has more frequency content included in the inversion. For each of the pings selected for inversion, the LFM and MT signals have a time separation of approximately 1–10 min.

The attenuation was assumed constant with depth in the seabed and was determined at 2, 5, and 10 km using both LFM and MT signals (see Table I). The results for 2- and 10-km are shown in Fig. 8. There was a slight increase of the mean inverted attenuation from 0.4 dB/λ at 2 km, to 0.5 dB/λ at 5 km, to 0.6 dB/λ at 10 km. This apparent range dependence is consistent with neglecting loss mechanisms (such as mode coupling caused by rough surface and seabed) in the range-independent modeling. Considering only the LFM signals, the 2-km data have a standard deviation of 0.06 dB/λ and for 10 km it is 0.2 dB/λ. And, the difference between the minimum and maximum values found are 0.16

TABLE I. Optimum environmental parameters for LFM signals. Results and search intervals are as shown. Attenuation and density are constant through the sediment and sub-bottom. Speeds refer to compressional acoustic waves, and attenuation is given in units of decibels per wavelength.

Parameter	Search bounds	2 km	5 km	10 km
Sediment speed: c_{sed} (m/s)	1500–1750	1559±8	1568±7	1569±32
Sediment thickness: h_{sed} (m)	0.1–20	4.3±0.7	5.4±0.7	6.6±6.7
Attenuation: α (dB/λ)	0.0–1.0	0.4±0.06	0.5±0.06	0.6±0.20
Density: ρ (g/cm^3)	1.1–2.5	1.53±0.05	1.50±0.2	1.58±0.10
Sub-bottom speed: c_{bot} (m/s)	c_{sed}+0–250	1637±17	1742±51	1702±68

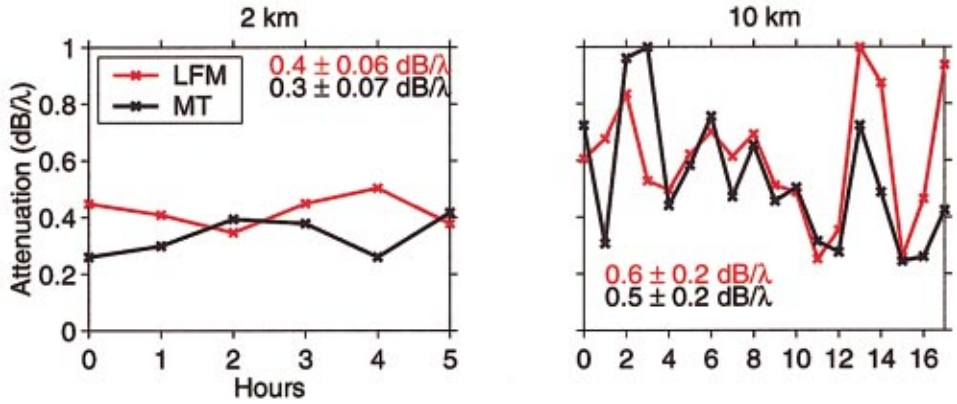

FIG. 8. Results for attenuation. Left panel is for 2 km and right for 10 km.

dB/λ at 2 km and 0.75 dB/λ at 10 km. The other geo-acoustic parameters along with standard deviations are summarized in Table I for the LFM signals at 2-, 5-, and 10-km source–receiver ranges.

B. Optimization for source and receiver positions

Although for MFP inversion the sound source and receiver positions are known, there is good reason to include an optimization of these parameters. In most cases, the positions have some experimental uncertainty which should be factored into the search. Additionally, slight mismatches in bathymetry or water sound speed between model and true environments often translate into shifts in apparent source position. If the apparent source position is included in the modeling, a better fit between measured and modeled data can be achieved (and presumably a better estimate of the bottom properties). The same is true for the receivers, except here there is both apparent and true receiver motion due to ocean currents which can cause the vertical array to tilt. Since the bottom of the array is moored to the seafloor, the horizontal deviation is largest near the sea surface where array tension is kept by a subsurface float. The array is designed to minimize tilt, but it is unavoidable when the currents are strong. The value for source and receiver positions are reasonably well known through direct measurements, and the positions found through the optimization (data inversion) are valuable as a quality check. Obtaining agreement between the measured and inverted values for source and receiver positions is a necessary but insufficient condition to indicate the model is a good representation of the reality.

The comparison between the inverted location for the source position is shown in Fig. 9 for both source range and depth at 2 and 10 km. The vertical axis of the figures indicates the search bounds. Although the source range was known from direct measurements to within about 10 m, and the source depth to within 1 m, the search bounds were kept large to allow flexibility for the optimization to find positions giving the best fit. The mean source range and depth results at both 2 and 10 km are correct to within the indicated uncertainty. While at 2 km the estimated range variability is only about 10 m, at 10 km the variability is quite large, exceeding 140 m. To show the consistency, as with the geo-

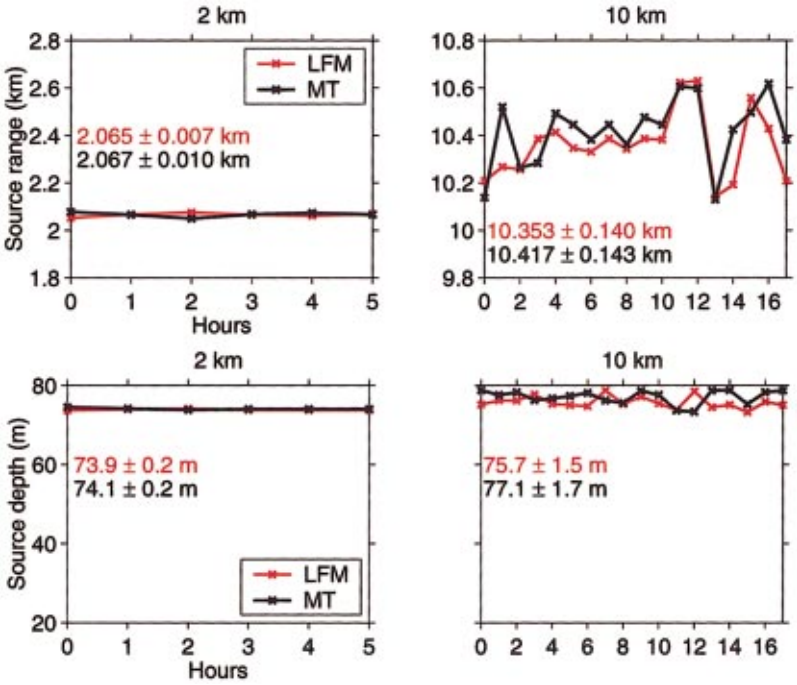

FIG. 9. Top left panel shows the estimated source range position at 2 km and the top right panel is for 10 km. Lower left panel is the estimate for source depth at 2 km and lower right for 10 km.

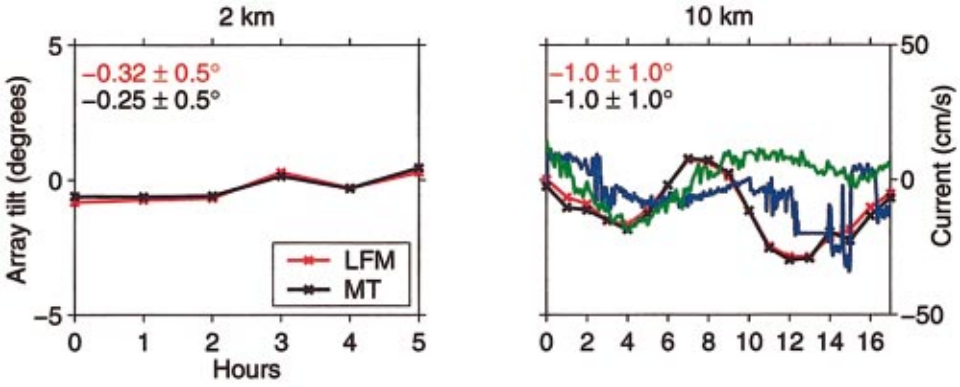

FIG. 10. Left panel shows the array tilt for 2 km and right panel for 10 km. The light-blue line is the tilt sensor data and the green line is the ADCP current estimate at depth near the tilt sensor. Note the second *y* axis for the current data on the right-hand side of the 10-km plot.

acoustic properties, both the LFM and MT results are shown in the figures.

The tilt of the vertical array was also estimated in the modeling (as a rigid line array); this is compared with the measurements of the ocean currents taken by the ADCP system near the VLA. Additionally, the array was equipped with a tilt sensor to give the local tilt on the array near the top hydrophone at about 10-m depth. The tilt results are shown in Fig. 10. The tilt derived from the acoustic data shows the same tendencies as both the tilt sensor and the ADCP measurements. The tilt sensor data do not include array shape and reflect only the tilt at one point. The ADCP measurements estimate currents which are related to array tilt but may not be in one-to-one correspondence.

C. Modeling of time variability

Modeling of sound propagation through different time snapshots of the measured oceanographic data has been performed in order to explain the time variability observed in the acoustic data. The coupled-mode model C-SNAP[24] was used to simulate the deterministic part of the propagation in the time- and range-dependent environment along the 2- and 10-km track. The range-dependent sound-speed profiles measured by the towed CTD chain were included in the modeling with mean source–receiver geometry and bottom properties found in subsection III A and III B. The modeled and experimental mean transmission loss at the center frequencies of 250, 450, and 750 Hz and averaged over a 10-Hz band are shown in Fig. 11. The data and model results have been further averaged over a time period of 4.5 h for the 2-km track and 18 h for the 10-km track. Figure 11 also shows modeled and experimental standard deviation of the transmission loss during 4.5 h of transmission along the 2-km track and 18 h along the 10-km track.

There is a very good agreement between the modeled and experimental mean levels at 2 km with a maximum standard deviation of around ±1 dB in the experimental data. At 10 km the match between model and data becomes worse, and the standard deviation increases to ±5 dB, caused by a longer averaging time and propagation range. The differences in the nulls between model and data are due to noise in the data. However, the mean modeling results are within the standard deviation of the data. The experimental standard deviation is poorly modeled at 10 km, although the measured profiles, taken every 140 m in range, are included in the modeling. This is due to insufficient modeling of the environment such as the effect of the rough sea surface on the acoustic propagation, and the absence of the ambient noise. A more direct comparison between data and modeling results

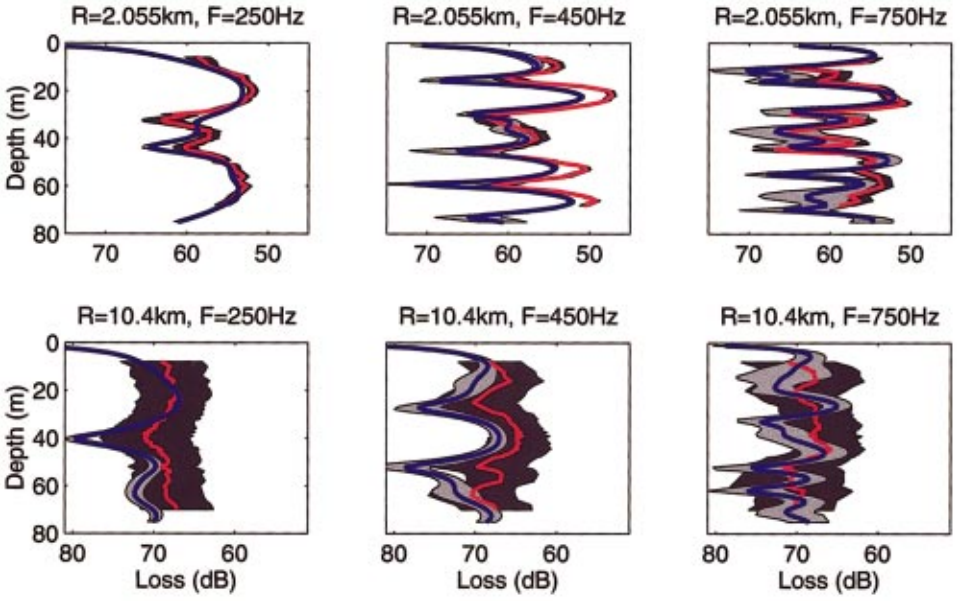

FIG. 11. Modeled (blue curve) and experimental (red curve) mean transmission loss (10-Hz band averaged) for the 2- and 10-km track. The gray- and black-shaded areas are the modeled and experimental standard deviation of the transmission loss, respectively, during 4.5 h of transmission along the 2-km track and 18 h along the 10-km track.

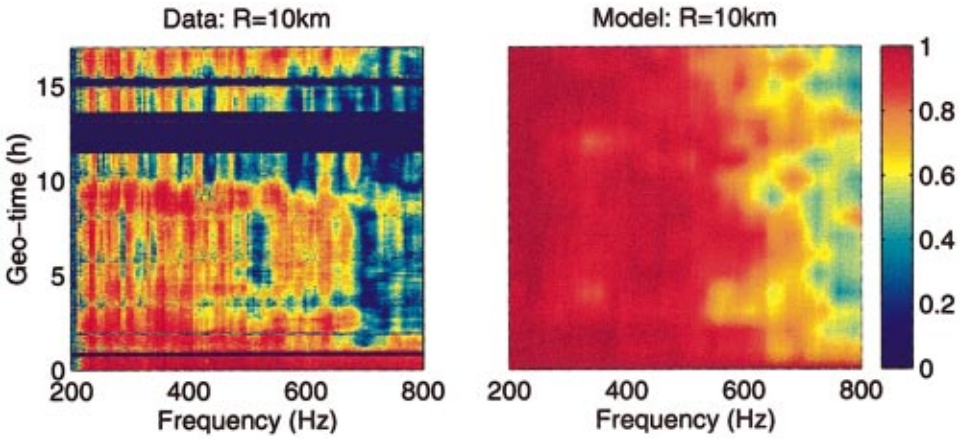

FIG. 12. Matched-field correlation of data and model. Eighteen sets of range-dependent sound-speed profiles are included in the modeling, corresponding to 18 h of transmission.

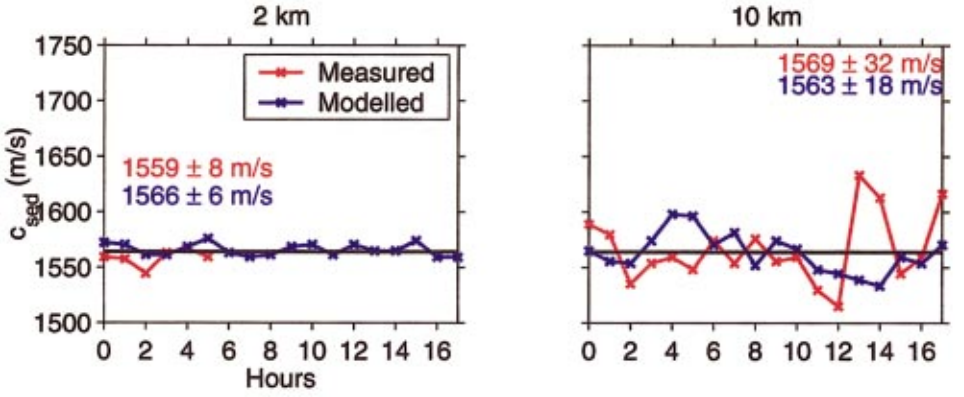

FIG. 13. Results for sediment sound speed. Left panel is for 2 km and right for 10 km.

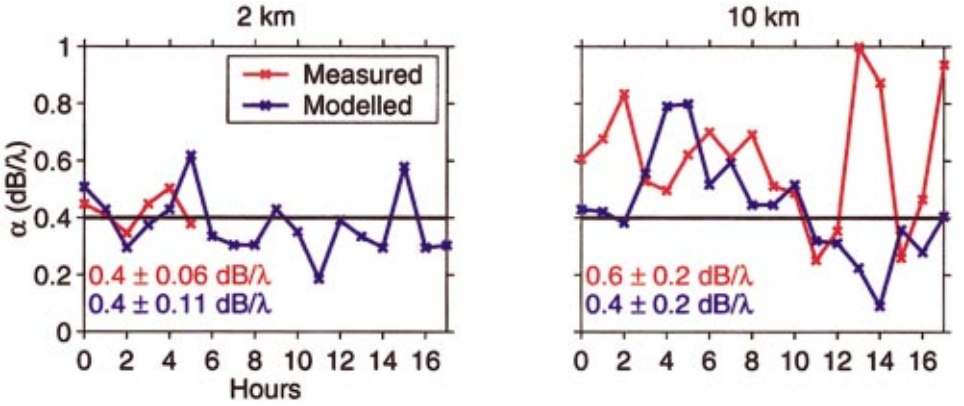

FIG. 14. Results for attenuation. Left panel is for 2 km and right for 10 km.

TABLE II. Optimum environmental parameters for the synthetic case. Results and search intervals are as shown. Attenuation and density are constant through the sediment and sub-bottom. Speeds refer to compressional acoustic waves, and attenuation is given in units of decibels per wavelength.

Parameter	Search bounds	True	Result—2 km	Result—10 km
Sediment speed: c_{sed} (m/s)	1500–1750	1559	1566±6	1563±18
Sediment thickness: h_{sed} (m)	0.1–20	4.3	5.8±1.0	5.6±2.9
Attenuation: α (dB/λ)	0.0–1.0	0.4	0.4±0.11	0.4±0.20
Density: ρ (g/cm^3)	1.1–2.5	1.53	1.52±0.03	1.56±0.10
Sub-bottom speed: c_{bot} (m/s)	c_{sed}+0–250	1637	1641±27	1693±62

is established by applying the matched-field correlation [Eq. (1)] for an 18-h time period of transmission. The propagation modeling for the same time period is performed by calculating the complex pressure at a range of 10 km for each of the 18 measured sound-speed sections corresponding to 1-h resolution in geo-time. The results are shown in Fig. 12.

The correlation shows more variability in the data than in the modeling results as the geo-time progresses. The abrupt decorrelation at frequencies around 650 Hz and a decorrelation time of around an hour at the higher frequencies observed in the data is correctly modeled. This indicates that the changes in the water column affect the propagation significantly at these frequencies, and that modeling of broadband, received time series in this frequency band and propagation range is extremely difficult if the environmental information is sparse.

Computer simulations are useful to isolate the contribution of various factors on the observed variability in both acoustic data and the subsequent optimal bottom properties. Among the factors which can contribute to time variability in the acoustic field are: ambient noise (including ship noise from NRV ALLIANCE and ITNS CICLOPE), surface waves, and ocean sound-speed profiles. While all of these factors were monitored, the amount each contributes to down-range acoustic fields is difficult to quantify. Using the propagation model C-SNAP, simulations of acoustic fields were made which included the range-dependent sound-speed profiles (as shown in Fig. 3). These simulations were used to study the effect of the time- and range-varying sound-speed profiles on propagation. Seabed properties were determined using the simulated data in exactly the same manner as for the measured data, and the results from the synthetic inversion for the sediment sound speed and attenuation are shown in Figs. 13 and 14, respectively.

For comparison, the optimum bottom properties found by using the experimental data (see Figs. 7 and 8) are also included in Figs. 13 and 14. The results show a variability in each of the inverted parameters which mimics the results of the measured data, and the variability of the optimum parameters found from the synthetic case is very similar to the experimental results. Note the variability in the synthetic optimum bottom properties is established solely by including the measured time- and range-dependent sound-speed profiles in the modeling. In the case of 2-km propagation, the simulation is carried out to 17 h, even though the measured data were only for 5 h for better comparison with the 10-km data.

A summary of the synthetic optimum bottom properties and the variability (standard deviation) is given in Table II.

IV. CONCLUSIONS

Acoustic experiments were conducted in the Strait of Sicily with several hours of data collected using a fixed sound source and vertical receiving array. These data were used with matched-field, geo-acoustic inversion to estimate the environmental properties at 2-, 5-, and 10-km source–receiver separation. Matched-field correlation of the data shows a strong time-, frequency-, and range-dependence. A decorrelation time of less than an hour was found in the data for the higher acoustic frequencies and at a 10-km propagation range. Prediction of broadband received time series is therefore extremely difficult (if not impossible) at ranges out to 10 km, even though extensive environmental information was available.

The Advent'99 experiment and numerical modeling analysis clearly demonstrate that significant time variability in received acoustic data is present, although the ocean variability was low compared to regions with known strong time-dependent oceanography. The experimental transmission loss averaged in frequency and time was modeled with sufficient accuracy. The mean, modeled transmission loss was within the standard deviation of the data for both the short and long propagation ranges. The modeled standard deviation of the transmission loss was in poor agreement with that of the data because of insufficient knowledge of the changing environment. When model parameters were optimized using matched field geo-acoustic inversion, a consistently high correlation between measured and modeled complex, broadband data was only possible at 2-km source–receiver separation. Although the source was localized for the three ranges of 2-, 5-, and 10-km, the predicted position varied from the known value with errors increasing with source–receiver separation. The inverted geo-acoustic properties were consistent only for the 2-km data.

Since the environmental parameters being estimated do not change with time, the inversion variability (errors) beyond the 2-km range is attributed primarily due to time-varying ocean properties. Although the mean, inverted environmental parameter estimates were in general agreement at the three ranges, the standard deviation was much higher for the longer range propagation. The ocean sound-speed spatial variability was not extreme. There was only 2–4-m/s sound-speed change from surface to bottom with very low internal wave activity. However, simulations of acoustic propagation through these measured ocean sound-speed profiles show that the sound speed alone is capable of producing the type of variability in inverted seabed properties seen here. These results show the impact of ocean time- and range variability on geo-acoustic inversion (and modeling). Beyond a few kilometers, at the frequencies considered here, the variability destroyed coherent processing and the possibility to predict acoustic propagation. Without reliable propagation prediction, the inverted geo-acoustic parameters showed an erroneous time variability. The ocean time variability also caused the optimized source position to vary slightly with time, even though the source–receiver geometry was fixed. The stability over time of the geo-acoustic inversion for the 2-km data indicates that the inversion methodology is sound. The degradation of the geo-acoustic inversion results at longer ranges signifies range- and frequency limitations on the method that depends on the oceanography.

ACKNOWLEDGMENTS

The authors wish to acknowledge all the members who participated in Advent'99. Special thanks to E. Michelozzi as engineering coordinator and P. Boni for acquisition of data. The authors would also like to gratefully acknowledge the crews of the NRV ALLIANCE and ITNS CICLOPE.

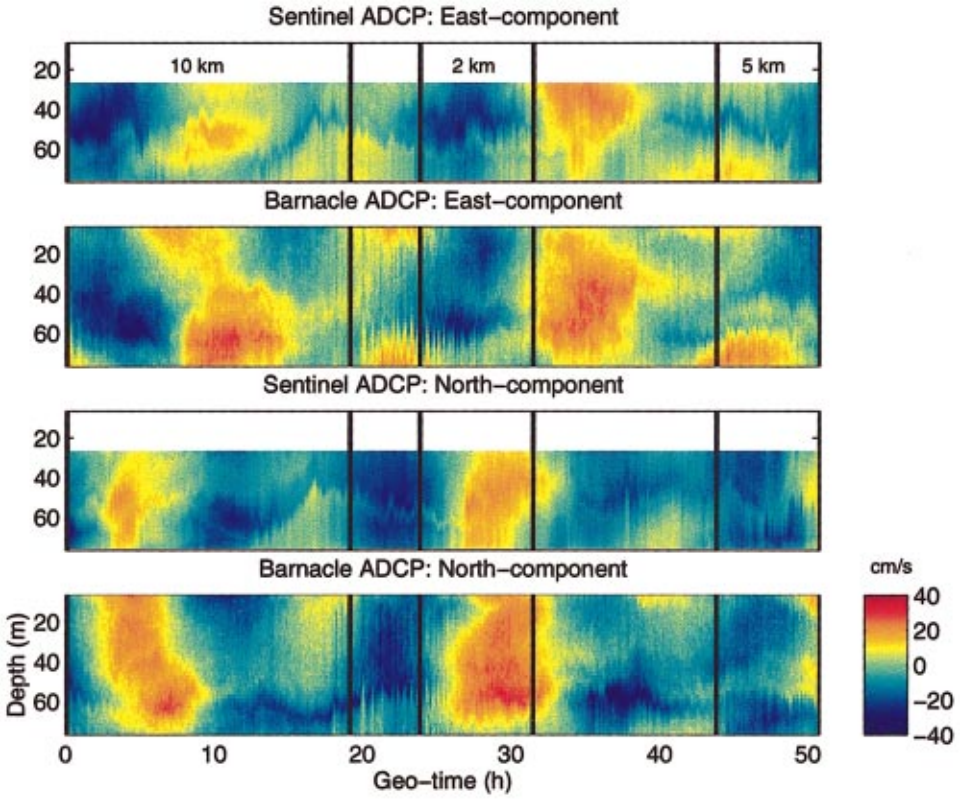

FIG. A1. Current during the fixed path propagation experiments measured by the Sentinel (at the source position) and the Barnacle (at the VLA for the 10-km acoustic track) ADCP system.

APPENDIX: CURRENT- AND WAVE-RIDER DATA

The north and east component of the current measured by the moored ADCP systems (Sentinel close to the source and Barnacle close to the VLA for the 10-km acoustic track) during the fixed path propagation experiment is shown in Fig. A1. The time periods of received acoustic signals along the three propagation paths are indicated by the vertical lines. By convention, a positive current in the east and north directions means flow from west towards east and south towards north, respectively. In general, the two ADCP systems show similar behavior of the current as a function of time and depth. A maximum current of around 40 cm/s was observed during the experiment, and the current is mainly driven by the tidal effect with a 24-h period. However, at a specific time the current direction depends on depth. This is particularly seen at times between 15 and 20 h for both the east and north components. The change of current direction in the water column introduces stratifications with shear interfaces. Furthermore, the current from the two positions is often shifted in phase, which is observed for example within the first 10 h of the measurements. This indicates strong range-dependent properties of the current in this region.

The observed properties of the current may have a strong impact on the tilt of the moored VLA, which has to be included before an optimum prediction of the sound propagation can be achieved. There was no indication of significant influence of the wind speed on the current, although high wind speeds were observed during the experiment. The significant wave height (an average of the 1/3-highest waves) measured during the fixed path propagation experiments is shown in Fig. A2. The significant waveheight does not exceed 0.5 m except for the 5-km fixed path experiment, where the waveheight increases monotonically up to 2.0 m at the end of the transmissions. As the experiment was conducted in the springtime, a strong thermocline in the sound-speed profile was not expected. Interaction of the propagating acoustic field with the rough dynamic sea surface is therefore most likely.

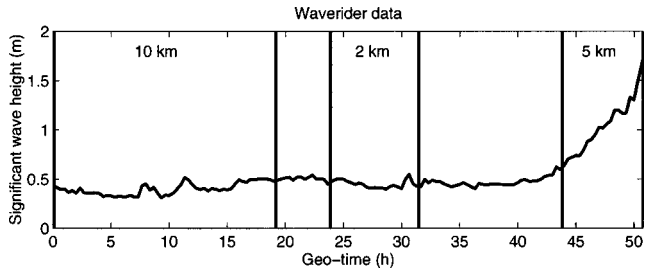

FIG. A2. Significant waveheight measured during the fixed path propagation experiments.

[1] F. B. Jensen, ''Comparison of transmission loss data for different shallow-water areas with theoretical results provided by a three-fluid normal-mode propagation model,'' in *Sound Propagation in Shallow Water* (SACLANTCEN CP-14, La Spezia, Italy, 1974), Vol. II, pp. 79–92.

[2] D. P. Knobles and R. A. Koch, ''A time-series analysis of sound propagation in a strongly multipath shallow-water environment with an adiabatic normal-mode approach,'' IEEE J. Ocean Eng. **21**, 1–13 (1996).

[3] D. P. Knobles, E. K. Westwood, and J. E. LeMon, ''Modal time-series structure in a shallow-water environment,'' IEEE J. Ocean Eng. **23**, 188–202 (1998).

[4] P. L. Nielsen, F. Bini-Verona, and F. B. Jensen, ''Time stability and predictability of broadband propagation in shallow water,'' in *Proceedings of the Fourth European Conference on Underwater Acoustics* (Instituto di Acustica, Rome, Italy, 1998), pp. 631–636, Italian National Research Council.

[5] P. L. Nielsen, M. Siderius, and F. B. Jensen, ''Ocean variability effects on

sound propagation in shallow water,'' in *Oceans '99* (IEEE, New York, 1999).
[6] J. Zhou, X. Zhang, and P. H. Rogers, ''Resonant interaction of sound wave with internal solitons in the coastal zone,'' J. Acoust. Soc. Am. **90**, 2042–2054 (1991).
[7] J. R. Apel, M. Badiey, C.-S. Chiu, S. Finette, R. Headrick, J. Kemp, J. F. Lynch, A. Newhall, M. H. Orr, B. H. Pasewark, K. Tielbürger, A. Turgut, K. von der Heydt, and S. Wolf, ''An overview of the 1995 SWARM shallow-water internal wave acoustic scattering experiment,'' IEEE J. Ocean Eng. **22**, 465–500 (1997).
[8] D. Tielbürger, S. Finette, and S. Wolf, ''Modeling mode arrivals in the 1995 SWARM experiment acoustic transmissions,'' J. Acoust. Soc. Am. **101**, 789–808 (1997).
[9] R. H. Headrick, J. F. Lynch, J. N. Kemp, A. E. Newhall, K. von der Heydt, J. Apel, M. Badiey, C. S. Chiu, S. Finette, M. Orr, B. Pasewark, A. Turgot, S. Wolf, and D. Tielbürger, ''Modeling mode arrivals in the 1995 SWARM experiment acoustic transmissions,'' J. Acoust. Soc. Am. **107**, 221–236 (2000).
[10] M. D. Collins, W. A. Kuperman, and H. Schmidt, ''Nonlinear inversion for ocean bottom properties,'' J. Acoust. Soc. Am. **92**, 2770–2783 (1992).
[11] C. E. Lindsay and N. R. Chapman, ''Matched field inversion for geophysical parameters using adaptive simulated annealing,'' IEEE J. Ocean Eng. **18**, 224–231 (1993).
[12] S. E. Dosso, M. L. Yeremy, J. M. Ozard, and N. R. Chapman, ''Estimation of ocean bottom properties by matched-field inversion of acoustic field data,'' IEEE J. Ocean Eng. **18**, 232–239 (1993).
[13] P. Gerstoft, ''Inversion of seismo-acoustic data using genetic algorithms and *a posteriori* probability distributions,'' J. Acoust. Soc. Am. **95**, 770–782 (1994).
[14] D. F. Gingras and P. Gerstoft, ''Inversion for geometric and geoacoustic parameters in shallow water: Experimental results,'' J. Acoust. Soc. Am. **97**, 3589–3598 (1995).
[15] J. P. Hermand and P. Gerstoft, ''Inversion of broadband multi-tone acoustic data from the Yellow Shark summer experiments,'' IEEE J. Ocean Eng. **21**, 324–346 (1996).
[16] M. Snellen, D. Simons, M. Siderius, J. Sellschopp, and P. Nielsen, ''An evaluation of the accuracy of shallow water matched field inversion results,'' J. Acoust. Soc. Am. **109**, 514–527 (2001).
[17] M. Siderius, M. Snellen, D. Simons, and R. Onken, ''An environmental assessment in the Strait of Sicily: Measurement and analysis techniques for determining bottom and oceanographic properties,'' IEEE J. Ocean Eng. **25**, 364–386 (2000).
[18] F. Bini-Verona, P. L. Nielsen, and F. B. Jensen, *PROSIM Broadband Normal-mode Model: A Users' Guide*, SM-358 (SACLANT Undersea Research Centre, La Spezia, Italy, 2000).
[19] F. B. Jensen and M. C. Ferla, *SNAP*: *The SACLANTCEN Normal-mode Acoustic Propagation Model*, SM-121 (SACLANT Undersea Research Centre, La Spezia, Italy, 1979).
[20] E. K. Westwood, C. T. Tindle, and N. R. Chapman, ''A normal mode model for acousto-elastic ocean environments,'' J. Acoust. Soc. Am. **100**, 3631–3645 (1996).
[21] F. B. Jensen, W. A. Kuperman, M. B. Porter, and Henrik Schmidt, *Computational Ocean Acoustics* (American Institute of Physics, New York, 1994).
[22] P. Gerstoft, *SAGA Users Manual 2.0, An Inversion Software Package*, Technical Report SM-333 (SACLANT Undersea Research Centre, La Spezia, Italy, 1997).
[23] M. Siderius, P. L. Nielsen, and F. B. Jensen, ''Geo-acoustic inversion of experimental data from two shallow water sites,'' in *Oceans '99* (IEEE, New York, 1999).
[24] M. C. Ferla, M. B. Porter, and F. B. Jensen, *C-SNAP*: *Coupled SACLANTCEN Normal Mode Propagation Loss Model*, SM-274 (SACLANT Undersea Research Centre, La Spezia, Italy, 1993).

Finite-difference time-domain modeling of low to moderate frequency sea-surface reverberation in the presence of a near-surface bubble layer

Richard S. Keiffer[a)]
Naval Research Laboratory, Code 7181, Stennis Space Center, Mississippi 39529-5004

J. C. Novarini
Planning Systems, Inc., 21294 Johnson Road, Long Beach, Mississippi 39560-9702

R. A. Zingarelli
Naval Research Laboratory, Code 7181, Stennis Space Center, Mississippi 39529-5004

(Received 18 December 2000; revised 19 March 2001; accepted 27 April 2001)

A finite-difference time-domain (FDTD) solution to the two-dimensional linear acoustic wave equation is utilized in numerical experiments to test the hypothesis that near-surface, bubble-induced refraction can have a significant impact on low to moderate frequency sea-surface reverberation. In order to isolate the effects of bubble-modified propagation on the scattering from the air/sea interface from other possible phenomena such as scattering from bubble clouds, the bubbly environment is assumed to be range independent. Results of the study show that both the strong wind-speed dependence and the enhanced scattering levels of the order found in the reverberation data are obtained when a wind-speed-dependent bubble layer is included in the modeling. © *2001 Acoustical Society of America.* [DOI: 10.1121/1.1383769]

PACS numbers: 43.30.Gv, 43.30.Es, 43.30.Hw [DLB]

I. INTRODUCTION

Breaking waves generate bubbles that populate the near-surface region of the ocean (see, e.g., Ref. 1). Higher wind speeds generally lead to more breaking waves and to greater numbers of bubbles injected into the ocean. For wind speeds above a few meters per second, the typical concentrations of bubbles found in this near-surface region can significantly lower the sound speed in the low-to-moderate frequency regime ($f<1.5$ kHz) (see, e.g., Ref. 2). In Ref. 3, the hypothesis that a persistent, bubble-induced, upward-refracting layer can enhance the backscattering from the air/sea interface in this frequency range was explored. In that study, this possible phenomenon was investigated using reasonable estimates for time- and range-averaged bubble populations and an *ad hoc* acoustics model that combined ray concepts to handle the propagation with first-order perturbation theory to describe the rough interface scattering. The main conclusion reached in Ref. 3 was that the refraction introduced by the bubble layer could strongly enhance the surface (air/sea interface) reverberation. Of particular significance was the observation that the assumed wind-speed dependence of the bubble layer gave rise to scattering strengths that followed (reasonably well) the strong wind-speed dependence of published scattering strength data (see, e.g., Ref. 4).

The primary purpose of this work is to make available new, highly accurate calculations based on a finite-difference time-domain (FDTD) solution to the two-dimensional (2D) linear acoustics wave equation for this problem. These new calculations avoid the *ad hoc* acoustic modeling assumptions employed in Ref. 3 and support the contention that bubble-induced refraction effects need to be considered when deriving sea-surface scattering strengths from reverberation data.

II. NUMERICAL EXPERIMENT

Although detailed observations of the temporal and spatial characteristics of the bubbly environment beneath rough sea surfaces are far from complete, there have been enough published oceanographic studies to form the basis of a semi-empirical model for a time-invariant, range-independent, depth-dependent bubble layer.[5] In the current work, we assume this idealized model for the environment and further restrict the frequency to the low-to-moderate range where the resonant scattering effects due to even the largest individual bubbles found in the ocean can be safely ignored. Under these assumptions, it is a straightforward matter to calculate a bubble-induced change to the sound speed[6] and effectively replace the bubbly environment with a depth-dependent, upward-refracting layer. In the frequency band of interest, the upward-refracting layer presented by the bubbles is, to a good approximation, frequency independent. Therefore, the numerical results computed for a single frequency in this band (say, 300 Hz) can be regarded as typical of the entire low-to-moderate frequency band.

The bubbly medium is also assumed to be lossless. This is a very good approximation in the frequency range of interest. For a 20-m/s wind and a source frequency of 300 Hz, the adopted bubble spectrum yields an attenuation of 0.02 dB/m at the surface, 5.0×10^{-3} dB/m at the e-folding depth (1.84 m), and 2.2×10^{-5} dB/m at the deepest extent of the bubble layer. A simple ray calculation for the integrated two-way loss between source/receiver and the surface, with due regard to the curvature of the sound path caused by the per-

a)Electronic mail: keiffer@nrlssc.navy.mil

 0001-4966/2001/110(2)/782/4/$18.00

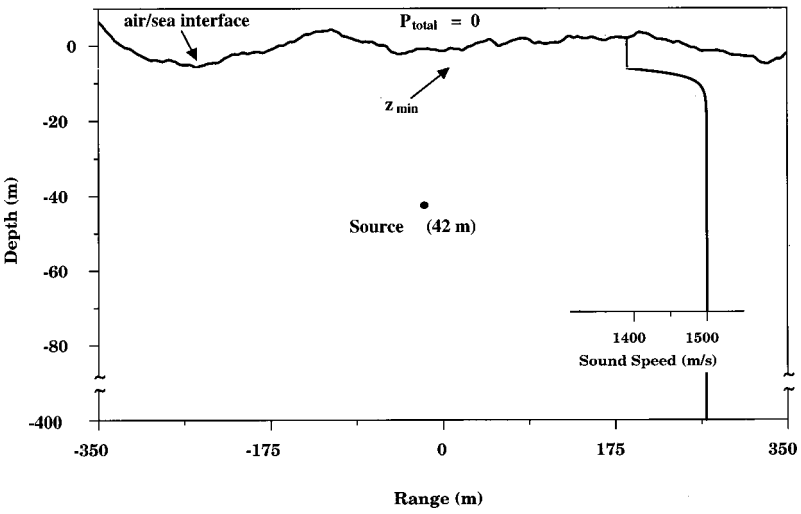

FIG. 1. Schematic of experiment geometry showing the rough sea surface and the bubble-perturbed sound-speed profile.

turbed sound profile, indicates that a ray launched at a 5° grazing angle will experience a total bubble-induced attenuation loss of only 0.2 dB.

The details of the FDTD model used in this study (named FIDO) have been described elsewhere[7] and are similar to other implementations which can be found in the literature.[8] In particular, FIDO solves the 2D linear acoustic wave equation in a second-order accurate algorithm assuming a nondispersive medium. The model was configured to enforce a pressure-release boundary condition on the rough air/sea interface and (partially) absorbing boundary conditions on the left, right, and bottom edges of the computational grid. FIDO has been tested (with excellent agreement) for backscattering by using test problems found in Alford *et al.*[8]

To determine if the bubble-induced refraction enhances the reverberation from the air/sea interface, FDTD calculations for the reverberation time series were computed for an ensemble of 50 rough sea surfaces assuming a homogeneous ($c=1500$ m/s) underwater environment. These results were then compared against FDTD calculations that used bubble-modified sound-speed profiles. Four values of wind speed (for a reference height of 10 m above the sea surface) were considered: 8, 10, 15, and 20 m/s. The wind speed affected the roughness of the air/sea interface as well as the number, size distribution, and depth dependence of the bubble population.

A schematic of the geometry adopted for these numerical experiments is shown in Fig. 1. An omnidirectional source is located 42 m below the mean ($\langle z\rangle=0$) surface height of a 700 m long "frozen," 1D, deterministic sea surface. The source was positioned so that there was an equal length (350 m) of rough sea surface to its left and right. For a sound speed of 1500 m/s, this geometry yielded a reverberation time series, uncontaminated by reflections from computational boundaries, that was approximately 0.42 s long. The minimum grazing angle of incidence associated with the latest return from the sea surface was approximately 7.7 deg.

The source emitted a finite-duration, Gaussian-shaped, cosinusoidal pulse

$$p(t)=\begin{cases} P_0\cos(2\pi f_0 t)\exp[-\pi(\alpha t)^2] & 0<t\leqslant T \\ 0 \quad t>T \end{cases}. \quad (1)$$

Here, $\alpha=44.46$ rad/s, $T=0.067$ s, $f_0=300$ Hz, and P_0 is the (unit) source amplitude. Note that the shallowest angles evaluated were slightly greater than expected from geometric considerations. This was due to the finite width of the source waveform, which caused some overlap between the very end of the scattering time series from the sea surface and the initial reflection from left and right vertical boundaries of the computational grid.

The deterministic 1D sea surfaces used in the study were generated using a linear filter technique[9] assuming a Pierson–Moskowitz sea-surface roughness spectrum.[10] The Pierson–Moskowitz spectrum is a nondirectional roughness spectrum (originally specified as a function of wave frequency) that was derived from point measurements of 2D fully developed wind-driven seas. To convert this spectrum to a form that can be used in the linear filtering technique, it is expressed as function of wave number using the dispersion relation for gravity waves in deep water ($\omega^2=gk$). Each 1D surface realization that is generated from the filtering process has total variance (of surface height) that equals the variance of the original Pierson–Moskowitz spectrum.

To prevent grid dispersion, the spatial and temporal sampling intervals were chosen as prescribed in Ref. 8. The FDTD calculations were performed using a spatial (grid) resolution of 0.25 m and a temporal resolution of 8.33×10^{-5} s. For a sound speed of 1500 m/s, this spatial resolution yielded 20 points per center wavelength of the source waveform. It can be noted that the spatial sampling easily satisfied the requirement from scattering theory that the "Bragg" component be included in the numerical realizations of the air/sea roughness.

Figure 1 also shows a plot of a typical bubble-perturbed sound-speed profile used in the study. Note that the sound speed is a constant 1500 m/s at the source depth and deeper. As the signal from the source travels upward toward the rough sea surface, it encounters the deepest extent of the bubble population at a depth of approximately 20 m. The sound speed begins to decrease at this point and reaches a

TABLE I. Parameters of modeled environments. Catalogue of the maximum sound speed defect due to the presence of the bubbles, Δc, (which occurs just below the sea surface), the e-folding depth of the modified sound-speed profile, and the rms roughness of the sea surfaces for each of the four wind speeds considered.

U (m/s)	$\Delta c_{\max}$ (m/s)	e-folding depth (m)	Max. void fraction	rms surface roughness (m)
8	−7	0.45	4.8×10^{-7}	0.39
10	−15	0.68	9.4×10^{-7}	0.61
15	−48	1.26	3.2×10^{-6}	1.37
20	−108	1.84	7.5×10^{-6}	2.44

minimum at depth $z_{\min}$. It was assumed in the modeling that the sound speed remains constant at this minimum speed for all water depths shallower than $z_{\min}$. This choice, in which the entire rough sea surface was ''bathed'' in a variable depth isospeed layer, was consistent with the methodology adopted in Ref. 3. It is an artifact that is the consequence of making the rough air/sea interface compatible with a range-independent stratified bubble layer. The value of $z_{\min}$ was determined from the deepest excursion in any set of sea-surface realizations. For example, in the 50 surface realizations that were generated for the 20-m/s wind speed, the deepest surface excursion was slightly less than 8.75 m. The three other wind speeds considered (15, 10, and 8 m/s) resulted in values of 6.0, 3.0, and 3.0 m, respectively, for $z_{\min}$. Additional details of the underwater- and sea-surface environments are listed in Table I. Included are the root-mean-square (rms) roughness of the interface, the e-folding depth of the bubble-modified sound-speed profile, the maximum void fraction, and the maximum sound-speed defect.

Before leaving this section, it should be emphasized that these sound-speed profiles assumed a particular relationship between the bubble population (and hence the void fraction) and the wind speed. Different factors, for example the air/sea temperature contrast, will influence this relationship. In addition, the bubble population model is based on oceanographic observations that were averaged over long times. The instantaneous void fractions (and sound-speed defects) near the surface may be much larger.

III. RESULTS AND DISCUSSION

As previously discussed, the FDTD solution method was used to generate reverberation time series from rough sea surfaces that were due to wind speeds of 8, 10, 15, and 20 m/s. For each wind speed, the average envelope[11] of the reverberation time series was calculated from 50 surface realizations. Identical numerical experiments were conducted with and without the inclusion of the bubble-induced sound-speed profile. Figure 2 shows the results of the FDTD calculations for the four wind speeds when the bubble layer is not included in the environmental modeling. As expected from scattering theory, the calculations show a weak variation in the reverberation level as a function of wind speed. The small increase in the reverberation level, which can be seen most clearly later in the time series, is due entirely to the increase in the surface roughness with wind speed (see Table I).

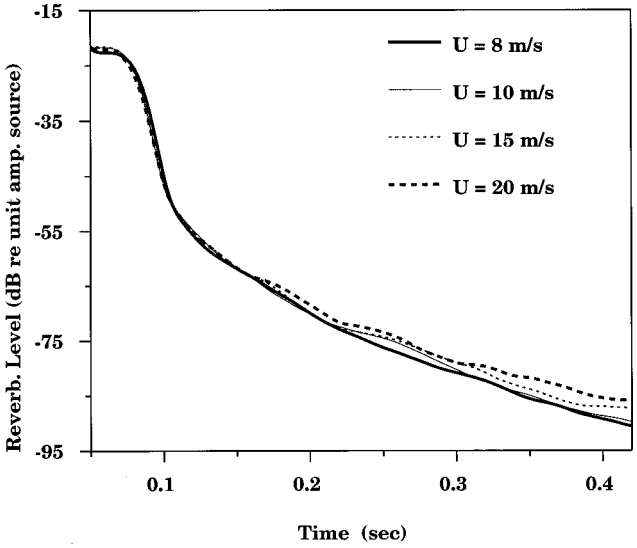

FIG. 2. Wind-speed (U) dependence of the average reverberation envelope at 300 Hz. Bubble-induced refraction effects are not included in the modeling. Reverberation levels are expressed in decibels relative to a unit amplitude source.

Figure 3 shows FDTD calculations from the numerical experiments that included a wind-speed-dependent bubble layer. Note that including the modeled bubble layer results in average reverberation levels that exhibit a strong wind-speed dependence. This behavior is particularly evident at later times or, equivalently, at shallower grazing angles. If Figs. 2 and 3 are compared, it can be noted that there is close agreement between the ''bubble'' and ''no-bubble'' reverberation levels near the beginning of the time series. At later times, however, it can be seen that for each of the four wind speeds studied the bubble case predicts a higher average reverbera-

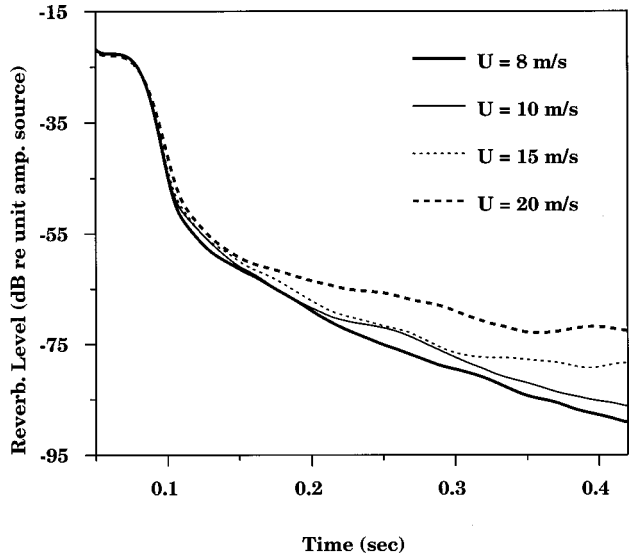

FIG. 3. Wind-speed (U) dependence of the average reverberation envelope at 300 Hz. Bubble-induced refraction effects are included in the modeling. Reverberation levels are expressed in decibels relative to a unit amplitude source.

tion envelope than the corresponding no-bubble case. The difference between the two predictions can also be seen to grow as the wind speed increases. For the 8-m/s case, the maximum difference between the two predictions is less than 2 dB, but for the 20-m/s comparison, the maximum difference exceeds 14 dB.

The *ad hoc* model described in Ref. 3 offers a simple explanation for the effect of the bubble layer on the FDTD reverberation calculations. At early times in the reverberation time series, the scattering is due to an insonifying field that strikes the rough sea surface at steep grazing angles. The bubble-induced change to the propagation direction of the insonifying field is small for these higher grazing angles; consequently, including the bubble layer in the modeling has little impact on the reverberation calculation. Similarly, the scattered field that propagates away from the surface at these higher grazing angles is only slightly affected as it propagates down through the bubble layer to the receiver. Later in the reverberation time series, the scattering is weaker because the insonifying field strikes the rough surface at shallower grazing angles. However, the presence of the bubble layer causes upward refraction. The main effect is to make the angle of insonification steeper and the scattering from the rough air/sea interface stronger.

This application of the FDTD solution to simulated bubble environments underlying rough sea surfaces has provided results which demonstrate that bubble-induced refraction can have a large impact on low-to-moderate frequency reverberation from the sea surface. When the refractive effect of the bubble layer was included in the modeling, both the strong wind-speed dependence and the enhanced scattering levels of the order found in the reverberation data[4] were obtained. On the other hand, in order to isolate the bubble-induced refraction effects, the bubbly environments used in this study were range- and time independent. The real ocean presents a range-, depth-, and time-dependent bubble population. This means that other phenomena, such as scattering from the range-dependent index of refraction introduced by the presence of the bubbles, will compete with the scattering from the sea surface in a complicated time-varying manner. The acoustic ramifications of increasingly realistic models for the environment need to be explored along with supporting field measurements in order to reach definitive conclusions about which combinations of scattering phenomena explain a particular data set.

ACKNOWLEDGMENTS

This work has been supported by the Office of Naval Research, Program Element No. 61153N-32, and by grants of computer time from the DoD High Performance Computing Shared Resource Centers at Stennis Space Center, MS. This document has been reviewed and is approved for public release.

[1] S. A. Thorpe, ''On the clouds of bubbles formed by breaking waves in the deep water and their role in the air–sea gas transfer,'' Philos. Trans. R. Soc. London, Ser. A **304**, 155–210 (1982).
[2] E. Terrill and W. K. Melville, ''Sound-speed measurements in the surface wave layer,'' J. Acoust. Soc. Am. **102**, 2607–2625 (1997).
[3] R. S. Keiffer, J. C. Novarini, and G. V. Norton, ''The impact of the background bubble layer on reverberation-derived scattering strengths in the low to moderate frequency range,'' J. Acoust. Soc. Am. **97**, 227–234 (1995).
[4] S. T. McDaniel, ''Sea surface reverberation: A review,'' J. Acoust. Soc. Am. **94**, 1905–1922 (1993).
[5] J. C. Novarini and G. V. Norton, ''Acoustic index of refraction in the background bubble layer of the ocean: An updated bubble spectrum and computer program CBUBBLY,'' Naval Research Laboratory Technical Report NRL/FR/7181–93-9432 (1994).
[6] C. S. Clay and H. Medwin, *Acoustical Oceanography* (Wiley, New York, 1977), Appendix A-6.
[7] R. A. Zingarelli, ''Finite Difference Solutions to the Workshop Problems,'' in Proceedings of the Reverberation and Scattering Workshop, edited by D. B. King, S. A. Chin-Bing, J. A. Davis, and R. B. Evans, May 1994, Gulfport, MS, 3.148–3.166, Naval Research Laboratory Book Contribution NRL/BE/7181-96-001.
[8] R. M. Alford, K. R. Kelly, and D. M. Boore, ''Accuracy of finite-difference modeling of the acoustic wave equation,'' Geophysics **39**, 834–842 (1974).
[9] J. W. Caruthers, R. S. Keiffer, and J. C. Novarini, ''Near-field acoustic scattering from simulated two-dimensional wind-driven sea surfaces,'' J. Acoust. Soc. Am. **91**, 813–822 (1992).
[10] W. J. Pierson and L. Moskowitz, ''A proposed spectral form for fully developed wind sea based on the similarity theory of S. A. Kitaigorodskii,'' J. Geophys. Res. **69**, 5181–5190 (1964).
[11] C. H. Horton, *Signal Processing of Underwater Acoustic Waves* (U. S. Gov. Printing Office, Washington, D. C., 1969).

Multi-section matched-peak tomographic inversion with a moving source

E. K. Skarsoulis
Institute of Applied and Computational Mathematics, Foundation for Research and Technology Hellas, P.O. Box 1527, 711 10 Heraklion, Crete, Greece

(Received 3 August 2000; revised 16 February 2001; accepted 29 May 2001)

An extended matched-peak inversion approach is proposed for the simultaneous analysis of travel-time data from multiple tomographic sections, from a moving source to a number of peripheral fixed receivers, to estimate the position of the source and the ocean state along the various sections. The proposed solution consists of finding those model states and source positions that maximize the joint number of peak identifications in the arrival patterns measured simultaneously along all sections. The offset calibration problem, associated with the uncertainty regarding mooring positions and possible unresolved internal instrument delays, is also addressed using the peak-matching principle. The time offsets are estimated such that the total number of identifications, over all sections and all transmissions, is maximized. The same analysis also applies to the case of a moving receiver listening to a number of fixed sources. The proposed approach is applied for the analysis of 9-month-long travel-time data from four conodal sections of the Thetis-2 tomography experiment.
[DOI: 10.1121/1.1387092]

PACS numbers: 43.30.Pc, 43.30.Bp, 43.60.Lq [DLB]

I. INTRODUCTION

Ocean acoustic travel-time tomography was introduced by Munk and Wunsch[1,2] as a remote-sensing technique for monitoring the ocean interior. Measuring the travel times of pulsed acoustic signals propagating through the water mass over a multitude of different paths, and exploiting the knowledge about how travel times are affected by the sound-speed (temperature) distribution in the water, the latter can be obtained by inversion. Nevertheless, the identification problem has to be solved first, i.e., the model arrival times must be associated with the observed travel times at the receiver.[3,4] Traditionally, this problem is solved by obtaining observed peak tracks (tracking problem) which are then associated with model peaks (identification problem), either manually or automatically.[5–9]

Recently, a matched-peak inversion approach was introduced[10] which by-passes the explicit solution of the tracking and identification problem. Using the linearized model relations between sound-speed and arrival-time perturbations about a set of background states, arrival times and associated model errors are calculated on a fine grid of model states discretizing the parameter space. Each model state can explain (identify) a number of observed peaks in a particular measurement lying within the uncertainty intervals of the corresponding predicted arrival times. The model states that explain the maximum number of observed peaks are considered as the more likely parametric descriptions of the measurement; these model states can be described in terms of mean values and variances providing a statistical answer (matched-peak solution) to the inversion problem. This approach has already been applied for the analysis (slice inversions) of large-scale tomography experiments, such as the 9-month-long Thetis-2 experiment in the western Mediterranean sea[10,11] and the ongoing multi-year experiment in the Labrador sea.[12]

In the Thetis-2 experiment one of the moored transceivers failed to receive tomography signals from other instruments as well as navigation signals from its associated bottom transponders used for motion tracking. The particular transceiver acted only as a source during the 9 months of the experiment. Its signals were recorded at a number of receivers within the tomographic array; nevertheless, the corresponding arrival times could not be corrected for the motion of the source, due to lack of navigation data, and thus absolute-time inversions could not be performed. In the present work the matched-peak approach is extended to allow the simultaneous analysis of travel-time data from multiple tomographic sections, from a moving source to a number of peripheral fixed receivers, to estimate the position of the source and the ocean state along the various sections. The proposed approach exploits the estimated peak arrival times from the simultaneous acoustic transmissions along the sections. The solution consists of finding the population of model states and source positions that maximize the joint number of peak identifications, over all sections. The same analysis also applies to the case of a moving receiver listening to a number of fixed sources.

Cornuelle[13] introduced a unified probabilistic approach for solving the inversion, mooring-motion, and clock-drift estimation problem for an arbitrary number of moving transceivers using ray theory and linear model relations (between ocean parameters and travel times). Gaillard[14] adapted a deterministic ray inversion scheme, introduced by Munk and Wunsch,[15] to the case of moving transceivers, assuming ocean perturbations about a canonical sound-speed profile. Also in that work the case was treated where three sources at fixed locations are used to track a moving receiver in the middle, simultaneously with the inversions along the three

sections. These approaches are simple and generic. Nevertheless, they both assume that identified peak tracks exist, and they also rely on linear model relations. The matched-peak approach applies directly to the estimated travel times, without requiring the identification problem to be solved beforehand, thus enabling the automatic analysis of travel-time data; furthermore, considering the background state as an unknown, the case of nonlinear model relations can be treated.

The lack of knowledge of the exact mooring positions, i.e., of the exact horizontal distance between any two moorings, and possible unresolved internal instrument delays cause a travel-time offset. This offset is usually estimated (and removed) by comparing acoustic measurements with acoustic predictions based on existing hydrographic measurements; this requires simultaneous acoustic and hydrographic measurements along each section.[9] In the case of multiple conodal sections a calibration method is proposed here, which is based on the peak-matching principle and which maximizes the total number of identifications over all sections and all transmissions. This calibration approach is based on acoustic data only, i.e., it does not require additional hydrographic measurements.

The contents of the work are organized as follows: Section II addresses the model relations between acoustic travel times and ocean parameters, as well as further sources of travel-time variability, such as mooring motion, clock drift, and time offsets. The derivative of arrival times with respect to the source–receiver range is expressed analytically using the notion of peak arrivals and normal-mode theory. In Sec. III the inversion problem for the case of multiple sections with a central moving transceiver is addressed, using the matched-peak approach. In the case of small transceiver displacements an invariance property of the matched-peak estimates of the time offsets is proven and discussed. In Sec. IV the proposed method is used for the analysis of 9-month-long travel-time data from four conodal sections of the Thetis-2 tomography experiment conducted from January to October 1994 in the western Mediterranean Sea. Further, a synthetic test case, based on the Thetis-2 data with simulated transceiver displacements, is considered. In Sec. V the main features of the proposed approach are discussed and conclusions are drawn.

II. MODEL RELATIONS AND TRAVEL-TIME VARIABILITY

A tomographic setting is considered with a broadband source and a distant receiver in a range-independent ocean. Due to the multi-path nature of acoustic propagation, a pulsed signal emitted by the source will arrive at the receiver as a sequence of peaks (the acoustic arrivals) at different time instants. The arrival times of the peaks can be modeled as functionals of the sound-speed profile $c(z)$ by expressing the arrival pattern a, defined as the amplitude of the acoustic pressure p_r at the receiver in the time domain, through the inverse Fourier transform

$$a(t;c;R,z_s,z_r)=|p_r(t;c;R,z_s,z_r)| = \frac{1}{2\pi}\left|\int_{-\infty}^{\infty} H_{sr}(\omega;c;R,z_s,z_r)P_s(\omega)e^{j\omega t}\,d\omega\right|, \tag{1}$$

where $P_s(\omega)$ is the source signal in the frequency domain and $H_{sr}(\omega;c;R,z_s,z_r)$ is the Green's function. The latter depends on the circular frequency ω, the sound-speed profile $c(z)$, and the relative source/receiver locations, i.e., on the source–receiver range R, the source and receiver depth z_s and z_r, respectively. From the mathematical viewpoint the arrivals can be defined as the local maxima of the arrival pattern with respect to time[16]

$$\frac{\partial a}{\partial t}(\tau_i;c;R,z_s,z_r)=0, \quad i=1,...,I. \tag{2}$$

This definition of arrivals (peak arrivals) is generic and encompasses the notions of ray arrivals[1,17] and modal arrivals[18,19] as special cases; it can also cope with any modeling approach for the arrival pattern, either ray- or wave theoretic. Since the arrival pattern depends on the sound-speed profile and the source–receiver locations, the peak arrival times do so as well, i.e., $\tau_i=\tau_i(c;R,z_s,z_r)$.

The sound-speed variability in a certain area can be represented through a modal expansion

$$c(z)=c_0(z)+\sum_{l=1}^{L}\vartheta_l f_l(z), \tag{3}$$

where $c_0(z)$ is a basic reference profile and $f_l(z)$, $l=1,...,L$, is a set of sound-speed modes, e.g., empirical orthogonal functions (EOFs).[20] The functional dependence of τ_i on the sound speed, assuming fixed source/receiver positions, can be written as a parametric dependence on the modal parameter vector $\boldsymbol{\vartheta}=(\vartheta_1,\ldots,\vartheta_L)'$

$$\tau_i=g_i(\boldsymbol{\vartheta}), \quad i=1,2,...,I, \quad \boldsymbol{\vartheta}\in\Theta, \tag{4}$$

where Θ is the parameter domain spanning the anticipated sound-speed variability. Although the dependence $g_i(\boldsymbol{\vartheta})$ is in general nonlinear, in the case of small variations about a background state $\boldsymbol{\vartheta}^{(b)}$ it can be linearized

$$\boldsymbol{\tau}(\boldsymbol{\vartheta})=\boldsymbol{\tau}^{(b)}+\mathbf{G}^{(b)}(\boldsymbol{\vartheta}-\boldsymbol{\vartheta}^{(b)}), \tag{5}$$

where $\boldsymbol{\tau}=(\tau_1,\ldots,\tau_I)'$ is the arrival-time vector, $\boldsymbol{\tau}^{(b)}=\boldsymbol{\tau}(\boldsymbol{\vartheta}^{(b)})$ denotes the background arrival times, and $\mathbf{G}^{(b)}$ is the observation (influence) matrix corresponding to the background state $\boldsymbol{\vartheta}^{(b)}$ and relating the sound-speed and travel-time variability, $G_{il}^{(b)}=\partial g_i(\boldsymbol{\vartheta}^{(b)})/\partial\vartheta_l$. Using the notions of ray, modal, or peak arrivals, the matrix $\mathbf{G}^{(b)}$ can be analytically expressed in terms of background quantities,[16,17,21] and Eq. (5) can be used as a basis for linear $\boldsymbol{\vartheta}$ inversions of travel-time data.

In the case where the nonlinear dependence of the arrival times on the sound-speed parameters becomes significant (e.g., large sound-speed variations), the above linearization about a single background state is insufficient and cannot be used for inversions. Nevertheless, it can be extended in a straightforward manner by considering a set of discrete background states, rather than a single background

state, whose extent depends on the anticipated sound-speed variability and the degree of nonlinearity;[9] then, Eq. (5) can be used with respect to the nearest background state each time. In this connection, the index b will be considered in the following as a variable, $b \in \mathcal{B}$, from the set $\mathcal{B}$ of discrete background states. Thus, the nonlinear model relation (4) is replaced by a set of linear ones. The cost to be paid, with respect to the inverse problem, is that an additional unknown is introduced, the background variable b.

In addition to sound-speed changes there are also other sources of travel-time variability in a range-independent ocean environment, such as mooring motions and clock drifts. Furthermore, the lack of knowledge of the exact mooring positions, and possible unresolved internal instrument delays cause travel-time offsets and displacements that have to be accounted for. Taking these factors into account, the observed travel times $\boldsymbol{\tau}^{(o)}$ can be written in the form

$$\boldsymbol{\tau}^{(o)} = \boldsymbol{\tau}^{(b)} + \mathbf{G}^{(b)}(\boldsymbol{\vartheta} - \boldsymbol{\vartheta}^{(b)}) + \frac{\partial \boldsymbol{\tau}}{\partial R}(\delta r + \Delta R) + \mathbf{u}(\delta t + \Delta T) + \boldsymbol{\nu}. \tag{6}$$

The vector $\partial\boldsymbol{\tau}/\partial R$ is the derivative of travel times with respect to the horizontal source–receiver range. The variable δr denotes the range perturbation due to mooring motion, whereas ΔR denotes the difference of the actual distance between moorings (after deployment) and the assumed (best estimated) distance used for acoustic modeling. The vertical motions of the source or receiver are not accounted for here. One reason is that for moored instruments and small mooring deviations from the vertical, displacements in the vertical are much smaller than in the horizontal. Furthermore, the derivative of travel times with respect to the vertical mooring displacement for typical underwater propagation conditions has been estimated by Cornuelle[13] to be about one order of magnitude smaller than the horizontal-motion derivative.[22]

If the source and receiver location is tracked during the experiment, e.g., through bottom-mounted navigation transponders, the range perturbation δr can be estimated for each transmission and the corresponding mooring motion effect can be removed from the observed travel times. Since the source and the receiver change their positions with time, following the mooring motions, the range perturbation δr will be in general different from transmission to transmission. The deviation ΔR, on the other hand, is a constant which accounts for the difference between the actual and the nominal (best estimated) source–receiver range, which remains even after removal of the mooring-motion effect. Since the mooring locations can be known today with GPS accuracy, the correction ΔR will be of the order of a few meters at most.

The vector $\mathbf{u}$ in (6) is a unity vector, with all its elements equal to 1. The variable δt denotes the differential clock drift, i.e., the difference between receiver and source clock drifts, during the experiment. This is expected to be a smooth function of time and is commonly approximated by a low-order polynomial. The term ΔT accounts for a differential internal instrument delay which is assumed constant. Finally, the vector $\boldsymbol{\nu}$ in (6) accounts for the cumulative modeling and observation error.

A. Range derivatives of arrival times

As already mentioned, the arrival pattern a—and thus the arrival times—in a range-independent ocean environment depend on the sound-speed profile and also on the location of the source and receiver, i.e., on the source–receiver range and depths. Applying Eq. (2) at a perturbed range and using a Taylor expansion about the unperturbed state, the following expression can be obtained for the derivative of peak arrival times with respect to the source–receiver range:

$$\frac{\partial \tau_i}{\partial R} = \frac{-\dfrac{\partial^2 a(\tau_i; c; R, z_s, z_r)}{\partial R \partial t}}{\dfrac{\partial^2 a(\tau_i; c; R, z_s, z_r)}{\partial t^2}}. \tag{7}$$

The time derivatives of the arrival pattern can be obtained from H_{sr} through (1) by using elementary properties of the Fourier transform. Further, the calculation of $\partial a/\partial R$ can be reduced to the calculation of H_{sr} and $\partial H_{sr}/\partial R$.[16] The expression (7) is generic and can be used in connection with any propagation model, either geometric or wave theoretic. Using normal-mode theory[23,24] the Green's function H_{sr} in the far field can be written as a sum of modes

$$H_{sr}(\omega; c; R, z_s, z_r) = \frac{\omega\rho^2}{\sqrt{8\pi}} \sum_{n=1}^{N} \frac{u_n(z_s) u_n(z_r)}{\sqrt{k_n R}} \times \exp\{j k_n R - j\pi/4\}, \tag{8}$$

where ρ is the water density. The quantities k_n and u_n, $n = 1,...,N$ are the real eigenvalues and the corresponding eigenfunctions (propagating modes), respectively, of the vertical Sturm–Liouville problem

$$\frac{d^2 u_n(z)}{dz^2} + \frac{\omega^2}{c^2(z)} u_n(z) = k_n^2 u_n(z), \tag{9}$$

supplemented by the conditions that $u_n = 0$ at the sea surface, ρu_n and du_n/dz are continuous across the interfaces, and u_n and du_n/dz are vanishing as $z \to \infty$. The range derivative of the Green's function (8) can be expressed as

$$\frac{\partial H_{sr}}{\partial R} = -\frac{1}{2R} H_{sr} + \frac{\omega\rho^2}{\sqrt{8\pi}} \sum_{n=1}^{N} k_n \frac{u_n(z_s) u_n(z_r)}{\sqrt{k_n R}} \times \exp\{j k_n R + j\pi/4\}. \tag{10}$$

The first term in the above expression is due to the variation of the geometrical attenuation term $\sqrt{k_n R}$. The second term is due to the phase variation and is dominant, since the first term contains the range R in the denominator. Using the above expressions (8) and (10), in connection with (1) and (7), the range derivatives of the peak arrival times can be calculated.

Table I shows calculated values of these derivatives for eight peak arrivals along four Thetis-2 sections (details are given in Sec. IV). It is seen from this table that early arrivals are characterized by smaller values of the range derivatives than late arrivals. Furthermore, the range of values is very

TABLE I. Range derivatives of peak-arrival times based on normal-mode calculations for four Thetis-2 sections.

τ_i (s)	$\partial\tau_i/\partial R$ (s/m)	τ_i (s)	$\partial\tau_i/\partial R$ (s/m)
H-W4		W5-W4	
201.474	$6.626\cdot10^{-4}$	157.361	$6.617\cdot10^{-4}$
201.053	$6.612\cdot10^{-4}$	157.161	$6.602\cdot10^{-4}$
200.995	$6.607\cdot10^{-4}$	157.078	$6.592\cdot10^{-4}$
200.924	$6.587\cdot10^{-4}$	157.024	$6.586\cdot10^{-4}$
200.841	$6.576\cdot10^{-4}$	156.963	$6.566\cdot10^{-4}$
200.697	$6.552\cdot10^{-4}$	156.851	$6.554\cdot10^{-4}$
200.494	$6.534\cdot10^{-4}$	156.665	$6.527\cdot10^{-4}$
200.186	$6.497\cdot10^{-4}$	156.343	$6.483\cdot10^{-4}$
S-W4		W3-W4	
169.404	$6.646\cdot10^{-4}$	235.091	$6.632\cdot10^{-4}$
169.218	$6.616\cdot10^{-4}$	234.864	$6.604\cdot10^{-4}$
169.123	$6.591\cdot10^{-4}$	234.717	$6.587\cdot10^{-4}$
169.052	$6.578\cdot10^{-4}$	234.632	$6.576\cdot10^{-4}$
168.947	$6.563\cdot10^{-4}$	234.534	$6.568\cdot10^{-4}$
168.793	$6.546\cdot10^{-4}$	234.375	$6.541\cdot10^{-4}$
168.544	$6.509\cdot10^{-4}$	234.136	$6.520\cdot10^{-4}$
168.124	$6.462\cdot10^{-4}$	233.789	$6.485\cdot10^{-4}$

small, from above $6.45\cdot10^{-4}$ s/m to less than $6.65\cdot10^{-4}$ s/m for all sections; the variability in all cases is less than 3%. Thus, a 10-m range increase will cause a time delay of about 6.45 ms to the earliest arrivals and 6.65 ms to the latest ones; i.e., the relative displacement of the arrivals will be as small as 0.2 ms. On the other hand, a 1000-m range increase will cause a delay of about 645 ms to the early arrivals and 665 ms to the late ones; i.e., the arrival pattern will stretch by approximately 20 ms. These findings are in agreement with the results by Cornuelle[13] for the range derivatives of ray-arrival times

$$\frac{\partial\tau_i}{\partial R}=\frac{\cos\psi_{r,i}}{c(z_r)}=\frac{\cos\psi_{s,i}}{c(z_s)}, \tag{11}$$

where $\psi_{r,i}$ and $\psi_{s,i}$ are the grazing angle of the ith eigenray at the source and at the receiver, respectively. Since ray grazing angles are typically less than 12 deg, with larger angles corresponding to earlier ray arrivals, using a typical sound speed of 1500 m/s yields a range for the derivative values similar to that obtained for the peak arrivals above.

In conclusion, a range variation causes a translation and a relative deformation (stretching/shrinking) to the arrival pattern. The translation effect is dominant while the deformation is much weaker. If the range variation is small, of the order of a few tens of meters, the deformation effect is very small, of the order of 1 ms. As mentioned earlier, the magnitude ΔR, accounting for the difference between actual and nominal (best estimated from GPS) mooring distance, is expected to reach a few meters at most. In this connection, the stretching/shrinking effect of ΔR on the travel times can be neglected. Since the remaining translation effect due to ΔR is similar to the effect of the internal instrument delay ΔT, the two effects can be merged in (6), resulting in

$$\boldsymbol{\tau}^{(o)}=\boldsymbol{\tau}^{(b)}+\mathbf{G}^{(b)}(\boldsymbol{\vartheta}-\boldsymbol{\vartheta}^{(b)})+\frac{\partial\boldsymbol{\tau}}{\partial R}\delta r+\mathbf{u}(\delta t+\Delta T)+\boldsymbol{\nu}. \tag{12}$$

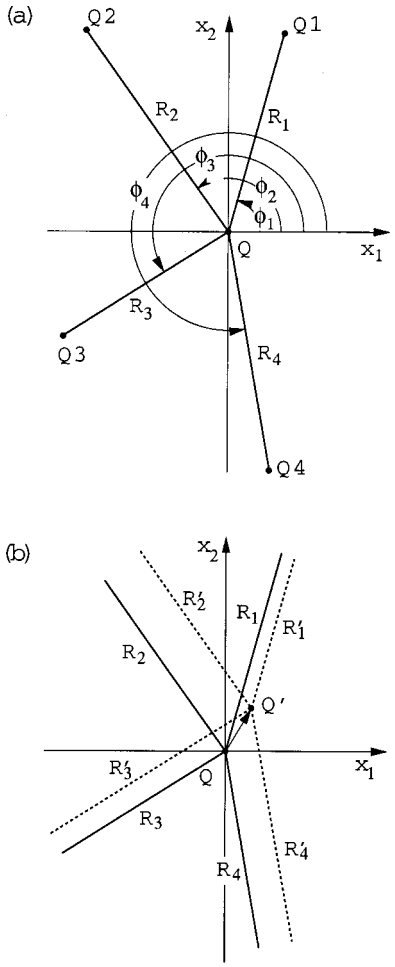

FIG. 1. (a) The geometry of multiple conodal sections defined by a central transceiver Q and a set of peripheral transceivers Q1, Q2, etc. (b) Perturbed geometry due to a horizontal displacement of the central transceiver (detail).

III. MULTI-SECTION MATCHED-PEAK INVERSION

In this section the matched-peak approach is applied to travel-time data from multiple conodal tomographic sections, e.g., from a moving source to a number of peripheral fixed receivers, as shown in Fig. 1(a). The same analysis also applies to the case of a moving receiver listening to a number of fixed sources. The observed travel-time data in the simultaneous transmissions along the various sections will be exploited in order to estimate the position of the central transceiver, the ocean state, and the constant offset along each section. Clock-drift errors are not accounted for, i.e., it is assumed that the observed arrival times have been corrected for the differential clock drift.

Any deviation of the central mooring from the vertical will induce a horizontal displacement $\mathbf{x}=(x_1,x_2)$ to the central transceiver which in turn will affect the horizontal range of each section. Assuming that the horizontal deviations of the central transceiver are much smaller than the horizontal ranges of the sections, the perturbed sections will be nearly parallel to the nominal ones, as shown in Fig. 1(b), and thus the change in range for each section will be given by the projection of the vector $\mathbf{x}$ on the original section direction

$$\delta r_s(\mathbf{x})=-x_1\cos\phi_s-x_2\sin\phi_s, \quad s=1,...,S, \tag{13}$$

where ϕ_s is the angle that section s builds with the axis x_1, as shown in Fig. 1(a), and δr_s the range perturbation of section s due to $\mathbf{x}$. The subscript s is used in the following to denote section-specific quantities. Neglecting the clock-drift term from (12), the observed travel times for the sth section become

$$\boldsymbol{\tau}_s^{(o)} = \boldsymbol{\tau}_s^{(b)} + \mathbf{G}_s^{(b)}(\boldsymbol{\vartheta}_s - \boldsymbol{\vartheta}_s^{(b)}) + \frac{\partial \boldsymbol{\tau}_s}{\partial R_s}\,\delta r_s(\mathbf{x}) + \mathbf{u}_s \Delta T_s + \boldsymbol{\nu}_s . \tag{14}$$

For each set of simultaneous transmissions the unknowns are the horizontal displacement $\mathbf{x}$ of the central transceiver, the background state b_s, and the parameter vector $\boldsymbol{\vartheta}_s$ (or, alternatively, the perturbation $\boldsymbol{\vartheta}_s - \boldsymbol{\vartheta}_s^{(b)}$), $s = 1,...,S$, along each section. In addition, the constants (offsets) ΔT_s have to be estimated.

In the matched-peak approach the parameter domain referring to each section is discretized into a regular grid, with discretization steps $\delta\boldsymbol{\vartheta}_s$,[10] which is superposed on the grid of background states for that section. Using the model relations, arrival-time predictions are made for each discrete model state $\tilde{\boldsymbol{\vartheta}}_s$ (a tilde denotes quantities referring to the discretization grid), depending also on the displacement $\mathbf{x}$ and the constant ΔT_s

$$\tilde{\boldsymbol{\tau}}_s(\tilde{\boldsymbol{\vartheta}}_s;\mathbf{x};\Delta T_s) = \boldsymbol{\tau}_s^{(b)} + \mathbf{G}_s^{(b)}(\tilde{\boldsymbol{\vartheta}}_s - \boldsymbol{\vartheta}_s^{(b)}) + \frac{\partial \boldsymbol{\tau}_s}{\partial R_s}\,\delta r_s(\mathbf{x}) + \mathbf{u}_s \Delta T_s . \tag{15}$$

Each discrete model state corresponds to a particular background state. An estimate for the upper bound of the prediction error is given by the sum of the observation/modeling error $\boldsymbol{\nu}_s$ and a discretization error, which depends on the background state and the discretization steps

$$\mathbf{e}_s(b_s, \delta\boldsymbol{\vartheta}_s) = \tfrac{1}{2}|\mathbf{G}_s^{(b)}|\,\delta\boldsymbol{\vartheta}_s + \boldsymbol{\nu}_s , \tag{16}$$

where $|\mathbf{G}_s^{(b)}|$ denotes the matrix whose elements are the absolute values of the elements of $\mathbf{G}_s^{(b)}$. Each of the predicted arrival times (15) is allowed to associate with observed arrival times if its time difference is smaller than the corresponding travel-time error (16). A matching index Λ_s can be thus calculated along each section, depending on $\tilde{\boldsymbol{\vartheta}}_s$, $\mathbf{x}$, and ΔT_s, and denoting the number of identifiable peaks, i.e., the number of peaks in the measured arrival pattern that can be associated with the predicted arrival times $\tilde{\boldsymbol{\tau}}_s(\tilde{\boldsymbol{\vartheta}}_s;\mathbf{x};\Delta T_s)$

$$\Lambda_s = \Lambda_s(\tilde{\boldsymbol{\vartheta}}_s;\mathbf{x};\Delta T_s). \tag{17}$$

Λ_s can be calculated in a straightforward and simple way as explained in Ref. 10; the associated computational burden is much smaller than for building up the set of all possible trial identifications (possible associations between predicted and observed peaks), which is necessary, e.g., for explicitly solving the identification problem.[9]

According to the peak-matching principle, the sound-speed parameters $\boldsymbol{\vartheta}_s$ along the various sections and the horizontal displacement $\mathbf{x}$ of the central transceiver can be estimated from each set of simultaneous transmissions, for given offsets ΔT_s, by finding the population of discrete model states and corresponding displacements that maximize the joint number of peak identifications over all sections

$$V(\Delta\mathbf{T}) = \left\{ (\tilde{\boldsymbol{\vartheta}}_1,\ldots,\tilde{\boldsymbol{\vartheta}}_S;\mathbf{x}) : \sum_{s=1}^{S} \Lambda_s(\tilde{\boldsymbol{\vartheta}}_s;\mathbf{x};\Delta T_s) = \max \right\}, \tag{18}$$

where $\Delta\mathbf{T} = (\Delta T_1,\ldots,\Delta T_S)$ denotes the vector of offsets along all sections. The maximum value of the joint matching index corresponding to the elements of $V(\Delta\mathbf{T})$ is denoted by $M(\Delta\mathbf{T})$

$$(\tilde{\boldsymbol{\vartheta}}_1,\ldots,\tilde{\boldsymbol{\vartheta}}_S;\mathbf{x}) \in V(\Delta\mathbf{T}) \Leftrightarrow \sum_{s=1}^{S} \Lambda_s(\tilde{\boldsymbol{\vartheta}}_s;\mathbf{x};\Delta T_s) = M(\Delta\mathbf{T}). \tag{19}$$

Since $\Delta\mathbf{T}$ is valid for the entire experiment duration, from deployment to recovery, it is estimated from the entire data set, i.e., from the entirety of the sets of simultaneous transmissions. Assuming that there are K sets of simultaneous transmissions along the sections considered, and denoting by $M_k(\Delta\mathbf{T})$ the maximum of the joint matching index corresponding to the kth transmission set, the matched-peak estimate of $\Delta\mathbf{T}$ is set to maximize the sum $\mathcal{M}(\Delta\mathbf{T}) = \Sigma_{k=1}^{K} M_k(\Delta\mathbf{T})$ over all transmissions. It is shown in the following subsection, for the case of small motions, that this estimate is not a unique one, but rather a class

$$\mathcal{D} = \{\Delta\mathbf{T} : \mathcal{M}(\Delta\mathbf{T}) = \max\} \tag{20}$$

of estimates, based on the fact that the global matching index $\mathcal{M}$ is invariant to translations of the (x_1, x_2) coordinate system. The maximum of the global matching index, over all sections and all transmissions, corresponding to the elements of $\mathcal{D}$, will be denoted by $\mathcal{M}_{\max}$

$$\Delta\mathbf{T} \in \mathcal{D} \Leftrightarrow \mathcal{M}(\Delta\mathbf{T}) = \mathcal{M}_{\max}. \tag{21}$$

In summary, the offset calibration (determination of $\Delta\mathbf{T}$) is performed by maximizing the global matching index, over all sections and all transmissions. At the level of each single set of simultaneous transmissions the oceanographic inversion problem along the sections as well as the navigation problem for the central transceiver is solved by maximizing the joint matching index, over all sections. In other words, using probabilistic terminology, the offset calibration problem is solved by maximizing the marginal likelihood over all sections and transmissions, the likelihood being represented by the matching index for each section and each transmission, whereas the oceanographic inversion and navigation problems are solved at the level of each single set of simultaneous transmissions, by maximizing the marginal likelihood over all sections.

A. Small motions

If the horizontal displacement $\mathbf{x}$ of the central transceiver is small, the range effects on the arrival pattern can be considered limited to the translation only, since the time stretching/shrinking of the arrival pattern will be negligible, as discussed in Sec. II A. In the matched-peak context, negligible means that it is small compared to the cumulative observation, modeling, and discretization errors. For assumed errors of the order of 10 ms, horizontal displacements

up to about 50 m can be considered to be small, since the induced relative deformation of the arrival pattern is less than 1 ms. The horizontal displacements of the Thetis-2 transceivers are of the above order and can thus be considered as small motions. Neglecting the deformation effect of the horizontal displacement $\mathbf{x}$, the arrival-time predictions are written in the form

$$\tilde{\boldsymbol{\tau}}_s(\tilde{\boldsymbol{\vartheta}}_s;\mathbf{x};\Delta T_s)=\boldsymbol{\tau}_s^{(b)}+\mathbf{G}_s^{(b)}(\tilde{\boldsymbol{\vartheta}}_s-\boldsymbol{\vartheta}_s^{(b)})+\mathbf{u}_s(c_r^{-1}\delta r_s(\mathbf{x})+\Delta T_s), \quad (22)$$

where c_r is an arbitrary reference sound speed, e.g., 1500 m/s (a change in c_r of 10 m/s will cause a travel-time error as small as 0.2 ms).

It is shown in the following that if $\Delta\mathbf{T}$ belongs to $\mathcal{D}$, then any other delay vector $\Delta\mathbf{T}'$ defined through the relation

$$\Delta T_s'=\Delta T_s+A_1\cos\phi_s+A_2\sin\phi_s, \quad s=1,2,...,S, \quad (23)$$

where A_1 and A_2 are constants, will also belong to $\mathcal{D}$. Substituting (23) into (22) and taking into account the kinematic condition (13), the predicted arrival times can be written

$$\begin{aligned}\tilde{\boldsymbol{\tau}}_s(\tilde{\boldsymbol{\vartheta}}_s;\mathbf{x};\Delta T_s)&=\boldsymbol{\tau}_s^{(b)}+\mathbf{G}_s^{(b)}(\tilde{\boldsymbol{\vartheta}}_s-\boldsymbol{\vartheta}_s^{(b)})\\&\quad+\mathbf{u}_s(c_r^{-1}\delta r_s(\mathbf{x}+c_r\mathbf{A})+\Delta T_s')\\&=\tilde{\boldsymbol{\tau}}_s(\tilde{\boldsymbol{\vartheta}}_s;\mathbf{x}+c_r\mathbf{A};\Delta T_s'),\end{aligned} \quad (24)$$

where $\mathbf{A}=(A_1,A_2)$. The above equality of the predicted arrival times for $\Delta\mathbf{T}$ and $\Delta\mathbf{T}'$, for the same discrete model state $\tilde{\boldsymbol{\vartheta}}_s$ but different displacements $\mathbf{x}$ and $\mathbf{x}+c_r\mathbf{A}$, respectively, passes to the matching index for each section at the level of a single transmission

$$\Lambda_s(\tilde{\boldsymbol{\vartheta}}_s;\mathbf{x};\Delta T_s)=\Lambda_s(\tilde{\boldsymbol{\vartheta}}_s;\mathbf{x}+c_r\mathbf{A};\Delta T_s'), \quad (25)$$

which in turn results in identical optimum (maximum) values for the joint matching indices

$$M(\Delta\mathbf{T})=M(\Delta\mathbf{T}'). \quad (26)$$

In the case of K sets of simultaneous transmissions, Eq. (26) holds for each set of simultaneous transmissions, i.e., it becomes $M_k(\Delta\mathbf{T})=M_k(\Delta\mathbf{T}')$, $k=1,...,K$. The global matching index corresponding to $\Delta\mathbf{T}'$ will then read

$$\begin{aligned}\mathcal{M}(\Delta\mathbf{T}')&=\sum_{k=1}^{K}M_k(\Delta\mathbf{T}')=\sum_{k=1}^{K}M_k(\Delta\mathbf{T})\\&=\mathcal{M}(\Delta\mathbf{T})=\mathcal{M}_{\max},\end{aligned} \quad (27)$$

since $\Delta\mathbf{T}\in\mathcal{D}$. Equation (27) implies that $\Delta\mathbf{T}'$ also belongs to $\mathcal{D}$. Accordingly, for each offset vector $\Delta\mathbf{T}$ in $\mathcal{D}$ there is a multiplicity of equivalent offset vectors $\Delta\mathbf{T}'$ which correspond to translations of the (x_1,x_2)-coordinate system; the transformation (23), in particular, corresponds to a translation by $c_r\mathbf{A}$. Consequently, any two components of $\Delta\mathbf{T}$ can be arbitrarily fixed, e.g., $\Delta T_1=\Delta T_2=0$; i.e., the dimension of the $\Delta\mathbf{T}$ search can be reduced by 2. From the above it is clear that the global matching index $\mathcal{M}(\Delta\mathbf{T})$ and the associated model states at the level of each section and each transmission are invariant to translations of the (x_1,x_2)-coordinate system. The same can be shown to be also true for rotations, which however do not affect the dimensionality of the ΔT-search.

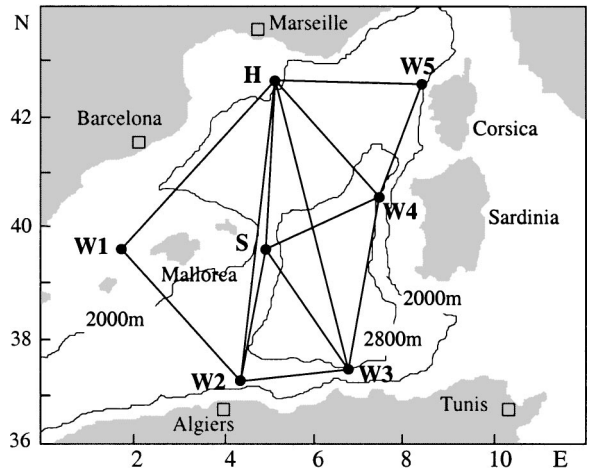

FIG. 2. The geometry of the Thetis-2 experiment in the western Mediterranean Sea.

IV. APPLICATION TO THETIS-2 EXPERIMENT

In this section the proposed inversion approach is applied to multi-section travel-time data from the Thetis-2 tomography experiment conducted from January to October 1994 in the western Mediterranean Sea.[11,25] Figure 2 shows the experimental site and geometry. The tomographic array contained seven moored transceivers, all deployed at a nominal depth of 150 m. An HLF-5 source, marked by H, of central frequency 250 Hz and effective bandwidth 62.5 Hz, insonified the basin at 8-h intervals. The remaining six sources (W1–W5 and S), transmitting six times per day, were of Webb type with central frequency 400 Hz and effective bandwidth 100 Hz. The receiver parts of H and S could listen to 400-Hz signals only, whereas the receivers at W1–W5 were modified to listen to both 400-Hz and 250-Hz signals.

After completion of the experiment it was discovered that the instrument W4 had very few good records. A leakage had resulted in a short circuit at both the receiver and navigation inputs, such that neither navigation nor receiver data were available at this instrument.[26] Fortunately, the W4 transmitter continued to work properly and the W4 transmissions were recorded at the other instruments, in particular at W3, W5, H, and S. These receptions, however, cannot be corrected for the motions of W4 due to missing navigation data. Accordingly, absolute-time inversions cannot be performed along the corresponding sections. The multi-section matched-peak inversion method is applied in the following to the sections W3–W4, W5–W4, H–W4, and S–W4, with nominal ranges 354.7, 237.2, 303.5, and 255.4 km, respectively, to simultaneously estimate the ocean state and navigate the source W4.

A. Data

Figure 3 shows the observed peak arrival times (light dots) and cutoff peaks (heavier dots) corresponding to the daily averaged transmissions along the four sections, after

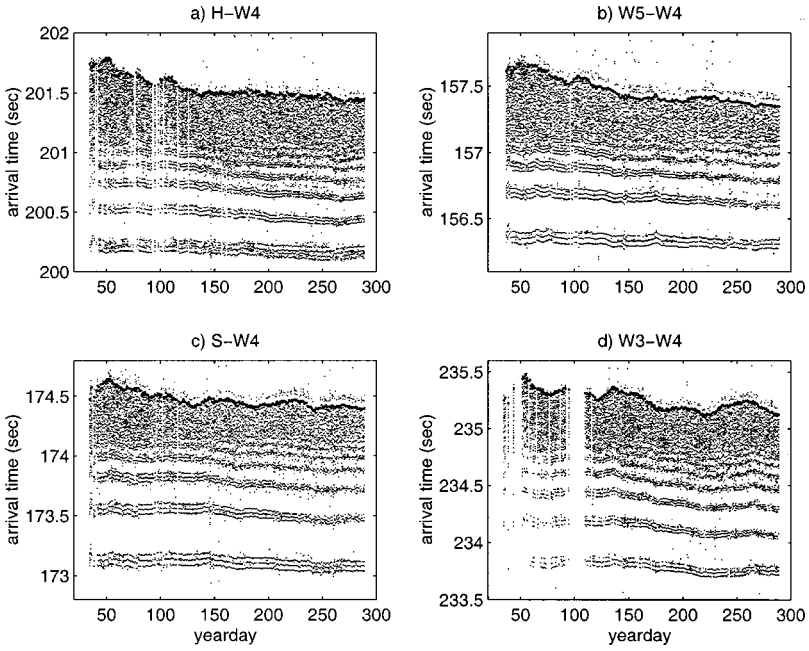

FIG. 3. Measured arrival times from W4 at H, W5, S, and W3, respectively. The cutoff peaks are denoted by heavier dots.

correlation processing and clock-drift correction. Mooring-motion correction has also been applied for all instruments except W4, i.e., the data of Fig. 3 contain the cumulative effects of ocean changes and W4 motions. The horizontal axes in Fig. 3 represent yeardays of 1994 and span the 9-month duration of the experiment, whereas the vertical axes measure travel times. Low-SNR receptions have been omitted from this figure and are neglected in the subsequent analysis. It is seen, e.g., in Fig. 3(d) that there is a nearly 15-day interruption in the W3–W4 data, around yearday 100; during this period the simultaneous four-section inversion cannot be applied.

Five to six arrival groups can be distinguished in the early part of most receptions along the four sections. These can be associated with particular ray groups corresponding to steep propagation angles. The remaining intermediate and late arrivals are difficult to interpret in terms of ray arrivals because ray groups overlap with each other in this interval. To exploit some of the information contained in the intermediate and late part of the arrival patterns the peak-arrival approach[8,16] is used, combined with normal-mode propagation modeling.

Figure 4 shows the basic reference sound-speed profile for each section and also the three most significant EOFs for the western Mediterranean basin. The historical rms values of the EOF amplitudes are $\vartheta_{1,\mathrm{rms}}=18.48$, $\vartheta_{2,\mathrm{rms}}=2.88$, and $\vartheta_{3,\mathrm{rms}}=0.96$. EOF-1 accounts for the bulk of the seasonal variability taking place close to the surface, and this explains the large rms value of the corresponding amplitude, whereas higher-order EOFs extend to increasingly deeper layers. The first three EOFs explain 99.6% of the total variance.

The behavior of peak-arrival times with respect to ϑ_1 variations, i.e., seasonal variations, is illustrated in Fig. 5. The KRAKEN[27] normal-mode code was used to calculate arrival patterns for each ϑ_1 value; the emitted signal was approximated by a Gaussian pulse. Only the peaks that can be continuously traced over the ϑ_1-variability range are plotted in Fig. 5. A nonlinear character is evident for all sections and peaks; in particular, transition intervals can be seen, different for different peaks, where the nonlinearity is stronger. These intervals correspond to the passage from surface-reflected to refracted propagation, which, in terms of rays, occurs when the sound speed at the surface equals the sound speed at the ray up-turning depth. The latter is larger for deep rays—corresponding to early arrivals—than for shallower rays—corresponding to late arrivals. Accordingly, the transition will take place at larger ϑ_1 values for early arrivals than for late ones; this behavior is seen in Fig. 5. It is remarkable that the cutoff peak-arrival time along the southmost section W3–W4, Fig. 5(d), is nearly insensitive to ϑ_1 variations; in that case the source and receiver both lie on the channel axis (150 m). Neither the presence of the channel nor the sound speed at the channel axis is affected by the first EOF, since the latter extends up to 100 m only. The particular cutoff

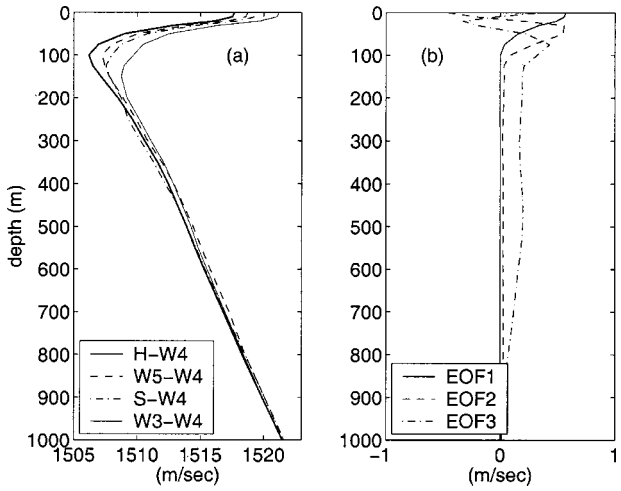

FIG. 4. (a) The basic reference sound-speed profiles along the four sections in the upper 1000 m. (b) The first three empirical orthogonal functions (EOFs) for the western Mediterranean basin.

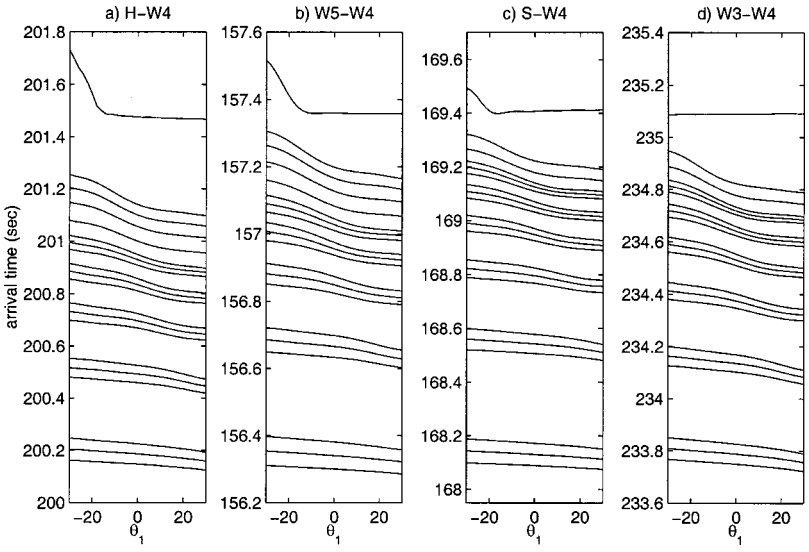

FIG. 5. The predicted arrival times along the four sections as functions of the first EOF amplitude.

peak is affected by the higher-order EOFs only.

Using the model peaks shown in Fig. 5 the matched-peak inversion approach is applied to the data of Fig. 3 to perform offset calibration and inversion along the four sections, as well as navigation of the central mooring W4. For the calculation of the observation (influence) matrix the peak-arrival approach is used. To account for large-scale range-dependence effects, travel-time corrections are calculated from hydrographic data and applied to the cutoff peaks;[9] a cold bias is predicted along all sections, with an estimated mean delay of 53, 46, 25, and 6 ms along W3–W4, W5–W4, H–W4, and S–W4, respectively. The search space for the EOF-1 amplitude along each section is set to ± 8 about the historical value for each day of the year, whereas for the remaining EOFs it is set to ± 2.5 times the corresponding rms value. The discretization steps taken are $\delta\vartheta_1 = 0.7$, $\delta\vartheta_2 = 0.5$, and $\delta\vartheta_3 = 0.25$. The resulting discretization errors range from about 2 ms for the early arrivals to 10 ms or higher for the late ones, depending on the background state. A 10-ms observation/modeling error is considered for all peaks except the cutoff, for which a larger value of 50 ms is used to account for increased variability.[9,10]

The maximum horizontal deviations of the Thetis-2 transceivers are of the order of 50–100 m.[26] In this connection, the small-motion assumption is made for the horizontal displacements of the instrument W4. The navigation results for W4 support this assumption.

B. Results

Figure 6 shows the total number of identifications $\mathcal{M}$, over all sections and all transmissions, as a function of the time offset along S–W4 and H–W4; the time offsets for the W3–W4 and W5–W4 data have been arbitrarily set to zero, in accordance with the conclusion of Sec. III A. The global matching index $\mathcal{M}$ reaches its maximum value at a single point, denoted by an asterisk in Fig. 6, with $\Delta T_{S-W4} = 20$ ms and $\Delta T_{H-W4} = 0$, corresponding to 15 077 identified peaks over all sections and transmissions (an average of about 17 identifications per section and transmission). The contours shown in Fig. 6 are separated by 10, starting from the maximum value.

It is seen from this figure that the time offsets close to the optimum, with respect to the total number of identified peaks, are distributed about a straight line with positive inclination passing through the optimum point (0,0.02). This means that an increase/decrease in the offset along H–W4 must be accompanied by an appropriate increase/decrease in the offset along S–W4 to ensure the best possible identification results, i.e., the best possible matching. This can be explained by looking at the geometry of the four sections in Fig. 2: since the offset along the nearly coaxial sections W3–W4 and W5–W4 is fixed to zero, there is only one degree of freedom left for the motion of W4, namely perpendicular to these sections, i.e., along a direction close to the east–west axis. This means that the resulting optimum offsets along H–W4 and S–W4 must be close to each other; this is observed in Fig. 6. Thus, the possibility to arbitrarily select any two of the time delays and the above behavior

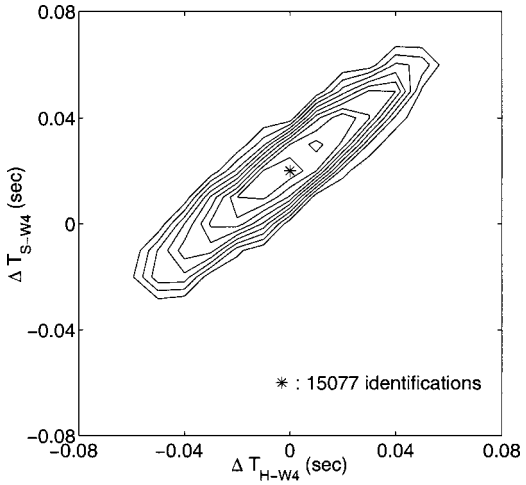

FIG. 6. Offset calibration: The global matching index $\mathcal{M}$ as function of the time offsets along H–W4 and S–W4, assuming zero offsets along W3–W4 and W5–W4. The maximum of $\mathcal{M}$ is denoted by an asterisk. The contours shown are separated by 10.

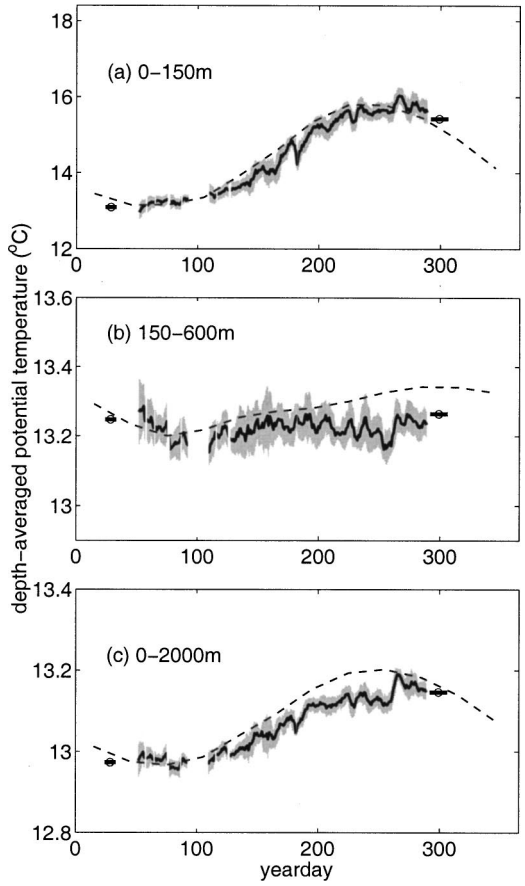

FIG. 7. Inversion results along H–W4: Evolution of depth-averaged potential temperatures in the 0–150, 150–600, and 0–2000-m layers. The retrieved mean temperatures (solid lines) and inversion errors (gray areas) are superimposed on the historical mean temperatures (dashed lines). Available hydrographic data are denoted through circles, with horizontal lines indicating the duration of observations.

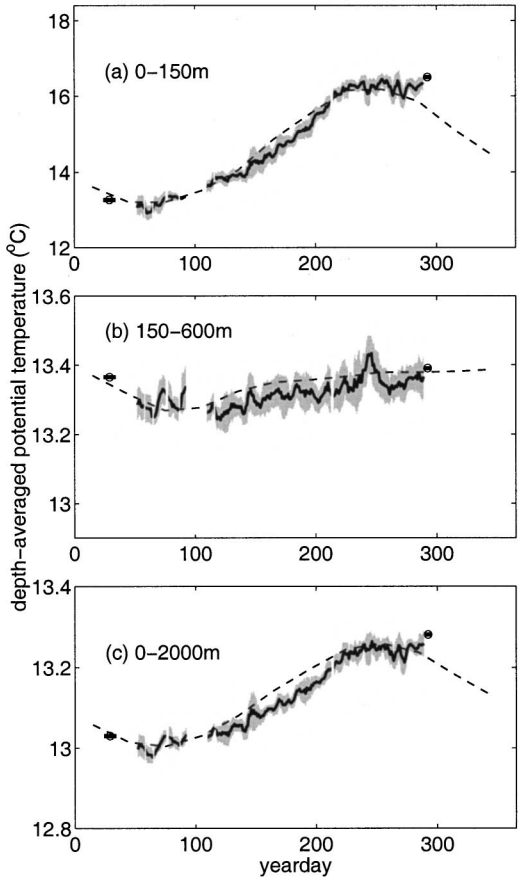

FIG. 8. Inversion results along W5–W4 (description as in Fig. 7).

render the offset calibration practically one-dimensional.

The inversion results corresponding to the optimum time offsets along the four sections are shown in Figs. 7–10, in the form of depth-averaged temperatures over three layers: a surface layer, from the surface down to 150 m, an intermediate layer from 150 to 600 m, and a deep layer from the surface down to 2000 m, representing the total heat content of the water column. For converting the estimated sound speed to temperature a depth-dependent conversion relation has been used, of the form $\theta(z)=\theta_*(z)+d_*(z)[c(z)-c_*(z)]$ where θ_*, d_*, and c_* are depth functions estimated from historical data in the area of the experiment;[9] conversion errors have also been estimated and accounted for. The inversion results (mean values and rms errors) are shown through the solid lines and the gray areas, respectively, in Figs. 7–10. These results are based on simultaneous four-section inversions. In this connection, they cover only periods where simultaneous acoustic data exist along all four sections; e.g., the 15-day gap about yearday 100 in the W3–W4 data reflects in the inversion results along all sections.

The dashed lines in Figs. 7–10 represent the historical mean temperatures for each day of the year. Finally, the hydrographic data, collected before the start and after the end of the experiment, are marked through circles with horizontal lines representing the duration of observations. In comparing these observations with the inversion results, their temporal distance (more than 30 days in some cases) as well as the temporal spread of the hydrographic data (reaching, e.g., 14 days in the case of late H–W4 data) have to be taken into account. The inversion results are in general agreement with the hydrographic data. Since the offset calibration in Fig. 6 has been based on the matched-peak approach, *not* on the hydrographic data, the inversion results and the hydrographic data are fully independent. The inversion results follow the anticipated gross seasonal behavior in the near-surface and the deep layer. The variability in the intermediate layer, below 150 m, is mainly due to mesoscale activity. A comparison of both the inversion results and the hydrographic data with the climatological data shows that there are significant deviations from the historical mean conditions in all three layers.

The horizontal displacement of the source W4 estimated from the multi-section matched-peak approach is shown in Fig. 11; for the time-to-distance conversion a reference sound speed $c_r=1500$ m/s was used. The upper two panels of Fig. 11 show the north–south and east–west mean deviation along with the corresponding rms errors as a function of yearday. It is seen that the retrieved displacements exhibit a certain degree of temporal coherence, i.e., subsequent estimates of the displacement of W4 are statistically dependent on each other. This is particularly important considering the fact that subsequent receptions have been analyzed independently of each other.

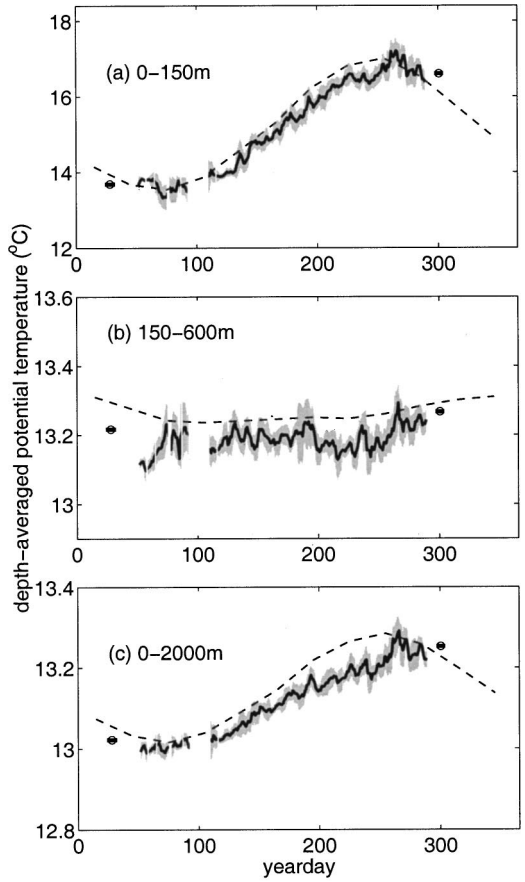

FIG. 9. Inversion results along S–W4 (description as in Fig. 7).

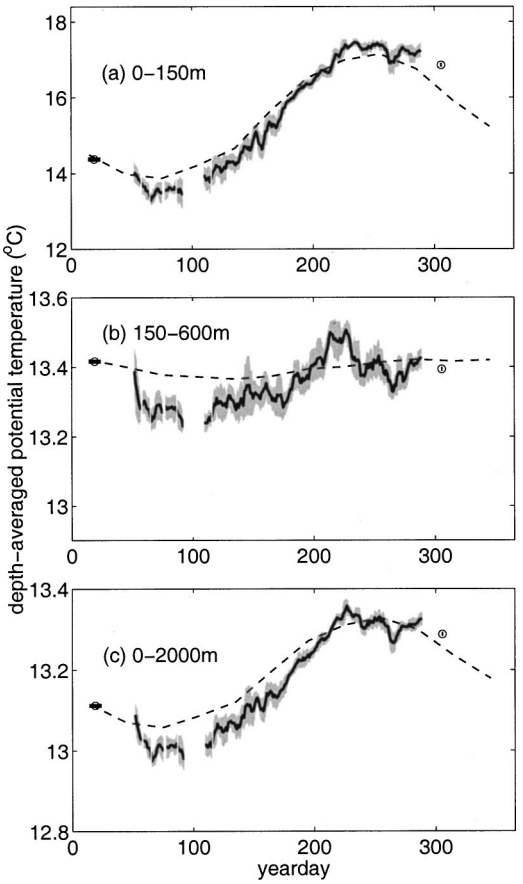

FIG. 10. Inversion results along W3–W4 (description as in Fig. 7).

The results shown are based on daily averages and accordingly, existing mooring motions with time scales less than 24 h are not resolved; moreover, such ''fast'' mooring motions may cause a certain degradation of the averaged data since their effects cannot be removed prior to averaging. Nevertheless, despite these shortcomings, the estimated horizontal deviations of the transceiver W4 explain most of the abrupt changes in the behavior of the observed travel-time data in Fig. 3. For example, the southward drift of the transceiver W4 between yeardays 170 and 175 [Fig. 11(a)] is seen in the observed travel times along the sections W5–W4 and W3–W4, close to the north–south axis. The arrivals along W5–W4 are delayed, whereas the ones along W3–W4 are advanced. Similarly, the drift of W4 to the south/southwest observed in Figs. 11(a) and (b) over the yeardays 50–75 causes a warm-bias effect (advancement of arrival times) along S–W4 and at the same time a delay (cold bias) in the arrival times along W5–W4, which can be seen in Fig. 3.

The lower panel in Fig. 11 shows the estimated horizontal trajectory of W4. The overall mean position of the transceiver is denoted by a dot. It is seen that the estimated horizontal deviations from the nominal position are less than 100 m, and in most cases less than 50 m. These values lie within the expectation limits for the particular mooring, and they further justify the small-motion assumption. The deviation of the overall mean position from the nominal position is about 16 m. This difference can be eliminated by appropriately modifying the time offsets, according to Eq. (23), such that the nominal W4 position is shifted by 16 m to the north; see the concluding remarks of Sec. III A.

To assess the efficiency of the method for estimating the position of the central transceiver a synthetic test case is considered using simulated travel-time data: the measured arrival pattens along the four Thetis-2 sections are first corrected for the estimated displacements of W4, shown in Fig. 11, and then, assuming a harmonic motion of the central mooring, the travel-time data are modified accordingly. The synthetic data are used as input to the multi-section matched-peak approach. The navigation results for this synthetic case are shown in Fig. 12 along with the assumed harmonic motion (dashed line); the inversion results are nearly identical to those shown in Figs. 7–10 and are omitted. It is seen from Fig. 12 that the assumed mooring motion is reproduced with remarkable accuracy, with the dashed lines in most cases lying within the estimated error bars. This means that the method can separate the travel-time changes due to oceanographic conditions from those induced from motions of the central transceiver.

V. DISCUSSION—CONCLUSIONS

An extended matched-peak approach was presented allowing the simultaneous analysis of travel-time data from multiple tomographic sections, from a moving source or receiver to a number of peripheral fixed transceivers, to estimate the position of the moving instrument and the ocean state along the various sections. This can be useful, e.g., in

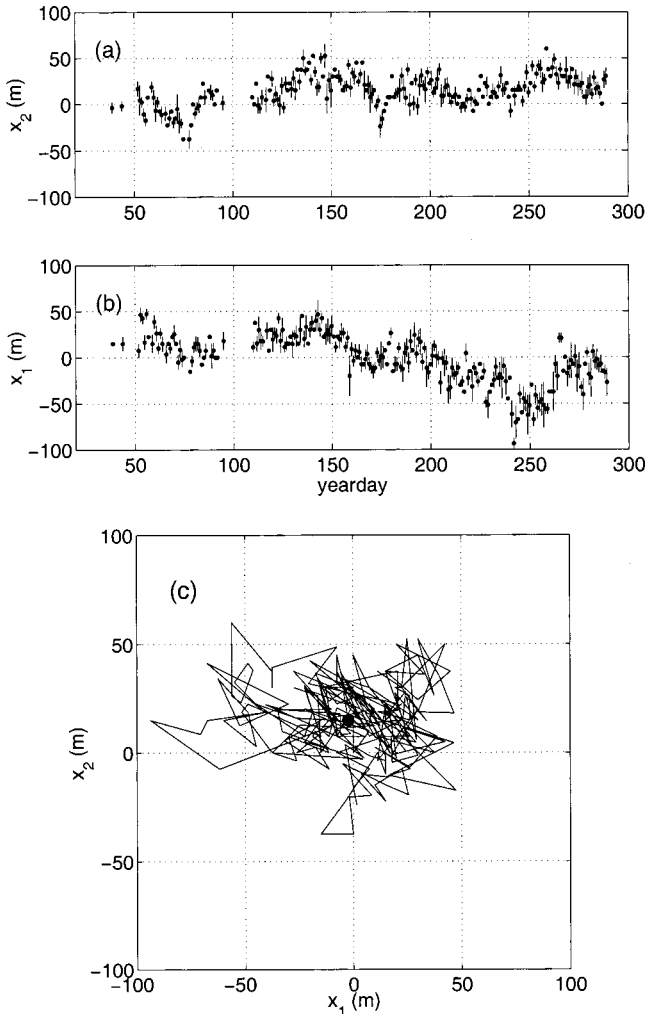

FIG. 11. Navigation results: The estimated (a) northward and (b) eastward displacements of the transceiver W4 and the corresponding rms errors. (c) The horizontal trajectory of the transceiver over the 9 months of the experiment. The overall mean position is denoted by a dot.

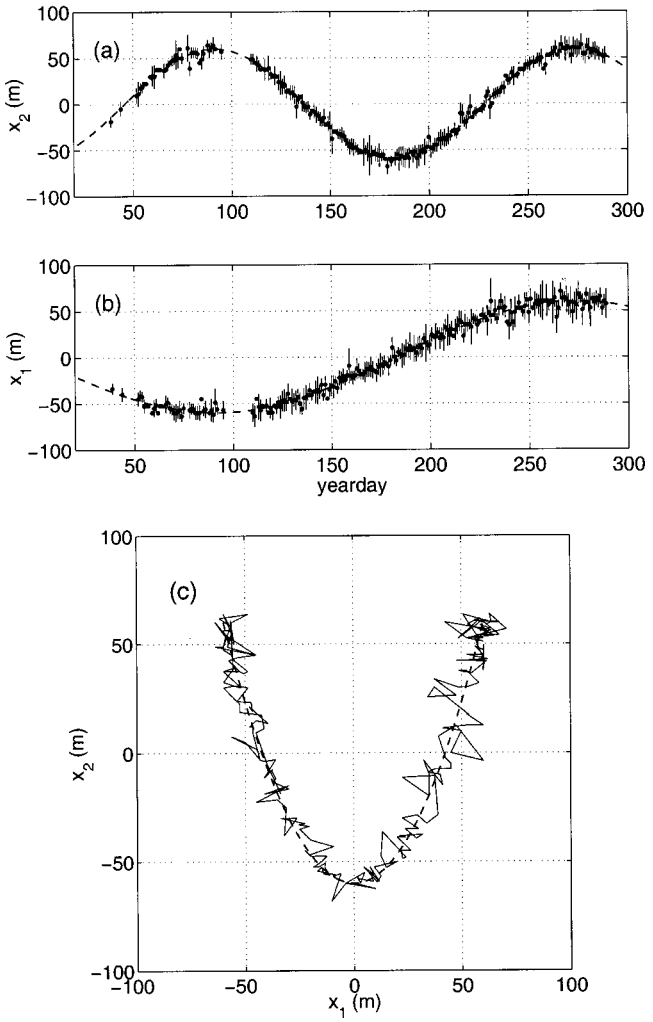

FIG. 12. Navigation results based on simulated travel-time data corresponding to a harmonic motion of the transceiver W4 (dashed lines). (a) Northward displacement; (b) eastward displacement. (c) The horizontal trajectory of W4.

case of missing navigation data for a particular transceiver within a tomographic array. The proposed scheme uses the simultaneous acoustic receptions along the sections originating/ending at the particular instrument to provide a solution to the inversion problem as well as an estimate for the instrument position. The solution consists of the kinematically compatible model states and instrument positions that maximize the joint matching index, i.e., the number of peak identifications over all sections.

A further problem addressed is the offset calibration along each section, which accounts for the difference between the actual and the nominal (best estimated) source–receiver range, as well as for internal instrument delays. This problem is usually solved by comparing measured acoustic arrival patterns and acoustic predictions based on hydrographic measurements, provided that the latter have been conducted simultaneously with the acoustic measurements along each section. The solution proposed here is based on a global matched-peak approach; the time offsets are estimated such that the total number of identifications over all sections and acoustic transmissions (global matching index) is maximized. This calibration approach is based on acoustic data only, i.e., it does not require additional hydrographic measurements. In the case of small motions, the global matching index and the associated model states are invariant to translations of the (x_1,x_2)-coordinate system, corresponding to shifts of the nominal transceiver position. As a result, any two of the time offsets can be arbitrarily specified, reducing the dimension of the calibration problem by 2.

A main feature of the matched-peak approach is that it provides inversion and navigation results directly from travel-time data without requiring that identified peak tracks exist, thus enabling the automatic analysis of travel-time data, even in the presence of long interruption intervals between transmissions. Furthermore, by using an appropriate set of background states the problem of nonlinear model relations can be treated. All model states, i.e., all points within the parameter domain, are considered equally probable for describing a particular reception. The *a priori* rms values of the sound-speed parameters (e.g., the EOF amplitudes) are used to specify the extent of the parameter domain. The observation/modeling travel-time errors, together with the discretization errors, specify the maximum allowable tolerance for associating predicted and observed arrival times.

The inversion and position estimation errors depend on the travel-time data, i.e., they are in general different from transmission to transmission, in contrast to linear-inversion errors which are fixed and known *a priori*.

The application to the Thetis-2 data used the acoustic recordings of a moored source, for which navigation data were missing, at four other instruments, for which navigation data exist such that the effect of their horizontal motion could be removed from the acoustic data. The simultaneous acoustic measurements along the four sections were used to specify the optimum time offsets by applying the global matched-peak approach. Then, simultaneous four-section inversions were performed to specify the corresponding model states and source positions. The inversion results are in good agreement with the independent hydrographic observations. The time series of the estimated horizontal displacements of the central transceiver exhibit temporal coherence, i.e., subsequent estimates are statistically dependent on each other. The efficiency of the proposed approach for solving the navigation problem was illustrated using simulated data.

The above inversions covered only the cases of simultaneous data along all four sections, i.e., no results were produced in periods of data interruption along any of the sections. The best strategy in case of gaps in the data would be to adapt the analysis to the data available on each day. If data along a single section are available, then simple relative-time inversions can be performed. If there exist simultaneous data along two conodal sections (i.e., with a common mooring), the matched-peak approach can be used both for solving the inversion problem and for specifying the transceiver position. If the number of conodal sections is larger than two the same applies, but in addition the offset calibration problem can be addressed since only two time delays can be set arbitrarily, as shown in Sec. III A. The latter applies also to the case of two coaxial sections, with three moorings in line, since Eq. (13) becomes essentially one-dimensional (which means that only one time delay can be set arbitrarily).

The proposed multi-section matched-peak approach for solving the inversion and mooring navigation problem is based on the assumption that the horizontal deviation of the central transceiver is much smaller than the horizontal ranges of the corresponding sections. By relaxing this assumption the proposed method could be extended to address, e.g., the case of a central drifting source with moored/fixed peripheral receivers. Such a configuration might be useful, e.g., under ice, where the deployment of moored instruments is difficult.

ACKNOWLEDGMENTS

This work was supported by the European Union MAST-III program under Contract No. MAS3-CT97-0147. Fruitful discussions with U. Send (IfM, Kiel) are acknowledged. The author would like to thank the anonymous reviewers for providing helpful comments and suggestions.

[1] W. H. Munk and C. Wunsch, ''Ocean acoustic tomography: A scheme for large scale monitoring,'' Deep-Sea Res., Part A **26**, 123–161 (1979).
[2] W. H. Munk, P. F. Worcester, and C. Wunsch, *Ocean Acoustic Tomography* (Cambridge University Press, New York, 1995).
[3] J. L. Spiesberger, R. C. Spindel, and K. Metzger, ''Stability and identification of ocean acoustic multipaths,'' J. Acoust. Soc. Am. **67**, 2011–2017 (1980).
[4] G. R. Legters, N. L. Weinberg, and J. G. Clark, ''Long-range Atlantic acoustic multipath identification,'' J. Acoust. Soc. Am. **73**, 1571–1580 (1983).
[5] P. F. Worcester, ''An example of ocean acoustic multipath identification at long range using both travel time and arrival angle,'' J. Acoust. Soc. Am. **70**, 1743–1747 (1981).
[6] B. M. Howe, P. F. Worcester, and R. C. Spindel, ''Ocean acoustic tomography: Mesoscale velocity,'' J. Geophys. Res. **92**, 3785–3805 (1987).
[7] F. R. Martin-Lauzer and D. Mauuary, ''Probabilistic ray identification: A new tool for ocean acoustic tomography,'' in P*roc. ICASSP 94* (Adelaide, 1994).
[8] E. K. Skarsoulis, G. A. Athanassoulis, and U. Send, ''Ocean acoustic tomography based on peak arrivals,'' J. Acoust. Soc. Am. **100**, 797–813 (1996).
[9] E. K. Skarsoulis and U. Send, ''One-step analysis of non-linear traveltime data in ocean acoustic tomography,'' J. Atmos. Ocean. Technol. **17**, 240–254 (2000).
[10] E. K. Skarsoulis, ''A matched-peak inversion approach for ocean acoustic travel-time tomography,'' J. Acoust. Soc. Am. **107**, 1324–1332 (2000).
[11] U. Send, G. Krahmann, D. Mauuary, Y. Desaubies, F. Gaillard, T. Terre, J. Papadakis, M. Taroudakis, E. Skarsoulis, and C. Millot, ''Acoustic observations of heat content across the Mediterranean Sea,'' Nature (London) **385**, 615–617 (1997).
[12] J. Marshall, F. Dobson, K. Moore, P. Rhines, M. Visbeck, E. d'Asaro, K. Bumke, S. Chang, R. Davis, K. Fisher, R. Garwood, P. Guest, R. Harcourt, C. Herbaut, T. Holt, J. Lazier, S. Legg, J. McWilliams, R. Pickart, M. Prater, I. Renfrew, F. Schott, U. Send, and W. Smethie, ''The Labrador Sea deep convection experiment,'' Bull. Am. Meteorol. Soc. **79**, 2033–2058 (1998).
[13] B. Cornuelle, ''Simulation of acoustic tomography array performance with untracked or drifting sources and receivers,'' J. Geophys. Res. **90**, 9079–9088 (1985).
[14] F. Gaillard, ''Ocean acoustic tomography with moving sources or receivers,'' J. Geophys. Res. **90**, 11891–11898 (1985).
[15] W. H. Munk and C. Wunsch, ''Up-down resolution in ocean acoustic tomography: Rays and modes,'' Deep-Sea Res., Part A **29**, 1415–1436 (1982).
[16] G. A. Athanassoulis and E. K. Skarsoulis, ''Arrival-time perturbations of broadband tomographic signals due to sound-speed disturbances. A wave-theoretic approach,'' J. Acoust. Soc. Am. **97**, 3575–3588 (1995).
[17] J. L. Spiesberger and P. F. Worcester, ''Perturbations in travel time and ray geometry due to mesoscale disturbances: A comparison of exact and approximate calculations,'' J. Acoust. Soc. Am. **74**, 219–225 (1983).
[18] W. H. Munk and C. Wunsch, ''Ocean acoustic tomography: Rays and modes,'' Rev. Geophys. Space Phys. **21**, 777–793 (1983).
[19] E. C. Shang, ''Ocean acoustic tomography based on adiabatic mode theory,'' J. Acoust. Soc. Am. **85**, 1531–1537 (1989).
[20] R. W. Preisendorfer and C. D. Mobley, *Principal Component Analysis in Meteorology and Oceanography* (Elsevier, Amsterdam, 1988).
[21] E. C. Shang and Y. Y. Wang, ''On the calculation of modal travel time perturbation,'' Sov. Phys. Acoust. **37**, 411–413 (1991).
[22] For example, if a 3-km mooring leans to the side by 100 m the time shift associated with the horizontal displacement of the mooring top (100 m) is about 65 ms. The time shift due to the vertical displacement of the mooring top will be 0.5 ms at most, assuming that the mooring remains linear.
[23] L. Brekhovskikh and O. Godin, *Acoustics of Layered Media II. Point Sources and Bounded Beams* (Springer, Berlin, 1992).
[24] F. B. Jensen, W. A. Kuperman, M. B. Porter, and H. Schmidt, *Computational Ocean Acoustics* (AIP, New York, 1994).
[25] Thetis-2, A pilot tomography system for monitoring the western Mediterranean basin, Final Report, edited by U. Send, EU MAST-2 project CT91-0006, March 1996.
[26] Thetis group, A pilot tomography system for monitoring the western Mediterranean basin, Tomography Data Report, EU MAST-2 project CT91-0006, March 1996.
[27] M. B. Porter and E. L. Reiss, ''A numerical method for ocean acoustic normal modes,'' J. Acoust. Soc. Am. **76**, 244–252 (1984).

Acoustic remote sensing of internal solitary waves and internal tides in the Strait of Gibraltar

Christopher O. Tiemann,[a] Peter F. Worcester, and Bruce D. Cornuelle
Scripps Institution of Oceanography, University of California at San Diego, La Jolla, California 92093

(Received 20 July 2000; revised 26 February 2001; accepted 27 April 2001)

High-frequency underwater acoustic transmissions across the Strait of Gibraltar are used to examine the feasibility of acoustically measuring several physical processes in the Strait, a difficult area to sample with conventional instruments. Internal undular bores propagate along the interface between an upper layer of Atlantic water and a lower layer of Mediterranean water. As they cross the acoustic path they are recognized by their scattering effects in the acoustic record. The time between internal bore crossings is influenced more by the tidal phase of the bore release at the Camarinal Sill than by variability in the bore's propagation time to the acoustic path. When internal bores were present, the acoustic arrival patterns could be classified as one of three types with different internal bore and internal tide amplitudes. The arrival types alternate during spring to neap tide transitions, suggesting that internal bore amplitude is not linearly related to tidal height. The sensitivity of acoustic observables to several physical parameters is investigated using a forward model, and a demonstration of inverse techniques provides estimates of several physical parameters from spring tidal cycles. © *2001 Acoustical Society of America.* [DOI: 10.1121/1.1382617]

PACS numbers: 43.30.Pc, 43.30.Cq [DLB]

I. INTRODUCTION

The Strait of Gibraltar is a challenging environment to observe with conventional instruments. Its large variability over small time and space scales makes it difficult to sample adequately, and the strong tidal currents and extensive ship and fishing traffic there are inhospitable to moored instruments. CTD casts and moorings have provided most historical information about internal tides in the Strait (Armi and Farmer, 1988; Farmer and Armi, 1988; Boyce, 1975; Bray *et al.*, 1990, 1995; Candela *et al.*, 1990; Ziegenbein, 1970), but CTD data can suffer from temporal aliasing problems because of the brevity of some important physical processes in the Strait. While moored instruments can sample quickly, they are point measurements subject to spatial aliasing and contamination from local, small-scale variability.

Packets of large internal solitary waves routinely propagate west through the Strait and have received considerable attention (Boyce, 1975; Watson, 1994; Watson and Robinson, 1990; Ziegenbein, 1970). These solitary waves are difficult to observe using CTD measurements because of their short duration at any one point. Satellite and surface radar images have been successful in observing their speed and horizontal wave-front shape but give no indication of their vertical structure (Alpers and La Violette, 1993; Richez, 1994; Watson, 1994; Watson and Robinson, 1990). Echosounders have successfully observed the vertical displacement of internal solitary wave packets (Armi and Farmer, 1988; Farmer and Armi, 1988; Watson, 1994), but the variability of their shape with range across the Strait has not been directly observed.

Although conventional measurement techniques are suitable in some situations, they all have limitations in the environment of the Strait of Gibraltar. A technique that has received less attention in the Strait, yet offers some advantages over conventional methods, is that of acoustic remote sensing. A key virtue of using acoustics is the ability to make rapidly repeated measurements which eliminates any problems of aliasing in time. Acoustic transmissions across the Strait of Gibraltar are practically instantaneous relative to the time scales of even the briefest physical processes. Acoustic measurements inherently integrate horizontally, which suppresses small-scale variability, and they can even be used to measure several parameters simultaneously, as this work will show.

The Strait of Gibraltar Acoustic Monitoring Experiment was conducted in April 1996 as a joint project between the Scripps Institution of Oceanography and the Institut für Meereskunde, University of Kiel. The Gibraltar experiment has already provided acoustically derived estimates of transport through the Strait (Send *et al.*, 2001), but this paper provides examples of additional information that can be sensed acoustically and offers new insight into the interesting physical processes in the Strait. The potential exists to learn much about the physical oceanography in the Strait without deploying extensive instrumentation in its interior.

Tiemann *et al.* (2001) investigated the scattering effects of internal solitary waves and internal tides on acoustic transmissions across the Strait of Gibraltar by using a multiparameter physical model of the Strait in the forward problem. This model can qualitatively explain many important features of the observed acoustic scattering by showing how acoustic ray paths across the Strait evolve over a tidal cycle. The same model was further used in this work to determine how sensitive acoustic travel times are to changes in several physical parameters such as internal solitary wave amplitude, internal solitary wave speed, and internal tide amplitude.

[a]Now at: Science Applications International Corporation, La Jolla, CA 92037.

 0001-4966/2001/110(2)/798/14/$18.00

This paper will demonstrate three different techniques for extracting oceanographic information from an acoustic record. These analyses are independent of each other and will each appear in their own section, ordered in increasing complexity. Section II provides a general overview of the environment of the Strait of Gibraltar, the experiment instrumentation, and the physical model used in the forward problem. Section III shows an example of how acoustics can be used to determine when internal solitary waves are present and, when used in conjunction with conventional measurements, to time the travels of internal bores through the Strait. In Sec. IV, three generalized acoustic travel time arrival patterns are identified. These patterns are repeated frequently in the acoustic record, and their sequence shows some interesting long term trends. In Sec. V, the sensitivity of acoustic propagation in the Strait to perturbations in the physical model parameters is examined, and in some cases a qualitative explanation for the resulting travel time changes is provided. Following this is a description of the linear inverse technique used to estimate several physical parameters from the acoustic data.

II. OVERVIEW

An understanding of the physical processes in the Strait of Gibraltar is necessary for modeling acoustic propagation in the region. Tiemann *et al.* (2001) describe in detail the model previously developed to describe the oceanographic processes in the Strait and aid in acoustic propagation studies, but key features of the environment, experimental approach, and model parameters are repeated briefly here.

The basic circulation of the Strait is relatively simple, with an upper layer of relatively warm, fresh Atlantic water about 100 m thick flowing east into the Mediterranean Sea and a lower layer of relatively salty, cold Mediterranean water flowing back west through the Strait into the Atlantic. This mean flow is modulated by large semidiurnal tidal flows, and there are tidal fluctuations in the depth of the interface between the upper Atlantic and lower Mediterranean water layers. Within the model, these fluctuations from the internal tide are reproduced by sinusoidal vertical shifts of the background sound-speed field of up to 25 m on the northern side of the Strait and 40 m on the southern side.

Perhaps the most interesting feature, though, is the propagation of internal bores which are released at the Camarinal Sill on the west side of the Strait at the relaxation of most high tides. As the bore propagates east through the Strait it eventually disintegrates into a train of internal solitary waves, with waves of larger amplitude and wavelength at the head of the packet. Within the model, the vertical amplitude of the internal solitary wave packets is based on an echosounder observation of a packet near the acoustic path but is scaled with position across the Strait, increasing from north to south, with an average 100 m amplitude near the center of the Strait. The modeled packet crosses the experiment's acoustic path with a speed of 2.5 m/s and with a horizontal wave-front curvature based on one observed in a satellite image.

The geometry of the Gibraltar experiment was selected to give both lower acoustic ray paths across the Strait that were confined to the lower layer of Mediterranean water and upper ray paths that acoustically sampled the interface between Atlantic and Mediterranean waters and the internal solitary waves which propagate along that interface. Three 2 kHz transceivers (labeled T1, T2, and T3 in Fig. 1) were installed just above the sea floor at about 200 m depth, at the endpoints of two acoustic paths. Transmissions every 2 min from T1 to T3 will be examined in this paper; the T1–T3 path was perpendicular to the current flow to minimize any acoustic travel time variation due to currents. The tilts and orientations of the instrument moorings were measured every 5 min and used to correct acoustic travel times for instrument motion, but close examination of the T1 instrument tilt data showed brief but violent tilts occurring roughly every 12 h. These ''kicks'' are due to the passing of an internal solitary wave over the instrument and provide a hint as to where to look in the acoustic data for internal solitary wave effects.

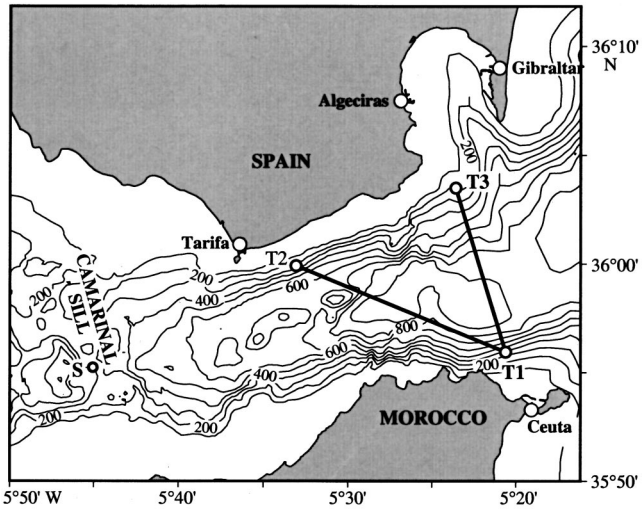

FIG. 1. Bathymetry of the Strait of Gibraltar with instrument positions and acoustic paths indicated. Due to inaccuracies in bathymetry, depth contours do not exactly match instrument depths.

The observed acoustic scattering was quite complicated as ray paths were repeatedly created and destroyed with the passing of internal solitary waves and the evolution of the internal tide. The background sound-speed field used in the model was constructed from environmental data taken during the experiment and has double minimums in the sound-speed profiles at every range. Within the model, the sound-speed field is shifted vertically and adiabatically in accord with a mode 1 internal tide. Furthermore, when an internal solitary wave crosses the acoustic path, it temporarily displaces warm shallow water deeper, perturbing the sound-speed profiles even further. The internal solitary wave is modeled as another mode 1 vertical displacement which sharpens sound-speed gradients. The increased sound-speed gradients can then refract acoustic rays away from their usual sound channels. To illustrate this, Fig. 2 shows absolute acoustic travel times to the T3 instrument over two tidal cycles, and Fig. 3 shows the predicted ray paths and soundspeed field along the T1–T3 acoustic path at several instances in a tidal cycle. The ray identifiers (''a'' through ''e'') of Fig. 3 correspond to the same labels on the travel times of Fig. 2. Ray path ''a'' will be referred to as the ''lower ray'' because it consistently

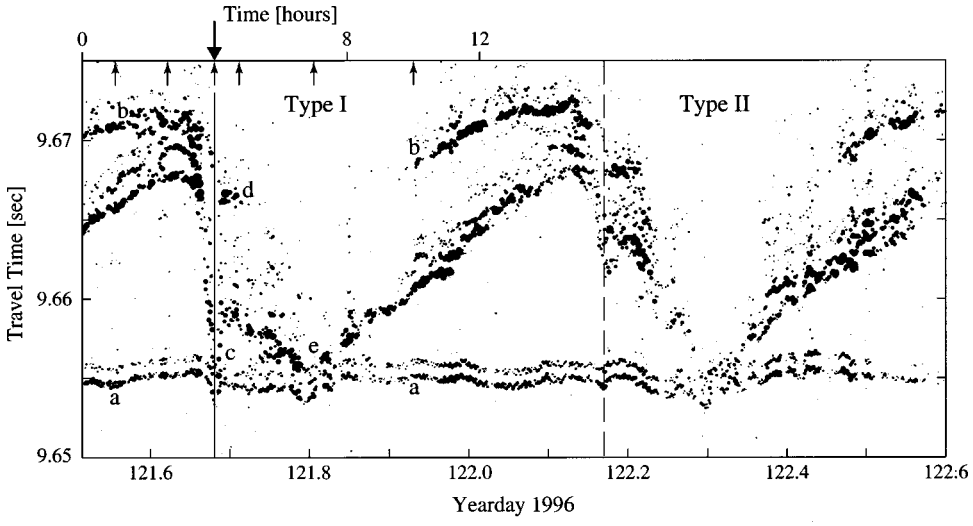

FIG. 2. Absolute travel times as a function of yearday 1996 for transmissions from T1 to T3. Each arrival peak is plotted as a dot, with size proportional to SNR. Vertical lines indicate times of internal bore crossings and arrival structure type (Type I solid, Type II long dash). Labels "a" through "e" identify key features of the acoustic data which were matched in the predicted data and correspond to the ray identifiers of Fig. 3. Small arrows indicate times for which ray paths are shown in Fig. 3. Large arrow indicates time of a large tilt of the T1 instrument. Type I and II arrival structure labels are described further in Sec. IV.

sampled the lower water layer. Its travel time of 9.655 s is nearly constant throughout the tidal cycle. Ray paths "b" through "e" will collectively be called "upper rays," and they showed much more travel time variability, such as the rapid 15 ms decrease in travel time near Hour 4 of Fig. 2. Despite such complexity, the acoustic scattering is surprisingly robust, and the repeatability of key acoustic features made the Gibraltar data set a good candidate for modeling.

III. INTERNAL BORE TRAVEL TIME

The internal undular bores in the Strait of Gibraltar originate at the Camarinal Sill to the west. A lee wave in the form of an internal hydraulic jump appears behind the sill during strong westward tidal flows. When the tide relaxes, this wave is free to cross the sill and moves east as an internal bore along the interface between the Atlantic and Mediterranean waters. Using temperature and salinity records from several moorings along the main axis of the Strait, Armi and Farmer (1988) timed the passage of a mode 1 internal bore through the Strait; they predict the bore should cross the Gibraltar experiment's T1–T3 acoustic path approximately 5.5 h after its release from the Camarinal Sill. Acoustic data can also be used to time the passing of a bore over the acoustic path because its scattering effects in the acoustic record are recognizable. Note that by that time, the bore will have evolved into a packet of internal solitary waves.

As an internal solitary wave train crosses the T1–T3 acoustic path the travel times for both upper and lower eigenray paths should decrease sharply as they are refracted down deep due to large sound-speed gradients at the source. This ray path refraction is illustrated in Fig. 3, Hour 4. The horizontal wave-front curvature of the solitary wave packet prevents discrete oscillations for each solitary wave from appearing in the acoustic record (Tiemann *et al.*, 2001). The severity of the travel time drop varies with the vertical amplitude of the passing internal solitary waves; larger waves cause larger sound-speed gradients and steeper ray path refractions. Such rapid drops in travel time are often seen in the acoustic data, once per tidal cycle, and they coincide with the violent kicks seen in the T1 instrument's tilt data. (The 10–15 ms travel time decrease for upper ray paths is not the result of instrument motion.) However, not every abrupt travel time decrease has a corresponding indicator in the instrument's motion data. The data from both semidiurnal tidal cycles of Fig. 2 show sharp decreases in travel time, at yeardays 121.68 and 122.17, indicative of an internal solitary wave packet crossing the acoustic path, but the acoustic data suggest that the earlier packet at day 121.68 has a bigger amplitude because the travel time decrease of the upper rays is larger (15 ms drop vs 10 ms drop). The T1 instrument motion confirms a larger internal solitary wave at day 121.68 as a violent tilt was recorded at the instrument, moored at a depth of 165 m, but not in the later case when smaller amplitude waves did not extend deep enough to move the instrument.

A sudden travel time decrease is the acoustic signature of a passing internal solitary wave, and for every tidal cycle where one occurred, the yearday at the maximum decrease was noted as the time of the internal solitary wave crossing. Not every tidal cycle has an associated crossing, particularly during neap tides when the internal bores are smaller in amplitude or nonexistent. Figure 4(a) shows the spacing in time, as a function of yearday, between internal bores crossing the acoustic path; spacings between bores more than one tidal cycle apart are not considered here. The tidal height record from Ceuta is shown beneath to illustrate days of spring and neap tides and the tidal daily inequality. The mean time between bore occurrences is 12.56 h, but their spacing oscillates shorter or longer than the mean on consecutive tides. The bore spacing also seems to vary more with the size of the tidal daily inequality than with overall tidal amplitude; Figure 5 suggests a roughly linear relationship between the time separating two internal bore occurrences and the difference in low tide heights from their tidal cycles. For the tidal record shown in Fig. 4(d), the time between consecutive high tides varies up to $\pm.7$ h, usually alternating above and below the mean period of 12.46 h. This variation in tidal period helps account for part of the ± 3.5 h maximum variation in bore spacings. The remaining variation could be due to changes in a bore's release time from the Camarinal Sill, relative to high tide, or to differences in some physical prop-

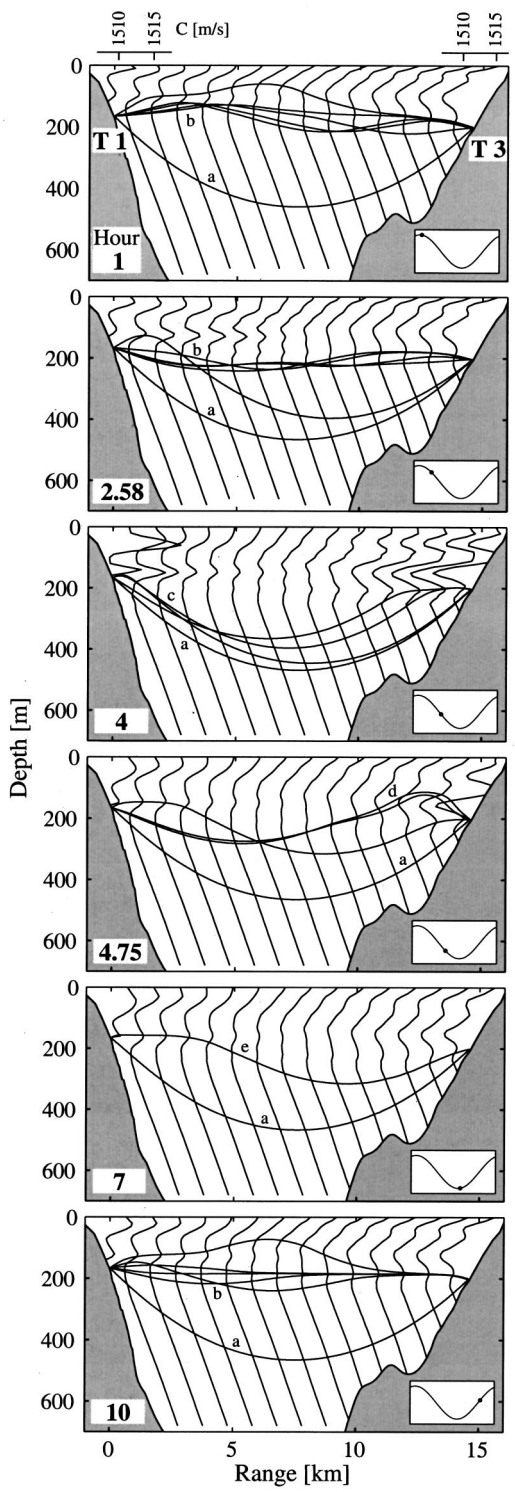

FIG. 3. Vertical sections along the T1–T3 acoustic path showing background sound-speed profiles and predicted ray paths at several times in a 12 h spring tidal cycle. Inset shows phase within the tidal cycle. The view is looking west with the southern T1 source on the left. The ray identifiers (''a'' through ''e'') correspond to the same labels of Fig. 2. Scale for profile values is the same for all profiles but offset in range. This figure is reproduced from Tiemann *et al.* (2001).

erties such as the bore's phase speed or currents in the Strait.

Determining a bore's release time from the Camarinal Sill is necessary in calculating its travel time to the acoustic path and its phase in the tidal cycle. To do so in this experiment, conventional instruments were essential. It is difficult

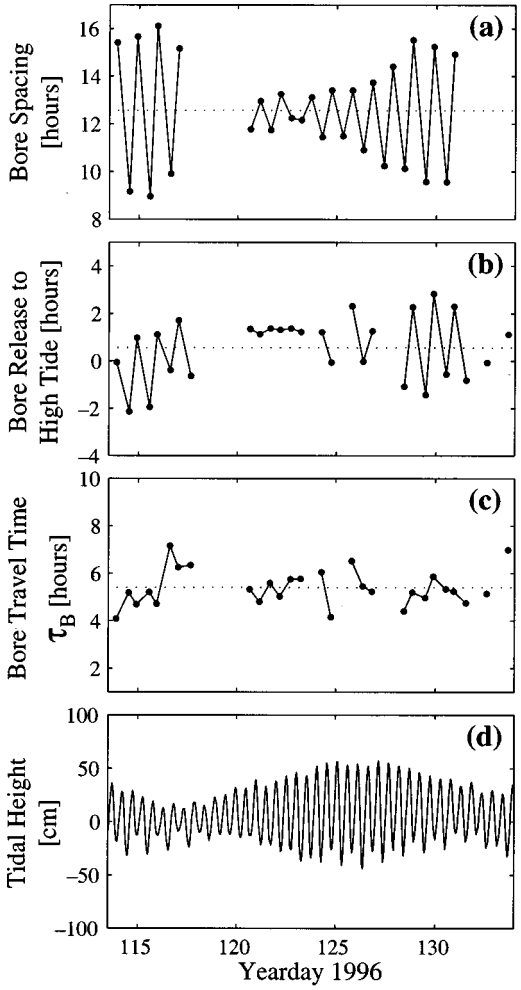

FIG. 4. (a) Time between internal bore crossings separated by no more than one tidal cycle. (b) Time from a bore release to the nearest high tide at Ceuta. Positive values indicate a bore release prior to the high tide. (c) τ_B, bore travel time from the Camarinal Sill to the acoustic path. In (a) through (c), data points from adjacent tidal cycles are connected by a line. The mean is shown as a dotted line. (d) Tidal height record from Ceuta.

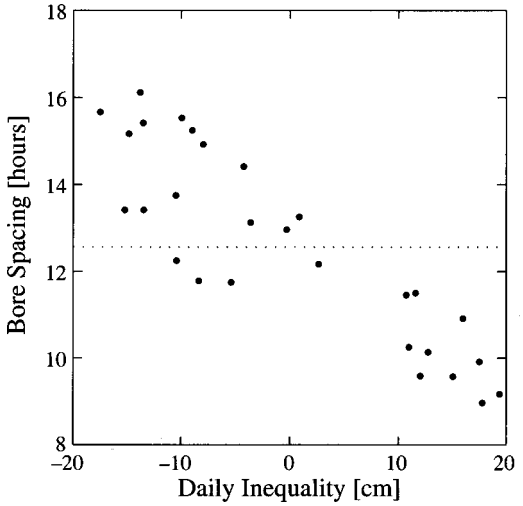

FIG. 5. Time between internal bore crossings vs the tidal daily inequality at Ceuta for yeardays 114 to 135. The daily inequality is the difference in tidal height between adjacent low tides. Dotted line indicates the mean internal bore spacing of 12.56 h.

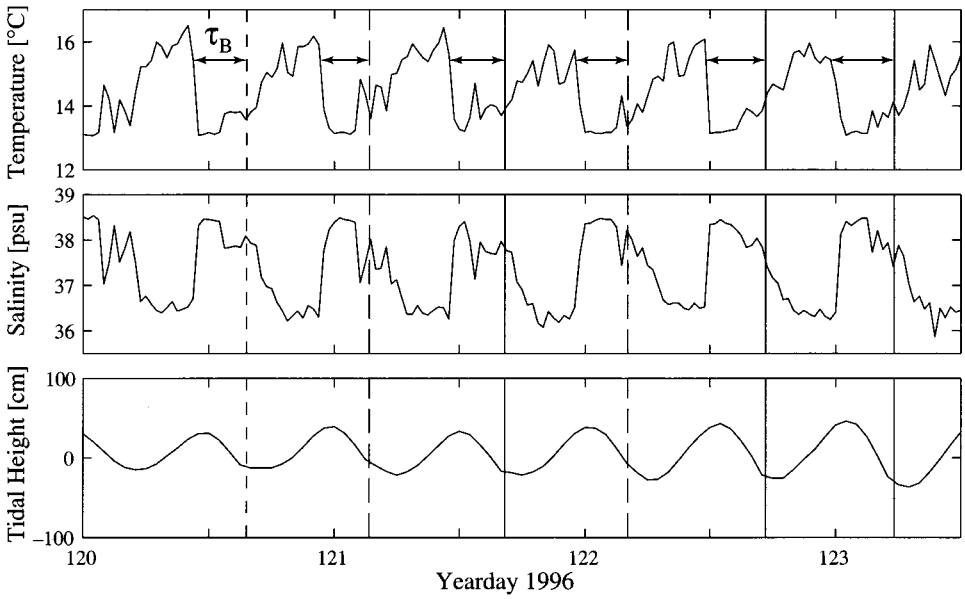

FIG. 6. Temperature and salinity records from 118 m depth at mooring "S" on Camarinal Sill, plus the tidal height record from Ceuta, for six tidal cycles. Vertical lines indicate times of internal bore crossings at the acoustic path and arrival structure type (Type I solid, Type II long dash, Type III short dash). The bore's travel time, τ_B, is dimensioned six times in the temperature series. The complete time series for τ_B is shown in Fig. 4(c).

to estimate the time of a bore's release using current meter data from the sill because of uncertainties in how strong a current is necessary to hold a bore in place. Instead, abrupt changes in the temperature and salinity record from the sill are a better indicator of an internal bore release. Figure 6 shows the temperature and salinity record at 118 m depth from the sill mooring (labeled "*S*" in Fig. 1). Data from six consecutive tidal cycles are shown, with the tidal height at Ceuta provided for reference. The vertical bars on the figure indicate times of internal bore crossings at the acoustic path as determined from the acoustic data. Approximately 5 h before each bore crossing, there is a rapid drop in temperature at the sill of about 3 °C and a simultaneous rise in salinity of about 2 psu; this event designates the time of the bore release. The clearest examples of bore releases are shown in Fig. 6, however, the temperature and salinity records were not consistently good markers. In ambiguous cases where there was no sharp temperature or salinity change, no attempt was made to time the bore release.

The time from all bore releases to their nearest high tide in the tidal record is shown in Fig. 4(b). The bore was released an average of 34 min before the high tide, but release can occur over 2 h before or after the high tide, often alternating above and below the mean on successive tidal cycles. This series is another example where the bore's characteristics are steadiest during days of small daily inequalities. Armi and Farmer (1988) observed a 1 h variation in the tidal phase of the bore release and also attributed this to the diurnal inequality in the tide.

The travel time for an internal bore to propagate from the Camarinal Sill to the acoustic path is the difference between a bore's release time and the time of its crossing as determined from the acoustic data. This quantity is labeled in Fig. 6 as τ_B and its time series is shown in Fig. 4(c). The mean bore travel time is 5.4 h, and this is in agreement with Armi and Farmer's measurement of 5.5 h along the same path (1988). The time series for bore travel time is considerably less variable than that of the bore's tidal phasing, with rms values of 0.76 and 1.31 h, respectively. The variation in the time between internal bore arrivals is influenced more by variability in the tidal phase of the bore release than by variability in the bore's travel time.

IV. ARRIVAL PATTERN IDENTIFICATION

The repeatability of key features in the acoustic data during spring tidal cycles is what made the Gibraltar data set such a good candidate for modeling attempts, and the model developed previously (Tiemann *et al.*, 2001) successfully reproduced many properties of the acoustic arrival pattern for spring tides. The data set shows robustness outside of the spring tides as well. Examination of acoustic data during the transitions between spring and neap tides reveals that there are two more broad categories of arrival structures, repeated often and usually on alternating tidal cycles.

The acoustic data from the three consecutive tidal cycles shown in Fig. 7(a) were used as archetypes for classifying arrival structures according to their distinguishing characteristics. The three arrival structures will be identified simply as Type I, II, and III, and their key features are listed in Table I and labeled on the dot plot of Fig. 7(a). The times of an internal bore crossing the acoustic path are indicated by vertical lines where the line type (solid, long dash, short dash) corresponds to the classification of the arrival pattern (Type I, II, or III) for that tidal cycle. The analysis to follow takes advantage of the qualitative differences among arrival patterns as listed in Table I. A later section will quantitatively examine the features of Type I arrivals.

Note that after yearday 128.0, the acoustic travel times will appear shifted 15 ms earlier [compare Figs. 2 and 7(a)] because the T1 instrument autonomously redeployed itself about 23 m closer to the T3 receiver. As mentioned earlier, the Strait of Gibraltar is a difficult environment for moored instruments! That shift will not adversely affect this work as only relative travel time changes are of interest, and the eigenray paths predicted by the model are essentially the same for the new, slightly shorter acoustic path.

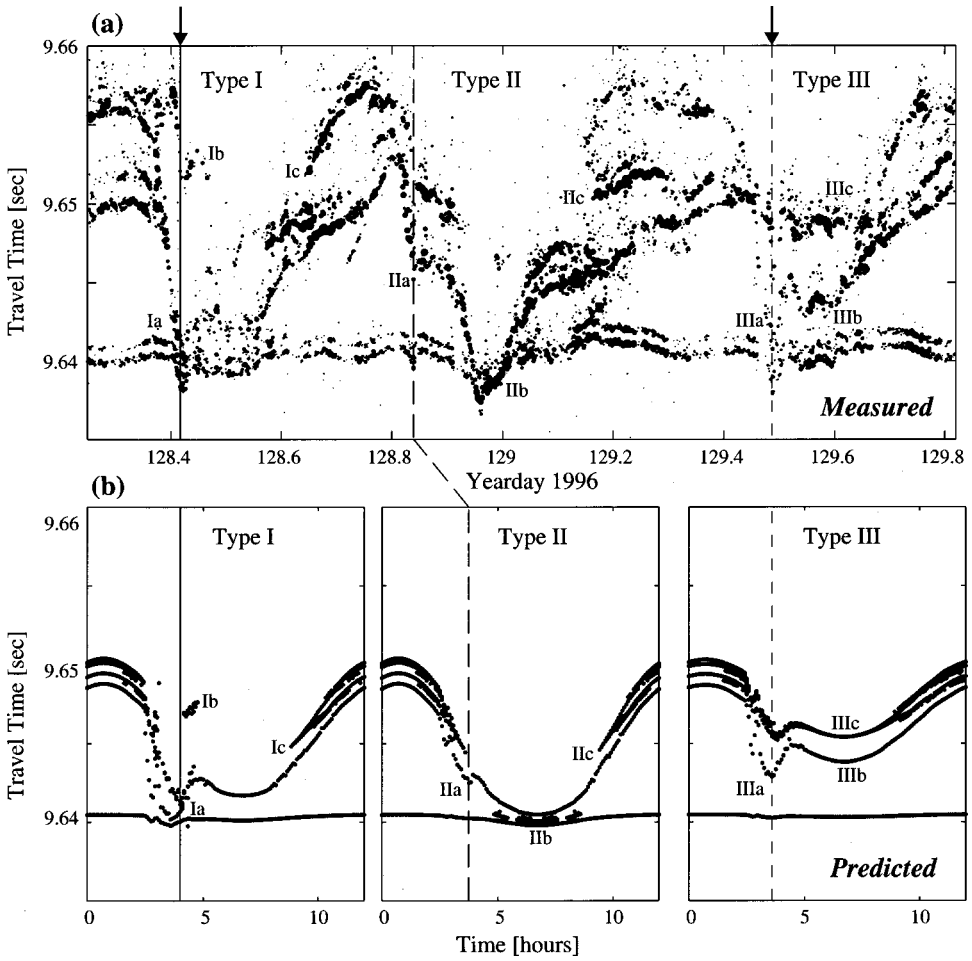

FIG. 7. Measured and predicted ray travel times over three tidal cycles. The labels (''Ia'' through ''IIIc'') identify key features of the measured data matched by the model output and are described in the text and in Table I. Vertical lines indicate times of internal bore crossings and arrival structure type (Type I solid, Type II long dash, Type III short dash). Arrows indicate times of a large tilt of the T1 instrument.

The three tidal cycles of Fig. 7(a) are from a transition period from spring to neap tides. The Type I arrival structure shows the last of spring tides; reproducing this structure was the goal of the first modeling attempts. By changing some model input parameters, key features of the Type II and Type III arrival structures can be reproduced as well, providing an understanding of the relative changes in physical processes between the different arrival types. Figure 7(b) shows predicted travel times for three tidal cycles as output by the model in attempts to match the three types of arrival structures. Although the key features listed in Table I were qualitatively reproduced by the models, other details of the measured data are not reproduced. This is mainly due to errors in the background sound-speed field as environmental data were limited during sound-speed profile construction. Attempts to more closely match the travel time separation between lower and upper ray arrivals (''a'' and ''b'' of Fig. 2) by ''speeding up'' the lower water layer and ''slowing down'' the upper water layer complicated other ray paths beyond what is seen in the data. Although the model for Type I arrivals does not exactly reproduce the observed travel times, its model parameters are suitable for use as a reference state in the sensitivity studies to follow.

TABLE I. Features of travel time arrival patterns.

Feature		Description
Type I	Ia	Sudden upper ray travel time decrease of about 15 ms.
	Ib	Isolated cloud of upper ray arrivals shortly after bore crossing.
	Ic	Absence of late-arriving upper rays for several hours.
Type II	IIa	Sudden upper ray travel time decrease of about 10 ms.
	IIb	Upper ray travel times continue to decrease following bore crossing.
	IIc	Absence of late-arriving upper rays for several hours.
Type III	IIIa	Sudden upper ray travel time decrease of 10–15 ms.
	IIIb	Lower and upper ray arrivals separated through most of tidal cycle.
	IIIc	Late-arriving upper rays present through entire tidal cycle.

The model parameters used to match the Type I case are described in Sec. II and in detail in Tiemann *et al.* (2001). When matching the Type II case, the internal bore amplitude was reduced to 20% of the reference case; this prevents the initial upper ray travel time decrease from being so severe (feature ''IIa'' from Table I) and allows the late-arriving upper rays to persist longer before disappearing (''IIc''). The continued drop in upper ray travel times, reaching a minimum in the middle of the tidal cycle (''IIb''), is more likely the result of internal tides vertically shifting the background

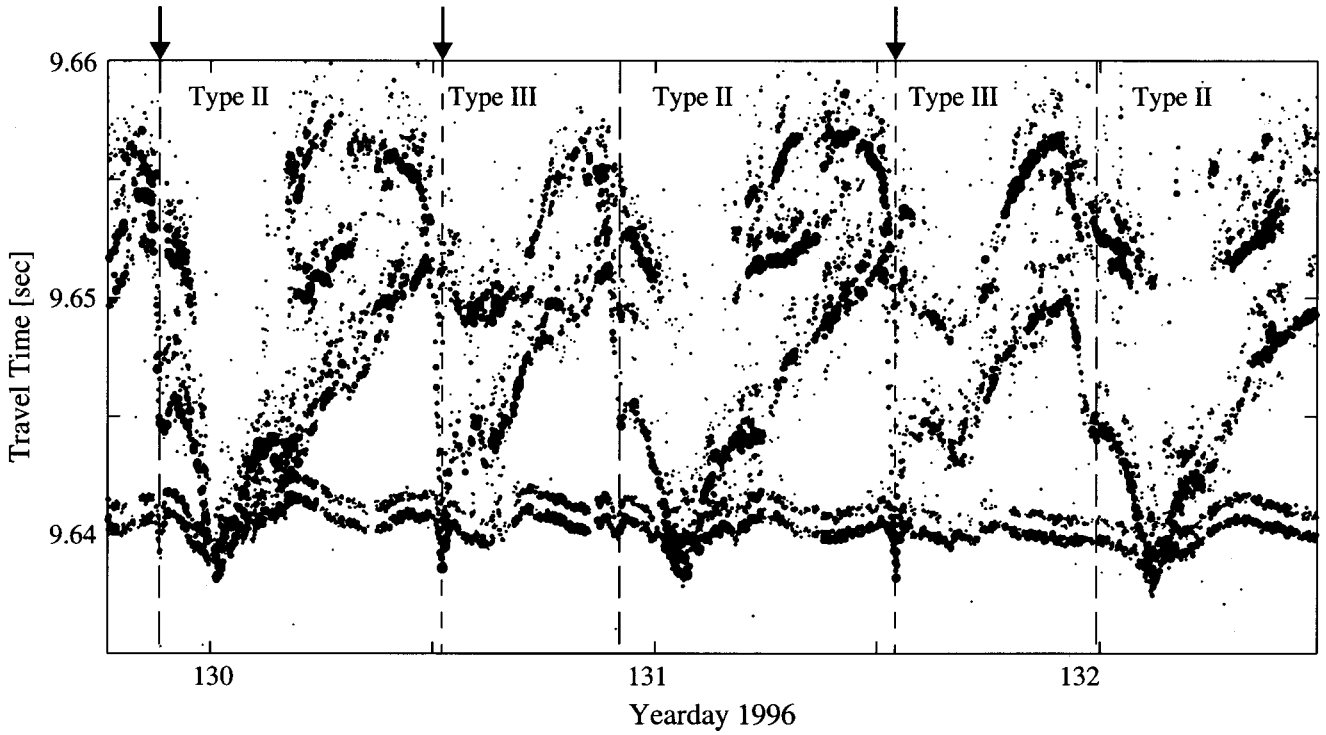

FIG. 8. Absolute travel times for five tidal cycles as a function of yearday 1996 for transmissions from T1 to T3. Vertical lines indicate times of internal bore crossings and arrival structure type (Type II long dash, Type III short dash). Arrows indicate times of a large tilt of the T1 instrument.

sound-speed field rather than internal solitary wave effects. Thus internal tide amplitude was increased slightly by 10 m, and the background sound-speed profiles were uniformly shifted deeper by 10 m in order to minimize the lower/upper ray travel time separation at the bottom of the tidal cycle. Offsetting the background sound-speed profiles from their reference state is equivalent to changing the depth of the Atlantic/Mediterranean interface, which could reasonably be varying from one tidal cycle to the next. Furthermore, shifting the sound-speed field slightly is not unreasonable given the uncertainties in the range-dependent sound-speed field construction.

Because the variation in upper ray travel times for the Type III case is smaller and the lower/upper ray travel time separation larger, the opposite model parameter change was made: internal tide amplitude was decreased by 12 m and the background sound-speed field was shifted shallower by 10 m. Shifting the background sound-speed field shallower maintains late-arriving upper rays throughout the entire tidal cycle (''IIIc''). The internal solitary wave amplitude in the Type III case is decreased to 30% of the reference state in order to provide an initial upper ray travel time decrease of a size between the Type I and Type II cases (''IIIa'') but yet not be so large that the late-arriving upper ray paths disap-

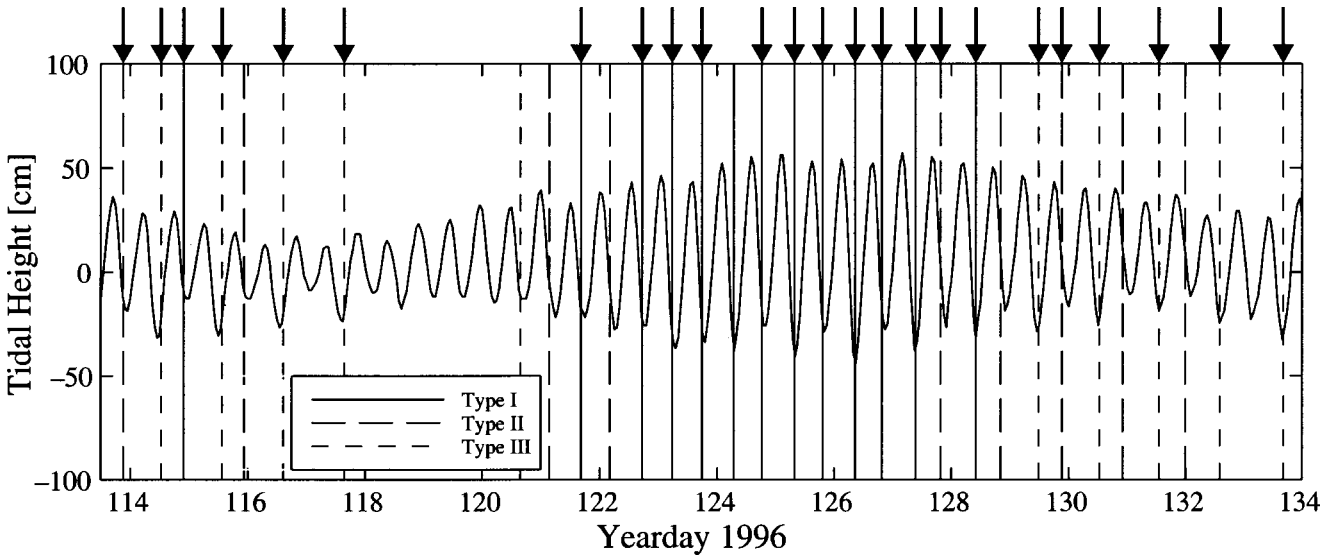

FIG. 9. Tidal height at Ceuta as a function of yearday 1996 overlaid with vertical lines indicating times of internal bore crossings and arrival structure type (Type I solid, Type II long dash, Type III short dash). Arrows indicate times of a large tilt of the T1 instrument.

pear. In summary, the Type I arrivals assume the largest internal solitary wave amplitude. The Type II arrivals use the smallest internal solitary wave amplitude but the largest internal tide amplitude. The Type III arrivals assume a middle-sized solitary wave, but the smallest internal tide.

Every tidal cycle where an internal bore crossing was seen was catalogued as one of the three types of arrival structures shown in Fig. 7(a). Although this was done by a visual pattern matching, there was usually little doubt as to which archetype most closely resembled each tidal cycle's arrival structure. For example, note how the presence of late arriving upper rays in a Type III arrival (feature IIIc) distinguish it from Types I and II where those rays are absent. Additionally, in a Type II arrival, the convergence of upper and lower ray travel times happens hours after the initial upper ray travel time decrease (feature IIb), distinguishing it from Types I and III. Figure 8 shows acoustic data from five more tidal cycles where alternating Type II and Type III arrival structures are relatively obvious. Again, the vertical bars in this figure indicate times of an internal bore crossing, and arrows indicate an accompanying severe tilt in the T1 instrument. As additional examples, the travel times of Fig. 2 would be classified as a Type I and Type II arrival (Fig. 10 is a Type I arrival).

After classifying all of the tidal cycles with bore occurrences by arrival type, an interesting pattern emerged when plotting arrival type on a tidal height record from Ceuta. Figure 9 shows times of internal bore crossings as vertical lines where line type distinguishes arrival type. The tidal record identifies days of spring and neap tides and the daily inequality. Note how Type I arrivals, modeled with the largest internal bore amplitude, occur during the spring tides, while Type II and Type III arrivals are seen on days to either side of the Type I arrivals during the transition to neap tides. Outside of the spring tides, the tidal cycles alternate between the small and medium bore amplitudes of Type II and Type III arrivals, just as the tidal height record alternates with the highs and lows of the daily inequality. Lastly, evidence of internal bore crossings are absent only on days of neap tides, as expected. Note that even if a few arrival pattern types have been misidentified by visual inspection, the basic patterns presented here would still exist.

V. LINEAR INVERSE METHODS

Section IV demonstrated how the acoustic record can be used to determine the presence or absence of internal bores and make general estimates of internal bore and internal tide amplitude from different tidal cycle types. However, acoustic data can also be used to estimate the subtle variations in several physical parameters among tidal cycles of the same type through the use of linear inverse methods. This section offers a demonstration of that technique using cases of spring tide (Type I) arrival structures. By varying the model's input parameters, one can calculate how a small perturbation to a modeled physical process, such as an increased tidal swing or internal bore amplitude, leads in the real acoustic data to small changes in acoustic travel times. Perturbing model parameters also helps quantify model stability and sensitivity. Because any single datum from the acoustic data can often be influenced by several physical processes simultaneously, inverse methods are used to determine how much each model parameter contributes to the total travel time perturbation.

TABLE II. Acoustic observables and uncertainties.

Observable	Description	Uncertainty
d_1	Upper/lower ray travel time separation at 1 h	1 ms
d_2	Upper/lower ray travel time separation at bore crossing	0.2 ms
d_3	Upper/lower ray travel time separation at 7 h	1 ms
d_4	Time of bore crossing	0.2 h
d_5	Time of upper ray disappearance	1.5 h
d_6	Time of upper ray reappearance	2 h
d_7	Duration of cloud of upper ray arrivals following bore crossing	1 h
d_8	Travel time separation in cloud of upper ray arrivals	1 ms

After observing how the real acoustic record varies with time, estimates can be made of how the physical processes of the Strait varied with time as well. Unfortunately, there are few simultaneous, independent environmental measurements to compare to the estimates calculated here, but comparisons to historical data are attempted when no direct observations are available. These estimates do provide examples of the variability in physical processes in the Strait, but because of the limited duration of the acoustic record, they are too short to serve as other than examples.

A. Sensitivity analysis

The model can help determine to which physical processes in the Strait of Gibraltar the acoustic transmissions are most sensitive, and learning how the predicted acoustic travel times vary with changing model parameters is a necessary step in the inverse calculation. In order to objectively measure travel time variability, acoustic features that could be measured on all spring tidal cycles were identified and will be called ''observables.'' The eight observables that were measured for each of 12 spring tidal cycles are described in Table II and identified in Fig. 10. Observables d_4, d_5, and d_6 are dependent upon placement of a 12 h window defining the start and end of a tidal cycle; they refer to times relative to a tidal cycle window, not an absolute time. For consistency, the times of the internal solitary wave crossings (d_4), seen in the acoustic data as the bottom of the upper ray travel time drop, were designated the 4 h mark for every tidal cycle window.

Figure 11 shows time series for seven of the eight acoustic observables listed in Table II in an effort to identify any trends over the seven days of spring tides. (Observable d_4, not shown, equals 4 h for all tidal cycles by definition, and in the inverse calculation to follow, it serves as a constraint on the time of the bore crossing.) Over this short time series, no strong trends are seen. Some of the variability is due in part to the difficulty in making the measurements.

It would be simplest if the sensitivity studies indicate

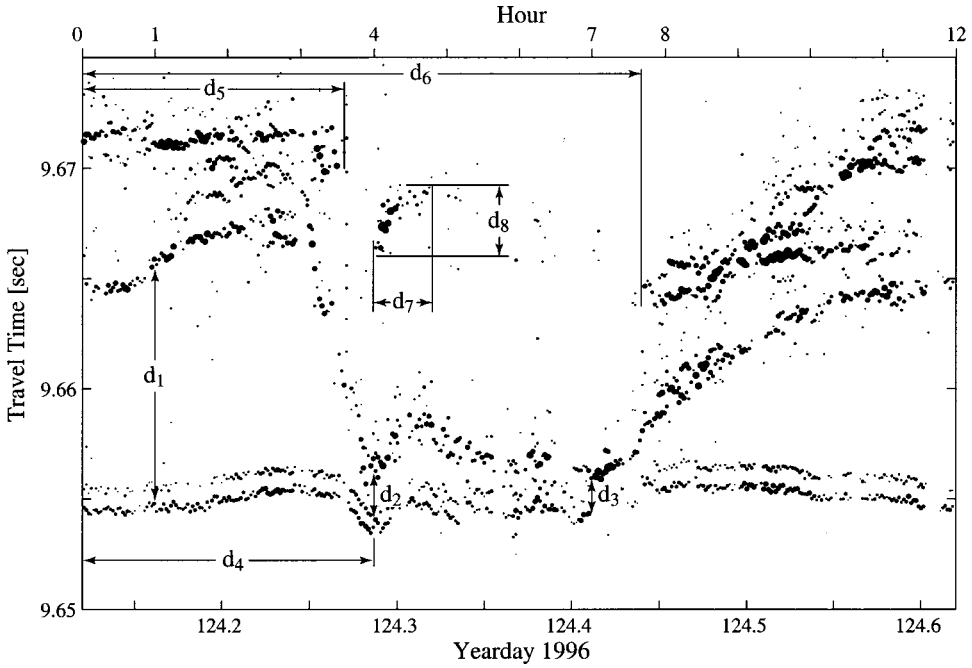

FIG. 10. Dimension lines illustrating the eight observables (d_1 through d_8) for a Type I arrival pattern. Observables are defined in Table II.

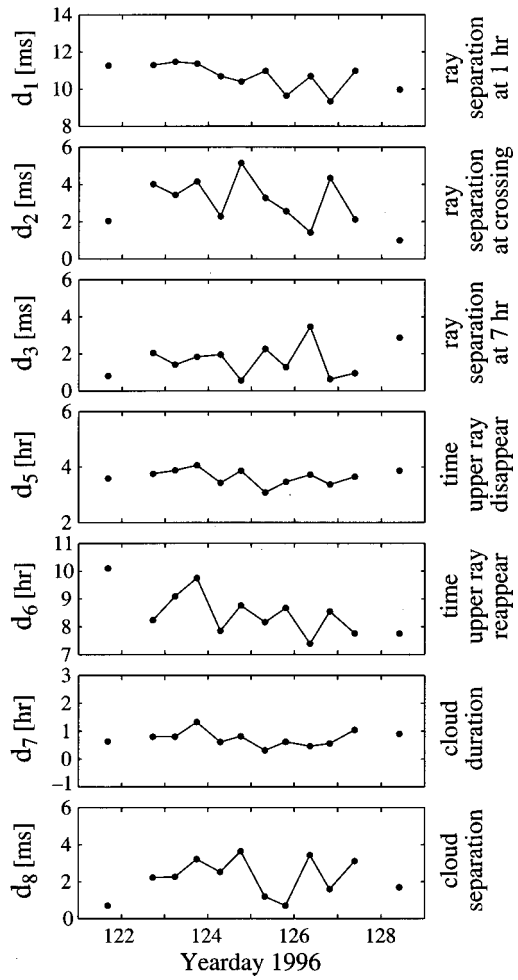

FIG. 11. Time series for seven observables from Type I arrivals. Data points from adjacent tidal cycles are connected by a line. Observables are defined in Table II.

that a travel time observable is affected by only a single model parameter, and thus the physical process that model parameter represents would be a good candidate for acoustic remote sensing. However, the inverse method is still able to provide model parameter estimates even when an observable is influenced by many parameters simultaneously, as is often the case here.

Eight model parameters were perturbed slightly, one at a time, in both a positive and negative direction from the reference state. The model was rerun after each perturbation and changes in the eight observables from the reference travel times were recorded. The result was a matrix of derivatives describing how each observable responds to perturbations in each model parameter. Table III lists all the model parameters along with the size of their perturbations. Perturbation sizes were chosen with the goal of being large enough to make a noticeable difference in travel time observables (about 0.5 ms or 0.5 h) but small enough so that the perturbations remained linear. If perturbed too far, eigenray paths change and some observables would no longer be measurable.

Because the internal bore amplitude is scaled with range across the Strait, perturbations to its associated model parameter, m_1, will be by a percentage of the reference state instead of an absolute number of meters. Model parameters m_3 and m_4, internal tide amplitude at the source and receiver, define the maximum and minimum for the range-dependent internal tide amplitude. Linearly interpolated between the endpoints, the internal tide amplitude is larger on the southern side of the Strait, near the source. The background sound-speed profiles can be offset vertically from their reference state, with the amount of offset interpolated linearly in range across the Strait between the values in m_5 and m_6, profile offsets at the source and receiver. This is equivalent to changing the depth and slope of the Atlantic/

TABLE III. Model parameter uncertainties and perturbations used in sensitivity studies.

Parameter	Description	Uncertainty	Perturbation (±)
m_1	Internal bore amplitude	12%	20%
m_2	Internal bore phase speed	0.5 m/s	0.3 m/s
m_3	Internal tide amplitude at source	12 m	10 m
m_4	Internal tide amplitude at receiver	10 m	10 m
m_5	Sound-speed profile vertical offset at source	8 m	10 m
m_6	Sound-speed profile vertical offset at receiver	8 m	10 m
m_7	Internal tide phase at source	0.12 rad	0.4 rad
m_8	Internal tide phase at receiver	0.12 rad	0.4 rad

Mediterranean interface. The tidal phase is also interpolated linearly in range across the Strait between the phase at the source and receiver, parameters m_7 and m_8. If the source and receiver phases are unequal, this makes the Atlantic/Mediterranean interface "rock" as the tide will at times be rising on one side of the acoustic path and falling on the other side.

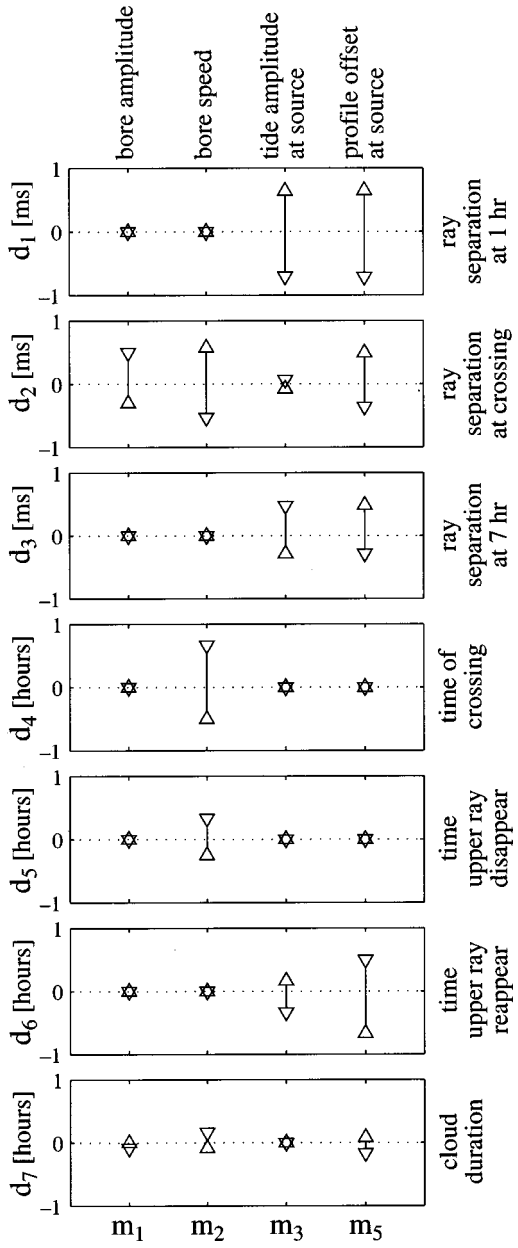

FIG. 12. Change in observable's (d_i) reference state in response to a model parameter (m_j) perturbation. For each observable/parameter combination, △ indicates the change due to a positive model parameter perturbation, and ▽ indicates a negative perturbation. Observables and model parameters are defined in Tables II and III.

When displayed graphically, linearity of the observables' derivatives with respect to model parameters ($\delta d_i / \delta m_j$) can quickly be verified and sensitivities to model parameters compared. Figure 12 shows a selected subset from the 8×8 matrix of derivatives. The changes to seven travel time observables, from both positive and negative perturbations to four model parameters, are shown. If the model reacts linearly to a perturbation, the changes to a travel time observable will be equal and opposite for the positive and negative perturbations. If a model parameter has no influence on an observable, its positive and negative derivatives will both be zero. For example, internal bore amplitude (m_1) has no effect on upper/lower ray travel time separation at the 1 h mark (d_1), but it does have an effect on upper/lower ray separation during the bore crossing (d_2). The relative strength with which a model parameter affects different observables can be compared by looking along any column of Fig. 12. For example, internal tide amplitude at the source (m_3) has a larger influence on observable d_1 than on any other observable.

While the impact of model parameter perturbations can be described numerically by the derivatives calculated above, enough was previously learned of the acoustic scattering to provide a qualitative explanation of why the acoustic observables change as they do. Figure 3 shows the modeled evolution of sound-speed profiles along the acoustic path, and the eigenray paths that result, at several times during a tidal cycle. Figure 3 will be referred to in the descriptions to follow, and the qualitative descriptions can be confirmed with the values shown in Fig. 12.

1. Internal bore amplitude

In Fig. 3, Hour 4, the presence of the internal bore over the source (T1) and receiver (T3) causes large sound-speed gradients which refract all upper rays ("c") down deep, paralleling the lower ray ("a"). If m_1, the internal bore amplitude, is increased, sound-speed gradients increase and all upper rays will be refracted even deeper, more closely following the lower ray. Because upper rays follow almost the same path as the lower ray, their travel times are nearly identical, and the observable d_2, upper/lower ray travel time separation at the bore crossing, decreases. Internal bore amplitude affects the fewest number of observables because

the internal bores are over the acoustic path for only a short time.

2. Internal bore phase speed

Changing the modeled phase speed of the internal bore mainly affects the timing of the upper ray travel time decrease and the disappearance of the late-arriving upper rays. Increasing m_2 causes the internal bore to pass over the acoustic path earlier and quicker, resulting in a decrease in the observable d_4, time of the bore crossing. An internal bore over the source also deflects the shallowest ray away from the shallowest sound channel, as seen in Fig. 3, Hour 2.58. This effect happens sooner with a faster bore, an effect measured by the observable d_5, the time of upper ray disappearance. The isolated clouds of upper ray arrivals at Hour 4.75 (''d'') are due to an internal bore over the receiver causing sound-speed gradients which refract shallow rays down on to the receiver from above. A slower moving internal bore will remain over the receiver for a longer time, thus increasing the duration of this effect. This increase is seen by observable d_7.

3. Internal tide amplitude

The model parameters m_3 and m_4 for internal tide amplitude dictate the maximum extent the background sound-speed profile will be shifted vertically over a tidal cycle. Comparing the soundspeed profiles of Fig. 3, Hour 1 and Hour 7 most clearly illustrates this shifting (after scaling by a vertical mode 1 function). Outside of Hours 2 to 5, changes in upper ray travel times are due to the internal tide's changes to the sound-speed field instead of from internal bore activity. As an upper ray will stay within the same sound channel over much of the tidal cycle, its path length changes as the sound channels shift vertically, thus changing its travel time. Lower ray travel times do not change significantly with the internal tide because sound-speed perturbations are small in deep water due to scaling by the vertical mode 1 function. An increased internal tide amplitude causes (at Hour 1) a larger upward vertical excursion by shallow sound channels, longer path lengths for that channel's eigenrays, and longer ray travel times. This is seen as in increase in observable d_1, upper/lower ray travel time separation at 1 h, since the upper ray takes longer to arrive but the lower ray travel time remains constant. During times of downward internal tide displacements (Hour 7), the sound channels carry rays into slightly faster water, thus decreasing a shallow ray's travel time and decreasing observable d_3. In all cases, observables seem more sensitive to internal tide amplitude changes on the source (southern) end of the acoustic path than at the receiver end. This may be because the source is shallower than the receiver and often within the double minimums of the sound-speed profiles where sound-speed gradients are stronger.

4. Sound-speed profile offset

The model parameters for adding a constant vertical offset to the background sound-speed field, m_5 and m_6, affect observables similarly to parameters of internal tide amplitude. The profile offset parameter defines a constant vertical shift to be added to the sinusoidal shifting defined by the internal tide parameters. Interestingly, parameter m_5, the profile offset at the source, has a large effect on observable d_6, the reappearance time of the late-arriving upper rays, while parameter m_6 has no effect. The reappearance of the upper ray arrivals indicates that the shallowest sound channel is once again being used. Rays refract up into the shallow sound channel immediately after leaving the source only when the source is below the deeper sound-speed minimum. This happens sooner when profiles at the source are offset shallower, and thus observable d_6 decreases.

In most cases the observables respond linearly to perturbations of a single model parameter; some may show a slightly unequal response to the positive and negative perturbation for a given parameter. Their successful use in an inverse calculation also requires that their responses be linear when several model parameters are perturbed simultaneously. Fortunately, the derivatives of the observables did add linearly when tested with several combinations of perturbations to internal tide amplitude, profile offset, tidal phase, and bore amplitude. However, testing the linearity for every combination of eight model parameters before proceeding with the inverse calculation was not feasible. It was assumed that the observables would behave linearly provided that model perturbations were small, and this was tested and confirmed in calculations using the new model parameter estimates provided by the inverse.

B. Linear inverse calculation

The sensitivity studies confirm that most observables are dependent upon more than one model parameter; observable d_5, time of shallow ray disappearance, is the only exception. When many observables change from their reference state simultaneously, inverse techniques can estimate what combination of model parameter perturbations will provide output that most closely matches the observables. The following matrices are used in the inverse calculation (Wunsch, 1996):

- d Data vector. For each of 12 spring tidal cycles, the difference between observables predicted for the reference state and measured observables.
- G Derivatives $(\delta d_i/\delta m_j)$ as measured in the sensitivity studies.
- R Data uncertainty covariance matrix. The diagonal of this matrix is the expected uncertainty for each observable, shown in Table II.
- P Model parameter uncertainty covariance matrix. The diagonal of this matrix guides how far the inverse is allowed to perturb each model parameter. Values are shown in Table III.

Once the above matrices are defined, they can be used in the inverse equation (1) to calculate $\hat{m}$, estimates of the amount to perturb each model parameter in order to match the data from each tidal cycle:

$$\hat{m} = (G^T R^{-1} G + P^{-1})^{-1} G^T R^{-1} d. \quad (1)$$

Uncertainties for the $\hat{m}$ estimates are calculated as follows:

$$\hat{P} = (G^T R^{-1} G + P^{-1})^{-1}. \quad (2)$$

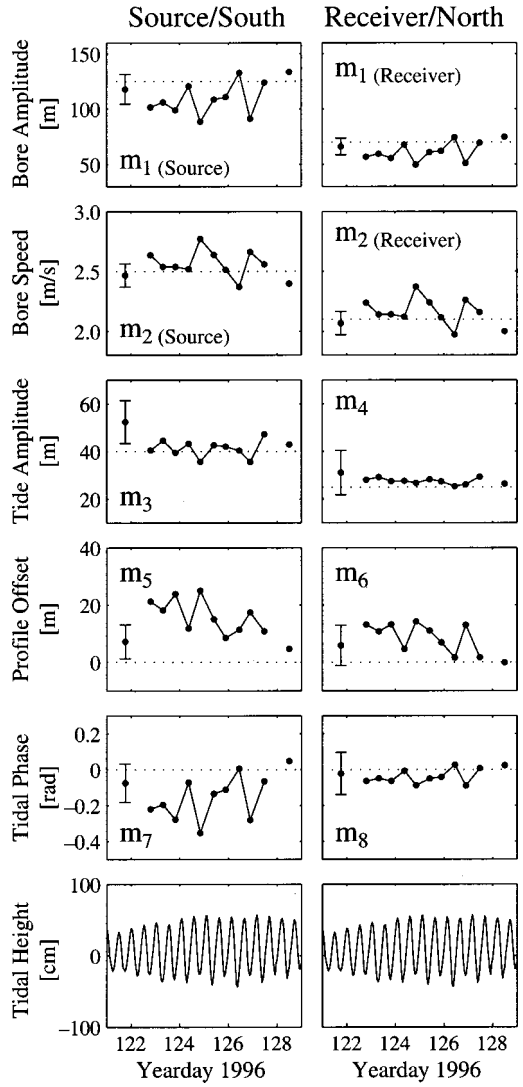

FIG. 13. Time series for eight corrected model parameters (m_j), plus the tidal height record from Ceuta. The uncertainty for each parameter is independent of yearday and shown only on the first data point. Data points from adjacent tidal cycles are connected by a solid line. Dotted lines indicate the model parameter value for the reference state. Model parameters are defined in Table III.

The precision with which the observations were required to match the model output depended on both the precision of the data (observation error) and the ability of the model to reproduce the observable (representation error). The uncertainty assigned to a given observable has variance that is the sum of the variance of the observational and representational error. While observational error was similar for most observables, representational error varied greatly, and dominated the uncertainties in matrix *R*. Observables that could be reproduced well in spite of the limited parameterization of the inverse model were given smaller uncertainties, thus requiring the inverse to match them more closely. In assigning values for the data error uncertainty matrix, the smallest uncertainties were given to d_2 and d_4, the observables from the time of the bore crossing.

The difference between the measured and modeled values for an observable is the residual, and the least square inverse procedure more strongly penalizes residuals for observables with small expected uncertainties. The inverse solution ($\hat{m}$) was optimized to have a low data misfit penalty while also minimizing the weighted magnitudes of the model parameter perturbations. The estimated model parameter perturbations were added to the reference model parameters to make corrected model parameters. Time series for the corrected model parameters, and thus the physical processes they represent, are shown in Fig. 13. Parameters m_1 and m_2 are not specific to the source or receiver side of the acoustic path as the other parameters are. However, they have been scaled per the range-dependent functions used in the model (detailed in Tiemann *et al.*, 2001) before being presented in Fig. 13. Error bars showing the standard deviations of the model parameter estimates are independent of yearday and are shown on the first data point only.

Despite the short time series available, some conclusions can be drawn. There is more variability in physical processes on the source (southern) side of the acoustic path than on the receiver (northern) side, but in most cases, perturbations at the source and receiver are in the same direction for a given parameter. The estimated internal bore amplitude, m_1, is usually smaller than the reference case, and as predicted from the sensitivity studies, it moves exactly opposite the time series for observable d_2, upper/lower ray separation at the time of the bore crossing. Observable d_2 would be the best choice to use in quickly estimating internal bore strength. The estimates of internal tide amplitude are consistent with historic observations that internal tides are larger on the southern side of the Strait, but it is unfortunate that the error bars for the tidal amplitude at the receiver are so relatively large. The tidal phase estimates suggest that the internal tides at the source and receiver should not be exactly in phase. As the Atlantic/Mediterranean interface depth rises and falls with the internal tide, the northern side is slightly ahead of the southern side, causing the interface to rock. This rocking was also seen in environmental data from three moorings, parallel to the acoustic path, measured concurrently with the Gibraltar experiment's acoustic data (B. Baschek, personal communication). The estimates of sound-speed profile offsets are equivalent to a change in the reference interface depth, and they might be used to measure the changing thickness of the Atlantic and Mediterranean water layers.

While the time series of Fig. 13 show no obvious trends with the tidal height record, their fluctuations and uncertainties give insight into how variable the physical processes in the Strait are, even over such a short time period. More obvious trends might be seen in longer series through both spring and neap tides or when compared to other processes such as the size of the hydraulic jump at the Camarinal Sill or the current flow through the narrows. This demonstration of the linear inverse calculation also confirms the model's stability and hopefully the usefulness of acoustic remote sensing. In recalculations of the forward problem using newly estimated model parameters, the model responds well to changes of multiple parameters simultaneously, providing reasonable matches to many spring tide arrivals and not just the one pattern to which it was originally fit.

VI. DISCUSSION

The Gibraltar experiment was designed to test the feasibility of using acoustic methods to measure physical oceanographic processes in an environment difficult for conventional instruments. The opportunity for rapid sampling in time, inherent integration in space, and ability to measure several physical parameters simultaneously and nonintrusively are key advantages of using acoustic techniques in the Strait of Gibraltar. This paper has offered demonstrations of a few techniques used to extract information from the acoustic record. More thorough environmental measurements would have been helpful in improving the model used in forward problem calculations and for verifying the acoustically derived estimates presented here. Long-term trends in the physical processes still need to be identified with a longer time series of data. The distribution of physical parameters is of interest as well; a longer time series of estimates could determine if the parameters behave as purely random variables.

As shown in Sec. IV, there were at least three different types of travel time arrival patterns observed during the few weeks of the experiment. Reproduction of those travel times assumed a mode 1 internal bore in every case, but with varying amplitudes. Armi and Farmer (1988) reported seeing some mode 2 internal bores in the narrows of the Strait in addition to numerous observations of mode 1 bores, and so the use of acoustic methods to determine the modal content of a passing bore was briefly investigated as well. The model was modified to scale the internal bore amplitude with a vertical mode 2 function, instead of the usual mode 1 function, and predicted acoustic travel times over a spring tidal cycle were recalculated. According to the model, a mode 2 bore would have caused acoustic rays to refract sharply down as they left the source, reflecting first off the sea floor and then the sea surface, but missing the receiver for 2 h out of the tidal cycle. As there is a continuous record of travel times recorded at the T3 receiver, it is possible that there were no instances of a mode 2 bore, especially since the three different types of arrival patterns can be explained using mode 1 bores of varying amplitude. However, the model may be tuned to work only with mode 1 bores as there is no other environmental data showing occurrences of mode 2 internal bores.

It has been suggested from studies of satellite images of the Strait that most internal solitary wave packets entering the Mediterranean Sea can be identified as either Northeast or Southeast Modes, named for their tendency to propagate in the directions indicated (Apel, 2000). Furthermore, there is evidence that the packets may alternate modes on a semidiurnal basis. If the Northeast and Southeast Modes have horizontal wave-fronts with significantly different shapes as they cross the acoustic path, that might also help explain the alternating Type II and Type III arrival structures seen in the acoustic data.

Lastly, this work has offered examples where acoustic remote sensing has not only confirmed previous observations of physical processes in the Strait but also offered some new insight and questioned historic understanding. For example, the average 5.4 h measured here for an internal bore to travel from the Camarinal Sill to the T1–T3 acoustic path agrees with Armi and Farmer's estimates (1988). This work has also confirmed that an internal bore passes through the narrows on average every 12.56 h with the semidiurnal tide. However, this brief acoustic record suggests that successive bore occurrences typically alternate longer and shorter than the mean spacing, increasing in variability with the daily inequality. The amplitude of an internal bore is reported to vary with tidal height, being largest during the spring tides. This work confirmed that is generally true when classifying tidal cycles according to their acoustic arrival pattern; the Type I patterns occur during the spring tides and are modeled with largest internal bore amplitudes of the three arrival types. However, this work suggests that internal bore amplitude does not always scale linearly with tidal height. Rather, during spring to neap tide transitions, it alternates between small and medium sized internal bores on adjacent tidal cycles, as seen in the ordering of Type II and Type III arrival pattern occurrences.

ACKNOWLEDGMENTS

U. Send was the principal investigator for the Gibraltar Acoustic Monitoring Experiment at the University of Kiel. B. Baschek provided analysis of the environmental data taken during the experiment. T. Birdsall and K. Metzger designed the 2 kHz signals and signal processing. M. Dzieciuch assisted with the data analysis. D. Farmer and L. Armi participated in many helpful discussions during the design and analysis of the experiment. The first phase of the field work was conducted with the able assistance of the crew of the German research vessel F/S POSEIDON. The Camarinal Sill mooring (S) was installed and data provided by J. Candela and D. Limeburner. The 2 kHz instruments were recovered by the Spanish Naval research vessel MALASPINA, which was generously made available to us by the Spanish Navy, with J. Rico (Instituto Hidrografico de la Marina, Cádiz, Spain) as Chief Scientist. The acoustic instrumentation was designed, fabricated, tested, and fielded by L. Day, K. Hardy, D. Horwitt, D. Peckham, and A. Rivera. B. Betts prepared the illustrations. This work was supported by the Office of Naval Research (ONR Grant No. N00014-95-1-0072) and the European Community MAST program (EC MAST-3 Contract No. MAS3-CT96-0060). C. Tiemann was supported by an ONR AASERT grant (ONR Grant No. N00014-95-1-0795).

Alpers, W., and La Violette, P. (**1993**). ''Tide-generated nonlinear internal wave packets in the Strait of Gibraltar observed by the synthetic aperture radar aboard the ERS-1 satellite,'' in *Proc. of the First ERS-1 Symposium, Eur. Space Agency Spec. Publ. ESA-SP 359(2)*, edited by B. Kaldeich (ESA Publications Division, Noordwijk, The Netherlands), pp. 753–758.

Apel, John R. (**2000**). ''Solitons near Gibraltar: Views from the European Remote Sensing Satellites,'' Data Report 2000-1, Global Ocean Associates, Silver Spring, Maryland.

Armi, L., and Farmer, D. M. (**1988**). ''The flow of Mediterranean water through the Strait of Gibraltar,'' Prog. Oceanogr. **21**, 1–105.

Boyce, F. (**1975**). ''Internal waves in the Straits of Gibraltar,'' Deep-Sea Res. **22**, 597–610.

Bray, N., Winant, C., Kinder, T., and Candela, J. (**1990**). ''Generation and kinematics of the internal tide in the Strait of Gibraltar,'' in *The Physical Oceanography of Sea Straits*, edited by L. Pratt (Kluwer Academic, Dordrecht), pp. 477–491.

Bray, N., Ochoa, J., and Kinder, T. (**1995**). ''The role of the interface in exchange through the Strait of Gibraltar,'' J. Geophys. Res. **100**, 10755–10776.
Candela, J., Winant, C., and Ruiz, A. (**1990**). ''Tides in the Strait of Gibraltar,'' J. Geophys. Res. **95**, 7313–7335.
Farmer, D. M., and Armi, L. (**1988**). ''The flow of Atlantic water through the Strait of Gibraltar,'' Prog. Oceanogr. **21**, 1–105.
Richez, C. (**1994**). ''Airborne synthetic aperture radar tracking of internal waves in the Strait of Gibraltar,'' Prog. Oceanogr. **33**, 93–159.
Send, U., Worcester, P. F., Cornuelle, B. D., Tiemann, C. O., and Baschek, B. (**2001**). ''Integral measurements of mass transport and heat content in straits from acoustic transmissions,'' Deep-Sea Res. (in press).
Tiemann, C. O., Worcester, P. F., and Cornuelle, B. D. (**2001**). ''Acoustic scattering by internal solitary waves in the Strait of Gibraltar,'' J. Acoust. Soc. Am. **109**, 143–154.
Watson, G., and Robinson, I. (**1990**). ''A study of internal wave propagation in the Strait of Gibraltar using shore-based marine radar images,'' J. Phys. Oceanogr. **20**, 374–395.
Watson, G. (**1994**). ''Internal waves in a stratified shear flow: The Strait of Gibraltar,'' J. Phys. Oceanogr. **24**, 509–517.
Wunsch, C. (**1996**). *The Ocean Circulation Inverse Problem* (Cambridge University Press, New York).
Ziegenbein, J. (**1970**). ''Spatial observations of short internal waves in the Strait of Gibraltar,'' Deep-Sea Res. **17**, 867–875.

Target strength measurements of Hawaiian mesopelagic boundary community animals

Kelly J. Benoit-Bird[a] and Whitlow W. L. Au
Hawaii Institute of Marine Biology, P. O. Box 1106, Kailua, Hawaii 96734

(Received 18 December 2000; revised 12 March 2001; accepted 27 April 2001)

A 200-kHz echosounder modified to digitize the envelope of the received echoes directly into a computer was used to measure the *ex situ* target strength (TS) of live animals from the Hawaiian mesopelagic boundary community as a function of animal size, tilt and roll angle, and biological classification. Dorsal aspect TS (in dB//1 m) at 200 kHz was related to the animal's length: myctophid fish TS = 20 log (standard length in cm) − 58.8, $r^2 = 0.91$, squid TS = 18.8 log (mantle length in cm) − 61.7, $r^2 = 0.81$, shrimp TS = 19.4 log (length in cm) − 74.1, $r^2 = 0.83$. Tilting the fish 5° and 10° changed the measured TS by up to 3.0 dB, decreasing TS as the fish was tilted forward and increasing TS as the fish was tilted backwards. In shrimp, forward tilt increased TS while backward tilt decreased TS by up to 3.3 dB. No consistent trend in squid TS change was observed with tilt angle. Roll angles of 5° and 10° increased the TS of all groups by up to 3.0 dB. Myctophid lateral aspect TS was consistently about 6 dB higher than the dorsal TS. Physiological analysis of the fishes' swimbladders revealed that the swimbladder is not the dominant scattering mechanism in the myctophid fishes studied.
[DOI: 10.1121/1.1382620]

PACS numbers: 43.30.Sf, 43.30.Ft, 43.20.Fn [DLB]

I. INTRODUCTION

The mesopelagic boundary community found in the waters over the slopes of the Hawaiian Islands is a distinct, land-associated community of micronektonic fish, shrimp, and squid (Reid *et al.*, 1991). The species composition of the boundary community is different from that of the sound-scattering layer found in the open ocean surrounding the islands (Reid, 1994). Gut-content analyses of a variety of fish including snappers (*Etelis coruscans* and *Etelis carbunculus*) (Haight *et al.*, 1993), tunas (He *et al.*, 1997), billfish (Skillman, 1998) as well as spinner dolphins (*Stenella longirostris*) (Norris and Dohl, 1980) in Hawaii have established that much of their prey is taken from the boundary community. Clearly, the mesopelagic boundary community is an important component of the coastal ecosystem in Hawaii, and other Pacific islands. This layer, however, has not been well studied. Only one study has concentrated specifically on this important zone (Reid, 1994; Reid *et al.*, 1991), with two others looking at it incidentally (Amesbury, 1975; Struhsaker, 1973). All of these studies used trawling as their primary method of sample collection.

Midwater trawling research (Amesbury, 1975; Reid, 1994; Ried *et al.*, 1991; Struhsaker, 1973) has been very valuable in identifying specific species and obtaining some general information about the spatial structure of this boundary community of micronekton. However, trawling techniques alone have severe disadvantages. Trawling studies are relatively localized. Reid's work, for example, consisted of 3 stations around Oahu and another 11 stations around the Maui area. Trawls must be launched from a large ship and are therefore expensive and time consuming. In addition, and probably most importantly, there is the inherent bias associated with ''net avoidance'' (Holliday and Pieper, 1995; Medwin and Clay, 1998). In one study a comparison of trawl sampling and acoustic methods found that acoustic sampling estimated biomass seven times greater than trawl estimates (Koslow, 1997). Sampling with nets yields a highly biased assessment of overall biomass and relative composition of marine pelagic communities (Kenchington, 1989). Moreover, trawling cannot assess small-scale spatial and temporal heterogeneity effectively. The combined difficulties of trawling used alone severely hinder any attempt to assess the biomass, diversity, community structure, and trophic organization of marine communities (Koslow, 1997).

The use of acoustic methods to estimate animal abundance in the wild requires information on the acoustic size, target strength, or backscattering cross section, of individual organisms (MacLennan, 1990; Thiebaux *et al.*, 1991) as well as knowledge about other reflective characteristics of individual animals in the community (Love, 1969). Both echo-energy integration and echo-counting techniques require an estimate of the target strength of individual targets (MacLennan, 1990). No target strength measurements are available for myctophid fishes, which comprise more than 50% of the species and individuals of the Hawaiian mesopelagic boundary community (Reid *et al.*, 1991). To understand the dependence of target strength on length and tilt or roll angle, live mesopelagic organisms were tethered in a shipboard seawater tank and ensonified with a 200-kHz signal. The validity and field applicability of tethered single-fish measurements have been established (Foote, 1983). The goal of this work was to obtain reliable estimates of target strength and its variability for use in acoustic surveys of the Hawaiian mesopelagic boundary community.

[a]Electronic mail: benoit@hawaii.edu

TABLE I. Summary of mesopelagic boundary animals measured.

	Family	Species	Number measured	Size range (cm)	Mean size (cm)
Fishes					
	Myctophidae				
		Benthosema fibulatum	29	2.4–7.9	5.2
		Diaphus adenomus	8	3.7–6.4	5.3
		Diaphus chrysorhynchus	7	3.2–6.4	4.7
		Diaphus trachops	3	3.3–3.9	3.7
		Idiolychnus urolampus	2	3.6–4.7	···
		Myctophum brachygnathos	5	4.4–8.2	6.1
	Astronesthidae				
		Astronesthes lucifer	1	5.9	···
	Bregmacerotidae				
		Bregmaceros sp.	1	5.0	···
Squids					
	Endoploteuthidae				
		Abralia trigonura	5	1.2–4.2	2.5
	Chiroteuthidae				
		Chrioteuthis imperator	2	1.8–2.2	···
	Cranchiidae				
		Liocranchia reinhardti	1	3.6	···
Shrimps					
	Gnathophausidae				
		Gnathophausia longispina	2	4.5–7.4	···
	Pasiphaeidae				
		Pasiphaea truncata	1	6.8	···
	Sergestidae				
		Sergia fulgens	11	2.6–8.3	5.8

II. METHODS

Trawling for micronektonic organisms was conducted using a 2-m-opening Isaacs-Kidd Midwater Trawl (IKMT) during two cruises in May and July of 2000 aboard the NOAA ship TOWNSEND CROMWELL. The trawl was towed obliquely for 20 to 30 min, reaching a maximum depth of 200 m. The ship was traveling between 3 and 4 kn with wire sent out at 25 m per min. The various live animals from the mesopelagic boundary community that target strength measurements were obtained from are shown in Table I.

Live organisms from the mesopelagic boundary community and other organisms in the same size range were transferred into an aerated seawater container on deck to await study. Within one-half hour of initial retrieval, a single, robust individual was transferred into a container filled with 1 liter of water. To tranquilize the animal for study, bubbling CO_2 was administered via Alka-Seltzer tablets. Tablets were added one-quarter at a time until the animal was subdued. The anesthetized individual was then mounted upside down over an upward-looking transducer on the bottom of the tank. Animals were mounted with monofilament lines as shown in Fig. 1, to a wooden frame that kept the animal motionless. The frame rested on the top of a 2000-L freestanding shipboard tank filled with seawater. Animals were held 0.3 m from the surface of the water, 1 m above the transducer (Fig. 2). Air bubbles were removed from the surface of the animal and the monofilament tethers with streaming seawater. To observe the effect of angle on the measured target strengths, the wooden frame could be rotated 5- and 10 deg about the dorso-ventral and lateral axes of the animal by raising one side of the frame with a wooden block and recentering the target animal.

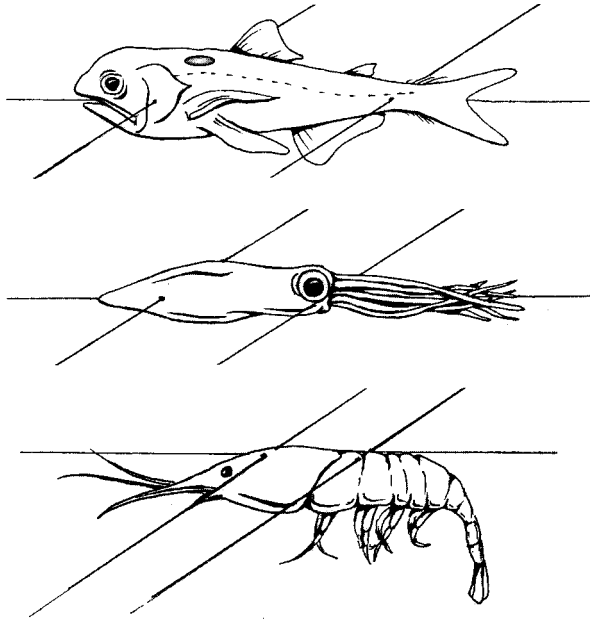

FIG. 1. Illustration of a representative fish, squid, and shrimp showing how they were mounted with six monofilament lines.

One hundred echoes were obtained from the dorsal aspect of each animal using a Computrol, Tournament Master Echosounder NCC 5300 modified to read directly into a laptop computer. The envelope of the echo was digitized at a sampling rate of 10 kHz with a Rapid System R1200. The echosounder used a 200-kHz outgoing signal with a pulse length of 130 μs. The acoustic reflection of 20 individuals was also measured 5- and 10-deg from dorsal in both the tilt and roll planes, and 8 individuals were measured from the lateral aspect.

Target strengths of individual animals were calculated using an indirect calibration procedure incorporating reference targets. Calibration of the experimental setup was ac-

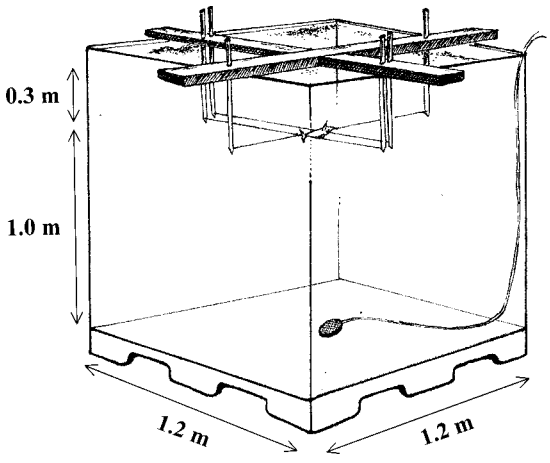

FIG. 2. Experimental setup. A wooden frame that held the subject upside down 0.3 m from the surface of the water and 1 m above an upward-looking transducer rested on a 2000-L seawater tank aboard the ship. The frame could be rotated 5° and 10° about the dorso-ventral and lateral axes of the animal by raising one side of the frame with a wooden block and recentering the target.

TABLE II. Gelatinous mesopelagic organisms caught in the IKMT along with mesopelagic boundary animals. These animals were also measured but none returned an echo above the threshold of the echosounder, −63 dB.

Order Species	Number measured	Size range (cm)	Inclusions
Salps			
Salpida			
Salpa spp.	4	3.8–6.5	gas
Pyrosomes			
Pyrosomidae			
Pyrosomas spp.	3	11.0–16.4	none
Heteropods			
Mesogastropoda			
Family Heteropoda, sp. unknown	2	3.1–4.2	shell
Siphonophores			
Calycophora			
unknown	5	6.2–17.1	gas

complished by substituting a 0.79-cm-diameter solid-steel sphere for the fish and comparing the echo level of the target fish to that of the reference target. A 0.64-cm and 1.11-cm sphere were also measured to confirm the calibration. The target strength of each sphere was measured from the levels of the incident and reflected signal from the sphere measured with a separate, calibrated hydrophone. The target strength of an individual animal from the mesopelagic layer (TS_{mbl}) was determined from the equation

$$TS_{mbl} = 20 \log(V_{envelope}/V_{calibrated}) + TS_{sphere}, \quad (1)$$

where $V_{envelope}$ is the voltage received by the echosounder from the animal, $V_{calibrated}$ is the voltage received from a sphere at the same range, and TS_{sphere} is the known target strength of the sphere.

The standard length of fishes (the distance between the snout to the end of the caudal peduncle), the mantle length of the dorsal side of the squids, and the total length of the shrimp species was measured with vernier calipers to the nearest 1 mm. Boundary community organisms were then identified to species and frozen for later analysis. Dorsal aspect target strengths of individuals as a function of the log of their length for practically definable biological classes were analyzed using regressions. *F* tests were used to test the significance of each regression's slope.

Frozen fish were thawed and dissected under a dissecting microscope to look at the characteristics of their swimbladders. An ocular micrometer was used to measure the maximum length of the major and minor axes of the swimbladder. The state of the swimbladder, inflated or not, was noted and the swimbladder was completely removed. Thin sections were made of the extracted swimbladder to analyze its contents.

III. RESULTS

Echoes from 14 gelatinous animals, shown in Table II, from four major groups were not detectable with the echosounder system. Eleven of the organisms had gas inclusions or shells. The threshold level of the echosounder system was measured to be −63 dB.

Variation among the 100 echoes measured for each individual fish, shrimp, or squid at each aspect was limited to ±2.6 dB and was distributed normally about the mean. The dorsal aspect target strength at 200 kHz of mesopelagic fish ($n=56$) was a function of the log of the fish's standard length [Fig. 3(A)]. All measurements are within the range of geometric scattering. This relationship can be expressed as

$$TS = 20 \log(\text{standard length in cm}) - 58.8. \quad (2)$$

in dB *re* 1 m. The r^2 of this relationship was 0.83. An *F* test revealed that the slope of the regression was significantly different from zero ($P<0.05$). If only myctophid fish are considered by removing the bregmaceroid and astronesthid, the relationship remains the same; however, the r^2 for this relationship was 0.91 and was significant at $P<0.01$. One myctophid fish species was abundant enough to be considered independently. The regression for *Benthosema fibulatum* can be represented by the same equation; however, the r^2 increased to 0.94. An *F* test revealed the slope of the regression was significantly different from zero at $P<0.01$. Myctophid fish from the genus *Diaphus*, represented by three species, *D. adenomus*, *D chrysorhynchus*, and *D. trachops*, had the same relationship as well. The r^2 for *Diaphus* was 0.91 and the slope was significant at the $P<0.05$ level.

The dorsal aspect target strength of eight individuals from three squid species, *Abralia trigonura*, *Chrioteuthis imperator*, and *Liocranchia reinhardti*, was correlated with the log of the squid's mantle length [Fig. 3(B)]. The best-fit regression for these measurements, which are within the range of geometric scattering, can be expressed as

$$TS = 18.8 \log(\text{mantle length in cm}) - 61.7, \quad (3)$$

in dB *re* 1 m. The data had an $r^2=0.81$ and an *F* test revealed that the slope of the regression was significant ($P<0.05$).

The dorsal aspect target strength of 12 individuals of three species of mesopelagic shrimps, *Gnathophausia longispina*, *Pasiphaea truncata*, and *Sergia fulgens* was correlated with the log of the shrimp's total length [Fig. 3(C)]. The best-fit regression line can be expressed by the equation

$$TS = 19.4 \log(\text{length in cm}) - 74.1, \quad (4)$$

in dB *re* 1 m. The data were within the range of geometric scattering and had an $r^2=0.83$ and the slope was significant at the $P<0.05$ level. The echoes from two shrimps, 2.6- and 3.2-cm long, were not detectable.

The effect of tilt angle and roll angle on the target strength of 13 myctophids is shown in Fig. 4(A). Target strengths of fish tilted 5° head down were, on average, 1.6 dB lower than the dorsal aspect target strength of the same individual. Tilting the fish head down by 10° decreased the target strength by an average of 2.3 dB relative to dorsal aspect target strengths. Tilting the fish's head up 5° increased the target strength relative to the dorsal target strength by an average of 0.9 dB. Tilting the fish head up by 10° increased the target strength relative to the dorsal aspect target strength by an average of 1.7 dB. When the fish was angled 5° to one side, the target strength increased an average of 1.0 dB. A roll angle of 10° caused an increase of an average of 1.8 dB.

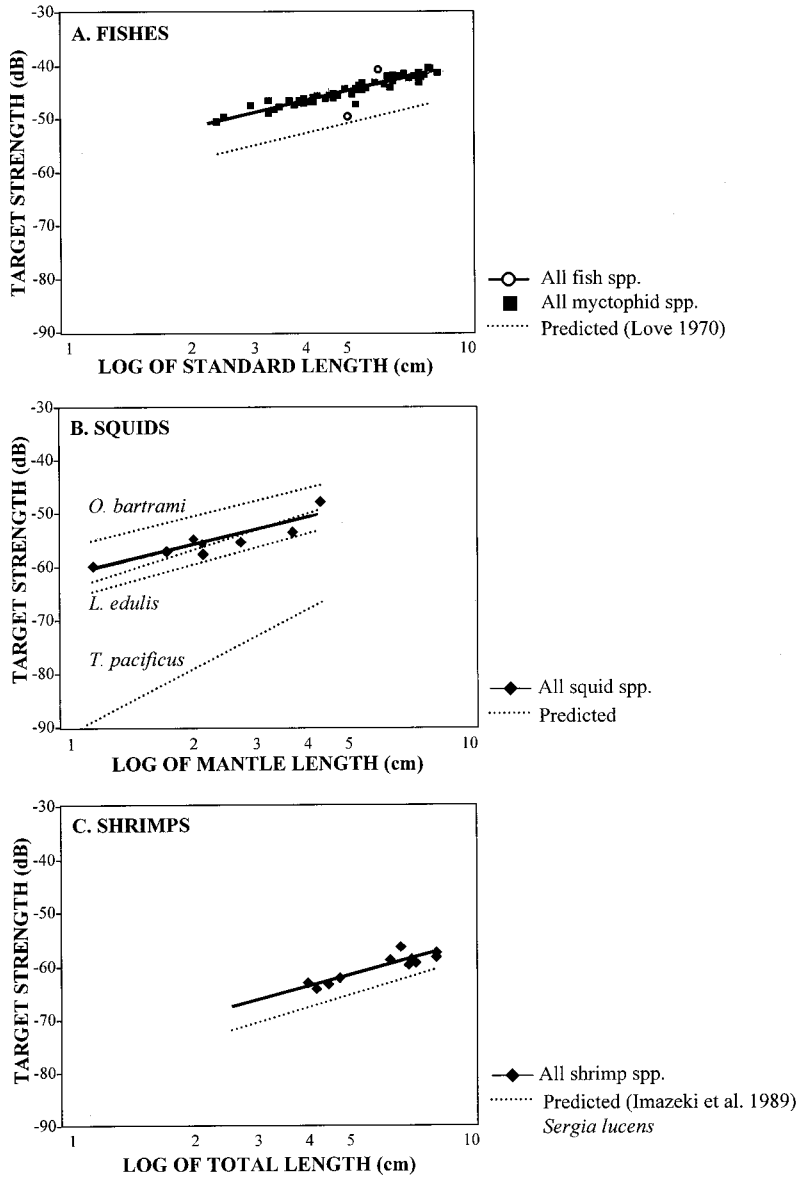

FIG. 3. (A) Dorsal aspect target strengths at 200 kHz of 56 individuals of various mesopelagic fish species plotted against the log of the fish's standard length in cm. The predictions of Love (1970) for dorsal aspect target strength values for fish equal in size to the measured individuals are represented by the dashed line. All mesopelagic fish are represented by empty circles, the best-fit logarithmic curve for all fish, TS = 20 log (standard length) − 58.8, had an r^2 of 0.83. Only myctophid species are represented by a square ($n = 54$), including only this data, the curve had an r^2 of 0.91. (B) Dorsal aspect target strengths at 200 kHz of eight individuals representing three mesopelagic squid species plotted against the log of the squid's mantle length in cm. The measured dorsal target strengths are represented by the filled diamonds. The best-fit logarithmic curve, TS = 18.8* log (mantle length) − 61.7, had an $r^2 = 0.81$ and a significant slope ($P < 0.05$). The predictions of dorsal aspect target strength at 200 kHz for individuals of the same size as the measured individuals are represented by the dashed lines: flying squid, *Ommastrephes bartrami* (Arnaya *et al.*, 1989; Kajiwara *et al.*, 1990), *Loligo edulis* (Lee *et al.*, 1991), and *Todarodes pacificus* (Arnaya *et al.*, 1989). (C) Dorsal aspect target strengths at 200 kHz of 12 individuals representing three mesopelagic shrimp species plotted against the log of the shrimp's length in cm. The best-fit logarithmic curve, TS = 19.4* log (length) − 74.1, had an $r^2 = 0.83$ and had a significant slope ($P < 0.05$). The dashed line represents the dorsal target strength at 200 kHz of *Sergia lucens* (Imazeki *et al.*, 1989), a species closely related to *Sergia fulgens*, the most abundant species in this sample.

The lateral (side aspect) target strength at 200 kHz of eight mesopelagic fishes, one astronesthid, and seven myctophids is given in Table III. The lateral target strength of the astronesthid was 0.8 dB lower than its dorsal target strength. The lateral target strengths of the myctophids were an average of 6.0 dB higher than their dorsal target strengths.

The effect of tilt and roll angle on the target strength of four squids showed that tilting the squid head down 5° increased the target strength relative to the dorsal aspect target strength an average of 0.6 dB [Fig. 4(B)]. Tilting the squid's head down 10° increased its target strength by an average of 0.7 dB, while tilting the squid head back 5° increased its target strength relative to its dorsal target strength by an average of 0.6 dB. Tilting the squid back 10° increased its target strength by 0.9 dB, on average. Changing the squid's angle by rolling it 5° to one side increased its target strength by an average of 0.7 dB relative to its dorsal aspect target strength, while rolling the squid 10° to one side increased the target strength by 0.6 dB.

The effects of tilt and roll angle on the target strengths of three shrimps are shown in Fig. 4(C). Tilting the shrimps forward, head down, by 5° increased their target strength relative to their dorsal target strength by an average of 1.6 dB. Tilting the shrimps forward by 10° increased their target strength relative to their dorsal target strength by an average of 2.6 dB. Tilting the shrimps backward by 5° and 10° decreased their target strengths relative to dorsal by an average of 2.0- and 3.3-dB, respectively. Rolling the shrimp 5° to one side increased its target strength relative to dorsal by an average of 0.7 dB. The target strengths of shrimps rolled 10° to one side also increased their target strength by an average of 0.7 dB.

The relationship between the standard length of fish and the maximum length of the major and minor axes of the fish's swimbladder was not regressive (Fig. 5). The r^2 for fish standard length against the length of the swimbladder's major axis was 0.02. For the swimbladder's minor axis, the r^2 was 0.01. F tests show that neither line has a significant slope ($P \gg 0.05$). There is also no relationship between the log length of the major or minor axes of the swimbladder and

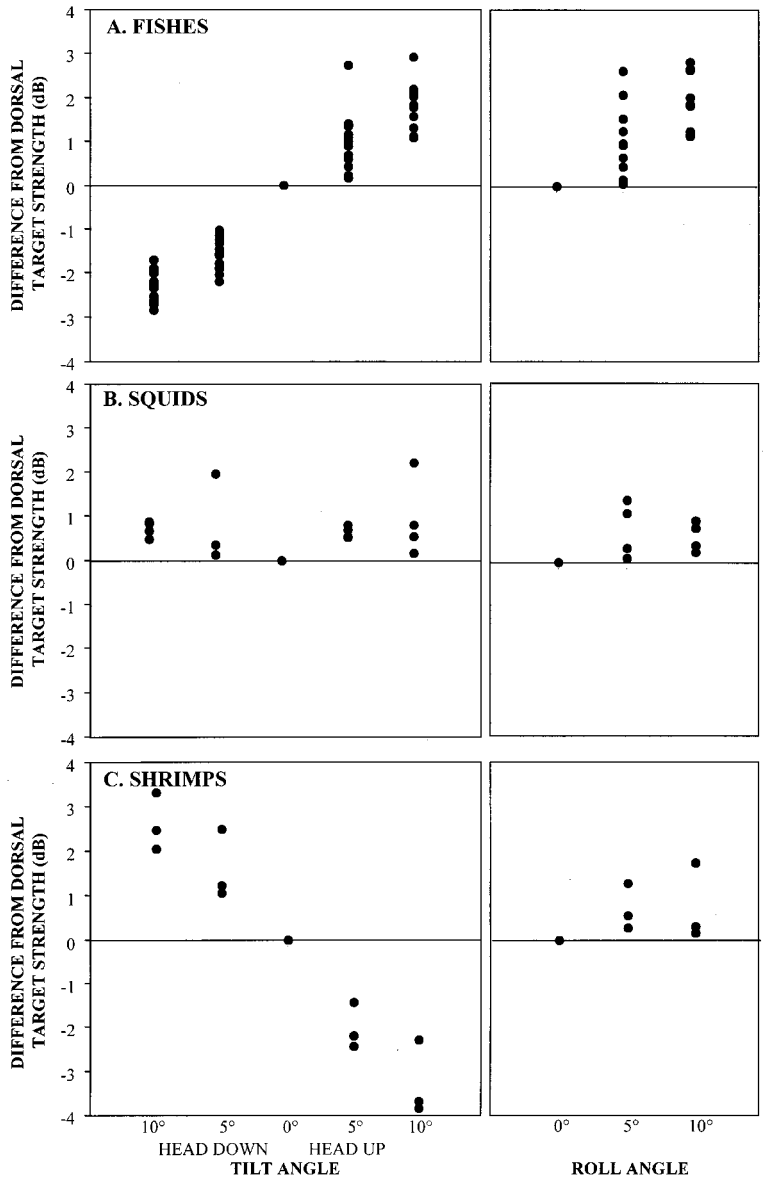

FIG. 4. (A) The effect of tilt angle (left) and roll angle (right) on the 200-kHz target strength of 13 myctophid fish. The *y* axis shows the difference of the measured target strength from the dorsal aspect target strength of the same individual. (B) The effect of tilt angle (left) and roll angle (right) on the target strengths of four squids. The *y* axis shows the difference of the measured target strength from the dorsal aspect target strength of the same individual. (C) The effect of tilt angle (left) and roll angle (right) on the target strengths of three shrimps. The *y* axis shows the difference of the measured target strength from the dorsal aspect target strength of the same individual.

target strength. The r^2 for each comparison was less than 0.1 with $P \geqslant 0.05$. Of the 38 swimbladders examined, 11 were completely empty, 1 was filled only with gas, 16 were filled only with a solid wax, and 10 had a solid wax core surrounded by a thin layer (1 mm or less) of gas. The empty swimbladders looked like two thin layers of tissue completely adhered to each other; there appeared to be no gas content in these swimbladders. Only one species, *Diaphus adenomus*, was observed with all swimbladders in the same state (empty). All other species had at least one individual with an empty swimbladder and at least one with solid wax in its swimbladder. The lack of relationships between fish length or target strength and swimbladder length did not change if animals were broken down by species or by swimbladder content. The lengths of the two axes of the same swimbladder were significantly correlated with an r^2 of 0.49 and $P < 0.01$. It is important to note that, unlike many other species of fish whose swimbladder's length is often more than 70% of the length of the fish (Saenger, 1989), the maximum length of the swimbladder in these myctophid fishes was, on average, 5% of the length of the fish. The small sizes of these swimbladders, represented by the filled oval within the fish in Fig. 1, all less than 12 mm in maximum length, precluded any measures of the position of the swimbladder relative to the fish.

TABLE III. Lateral target strengths at 200 kHz for 8 mesopelagic fishes, 1 astronesthid and 7 myctophids. The lateral target strength of the astronesthid was 0.81 dB lower than its dorsal target strength. The lateral target strengths of the myctophids were an average of 6.0 dB higher than their dorsal target strengths.

Species	Dorsal TS (dB)	Lateral TS (dB)	TS diff (dB)
Astronesthes lucifer	−41.6	−42.4	−0.8
Benthosema fibulatum	−51.2	−44.6	6.6
Benthosema fibulatum	−43.3	−35.4	7.9
Benthosema fibulatum	−41.8	−34.9	6.9
Benthosema fibulatum	−41.4	−35.3	6.1
Diaphus adenomus	−44.2	−39.1	5.2
Diaphus chrysorhynchus	−43.2	−38.6	4.6
Myctophum brachygnathos	−42.2	−37.3	4.9

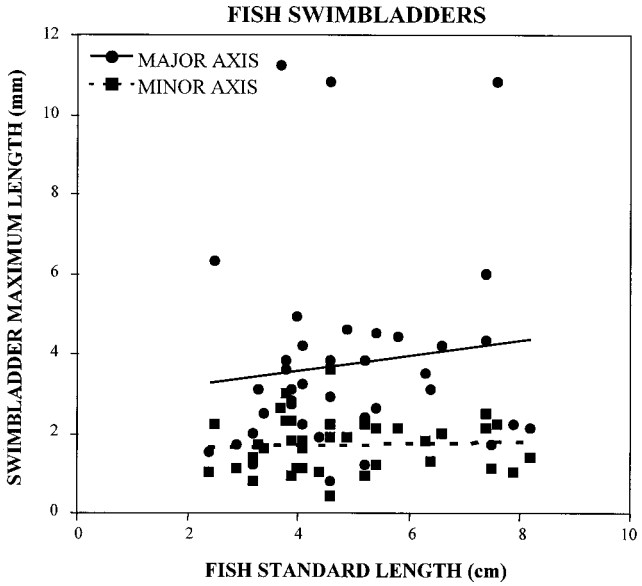

FIG. 5. The standard length of myctophid fish against the maximum length of the major and minor axes of their swimbladders. No regressive relationship was found for either measurement. The r^2 for fish length against the major axis was 0.02 with a $P \gg 0.05$. The r^2 for fish length against the minor axis was 0.01 with a $P \gg 0.05$.

IV. DISCUSSION

The gelatinous animals captured in the same trawls as the mesopelagic boundary community animals did not return echoes high enough to be detected by the echosounder system. Many of these animals had intact gas inclusions or shells that might have been predicted to serve as strong targets. However, Stanton and his colleagues (1998) found that siphonophores with gas enclosures had a target strength near −70 dB, at 200 kHz. They also found that shelled pelagic gastropods, morphologically similar to the heteropods examined here, had target strengths less than −70 dB at 200 kHz. The target strength of a gelatinous animal lacking either a shell or gas inclusion, *Aurelius aurelia*, equivalent in size to the animals observed in this study would have a target strength of about −75 dB (Mutlu, 1996). The lowest target strength the echosounder system can measure was measured to be −63 dB, well above the various target strength measures for gelatinous animals. Wiebe *et al.* (1990) found that it took more than a thousand pelagic gastropods per cubic meter to create a scattering strength of −43 dB, in the range of the target strength of one mesopelagic boundary community animal. While densities of gelatinous animals with inclusions might occur in Hawaii, the change in echo-energy estimates of density in the field would be very small relative to the high densities of the boundary community that have been observed (Benoit-Bird *et al.*, 2001).

The dorsal aspect target strength of myctophid fish was strongly dependent on the log of their standard length. The slope and *y* intercept of the regression were not affected by including only the most abundant species or genus. There appears to be little effect of taxonomy on target strength within the myctophids represented in this sample. The *y* intercept of the regression line for myctophids was 5.2 dB *re* 1 m higher than the generalized regression for fish presented by Love (1970) corrected to be referenced to 1 m. It is unclear why the observed target strengths of the myctophids in this study were consistently so high. The pulse length used was not short enough to resolve parts of an individual fish except perhaps of our largest specimens. The use of only the envelope of the echo limits the possibility that highlights from the echo could be resolved even on the largest specimens because of their relatively small size, further eliminating the possibility that target strength based on a highlight could be obtained. If target strength based on a highlight was measured, we would expect the largest individuals to be outliers on the graph, which is not the case. The values measured for the myctophids in this study are within the range of values presented by Love (1970) for fish in the same size range. It is probable that morphological differences between the species used in previous work and the myctophids used here, as well as differences between individual fish, the relatively small sample sizes, and the different methodologies used, could explain the variation.

Other researchers have found that the swimbladders of fish from the myctophid geni that are represented in this study are often uninflated, wax invested, or apparently nonfunctional (Brooks, 1977; Neighbors, 1992; Neighbors and Nafpaktitis, 1982; Saenger, 1989). The fish of the species investigated here also were rarely filled with only gas. Most were empty or wax invested. Depth of capture was apparently not the cause of the observation of empty swimbladders, as two of the fish with empty swimbladders, two with a mixture of solid wax and gas in their swimbladders, and one with only solid wax in its swimbladder were caught at the surface with a dipnet. This reduction or loss of a gas-filled bladder, shown to be the largest component of backscattering from swimbladdered fish (Foote, 1980), raises the question: what is the dominant scattering mechanism of these fish? Our data show no relationship between a fish's length or target strength and the size of its swimbladder or its content. Clearly, the swimbladder is not causing the echoes observed here. Perhaps as in other fish observed, the head region, primarily the skull, is an important source of scattering (Reeder *et al.*, Sun *et al.*, 1985).

The target strength of mesopelagic squids was positively correlated with their mantle length. The target strengths of the squids in this study were similar to the 200-kHz target strengths of the flying squid, *Ommastrephes bartrami*, of the same size. The target strengths measured in this study were 3.9 dB less than those measured by Kajiwara *et al.* (1990) for flying squid and 3.1 dB higher than those of Arnaya *et al.* (1989) for the flying squid. The target strengths for the mesopelagic squids in this study were also only 4 dB higher than the target strengths measured by Arnaya *et al.* (1989) for equally sized *Loligo edulis*. Target strengths have been reported for *Todarodes pacificus* which were about 30 dB less than those observed for the mesopelagic squids in this study (Lee *et al.*, 1991). The slope of the regression of length versus target strength for mesopelagic squids was somewhat less than those of the other squids, suggesting that target strength is less dependent on mantle length in this sample. This difference might be attributable to differences in morphology and scattering characteristics between the three spe-

cies of squids in this sample, as well as the relatively small sample size.

The dorsal target strength at 200 kHz of the three mesopelagic shrimp species was significantly correlated with the total length of the shrimp. Eleven of the 14 shrimps in this sample were *Sergia fulgens*. The target strengths of the shrimps in this sample were 4.1 dB higher than those found for *Sergia lucens* (Imazeki *et al.*, 1989), a species closely related to *Sergia fulgens*. The difference in target strength between the two samples is likely a result of the multispecies composition of this sample, differences between *S. fulgens* and *S. lucens*, and differences in methodology and equipment.

Tilting myctophid fish by 5° and 10° changed the measured target strengths by up to 3 dB. The target strength decreased as the fish was tilted forward, head down. The farther the fish was tilted forward, the more the target strength decreased relative to dorsal target strength. Target strength increased as the fish was tilted backward, increasing more with increased tilt angle. This agrees with the pattern observed for target strength changes as a function of tilt angle in many species of fish (Kubecka, 1994; MacLennan and Simmonds, 1992). The opposite pattern has been observed in other fish species (Do and Surti, 1990). Maximum target strength is generally observed when the primary source of scattering is oriented perpendicular to the acoustic beam (Kubecka, 1994). Thus, the orientation of the primary source of scattering relative to the axis of the fish determines the tilt angle that will produce the maximum scattering strength. The source of scattering in myctophid fish appears to be tilted forward (about 10° down) relative to the axis of the fish.

The pattern of target strength changes observed for myctophids was reversed for shrimps; forward tilt increased target strength while backward tilt decreased it. The magnitude of the change could reach 3.3 dB. This fits the direction of change predicted by the bent cylinder model of Clay (1992) when defining dorsal aspect the way we have here, as parallel to the carapace.

No consistent pattern in target strength was observed with changing tilt angle for squids. The greatest change was 2.2 dB. This is consistent with the observations of Lee *et al.* (1991) and Arnaya and Sano (1990), who found that the species of squids they measured were omnidirectional with respect to acoustic scattering strength. The scattering process associated with squid is still poorly understood and, unfortunately, these data are not helpful at obtaining a deeper understanding of the process.

Roll angles of 5° and 10° increased the target strength of myctophid fish relative to their dorsal aspect target strength. The greater angle had a greater effect on the target strength, causing a maximum change in target strength of 3 dB. Lateral target strength of myctophids was consistently approximately 6 dB higher than the dorsal target strength for the same individual. The single astronesthid measured had a lateral target strength lower than its dorsal target strength, by less than 1 dB. Rolling shrimps 5- and 10-deg showed a similar pattern in target strength change as myctophids, an increase in target strength with increasing roll angle. The maximum effect of roll angle on shrimp target strength was 1.7 dB. Again, no pattern was evident for squids where the maximum change in target strength due to roll angle for an individual was 1.3 dB. There was large variability in the effect of tilt or roll on target strength changes and not every individual conformed to these generalities.

Tilt and roll angles have been shown to have a profound impact on acoustic field measures of animal abundance (Huse and Ona, 1996; Mukai and Iida, 1995). These observations, however, were made on single species aggregations. The use of information on the effect of tilt and roll angle on target strength in the field is most effective when studying not only single species aggregations, but also animals from the same size class. The mesopelagic boundary community is diverse and is found in assemblages composed of many size classes and not only a variety of species, but also species from more than one biological group. The differences in target strength as a function of tilt angle observed in animals from the Hawaiian mesopelagic boundary community were relatively small, less than 3.5 dB. In the field, these differences would be overshadowed by the differences caused by species and size class variability. Consequently, these measurements of tilt angle provide valuable information for error estimation in the field, particularly on this vertically migrating community. As the community rises early in the evening, the target strength of fish will be lower than their target strength as they swim downwards later in the evening. The opposite will be true for the shrimps. These differences may cause the echo-energy integration estimates of density or biomass to appear different between two times at the opposite ends of the migration when the real densities are equivalent. They could also cause field estimates of the size of individuals creating echoes to be under- or overestimated, depending on the animal group being measured and the time observed as even at rest, myctophids, for example, are often observed at a significant tilt (Barham, 1971). However, tilt angle data cannot be directly applied to abundance estimates or used for identification of animal behavior without more information on community composition than can be obtained from single-frequency acoustics alone.

The information obtained in this study will support quantitative estimates of abundance in future acoustic field studies of the Hawaiian mesopelagic boundary community. These data will also allow estimation of the levels of variation and uncertainty in field data and may permit major compositional differences in the boundary community to be observed with acoustics, particularly since the fishes and squids have such different target strength–length relationship than the shrimps.

ACKNOWLEDGMENTS

The National Marine Fisheries Service's Honolulu Laboratory generously provided ship time aboard the TOWNSEND CROMWELL and Chief Scientist Robert Humphreys kindly worked with us to maximize accomplishment of both his and our cruise objectives. The officers and crew of the TOWNSEND CROMWELL provided excellent scientific support, especially Phil White. NMFS also supplied the free-standing tank. Bruce Mundy provided assistance in the field

and fish species identification while Curt Fiedler assisted in identifying the shrimp species. Chris Bird provided assistance constructing the mounting frame and conducting field work. Mark Latham of Computrol provided invaluable assistance in modifying the echosounder. Timothy Stanton, Andone Lavery, Paul Nachtigall, and two anonymous reviewers made helpful comments on earlier drafts of this manuscript. This is HIMB Contribution No. 1110.

Amesbury, S. S. (**1975**). ''The vertical structure of the midwater fish community off leeward Oahu, Hawaii,'' Ph.D. dissertation (University of Hawaii).

Arnaya, I. N., and Sano, N. (**1990**). ''Studies on acoustic target strength of squid. V. Effect of swimming on target strength of squid,'' Bull. Fac. Fish., Hokkaido Univ. **41**, 18–31.

Arnaya, I. N., Sano, N., and Iida, K. (**1989**). ''Studies on acoustic target strength of squid. III. Measurement of the mean target strength of small live squid,'' Bull. Fac. Fish., Hokkaido Univ. **40**, 110.

Barham, E. G. (**1971**). ''Deep sea fishes: Lethargy and vertical orientation,'' in *Biological Sound Scattering in the Ocean*, edited by G. B. Farquar (U.S. Government Printing Office, W100–118).

Benoit-Bird, K. J., Au, W. W. L., Brainard, R. E., and Lammers, M. O. (**2001**). ''Diel horizontal migration of the Hawaiian mesopelagic boundary community observed acoustically,'' Mar. Ecol.: Prog. Ser. (in press).

Brooks, A. H. (**1977**). ''A study of the swimbladders of selected mesopelagic fish species,'' in *Oceanic Sound Scattering Prediction*, edited by N. R. Andersen and B. J. Zahuranec (Plenum, New York), pp. 565–590.

Clay, C. S. (**1992**). ''Composite ray-mode approximations for backscattered sound from gas-filled cylinders and swimbladders,'' J. Acoust. Soc. Am. **94**, 2173–2180.

Do, M. A., and Surti, A. M. (**1990**). ''Estimation of dorsal aspect target strength of deep-water fish using a simple model of swimbladder backscattering,'' J. Acoust. Soc. Am. **87**, 1588–1596.

Foote, K. G. (**1980**). ''Importance of the swimbladder in acoustic scattering by fish: A comparison of gadoid and mackeral target strengths,'' J. Acoust. Soc. Am. **67**, 2084–2089.

Foote, K. G. (**1983**). ''Linearity of fisheries acoustics with addition theorem,'' J. Acoust. Soc. Am. **73**, 1932–1940.

Haight, W. R., Parrish, J. D., and Hayes, T. A. (**1993**). ''Feeding ecology of deepwater lutjanid snappers at Penguin Bank, Hawaii,'' Proc. Am. Fish. Soc. **122**, 328–347.

He, X., Bigelow, K. A., and Boggs, C. H. (**1997**). ''Cluster analysis of longline sets and fishing strategies within the Hawaii-based fishery,'' Fish. Res. **31**, 147–158.

Holliday, D. V., and Pieper, R. E. (**1995**). ''Bioacoustical oceanography at high frequencies,'' ICES J. Mar. Sci. **52**, 279–296.

Huse, I., and Ona, E. (**1996**). ''Tilt angle distribution and swimming speed of overwintering Norwegian spring spawning herring,'' ICES J. Mar. Sci. **53**, 863–873.

Imazeki, A., Yonemoto, H., Saotome, Y., Isouchi, T., and Hamada, Y. (**1989**). ''Multifrequency measurements of target strength of the sergestid shrimp *Sergia lucens*,'' J. Tokyo Univ. Fish. **76**, 37–44.

Kajiwara, Y., Iizka, K., and Kamei, Y. (**1990**). ''Measurement of target strength for the flying squid (*Ommastrephes bartrami*),'' Bull. Fac. Fish., Hokkaido Univ. **41**, 205–212.

Kenchington, T. J. (**1989**). ''Estimation of catchability coefficients,'' Mar. Biol. (Berlin) **101**, 24–35.

Koslow, J. A. (**1997**). ''Seamounts and the ecology of deep-sea fisheries,'' Am. Sci. **85**, 168–176.

Kubecka, J. (**1994**). ''Simple model on the relationship between fish acoustical target strength and aspect for high-frequency sonar in shallow waters,'' J. Appl. Ichthyol. **10**, 75–81.

Lee, K.-T., Shih, W.-H., Liao, C.-H., and Wang, J.-P. (**1991**). ''Studies on the hydroacoustic scattering properties of individual squid, *Loligo edulis*,'' J. Fish. Soc. Taiwan **18**, 215–225.

Love, R. H. (**1969**). ''Maximum side-aspect target strength of an individual fish,'' J. Acoust. Soc. Am. **46**, 746–752.

Love, R. H. (**1970**). ''Dorsal-aspect target strength of an individual fish,'' J. Acoust. Soc. Am. **49**, 816–823.

MacLennan, D. N. (**1990**). ''Acoustical measurement of fish abundance,'' J. Acoust. Soc. Am. **87**, 1–15.

MacLennan, D. N., and Simmonds, E. J. (**1992**). *Fisheries Acoustics* (Chapman and Hall, New York).

Medwin, H., and Clay, C. (**1998**). *Fundamentals of Acoustical Oceanography* (Academic, San Diego).

Mukai, T., and Iida, K. (**1995**). ''Diurnal variation of encaged fish echoes, and estimation of fish tilt angle distribution,'' Fish. Sci. **61**, 647–652.

Mutlu, E. (**1996**). ''Target strength of the common jellyfish (*Aurelia aurita*): A preliminary experimental study with a dual-beam acoustic system,'' ICES J. Mar. Sci. **53**, 309–311.

Neighbors, M. A. (**1992**). ''Occurrence of inflated swimbladders in five species of lanternfishes (family Myctophidae) from waters off southern California,'' Mar. Biol. (Berlin) **114**, 355–363.

Neighbors, M. A., and Nafpaktitis, B. G. (**1982**). ''Lipid compositions, water contents, swimbladder morphologies and buoyancies of nineteen species of midwater fishes (18 myctophids and 1 neoscopelid),'' Mar. Biol. (Berlin) **66**, 207–215.

Norris, K. S., and Dohl, T. P. (**1980**). ''Behavior of the Hawaiian spinner dolphin, *Stenella longirostris*,'' Fish. Bull. **77**, 821–849.

Reeder, D. B., Stanton, T. K., Chu, D. and Jech, M. (**2000**) ''Broadband acoustic backscattering by Alewife fish: Experiment and analysis,'' J. Acoust. Soc. Am. **108**, 2457.

Reid, S. B. (**1994**). ''Spatial structure of the mesopelagic fish community in the Hawaiian boundary region,'' Ph.D. dissertation (University of Hawaii).

Reid, S. B., Hirota, J., Young, R. E., and Hallacher, L. E. (**1991**). ''Mesopelagic-boundary community in Hawaii: Micronekton at the interface between neritic and oceanic ecosystems,'' Mar. Biol. (Berlin) **109**, 427–440.

Saenger, R. A. (**1989**). ''Bivariate normal swimbladder size allometry models and allometric exponents for 38 mesopelagic swimbladdered fish species commonly found in north Sargasso Sea,'' Can. J. Fish. Aquat. Sci. **46**, 1986–2002.

Skillman, R. A. (**1998**). ''Central Pacific swordfish, *Xiphias gladius*, fishery development, biology, and research,'' NOAA Technical Report 142.

Stanton, T. K., Chu, D., Wiebe, P. H., Martin, L. V., and Eastwood, R. L. (**1998**). ''Sound scattering by several zooplankton groups. I. Experimental determination of dominant scattering mechanisms,'' J. Acoust. Soc. Am. **103**, 225–235.

Struhsaker, P. (**1973**). ''A contribution to the systematics and ecology of Hawaiian bathyal fishes,'' Ph.D. dissertation (University of Hawaii).

Sun, Y., Nash, R. D. M., and Clay, C. S. (**1985**). ''Acoustic measurements of the anatomy of fish at 220 kHz,'' J. Acoust. Soc. Am. **78**, 1772–1776.

Thiebaux, M. L., Boudreau, P. R., and Dickie, L. M. (**1991**). ''An analytical model of acoustic fish reflection for estimation of maximum dorsal aspect target strength,'' Can. J. Fish. Aquat. Sci. **48**, 1772–1782.

Wiebe, P. H., Greene, C. H., Stanton, T. K., and Burczynski, J. (**1990**). ''Sound scattering by live zooplankton and micronekton: Empirical studies with a dual-beam acoustical system,'' J. Acoust. Soc. Am. **88**, 2346–2360.

Spatial resolution of time-reversal arrays in shallow water

Seongil Kim,[a] G. F. Edelmann, W. A. Kuperman, W. S. Hodgkiss, and H. C. Song
Marine Physical Laboratory, Scripps Institution of Oceanography, La Jolla, California 92093-0238

T. Akal
SACLANT Undersea Research Centre, 19138 La Spezia, Italy

(Received 25 September 2000; revised 16 April 2001; accepted 27 April 2001)

A series of time-reversal experiments was performed in shallow water including a range-dependent slope environment. Time-reversal arrays implemented with center frequencies of 445 and 3500 Hz achieved sharp focal regions up to ranges of 30 and 13 km, respectively in 110–130-m shallow water. In this paper, resolution expressions are derived using an image method to describe the focal sizes achieved with time-reversal arrays in various ocean environments. Analysis for the measured data indicates that the focal size approaches the diffraction limit of an array for given waveguide conditions, i.e., waveguide geometry and attenuation. The measured focal size has implications for the maximum achievable resolution of linear matched-field processing which is a computational implementation of the time-reversal process. © *2001 Acoustical Society of America.*
[DOI: 10.1121/1.1382619]

PACS numbers: 43.30.Vh, 43.30.Pc, 43.60.Gk [DLB]

I. INTRODUCTION

Recently, acoustic time-reversal mirrors (TRMs) have been demonstrated in the laboratory[1,2] and in the ocean.[3–5] Time reversal, also referred to as the process of phase conjugation[6] in the frequency domain, refocuses the incident acoustic field back to the origin of a probe signal regardless of the complexity of the medium. The focusing or the resolution of a TRM can be described by wave diffraction limits; Rayleigh and Fresnel limits for the transverse and the longitudinal resolution.[7] In free space, the resolution is described with the physical extent of an aperture, but in an ocean waveguide, the spatial complexity of the sound field resulting from multipath propagation increases the resolution over free space. The purpose of this paper is to describe the resolution accomplished with time-reversal arrays in various ocean environments.

The resolution issue for TRMs is the same as the resolution of matched-field processing (MFP).[8] While a propagation model is used to match the source-generated sound fields in MFP, the time-reversed signal is physically backpropagated to the original source position using a source–receiver array in a TRM. MFP requires *a priori* environmental information along the propagation path for accurate simulation of wave fields, but such measurements often are not practical. On the other hand, time reversal is an environmental self-adaptive process. Hence, the focal size realized with a TRM can be considered as the maximum achievable resolution of MFP for given waveguide conditions.

Greater performance of an array in a waveguide over the free-space diffraction limit already has been mentioned in the context of MFP using Cramer–Rao bounds,[8] in ultrasonic experiments,[9] and in ocean experiments.[3] A simple way to look at resolution is to recognize that a water-column-spanning array can produce a focal spot with vertical extent of approximately the waveguide depth divided by the number of modes, i.e., the shortest vertical wavelength which results from the highest order effective mode. In this paper we present foci achieved with low- (445 Hz) and high-frequency (3500 Hz) TRMs in various ocean environments. Resolution expressions using an image method are derived for a Pekeris waveguide and a wedge ocean to describe the measured focal sizes. This description provides physical and quantitative insight into how waveguide parameters such as geometry and attenuation affect resolution in MFP as well as in the time-reversal process.

In this study, we do not consider dynamic ocean effects[10,11] under the assumption that the ocean is static during the time between the forward propagation and the time-reversal backpropagation. The measured data presented here were selected from the signals which were backpropagated within 2 min of reception. The possible components of time-dependent ocean variations on this time scale are surface and internal waves. Since the observed sound-speed profiles during the experiments were strongly downward refracting and the periods of internal waves are much longer than this time scale, the effect of these dynamic feature is assumed to be negligible.

In the next section, time-reversal experiments are briefly described and the measured foci in various ocean environments are presented. In Sec. III, we formulate the equations describing time-reversal focusing in free space and ocean waveguides. The equation describing the focused acoustic field is interpreted as the near-field beam pattern of an array. In Sec. IV, the transverse (doped) and longitudinal (range) resolution expressions are derived from the beam-pattern equations. The bottom attenuation serves as an aperture shading and reduces the effective aperture of TRM. In Sec. V the measured time-reversal foci are compared with the theory.

[a]Electronic mail: seongil@mpl.ucsd.edu

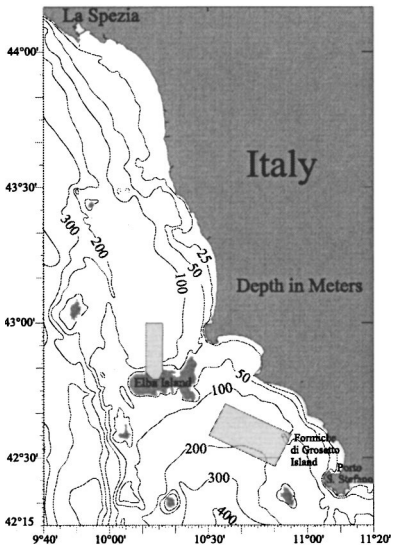

FIG. 1. Locations of the time-reversal experiments. In April 1996 and May 1997, low-frequency (445-Hz) experiments were performed near the Formiche di Grosseto. In July 1999, a high-frequency (3500-Hz) experiment was carried out both north of Elba and in the Formiche area.

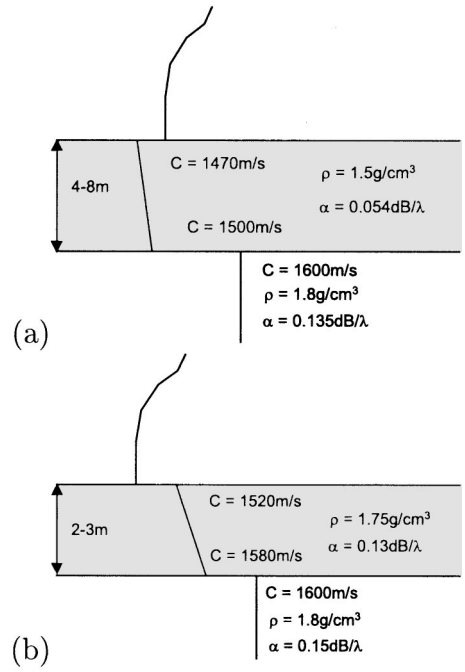

FIG. 2. Two-layer geoacoustic models for the experimental area: (a) Formiche (slow bottom) and (b) North Elba (fast bottom).

II. TIME-REVERSAL EXPERIMENTS

A. Experimental setup

Here, we briefly describe the experimental equipment and the environmental conditions of the sites where the time-reversal experiments were performed.[3–5] Refer to the cited references for the detailed descriptions of hardware and ocean environments. The important point is the difference in geoacoustic properties between the Formiche and Elba areas, which resulted in different attenuation and focal sizes.

We performed a series of time-reversal experiments in two areas (near Formiche and Elba islands) off the west coast of Italy (see the boxes in Fig. 1). The two experimental sites have very different seabed properties.[12–15] The area near Formiche is a relatively flat environment with water depth of about 120–130 m. The sediment contains a homogeneous clay layer with thickness varying between 4 to 8 m. Since the sound speed in the sediment layer is less than the water column (slow bottom), most of the acoustic energy penetrates into the sediment layer and interacts with the silt sub-bottom resulting in large attenuation. The area north of Elba has 2- to 3-m-thick sand sediments where sound speed in the sediment is known to be greater than that of the water column (fast bottom). The water depth in the flat Elba area is about 110–120 m. Experiments were performed both in the flat area and the slope environment close to the island. In the slope environment, the water depth decreases from 115 to 0 m in about a 10-km range. The slope is steeper near the island (~2°). Figure 2 shows the two-layer geoacoustic models for these areas.[14,16]

Figure 3 shows the experimental setup for acoustic and oceanographic measurements. A TRM was implemented with a vertical source–receiver array (SRA). The SRA receives an incident signal from a probe source (PS) and retransmits the time-reversed signal to the receiving array which is collocated with the PS. In April 1996 and May 1997, a TRM was deployed near Formiche di Grosseto consisting of a 77-m SRA with 20 hydrophones and 20 contiguously located slotted cylinder sources with a frequency of 445 Hz. Each element of the SRA was operated at a nominal source level of 160 dB/1 μPa with 50-ms pure-tone pulses. The SRA was hardwired to the island for time-reversal processing. A PS was located in the vicinity of a 48-element vertical receive array (VRA) which radio telemetered all data back to the R/V ALLIANCE. The July 1999 experiment was performed with a center frequency of 3500 Hz both north of Elba and in the Formiche area. The experimental setup was similar to the previous ones but the SRA had 29 transducers spanning a 78-m aperture. The source level of the SRA was 178 dB/1 μPa and the nominal pulse lengths were 2 and 10 ms at 3500 Hz. The VRA covered 93 m of the water column with 32 hydrophones. This time, both the VRA and SRA were radio linked to the R/V ALLIANCE.

Oceanographic measurements included a wave rider, current meters, and conductivity-temperature chains. Sound-speed profiles (SSP) were measured frequently by conductivity-temperature-depth (CTD) casts. The SSPs collected over the experiment period indicate the variability of the upper water column, especially in the thermocline region (Fig. 4). The downward-refracting sound-speed structure resulted in substantial interaction of the sound field with the ocean bottom.

B. Measured time-reversal foci

In this section, we describe the measured focal structure. Of interest are focal size variations: (1) with frequency; (2) with waveguide conditions; and (3) with range. The results presented in this paper are limited to the vertical focal structure. Although the horizontal focal structure also was investigated in the experiments, we do not include the results in this study since the measured data did not cover the whole

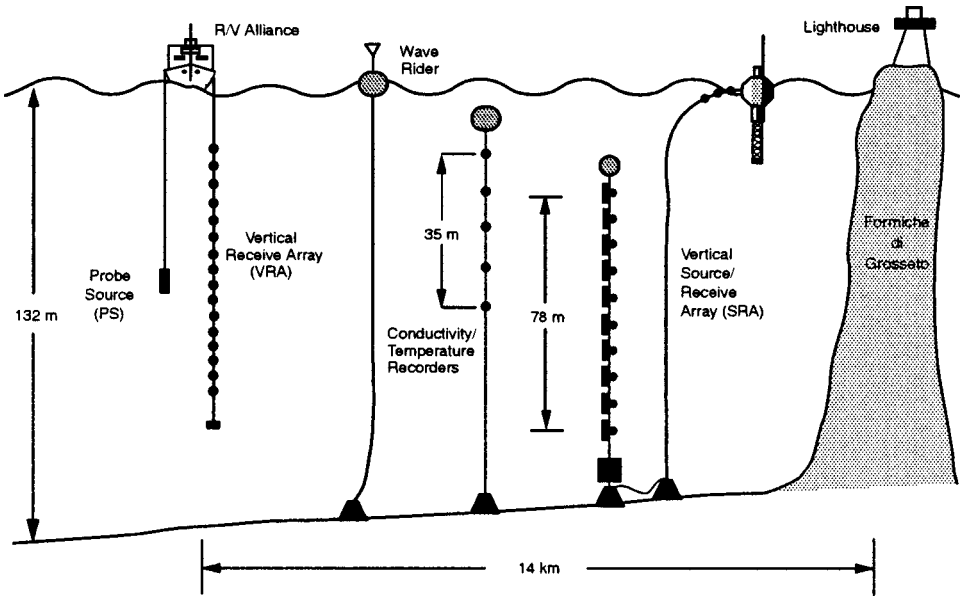

FIG. 3. Experimental setup for the July 1999 high-frequency (3500-Hz) time-reversal experiment near Formiche di Grosseto. The time-reversal array (vertical source–receiver array) consisted of 29 transducers with interelement spacing 2.786 m spanning 78 m of the water column. Oceanographic measurements included regular CTDs, a wave rider buoy, conductivity-temperature recorders, current meters, etc. The setups were similar for the low-frequency (445-Hz) experiments except that the source–receiver array had 20 elements spanning an aperture of 77 m. The VRA covered 93 m of the water column with 32 hydrophones in the high-frequency experiment and 96-m of one water column with 48 hydrophones in the low-frequency experiments.

scale of the horizontal resolution and the elapsed time over which the measurements were made does not guarantee static ocean conditions.

The focused acoustic fields were measured by the VRA. The received signals were bandpass filtered and envelopes of each signal was extracted using a discrete Hilbert transform.[17] A spline interpolation scheme was applied in depth direction for the intensity data of time vs depth. The depth focal size was defined at the 3-dB down points from the peak level with integrations for the pulse length.

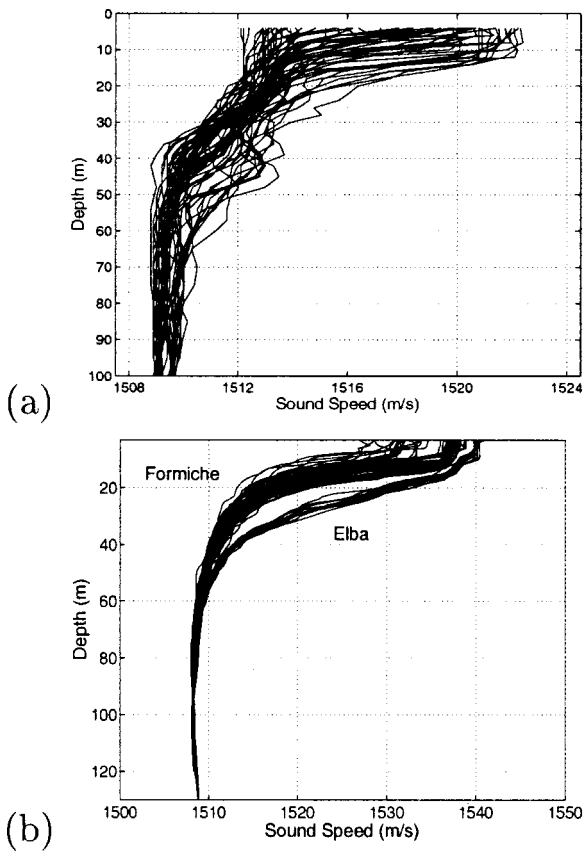

FIG. 4. Sound-speed profiles measured with CTD casts from the R/V ALLIANCE: (a) in the 1997 experiment and (b) in the 1999 experiment.

In free space, the transverse focal sizes are directly proportional to the wavelengths or inversely to the frequencies. In a waveguide, the different loss mechanisms at the boundaries between low- and high-frequency propagation sometimes prevent the focal sizes from being proportional to the wavelengths. Figure 5 shows the results for two different frequencies measured in the Formiche area (130-m water depth). The foci were observed at a range of 15 km with a 50-ms pure-tone pulse with a center frequency of 445 Hz [Fig. 5(a)] and at a range of 12.73 km with a 10-ms pure-tone pulse with a center frequency of 3500 Hz [Fig. 5(b)]. The probe source depths were 80 m for both cases. The vertical focal sizes are 20 and 7.5 m, respectively, with a size ratio of 2.7 between the low-frequency and the high-frequency focus. In this case the ratio of wavelengths is 7.8, which is substantially different from the ratio of focal sizes.

The waveguide attenuation and geometry play important roles for determining the focal size. Figure 6 represents the foci obtained in three different environments: (a) Formiche area (slow bottom); (b) flat Elba area (fast bottom); and (c) sloping Elba area. The water depths were 130 m in the Formiche area and 120 m in the flat Elba area. In the slope experiment, the SRA was located in 120-m-deep water and the probe source in 33-m-deep water. The bathymetry sloped upwards about 1°–2° from shallow water to the island. The focus was realized with 2-ms rectangular pulses at a center frequency of 3500 Hz. The ranges were 7.9, 7.4, and 9.6 km, and the probe sources were 70, 60, and 22 m deep, respectively. The vertical focal sizes at the 3-dB down points are 6.3, 3.8, and 1.7 m. The main reason for the different focal sizes is the difference in bottom attenuation between the Formiche and Elba areas and additional geometric effects in the sloping environment. The slow bottom in the Formiche area causes greater attenuation than the fast bottom in the Elba area. The geometric effects in the slope environment are discussed in Sec. IV.

The spatial focus broadens with range due to mode stripping.[4] Figure 7 shows the foci achieved with different

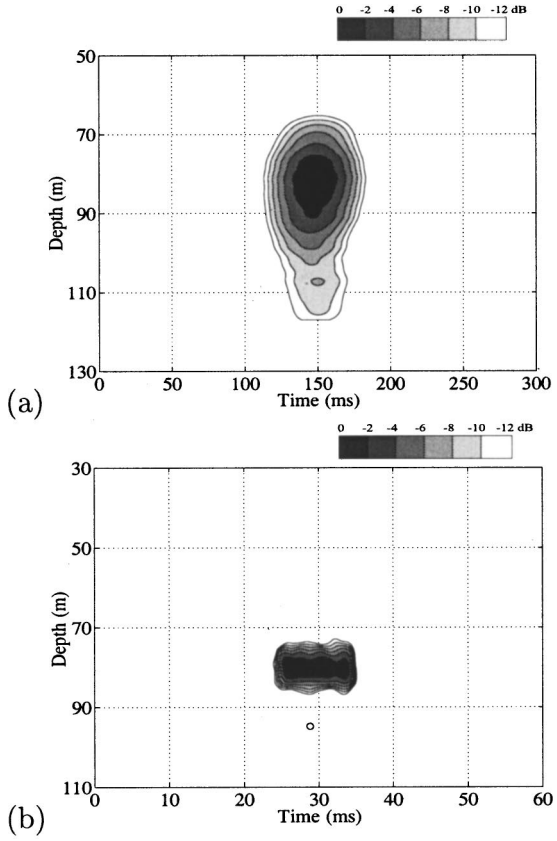

FIG. 5. Measured time reversal foci: (a) for 445 Hz with a 50-ms pulse at 15 km and (b) for 3500 Hz with a 10-ms pulse at 12.73 km. The source depths were both 80 m. The focal size is proportional to the wavelength but the relationship is not linear due to the differential effect of attenuation with frequency in the ocean bottom.

ranges in the Formiche area. The focus was observed out to 30 km at 445 Hz with a 50-ms pulse and 13 km at 3500 Hz with a 2-ms pulse. The focal size changes from 12 m at 4.5 km to 28 m at 30 km for 445 Hz and from 3.8 m at 2.2 km to 7.3 m at 12.8 km for 3500 Hz, which shows that the focal size is somewhat proportional to the square root of range.

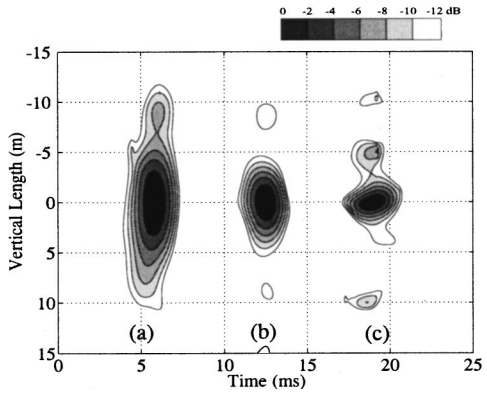

FIG. 6. Measured foci for 3500 Hz with a 2-ms pulse in three different environments: (a) Formiche area at 7.9 km range with PS at 70-m depth; (b) flat Elba area at 7.4 km with PS at 60-m depth; and (c) sloping Elba area at 9.6 km range with PS at 22-m depth in 33-m water depth. The main reasons for the different focal sizes are due to the difference in bottom attenuation between the Formiche and flat Elba areas and additional geometrical effects in a sloping environment.

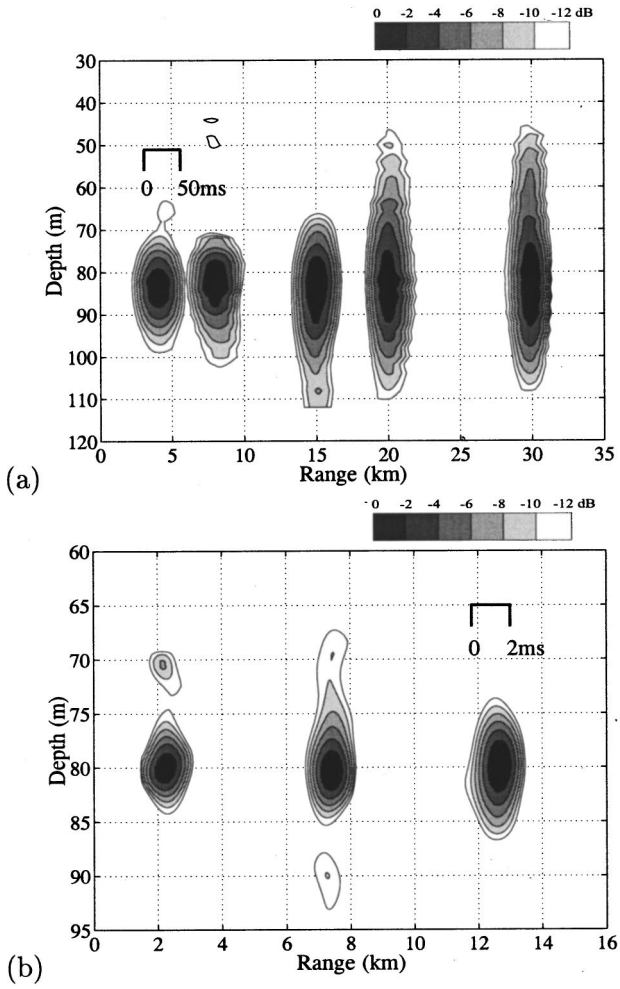

FIG. 7. Measured focal sizes at different ranges from SRA: (a) for 445 Hz and (b) for 3500 Hz. As expected, the spatial focus in depth broadens with range due to mode stripping. Note the different scales in pulse length, range, and depth.

III. TIME-REVERSAL FOCUSING WITH A LINE ARRAY

A. Free space

Here, we briefly review the time-reversal focusing with a line array in free space.[18] Figure 8 shows a line array of an aperture L associated with a spherical coordinate. The pressure field received at a field point (r,φ) from an element dz of the array is

$$dp = \frac{S(z)}{l}\exp(jkl)dz, \tag{1}$$

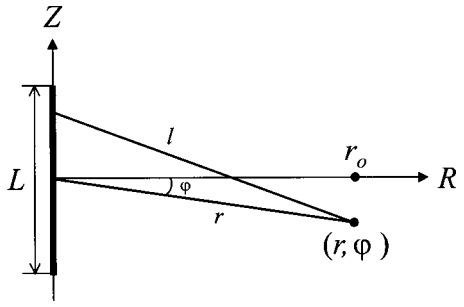

FIG. 8. A line array of aperture L associated with spherical coordinate.

where $S(z)$ is either a source amplitude or an aperture shading along the array, $j=\sqrt{-1}$, k is the wave number, and l is the path length from a source point to a receiver point. Inserting a phase-conjugated probe signal $A\exp(-jkl_0)/l_0$ into $S(z)$, the pressure field observed at a field point (r,φ) from the time-reversal array is

$$p(l)=\int_{-L/2}^{L/2}\frac{A}{ll_0}\exp jk(l-l_0)dz, \tag{2}$$

where A is the amplitude of the probe source and l_0 is the distance from a probe source to an element of the array. The path length is given by

$$l^2=r^2+z^2+2rz\sin\varphi, \tag{3}$$

and using a binomial expansion, l can be represented as

$$l=r+z\sin\varphi+\frac{z^2}{2r}\cos^2\varphi-\frac{z^3}{2r^2}\sin\varphi\cos^2\varphi+\cdots. \tag{4}$$

In the near field $(1.356L<r<kL^2/2)$,[19] only the first term of the expansion is necessary for approximating the amplitude term in Eq. (2), but we need to consider to the second-order term for the phase term since a small path-length difference causes a large phase difference. With this Fresnel approximation[19] and the probe source position of $(r_0,0)$, Eq. (2) becomes

$$p(r,\varphi)=A\frac{\exp jk(r-r_0)}{rr_0}\int_{-L/2}^{L/2}\exp\left[jk\frac{z^2}{2}\left(\frac{\cos^2\varphi}{r}-\frac{1}{r_0}\right)\right]\times\exp(jkz\sin\varphi)dz. \tag{5}$$

This is a one-dimensional spatial Fourier transform expression which can be interpreted as a near-field directional function (beam pattern) of a line array lying along the z axis. The exponential terms associated with r become unity with $r\rightarrow r_0$ and $\varphi\rightarrow 0$, i.e., to the probe source position, indicating that the time-reversal propagation compensates for the quadratic phase differences caused by the path-length differences. Along the locus of points $r=r_0\cos^2\varphi$ the field becomes exactly that of a uniform line array at infinity (Fraunhofer zone), i.e., the far-field beam pattern. Although the focal surface bows slightly with the z direction, it is not enough to be of concern for a small φ. Ignoring the amplitude spreading term A/rr_0, the far-field beam pattern near the focal region is

$$D(\chi)=\int_{-L/2}^{L/2}\exp(j\chi z)dz, \tag{6}$$

where $\chi=k\sin\varphi$. Notice that the beam pattern along the z direction is determined by the angle φ; in other words, the relative position difference between the probe source and the observation field point, and by the wave number k.

B. Ocean waveguide

Similarly, we can define a time-reversal focusing in a ocean waveguide using an image method.[20] Although the image method is only applicable to the waveguide with a homogeneous water column, the method well describes most shallow-water propagations. The ocean surface is assumed to be a perfect reflector, while the bottom is an interface which reduces the pressure amplitude by a reflection coefficient which can be determined by the geoacoustic properties of the bottom. As a consequence of multiple reflection from the surface and bottom boundaries, the field at the receiver is represented as the summation of contributions from image sources (Fig. 9). Each image source represents the image of a time-reversal array which spans the whole water column of the waveguide. The higher angle image has more interactions with the bottom and contributes less to the total field.

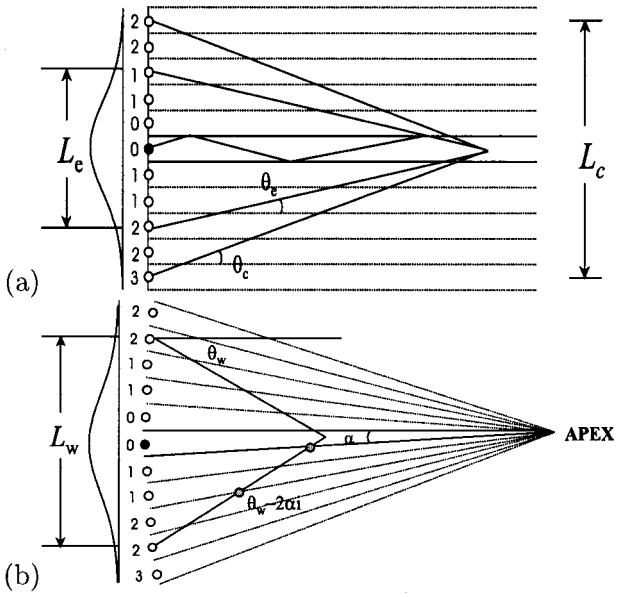

FIG. 9. Schematic of image arrays: (a) for a Pekeris waveguide and (b) for a sloping environment. The image aperture L_c is determined by the critical angle (θ_c) of the bottom. The effective aperture L_e is smaller due to attenuation in the ocean bottom which causes shading of the image sources. In a sloping environment, the grazing angle changes by 2α for each bounce with the bottom which results in a difference in the effective aperture L_w. The labels at the image sources indicate the number of interaction with the bottom.

If we label the images with the number of interactions they have with the bottom (Fig. 9), the distance l_i for each set of two images whose contributions make i interactions with bottom can be approximated as

$$l_i\approx r^2+(2Di)^2+2r(2Di)\sin\varphi. \tag{7}$$

This is same as Eq. (3) except z is replaced with $2Di$. Although the exact path length is important to describe one-way acoustic propagations, the exact locations of the array elements are not important for the calculation of the time-reversed field since the time-reversal process compensates for the phase delays caused by the path differences to each image.[6] The pressure field received by an image source from a point source located in a waveguide is

$$p_i=\frac{S(\theta_i)V(\theta_i)^{i\text{th}}}{l_i}\exp(jkl_i), \tag{8}$$

where $S(\theta_i)$ is the source amplitude, $V(\theta_i)$ is the reflection coefficient of the bottom, θ_i is the grazing angle of the image source which has i interactions with bottom, and k is the wave number. $V(\theta_i)^{i\text{th}}$ is the accumulated attenuation with i-time bottom interactions. The pressure field observed at a

field point after a time-reversal process with a probe signal $AV(\theta_i)^{i\text{th}}\exp(jkl_{0i})/l_{0i}$ can be represented as the summation of contributions from each image source as

$$p(l)=A\sum_{i=-\infty}^{\infty}\frac{|V(\theta_i)|^{2|i|}}{l_i l_{0i}}\exp jk(l_i-l_{0i}), \tag{9}$$

where l_i^0 is the distance from a probe source to the ith image source. Negative values in i mean the contribution from the image sources corresponding to negative θ. In the above equation we used $V(\theta_i)V(\theta_{0i})^{+}\approx|V(\theta_i)|^2$, where θ_{0i} is the grazing angle corresponding to the probe source and $[\,]^{+}$ is complex conjugation. Although $V(\theta_i)$ is normally a complex value, we assumed that the phase difference caused by the difference in grazing angles between θ_{0i} and θ_i is negligible and the phase changes caused by the bottom reflection are recovered by the two-way propagation of time-reversal processes.

Assume the array element spacing to be dense enough to be considered as a continuous array and the range from the array to the receiver to be much greater than the channel depth, $D\ll R$; then, the summation can be replaced by an integration[21]

$$p(l)\approx\frac{A}{2D}\int_{-\infty}^{\infty}\frac{|V(\theta)|^{|z|/D}}{ll_0}\exp jk(l-l_0)dz, \tag{10}$$

where z replaced the index i with $z=2Di$, θ_i and l_{0i} are changed to θ and l_0, respectively. The Fresnel approximation[19] for the path length in Eq. (10) becomes

$$p(r,\varphi)=A\frac{\exp jk(r-r_0)}{2Drr_0}\int_{-\infty}^{\infty}|V(\theta)|^{|z|/D}\times\exp\left[jk\frac{z^2}{2}\left(\frac{\cos^2\varphi}{r}-\frac{1}{r_0}\right)\right]\exp(jkz\sin\varphi)dz, \tag{11}$$

and the corresponding far-field beam-pattern expression is

$$D(\chi)=\int_{-\infty}^{\infty}|V(\theta)|^{|z|/D}\exp(j\chi z)dz, \tag{12}$$

where $\chi=k\sin\varphi$. Comparing Eq. (12) with the free-space beam pattern of Eq. (6), the factor from the bottom attenuation $|V(\theta)|^{|z|/D}$ serves as an aperture shading which eventually determines the effective aperture of the image array.

This image approach can be further extended to a range-dependent geometry, a wedge-shaped ocean. The slope of the bottom interface α is associated with the range to the apex R_a and the water depth D as $R_a\alpha\approx D$ (Fig. 9). A time-reversal mirror is located at the mouth of the wedge and a probe source at a range R. The probe signal propagates down slope to the array and the time-reversed signal is backpropagated up slope to the receiver. The main difference from the flat waveguide is that sound waves experience successive bottom reflections at incident angles 2α steeper (smaller) for up-slope (down-slope) propagation. Noting that the grazing angles for the first bounce and the last bounce are $\theta_i-\alpha$ and $\theta_i-(2i-1)\alpha$, respectively, the mean bottom reflection coefficient for the ith image source is $V(\theta_i-\alpha i)$. The accumulated attenuation of the ith image source during the two-way propagation is $V(\theta-\alpha i)^{2i}$. Using the relation of $2Di=z$, the corresponding far-field beam-pattern expression for a wedge ocean is

$$D(\chi)=\int_{-\infty}^{\infty}\left|V\left(\theta-\alpha\frac{|z|}{2D}\right)\right|^{|z|/D}\exp(j\chi z)dz, \tag{13}$$

where $\chi=k\sin\varphi$. Notice that the far-field beam pattern is modified by the waveguide geometry, which is realized through the change of the reflection coefficient.

IV. SPATIAL RESOLUTION OF AN ARRAY

A. Free space

In this section, we derive formulas describing the resolution of time-reversal arrays in free space. The transverse (Δ_z) resolution (breadth of focus) can be defined from the mainlobe width of the far-field beam pattern of Eq. (6). The solution of the beam-pattern function is

$$D(\varphi)=L\,\mathrm{sinc}\left(\frac{L\sin\varphi}{\lambda}\right), \tag{14}$$

where λ is the wavelength and L is the aperture. Following the conventional definition of the 3-dB beamwidth of the mainlobe ($\varphi_{3\text{ dB}}\approx0.886\lambda/L$), the transverse resolution is

$$\Delta_z=0.886\lambda\frac{R}{L}, \tag{15}$$

where $\sin\varphi$ is approximated as φ and R is the range from the array.

Although the transverse focal structure is symmetric along the R axis, the longitudinal structure is not symmetric due to the r dependence in the near-field beam pattern. One method to define the longitudinal resolution is to examine the maximum range ($r_{\max}$) and the minimum range ($r_{\min}$) along the R axis within which there is a good focus with phase difference from the focal center (R_0,0) less than $3\pi/4$. Since the maximum phase difference is caused by the end of the aperture ($\pm L/2$), the $r_{\max}$ and $r_{\min}$ can be defined from Eq. (5) as

$$r_{\max}\approx R_0\left(1+\frac{3\lambda}{L^2}R_0\right), \tag{16}$$

$$r_{\min}\approx R_0\left(1-\frac{3\lambda}{L^2}R_0\right). \tag{17}$$

Then, the longitudinal resolution ($\Delta_r=r_{\max}-r_{\min}$) expression becomes

$$\Delta_r=6\lambda\left(\frac{R}{L}\right)^2. \tag{18}$$

The ranges of $r_{\max}$ and $r_{\min}$ roughly correspond to 3-dB down points in amplitude from the focal center. Although the proportionality constants needed in the above equations depend on the specific resolution criteria, for a given range (R) and wavelength (λ) the focal sizes in free space are directly proportional to the physical extent of the aperture (L) and the

square of the aperture (L^2) for the transverse and longitudinal directions, respectively.

B. Ocean waveguide

The resolution expression derived for free space can be used to define the resolution in an ocean waveguide. In the ocean, the effective aperture increases due to the multipath propagation caused by boundary reflections. Hence, the resolution increases over a free-space environment. The effective aperture is limited by the waveguide nature of acoustic propagation and attenuation in the bottom. For a lossless Pekeris waveguide of depth D, there exists a critical angle of reflection given by $\theta_c = \cos^{-1}(c_w/c_b)$ where c_w and c_b are the sound speeds in the water column and in the bottom, respectively. Sound propagating within the critical angle suffers no bottom loss and hence propagates to long distances. The length of the image array can be roughly written as

$$L_c \approx 2R \tan\theta_c, \tag{19}$$

and the corresponding resolution expressions are

$$\Delta_z \sim \frac{\lambda}{2\tan\theta_c}, \tag{20}$$

$$\Delta_r \sim \frac{\lambda}{(2\tan\theta_c)^2}. \tag{21}$$

For a lossy waveguide, we can use the far-field beam-pattern expression of Eq. (12) to derive resolution formulas. Although the integration in Eq. (12) can be evaluated numerically with any arbitrary reflection coefficient function $V(\theta)$, here we use a simple functional approximation of $V(\theta) \approx \exp(-\gamma\theta)$ to analytically solve the beam-pattern equation.[21] Although a more complicated functional form would give a more accurate $V(\theta)$, $\exp(-\gamma\theta)$ is a good approximation for low grazing angle incidences and leads to closed-form expressions for resolution which are sufficient for the purpose of this paper for giving physical insight into how waveguide attenuation affects resolution or focal sizes associated with waveguide geometry. γ is an attenuation factor which can be determined by least-squares curve fitting for the known reflection coefficient curves with angles which would be obtained either from a geoacoustic model[20] or measured data.

With $V(\theta) \approx \exp(-\gamma\theta)$, the solution of the far-field beam pattern of Eq. (12) is (see the Appendix for details)

$$D(z) \sim \exp\left(-\frac{\gamma R}{4D}k^2 z^2\right). \tag{22}$$

The depth resolution for the 3-dB beamwidth can be defined as

$$\Delta_z = 0.374\lambda \sqrt{\frac{\gamma R}{D}}. \tag{23}$$

Using Eqs. (15) and (23), the corresponding linear, uniform array having the same 3-dB depth resolution would have an effective aperture

$$L_e = 2.368 \sqrt{\frac{DR}{\gamma}}. \tag{24}$$

From Eqs. (18) and (24), the range resolution in a lossy Pekeris waveguide would be

$$\Delta_r = 1.07\lambda \frac{\gamma R}{D}. \tag{25}$$

In a lossy waveguide, the resolution is a function of water depth D, medium attenuation γ, and range R. With the approximation of $V(\theta) \approx \exp(-\gamma\theta)$, the depth resolution ($\Delta_z$) is found to be proportional to the square root of the attenuation factor γ and the range R, and the inverse square root of the waveguide depth D, while the range resolution (Δ_r) is proportional to the attenuation and the range and inversely proportional to the waveguide depth.

Using a similar approximation for the reflection coefficient in a wedge ocean, the far-field beam pattern of Eq. (13) becomes (see the Appendix for details)

$$D(z) \sim \exp\left[-\frac{\gamma R}{4D}\left(1 - \frac{R}{2R_a}\right)k^2 z^2\right]. \tag{26}$$

The corresponding depth and range resolution expressions are

$$\Delta_z = 0.374\lambda \sqrt{\frac{\gamma R}{D}\left(1 - \frac{R}{2R_a}\right)}, \tag{27}$$

$$\Delta_r = 1.07\lambda \frac{\gamma R}{D}\left(1 - \frac{R}{2R_a}\right). \tag{28}$$

A uniform array having the same 3-dB focal width would have an effective aperture

$$L_e = 2.368 \sqrt{\frac{DR}{\gamma(1 - R/2R_a)}}. \tag{29}$$

In a wedge ocean, an additional factor R_a is included for determining the image aperture which represents the geometry of the wedge ocean with depth D. This geometric factor results from the fact that each bounce of sound propagating from a probe source to a time-reversal array reduces the reflection angle by 2α. It is apparent from Fig. 9 that for an image interacting with the bottom in two-way transmission, the accumulated attenuation is smaller in a wedge ocean than in a flat ocean of constant depth D, which results in a larger image aperture in a wedge geometry. From the perspective of adiabatic modal propagation,[20] modes are compressed with up-slope propagation, which results in higher resolution for the time-reversal process in sloping environments.

C. Numerical example

Here, we present a numerical example of resolution calculation illustrating the depth and range resolution changes with range in a Pekeris waveguide and in a wedge ocean. In order to validate the accuracy of the results, we compare them with the focal sizes obtained with a parabolic equation full wave model.[22] The model ocean consists of the pressure release surface, 100-m water column, and infinite bottom half space. The sound speeds are 1500 and 1600 m/s for the water and bottom, respectively, and the corresponding densities are 1.0 and 1.8 g/cm^3. The bottom attenuation is 0.7

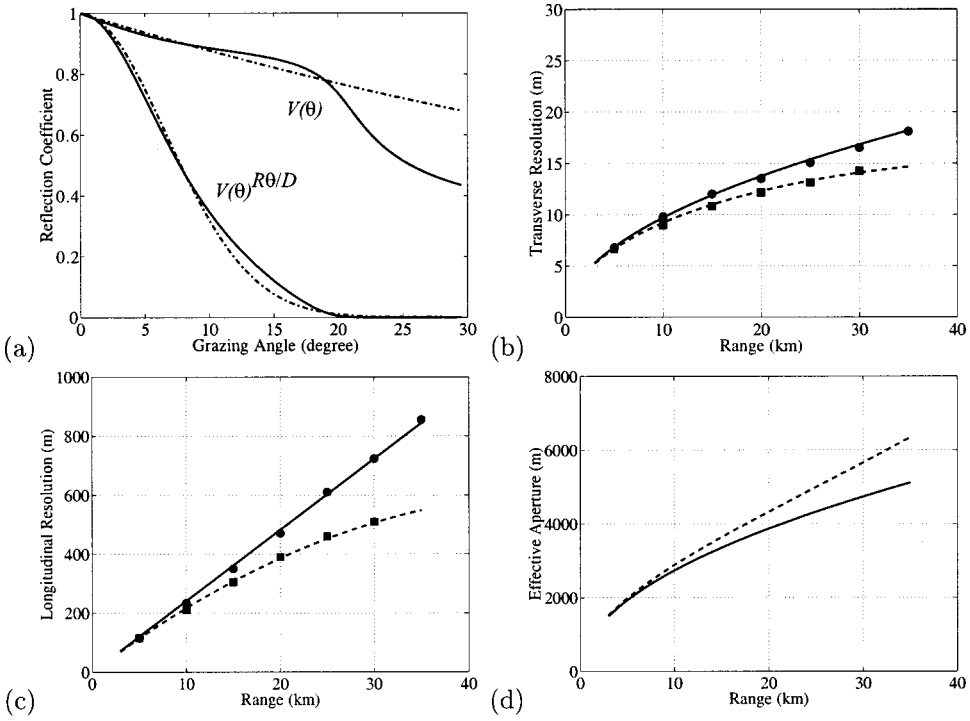

FIG. 10. An example of resolution calculation in a Pekeris waveguide and in a wedge ocean. The waveguide geometries are with $D=100$ m, $R_a=50$ km. The sound speeds are 1500 m/s and 1600 for water and bottom, respectively, and the corresponding densities are 1.0 and 1.8 g/cm^3. The bottom attenuation is 0.7 dB/λ. (a) The calculated reflection coefficient $V(\theta)$ and the accumulated attenuation $V(\theta)^{R\theta/D}$ at 10-km range (solid line) and the approximation with $\exp(-\gamma\theta)$ (dot-dashed lines). (b) The depth resolution in a Pekeris waveguide (solid line) and in a wedge ocean (dashed line). The solid circles and squares are from simulation results with a parabolic equation model. (c) The range resolution. (d) The calculated effective apertures (L_e).

dB/λ. In a wedge ocean the water depth decreases from 100 to 0 m in a distance of 50 km having slope of 0.114°.

The resolution calculations are at 500-Hz and the corresponding wavelength is 3 m in the water column. Since the bottom is homogeneous, the reflection coefficient is independent of frequency. The solid line in Fig. 10(a) shows the reflection coefficient curve as a function of angle calculated with the geoacoustic properties. The dot-dashed line represents the approximation with $\exp(-\gamma\theta)$ where $\gamma=0.75$. Although there are some discrepancies between those two curves in $V(\theta)$ after the critical angle (20.4°), the difference turns out to be very small in the accumulated attenuation of $V(\theta)^{R\theta/D}$ due to the multiple interactions for the higher angle images. The overall effect on the pressure field from the difference would be negligible.

As shown in Figs. 10(b) and (c), the depth and range focal sizes increase with range due to the bottom attenuation. As expected, the focal sizes are smaller in the wedge ocean (dashed lines) than those in the flat ocean (solid lines) due to the geometric effect under the same geoacoustic conditions. The simulation results with a parabolic equation model[22] (the solid circles and squares for the flat ocean and the wedge ocean, respectively) match well with the resolution curves obtained with the Eqs. (23), (25), (27), and (28), verifying the resolution equations derived in this paper for flat oceans as well as wedge oceans. The effective apertures (L_e) in Fig. 2(d) show that the aperture of the image array becomes much bigger than the physical extent of the array (100 m), resulting in finer resolution in a waveguide over the resolution in free space.

V. COMPARISON WITH MEASURED DATA

Here, we compare the resolution formulas with measured data. The main purpose is to describe the measured focal sizes along with their waveguide conditions: water depth, range, and attenuation which are parametrized in the resolution formulation. The foci were realized with probe source depths at 60–80 m. For these depths, the focal structures of the high-frequency (3500-Hz) signals were stable for tens of minutes. The focal structures of the low-frequency (445-Hz) signals were stable for longer periods of time (several hours).[3,4] Since the data collected for this comparison were from cases where the received probe-source pulse was retransmitted within a few minutes, we can assume that the foci were realized under relatively static ocean conditions. The resolution is defined as the focal size at the 3-dB down points from the peak signal level.

Figure 11(a) shows the comparison at 445-Hz in the Formiche area. The resolution curve is calculated with $\gamma=1.55$ and $D=110$ m. The attenuation factor γ is obtained by approximating the reflection coefficient as $V(\theta)\approx\exp(-\gamma\theta)$ which is calculated from the two-layer geoacoustic model for this area in Fig. 2(a). Since the effective modes contributing to the focal field are trapped below the thermocline, the effective waveguide depth[23] D is determined by removing the upper mixed layer (15 m) from the total water depth. The calculated resolution curve based on known geoacoustic parameters approximates closely the measured focal sizes. A numerical simulation[4] using a normal-mode method also showed similar focal sizes for these 445-Hz data.

Figure 11(b) is at 3500-Hz in three different environments: the Formiche, flat Elba, and sloping Elba areas. The measured focal sizes are easily differentiated into three groups, with the largest focal size in the Formiche area and the smallest in the sloping Elba area for a given range. The calculated resolution curves match the measured data well with $\gamma=16$ and $D=115$ m for the Formiche area, with $\gamma=5$ and $D=90$ m for the flat Elba area, and with $\gamma=1.6$ and $D=90$ m for the sloping Elba area. The main difference in

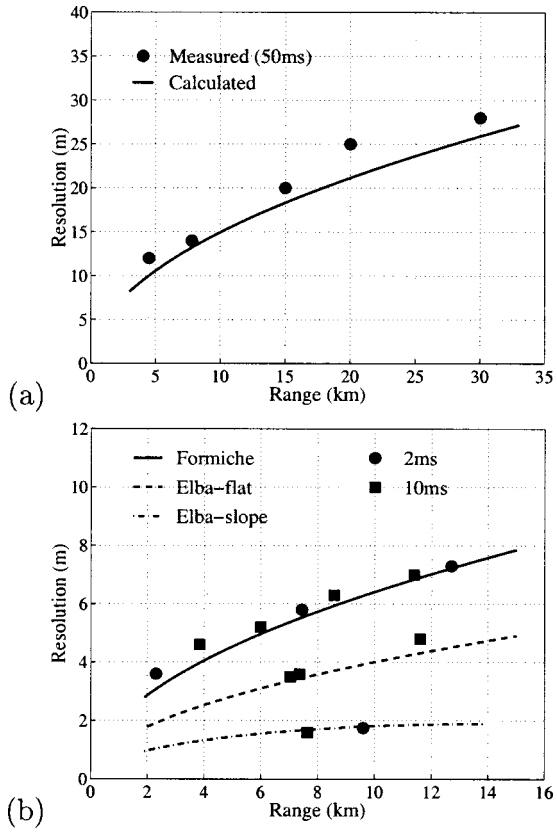

FIG. 11. Comparison between the measured vertical focal sizes and the calculated resolution based on the image aperture method with appropriate bottom attenuation: (a) for 445 Hz in the Formiche area with $\gamma=1.55$ and (b) for 3500 Hz in three different environments with $\gamma=16$, 5, 1.6 for the Formiche, flat Elba, and sloping Elba area, respectively.

effective depth between the Formiche area (115 m) and the Elba area (90 m) is due to the differences in the thermocline depth and the total water depth. The larger γ in the Formiche area indicates higher attenuation for waveguide propagation and larger focal sizes. The focal size is smaller in the sloping Elba area than that in the flat Elba area for the same γ due to the geometric effect in a sloping environment, but an additional adjustment of γ from 5 to 1.6 was needed to explain the measured data in the sloping area.

The attenuation factors ($\gamma=16$ for the Formiche area and $\gamma=5$ for the flat Elba area) used for the resolution calculation in Fig. 11(b) are larger than the values ($\gamma=7$ and $\gamma=1.5$, respectively) obtained from the geoacoustic models in Fig. 2. There can be several reasons for this mismatch. One of them is measurement error caused by range mismatch between the PS and the VRA. From the calculation with Eq. (25), the longitudinal focal sizes were about 300 and 100 m at 5-km range for the Formiche and Elba areas, respectively. During the experiment the PS was located within 50 m from the VRA in the Formiche area and 20 m in the Elba area. Although the focal size was affected by this range mismatch, the VRA was inside the focal zone. The other possible factor is the uncertainty in geoacoustic parameters. Since these geoacoustic models are based on low-frequency (<800 Hz) experiments,[14,16] high-frequency sound propagation appears to experience different loss mechanisms. The frequency-dependent attenuation in layered sediment or additional loss from rough boundary scattering[24] can be important in high-frequency propagation. Transmission loss measurements performed during the experiment also showed higher attenuation for 3500-Hz sound than attenuation values based on lower-frequency experiments in the area.

VI. SUMMARY

Acoustic foci realized with vertical time-reversal arrays in various shallow-water environments were presented and analyzed using an image aperture method. For a given frequency and range, the resolution is determined by waveguide attenuation and water depth in the ocean waveguide while the resolution is determined by the physical extent of the array in free space. With the approximation of $V(\theta)\approx\exp(-\gamma\theta)$ for the bottom reflection coefficient, the vertical focal size is found to be proportional to the square root of attenuation and inversely proportional to the square root of waveguide depth, while the horizontal focal size is found to be proportional to the attenuation and range and inversely proportional to the waveguide depth. In a sloping ocean, an additional geometric effect results in higher resolution for up-slope focusing.

ACKNOWLEDGMENTS

This research was supported by the Office of Naval Research, Contract No. N00014-94-1-0458.

APPENDIX: SOLUTIONS OF THE FAR-FIELD BEAM-PATTERN EQUATIONS

The accumulated attenuation for the two-way propagation between the probe source and ith image source are $V(\theta)^{2i}$ and $V(\theta-\alpha i)^{2i}$ for a flat ocean and a wedge ocean, respectively. Using the approximation $V(\theta)\approx\exp(-\gamma\theta)$ with relations of $2Di=z$, $R\theta\approx z$, and $R_a\alpha\approx D$, the attenuation expressions become $\exp(-\gamma z^2/RD)$ for a flat ocean and $\exp(-\gamma z^2(1-R/2R_a)/RD)$ for a wedge ocean. Then, Eqs. (12) and (13) can be written as

$$D(\chi)=\int_{-\infty}^{\infty}\exp(-az^2)\exp(j\chi z)dz$$

$$=\frac{1}{\sqrt{2a}}\exp\left(-\frac{\chi^2}{4a}\right), \tag{A1}$$

where $a=\gamma/DR$ for a flat ocean and $a=\gamma(1-R/2R_a)/DR$ for a wedge ocean, respectively, and $\chi=k\sin\varphi$. Noticing that $\varphi\approx Rz$, Eq. (A1) becomes

$$D(z)=\sqrt{\frac{DR}{2\gamma}}\exp\left(-\frac{\gamma R}{4D}k^2z^2\right), \tag{A2}$$

and

$$D(z)=\sqrt{\frac{DR}{2\gamma(1-R/2R_a)}}\exp\left[-\frac{\gamma R}{4D}\left(1-\frac{R}{2R_a}\right)k^2z^2\right] \tag{A3}$$

for a flat ocean and a wedge ocean, respectively.

[1] M. Fink, ''Time reversal mirrors,'' in *Acoustical Imaging*, edited by B. F. Jones (Plenum, New York, 1995), Vol. 25, pp. 1–15.
[2] M. Fink, ''Time reversed acoustics,'' Phys. Today **50**, 34–40 (1997).
[3] W. A. Kuperman, W. S. Hodgkiss, H. C. Song, T. Akal, C. Ferla, and D. Jackson, ''Phase conjugation in the ocean: Experimental demonstration of an acoustic time-reversal mirror,'' J. Acoust. Soc. Am. **102**, 25–40 (1998).
[4] W. S. Hodgkiss, H. C. Song, W. A. Kuperman, T. Akal, C. Ferla, and D. R. Jackson, ''A long-range and variable focus phase conjugation experiment in shallow water,'' J. Acoust. Soc. Am. **105**, 1597–1604 (1999).
[5] T. Akal, G. Edelmann, S. Kim, W. S. Hodgkiss, W. A. Kuperman, and H. C. Song, ''Low and high frequency ocean acoustic phase conjugation experiments,'' Proceedings of the Sixth European Conference of Underwater Acoustics, pp. 493–498 (2000).
[6] D. R. Jackson and D. R. Dowling, ''Phase conjugation in underwater acoustics,'' J. Acoust. Soc. Am. **89**, 171–181 (1991).
[7] M. Born and E. Wolf, *Principles of Optics: Electromagnetic Theory of Propagation, Interference and Diffraction of Light* (Pergamon, New York, 1964), pp. 435–449.
[8] A. B. Baggeroer, W. A. Kuperman, and H. Schmidt, ''Matched field processing: Source localization in correlated noise as an optimum parameter estimation problem,'' J. Acoust. Soc. Am. **83**, 571–587 (1988).
[9] P. Roux and M. Fink, ''Time reversal in a waveguide: Study of the temporal and spatial focusing,'' J. Acoust. Soc. Am. **107**, 2418–2429 (2000).
[10] D. R. Dowling and D. R. Jackson, ''Narrow-band performance of phase-conjugate arrays in dynamic random media,'' J. Acoust. Soc. Am. **91**, 3257–3277 (1992).
[11] M. Dungan and D. R. Dowling, ''Computed narrow-band time-reversing array retrofocusing in a dynamic shallow ocean,'' J. Acoust. Soc. Am. **107**, 3101–3112 (2000).
[12] T. Akal, ''Bathymetry and bottom structure of zones near the island of Elba used for acoustical trials in shallow water,'' Technical Report, TM-162, SACLANT Undersea Research Centre, La Spezia, Italy, 1970.
[13] T. Akal, C. Gehin, B. Matteucci, and B. Tonarelli, ''Measured and computed physical properties of sediment cores, island of Elba zone,'' Technical report, M-82, SACLANT Undersea Research Centre, La Spezia, Italy, 1972.
[14] J.-P. Hermand and P. Gerstoft, ''Inversion of broad-band multitone acoustic data from the yellow shark summer experiments,'' IEEE J. Ocean. Eng. **21**, 324–346 (1996).
[15] D. F. Gingras and P. Gerstoft, ''Inversion for geometric and geoacoustic parameters in shallow water: Experimental results,'' J. Acoust. Soc. Am. **97**, 3589–3598 (1995).
[16] F. B. Jensen, ''Comparison of transmission loss data for different shallow water area with theoretical results provided by a three-fluid normal-mode propagation model,'' in *Sound Propagation in Shallow Water*, edited by O. F. Hastrup and O. V. Olesen (CP-14, SACLANT ASW Research Centre, La Spezia Italy, 1974), pp. 79–92.
[17] R. N. Bracewell, *The Fourier Transform and its Applications* (McGraw-Hill, New York, 1978), pp. 267–272.
[18] H. C. Song, P. R. Roux, and W. A. Kuperman, ''Focal translation by frequency shift in free space,'' IEEE Trans. Ultrason. Ferroelectr. Freq. Control **47**, 687–695 (1999).
[19] L. J. Ziomek, ''Three necessary conditions for the validity of the Fresnel phase approximation for the near-field beam pattern of an aperture,'' IEEE J. Ocean Eng. **18**, 73–75 (1993).
[20] F. B. Jensen, W. A. Kuperman, M. B. Porter, and H. Schmidt, *Computational Ocean Acoustics* (American Institute of Physics, New York, 1994).
[21] L. E. Kinsler, A. R. Frey, A. B. Coppens, and J. V. Sanders, *Fundamentals of Acoustics* (Wiley, New York, 1982), pp. 427–430.
[22] M. D. Collins, ''Generalization of the split-step pade solution,'' J. Acoust. Soc. Am. **96**, 382–385 (1994).
[23] F. B. Jensen and W. A. Kuperman, ''Optimum frequency of propagation in shallow water environments,'' J. Acoust. Soc. Am. **73**, 1979–1984 (1983).
[24] W. A. Kuperman and F. Ingenito, ''Attenuation of the coherent component of sound propagating in shallow water with rough boundaries,'' J. Acoust. Soc. Am. **61**, 1178–1187 (1977).

Pressure dependence of the elasticity of a steel sphere measured by the cavity resonance method

Ichiro Ohno
Department of Earth Sciences, Ehime University, Matsuyama 790-8577, Japan

Masaki Kimura
Department of Materials Science and Engineering, Ehime University, Matsuyama 790-8577, Japan

Yoichi Hanayama
Department of Mechanical Engineering, Ehime University, Matsuyama 790-8577, Japan

Hitoshi Oda and Isao Suzuki
Department of Earth Sciences, Okayama University, Okayama 700-8530, Japan

(Received 19 December 2000; revised 24 May 2001; accepted 29 May 2001)

The pressure derivatives of elastic moduli of a steel sphere were measured by the cavity resonance method, a modified resonant sphere technique under gas pressure using a spherical three-layered structure (3LS) consisting of a sample-thin gas layer–cavity container system. The pressure-induced shifts of resonance peaks of both toroidal and spheroidal modes were observed up to 100 MPa (1 kbar) under gas pressure with helium gas. The resultant pressure derivatives of frequencies of toroidal modes yielded a pressure derivative of shear modulus of $\partial G/\partial P = 2.01 \pm 0.08$. The pressure derivative of the bulk modulus was determined from the data of spheroidal modes, $\partial K/\partial P = 5.0 \pm 0.4$, by analyzing these data as free oscillations of the 3LS superimposed on the static compression. The results demonstrate the efficiency of the cavity resonance method for measuring pressure derivatives of elastic moduli of solids. © *2001 Acoustical Society of America.*
[DOI: 10.1121/1.1387085]

PACS numbers: 43.35.Cg, 43.35.Yb [SGK]

I. INTRODUCTION

The rectangular parallelepiped resonance (RPR) method that uses a rectangular parallelepiped specimen to measure elastic and anelastic properties of isotropic and anisotropic solids has been developed based on the work of Demarest (1971) and Ohno (1976). The resonant sphere technique (RST), a resonance method using a spherical specimen, was originated by Fraser and LeCraw (1964) and Soga and Anderson (1967). RST has been extended to anisotropic materials through the contributions of Mochizuki (1988), Visscher *et al.* (1991), Suzuki *et al.* (1992), and Oda *et al.* (1994). Oda *et al.* (1993) gave the analytical expressions of partial derivatives of eigenfrequencies with respect to elastic constants for both RPR and RST, which are very important in the inversion procedure from eigenfrequencies to elastic constants. Reviews of the resonance method have been published by Maynard (1996), Leisure and Willis (1997), and Migliori and Sarrao (1997); in these reviews, the method is called resonant ultrasound spectroscopy (RUS).

In the resonance methods, eigenfrequencies of a sample shaped into a cube, rectangular parallelepiped, or sphere are measured, and elastic constants are determined by the inversion of the frequency data. Since frequencies of a redundant number of modes can be acquired at a time, the complete set of elastic constants can be determined without repeating further measurements. This point constitutes a major advantage of the resonance method, especially when we want to measure anisotropic materials while changing temperature or other physical conditions. The resonance method has therefore been applied to measure temperature variations in the elasticity of various materials across a wide range of temperature (e.g., Isaak *et al.*, 1998a; Suzuki *et al.*, 2000).

Attempts have been made to apply the resonance method under a high-pressure condition in order to measure the pressure dependency of elastic constants. For this purpose Ohno *et al.* (1994) proposed the ''cavity resonance'' method (see Sec. II) and demonstrated a pressure-induced shift of resonance peaks of a steel sphere under gas pressure, and gave preliminary results on the pressure derivatives of shear and bulk moduli. Isaak *et al.* (1998b) measured silica glass spheres under gas pressure, and determined the pressure derivative of the shear modulus. Ohno *et al.* (2000) demonstrated on a silica glass sphere that the cavity resonance method yields pressure derivatives of shear and bulk moduli that are in good agreement compared with those derived previously. In this paper we show the results of measurement and analysis of a steel sphere using the cavity resonance method.

II. METHODS

In the present study we apply the cavity resonance method to a spherical sample of steel. There exist two types of normal modes, toroidal (torsional) and spheroidal, in the oscillation of an isotropic sphere. The notations ${}_nT_l$ and ${}_nS_l$ are used to denote the toroidal and spheroidal modes of angular order l and radial order n, respectively. The toroidal mode has only displacement tangential to the surface, and thus does not couple with the surrounding gas when the vis-

 0001-4966/2001/110(2)/830/7/$18.00

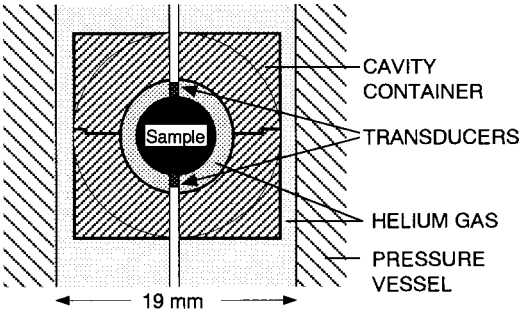

FIG. 1. Schematic drawing of the sample–cavity container assembly for the cavity resonance method under gas pressure. The sample is placed at the center of the spherical cavity. The spheroidal modes of the sample are analyzed as the free vibration of the three-layered structure (3LS) of the sample-thin gas layer–cavity container. The cavity container has a cylindrical outer shape shown by thick lines. The large circle shown by thin line indicates the imaginary spherical outer shape assumed in the theoretical calculation.

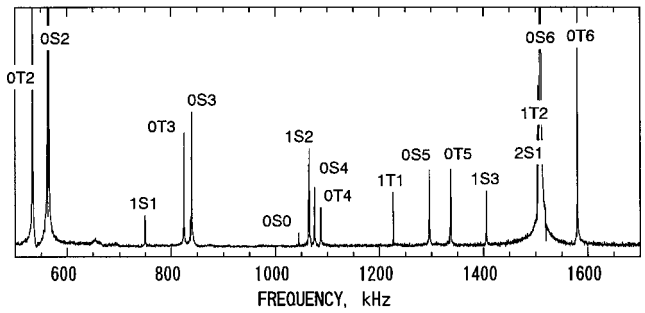

FIG. 2. Spectrum of the steel-sphere sample obtained at the atmospheric pressure.

cosity of gas is ignored. We can therefore obtain the pressure derivative of the shear modulus by simply measuring the pressure derivative of the frequency of a toroidal mode. This is the reason we adopt a spherical sample of isotropic material in this study.

On the other hand, the spheroidal mode has a displacement component perpendicular to the surface, and couples with the surrounding gas. Accordingly, to accomplish the data reduction of spheroidal modes, we must analyze the coupled sample–gas system. For such analysis we need to specify suitable boundary conditions of the system. To realize this we use the ''cavity container'' shown in Fig. 1.

Figure 1 shows a schematic of the assembly of the sample, cavity container, and transducers used to measure eigenfrequencies under gas pressure. At the center of the cavity container is a spherical cavity in which the sample is located with spacers of suitable thickness. The cavity is open to the outside of the container and filled with helium gas as a pressure medium. We analyze the measured spheroidal modes as the free oscillation of a spherical three-layered structure consisting of the sample, the gas layer, and the cavity container, evaluating the effect of hydrostatic compression beforehand. We call this method the cavity resonance method.

III. EXPERIMENTAL PROCEDURE AND RESULTS

A steel sphere (ball bearing) with radius of 2.384 mm and density of 7.798 g/cm^3 was used as a sample. Figure 2 shows a spectrum obtained at atmospheric pressure. The shear and bulk moduli were determined to be $G_0=79.5$ GPa and $K_0=165$ GPa, respectively, from frequencies of the lower 14 modes.

The assembly mentioned above was placed in the pressure vessel of the high-pressure gas apparatus. The high-pressure vessel was 19 mm in diameter and 200 mm in height. Details of the gas apparatus are described in Kimura *et al.* (1987). The outer shape was cylindrical, with a diameter of 17 mm and a height of 19 mm. In the theoretical calculation, the outer shape was assumed to be spherical with a diameter of 17 mm, as indicated by a large circle in Fig. 1. The cavity container was made of tungsten carbide alloy, and divided into two parts for placement of the sample, as shown by horizontal lines in Fig. 1.

A pair of lead zirconate–titanate transducers of shear type was used in this study. The transducers were placed in contact with the sample by the weight of the jig holding the top transducer. Continuous sinusoidal voltage was input to one of the transducers. The output amplitude was measured while scanning the frequency of the input voltage (cw method). Measurements were made at several points up to 100 MPa (1 kbar). Each measurement at a pressure was begun 20 min after the pressure was increased or decreased to avoid the influence of adiabatic compression or expansion of helium gas. Pressure was measured with a Bourdon's tube.

We monitored the temperature at the outer surface of the pressure vessel. During the 2-day measurement period the room temperature fluctuated within a few degrees, and it was necessary to correct this effect in order to obtain an accurate pressure dependence of the frequencies. For this purpose we also measured the temperature dependence of the frequency of the measured modes at atmospheric pressure, independently of the measurement under pressure. An example of the temperature correction is shown in Fig. 4(a).

Three toroidal modes, ${}_0T_4$, ${}_1T_1$, and ${}_0T_5$ and two spheroidal modes, ${}_1S_2$ and ${}_1S_3$, were detected under gas pressure up to 100 MPa. Figure 3 shows some examples of spectra recorded at various pressures. We can see in this figure that the resonance peaks shift to higher frequency as the pressure increases. The frequencies of four modes are plotted as a function of pressure in Fig. 4. The multiple peaks and lines in Figs. 3 and 4 occur due to the splitting of the degenerate modes. The pressure gradients of the frequencies were determined by least-squares fitting, and are listed in Tables I and II.

IV. DATA REDUCTION

The frequency of toroidal modes of a homogeneous sphere is expressed as follows (Sato and Usami, 1962):

$$f=\eta V_s/(2\pi a), \tag{1}$$

where f is the modal frequency, V_s is the shear wave velocity, a is the radius, and η is the numerical factor or dimensionless frequency, which depends only on the radial and angular orders n and l, as ${}_n\eta_l$. Since the toroidal mode does not

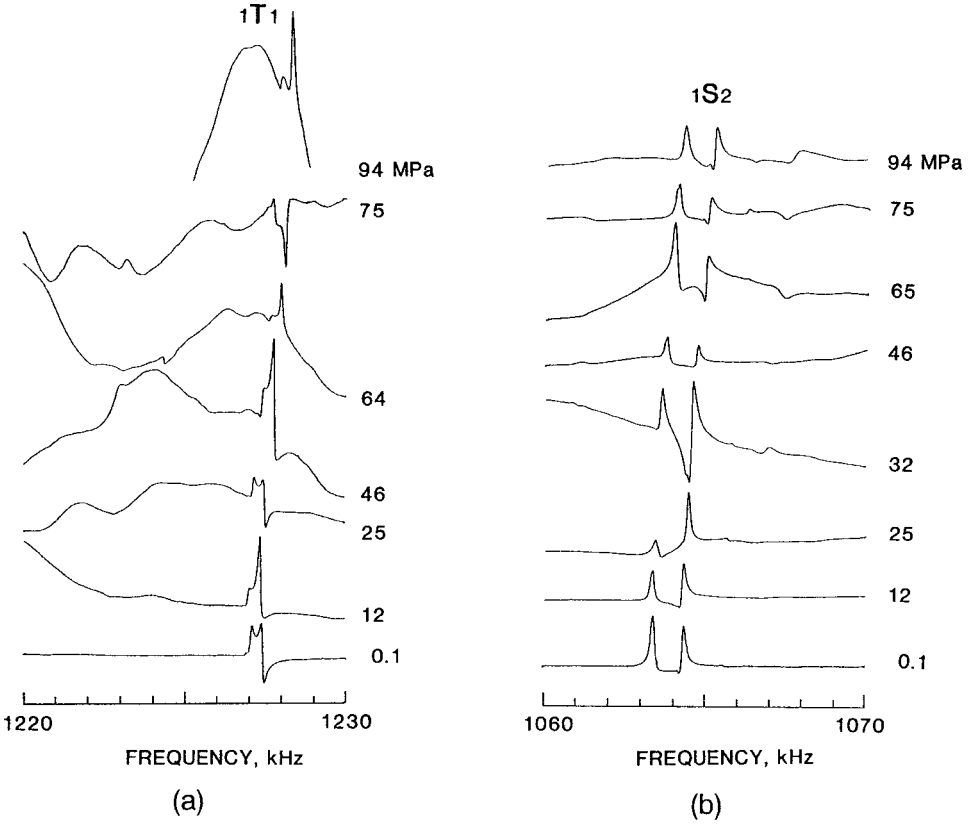

FIG. 3. Spectra obtained at various pressures and showing the pressure-induced shift of the peaks of (a) $_1T_1$ and (b) $_1S_2$ modes. The multiple peaks are caused by the splitting of the degenerate mode.

couple with the surrounding gas, differentiating (1) with respect to pressure P, we have

$$\frac{1}{f}\frac{\partial f}{\partial P}=\frac{1}{2}\left(\frac{1}{G}\frac{\partial G}{\partial P}-\frac{1}{3K}\right), \tag{2}$$

where G and K are the shear modulus and bulk modulus, respectively. Using Eq. (2) along with the values of K and G determined at 1 atm, we have the pressure derivative of the shear modulus at zero pressure, $\partial G/\partial P=G_0'$. The results are listed in Table I. The data of five peaks of three modes give $G_0'=2.01$ with one σ of 0.08.

In the above discussion we neglected the effect of the viscosity of helium gas upon toroidal mode frequencies. Sorbello *et al.* (2000) theoretically evaluated the gas-loading effect for isotropic spheres. When f_0 is the frequency of a toroidal mode without gas loading and $f=f_0+\Delta f$ is that of such a mode with gas loading, the order of magnitude of the difference Δf is given by $\Delta f/f_0\approx(\rho_g\eta_g f_0/\rho G)^{1/2}$. Here, ρ_g and η_g are the density and viscosity coefficient of the gas, and ρ and G are the density and shear modulus of the solid sample, respectively. The viscosity η_g of helium gas at 1 atm and 80 MPa is 1.860×10^{-5} and 2.073×10^{-5} Pa·s, respectively (Vargaftik, 1983), and is $\rho_g\approx0.1$ g/cm^3 at 100 MPa. Then, the frequency difference becomes $\Delta f\approx6$ Hz for $f_0\approx2$ MHz. This is negligible compared with the experimental error, and the gas-loading effect on toroidal modes can be ignored.

If the spheroidal mode does not couple with the surrounding gas, or the coupling is so small as to be negligible, we have

$$\frac{1}{f}\frac{\partial f}{\partial P}=\frac{1}{2}\left(\frac{1}{G}\frac{\partial G}{\partial P}-\frac{1}{3K}\right)+\frac{1}{\eta}\frac{\partial \eta}{\partial \nu}\frac{\partial \nu}{\partial P}, \tag{3}$$

where ν is Poisson's ratio. In the case of spheroidal modes, η depends not only on the orders of n and l but also on Poisson's ratio. For the isotropic elastic body $K=(2(1+\nu)/3(1-2\nu))G$, we have

$$\frac{\partial K}{\partial P}=\frac{2(1+\nu)}{3(1-2\nu)}\frac{\partial G}{\partial P}+\frac{2G}{(1-2\nu)^2}\frac{\partial \nu}{\partial P}. \tag{4}$$

From Eqs. (3) and (4), together with the measured $\partial f/\partial P$ and $G_0'=2.01$ from Table I, we have $\partial K/\partial P=K_0'$. The values of K_0' obtained in this manner are listed in column HS in Table II.

The spheroidal mode, however, has a displacement component perpendicular to the spherical surface and does couple with the surrounding fluid, more or less. In this study we treat the problem by solving the normal modes of the hydrostatically compressed spherical three-layered structure (3LS) of the sample–gas–cavity container. The calculation was made using the subroutine package developed by Saito (1988) for the earth's free oscillation. This means that the problem is regarded as a problem of the free oscillation of the 3LS superimposed on the static compression. Although the cavity container is cylindrical in its external shape, we regarded it as spherical for the first approximation, as shown in Fig. 1.

In order to determine the static compression of 3LS, we must first obtain the elastic properties of the helium gas, the cavity container, and the sample under high pressure. For helium gas we used the data of Kimura *et al.* (1995). For the

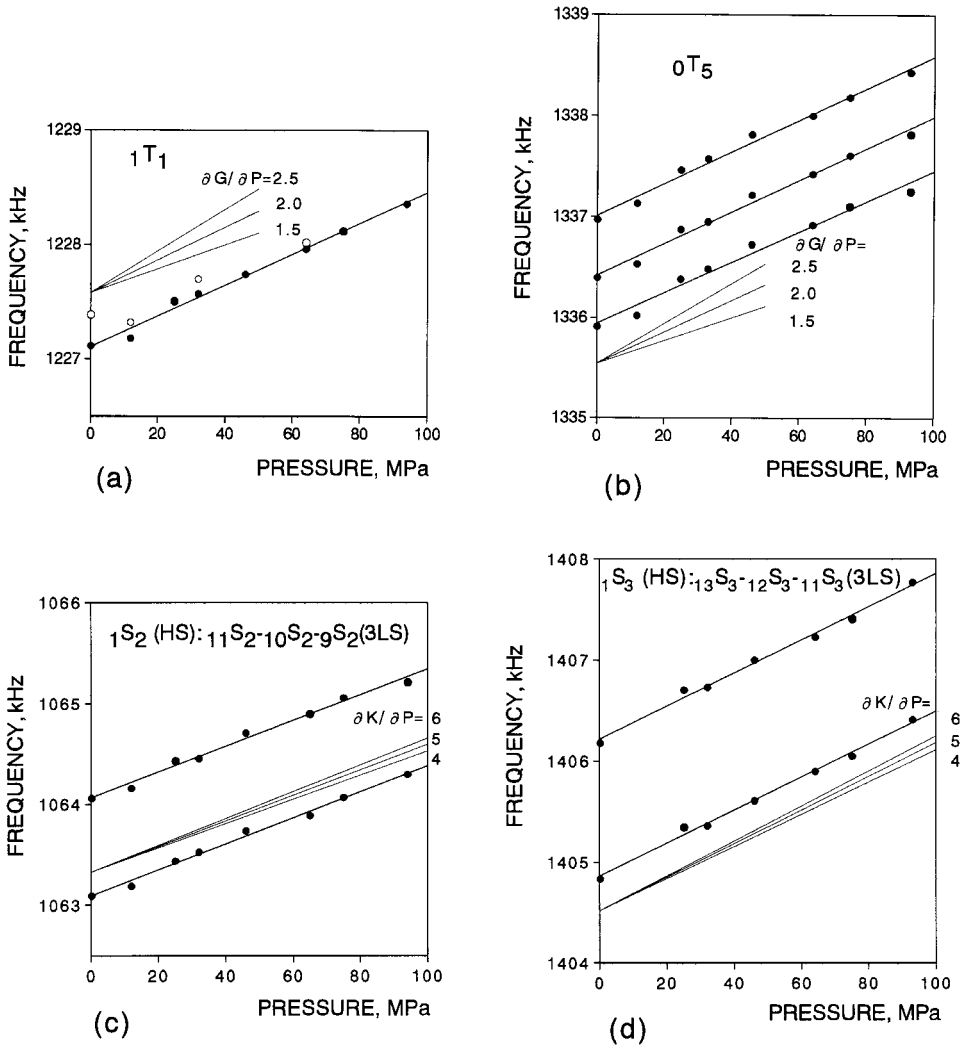

FIG. 4. Plots of the observed frequencies as a function of pressure on (a) $_1T_1$; (b) $_0T_5$; (c) $_1S_2$; and (d) $_1S_3$. Open circles in (a) denote the uncorrected data for temperature change, and solid circles denote the corrected frequencies. Theoretical slopes are also shown for comparison for the indicated values of $\partial G/\partial P$ or $\partial K/\partial P$, the pressure derivatives of the shear modulus and bulk modulus, respectively. Notation such as $_1S_2$(HS): $_{11}S_2-_{10}S_2-_9S_2$ (3LS) in (c) and (d) means that the $_1S_2$ mode in the homogeneous structure (HS) corresponds to $_{11}S_2$, $_{10}S_2$, and $_9S_2$ in the three-layered structure (3LS).

cavity container made of tungsten carbide alloy, we used the data of Hanayama *et al.* (1995). For the sample we used the following Birch–Murnaghan's formulas based on the finite strain theory (Birch, 1938):

$$\begin{aligned}
&\varepsilon=\tfrac{1}{2}\{(\rho/\rho_0)^{2/3}-1\}\\
&P=3K_0(1+2\varepsilon)^{5/2}\varepsilon\{1+(3/2)(K_0'-4)\varepsilon\}\\
&K=K_0(1+2\varepsilon)^{5/2}\{1+(3K_0'-5)\varepsilon\}\\
&G=G_0(1+2\varepsilon)^{5/2}\{1+(3G_0'K_0/G_0-5)\varepsilon\},
\end{aligned}\tag{5}$$

where ρ is the density, ε is the Eulerian strain, P is the pressure, the prime denotes the derivative with respect to pressure, and the suffix 0 denotes the value at zero pressure. Since the pressure range measured in this study is as low as up to 100 MPa, it may not be necessary to use the finite strain formulas. But, we do so in order to allow for future measurement at higher pressure.

Assuming values of 4.0, 5.0, and 6.0 for K_0', we calculated the elastic properties of the sample at high pressure with $K_0=165$ GPa, $G_0=79.5$ GPa, and $\rho_0=7.798$ g/cm^3 from the measurement at ambient pressure, and $G_0'=2.01$ from Table I. In this way, we evaluated the elastic properties of 3LS compressed statically, and calculated the frequencies as a function of pressure. An example is shown in Fig. 5 for

TABLE I. Measured frequencies and their pressure derivatives of toroidal modes, and the resulting pressure derivative of shear modulus.

Mode	Frequency at 1 atm (kHz)	$\partial f/\partial P$ (kHz/GPa)	$G_0'=\partial G/\partial P$
$_0T_4$	1087.0	13.4(7)	2.12
$_1T_1$	1227.1	13.5(6)	1.91
$_0T_5$	1335.9	15.1(9)	1.96
$_0T_5$	1336.4	15.7(7)	2.03
$_0T_5$	1337.0	15.8(6)	2.01
		Average	2.01(8)

TABLE II. Measured frequencies and their pressure derivatives of spheroidal modes, and the resulting pressure derivative of bulk modulus.

Mode		Frequency at 1 atm	$\partial f/\partial P$	$K_0'=\partial K/\partial P$	
HS[a]	3LS[b]	(kHz)	(kHz/GPa)	HS[a]	3LS[b]
$_1S_2$	$_{11}S_2-_{10}S_2-_9S_2$	1063.1	13.0(4)	5.28	5.45
$_1S_2$		1064.1	12.8(6)	4.88	5.18
$_1S_3$	$_{13}S_3-_{12}S_3-_{11}S_3$	1404.8	16.3(9)	4.39	4.61
$_1S_3$		1406.2	16.4(7)	4.49	4.73
			Average	4.8(4)	5.0(4)

[a]Analyzed as homogeneous sphere of sample only.
[b]Analyzed as spherical three-layered structure.

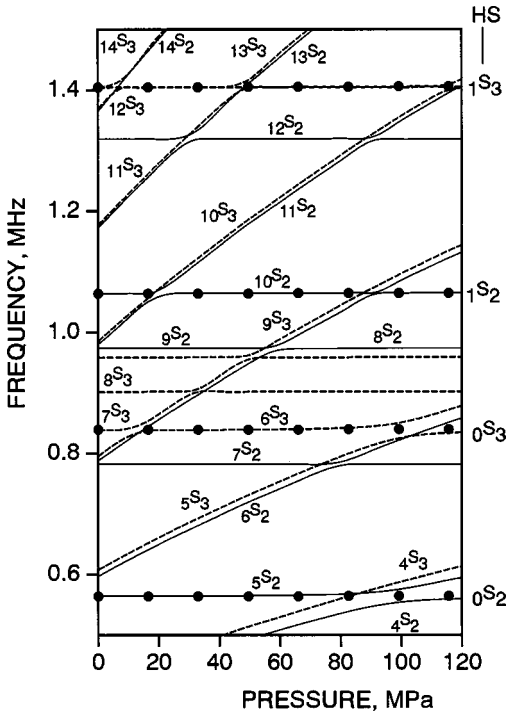

FIG. 5. Theoretical frequencies of the spherical three-layered structure of the sample-gas-layer–cavity container system as a function of pressure. Only modes of $l=2$ (solid lines) and $l=3$ (broken lines) are shown, and $\partial K/\partial P$ is assumed to be 5.0. Solid circles denote the frequencies of the corresponding modes of the HS indicated at right.

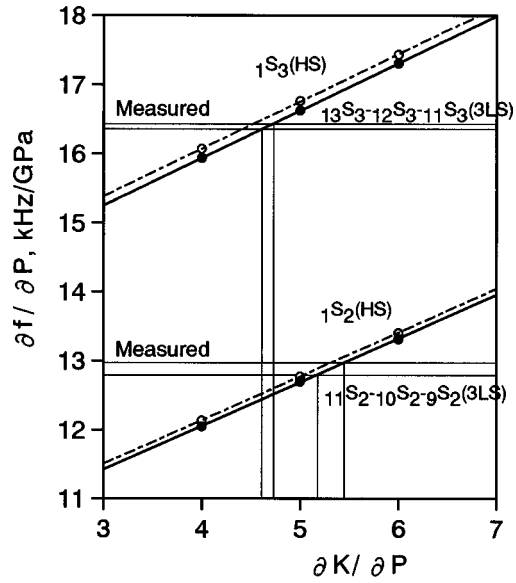

FIG. 6. Theoretical $\partial f/\partial P$ plotted as a function of assumed $K_0'=\partial K/\partial P$. Open circles and broken lines show the value for the HS, and solid circles and solid lines show the values for the 3LS. Measured data of $\partial f/\partial P$ are also shown by horizontal lines.

the case of $K_0'=5.0$. For the purpose of simplicity, only the modes of $l=2$ and $l=3$ are shown in Fig. 5. There appear to be many more modes in 3LS than in the corresponding homogeneous sphere (HS) of the sample only (see the solid circles in Fig. 5).

In 3LS the vibrational energy is localized to one of three layers due to the existence of the intermediate gas layer with extremely low impedance. Thus, the normal modes of the three-layered structure can be classified as either ''sample mode,'' ''gas mode,'' or ''container mode'' (Oda and Suzuki, 1999). The frequencies of gas modes have a large pressure gradient because of the large compressibility of gas, and often come close to the sample mode or container mode when pressure increases. In such situations the two traces of frequency cross each other without interaction if they have different angular order *l*. However, when the two modes have the same *l*, they do not cross but interact or couple with each other, changing their pressure gradients gradually, then part again after the interaction or coupling. Figure 5 provides numerous examples of such mode coupling: e.g., the coupling between $_6S_3$ and $_7S_3$ near 15 MPa, and that between $_{10}S_2$ and $_{11}S_2$ near 20 MPa. After such mode coupling the properties of the two modes are exchanged (Oda and Suzuki, 1999); for example, $_{10}S_2$ is in gas mode and $_{11}S_2$ is in sample mode before the coupling around 20 MPa, but $_{10}S_2$ is in sample mode after the mode coupling. Thus, with the pressure increase the mode $_1S_2$ of HS corresponds to $_{11}S_2$, $_{10}S_2$, and then $_9S_2$ in 3LS, which is represented as $_{11}S_2-_{10}S_2-_9S_2$. Similarly, $_1S_3$ in HS corresponds to $_{13}S_3-_{12}S_3-_{11}S_3$ in 3LS.

Assuming K_0' to be 4.0, 5.0, and 6.0, we calculated the frequencies of the $_{11}S_2-_{10}S_2-_9S_2$ modes and $_{13}S_3-_{12}S_3-_{11}S_3$ modes as a function of pressure. The results are shown in Figs. 4(c) and (d), and are compared with the measured data. The pressure gradient of the calculated frequency is plotted against the assumed K_0' in Fig. 6. The pressure gradient in 3LS, shown with solid lines, is a little smaller than that in HS, shown with dashed lines. K_0' is determined such that the calculated gradient meets the measured one. The measured data represented by horizontal lines give K_0' around 5.0 as shown in Fig. 6 and Table II.

Figure 6 also shows that the differences caused by the HS and 3LS calculations are smaller than the differences caused by the ambiguity in the measured $\partial f/\partial P$ listed in Table II. This means the analysis in 3LS is not necessarily essential, at least on the two modes.

V. DISCUSSION

The resulting pressure derivative of the shear modulus, $G_0'=2.01$, is consistent with the values of 2.4 (Hughes and Maurette, 1956), 1.7 (Bridgman, 1958), and 2.6 (Nishitake *et al.*, 1967) reported for steel. The result of the pressure derivative of the bulk modulus, $K_0'=5.0$, is also comparable with the value of 6.0 (Hughes and Maurette, 1956), and of 6.5 (Nishitake *et al.*, 1967), except for 11.9 (Bridgman, 1958).

We next compared the measurements obtained for the spheroidal modes using a 3LS approach with those obtained using a simple HS analysis. The difference in the resulting K_0' was about 0.2 (4%), as seen in Fig. 6 and Table II. Since the ambiguity due to the experimental error in $\partial f/\partial P$ (Table II) was larger than this, the simple HS analysis with Eq. (3) is a convenient method for analyzing data in such a pressure range.

As mentioned above, a sample mode in 3LS sometimes couples with gas modes of the same angular order *l* when the frequencies are close to each other in value. Figure 7 shows

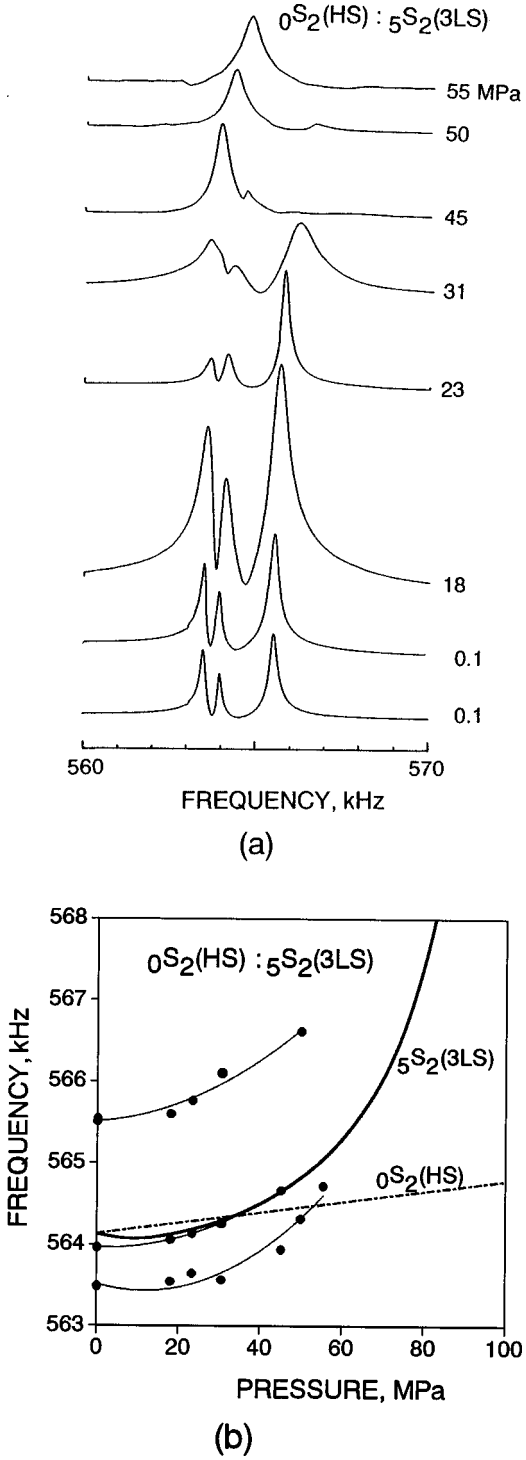

FIG. 7. (a) Measured pressure-induced shifts of resonance peaks of $_0S_2$ (HS). Three peaks were recorded split from the degenerated mode. (b) The frequency of the $_0S_2$ (HS) mode as a function of pressure. The broken line is the theoretical frequency calculated for the HS, and the thick solid line is that for the 3LS. Measured data (solid circles) show a trend to agree with the 3LS curve rather than the HS line.

an example measured on $_5S_2$ in 3LS, which corresponds to $_0S_2$ in HS. The frequencies of triplet peaks increase very rapidly and nonlinearly with pressure. This phenomenon cannot be explained by the calculated trace of $_0S_2$ of HS (dashed line), but can be adequately explained by those of $_5S_2$ of 3LS (thick solid line). This means we have actually observed the modes of 3LS. It seems that the mode $_5S_2$ could be observed because this mode couples with $_4S_2$ over a particularly wide pressure range, as shown in Fig. 5.

When the mode coupling takes place over a wide pressure range, as seen between $_5S_2$ and $_4S_2$, this prevents us from accurately determining K_0' with frequency data in a narrow pressure range. It is thus best to reduce the number of gas modes to as few as possible. For this purpose we should make the thickness of the gas layer as thin as possible (Suzuki *et al.*, 1998). In the present study the gas layer was as thick as 2.6 mm, and there were many gas modes, as shown in Fig. 5. Ohno *et al.* (2000) made the same kind of measurement on a silica glass sphere, but with a thinner gas layer of 0.36 mm, where only one gas mode was seen for each l in the frequency range concerned.

Although the cavity container had a cylindrical outer shape and was divided into upper and lower parts (Fig. 1), in the present calculation it was regarded as a closed spherical shell. For this reason, the calculated frequencies of container modes are rather meaningless. More important, however, are the frequencies of the sample modes and the interacting gas modes, which are hardly affected by the outer shape and size of the container.

VI. SUMMARY

(1) We measured eigenfrequencies of a steel-sphere sample under gas pressure with a spherical three-layered structure (3LS) composed of a sample-gas–container system (cavity resonance method). The pressure-induced shifts of frequencies were observed up to 100 MPa (=1 kbar) for both toroidal and spheroidal modes, and the pressure derivatives of frequency, $\partial f/\partial P$, were obtained. The $\partial f/\partial P$ data of the toroidal modes were reduced to the pressure derivative of shear modulus, $\partial G/\partial P = G_0' = 2.01 \pm 0.08$. This result is within the range of the previous values reported for steel, 2.0 (Hughes and Maurette, 1956), 1.7 (Bridgman, 1958), and 2.6 (Nishitake *et al.*, 1967).

(2) The $\partial f/\partial P$ data of spheroidal modes were reduced to the pressure derivative of the bulk modulus, $\partial K/\partial P = K_0'$, in two ways: first, as the homogeneous sphere (HS) of the sample alone, in which the coupling between the sample and the surrounding gas was ignored, and second, as a 3LS, in which the coupling was taken into account. The former analysis yielded $K_0' = 4.8 \pm 0.4$, and the latter $K_0' = 5.0 \pm 0.4$. The difference of 0.2 between these two methods of analysis is smaller than the standard deviation of the present measurements. The result of $K_0' = 5.0 \pm 0.4$ is comparable with the previous value of 6.0 (Hughes and Maurette, 1956) and 6.5 (Nishitake *et al.*, 1967) within 30% difference, except for 11.9 (Bridgman, 1958).

(3) In summary, we demonstrated that the cavity resonance method, an application of resonant sphere technique under high pressure using a gas medium, is effective to measure the pressure dependence of elastic moduli.

ACKNOWLEDGMENTS

We thank M. Kumazawa for his invaluable suggestions and input, and the anonymous reviewers for their critical comments. We also thank S. Ishikawa (Nagoya University, Japan) for his help in preparing the cavity containers, and M. Mori (Ehime University, Japan) for his support in operating the gas apparatus. This work was supported by Grants-In-Aid for Scientific Research (Nos. 06640547, 10640465, and 12640410) from the Japanese Ministry of Education.

Birch, F. (**1938**). ''The effect of pressure upon the elastic properties of isotropic solids, according to Murnaghan's theory of finite strain,'' J. Appl. Phys. **9**, 279–288.

Bridgman, P. W. (**1958**). *The Physics of High Pressure* (Bell, London), p. 386.

Demarest, H. (**1971**). ''Cube resonance method to determine the elastic constants of solids,'' J. Acoust. Soc. Am. **49**, 768–775.

Fraser, D. B., and LeCraw, R. C. (**1964**). ''Novel method of measuring elastic and anelastic properties of solids,'' Rev. Sci. Instrum. **35**, 1113–1115.

Hanayama, Y., Nishioka, N., Kumura, M., and Ishizuka, S. (**1995**). ''Measurement on the ultrasound velocities and elastic constants of WC-Co superhard alloy under high pressure,'' Mem. Faculty Eng., Ehime Univer. **14**, 419–427 (in Japanese).

Hughes, D. S., and Maurette, C. (**1956**). ''Dynamic elastic moduli of iron, aluminum and fused quartz,'' J. Appl. Phys. **27**, 1184–1186.

Isaak, D. G., Carnes, J. D., Anderson, O. L., and Cynn, H. (**1998a**). ''Elasticity of TiO_2 rutile to 1800 K,'' Phys. Chem. Miner. **26**, 31–43.

Isaak, D. G., Carnes, J. D., Anderson, O. L., and Oda, H. (**1998b**). ''Elasticity of fused silica spheres under pressure using rsonant ultrasound spectroscopy,'' J. Acoust. Soc. Am. **104**, 2200–2206.

Kimura, M., Hanayama, Y., and Nishitake, T. (**1987**). ''High pressure gas apparatus for measuring ultrasound velocity in matters up to 4 GPa,'' Jpn. J. Appl. Phys., Part 1 **26**, 1361–1365.

Kimura, M., Masui, T., Miyata, K., Nishioka, N., Hanayama, Y., and Nishitake, T. (**1995**). ''Measurement of ultrasound velocity in condensed helium gas up to 3 GPa,'' Mem. Faculty Eng, Ehime Univer. **14**, 411–418 (in Japanese).

Leisure, R. G., and Willis, F. A. (**1997**). ''Resonant ultrasound spectroscopy,'' J. Phys.: Condens. Matter **9**, 6001–6029.

Maynard, J. (**1996**). ''Resonant ultrasound spectroscopy,'' Phys. Today **49**(1), 26–29.

Migliori, A., and Sarrao, J. L. (**1997**). *Resonant Ultrasound Spectroscopy* (Wiley, New York).

Mochizuki, E. (**1988**). ''The sphere resonance method to determine the elastic constants of crystal,'' J. Appl. Phys. **63**, 5668–5673.

Nishitake, T., Araki, J., and Miyoshi, Y. (**1967**). ''Elastic wave velocities in stainless steels at high pressures,'' Mem. Ehime Univ., Sect. III **5**, 11–16.

Oda, H., Suzuki, I., and Ohno, I. (**1993**). ''Partial derviatives of eigenfrequencies of a rectangular parallelepiped and a sphere of elastically anisotropic solid,'' J. Phys. Earth **41**, 271–289.

Oda, H., Isoda, S., Inouye, Y., and Suzuki, I. (**1994**). ''Elastic constants and anelastic properties of an anisotropic periclase sphere as determined by the resonant sphere technique,'' J. Geophys. Res. **99**, 15517–15527.

Oda, H., and Suzuki, I. (**1999**). ''Normal mode oscillation of a sphere with solid–gas–solid structure,'' J. Acoust. Soc. Am. **105**, 693–699.

Ohno, I. (**1976**). ''Free vibration of a rectangular parallelepiped crystal and its application to determination of elastic constants of orthorhombic crystals,'' J. Phys. Earth **24**, 355–379.

Ohno, I., Hanayama, Y., Kimura, M., Suzuki, I., Oda, H., and Kumazawa, M. (**1994**). ''Pressure derivatives of elastic constants of iron by cavity resonance method,'' in *High Pressure Science and Technology—1993*, edited by S. C. Schmidt, J. W. Shaner, G. A. Samara, and M. Ross (AIP, New York), pp. 931–934.

Ohno, I., Abe, M., Kimura, M., Hanayama, Y., Oda, H., and Suzuki, I. (**2000**). ''Elasticity measurement of silicia glass under gas pressure,'' Am. Mineral. **85**, 288–291.

Sato, Y., and Usami, T. (**1962**). ''Basic study on the oscillation of a homogeneous elastic sphere. I. Frequency of the free oscillations,'' Geophys. Mag. **31**, 15–24.

Saito, M. (**1988**). ''DISPER80: A subroutine package for the calculation of seismic normal mode solution,'' in *Seismological Algorithm*, edited by D. J. Doornbos (Academic, New York), pp. 293–319.

Soga, N., and Anderson, O. L. (**1967**). ''Elastic properties of tektites measured by resonant sphere technique,'' J. Geophys. Res. **72**, 1733–1739.

Sorbello, R. S., Feller, J., Levy, M., Isaak, D. G., Carnes, J. D., and Anderson, O. L. (**2000**). ''The effect of gas loading on the RUS spectra of spheres,'' J. Acoust. Soc. Am. **107**, 808–818.

Suzuki, I., Oda, H., Isoda, S., Saito, T., and Seya, K. (**1992**). ''Free oscillation of an elastically anisotropic sphere and its application to determining the elastic constants of rutile,'' J. Phys. Earth **40**, 601–616.

Suzuki, I., Oda, H., Yamada, K., and Ohno, I. (**1998**). ''Theoretical analysis for high pressure resonance method: Vibration of a three layered shell structure with an isotropic or anisotropic core,'' Rev. High Pressure Sci. Technol. **7**, 1517–1519.

Suzuki, I., Ohno, I., and Anderson, O. L. (**2000**). ''Harmonic and anharmonic properties of spinel $MgAl_2O_4$,'' Am. Mineral. **85**, 304–311.

Vargaftik, N. B. (**1983**). *Handbook of Physical Properties of Liquids and Gases* (Hemisphere, Washington, D.C.), p. 535.

Visscher, W. M., Miglioli, A., Bell, T. M., and Reinert, R. A. (**1991**). ''On the normal modes of free vibration of inhomogeneous and anisotropic elastic objects,'' J. Acoust. Soc. Am. **90**, 2154–2162.

Surface waves in orthotropic incompressible materials

Michel Destrade[a)]
Mathematics, Texas A&M University, College Station, Texas 77843-3368

(Received 1 October 2000; accepted for publication 17 April 2001)

The secular equation for surface acoustic waves propagating on an orthotropic incompressible half-space is derived in a direct manner, using the method of first integrals. © *2001 Acoustical Society of America.* [DOI: 10.1121/1.1378346]

PACS numbers: 43.35.Pt [ANN]

I. INTRODUCTION

The problem of elastic waves propagating on the free surface of a semi-infinite elastic body is a well-covered research topic, initiated by Rayleigh[1] in his study of seismic waves within the context of classical linear elasticity. For anisotropic crystals, Barnett and Lothe[2] have drawn on the works of Stroh[3] to build a complete theory of surface waves based on an analogy between surface wave propagation and straight line dislocation motion. Extensive coverage and surveys of that topic can be found, for instance, in a textbook by Ting.[4]

Recently, there has been some interest[5–7] in the study of wave propagation in anisotropic materials subjected to the constraint of *incompressibility*. Our purpose in the present paper is to establish the secular equation for surface (Rayleigh) waves propagating on the free plane surface of an incompressible orthotropic half-space. A similar problem was solved by Chadwick[8] within the context of finite elasticity: he considered the propagation of small-amplitude surface waves in a finitely deformed incompressible material; the deformation was static and purely homogeneous, and the strain energy function for the incompressible nonlinearly elastic material was such that the deformed body presented orthotropic anisotropy. Following Nair and Sotiropoulos,[7] in the present article we focus on an orthotropic linearly elastic material for which the usual stress–strain relations are modified to take the incompressibility constraint into account, by adding an isotropic pressure term. These authors have argued that ''the assumptions of incompressibility and orthotropy are applicable to several materials as, for example, polymer Kratons, thermoplastic elastomers, rubber composites when low frequency waves are considered to justify the assumption of material homogeneity, etc.'' Other studies use these assumptions for the modeling of laminated composites made alternatively with reinforcing (filler) layers and matrix (binder) layers,[9] or with stiff fibers and incompressible epoxy matrices.[10]

Our primary purpose in this paper is to show that the method of first integrals used by Mozhaev[11] to derive, in a rapid and elegant manner, the secular equation for surface waves in (compressible) orthotropic materials, can also be employed in the case of incompressible orthotropic materials. This can be achieved by applying the method of first integrals to a system of second order ordinary differential equations for the components of the *tractions* on surfaces parallel to the free surface, rather than for the components of the mechanical displacement (as in Ref. 11). In the latter case, the pressure appears in the system of differential equations, whereas in the former case, it does not, and hence the number of unknowns is reduced from four (the pressure and the components of the mechanical displacement) to three (the components of the traction on surfaces parallel to the free surface). Also, the mechanical boundary conditions are easily written, because they correspond to the nullity of these traction components on the free surface of the half-space, and at an infinite distance from this surface. A third advantage of this approach is that the assumption of plane strain[7] is not required *a priori*.

The paper is organized as follows. In Sec. II, the basic equations governing the propagation of elastic waves in an orthotropic incompressible material are recalled. In Sec. III, these equations are written for the case of surface acoustic waves. Then a system of six first order differential equations for the displacement and the traction components is derived. Eventually a system of three second order differential equations is found for the traction components. One of these three equations is trivially solved when the boundary conditions are applied. In Sec. IV, the method of first integrals[11,12] is applied to the two remaining equations, and the secular equation for surface waves in orthotropic incompressible materials is quickly derived. As a check, the isotropic case is treated and Rayleigh's original equation[1] is recovered. Also, the correspondence between this paper's result and Chadwick's result[8] is shown. Finally in Sec. V, possible developments for this work are presented.

II. PRELIMINARIES

First, the governing equations for an incompressible orthotropic elastic material are recalled. The material axes of the body are denoted by x_1, x_2, and x_3. The equations may be derived from the classical linearized equations of anisotropic elasticity[13] by adding an isotropic pressure term $p\mathbf{1}$ (say) to the nominal stress $\boldsymbol{\sigma}$ (say). Hence, for orthotropic incompressible elastic bodies,[7]

$$\begin{aligned}
\sigma_{11} &= -p + C_{11}\epsilon_{11} + C_{12}\epsilon_{22} + C_{13}\epsilon_{33},\\
\sigma_{22} &= -p + C_{12}\epsilon_{11} + C_{22}\epsilon_{22} + C_{23}\epsilon_{33},\\
\sigma_{33} &= -p + C_{13}\epsilon_{11} + C_{23}\epsilon_{22} + C_{33}\epsilon_{33},\\
\sigma_{32} &= 2C_{44}\epsilon_{32}, \quad \sigma_{13} = 2C_{55}\epsilon_{31}, \quad \sigma_{12} = 2C_{66}\epsilon_{12},
\end{aligned} \tag{1}$$

a)Electronic mail: michel.destrade@math.tamu.edu

where ϵ's denote the strain components, and C's the elastic constants. The strain components are related to the displacement components u_1, u_2, u_3 through

$$\epsilon_{ij}=(u_{i,j}+u_{j,i})/2 \quad (i,j=1,2,3). \tag{2}$$

Finally, the incompressibility constraint reads as

$$u_{1,1}+u_{2,2}+u_{3,3}=0, \tag{3}$$

and the equations of motion, in the absence of body forces, are written as

$$\sigma_{ij,j}=\rho u_{i,tt} \quad (i=1,2,3), \tag{4}$$

where ρ is the mass density of the material, and the comma denotes differentiation. These are the equations established by Nair and Sotiropoulos.[7] These authors also note that for plane strain, the strain–energy function density is positive definite when the following inequalities are satisfied:

$$C_{66}\geqslant 0, \quad C_{11}+C_{22}-2C_{12}\geqslant 0. \tag{5}$$

III. SURFACE WAVES

Here the equations of motion for a surface wave in a semi-infinite body made of an orthotropic incompressible elastic material are established. Attention is restricted to propagating inhomogeneous surface waves which are subsonic with respect to homogeneous body waves. The modelization of the surface wave follows that of Mozhaev:[11] the plane wave propagates with speed v, wave number k, and corresponding displacement and pressure of the form

$$[u_j(x_1,x_2,x_3),p(x_1,x_2,x_3)]=[U_j(x_2),kP(x_2)]e^{ik(x_1-vt)} \quad (j=1,2,3), \tag{6}$$

where the U's and P are unknowns functions of x_2 alone. For these waves, the planes of constant phase are orthogonal to the x_1-axis, and the planes of constant amplitude are orthogonal to the x_2-axis. The stress–strain relations (1) reduce to

$$\begin{aligned} t_{11}&=-P+iC_{11}U_1+C_{12}U_2', \\ t_{22}&=-P+iC_{12}U_1+C_{22}U_2', \\ t_{33}&=-P+iC_{13}U_1+C_{23}U_2', \\ t_{32}&=C_{44}U_3', \quad t_{13}=iC_{55}U_3, \quad t_{12}=C_{66}(U_1'+iU_2), \end{aligned} \tag{7}$$

where the prime denotes differentiation with respect to kx_2, and the t's are defined by

$$\sigma_{ij}(x_1,x_2,x_3)=kt_{ij}(x_2)e^{ik(x_1-vt)} \quad (i,j=1,2,3). \tag{8}$$

The surface $x_2=0$ is assumed to be free of tractions, and the mechanical displacement and pressure are assumed to be vanishing as x_2 tends to infinity. These conditions lead to the following boundary conditions:

$$t_{i2}(0)=0, \quad U_i(\infty)=0 \quad (i=1,2,3), \quad P(\infty)=0. \tag{9}$$

Finally, the equations of motion (4) and the incompressibility constraint (3) reduce to

$$\begin{aligned} &it_{11}+t_{12}'=-\rho v^2U_1, \quad it_{12}+t_{22}'=-\rho v^2U_2, \\ &it_{13}+t_{32}'=-\rho v^2U_3, \quad iU_1+U_2'=0. \end{aligned} \tag{10}$$

Note that a classical approach would be to substitute in these last equations, the expressions obtained earlier for the stress tensor components, which would lead to a system of four second order differential equations for the unknown functions U_1, U_2, U_3, P. Instead, the Stroh formalism is now used to derive a system of six first order differential equations for the components of the displacement and the tractions on the surface $x_2=$ const. Thus, introducing the notation

$$t_i=t_{i2} \quad (i=1,2,3), \tag{11}$$

and using Eqs. (7)–(10), the system is found as

$$\begin{aligned} &U_1'=-iU_2+(1/C_{66})t_1, \quad U_2'=-iU_1, \quad U_3'=(1/C_{44})t_3, \\ &t_1'=(C_{11}+C_{22}-2C_{12}-\rho v^2)U_1-it_2, \\ &t_2'=-\rho v^2U_2-it_1, \quad t_3'=(C_{55}-\rho v^2)U_3. \end{aligned} \tag{12}$$

Now a system of three second order differential equations for t_1, t_2, t_3 is derived as follows. First, the differentiation of $(12)_{4-6}$ yields relations between the t_i'' and the u_i', t_i', or equivalently, using $(12)_{1-3}$ between the t_i'' and the u_i, t_i', t_i. Then, substitution for the u_i by their expression in terms of the t_i', t_i obtained from $(12)_{4-6}$ is performed. Eventually it is found that the t_i'', t_i', t_i $(i=1,2,3)$ must satisfy the following equations,

$$\begin{aligned} &(\rho v^2)t_1''-i(C_{11}+C_{22}-2C_{12}-2\rho v^2)t_2' \\ &\quad +(C_{11}+C_{22}-2C_{12}-\rho v^2)(1-\rho v^2/C_{66})t_1=0, \\ &(C_{11}+C_{22}-2C_{12}-\rho v^2)t_2''+i(C_{11}+C_{22}-2C_{12}-2\rho v^2)t_1' \\ &\quad +\rho v^2t_2=0, \\ &C_{44}t_3''-(C_{55}-\rho v^2)t_3=0, \end{aligned} \tag{13}$$

and are subject to the following boundary conditions:

$$t_i(0)=t_i(\infty)=0 \quad (i=1,2,3). \tag{14}$$

The third differential equation in the system (13) is decoupled from the two others, and can be solved exactly. Taking the boundary conditions $(14)_3$ into account, it is seen that

$$t_3(x_2)=0, \quad \text{for all } x_2, \tag{15}$$

and hence the motion is a pure mode[14] for the tractions on the surface $x_2=$ const. Now the coupled system of the two remaining equations may be solved.

IV. SECULAR EQUATION

For surface waves in compressible orthotropic materials, Mozhaev[11] applied the method of first integrals to a system of two differential equations for the two nonzero components of the mechanical displacement. Here a similar procedure for the two nonzero components t_1, t_2 of the tractions on the surface $x_2=$ const is followed, and the secular equation for surface waves in incompressible orthotropic materials is obtained in a direct manner.

The differential equations $(13)_{1,2}$ for t_1, t_2 are expressed as

$$\xi t_1'' - i(\delta - 2\xi)t_2' + (\delta - \xi)(1-\xi)t_1 = 0,$$
$$(\delta - \xi)t_2'' + i(\delta - 2\xi)t_1' + \xi t_2 = 0, \tag{16}$$

where ξ and δ are defined by

$$\xi = (\rho v^2)/C_{66}, \quad \delta = (C_{11} + C_{22} - 2C_{12})/C_{66}. \tag{17}$$

The speed given by $\xi = 1$ (that is $\rho v^2 = C_{66}$) corresponds to the speed of a body (homogeneous) wave propagating in the x_1-direction, and gives therefore an upper bound for the speed of subsonic waves. Throughout the rest of the paper, it is assumed that the surface wave travels with a speed distinct from that given by $\xi = \delta$ (that is $\rho v^2 \neq (C_{11} + C_{22} - 2C_{12})/C_{66}$).

Now multiplication of $(16)_1$ by t_1' and $(16)_2$ by t_2', and integration between $x_2 = 0$ and $x_2 = \infty$, yields, using the boundary conditions (14),

$$\xi t_1'(0)^2 - 2i(\delta - 2\xi)\int t_1' t_2' = 0, \tag{18}$$

and

$$(\delta - \xi)t_2'(0)^2 + 2i(\delta - 2\xi)\int t_1' t_2' = 0,$$

so that

$$\xi t_1'(0)^2 + (\delta - \xi)t_2'(0)^2 = 0. \tag{19}$$

Similarly, multiplication of $(16)_1$ by $\xi t_1' + i(\delta - 2\xi)t_2$ and $(16)_2$ by $(\delta - \xi)t_2' - i(\delta - 2\xi)t_1$, and integration between $x_2 = 0$ and $x_2 = \infty$, yields

$$\xi^2 t_1'(0)^2 + 2i(\delta - 2\xi)(\delta - \xi)(1-\xi)\int t_1 t_2 = 0,$$

and

$$(\delta - \xi)^2 t_2'(0)^2 - 2i(\delta - 2\xi)\xi \int t_1 t_2 = 0, \tag{20}$$

so that

$$\xi^3 t_1'(0)^2 + (\delta - \xi)^3(1-\xi)t_2'(0)^2 = 0. \tag{21}$$

Equations (19) and (21) form a trivial system of two equations for the unknowns $t_1'(0)^2$ and $t_2'(0)^2$, whose determinant must be zero:

$$\xi(\delta - \xi)[(\delta - \xi)^2(1-\xi) - \xi^2] = 0. \tag{22}$$

It follows that the *secular equation* is given by

$$(\delta - \xi)^2(1-\xi) = \xi^2,$$

i.e.,

$$(C_{11} + C_{22} - 2C_{12} - \rho v^2)^2 (C_{66} - \rho v^2) = C_{66}(\rho v^2)^2. \tag{23}$$

This equation constitutes the main result of the paper: the direct and explicit derivation of the secular equation for subsonic surface waves propagating in a semi-infinite body made of orthotropic incompressible linearly elastic material. It is worth mentioning that this result can be used for other types of anisotropy: Royer and Dieulesaint[15] have indeed proved that with respect to surface waves, results established for the orthotropic case may be applied to 16 different configurations, including cubic, tetragonal, and hexagonal anisotropy.

In order to justify the existence of a real wave speed, the secular equation (23) is expressed as

$$f(\xi) = 0, \quad \text{where} \quad f(\xi) = \xi^2 - (\delta - \xi)^2(1-\xi). \tag{24}$$

As noted earlier, for traveling subsonic surface waves, this secular equation is subject to

$$0 \leqslant \xi \leqslant 1. \tag{25}$$

Within this range, it is easy to prove that f is a monotonic increasing function of ξ, and that

$$f(0) = -\delta^2, \quad f(1) = 1. \tag{26}$$

It follows that the secular equation has a unique positive root in the interval (25).

For consistency purposes, the main result established in this paper is related to previous studies. First, attention is given to the isotropic limit, when $C_{11} = C_{22} = \lambda + 2\mu$, $C_{12} = \lambda$, $C_{66} = \mu$, where λ and μ are the classical Lamé moduli of elasticity. In this case, the secular equation, written for $\xi = \rho v^2/\mu$, reduces to

$$(4-\xi)^2(1-\xi) = \xi^2, \quad \text{or} \quad \xi^3 - 8\xi^2 + 24\xi - 16 = 0, \tag{27}$$

which is the well-known equation derived by Lord Rayleigh,[1] by considering the incompressible limit ($\lambda = \infty$) for an isotropic linear elastic material.

Next, another previous result is put into perspective. Chadwick[8] has adapted the Stroh formalism to the theory of prestressed incompressible nonlinearly elastic materials. Considering a material whose stored energy function is such that the body will present orthorhombic anisotropy once it has been subjected to a large pure homogeneous deformation, he obtained the secular equation for surface waves propagating in a principal direction as

$$[2(B + C - \overline{\sigma}) - \rho v^2][C(A - \rho v^2)]^{1/2} = (C - \overline{\sigma})^2 - C(A - \rho v^2), \tag{28}$$

where A, B, C are constants defined in terms of the strain energy, initial pressure, and initial stretch ratios, and $\overline{\sigma}$ is the normal stress applied on the surface $x_2 = 0$. When this surface is free of tractions, $\overline{\sigma} = 0$ and after squaring, Eq. (28) reduces to

$$(2B + C - A - \eta^2)^2 (C - \eta^2) = C(\eta^2)^2, \tag{29}$$

where $\eta^2 = C - A + \rho v^2$. This equation may be formally compared to Eq. $(23)_2$, where η^2, C, and $2B - A$ play the role of ρv^2, C_{66}, and $C_{11} + C_{22} - C_{66} - 2C_{12}$, respectively.

Finally, Nair and Sotiropoulos[6] have obtained an *implicit* form of the secular equation for surface waves propagating in a monoclinic incompressible material. By taking the elastic coefficients C_{16} and C_{26} to be zero in their analysis, the reader may check that the explicit secular equation (23) is recovered.

V. DISCUSSION

The secular equation for surface waves on an incompressible orthotropic half-space was derived directly. Hence it has been shown that a powerful method presented by Mozhaev,[11] but which seems to have remained unnoticed, can be adapted to take the constraint of incompressibility into account.

For monoclinic or triclinic materials, the method of first integrals cannot be applied in the case of a three dimensional displacement. As demonstrated by Mozhaev,[11] it leads to a trivial system of 18 equations for 18 unknowns, but the rank of the system turns out to be 17 at most, a fact which appears to have been overlooked by the author.

However, for *plane strain* deformations, some further results may be established. For instance, Sotiropoulos and Nair[5] have studied the reflection of plane elastic waves from a free surface in incompressible monoclinic materials with plane of symmetry at $x_3=0$, and Nair and Sotiropoulos[6] have considered interfacial waves with an interlayer in the same type of materials. In particular, they derived the secular equation for surface (Rayleigh) waves in an implicit form. The first integrals method makes it possible to write the secular equation in explicit form, as is proved in a forthcoming article. Possibly, interfacial (Stoneley) waves may also be investigated

.

ACKNOWLEDGMENTS

I am greatly indebted to Professor M. Hayes (University College, Dublin) for pointing out and providing Ref. 11, and for his patient guidance. I also thank Dr. A. L. Shuvalov (Institute of Crystallography, Moscow) for his insightful and encouraging comments, and Dr. Y. Fu (Keele University, Keele) for suggesting a link between Ref. 11 and the Stroh formalism.

In its early stages, this work was conducted at the Department of Mathematical Physics, University College Dublin, Ireland, and supported by a grant from the European Commission under the TMR Program, Contract No. FMBICT983468.

[1] Lord Rayleigh, ''On waves propagated along the plane surface of an elastic solid,'' Proc. R. Soc. London, Ser. A **17**, 4–11 (1885).
[2] D. M. Barnett and J. Lothe, ''Free surface (Rayleigh) waves in anisotropic elastic half-spaces: The surface impedance method,'' Proc. R. Soc. London, Ser. A **402**, 135–152 (1985).
[3] A. N. Stroh, ''Steady state problems in anisotropic elasticity,'' J. Math. Phys. (Cambridge, Mass.) **41**, 77–103 (1962).
[4] T. C. T. Ting, *Anisotropic Elasticity: Theory and Applications* (Oxford University Press, New York, 1996).
[5] D. A. Sotiropoulos and S. Nair, ''Elastic waves in monoclinic incompressible materials and reflection from an interface,'' J. Acoust. Soc. Am. **105**, 2981–2983 (1999).
[6] S. Nair and D. A. Sotiropoulos, ''Interfacial waves in incompressible monoclinic materials with an interlayer,'' Mech. Mater. **31**, 225–233 (1999).
[7] S. Nair and D. A. Sotiropoulos, ''Elastic waves in orthotropic incompressible materials and reflection from an interface,'' J. Acoust. Soc. Am. **102**, 102–109 (1997).
[8] P. Chadwick, ''The application of the Stroh formalism to prestressed elastic media,'' Math. Mech. Sol. **97**, 379–403 (1997).
[9] A. N. Guz' and I. A. Guz', ''On the theory of stability of laminated composites,'' Int. Appl. Mech. **35**, 323–329 (1999).
[10] M. Sutcu, ''Orthotropic and transversely isotropic stress–strain relations with built-in coordinate transformation,'' Int. J. Solids Struct. **29**, 503–518 (1992).
[11] V. G. Mozhaev, ''Some new ideas in the theory of surface acoustic waves in anisotropic media,'' *IUTAM Symposium on Anisotropy, Inhomogeneity and Nonlinearity in Solids,* edited by D. F. Parker and A. H. England (Kluwer, Holland, 1994), pp. 455–462.
[12] M. Y. Yu, ''Surface polaritons in nonlinear media,'' Phys. Rev. A **28**, 1855–1856 (1987).
[13] A. E. H. Love, *A Treatise on the Mathematical Theory of Elasticity* (Cambridge University Press, England, 1927).
[14] P. Chadwick, ''The existence of pure surface modes in elastic materials with orthorhombic symmetry,'' J. Sound Vib. **47**, 39–52 (1976).
[15] D. Royer and E. Dieulesaint, ''Rayleigh wave velocity and displacement in orthorhombic, tetragonal, and cubic crystals,'' J. Acoust. Soc. Am. **76**, 1438–1444 (1984).

Heat transfer from transverse tubes adjacent to a thermoacoustic stack

George Mozurkewich[a)]
Ford Motor Company Research Laboratory, Mail Drop 3028/SRL, P.O. Box 2053, Dearborn, Michigan 48121-2053

(Received 13 March 2000; revised 14 May 2001; accepted 16 May 2001)

The goal of this work was to test the usefulness of the time-average steady-flow equivalent (TASFE) approximation for the analysis of heat exchangers for thermoacoustic engines. The TASFE approximation assumes that the heat transfer in an acoustic standing wave with zero mean flow is equivalent to averaging the corresponding steady-flow correlation over a sinusoidal distribution of gas speeds. The experiment tested three simple heat-exchanger configurations located immediately adjacent to the hot end of a thermoacoustic stack. Two configurations consisted of bare, parallel, water-carrying tubes oriented transverse to the mean acoustic flow. A third configuration consisted of a single layer of woven copper screen soldered to transverse tubes. Experiments with pure helium and with a mixture of helium and argon found qualitative, and sometimes quantitative, agreement with expectations of the TASFE approximation at both large and small acoustic amplitudes. In addition, large heat transfer with zero temperature difference between the heat exchanger and the stack was observed and interpreted.
[DOI: 10.1121/1.1385180]

PACS numbers: 43.35.Ud, 44.25.–f [SGK]

I. INTRODUCTION

Thermoacoustic refrigeration uses an intense sound wave to produce cooling.[1] In the traditional, standing-wave approach, an acoustic oscillation involving cyclic compression and rarefaction produces an associated temperature oscillation, and the refrigeration is based on the thermodynamic cycle that packets of gas undergo as they partake in the oscillation. Only those gas packets which oscillate ''near'' a solid surface contribute to the refrigerating effect. ''Near'' is defined in terms of the thermal penetration depth in the gas, which is usually on the order of 10^{-4} m.[1]

A typical, standing-wave thermoacoustic refrigerator consists of an acoustic resonator, some means to feed acoustic power into the resonator (such as a loudspeaker), and a thermoacoustic stack.[1,2] The latter component is a porous medium (such as honeycomb,[3] jelly roll,[4] catalytic-converter monolith,[5] stacked screens,[6] reticulated foam,[7] or pin stack[8]) that increases the amount of cooling by increasing the proportion of the oscillating gas that resides ''near'' a solid surface. In order to make use of this cooling effect, it is necessary to provide a means for heat to enter the gas at the cold end of the stack from the medium to be cooled, and to leave the hot end for rejection to an ambient heat reservoir. These roles are filled by two heat exchangers.

The performance of a practical refrigeration system is strongly linked with the effectiveness of its heat exchangers,[9] and a major factor controlling effectiveness is the size of the exchanger. This fact presents a particular challenge in thermoacoustic refrigerators (and also prime movers) because the useful length of a heat exchanger in a thermoacoustic engine is roughly equal to the acoustic displacement amplitude, typically only 10^{-3}–10^{-2} m. Therefore, improved understanding of these heat exchangers is a key requirement for the practical development of thermoacoustic refrigeration. This important issue has been addressed by both experimental[3,10–13] and theoretical[14–18] approaches.

The experiment described in Ref. 11 sets the stage for the present investigation. A heated wire was introduced into an acoustic standing wave at a velocity antinode in an otherwise empty resonator. The heat-transfer coefficient, h, from the wire to the acoustic medium (air) was measured by electrical means. As a function of acoustic velocity amplitude, u_1, the behavior of h falls into three regimes. At small u_1, h is independent of acoustic amplitude and takes the well-known value for natural convection. At large u_1, h varies like $u_1^{1/2}$ and agrees quantitatively with the appropriate steady-flow heat-transfer correlation for forced convection, after averaging over the instantaneous speeds occurring throughout an acoustic cycle; this is called the ''time-average steady-flow equivalent'' (TASFE) approximation.[19] At intermediate u_1, the value of h falls substantially below that for forced convection; this last regime is described as being ''bottlenecked.''

The origin of the bottleneck lies in the character of the acoustic motion.[11] In steady flow, a representative packet of gas approaches the heated wire from one direction, removes some heat from it, and flows off to infinity in the opposite direction, where it cannot influence subsequent behavior. In acoustic flow, the packet of gas oscillates back and forth, repeatedly returning to the vicinity of the heated wire; without some other mechanism for removing heat from the packet, the temperature of the gas in the packet must eventually approach that of the wire. From the perspective of this physical argument, the surprising feature of the heated-wire experiment is not that a bottleneck exists at moderate ampli-

a)Electronic mail: gmozurke@ford.com

TABLE I. Characteristics of the heat exchangers used in this study.

Configuration	Number of tubes	Outer diameter, d (mm)	Inner diameter (mm)	Spacing (mm)	Surface area, S (cm^2)	Distance from velocity node, z (m)
A	12	2.36	1.65	5.08	50.3	0.028
B	7	3.97	3.26	8.89	49.6	0.32
C	screen	0.34	⋯	1.23	55.8	0.028

tude, but rather that the TASFE approximation holds at large amplitude. Reference 11 argues that acoustic streaming is the ''other mechanism'' that opens the bottleneck.

The experiment just described, performed for an isolated wire in an otherwise empty acoustic resonator, has limited relevance to thermoacoustic engines. The geometry of actual interest places the heat exchanger immediately adjacent to a thermoacoustic stack. In this geometry, the same packet of gas that interacts with the heat exchanger during one part of its motion can also interact with the stack during another part of its motion. Therefore the interpretation of the bottleneck given in the previous paragraph makes a clear physical prediction: Because the gas packet now has a place to reject its heat (namely, into the adjacent end of the stack), the heat-transfer bottleneck in the intermediate regime should disappear. That is, the TASFE heat-transfer rate should be observed whenever it exceeds that from natural convection. The experiment described in this paper was undertaken largely to test this prediction.

II. EXPERIMENTAL METHOD

A. Apparatus

Measurements were performed using a modular thermoacoustic refrigerator.[20] The thermoacoustic stack, 25.4 mm long, consisted of stainless-steel honeycomb having 0.8-mm hexagonal pores and a total pore perimeter of 14 m. The stack and flanking heat exchangers were contained in a plastic housing that formed part of a quarter-wave resonator. The majority of the resonator was constructed from stainless-steel tubes of approximately 6.6 cm inside diameter, and the total length of the resonator could be changed by adding or omitting tube segments. The vertically oriented resonator was driven from the bottom, near a velocity antinode, by a commercial, high excursion loudspeaker (Model DL-10X, ElectroVoice, Buchanan, MI), and the stack was located near the velocity node at the upper end. The velocity amplitude at the heat-exchanger location was calculated from

$$u_1(z) = \frac{p_L}{\rho c} \sin\left(2\pi \frac{fz}{c}\right), \tag{1}$$

where f is the frequency of the standing wave, z is the distance from the closed, upper end of the resonator, p_L is the measured dynamic pressure at the velocity node ($z=0$), and ρ and c are the mean gas density and speed of sound.

Measurements were made on the heat exchanger adjacent to the upper end of the stack, facing the velocity node. When the thermoacoustic engine is acting as a refrigerator, this is the ''hot-end'' exchanger, i.e., the one that extracts heat. For the present experiment, however, the temperatures of the two heat exchangers were varied over such wide ranges that either one could be hotter or colder. Nevertheless, I will call the exchanger facing the velocity node the ''hot-end'' exchanger as a convention. The ''cold-end'' exchanger is adjacent to the end of the stack facing the loudspeaker. Through the nonlinear terms in the Navier–Stokes equation, an intense sound wave can be ''rectified,'' causing steady convection of the gas inside the resonator. This process, known as acoustic streaming,[21,22] can transfer heat from the Joule-heated loudspeaker to the cold-end heat exchanger.[20,23] It is because the amount of heat thus transported is uncertain that the measurements were made on the opposite end of the stack.

Although the heat exchangers used in previous work[20] consisted of aluminum tubes surrounded by and soldered to reticulated aluminum foam, simpler geometries were chosen for the present investigation. Each hot-end heat exchanger consisted of several equally spaced, parallel copper tubes oriented transverse to the resonator axis, mounted into an acrylonitrile–butadiene–styrene (ABS) housing using a cyanoacrylate adhesive (Loctite #495). The housing formed a segment of the modular resonator. The tubes were located as close as possible to the stack without touching it, the estimated gap between stack and tubes being <0.3 mm. Configuration A consisted of 12 parallel, evenly spaced tubes mounted in a closed-end housing that fixed the distance from the end of the resonator to the tube centerline at 28 mm. Configuration B consisted of 7 tubes mounted in an open-ended housing, allowing the exchanger to be located at a substantial distance (0.32 m) from the end of the resonator, in order to increase the acoustic velocity at the exchanger. A third heat exchanger (configuration C) was constructed by soldering a copper screen to four parallel tubes in a closed-end ABS housing similar to that used in configuration A. The diameter of the wires in the screen was 0.34 mm and their center-to-center spacing was 1.23 mm. This geometry represents a first small step beyond the idealized, parallel-tube heat-exchanger geometry toward a more practical, finned-tube design. Parameters relevant to all three geometries are presented in Table I.

B. Measurements

The experiment involved establishing an acoustic standing wave of known amplitude, measuring the quantity of heat transferred in steady state through the hot-end heat exchanger, and measuring the temperature difference across which the heat transfer occurred.

On theoretical grounds, one expects the quantity of heat transferred to the hot-end heat exchanger, Q_H, to depend on

the temperature difference between the exchanger, T_{hhx}, and the surrounding gas, T_g. For engineering purposes, on the other hand, the more useful temperature difference is that between the heat exchanger and the adjacent end of the stack, T_H. T_H is a well-defined and easily measured quantity that enters into the theory of thermoacoustic heat transport in the stack, while T_g varies with position near the end of the stack and around the heat-exchanger tubes. Therefore the heat-transfer rates in this experiment were referred to $T_H - T_{hhx}$.

The temperature of the heat exchanger was adjusted by circulating water in a closed loop containing the heat exchanger, a temperature-controlled bath, a peristaltic pump, and a variable-area flow meter. The temperature of the water entering the exchanger was determined using a chromel–alumel (type *K*) thermocouple, and the temperature change ΔT between the inlet and outlet manifolds was determined by a copper–constantan (type *T*) differential thermocouple. The average temperature, $T_{hhx}=T_{\text{inlet}}+\Delta T/2$, is reported. The hot-end heat flow was determined from

$$Q_H=\rho_w \dot{V} C_w \Delta T, \tag{2}$$

where ρ_w and C_w are the density and heat capacity of water and $\dot{V}$ is its volume flow rate. $\dot{V}$ was set to 3.8 cm^3/s with an uncertainty of $\pm 8\%$, which was the dominant determinant of the overall accuracy of the heat measurement. Accordingly, ΔT was roughly 7 K for the largest heat flow encountered. Systematic error was assessed by running water through the hot heat exchanger in the absence of acoustic excitation. The temperature difference between the water and ambient was varied over the range ± 15 K to simulate circumstances in the actual experiment. The largest observed $|Q_H|$ initially was 4.5 W but was reduced to 2 W by wrapping foam around the portions of the tubes exposed to ambient temperature. Viscous heating of the flowing water was calculated to be not more than a few mW. The remaining, unaccounted 2 W presumably involved conduction through solid portions of the apparatus.

The temperature of the hot end of the stack, T_H, was measured using a chromel–alumel thermocouple sheathed in stainless steel, with the junction grounded to the end of the sheath. To ensure that the measurement was not influenced by the gas temperature adjacent to the end of the stack, the thermocouple was greased and inserted through a stack pore. Because the sheath diameter was chosen to fit snugly into the pore, sheath-to-pore contact was maintained over the entire length of the stack. The junction was located flush with the hot end of the stack while the leads issued from the cold end. Based on an approximate dimensional argument, the systematic error arising from temperature difference between the thermocouple and the hot end of the stack was estimated to be less than 1 K.

The value of T_H was not controlled. In steady state, T_H took whatever value was required to equalize the net heat pumped up the stack (thermoacoustic heat flux less thermal conduction through stack material and gas) and the heat extracted into the hot-end heat exchanger. When the temperature difference across the stack was small, or when the ''hot'' end was colder than the ''cold'' end, the large amount of thermoacoustically pumped heat produced a large temperature drop between stack and heat exchanger. Increasing the temperature of the hot end or decreasing the temperature of the cold end reduced the quantity of heat pumped, and the temperature drop to the heat exchanger decreased accordingly.

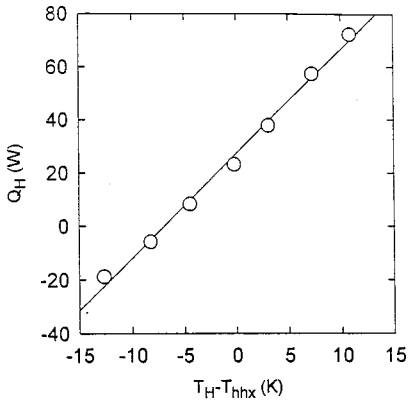

FIG. 1. Measured heat flow through the hot-end heat exchanger vs temperature difference between the hot end of stack and the hot-end heat exchanger. Configuration B, helium–argon mixture at 10 bar, $p_L=30$ kPa, $f=224$ Hz.

To establish the standing wave, the loudspeaker was driven from a signal synthesizer through a power amplifier. Operation was maintained at a specified dynamic pressure amplitude and on resonance by means of computer-controlled adjustment of the synthesizer's amplitude and frequency, using feedback from a dynamic pressure sensor (PCB Piezotronics model 121A) in the closed end of the resonator. Temperatures were monitored and Q_H was calculated several times per minute.

The first step of the experimental procedure consisted of establishing the two heat exchangers' flow rates and bath temperatures, after which the signal to the loudspeaker was turned on and maintained on resonance at the designated amplitude. The temperatures and Q_H were monitored until they reached steady state and were recorded. The loudspeaker signal was adjusted to a new amplitude, and the monitoring and recording were repeated. Once a sequence of amplitudes was completed, the loudspeaker was turned off (to reduce heating of the working fluid and to save wear and tear on the loudspeaker) until new bath temperatures were established. The temperatures of the baths were adjusted in tandem, such that their mean temperature was held approximately at room temperature.

III. RESULTS

For each dynamic pressure level, the steady-state heat flow through the hot-end heat exchanger, Q_H, was plotted against T_H-T_{hhx} (Fig. 1). The data shown in Fig. 1 were generated by changing the temperatures of the hot- and cold-end heat exchangers through changes in the bath temperatures. A least-squares fit to the form $Q_H=Q_0+q'(T_H-T_{hhx})$ is superimposed.

The intercept, Q_0, in Fig. 1 is approximately 20 W. Based on the expectation that no heat should flow through zero temperature difference, one may be inclined to attribute this offset to experimental error. Yet the systematic errors in

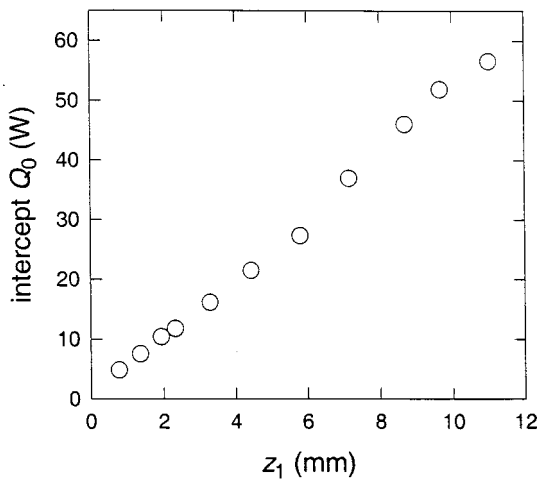

FIG. 2. Heat flow at zero temperature difference, Q_0, vs free-stream displacement amplitude, z_1. Configuration B, helium–argon mixture, 224 Hz.

heat flow (2 W) and temperature difference (1 K), estimated as described in Sec. II B, are too small to explain the magnitude of Q_0. The dependence of the offset on free-stream acoustic displacement amplitude, $z_1 = u_1/(2\pi f)$, is shown in Fig. 2 for configuration B. For this set of data, T_H happened to fall within 2 K of ambient for all measurements. Thus the large offsets plotted in Fig. 2 all occurred for *both* T_H *and* T_{hhx} within 2 K of ambient. It seems unlikely that such large heat flows could be caused by heat leaks through a temperature difference of 2 K. Therefore the offsets are real. A physical interpretation of the origin of Q_0 is proposed in Sec. IV.

Because of the offset, the slope q' was used to define the heat-transfer coefficient unconventionally by $h = q'/S$, where S is the surface area of the tubes. Values thus obtained were converted to nondimensional Nusselt number, Nu, in the conventional manner,

$$\mathrm{Nu} = \frac{hd}{k_g}, \tag{3}$$

where d is the outside diameter of the tubes and k_g is the thermal conductivity of the gas. The acoustic velocity amplitude was converted into an ''acoustic'' Reynolds number by

$$\mathrm{Re}_1 = \frac{\rho u_{1,\mathrm{corr}} d}{\mu}, \tag{4}$$

where μ is the viscosity of the gas and $u_{1,\mathrm{corr}}$ equals u_1 multiplied by the ratio of the total cross-sectional area of the resonator to the unobstructed area between the tubes. The correction is required by the convention that the Reynolds number for an obstructed flow is based not on the free-stream velocity but on the maximum velocity in the plane of the obstruction.

The TASFE prediction for heat transfer from transverse tubes was derived from the corresponding steady-flow correlation. Zukauskas has thoroughly reviewed heat transfer from a single tube in steady cross flow.[24] He recommends the following correlation:

$$\mathrm{Nu}\,\mathrm{Pr}^{-0.37} = \begin{cases} 0.75\,\mathrm{Re}^{0.4}, & 1 < \mathrm{Re} < 40 \\ 0.51\,\mathrm{Re}^{0.5}, & 40 < \mathrm{Re} < 1000 \\ 0.26\,\mathrm{Re}^{0.6}, & 1000 < \mathrm{Re} < 20\,000, \end{cases} \tag{5}$$

where Pr is the Prandtl number. To obtain the TASFE prediction for heat transfer from a single tube in oscillatory cross flow, this correlation was assumed to extend to $\mathrm{Re}=0$, $\mathrm{Re}_1 \sin(2\pi f t)$ was substituted for Re, and the time average over one half cycle was computed numerically. The numerical results were parametrized by

$$\log_{10}(\mathrm{Nu}\,\mathrm{Pr}^{-0.37}) = -0.2065 + 0.3369x + 0.033\,22x^2, \tag{6}$$

where $x = \log_{10}(\mathrm{Re}_1)$. Values of Nu obtained from this parametrization agree with the numerical results within $\pm 3\%$ over the range $2 < \mathrm{Re}_1 < 20\,000$. In a previous work, the author used the expression[11]

$$\mathrm{Nu}_{\mathrm{old}}\mathrm{Pr}^{-0.37} = 0.39\,\mathrm{Re}_1^{0.5}, \tag{7}$$

over the limited range $\mathrm{Re}_1 < 1000$. This ''old'' expression was obtained by assuming that the square-root dependence in the second line of Eq. (5) holds to zero velocity and numerically averaging over one half cycle. The ratio of Nu from Eq. (6) to $\mathrm{Nu}_{\mathrm{old}}$ from Eq. (7) is 1.22, 1.013, 1.000, and 1.229 at $\mathrm{Re}_1 = 10,\ 10^2,\ 10^3$, and 10^4, respectively.

The experiments reported here used not a single tube but a row of tubes. In general, heat transfer from a bank of tubes exposed to cross flow is larger than that given by Eq. (5). Yet a careful reading of Zukauskas and detailed examination of his figures reveals that the first row of tubes in a bank generally obeys Eq. (5) while rows deeper into the bank exhibit increased heat transfer due to flow disturbances propagating from the first row. Therefore it is assumed here that the single-tube result applies equally well to a single row of tubes, and Eq. (6) is used as the basis for comparison with the experimental data. With some effort it can be shown that Zukauskas's correlation for a staggered bank of tubes gives moderate to good agreement (depending on porosity) with correlations for stacks of woven screens.[25] Therefore Eq. (6) will also be used for comparison with a single layer of screen.

The experimental results will also be compared to an empirical expression that was used to represent heat transfer for an isolated tube in an acoustic standing wave.[11] As described in Sec. I, the heat-transfer coefficient for an isolated tube falls substantially below the values predicted by Eq. (7) over a certain range of Re_1 that is described as being ''bottlenecked.'' For $\mathrm{Re}_1 < 1000$, this bottlenecked behavior can be expressed in the form[11]

$$\mathrm{Nu}_{\mathrm{bottleneck}}\,\mathrm{Pr}^{-0.37} = \frac{0.39\,\mathrm{Re}_1^{0.5}}{1 + 88/\mathrm{Re}_S}, \tag{8}$$

from which I have omitted a contribution from natural convection. The streaming Reynolds number is defined by $\mathrm{Re}_S = \rho u_{1,\mathrm{corr}}^2/(2\pi f \mu)$.

Figure 3 shows the nondimensional heat-transfer coefficient for configuration A with pure helium ($\mathrm{Pr}=0.68$) and with a mixture consisting of 80 at.% He and 20 at.% Ar ($\mathrm{Pr}=0.40$). Measurements for the mixture were obtained at

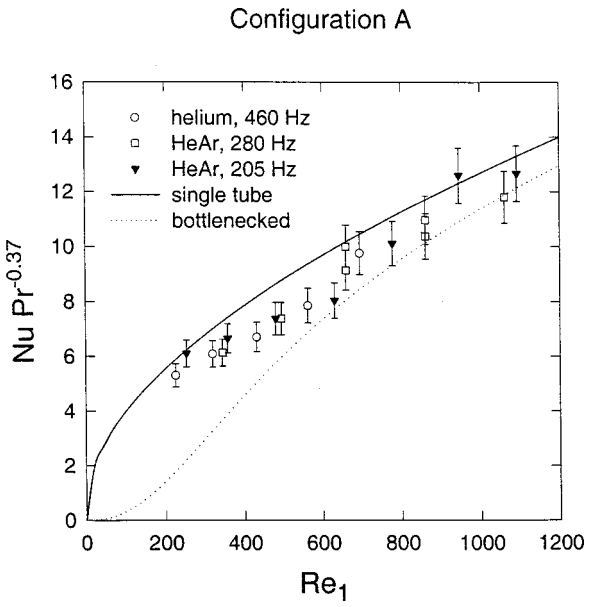

FIG. 3. Nondimensional heat-transfer coefficient for configuration A (12 parallel tubes) using pure helium and a mixture of 20 at. % argon in helium at 10 bar. The lines show the prediction of the TASFE approximation, Eq. (6) and the bottleneck expectation, Eq. (8).

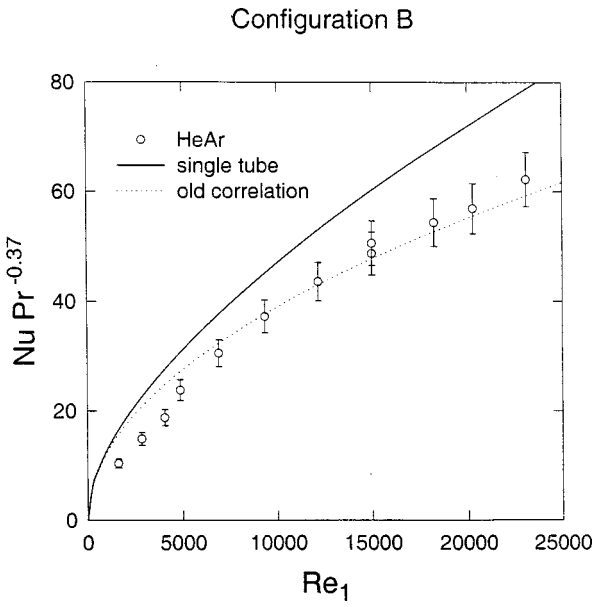

FIG. 4. Nondimensional heat-transfer coefficient for configuration B (7 parallel tubes) at 225 Hz using a mixture of 20 at. % argon in helium at 10 bar. Solid line: Eq. (6); dotted line: Eq. (7).

two different frequencies by changing the length of the resonator between the loudspeaker and stack. Each data point results from analysis of a data set similar to that shown in Fig. 1. For He and for the mixture at 280 Hz, the peak, free-stream acoustic displacement amplitude ranged from 0.22 to 0.68 mm; for the mixture at 205 Hz, it ranged from 0.30 to 1.30 mm. These peak-to-peak displacements are less than or comparable to the 2.36-mm tube diameter. The solid line is the prediction of the TASFE approximation for flow past a single transverse tube, Eq. (6), which differs little from Eq. (7) over this range of Re_1. The dotted line is the bottleneck expression, Eq. (8), calculated for pure helium; because Re_S depends on the viscosity of the gas, the bottleneck line for the mixture is slightly different. Although measurements at $\mathrm{Re}_1 > 600$ agree equally well with both expressions, the TASFE approximation fits better at smaller Re_1.

Configuration B permitted the data to be extended to larger Re_1 by increasing the diameter of the heat-exchanger tubes and moving the velocity node away from the plane of the tubes. Figure 4 shows the resulting nondimensional heat-transfer coefficients with a mixture of helium and argon in the same 80:20 proportion. The displacement amplitude ranged from 0.77 to 11.0 mm. The data fall 20%–30% below the TASFE approximation for a single tube. The data agree better with the old correlation, Eq. (7), which was expected to apply only for $40 < \mathrm{Re}_1 < 1000$. (The bottlenecked behavior is not plotted here because it differs from the TASFE approximation only at small Re_1.)

Figure 5 shows nondimensional heat-transfer coefficients for configuration C, consisting of copper screen soldered onto tubes. The working fluid was the 80:20 helium–argon mixture at 10 bar, and the displacement amplitude ranged from 0.22 to 0.90 mm. As discussed previously, the prediction of the TASFE approximation was calculated for a single bank of tubes. The data points fall appreciably below that prediction and also do not follow the bottleneck expression, but satisfactory agreement with the TASFE prediction is obtained after accounting for imperfect fin efficiency.

Fin efficiency, η, is the ratio of actual heat flow to "ideal" heat flow, i.e., assuming that all solids are perfect thermal conductors and therefore all heat-exchange surfaces reside at the same temperature. For a fin of uniform cross section extending between two tubes held at a base temperature, it is given by[26]

$$\eta = \frac{\tanh(L/\lambda)}{L/\lambda}, \quad \lambda = (k_s A/h\Pi)^{1/2}, \tag{9}$$

where A is the fin's cross-sectional area, Π is its perimeter, and L is the half the length of the fin between the two tubes.

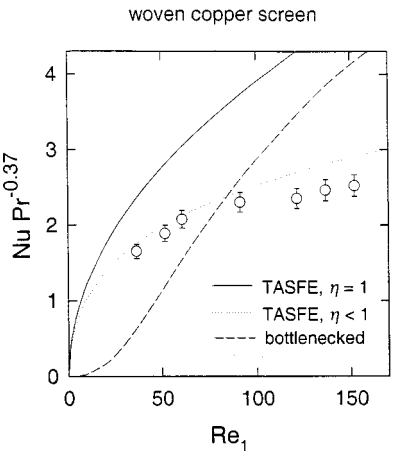

FIG. 5. Nondimensional heat-transfer coefficient for configuration C (copper screen) at 283 Hz using a mixture of 20 at. % argon in helium at 10 bar. Predictions of the TASFE approximation, Eq. (6), are shown for perfectly efficient fins (solid line) and for estimated actual fin efficiency (dotted line). The dashed line shows the bottleneck expression, Eq. (8), for perfect fins.

The thermal conductivity of the fin material is k_s. Equation (9) would apply directly, for example, to an array of wire fins oriented perpendicular to the water-bearing tubes. The copper screen, however, has a more complicated geometry, consisting of wires oriented at $\pm 45°$ with respect to the tubes. Nevertheless, because the total quantity of solid that must be heated is proportional to A and the total heat-transfer surface area is proportional to Π, it seems reasonable to approximate the behavior of the screen using these equations. Note that both λ and η decrease with increasing h. Values in Fig. 5 were computed using $k_s = 300$ W/m K, $L = 7.64$ mm, and $A/\Pi = d/4$, where d is the diameter of the wire forming the screen.

IV. DISCUSSION

One may be surprised to find nonzero heat flow when the heat exchanger is at the same temperature as the adjacent end of the stack. What matters, however, is the temperature of the gas relative to the heat exchanger, and the temperature of the gas outside the stack varies with distance along the resonator's axis. Specifically, the temperature increases with distance beyond the hot end of the stack because the thermoacoustic energy flux persists a short distance past the end of the stack,[27] and the heat deposited within the short region over which the axial component of flux approaches zero creates a time-average temperature gradient.[14] The transverse tubes, being solid surfaces interposed into an acoustic standing wave, will themselves induce thermoacoustic effects in their vicinity, causing an additional time-average axial temperature gradient. The resulting heat transfer to the tubes will depend on some appropriate spatial average of the gas temperature near the tubes. Although the detailed calculation of that average would presumably be very messy for this geometry, the qualitative behavior should be similar to that for duct-like exchangers immediately adjacent to the end of the stack. An approximate, one-dimensional model for the duct geometry[16] predicts substantial heat flow from the gas into the hot-end heat exchanger when $T_H = T_{hhx}$. In fact, for the case of perfect registry between stack and heat exchanger, a substantial fraction of the entire thermoacoustic flux pumped by the stack can be transferred to the exchanger when $T_H = T_{hhx}$.[28]

The results for configurations A and C agree fairly well with the TASFE approximation, Eq. (6). Curiously, the data for configuration B agree better with Eq. (7), which does not take into account the stronger power-law dependence on Reynolds number for $\mathrm{Re}_1 > 1000$. Thus the variation of heat transfer with square root of velocity, Eq. (7), holds at larger velocities than anticipated. The reason is unknown and could be a fruitful area for theoretical investigation.

The behavior $h \propto u_1^{0.5}$ also persists at acoustic displacements smaller than the diameter of the tubes. It is instructive to compare this behavior with an observation by Swift for parallel-duct heat exchangers.[3] For displacement amplitudes less than the length of the ducts, Swift found heat flow, Q, proportional to the square of acoustic amplitude and temperature difference between exchanger and gas, ΔT, linear in amplitude. To interpret these results, he wrote $Q = h_{\mathrm{local}} S_{\mathrm{eff}} \Delta T$, where S_{eff}, the effective surface area of the ducts, is proportional to amplitude. (In a duct, the local heat-transfer coefficient is proportional to the thermal conductivity of the gas divided by the thermal penetration depth, $h_{\mathrm{local}} \propto k_g / \delta_k$, and thus is independent of amplitude.[3,10,14]) Defining a mean heat-transfer coefficient, $h = Q/S\Delta T$, using the total heat-transfer area of the ducts, S, one finds $h = h_{\mathrm{local}} S_{\mathrm{eff}}/S \propto u_1$. Swift also observed that ΔT increased more quickly with amplitude when the displacement exceeded the duct length. This implies $h \propto u_1^b$ with $b < 1$; on the grounds that $S_{\mathrm{eff}} \rightarrow S$ in this limit, Swift anticipated $b = 0$.

Applying the same approach to transverse tubes, one may expect $h_{\mathrm{local}} \propto u_1^{0.5}$ in analogy with steady flow. Therefore, for displacements large compared to the tube diameter, one finds $h \propto u_1^{0.5}$, in agreement with the present results. For small displacements, however, h should vary more rapidly with u_1, in disagreement with the data presented here. The reason for this discrepancy is not known and remains an area for further investigation.

The expectation $b = 0.5$ in the previous paragraph is qualitatively consistent with Swift's large-amplitude results. Indeed, for displacements large compared to the length of a duct, the distinction between internal, duct flow and external flow, like that around a tube, becomes fuzzy. In a large-displacement flow, duct walls look like flattened cylinders, and the TASFE approximation should apply.

Brewster *et al.*[12] presented another model in which heat transfer is linear in acoustic amplitude, but their model seems to require ''perfect'' heat exchange, both between gas and stack and between gas and heat exchanger. Given the small surface area of the heat exchangers in the present experiment, the thermal contact between gas and exchanger must be highly imperfect.

The TASFE approximation does not apply to Gopinath and Harder's measurements of heat transport from an *isolated* cylinder in oscillatory flow, which were intentionally limited to displacement amplitudes smaller than the cylinder diameter.[13] For the case of an isolated cylinder, small amplitudes preclude observation of the TASFE regime[11,19] because heat transport is limited by the smallness of the associated streaming flows. In contrast, as demonstrated in the present work, the proximity of a thermoacoustic stack (within roughly an acoustic displacement amplitude of the exchanger) opens the streaming bottleneck by providing a more efficient path for heat removal, thereby making the TASFE approximation relevant.

V. CONCLUSION

These results show that the time-average steady-flow equivalent approximation is useful for the analysis of heat exchangers consisting primarily of transversely oriented cylindrical elements in an acoustic standing wave. Results for transverse-tube heat exchangers agree quantitatively with the TASFE approximation for acoustic Reynolds numbers less than ≈ 1000 and qualitatively for larger Re_1. Results with copper screens affixed to tubes also agree with the TASFE approximation, once imperfect fin efficiency is taken into account. It seems likely that this conclusion will also hold for

other shapes of heat-exchanger elements, as long as the flow may be broadly characterized as external flow rather than duct flow.

The regime of validity of the TASFE approximation for heat transfer from transverse tubes adjacent to a stack extends to lower Re_1 than for similar tubes in an otherwise empty resonator. In the absence of the stack, heat that has been transferred from a heat exchanger to the gas can be removed from the gas only by the relatively slow process of advection by acoustic streaming. Except at very large Re_1, this slow process controls the overall heat-transfer rate. With a stack nearby, however, the reciprocating motion of the gas allows the heat to be removed to the stack on each acoustic cycle. In this case, the overall heat-transfer rate is dominated by the process described by Eq. (5), and the TASFE approximation applies.

The heat-transfer coefficients presented here describe the *change* of heat flow with a *change* in the temperature difference between the heat exchanger and the end of the stack. A full description of the heat-transfer process requires additional knowledge of the heat flow that occurs through zero temperature difference. Qualitatively, such heat flow occurs because the gas interacting with the heat exchanger does not have the same time-average temperature as the end of the stack. Quantitatively, the specification of that additional heat flow awaits fuller characterization.

ACKNOWLEDGMENTS

I thank Steven R. Murrell and Steven R. Volkman for experimental assistance.

[1] G. W. Swift, ''Thermoacoustic engines,'' J. Acoust. Soc. Am. **84**, 1145–1180 (1988).
[2] G. W. Swift, ''Thermoacoustic engines and refrigerators,'' Phys. Today **48**, 22–28 (1995).
[3] G. W. Swift, ''Analysis and performance of a large thermoacoustic engine,'' J. Acoust. Soc. Am. **92**, 1551–1563 (1992).
[4] T. J. Hofler, ''Thermoacoustic refrigerator design and performance,'' Ph.D. dissertation, University of California San Diego, 1986.
[5] W. P. Arnott, H. E. Bass, and R. Raspet, ''General formulation of thermoacoustics for stacks having arbitrarily shaped pore cross sections,'' J. Acoust. Soc. Am. **90**, 3228–3237 (1991).
[6] M. S. Reed and T. J. Hofler, ''Measurements with wire mesh stacks in thermoacoustic prime movers,'' J. Acoust. Soc. Am. **99**, 2559 (1996). Abstract only.
[7] J. A. Adeff, T. J. Hofler, and W. C. Moss, ''Measurements with reticulated vitreous carbon stacks in thermoacoustic prime movers and refrigerators,'' J. Acoust. Soc. Am. **104**, 32–38 (1999).
[8] G. W. Swift and R. M. Keolian, ''Thermoacoustics in pin-array stacks,'' J. Acoust. Soc. Am. **94**, 941–943 (1993).
[9] See, for example, A. Bejan, *Thermal Design and Optimization* (Wiley, New York, 1996)
[10] S. L. Garrett, D. K. Perkins, and A. Gopinath, in Proceedings of the Tenth International Heat Transfer Conference, 1994, Vol. IV, pp. 375–380.
[11] G. Mozurkewich, ''Heat transfer from a cylinder in an acoustic standing wave,'' J. Acoust. Soc. Am. **98**, 2209–2216 (1995).
[12] J. R. Brewster, R. Raspet, and H. E. Bass, ''Temperature discontinuities between elements in thermoacoustic devices,'' J. Acoust. Soc. Am. **102**, 3355–3360 (1997).
[13] A. Gopinath and D. R. Harder, ''An experimental study of heat transfer from a cylinder in low-amplitude oscillatory flows,'' Int. J. Heat Mass Transf. **43**, 505–520 (2000).
[14] G. Mozurkewich, ''Time-average temperature distribution in a thermoacoustic stack,'' J. Acoust. Soc. Am. **103**, 380–388 (1998); erratum **105**, 567 (1999).
[15] G. Mozurkewich, ''Temperature distribution in a circular thermoacoustic pore,'' in *Proceedings of the 16th International Congress on Acoustics*, Seattle, WA, 1998, pp. 819–820.
[16] G. Mozurkewich, ''A model for transverse heat transfer in thermoacoustics,'' J. Acoust. Soc. Am. **103**, 3318–3326 (1998).
[17] A. Gopinath, N. Tait, and S. L. Garrett, ''Thermoacoustic streaming in a resonant channel: The time-averaged temperature distribution,'' J. Acoust. Soc. Am. **103**, 1388–1405 (1998).
[18] V. Gusev, P. Lotton, H. Baillet, S. Job, and M. Bruneau, ''Relaxation-time approximation for analytical evaluation of temperature field in thermoacoustic stack,'' J. Sound Vib. **235**, 711–726 (2000).
[19] P. D. Richardson, ''Effects of sound and vibration on heat transfer,'' Appl. Mech. Rev. **20**, 201–217 (1967).
[20] S. R. Murrell and G. Mozurkewich, ''Modular thermoacoustic refrigerator,'' J. Acoust. Soc. Am. **94**, 1772 (1993). Abstract only. An artist's rendition of the apparatus appears on the cover of Phys. Today, July 1995.
[21] W. L. Nyborg, ''Acoustic streaming,'' in *Physical Acoustics*, edited by W. P. Mason (Academic, New York, 1965), Vol. II, Part B, pp. 265–331.
[22] J. Lighthill, ''Acoustic streaming,'' J. Sound Vib. **61**, 391–421 (1978).
[23] J. C. Wheatley, T. Hofler, G. W. Swift, and A. Migliori, ''An intrinsically irreversible thermoacoustic heat engine,'' J. Acoust. Soc. Am. **74**, 153 (1983). See p. 159.
[24] A. Zukauskas, ''Heat transfer from tubes in crossflow,'' Adv. Heat Transfer **8**, 93 (1972). See especially Figs. 35, 36, 45, and 46. The correlation quoted in the present work assumes the special case of temperature-independent fluid properties.
[25] W. M. Kays and A. L. London, *Compact Heat Exchangers*, 3rd ed. (McGraw–Hill, New York, 1984). Note that their Reynolds and Nusselt numbers are based on the hydraulic diameter of the fluid space, not on the diameter of the wires.
[26] F. M. White, *Heat and Mass Transfer*, revised edition (Addison–Wesley, Reading, MA, 1988), Eqs. (2.66) and (2.56).
[27] N. Cao, J. R. Olson, G. W. Swift, and S. Chen, ''Energy flux density in a thermoacoustic couple,'' J. Acoust. Soc. Am. **99**, 3456–3464 (1996). See Fig. 2(b).
[28] See Figs. 6(c), 7(b), and Eq. (24) in Ref. 16.

Simulation of laser-generated ultrasonic waves in layered plates

A. Cheng, T. W. Murray,[a] and J. D. Achenbach
Center for Quality Engineering and Failure Prevention, Northwestern University, Evanston, Illinois 60208-3020

(Received 9 May 2000; revised 17 April 2001; accepted 23 April 2001)

A model is presented for the pulsed laser generation of ultrasound in isotropic layered plates. The stresses and displacements of the plate have been formulated in the Hankel and Laplace transform domains using the Thompson transfer matrix approach. The time domain response has been obtained by numerically inverting the transforms. Several numerical results are presented showing the normal surface displacement in the following configurations: single-layer film on a semi-infinite substrate, two layers on a semi-infinite substrate, and three-layer plates. The model provides a useful tool for the determination of which modes are generated by a laser source in a layered system. It can also be used to determine how sensitive the modes are to small changes in density, thickness, or elastic properties of the layers and to help in the selection of experimental parameters (laser spot size, pulse length, and source to receiver distance) for optimal sensitivity. © *2001 Acoustical Society of America.* [DOI: 10.1121/1.1381536]

PACS numbers: 43.35.Ud, 43.35.Zc [SGK]

I. INTRODUCTION

Optical techniques for the generation and detection of ultrasound are well established and have been utilized in a wide variety of nondestructive evaluation (NDE) and materials characterization applications.[1–3] Pulsed laser sources provide a nondestructive, noncontact means of wide-bandwidth acoustic wave generation. In order to determine the properties of a given structural system, the signal generated by a laser source in such a system must be well understood. The signals become increasingly more difficult to interpret as the structural system becomes more complex. Of particular interest in this article are the acoustic signals generated by a pulsed laser source in multilayer isotropic plates and films. Applications include the inspection of multi-layer hard coatings widely used to protect materials against wear and abrasion as well as the evaluation of the properties of bonding layers between plates.

The laser generation of ultrasound in a half-space as well as in thin plates has previously been addressed.[4–9] More recently, a model for laser generation in a thin film on a substrate has been presented.[10] In the present work, the model is extended to calculate the acoustic signal generated by a laser source in a layered isotropic plate with an arbitrary number of layers. Several interesting theoretical results are presented for coatings with a slow layer on a fast substrate and a fast layer on a slow substrate, two layers on a half-space, and a three-layer plate. The calculated time domain signals provide information about the wave modes that are generated in the various systems and may be useful, for example, for extracting, density, thickness, and elastic property data directly by comparing calculated and experimental displacements. The model also provides a tool for the selection of laser pulse parameters such as spot size and pulse width for optimal acoustic wave generation in a particular system. Dispersion curves are also presented for the layered systems to aid in the interpretation of the time domain data.

Several techniques are presented in the literature for the analysis of transient waves in both isotropic and anisotropic single-and multi-layer plates.[11–18] One approach is generalized ray theory in which the elastic waves associated with each possible sound path or ray between the source and receiver have to be determined. However, the number of sound paths that do not degenerate may be considerable for a plate with a number of thin layers, making the technique computationally intensive. The other conventional approach is by the use of the integral transform techniques which eliminate the need for sound path tracing. In this work, Hankel and one-side Laplace transforms are used to calculate the response of an elastic isotropic layered plate to an axisymmetric laser source. The response is first formulated in the Hankel and Laplace domains using the Thompson transfer matrix method.[19] The time domain response is then obtained through numerical inversion of the Hankel and Laplace transforms.

II. THEORY

A. Governing equations

Consider a multi-layered plate, which consists of n homogenous, isotropic, and linearly elastic layers, each with a thickness of h_j $(j=1,2,...,n)$. The top surface is subject to laser pulse illumination, as depicted in Fig. 1. Following the work of other authors, the laser source may be represented as an equivalent elastic boundary source consisting of distributed normal and shear loading on the plate surface.[4–6] In the following, the normal and shear loading boundary conditions are represented as f and g, respectively. Details of the source representation will be discussed later.

For a cylindrical coordinate system, the decomposition of the displacement vector in terms of the vector potential ψ (which has a component in the θ direction only) and the

[a]Author to whom correspondence should be addressed. Electronic mail: tmurray@nwu.edu

 0001-4966/2001/110(2)/848/8/$18.00

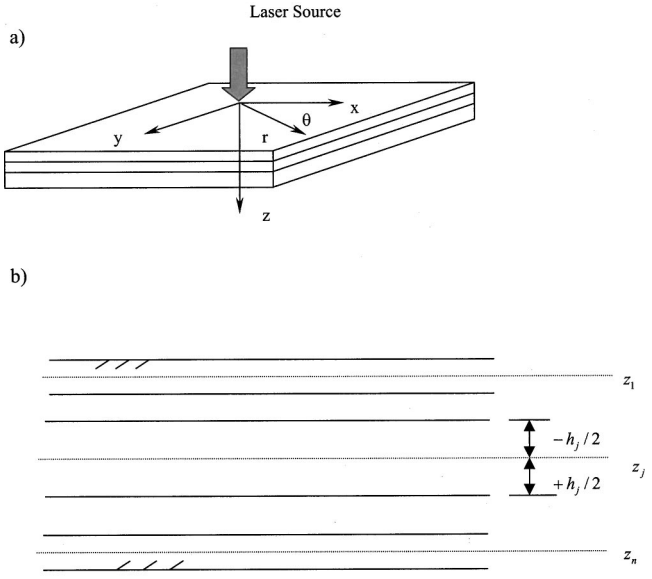

FIG. 1. Geometry used for calculation (a) and definition of variables in each layer (b).

scalar potential φ, the equation of motion in a layer can be written as

$$\varphi_{,rr}+\frac{1}{r}\varphi_{,r}+\varphi_{,zz}=s_L^2\varphi_{,tt}, \tag{1}$$

$$\psi_{,rr}+\frac{1}{r}\psi_{,r}+\psi_{,zz}-\frac{1}{r^2}\psi=s_T^2\psi_{,tt}, \tag{2}$$

where $s_L=1/c_L$ and $s_T=1/c_T$ are the slownesses of the longitudinal and transverse waves with the corresponding phase velocities c_L and c_T. The corresponding displacements and stresses may be expressed as

$$u=\varphi_{,r}-\psi_{,z}, \tag{3}$$

$$w=\varphi_{,z}+\frac{1}{r}(r\psi)_{,r}, \tag{4}$$

$$\tau_{zr}=\mu(u_{,z}+w_{,r}), \tag{5}$$

$$\tau_z=(\lambda+2\mu)w_{,z}+\frac{\lambda}{r}(ru)_{,r}, \tag{6}$$

where μ and λ are the Lamé constants. The application of Hankel and one-sided Laplace transforms to Eqs. (1) and (2) yields

$$\overline{\varphi}^{H_0}_{,zz}-\alpha^2\overline{\varphi}^{H_0}=0, \tag{7}$$

$$\overline{\psi}^{H_1}_{,zz}-\beta^2\overline{\psi}^{H_1}=0, \tag{8}$$

where the top bar "-" represents the Laplace transform and H_0 and H_1 represent the Hankel transform of order zero and unity, respectively. Also $\alpha^2=\xi^2+s_L^2p^2$ and $\beta^2=\xi^2+s_T^2p^2$. Here, ξ and p represent the spatial frequency and the time frequency, respectively. For a layer, the appropriate solutions of these equations are

$$\overline{\varphi}^{H_0}=A(\xi,p)e^{-\alpha z}+B(\xi,p)e^{\alpha z}, \tag{9}$$

$$\overline{\psi}^{H_1}=C(\xi,p)e^{-\beta z}+D(\xi,p)e^{\beta z}, \tag{10}$$

where A, B, C, and D are functions of ξ and p. Application of the Laplace and Hankel transform to the displacements and stresses in Eqs. (3)–(6) yields

$$\overline{u}^{H_1}=-\xi\overline{\varphi}^{H_0}-\overline{\psi}^{H_1}_{,z}, \tag{11}$$

$$\overline{w}^{H_0}=\overline{\varphi}^{H_0}_{,z}+\xi\overline{\psi}^{H_1}, \tag{12}$$

$$\overline{\tau}^{H_1}_{zr}=-\mu(2\xi\overline{\varphi}^{H_0}_{,z}+(s_T^2p^2+2\xi^2)\overline{\psi}^{H_1}), \tag{13}$$

$$\overline{\tau}^{H_0}_{z}=\mu((s_T^2p^2+2\xi^2)\overline{\varphi}^{H_0}+2\xi\overline{\psi}^{H_1}_{,z}). \tag{14}$$

The boundary condition at the top and bottom surfaces can be written in the Laplace and Hankel domain as

$$\overline{\tau}^{H_1}_{rz}(z=z_1-h_1/2)=\overline{g}^{H_1}(\xi,p), \tag{15}$$

$$\overline{\tau}^{H_0}_{z}(z=z_1-h_1/2)=\overline{f}^{H_0}(\xi,p), \tag{16}$$

$$\overline{\tau}^{H_1}_{rz}(z=z_n+h_n/2)=0, \tag{17}$$

$$\overline{\tau}^{H_0}_{z}(z=z_n+h_n/2)=0, \tag{18}$$

where $\overline{g}^{H_1}(\xi,p)$ and $\overline{f}^{H_0}(\xi,p)$ are equivalent elastic boundary sources used to represent acoustic wave generation by an incident laser pulse. They have been given as[5]

$$\overline{g}^{H_1}(\xi,p)=-2\frac{\xi}{p}C_0Q_0Q(\xi)Q(p), \tag{19}$$

$$\overline{f}^{H_0}(\xi,p)=-\frac{(\beta^2+\xi^2)}{p\chi}C_0Q_0Q(\xi)Q(p), \tag{20}$$

where $\chi^2=\alpha^2+p/\kappa$, κ is the thermal diffusion coefficient, C_0 is constant related to the thermal and elastic properties of the top layer, and $Q_0Q(\xi)Q(p)$ is the Hankel and Laplace transform of the laser source function $Q(r,t)$. The laser source function has been given by

$$Q(r,t)=Q_0\left[\frac{2}{R^2}e^{-2r^2/R^2}\right]\left[\frac{8t^3}{\tau^4}e^{-2t^2/\tau^2}\right], \tag{21}$$

where R is the laser spot size, τ is the laser pulse rise time, and Q_0 is the absorbed laser energy. This source has been shown to accurately represent the stress field induced by a laser in a number of practical cases.[4,5,10] The representation is subject to the following assumptions: the heating is localized to the surface layer, the point of observation is outside of the volume defined by significant thermal diffusion, and the optical energy is converted to heat close to the irradiated boundary. The first and second assumptions hold if the thermal diffusion length $(4k\tau)^{1/2}$, where τ is the laser pulse width, is sufficiently less than the top layer thickness and the source to receiver distance, respectively. The third assumption holds as long as the top layer material is a strong absorber at the generation laser wavelength.

B. Total transfer relation of a layered plate

By substituting Eqs. (9) and (10) into Eqs. (11)–(14) and considering the displacements and stresses of layer j at $z=z_j-h_j/2$ [see Fig. 1(b)], we obtain

$$\{S(z)\}_{z=z_j-h_j/2}$$

$$=\begin{bmatrix} -\xi & -\xi e^{-\alpha_j h_j} & \beta_j & -\beta_j e^{-\beta_j h_j} \\ -\alpha_j & \alpha_j e^{-\alpha_j h_j} & \xi & \xi e^{-\beta_j h_j} \\ b_j & -b_j e^{-\alpha_j h_j} & -a_j & -a_j e^{-\beta_j h_j} \\ a_j & a_j e^{-\alpha_j h_j} & -c_j & c_j e^{-\beta_j h_j} \end{bmatrix}\{\Lambda\}, \quad (22)$$

where $a_j=\mu_j(s_{Tj}^2 p^2+2\xi^2)$, $b_j=2\mu_j\xi\alpha_j$, and $c_j=2\mu_j\xi\beta_j$. The vectors

$$\{\Lambda\}=\{Ae^{-\alpha_j(z_j-h_j/2)} \;\; Be^{\alpha_j(z_j+h_j/2)} \;\; Ce^{-\beta_j(z_j+h_j/2)} \;\; De^{\beta_j(z_j+h_j/2)}\}^T$$

and

$$\{S(z)\}=\{\overline{u}^{H_1} \quad \overline{w}^{H_0} \;\; \overline{\tau}_{zr}^{H_1} \quad \overline{\tau}_z^{H_0}\}^T$$

have been introduced to simplify the notation. Similarly, at $z=z_j+h_j/2$, we have

$$\{S(z)\}_{z=z_j+h_j/2}$$

$$=\begin{bmatrix} -\xi e^{-\alpha_j h_j} & -\xi & \beta e^{-\beta_j h_j} & -\beta_j \\ -\alpha_j e^{-\alpha_j h_j} & \alpha_j & \xi e^{-\beta_j h_j} & \xi \\ b_j e^{-\alpha_j h_j} & -b_j & -a_j e^{-\beta_j h_j} & -a_j \\ a_j e^{-\alpha_j h_j} & a_j & -c_j e^{-\beta_j h_j} & c_j \end{bmatrix}\{\Lambda\}. \quad (23)$$

Substitution of Eq. (22) into (23) to eliminate the common vector $\{\Lambda\}$ yields the transfer relation of the stress-displacement vectors at the two sides of layer j,

$$\{S(z)\}_{z=z_j+h_j/2}=M_j\{S(z)\}_{z=z_j-h_j/2}, \quad (24)$$

where the layer transfer matrix M_j is obtained as

$$M_j=\begin{bmatrix} -\xi e^{-\alpha_j h_j} & -\xi & \beta e^{-\beta_j h_j} j & -\beta_j \\ -\alpha_j e^{-\alpha_j h_j} & \alpha_j & \xi e^{-\beta_j h_j} & \xi \\ b_j e^{-\alpha_j h_j} & -b_j & -a_j e^{-\beta_j h_j} & -\alpha_j \\ a_j e^{-a_j h_j} & a_j & -c_j e^{-\beta_j h_j} & c_j \end{bmatrix}$$

$$\times\begin{bmatrix} -\xi & -\xi e^{-\alpha_j h_j} & \beta_j & -\beta_j e^{-\beta_j h_j} \\ -\alpha_j & \alpha_j e^{-\alpha_j h_j} & \xi & \xi e^{-\beta_j h_j} \\ b_j & -b_j e^{-\alpha_j h_j} & -a_j & -a_j e^{-\beta_j h_j} \\ a_j & a_j e^{-\alpha_j h_j} & -c_j & c_j e^{-\beta_j h_j} \end{bmatrix}^{-1}. \quad (25)$$

Now, the application of the continuity conditions at layer interfaces from 1 to n yields

$$\{S(z)\}_{z=z_n+h_n/2}=T\{S(z)\}_{z=z_1-h_1/2}, \quad (26)$$

where the total transfer matrix T is obtained as

$$T=M_n M_{n-1} M_{n-2}\cdots M_{j+1} M_j M_{j-1}\cdots M_3 M_2 M_1, \quad (27)$$

which transfers the displacements and stresses from one side of the layered plate to the other side.

C. Total transfer relation for a layered plate on a half-space

For a homogeneous, isotropic, and linearly elastic half-space, the two upgoing bulk wave modes vanish such that B and D in Eqs. (9) and (10) are equal to zero. Following the same procedure that leads to the layer transfer matrix, one can obtain the transfer relation for a half-space, labeled by $n+1$, as

$$\{S(z)\}_{z=z_n+h_n/2}=\begin{bmatrix} -\xi & \beta_{n+1} & 0 & 0 \\ -\alpha_{n+1} & \xi & 0 & 0 \\ b_{n+1} & -a_{n+1} & 1 & 0 \\ a_{n+1} & -c_{n+1} & 0 & 1 \end{bmatrix}\{\Lambda^*\}$$

$$=M_{n+1}\{\Lambda^*\}. \quad (28)$$

where

$$\{\Lambda^*\}=\{Ae^{-\alpha_{n+1}(z_n+h_n/2)} \quad Ce^{-\beta_{n+1}(z_n+h_n/2)} \quad 0 \quad 0\}^T.$$

The application of the continuity conditions at the interface in between the layered plate and the half-space, i.e., substituting Eq. (28) into (26), yields

$$\{\Lambda^*\}=T^*\{S(z)\}_{z=z_1-h_1/2}=M_{n+1}^{-1}T\{S(z)\}_{z=z_1-h_1/2}. \quad (29)$$

Now, the total transfer matrix T^* consists of the total transfer matrix of the layers T and the transfer matrix M_{n+1} for the half-space.

D. Transient response

Introduction of the boundary conditions defined by Eqs. (15)–(18) into Eq. (26) yields the displacements at the top surface of the layered plate in the Hankel and Laplace domains:

$$\begin{Bmatrix} \overline{u}^{H_1}(\xi,p) \\ \overline{w}^{H_0}(\xi,p) \end{Bmatrix}_{z=z_1-h_1/2}$$

$$=-\begin{bmatrix} T_{33} & T_{34} \\ T_{43} & T_{44} \end{bmatrix}\begin{bmatrix} T_{31} & T_{32} \\ T_{41} & T_{42} \end{bmatrix}^{-1}\begin{Bmatrix} \overline{g}^{H_1}(\xi,p) \\ \overline{f}^{H_0}(\xi,p) \end{Bmatrix}. \quad (30)$$

From Eq. (30), the Rayleigh–Lamb frequency equation for a layered plate can be derived as

$$\Delta(\xi,p)=T_{31}T_{42}-T_{32}T_{41}=0. \quad (31)$$

The transient response of the layered plate under laser source illumination can now be obtained by using the inverse Laplace and Hankel transforms as

$$u(r,t)=\frac{1}{2\pi i}\int_0^\infty\left(\int_{a-i\infty}^{a+i\infty}\overline{u}^{H_1}(\xi,p)e^{pt}\,dp\right)J_1(r\xi)\xi\,d\xi, \quad (32)$$

$$w(r,t)=\frac{1}{2\pi i}\int_0^\infty\left(\int_{a-i\infty}^{a+i\infty}\overline{w}^{H_0}(\xi,p)e^{pt}dp\right)J_0(r\xi)\xi\,d\xi, \quad (33)$$

where a is a real arbitrary constant. To solve Eqs. (32) and (33) analytically is very difficult as we are dealing with a multi-layered plate. However, they can be solved using numerical techniques. Note that for a case of a layered plate on a half-space the transfer matrix T^* instead of T will be used accordingly.

TABLE I. Material parameters and thermal coefficients.

Materials	c_t (km/s)	c_l (km/s)	ρ (g/cm^3)	κ (mm^2/μs)
Aluminum	3.13	6.32	2.72	$8e^{-5}$
Titanium	2.71	5.28	4.5	$7e^{-6}$
Epoxy	1.3	2.73	1.4	NA

III. NUMERICAL SIMULATION

Equations (32) and (33) are used to calculate the transient response of a layered plate. For an elastic multi-layered plate, there are an infinite number of singularities for particular frequency values in the integrand of the equations. These values correspond to an infinite number of poles associated with the zeroes of the Rayleigh–Lamb frequency equation that relates frequency and wave number for guided waves in a layered plate. Since all of the poles are simple poles for an isotropic layered plate, the integral is carried out along a contour that is not on the imaginary axis so that the singularities can be avoided. This is done by simply setting a in the inverse Laplace integral equal to a real positive constant. In this study, the quadrature numerical integration method[20] has been used to calculate the inverse Hankel transform. The numerical algorithm described by Crump[21] has been used to complete the one-sided Laplace inversion. The dispersion curves are calculated using Eq. (31). The material properties and the thermal coefficients that have been used in the calculation are listed in Table I. Here C_0 and Q_0 have been set to be unity for all cases.

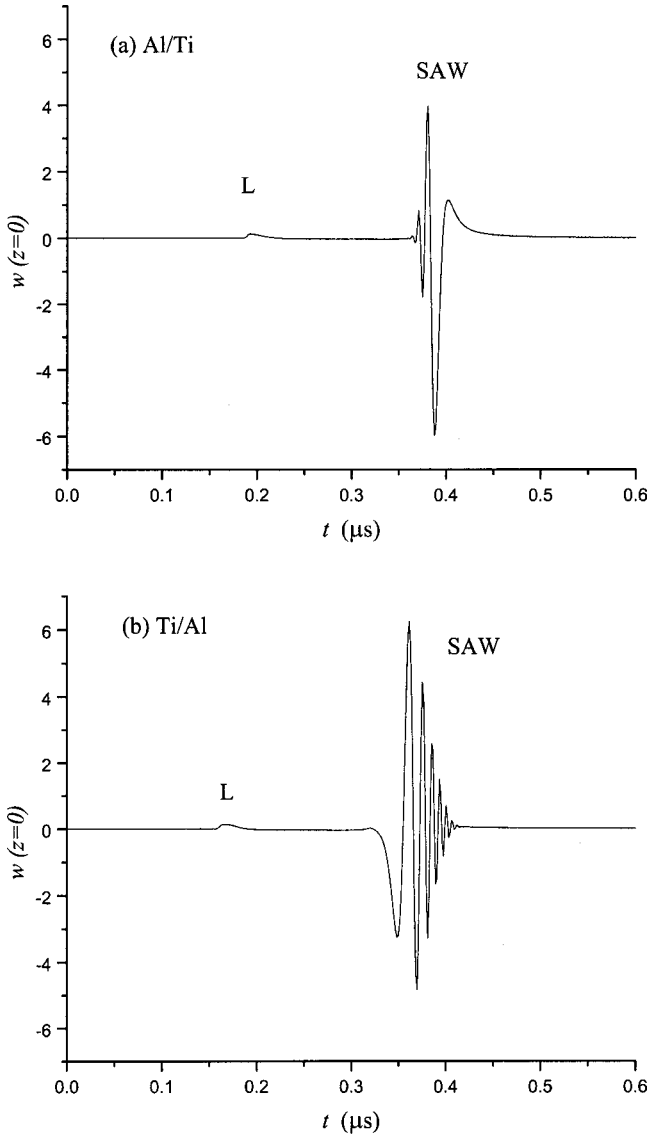

FIG. 2. Transient responses of (a) a fast layer on a slow substrate (Al/Ti) and (b) a slow layer on a fast substrate (Ti/Al).

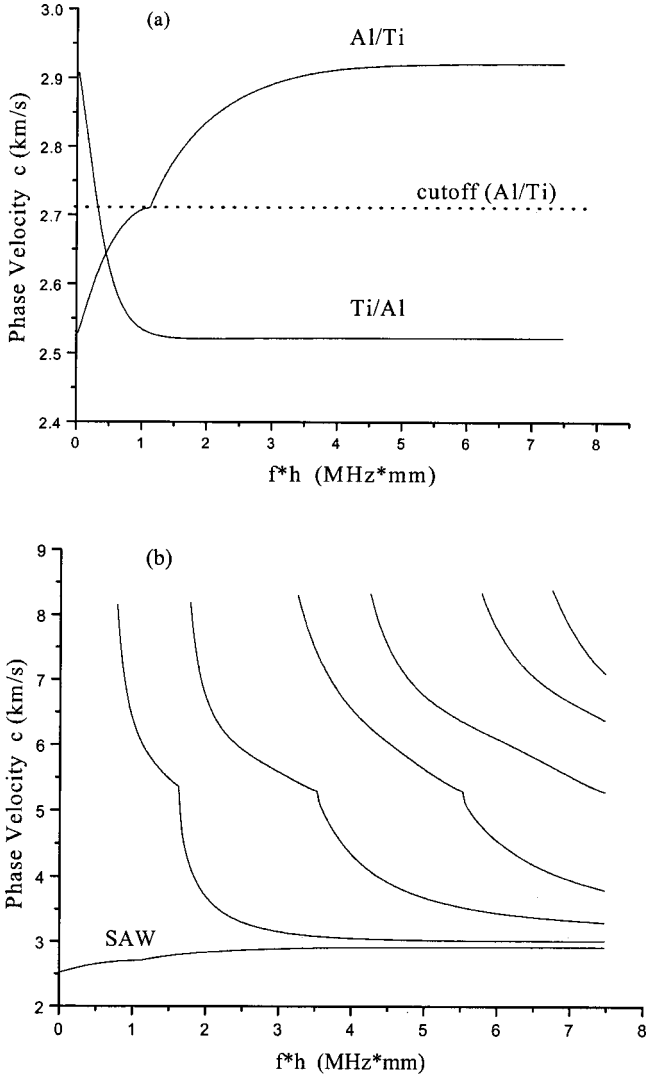

FIG. 3. Dispersion curves: (a) surface waves (lowest modes) for a slow layer on a fast substrate (Ti/Al) and a fast layer on a slow substrate (Al/Ti); (b) all modes in a fast layer on a slow substrate (Al/Ti).

As a first example, the response of a single layer on a half-space is calculated. The behavior of the generated surface waves depends on the properties of the film and the substrate and can be divided into two general cases: a slow layer on a fast substrate and a fast layer on a slow substrate.[22] In the case of a slow layer on a fast substrate, the presence of the top layer decreases the surface wave velocity below that of the Rayleigh velocity of the substrate and normal dispersion is expected. The case of a fast layer on a slow substrate shows the opposite behavior and anomalous dispersion is expected. Here, the two cases are configured as titanium/aluminum and aluminum/titanium, respectively. The

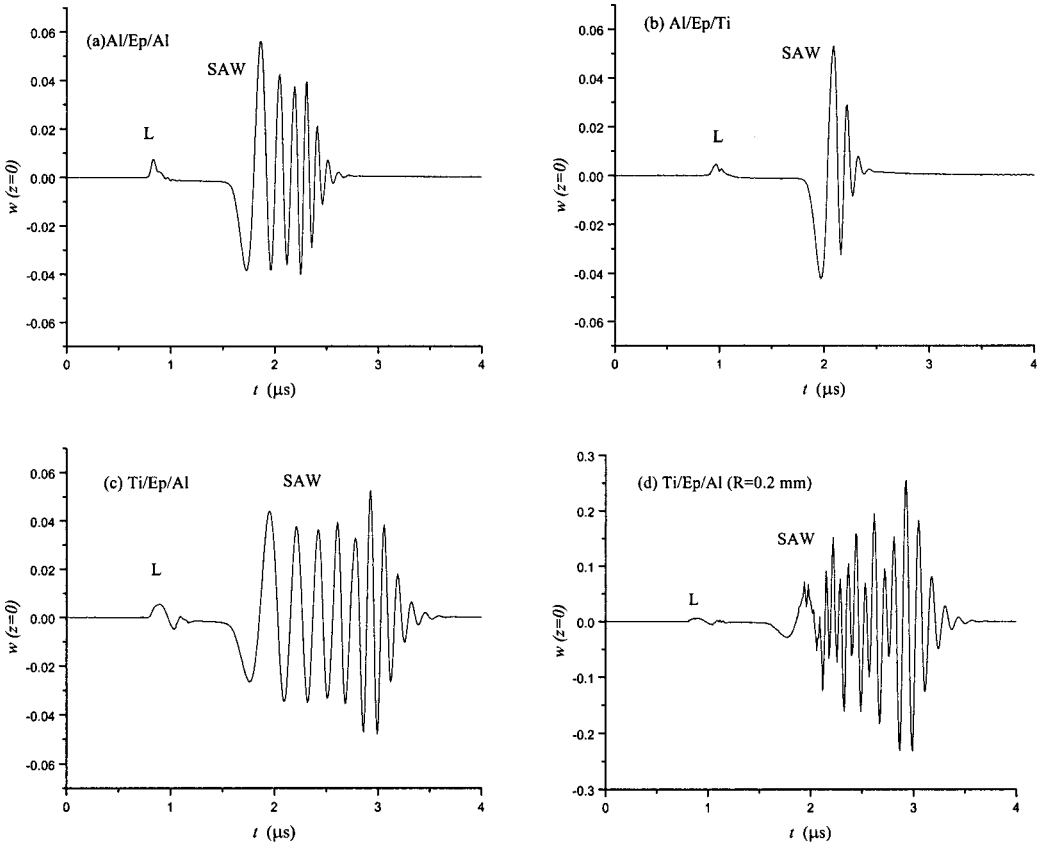

FIG. 4. Transient response of two layers on a half-space: (a) aluminum/epoxy layers on aluminum substrate, (b) aluminum/epoxy layers on titanium substrate, (c) titanium/epoxy layers on aluminum substrate, and (d) titanium/epoxy layers on aluminum substrate with the laser beam radius of $R=0.2$ mm.

transient responses at the top surfaces were calculated with a laser source-to-receiver distance of 1 mm, a laser source rise time of 1 ns, and a laser beam radius of 40 μm. The thickness of the coating layer for each case is 2.2 μm. The results are shown in Fig. 2. In each case, we first see the arrival of the grazing longitudinal wave followed by the arrival of the surface wave. The surface waves are, as expected, dispersive. For the fast layer on a slow substrate, the high-frequency components of the surface wave travel faster than the lower frequency components. Conversely, the high-frequency components of the surface wave travel slower than the lower frequency ones for the case of a slow layer on a fast substrate.

The dispersion curves of the surface waves are given in Fig. 3. The laser source primarily generates the lowest order modes, shown in Fig. 3(a), in each system. For the case of a slow layer on a fast substrate, the dispersion curve starts at the Rayleigh velocity of the substrate and slopes downward to asymptotically approach the Rayleigh velocity of the film. Just as for a simple Rayleigh wave on a free surface, there is no energy leakage into the substrate. For the case of a fast layer on a slow substrate, the situation is complicated by the presence of the cutoff velocity occurring at the transverse wave velocity of the substrate. Below the cutoff, a surface acoustic wave (SAW) solution exists which begins at the Rayleigh velocity of the substrate and proceeds to the transverse wave velocity of the substrate. Above the cutoff pseudo SAWs propagate which leak energy into the substrate. The attenuation of the pseudo SAWs is strongest just above the cutoff frequency and decreases for higher frequencies, as the SAW no longer penetrates into the substrate.[23] Note that the signal shown in Fig. 2(a) is well below cutoff and propagates as a true surface wave. Besides the modes presented in Fig. 3(a), we also see some other higher modes in the full dispersion curve given in Fig. 3(b) for the fast on slow case. There is a cutoff associated with the longitudinal wave velocity of the substrate for each of the higher modes. After passing their cutoffs, all of the higher modes will approach the transverse wave velocity of the layer as f*h increases. Similar dispersion phenomena have also been observed for the higher modes of a slow layer on a fast substrate.

Next, the displacement normal to the surface is calculated for the case of two layers on a half-space using a 2-ns laser source with a radius of 0.5 mm. The source-to-receiver distance was 5 mm. For two layers on a half-space, three configurations are considered; aluminum/epoxy on an aluminum substrate, aluminum/epoxy on a titanium substrate, and titanium/epoxy on an aluminum substrate. The thickness for the two top layers was taken as 0.045/0.01 mm. The transient responses were calculated and are shown in Fig. 4. The transient response of two layers on a half-space is different than for the single-layer case. Here, the high-frequency components of the surface waves travel slower than the lower frequency ones for all the cases in Figs. 4(a)–(c). To understand this, the dispersion curves for the three configurations have been calculated. The lowest modes are plotted in Fig. 5. All three of the phase velocity curves decrease with increasing

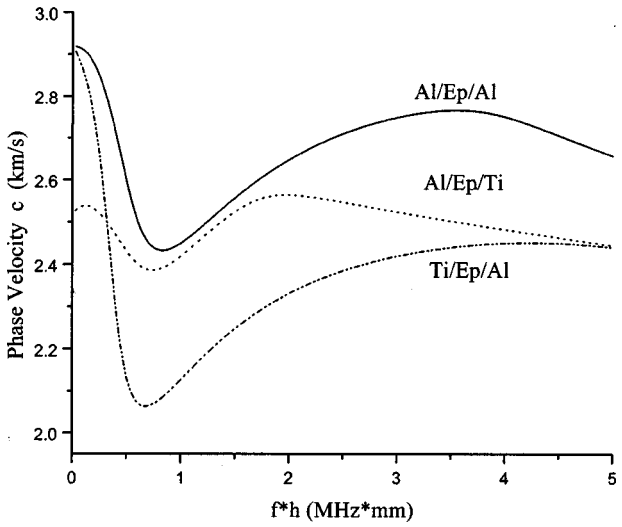

FIG. 5. Dispersion curves of lowest wave modes for two layers on a half-space including aluminum/epoxy layers on titanium substrate, titanium/epoxy layers on aluminum substrate, and aluminum/epoxy layers on aluminum substrate.

f*h in the frequency thickness range less than 0.5 MHz*mm, where the signals in Figs. 4(a)–(c) have been calculated. The dispersion curves show interesting behavior in that the arrival of two (or more) different frequency component should overlap in the time domain waveforms provided that the correct f*h range is generated. The transient response for the case (c) has been recalculated by decreasing the laser beam radius to 0.2 mm in order to generate higher-frequency components. The result is plotted in Fig. 4(d). Now the center frequency of the generated wave packet falls in the valley of the dispersion curve such that both the low-and high-frequency components of the signal travel faster than the center frequency. The higher-and lower-frequency components of the same mode are on top of each other in the time domain and what, at first inspection, appears to be the superposition of two different modes is actually the superposition of arrivals from the same mode.

We also calculated the normal displacement at the top surfaces for the case of a three-layer plate with a source-to-receiver distance of 5 mm, laser pulse rise time of 2 ns and laser beam radius of 0.5 mm. For a three-layer plate, calculations have been made for the following configurations: aluminum (0.045 mm)/epoxy (0.01 mm)/aluminum (0.045 mm). The time domain trace is shown in Fig. 6(a). The waveform looks very similar to those presented in the literature for laser-generated ultrasound in a single plate.[1] The initial arrival shows the symmetric mode (s_0) and the latter arrival the asymmetric mode (a_0). The effects of the epoxy layer are shown in the dispersion curve in Fig. 6(b) which compares the layered plate with a single aluminum plate of the same total thickness (0.1 mm). The presence of the epoxy layer causes a marked decrease in the velocity of both the symmetric and asymmetric modes. It is noted that the presence of the epoxy layer also causes a decrease in the amplitudes of both modes.

To evaluate unknown material properties of a layered structure from measured data by using an inverse technique

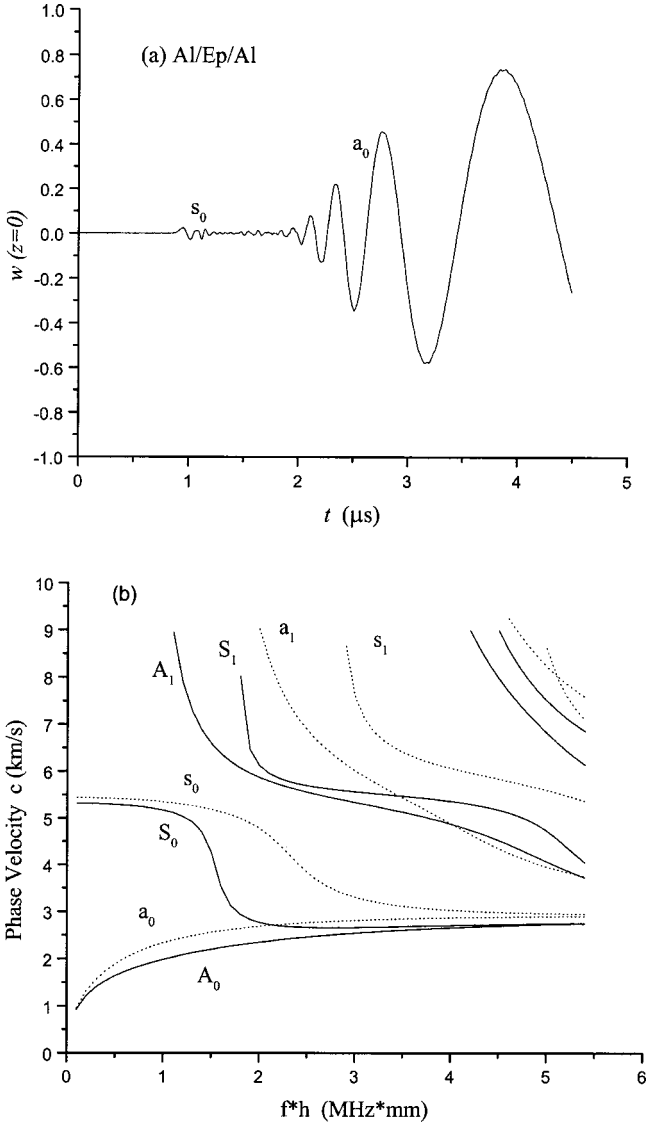

FIG. 6. (a) Transient response of the three-layer (aluminum/epoxy/aluminum) plate and (b) dispersion curves of the three-layer aluminum/epoxy/aluminum plate (solid line) as compared to the one-layer aluminum plate (dotted line) of the same total thickness.

requires a sensitivity analysis of the signals to variations of the material parameters. It can then be determined whether the unknown parameters can be extracted. As examples, we recalculated the signals in Figs. 4(c) and 6(a) with both the shear and longitudinal velocities of the epoxy layer varying ±10%. The results are shown in Figs. 7(a) and (b), where the dotted lines represent the variations (±10%) and the solid line represents the original values. It can be seen that not all the modes in the laser-generated signals are sensitive to the variation of material properties. For the case that is presented in Fig. 7(a), the surface wave mode is much more sensitive than the grazing longitudinal mode. It can also be seen that even for the surface mode itself the sensitivity is different with respect to the frequency, where the higher-frequency components of the surface wave mode vary much more than the lower-frequency ones. This suggests that the sensitivity may be improved by using a smaller spot size to generate higher frequencies. The grazing longitudinal mode, on the other hand, is not very affected by the change in the middle

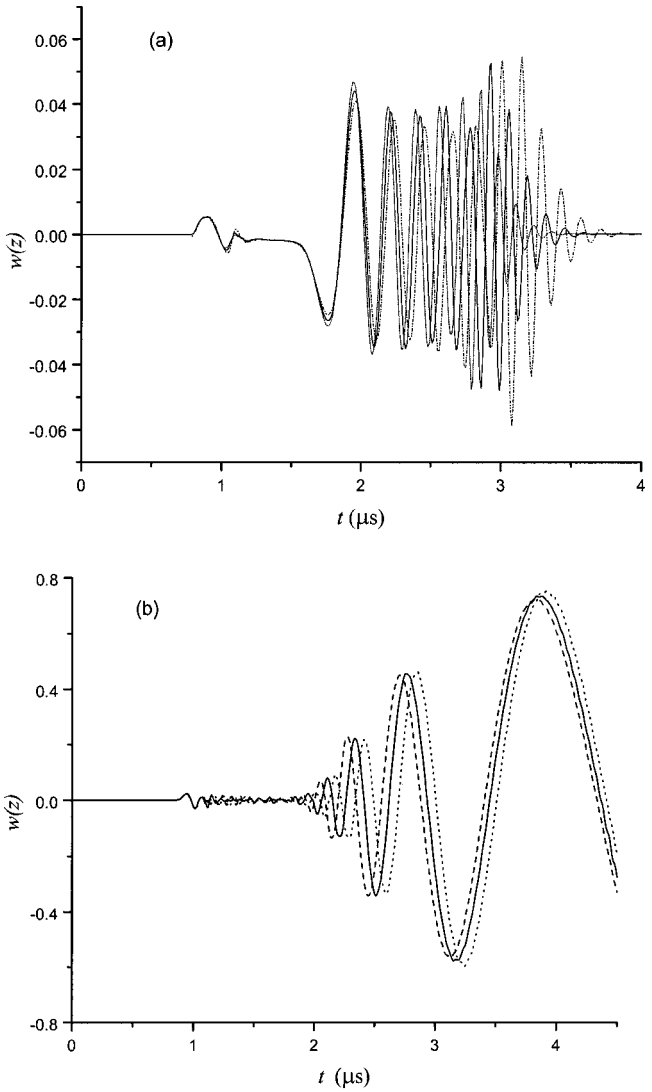

FIG. 7. Sensitivity of the signal to the variation of material properties of the second layer of (a) two layers on a half-space with Ti/Ep/Al configuration and (b) a three-layer plate with Al/Ep/Al configuration.

layer because it is primarily sensitive to the properties of the top layer. For the case that is presented in Fig. 7(b), it can be observed that the arrival of the a_0 mode is much more sensitive than that of the s_0 mode. The a_0 mode shows a relatively large shift with changes in bonding layer properties and should be able to be used to effectively extract these properties experimentally.

IV. CONCLUSIONS

The transient response of an elastic isotropic layered plate subject to laser source illumination has been studied in this work. The stresses and displacements of the layered plate generated by the laser source have been formulated in the Hankel and Laplace transform domains using the Thompson transfer matrix approach. The time domain response has been obtained by numerically inverting the transforms. Numerical results are calculated giving the normal displacement for several configurations: coatings with a slow layer on a fast substrate and a fast layer on a slow substrate, two thin layers on a half-space, and a three-layered plate. The characteristics of the laser-generated transient signals and their dispersion phenomena for each particular case have been studied in detail. The sensitivity of the signals to variations of material properties of layers has been demonstrated. The model provides a useful tool for the determination of which modes are generated by a laser source in a layered system. It can also be used to determine how sensitive the generated modes are to changes in density, thickness, or elastic properties of the layers and to help in the selection of experimental parameters (laser spot size, pulse length, and source to receiver distance) for optimal sensitivity. Future work will focus on using the model to determine the properties of layered structures using an inverse method.

ACKNOWLEDGMENT

This work was carried out in the course of research sponsored by the Office of Naval Research under Contract No. N00014-89-1362.

[1] C. E. Scruby and L. E. Drain, *Laser Ultrasonics, Techniques and Applications* (Hilger, New York, 1990).
[2] S. J. Davis, C. Edwards, G. S. Taylor, and S. B. Palmer, ''Laser-Generated Ultrasound: its properties, mechanisms, and multifarious applications,'' J. Phys. D **26**, 329–348 (1993).
[3] D. A. Hutchins, ''Mechanisms of pulsed photoacoustic generation,'' Can. J. Phys. **64**, 1247–1264 (1986).
[4] J. B. Spicer, A. D. W. McKie, and J. W. Wagner, ''Quantitative theory for laser ultrasonic waves in a thin plate,'' Appl. Phys. Lett. **57**(18), 1882–1884 (1990).
[5] J. B. Spicer, ''Laser Ultrasonics in Finite Structures: Comprehensive Modeling with Supporting Experiment,'' Ph.D. thesis, Johns Hopkins University, 1991.
[6] L. R. F. Rose, ''Point-source representation for Laser generated ultrasound,'' J. Acoust. Soc. Am. **75**, 723–732 (1984).
[7] F. A. McDonald, ''On the precursor in laser-generated ultrasound in metals,'' Appl. Phys. Lett. **56**, 230 (1990).
[8] J. Cheng, L. Wu, and S. Zhang, ''Thermoelastic response of pulsed photothermal deformation of thin plates,'' J. Appl. Phys. **76**(2), 716 (1994).
[9] T. Sanderson, C. Ume, and J. Jarzynski, ''Laser generated ultrasound: a thermoelastic analysis of the source,'' Ultrasonics **35**, 115–124 (1997).
[10] T. W. Murray, S. Krishnaswamy, and J. D. Achenbach, ''Laser generation of ultrasound in films and coatings,'' Appl. Phys. Lett. **74**(23), 3561 (1999).
[11] J. D. Achenbach, *Wave Propagation in Elastic Solids* (North-Holland, Elsevier, Amsterdam, 1973).
[12] N. Vasudevan and A. K. Mal, ''Response of an elastic plate to localized transient source,'' J. Appl. Mech. **52**, 356–362 (1985).
[13] J. Miklowitz, ''Transient compressional waves in an infinite elastic plate or elastic layer overlaying a rigid half-space,'' J. Appl. Mech. **29**, 53–60 (1962).
[14] F. Santosa and Y.-H. Pao, ''Transient axially symmetric response of an elastic plate,'' Wave Motion **11**, 271–296 (1989).
[15] D. E. Chimenti, ''Guided waves in plates and their use in materials characterization,'' Appl. Mech. Rev. **50**, 247–284 (1997).
[16] Y.-H. Pao and R. R. Gajewski, ''The generalized ray theory and transient response of layered elastic solids,'' *Phys. Acoust.*, edited by R. N. Thurston (Academic, New York, 1997), Vol. XIII.
[17] G. P. Eatwell, J. A. Simmons, and J. R. Willis, ''A New Representation for the Dynamic Green's Tensor of an Elastic Half-Space of Layered Medium,'' Wave Motion **4**, 53–73 (1982).
[18] J. H. M. T. van der Hijden, *Propagation of Transient Elastic Waves in Stratified Anisotropic Media* (North-Holland, Elsevier, Amsterdam, 1987).
[19] W. T. Thomson, ''Transmission of elastic waves through a stratified solid medium,'' J. Appl. Phys. **21**, 89–93 (1950).
[20] H. T. Lau, *A Numerical Library in C for Scientists and Engineers* (CRC Press, Inc., 1995), pp. 297–299.

[21] K. S. Crump, ''Numerical inversion of Laplace transforms using a Fourier series approximation,'' J. ACM **23**(1), 89–96 (1976).
[22] G. W. Farnell and A. L. Adler, in *Physical Acoustics*, edited by W. Mason and R. Thurston (Academic, New York, 1972), Vol. IX, pp. 35–127.
[23] P. Zinin, O. Lefeuvre, G. A. D. Briggs, B. D. Zeller, P. Cawley, A. J. Kinloch, and G. E. Thompson, ''Anomalous behavior of leaky surface waves for stiffening layer near cutoff,'' J. Appl. Phys. **82**(3), 1031 (1997).

Analysis of the asymmetric triple-layered piezoelectric bimorph using equivalent circuit models

Sung Kyu Ha[a)]
Smart Structures and Materials Laboratory, Department of Mechanical Engineering, Hanyang University, 1271 Sal-Dong, Ansan, Kyounggi-do 425-791, Korea

(Received 28 December 2000; accepted for publication 2 June 2001)

An eight-port impedance matrix and an equivalent circuit are presented for the analysis of an asymmetric triple-layered piezoelectric bimorph with separate electrical ports. The separate electric ports for the top and bottom piezoelectric layers operate independently of each other: they generate and/or sense the coupled extensional and flexural motions. Taking into account shear and rotatory inertia, the eight-port impedance model is first obtained for the bimorph. The electromechanical behavior of the piezoelectric layers, and the mechanical motions of the bimorph, are separately represented by equivalent circuits with common ports. Connecting the circuits through the common ports then leads to the overall equivalent circuit. It is demonstrated that the resonance/antiresonance frequencies and the sensor-to-actuator signal of the cantilevered bimorph for various length-to-thickness ratios can be effectively calculated by the application of the electrical network theory to the equivalent circuit. It is also shown that the electric circuit conditions on the piezoelectric layers can alter the resonance frequencies of the bimorph without changing the mechanical conditions. All the results by the present method are in excellent agreement with those by three-dimensional finite-element methods.
[DOI: 10.1121/1.1387090]

PACS numbers: 43.38.Ar, 43.38.Fx, 43.40.At, 43.40.Dx [SLE]

I. INTRODUCTION

Beam types of piezoelectric transducers have been widely used in many applications such as biomedical ultrasonic imaging analyzers, accelerometers, acoustic sensors, resonators, ultrasonic driers, inkjet printer heads, underwater electroacoustic projectors, etc.[1–4] To generate the flexural motion in the electromechanical transducers, a piezoelectric layer is bonded on each side of the thin shim layer, and they are electrically interconnected in series or parallel. The analysis so far has been mainly based on the Euler beam theory, which is accurate enough to analyze the slender piezoelectric bimorph in flexural motion.[5–10] However, as the aspect ratio of the length to the thickness decreases, such elementary theory cannot accurately predict the electromechanical behavior of the bimorph. In this case, according to the Timoshenko beam theory, the transverse shear deformation and the rotatory inertia should be taken into account. Unlike the symmetric piezoelectric bimorph with one electric port, both extensional and flexural motions can be excited in the asymmetric bimorph with the two separate electric ports.[11] In this bimorph, the electrical signals generated by the mechanical motions can be monitored separately by the two piezoelectric layers.

The impedance and admittance matrices are often used in the analysis of piezoelectric transducers since the lumped parameters conveniently describe the electromechanical behavior, including the resonance and antiresonance frequencies.[12–17] However, it is more convenient to use the electrical equivalent circuits, which represent the electromechanical behavior of the piezoelectric bimorph.[18–24] The circuits offer visual interactions of the compound transducers with external systems, such as electrical driving devices and wave propagation media.[19] The electromechanical behavior can then be easily analyzed by virtue of the powerful methods of electrical network theory.[20] The rotational angular velocity of the Langevin flexural transducer was obtained from the single-port equivalent circuit.[21] Both the vertical and angular displacements were taken into account, and a block equivalent circuit together with a four-by-four transmission matrix was then presented.[22] The dynamic models of piezoelectric actuators which included the axial deflection were later derived.[23] Most recently, an equivalent circuit of the bimorph in flexural motion was derived using the five-by-five impedance matrix.[24]

However, the shear deformation and the rotational inertia have not been taken into account yet in the analysis of the asymmetric triple-layered piezoelectric bimorph with separate electric ports. The purpose of this paper is thus to analyze the piezoelectric transducers in extensional and flexural motions by including the thickness effects. An eight-by-eight impedance matrix is first derived: one electric port for each top and bottom layer, one for extensional motion, and two flexural motions at each end. An equivalent circuit is then presented which further facilitates the analysis of the bimorph. Three cases are then studied: (1) the effects of shear and rotatory inertia on the resonance and antiresonance frequencies for various aspect ratios; (2) the variation of the resonance frequencies according to the electric open- or short-circuit conditions imposed on the two piezoelectric layers; and (3) the voltage response of one piezoelectric layer actuated by the other.

[a)]Electronic mail: sungha@hanyang.ac.kr

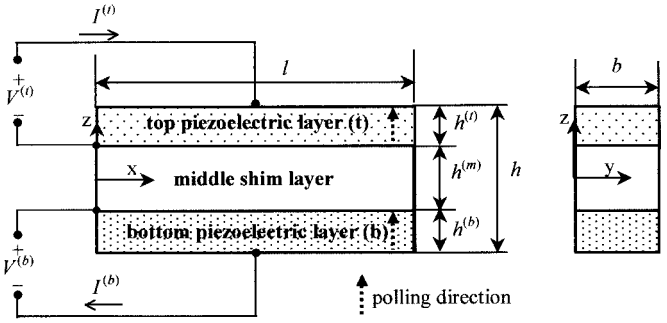

FIG. 1. Configuration of the asymmetric triple-layered piezoelectric bimorph with the electrically separate ports.

II. BASIC EQUATIONS

The asymmetric triple-layered piezoelectric bimorph considered in this study is comprised of a relatively thick middle shim and two piezoelectric layers of different material properties and thickness, as shown in Fig. 1. The piezoelectric layers are electroded on the top and bottom faces, and they have separate electrical ports. The polarizations of the piezoelectric layers direct upward; the bimorph deforms vertically and/or axially according to the directions of the electric fields and the thickness of the piezoelectric layers. The length (x direction), the total thickness (z direction), and the width (y direction) are denoted, respectively, by l, h, and b; each thickness for the middle shim and the top and bottom layers is denoted respectively by $h^{(m)}$, $h^{(t)}$, and $h^{(b)}$. The mechanical and electrical responses as well as the applied voltages and loads are supposed to be in harmonic vibration with a common angular frequency ω.

In the Thimoshenko beam theory, the total vertical deflection $u_z(x)$ of the beam is generated by both bending and shear, so that the slope of the deflection curve and the axial displacement $u_x(x,z)$ can be written as[25]

$$\frac{\partial u_z(x)}{\partial x}=\theta(x)+\psi(x), \quad u_x(x,z)=u_o(x)-z\,\theta(x), \tag{1}$$

where θ is the angle of rotation due to bending, ψ is the angle of distortion due to shear, and u_o is the axial extensional displacement at the neutral axis ($z=0$). The strain–displacement relationship thus yields the axial S_{xx} and shear strain S_{xz}

$$S_{xx}=\frac{\partial u_x}{\partial x}=\frac{\partial u_o}{\partial x}-z\frac{\partial \theta}{\partial x}, \quad S_{xz}=\frac{\partial u_x}{\partial z}+\frac{\partial u_z}{\partial x}=\psi. \tag{2}$$

The z-directional electric field $E_z^{(p)}$ of each pth piezoelectric layer ($p=t$ for the top layer and b for the bottom layer) is assumed to be constant

$$E_z^{(p)}=\frac{V^{(p)}}{h^{(p)}}, \tag{3}$$

where $V^{(p)}$ denotes the electric potential difference, or the voltage in the pth piezoelectric layer.

The one-dimensional constitutive equation for a piezoelement is written as[1]

$$\begin{aligned} &T_{xx}=c_{11}S_{xx}-e_{31}E_z, \quad T_{xz}=c_{55}S_{xz},\\ &D_z=e_{31}S_{xx}+\varepsilon_{33}E_z, \end{aligned} \tag{4}$$

where T_{xx} and T_{xz} are the axial normal and shear stresses, and D_z is the z-directional electric displacement. The material properties in Eq. (4) are defined as

$$c_{11}=\frac{1}{s_{11}^E}, \quad c_{55}=\frac{1}{s_{55}^E}, \quad e_{31}=\frac{d_{31}}{s_{11}^E}, \quad \varepsilon_{33}=\varepsilon_{33}^T-\frac{d_{31}^2}{s_{11}^E}, \tag{5}$$

where s_{11}^E and s_{55}^E denote the elastic extensional and shear compliances under the constant electric field; d_{31} the piezoelectric strain constant; and ε_{33}^T the permittivity under the constant stress.

With Eqs. (1)–(4), the extensional load N_x, the flexural moment M_x, and the transverse shear force R_x can be written as

$$N_x=\int\int T_{xx}dz\,dy=A_{11}\frac{\partial u_o}{\partial x}-e_{31}^{(t)}bV^{(t)}-e_{31}^{(b)}bV^{(b)}, \tag{6a}$$

$$\begin{aligned} M_x&=-\int\int T_{xx}z\,dz\,dy\\ &=D_{11}\frac{\partial \theta}{\partial x}+z_c^{(t)}e_{31}^{(t)}bV^{(t)}+z_c^{(b)}e_{31}^{(b)}bV^{(b)}, \end{aligned} \tag{6b}$$

$$R_x=\int\int T_{xz}dz\,dy=A_{55}\psi, \tag{6c}$$

where $z_c^{(p)}$ denotes the z-directional center coordinate of the pth layer with respect to the neutral axis, i.e., $z=0$, which is determined from the condition

$$\int c_{11}z\,dz=0. \tag{7}$$

Each stiffness A_{11}, D_{11}, and A_{55} in Eq. (6) is defined as

$$(A_{11},D_{11},A_{55})=b\int (c_{11},c_{11}z^2,\gamma c_{55})dz, \tag{8}$$

where the y-directional integration simply yielded the multiplication of the width b, and γ is a shear correction factor ($\gamma=5/6$ for the rectangular cross section).

The electric charge for each piezoelectric layer is defined as

$$Q^{(p)}=\frac{b}{h^{(p)}}\int\int D_z^{(p)}\,dz\,dx, \tag{9}$$

which is the conjugate of the voltage when the electric field is assumed as in Eq. (3).[13] Substituting Eqs. (1)–(4) into Eq. (9) yields

$$\begin{aligned} Q^{(p)}&=e_{31}^{(p)}b[u_o(l)-u_o(0)]-e_{31}^{(p)}z_c^{(p)}b[\theta(l)-\theta(0)]\\ &\quad+lb\frac{\varepsilon_{33}^{(p)}}{h^{(p)}}V^{(p)}. \end{aligned} \tag{10}$$

Note that the electric charge is generated by both extensional and flexural motions from which the rigid body translation and rotation are excluded. It is also observed that the net rotation, i.e., $\theta(l)-\theta(0)$ multiplied by the distance $z_c^{(p)}$ pro-

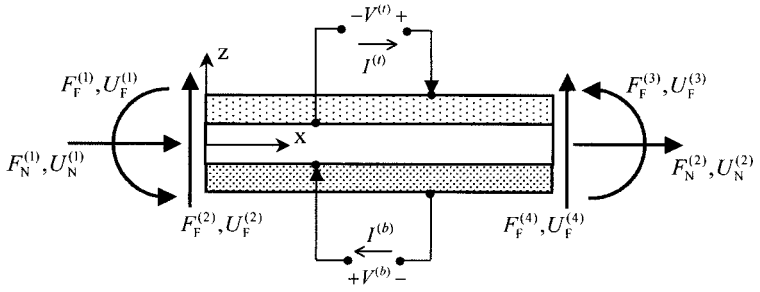

FIG. 2. The mechanical and electrical effort and flow vectors: one extensional and two flexural motions at each boundary, and one electric port for each piezoelectric layer.

duces the axial extension, which adds to the net axial extension, i.e., $u_o(l)-u_o(0)$.

Substituting Eq. (6) into the extensional and flexural equilibrium equations yields two differential equations

$$\frac{\partial^2 u_o}{\partial x^2}-\frac{\rho_h}{A_{11}}\frac{\partial^2 u_o}{\partial t^2}=0, \tag{11a}$$

$$\frac{\partial^4 u_z}{\partial x^4}-\left(\frac{\rho_h}{A_{55}}+\frac{\rho_r}{D_{11}}\right)\frac{\partial^4 u_z}{\partial x^2\partial t^2}+\frac{\rho_h}{D_{11}}\frac{\partial^2 u_z}{\partial t^2}+\frac{\rho_h}{A_{55}}+\frac{\rho_r}{D_{11}}\frac{\partial^4 u_z}{\partial t^4}=0, \tag{11b}$$

where ρ_h now indicates the mass density per unit length and ρ_r the rotatory mass density. The general solutions of Eq. (11) for the harmonic motion with the frequency ω are[25]

$$u_o(x,t)=[A_1\cos\lambda_o x+A_2\sin\lambda_o x]^{j\omega t}, \tag{12a}$$

$$u_z(x,t)=[A_3\cos\lambda_a x+A_4\sin\lambda_a x+A_5\cosh\lambda_b x+A_6\sinh\lambda_b x]e^{j\omega t}, \tag{12b}$$

where A_i $(i=1,2,...,6)$ are the coefficients to be determined using either the force or the displacement conditions at the boundary. The parameters λ_o, λ_a, and λ_b in Eq. (12) are defined as

$$\lambda_o=\omega\sqrt{\frac{\rho_h}{A_{11}}}, \tag{13a}$$

$$\lambda_a=\sqrt{\tfrac{1}{2}(\rho_S+\rho_R)+\sqrt{\tfrac{1}{4}(\rho_S-\rho_R)^2+\rho_D}}, \tag{13b}$$

$$\lambda_b=\sqrt{-\tfrac{1}{2}(\rho_S+\rho_R)+\sqrt{\tfrac{1}{4}(\rho_S-\rho_R)^2+\rho_D}}, \tag{13c}$$

where $\rho_S=\rho_h\omega^2/A_{55}$, $\rho_R=\rho_r\omega^2/D_{11}$, and $\rho_D=\rho_h\omega^2/D_{11}$. It can be observed that the shear deformation and the rotatory inertia are associated, respectively, with ρ_S and ρ_R.

III. DERIVATION OF IMPEDANCE AND ADMITTANCE MATRICES

In this section, the impedance and admittance matrices are derived from the results obtained in the previous section. The mechanical effort and flow vectors for extensional and flexural motions together with the electric voltages and currents are now defined as shown in Fig. 2. For extensional motion (denoted by the subscript N in the following notations), the mechanical effort $\mathbf{F}_N$ and flow vectors $\mathbf{U}_N$ are defined, respectively, in terms of the forces and displacements at the boundary

$$\mathbf{F}_N=\begin{pmatrix}F_N^{(1)}\\F_N^{(2)}\end{pmatrix}=\begin{pmatrix}-N_x(0)\\N_x(l)\end{pmatrix}$$

and

$$\mathbf{U}_N=\begin{pmatrix}U_N^{(1)}\\U_N^{(2)}\end{pmatrix}=j\omega\begin{pmatrix}u_o(0)\\u_o(l)\end{pmatrix}. \tag{14}$$

The common time-dependence term $e^{j\omega x}$ is omitted in the derivation. Substituting Eq. (12a) into Eq. (6a) and eliminating the coefficients A_1 and A_2 yields the relationship between $\mathbf{F}_N$ and $\mathbf{U}_N$

$$\mathbf{F}_N=\mathbf{Z}_N\mathbf{U}_N+e_{31}^{(t)}bV^{(t)}\begin{pmatrix}-1\\1\end{pmatrix}+e_{31}^{(b)}bV^{(b)}\begin{pmatrix}-1\\1\end{pmatrix}, \tag{15}$$

where Z_N now denotes a two-by-two symmetric impedance matrix for extensional motion, each component $Z_N^{(i,j)}$ given by

$$Z_N^{(1,1)}=Z_N^{(2,2)}=A_{11}\frac{\lambda_o c_o}{j\omega s_o},\quad Z_N^{(1,2)}=-A_{11}\frac{\lambda_o}{j\omega s_o}. \tag{16}$$

For notation brevity, $c_o=\cos\lambda_o l$ and $s_o=\sin\lambda_o l$. The mechanical effort $\mathbf{F}_F$ and flow vectors $\mathbf{U}_F$ for flexural motion (denoted by the subscript F) are also defined as

$$\mathbf{F}_F=\begin{pmatrix}F_F^{(1)}\\F_F^{(2)}\\F_F^{(3)}\\F_F^{(4)}\end{pmatrix}=\begin{pmatrix}-M_x(0)\\-R_x(0)\\M_x(l)\\R_x(l)\end{pmatrix}$$

and

$$\mathbf{U}_F=\begin{pmatrix}U_F^{(1)}\\U_F^{(2)}\\U_F^{(3)}\\U_F^{(4)}\end{pmatrix}=j\omega\begin{pmatrix}\theta(0)\\u_z(0)\\\theta(l)\\u_z(l)\end{pmatrix}. \tag{17}$$

Substituting Eq. (12b) into Eqs. (6b) and (6c) now yields the relationship between $\mathbf{F}_F$ and $\mathbf{U}_F$

$$\mathbf{F}_F=\mathbf{Z}_F\mathbf{U}_F+z_c^{(t)}e_{31}^{(t)}bV^{(t)}\begin{pmatrix}-1\\0\\1\\0\end{pmatrix}+z_c^{(b)}e_{31}^{(b)}bV^{(b)}\begin{pmatrix}-1\\0\\1\\0\end{pmatrix}. \tag{18}$$

The four-by-four impedance matrix $\mathbf{Z}_F$ is symmetric, and its component $Z_F^{(i,j)}$ is given by

$$
\begin{aligned}
Z_{\mathrm{F}}^{(1,1)} &= Z_{\mathrm{F}}^{(3,3)} = D_{11}\lambda_a\lambda_b(\lambda_a^2+\lambda_b^2) \\
&\quad \times(\lambda_b\lambda_1^2 c_a s_b - \lambda_a\lambda_2^2 c_b s_a)/X, \\
Z_{\mathrm{F}}^{(1,2)} &= -Z_{\mathrm{F}}^{(3,4)} = D_{11}\rho_D[\lambda_a\lambda_b(\lambda_1^2-\lambda_2^2)(c_a c_b-1) \\
&\quad -(\lambda_2^2\lambda_a^2+\lambda_1^2\lambda_b^2)s_a s_b]/X, \\
Z_{\mathrm{F}}^{(1,3)} &= D_{11}\lambda_a\lambda_b(\lambda_a^2+\lambda_b^2)(\lambda_2^2\lambda_a s_a - \lambda_1^2\lambda_b s_b)/X, \\
Z_{\mathrm{F}}^{(1,4)} &= -Z_{\mathrm{F}}^{(2,3)} = -D_{11}\rho_D\lambda_a\lambda_b(\lambda_a^2+\lambda_b^2)(c_a-c_b)/X, \\
Z_{\mathrm{F}}^{(2,2)} &= Z_{\mathrm{F}}^{(4,4)} = D_{11}\rho_D(\lambda_a^2+\lambda_b^2) \\
&\quad \times(\lambda_a\lambda_2^2 c_a s_b + \lambda_b\lambda_1^2 c_b s_a)/X, \\
Z_{\mathrm{F}}^{(2,4)} &= D_{11}\rho_D(\lambda_a^2+\lambda_b^2)(\lambda_a\lambda_2^2 s_b + \lambda_b\lambda_1^2 s_a)/X,
\end{aligned}
\tag{19}
$$

where $c_a=\cos\lambda_a l$, $s_a=\sin\lambda_a l$, $c_b=\cosh\lambda_b l$, and $s_b=\sinh\lambda_b l$; $\lambda_1^2=\lambda_a^2-\rho_S$ and $\lambda_2^2=\lambda_b^2+\rho_S$; and

$$
X=j\omega[2\rho_D\lambda_a\lambda_b(c_a c_b-1)+s_a s_b(\lambda_1^4\lambda_b^2-\lambda_2^4\lambda_a^2)]. \tag{20}
$$

With the following definitions of the current and voltage vectors as

$$
\mathbf{I}=\begin{pmatrix} I^{(t)} \\ I^{(b)} \end{pmatrix} \quad \text{and} \quad \mathbf{V}=\begin{pmatrix} V^{(t)} \\ V^{(b)} \end{pmatrix}, \tag{21}
$$

and with Eq. (10), the electric currents for the top and bottom piezoelectric layers can then be expressed as

$$
\mathbf{I}=\begin{pmatrix} e_{31}^{(t)}b \\ e_{31}^{(b)}b \end{pmatrix}(U_{\mathrm{N}}^{(2)}-U_{\mathrm{N}}^{(1)})-\begin{pmatrix} z_c^{(t)}e_{31}^{(t)}b \\ z_c^{(b)}e_{31}^{(b)}b \end{pmatrix}(U_{\mathrm{F}}^{(3)}-U_{\mathrm{F}}^{(1)})+\mathbf{C}\mathbf{V}, \tag{22}
$$

where the clamped admittance $\mathbf{C}$ is a diagonal matrix, defined as

$$
\mathbf{C}=j\omega lb\begin{bmatrix} \varepsilon_{33}^{(t)}/h^{(t)} & 0 \\ 0 & \varepsilon_{33}^{(b)}/h^{(b)} \end{bmatrix}. \tag{23}
$$

Equation (22) shows how the currents are generated by the mechanical motions in addition to the voltages.

As a result, Eqs. (15), (18), and (22) are combined into a matrix form

$$
\begin{pmatrix} \mathbf{F}_{\mathrm{N}} \\ \mathbf{F}_{\mathrm{F}} \\ \mathbf{I} \end{pmatrix}=\begin{bmatrix} \mathbf{Z}_{\mathrm{N}} & \mathbf{0} & \mathbf{P}_{\mathrm{N}} \\ \mathbf{0} & \mathbf{Z}_{\mathrm{F}} & \mathbf{P}_{\mathrm{F}} \\ -\mathbf{P}_{\mathrm{N}}^{\mathrm{T}} & -\mathbf{P}_{\mathrm{F}}^{\mathrm{T}} & \mathbf{C} \end{bmatrix}\begin{pmatrix} \mathbf{U}_{\mathrm{N}} \\ \mathbf{U}_{\mathrm{F}} \\ \mathbf{V} \end{pmatrix}, \tag{24}
$$

where the electromechanical coupling matrices $\mathbf{P}_{\mathrm{N}}$ and $\mathbf{P}_{\mathrm{F}}$ for extensional and flexural motions are obtained

$$
\begin{aligned}
\mathbf{P}_{\mathrm{N}} &= b\begin{bmatrix} e_{31}^{(t)} & e_{31}^{(b)} \\ -e_{31}^{(t)} & -e_{31}^{(b)} \end{bmatrix}, \\
\mathbf{P}_{\mathrm{F}} &= b\begin{bmatrix} -z_c^{(t)}e_{31}^{(t)} & -z_c^{(b)}e_{31}^{(b)} \\ 0 & 0 \\ z_c^{(t)}e_{31}^{(t)} & z_c^{(b)}e_{31}^{(b)} \\ 0 & 0 \end{bmatrix}.
\end{aligned}
\tag{25}
$$

Now, the impedance and admittance matrices can be easily obtained from Eq. (24). The exchange of the current vector with the voltage vector in Eq. (24) yields the impedance matrix

$$
\begin{pmatrix} \mathbf{F}_{\mathrm{N}} \\ \mathbf{F}_{\mathrm{F}} \\ \mathbf{V} \end{pmatrix}=\begin{bmatrix} \mathbf{Z}_{\mathrm{N}}+\mathbf{P}_{\mathrm{N}}\mathbf{C}^{-1}\mathbf{P}_{\mathrm{N}}^{\mathrm{T}} & \mathbf{P}_{\mathrm{N}}\mathbf{C}^{-1}\mathbf{P}_{\mathrm{F}}^{\mathrm{T}} & \mathbf{P}_{\mathrm{N}}\mathbf{C}^{-1} \\ & \mathbf{Z}_{\mathrm{F}}+\mathbf{P}_{\mathrm{F}}\mathbf{C}^{-1}\mathbf{P}_{\mathrm{F}}^{\mathrm{T}} & \mathbf{P}_{\mathrm{F}}\mathbf{C}^{-1} \\ \text{sym.} & & \mathbf{C}^{-1} \end{bmatrix}\times\begin{pmatrix} \mathbf{U}_{\mathrm{N}} \\ \mathbf{U}_{\mathrm{F}} \\ \mathbf{I} \end{pmatrix}, \tag{26}
$$

whereas the exchange of the effort vector with the flow vector in Eq. (24) yields the admittance matrix

$$
\begin{pmatrix} \mathbf{U}_{\mathrm{N}} \\ \mathbf{U}_{\mathrm{F}} \\ \mathbf{I} \end{pmatrix}=\begin{bmatrix} \mathbf{Z}_{\mathrm{N}}^{-1} & \mathbf{0} & -\mathbf{Z}_{\mathrm{N}}^{-1}\mathbf{P}_{\mathrm{N}} \\ & \mathbf{Z}_{\mathrm{F}}^{-1} & -\mathbf{Z}_{\mathrm{F}}^{-1}\mathbf{P}_{\mathrm{F}} \\ \text{sym.} & & \mathbf{C}+\mathbf{P}_{\mathrm{N}}^{\mathrm{T}}\mathbf{Z}_{\mathrm{N}}^{-1}\mathbf{P}_{\mathrm{N}}+\mathbf{P}_{\mathrm{F}}^{\mathrm{T}}\mathbf{Z}_{\mathrm{F}}^{-1}\mathbf{P}_{\mathrm{F}} \end{bmatrix}\times\begin{pmatrix} \mathbf{F}_{\mathrm{N}} \\ \mathbf{F}_{\mathrm{F}} \\ \mathbf{V} \end{pmatrix}. \tag{27}
$$

It is clearly shown in Eqs. (24), (26), and (27) how mechanical extensional and flexural motions are related and coupled with the electric voltages and currents of the piezoelectric layers; for instance, Eq. (27) shows how the electric voltages excite extensional and flexural motions. The electrical and mechanical conditions assigned to the bimorph can be easily realized in the matrices, e.g., the electrically open- or short circuits, the parallel or series connections in the piezoelectric layers, and the mechanical boundary conditions. It is noticed that the impedance and admittance matrices are symmetric, which is one of the reciprocity conditions often observed in electromechanical systems.

IV. EQUIVALENT CIRCUIT MODEL

In this section, an equivalent circuit representation of the asymmetric triple-layered bimorph is derived from the equations obtained in the previous sections. In order to do so, each equivalent circuit for the top and bottom piezoelectric layers and for the extensional and flexural motions is separately derived, and the overall equivalent circuit is then completed by connecting the circuits to each other through common terminals.

First, we define the equivalent currents $\overline{I_{\mathrm{N}}}$ and $\overline{I_{\mathrm{F}}}$, each corresponding to extensional and flexural motion as

$$
\overline{I_{\mathrm{N}}}=U_{\mathrm{N}}^{(2)}-U_{\mathrm{N}}^{(1)}, \quad \overline{I_{\mathrm{F}}}=U_{\mathrm{F}}^{(3)}-U_{\mathrm{F}}^{(1)} \tag{28}
$$

and the turns ratios of the transformers and the capacitance for the pth piezoelectric layer as

$$
\Gamma_{\mathrm{N}}^{(p)}=-e_{31}^{(p)}b, \quad \Gamma_{\mathrm{F}}^{(p)}=z_c^{(p)}e_{31}^{(p)}b, \quad C^{(p)}=\frac{lb\varepsilon_{33}^{(p)}}{h^{(p)}}. \tag{29}
$$

The electric current $I^{(p)}$ of Eq. (22) is then rewritten as

$$
I^{(p)}=-\Gamma_{\mathrm{N}}^{(p)}\overline{I_{\mathrm{N}}}-\Gamma_{\mathrm{F}}^{(p)}\overline{I_{\mathrm{F}}}+j\omega C^{(p)}V^{(p)}. \tag{30}
$$

With Kirchhoff's current laws (KCL), Eq. (30) can be represented by an equivalent circuit, as shown in Fig. 3(a), where the transformers convert the extensional and flexural motions

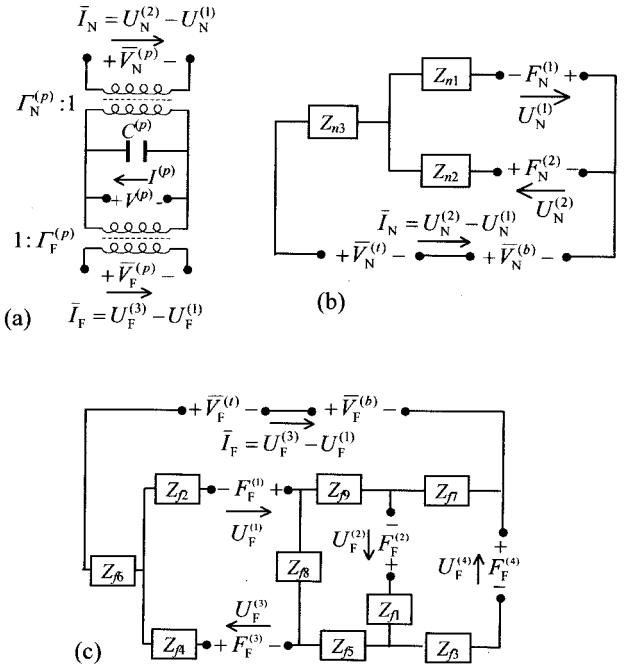

FIG. 3. Equivalent circuits (a) for the piezoelectric layer; (b) for the extensional motion; and (c) for the flexural motion of the bimorph.

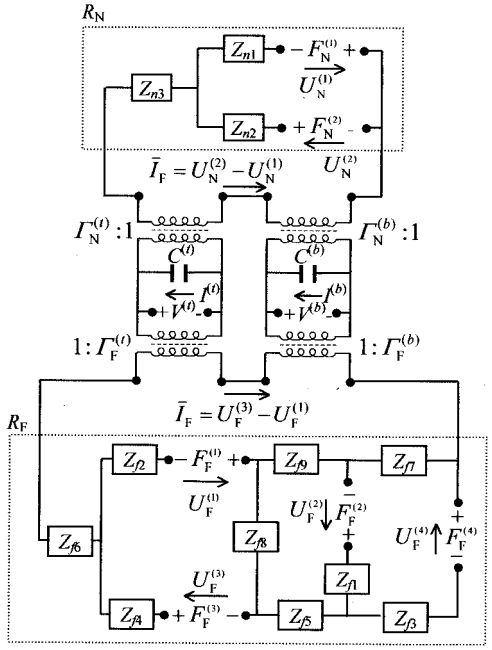

FIG. 4. Eight-port overall equivalent circuit; the circuits enclosed by the dotted box denote the impedances R_N and R_M, respectively, due to the extensional and flexural motions.

to the equivalent currents $\bar{I}_N$ and $\bar{I}_F$, respectively, by the ratios $\Gamma_N^{(p)}$ and $\Gamma_F^{(p)}$. At the same time, the transformers conversely convert the electric voltage $V^{(p)}$ to the equivalent voltages, or driving forces for extensional and flexural motions, each denoted respectively by $\bar{V}_N^{(p)}$ and $\bar{V}_F^{(p)}$

$$\bar{V}_N^{(p)} = \Gamma_N^{(p)} V^{(p)}, \quad \bar{V}_F^{(p)} = \Gamma_F^{(p)} V^{(p)}. \tag{31}$$

The terminals with $\bar{I}_N$ as current and $\bar{V}_N^{(p)}$ as voltage, denoted by $(\bar{V}_N^{(p)}, \bar{I}_N)$, will be a common port through which a circuit for extensional motion is connected to the one for the piezoelectric layer; the terminals $(\bar{V}_F^{(p)}, \bar{I}_F)$ are for flexural motion.

Next, the extensional motion in Eq. (15) is represented by an equivalent circuit with two coupled closed loops which contain two mechanical terminals, i.e., $(F_N^{(1)}, U_N^{(1)})$ and $(F_N^{(2)}, U_N^{(2)})$, and the two source terminals, i.e., $(\bar{V}_N^{(t)}, \bar{I}_N)$ and $(\bar{V}_N^{(b)}, \bar{I}_N)$. Since the equivalent current $\bar{I}_N = U_N^{(2)} - U_N^{(1)}$ for the extensional motion is common to the two piezoelectric layers, as shown in Eq. (30), two flow loops are drawn as depicted in Fig. 3(b). The impedances Z_{ni} $(i=1,2,3)$ in the circuit are now determined by applying Kirchhoff's voltage laws (KVL) to the two closed loops and using Eq. (15), and expressed in terms of the components of the impedance matrix $Z_N^{(i,j)}$

$$Z_{n1} = Z_{n2} = Z_N^{(1,1)} + Z_N^{(1,2)}, \quad Z_{n3} = -Z_N^{(1,2)}. \tag{32}$$

Next, the mechanical flexural motion described by Eq. (18) implies four closed loops in an equivalent circuit with four mechanical terminals $(F_F^{(i)}, U_F^{(i)})$, where $i=1,2,3,4$, and with the two source terminals $(\bar{V}_F^{(t)}, \bar{I}_F)$, $(\bar{V}_F^{(b)}, \bar{I}_F)$. Since the equivalent current $\bar{I}_F = U_F^{(3)} - U_F^{(1)}$ is common to the two piezoelectric layers as shown in Eq. (30), a flow loop is formed which includes both $U_F^{(1)}$ and $U_F^{(3)}$. Other loops are consequently induced, and the full circuit is drawn in Fig. 3(c). Similar to the extensional motion, the equivalent circuit is connected to those for the piezoelectric layers through the terminals $(\bar{V}_F^{(t)}, \bar{I}_F)$ and $(\bar{V}_F^{(b)}, \bar{I}_F)$. By applying KVL to the four loops in the circuit and using Eq. (18), we obtain Z_{fi} $(i=1,2,3,...,9)$ in terms of $Z_F^{(i,j)}$

$$\begin{aligned}
&Z_{f1} = Z_F^{(2,2)} + Z_F^{(2,4)}, \quad Z_{f6} = Z_F^{(1,4)} - Z_F^{(1,3)}, \\
&Z_{f2} = Z_F^{(1,1)} + Z_F^{(1,3)}, \quad Z_{f7} = -Z_F^{(1,2)} - Z_F^{(1,4)}, \\
&Z_{f3} = Z_F^{(2,2)} + Z_F^{(1,2)} + Z_F^{(2,4)} + Z_F^{(1,4)}, \\
&Z_{f8} = -Z_F^{(1,2)} + Z_F^{(1,4)}, \\
&Z_{f4} = Z_F^{(1,2)} - Z_F^{(1,4)} + Z_F^{(1,1)} + Z_F^{(1,3)}, \quad Z_{f9} = Z_F^{(1,2)}, \\
&Z_{f5} = -Z_F^{(2,4)} - Z_F^{(1,4)}.
\end{aligned} \tag{33}$$

The overall equivalent circuit is now obtained by connecting the circuits for the top and bottom piezoelectric layers to those for extensional and flexural motions through the common terminals, i.e., $(\bar{V}_N^{(t)}, \bar{I}_N)$, $(\bar{V}_N^{(b)}, \bar{I}_N)$, $(\bar{V}_F^{(t)}, \bar{I}_F)$, and $(\bar{V}_F^{(b)}, \bar{I}_F)$, as shown in Fig. 4. This equivalent circuit clearly shows how each mechanical, electrical, and electromechanical component is related to the other. Most importantly, all the circuit components are completely expressed in terms of the impedance matrix components as noted in Eqs. (16), (19), (32()), and (33). Using the circuit, we can thus observe the effects of such parameters on the transducing performance as the thickness, the length, and the material properties of the bimorph. The specified mechanical or electrical conditions are easily realized by the electromechanical equivalence: the zero-prescribed displacement and force are electrically equivalent to opening and closing the corresponding mechanical ports, respectively. We can also con-

nect other equivalent circuits to this circuit through the proper terminals in accordance with the external mechanical and electrical components attached to the bimorph.

Although the overall admittance matrix in Eq. (27) can yield the electrical admittance under the given mechanical boundary conditions, the equivalent circuit enables us to derive the electrical admittance more easily. Once the mechanical boundary conditions are assigned to the corresponding ports, the extensional R_N and flexural impedances R_F can replace the circuits enclosed, respectively, by the dotted boxes as shown in Fig. 4. Applying KVL to the circuit with the impedances yields the electrical admittance

$$\begin{pmatrix} I^{(t)} \\ I^{(b)} \end{pmatrix} = \begin{bmatrix} Y^{(t,t)} & Y^{(t,b)} \\ Y^{(b,t)} & Y^{(b,b)} \end{bmatrix} \begin{pmatrix} V^{(t)} \\ V^{(b)} \end{pmatrix}, \tag{34}$$

where each component of the admittance is obtained as

$$Y^{(t,t)} = j\omega C^{(t)} + \frac{\Gamma_N^{(t)2}}{R_N} + \frac{\Gamma_F^{(t)2}}{R_F}, \tag{35a}$$

$$Y^{(t,b)} = Y^{(b,t)} = \frac{\Gamma_N^{(t)}\Gamma_N^{(b)}}{R_N} + \frac{\Gamma_F^{(t)}\Gamma_F^{(b)}}{R_F}, \tag{35b}$$

$$Y^{(b,b)} = j\omega C^{(b)} + \frac{\Gamma_N^{(b)2}}{R_N} + \frac{\Gamma_F^{(b)2}}{R_F}. \tag{35c}$$

The poles and zeros of the admittance yield, respectively, the resonance and antiresonance frequencies of the bimorph. The electrical parallel connection conditions ($I = I^{(b)} - I^{(t)}$ and $V = -V^{(t)} = V^{(b)}$) simplify Eqs. (34) and (35) as

$$Y = \frac{1}{V} = j\omega(C^{(t)} + C^{(b)}) + \frac{(\Gamma_N^{(t)} - \Gamma_N^{(b)})^2}{R_N} + \frac{(\Gamma_F^{(t)} - \Gamma_F^{(b)})^2}{R_F}. \tag{36}$$

In the case of the symmetric layer sequence ($e_{31}^{(t)} = e_{31}^{(b)}$, $z_c^{(t)} = -z_c^{(b)}$, $\varepsilon_{33}^{(t)} = \varepsilon_{33}^{(b)}$; $C_t = C_b = C/2$, $\Gamma_N^{(t)} = \Gamma_N^{(b)}$, $\Gamma_F^{(t)} = -\Gamma_F^{(b)} = \Gamma_F/2$), Eq. (36) further reduces to

$$Y = \frac{1}{V} = j\omega C + \frac{\Gamma_F^2}{R_F}. \tag{37}$$

It is noted in Eqs. (34)–(37) that mechanical extensional and flexural conditions at the boundary can be easily realized, respectively, by R_N and R_F.

For the fixed-free end condition as shown in Fig. 5, as an example, the mechanical flows and efforts are given by

$$\begin{aligned} &U_N^{(1)} = U_F^{(1)} = U_F^{(2)} = 0, \\ &F_N^{(2)} = F_F^{(3)} = F_F^{(4)} = 0. \end{aligned} \tag{38}$$

The reduced equivalent circuits are easily drawn and illustrated in Fig. 5 using the electromechanical equivalence. Applying KVL to the circuit enclosed by the dotted box in Fig. 5 leads to the impedances R_N and R_F, each simplified, respectively, by Eqs. (32) and (33)

$$R_N = Z_{n3} + Z_{n2} = Z_N^{(1,1)}, \tag{39a}$$

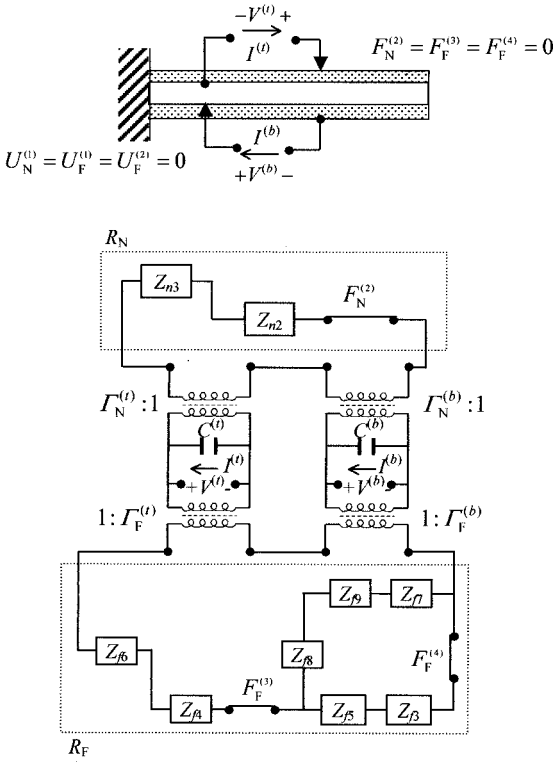

FIG. 5. Equivalent circuit of the bimorph with one end fixed and the other free.

$$R_F = Z_{f6} + Z_{f4} + \frac{(Z_{f3} + Z_{f5})(Z_{f7} + Z_{f8} + Z_{f9})}{Z_{f3} + Z_{f5} + Z_{f7} + Z_{f8} + Z_{f9}} = Z_F^{(1,1)} - \frac{(Z_F^{(1,2)})^2}{Z_F^{(2,2)}}. \tag{39b}$$

Substitution of Eq. (39) into Eq. (35) yields the electrical admittances of the bimorph subjected to the fixed-free end conditions. The electric admittance could also be derived by assigning the mechanical boundary conditions of Eq. (38) to the admittance matrix in Eq. (27), but the results by the equivalent circuit give a better understanding and visualization of the system.

One of the two piezoelectric layers can be used as an actuator and the other as a sensor. In this case, the voltage at the sensor, e.g., $V^{(b)}$, is generated by the deformation due to the actuator voltage, e.g., $V^{(t)}$. We can then calculate the sensor-to-actuator voltage signal using the condition that $I^{(b)} = 0$ in Eq. (34)

$$\frac{V^{(b)}}{V^{(t)}} = -\frac{Y^{(b,t)}}{Y^{(b,b)}}. \tag{40}$$

This type of transducer can be applied to the resonance sensor for static force measurement.[26]

V. APPLICATIONS AND DISCUSSIONS

In this section, the electromechanical behavior of the asymmetric triple-layered bimorphs in extensional and flexural motion is investigated using the equivalent circuit derived in the previous sections. The bimorph under consideration consists of PZT G1195N (point group 6 mm)

piezoelectric ceramics and stainless-steel layer for the middle shim. The material properties are as follows: for the PZT G1195N, $1/s_{11}^{E}=61.0\,\mathrm{GPa}$, $\nu=0.3$, $\rho=7600\,\mathrm{kg/m^3}$, $d_{31}=0.254\,\mathrm{nm/V}$, and $\varepsilon_{33}^{T}=15.0\,\mathrm{nF/m}$, and for the stainless steel, $1/s_{11}^{E}=200.0\,\mathrm{GPa}$, $\nu=0.3$, and $\rho=7830\,\mathrm{kg/m^3}$.

In the first case, the effects of the thickness aspect ratio $(=l/h)$, ranging from 2.5 to 15, on the resonance and antiresonance frequencies of the bimorph with the fixed-free boundary condition are probed; the thickness of each layer is given by $h^{(t)}=h^{(b)}=0.15\,\mathrm{mm}$ and $h^{(m)}=0.7\,\mathrm{mm}$. Four cases are thus considered: (1) Euler beam (no shear and no rotatory inertia); (2) only rotatory inertia; (3) only shear; and (4) Timoshenko beam (both shear and rotatory inertia). We can easily neglect the effects of shear and rotatory inertia in the analysis by assigning zero values, respectively, to ρ_S $(=\rho_h\omega^2/A_{55})$ and $\rho_R(=\rho_r\omega^2/D_{11})$ in Eq. (13). For the purpose of verification, the three-dimensional finite-element method (FEM) is used where a node in the element has four degrees of freedom, i.e., three mechanical displacements and one electric potential.[27] To assure the convergence of the frequencies within 0.1% of errors, 150 elements are used for the axial direction, and 20 elements for the thickness direction. The calculated frequencies are normalized as follows:

$$\omega^{*}=\sqrt{\frac{\rho_h\omega^2}{D_{11}}}\,l^2=\omega\sqrt{\rho_{hD}}\,l^2. \tag{41}$$

The resonance frequencies are calculated and shown in Fig. 6. It is evident that the effects of shear and rotatory inertia on the frequencies become more significant, as the bimorph gets shorter. In the higher modes, the differences are still obvious even for the high aspect ratio. The resonance frequencies calculated under the consideration of both shear and rotatory inertia agree very well with the results by the FEM for all ranges of aspect ratios. The antiresonance frequencies are shown in Fig. 7, and similar to the resonance frequencies, the effects of shear and rotatory inertia are remarkable for shorter beams and higher modes. The overall antiresonance frequencies are higher than the resonance frequencies; they show greater differences in the first frequency. In both resonance and antiresonance frequencies, the effects of the shear deformation are more significant than those of the rotatory inertia.

In the second case, we observe the changes of the fundamental frequencies according to the circuit conditions of the piezoelectric layers. All possible circuit conditions are considered, i.e., short–short, open–short, short–open, and open–open imposed on the top and bottom piezoelectric layers. The normalized frequencies versus the thickness ratios of the two piezoelectric layers $h^{(t)}/h^{(b)}$ are calculated and shown in Fig. 8; $h^{(t)}+h^{(b)}=0.3\,\mathrm{mm}$, $h^{(m)}=0.7\,\mathrm{mm}$, and $l/h=10$. The results agree very well with those by the FEM. It is observed that the fundamental frequencies increase as the number of open ports increases, and that the short–open ports yield higher frequency than the open–short ports for the asymmetric layers of $h^{(t)}/h^{(b)}<1$. Thus, depending upon the type of actuation used, the same actuator setup can generate a very different structural actuation and response.

In the third case, we examine the sensor voltage $V^{(b)}$ generated by the actuator voltage $V^{(t)}$ for three different exciting frequencies, i.e., 80% and 40% of the resonance frequencies ω_r, and the static one. The statically exciting voltage is realized by taking a very low value for the exciting frequency. The geometric dimensions and material properties are the same as in the second case. We have obtained the sensor-to-actuator voltage ratios $V^{(b)}/V^{(t)}$ versus the thickness ratios $h^{(t)}/h^{(b)}$ using Eq. (40), as shown in Fig. 9. For the given geometry and materials, the voltage ratio $V^{(b)}/V^{(t)}$ decreases as the ratio $h^{(t)}/h^{(b)}$ increases for all cases. Excellent agreements are also observed between the results by the equivalent circuit and the FEM.

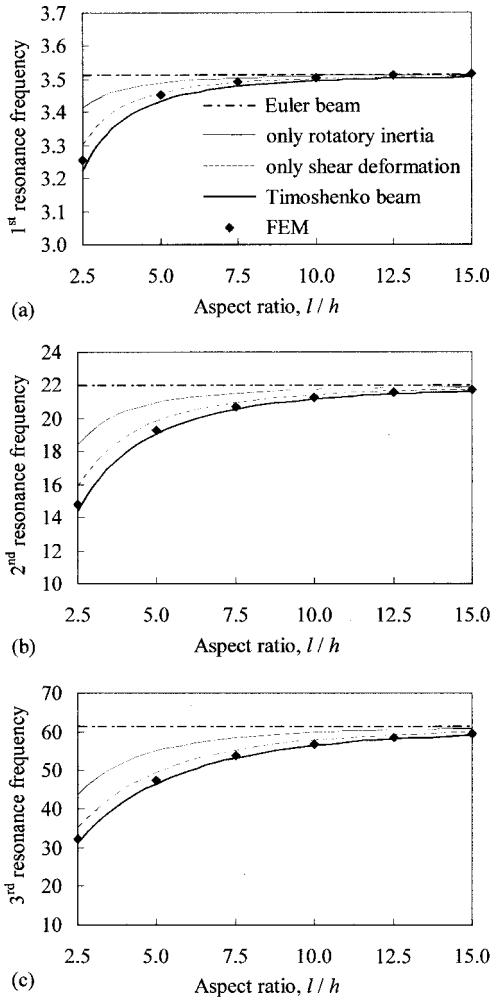

FIG. 6. The normalized resonance frequencies versus the aspect ratios, calculated by the equivalent circuit and the FEM; (a) the first; (b) the second; and (c) the third frequencies.

VI. CONCLUSIONS

To analyze the electromechanical behavior of the asymmetric triple-layered bimorph with two separate electric ports, we have derived an eight-by-eight impedance matrix and eventually an equivalent circuit. It has been demonstrated that the mechanical conditions as well as the electric port conditions can be easily realized with the electromechanical equivalence in the circuit. The electrical admittances have also been obtained from the circuit and expressed in terms of the geometric dimension and the material properties of the bimorph. The effects of shear and rotational

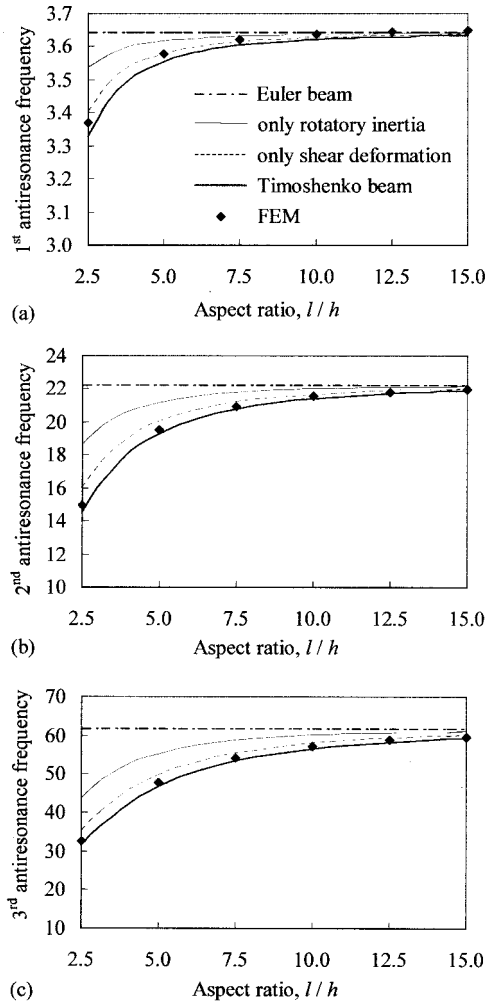

FIG. 7. The normalized antiresonance frequencies versus the aspect ratios, calculated by the equivalent circuit and the FEM; (a) the first; (b) the second; and (c) the third frequencies.

inertia and the circuit conditions on the resonance/antiresonance frequencies for a wide range of thickness ratios have been thus studied using the circuit.

The equivalent circuits are expected to facilitate further analyses of the electromechanical system for probing the effects of connecting external systems, or of making modifications to the bimorph. It is also expected that the admittance matrix and the equivalent circuit presented in this paper can be expanded to other types of piezoelectric transducers for future applications including the multilayered piezoelectric sensors and actuators subjected to the multiple electrical excitation and general loading conditions.

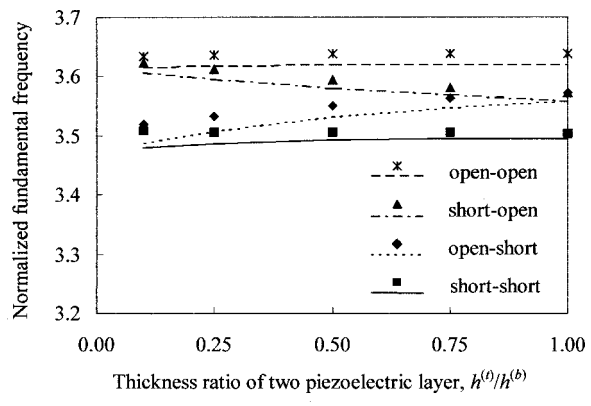

FIG. 8. The fundamental frequencies versus the thickness ratios $h^{(t)}/h^{(b)}$ for the possible circuit conditions imposed on the top and bottom piezoelectric layers. Lines and symbols for the results, respectively, by the equivalent circuit and the FEM.

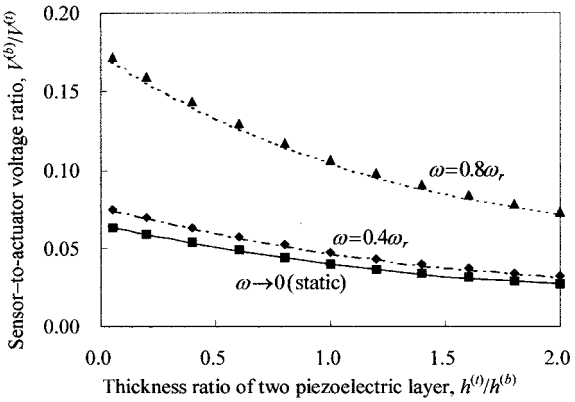

FIG. 9. The sensor-to-actuator voltage ratios $V^{(b)}/V^{(t)}$ versus the thickness ratios $h^{(t)}/h^{(b)}$ for three different exciting frequencies. Lines and symbols for the results, respectively, by the impedance matrix and the FEM.

ACKNOWLEDGMENT

This work was partially supported by the center of IDOT and the Brain Korea 21 Project.

[1] K. Uchino, *Piezoelectric Actuator and Ultrasonic Motors* (Kluwer Academic, Dordrecht, 1996).
[2] D. A. Berlincourt, D. R. Curran, and H. Jaffe, "Piezoelectric and Piezomagnetic materials and Their Function in Transducers," Phys. Acoust. **1**, 169–267 (1964).
[3] P. L. Chen, R. S. Muller, R. D. Jolly, G. L. Halac, R. M. White, A. P. Andrews, T. C. Lim, and M. F. Motamedi, "Integrated Silicon Microbeam PI-FET Accelerometer," IEEE Trans. Electron Devices **29**(1), 27–33 (1982).
[4] G. Percin, L. Levin, and B. T. Khuri-Yakub, "Piezoelectrically Actuated Droplet Ejector," Rev. Sci. Instrum. **68**(12), 4561–4563 (1997).
[5] I. Jung and Y. Roh, "Design and Fabrication of Piezoceramic Bimorph Vibration Sensors," Sens. Actuators A **69**, 259–266 (1998).
[6] X. Wang, C. Ehlers, and M. Neitzel, "Dynamic Analysis of Piezoelectric Actuator Bonded on Beam," Proceedings of the Third International Conference on Intelligent Materials, Lyon, France, June (1996), pp. 883–890.
[7] C. M. LaPeter and H. H. Cudney, "Design Methodology for Piezoelectric Actuators," Smart Structures and Materials—Proceedings of the Annual Meeting of the ASME, Atlanta, Georgia, December (1991), pp. 139–143.
[8] Q. M. Wang, X. H. Du, B. Xu, and L. Eric Cross, "Electromechanical Coupling and Output Efficiency of Piezoelectric Bending Actuator," IEEE Trans. Ultrason. Ferroelectr. Freq. Control **46**(3), 638–646 (1999).
[9] H. Tanaka, "Generalized Basic Equations for Bending Vibrations of Piezoelectric Bars from Hamilton's Principle," J. Acoust. Soc. Am. **95**, 1768–1772 (1994).
[10] T. S. Low and W. Guo, "Modeling of a Three-Layer Piezoelectric Bimorph Beam with Hysteresis," J. Microelectromech. Syst. **4**(4), 230–237 (1995).
[11] N. N. Rogacheva, C. C. Chou, and S. H. Chang, "Electromechanical Analysis of a Symmetric Piezoelectric/Elastic Laminate Structure: Theory and Experiment," IEEE Trans. Ultrason. Ferroelectr. Freq. Control **45**(2), 285–294 (1998).
[12] A. Iula, N. Lamberti, and M. Pappalardo, "A Model for the Theoretical Characterization of Thin Piezoceramic Rings," IEEE Trans. Ultrason. Ferroelectr. Freq. Control **43**(3), 370–375 (1996).

[13] S. K. Ha and Y. H. Kim, ''Impedance and admittance matrices of symmetric piezoelectric annular bimorphs and their applications,'' J. Acoust. Soc. Am. **108**, 2125–2133 (2000).
[14] L. Shuyu, ''Vibration Analysis and Frequency Equation for an Ultrasonic Transducer Consisting of a Longitudinal Vibrator and a Flexural Circular Plate,'' Acustica **81**(1), 53–57 (1995).
[15] Q. M. Wang and L. E. Cross, ''Constitutive Equation of Symmetric Triple Layer Piezoelectric Benders,'' IEEE Trans. Ultrason. Ferroelectr. Freq. Control **46**(6), 1343–1351 (1999).
[16] J. G. Smits and A. Ballato, ''Dynamic Admittance Matrix of Piezoelectric Cantilever Bimorphs,'' J. Microelectromech. Syst. **3**, 105–112 (1994).
[17] J. G. Smits, W. Choi, and A. Ballato, ''Resonance and Antiresonance of Symmetric and Asymmetric Cantilevered Piezoelectric Flexors,'' IEEE Trans. Ultrason. Ferroelectr. Freq. Control **44**(2), 250–258 (1997).
[18] D. D. Ebenezer, ''Three-port Parameters and Equivalent Circuit of Radially Polarized Piezoelectric Ceramic Cylinders of Finite Length,'' J. Acoust. Soc. Am. **99**, 2908–2912 (1996).
[19] L. Shuyu, ''Equivalent Circuits and Directivity Patterns of Air-coupled Ultrasonic Transducers,'' J. Acoust. Soc. Am. **109**, 949–957 (2001).
[20] Y. C. Chen, L. Wu, K. K. Chang, and C. L. Huang, ''Analysis and Simulation of Stacked-Segment Electromechanical Transducers with Partial Electrical Exitation by PSPICE,'' Jpn. J. Appl. Phys. **36**(10), Part 1, 6550–6557 (1997).
[21] Y. Koike, T. Tamura, and S. Ueha, ''Electrical Equivalent Circuit of Loaded Thick Langevin Flexural Transducer,'' Jpn. J. Appl. Phys. **36**(5B), Part 1, 3121–3125 (1997).
[22] H. Tanaka and R. Aoyagi, ''Analysis of Piezoelectric Bending Accelerometer Using the Equivalent Circuit,'' Jpn. J. Appl. Phys. **35**(5B), Part 1, 3035–3037 (1996).
[23] X. Wang, C. Ehlers, and M. Neitzel, ''Dynamic Analysis of Piezoelectric Actuator Bonded on Beam,'' Proceedings of the Third International Conference on Intelligent Materials, Lyon, France, June (1996), pp. 883–890.
[24] Y. S. Cho, Y. E. Park, C. S. Han, and S. K. Ha, ''Five-port Equivalent Electric Circuit of Piezoelectric Bimorph Beam,'' Sens. Actuators A **84**, 140–148 (2000).
[25] W. Weaver, S. P. Timoshenko, and D. H. Young, *Vibration Problems in Engineering*, 5th ed. (Wiley, New York, 1990).
[26] C. Gehin, C. Barthod, and Y. Teisseyre, ''Design and Characterization of a New Force Resonant Sensor,'' Sens. Actuators A **84**, 65–69 (2000).
[27] S. K. Ha, C. Keilers, and F. K. Chang, ''Finite Element Analysis of Composite Structures Containing Distributed Piezoceramic Sensors and Actuators,'' AIAA J. **30**(3), 772–780 (1992).

Nonlinear output control in hysteretic, saturating materials[a)]

Jean C. Piquette and Elizabeth A. McLaughlin
Naval Undersea Warfare Center, Division Newport, 1176 Howell Street, Newport, Rhode Island 02841

G. Yang and B. K. Mukherjee
Department of Physics, Royal Military College of Canada, Kingston, Ontario K7K 7B4, Canada

(Received 7 July 2000; accepted for publication 3 May 2001)

The problem of determining the drive waveform that produces a desired output from a hysteretic, saturating material is considered both theoretically and experimentally. The specific problem of interest is the production of a high-amplitude, but monofrequency, sinusoidal polarization response. (The techniques presented could also be used to control other physical variables, such as the strain, if desired.) Two sample materials were considered, one of which is characterized by relatively low hysteresis ($\tan\delta\approx 0.03$) and tested using mechanical prestresses of 20.7 MPa (3 kpsi) and 41.4 MPa (6 kpsi), and the other of which is characterized by relatively high hysteresis ($\tan\delta\approx 0.11$), and tested without a prestress. Both samples were fabricated from the electrostrictive material lead magnesium niobate (PMN), although a magnetostrictive material (such as Terfenol-D) could have been tested instead. The samples were subjected to a bias voltage and prestress in order to simulate conditions that might arise in a full transducer. By analytically inverting a theory of hysteresis [J. C. Piquette and S. E. Forsythe, J. Acoust. Soc. Am. **106**, 3317–3327 (1999) and J. Acoust Soc. Am. **106**, 3328–3334 (1999)], the required (predistorted) drive waveform was determined. Both semi-major and minor hysteresis loops, in both polarization and strain, were measured and the parameters of the theory determined by least-squares fitting. The measurements were obtained under quasi-static conditions, with drive frequencies at or below 10 Hz. The observed fits of theory to data are of high quality. The theory was then inverted analytically to determine the drive required to produce the desired monofrequency polarization response, having a peak polarization value approximately equal to that achieved using a biased sinusoid of AC amplitude equal to the bias. The total harmonic distortion (THD) in the output polarization resulting from the inverting drive, computed using 10 harmonics, was experimentally observed to be about an order of magnitude less than that resulting from a biased sinusoid in all cases. It is shown that the hysteresis loop arising when using the distortion-reducing drive is of smaller area than that obtained when driving with a sinusoid to achieve the same polarization amplitude. Thus, the distortion-reducing drive results in a smaller loss per cycle than is obtained with a sinusoidal drive. [DOI: 10.1121/1.1381537]

PACS numbers: 43.38.Ar, 43.20.Px, 43.30.Yj, 43.58.Vb [SLE]

I. INTRODUCTION

Active transducer materials generally exhibit both saturation and hysteresis. (''Saturation'' is the phenomenon of the departure of the polarization versus electric field curve from a straight line, and is associated with the depletion of dipoles available to realign with an increasing applied field. ''Hysteresis'' is the phenomenon of the failure of the polarization versus electric field curve to retrace the same path when an electric field is applied and then removed, and is associated with the presence of irreversible loss mechanisms in the material or time-dependent phenomena.) This is true both for the older active materials,[1,2] such as barium titanate and lead zirconate titanate (PZT), and for the newer active materials[3,4] such as lead magnesium niobate (PMN) and Terfenol-D. Saturation and hysteresis can lead to significant harmonic distortion of the output, since both of these phenomena are nonlinear in character. In the case of PZT, the problem of significant harmonic distortion is avoided by utilizing drive levels that produce changes in polarization that are small relative to the remanent polarization of the material. While PMN and Terfenol-D do not retain large remanent polarizations, a similar approach can be utilized if the drive amplitudes considered are a small percentage of the bias voltages used to simulate the effects of a remanence (in PMN), or a small percentage of the biasing magnetic field (in Terfenol-D). However, these newer transduction materials are much more temperature sensitive than is PZT, and as temperature is lowered, significant hysteresis can appear in them. Moreover, even at elevated temperatures, where hysteresis can be insignificant, the requirement to operate the transducer at drive levels that are a small percentage of the bias level to avoid the harmonic distortion significantly reduces the possible output level obtainable by the device. In PZT drive levels also must be kept relatively low in order to avoid depoling. However, in PMN and Terfenol-D the remanent polarization is relatively insignificant, and drive levels

[a)]Preliminary reports on this work were presented at the 1999 PMN Workshop (Alfred University, Alfred, NY, October 1999) and at the 2000 ONR Workshop on Transducers and Transducer Materials (Penn State University, State College, PA, April 2000).

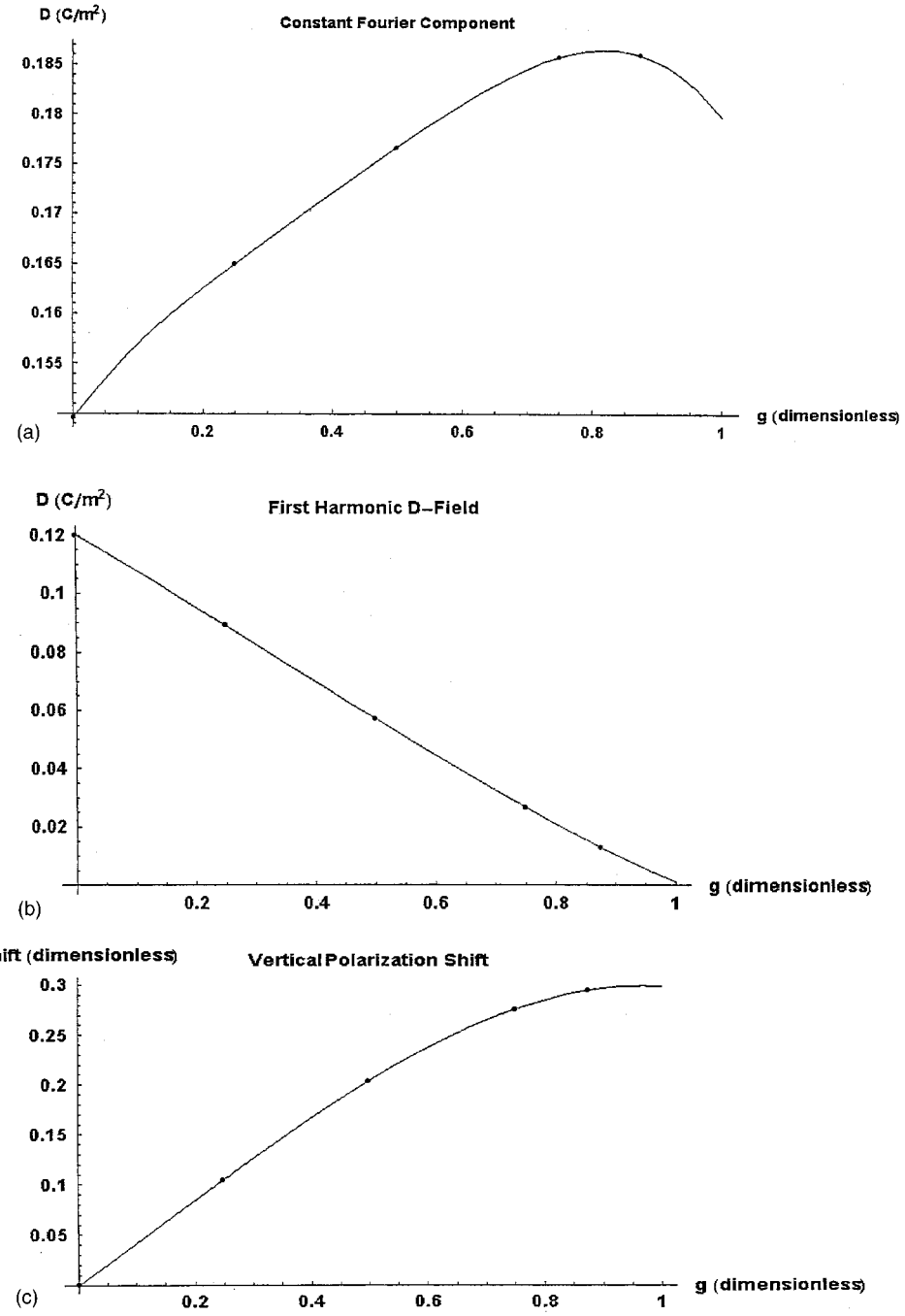

FIG. 1. (a) Fourth-degree polynomial fit (solid line) of the constant Fourier component of the anhysteretic *D*-field compared with the directly measured values (dots). [Measured data are rendered anhysteretic by a transformation introduced in Ref. 6, Eq. (6).] The case considered is the low-hysteresis sample as measured under 20.7 MPa (3 kpsi) prestress. The extreme left end of the *g*-axis ($g=0$) is associated with the semi-major loop, for which the ac drive amplitude is equal to the bias. The extreme right end of the *g*-axis ($g=1$) corresponds to an ac drive level of zero. (b) Fourth-degree polynomial fit (solid line) of the amplitude of the first harmonic of the anhysteretic *D*-field compared with the directly measured values (dots). [Measured data are rendered anhysteretic by a transformation introduced in Ref. 6, Eq. (6).] The case considered is the low-hysteresis sample as measured under 20.7 MPa (3 kpsi) prestress. The value on the *D*-axis ($g=0$) is the first-harmonic amplitude of the polarization found in the anhysteretic version in the semi-major loop. (c) Fourth-degree polynomial fit (solid line) of the residual vertical polarization shift compared with the directly measured values (dots). The case considered is the low-hysteresis sample as measured under 20.7 MPa (3 kpsi) prestress. Data have been normalized to the amplitude of the first harmonic polarization in each minor loop. The data point at the origin is associated with the semi-major loop, for which the ac drive amplitude is equal to the bias, and is *defined* to have zero polarization shift.

right up to the bias levels can be considered. However, to do so requires the ability to deal with the attendant harmonic distortions.

The output harmonics that appear owing to the use of high drive levels can be suppressed by a suitable predistortion of the drive waveform. That is, by introducing suitable harmonic distortion into the drive, the harmonics appearing in the output can be eliminated, or at least greatly reduced. The determination of the required drive can be effected if a sufficiently accurate model of the material behavior is available. One such model, applicable to both electrostrictive and magnetostrictive materials, has recently appeared.[5,6] In Ref. 6, applications of the theory to minor hysteresis loops obtained from Terfenol-D were presented. (The measurements used in the example presented in Ref. 6 were first reported in Ref. 4.) The first applications of the theory of Refs. 5 and 6 to minor hysteresis loops acquired from PMN, however, are described in the present article, together with experimental demonstrations of nonlinear output control.

Since a direct application of a high-amplitude, biased, sinusoidal drive produces a distorted (i.e., nonsinusoidal) response, it is obvious that a nonsinusoidal drive is required to produce the desired distortion-free sinusoidal output. Owing to the effects of saturation, in order to produce the positive-going half-cycle of the response it is necessary to drive the material at an amplitude greater than that used to produce the negative-going half-cycle, assuming unipolar drive and taking the bias point to be the reference. Each such drive amplitude has associated with it a distinct hysteresis loop. Thus it will be shown that in order to deduce a theoretical hyster-

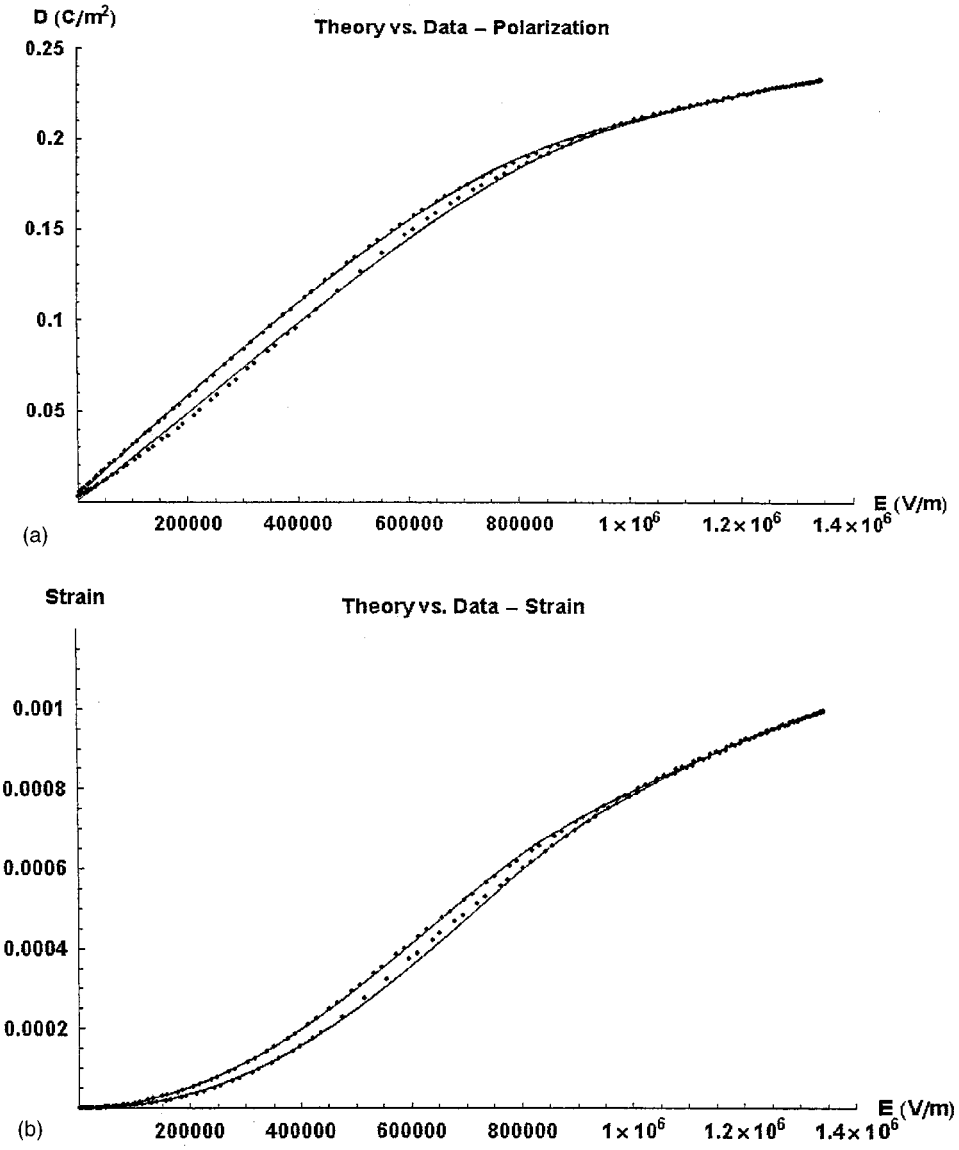

FIG. 2. (a) Theory (solid line) compared with data (dots) for the semi-major-loop polarization for the 41.4 MPa (6 kpsi) prestress, low-hysteresis case. (b) Theory (solid line) compared with data (dots) for the semi-major-loop strain for the 41.4 MPa (6 kpsi) prestress, low-hysteresis case.

esis loop that can be inverted to yield a drive waveform that produces the desired sinusoidal output response, it is necessary to combine (at least) two theoretical loops into one.

We note that hysteresis can also be controlled to a significant extent through the use of charge-control methods,[7] and we have used such methods in several US patents.[8–10] However, these methods do not solve all of the output-control problems considered here. First, these methods do not entirely eliminate hysteresis (see Ref. 7, Fig. 9). Second, the essentially *quadratic* dependence of the strain upon the polarization (or charge), as is true for the *electrostrictive* material PMN, would cause the techniques of Ref. 7 to fail to linearize the strain for this material. This is especially so for the very large drives of interest to us, over which the quadratic response is manifest. Our method, on the other hand, accounts fully for the quadratic nature of the strain, and thus would control it as effectively as it controls the polarization.

In order to achieve the relatively high degree of accuracy of fits of theory to experiment considered necessary to permit the desired level of output control, the procedure introduced in Ref. 6 for interpolating between measured minor loops had to be modified slightly. A description of the modifications is given in Sec. II A. Applications of the theory to newly acquired experimental data are given in Sec. II B. Both semi-major and minor hysteresis loops in both polarization and strain were acquired in the experiments. (The term ''semi-major hysteresis loop'' refers to any loop obtained when the drive applied to a sample consists of a biased sinusoid where the ac amplitude is equal to the bias. The notion of the semi-major loop was introduced in Ref. 6 in order to distinguish this case from that of the major loop, which applies when no bias is used.) The measurements were carried out on two samples of PMN, one of which is characterized by relatively high hysteresis ($\tan\delta \approx 0.11$), the other of which is characterized by relatively low hysteresis ($\tan\delta \approx 0.03$). The high-hysteresis sample was measured without a mechanical prestress, while the low-hysteresis sample was measured at two nonzero prestress levels that are typical of those used in transducers to avoid sample extension. The methods used to deduce the composite hysteresis loop, which is required to compute the inverting drive, are described in Sec. III. The results of experimental tests of the drives designed using the methods given in Sec. III are reported in

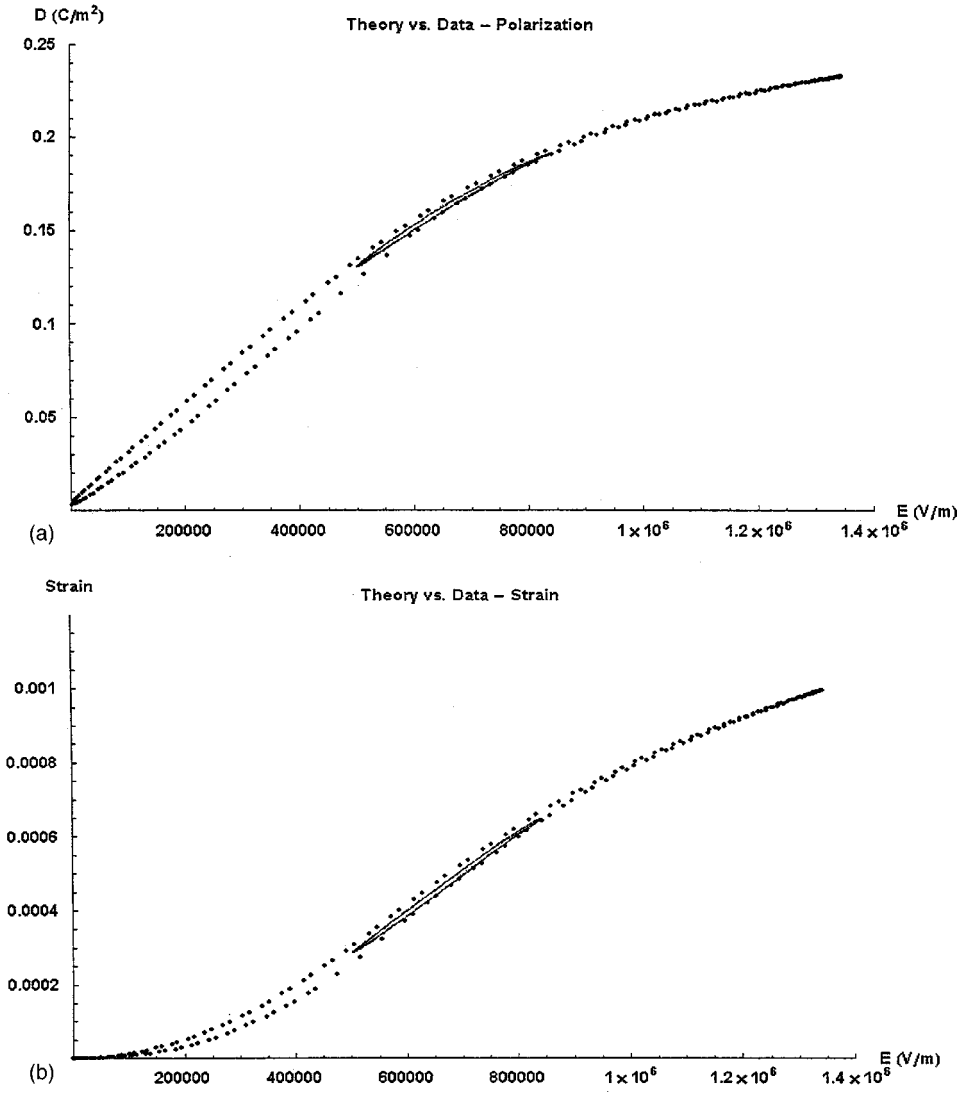

FIG. 3. (a) Theory (solid line) compared with data (dots) for one of the minor polarization loops obtained for the 41.4 MPa (6 kpsi) prestress, low-hysteresis case. Experimental semi-major loop data are also shown for reference, in order that the relative positioning of the minor loop might be seen. (b) Theory (solid line) compared with data (dots) for one of the minor strain loops obtained for the 41.4 MPa (6 kpsi) prestress, low-hysteresis case. Experimental semi-major loop data are also shown for reference, in order that the relative positioning of the minor loop might be seen.

Sec. V. A summary, discussion, and the conclusions are given in Sec. V.

II. INITIAL EXPERIMENTS

Prior to designing the inverting waveforms it is necessary to determine numerical values for the parameters of the theory.[5,6] Among the required parameters are the low-field permittivity, the ''saturation parameter'' (which is a measure of the rate at which saturation occurs in the material), as well as ''field-space'' [5] rotation angles required to transform the measured hysteretic data into anhysteretic form. These parameters are determined experimentally by first driving the sample with a series of biased sinusoids, each having the same bias voltage but differing in ac amplitude. These drives produce a set of nested polarization, and strain, hysteresis loops. A data transformation, introduced in Refs. 5 and 6, is then applied to these nested loops, thus converting the data into anhysteretic form. The theory is then simultaneously least squares fitted to the anhysteretic versions of the polarization and strain data to determine the parameters of the theory. The reader may wish to consult Refs. 5 and 6 for a complete description of the theory, and for a fuller description of how the parameters are determined.

There were two samples tested in the experiments. The ''low-hysteresis'' sample, PMN/PT/La 85/15/1, consists of 85 molecular percent of lead magnesium niobate in solid solution with 15 molecular percent lead titanate, doped with 1 weight percent lanthanum. It has a ''$T_{\max}$,'' measured at 0.1 kHz, of 38 °C. (The quantity $T_{\max}$ is the temperature at which the small signal permittivity peaks at a given frequency with no prestress applied to the sample.) The ''high-hysteresis'' sample, PMN/PT 85/15, consists of 85 molecular percent of lead magnesium niobate, in solid solution with 15 molecular percent lead titanate. It has a $T_{\max}$, measured at 1 kHz, of 62 °C.

A. Revised minor-loop analysis

In order to obtain the very high quality of fits of theory to data desired to help achieve a high degree of output control, it was found necessary to revise somewhat the procedure described in Ref. 6 for evaluating the minor loops. Each experimentally acquired minor hysteresis loop exhibits both an in-plane rotation, and a vertical shift, of its major axis relative to the major axis of the semi-major loop. Or at least such a rotation and shift can be accurately defined for the major axis of the two-dimensional ''reference ellipse'' asso-

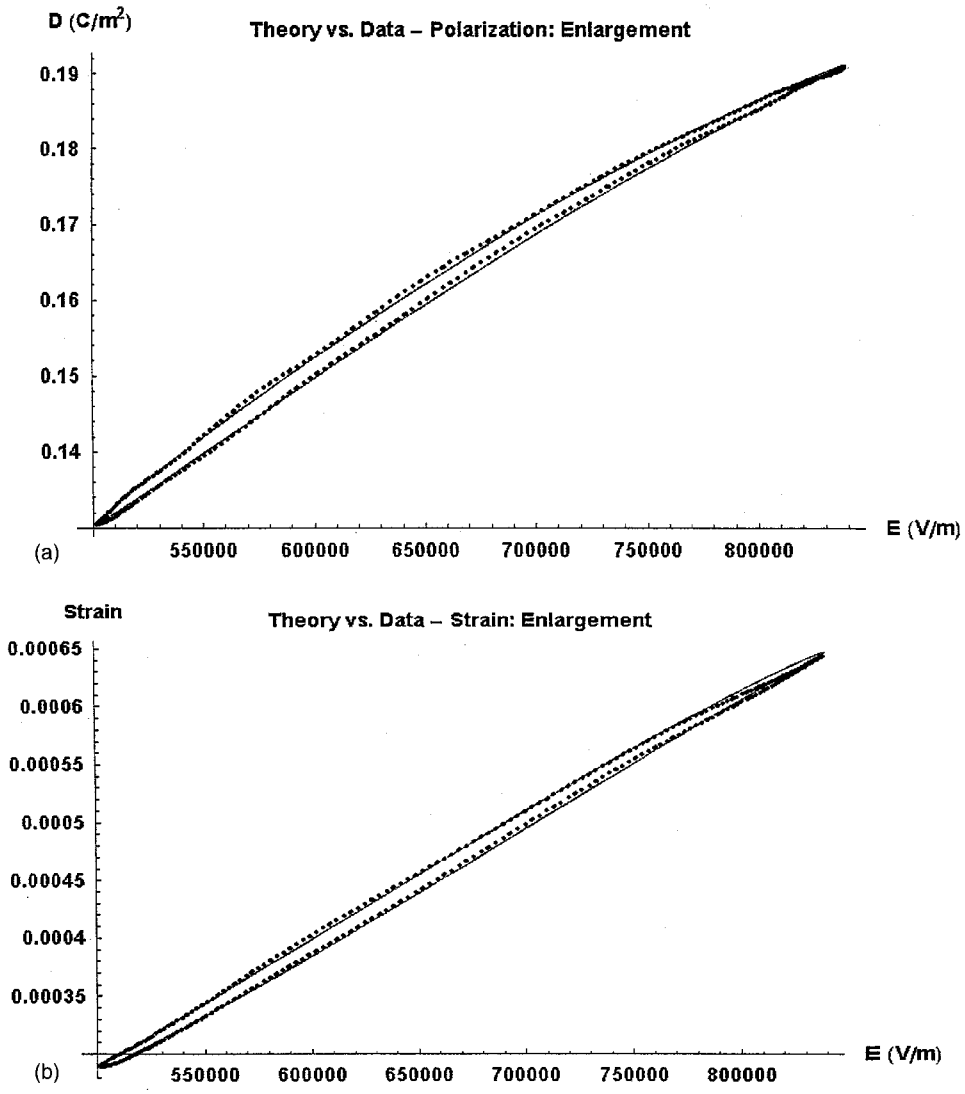

FIG. 4. (a) Theory (solid line) compared with data (dots) for one of the minor polarization loops obtained for the 41.4 MPa (6 kpsi) prestress, low-hysteresis case. This is an enlargement of the minor loop shown in Fig. 3(a), presented without the semi-major-loop background data in order that theory and data might be more readily compared. (b) Theory (solid line) compared with data (dots) for one of the minor strain loops obtained for the 41.4 MPa (6 kpsi) prestress, low-hysteresis case. This is an enlargement of the minor loop shown in Fig. 3(b), presented without the semi-major-loop background data in order that theory and data might be more readily compared.

ciated with each loop. (The reference ellipse is another concept that was introduced in Ref. 5, Appendix B.) Readers unfamiliar with the rotation-plus-shift phenomenon may wish to refer to Figs. 1 and 2 of Ref. 6, p. 3329, where it can be readily seen.

Equation (6) of Ref. 6 is a data-transformation equation. One effect of this data transformation is the ''collapse'' of each hysteresis loop to an approximately one-dimensional figure; i.e., a figure of approximately zero area. This portion of the transformation effectively eliminates hysteresis from the data. Comparing Figs. 1 and 2 of Ref. 6, one can see the effects of the area-collapsing portion of the transformation.

A second effect of the data transformation of Eq. (6) of Ref. 6 is the alignment of each collapsed minor loop with the collapsed semi-major loop. This second portion of the data transformation thus inverts the rotation-plus-shift of the major axes described above. Comparing Figs. 2 and 3 of Ref. 6, one can see the results of applying this shift-plus-rotation portion of the transformation to the smallest minor loop. It is the empirical ''vertical shift'' formula given by Eq. (5) of Ref. 6 that now has been modified. (The rotation portion of the transformation remains unchanged.) Equation (5) was introduced in Ref. 6 to allow interpolations between the directly measured vertical polarization (or magnetization) shifts. Although the original empirical formula was still found to work reasonably well on the data obtained in the present experiments, it did not provide the highly accurate fits of theory to data that are probably required to achieve the high degree of output control desired here. Hence a modified procedure for interpolating the vertical shifts, described below, is introduced.

The new procedure involves first determining the Fourier components of the *anhysteretic* versions of the data. (As already noted, after the areas of the loops have been collapsed by the data transformation, the measurements have been effectively rendered anhysteretic.) The constant component from those spectra is then subtracted from the corresponding anhysteretic data. Dividing by the first-harmonic amplitude normalizes the data.

However, subtracting the constant Fourier components from the anhysteretic data does *not* entirely eliminate the vertical polarization displacements between the various anhysteretic D vs E curves. Afterward, there remains a ''residual'' vertical difference between the various data sets, which still must be subtracted to eliminate the vertical displacements. (This residual difference is purely a vertical dis-

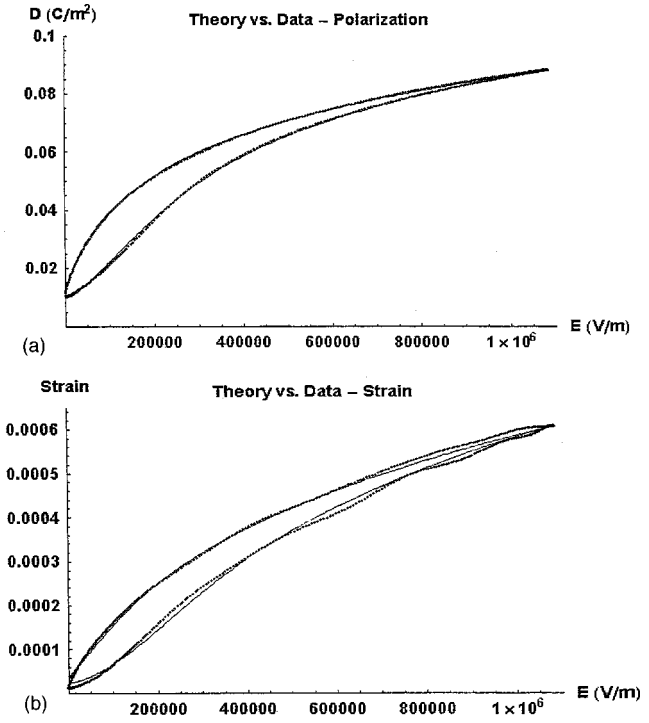

FIG. 5. (a) Theory (solid line) compared with data (dots) for the semi-major-loop polarization for the high-hysteresis case. No prestress was applied in this measurement. (b) Theory (solid line) compared with data (dots) for the semi-major-loop strain for the high-hysteresis case. No prestress was applied in this measurement.

placement of the data, since the angular portion of the data transformation has eliminated any *rotational* difference.) That is, owing primarily to the effects of saturation, *the constant Fourier components of the various anhysteretic data sets are unequal*. Thus, subtraction of each such constant Fourier component from the data does *not* cause the resulting curves of D vs E to align vertically. The value of the residual constant polarization component is determined by fitting each of the anhysteretic D vs E curves to a polynomial in E. The constant component resulting from this fit is the residual portion of the polarization shift.

In order to allow interpolation and extrapolation, equations are required for estimating the constant and first harmonic Fourier components of the anhysteretic D field, as well as the residual polarization shift described above. (Interpolation is needed because the drive-design process requires the ability to determine how the sample will respond to drive conditions that have not been measured experimentally.) The required equations were obtained by performing a polynomial fit to each of the directly measured values. In each case, the polynomial is expressed in terms of the dimensionless drive parameter g, where

$$g \equiv \frac{(E_{\text{bias}} - E_{\text{drive}})}{E_{\text{bias}}}. \tag{1}$$

Here, E_{bias} denotes the electric field created by the bias voltage and E_{drive} denotes the electric field created by the ac drive voltage. (The reader should keep in mind that, in the initial experiments currently under discussion, the total voltage applied to the sample always consisted of a dc bias voltage plus a monofrequency sinusoidal ac voltage.) Notice that as defined, g is a dimensionless parameter that measures the "strength" of the drive field, although it varies in an opposite way to the variation in E_{drive}. That is, g is zero when $E_{\text{bias}} = E_{\text{drive}}$, and is unity when $E_{\text{drive}} = 0$.

The results of the fitting process are shown, for one case, in Figs. 1(a)–(c). The case considered is that of the low-hysteresis sample tested at 20.7 MPa (3 kpsi) prestress. In Fig. 1(a) is shown the constant Fourier component of the anhysteretic D field. Dots represent the directly measured values, while the solid line is the result of the polynomial fit. [A fourth-degree polynomial was used to accommodate the five measured data points, viz., the semi-major loop and four minor loops. However, a polynomial of the fourth degree was used only in this one case, because in the other cases fewer than four minor loops were measured in addition to the semi-major loop. Thus a polynomial of degree less than the fourth is sufficient for the other cases. The slowness of the variations of the functions depicted in Figs. 1(a)–(c) establishes the validity of this procedure. The case considered in these figures was selected for presentation because the high-order polynomial used would be expected to exhibit the greatest variations with respect to g, if such large variations were needed to accommodate the measurements. As can be seen, however, the observed variations are quite modest.] Figure 1(b) is similar to Fig. 1(a), except in this case it is the first harmonic Fourier component of the anhysteretic data that is shown. Finally, Fig. 1(c) shows the data and the polynomial fit for the residual polarization shift that is required to cause each minor loop to overlay the semi-major loop, once the constant Fourier component has been subtracted. In this case, the shift values are dimensionless because the data have been normalized by the process introduced in Ref. 5, viz., they have been normalized to the amplitude of the first harmonic. [Note again from Eq. (1) that $g = 0$ corresponds to the semi-major loop condition, i.e., drive amplitude equal to the bias. Thus, since the shift is defined relative to the semi-major loop, zero shift is required at $g = 0$, as is seen in Fig. 1(c).]

B. "Direct" experiment versus theory

Considered next are the results of applying the theory of Refs. 5 and 6 to measurements acquired when the samples are driven with biased sinusoids. Both samples were tested at room temperature. The low-hysteresis sample was tested at two different conditions of prestress: 20.7 MPa (3 kpsi) and 41.4 MPa (6 kpsi). For both prestress conditions the test frequency was 10 Hz. The high-hysteresis sample was tested without mechanical load, and was tested at an ac frequency of 0.1 Hz

A few of the results obtained for the low-hysteresis sample, prestressed at 41.4 MPa (6 kpsi), are presented in Figs. 2–4. The results shown are typical of all those obtained for the low-hysteresis sample. Dots denote data and solid lines denote theory. Figure 2(a) presents the semi-major polarization loop, while Fig. 2(b) shows the strain for this case. Figures 3(a) and (b) present results for one of the minor-loop measurements. Again the case considered is that of the low-

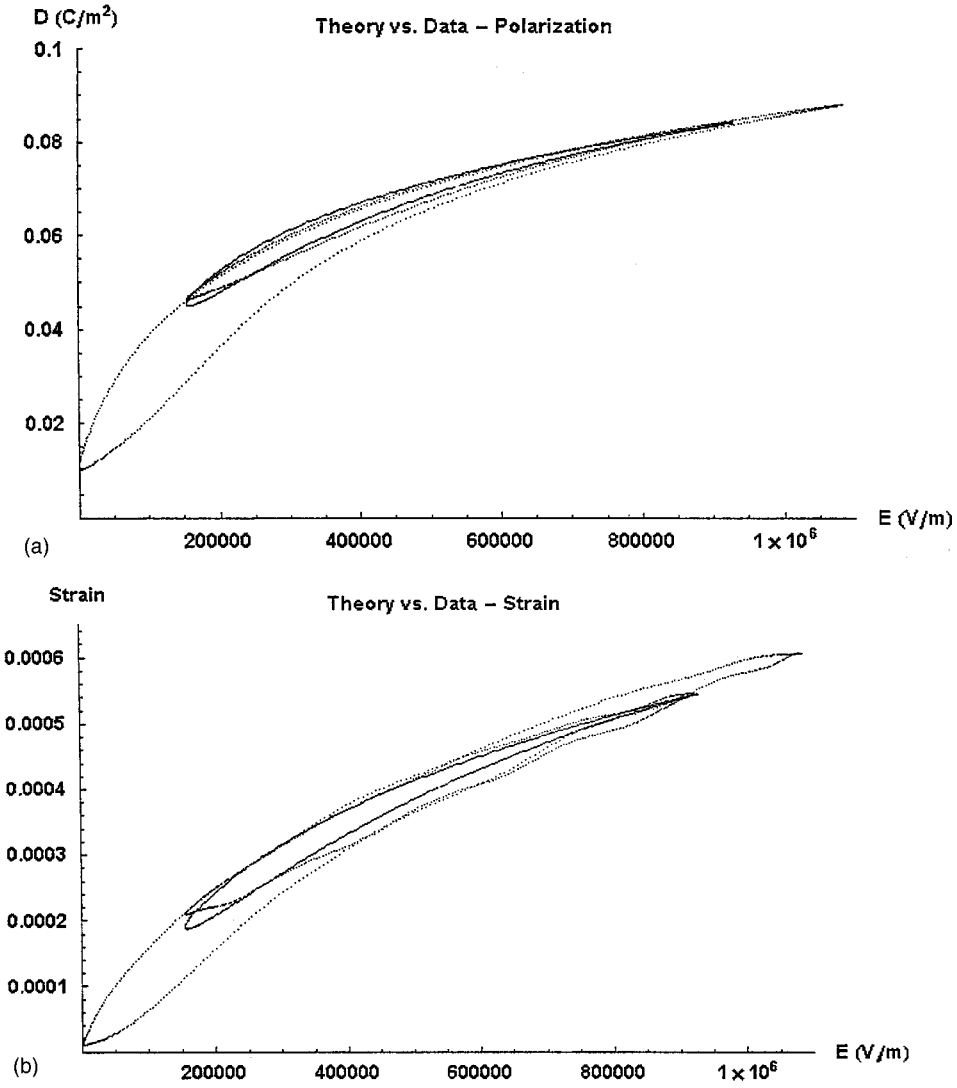

FIG. 6. (a) Theory (solid line) compared with data (dots) for one of the minor polarization loops obtained for the high-hysteresis case. No prestress was used. Experimental semi-major-loop data are also shown for reference, in order that the relative positioning of the minor loop might be seen. (b) Theory (solid line) compared with data (dots) for one of the minor strain loops obtained for the high-hysteresis case. No prestress was used. Experimental semi-major-loop data are also shown for reference, in order that the relative positioning of the minor loop might be seen.

hysteresis sample prestressed at 41.4 MPa (6 kpsi). Figure 3(a) shows the polarization, while Fig. 3(b) shows the strain. Here the semi-major-loop data have also been plotted so that the relative positions of the nested minor loops can be seen. In order that a comparison between theory and data can be more easily made, enlargements of the minor-loop results for this case are shown in Figs. 4(a) and (b), without the semi-major-loop background. As can be seen, the agreement is quite good.

Results obtained from the high-hysteresis sample are shown in Figs. 5(a) and (b) and 6(a) and (b). Figure 5(a) shows the semi-major polarization loop, while Fig. 5(b) shows the strain for this case. Figure 6(a) shows the polarization for one of the minor loops obtained in this case, while Fig. 6(b) shows the strain. As was done in presenting the results for the low-hysteresis sample, the semi-major-loop data are also shown for reference in both figures. Again, the agreement seen between theory and data is quite good, except possibly for the minor-loop strain shown in Fig. 6(b). However, the noise seen in this case is larger than for the other cases, and some of this disagreement might be attributable to this cause.

III. OUTPUT CONTROL THEORY

The theoretical methods used to achieve output control were detailed in Ref. 6, so they will only be summarized briefly here. However, details concerning the necessity of using multiple theoretical hysteresis loops to achieve the desired control, which were not supplied in Ref. 6, will be furnished here. In considering the method used to achieve output control, the reader should bear in mind that the theory of Refs. 5 and 6 is quasi-static in character. This means that the observed responses are assumed to be frequency independent. The primary consequence of this assumption is that only the bias voltage and wave *amplitude* are considered responsible for creating the hysteresis-loop shape and orientation. Thus, the loop shape and orientation are assumed to be unaffected by the specific drive wave *shape* associated with a given drive wave *amplitude*.

This assumed independence of hysteresis loop shape from the details of the drive wave shape might lead one to suppose that the drive waveform required to produce a desired output could be deduced by directly inverting the measured data. However, that is not so since the loop shapes and orientations are clearly functions of drive amplitude, as can

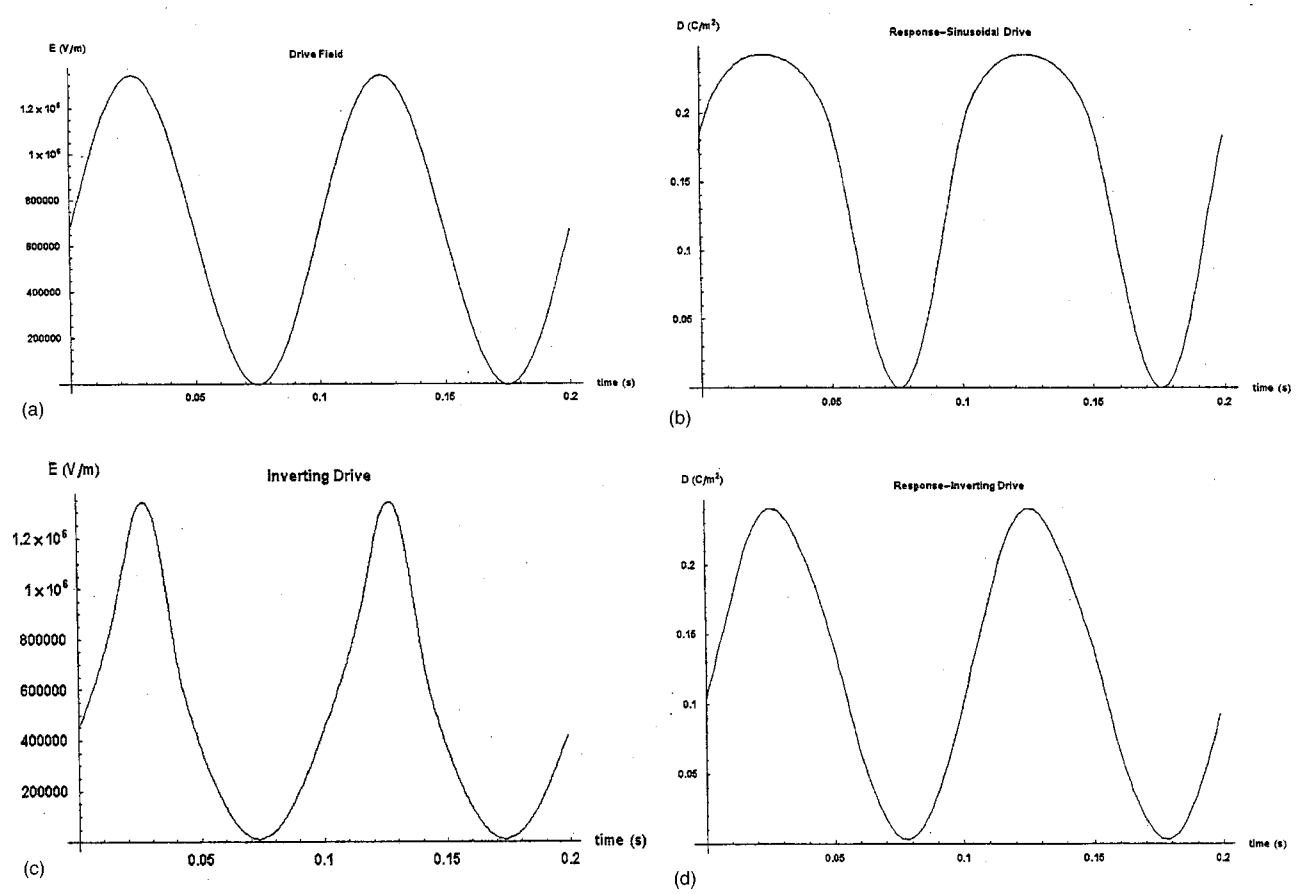

FIG. 7. (a) Theoretical biased sinusoidal electric-field drive. (b) Theoretical response of the low-hysteresis sample prestressed at 20.7 MPa (3 kpsi) to the drive of (a). (c) Inverting electric-field drive waveform, designed theoretically to produce a monofrequency sinusoidal output polarization from the low-hysteresis sample prestressed at 20.7 MPa (3 kpsi), with peak polarization approximately equal to that achieved with the biased sinusoidal drive. (d) Theoretical response of the low-hysteresis sample prestressed at 20.7 MPa (3 kpsi) to the drive of (c). Compare with (b).

be seen by examining Figs. 2(a), 2(b), 3(a), 3(b), 5(a), 5(b), 6(a) and 6(b). In order to achieve a desired output response it is necessary to know what the loop shape and orientation will be for *any possible* drive amplitude, since one does not know in advance what drive amplitude will be needed to produce a desired output. There are, of course, a continuum infinity of possible drive amplitudes. Owing to the necessarily sparse measurements of minor loops that can be acquired experimentally, it is unlikely that all the drive amplitudes that will be needed in fabricating the desired drive will have been measured. However, the theory of Refs. 5 and 6 permits interpolation or extrapolation to any drive amplitude that is equal to, or less than, the bias level.

Time is taken to be a parameter in generating the distortion-reducing drive from its associated theoretical loop. In essence, the process of creating the drive waveform begins with the assumption that the *same hysteresis loop associated with the observed distorted response to a sinusoidal drive will still appear when the sample is driven with the inverting drive*, at least over a segment of the waveform. (This matter will be considered further presently.) Thus, the process of eliminating (or reducing) output distortion does *not* eliminate hysteresis. However, the *times* at which the sampled points of the drive appear must differ from the times at which these points appear in the original (sinusoidal) drive, in order that the desired output might result. By varying the times of the sampled points in the drive waveform, the originally sinusoidal *drive* becomes distorted in such a way that distortion is eliminated, or at least greatly reduced, in the *response*.

An appreciation for how the wave shape of the distortion-correcting drive is determined can perhaps be gained by examining Figs. 7(a)–(d). These theoretical waveforms were generated using the model parameters determined in the least-squares fit to the 20.7 MPa (3 kpsi) prestress, low hysteresis-sample data. In Fig. 7(a) is shown a biased sinusoidal drive approximating that used in the experiment to obtain the semi-major-loop data. In Fig. 7(b) the computed polarization response to the drive of Fig. 7(a) is shown. Distortion in the response is evident.

Essentially, by ''retiming'' the sampled drive points of Fig. 7(a) appropriately, the distorted drive of Fig. 7(c) can be produced. (This is actually an oversimplification. This oversimplification is corrected in the next, and subsequent, paragraphs.) Prior to drawing Fig. 7(c), however, the drive points are interpolated so that they again appear at equally spaced time points. The predicted response to the drive of Fig. 7(c) is shown in Fig. 7(d). By comparing Fig. 7(b) with Fig. 7(d), the reduction in distortion theoretically predicted to occur is apparent.

One subtlety, which has been ignored in the discussion thus far, arises in producing the drive waveform shown in Fig. 7(c). Owing to the effects of saturation, the drive ampli-

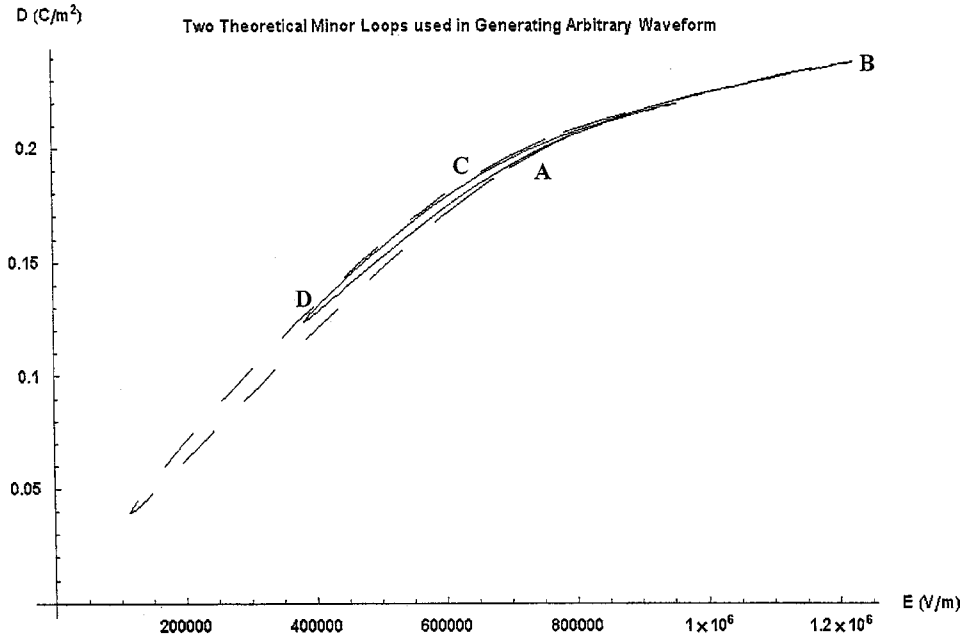

FIG. 8. Two nested theoretical minor loops required to design the inverting waveform. Two loops are needed owing to the effects of saturation. Segments of each of the depicted loops are combined to create a single loop, which is then used to design the inverting drive. Points used to fabricate the composite loop are taken from the lower segment of the outer loop (dashed-line curve) beginning at point A, and are taken from that loop segment up to point B. Starting at point B, the composite loop is fabricated from points appearing along the upper segment of the outer loop, at least up to point C. At some location between points C and D, the composite-loop-determining algorithm then "hops" to the upper segment of the inner loop (solid-line curve). (The exact position at which the hop is done is determined by minimizing a cost function that gives equal weights to matching the slopes, and the field values, on each of the two loops.) The composite loop is then fabricated from points appearing along the upper segment of the inner loop, until point D is reached. After point D, the composite loop is fabricated from points appearing along the lower segment of the inner loop, until point A is reached. There another hop, this time to the lower segment of the outer loop, is required. The difference in the sizes of the two loops shown has been exaggerated for clarity.

tude required to produce the *positive*-going segment of the response of Fig. 7(d) is unequal to the drive amplitude required to produce the *negative*-going segment. Since the theory of Refs. 5 and 6 is drive amplitude based, it therefore becomes necessary to generate at least two theoretical hysteresis loops to produce the desired distortion-correcting drive waveform. That is, in order to cause the sample polarization response to "swing" to the *equal* levels that are characteristic of a sinusoid, i.e., *equal* responses in both the positive- and negative-going output-wave segments, it is necessary to use *unequal* drive amplitudes in each corresponding drive-wave segment. Each such drive amplitude results in a unique associated hysteresis loop. Thus, the actual loop used to produce the desired response is a composite of at least two loops.

The two nested theoretical loops shown in Fig. 8 can be used to help understand how two theoretical loops are combined in producing the distortion-reducing drive. [The loops shown are not the loops that were used to produce the drive shown in Fig. 7(c). The size difference of the loops shown has been exaggerated for clarity.] The outer loop (dashed-line curve) is the theoretical polarization response resulting from a higher-amplitude sinusoidal drive, while the inner loop (solid-line curve) is that resulting from a lower-amplitude sinusoidal drive.

The drive cycle used to produce the distortion-corrected response proceeds along the path defined by the sequence of points A→B→C→D→A. The drive cycle is partially fabricated from points that appear on the lower segment of the outer loop, starting in the vicinity of point "A." At point "A," the drive field is increasing in amplitude ($dE/dt>0$). At point "B," the rate of change of the drive field becomes zero ($dE/dt=0$). After point "B," the drive cycle is fabricated from points that appear along the upper segment of the outer loop, at least up to point C. Along the path B→C the drive amplitude is decreasing ($dE/dt<0$). Thus, we see that the composite loop consists entirely of points taken from the outer loop over the path A→B→C. At some location between points "C" and "D," it is necessary for the algorithm that determines the shape of the distortion-reducing drive to "hop" over to the upper segment of the inner loop (solid-line curve). Note, however, that the amplitudes and slopes of both loops between "C" and "D" are rather similar. The optimum jump point is determined by minimizing a cost function that gives equal weights to matching the slopes and amplitudes of the responses appearing on each loop, in order that the disturbing influence of hopping from one loop to the other is minimized. Once the hop to the inner loop is complete, the algorithm begins to use points from the upper segment of the inner loop to fabricate the drive cycle, until point "D" is reached. At point D, the rate of change of the drive field becomes zero ($dE/dt=0$) once again. The algorithm then uses points appearing along the lower segment of the inner loop from point "D" to point "A," where another hop is required. [Between points "D" and"A," the drive amplitude is again increasing ($dE/dt>0$).] The second hop returns the algorithm to the lower segment of the outer loop, where the cycle begins anew.

It will be appreciated that the loop-hopping algorithm described here is inherently subject to producing some dis-

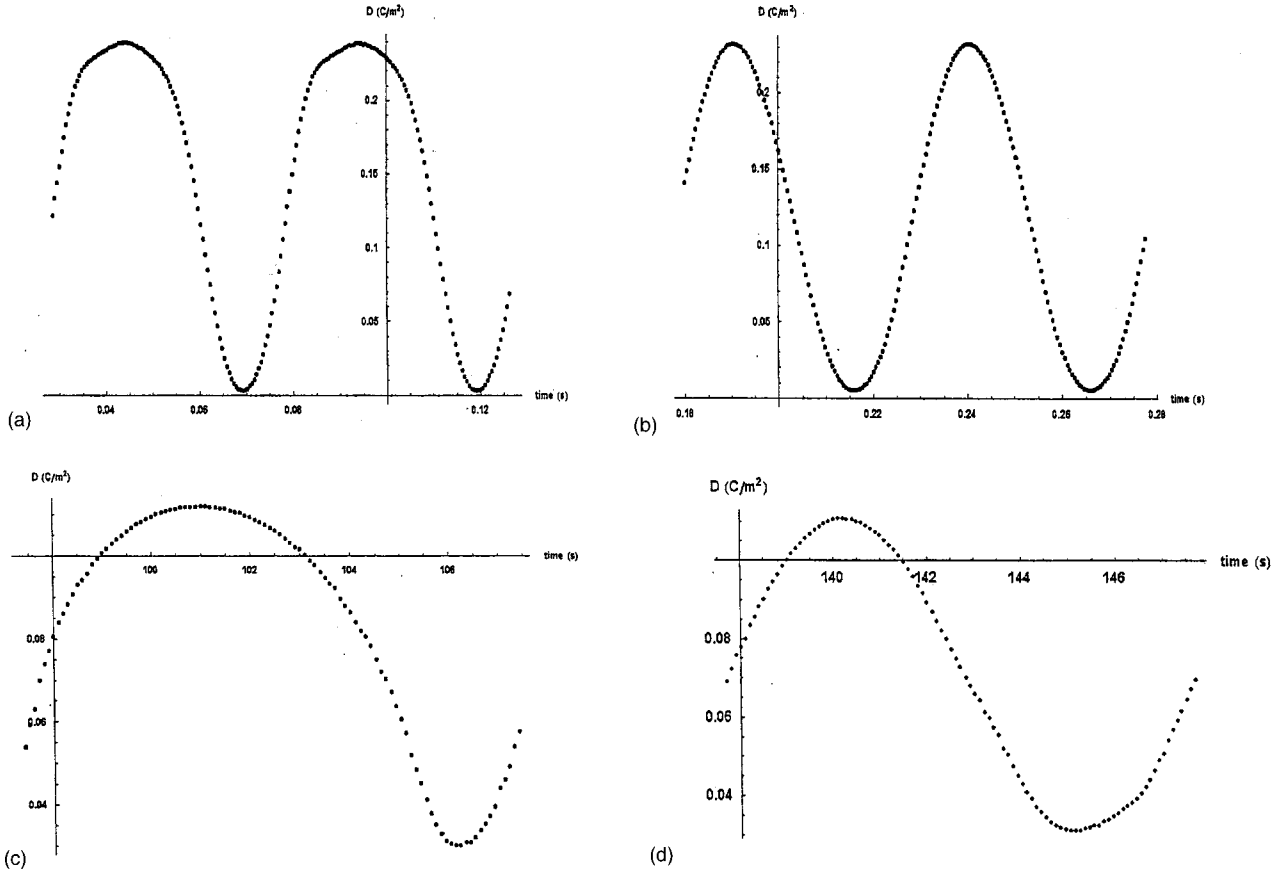

FIG. 9. (a) Experimental time-domain polarization response to a biased sinusoidal drive applied to the low-hysteresis sample prestressed at 20.7 MPa (3 kpsi), semi-major loop drive condition. (b) Experimental time-domain polarization response to the inverting drive applied to the low-hysteresis sample prestressed at 20.7 MPa (3 kpsi). (c) Experimental time-domain polarization response to a biased sinusoidal drive applied to the high-hysteresis sample, semi-major loop drive condition. (d) Experimental time-domain polarization response to the inverting drive applied to the high-hysteresis sample.

tortion in the response. A better algorithm could probably be devised in which more than two loops are used to generate the composite loop. The greater the number of loops used in creating the composite loop, the smaller would be the levels of the undesirable abrupt changes in drive level occurring at the hop points. These abrupt changes in drive level limit the extent to which output distortion can be corrected with the present algorithm. (A modified algorithm is the subject of future research.)

IV. OUTPUT CONTROL EXPERIMENT

The algorithm described in Ref. 6 (and summarized, and expanded upon, here in Sec. III) was used to design drive-voltage waveforms to produce monofrequency sinusoidal polarization responses of amplitudes approximately equal to those achieved in the semi-major loops. The design was based on the model parameters determined by fitting to the experimental data presented in Sec. II. The designed waveforms were then applied experimentally, and the resulting responses captured and analyzed. The results are shown in Figs. 9(a)–(d) and 10(a)–(d). Figures 9(a)–(d) show time domain results, while Figs. 10(a)–(d) show frequency domain results. Figure 9(a) shows the response to a high-amplitude, biased, sinusoidal drive applied to the low-hysteresis sample at the 20.7 MPa (3 kpsi) prestress, as described in Sec. I, while Fig. 9(b) shows the response to the inverting drive. The results shown are similar to those obtained for this sample at the 41.4 MPa (6 kpsi) prestress, although the distortion was somewhat greater in the case selected for depiction. Figures 10(a) and (b) show the corresponding results in the frequency domain for this case. As can be seen, the distortion has been reduced significantly. The total harmonic distortion (THD) occurring in the response to the biased sinusoidal drive, shown in Figs. 9(a) and 10(a), is 26.3%, while that for the designed drive, shown in Figs. 9(b) and 10(b), is 2.60%. Thus, harmonic distortion was reduced by slightly more than an order of magnitude.

In Figs. 9(c), 9(d), 10(c), and 10(d) are shown the results obtained from the high-hysteresis sample. Again, it can be seen that a significant reduction in harmonic distortion was achieved. The THD for the response shown in Figs. 9(c) and 10(c) is 33.5%, while that for the response shown in Figs. 9(d) and 10(d) is 3.0%. As with the THD reported for the results shown for the low-hysteresis case, the ten harmonics depicted were used in the calculation. Once again, this is a reduction in distortion somewhat in excess of an order of magnitude. This level of distortion reduction was observed in all the tests that were conducted.

The reader should not draw the conclusion from the results presented that the energetics of the system have been modified in any way by the drive that has been applied to reduce the harmonic content of the output. Indeed, the hys-

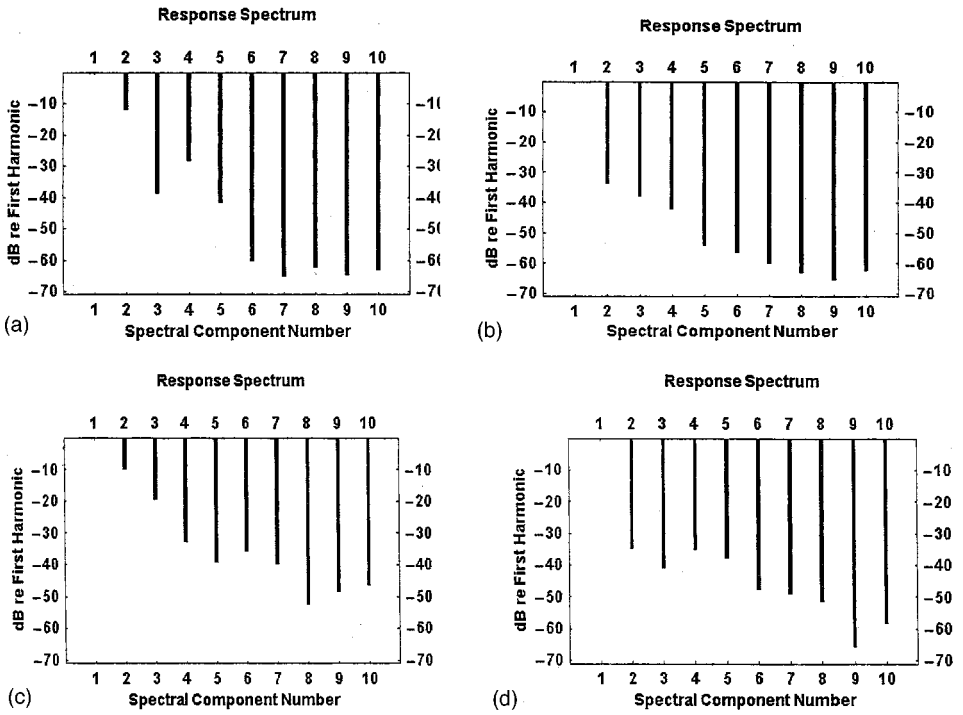

FIG. 10. (a) Experimental frequency-domain polarization response to a biased sinusoidal drive applied to the low-hysteresis sample prestressed at 20.7 MPa (3 kpsi), semi-major loop drive condition. THD=26.3%. (Ten harmonics were used in the THD calculation.) (b) Experimental frequency-domain polarization response to the inverting drive applied to the low-hysteresis sample prestressed at 20.7 MPa (3 kpsi). THD=2.60%. (Ten harmonics were used in the THD calculation.) (c) Experimental frequency-domain polarization response to a biased sinusoidal drive applied to the high-hysteresis sample, semi-major loop drive condition. THD=33.5%. (Ten harmonics were used in the THD calculation.) (d) Experimental frequency-domain polarization response to the inverting drive applied to the high-hysteresis sample. THD =3.0%. (Ten harmonics were used in the THD calculation.)

teresis loops arising under sinusoidal drives also appear under the inverting drive, so that the energy lost over each *corresponding* cycle is the same in both cases. As noted in Ref. 5, the harmonics above the first do not contribute to the area of the hysteresis loop, but only to its shape. However, in creating the *negative-going segment* of the distortion-reduced response, the hysteresis loop used to construct the drive corresponds to a sinusoid of reduced amplitude (segment D to A of Fig. 8). Thus, effectively, there is a hysteresis loop of smaller area generated, and a lower energy loss per cycle occurs, when the distortion-reducing drive is used.

V. SUMMARY, DISCUSSION, AND CONCLUSION

Experimental tests of the ability of the theory of Refs. 5 and 6 to accommodate hysteretic data acquired from PMN were reported. While the ability of the theory to accommodate semi-major hysteresis loops obtained from PMN was previously reported in Ref. 5, heretofore no experimental confirmation of its minor-loop capabilities for this material had been reported. The ability of the theory to accommodate both semi-major and minor hysteresis loops, in both polarization and strain, and both with and without prestress, was found to be quite good. However, in order to obtain the high quality of fit of theory to data believed required to achieve significant output control, it was found to be necessary to modify the vertical-shift interpolation algorithm of Ref. 6.

The theoretical method used for achieving output control was summarized. It was shown that in order to achieve a good approximation to the desired output trajectory, it is necessary to generate a composite hysteresis loop from at least two loops. This is due to the effects of saturation, which necessitate driving the material at higher amplitude in the positive-going region of the signal than in the negative-going region.

A high degree of success was obtained in achieving the desired goal of producing a monofrequency sinusoidal polarization output at high amplitude. In all cases tested, the total harmonic distortion (THD) was reduced by more than an order of magnitude compared with that resulting from a biased sinusoid. Similar methods could also be applied to the control of other output variables, such as the strain.

Although the reduction in THD was significant, there is still room for improvement. Most of the remaining distortion is attributable to the simple two-loop algorithm used to produce the required composite hysteresis loop, rather than due to any failure of the hysteresis theory of Refs. 5 and 6 to properly accommodate the data. This claim is based on a spectral analysis of the *predicted* polarization responses to the designed drive waveforms. For example, a spectral analysis of the waveform of Fig. 7(d), which is the *theoretical* response to the designed inverting waveform shown in Fig. 7(c), shows that the THD should, in fact, be approximately an order of magnitude less than that produced by a biased sinusoidal drive, as shown in Fig. 7(b). Since this is quite similar to the reduction in THD that was achieved in the experiments, the theory is seen to accord quite well with the observations.

If more than the achieved order of magnitude reduction in THD is desired, it will be necessary to design a more sophisticated algorithm to produce the required composite hysteresis loop than the simple two-loop composite used here. Development of such an algorithm is the subject of future research.

ACKNOWLEDGMENTS

This work was supported in part by the Office of Naval Research, Code 321. It was also supported in part by the In-house Laboratory Independent Research (ILIR) program of the Naval Undersea Warfare Center.

[1] W. P. Mason, *Piezoelectric Materials and Their Application to Ultrasonics* (Van Nostrand, New York, 1950), Fig. 12.6, p. 295.
[2] D. A. Berlincourt, D. R. Curran, and H. Jaffe, ''Piezoelectric and piezomagnetic materials and their function in transducers,'' in *Physical Acoustics I* (Part A), edited by W. P. Mason (Academic, New York, 1964), Fig. 9, p. 209.
[3] K. M. Rittenmeyer, ''Electrostrictive ceramics for underwater applications,'' J. Acoust. Soc. Am. **95**, 849–856 (1994).
[4] M. B. Moffett, A. E. Clark, M. Wun-Fogle, J. F. Lindberg, J. P. Teter, and E. A. McLaughlin, ''Characterization of Terfenol-D for magnetostrictive transducers,'' J. Acoust. Soc. Am. **89**, 1448–1455 (1991).
[5] J. C. Piquette and S. E. Forsythe, ''One-dimensional phenomenological theory of hysteresis. I. Development of the model,'' J. Acoust. Soc. Am. **106**, 3317–3327 (1999).
[6] J. C. Piquette and S. E. Forsythe, ''One-dimensional phenomenological theory of hysteresis. II. Applications,'' J. Acoust. Soc. Am. **106**, 3328–3334 (1999).
[7] J. A. Main, E. Garcia, and D. V. Newton, ''Precision position control of piezoelectric actuators using charge feedback,'' J. Guid. Control Dyn. **18**, 1068–1073 (1995).
[8] J. C. Piquette and S. E. Forsythe, ''An Underwater Acoustic Projector,'' Notice of Allowability serial number 08/919.071, 19 March 1998.
[9] J. C. Piquette, ''Dual-Section Push-Pull Underwater Projector,'' U.S. Patent Number 5,949,741, issued 7 Sept. 1999.
[10] J. C. Piquette, ''Flextentional Dual-Section Push-Pull Underwater Projector,'' U.S. Patent Number 5,926,439, issued 20 July 1999.

Modeling, vibration, and stability of elastically tailored composite thin-walled beams carrying a spinning tip rotor

Ohseop Song
Mechanical Engineering Department, Chungnam National University, Taejon 305-764, South Korea

Hyuck-Dong Kwon
Mechanical Engineering Department, Yonsei University, Seoul 120-749, South Korea

Liviu Librescu[a)]
Engineering Science and Mechanics Department, Virginia Polytechnic Institute and State University, Blacksburg, Virginia 24061

(Received 5 September 2000; revised 6 April 2001; accepted 14 April 2001)

The problems of the mathematical modeling, eigenvibration, and stability of cantilevered thin-walled beams carrying a spinning rotor at its tip are investigated. The structure modeled as a thin-walled beam encompasses nonclassical features such as anisotropy, transverse shear, and secondary warping, and in this context, a special ply-angle configuration inducing a structural coupling between flapping-lagging-transverse shear is implemented. The implications of combined gyroscopic effects and conservative force upon the free vibration and stability of this structural system are revealed and a number of pertinent conclusions are outlined. Among others, it is shown that the judicious implementation of the tailoring technique can yield dramatic enhancements of both the vibrational and stability behavior of the system. © *2001 Acoustical Society of America.*
[DOI: 10.1121/1.1377292]

PACS numbers: 43.40.At [CBB]

I. INTRODUCTION

A great deal of interest for the study of gyroscopic systems has been manifested in the last decade. This interest was stimulated by the need of a better understanding of the behavior of a number of important technological devices such as the drive shafts of gas turbines, of rotor systems used in helicopter and tilt rotor aircraft, as well as of robotic manipulators and gyro-devices used in space applications. Some of these robots carry tools, such as drills or grinding wheels that rotate. The extensive lists of references supplied in Refs. 1 and 2 reflect in full the interest afforded to the study of this problem. However, in the last years (see Refs. 3 and 4), a more encompassing concept of gyroscropic systems, referred to as gyroelastic ones, was developed. According to this concept, a gyroelastic system is constituted of a body considered to be continuous in mass, stiffness, and in gyricity, as well. Based on this concept, an efficient possibility of modeling elastic structures that are equipped with a large number of small spinning rotors spread over the structure can be devised. Moreover, within this concept, also the case of the continuum equipped with discrete spinning rotors can be accommodated. In several recent papers this concept was exemplified for the case of a Bernoulli–Euler solid beam containing a 1-D distribution of gyricity along the beam neutral axis and subjected to a conservative load (see, e.g., Ref. 4), whereas in Ref. 5 this concept was applied to the case of a solid beam carrying a spinning rotor located at the beam tip. In the present article, an encompassing structural model equipped with a gyrodevice is considered. In this sense, an anisotropic thin-walled beam equipped at its free end with a small spinning rotor is considered. The beam model as considered in this article was developed in Refs. 6–8. In this context, one of the goals of this article is to model and analyze the vibrational behavior of the gyroelastic system (see Fig. 1) as a function of the spin rate Ω_z of the rotor and on the conservative compressive force acting along the longitudinal z axis. Another goal of this research is to put into evidence the conditions under which, for the present gyroscopic system, the instabilities by divergence (i.e., the static one) and by flutter (i.e., the dynamic one) occur. In this context, it will be shown that the directionality property featured by the anisotropic materials of the structure can constitute important tools towards postponing the occurrence of such instabilities. To this end, in order to induce specific structural couplings beneficial for the structure, a *circumferentially uniform stiffness configuration* is considered. Within this ply-angle configuration the entire system of governing equations splits exactly into two independent systems, one of them involving the flapping-lagging-transverse shear coupling, and the other one involving the twist-extension coupling. For the problem at hand, only the case of the system undergoing the flapping-lagging-transverse shear coupled motion will be considered.

II. COORDINATE SYSTEMS. BASIC ASSUMPTIONS

The case of a straight flexible thin-walled beam of length L that is clamped at $Z=0$ and free at $Z=L$ where it carries a spinning rigid rotor of mass m is considered (see

a)Electronic mail: librescu@vt.edu

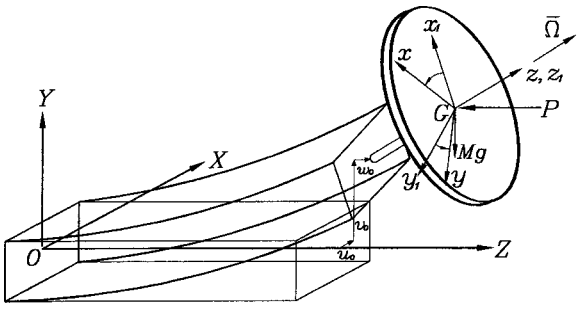

FIG. 1. Thin-walled box-beam with a spinning tip rotor.

Fig. 1). The offset between the beam tip and the centroid of the rotor is denoted as r_m. The rotor is assumed to have an axis of inertial symmetry which is coincident with the longitudinal axis of the beam.

Two sets of coordinates are considered, an inertial frame $OXYZ$ and a body fixed frame $Gxyz$ attached to the rotor, where G is the rotor mass center. Associated to these two coordinate frames, the systems of the unit vectors are $\mathbf{I}$, $\mathbf{J}$, $\mathbf{K}$, and $\mathbf{i}$, $\mathbf{j}$, $\mathbf{k}$, respectively. The external force P acting at the beam tip is assumed to remain parallel to the Z axis of the inertial frame, whereas the spin rate vector of the rotor, $\mathbf{\Omega}_z$, is $\mathbf{\Omega}_z = \Omega_z \mathbf{k}$.

The adopted structural model is that of a thin-walled beam of arbitrary cross-sectional shape. Toward its modeling, the following assumptions are adopted: (*i*) the original cross-section of the beam is preserved, (*ii*) the secondary warping effect is included, (*iii*) transverse shear effects are incorporated, and, finally, (*iv*) the constituent material of the structure features anisotropic properties, and, in this context, a special lay-up inducing flapping-lagging-transverse shear coupling is implemented. As a result, conditions preventing the occurrence of the twist motion should be implemented. Consequently, in this analysis the existence of the mass unbalance of the rotor is precluded.

III. KINEMATICS

In light of the previously mentioned assumptions and in order to reduce the 3-D elasticity problem to an equivalent 1-D one, the components of the displacement vector are represented as in Refs. 1, 2 and 6–9 as

$$u(X,Y,Z;t) = u_0(Z;t) - Y\phi(Z,t), \tag{1a}$$

$$v(X,Y,Z;t) = v_0(Z;t) + X\phi(Z,t), \tag{1b}$$

$$w(X,Y,Z;t) = w_0(Z,t) + \theta_X(Z;t)\left[Y(s) - n\frac{dX}{ds}\right] + \theta_Y(Z;t)\left[X(s) + n\frac{dY}{ds}\right] - \phi'(Z;t)[F_\omega(s) + na(s)]. \tag{1c}$$

In these equations $u_0(Z;t)$, $v_0(Z;t)$, and $w_0(Z;t)$ denote the displacements along the X, Y and Z axes, respectively, while $\phi(Z,t)$, $\theta_X(Z;t)$, and $\theta_Y(Z;t)$ denote the twist about the Z axis and rotations about the X and Y axes, respectively, $F_\omega(s)$ and $na(s)$ that appear in the longitudinal displacement play the role of primary and secondary warping functions, respectively. For their definition see Refs. 6–8. In these equations, as well as in the forthcoming ones, the primes denote differentiation with respect to the longitudinal Z-coordinate, s is the local circumferential coordinate measured along the mid-surface beam contour, while n is the local normal coordinate measured from the mid-surface of the beam cross-section through the wall thickness. The rotational displacement of the beam tip can be expressed as $\Theta = [\theta_X, -\theta_Y, \phi]^T$, while the angular velocity $\mathbf{\Omega_B}$ of the beam cross-section where the rotor is attached is represented in the absolute system of coordinates through the symbolism of Hughes (see Ref. 10) as

$$\Omega_B = \dot{\Theta} - \tfrac{1}{2}\Theta^X\dot{\Theta} = [\dot{\theta}_X + \tfrac{1}{2}(\theta_Y\dot{\phi} - \dot{\theta}_Y\phi); -\dot{\theta}_Y + \tfrac{1}{2}(\theta_X\dot{\phi} - \dot{\theta}_X\phi); \dot{\phi} + \tfrac{1}{2}(\theta_X\dot{\theta}_Y - \dot{\theta}_X\theta_Y)]^T. \tag{2}$$

In Eq. (2), Θ^X is the skew-symmetric matrix expressed in terms of the elements of the column matrix Θ as

$$\Theta^X = \begin{vmatrix} 0 & -\phi & -\theta_Y \\ \phi & 0 & -\theta_X \\ \theta_Y & \theta_X & 0 \end{vmatrix}. \tag{3}$$

In addition, the superposed dots and superscript T denote time derivatives and transpose of a matrix, respectively. Since Ω_B as expressed by Eq. (2) has to be evaluated at the beam tip, the terms associated with its effect appear in the boundary conditions at $Z = L$.

IV. GOVERNING EQUATIONS

Toward the goal of deriving the equations of motion of beams equipped with a spinning rotor at its tip and the associated boundary conditions, Hamilton's variational principle is used. It may be stated as

$$\delta J = \int_{t_0}^{t_1} (\delta U - \delta K_B - \delta K_R - \delta W_R - \delta W_A)\, dt = 0, \tag{4}$$

where U denotes the strain energy of the elastic beam, K_B and K_R denote the kinetic energy of the beam, and of the spinning rotor, respectively, W_R and W_A denote the work done by spinning rotor and axial load, respectively, while δ denotes the variation operator.

In the forthcoming developments, in order to render explicitly the various energies intervening in Eq. (4), the relationship between the unit vectors $(\mathbf{I},\mathbf{J},\mathbf{K})$ and $(\mathbf{i},\mathbf{j},\mathbf{k})$ has to be established. To this end, after lengthy but straightforward manipulations one obtains the relationship

$$\begin{pmatrix} \mathbf{I} \\ \mathbf{J} \\ \mathbf{K} \end{pmatrix} = [H] \begin{pmatrix} \mathbf{i} \\ \mathbf{j} \\ \mathbf{k} \end{pmatrix}, \tag{5}$$

where, by using the concept of small angles of rotation, we have

$$[H]\equiv h_{ij}=\begin{bmatrix} \cos\Omega t-\phi\sin\Omega t & -(\sin\Omega t+\phi\cos\Omega t) & -\theta_Y \\ \sin\Omega t+\phi\cos\Omega t & \cos\Omega t-\phi\sin\Omega t & -\theta_X \\ \theta_X\sin\Omega t+\theta_Y\cos\Omega t & \theta_X\cos\Omega t-\theta_Y\sin\Omega t & 1 \end{bmatrix}. \tag{6}$$

By virtue of (2), the total angular velocity of the rotor can be expressed as

$$\begin{aligned}\boldsymbol{\Omega}_R&=\boldsymbol{\Omega}_B+\Omega_z\mathbf{k}\\ &=[\dot\theta_X+\tfrac{1}{2}(\theta_Y\dot\phi-\dot\theta_Y\phi)]\mathbf{I}+[-\dot\theta_Y+\tfrac{1}{2}(\theta_X\dot\phi-\dot\theta_X\phi)]\mathbf{J}\\ &\quad+[\dot\phi+\tfrac{1}{2}(\theta_X\dot\theta_Y-\dot\theta_X\theta_Y)]\mathbf{K}+\Omega_z\mathbf{k}\\ &=\omega_{BX}\mathbf{I}+\omega_{BY}\mathbf{J}+\omega_{BZ}\mathbf{K}+\Omega_z\mathbf{k}\\ &=(\omega_{BX}h_{11}+\omega_{BY}h_{21}+\omega_{BZ}h_{31})\mathbf{i}+(\omega_{BX}h_{12}+\omega_{BY}h_{22}\\ &\quad+\omega_{BZ}h_{32})\mathbf{j}+(\omega_{BX}h_{13}+\omega_{BY}h_{23}+\omega_{BZ}h_{33}+\Omega_z)\mathbf{k}\\ &\equiv\omega_{Rx}\mathbf{i}+\omega_{Ry}\mathbf{j}+\omega_{Rz}\mathbf{k}.\end{aligned} \tag{7}$$

On the other hand, keeping in mind the expression of the position vector of the rotor

$$\mathbf{R}_R(x,y,z;t)=u_0\mathbf{I}+v_0\mathbf{J}+(L+w_0)\mathbf{K}+x\mathbf{i}+y\mathbf{j}+(r_m+z)\mathbf{k}, \tag{8}$$

one obtains

$$\dot{\mathbf{R}}_R=\dot u_0\mathbf{I}+\dot v_0\mathbf{J}+\dot w_0\mathbf{K}+x\dot{\mathbf{i}}+y\dot{\mathbf{j}}+z\dot{\mathbf{k}}, \tag{9}$$

wherefrom, by virtue of Eqs. (5) and (6), its expression becomes

$$\begin{aligned}\dot{\mathbf{R}}_R&=\dot u_o\mathbf{I}+\dot v_o\mathbf{J}+\dot w_o\mathbf{K}+(-y\omega_{Rz}+z\omega_{Ry})\mathbf{i}\\ &\quad+(x\omega_{Rz}-z\omega_{Rx})\mathbf{j}+(-x\omega_{Ry}+y\omega_{Rx})\mathbf{k}.\end{aligned} \tag{10}$$

As a result, it is possible to obtain the kinetic energy of the rotor as

$$\begin{aligned}K_R&=\frac{1}{2}\int_{\tau_R}\rho_R(\dot{\mathbf{R}}_R\cdot\dot{\mathbf{R}}_R)\,\delta_{\mathrm{D}}(Z-L)\,d\tau_R\\ &=\tfrac{1}{2}\{m_R(\dot u_o^2+\dot v_o^2+\dot w_o^2)+J^R_{xxyy}(\dot\theta_X^2+\dot\theta_Y^2)+J^R_{zz}[(\dot\phi+\Omega)^2\\ &\quad+3\Omega_z(\theta_X\dot\theta_Y-\dot\theta_X\theta_Y)]\}_{Z=L}.\end{aligned} \tag{11}$$

Herein, $J^R_{xx}=J^R_{yy}=J^R_{xxyy}=m_R(r_m^2+\frac{1}{4}k_R^2)$ are the rotor mass moments of inertia, $J^R_{zz}=\frac{1}{2}m_Rk_R^2$ is the polar moment of inertia, k_R is the radius of gyration of the rotor, and m_R is the rotor mass, while $\delta_{\mathrm{D}}(\cdot)$ stands for the Dirac's delta function.

As a result, by using Hamilton's condition consisting of $\delta v_i=0$, at t_0, t_1, one obtains

$$\begin{aligned}\int_{t_0}^{t_1}\delta K_R\,dt&\equiv\left(\int_{t_0}^{t}dt\int_{\tau_R}\rho_R\ddot{\mathbf{R}}_R\cdot\delta\mathbf{R}_R\,d\tau_R\right)\\ &=[-m_R\ddot u_o\delta u_o-m_R\ddot v_o\delta v_o-m_R\ddot w_o\delta w_o\\ &\quad-(J^R_{xxyy}\ddot\theta_X-3\Omega J^R_{zz}\dot\theta_Y)\delta\theta_X-(J^R_{xxyy}\ddot\theta_Y\\ &\quad+3\Omega J^R_{zz}\dot\theta_X)\delta\theta_Y-J^R_{zz}\ddot\phi\,\delta\phi]_{Z=L}.\end{aligned} \tag{12}$$

As basic prequisites, we will list also the variation of the work done by the spinning tip rotor:

$$\begin{aligned}\delta W_R&=[m_Rr_m\ddot\theta_Y\delta u_o+m_R(r_m\ddot\theta_X-g)\,\delta v_o+m_Rr_m(\ddot v_o+g)\\ &\quad\times\delta\theta_X+m_Rr_m\ddot u_o\delta\theta_Y]_{Z=L}\end{aligned} \tag{13}$$

and also that done by the axial load

$$\delta W_A=-P\int_0^L(u_o''\delta u_o+v_o''\delta v_o)\,dZ+P[u_o'\delta u_0+v_o'\delta v_o]_0^L. \tag{14}$$

Finally, keeping in mind that the position vector and its time derivative of a deformed point of the beam are given, respectively, as

$$\begin{aligned}\mathbf{R}_b(X,Y,Z;t)&=(X+u)\mathbf{I}+(Y+v)\mathbf{J}+(Z+w)\mathbf{K},\\ \dot{\mathbf{R}}_b(X,Y,Z;t)&=\dot u\mathbf{I}+\dot v\mathbf{J}+\dot w\mathbf{K},\end{aligned} \tag{15}$$

one can easily obtain the associated kinetic energy K_b and also

$$\begin{aligned}\int_{t_0}^{t_1}\delta K_b\,dt&\equiv\left(-\int_{t_0}^{t_1}dt\int_{\tau}\ddot{\mathbf{R}}_b\cdot\delta\mathbf{R}_b\,d\tau\right)\\ &=-\int_{t_0}^{t_1}dt\int_{\tau}\left\{(\ddot u_0-Y\ddot\phi)\,\delta u+(\ddot v_0+X\ddot\phi)\,\delta v\right.\\ &\quad+\left(\ddot w_0+\ddot\theta_X\left[Y-n\frac{dX}{ds}\right]+\ddot\theta_Y\left[X+\frac{dY}{ds}\right]\right.\\ &\quad\left.\left.-\ddot\phi'[F_w+na]\right)\delta w\right\}\rho\,d\tau\\ &=-\int_{t_0}^{t_1}dt\left[\int_0^L\{K_1\delta u_0+K_2\delta v_0\right.\\ &\quad+K_3\delta w_0\delta\theta_X+K_4\theta_X+K_5\delta\theta_Y\\ &\quad\left.+(K_6-K_7)\,\delta\phi\}dZ-[K_7\delta\phi]_0^L\right]dt.\end{aligned} \tag{16}$$

In the above equation K_i $(i=\overline{1,7})$ denote inertia terms. Their expressions, restricted to *circumferentially uniform*

stiffness configuration case that is considered in this article, are provided in Appendix A.

As concerns the variation of strain energy U_b of the beam, its expression is

$$\delta U_b = \frac{1}{2}\int_\tau \sigma_{ij}\delta\epsilon_{ij}d\tau$$

$$= -\int_0^L \{Q'_X\delta u_0 + Q'_Y\delta v_0 + T_Z\delta w_0 + (M'_X - Q_Y)\delta\theta_X + (M'_Y - Q_X)\delta\theta_Y + (B''_w + M'_Z)\delta\phi\}dZ + [Q_X\delta u_0 + Q_Y\delta v_0 + T_A\delta w_0 + M_x\delta\theta_X + M_Y\delta\theta_Y + (B'_w + M_Z)\delta\phi - B_w\delta\phi']_0^L, \quad (17a)$$

where Q_X, Q_Y, T_Z, M_X, M_Y, M_Z and B_ω are 1-D stress-resultants and stress-couples defined in Refs. 1, 6, and 7.

In addition, the variation of the work done by the gravitational force is

$$\delta W_{bg} = -\int_0^L b_1 g\,\delta v_0 dZ, \quad (17b)$$

where g is the gravitational acceleration while b_1 is a mass term whose expression is provided in Appendix A. In such a context, Hamilton's variational principle, Eq. (4), provides the equations of motion of the entire system and the associated boundary conditions. One of the main features of the obtained governing equation system is the full coupling between flapwise-bending, lateral (or chordwise) bending, extension, twist and transverse shear.

In order to induce the elastic coupling between flapwise-bending, chordwise-bending and transverse shear, a special ply-angle distribution referred to as *circumferentially uniform stiffness* (CUS) configuration (see Refs. 6 and 7), generated by skewing angle plies with respect to the beam axis according to the law $\theta(Y) = \theta(-Y)$ and $\theta(X) = \theta(-X)$, is implemented.

The ply-angle configuration of this type is achievable via winding technology. Angle θ denotes the dominant ply orientation in the top and bottom, as well as in the lateral walls of the beam, measured from the positive s axis toward the positive Z axis.

In this case, from the variational equation (4) expressed in full, bearing in mind that δu_0, δv_0, $\delta\theta_X$ and $\delta\theta_Y$ are independent and arbitrary, and setting the coefficients of these variations to zero in the variational principle, the equations of motion and the boundary conditions featuring this type of coupling are obtained.

Employing constitutive equations and strain-displacement relationships in the equations of motion, the governing equations about a static equilibrium position featuring the flap-lag-transverse shear coupling expressed in terms of displacement quantities are obtained as

$$\delta u_o : a_{43}\theta''_X + a_{44}(u''_o + \theta'_Y) - b_1\ddot{u}_o - Pu''_o = 0, \quad (18a)$$

$$\delta v_o : a_{52}\theta''_Y + a_{55}(v''_o + \theta'_X) - b_1\ddot{v}_o - Pv''_o = 0, \quad (18b)$$

$$\delta\theta_X : a_{33}\theta''_X + a_{34}(u''_o + \theta'_Y) - a_{55}(v'_o + \theta_X) - a_{52}\theta'_Y - \underbrace{(b_4 + \delta_n b_{14})}\ddot{\theta}_X = 0, \quad (18c)$$

$$\delta\theta_Y : a_{22}\theta''_Y + a_{25}(v''_o + \theta'_X) - a_{44}(u'_o + \theta_Y) - a_{43}\theta'_X - \underbrace{(b_5 + \delta_n b_{15})}\ddot{\theta}_Y = 0. \quad (18d)$$

Associated to the governing system, the boundary conditions are at $Z = 0$

$$u_o = v_o = \theta_X = \theta_Y = 0, \quad (19)$$

and at $Z = L$,

$$\delta u_o : a_{43}\theta'_X + a_{44}(u'_o + \theta_Y) - Pu'_o + m_R(\ddot{u}_o - \underbrace{r_m\ddot{\theta}_Y}) = 0, \quad (20a)$$

$$\delta v_o : a_{52}\theta'_Y + a_{55}(v'_o + \theta_X) - Pv'_o + m_R(\ddot{v}_o - \underbrace{r_m\ddot{\theta}_X}) = 0, \quad (20b)$$

$$\delta\theta_X : a_{33}\theta_X{}' + a_{34}(u'_o + \theta_Y) + \underbrace{J^R_{xxyy}\ddot{\theta}_X} - \underline{3\Omega_z J^R_{zz}\dot{\theta}_Y} - m_R r_m\ddot{v}_o = 0, \quad (20c)$$

$$\delta\theta_Y : a_{22}\theta'_Y + a_{25}(v_o{}' + \theta_X) + \underbrace{J^R_{xxyy}\ddot{\theta}_Y} + \underline{3\Omega_z J^R_{zz}\dot{\theta}_X} - m_R r_m\ddot{u}_o = 0. \quad (20d)$$

The coefficients $a_{ij} = a_{ji}$ appearing in these equations as well as in the forthcoming ones denote stiffness quantities. Their expression can be found in Refs. 1 and 6–8. The terms in Eqs. (19) underscored by a solid line are associated with the gyroscopic effects, whereas those marked by an undulated line correspond to rotatory inertia terms. The tracer δ_n identifies the inertia effects associated to the points off the mid-surface of the beam. This tracer takes the value 1 or 0 depending on whether this effect is accounted for or discarded, respectively.

For locations of the spinning rotor different from that of the beam tip, the gryoscopic effects would have to appear in the governing equations and not in the boundary conditions at $Z = L$.

It should be remarked that for $\theta = 0°$ and 90°, the coupling stiffness quantities a_{43}, a_{52}, a_{17} become immaterial, and when also $\Omega_z = 0$, the governing system and boundary conditions split exactly into two independent groups associated with flapping and lagging motions. It should be mentioned that within the same ply-angle configuration an additional system of governing equations and boundary conditions involving the extension-twist coupling are obtained. Being decoupled from the system involving flapwise-chordwise bending, these equations are not used in the article, and as such are not displayed here.

V. THE CASE OF UNSHEARABLE BEAMS

Equations (18)–(20), correspond to shearable beams. In order to determine their unshearable counterpart, elimination of $a_{44}(u'_0 + \theta_Y)$ and $a_{55}(v'_0 + \theta_X)$ in Eqs. (18a) and (18b) and in the boundary conditions (20a) and (20b) followed by consideration of $\theta_X = -v'_0$ and $\theta_Y = -u'_0$ results in the governing equations of the unshearable beams,

$$\delta u_o: a_{22}u_0''''-(\underbrace{b_5+\delta_n b_{15}})\ddot{u}_0''+b_1\ddot{u}_0+Pu_0''=0,$$
$$\delta v_0: a_{33}v_0''''-(\underbrace{b_4+\delta_n b_{14}})\ddot{v}_0''+b_1\ddot{v}_0+Pv_0''=0, \tag{21}$$

and the boundary conditions at $Z=0$,

$$u_o=v_0=u_0'=v_0'=0, \tag{22}$$

and at $Z=L$,

$$\delta u_o: a_{22}u_0'''-(\underbrace{b_5+b_{15}})\ddot{u}_0'+Pu_0'-m_R(\ddot{u}_0+\underbrace{r_m\ddot{v}_0'})=0,$$
$$\delta v_0: a_{33}v_0'''-(\underbrace{b_4+b_{14}})\ddot{v}_0'+Pv_0'-m_R(\ddot{v}_0+\underbrace{r_m\ddot{v}_0'})=0,$$
$$\delta u_0': a_{22}u_0''+\underbrace{J^R_{xxyy}\ddot{u}_0'}+\underline{3\Omega_z J^R_{zz}\dot{v}_0'}+m_R r_m\ddot{u}_0=0, \tag{23}$$
$$\delta v_0': a_{33}v_0''+\underbrace{J^R_{xxyy}\ddot{v}_0'}-\underline{3\Omega_z J^R_{zz}\dot{u}_0'}+m_R r_m\ddot{v}_0=0.$$

In contrast to the case of shearable beams, it becomes evident that for the unshearable beam counterpart, the flapping-lagging coupling arises only in the boundary conditions at the beam tip, and when $r_m=0$, it is due entirely to the gyroscopic effects.

VI. SOLUTION METHODOLOGY

Toward the goal of solving the eigenvalue problem of the gyroelastic system acted on by a compressive edge load applied at its tip, the following steps will be implemented. The first one consists of the representation of displacement quantities in the form

$$u_o(Z;t)=\mathbf{U}^T(Z)\mathbf{q}_u(t), \quad v_o(Z;t)=\mathbf{V}^T(Z)\mathbf{q}_v(t),$$
$$\theta_X(Z;t)=\mathbf{X}^T(Z)\mathbf{q}_x(t), \quad \theta_Y(Z;t)=\mathbf{Y}^T(Z)\mathbf{q}_y(t). \tag{24}$$

Herein $\mathbf{U}$, $\mathbf{V}$, $\mathbf{X}$, $\mathbf{Y}$ are the vectors of trial functions that are chosen as to satisfy at least the kinematic boundary conditions; $\mathbf{q}_u$, $\mathbf{q}_v$, $\mathbf{q}_x$, $\mathbf{q}_y$ are the vectors of generalized coordinates, while superscript T denotes transpose operation. Replacing the energy quantities and representations (24) in the variational integral, Eq. (4), carrying out the indicated variations and the required integrations, leads to the equation

$$\mathbf{M}\ddot{\mathbf{q}}(t)+\mathbf{G}\dot{\mathbf{q}}(t)+\mathbf{K}\mathbf{q}(t)=\mathbf{0}, \tag{25}$$

where $\mathbf{M}$ is the real, symmetric, positive definite mass matrix, $\mathbf{K}$ is the symmetric stiffness matrix, including in its elements the external load P, $\mathbf{G}$ is the skew-symmetric gyroscopic matrix, while $\mathbf{q}\equiv[\mathbf{q}_u^T,\mathbf{q}_v^T,\mathbf{q}_x^T,\mathbf{q}_y^T]^T$ is the overall vector of the generalized coordinates. Notice that in the case of the nonspinning rotor, i.e., when $\Omega_z=0$, in the absence of structural damping the matrix $\mathbf{G}$ becomes immaterial. The expressions of the matrices $\mathbf{M}$, $\mathbf{K}$, and $\mathbf{G}$ are supplied in Appendix B.

For synchronous motion, upon expressing $\mathbf{q}(t)=\mathbf{Z}\exp(i\omega t)$, where $\mathbf{Z}$ is a constant vector and ω is a constant valued quantity, both generally complex, and following the usual steps, one obtains the eigenvalue problem

$$-\omega^2\mathbf{M}\mathbf{Z}+i\omega\mathbf{G}\mathbf{Z}+\mathbf{K}\mathbf{Z}=\mathbf{0}, \tag{26}$$

where ω must satisfy the characteristic equation

$$\Delta(\omega^2,P,\Omega_z)=\det|-\omega^2\mathbf{M}+i\omega\mathbf{G}+\mathbf{K}|=0. \tag{27}$$

In this connection we have to remark that the characteristic polynomial Δ contains only even powers of ω and, as such, the stability will be analyzed in terms of the nature of ω^2. Since $\mathbf{K}$ includes the contribution of the external load which can be tensile or compressive, we can have $\mathbf{K}>0, \mathbf{K}=0$ or $\mathbf{K}<0$. As a result, one can distinguish three cases (see Ref. 11):

(1) Pure oscillatory motion, i.e., stable motion, occurring when $\mathbf{K}$ is positive definite, as long as ω_k^2 are real and positive.
(2) Instability by divergence is found from the equation $\Delta(\omega^2,P)=0$ when $\omega^2=0$. As clearly emerges, the instability by divergence depends on the external load P only and is the same for both the gyroscopic and nongyroscopic systems.
(3) $\mathbf{K}$ is negative definite. In this case it is still possible to have stable motion. In such a case the gyroscopic effects stabilize the unstable conservative system. However, also in the case, when $\mathbf{K}$ is negative definite, the eigenvalues can be complex conjugate with at least one of them having a negative imaginary part, which results in unstable motion of the flutter type. As the rotational speed of the rotor Ω_z and the compressive load P increase, two consecutive eigenvalues ω_p^2 and ω_p^2+1 may coalesce, and beyond that point of coalescence, the eigenfrequencies become complex conjugate, and correspondingly, bending oscillations with exponentially increasing amplitudes will occur. The values of ω and Ω_z corresponding to the coalescence point are referred to as the flutter frequency ω_{fl}, and the flutter rotational speed $(\Omega_z)_{fl}$, respectively. Certainly, at each magnitude of the external load P, ω_{fl} and $(\Omega_z)_{fl}$ can be determined. Although this type of instability is typical to nonconservative systems, this can occur in conservative gyroscopic systems as well.

VII. NUMERICAL SIMULATIONS

The numerical illustrations are carried out for the case a composite box-beam. It features the following dimensions: $c=10$ in., $h=0.4$ in., $L=80$ in. It is also assumed that the material of the beam structure is of a Graphite/Epoxy composite whose on-axes elastic properties can be found in Refs. 1 and 6–8.

The numerical simulations are displayed in terms of the following dimensionless parameters of the system:

$$\overline{\omega}_i=\frac{\omega_i}{\omega_0}, \quad \overline{\Omega}_z=\frac{\Omega_z}{\omega_o}, \quad R=\frac{b}{c}; \quad \overline{P}=\frac{\overline{P}}{\hat{P}},$$
$$\overline{m}_R=\frac{m_R}{b_1 L}=0.5, \quad \overline{r}_m=\frac{r_m}{L}=0.2, \quad \overline{k}_R=\frac{k_R}{L}=0.2. \tag{28}$$

Herein $\omega_0=164.73$ rad/s while $\hat{P}=81178.1$ lb.

In Figs. 2(a)–4(a) there are depicted, in the absence of the compressive load $\overline{P}$, the dependence of the three normalized eigenfrequencies $\overline{\omega}_i$ $(i=1,2,3)$ versus the normalized rotor spin speed $\overline{\Omega}_z$. The results were generated for a square cross-section $(R=1)$, unshearable beam, and for selected

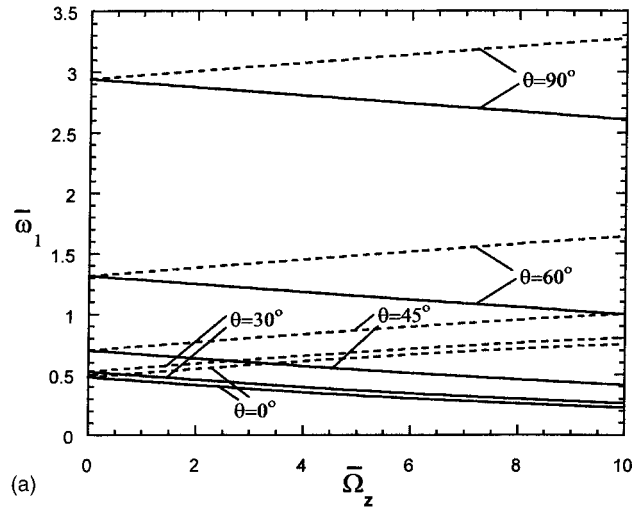

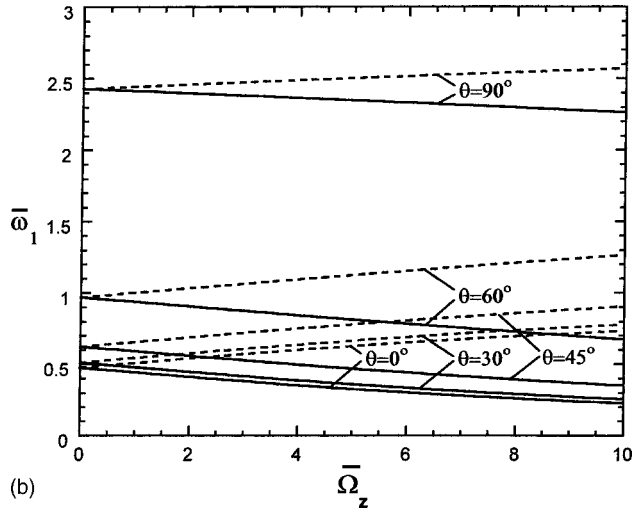

FIG. 2. (a) Influence of the ply-angle of the beam material on the upper and lower branches of the rotating dimensionless fundamental frequency. Unshearable beam model $R=1$. (b) The counterpart of (a) for the shearable beam model.

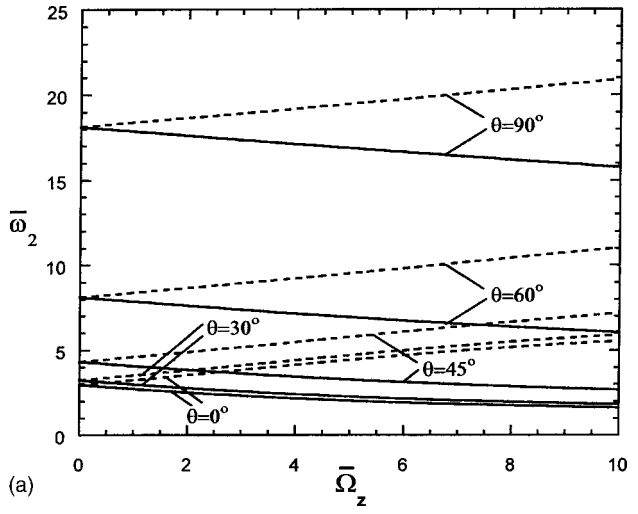

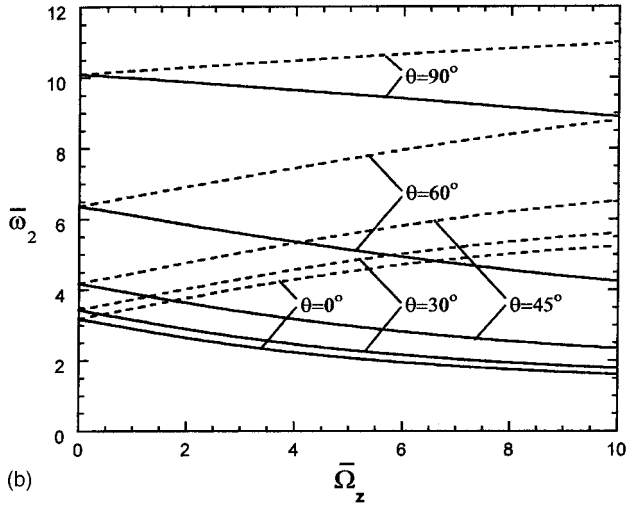

FIG. 3. (a) The counterpart of Fig. 2(a) for the second mode natural dimensionless frequency. (b) The counterpart of (a) for the shearable beam model.

values of the ply-angle θ. For $\bar{\Omega}_z=0$, i.e., for the nonspinning rotor, having in view that for this case the bending stiffnesses in X and Y directions are equal, the flapping and lagging eigenfrequencies in each mode coincide. As soon as the rotation starts, i.e., for $\bar{\Omega}_z\neq 0$, implying that gyroscopic forces are generated, a bifurcation of rotating eigenfrequencies is experienced, resulting in the upper and lower frequency branches. The rotor spin rate at which the lowest rotating eigenfrequency becomes zero-valued is referred to as the critical spinning speed, $(\bar{\Omega}_z)_{cr}$, and corresponds to the divergence instability. However, as it will appear later in Fig. 5, this critical spinning speed is extremely large. From these plots it can readily be seen that implementation of the tailoring technique can yield a dramatic enhancement of the vibrational behavior of the system. In this sense, the increase of the ply-angle θ, which is accompanied by an increase of bending stiffnesses (see Ref. 7), results in an increase of both nonrotating and rotating eigenfrequencies.

From the same figure it clearly appears that, with the increase of the mode number, for fixed spin rates the distances between the upper and lower frequency branches as compared to those appearing in the lower modes tend to reduce in magnitude, a trend that is independent of the variation of the ply-angle. In Figs. 2(b)–4(b) the shearable counterparts of Figs. 2(a)–4(b) are depicted. Comparison of these figures reveals that the classical (unshearable) beam model overestimates both the nonrotating and the rotating frequencies.

In Fig. 5 the variation of the lower branch of the first eigenfrequency of the system versus the rotor spinning rate $\bar{\Omega}_z$ is depicted in logarithmic scale, for selected values of the ply-angle. The beneficial effects induced by the increase of the ply-angle on both the lower branch of rotating fundamental eigenfrequency and on the rotor spinning divergence speed clearly emerge from this plot. The same trend appears also in the case of the variation of the cross-section parameter R, in the sense that the increase of R yields an increase of both the rotating/nonrotating lower branch of eigenfrequencies and of the divergence spinning speed of the rotor.

In Figs. 6–8 there are plots depicting the variation of the first three eigenfrequencies versus $\bar{\Omega}_z$ for selected values of the cross-sectional parameter R, and for a fixed value of the

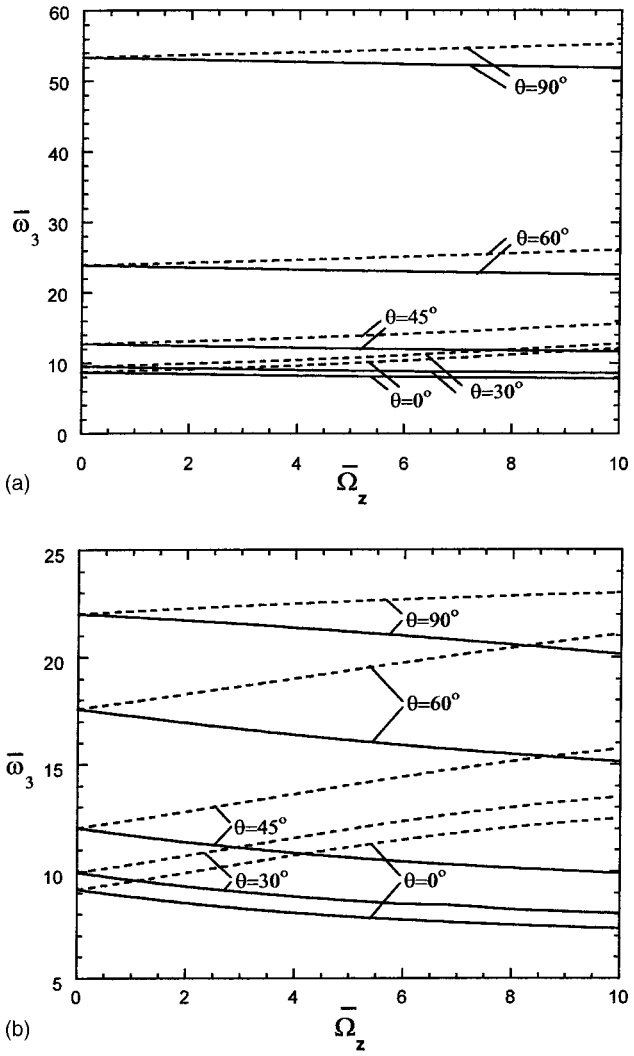

FIG. 4. (a) The counterpart of Fig. 2(a) for the third mode natural dimensionless frequency. (b) The counterpart of (a) for the shearable beam model.

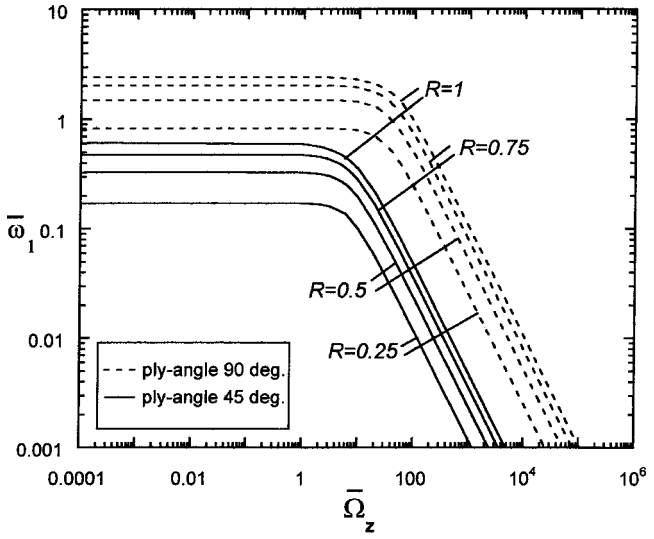

FIG. 5. Variation of the lower branch of the first natural rotating frequency for selected values of the cross-section parameter R, and two values of the ply-angle, $\theta = 45$ and 90 degrees.

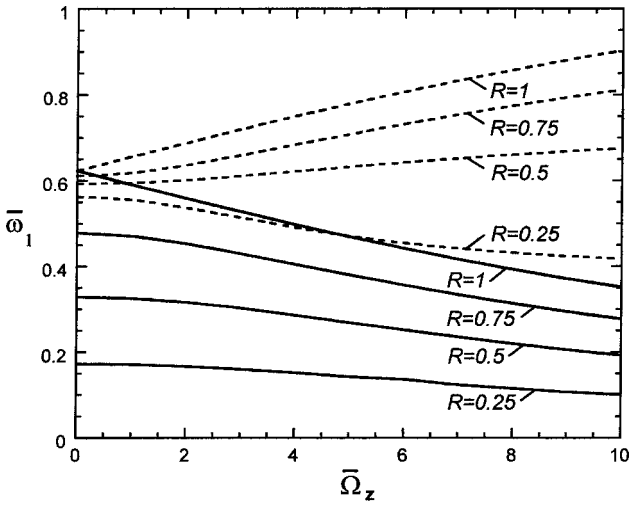

FIG. 6. Influence of the cross-section parameter R on the upper and lower branches of the first natural dimensionless rotating frequency, $\theta = 45$ degrees.

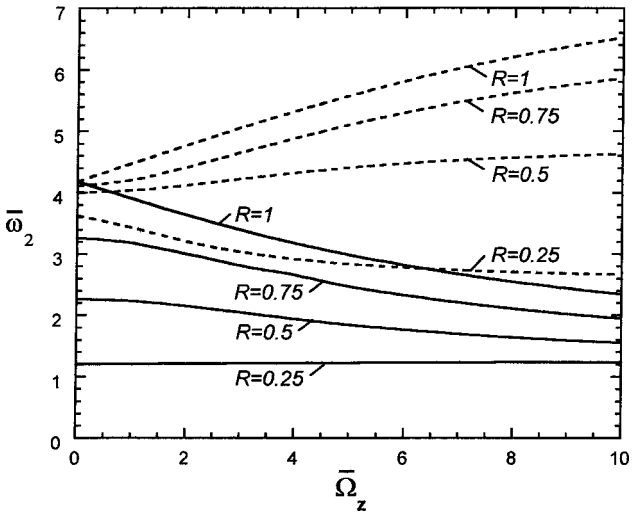

FIG. 7. Counterpart of Fig. 6 for the second rotating natural frequency.

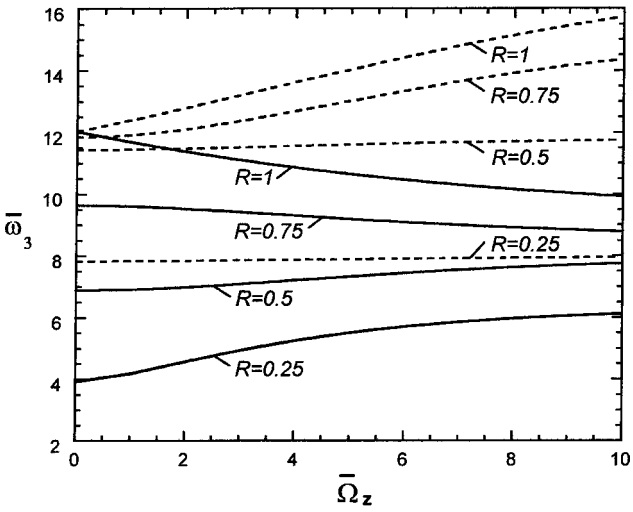

FIG. 8. Counterpart of Fig. 6 for the third rotating natural frequency.

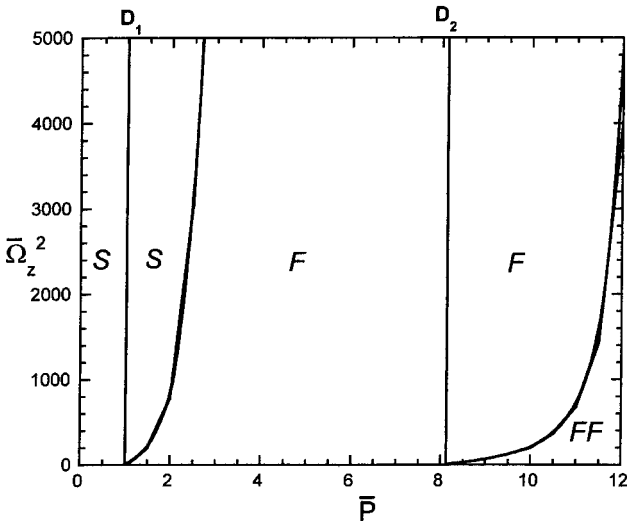

FIG. 9. Stability boundaries for the box-beam with a spinning rotor ($R=1$, $\theta=0$).

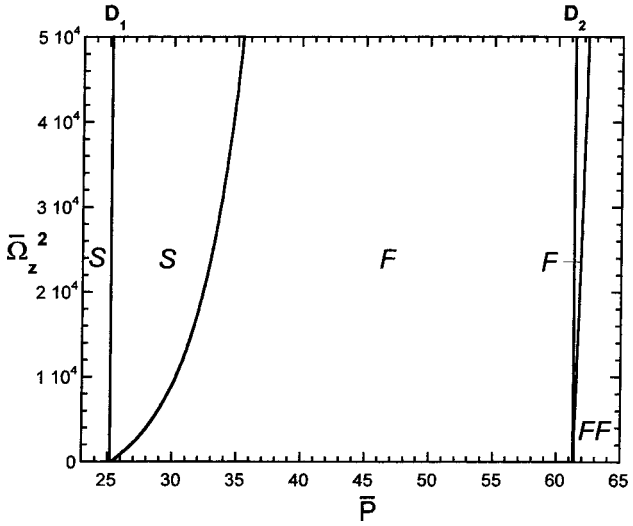

FIG. 11. Counterpart of Fig. 9 for $\theta=90$ degrees.

ply-angle $\theta=45$ degrees. The figures reveal that for beams characterized by $R\neq 1$, the nonrotating frequencies in flapping and lagging do not coincide.

It clearly appears that the natural frequency pairs associated to the case $R\neq 1$ are lower as compared to the ones associated to a square beam cross-section counterpart.

Moreover, with the increase of the mode number, the eigenfrequencies associated to the lower branch of each frequency pair, instead of decreasing, have the tendency of increasing with the increase of $\bar{\Omega}_z$, a trend that is more prominent for lower values of the parameter R.

In Figs. 9–11 stability plots for the case of a square ($R=1$) cross-section beam are supplied. These were generated by representing the trial functions in Eqs. (24) by six-function approximation. In these figures the domains of stability are marked by S, and those by single and double flutter instability by F and FF, respectively. For this case, since the beam features equal bending stiffnesses in both X and Y directions, the divergence instability under the compressive axial load occurs simultaneously in both X and Y directions.

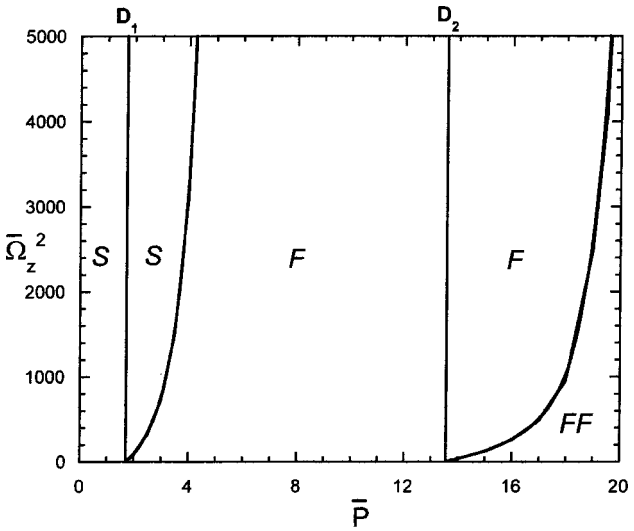

FIG. 10. Counterpart of Fig. 9 for $\theta=45$ degrees.

In this case the divergence boundaries marked as D_1 and D_2 are associated with double roots, and consequently these can be interpreted as divergence regions of zero thickness.

In the load interval $0\leqslant\bar{P}<\bar{P}_{D_1}$, the frequencies ω_k^2 remain positive for any value of $\bar{\Omega}_z^2$, indicating that in this load range the system is stable.

For a slight increase of $\bar{P}$ beyond $\bar{P}_{D_1}$ and for low values of $\bar{\Omega}_z^2$, a pair of complex conjugate eigenfrequencies indicating instability by single flutter is observed. However, as $\bar{\Omega}_z^2$ increases, due to the gyroscopic effects, the system featuring real positive roots ω_k^2 enters into a stable region. One can interpret this behavior as the stabilization of a conservative system by gyroscopic forces.

However, at the right of the resulting stability boundary, until $P=\bar{P}_{D_2}$ and for arbitrary $\bar{\Omega}_z^2$, the frequencies consist of two positive values and a pair of complex conjugates indicating instability by single flutter. For $\bar{P}>\bar{P}_{D_2}$, two flutter regions are featured.

In one of these, the frequencies consist of two positive values and a pair of complex conjugates, indicating instability by single flutter (region F), while in another one, frequencies consist of two pairs of complex conjungates, indicating instability by double flutter (region FF).

From Figs. 9–11 one can infer that with the increase of the ply-angle the stability domains are greatly enlarged and, at the same time, the instability boundaries by divergence and flutter are shifted towards larger compressive loads $\bar{P}$.

It should be remarked that the stability behavior of the beam modeled within the thin-walled beam theory, as reported here, agrees qualitatively well with that obtained within the solid isotropic beam modeled within Bernoulli–Euler theory (see Ref. 5).

As concerns the stability of rectangular cross-section ($R\neq 1$) thin-walled beams, their behavior is much more complex than that featured by their square cross-section beam counterparts, in the sense that in addition to regions corresponding to instability regions by single flutter (F) and divergence (D), regions by double (DD), triple (DDD),

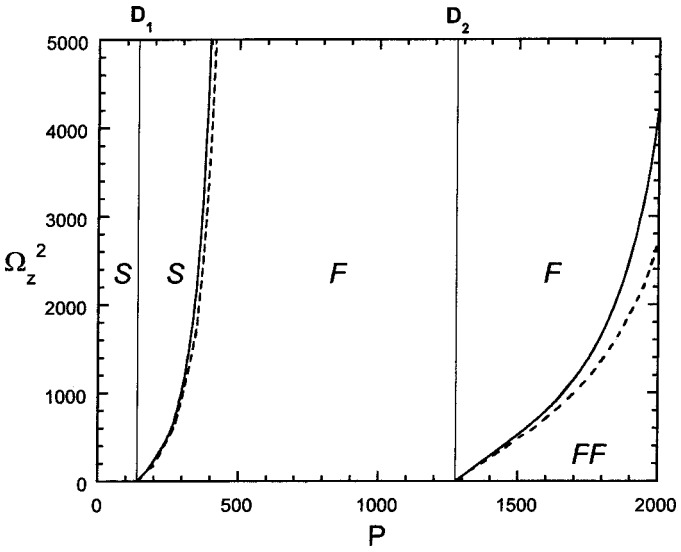

FIG. 12. Validation of the solution methodology based on the Heppler's gyroscopic model (Ref. 5); (————–) present EGM versus (–––––) Heppler's methodology. Stability diagram in the plane $(\Omega_z^2[(\mathrm{rad/s})^2] - P[N]$.

and quaternary $(DDDD)$ divergence and double flutter (FF), as well as instability regions by mixed, single and double divergence and flutter, i.e., DF and DDF, respectively, are featured.

For the case of a solid isotropic beam of cross-sections characterized by $R \neq 1$, the complexity of the stability behavior was illustrated in Ref. 5.

Having in view that, to the best of the authors' knowledge, there are no similar results in the specialized literature based on the thin-walled structural model, the only possible validation would concern the solution methodology used to derive the instability boundaries. In this context, it is possible to apply the present methodology based on the extended Galerkin method (see Ref. 9) to the very simple structural model developed in Ref. 5, where the Ritz method used in conjunction with the eigenfunctions proper to a cantilevered beam have been used. For the data characterizing the gyroscopic system considered in Ref. 5, Fig. 12 displays the instability boundaries obtained via the use of both methodologies, and a good agreement of predictions of the boundaries of stability/instability is revealed.

VIII. CONCLUSIONS

The equations governing the motion of robotic arm systems consisting of a thin-walled elastic beam carrying at its tip a spinning tip rotor loaded by a compressive conservative force have been established.

In this context, the vibrational and stability responses of the considered gyroscopic system have been analyzed, and ways to enhance its behavior, based on the directionality property of the constituent composite material, have been emphasized. The results have also revealed that the system can lose its stability by divergence by the separate actions of $\overline{P}$ and $\overline{\Omega}_z$, and by flutter, through the joint action of $\overline{P}$ and $\overline{\Omega}_z$. This implies that in the absence of the compressive load, the system cannot lose its stability by flutter.

The results have also revealed that in some cases the gyroscopic effects can stabilize the conservative system.

APPENDIX A: EXPRESSIONS OF THE INERTIA TERMS

When restricted to the CUS beam configuration the expressions of the inertia terms are

$$K_1 = b_1 \ddot{u}_0; \quad K_2 = b_1 \ddot{v}_0; \quad K_4 = (b_4 + \delta_n b_{14}) \ddot{\theta}_X;$$

$$K_5 = (b_5 + \delta_n b_{15}) \ddot{\theta}_Y.$$

In these expressions b_i are reduced mass terms defined as

$$(b_1, b_4, b_5) = \oint m_0 (1, Y^2, X^2) ds,$$

$$(b_{14}, b_{15}) = \oint m_2 \left(\left(\frac{dX}{ds} \right)^2, \left(\frac{dY}{ds} \right)^2 \right) ds,$$

where

$$(m_0, m_2) = \sum_{k=1}^{N} \int_{h_{k-1}}^{h_{(k)}} \rho_{(k)} (1, n^2) dn,$$

$\rho_{(k)}$ being the mass density of the kth constituent material layer, while N is the total number of layers.

APPENDIX B: EXPRESSIONS OF THE MASS MATRIX M, STIFFNESS MATRIX K AND SKEW-SYMMETRIC MATRIX G

The entries of the mass matrix $\mathbf{M}(\equiv \mathbf{M}_{4\times 4})$ are the following.

$\mathbf{M} \equiv (m_{ij})$	Their expression
m_{11}	$-\int_0^L (b_1 \mathbf{U}\mathbf{U}^T) dZ - [m_R \mathbf{U}\mathbf{U}^T]_{Z=L}$
$m_{12} = m_{21}$	0
$m_{13} = m_{31}$	0
m_{14}	$[m_R r_m \mathbf{U}\mathbf{Y}^T]_{Z=L}$
m_{22}	$-\int_0^L (b_1 \mathbf{V}\mathbf{V}^T) dZ - [m_R \mathbf{V}\mathbf{V}^T]_{Z=L}$
m_{23}	$[m_R r_m \mathbf{V}\mathbf{X}^T]_{Z=L}$
$m_{24} = m_{42}$	0
m_{32}	$[m_R r_m \mathbf{X}\mathbf{V}^T]_{Z=L}$
m_{33}	$-\int_0^L (b_4 + \delta_n b_{14}) \mathbf{X}\mathbf{X}^T dZ - [J^R_{xxyy} X X^T]_{Z=L}$
$m_{34} = m_{43}$	0
m_{41}	$[m_R r_m \mathbf{Y}\mathbf{U}^T]_{Z=L}$
m_{44}	$-\int_0^L (b_5 + \delta_n b_{15}) \mathbf{Y}\mathbf{Y}^T dZ - [J^R_{xxyy} \mathbf{Y}\mathbf{Y}^T]_{Z=L}$

The entries of the gyroscopic matrix $\mathbf{G}(\equiv \mathbf{G}_{4\times 4})$ different of zero are the following.

$\mathbf{G} \equiv (g_{ij})$	Their expressions
g_{34}	$[3 J^R_{zz} \Omega_z \mathbf{X}\mathbf{Y}^T]_{Z=L}$
g_{43}	$-[3 J^R_{zz} \Omega_z \mathbf{Y}\mathbf{X}^T]_{Z=L}$

The entries of the stiffness matrix $\mathbf{K}(\equiv K_{4\times 4})$ are

$\mathbf{K}\equiv(K_{ij})$	Their expression
k_{11}	$\int_0^L (a_{44}\mathbf{U}\mathbf{U}''^T - P\mathbf{U}\mathbf{U}''^T)dZ$ $-[a_{44}\mathbf{U}\mathbf{U}'^T - P\mathbf{U}\mathbf{U}'^T]_{Z=L}$
$k_{12}=k_{21}$	0
k_{13}	$\int_0^L (a_{43}\mathbf{U}\mathbf{X}''^T)dZ - [a_{43}\mathbf{U}\mathbf{X}'^T]_{Z=L}$
k_{14}	$\int_0^L (a_{44}\mathbf{U}\mathbf{Y}'^T)dZ - [a_{44}\mathbf{U}\mathbf{Y}^T]_{Z=L}$
k_{22}	$\int_0^L (a_{55}\mathbf{V}\mathbf{V}''^T - P\mathbf{V}\mathbf{V}''^T)dZ$ $-[a_{55}\mathbf{V}\mathbf{V}'^T - P\mathbf{V}\mathbf{V}'^T]_{Z=L}$
k_{23}	$\int_0^L (a_{55}\mathbf{V}\mathbf{X}'^T)dZ - [a_{55}\mathbf{V}\mathbf{X}^T]_{Z=L}$
k_{24}	$\int_0^L (a_{52}\mathbf{V}\mathbf{Y}''^T)dZ - [a_{52}\mathbf{V}\mathbf{Y}'^T]_{Z=L}$
k_{31}	$\int_0^L (a_{34}\mathbf{X}\mathbf{U}''^T)dZ - [a_{34}\mathbf{X}\mathbf{U}'^T]_{Z=L}$
k_{32}	$-\int_0^L (a_{55}\mathbf{X}\mathbf{V}'^T)dZ$
k_{33}	$\int_0^L (a_{33}\mathbf{X}\mathbf{X}''^T - a_{55}\mathbf{X}\mathbf{X}^T)dZ - [a_{33}\mathbf{X}\mathbf{X}'^T]_{Z=L}$
k_{34}	$\int_0^L (a_{34}\mathbf{X}\mathbf{Y}'^T - a_{52}\mathbf{X}\mathbf{Y}'^T)dZ - [a_{34}\mathbf{X}\mathbf{Y}^T]_{Z=L}$
k_{41}	$-\int_0^L (a_{44}\mathbf{Y}\mathbf{U}'^T)dZ$
k_{42}	$\int_0^L (a_{25}\mathbf{Y}\mathbf{V}''^T)dZ - [a_{25}\mathbf{Y}\mathbf{V}'^T]_{Z=L}$
k_{43}	$\int_0^L (a_{25}\mathbf{Y}\mathbf{X}'^T - a_{43}\mathbf{Y}\mathbf{X}'^T)dZ - [a_{25}\mathbf{Y}\mathbf{X}^T]_{Z=L}$
k_{44}	$\int_0^L (a_{22}\mathbf{Y}\mathbf{Y}''^T - a_{44}\mathbf{Y}\mathbf{Y}^T)dZ - [a_{22}\mathbf{Y}\mathbf{Y}'^T]_{Z=L}$

We should remark that applying an integration by parts in the expressions of k_{14} and k_{23} one obtains, in conjunction with the boundary conditions that k_{14} and k_{23} reduce to

$$k_{14}=-\int_0^L (a_{44}\mathbf{U}'\mathbf{Y}^T)dZ$$

and

$$k_{23}=-\int_0^L (a_{55}\mathbf{V}'\mathbf{X}^T)dZ,$$

respectively, wherefrom one arrives at the conclusion that the stiffness matrix $\mathbf{K}$ is symmetric.

[1] O. Song, and L. Librescu, "Anisotropy and Structural Coupling on Vibration and Instability of Spinning Thin-Walled Beams," J. Sound Vib. **204**(3), 477–494 (1997).

[2] O. Song and L. Librescu, "Modeling and Vibration of Pretwisted Spinning Composite Thin-Walled Beams," Proceedings of the 38th AIAA/ASME/ASCE/AHS/ASC, Structures, Structural Dynamics, Materials Conference and Exhibition and AIAA/ASME/AHS/Adaptive Structures Forum, Part I, AIAA 97-1091, pp. 312–322, Kissimmee FL, 7–10 April 1997.

[3] G. M. T. D'Eleuterio and P. C. Hughes, "Dynamics of Gyroelastic Spacecraft," J. Guid. Control Dyn. **10**(4), 401–405 (1987).

[4] K. Yamanaka, G. R. Heppler, and K. Huseyin, "Stability of Gyroelastic Beams," AIAA J. **34**(6), 1270–1278 (1996).

[5] K. Yamanaka, G. R. Heppler, and K. Huseyin, "The Stability of a Flexible Link with a Tip Rotor and a Compressive Tip Load," IEEE Trans. Rob. Autom. **11**(6), 882–886 (1995).

[6] O. Song and L. Librescu, "Free Vibration of Anisotropic Composite Thin-Walled Beams of Closed Cross-Section Contour," J. Sound Vib. **167**(1), 129–147 (1993).

[7] L. Librescu, L. Meirovitch, and O. Song, "Refined Structural Modeling for Enhancing Vibrational and Aeroelastic Characteristics of Composite Aircraft Wings," Rech. Aerosp. **1**, 23–35 (1996).

[8] L. Librescu, O. Song, and H. D. Kwon, "Vibration and Stability of Gyroelastic Beams Via Smart Materials Technology," *Smart Structures*, NATO Science Series, 3. High Technology—Vol. 65, edited by J. Holnicki-Szulc and J. Rodellar (Kluwer Academic, Dordrecht, 1999), pp. 163–172.

[9] L. Librescu, L. Meirovitch, and S. S. Na, "Control of Cantilever Vibration via Structural Tailoring and Adaptive Materials," AIAA J. **35**(8), 1309–1315 (1997).

[10] P. C. Hughes, *Spacecraft Attitude Dynamics* (Wiley, New York, 1986).

[11] K. Huseyin, *Vibrations and Stability of Multiple Parameters Systems* (Noordhoff, Alphen Aan Den Rijn, The Netherlands, 1978).

Noise source identification in a rotary compressor: A multidisciplinary synergetic approach

Han-Jun Kim
ArvinMeritor Exhaust, 950 West 450 S, West Columbus, Indiana 47201

Young Man Cho
School of Mechanical and Aerospace Engineering, Seoul National University, San 56-1, Shilim-dong, Kwanak-gu, Seoul 151-742, Korea

(Received 10 July 2000; accepted for publication 30 March 2001)

The complex nature of noise/vibration generation and transmission in rotating machinery has made it indispensable to employ various techniques to identify the corresponding sources and paths. A theoretical approach via finite-element analysis (FEA), an experimental approach via direct measurement, and a signal processing approach via feature extraction of the measured data have all made significant contributions. Yet, there has not been much interdisciplinary effort among the three areas although their mutually complementary roles have long been recognized. In this paper, a synergetic approach is proposed to noise/vibration source and transmission path identification in order to take advantage of all the merits of the three different approaches. The proposed approach is discussed with a rotary compressor as a testbed. In the new approach, the experimentally measured sound intensity map is initially used to suggest the active radiation area, which guides us to instrument the rotary compressor at the suspected noise/vibration source positions. The collected data from the compressor is then processed to unravel the candidate source(s). Various signal processing techniques such as filtering, Hilbert transform, and fast Fourier transform are used to enhance the desired features buried in the experimental data. Finally, modal analysis via FEA and direct measurement further help to pinpoint the true source(s) and simultaneously verifies the conjecture following the experimental data processing.
[DOI: 10.1121/1.1378353]

PACS numbers: 43.40.Le [PJR]

I. INTRODUCTION

It has long been recognized that the comfort level of any commercial product plays a role as a definite market discriminator. It is an irreversible trend that the importance of the comfort level is exceeding that of the functionality, as the living standard of human beings is ever improving. This is especially true for residential systems, e.g., air conditioners, refrigerators, vacuum cleaners, etc. Among many factors determining the comfort level, acoustic noise and mechanical vibration are two nuisances that affect human perception most and, accordingly, have been studied intensively in (Harris, 1957; Croker, 1975; Yerges, 1978; Beranek, 1971; Foreman, 1990; Ewins, 1984; Allemang, 1984).

The complex nature of noise/vibration generation and transmission in these residential systems naturally requires efforts from multiple disciplines for successful control of the comfort level. Modal analysis via the finite-element method (FEM) has offered tremendous insight into the qualitative understanding of noise/vibration generation and transmission without explicit instrumentation. On the other hand, the direct measurement of noise/vibration such as obtaining a sound intensity map has presented a guideline to the localization of noise/vibration sources. Signal processing techniques have provided another alternative by extracting relevant features from *raw* experimental data or simulation output that are not often self-revealing and by presenting these features in a more readily analyzable manner. Notwithstanding their individual success in attacking the problem of noise/vibration generation and transmission, the extent of multidisciplinary efforts has been quite limited. In this paper, a synergetic approach is proposed to noise/vibration source and transmission path identification by employing several techniques from multiple disciplines in order to take advantage of the merits of each technique at different stages of problem solving. A *prima-facie* case is made to demonstrate the role that the synergetic approach can play in the identification of noise/vibration sources and transmission paths. Despite its virtually unlimited realm of application, the proposed approach is discussed with a rotary compressor as a testbed for simplicity and clarity.

First, the frequency range of interest (typically, narrow band) is determined where the noise of the rotary compressor is actively radiating. Then, the sound intensity map around the compressor shows where the excessive sound radiation is physically emanating. The vibration is measured on the compressor shell where the sound intensity map indicates high radiation. The vibration signals are analyzed via various signal processing techniques to identify noise sources and transmission paths. *A priori* knowledge about the compressor running cycle is then used to locate the noise sources. Modal analysis via FEM and direct measurement of the cylinder pressure help to pinpoint the noise source(s). Two noise generation mechanisms are identified in the rotary compressor via the proposed technique: overpressurization in the cylinder chamber and structural resonance of the cylinder.

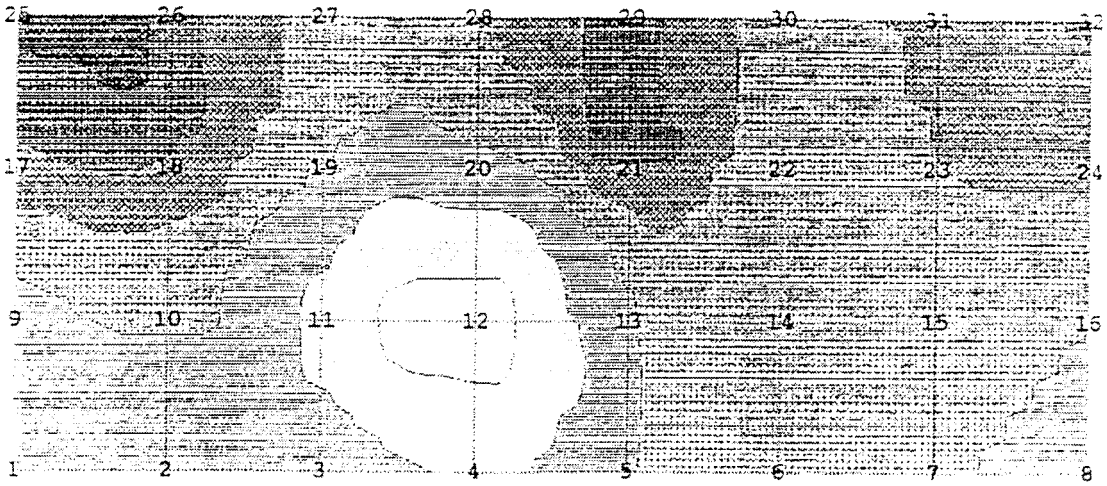

FIG. 1. Sound intensity map of the rotary compressor in the gray scale. The lighter the color is, the stronger the sound intensity is.

Section II shows how acoustic radiation is distributed in the rotary compressor, which leads to further instrumentation of vibration and pressure signals in the compressor. Section III describes the signal processing applications to extract the desired features from the measurements. In Section IV, the noise sources are finally determined by virtue of internal measurement and modal analysis.

II. SOUND INTENSITY MAP ANALYSIS

Identification of noise/vibration sources and transmission paths begins with defining the frequency range of interest. In the rotary compressor under consideration, the 5 kHz band is of interest. Our goal is to localize this 5 kHz band noise so that a remedy may be developed. The requirement for the experimental data collection naturally leads to an ''outside-to-inside'' approach, where experimental data are collected in the following order: (1) outside the compressor, (2) on the compressor shell, and (3) inside the compressor. For example, the internal instrumentation via an accelerometer(s) is much harder to achieve than the external instrumentation via sound intensity measurement using a microphone(s). In the outside-to-inside approach, the external instrumentation sheds light on the potential noise source(s), which alleviates the burden of detailed internal instrumentation. The alternative is to instrument a compressor in detail internally from the beginning.

The operating condition of the compressor is as follows: condensing temperature 130 °F, evaporating temperature 45 °F, and returned gas temperature 65 °F. The sound intensity map of the rotary compressor is measured around the compressor with an intensity probe. The probe is placed 30 cm from the compressor shell so that the sound radiation in the direction normal to the compressor shell is measured. Figure 1 gives an unwrapped view of the sound intensity map around the cylindrical surface of the compressor, where the intensity is measured in the 1/3 octave band centered at 5 kHz. The cylindrical surface is divided into a 4×8 grid. The intensity is represented in the gray scale, i.e., the lighter the color is, the stronger the sound intensity is. It is obvious in Fig. 1 that the sound intensity level at the 5 kHz band was high at location 12 (location ''A''), which is close to the discharge port in the compressor. The intensity level at the location A region is about 10 dB higher than anywhere else on the compressor shell, which suggests measuring the surface vibration (or acceleration) and the near-field sound pressure at the corresponding locations. Then, the coherence is examined between the vibration and the sound pressure.

Figure 2 shows the schematic of the rotary compressor cylinder. The state of the rotary compressor during the compression cycle is represented by the crank angle throughout this paper. The crank angles are measured counterclockwise from the top of the page in Fig. 2. The vibration at location A is measured with an accelerometer in the time domain and is shown in Fig. 3. The sampling rate is 16 kHz. The Fourier transform of the vibration signal at location A indicates the existence of strong vibration peaks in the 5 kHz band. The sound pressure is measured in a similar manner. Then, the coherence between the vibration and the sound pressure in the 5 kHz band is measured in order to determine whether the 5 kHz vibration is the cause of the 5 kHz sound radiation. Such a coherence test can eliminate any possible existence of a nonlinear sound radiation mechanism that would nullify the subsequent analysis of the 5 kHz vibration signal. It is always possible that the vibration at different frequency bands can be shifted into the 5 kHz band when it generates the noise via a nonlinear mechanism. The measured coherence at 5 kHz between the vibration and the sound pressure is 0.95, which proves that the 5 kHz noise is truly vibration induced and that the radiation mechanism is linear. Once the origin of the noise in the 5 kHz band is identified as the vibration at the location A, it is sufficient to analyze the vibration signal instead of the unwieldy sound intensity map, in order to perform the noise source and transmission path identification. In what follows, various signal processing techniques such as filtering, Hilbert transform, and fast Fourier transform are employed to analyze the vibration signals.

III. FEATURE EXTRACTION VIA SIGNAL PROCESSING

In this section, various signal processing techniques are used to extract the necessary features for identifying noise sources in the 5 kHz band. Our approach is to (1) locate the time instant when the maximum vibration occurs, (2) map

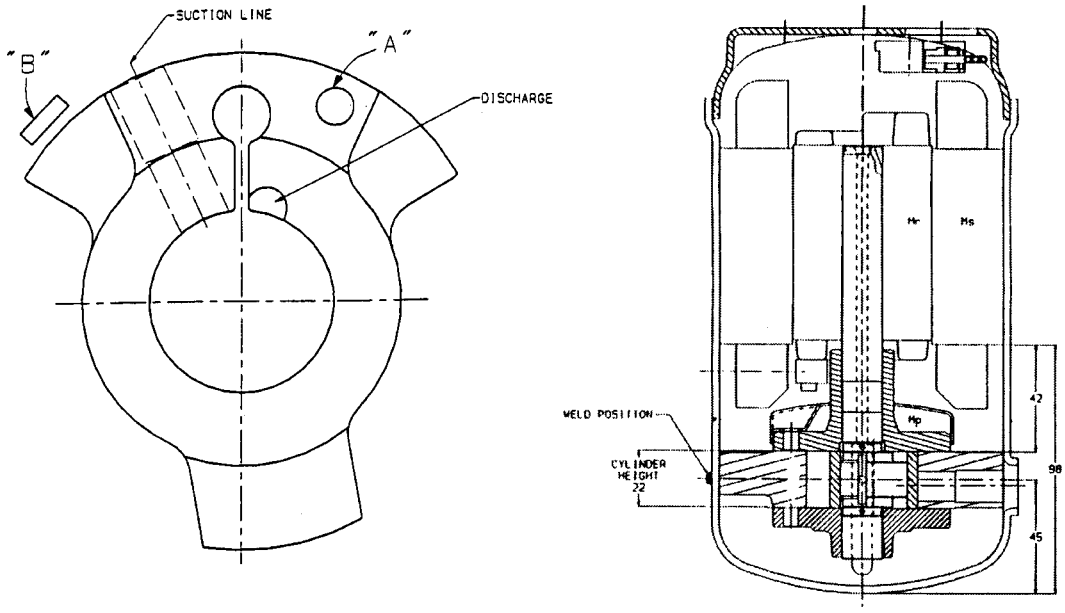

FIG. 2. Schematic diagram of the rotary compressor cylinder. The crank angle is measured counterclockwise from the top of the page.

the time instant into the crank angle, and (3) identify the possible vibration source(s) from the crank angle of the maximum vibration. In this respect, the signal processing techniques adopted in this section should not corrupt the 5 kHz band component or change the timing (or phase) information of the signal. Throughout this section, it is worthwhile noting how such features are preserved.

A. Bandpass filtering of vibration signals

The time-domain signal of vibration contains some unwanted information. A fourth-order Butterworth filter, with passband 4800–5200 Hz, is designed to isolate the 5 kHz component of the vibration signals. The MATLAB signal processing toolbox was used for the filter design (Mathworks, Inc., 1992). Since any causal filter inevitably introduces some phase delay into the filtered signal, special attention must be paid in order to preserve the phase information of the signal, which turns out to be crucial to noise source identification. Since a causal filter cannot preserve the phase, the concept of forward–backward filtering is adopted (Mathworks, Inc., 1992; Oppenheim and Schafer, 1989). Since the gain responses of the forward and backward filters are identical, the signal outside the passband of the Butterworth filter is attenuated twice by the forward–backward filtering. The MATLAB toolbox provides a convenient function to perform the forward–backward filtering (filtfilt.m) with a given filter (in our case, the Butterworth filter). The vibration signal is then filtered with filtfilt.m and the Butterworth filter, which is shown in Fig. 4.

The filtered vibration signal is used to determine the instants in time when high amplitudes occur. Once the time

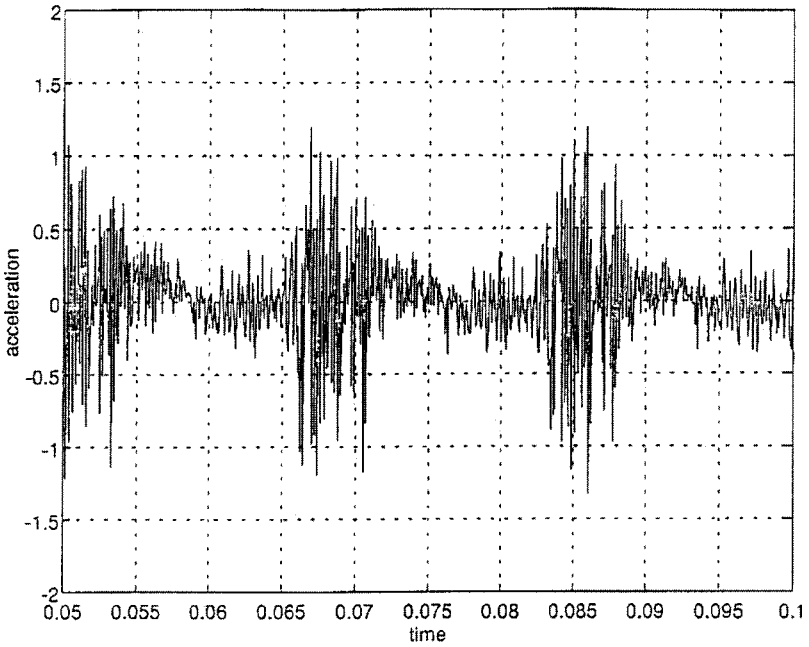

FIG. 3. Acceleration in the time domain at location "A."

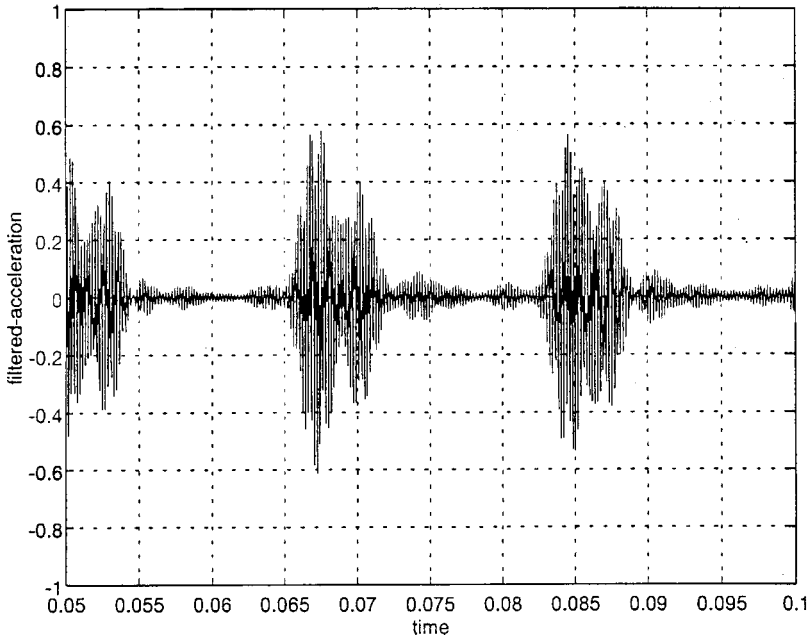

FIG. 4. Acceleration signal filtered by the 5 kHz bandpass filter.

instants are identified, the corresponding states of the compressor during the compression cycle can be inferred such as the position of the piston and the crank angle. Our goal is to identify the corresponding state of the compressor (identified with the crank angle) when the maximum instantaneous amplitude of the vibration signal is achieved, where it is assumed that the maximum instantaneous vibration results in maximum sound (or noise) radiation. However, the filtered signal itself cannot provide *precise* information on its instantaneous amplitude and the corresponding crank angle. In the following, it is shown how to determine the instantaneous amplitude via the Hilbert transform

B. Estimation of instantaneous amplitude via Hilbert transform

The Hilbert transform can help to pinpoint the crank angle corresponding to maximum vibration (Simon and Tomlinson, 1984). The Hilbert transform (or, equivalently, Hilbert filter) of $x(t)$ is defined as follows (Bracewell, 1986):

$$X_{\mathrm{Hi}} \underline{\underline{\mathrm{def}}} \frac{1}{\pi}\int_{-\infty}^{\infty}\frac{x(\tau)}{\tau - t}\,d\tau.$$

In the frequency domain, the Hilbert transform of $x(t)$ is given by $j\,\mathrm{sgn}(f)X(f)$, where $\mathrm{sgn}(f)$ is 1 for positive f and -1 for negative f, and $X(f)$ is the Fourier transform of $x(t)$ (Bracewell, 1986). Hence, the Hilbert transformation is equivalent to the filtering in which the amplitudes of spectral components are left unchanged, but their phases are altered by $\pi/2$ rad, positively or negatively according to the sign of f.

Now it is shown how the Hilbert transform can be used to obtain the instantaneous amplitude of a signal. Consider a real signal $x(t)$, which may be associated with a complex function $\hat{x}(t)=x(t)-jX_{\mathrm{Hi}}(t)$, called the analytic signal of $x(t)$. It is interesting to note that the instantaneous amplitude of a signal can be defined via the analytic signal. For example, let $x(t)=\cos(2\pi f_c t)$. Then, $\hat{x}(t)=\cos(2\pi f_c t)+j\sin(2\pi f_c t)=\exp(2\pi f_c t)$. The instantaneous amplitude of $\cos(2\pi f_c t)$ is $|\hat{x}(t)|=1$. By generalizing this result, the magnitude of the analytic signal in the time domain is defined as the instantaneous amplitude, or envelope of $x(t)$ (Bracewell, 1986). Figure 5 shows the instantaneous amplitude of the acceleration signal (IAA) at the location A. With the IAA available, it remains to map the time instant of the maximum vibration signal into the corresponding state of the compressor (crank position). Although seemingly straightforward, it is not easy to map the specific time instant into the state of the compressor since the crank position cannot be readily revealed without internal instrumentation. However, the internal instrumentation inevitably alters the structure of the compressor, which must be avoided in order for the results of noise source identification to be valid for an undisturbed compressor. This apparent impasse is resolved through judicious selection of a secondary signal that bridges between two compressors: one with internal instrumentation and the other without internal instrumentation.

The pressure pulse signal of a compressor at the discharge line (connected to the top shell) maintains an invariant relation to the crank angle, which makes it possible to obtain the crank angle at a certain instant from the pressure signal. The relation between the discharge pulse and the crank angle depends only upon the rotational speed of the motor. The rotational speed of the motor is fairly constant around 58.5 Hz (within ± 3 Hz). With this information, the following approach is proposed to measuring the vibration signal versus crank angle without internal instrumentation and, consequently, without altering the compressor structure. First, a bolted-shell compressor is instrumented to measure the vibration signal, the pressure pulse at the discharge line, and the crank position via magnetic pick-up. (The internally instrumented compressor is normally bolted after instrumentation is installed.) Second, the vibration signal and the pressure pulse at the discharge line are measured in a compressor instrumented only externally (typically, called a welded-shell

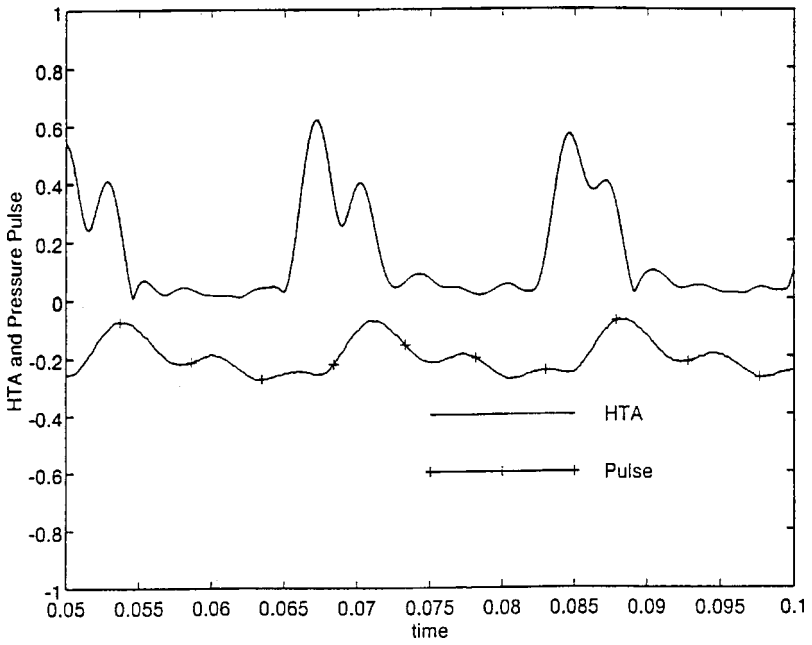

FIG. 5. Instantaneous amplitude of the acceleration signal at location "A" ("HTA") and pressure pulse at the discharge line (pulse) in a welded-shell rotary compressor.

compressor). Then, the pressure pulse from the bolted-shell compressor is shifted in time to match the pressure pulse from the welded-shell compressor. The delay required to match the two pressure pulses is then used to shift the magnetic pick-up from the bolted-shell compressor, which correspondingly provides information on the crank angle for the welded-shell compressor. In this way, the vibration signals and pressure pulses in the welded-shell compressor can be analyzed with respect to its own crank angle information. It is worth noting that the discharge cavity in the bolted-shell compressor is kept identical to that of the welded-shell compressor. Otherwise, the discharge pulse waveform would be distorted due to the different delays, which makes it impossible to compare the data obtained from the two compressors. Figures 5 and 6 show the similarity between the pressure pulses from the bolted-shell and welded-shell compressors, which further supports our claim. Equipped with this information, the following conclusion can be drawn: the IAA over one cycle indicates that the high levels of IAA occur mostly at around 220° and 300°.

IV. IDENTIFICATION OF NOISE SOURCES VIA INTERNAL MEASUREMENT AND MODAL ANALYSIS

Two noise sources are identified from the information on the crank positions where the high levels of IAA occur: (1) overpressurization in the cylinder chamber, and (2) structural resonance of the cylinder. The former is related to the crank angle of 220° and the latter, 300°. The direct measurement of the cylinder pressure and the modal analysis serve as two essential vehicles in pinpointing true sources.

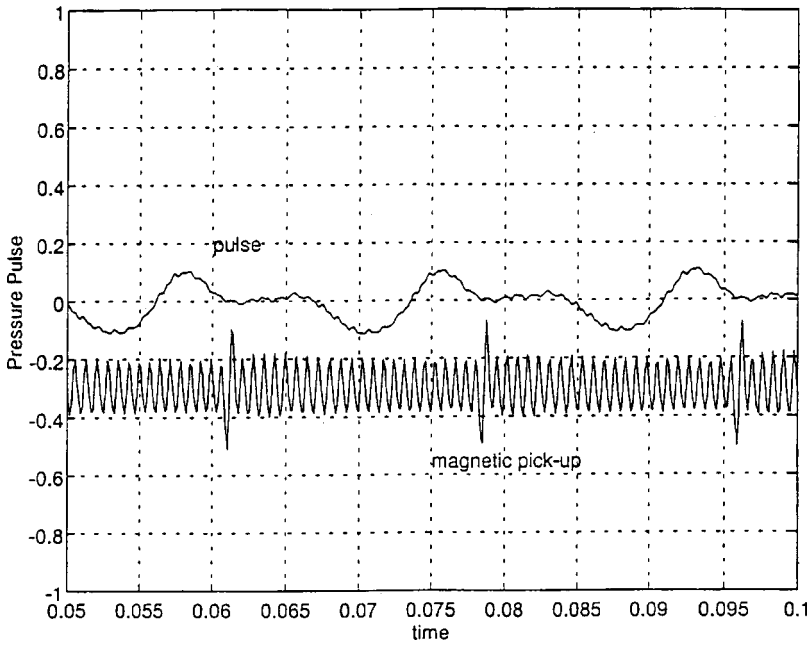

FIG. 6. Pressure pulse and magnetic pick-up in the bolted-shell rotary compressor.

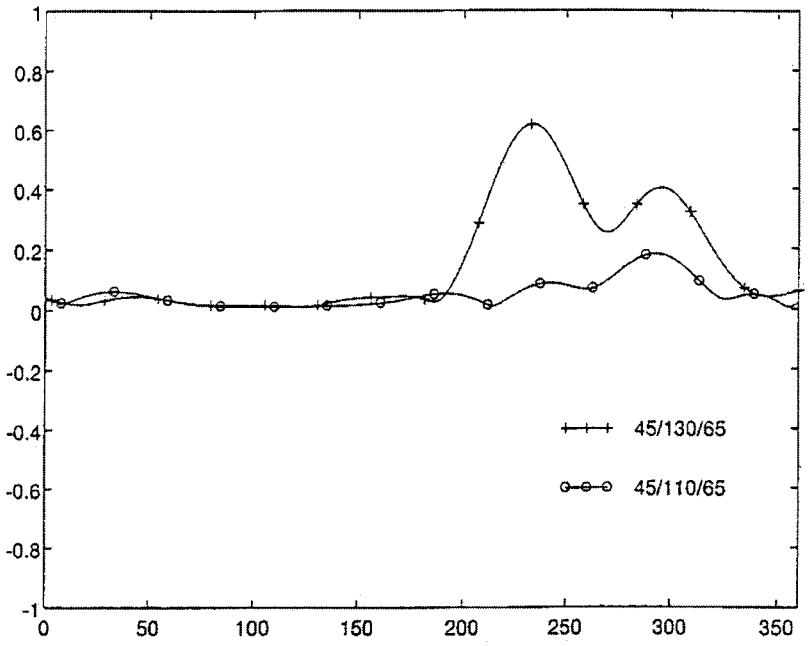

FIG. 7. Comparison of IAAs for two different discharge pressure conditions: (1) 311 psig and (2) 250 psig.

A. Overpressurization in the cylinder chamber

The discharge valve in a rotary compressor is an automatic-type valve, the name of which is coined from the fact that the pressure difference between the cylinder and the discharge plenum governs the fundamental valve opening/closing operations. Opening/closing operations of ordinary mechanical valves are mechanically synchronized with other parts of the whole system, e.g., via cams. The valve starts to open when the cylinder pressure reaches the discharge plenum pressure inside the discharge muffler. Both the cylinder pressure and the crank angle are measured in the bolted-shell compressor, noting that the cylinder pressure fluctuation is invariant to the compressor type, whether it is welded or bolted. The experimental results show that the discharge valve starts to open at a crank angle of 200° when the cylinder pressure reaches the discharge plenum pressure, 311 psig, as shown in Fig. 7. The cylinder pressure continues to increase even after the discharge valve is open due mainly to the compressibility of the refrigerant. In other words, it takes a while for the cylinder pressure to reach the discharge plenum pressure because the refrigerant in the cylinder is compressed while the valve is open. As a result, the maximum pressure occurs at around 220°.

Based on the above argument and supporting experimental data, the overpressurization is conjectured to be the candidate cause of the high level of IAA at 220°. In order to verify such a claim, the compressor is tested at a different discharge plenum pressure without altering the other condition: 250 psig instead of 311 psig. The experimental results show that (1) the discharge valve opens earlier than in the previous measurement, (2) the overpressurization magnitude is decreased, and (3) the crank angle where the cylinder pressure achieves its maximum remains unchanged at 220°. In Fig. 7, it is observed that the first hump at 220° is reduced to a great extent due to the discharge pressure change. This validates our claim that the overpressurization in the compression chamber is the source of the high level of IAA at 220°.

In order to reduce the overcompressed pressure, a design modification is sought after. The discharge notch is connected to the motor-end bearing (Fig. 2), and the compressor discharge valve is attached to the top of the bearing. The motor-end bearing has a straight hole through which the discharge gas passes from the discharge notch as shown in Fig. 2. The hole in the motor-end bearing is then modified to provide larger clearance volume in the cylinder. The extra volume results in the reduction of the overcompressed pressure and, subsequently, 3 dB sound pressure level in the 5 kHz band.

B. Structural resonance of the cylinder via finite-element analysis

Although the first peak is significantly suppressed via the hole-design modification, the second peak still remains unchanged as shown in Fig. 7. In order to locate the origin of the second peak, the compressor structure is examined at the crank angle of 300°, which identifies a structural weakness (notch at the cylinder) at the position. Finite-element analysis is conducted to examine whether the structural weakness is indeed the root cause of the second peak.

The modal analysis via finite-element analysis is first conducted to obtain the resonance frequencies of the cylinder and the corresponding mode shapes. The finite-element model is shown in Fig. 8. The cylinder is welded to the compressor shell, and the modeling of the welds in the cylinder is simplified as a fixed boundary condition. The excitation force is simulated from the resultant pressure in the cylinder. The results show that one of the resonance frequencies with three weld points (W1, W2, and W3 in Fig. 8) is 5 kHz, which falls within our frequency range of interest. The corresponding mode shape shows that the portion of the cylinder at the crank angle of 300° is the most active part of the

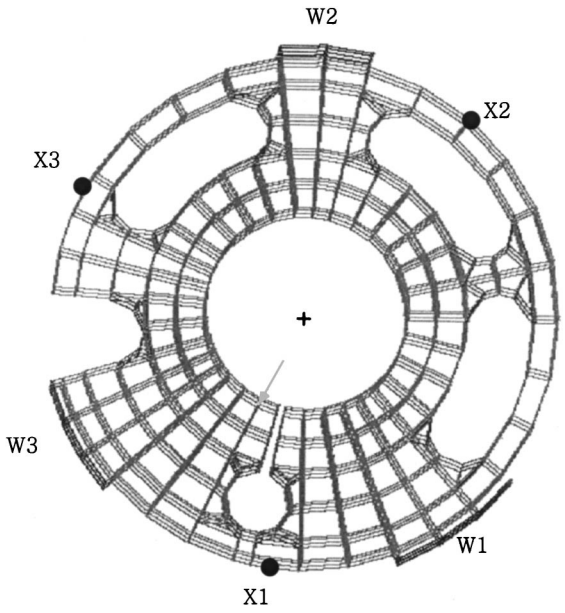

FIG. 8. Finite-element model of the rotary compressor cylinder with old and new weld points.

cylinder at 5 kHz. Then, the vibration level is calculated using the simulated force around the cylinder, and the highest vibration level is shown at the crank angle of 300°.

The theoretical modal analysis is further validated experimentally via the frequency response function (FRF) measurement. The goal of the FRF test is to experimentally verify the structural resonance frequency estimates obtained via finite-element analysis. The FRF measurement is the most commonly used approach to the estimation of modal parameters (Halvosen and Brown, 1977; Goyder, 1980). The FRF is the complex ratio of the Fourier transform of output response to the Fourier transform of input excitation as a function of frequency for a single input and a single output system. The FRFs are measured using excitation at a single point (location A). The experimental results verify the existence of the 5 kHz resonance frequency in the cylinder, which is consistent with the result of the FEA. PATRAN is used for the pre- and post-processor and ANSYS for the analysis tool (PDA Engineering, 1993; Swanson Analysis System, Inc., 1992).

In order to suppress the structural vibration level at the 5 kHz, three different weld points ($\times 1$, $\times 2$, and $\times 3$) are proposed as shown in Fig. 8, which restrict the vibrations at the crank angle of 300°. As a result of new weld points, the vibration level is significantly reduced and the resulting sound pressure level is decreased by 2 dB in the 5 kHz band.

V. CONCLUDING REMARKS

A synergetic approach is proposed for vibration-induced noise source and transmission path identification. First, the sound intensity map of a rotary compressor reveals the active region of acoustic radiation. The vibration signal is measured near the active region of the acoustic radiation. The coherence test indicates that the mechanical vibration is the main cause of the acoustic noise. Then, various signal processing techniques including bandpass filtering and the Hilbert transform are used to extract the features related to noise generation from the raw vibration signals. Finally, direct measurement and modal analysis guide us to the noise sources. The findings of the noise source identification have resulted in a successful design of quieter compressors at Carrier, Inc. By virtue of its generic nature, the applicability of the synergetic approach should be unlimited even if it has been applied to a rotary compressor.

ACKNOWLEDGMENTS

This work has been supported by United Technologies Carrier, the Brain Korea 21 Project, Institute of Advanced Machinery and Design at Seoul National University.

Allemang, R. J. (**1984**). ''Experimental modal analysis bibliography,'' Proc. IMAC, 13-13.
Beranek, L. (**1971**). *Noise and Vibration Control* (Institute of Noise Control Engineering, Poughkeepsie, NY).
Bracewell, R. N. (**1986**). *The Fourier Transform and Its Applications*, 2nd ed. (McGraw-Hill, New York).
Crocker, M. J. (**1975**). *Reduction of Machinery Noise* (Purdue University, West Lafayette, IN).
Ewins, D. J. (**1984**). *Modal Testing: Theory and Practice—Research Studies* (John Wiley and Sons, New York, NY).
Foreman, J. (**1990**). *Sound Analysis and Noise Control* (Van Nostrand Reinhold, New York).
Goyder, H. (**1980**). ''Methods and application of structural modeling from measured structural frequency response data,'' J. Sound Vib. **68**, 209–230.
Halvorsen, W., and Brown, D. (**1977**). ''Impulse technique for structural frequency response testing,'' J. Sound Vib. **11**, 8–21.
Harris, C. (**1957**). *Handbook of Noise Control* (McGraw-Hill, New York).
MathWorks, Inc. (**1992**). *The PRO-MATLAB User's Guide* (MathWorks, South Natick, MA).
Oppenheim, A. V., and Schafer, R. W. (**1989**). *Discrete-time Signal Processing* (Prentice-Hall, Englewood Cliffs, NJ).
PDA Engineering (**1993**). *PATRAN User's Manual* (PDA Engineering, Costa Mesa, CA).
Simon, M., and Tomlinson, G. (**1984**). ''Application of the Hilbert transforms in the modal analysis of nonlinear systems,'' J. Sound Vib. **96**, 421–436.
Swanson Analysis System, Inc. (**1992**). *ANSYS User's Manual* (Swanson Analysis System, Houston, TX).
Yerges, L. F. (**1978**). *Sound, Noise and Vibration Control*, 2nd ed. (Van Nostrand Reinhold, New York).

Equipartition and mean-square responses in large undamped structures

Richard L. Weaver
Theoretical & Applied Mechanics, University of Illinois, 104 South Wright Street, Urbana, Illinois 61801

(Received 1 May 2001; accepted for publication 22 May 2001)

It is shown that the smoothed spectral energy density at one point in a large complex structure may be approximated in a simple manner as proportional to the frequency-smoothed admittance at the receiver and at the source, and inversely proportional to the global modal density. Thus, the mean-square response may be estimated with little computational burden, knowing only the local properties at source and receiver and the size of the system. The approximate predictions are compared with the results of direct numerical simulations and found to be accurate except in the presence of Anderson localization. © *2001 Acoustical Society of America.*
[DOI: 10.1121/1.1385566]

PACS numbers: 43.40.Qi, 43.40.Hb, 43.20.Ks [JGM]

I. INTRODUCTION

It is well accepted that direct numerical solutions of the governing equations of large structural acoustic systems, while possible in principle, can be so computationally demanding as to be impractical. This is particularly true if the structure is large and irregular, and if the solution is desired at late times or high frequencies or fine frequency resolution. Furthermore, any such solution is necessarily sensitive to uncertainties and details in the modeling. An exact solution by direct numerical simulation can therefore be of questionable value. For these reasons statistical estimates of responses have long been sought.

Statistical energy analysis[1–5] is one approach to obtaining such estimates. In conventional SEA, steady-state energy densities are predicted for bandlimited responses in the presence of dissipation. SEA models require a partition of the system into weakly coupled substructures, modal density, and dissipation estimates for each substructure, and estimates of coupling loss factors for energy flow between them. Direct Finite Element numerical simulations[5–9] have been used to estimate the parameters of an SEA model, though more commonly they are estimated from analytic models or experimental observations. Recent years have seen extensions of SEA to the time domain[10,11] and development of some hybrid methods.[12]

Throughout all the work in SEA there has been less attention paid to error estimates than to the mean SEA predictions themselves. Fluctuations away from the means are of at least two kinds, and may be termed ''secular,'' and ''universal.'' Quantitative understanding of each is a prerequisite to any complete statistical energy theory.

Universal fluctuations are due to resonances of the system modes. They may be so termed because their statistics are expected to be functions of only a small number of structural parameters, modal density, and dissipation for example, and otherwise expected to be identical in widely differing systems. Because the modes are global and sensitive to small details in the structure, no efficient theory should be expected to model the details of the resonance peaks and troughs. In the presence of sufficient dissipation however (the Schroeder criterion requires modal overlap to be greater than 3), these fluctuations are weak. At small modal overlap these fluctuations are strong, and there is an ongoing effort in the literature seeking to make quantitative estimates of the rms magnitude of the fluctuations in terms of modal density and dissipation.[13–19] This paper is not concerned with universal fluctuations.

Secular variations have received relatively little attention. Throughout SEA, little attention has been paid to the problem of strongly coupled substructures, or to the equivalent case in which there are structural features with broad resonances that affect spectral power densities but which do not correspond to well-delimited ''substructures.'' Consider for example a reverberation room, with a source or receiver placed a short distance from a wall or corner. Spectral variations can be expected on frequency scales corresponding to the inverse of travel times to and from the wall. These are neglected in conventional SEA.

This paper considers the problem of estimating bandlimited mean-square responses in large undamped systems excited by transient forces, with particular attention paid to the prediction of secular variations in the spectra. The work is conceived as part of an endeavor seeking improved models of energy flow in damped and undamped complex systems. The study of undamped vibrations in complex systems has clarified many issues in the past,[20–24] and is, moreover, sometimes relevant to actual practice. The undamped problem is substantially simpler than the more general damped case, but sufficiently replete with relevant and subtle issues to recommend its consideration for present purposes as well.

In the next section the formal mathematical treatment of the vibrations of large linear systems is posed and formal expressions for mean-square responses (loosely equivalent to ''energy'') are derived. A plausible approximate formula is then suggested, whose evaluation does not require substructuring and which promises to be computationally undemanding compared to that of an exact calculation. The expression is proportional to the admittance at the source and receiver positions, and inversely proportional to the size of the system. The approximation is related to equipartition and the

result is reminiscent of SEA notions that local responses are proportional to local modal densities. The formula is then confirmed in Sec. V by comparing its predictions with the results of direct numerical simulations.

II. MATHEMATICAL PRELIMINARIES

The formal problem of transient linear vibrations in a continuous finite structure is well developed. It is commonly recast in discrete finite degree-of-freedom form, most often by using a finite number of spatially compact generalized displacements. The result is a set of coupled linear ordinary second-order differential equations in terms of Rayleigh–Ritz highly sparse real symmetric mass and stiffness matrices. In this section those governing equations are formally solved in terms of the eigenmodes. Expressions are derived for the (bandlimited) energy deposited by transient loads, and for the (bandlimited) mean-square signal received.

A. Governing equations

The governing equations of undamped linear vibrations of a discrete finite system may be stated in matrix form

$$[K]\{v(t)\}+[M]\frac{d^2}{dt^2}\{v(t)\}=\{s\}S(t);$$
$$\{v(0)\}=\frac{d}{dt}\{v(0)\}=\{0\}, \tag{1}$$

in which the response $\{v(t)\}$ is an N-component column vector whose components represent the displacement at various positions in the structure. Quiescent initial conditions are assumed. The source time function S is taken to vanish for negative times, and to vanish for all times t greater than some time T_S. The vector $\{s\}$ is taken to be normalized

$$\{s\}^T[M]\{s\}=1. \tag{2}$$

B. Response

The structure has a Green's matrix with a spectral representation in terms of the (normalized) modes $\{u^n\}$, $n=1,2,...,N$.

$$[G(t)]=\sum_{n=1}^{N}\{u^n\}\{u^n\}^T\frac{\sin(\omega_n t)}{\omega_n} \quad \text{for } t>0;$$
$$=0 \quad \text{otherwise.} \tag{3}$$

It has Fourier transform

$$[\tilde{G}(\omega)]=\int_0^\infty [G(t)]\exp\{-i\omega t\}dt$$
$$=\sum_{n=1}^{N}\{u^n\}\{u^n\}^T\frac{1}{\omega_n^2-(\omega-i\varepsilon)^2}, \tag{4}$$

where the infinitesimal $-i\varepsilon$ emphasizes that $[G(\omega)]$ is the continuation to the real ω axis of a quantity whose definition is guaranteed only in the lower half plane.

The response, to source distribution $\{s\}$ with real time function $S(t)$, is obtained by a convolution with $[G]$

$$\{v(t)\}_{s,S}=\sum_{n=1}^{N}\{u^n\}s_n\int_0^t S(\tau)\sin(\omega_n(t-\tau))/\omega_n\,d\tau, \tag{5}$$

where the source strength for the nth mode is defined by

$$s_n=\{u^n\}^T\{s\}. \tag{6}$$

At times t greater than T_S the expression is especially simple

$$\{v(t)\}_{s,S}=\sum_{n=1}^{N}\{u^n\}s_n\,\mathrm{Im}[\tilde{S}(\omega_n)\exp\{i\omega_n t\}/\omega_n], \tag{7}$$

where Im indicates imaginary part.

C. Energy

The total kinetic energy in a field $\{v(t)\}$ is given by

$$\mathrm{KE}=\frac{1}{2}\frac{d}{dt}\{v(t)\}^T[M]\frac{d}{dt}\{v(t)\}. \tag{8}$$

Equation (7) for $\{v\}_{s,S}$ is substituted into the expression (8) for the kinetic energy. After time averaging and doubling to account for the strain energy, the total energy, $E_{s,S}$, deposited by the source $\{s\}S(t)$ is found to be

$$E_{s,S}=\frac{1}{2}\sum_{n=1}^{N}|\tilde{S}(\omega_n)|^2 s_n^2, \tag{9}$$

where the orthonormality of the modes has been invoked

$$\{u^n\}^T[M]\{u^m\}=\delta_{mn}. \tag{10}$$

The same result can also be obtained, with greater analytic effort, by time-integrating the power output (force times velocity) from the source

$$E_{s,S}=\int_0^{T_S}S(t)\{s\}^T\frac{d}{dt}\{v(t)\}_{s,S}dt$$
$$=\int_{-\infty}^{\infty}S(t)\{s\}^T\frac{d}{dt}\{v(t)\}_{s,S}dt$$
$$=\frac{1}{2\pi}\int_{-\infty}^{\infty}\tilde{S}^*(\omega)\{s\}^T i\omega\{\tilde{v}(\omega)\}d\omega$$
$$=\frac{1}{2\pi}\int_{-\infty}^{\infty}|\tilde{S}(\omega)|^2 i\omega\{s\}^T[\tilde{G}(\omega)]\{s\}d\omega$$
$$=\frac{1}{2\pi}\sum_{n=1}^{N}s_n^2\int_{-\infty}^{\infty}|\tilde{S}(\omega)|^2\frac{i\omega}{\omega_n^2-(\omega-i\varepsilon)^2}d\omega$$
$$=\frac{1}{2}\sum_{n=1}^{N}|\tilde{S}(\omega_n)|^2 s_n^2. \tag{11}$$

D. Mean-square signal at receiver

Now consider a receiver, with spatial distribution defined by $\{r\}$ (a normalized vector). Its signal is passed through a filter $R(t)$. $R(t)$ is taken to be causal [so that $R(t<0)=0$], to be real, and to have finite compact support [such that $R(t>T_R)=0$]. The output of the filter is

$$\psi(t) \equiv \int_0^t \{r\}^T \{v(\tau)\} R(t-\tau)\, d\tau, \tag{12}$$

which for times $t > T_S + T_R$ is (after defining $r_n = \{u^n\}^T \{r\}$)

$$\psi(t) = \sum_{n=1}^{N} r_n s_n \, \mathrm{Im}[\tilde{R}(\omega_n)\tilde{S}(\omega_n)\exp(i\omega_n t)/\omega_n]. \tag{13}$$

It is this quantity, being the bandpassed signal from the receiver, for which an estimate is required. The response is oscillatory and the mean is clearly zero. The first nontrivial moment is the (time-averaged) mean-square response.

$$\overline{\psi^2} = \sum_{n=1}^{N} r_n^2 s_n^2 |\tilde{R}(\omega_n)\tilde{S}(\omega_n)|^2 / 2\omega_n^2. \tag{14}$$

The time averaging has caused the cross terms to vanish.

III. APPROXIMATE MEAN-SQUARE SIGNAL

The above expression has, in large or disordered structures, two stochastic factors, r and s. The expression may be estimated by assuming that these two factors are uncorrelated; that is, that the overlap of a given mode with the source is independent of its overlap with the receiver. Following the spirit of random matrix theory,[25,26] it is imagined that the overlaps of a mode $\{u^n\}$ with source and receiver are its projections in two arbitrary uncorrelated random ''directions'' $\{s\}$ and $\{r\}$. If one defines a weighted modal average, of an n-dependent quantity Q_n over the modes n in a band B, by

$$\langle Q \rangle_B \equiv \sum_{n=1}^{N} Q_n |B(\omega_n)|^2 \Big/ \sum_{n=1}^{N} |B(\omega_n)|^2,$$

then a statement that Q and P are uncorrelated implies

$$\langle QP \rangle_B = \langle Q \rangle_B \langle P \rangle_B .$$

Making this assumption about r^2 and s^2 leads to an estimate for (14) of the form

$$\overline{\psi^2} \approx \frac{\Sigma_{n=1}^{N} \tfrac{1}{2} r_n^2 \, |\tilde{B}(\omega_n)|^2 \; \Sigma_{n=1}^{N} \tfrac{1}{2} s_n^2 |\tilde{B}(\omega_n)|^2}{\omega_c^2 \; \Sigma_{n=1}^{N} \tfrac{1}{2} \, |\tilde{B}(\omega_n)|^2}, \tag{15}$$

where B is the convolution of S and R; $B = R * S$; $\tilde{B} = \tilde{R}\tilde{S}$. The assumption that the band B is narrow, with central frequency ω_c, has allowed the factor $1/\omega^2$ to be extracted from the sums.

This approximation is related to equipartition. If the source at s has deposited equal amounts of energy in each mode, then the s^2 are all equal and the assumed decorrelation follows immediately. Strict equipartition is of course nonsense; mode amplitudes at a point s are not equal. Here, we have invoked a different assumption, one with utility similar to that of equipartition, but which is more tenable. Rather than asserting equipartition, we now require merely a lack of correlation between the r_n and s_n.

The approximation is quite clearly *not* correct if the structure is Anderson localized and the source and receiver are distant. In that case those modes which have large overlap s with the source are the modes that are localized near the source; they are not the same as those modes with large overlap r near the receiver. That SEA fails in the presence of Anderson localization is clear from the literature.[3,20–22,27,28] Nor is our approximation valid if the source and receiver coincide; $r = s$, in which case weak Anderson localization[23,29] is expected. It should be possible to introduce *ad hoc* correction factors for the effect of weak Anderson localization. For example, one could augment the present predictions by a factor of 2 at times short compared to the break time if the source and receiver coincide exactly, by a quantity closer to 3 at late times, and by a smaller quantity if source and receiver do not coincide precisely. The weak localization enhancement is discussed in the literature.[23,29] It may be more difficult to insert corrections for full localization.

There are at least three potential sources of error in the above approximation. There may be some Anderson localization. The bandpass filter B may be too wide in frequency to resolve secular variations in the mean values of r^2 and s^2. Random universal fluctuations of r^2 and s^2 away from their means may have a random impact on the accuracy of (15). The problem of *a priori* quantification and estimation of errors in (15) is assigned to another occasion. Here, the focus is primarily on the simpler questions of the practical utility and general validity of (15).

IV. EVALUATION OF THE APPROXIMATE EXPRESSION

A. The numerator

The factors in the above are expressed in terms of modal sums, but they have simple interpretations that allow them to be determined efficiently and without modal analysis. A comparison with Eq. (11) shows that the factors in the numerator are each the work done by a source with spatial distribution $\{r\}$ (or $\{s\}$) and time dependence $B(t)$. They are $E_{r,B}$ and $E_{s,B}$. That identification allows them to be estimated efficiently. Each may be found in numerical simulation by integrating the power output (force times velocity) of a source $B(t)$

$$\sum_{n=1}^{N} \frac{1}{2} r_n^2 |\tilde{B}(\omega_n)|^2$$

$$= E_{r,B} = \int_0^{T_B = T_S + T_R} B(t) \{r\}^T \frac{d}{dt} \{v(t)\}_{r,B} dt$$

$$= \int_0^{T_B} B(t) \times \left[\frac{d}{dt} \int_0^t (\{r\}^T [G(t-\tau)] \{r\}) B(\tau)\, d\tau \right] dt, \tag{16a}$$

with a similar expression for $E_{s,B}$. Use of (16a) requires knowledge of G, i.e., the direct numerical solution of an equation like (1), but only over a short time. Thus, the computational requirements in (16a) are slight. If the wave field over this short time may be assumed to have visited (and returned from) only a small part of the structure near the source, then distant parts of the structure may be omitted

from such a solution, with an additional saving of computational effort. It may be possible to approximate the effect of less distant parts of the structure by the (frequency-smoothed) impedance they present to the region near the source, i.e., as a "fuzzy."[24,30–34] Even in the absence of modal overlap, smoothed fuzzy impedances are good representations of the effect of substructures if attention is confined to short times.[24] Modeling of these less distant parts of the structure by means of fuzzy impedances would lend additional efficiency to the computation.

The expression (15), with the use of (16a) to evaluate its factors, is reminiscent of Skudrzyk's observation[35] that spectral responses, although often irregular functions of frequency are, when smoothed, identical to those of a uniformly extended infinite structure, i.e., independent of distant regions. It is also reminiscent of Weaver's proof[36] that smoothed spectral energy density consequent to a transient load (or equivalently, smoothed admittance) depends on structural details in the vicinity of the load, and is independent of distant features.

As an alternative to the evaluation of E by means of an integral over time of a quantity that depends on a time-domain integration of the equations of motion, one may consider E's evaluation in the frequency domain. Time-domain integrations of equations of motion are often avoided, as they can require fine time stepping to assure stability and accuracy where fine spatial discretization is required to resolve stress concentrations. Time-domain solutions are also problematic when dissipation mechanisms are defined in the frequency domain but not in the time domain. In order to avoid time-domain integrations of the equations of motion, Eq. (16a) may be rewritten as

$$E_{r,B}=\int_0^{T_B}B(t)\left[\frac{d}{dt}\int_0^t(\{r\}^T[G(t-\tau)]\{r\})B(\tau)d\tau\right]dt$$
$$=\frac{1}{2\pi}\int_{-\infty}^{\infty}i\omega|\tilde{B}(\omega)|^2\{r\}^T[\tilde{G}(\omega)]\{r\}d\omega$$
$$=\frac{-2}{2\pi}\int_0^{\infty}\omega|\tilde{B}(\omega)|^2\{r\}^T[\mathrm{Im}\,G(\omega)]\{r\}d\omega. \quad (16b)$$

In this form the integral is not very useful; $G(\omega)$ varies rapidly on a scale of the global modal density, and direct numerical evaluation of (16b) therefore requires a fine step size in ω. Indeed, $G(\omega)$ has poles at all points $\omega=\pm\omega_n+i\varepsilon$. But, if the integration contour, now along the real ω axis, is deformed into the lower half plane, these poles are smoothed and no new poles are encountered. It is then not difficult to show that E may also be expressed as

$$E_{r,B}=\frac{1}{2\pi}\int_{-\infty}^{\infty}i\omega|\tilde{B}(\omega)|^2(\{r\}^T[\tilde{G}(\omega)]\{r\})d\omega$$
$$=\frac{1}{2\pi}\int_{-\infty}^{\infty}i(\omega-iH)|\tilde{B}(\omega-iH)|^2$$
$$\times(\{r\}^T[\tilde{G}(\omega-iH)]\{r\})d\omega, \quad (16c)$$

for all positive H. At an optimal value for H, this expression for E may be computationally less demanding than (16a).

B. The denominator

The denominator of (15) is essentially the number of modes in the band B, and is more problematic. Modal density estimates are required in standard SEA as well. There may be ways to estimate this quantity analytically, e.g., by means of a Weyl series, as in the next section. If there is reason to think it varies only slowly with frequency, then the numerator alone provides the more important information on how the mean-square response varies with frequency. If more precision is required, then a numerical scheme (e.g., Ref. 37) for estimating the number of eigenvalues of a matrix within a specified band may be indicated. In any case, a known modal density $D(\omega)=dN/d\omega$ allows the denominator to be constructed as

$$\omega_c^2\sum_{n=1}^{N}\frac{1}{2}|\tilde{B}(\omega_n)|^2\approx 2\pi^2 f_c^2\int_0^{\infty}\tilde{B}(\omega)^2D(\omega)d\omega$$
$$\approx 2\pi^3 f_c^2 D(2\pi f_c)\int_0^{T_B}B(t)^2\,dt, \quad (17)$$

where f_c is the central frequency of the assumed-narrow filter B.

If $D(\omega)$ is not known, there is at least one computational scheme for estimating it numerically. Consider the expression

$$A_B\equiv\int_0^{T_B}B(t)\frac{d}{dt}\left[\int_0^t\mathrm{Trace}([M][G(t-\tau)])B(\tau)d\tau\right]dt$$
$$=\sum_{n=1}^{N}\int_{-\infty}^{\infty}B(t)\left[\int_{-\infty}^{t}\mathrm{Trace}([M]\{u^n\}\{u^n\}^T)\right.$$
$$\left.\times\cos(\omega_n(t-\tau))B(\tau)d\tau\right]dt. \quad (18)$$

The above trace $[M]\{u\}\{u\}^T$ is unity, by virtue of normalization of the modes, and the expression becomes

$$A_B=\frac{1}{2}\sum_{n=1}^{N}|\tilde{B}(\omega_n)|^2, \quad (19)$$

which establishes (18) as a method for calculating the sum in the denominator of (15). It also establishes the sum A_B as a kind of system-wide sum of energy deposits $E_{x,B}$ over all sites x. If M is diagonal, then

$$A_B=\sum_{x=1}^{N}E_{x,B}M_{xx}. \quad (20)$$

If M is not diagonal, the expression is slightly more complicated.

Any individual term in this sum is readily calculated by numerically integrating the governing differential equations (1) for point sources $\{x\}$ over short times, as in Eq. (16a), and thereby constructing the $E_{x,B}$. Alternatively, E_x may be found by a numerical construction of the elements of $G(\omega-iH)$ for a small number of ω's, followed by numerical evaluation of the integral (16c). Precise evaluation of (20), however, requires that this process be repeated for all sites $\{x\}$ and then summed, at potentially prohibitive cost.

It is therefore suggested that the sum could be evaluated by summing over a sufficiently large and unbiased subspace, a kind of Monte Carlo evaluation of the trace

$$\sum_{n=1}^{N} \frac{1}{2}|\tilde{B}(\omega_n)|^2 \approx \lim_{\mathcal{N}\to N} \frac{N}{\mathcal{N}} \sum_{x=1}^{\mathcal{N}} \sum_{y} M_{yx} \int_0^{T_s+T_r} B(t) \times \left[\frac{d}{dt} \int_0^t [G_{yx}(t-\tau)] B(\tau) d\tau \right] dt. \quad (21)$$

In the particular case where $[M]$ is diagonal, this prescription becomes

$$\sum_{n=1}^{N} \frac{1}{2}|\tilde{B}(\omega_n)|^2 \approx \lim_{\mathcal{N}\to N} \frac{N}{\mathcal{N}} \sum_{x=1}^{\mathcal{N}} M_{xx} \int_0^{T_s+T_r} B(t) \times \left[\frac{d}{dt} \int_0^t G_{xx}(t-\tau) B(\tau) d\tau \right] dt = \lim_{\mathcal{N}\to N} \frac{N}{\mathcal{N}} \sum_{x=1}^{\mathcal{N}} M_{xx} E_{x,B}. \quad (22)$$

The limit can be expected to be approximately achieved at modest value of $\mathcal{N} \ll N$, if the order with which the sites $\{x\}$ are studied is chosen without bias, e.g., by a random number generator.

C. Summary

The results of this section are now summarized. The mean-square bandpassed signal in a receiver may be estimated by

$$\overline{\psi^2} \sim \frac{E_{r,B} E_{s,B}}{\omega_c^2 \Sigma_{x=1}^{N} M_{xx} E_{x,B}} = \frac{E_{r,B} E_{s,B}}{2\pi^3 f_c^2 D(2\pi f_c) \int B^2(t) dt}. \quad (23)$$

The estimate is proportional to the local admittance (i.e., the local modal density) at the source and at the receiver, and inversely proportional to the global modal density. The factors E may be calculated by means of (16a) in terms of an integration of the governing differential equations over only a short time. Or, they may be calculated by means of (16c) in terms of frequency-domain responses at only a few well-separated complex frequencies $\omega - iH$. The denominator is written in terms of the modal density, which is often known independently. Thus, the estimate is expected to be computationally much less demanding than an exact direct numerical simulation. In the next section this formula is applied to the case of a specific complex many-degree-of-freedom system, and its predictions are compared with the results of an exact calculation.

V. NUMERICAL EXPERIMENT

A. Direct numerical simulation

The above theory is tested in a finite-difference version of a two-dimensional membrane. This structure is an exact model of a discrete set of unit masses supported at the intersections of unit tensioned strings in a square array fixed at its boundary. We have studied this kind of system on several previous occasions.[20,22,27–29] The present simulation consists of a 100×200 array of such unit masses. All sites just outside the edges are constrained to zero displacement, thus mimicking the membrane's rigid boundary. To add some nontrivial inhomogeneous features to the system, a large point mass m has been attached to one point of the structure by means of a stiff spring k. A few internal sites are constrained to zero displacement in order to create a small open cavity within the system. These additions modify the local admittance and add some interesting features to the spectrum. In order to minimize coherent echoes from the walls, part of the boundary is roughened. The array is illustrated in Fig. 1.

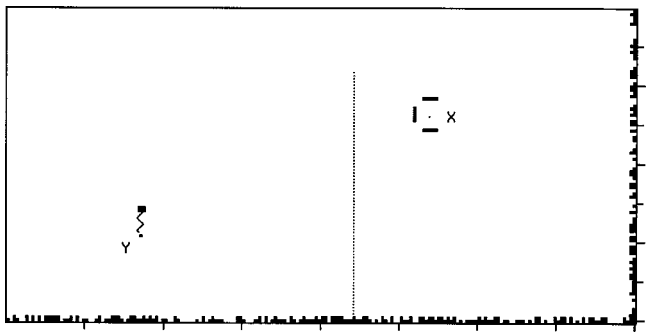

FIG. 1. The domain studied is a rectangular membrane, with a small open cavity embedded within it. The boundaries are rigid, two of them are roughened (Refs. 20, 29) by blocking a random number (0 to 2) of sites next to the wall. The structure is discretized spatially by means of 200×100-element central differences. Sources and receivers are considered at the indicated sites, X near or within the cavity, and Y near an attached mass/spring. The dotted line indicates the rigid wall (with window of length 20) inserted to generate the data of Fig. 6.

The nearly 20 000 coupled ordinary differential equations (ODEs) that describe this system are solved by central differences in the time domain, with step size $\delta t = 0.4$, about 40% more conservative than is required for stability. (Stability requires $\delta t < 2/\omega_{\max}$, where $\omega_{\max}$ is the highest natural frequency in the structure $\approx \sqrt{8}$.) Attention is confined to frequencies $\omega_c < 1.2$, where the mesh is very nearly isotropic and nondispersive, and the temporal differencing is very nearly nondispersive. The transient dynamics was studied for a period of $N_T = 32\,768$ time steps, for a total time of $T \approx 13\,000$.

To construct the central-difference response $\{u\}$ to a unit impulse acting at time 0 on a site X, the free vibration subsequent to certain initial conditions was formed. The scheme recognizes initial conditions $u_x(t=0) = 0$, and $u_x(t=\delta t) = \delta t$, corresponding to a unit impulse that acts at time 0 on site X. All other initial u's were zero. The difference equations were of the form

$$[K]\{u(t)\} + \frac{\{u(t+\delta t) - 2u(t) + u(t-\delta t)\}}{\delta t^2} = \{0\}. \quad (24)$$

The approximately $20\,000 \times 20\,000$ matrix $[M]$ is diagonal. The mass matrix $[M]$ is the identity, except for that diagonal element corresponding to the attached mass, where it has a value m. $[K]$ is sparse; most of its diagonal elements are 4. The diagonal element corresponding to the site where the mesh is connected to the mass/spring has a value $4 + k$.

The diagonal element of $[K]$ corresponding to the added mass m is k. Each off-diagonal element connecting nearest-neighbor sites of the mesh is -1, except for that off-diagonal site connecting the mesh and the added mass where it is $-k$. All other elements are zero. The solution is obtained by explicitly solving (24) for $\{u(t+\delta t)\}$ and iterating the resulting formula in time. $G_{ZX}(t)$ is the Zth element of the solution $\{u(t)\}$.

Four waveforms, $G_{XX}(t)$, $G_{XY}(t)$, $G_{YX}(t)$, and $G_{YY}(t)$, were obtained, for impulse sources at sites X and Y, and displacement receivers at X and Y (see Fig. 1). Reciprocity demands that $G_{XY}(t)=G_{YX}(t)$; this was confirmed in the simulations. Energy conservation demands that a finite-difference version of energy

$$\mathcal{E}_{t+\delta t/2} \equiv \frac{\{u(t+\delta t)\}^T[K]\{u(t)\}}{2} + \frac{\{u(t+\delta t)-u(t)\}^T[M]\{u(t+\delta t)-u(t)\}}{2\,\delta t^2}, \tag{25}$$

is independent of t. This also was confirmed.

Modal densities for this structure are approximated by means of the two-term Weyl series for continuous membranes with Dirichlet boundary conditions. The mesh is conceptualized as an approximation to a membrane of dimensions 200.5×100.5 and the number of modes per unit circular frequency is obtained as

$$dN/d\omega = \omega A/2\pi - P/16, \tag{26}$$

where A is the area$=20\,150$, and P is the Dirichlet perimeter≈ 600. There are minor corrections (ignored here) to these values, related to the discrete microstructure and to the extra perimeter and smaller volume associated with the rough boundary and the open cavity. At $\omega=0.3$ the modal density is about 925; at $\omega=1.2$ it is about 3811. Break times at which individual resonances may be resolved, $T_{\text{break}}=2\pi dN/d\omega$, are 5800 and 24 000, respectively.

B. Bandpassed energies

To investigate the validity of Eq. (23), it is necessary to choose a frequency resolution, i.e., the width of the bandpass filter B. In order to capture the potentially interesting time scales of reverberation and decay within the small cavity, and also that of the radiation damping of the mass spring {not true damping, but rather the radiation of energy from the mass spring into the mesh}, we need sufficiently fine frequency resolution. This in turn requires that we choose the duration of the filter $B(t)$ to be long enough. In the examples below T_B is chosen to be 100 and 200. In order to diminish the strength of the bandpass filter's side lobes, the envelope of $B(t)$ is chosen to be smooth in the time domain. According to our constraints, B is also chosen to vanish for times $|t|>T_B$ and for $t<0$. Thus, for the filter centered on frequency f_c, a cosine-bell tone burst is chosen of the following form:

$$B_f(t)=\begin{cases} 0 & |t-T_B/2|>T_B/2 \\ \frac{1}{2}[1-\cos(2\pi t/T_B)]\cos\{2\pi f_c(t-T_B/2)\} & \\ & |t-T_B/2|<T_B/2. \end{cases} \tag{27}$$

Its Fourier transform, which has a full width at half power of $\Delta\omega=9/T_B$, is plotted in Fig. 2.

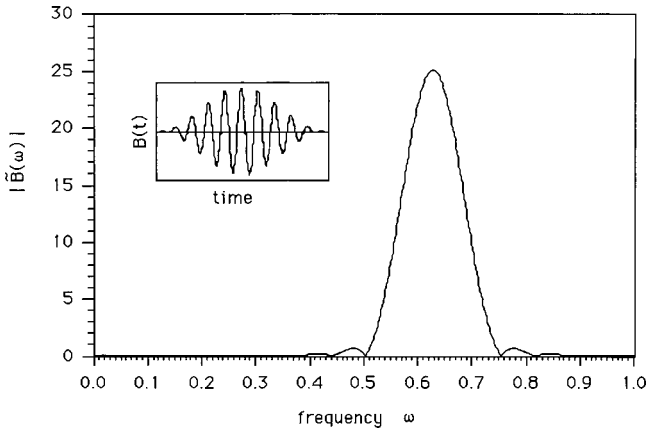

FIG. 2. The bandpass filter B for the case $T_B=100$ and frequency $f_c=0.1$. The inset shows B in the time domain, a cosine-bell tone burst.

The theory developed above predicts that the smoothed power spectrum of G_{XY} may be approximated as the product of the energy that would be deposited by sources at X and Y, divided by something proportional to modal density

$$\langle [B_{f_c}(t)*G_{XY}(t)]^2\rangle \approx \frac{\left[\int_0^{T_B} B_{f_c}(t)\left\{\frac{d}{dt}\int_0^t G_{XX}(t-\tau)B_{f_c}(\tau)d\tau\right\}dt\right]\left[\int_0^{T_B} B_{f_c}(t)\left\{\frac{d}{dt}\int_0^t G_{YY}(t-\tau)B_{f_c}(\tau)d\tau\right\}dt\right]}{2\pi^3 f_c^2 D(2\pi f_c)\int_0^{T_B} B_{f_c}^2(t)dt}. \tag{28}$$

For each frequency f_c of interest, the left and right sides were evaluated and compared. Each is plotted, versus f_c, in Figs. 3–6. Rather than laboriously programming the convolution and time average required by the left-hand side (LHS) above, it is evaluated by Fourier transforming the entire history $G_{XY}(t)$, multiplying by the Fourier transform of B, and integrating with respect to frequency

$$\text{LHS}=\frac{1}{2\pi T}\int_{-\infty}^{\infty}|\tilde{B}_{f_c}(\omega)\tilde{G}_{XY}(\omega)|^2 d\omega, \tag{29a}$$

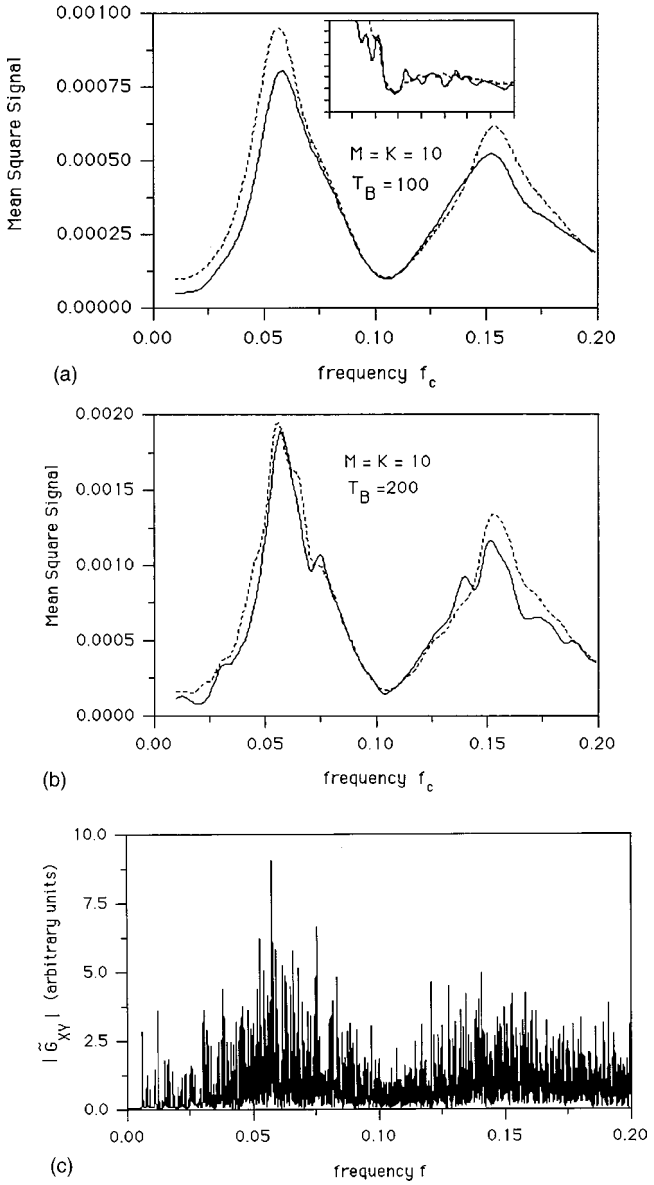

FIG. 3. (a) The actual mean-square signal at Y near (two mesh spacings away from) the attached mass/spring [Eq. (29b), solid line] is compared to the prediction [Eq. (32), dashed line]. The case is shown in which the stiffness and mass of the attachment are each 10 and the source is at X in the center of the open cavity. The bandpass filter $B(t)$ was that of Fig. 2 with a duration $T_B=100$, corresponding to a full width at half power of $\Delta f=0.015$. The inset shows (on the same scales but with a finer frequency resolution obtained by setting $T_B=200$) the behavior when the cavity walls are removed. The low-frequency response is greater; the broad resonances associated with the modes of the cavity are not present. (b) The approximation (dashed line) is compared to the exact result (solid line) for the case of a finer frequency resolution. (c) A high-resolution Fourier transform of the signal G_{XY} for the case shown in (a) and (b). The FFT is taken of the full signal, over the finite time $T=13\,107$ and shows the secular variations indicated in (a) and (b). It also shows rapid fluctuations corresponding to individual modes.

where $T=13\,107.2$ is the length of the time record of G_{XY} used to construct its Fourier transform. As the transforms are effected by N_T-point FFT, (29a) is reexpressed as

$$\mathrm{LHS}=\frac{2(\delta t)^2}{N_T^2}\sum_{\nu=1}^{N_T/2}|\tilde{B}_\nu\tilde{G}_{XY\nu}|^2, \tag{29b}$$

where B_ν and G_ν are the νth elements of the FFT of B and G

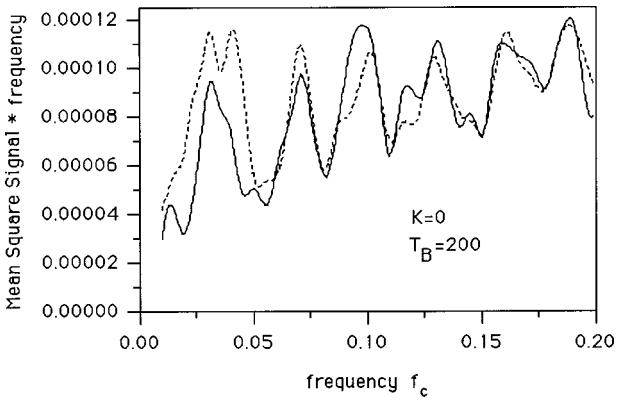

FIG. 4. Comparison of exact (solid line) and approximate (dashed line) power spectra for a modified structure. The spring is deleted and the source position X is moved outside the cavity.

$$\tilde{B}_\nu=\sum_{m=1}^{N_r}B(t=m\delta t)\exp\{-2i\pi(\nu-1)(m-1)/N_T\}. \tag{30}$$

The factors in the numerator of the right-hand side (RHS) of (28) were constructed in terms of the values of G_{XX} and G_{YY} at early times. As G was obtained by central differences, it is a central-difference version of the convolution and energy continuity equations that is required

$$v_{Z,n}=\sum_{m=1}^{n-1}G_{ZZ}(t=\{n-m\}\delta t)B_{f_c}(t=m\delta t)\,\delta t,$$
$$E_{Z,B}=\sum_{m=1}^{T_B/\delta t}B_{f_c}(t=m\delta t)[v_{Z,m+1}-v_{Z,m-1}]/2, \tag{31}$$

for $Z=X$ or $Z=Y$. Thus, v_z is the displacement response at Z to a force $B(t)$ applied at point Z. It is obtained by convolution of B with the recorded G_{ZZ}. The discrete-time version of the right-hand side of (28) is thus

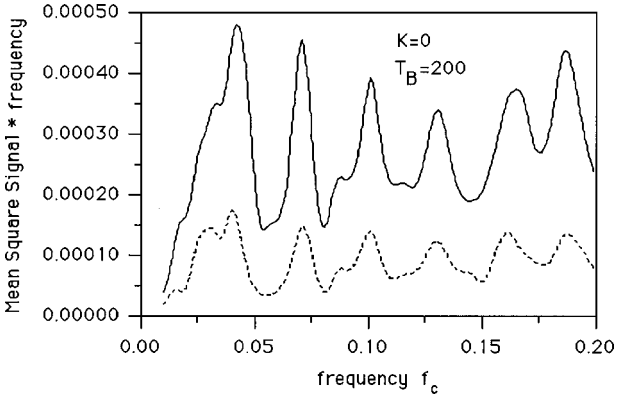

FIG. 5. A comparison of the exact (solid line) and approximate (dashed line) power spectra for a source coincident with the receiver at the point X just outside the cavity. The undulations seen are similar to those of Fig. 4. The most striking difference is that the approximate formula is now in error. The error is in the expected amount, the enhanced backscatter coefficient of 3.

$$\mathrm{RHS}=\frac{[\Sigma_{m=1}^{T_B/\delta t}B_{f_c}(t=m\,\delta t)[v_{X,m+1}-v_{X,m-1}]/2][\Sigma_{m=1}^{T_B/\delta t}B_{f_c}(t=m\,\delta t)[v_{Y,m+1}-v_{Y,m-1}]/2]}{2\pi^3 f_c^2\{f_c A-P/16\}\Sigma_{m=1}^{T_B/\delta t}B_{f_c}^2(t=m\,\delta t)\,\delta t}. \tag{32}$$

C. Comparisons

Numerical evaluations of Eqs. (29b) and 32 are compared in Figs. 3–6. Figure 3(a) shows the observed long-time scale mean-square bandpassed signal (29a) at position Y near (two mesh spacings away from) the attached mass spring. The source is at X in the center of the cavity. Figure 3(a) also shows the prediction (32) based on short-time integrations of the power deposited by forces $B(t)$ applied at positions X and Y. The approximate theory has captured all the significant spectral features. Except at very low frequency, it is correct within several percent. The figure also shows the effect of removing the cavity. As might have been expected, the rigid cavity walls depressed the long wavelength response, leading to small response at low frequencies. A sort of resonance at $f=0.16$ and 0.06, and an antiresonance at 0.11 are also apparent, and ascribed to standing waves in the cavity.

The calculational resources consumed by the estimate are much less than those required by the direct numerical simulation. The full calculation involved an integration over a time period of 13 000, while the estimate required two integrations, each over a period T_B. Savings of about 98% were realized. Savings would be greater yet if the approximate computations had omitted the less important distant parts of the structure far from the source, or modeled them with a view towards more computational efficiency. In the short-time T_B, distant parts of the structure are not in communication with the source and do not contribute to the factors in the numerator of (23).

Figure 3(b) is based on the same wave forms as those of Fig. 3(a) but is generated with a finer resolution in frequency, effected by the choice $T_B=200$. Both the exact result (solid line) and the approximate result (dashed line) show finer variations. As expected, though, the overall error is somewhat less with the finer resolution.

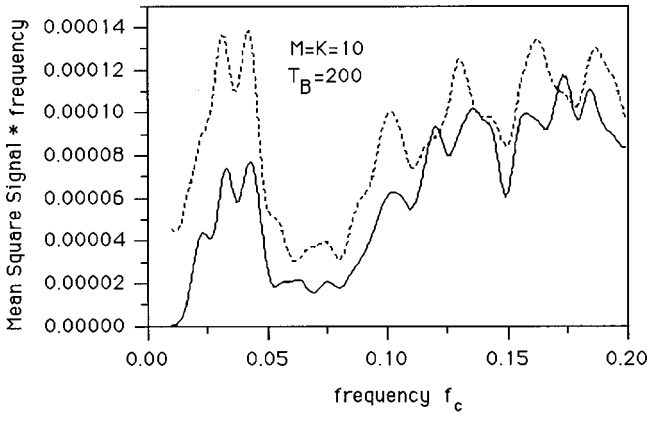

FIG. 6. Comparison of exact and approximate spectral energy densities for the case of a source at X near the cavity, a receiver at Y near the attached mass and spring, and a vertical wall that bisects the structure into two approximately square domains. A window of length 20 is in the wall. There is a discrepancy between exact and approximate energy densities that is most severe at long wavelengths; it is ascribed to Anderson localization.

Figure 3(c) shows the spectrum of G_{XY} without the frequency-smoothing induced by the bandpass filtering, squaring, and time-domain averaging discussed in Sec. II D. Here, the spectrum has high-resolution inherited from the long-time record signal $G_{XY}(t)$ of duration 13 000. The spectrum shows smooth secular features that are correctly captured by the curves in Figs. 3(a) and (b). It also shows rapid universal fluctuations that are related to the individual modes of the entire structure. Such rapidly varying features cannot be predicted without a full global analysis. No statistical energy theory should be asked to do so. It may, however, be possible to construct simple estimates for the statistics of fluctuation in Fig. 3(c) away from energy means of Figs. 3(a) and (b). Power transfer function covariances have received attention in the literature[13–19] and formulas exist, for mean-square fluctuations, that appear to be reliable to within about 50%, at least in reverberation rooms.

Figure 4 shows a comparison like that of Fig. 3(b), this time with the mass and spring deleted, and site X chosen near but not within the cavity. Again, the approximate theory does a good job of predicting the mean-square signal.

Figures 5 and 6 compare the spectral energy densities in cases in which discrepancies are expected. In Fig. 5, for which source and receiver coincide, weak Anderson localization[23,29] is expected to augment backscattered energy at all frequencies by factors up to 3. This is precisely what is observed; the prediction is low by about that amount. In Fig. 6, for which a wall nearly bisects the rectangular domain into two nearly square substructures, and for which source and receiver are in different substructures, Anderson localization will tend to depress actual energy densities below the simple predictions. Pairs of coupled reverberation rooms have recently been shown to Anderson localize.[20] The effect is especially significant when wavelengths are comparable to or longer than window size. That is observed here also; the discrepancy is strongest at the longer wavelengths. The severity of the discrepancy, even at $f_c=0.1$, where the window is two wavelengths wide, is striking, but is consistent with that seen in Ref. 20.

VI. SUMMARY

The concepts that underlie Eq. (23), and in particular those used in deriving the approximate (15) from the exact (14), have implications beyond those developed here. A case has been made that they lend themselves to the longstanding problem of efficient estimation of responses in large structures. But, Eq. (23) could be used to estimate any of its factors in terms of the others; it need not be confined to estimates of mean-square ψ. Ultrasonic laboratory work is now in progress in which local responses (for example, one

of the factors in the numerator) are obtained from measurements of responses ψ to distant sources. Applications in seismology and ultrasonics are being considered.

Here, the approximation has been shown to be of value for the problem of estimating mean-square responses in undamped systems. It is far less computationally demanding than direct numerical simulations, but nevertheless makes good estimates for bandlimited mean-square responses. While similar in spirit to statistical energy analysis, it is not SEA, at least in any ordinary sense of the term, as it does not require any substructuring or weak coupling between substructures. The present formulation has one paramount virtue in comparison to SEA: that it treats (sub)structures with internal features and broad resonances, and can distinguish different positions of sources and receivers within the same (sub)structure.

But, there is much that might still be done to extend the approximation to more practical cases. Its chief weakness is its neglect of damping. It is easy to see that if damping is weak on the time scale of transport within a structure, then damping should be of little consequence to the approximation's accuracy. This could be confirmed by further studies. If damping is stronger than that, the theory requires extension and modification. To put it differently, the theory needs to be extended to encompass time-dependent energy transport, not just asymptotic late-time energy distributions.

The work so far has shown that early time responses determine smoothed late-time asymptotic energies. But, early time responses also describe a degree of transport. The statistical energy ansatz supposes that energy transport is diffusive. If the coefficients of that diffusion operator can be taken from the behavior of short-time-scale direct numerical simulations, it may be that long-time-scale energy flow can be constructed by concatenation of these short-time operators. It remains to be seen whether the transport behavior described by the short-time dynamics is statistically equivalent to the transport behavior that takes place at later times. But this much is clear at this point: the methodology would work in a multiply scattering random wave medium where the energy transport *is* governed by a diffusion equation, and for which a concatenation of short-time diffusions to late times gives the correct description at late times. It is also clear that the method will fail if Anderson localization is significant.

If successful, the result would be a methodology for constructing energy flow equations for large, irregular, damped structures. The methodology would require no substructuring, or determination of coupling factors. It would be based on a numerical description of the structure, and require the direct numerical integration of the dynamical equations for short times and small regions only, thus leading to substantial savings of computational effort compared to direct numerical integration of the entire structure over long times.

ACKNOWLEDGMENTS

This work was supported by the National Science Foundation through Grant Number 9988645.

[1] R. H. Lyon and R. G. DeJong, *Theory and Application of Statistical Energy Analysis* (Butterworths-Heimann, Boston, 1995).
[2] E. H. Dowell and Yuji Kubota, ''Asymptotic modal analysis and SEA of dynamical systems,'' J. Appl. Mech. **52**, 949–957 (1985).
[3] C. H. Hodges and J. Woodhouse, ''Theories of noise and vibration transmission in complex structures,'' Rep. Prog. Phys. **49**, 107–170 (1986).
[4] J. Woodhouse, ''An approach to the theoretical background of SEA applied to structural vibration,'' J. Acoust. Soc. Am. **69**, 1695–1709 (1981).
[5] B. R. Mace and P. J. Shorter, ''Energy flow models from finite element analysis,'' J. Sound Vib. **233**, 369–389 (2000).
[6] C. Simmons, ''Structure-borne sound transmission through plate junctions and estimates of SEA coupling loss factors using the FE method,'' J. Sound Vib. **144**, 215–227 (1991).
[7] J. A. Steel and R. J. M. Craik, ''Statistical energy analysis of structure-borne sound transmission by FEM,'' Sound Vib. **178**, 553–561 (1993).
[8] K. Shankar and A. J. Keane, ''A study of the vibrational energies of two coupled beams by FE and receptance methods,'' Sound Vib. **181**, 801–838 (1995).
[9] C. R. Fredo, ''SEA-like approach for the derivation of energy flow coefficients with a finite element model,'' Sound Vib. **199**, 645–666 (1997).
[10] M. L. Lai and A. Soom, ''Prediction of transient vibration envelopes using SEA techniques,'' J. Vibr. Acoust. **112**, 127–137 (1990).
[11] R. J. Pinnington and D. Lednik, ''Transient SEA of an impulsively excited two oscillator system,'' J. Sound Vib. **189**, 249–264 (1996).
[12] R. S. Langley and P. G. Bremner, ''A hybrid method for the vibrational analysis of complex structural-acoustic systems,'' J. Acoust. Soc. Am. **105**, 1657–1671 (1999).
[13] J. L. Davy, ''The ensemble variance of random noise in a reverberation room,'' J. Sound Vib. **107**, 361–373 (1986).
[14] J. L. Davy, ''Improvements on formulae for the ensemble relative variance of random noise in a reverberation room,'' J. Sound Vib. **115**, 145–161 (1987).
[15] J. L. Davy, ''The relative variance of the transmission function of a reverberation room,'' J. Sound Vib. **77**, 455–479 (1981).
[16] R. H. Lyon, ''Statistical analysis of power injection and response in structures and rooms,'' J. Acoust. Soc. Am. **45**, 545–565 (1969).
[17] R. V. Waterhouse, ''Estimation of monopole power radiated in a reverberation chamber,'' J. Acoust. Soc. Am. **64**, 1443–1446 (1978).
[18] R. L. Weaver, ''On the ensemble variance of reverberation room transfer functions, the effect of spectral rigidity,'' J. Sound Vib. **130**, 487–491 (1989).
[19] O. I. Lobkis, R. L. Weaver, and I. Rozhkov, ''Power variances and decay curvature in a reverberant system,'' J. Sound Vib. **237**, 281–302 (2000).
[20] R. L. Weaver and O. I. Lobkis, ''Anderson localization in coupled reverberation rooms,'' J. Sound Vib. **231**(4), 1111–1134 (2000).
[21] C. H. Hodges, ''Confinement of vibration by structural irregularity,'' J. Sound Vib. **82**, 411–424 (1982).
[22] R. L. Weaver, ''Anderson localization in the time domain: Numerical studies of waves in two-dimensional disordered media,'' Phys. Rev. B **49**, 5881–5895 (1994).
[23] R. L. Weaver and O. I. Lobkis, ''Enhanced backscattering and modal echo of reverberant elastic waves,'' Phys. Rev. Lett. **84**, 4942–4945 (2000); see also J. de Rosny, A. Tourin, and M. Fink, ''Coherent backscattering of an elastic wave in a chaotic cavity,'' *ibid.* **84**, 1693 (2000).
[24] R. L. Weaver, ''The effect of an undamped finite degree of freedom ''fuzzy'' substructure: Numerical solutions and theoretical discussion,'' J. Acoust. Soc. Am. **100**, 3159–3164 (1996); ''Mean and mean square responses of a prototypical master/fuzzy system,'' *ibid.* **101**, 1441–49 (1997).
[25] M. L. Mehta, *Random Matrices* (Academic, Boston, 1990).
[26] T. A. Brody, J. Flores, J. B. French, P. A. Mello, A. Pandey, and S. S. M. Wong, ''Random matrix physics: Spectrum and strength fluctuations,'' Rev. Mod. Phys. **53**, 385–478 (1981).
[27] R. Weaver, ''Localization, scaling, and diffuse transport of wave energy in disordered media,'' Appl. Mech. Rev. **49**, 111–120 (1996).
[28] R. L. Weaver and J. Burkhardt, ''Transport in multi-coupled Anderson localizing systems,'' Chaos, Solitons Fractals **11**, 1611–20 (2000).
[29] R. Weaver and J. Burkhardt Weak, ''Anderson localization and enhanced backscatter in reverberation rooms and quantum dots,'' J. Acoust. Soc. Am. **96**, 3186–3190 (1994); see also Prigodin, Altshuler, Efetov, and Ida, ''Mesoscopical dynamical echo in quantum dots,'' Phys. Rev. Lett. **72**, 546 (1994).
[30] C. Soize, ''Probabalistic structural modeling in linear dynamic analysis of

complex mechanical systems. I. Theoretical elements,'' Rech. Aerosp. **5**, 23–48 (1986).
[31] C. Soize, ''A model and numerical method in the medium frequency range for vibroacoustic predictions using the theory of structural fuzzy,'' J. Acoust. Soc. Am. **94**, 849–865 (1993).
[32] A. D. Pierce, V. W. Sparrow, and D. A. Russell, ''Fundamental structural-acoustic idealizations for structures with fuzzy internals,'' J. Vibr. Acoust. **117**, 339–348 (1995).
[33] M. Strasberg and D. Feit, ''Vibration damping of large structures induced by attached small resonant structures,'' J. Acoust. Soc. Am. **99**, 335–344 (1996).
[34] R. H. Lyon, ''Statistical energy analysis and structural fuzzy,'' J. Acoust. Soc. Am. **97**, 2878–2881 (1995).
[35] E. J. Skudrzyk, *Simple and Complex Vibratory Systems* (Pennsylvania State University Press, University Park, PA, 1968); also, ''Understanding the dynamic behavior of complex vibrators,'' Acustica **64**, 123–147 (1987).
[36] R. L. Weaver, ''On the time and geometry independence of elastodynamic spectral energy density,'' J. Acoust. Soc. Am. **80**, 1539–1541 (1986).
[37] T. R. Hughes, ''Sylvester's Inertia Theorem,'' in *The Finite Element Method* (Prentice-Hall, Englewood Cliffs, NJ, 1987); see also P. Shorter, J. Acoust. Soc. Am. **108**, 2557 (2000).

A method to calculate the acoustic response of a thin, baffled, simply supported poroelastic plate

K. V. Horoshenkov[a)]
School of Engineering, University of Bradford, Bradford BD7 1DP, England

K. Sakagami[b)]
Environmental Acoustics Laboratory, Faculty of Engineering, Kobe University, Rokko, Nada, Kobe 657-8501, Japan

(Received 19 December 2000; accepted for publication 18 May 2001)

The Helmholtz integral equation formulation is used to produce the solution for the acoustic field reflected from a finite, thin, poroelastic plate in a rigid baffle with simply supported edges. The acoustic properties of the porous material are predicted using the effective fluid assumption. The solutions for the displacement of the plate and for the loading acoustic pressures are given in the form of the sine transform. The sine transform coefficients are obtained from the solution of a system of linear equations resulting from three integral Helmholtz formulations which relate the displacement of the plate and the acoustic pressures on the front and on the back of the plate. The effect of an air gap behind the plate in the front of a rigid wall is also considered. A parametric study is performed to predict the effect of variations in the parameters of the poroelastic plate. It is shown that thin, light, poroelastic plates can provide high values of the acoustic absorption even for low frequency sound. This effect can be exploited to design compact noise control systems with improved acoustic performance.
[DOI: 10.1121/1.1385900]

PACS numbers: 43.50.Gf, 43.55.Ev, 43.40.Fz [MRS]

I. INTRODUCTION

Porous media such as glass and mineral wool fiber blanket have been used extensively for many years for sound reduction. These materials have been mainly used indoors although there have been some outdoor applications, with suitable protective covers, in road traffic noise abatement. The susceptibility of these materials to degradation and the subsequent need for protection outdoors has lead to the search for more robust alternatives of equal acoustic efficiency. The relatively recent work on thin, elastic, porous plates[1–3] suggests the possibility of producing porous media that possess not only sound absorption properties but also pronounced resonant structural vibrational characteristics. In this way, the desirable combination of structural motion and viscothermal boundary layer acoustic absorption in the pores of the material may be exploited, in a single structure. The microstructure of consolidated granular materials can be readily designed since it is a function of the granules and the consolidation process.[3] This is a considerable asset, because it permits optimization of the structural and acoustic parameters of layers of these materials.

There have been a number of works (e.g., Refs. 4–7) which are primarily based on the finite element formulation (FEM) and the original Biot theory.[8] These formulations are more suited for the case when the wavelength of sound is comparable to the thickness of the acoustic porous layer so that the longitudinal variation of the frame displacement can be predicted. Because these works are based on a numerical method, they may fail to provide a fundamental physical inside into the phenomenon nature. Unlike many previous works this paper presents a more simple analytical method to study the effect of the elastic frame of finite density on the acoustic properties of a thin, porous, fluid-loaded elastic plate, which is simply supported in a rigid baffle.

II. THEORETICAL FORMULATION

Let us consider a thin, fluid-loaded poroelastic plate of a finite width, L, which is simply supported in a rigid baffle (see Fig. 1). We assume that the plate is infinitely long in y-direction and that a plane acoustic wave $p_i = e^{ik_o(\sin\theta_0 x + \cos\theta_0 z)}$ is incident on the front surface of the plate at the angle θ_0 in the plane $x-z$. In this expression k_o is the wave number in air. The direction of the plane wave is normal to the surface of the plate in the plane $y-z$. It is also assumed that all acoustic quantities have a harmonic time dependence $e^{-i\omega t}$ which we suppress in the following expressions.

To derive the formulation of the problem we shall begin with the boundary conditions, which are obtained from the continuity of acoustic pressures and velocities, so that on the front surface of the plate, at $z=0$

$$p_s = p_i + p_r = p_b, \tag{1}$$

where $p_b = p_b^+ + p_b^-$ is the pressure in the wave transmitted in the plate and p_r is the pressure in the wave reflected from the plate. The terms p_b^+ and p_b^- stand for the pressure in the

a)Electronic mail: K.Horoshenkov@bradford.ac.uk
b)Electronic mail: saka@kobe-u.ac.jp

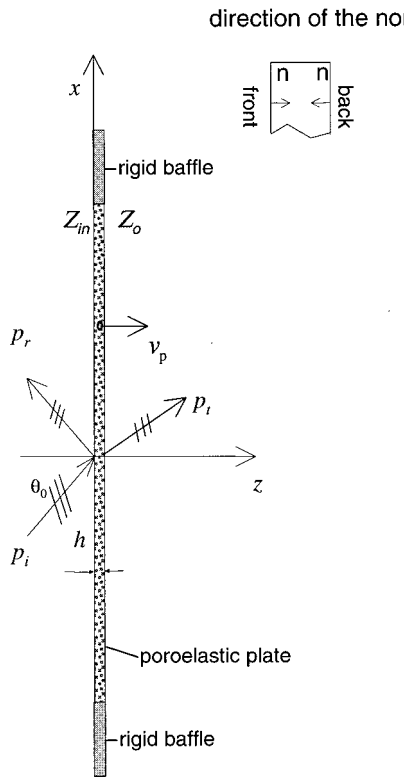

FIG. 1. On the reflection from a baffled poroelastic plate loaded with two fluid half-spaces.

direct wave excited in the porous plate and the wave reflected from the back of the plate, respectively.

Taking the outward normal, the boundary conditions for the acoustic velocities at the front surface of the plate are written as

$$\frac{\nabla p_s}{i\omega\rho_o}=\frac{\nabla p_b}{i\omega\rho_b}+v_p \tag{2}$$

or

$$\frac{\nabla p_s}{i\omega\rho_o}=\frac{p_s}{Z_{in}}+v_p, \tag{3}$$

where Z_{in} is the front specific acoustic impedance of the plate and v_p is the velocity of the plate, ρ_o and ρ_b are the density of air and the effective fluid, respectively.

Similarly, on the back of the plate at $z=h$ the boundary conditions for the acoustic pressures and velocities are written as

$$p_t=p_b^+e^{i\gamma_b}+p_b^-e^{-i\gamma_b}, \tag{4}$$

$$\frac{\nabla p_b}{i\omega\rho_b}+v_p=\frac{\nabla p_t}{i\omega\rho_o}, \tag{5}$$

where p_t is the transmitted pressure and $\gamma_b=k_bh\cos\theta_b$.

In this work we consider two cases: (a) the case when the plate and the baffle separate two fluid half-spaces (see Fig. 1); and (b) when the plate and the baffle are separated from a rigid wall by an infinitely long acoustic layer of finite

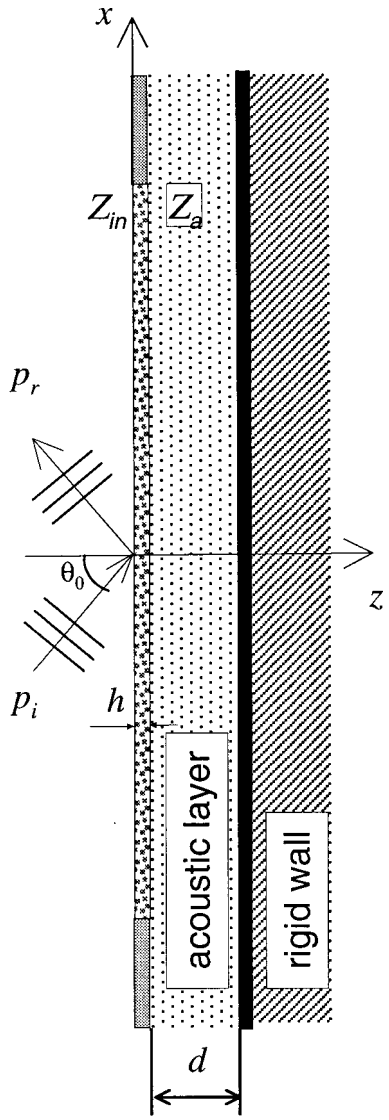

FIG. 2. On the reflection from a poroelastic plate loaded with an infinitely long acoustic layer of finite impedance.

thickness, d (see Fig. 2). In the first case, when the loading is provided by a fluid half-space, the front surface acoustic impedance is given by (e.g., see Ref. 9, page 46)

$$Z_{in}=Z_b\frac{Z_o+Z_b\tanh(-ik_bh\cos\theta_b)}{Z_b+Z_o\tanh(-ik_bh\cos\theta_b)}, \tag{6}$$

where $Z_b=\rho_bc_b/\cos\theta_b$ and k_b are the characteristic impedance and wave number of the porous material, $Z_o=\rho_oc_o/\cos\theta_0$ is the acoustic impedance of the fluid half-space. Here c_b is the complex sound speed in the porous material, c_o is the sound speed in air and the angle of refraction $\sin\theta_b=(c_b/c_o)\sin\theta_0$.

Alternatively, when the plate is loaded with an ininitely long acoustic layer confined between the plate and the rigid backing (see Fig. 2) Eq. (6) becomes

$$Z_{in}=Z_b\frac{Z_a+Z_b\tanh(-ik_bh\cos\theta_b)}{Z_b+Z_a\tanh(-ik_bh\cos\theta_b)}, \tag{7}$$

where $Z_a=\rho_a c_a/\cos\theta_a \coth(-ik_a d\cos\theta_a)$ for an acoustic layer of thickness d. In the last expression ρ_a, c_a and k_a are the complex density, sound speed and the wave number of the acoustic layer, respectively. These properties as well as the properties of the effective fluid in the plate can be predicted using, for example, expressions given in Ref. 10. The angle of refraction in the absorbing layer $\sin\theta_a=(c_a/c_b)\sin\theta_b$.

III. DISPLACEMENT OF A POROELASTIC PLATE

To derive the expression for the displacement of the plate we assume that the plate is composed of an elastic material of a finite acoustic impedance, which can represent, for example, the impedance of the effective fluid filling the porous space.

We assume that the vibration of the plate is generated due to the pressure gradient between its front and back faces, so that the displacement $w_p(x)=v_p(x)/(-i\omega)$ can be determined from the equation of plate motion (e.g., see Ref. 11, Chap. 8)

$$D\nabla^4 w_p(x)-\omega^2\rho_p h w_p(x)=p_s(x)-p_t(x), \tag{8}$$

in which the structural rigidity $D=[E(1-i\eta)h^3/12(1-\nu^2)]$, E is the Young's modulus, ρ_p is the density of the plate, expressed in kg/m^3, η is the structural loss factor and ν is the Poisson ratio.

The displacement of a finite, thin, simply supported elastic plate can be represented by a sine transform

$$w_p(x)=\sum_{m=1}^{\infty} w_m \sin\left(\frac{\pi m}{L}x\right). \tag{9}$$

The coefficients w_n in Eq. (9) are found by substituting this equation in Eq. (8), multiplying the result by $\sin((\pi n/L)x)$ followed by integrating within the plate dimension of $0\leqslant x\leqslant L$. Utilizing the orthogonality condition in which

$$\int_0^L \sin\left(\frac{\pi m}{L}\right)\sin\left(\frac{\pi n}{L}x\right)dx=\begin{cases} L/2, & m\neq n \\ 0, & m=n \end{cases}, \tag{10}$$

we obtain

$$(Dk_n^4-\omega^2\rho_p h)w_n=\frac{2}{L}\int_0^L (p_s(x)-p_t(x))\sin(k_n x)dx, \tag{11}$$

in which $k_n=(n\pi/L)$.

Since the expressions in the right-hand side of Eq. (11) are the sine transforms of the pressures on the front and on the back of the plate, i.e.,

$$p_n^{(s)}=\frac{2}{L}\int_0^L p_s(x)\sin(k_n x)dx$$

and

$$p_n^{(t)}=\frac{2}{L}\int_0^L p_t(x)\sin(k_n x)dx, \tag{12}$$

we can re-write Eq. (11) as

$$\gamma_n w_n=p_n^{(s)}-p_n^{(t)}, \tag{13}$$

where $\gamma_n=Dk_n^4-\omega^2\rho_p h$. Zeros of γ_n yield the eigenfrequencies of the plate, which correspond to the structural resonance. For poroelastic plates these frequencies are affected by the fluid–solid interactions in the porous structure. This effect is rather complex and it is suggested that in simple models these interactions may be accounted for by the dynamically measured loss factor $\eta(\omega)$.

The next step will be to express analytically the effect of the structural vibration on the acoustic pressures on the front and on the back faces of the fluid-loaded plate. In this way a system of three coupled equations, (8), (14) and (15), can be determined and resolved against the three unknowns: w_p, p_s and p_t.

Using the Helmholtz integral formulation and the boundary conditions (3) and (5) the acoustic pressures can be expressed as

$$p_s=2p_i(x)+\frac{i}{2}\int_0^L \{\omega^2\rho_o w(x_s) + ik_o\beta_{in}p_s(x_s)\}H_0^{(1)}(k_o|x-x_s|)dx_s \tag{14}$$

and

$$p_t=-\frac{i}{2}\int_0^L \left\{\omega^2\rho_o w(x_s)+\frac{\nabla p_b}{i\omega\rho_b}\right\}H_0^{(1)}(k_o|x-x_s|)dx_s, \tag{15}$$

respectively. Here the surface acoustic admittance is $\beta_{in}=(\rho_o c_o/Z_{in})$.

Since the material of the plate is porous, then due to the interfacial acoustic flow the acoustic velocities in the plate at $z=h$ and at $z=0$ are related as

$$(\nabla p_b)_{z=h}=\epsilon(\nabla p_b)_{z=0}, \tag{16}$$

where the velocity transfer coefficient

$$\epsilon=\frac{p_b^+ e^{i\gamma_b}-p_b^- e^{-i\gamma_b}}{p_b^+-p_b^-}=\frac{e^{i\gamma_b}-r_b e^{-i\gamma_b}}{1-r_b}. \tag{17}$$

The acoustic pressure reflection coefficient from the back of the plate is defined as

$$r_b=\frac{p_b^-}{p_b^+}=\frac{Z-Z_b}{Z+Z_b}e^{2i\gamma_b}, \tag{18}$$

where $Z=Z_o$ if the plate is loaded by a fluid half-space, and $Z=Z_a$ if the load is an acoustic layer of thickness d.

Using relations (2)–(5) and (16) the pressure on the back can now be expressed

$$p_t=-\frac{i}{2}\int_0^L \{\omega^2\rho_o w(x_s)+ik_o\beta_{in}\epsilon p_s(x_s)\} \times H_0^{(1)}(k_o|x-x_s|)dx_s. \tag{19}$$

Applying the sine transform to Eqs. (14) and (19) and using expressions (9) and (12) we obtain three integral forms, which relate the coefficients in the sine series expansions for the plate velocity and for the acoustic pressures

$$\gamma_n w_n = 2p_n^{(i)} + \frac{2i\omega^2\rho}{L}\sum_{m=1}^{\infty} B_{mn} w_m - \frac{k\beta_{in}(1+\epsilon)}{L}\sum_{m=1}^{\infty} B_{mn} p_m^{(s)}, \tag{20}$$

$$p_n^{(s)} = 2p_n^{(i)} + \frac{i\omega^2\rho}{L}\sum_{m=1}^{\infty} B_{mn} w_m - \frac{k\beta_{in}}{L}\sum_{m=1}^{\infty} B_{mn} p_m^{(s)}, \tag{21}$$

and

$$p_n^{(t)} = -\frac{i\omega^2\rho}{L}\sum_{m=1}^{\infty} B_{mn} w_m + \frac{k\beta_{in}\epsilon}{L}\sum_{m=1}^{\infty} B_{mn} p_m^{(s)}, \tag{22}$$

where

$$B_{mn} = \int_0^L \int_0^L \sin(k_m x_s)\sin(k_n x_s) \times H_0^{(1)}(k_o|x-x_s|)\,dx_s\,dx \tag{23}$$

and

$$p_n^{(i)} = \frac{2\pi n}{(k_o L)^2 \sin^2\theta - (\pi n)^2}((-1)^n e^{ik_o L\sin\theta} - 1). \tag{24}$$

For the particular case, when $\sin\theta_0 = \pm(\pi n/k_o L)$ expression (24) becomes

$$p_n^{(i)} = 2i. \tag{25}$$

Expressions (20)–(22) are a system of three infinite sets of linear equations. Each set can be reduced to a system of N linear equations, since it can be shown that the coefficient series $\Sigma_{m,n}^{\infty}|B_{mn}/\gamma_n|^2$ and $\Sigma_n^{\infty}|p_n^{(i)}|^2$ are converging series for each of these sets.

If we denote $a_1 = (2i\omega^2\rho_o/L)$, $a_2 = a_1/2$, $b_1 = [k_o\beta_{in}(1+\epsilon)]/L$ and $b_2 = (k_o\beta_{in}/L)$, then Eqs. (20)–(22) can be rewritten in the matrix form as

$$\mathbf{G}\mathbf{w_p} = \mathbf{2p_i} + a_1\mathbf{B}\mathbf{w_p} - b_1\mathbf{B}\mathbf{p_s}, \tag{26}$$

$$\mathbf{p_s} = \mathbf{2p_i} + a_2\mathbf{B}\mathbf{w_p} - b_2\mathbf{B}\mathbf{p_s} \tag{27}$$

and

$$\mathbf{p_t} = -a_2\mathbf{B}\mathbf{w_p} + b_2\epsilon\mathbf{B}\mathbf{p_s}, \tag{28}$$

where $\mathbf{G}$ is the diagonal matrix of structural impedance coefficients γ_{mm}, $\mathbf{B}$ is the matrix of the radiation impedance coefficients B_{mn}. The column vectors $\mathbf{p_s}$, $\mathbf{p_t}$ and $\mathbf{w_p}$ in these equations are composed of the coefficients of the sine transforms for the surface pressure, transmitted pressure and the plate displacement, respectively.

Equations (26) and (27) can be used to determine the sine transform coefficients for the displacement of the plate

$$\mathbf{w_p} = 2(\mathbf{G} - a_1\mathbf{B} + a_2\mathbf{A}\mathbf{B})^{-1}(\mathbf{I} - \mathbf{A})\mathbf{p_i}, \tag{29}$$

for the pressure on the front face

$$\mathbf{p_s} = (\mathbf{I} + b_2\mathbf{B})^{-1}(2\mathbf{p_i} + a_2\mathbf{B}\mathbf{w_p}), \tag{30}$$

where the matrix $\mathbf{A} = b_1\mathbf{B}(\mathbf{I} + b_2\mathbf{B})^{-1}$ and $\mathbf{I}$ is the unity matrix. The transmitted pressure is found from expression (28). The method of singular value decomposition can be used in the case when the system of Eqs. (28)–(30) is ill-posed, which can result if a very large number of structural modes is to be considered.

The acoustic pressures are calculated using the following expressions:

$$p_s(x) = \sum_{n=1}^{N} p_n^{(s)}\sin(k_n x)$$

and

$$p_t(x) = \sum_{n=1}^{N} p_n^{(t)}\sin(k_n x). \tag{31}$$

The plate displacement w_p is calculated using expression (9).

A particular difficulty is the calculation of the radiation impedance matrix given by convolution integral (23). Although the direct numerical calculation of the convolution integral is possible, the process can be slow and unstable due to the oscillatory nature of the integrand function, which has a singularity at $x = x_s$. To improve the numerical integration of Eq. (23) we will use the transformation method suggested by Shenderov.[12] In this method double convolution integral (23) is reduced to a single integral,

$$B_{mn} = \frac{\mu(1+(-1)^{m+n})}{k_o^2\pi(n^2-m^2)}\int_0^{\mu}\left\{n\sin\left(\frac{m\pi}{\mu}v\right) - m\sin\left(\frac{n\pi}{\mu}v\right)\right\} \times H_0^{(1)}(v)\,dv, \quad m \neq n,$$

and

$$B_{mn} = k_o^{-2}\int_0^{\mu}\left\{(\mu - v)\cos\left(\frac{m\pi}{\mu}v\right) + \frac{\mu}{m\pi}\sin\left(\frac{m\pi}{\mu}v\right)\right\} \times H_0^{(1)}(v)\,dv, \quad m = n, \tag{32}$$

TABLE I. Base values of the nonacoustic parameters used in the numerical investigation.

Material	LPHD material	Foam (YB102)
Flow resistivity, Pa s m^{-2}	10^{11}	10^4
Porosity	0.01	0.57
Tortuosity	1.0	1.563
Pore size deviation, ϕ-units	0.4	0.4
Young's modulus, N/m^2	10^{11}	10^8
Structural loss factor	0	0
Poisson ratio	0.3	0.3
Material density, kg/m^3	8×10^3	80
Plate thickness, m	0.01	0.01
Width of air gap, m	0.08	0.08
Width of plate, m	0.5	0.5
Angle of incidence, deg	0	0

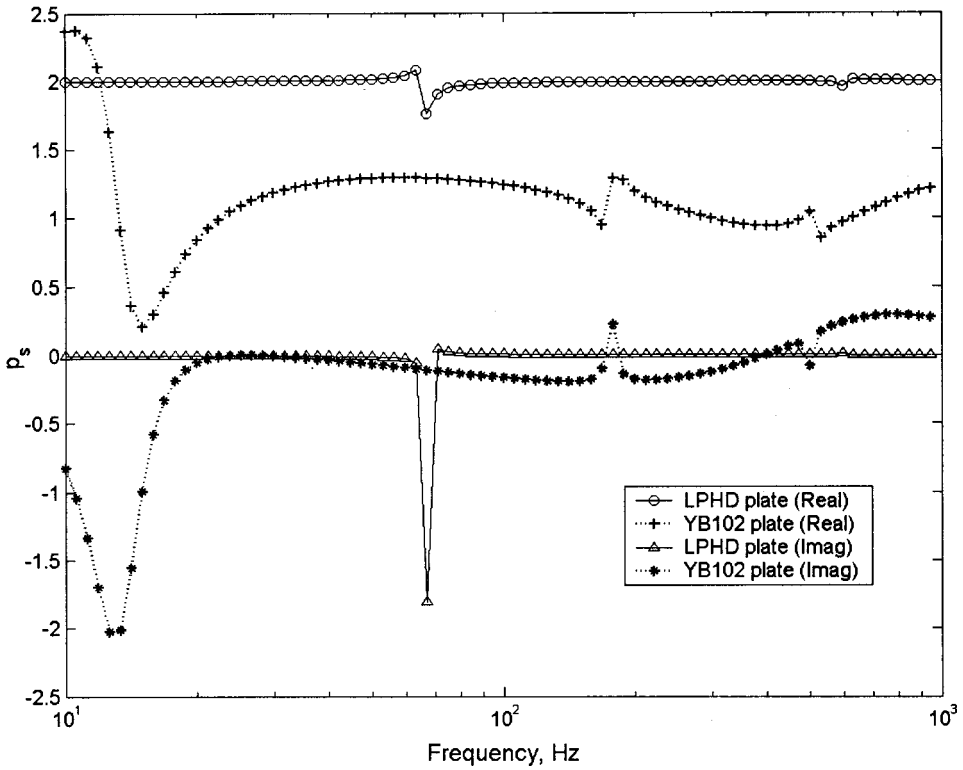

FIG. 3. The acoustic pressure spectra on the front surface of the plate predicted at $x=L/2$.

where $\mu=k_oL$. Integrals (32) are more suitable for numerical integration than original expression (23). It can be suggested to use the method of Gauss–Legendre quadrature, which is detailed in Ref. 13. The exact details of the transformation of Eq. (23) into Eq. (32) are provided in the Appendix.

IV. NUMERICAL RESULTS

Expressions (28)–(30) were used for a parametric investigation for the acoustic response as a function of the microscopic and elastic properties of a finite poroelastic plate. In

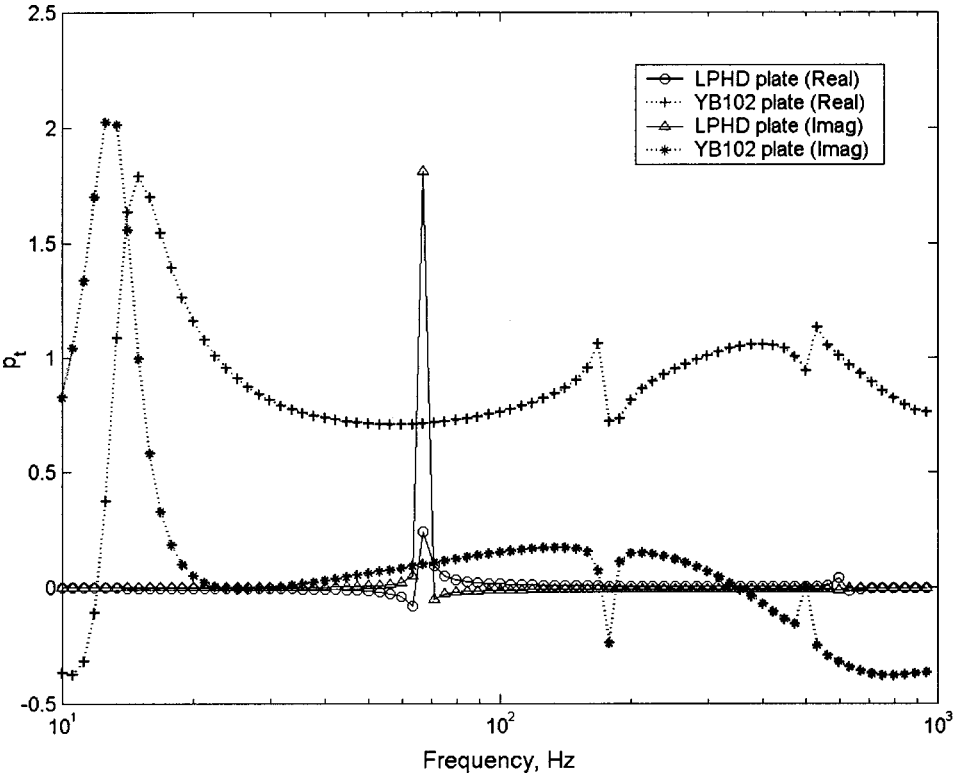

FIG. 4. The transmitted acoustic pressure predicted at $x=L/2$.

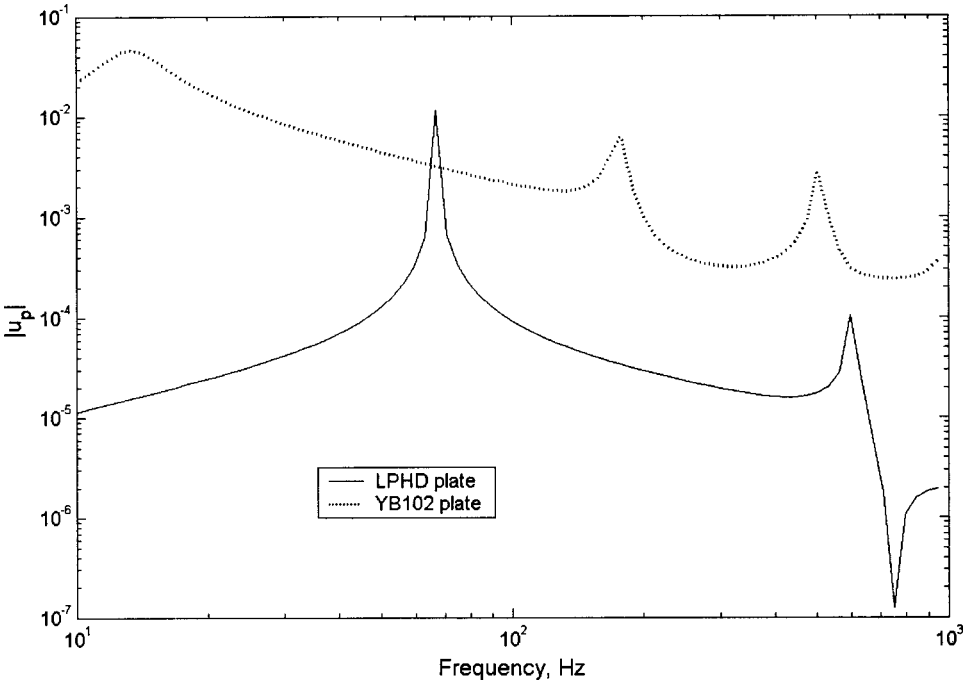

FIG. 5. The modulus of the velocity of the plates predicted at $x=L/2$.

this investigation the average surface acoustic impedance of the plate can be estimated using the following expression

$$\langle z\rangle(\omega,\theta_0)=\frac{\cos\theta_0\int_0^L p(x)ds}{\rho_o c_o\int_0^L(-i\omega w_p(x)+p_s(x)/Z_{in})dx}. \quad (33)$$

The plane wave acoustic absorption coefficient can be calculated using the above result as

$$\alpha(\omega,\theta_0)=1-\left|\frac{\langle z\rangle-\cos\theta}{\langle z\rangle+\cos\theta}\right|^2. \quad (34)$$

We limit the investigation to the values of the acoustic pressures, plate displacement, averaged surface acoustic impedance and the averaged plane wave absorption coefficient. Two plates have been considered: a low-permeability, high-density (LPHD) plate and a poroelastic plate YB102. Table I

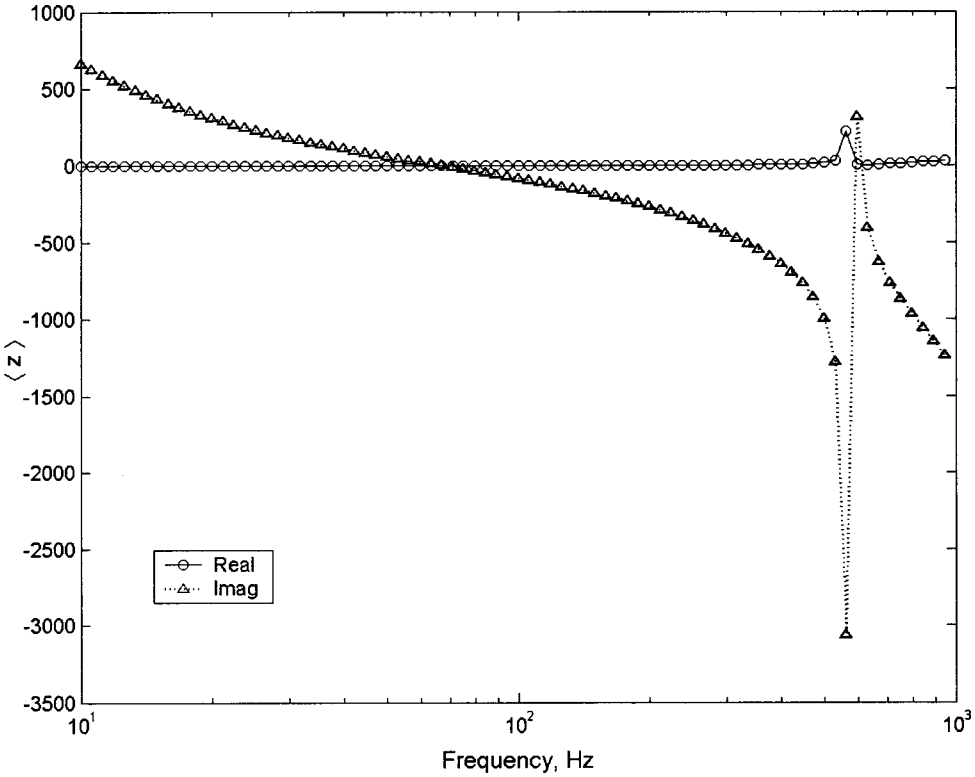

FIG. 6. The averaged, normalized, normal incidence surface acoustic impedance of the LPHD plate.

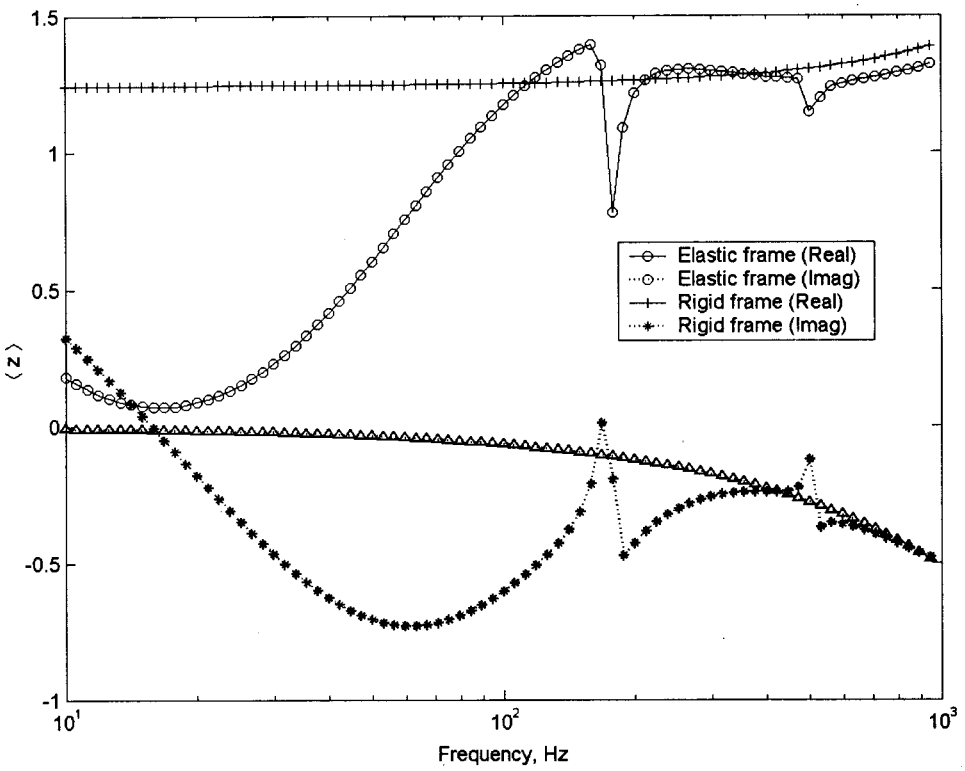

FIG. 7. The averaged, normalized, normal incidence surface acoustic impedance of the plate YB102.

provides the list of all the base values of the microscopic and elastic parameters for the materials used in the investigation. In this investigation the number of modes is limited to $N=64$.

A. Acoustic properties of poroelastic plates separating two fluid half-spaces

Figures 3 and 4 show the real and imaginary parts of the acoustic pressure spectra predicted on the front and on the back surface of the (LPHD) plate and those for poroelastic plate YB102. It is assumed that the plates are supported in a rigid baffle separating two air half-spaces as shown in Fig. 1. The Pade approximation model[10] was used to predict the acoustic impedance Z_b and the complex wave number k_b of the effective fluid. The model is based on the rational (Padé) approximation approach, which has been developed for some particular pore geometries and which accounts for viscous and thermal dissipation effects in rigid-frame porous media. In the case of the LPHD plate, the real part of the front surface acoustic pressure is very close to $2p_i$, while the imaginary part (see Fig. 3) as well as the transmitted pressure (see Fig. 4) is insignificantly small, except at the structural resonance frequencies of 67 Hz (mode 1) and 605 Hz (mode 3). This is the expected result due to poor coupling of the acoustic impedance of air and the mechanical impedance of the LPHD plate. The coupling can be improved if the density of the material of the plate, the Young's modulus and the flow resistivity of the material are reduced. In this case, then the real and imaginary parts of the acoustic pressure across the plate can vary considerably as illustrated in Fig. 3 for the case of the plate YB102. The front surface acoustic pressure in this case is affected by the flexural waves in a broader frequency range (see Fig. 3). The transmitted acoustic pressure in the case of the plate YB102 is induced by the vibration of the plate and by the acoustic flow through the porous structure and is nonzero throughout the considered frequency range (see Fig. 4).

Figure 5 shows the comparison of the absolute value of the structural velocity of LPHD plate and that of the poroelastic plate YB102. The velocity of the LPHD plate is limited throughout the considered frequency range except at the resonance frequencies and in the vicinity of these. It is easy to show that normally incident acoustic plane wave excites structural modes with odd indices $2n-1$, $n \in \mathcal{Z}^+$. Figure 5 shows that in the case of the poroelastic plate YB102, the width of the first resonance maximum is broadened as a result of the additional damping due to the finite value of the flow resistivity. It is also shown that the amplitude of the plate velocity is increased because of the reduced density and the elastic modulus of the material, which is the expected result.

Equation (33) was used to predict the average, normalized acoustic impedance of the elastic plates. Figures 6 and 7 show the results of the prediction for the LPHD plate and for the poroelastic plate YB102, respectively. As expected, the imaginary part of the acoustic impedance of the LPHD plate is positive and large in comparison with the real part in the low frequency range below the first resonance at 67 Hz corresponding to the ''spring'' characteristic of the mechanical impedance of the plate ($Z_m \propto 1/(-i\omega D)$). The result shown in Fig. 5 suggests that between the resonance frequencies the imaginary part of the acoustic impedance is negative corresponding to the ''mass'' characteristic of the mechanical impedance of the plate ($Z_m \propto -i\omega\rho_p h$). A similar result is ob-

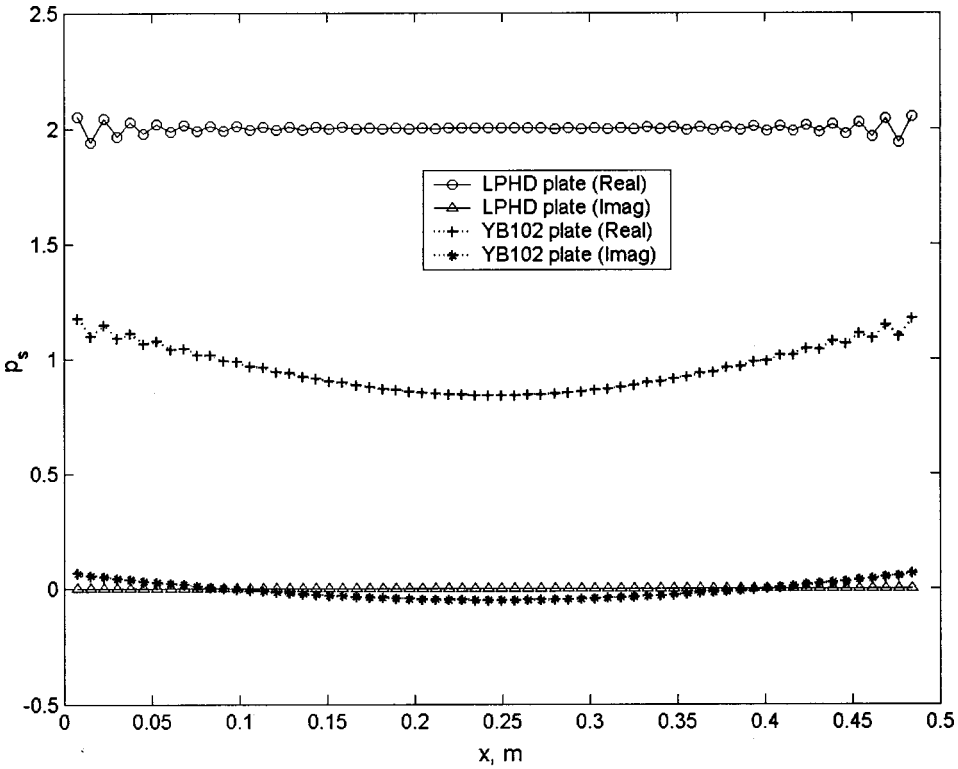

FIG. 8. The distribution of the acoustic pressure across the front surface of the plate, which is predicted for $f = 19.95$ Hz.

served in Fig. 6, but in this case the amplitude of the real and imaginary parts is comparable as the result of the finite values of the acoustic impedance of the plate material and lower values of its density and Young's modulus. In the lower frequency range, below 100 Hz, the amplitude of the real and imaginary part is primarily determined by the structural vibration of the plate. As the frequency of sound increases, the structural vibration effect become negligible and the values of the acoustic impedance approach asymptotically those predicted for the rigid frame case.

Figures 8–13 show the distribution of the real and imaginary parts of acoustic pressures on the surfaces of the LPHD and poroelastic plate and the velocity distribution across the plate for two arbitrarily chosen frequencies 20 Hz and 501 Hz. Figures 8, 9, 11 and 12 show that, as expected, the acoustic pressure is uniformly distributed across the

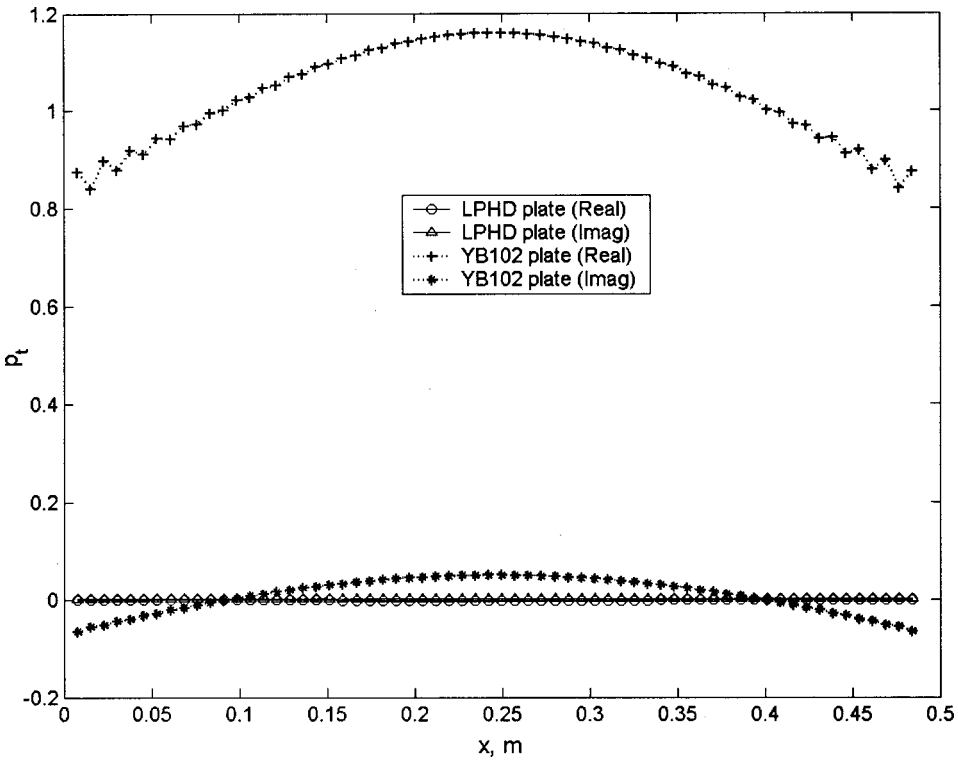

FIG. 9. The distribution of the transmitted acoustic pressure across the surface of the plate, which is predicted for $f = 19.95$ Hz.

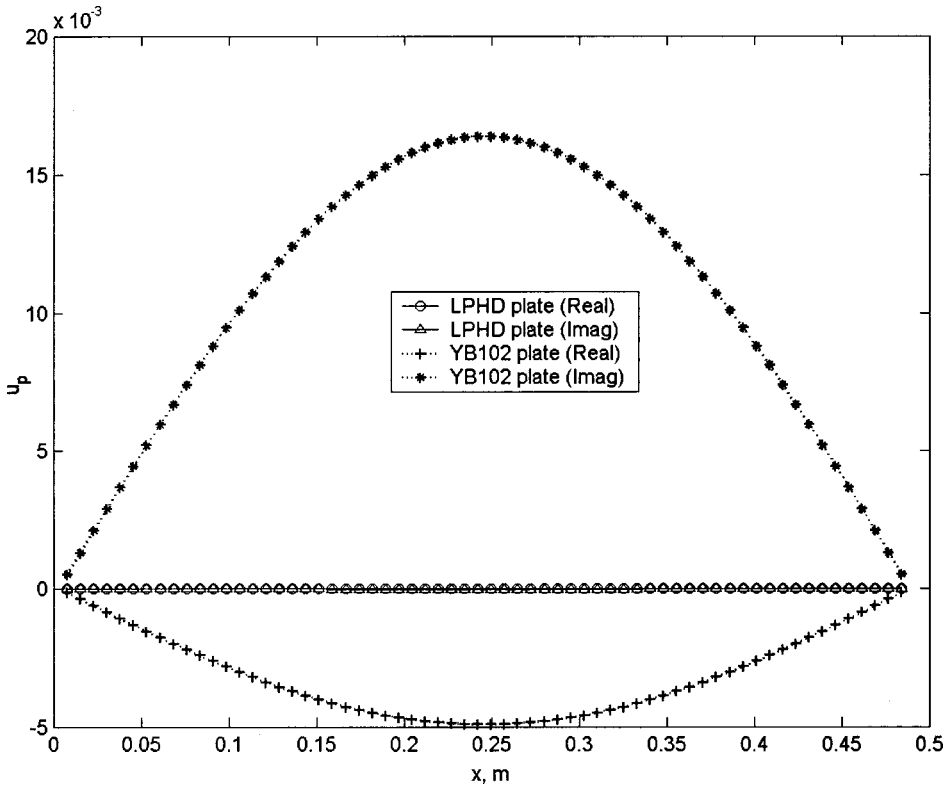

FIG. 10. The distribution of the plate velocity across the surface of the plate, which is predicted for $f=19.95$ Hz.

LPHD plate and that $p_s \cong 2p_i$ and $p_t \cong 0$ as the velocity of the structural vibration is negligibly small. The same figures suggest that the acoustic pressures across the front and the back of the poroelastic plate YB102 are more strongly affected by the structural vibration, for which the real and imaginary parts of the velocity are shown in Figs. 10 and 13 for 20 Hz and 501 Hz, respectively. In this case, the transmitted pressure is largely determined by the finite values of the acoustic impedance of the porous material of the plate which can be compared to the surface pressure on the front. Small fluctuations in the predicted acoustic pressures and velocities, which are particularly pronounced close to the edges of the plate $x \to 0$ and $x \to L$, are explained by the Gibbs phenomenon.

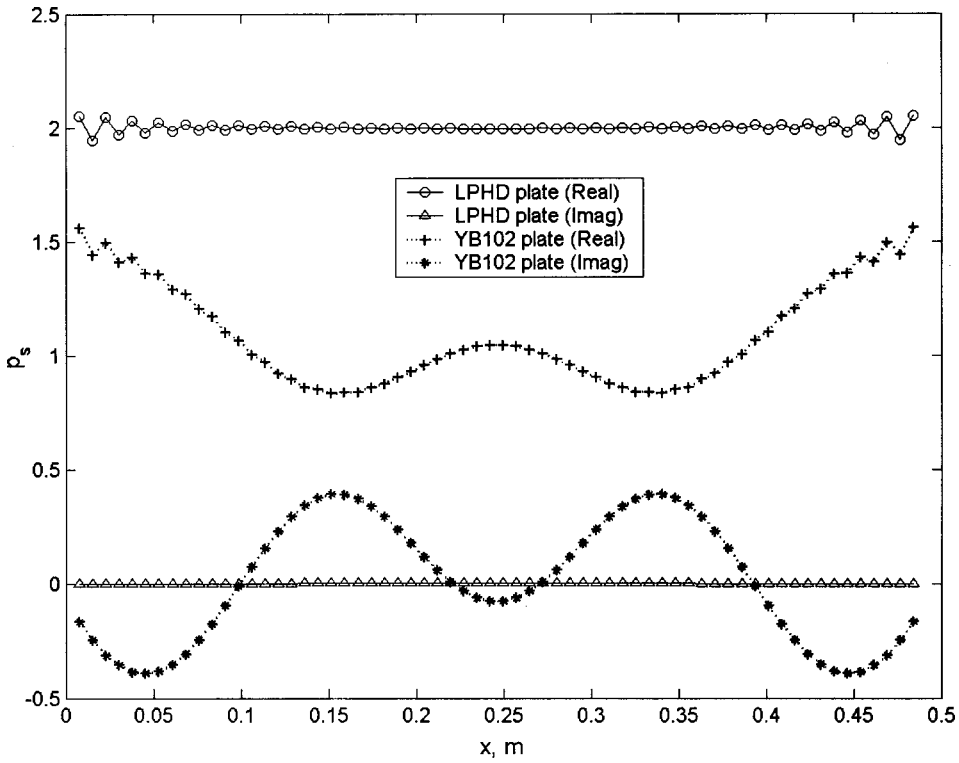

FIG. 11. The distribution of the acoustic pressure across the front surface of the plate, which is predicted for $f=501.19$ Hz.

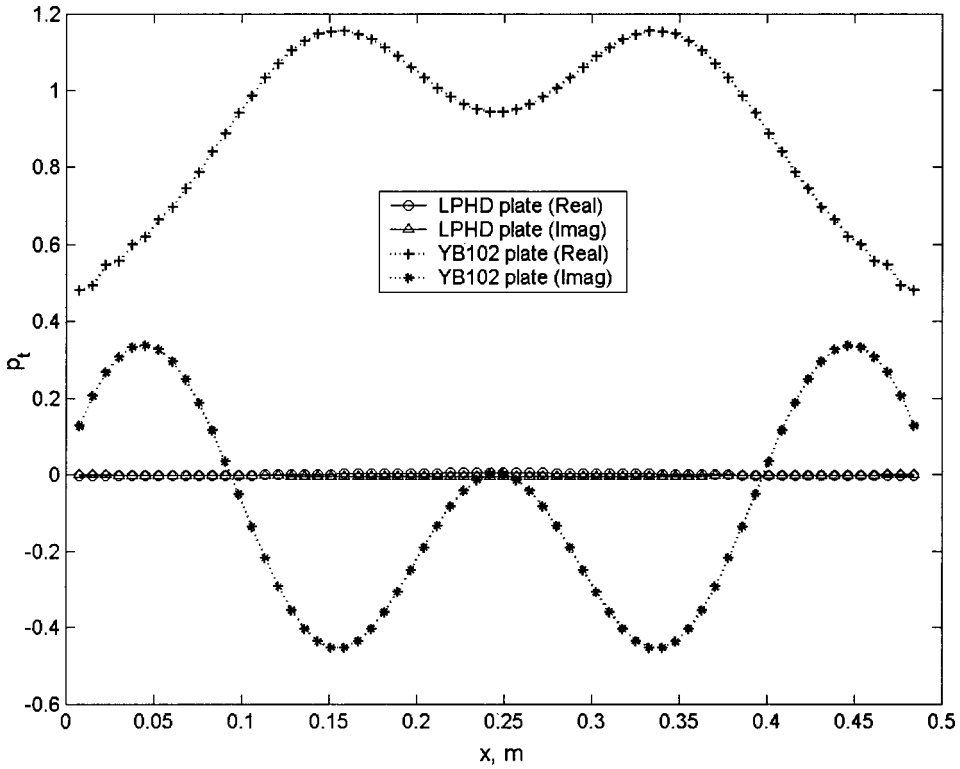

FIG. 12. The distribution of the transmitted acoustic pressure across the surface of the plate, which is predicted for $f = 501.19$ Hz.

B. Acoustic properties of poroelastic plates in the vicinity of rigid wall

It is common practice in noise control engineering and in architectural acoustics applications to install absorbing materials in the vicinity of impervious, reflecting walls as shown in Fig. 2. In this setup an air gap or acoustic layer of thickness d separates the porous slab and the impervious wall (see Fig. 2). Predictions were carried out to determine the effect of the mechanical parameters of a poroelastic plate system with an air gap on its acoustic impedance and the plane wave absorption coefficient. Figure 14 shows the real and imaginary parts of the averaged, normalized, normal incidence surface acoustic impedance of the plate YB102,

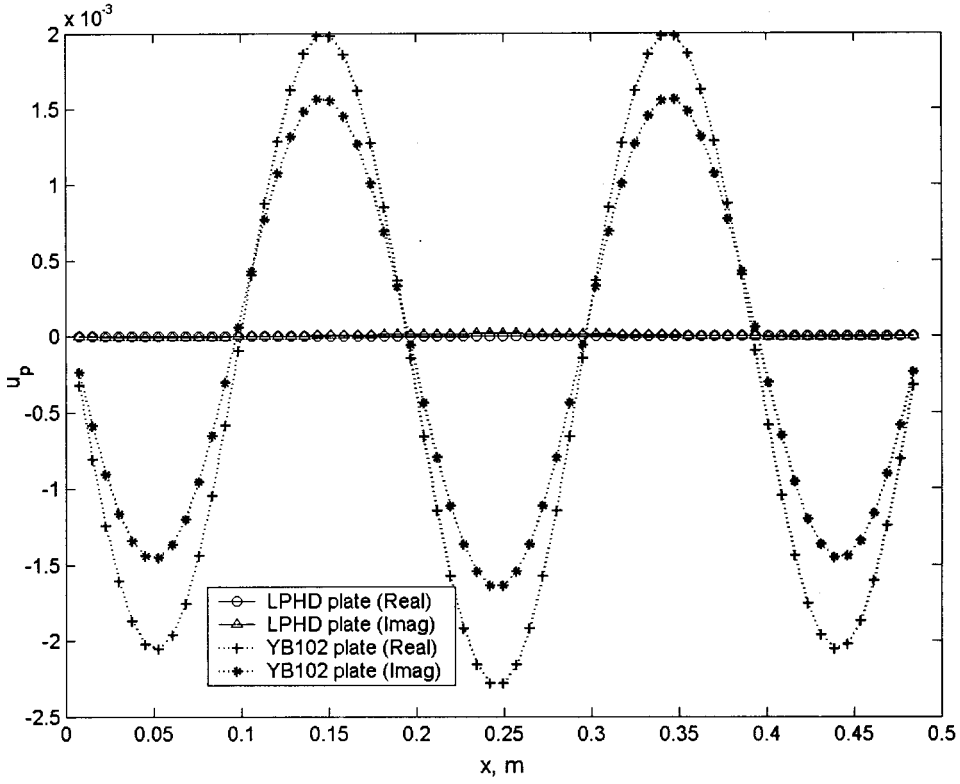

FIG. 13. The distribution of the plate velocity across the surface of the plate, which is predicted for $f = 501.19$ Hz.

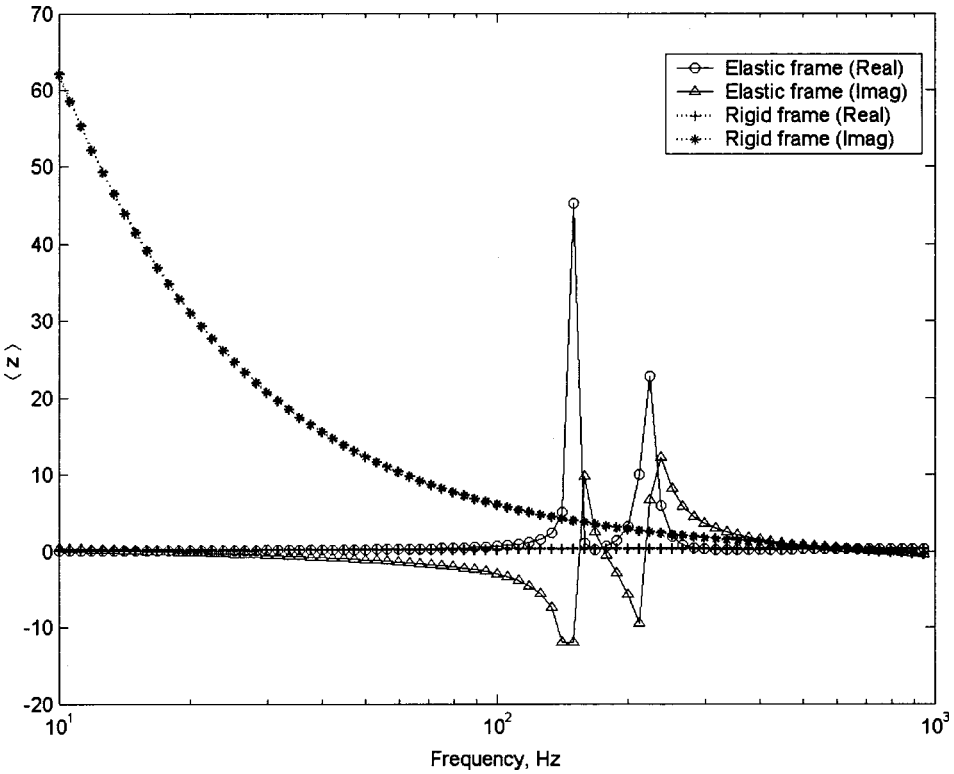

FIG. 14. The averaged, normalized, normal incidence surface acoustic impedance of the YB102 plate with an 80 mm air gap.

which is predicted using the developed model (solid line) and the Pade approximation model[10] for a rigid-frame case (dotted line). The plate is separated by a 0.08 m air gap from an impervious, rigid wall as shown in Fig. 2. The result suggests that in the case of poroelastic plate the imaginary part of the acoustic impedance is considerably reduced in comparison with the rigid-frame case due to the structural vibration, which results in the improved values of the absorption coefficient shown in Fig. 15.

The effect of the material density on the average, normal incidence absorption coefficient is illustrated in Fig. 16. In this figure a comparison is made between the result for the poroelastic plate and the rigid-frame plate (solid line). The maximum absorption in the low frequency range is attained for the lower values of the material density as a result of better coupling between the acoustic impedance of air and the mechanical impedance of the poroelastic plate.

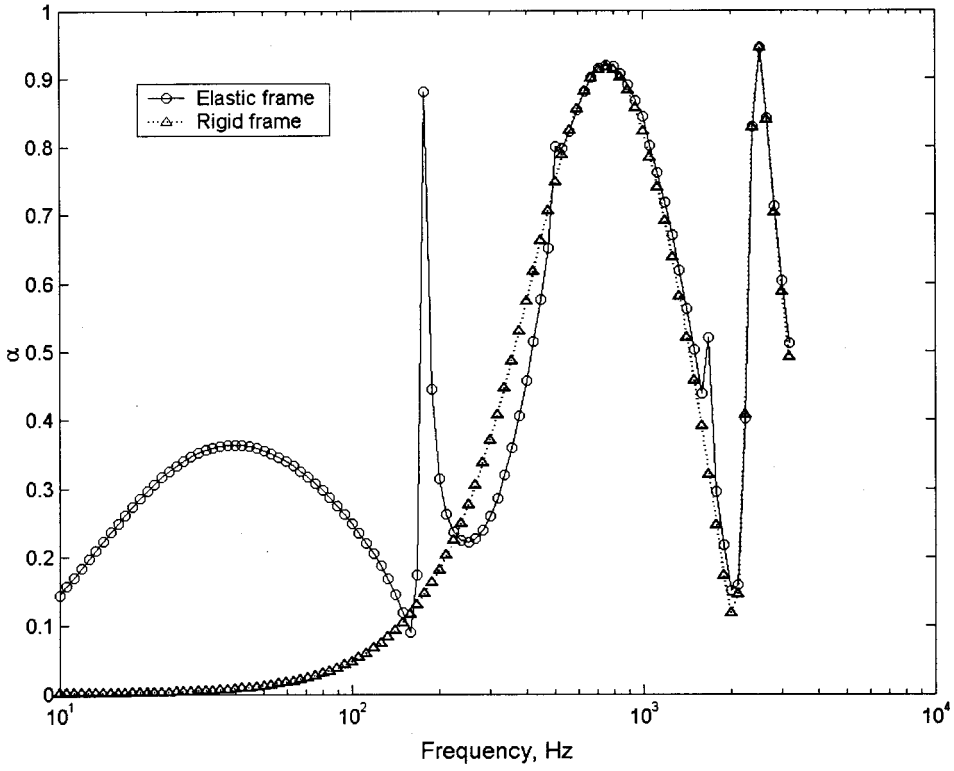

FIG. 15. The averaged, normal incidence absorption coefficient the YB102 plate with an 80 mm air gap.

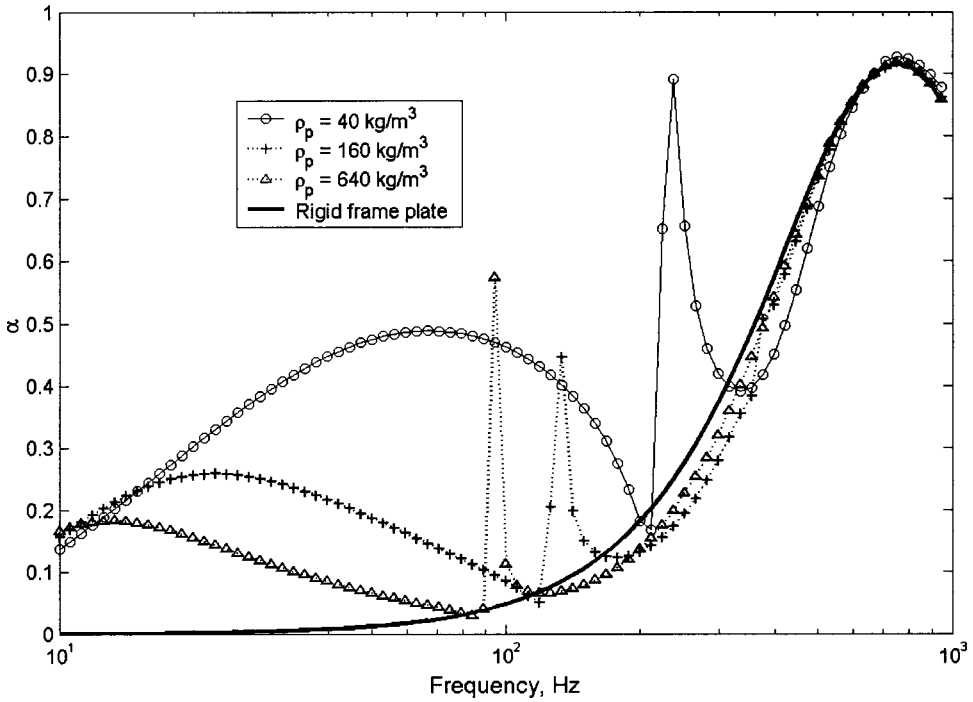

FIG. 16. The average absorption coefficient for a range of values of the density of the material of the plate YB102. Base values of the parameters are provided in Table I.

Figure 17 shows the effect of the Young's modulus on the acoustic absorption coefficient of the poroelastic plate YB102. It is shown that the absorption of the poroelastic plate can be improved by careful selection of the appropriate value of the Young's modulus. In a particular case of the result for $E=10^9$ N/m^2 there is considerable improvement in the absorption coefficient around 60 Hz, although there is a small reduction in the absorption coefficient around 200 Hz.

V. CONCLUSIONS

An analytical model has been developed to predict the structural velocity of and the acoustic pressures on the surface of a thin poroelastic plate. From these expressions the average value of the acoustic impedance and absorption coefficient can be predicted. The formulation allows the acoustic impedance of the backing layer to be also considered. Although the model is for an infinitely long fluid-loaded poroelastic plate of finite width, it can be easily extended to a rectangular plate by adopting the 3-D Green's function and carrying out the integration in the second dimension. The basic results for the considered plate indicate that a carefully chosen combination of microscopic and structural parameters can improve the acoustic absorption in a thin, porous, elastic plate. The major result of the finite density of the material frame and Young's modulus is the reduction of the

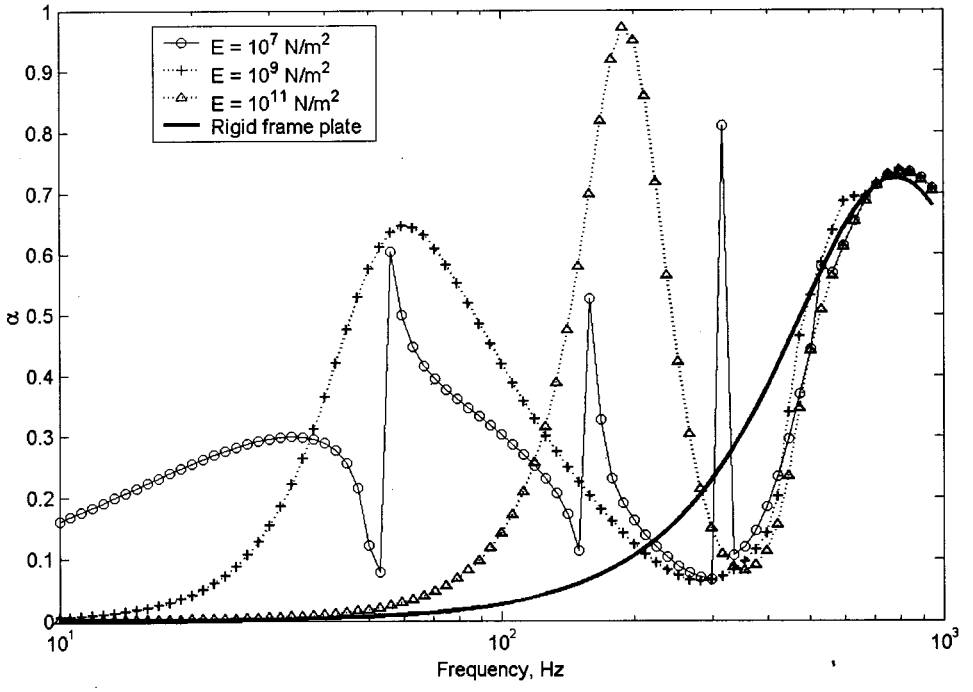

FIG. 17. The average absorption coefficient for a range of values of the Young's modulus of the material of the plate YB102. Base values of the parameters are provided in Table I.

imaginary part of the average acoustic impedance of the poroelastic plate, which is separated by an air gap from an impervious, rigid wall. In this case, the reduced density of the material and the value of the Young's modulus results in greater absorption at the lower frequencies.

ACKNOWLEDGMENTS

The authors are grateful to the Engineering and Physical Sciences Research Council (Grant No. GR/L54905) and the British Council in Tokyo for the support of this work. The authors would also like to thank Professor Shenderov for his very useful suggestions regarding the integral transformation technique and Professor Hothersall for his constructive comments.

APPENDIX: ON THE TRANSFORMATION OF THE DOUBLE INTEGRAL IN THE RADIATION IMPEDANCE COEFFICIENTS B_{mn}

The method of the integral transformation, which is proposed by Shenderov,[12] reduces considerably the computation time and effort to evaluate the radiation impedance coefficients in the matrix **B**. Shenderov omitted the details of the transformation from his book[12] and presented only final result Eq. (32) [there is also a typographical error in expressions (36.16) on page 268 in the original manuscript]. Because the method is very useful and efficient we illustrate in this section the intermediate steps in the integral transformation.

First, we introduce the new dimensionless variables $u=k_o x$ and $u_s=k_o x_s$ so that expression (23) can now be written as

$$B_{mn}=k_o^{-2}\int_0^{\mu}\int_0^{\mu}\sin\left(\frac{\pi m}{\mu}u_s\right)\sin\left(\frac{\pi n}{\mu}u\right)\times H_0^{(1)}(|u-u_s|)du_s\,du, \tag{A1}$$

where $\mu=k_o L$. Second, we split the integration path into two parts, i.e.,

$$B_{mn}=k_o^{-2}\int_0^{\mu}\left\{\int_0^{u}\sin\left(\frac{\pi m}{\mu}u_s\right)\sin\left(\frac{\pi n}{\mu}u\right)\times H_0^{(1)}(u-u_s)du_s+\int_u^{\mu}\sin\left(\frac{\pi m}{\mu}u_s\right)\sin\left(\frac{\pi n}{\mu}u\right)\times H_0^{(1)}(u_s-u)du_s\right\}du, \tag{A2}$$

and introduce two new variables in the inner integrals of Eq. (A2), $v=u-u_s$ for $u_s\in[0,\ u]$ and $v=u_s-u$ for $u_s\in[u,\mu]$ so that

$$B_{mn}=k_o^{-2}\int_0^{\mu}\left\{\int_0^{u}\sin\left(\frac{\pi m}{\mu}(u-v)\right)\sin\left(\frac{\pi n}{\mu}u\right)\times H_0^{(1)}(v)dv+\int_0^{\mu-u}\sin\left(\frac{\pi m}{\mu}(v+u)\right)\sin\left(\frac{\pi n}{\mu}u\right)\times H_0^{(1)}(v)dv\right\}du. \tag{A3}$$

Further substitution will be to replace $\mu-u=u'$ in the second outer integral, so that expression (A3) becomes

$$B_{mn}=k_o^{-2}\left\{\int_0^{\mu}\int_0^{u}\sin\left(\frac{\pi m}{\mu}(u-v)\right)\sin\left(\frac{\pi n}{\mu}u\right)\times H_0^{(1)}(v)dv+\int_0^{\mu}\int_0^{u'}\sin\left(\frac{\pi m}{\mu}(v+\mu-u')\right)\times\sin\left(\frac{\pi n}{\mu}(\mu-u')\right)H_0^{(1)}(v)dv\,du'\right\}, \tag{A4}$$

which reduces after the change of variable $u=u'$ in the second integral to

$$B_{mn}=k_o^{-2}(1+(-1)^{m+n})\int_0^{\mu}\int_0^{u}\sin\left(\frac{\pi m}{\mu}(u-v)\right)\times\sin\left(\frac{\pi n}{\mu}u\right)H_0^{(1)}(v)dv\,du. \tag{A5}$$

Using the Dirichlet formula for the interchange of variables in double integrals

$$\int_0^{a}\left\{\int_0^{v}f(v,u)dv\right\}du=\int_0^{a}\left\{\int_a^{v}f(v,u)du\right\}dv, \tag{A6}$$

we can finally rewrite Eq. (A5) in the following form

$$B_{mn}=\int_0^{\mu}b_{mn}H_0^{(1)}(v)dv, \tag{A7}$$

where

$$b_{mn}=k_o^{-2}(1+(-1)^{m+n})\int_v^{\mu}\sin\left(\frac{\pi m}{\mu}(u-v)\right)\times\sin\left(\frac{\pi n}{\mu}u\right)du. \tag{A8}$$

It is easy to show that integral (A8) can be reduced to the analytical form

$$b_{mn}=\frac{\mu(1+(-1)^{m+n})}{k_o^2\pi(n^2-m^2)}\left\{n\sin\left(\frac{m\pi}{\mu}v\right)-m\sin\left(\frac{n\pi}{\mu}v\right)\right\},\quad m\neq n,$$

and

$$b_{mn}=k_o^{-2}\left\{(\mu-v)\cos\left(\frac{m\pi}{\mu}v\right)+\frac{\mu}{m\pi}\sin\left(\frac{m\pi}{\mu}v\right)\right\},\quad m=n, \tag{A9}$$

which, together with expression (A7), is well-suited for the numerical integration. It can be proved that the integrand in Eq. (A7) is limited as the variable of integration $v\to 0$ (see Ref. 12, pp. 91–92).

[1] D. Takahashi, K. Sakagami, and M. Morimoto, "Acoustic properties of permeable membranes," J. Acoust. Soc. Am. **99**, 3003–3009 (1996).

[2] K. V. Horoshenkov and K. Sakagami, "Acoustic response of a thin poroelastic plate," in *Proc. of the 16th Int. Congress on Acoustics, 1998, Seattle, June 1998*, pp. 1897–1898,

[3] M. J. Swift, "Physical properties of porous recycled materials," Ph.D. thesis, University of Bradford, UK, November 2000.

[4] P. Goransson, "A weighted residual formulation of the acoustic wave propagation through a flexible porous material and comparison with a limp material model," J. Sound Vib. **182**, 479–494 (1995).

[5] Y. J. Kang and J. S. Bolton, ''Finite element modelling of isotropic elastic porous materials coupled with acoustical finite elements,'' J. Acoust. Soc. Am. **98**, 635–643 (1995).
[6] N. Atalla, R. Panneton, and P. Debergue, ''A mixed displacement-pressure formulation for poroelastic materials,'' J. Acoust. Soc. Am. **104**, 1444–1452 (1998).
[7] F. C. Sgard, N. Atalla, and J. Nicolas, ''A numerical model for the low frequency diffuse field sound transmission loss of double-wall sound barriers with elastic porous linings,'' J. Acoust. Soc. Am. **108**, 2865–2872 (2000).
[8] M. A. Biot, ''Theory of elastic wave propagation in a fluid saturated porous solid,'' J. Acoust. Soc. Am. **28**, 168–191 (1956), Parts I and II.
[9] L. M. Brekhovskikh, *Waves in Layered Media* (Academic, New York, 1960).
[10] K. V. Horoshenkov, K. Attenborough, and S. N. Chandler-Wilde, ''Padé approximant for the acoustical properties of rigid frame porous media with pore size distribution,'' J. Acoust. Soc. Am. **104**, 1198–1209 (1998).
[11] M. C. Junger and D. Feit, *Sound, Structures and Their Interaction* (Acoustical Society of America, American Institute of Physics, 1993).
[12] E. L. Shenderov, *Volnovye Zadachi Gidroakustiki (Wave Problems of Sonar)* (Sudostroenie, Leningrad, 1972), pp. 264–277 (in Russian).
[13] *Methods of Numerical Integration* (Academic, New York, 1975), p. 365.

A hybrid BIE/FFP scheme for predicting barrier efficiency outdoors[a)]

Shahram Taherzadeh[b)]
Department of Environmental and Mechanical Engineering, The Open University, Walton Hall, Milton Keynes MK7 6AA, United Kingdom

Kai Ming Li
Department of Mechanical Engineering, The Hong Kong Polytechnic University, Hung Hom, Kowloon, Hong Kong

Keith Attenborough
Department of Engineering, University of Hull, Hull HU6 7RX, United Kingdom

(Received 16 November 1998; revised 5 August 1999; accepted 2 May 2001)

To assess the acoustical performance of noise screens in the presence of an arbitrary sound speed profile, a numerical scheme based on a combination of the boundary integral and fast field program methods is developed. The Green's function required in the boundary integral is evaluated by a fast field formulation. The procedure is validated by comparing its predictions with other numerical results for simple cases and with measurements for indoor model experiments simulating downward refracting conditions. It is predicted that the performance of a noise screen placed 50 m from the source is reduced considerably by moderate downwind conditions. © *2001 Acoustical Society of America.* [DOI: 10.1121/1.1381539]

PACS numbers: 43.50.Gf, 43.50.Vt, 43.28.Fp [MRS]

I. INTRODUCTION

Recent years have produced a wealth of models and methods for predicting sound pressure in an outdoor environment. These include both analytical formulas for sound pressure in certain simple cases and numerical methods and algorithms with varying degrees of complexity and efficiency for more complex environments. The analytical models deal mainly with propagation in a homogeneous atmosphere above a plane impedance boundary or one with a simple sound speed gradient.[1] The numerical methods, which handle more general situations, include the fast field program[2–6] (FFP) for a range-independent environment, the parabolic equation method[7] (PE) for a range-dependent atmosphere above a plane boundary, and ray tracing techniques.[8] The first two techniques have found a wide spread use in both underwater and atmospheric acoustics. These numerical models have been able to explain many of the observed influences of atmospheric refraction and turbulence. However, all these methods deal with a plane boundary. If the ground is uneven at a scale that is large compared with the wavelengths of interest, as, for example, in the presence of a sound barrier or a hill, many current FFP and PE methods fail.

There has been a number of theoretical methods to calculate the sound field in presence of a barrier of simple shape by, for example, Pierce[9,10] and Rasmussen.[11] These earlier analyses were based on geometrical ray acoustics. On the other hand, numerical solution of the boundary integral equation [the boundary element method (BEM)] provides a comprehensive and accurate way of accounting for more complex boundaries such as a mixed impedance plane as well as an uneven terrain. This versatile numerical method has been utilized to solve a variety of problems involving nonuniform boundaries.[12–21] All these works have assumed neutral atmospheric conditions and no account has been made of the effects of sound wave refraction due to temperature and/or wind speed variation and turbulence. Moreover, many of these numerical schemes assume an infinitely long line source emitting cylindrical waves impinging on barriers or strips of infinite length parallel to the source.

Li *et al.*[22] have considered diffraction of sound from a bump or a trough with a Gaussian shape. They incorporated sound refraction in the medium by using an expression, originally due to Pekeris,[23] for the sound field in an unbounded medium with a linear sound speed profile. By considering only a rigid boundary or a pressure-release one, they simplified the problem considerably. They used an extension of the method of moments to evaluate the boundary integral (with a Gaussian bump). They reported that a soft ground with a bump or a hard ground with a trough causes a sound field enhancement beyond the shadow zone boundary. The significance of this apparent symmetry was not discussed in their predicted results. Uscinski[24] considered a similar problem above a rigid surface of random roughness. He used an expression derived from the parabolic equation approximation to the wave equation to account for the refraction in the medium. More recently, Salomons[25] has used a parabolic equation approach to study the effect of an absorbing barrier in a refracting medium. His numerical procedure involves starting a one-way parabolic marching solution and terminating the waves that impinge upon the barrier. Consequently, Salomons' method does not include backscattering. West

[a)]Based on a presentation at ICA/ASA '98, June 1998, Seattle.
[b)]Author to whom correspondence should be addressed. Electronic mail: S.Taherzadeh@open.ac.uk

 0001-4966/2001/110(2)/918/7/$18.00

et al.[26] derived the parabolic wave equation with a boundary profile function included. They then proceeded to solve the resulting equation by a ''wide angle'' PE. The formulation, however, is approximate and valid only for barriers or hills with small slopes. Most of the models discussed here are two-dimensional propagation models (propagation in a plane only) with a few exceptions such as the work of Duhamel.[21] There are few theoretical problems with extending a two-dimensional (2-D) model to a three-dimensional propagation method.[27] But the computational effort is large and would require some approximation. The procedure proposed here is also for two-dimensional propagation model.

Li and Wang[28] have introduced a novel method to simulate the effect of a noise barrier in a refracting atmosphere. In their approach, a conformal mapping technique is used to map the wave equation in a medium where the speed of sound varies exponentially with height above a flat boundary to that for a neutral fluid above a curved surface (a section of a cylinder). Subsequently, they use a BEM program, with a discretization of the resulting curved boundary as well as the barrier, to predict the insertion loss of the barrier. They have validated their method by comparing their predictions with measurements of the insertion loss of a thin barrier in a wind tunnel in downwind and upwind conditions.[29] Their method is restricted to relatively short ranges. Moreover, the requirement for discretizing the whole boundary puts a severe burden on the computation time.

The approach taken in this paper is to account for the refraction of the atmosphere as well as the reflection from the flat impedance boundary in the formulation of the Green's function. This approach is similar to that used by Gerstoft and Schmidt[30] for the evaluation of acoustic and seismic reverberation in an ocean environment.

In the next section, the starting boundary integral equation for our BEM is stated. In the subsequent sections we deal with the discretization of the boundary and the numerical solution of the Green's function. In the final section, some numerical examples are presented and discussed.

II. THEORY

A. The boundary integral equation

Assume that a line source produces a time-harmonic sound field in a medium, **D**, bounded by a locally reacting impedance surface, **S**. The surface **S** can have features such as barriers, hills, impedance discontinuities, etc. By means of the Green's theorem, the sound field can be written in an integral form as

$$\varepsilon\phi(\mathbf{r}) = G(\mathbf{r},\mathbf{r}_0) - \int_S \left\{ G(\mathbf{r},\mathbf{r}_s)\frac{\partial\phi(\mathbf{r}_s)}{\partial\mathbf{n}(\mathbf{r}_s)} - \phi(\mathbf{r}_s)\frac{\partial G(\mathbf{r},\mathbf{r}_s)}{\partial\mathbf{n}(\mathbf{r}_s)} \right\} ds, \tag{1}$$

where $G(\mathbf{r},\mathbf{r}_0)$, is the solution of the wave equation in the domain in the absence of scatterers, $\mathbf{r}_s$ is the position vector of the boundary element ds, and $\mathbf{n}$ is the unit normal vector out of ds. A time convention of $\exp(-i\omega t)$ is assumed. The parameter ε is dependent on the position of the receiver.[31] It is equal to 1 for $\mathbf{r}$ in the medium, $\frac{1}{2}$ for $\mathbf{r}$ on the flat boundary, and equal to the $\Omega/2\pi$ at edges, where Ω is the solid angle. The surface **S** contains the flat, locally reacting ground surface and additional features such as a barrier. The contribution to the total field from reflection by the flat ground surface can be taken into account in the Green's function, $G(\mathbf{r},\mathbf{r}_s)$. The surface **S** can be redefined to include the scatterer objects only, excluding the ground surface. The integral is then the contribution of the scattering elements to the total sound field at a receiver position. This integral formulation (first derived by Kirchhoff in 1882) is called the Helmhotz–Kirchhoff wave equation. It is the mathematical formulation of the Huygen's principle. If one allows the receiver points to approach the boundary, one obtains an integral equation for the field potential at the boundary. This boundary integral equation is a Fredholm integral equation of the second kind. Once solved, the contribution of the scatterers can be determined by evaluating the integral in Eq. (1) and calculating the total field for any point in the entire domain, **D**. This is the main boundary integral equation (BIE) for the acoustic field potential in the presence of a nonuniform boundary. The boundary element method (BEM) represents the acoustic propagation in a medium by the boundary integral equation and solves the set of integral equations numerically.

The imposition of a suitable boundary condition is required also. In most cases of interest one can assume a locally reacting impedance boundary condition:

$$\frac{d\varphi}{dn} - ik_0\beta\varphi = 0, \tag{2}$$

where β, the admittance, can be a function of the position on the boundary. This can be applied to the surface of the plane boundary and to the surfaces of the scatterers. Thus the derivative term of the unknown potential can be written in terms of the potential itself. Hence

$$\varepsilon\phi(r,z) = G(\mathbf{r},\mathbf{r}_0) - \int_S \phi(r_s,z_s)\left\{ ik_0\beta G(\mathbf{r},\mathbf{r}_s) - \frac{\partial G(\mathbf{r},\mathbf{r}_s)}{\partial\mathbf{n}(\mathbf{r}_s)} \right\} ds, \quad \mathbf{r},\mathbf{r}_s \in \mathbf{S}. \tag{3}$$

When discretizing the boundary surface it is assumed that the unknown potential is constant in each element, thereby reducing the integral equation to a set of linear equations.

B. Method of solving the BIE

The procedure for solving the integral equation (3) adopted here is the one suggested by Mayers[32] and used by Chandler-Wilde[15–17,19] These methods involve using a quadrature technique (Simpsons or Gauss) to discretize the integral and transform it to a set of linear equations. In one dimension it can be described as follows. The integration range is divided into M subdomains or elements, each of length or size h. The unknown potential, ϕ, is assumed to be constant within each element. Then the integral in Eq. (3) becomes

$$\int_S \phi(r_s,z_s)\left\{ ik_0\beta G(\mathbf{r},\mathbf{r}_0) - \frac{\partial G(\mathbf{r},\mathbf{r}_s)}{\partial \mathbf{n}(\mathbf{r}_s)}\right\} ds$$

$$= \sum_{m=1}^{M} \phi(r_m,z_m) \int_{t_m-h/2}^{t_m+h/2} \left\{ ik_0\beta G(\mathbf{r},\mathbf{r}_s) - \frac{\partial G(\mathbf{r},\mathbf{r}_s)}{\partial \mathbf{n}(\mathbf{r}_s)}\right\} ds. \tag{4}$$

In principle, the integral on the right-hand side can be evaluated numerically. Then the BIE [Eq. (4)] becomes

$$\varepsilon\phi(\mathbf{r}) = G(\mathbf{r},\mathbf{r}_0) - \sum_{m=1}^{M} \phi(\mathbf{r}_m)\Lambda(\mathbf{r},\mathbf{r}_m), \tag{5}$$

where $\Lambda(\,)$ denotes the integral on the right-hand side of Eq. (4). Substitution of $\mathbf{r}=\mathbf{r}_n$, $n=1,...,M$, produces a set of M linear equations:

$$\varepsilon\phi(\mathbf{r}_n) + \sum_{m=1}^{M} \phi(\mathbf{r}_m)\Lambda(\mathbf{r}_n,\mathbf{r}_m) = G(\mathbf{r}_n,\mathbf{r}_0), \quad n=1,...,M. \tag{6}$$

The Green's function $G(\mathbf{r},\mathbf{r}_s)$ will be singular at $\mathbf{r}=\mathbf{r}_s$, i.e., at diagonal elements when $n=m$. One can use the principal value of the integral for the integrals involving the singularities (see Ref. 31). Here we state only that the solution of the equation (3) is unique except near characteristic frequencies of the space enclosed by the barrier. The main methods suggested in the literature for overcoming this nonuniqueness problem are the so-called CHIEF method[33–35] and the method of Burton and Miller.[36,37]

III. THE GREEN'S FUNCTION

In Eq. (3), it remains to evaluate the Green's function and its derivative. The Green's function, $G(\mathbf{r},\mathbf{r}_0)$, represents the sound field in the medium in the absence of the scattering surfaces. In order to minimize the number of elements, the Green's function includes reflection from the flat impedance surface. The procedures for evaluation of this Green's function in different conditions are the concern of the rest of this section.

A. Neutral medium

As discussed in the Introduction, we consider a two-dimensional problem with an infinitely long line source radiating cylindrical waves in the medium. In this case the boundary integral is a line integral and their numerical evaluation is a relatively simple matter. The corresponding Green's function takes the form[19]

$$G_2(\mathbf{r},\mathbf{r}_0) = -(i/4)\{H_0^{(1)}(k|\mathbf{r}_0-\mathbf{r}|) + H_0^{(1)}(k|\mathbf{r}_0'-\mathbf{r}|)\} + P_\beta(\mathbf{r},\mathbf{r}_0), \tag{7}$$

with

$$P_\beta(\mathbf{r},\mathbf{r}_0) = \frac{i\beta}{2\pi}\int_{-\infty}^{+\infty} \frac{e^{ik[(z+z_0)\sqrt{1-s^2}-(x-x_0)s]}}{\sqrt{1-s^2}(\sqrt{1-s^2}-\beta)} ds, \quad \mathrm{Re}(\beta)>0. \tag{8}$$

In the above expression $H_0^{(1)}(\,)$ is the Hankel function of the first kind, $\mathbf{r}$, $\mathbf{r}_0$, and $\mathbf{r}_0'$ are the receiver, source, and image source positions, respectively. The wavenumber, k, and the complex admittance, β, are dependent on the frequency. The function P_β represents the ground wave term. The derivatives of the Green's function in the x and z directions are also given in Ref. 19. When the source and the receiver positions coincide, i.e., when $n=m$, the integral $\Lambda(\,)$ has a removable singularity. The integral can be evaluated analytically by replacing the Hankel functions by their small argument approximations and performing the integration.

Habault[18] uses the alternatives of single and double layer potential expressions to represent the Green's function and its derivative. These are again in terms of Hankel functions.

B. Evaluation of the Green's function by the FFP method

Since discretization of the boundaries is extremely time consuming, the Green's function must include as many calculations as possible in order to minimize the area of the boundary to be discretized. The Green's function includes the wave field propagating in the domain of the system. As such, it must contain the wave terms reflected from the ground if one is to avoid discretizing the whole ground surface. This device means that it is necessary only to discretize the "scatterer" elements above the ground surface, thus saving on the number of elements and equations to be solved. The method allows for the incorporation of an absorbing ground as well as a rigid one.

The Green's function for a line source radiating cylindrical waves above a locally reacting impedance plane can be written as[38]

$$G(\mathbf{r}_1,\mathbf{r}_2) = \frac{1}{\sqrt{2\pi}}\int_0^\infty \varphi(z_1,z_2,k_r)\exp(ik_rR)dk_r, \tag{9}$$

where $\mathbf{r}_2[=(x_2,z_2)]$ and $\mathbf{r}_1[=(x_1,z_1)]$ are the source and receiver position vectors, respectively, and $R[=x_2-x_1]$ is the horizontal separation between them.

In practice, the infinite integral is truncated at a suitable value, say $k_{\max}$, and the integral is replaced by a finite FFT sum. The variable of integration, k_r, can be thought of as the horizontal component of the wavenumber. To avoid the possible poles on or near the real k axis, the path of integration is deformed below the real axis,

$$\int_0^\infty = \int_0^{-i\alpha\,\delta k} + \int_{-i\alpha\,\delta k}^{k_{\max}-i\alpha\,\delta k}. \tag{10}$$

This is equivalent to making k_r a complex quantity with the imaginary part relating to an adjustable parameter (α). The wavenumber interval, δk, is given by $(k_{\max}/N_k)$ with N_k being the number of integration points.

The kernel function φ in Eq. (9) is now independent of range and is in one dimension only. This function is the solution of the one-dimensional Helmholtz equation in the presence of a plane impedance boundary. For a homogeneous fluid this solution is known and is given in terms of direct and reflected plane waves:

$$\varphi = \frac{1}{k_z}\left\{ e^{ik_z|z_1-z_2|} + \frac{k_z-k_0\beta}{k_z+k_0\beta} e^{ik_z(z_1+z_2)} \right\}, \tag{11}$$

with β being the specific normalized acoustic admittance of the ground; k_0 the wave number $(=\omega/c)$; and $k_z = \sqrt{k_0^2-k_r^2}$.

In an inhomogeneous medium such as a refracting atmosphere or in upwind or downwind conditions with an arbitrary sound speed profile, the potential function cannot be determined analytically. Instead, a scheme similar to the finite element method can be utilized[39,40] whereby the fluid is divided into uniform horizontal layers with the speed of sound and air density assumed to be constant within each layer. The potential in each layer is given by

$$\varphi_i = A_i^{\uparrow} e^{k_{z,i}(z-H_i)} + A_i^{\downarrow} e^{k_{z,i}(H_{i+1}-z)}, \tag{12}$$

with A_i's being the unknown amplitudes and H_i being the layer altitude. The boundary conditions at the layer boundaries determine the wave potential amplitudes in each layer. These conditions are the continuity of normal particle velocity and the pressure across the boundary. The resulting set of linear equations in unknown amplitudes is set in a global matrix form, $\mathbf{A}\times\mathbf{X}=\mathbf{B}$. Here $\mathbf{X}$ represents the unknown amplitude vector; $\mathbf{A}$, the matrix resulting from the known exponential terms, and $\mathbf{B}$ is the source term.[39,40] This matrix equation is solved to produce the wave amplitudes in all layers. The value of the kernel function at one or more desired positions can then be derived easily. An alternative method is to use a transmission line method to evaluate the transfer function between the source and the receiver layers. This method, however, is less efficient than the global matrix method used in our approach for multiple receiver elevations. The derivative of the Green's function required in the integral Λ can also be calculated easily. It has been used to calculate the sound field of an arbitrarily oriented dipole above an interface previously.[41,42] The derivatives of the kernel function in a homogeneous fluid above an absorbing boundary are given by

$$\varphi_x = -i\frac{k_r}{k_z}\left\{ e^{ik_z|z_1-z_2|} + \frac{k_z-k_0\beta}{k_z+k_0\beta} e^{ik_z(z_1+z_2)} \right\}, \tag{13}$$

$$\varphi_z = -i\left\{ \mathrm{sign}(z_2-z_1) e^{ik_z|z_1-z_2|} + \frac{k_z-k_0\beta}{k_z+k_0\beta} e^{ik_z(z_1+z_2)} \right\}. \tag{14}$$

The Green's function in each case is obtained easily by substituting the appropriate kernel function in Eq. (9). The k_r term in the numerator of Eq. (13) comes from differentiation of the exponential function in the Hankel transform [Eq. (9)]. In a layered medium, the boundary conditions are the same as for a monopole source. However, there is a slight difference in the source terms. At the fluid–solid interface where the boundary conditions apply, the source terms for the two derivatives are $e^{ik_z|z_1-z_2|}(k_z-k_0\beta)$ for the z derivative and $k_r e^{ik_z|z_1-z_2|}(1-k_0\beta/k_z)$ for the x derivative. The corresponding term for a monopole is $e^{ik_z|z_1-z_2|}(1-k_0\beta/k_z)$.

A simplifying feature of these calculations is that the Green's function and its two derivatives can be calculated simultaneously because the coefficient matrix is the same for all three and only the forcing term is different.

Once the kernel function is evaluated for all k_r, the integral in Eq. (9) can either be evaluated by a quadrature scheme or, since it is a Fourier integral, by the discrete Fourier transform method (DFT). This is the essence of the fast field program for calculating the sound pressure field in an arbitrary, range-independent sound speed profile. In the DFT scheme the integral in Eq. (9) is approximated by two discrete sums:[43]

$$G_m(\mathbf{r}) = \frac{i}{4}\frac{\delta k\, N_k^{1/2}}{\pi^{1/2}}\left[e^{2\pi m\alpha/N_k} \sum_{n=1}^{N_k-1} \varphi(z,k_n) e^{-2i\pi mn/N_k} + e^{-2\pi m\alpha/N_k} \sum_{n=1}^{N_k-1} \varphi(z,k_n) e^{2i\pi mn/N_k} \right], \tag{15}$$

where $G_m(\,)$ refers to the Green's function at the receiver point $\mathbf{r}_m$. One advantage of the FFT method is that the function values at an array of positions with a horizontal grid points $m\,\delta r = 2m\pi/k_{\max}$ $(m=1\cdots N_k)$ are evaluated at once, thus making possible savings on the number of FFP calculations. The horizontal wave number is given by

$$k_n = (n - i\alpha)\,\delta k. \tag{16}$$

Both summations can be performed by a single call to a DFT program. To evaluate the integral correctly, certain modifications are required to the kernel function to account for the truncation of the infinite integral at a finite value and for changing the path of integral away from the real axis to avoid the poles. Without these corrections superficial oscillations, called Gibbs oscillations, are superimposed on the kernel function and have detrimental effects on the accuracy of the final computation of the boundary element matrix. This is overcome in our method by applying a Hanning window to the kernel function.[44] With this windowing, accurate and oscillation-free values of the Fourier transform are obtained and lead to an accurate solution of the BIE.

It should be noted, however, that the Fourier transform is accurate only at distances greater than about two wavelengths. At distances shorter than two wavelengths, the Green's function for the homogeneous case is an accurate approximation since sound speed variations have little effect. This approximation has been implemented in our approach.

IV. NUMERICAL CONSIDERATIONS

A high level of accuracy is required in evaluating the Green's functions in the boundary integral equation. The FFP values for the pressure are accurate only at the spatial grid points. An interpolation scheme for range points lying between the grid points, while providing accurate values for the magnitude of the pressure, fails to give adequate accuracy for the phase values because of insufficient spatial sampling. In this respect, the midpoint of barrier elements must fall on the grid points of the FFP scheme. Hence, there are constraints on the integration parameters such as truncation value $(k_{\max})$ and the number of integration points (N_k). An alternative would be to use the Chirp-Z FFP formulation proposed by Li *et al.*[45] to decouple the wave number and space domain grid

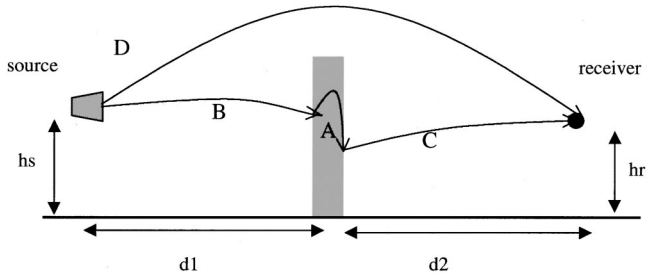

FIG. 1. Schematic diagram to show a typical outdoor environment consisting of a source, receiver, and noise barrier.

values in FFP and have arbitrary grid points in the space domain. However, this approach has not been adopted here.

The three stages to the calculations involving the Green's function and its derivatives are shown in Fig. 1. These stages include the following.

(a) Evaluating the radiation from each element to every other one [i.e., evaluating the matrix elements in Eq. (6)].

(b) Calculating the radiation from the source to each element on the barrier [the right-hand sides of Eq. (6)].

(c) Obtaining the contribution of each barrier element to the sound received at the observation point (i.e., evaluating the boundary integral after the matrix equation has been solved).

In addition, it is necessary to calculate the sound field from the source to the receiver in the absence of the barrier.

While, in principle, a single FFP step is sufficient to evaluate sound pressure at all points in the x-z plane, memory considerations make this impractical in most computer systems. Nevertheless, a considerable saving of time can be made at each of the three stages.

Apart from the case where a large area of the boundary has to be discretized (as in an uneven ground surface), the physical size of the scatterer is small compared with the radius of curvature. Furthermore, if the horizontal separation between the elements is small, the sound speed profile plays a very little role. In this case its homogeneous form [Eq. (7)] approximates the Green's function adequately.

The use of FFP in evaluating the Green's function allows one to make efficient computations in certain typical cases. In particular, if the scatterer is a barrier wall with vertical sides, the right-hand sides for each vertical section [case (b) above] can be evaluated with a single FFP step.

The same is true for the third stage (i.e., contributions from each element to a single observer point) by using the reciprocity property of the Green's function and its horizontal (or x) derivative.

V. RESULTS AND DISCUSSION

The numerical program proposed in this paper (BIE-FFP) has been validated by comparing its results to simplified cases where other predictions are available and to attenuation data obtained in laboratory conditions. BIE-FFP predictions for the relatively trivial (albeit computationally intensive, since the entire surface must be discretized) case of a sound field in a refracting medium above a flat absorbing surface, may be compared to theoretical values based on

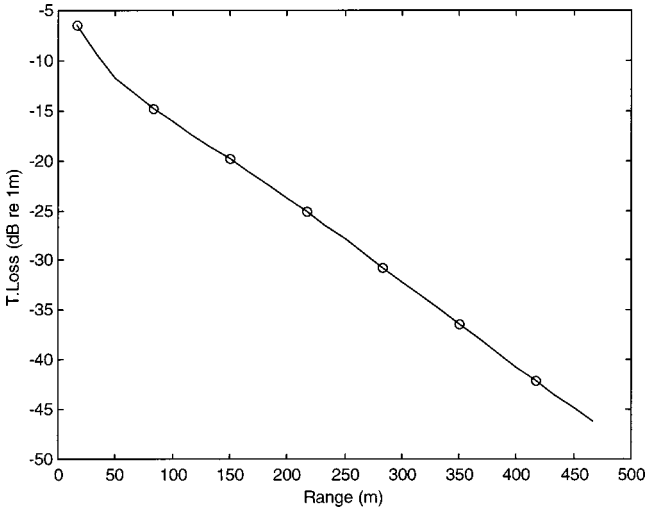

FIG. 2. Sound pressure level in an upwardly refracting medium above an impedance plane as predicted by a FFP code (solid line) and calculated by BIE-FFP and discretizing the boundary to test the code. The source and receiver heights are 10.0 and 1.2 m, respectively. The frequency is 10 Hz and the sound speed gradient is $-1.0\ \mathrm{m}^{-1}$.

the standard fast field program. The results are shown in Figs. 2 and 3 for upwind and downwind conditions, respectively. In both figures the solid line represents the results of standard FFP calculations of the transmission loss (db *re* field at 1 m) and the circles represent predictions of the BIE-FFP. It is clear that the scheme outlined in this paper is consistent with the standard FFP method for simple cases.

Data for the insertion loss of barriers in an arbitrary sound speed profile are rare. Rasmussen[29] has made scale model measurements of the excess attenuation spectra behind a thin barrier in a wind tunnel. The data is taken from Fig. 11 of Ref. 29 and the parameters are (see Ref. 29, Fig. 1): hs=2.0 m, hr=1.0 m, d1=20.0 m, d2=40.0, with the barrier height of 2.5 m. The input wind speed profile is the average of profiles 1 and 2 measured in front and beyond the barrier. Profile No. 3 gave slightly worse predictions. Figure 4 shows the predicted and measured values. There is reasonable agreement between these data (solid line) and the BIE-

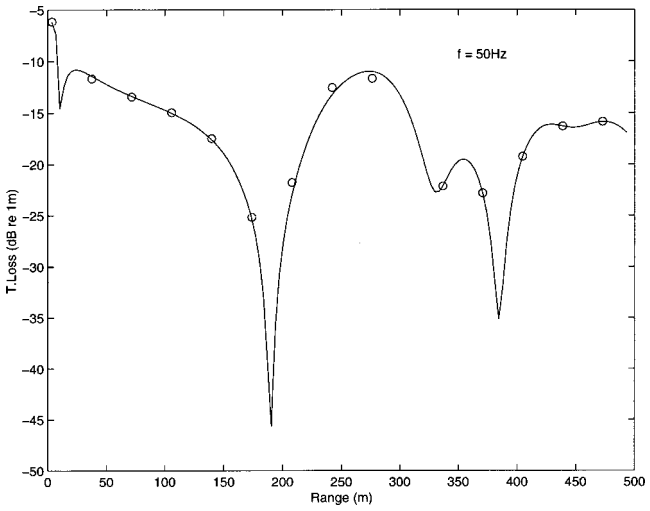

FIG. 3. The same as in Fig. 2, except that the frequency is 50 Hz and the medium is downward refracting. The sound speed gradient is $+1.0\ \mathrm{m}^{-1}$.

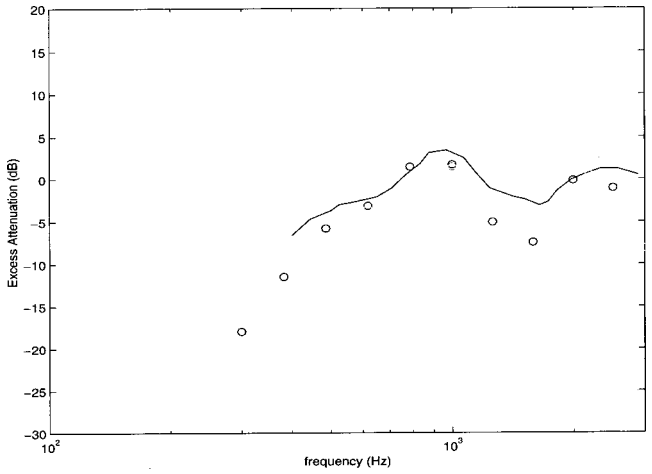

FIG. 4. Measured (solid line: see Fig. 11 of Ref. 24) and predicted (circles) excess attenuation of sound at a receiver behind a barrier 2.5 m high in downwind conditions. The measurement was made in 1:8 scale at a wind tunnel facility. Parameters are hs=2.0 m, hr=1.0 m, d1=20 m, and d2=40 m. A positve sound speed gradient of 0.5 m^{-1} was used.

FFP predictions (circles). These data have been used also by Li and Wang[28] to validate their scheme based on a conformal mapping of a refracting atmosphere to a curved boundary. The BIE-FFP predictions give improved agreement with the measured data.

Another set of measurements have been carried out by Gabillet *et al.*[46] over a hard concave surface with a thin barrier 15 cm high installed on it. The curvature of the surface is analogous to a positive sound speed gradient of 17.0 m^{-1}. The source height was 0.1 m, a distance of 4 m away from the barrier. The receiver was 3 m beyond the barrier also at a height of 0.1 m. Figure 5 shows the data [the solid line taken from Fig. 15(c) of Ref. 37] and our prediction (circles) using BIE-FFP. To achieve a stable result, an element size of 1 mm was used in the BIE, and 400 layers were utilized in the FFP

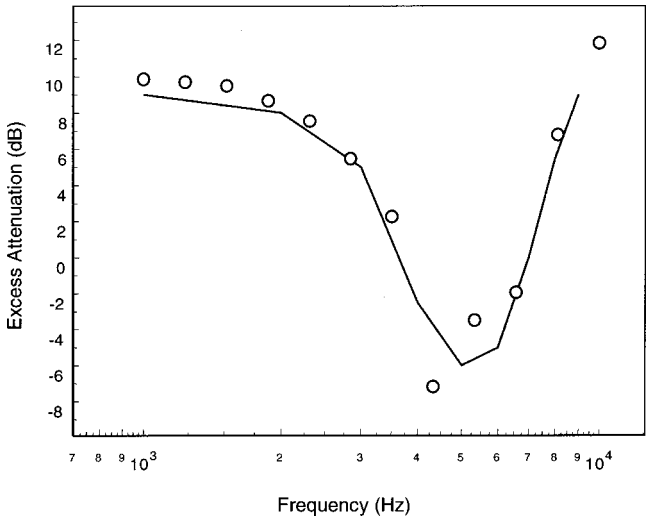

FIG. 5. Measured [solid line: see Fig. 15(c) of Ref. 37] and predicted (circles) excess attenuation of sound behind a thin barrier 0.15 m high on a hard concave surface. Parameters relating to Fig. 1 are hs=0.1 m, hr=0.1 m, d1=4 m, and d2=3 m. The curved surface mapped into a plane boundary resulted in a sound speed gradient of 17 m^{-1}.

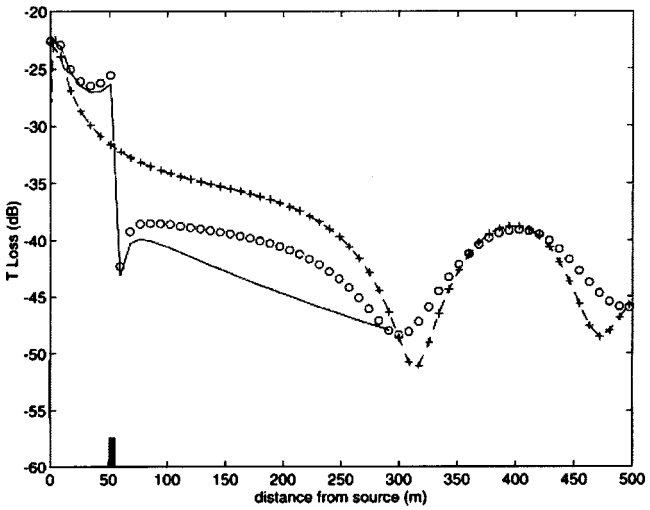

FIG. 6. Effectiveness of a noise barrier under downwind conditions. Crosses: sound level at 500 Hz downwind of the source in the absence of the barrier; Circles: sound level donwwind of the source with a barrier present at a distance of 50 m from the source. Solid line: barrier in the neutral atmosphere. The parameters are hs=0.5 m, hr=1.2 m, h_{barrier}=1.5 m, and a sound speed gradient of +1.0 m^{-1} is assumed. It is seen that after a distance of about 300 m the barrier is no longer effective.

calculations. Again, the BIE-FFP calculations show good agreement with scale model measurements.

We have used the BIE-FFP program to investigate the performance of noise barriers in downwind conditions. We have considered a situation in which an acoustically rigid barrier of height 1.55 m is positioned 50 m downwind of a noise source above an absorbing ground. The transmission loss has been calculated by the BIE-FFP at a frequency of 500 Hz and at observer positions up to a range of 500 m. The predictions of transmission loss with and without the barrier are given in Fig. 6. It is evident that at distances longer than 300 m the barrier is predicted to cause no effective reduction in sound levels. This is consistent with the view that the sound rays effectively curve over the barrier for long distances so that the barrier becomes ineffective.

VI. CONCLUSION

The model proposed in this paper represents considerable improvement on past applications of the boundary element method to sound propagation above a nonuniform boundary, including the condition of refracting atmosphere, since these have assumed a rigid boundary. We have described a numerical procedure for predicting the sound field in a refracting atmosphere above finite impedance surfaces that include noise barriers and other scatterers. The Green's functions required by the BIE are calculated by the FFP method.

The BIE-FFP has been validated by comparison with widely accepted results for simplified cases and with laboratory measurements reported by other workers.

ACKNOWLEDGMENT

This work was supported by the EPSRC (UK) Grant No. GR/L15326.

[1] K. M. Li, ''On the validity of the heuristic ray-trace-based modification to the Weyl Van der Pol formula,'' J. Acoust. Soc. Am. **93**, 1727–1735 (1993).
[2] F. R. DiNapoli, ''A fast field program for multilayered media,'' Naval Underwater Systems Center, Tech. Rep. 4103, 1971.
[3] R. Raspet, S. W. Lee, E. Kuester, D. C. Chang, W. F. Richards, R. Gilbert, and N. Bong, ''Fast field program for a layered medium bounded by complex impedance surfaces,'' J. Acoust. Soc. Am. **77**, 345–352 (1985).
[4] S. W. Lee, N. Bong, W. F. Richards, and R. Raspet, ''Impedance formulation of the fast field program for acoustic wave propagation in the atmosphere,'' J. Acoust. Soc. Am. **79**, 628–634 (1986).
[5] S. J. Franke and G. W. Swenson, Jr., ''A brief tutorial on the fast field program applied to sound propagation in the air,'' Appl. Acoust. **27**, 203–216 (1989).
[6] S. Tooms, S. Taherzadeh, and K. Attenborough, ''Sound propagation in a refracting fluid above a fluid-saturated porous elastic material,'' J. Acoust. Soc. Am. **93**, 173–181 (1993).
[7] M. J. White and K. E. Gilbert, ''Application of the parabolic equation to the outdoor propagation of sound,'' Appl. Acoust. **27**, 227–238 (1989).
[8] K. M. Li, S. Taherzadeh, and K. Attenborough, ''An improved ray-tracing algorithm for predicting sound propagation outdoors,'' J. Acoust. Soc. Am. **104**, 2077–2083 (1998).
[9] A. D. Pierce, ''Diffraction of sound around corners and over wide barriers,'' J. Acoust. Soc. Am. **55**, 941–955 (1974).
[10] A. D. Pierce, *Acoustics, An Introduction to its Physical Principles and Applications* (McGraw-Hill, New York, 1980).
[11] K. B. Rasmussen, ''On the effect of terrain profile on sound propagation outdoors,'' J. Sound Vib. **98**, 35–44 (1985).
[12] M. E. Friedman and R. P. Shaw, ''Diffraction of a plane shock wave by an arbitrary rigid cylindrical obstacle,'' J. Appl. Mech. **29**, 40–49 (1962).
[13] R. P. Shaw and M. E. Friedman, ''Diffraction of a plane shock wave by a free cylindrical obstacle at a free surface,'' 4th US National Congress of Applied Mechanics, 1962, pp. 371–379.
[14] R. Seznec, ''Diffraction of sound around barriers: use of the boundary elements technique,'' J. Sound Vib. **73**, 195–209 (1980).
[15] S. N. Chandler-Wilde and D. C. Hothersall, ''Sound above an inhomogeneous impedance plane,'' J. Sound Vib. **98**, 475–491 (1985).
[16] S. N. Chandler-Wilde and D. C. Hothersall, ''Propagation of road traffic noise over ground of mixed type,'' in *Preceedings of the Institute of Acoustics, 1985*, Vol. 7, pp. 367–374.
[17] S. N. Chandler-Wilde, ''Ground effects in environmental sound propagation,'' Ph.D. thesis, University of Bradford, 1988.
[18] D. Habault, ''Sound propagation above an inhomogeneous plane,'' J. Sound Vib. **100**, 55–67 (1985).
[19] D. C. Hothersall, S. N. Chandler-Wilde, and M. N. Hajmirzae, ''Efficiency of single noise barriers,'' J. Sound Vib. **146**, 303–322 (1991).
[20] K. Attenborough, P. Boulange, S. Taherzadeh, and K. M. Li, ''Rough hard surface ground effects,'' Inter-Noise97, Hungary, 1977.
[21] E. Duhamel, ''Efficient calculation of the three-dimensional sound pressure field around a noise barrier,'' J. Sound Vib. **197**, 547–571 (1996).
[22] Y. L. Li, S. J. Franke, and C. H. Liu, ''Wave scattering from a ground with a Gaussian bump or trough in an inhomogeneous medium,'' J. Acoust. Soc. Am. **94**, 1067–1675 (1993).
[23] C. L. Pekeris, ''Theory of propagation of sound in a half-space of variable sound velocity under conditions of formation of a shadow zone,'' J. Acoust. Soc. Am. **18**, 295–315 (1946).
[24] B. J. Uscinksi, ''Sound propagation with a linear sound-speed profile over a rough surface,'' J. Acoust. Soc. Am. **94**, 491–498 (1993).
[25] E. M. Salomons, ''Diffraction by a screen in a downwind sound propagation: A parabolic-equation approach,'' J. Acoust. Soc. Am. **95**, 3109–3117 (1994).
[26] M. West and R. A. Sack, ''A new generalized terrain parabolic equation (GT-PE),'' in *Proceedings of the 6th International Symposium on Long-Range Sound Propagation*, held in Ottawa, Canada, 1994, pp. 385–391.
[27] L. A. de Lacerda, L. A. Wrobel, H. Power, and W. J. Mansur, ''A novel boundary integral formulation for three-dimensional analysis of thin barriers over an impedance plane,'' J. Acoust. Soc. Am. **104**, 671–678 (1998).
[28] K. M. Li and Q. Wang, ''A BEM approach to assess the acoustic performance of noise barriers in the refracting atmosphere,'' J. Sound Vib. **211**, 663–681 (1998).
[29] K. B. Rasmussen, ''Sound propagation over screened ground under upwind conditions,'' J. Acoust. Soc. Am. **100**, 3581–3586 (1996).
[30] P. Gerstoft and H. Schmidt, ''A boundary element approach to ocean seismoacoustic facet reverberation,'' J. Acoust. Soc. Am. **89**, 1629–1642 (1991).
[31] R. P. Shaw, ''Boundary integral equation methods applied to wave problems,'' in *Developments in Boundary Element Methods—1*, edited by P. K. Banerjee and R. Field (Applied Science Publishers, London, 1980).
[32] D. F. Mayers, ''Quadrature methods for Fredholm equations of the second kind,'' in *Numerical Solution of Integral Equations*, edited by L. M. Delves and L. Walsh (Clarendon, Oxford, 1974).
[33] H. A. Schenck, ''Improved integral formulation for acoustic radiation problems,'' J. Acoust. Soc. Am. **44**, 41–58 (1968).
[34] A. F. Seybert and T. F. Rengarajan, ''The use of CHIEF to obtain unique solution for acoustic radiation using boundary integral equations,'' J. Acoust. Soc. Am. **81**, 1299–1306 (1987).
[35] T. W. Wu and A. F. Seybert, ''A weighted residual formulation for the CHIEF methods in acoustics,'' J. Acoust. Soc. Am. **90**, 1608–1914 (1996).
[36] W. S. Hwang, ''A boundary integral method for acoustic radiation and scattering,'' J. Acoust. Soc. Am. **101**, 3330–3335 (1997).
[37] A. J. Burton and G. F. Miller, ''The application of integral equation methods to the solution of some exterior boundary-value problems,'' Proc. R. Soc. London, Ser. A **323**, 201–210 (1971).
[38] P. M. Morse and K. U. Ingard, *Theoretical Acoustics* (McGraw-Hill, New York, 1968), Chap. 7.
[39] K. Attenborough, S. Taherzadeh *et al.*, ''Benchmark cases for outdoor sound propagation models,'' J. Acoust. Soc. Am. **97**, 173–191 (1995).
[40] F. B. Jensen, W. A. Kuperman, M. B. Porter, and H. Schmidt, *Computational Ocean Acoustics* (American Institute of Physics, Woodbury, NY, 1994), Appendix A4.
[41] S. Taherzadeh and K. Attenborough, ''Sound propagation from dipole and monopole sources in a stratified fluid above a layered poro-elastic solid,'' in *Proceedings of the Symposium on Computational Acoustics*, edited by C. A. Brebia (Southampton, UK, 1995), pp. 45–54.
[42] S. Taherzadeh, ''Sound propagation in inhomogeneous media,'' Ph.D. thesis, The Open University, 1996.
[43] T. L. Richards and K. Attenborough, ''Accurate FFT-based Hankel transforms for predictions of outdoor sound propagation,'' J. Sound Vib. **109**, 157–167 (1986).
[44] D. K. Wilson, ''Use of wavenumber-domain windows in fast field programs,'' J. Acoust. Soc. Am. **89**, 448–450 (1991).
[45] Y. L. Li, S. J. Franke, and C. H. Liu, ''Numerical implementation of an adaptive fast-field program for sound propagation in layered media using the chirp z transform,'' J. Acoust. Soc. Am. **89**, 2068–2075 (1991).
[46] Y. Gabillet, H. Schroeder, G. A. Daigle, and A. L'Esperance,, ''Application of the Gaussian beam approach to sound propagation in the atmosphere: Theory and experiments,'' J. Acoust. Soc. Am. **93**, 3105–3116 (1993).

Sound fields in a rectangular enclosure under active sound transmission control

S. K. Lau and S. K. Tang[a)]
Department of Building Services Engineering, The Hong Kong Polytechnic University, Hung Hom, Hong Kong, People's Republic of China

(Received 10 May 2000; revised 24 January 2001; accepted 24 May 2001)

The present study evaluates the effectiveness of active sound transmission control inside an enclosure using a purely acoustic source under the potential energy, squared pressure, and energy density control algorithms. Full coupling between a flexible boundary wall and the interior acoustic cavity is considered. Formulas based on the impedance-mobility approach are developed for the active control of sound transmission with the energy density control algorithm. The resultant total acoustic potential energy attenuation and sound fields under the three control algorithms are compared. Global amplification of the sound level with localized quiet zones under the squared pressure control is observed. This adverse effect can be removed by using the energy density control. It is also shown that the energy density control provides a more uniform control of sound field. Better performance of global and local control of sound field using the squared pressure and energy density controls can be achieved by locating the error sensors at the peak quiet zones and the areas of peak energy density attenuation, respectively, obtained under potential energy control.
 [DOI: 10.1121/1.1387095]

PACS numbers: 43.50.Ki, 43.55.Rg [MRS]

I. INTRODUCTION

Sound transmission through building fabrics has long been a problem in building noise control. This transmission of noise is mainly due to the interaction between sound fields and the flexible structure boundaries that make up the fabrics or simply a composite wall. However, such flexible structures can hardly be eliminated in reality. For example, in residential buildings, a certain level of window area is necessary for humans both from the physiological and psychological points of view,[1] as well as for providing natural lighting. Inside industrial buildings, windows provide transparency for monitoring purposes. Traditional passive control methods using a double-glazing setup or thicker glass are not usually cost effective, especially for low frequency applications.

Fuller and Jones[2] proposed the active structural acoustic control method (ASAC) to tackle sound transmission into the fuselage, and showed that it is highly effective to low frequency noise. Pan *et al.*[3–5] extended the analysis of ASAC to the rectangular panel-cavity system using total acoustic potential energy as the performance function. They discovered two modes of ASAC, namely the panel-controlled and cavity-controlled modes. The application of these control modes depends on the relative dominance of the panel structural and cavity modes. Since then, there have been rigorous studies into the use of a point force in ASAC (for instance, Qiu *et al.*[6]). Recently, Cazzolato and Hansen[7] proposed an error sensing criterion with surface mounted structural vibration sensors for ASAC. It appears that most of the previous studies were focused on using forces applied to the structure to control the panel-controlled modes. However, most of actuators and sensors for vibration control tend to obstruct the line of sight through windows. This is not desirable for either residential buildings or building services plantrooms. Also, ASAC is effective for suppressing panel modes only, and simply helps to reconstruct the panel velocity distribution in the case of cavity-controlled modes.[3] Some disadvantages of ASAC are discussed by Qui *et al.*,[6] such as the fact that the system requires higher accuracy to produce stable effective global sound attenuation and is not effective if the acoustic energy is transmitted from one structural mode to only one acoustic mode.

In the authors' opinion, the use of acoustic control sources in the active control of sound transmission is worth exploring in order to limit the numbers of vibration actuators and sensors required on critical structures. Snyder and Hansen[8,9] have considered the use of a hybrid control system with both acoustic and vibration control sources. Kim and Brennan[10] have tested the performance of such a concept in a long enclosure with the impedance and mobility approach. The acoustic control source has been shown to be very effective in controlling cavity-controlled modes inside an enclosed space.[9,10] Therefore, the effectiveness of acoustic control sources in the active control of sound transmission should not be overlooked.

For the error sensing criteria, the minimization of total acoustic potential energy (potential energy control) is difficult to implement in practice due to the lack of modal sensors. While the traditional error criterion of minimizing the sum of squared sound pressures at discrete locations (squared pressure control) can only provide local control of sound within confined zones of quiet[11] due to the limitation of the local information fed to the controller, Joseph *et al.*[11] found that the increase in the sound pressure level far from the 10

a)Author to whom correspondence should be addressed; electronic mail: besktang@polyu.edu.hk

dB quiet zone is negligible if the point of cancellation is very close to the secondary source. However, this may not be the case for a nondiffused sound field.[14] In order to cope with a more global control of the enclosed sound field, Sommerfeldt and Nashif[12] and Park and Sommerfeldt[13] suggested the minimization of the sum of energy densities at discrete locations (energy density control) as the error criterion. Lau and Tang[14] investigated the performance of various error criteria in the active control of indoor noise using acoustic secondary sources. Their results show that better sound fields and zones of quiet inside the enclosure could be achieved with energy density sensing. Sampath and Balachandran[15] also examined the effectiveness of various error functions for ASAC, while Cazzolato[16] and Kim[17] analyzed the resultant total acoustic potential energy of active sound transmission control using vibration and/or acoustic control sources under energy density and squared pressure controls, respectively.

Though the control of sound transmission into a rectangular enclosure is not a new topic, many previous works (for instance, Pan *et al.*,[3] Park and Sommerfeldt,[13] Cazzolato[16] and Kim[17]) evaluate the effectiveness of global noise control by using a single parameter of total acoustic potential energy. However, it is possible that the active control may produce an overall reduction of the total potential energy with localized areas of sound amplification. Direct comparison between the performance of different error sensing schemes and forcing methods in three-dimensional enclosed spaces in existing literature is therefore, in the opinion of the authors, incomplete. Also, the performance of error sensing in high energy density attenuation regions obtained under the potential energy control scheme is unknown.

The present study analyzes the sound field and the effectiveness of active sound transmission control with a purely internal acoustic control source under various error sensing schemes. Full couplings between the panel vibration and the room acoustic modes are considered. The existence of amplification and quiet zones and their distributions inside the enclosure are also discussed. Poor performance of active control is expected when the error sensor is located at the nodal plane of the sound field and energy density field for the squared pressure and the energy density control, respectively.[18] The performance of active sound transmission control with various error sensor locations not on the nodal planes is analyzed. It is hoped that a more complete picture of the use of active control in building acoustics can be revealed.

II. OPTIMIZED ACOUSTIC AND VIBRATION CONTROL SOURCE STRENGTHS

A. Potential energy control

Total acoustic potential energy in an enclosed space is widely used as the parameter in assessing the global control effectiveness of an error sensing scheme.[5,13] This total acoustic potential energy inside an enclosed space of volume V can be written as

$$\mathrm{PE}=\frac{1}{4\rho_a c^2}\int_V |p|^2\,dV, \tag{1}$$

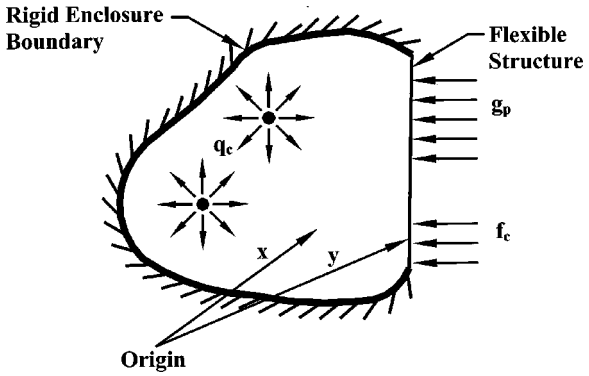

FIG. 1. Structural-acoustic coupled system.

where ρ_a and c are the air density and the speed of sound, and p denotes the complex sound pressure at a point inside the enclosed space. Considering an arbitrary shaped enclosure with a flexible boundary as shown in Fig. 1, $\mathbf{x}$ and $\mathbf{y}$ represent position vectors in the acoustic field inside the enclosure and on the flexible structure, respectively. The primary enclosed sound field (noise field) is due to the external modal force matrx, $\mathbf{g_p}$, on the flexible boundary. A matrix $\mathbf{t_c}=[\mathbf{f_c^T q_c^T}]^{\mathbf{T}}$ can be established, where $\mathbf{f_c}$ and $\mathbf{q_c}$ are the column vectors comprised of the strengths of the vibration control forces $[f_{c,1}\ f_{c,2}\ \cdots]^{\mathbf{T}}$ and acoustic control sources $[q_{c,1}\ q_{c,2}\ \cdots]^{\mathbf{T}}$ at discrete locations on the flexible boundary and inside the enclosure, respectively. Superscript $\mathbf{T}$ denotes the matrix transpose. The optimized secondary source strengths of the potential energy control for sound transmission are given by Kim[17] as

$$\mathbf{t_{c,PE}}=-\{\mathbf{R^H Z_a^H A^H A Z_a R}\}^{-1}\mathbf{R^H Z_a^H A^H A Z_a C Y_s g_p}, \tag{2}$$

where

$$\mathbf{R}=[\mathbf{C Y_s D_f}\ \ \mathbf{D_q}] \tag{3}$$

and

$$\mathbf{A}=(\mathbf{I}+\mathbf{Z_a Y_{cs}})^{-1}. \tag{4}$$

Superscript $\mathbf{H}$ denotes the Hermitian transpose. $\mathbf{Z_a}$ and $\mathbf{Y_s}$ are the uncoupled acoustic modal impedance matrix with N number of acoustic modes and the uncoupled structural modal mobility matrix with M number of structural modes, respectively. $\mathbf{C}$ is a $N\times M$ matrix of the structural-acoustic mode shape coupling coefficient with the elements $C_{n,m}$ as

$$C_{n,m}=\int_{S_f}\psi_n(\mathbf{x})\,\phi_m(\mathbf{y})\,dS,$$

where S_f denotes the area of the flexible boundary, and $\psi_n(\mathbf{x})$ and $\phi_m(\mathbf{y})$ represent the nth and the mth eigenfunctions of the acoustic and the structural mode distributions, respectively. $\mathbf{Y_{cs}}$ denotes the coupled structural modal mobility matrix ($\mathbf{C Y_s C^T}$) and $\mathbf{I}$ unit matrix. $\mathbf{D_q}$ is a $N\times Q$ matrix denoting the couplings between N number of acoustic modes and Q number of acoustic control source locations. $\mathbf{D_f}$ is an $M\times F$ matrix describing the couplings between M number of structural modes and F number of force control actuator locations. The (n,q) and (m,f) elements of $\mathbf{D_q}$ and $\mathbf{D_f}$ are given by

$$D_q(n,q)=\int_V \psi_n(\mathbf{x})\chi_a(\mathbf{x}_q)dV$$

and

$$D_f(m,f)=\int_{S_f} \phi_m(\mathbf{y})\chi_f(\mathbf{y}_f)dS,$$

respectively, where $\chi_a(\mathbf{x}_q)$ and $\chi_f(\mathbf{y}_f)$ are the acoustic and vibration source strength distribution functions at $\mathbf{x}_q$ and $\mathbf{y}_f$, respectively, and are normalized in the rest of this paper by their corresponding $q_{c,d}$ and $f_{c,f}$, respectively. A detailed derivation of Eq. (2) can be found in Kim.[17]

B. Squared pressure control

A control scheme that minimizes the sum of the measured squared sound pressures at discrete locations is the most practical and marketable of all those considered in the present study. In this section, the solution of optimal control source strengths for such a control algorithm will be obtained using the impedance and mobility approach.[17] Complex sound pressures at d number of measuring points inside an enclosure can be expressed as

$$\mathbf{p}=\mathbf{\Psi}^{\mathbf{H}}\mathbf{a}, \tag{5}$$

where $\mathbf{p}$ is a column vector of $[p(\mathbf{x}_1,\omega)p(\mathbf{x}_2,\omega)p(\mathbf{x}_3,\omega)\cdots p(\mathbf{x}_d,\omega)]^{\mathbf{T}}$, and $\mathbf{\Psi}$ and $\mathbf{a}$ are the $N\times d$ acoustic mode shape matrix and the $N\times 1$ complex amplitude matrix, respectively. Also, it can be shown that

$$\mathbf{\Psi}=\begin{bmatrix} \psi_1(\mathbf{x}) & \psi_1(\mathbf{x}_2) & \cdots & \psi_1(\mathbf{x}_d) \\ \psi_2(\mathbf{x}_1) & \ddots & & \\ \vdots & & \ddots & \\ \psi_N(\mathbf{x}_1) & & & \psi_N(\mathbf{x}_d) \end{bmatrix} \tag{6}$$

and

$$\mathbf{a}=\mathbf{A}\mathbf{Z}_{\mathbf{a}}(\mathbf{R}\mathbf{t}_{\mathbf{c}}+\mathbf{C}\mathbf{Y}_{\mathbf{s}}\mathbf{g}_{\mathbf{p}}). \tag{7}$$

The sum of the squared sound pressures for the measuring points is given as

$$\mathbf{p}^{\mathbf{H}}\mathbf{p}=\mathbf{a}^{\mathbf{H}}\mathbf{\Psi}\mathbf{\Psi}^{\mathbf{H}}\mathbf{a}. \tag{8}$$

A Hermitian quadratic equation is obtained by substituting Eqs. (6) and (7) into Eq. (8), and the optimal secondary source strength matrix that minimizes E number of sound pressure signals can be written as

$$\mathbf{t}_{\mathbf{c,SP}}=-\{\mathbf{R}^{\mathbf{H}}\mathbf{Z}_{\mathbf{a}}^{\mathbf{H}}\mathbf{A}^{\mathbf{H}}\mathbf{\Psi}_{\mathbf{e}}\mathbf{\Psi}_{\mathbf{e}}^{\mathbf{H}}\mathbf{A}\mathbf{Z}_{\mathbf{a}}\mathbf{R}\}^{-1} \times\mathbf{R}^{\mathbf{H}}\mathbf{Z}_{\mathbf{a}}^{\mathbf{H}}\mathbf{A}^{\mathbf{H}}\mathbf{\Psi}_{\mathbf{e}}\mathbf{\Psi}_{\mathbf{e}}^{\mathbf{H}}\mathbf{A}\mathbf{Z}_{\mathbf{a}}\mathbf{C}\mathbf{Y}_{\mathbf{s}}\mathbf{g}_{\mathbf{p}}, \tag{9}$$

where $\mathbf{\Psi}_{\mathbf{e}}$ is the acoustic mode shape matrix at the locations of the E number of sound pressure sensors that provide the error signals. Compared with Eq. (2) for the case of the potential energy control, Eq. (9) includes an extra term of error sensing mode shape matrix $\mathbf{\Psi}_{\mathbf{e}}$.

C. Energy density control

As discussed by Lau and Tang,[14] the energy density control is a promising algorithm for both global and local noise control inside an enclosed space. The energy density, ED, at a measuring point inside an enclosure is the sum of the acoustic potential and the kinetic energy densities:

$$\mathrm{ED}=\frac{|p|^2}{2\rho_a c^2}+\frac{\rho_a|u|^2}{2}, \tag{10}$$

where u is the particle velocity at the measuring point. ED provides more global information to the controller, as suggested by Eq. (10). It consists of the local sound pressure and particle velocity, and is less likely to vanish than the sound pressure. Though nodes in the three-dimensional energy density field exist, the nodal volumes for the total energy density field are much small than those of the squared pressure field.[18] Using Eq. (5), Eq. (10), and Euler's equation $\nabla p \approx -jk\rho_a cu$, the sum of the energy density at discrete points can be expressed in a matrix form as

$$\mathrm{ED}_{\mathrm{sum}}=\frac{1}{2\rho_a c^2}\left\{\mathbf{p}^{\mathbf{H}}\mathbf{p}+\frac{1}{k^2}\nabla\mathbf{p}^{\mathbf{H}}\cdot\nabla\mathbf{p}\right\}, \tag{11}$$

where k is the wave number. The sensing of energy density signals can be practically achieved by careful arrangement of microphones to measure the acoustic pressures and the three orthogonal components of pressure gradients shown in Eq. (11). The number of pressure microphones required to measure a local energy density can be reduced to four in the tetrahedral configuration.[16] Substituting Eqs. (5) and (7) into Eq. (11), one can find that $\mathrm{ED}_{\mathrm{sum}}$ for E number of local energy density signals can be expressed as

$$\mathrm{ED}_{\mathrm{sum}}=\frac{1}{2\rho_a c^2}J_{\mathrm{ED}},$$

where J_{ED}, the cost function of energy density control, is the Hermitian quadratic expression

$$J_{\mathrm{ED}}=\mathbf{t}_{\mathbf{c}}^{\mathbf{H}}\mathbf{F}_{\mathbf{1}}\mathbf{t}_{\mathbf{c}}+\mathbf{F}_{\mathbf{2}}^{\mathbf{H}}\mathbf{t}_{\mathbf{c}}+\mathbf{t}_{\mathbf{c}}^{\mathbf{H}}\mathbf{F}_{\mathbf{2}}+\mathbf{F}_{\mathbf{3}}$$

with

$$\mathbf{F}_{\mathbf{1}}=\mathbf{R}^{\mathbf{H}}\mathbf{Z}_{\mathbf{a}}^{\mathbf{H}}\mathbf{A}^{\mathbf{H}}\left[\mathbf{\Psi}_{\mathbf{e}}\mathbf{\Psi}_{\mathbf{e}}^{\mathbf{H}}+\frac{1}{k^2}\nabla\mathbf{\Psi}_{\mathbf{e}}\cdot\nabla\mathbf{\Psi}_{\mathbf{e}}^{\mathbf{H}}\right]\mathbf{A}\mathbf{Z}_{\mathbf{a}}\mathbf{R},$$

$$\mathbf{F}_{\mathbf{2}}=\mathbf{R}^{\mathbf{H}}\mathbf{Z}_{\mathbf{a}}^{\mathbf{H}}\mathbf{A}^{\mathbf{H}}\left[\mathbf{\Psi}_{\mathbf{e}}\mathbf{\Psi}_{\mathbf{e}}^{\mathbf{H}}+\frac{1}{k^2}\nabla\mathbf{\Psi}_{\mathbf{e}}\cdot\nabla\mathbf{\Psi}_{\mathbf{e}}^{\mathbf{H}}\right]\mathbf{A}\mathbf{Z}_{\mathbf{a}}\mathbf{C}\mathbf{Y}_{\mathbf{s}}\mathbf{g}_{\mathbf{p}},$$

and

$$\mathbf{F}_{\mathbf{3}}=\mathbf{g}_{\mathbf{p}}^{\mathbf{H}}\mathbf{Y}_{\mathbf{s}}^{\mathbf{H}}\mathbf{C}^{\mathbf{H}}\mathbf{Z}_{\mathbf{a}}^{\mathbf{H}}\mathbf{A}^{\mathbf{H}}\left[\mathbf{\Psi}_{\mathbf{e}}\mathbf{\Psi}_{\mathbf{e}}^{\mathbf{H}}+\frac{1}{k^2}\nabla\mathbf{\Psi}_{\mathbf{e}}\cdot\nabla\mathbf{\Psi}_{\mathbf{e}}^{\mathbf{H}}\right]\mathbf{A}\mathbf{Z}_{\mathbf{a}}\mathbf{C}\mathbf{Y}_{\mathbf{s}}\mathbf{g}_{\mathbf{p}}.$$

The optimal secondary source strengths of energy density control are derived herein by minimizing the resultant Hermitian quadratic expression for J_{ED}. One obtains

$$\mathbf{t}_{\mathbf{c,ED}}=-\left\{\mathbf{R}^{\mathbf{H}}\mathbf{Z}_{\mathbf{a}}^{\mathbf{H}}\mathbf{A}^{\mathbf{H}}\left[\mathbf{\Psi}_{\mathbf{e}}\mathbf{\Psi}_{\mathbf{e}}^{\mathbf{H}}+\frac{1}{k^2}\nabla\mathbf{\Psi}_{\mathbf{e}}\cdot\nabla\mathbf{\Psi}_{\mathbf{e}}^{\mathbf{H}}\right]\mathbf{A}\mathbf{Z}_{\mathbf{a}}\mathbf{R}\right\}^{-1} \cdot\mathbf{R}^{\mathbf{H}}\mathbf{Z}_{\mathbf{a}}^{\mathbf{H}}\mathbf{A}^{\mathbf{H}}\left[\mathbf{\Psi}_{\mathbf{e}}\mathbf{\Psi}_{\mathbf{e}}^{\mathbf{H}}+\frac{1}{k^2}\nabla\mathbf{\Psi}_{\mathbf{e}}\cdot\nabla\mathbf{\Psi}_{\mathbf{e}}^{\mathbf{H}}\right]\mathbf{A}\mathbf{Z}_{\mathbf{a}}\mathbf{C}\mathbf{Y}_{\mathbf{s}}\mathbf{g}_{\mathbf{p}}. \tag{12}$$

Equation (12) consists of an additional matrix of $(\mathbf{\Psi}_{\mathbf{e}}\mathbf{\Psi}_{\mathbf{e}}^{\mathbf{H}}+\nabla\mathbf{\Psi}_{\mathbf{e}}\cdot\nabla\mathbf{\Psi}_{\mathbf{e}}^{\mathbf{H}}/k^2)$, which consists of the normalized total energy density fields at the locations of the E number of energy

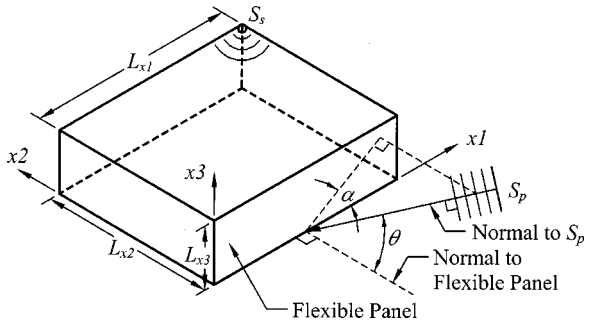

FIG. 2. Rectangular enclosed space and coordinate system.

density sensors that provide the error signals, compared with Eq. (2) for the potential energy control.

III. NUMERICAL MODEL AND COMPUTATIONAL CONVERGENCE

A numerical experiment was performed to evaluate the performance of various error sensing criteria for the active control of sound transmission. Figure 2 illustrates the rectangular enclosure and the coordinate system adopted in the present study. The dimensions of the enclosure are L_{x1} (length), L_{x2} (width), and L_{x3} (height) which were chosen such that $L_{x1}:L_{x2}:L_{x3}=1:e/\pi:1/\pi$ so as to avoid the degenerate acoustic modes.[19] The enclosure consists of five acoustically rigid walls and a simple supported flexible panel at $x2=0$. The primary enclosed sound fields are due to the interaction between the interior acoustic space and the structural vibration on the flexible panel excited by an external plane wave S_p of frequency ω. The propagation direction of S_p is defined by the incidence angle θ and azimuth α as shown in Fig. 2. The incidence angle θ is defined as the angle between the lines normal to the external plane wave and the flexible panel, while the azimuth α is the angle between the projected plane of the line normal to the external plane wave on the panel and the $x1$ axis. In the present investigation, the secondary acoustic control source, S_s, is located at the corner (L_{x1},L_{x2},L_{x3}) in order to avoid the nodal lines of any acoustic mode in the rectangular enclosure.[14,20] Two new dimensionless parameters, η_c and φ, are introduced herein as

$$\eta_c=\frac{K_a}{M_s\omega_{ac}\omega_{sc}}, \tag{13}$$

and

$$\varphi=\frac{\omega_{ac}}{\omega_{sc}}=\sqrt{\frac{\rho_s h}{D}}\left(\frac{1}{L_{y1}^2}+\frac{1}{L_{y2}^2}\right)^{-1}\frac{c}{\pi L_{x,\max}}, \tag{14}$$

respectively, where K_a and M_s are the acoustic bulk stiffness $(\rho_a c^2 S_f^2/V)$ and mass of the structure $(\rho_s h S_f)$, respectively, and ω_{ac} and ω_{sc} are the first eigenfrequencies of acoustic (cavity) and structural (panel) modes, respectively. D, ρ_s, S_f, and h are the bending stiffness, density, surface area and thickness of the flexible panel, respectively. $L_{x,\max}$ is the maximum perpendicular separation between two parallel walls inside the rectangular enclosure, and $L_{y1}\times L_{y2}$ are the dimensions of the flexible panel. In the present numerical model, $L_{x,\max}=L_{y1}=L_{x1}$ and $L_{y2}=L_{x3}$. Table I shows some possible values of η_c and φ. Then, Eqs. (3), (4), and (7) can be rearranged as follows:

TABLE I. Possible values of η_c and φ.[a]

Flexible structure	L_{x1} (m)	η_c	φ
6 mm glass (Ref. 21)	1	0.01	1.04
6 mm glass (Ref. 21)	5	0.26	5.21
12 mm glass (Ref. 21)	5	0.06	2.60
6 mm alumina (Al_2O_3) (Ref. 21)	5	0.10	3.05
Kim and Brennan (Refs. 10 and 22)	1.5	0.04	0.81

[a]Air density and speed of sound in air 20 °C are 1.21 kg/m^3 and 340 m/s, respectively.

$$\mathbf{a}=\eta_c\mathbf{A}\hat{\mathbf{Z}}_\mathbf{a}(\hat{\mathbf{R}}\hat{\mathbf{t}}_\mathbf{c}+\hat{\mathbf{C}}\hat{\mathbf{Y}}_\mathbf{s}\hat{\mathbf{g}}_\mathbf{p}), \tag{15}$$

$$\mathbf{A}=(\mathbf{I}+\eta_c\hat{\mathbf{Z}}_\mathbf{a}\hat{\mathbf{Y}}_\mathbf{cs})^{-1}, \tag{16}$$

and

$$\hat{\mathbf{R}}=[\hat{\mathbf{C}}\hat{\mathbf{Y}}_\mathbf{s}\mathbf{D}_\mathbf{f}\ \ \mathbf{D}_\mathbf{q}], \tag{17}$$

respectively, where $\hat{\mathbf{C}}=\mathbf{C}/S_f$, $\hat{\mathbf{g}}_\mathbf{p}=\mathbf{g}_\mathbf{p}/S_f$, and $\hat{\mathbf{Y}}_\mathbf{cs}=\hat{\mathbf{C}}\hat{\mathbf{Y}}_\mathbf{s}\hat{\mathbf{C}}^\mathbf{T}$. All the above variables are dimensionless except $\hat{\mathbf{g}}_\mathbf{p}$ and $\hat{\mathbf{t}}_\mathbf{c}$, whose units are Nm^{-2}. $\hat{\mathbf{Z}}_\mathbf{a}$ and $\hat{\mathbf{Y}}_\mathbf{s}$ are $(N\times N)$ and $(M\times M)$ diagonal matrices which equal $\{\omega_{ac}V/(\rho_a c^2)\}\mathbf{Z}_\mathbf{a}$ and $(\omega_{sc}\rho_s h S_f)\mathbf{Y}_\mathbf{s}$, respectively. The (n,n) and (m,m) diagonal elements of $\hat{\mathbf{Z}}_\mathbf{a}$ and $\hat{\mathbf{Y}}_\mathbf{s}$ consist, respectively, of $\hat{Z}_{a,n}$ and $\hat{Y}_{s,m}$ where

$$\hat{Z}_{a,n}=\frac{j\hat{\omega}}{\hat{\omega}_n^2-\hat{\omega}^2+2j\xi_n\hat{\omega}_n\hat{\omega}}, \tag{18}$$

$$\hat{Y}_{s,m}=\frac{j\hat{\omega}\varphi}{\hat{\omega}_m^2-\hat{\omega}^2\varphi^2+2j\zeta_m\hat{\omega}_m\hat{\omega}\varphi}, \tag{19}$$

and $\hat{\omega}$ is the normalized angular frequency (normalized by ω_{ac}). $\hat{\omega}_n$ and $\hat{\omega}_m$ are the acoustic and structural mode frequencies normalized by their first eigenfrequencies, respectively (ω_{ac} and ω_{sc}, respectively). ξ_n and ζ_m are the modal damping coefficients of the acoustic and structural modes, respectively. The secondary source strength matrix can be rewritten as

$$\hat{\mathbf{t}}_\mathbf{c}=\begin{bmatrix}\hat{\mathbf{f}}_\mathbf{c}\\ \hat{\mathbf{q}}_\mathbf{c}\end{bmatrix}, \tag{20}$$

where $\hat{\mathbf{f}}_\mathbf{c}=\mathbf{f}_\mathbf{c}/S_f$ and $\hat{\mathbf{q}}_\mathbf{c}=\mathbf{q}_\mathbf{c}(\omega_{sc}\rho_s h/S_f)$. Comparing the expression for $\hat{\mathbf{q}}_\mathbf{c}$ and $\hat{\mathbf{g}}_\mathbf{p}$, it can be noted that a weaker secondary acoustic control source is required to control a fixed external primary sound source under higher ω_{sc} and/or panel surface density, $\rho_s h$.

Equations (2), (9), and (12) for the optimal secondary source strength matrices can now be rewritten using the nondimensional parameters:

$$\hat{\mathbf{t}}_{\mathbf{c,PE}}=-\{\hat{\mathbf{R}}^\mathbf{H}\hat{\mathbf{Z}}_\mathbf{a}^\mathbf{H}\mathbf{A}^\mathbf{H}\mathbf{A}\hat{\mathbf{Z}}_\mathbf{a}\hat{\mathbf{R}}\}^{-1}\hat{\mathbf{R}}^\mathbf{H}\hat{\mathbf{Z}}_\mathbf{a}^\mathbf{H}\mathbf{A}^\mathbf{H}\mathbf{A}\hat{\mathbf{Z}}_\mathbf{a}\hat{\mathbf{C}}\hat{\mathbf{Y}}_\mathbf{s}\hat{\mathbf{g}}_\mathbf{p}, \tag{21}$$

$$\hat{\mathbf{t}}_{\mathbf{c,SP}}=-\{\hat{\mathbf{R}}^\mathbf{H}\hat{\mathbf{Z}}_\mathbf{a}^\mathbf{H}\mathbf{A}^\mathbf{H}\boldsymbol{\Psi}_\mathbf{e}\boldsymbol{\Psi}_\mathbf{e}^\mathbf{H}\mathbf{A}\hat{\mathbf{Z}}_\mathbf{a}\hat{\mathbf{R}}\}^{-1}\times\hat{\mathbf{R}}^\mathbf{H}\hat{\mathbf{Z}}_\mathbf{a}^\mathbf{H}\mathbf{A}^\mathbf{H}\boldsymbol{\Psi}_\mathbf{e}\boldsymbol{\Psi}_\mathbf{e}^\mathbf{H}\mathbf{A}\hat{\mathbf{Z}}_\mathbf{a}\hat{\mathbf{C}}\hat{\mathbf{Y}}_\mathbf{s}\hat{\mathbf{g}}_\mathbf{p}, \tag{22}$$

$$\hat{\mathbf{t}}_{\mathbf{c,ED}} = -\left\{\hat{\mathbf{R}}^{\mathbf{H}}\hat{\mathbf{Z}}_{\mathbf{a}}^{\mathbf{H}}\mathbf{A}^{\mathbf{H}}\left[\boldsymbol{\Psi}_{\mathbf{e}}\boldsymbol{\Psi}_{\mathbf{e}}^{\mathbf{H}} + \frac{1}{k^2}\nabla\boldsymbol{\Psi}_{\mathbf{e}}\cdot\nabla\boldsymbol{\Psi}_{\mathbf{e}}^{\mathbf{H}}\right]\mathbf{A}\hat{\mathbf{Z}}_{\mathbf{a}}\hat{\mathbf{R}}\right\}^{-1} \times \hat{\mathbf{R}}^{\mathbf{H}}\hat{\mathbf{Z}}_{\mathbf{a}}^{\mathbf{H}}\mathbf{A}^{\mathbf{H}}\left[\boldsymbol{\Psi}_{\mathbf{e}}\boldsymbol{\Psi}_{\mathbf{e}}^{\mathbf{H}} + \frac{1}{k^2}\nabla\boldsymbol{\Psi}_{\mathbf{e}}\cdot\nabla\boldsymbol{\Psi}_{\mathbf{e}}^{\mathbf{H}}\right]\mathbf{A}\hat{\mathbf{Z}}_{\mathbf{a}}\hat{\mathbf{C}}\hat{\mathbf{Y}}_{\mathbf{s}}\hat{\mathbf{g}}_{\mathbf{p}}. \tag{23}$$

In the foregoing discussions, suffices PE, SP, and ED denote quantities associated with the potential energy, squared pressure, and energy density control algorithms, respectively. $[\boldsymbol{\Psi}_{\mathbf{e}}\boldsymbol{\Psi}_{\mathbf{e}}^{\mathbf{H}}]$ and $[\boldsymbol{\Psi}_{\mathbf{e}}\boldsymbol{\Psi}_{\mathbf{e}}^{\mathbf{H}} + \nabla\boldsymbol{\Psi}_{\mathbf{e}}\cdot\nabla\boldsymbol{\Psi}_{\mathbf{e}}^{\mathbf{H}}/k^2]$ in Eqs. (22) and (23) govern the performance of the squared pressure and energy density controls. They depend directly on the error sensor locations. Parkins *et al.*[18] have investigated these two terms using node structures. As mentioned previously, the energy density control has the advantage of the lower probability of a randomly placed sensor being laid in a nodal volume for acoustic modes, and requiring much fewer sensors than the squared pressure control.

It can be seen from Eq. (15) that the effectiveness of passive sound transmission control depends on the structural-acoustic coupling transfer function (described by $\mathbf{A}$) and the effectiveness of the vibration force to acoustic pressure transfer function at weak structural-acoustic coupling (represented by $\eta_c\hat{\mathbf{Z}}_{\mathbf{a}}\hat{\mathbf{C}}\hat{\mathbf{Y}}_{\mathbf{s}}$). The two parameters, η_c and φ, are critical for passive sound transmission control. The speed of sound and the air density are practically constant. Thus, the traditional measure for controlling sound transmission is to reduce K_a/M_s in η_c, so that both the magnitudes of the structural-acoustic coupling transfer function and the vibration force to acoustic pressure transfer function at weak structural-acoustic coupling are reduced. Also, some reduction of sound transmission can be achieved by reducing both ω_{ac} and ω_{sc} [Eq. (15)]. Modification of the passive sound transmission control is possible by adjusting φ. However, the eigenfrequency of the flexible panel should not be near to the eigenfrequencies of the enclosure and/or the forcing frequency ω.

Using Eqs. (5), (15), (21), (22), and (23), the attenuation of sound pressure at a point inside the enclosure under the three sound transmission control algorithms can be expressed as

$$\Delta\mathrm{SP} = \boldsymbol{\Psi}^{\mathbf{H}}\{\eta_c\mathbf{A}\hat{\mathbf{Z}}_{\mathbf{a}}\hat{\mathbf{R}}\{\hat{\mathbf{R}}^{\mathbf{H}}\hat{\mathbf{Z}}_{\mathbf{a}}^{\mathbf{H}}\mathbf{A}^{\mathbf{H}}\mathbf{E}\mathbf{A}\hat{\mathbf{Z}}_{\mathbf{a}}\hat{\mathbf{R}}\}^{-1} \times \hat{\mathbf{R}}^{\mathbf{H}}\hat{\mathbf{Z}}_{\mathbf{a}}^{\mathbf{H}}\mathbf{A}^{\mathbf{H}}\mathbf{E}\mathbf{A}\hat{\mathbf{Z}}_{\mathbf{a}}\hat{\mathbf{C}}\hat{\mathbf{Y}}_{\mathbf{s}}\hat{\mathbf{g}}_{\mathbf{p}}\},$$

where $\mathbf{E}$ is $\mathbf{I}$, $\boldsymbol{\Psi}_{\mathbf{e}}\boldsymbol{\Psi}_{\mathbf{e}}^{\mathbf{H}}$, and $\boldsymbol{\Psi}_{\mathbf{e}}\boldsymbol{\Psi}_{\mathbf{e}}^{\mathbf{H}} + k^{-2}\nabla\boldsymbol{\Psi}_{\mathbf{e}}\cdot\nabla\boldsymbol{\Psi}_{\mathbf{e}}^{\mathbf{H}}$ for the potential energy, the squared pressure, and the energy density controls, respectively. Besides the terms for passive control, it can be shown that the effectiveness of the active sound transmission control relies on the matrix

$$\hat{\mathbf{R}}\{\hat{\mathbf{R}}^{\mathbf{H}}\hat{\mathbf{Z}}_{\mathbf{a}}^{\mathbf{H}}\mathbf{A}^{\mathbf{H}}\mathbf{E}\mathbf{A}\hat{\mathbf{Z}}_{\mathbf{a}}\hat{\mathbf{R}}\}^{-1}\hat{\mathbf{R}}^{\mathbf{H}}\hat{\mathbf{Z}}_{\mathbf{a}}^{\mathbf{H}}\mathbf{A}^{\mathbf{H}}\mathbf{E}\mathbf{A}\hat{\mathbf{Z}}_{\mathbf{a}}, \tag{24}$$

which is governed by the source frequency ω, the degree of structural-acoustic coupling, the modal characteristics of the enclosure and the flexible panel, and the error sensing matrix. Kim[17] has investigated the performance of active sound transmission control in a weakly coupled ductlike rectangular enclosure with potential energy control. For such a system, $\mathbf{A} \approx \mathbf{I}$ as $\eta_c\hat{\mathbf{Z}}_{\mathbf{a}}\hat{\mathbf{Y}}_{\mathbf{cs}} = 0$. This is consistent with the discussions of Kim and Brennan,[22] who stated the problem in a different way. Expression (24) becomes independent of η_c for weakly coupled systems. In this paper, fully structural-acoustic coupled systems are discussed with consideration of η_c and φ under three control algorithms, namely the potential energy, squared pressure, and energy density controls.

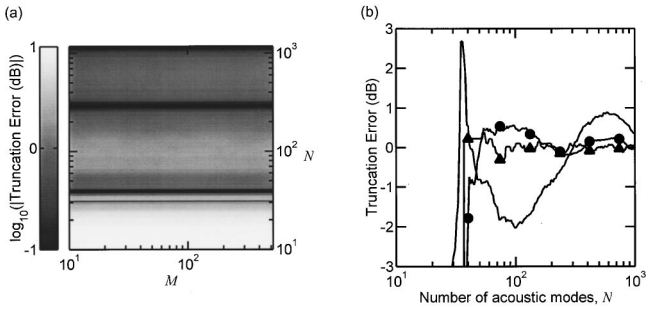

FIG. 3. Convergence of modal summation with point acoustic source at (L_{x1}, L_{x2}, L_{x3}) and forcing frequency $5\omega_{ac}$, $\eta_c = 0.0092$ and $\varphi = 9.2$. (a) At location $(0.9L_{x1}, 0.9L_{x2}, 0.9L_{x3})$ with $N < 1173$ and $M < 522$; (b) effect of location $(M = 522)$. — $(0.9L_{x1}, 0.9L_{x2}, 0.9L_{x3})$; —●— $(0.8L_{x1}, 0.8L_{x2}, 0.8L_{x3})$; —▲— $(0.5L_{x1}, 0.5L_{x2}, 0.5L_{x3})$.

Though an exact representation of the sound field is given by Eq. (5) with the summation of the contributions from infinite numbers of acoustic and structural modes ($N \to \infty$ and $M \to \infty$, respectively), truncating these summations with a finite number of modes in the calculations is reasonably accurate in the estimation of the sound field at low modal densities in practice. Therefore, a convergence test has to be done in the first place to determine the acceptable values for N and M. Equation (5) has an inherent convergence difficulty at locations close to a point acoustic source,[23] but it is not worth studying the sound pressure at these points. The acoustic modal impedance and the structural modal mobility in Eqs. (18) and (19) were obtained with both the acoustic and structural modal damping coefficients of 0.01 in the present study. All the simulations were computed by using MATLAB on a DEC workstation 600 a.u.

Figure 3(a) illustrates the convergence of the near field sound pressure calculated by Eq. (5) at the location $(0.9L_{x1}, 0.9L_{x2}, 0.9L_{x3})$ inside the enclosure shown in Fig. 2 with $\eta_c = 0.0092$, $\varphi = 9.2$ and an acoustic corner source located at (L_{x1}, L_{x2}, L_{x3}) operating at $5\omega_{ac}$. Defining truncation error as the difference between calculated result and that obtained with $N = 1173$ and $M = 522$, it is observed that there is a gradual reduction of such error for $N > 37$. The maximum deviation from the result obtained with $N = 1173$ and $M = 522$ is less than 0.86 dB for $N > 600$, regardless of the number of structural modes involved. Faster convergence can be found at increased distance away from the corner sound source for $N > 37$ in Fig. 3(b).

Figure 4(a) shows the convergence of sound pressure at the center of the enclosure due to an excitation from a point force acting at the center of the flexible panel. A sharp fall of truncation error is revealed for $N > 37$ and $M > 110$. The maximum deviation from the result obtained with $N = 1173$ and $M = 522$ is less than 0.97 dB for $N > 600$ and $M > 110$. Similar and even better convergence can be found at other

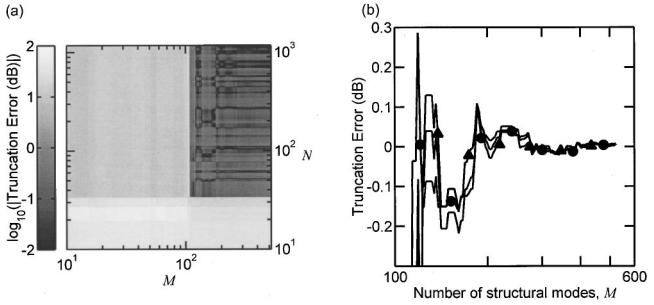

FIG. 4. Convergence of modal summation with point force actuator at $(0.5L_{y1},0.5L_{y2})$ and forcing frequency $5\omega_{ac}$, $\eta_c=0.0092$ and $\varphi=9.2$. (a) At center of enclosure $(0.5L_{x1},0.5L_{x2},0.5L_{x3})$; (b) effect of location ($N=1173$). — $(0.5L_{x1},0.5L_{x2},0.5L_{x3})$; —●— $(0.9L_{x1},0.9L_{x2},0.9L_{x3})$; —▲— $(0.5L_{x1},0,0.5L_{x3})$.

points inside the enclosure, as shown in Fig. 4(b). The same phenomenon is observed when the excitation is due to a plane acoustic external source (not shown here). The convergence test has been extended to cover the range $0.0092 \leqslant \eta_c \leqslant 0.92$ and $0.092 \leqslant \varphi \leqslant 9.2$. Similar or faster computational convergence as in Figs. 3 and 4 can be observed (not shown here). Thus 1173 and 522 numbers of acoustic and structural modes, respectively, were adopted in the present calculations with the consideration of computer power and accuracy. Compared with the details of Kim and Brennan,[10] the present investigation has included far more acoustic and structural modes in the calculations. Also, faster convergence can be achieved for $\omega<5\omega_{ac}$.

IV. TOTAL ACOUSTIC POTENTIAL ENERGY

A. Effects of η_c and φ under potential energy control

The effectiveness of passive sound transmission control depends mainly on the acoustic bulk stiffness and the mass of the structure, K_a/M_s,[22] which is related to η_c. However, for passive control of sound transmission, the principles of using lighter structures and smaller η_c are contradictory. The application of active sound transmission control will allow the use of lighter structures and/or even further reduce sound pressures inside the enclosure. As mentioned previously, a common metric for assessing the global control effectiveness inside an enclosure is the reduction of the total acoustic potential energy, PE. For orthogonal modal characteristic functions, the integration of potential energy [Eq. (1)] gives

$$\mathrm{PE}=\frac{V}{4\rho c^2}\mathbf{a}^{\mathbf{H}}\mathbf{a}. \tag{25}$$

Figure 5 shows the potential energy at frequency $0.2\omega_{ac}$, ω_{ac}, $2.4\omega_{ac}$, and $3\omega_{ac}$ under different combinations of η_c and φ, which are logarithmically distributed into 24×26 divisions between 0.0092 and 0.92 and between 0.092 and 9.2, respectively. The external modal force matrix, $\hat{\mathbf{g}}_\mathbf{p}$, results from an external plane wave of unity strength at $\theta=\pi/6$ and $\alpha=\pi/4$. There is, in general, a gradual decline of PE as η_c decreases for all frequencies. This is consistent with the deduction from the passive sound transmission control. Peak PE occurs at $\omega=\omega_{sc}$ for a weakly coupled system. As η_c increases, the peak PE occurs at lower frequency, especially

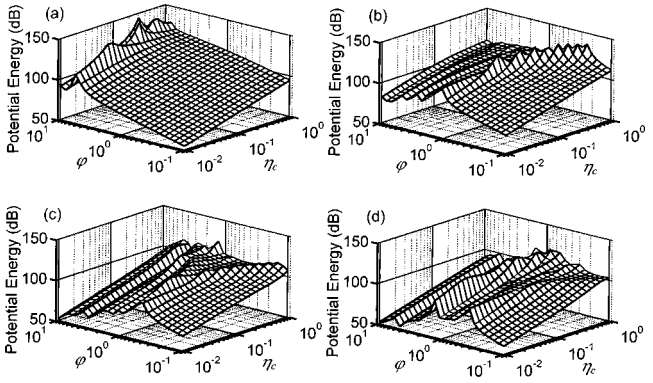

FIG. 5. Variation of total acoustic potential energy with η_c and φ at different forcing frequencies. (a) $0.2\omega_{ac}$; (b) ω_{ac}; (c) $2.4\omega_{ac}$; (d) $3\omega_{ac}$. Primary external plane source at $\theta=\pi/6$ and $\alpha=\pi/4$. All data presented are in dB ref 10^{-12} Nm.

for a strongly coupled system (where η_c is large). The shift of the PE is due to the effect of the coupling matrix $\mathbf{A}$ in Eq. (15). Such peak PE can be attenuated effectively by active means under the potential energy control using an acoustic control source at (L_{x1},L_{x2},L_{x3}) and a force control actuator at the center of the flexible panel, as shown in Fig. 6. Peak PE attenuations usually occur around the η_c and φ combinations that produce high PE at $\omega=\omega_{sc}$ (cf. Fig. 5). Relatively sharp reduction of the PE attenuation is observed at forcing frequency $\omega>\omega_{sc}$ for a weakly coupled system (small η_c), implying that this hybrid active sound transmission control of the global sound field is ineffective at frequencies higher than ω_{sc} when η_c is small. However, a certain degree of the PE attenuation can still be observed at frequency $\omega>\omega_{sc}$ if $\omega<\omega_{ac}$ [Figs. 6(a) and (b)] at the eigenfrequencies of the flexible panel. Also, the frequency at which this sharp fall of PE attenuation occurs is lower than ω_{sc} for a strongly coupled system (large η_c). A plateau of high PE attenuation can also be observed for small φ at $\omega<\omega_{sc}$.

Figures 7 and 8 illustrate the attenuation of PE under the potential energy control with a pure active force actuator at the center of the flexible panel and a pure acoustic control source at (L_{x1},L_{x2},L_{x3}), respectively, at frequency $0.2\omega_{ac}$, ω_{ac}, $2.4\omega_{ac}$, and $3\omega_{ac}$. Active vibration control produces

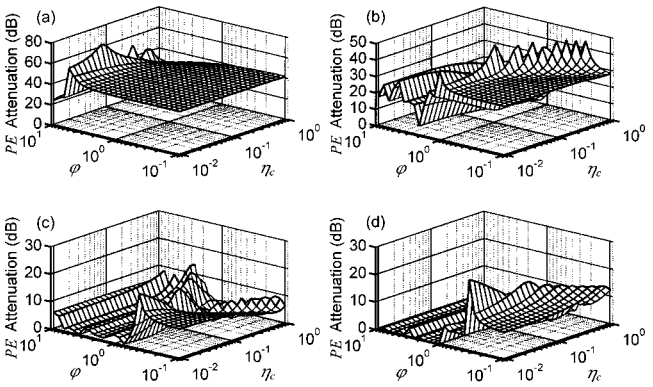

FIG. 6. Variation of total acoustic potential energy attenuation with η_c and φ under potential energy control using hybrid control system at different forcing frequencies. (a) $0.2\omega_{ac}$; (b) ω_{ac}; (c) $2.4\omega_{ac}$; (d) $3\omega_{ac}$. Primary external plane source at $\theta=\pi/6$ and $\alpha=\pi/4$; acoustic control source at (L_{x1},L_{x2},L_{x3}); force actuator at $(0.5L_{x1},0.5L_{x3})$.

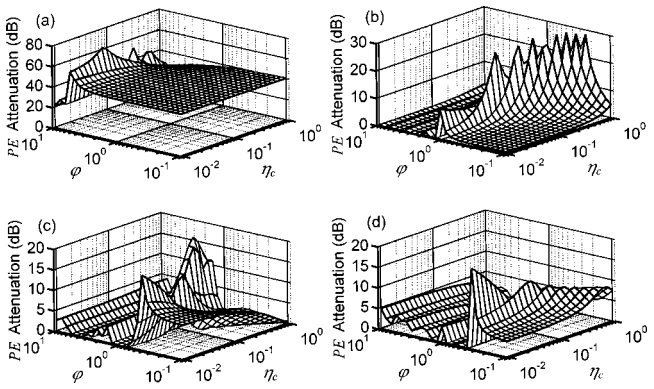

FIG. 7. Variation of total acoustic potential energy attenuation with η_c and φ under potential energy control using purely vibration control at $(0.5L_{x1},0.5L_{x3})$ at different forcing frequencies. (a) $0.2\omega_{ac}$; (b) ω_{ac}; (c) $2.4\omega_{ac}$; (d) $3\omega_{ac}$. Primary external plane source at $\theta=\pi/6$ and $\alpha=\pi/4$.

similar results as those under the hybrid control (Fig. 6). However, the high PE attenuation observed at $\omega=0.2\omega_{ac}$ falls rapidly as ω increases towards ω_{ac}. The control only becomes effective at the eigenfrequencies of the flexible panel in the cavity-controlled modes when $\omega=\omega_{ac}$, as shown in Fig. 7(b). For pure acoustic control (Fig. 8), high attenuation of PE can also be found at frequency $\omega>\omega_{sc}$ besides the plateau of PE attenuation at smaller η_c and φ pairs for $\omega\leqslant\omega_{ac}$. The acoustic control source is less effective to control the panel-controlled modes at ω_{sc} near to $\varphi=5$ and $\varphi=1$ as shown in Figs. 8(a) and (b), respectively. Only slight attenuation of PE can be found at higher frequencies [Figs. 8(c) and (d)]. Therefore, the pure acoustic control source is effective at frequencies less than ω_{ac} except at ω_{sc}. Comparing the results shown in Figs. 6–8, it is found that the pure acoustic control can provide reasonable acoustic potential energy attenuation in the practical range of φ and η_c (Table I), especially at low forcing frequency, despite its simplicity of construction. This better performance of the pure acoustic control is anticipated, as the higher structural modes of a weak panel structure are poorly excited by a plane wave as a result of modal filtering. However, this plane wave excitation is common in practical building noise transmission problems. A typical example of it is the noise emitted by a distant source transmitted into a room through the weak

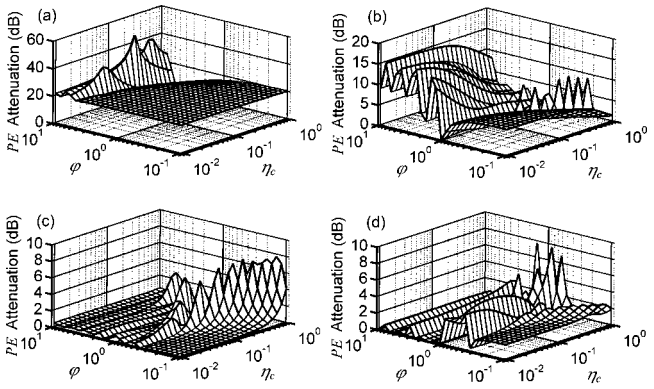

FIG. 8. Variation of total acoustic potential energy attenuation with η_c and φ under potential energy control using purely acoustic control source at (L_{x1},L_{x2},L_{x3}) at different forcing frequencies. (a) $0.2\omega_{ac}$; (b) ω_{ac}; (c) $2.4\omega_{ac}$; (d) $3\omega_{ac}$. Primary external plane source at $\theta=\pi/6$ and $\alpha=\pi/4$.

structures of building fabrics. Therefore, only this control is investigated in the rest of the paper.

B. Total potential energy under different control algorithms

Using the same external plane wave and the acoustic control source configuration as shown in Fig. 2, a single sensor was placed in five discrete locations within the enclosure for five control simulations. These five locations were equally spaced along a diagonal line between the points $(0.9L_{x1},0.9L_{x2},0.9L_{x3})$ and $(0.1L_{x1},0.1L_{x2},0.9L_{x3})$ close to the ceiling. At least four control channels are required for measuring the three orthogonal particle velocities and one sound pressure during each energy density sensing. Detailed comparisons between energy density error sensor and four microphones sensing can be found in Cazzolato.[16] Global control is then expected to be poorer for single squared pressure sensing than for energy density sensing. However, for a compact configuration of error sensing devices required in practice, the four microphone squared pressure signals are similar, especially in the practical frequency range of building noise control. Thus, the single microphone for squared pressure control is studied here for simplicity. Figures 9 and 10 show the attenuation of PE up to $5\omega_{ac}$ for each sensor location with $\eta_c=0.01$, $\varphi=1.04$ and $\eta_c=0.26$, $\varphi=5.21$, respectively. These combinations of η_c and φ correspond to data shown in the first and second rows of Table I for a small box and a room, respectively, with a 6 mm glass panel as the transmitting wall. The calculations were done at $0.02\omega_{ac}$ intervals. Also, attenuation greater than 40 dB and amplification higher than 30 dB were truncated.

It can be observed from Fig. 9 that the attenuation of total potential energy under the potential energy control scheme is high when the frequency of the external sound wave is less than ω_{ac}. Peak attenuation of PE also occurs at some eigenfrequencies, such as $1.16\omega_{ac}$, $1.53\omega_{ac}$, and $2.52\omega_{ac}$, which correspond to the (0,1,0), (1,1,0), and (1,2,0) acoustic modes, respectively. As the frequency increases beyond $3\omega_{ac}$, the attenuation of PE is poor.

The squared pressure control at the above error sensor locations gives a basically similar PE attenuation trend as the potential energy control, but significant amplifications are observed at some frequencies. The ineffective PE attenuation at $1.53\omega_{ac}$ [the (1,1,0) acoustic mode] shown in Fig. 9(c) is due to the location of the error sensor being on two nodal planes (the middle point of the ceiling). Besides the spillovers at some eigenfrequencies, the detrimental effects of the squared pressure control at frequencies between the room modes occur when the error sensor is located near to the region where the acoustic modes due to the secondary source are destructively interfering with each other. These effects are commonly found and are more significant for near field error sensing strategies at frequencies below ω_{ac}. Typical examples are the large PE amplifications at the frequencies $0.3\omega_{ac}$, $0.6\omega_{ac}$, and ω_{ac} shown in Figs. 9(a), (b), and (c), respectively. The first detrimental effect occurs at lower frequency when the error sensor gets closer to the secondary corner source.[14] The detrimental effects become less significant or can be eliminated when the error sensor is located

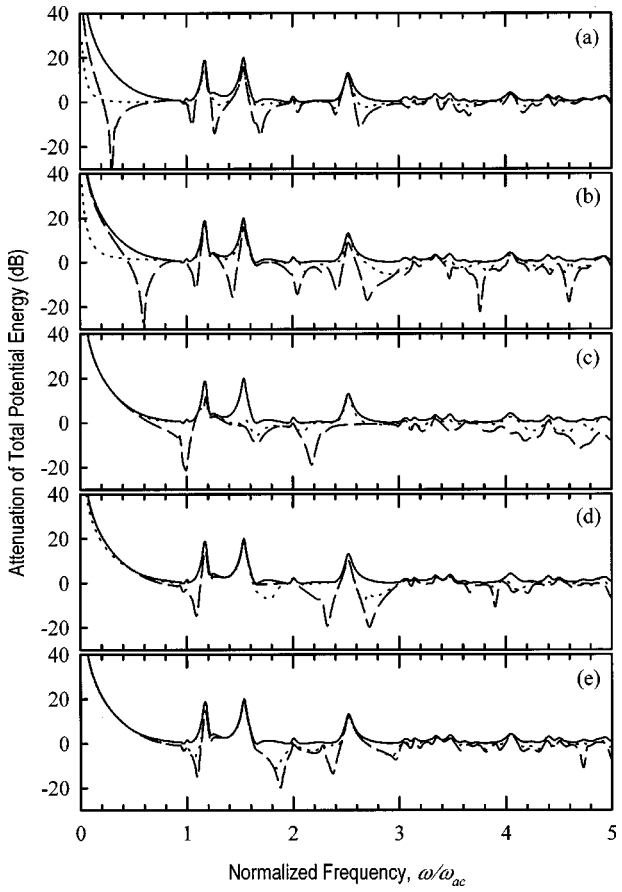

FIG. 9. Variation of total acoustic potential energy attenuation with frequency for primary acoustic source at $\theta=\pi/6$, $\alpha=\pi/4$ under various error sensor locations. (a) $(0.9L_{x1},0.9L_{x2},0.9L_{x3})$; (b) $(0.7L_{x1},0.7L_{x2},0.9L_{x3})$; (c) $(0.5L_{x1},0.5L_{x2},0.9L_{x3})$; (d) $(0.3L_{x1},0.3L_{x2},0.9L_{x3})$; (e) $(0.1L_{x1},0.1L_{x2},0.9L_{x3})$. —— Potential energy control; ——— squared pressure control; ——— energy density control. Secondary source at (L_{x1},L_{x2},L_{x3}); $\eta_c=0.01$ and $\varphi=1.04$.

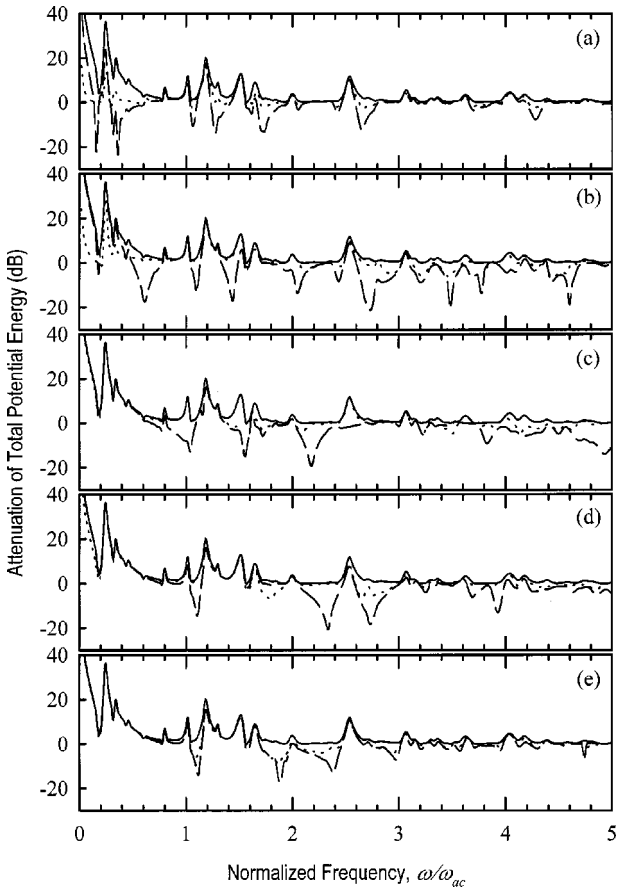

FIG. 10. Variation of total acoustic potential energy attenuation with frequency for primary acoustic source at $\theta=\pi/6$, $\alpha=\pi/4$ under various error sensor locations. (a) $(0.9L_{x1},0.9L_{x2},0.9L_{x3})$; (b) $(0.7L_{x1},0.7L_{x2},0.9L_{x3})$; (c) $(0.5L_{x1},0.5L_{x2},0.9L_{x3})$; (d) $(0.3L_{x1},0.3L_{x2},0.9L_{x3})$; (e) $(0.1L_{x1},0.1L_{x2},0.9L_{x3})$. Secondary source at (L_{x1},L_{x2},L_{x3}); $\eta_c=0.26$ and $\varphi=5.21$. Legends are the same as those in Fig. 9.

near to the corner opposite the secondary source due to the absence of destructively modal interference, as shown in Figs. 9(d) and (e), especially for frequency below ω_{ac}.[14]

The use of energy density as the cost function has the advantage of avoiding both detrimental effects and spillovers as suggested in Fig. 9, especially at frequencies below ω_{ac} for all error sensor locations investigated. This is expected, as the energy density control system is more heavily constrained. The particle velocities normal to the acoustically rigid walls of the enclosure vanish, and thus the particle velocities in the three orthogonal directions are zero at a corner of the rectangular enclosure. It can also be observed that the performance of the energy density control algorithm becomes closer to that of the squared pressure one as the error sensor is located towards the corner opposite to the secondary source [Figs. 9(d) and (e)], which is consistent with existing literature, for example, Cazzolato.[16] However, the energy density control becomes ineffective when the error sensor is placed closer to the secondary acoustic control source, due to the nonuniform energy density field produced solely by the secondary source, resulting in a small secondary source strength as shown by Lau and Tang[14] [Figs. 9(a) and (b)].

Basically similar results can be found for larger η_c $(=0.26)$ and φ $(=5.21)$ (that is, stronger acoustic-panel coupling), as shown in Fig. 10. However, the PE at frequencies near to $0.19\omega_{ac}(=\omega_{sc})$ is not effectively attenuated by all the three control algorithms even though they are far below ω_{ac} and the associated secondary acoustic source strength is high [Fig. 11(a)]. This is because of the ineffective generation of PE by the secondary acoustic source at ω_{sc}, as shown in Fig. 11(b), especially for $\omega_{sc}\ll\omega_{ac}$. Additional detrimental effects at frequency $0.16\omega_{ac}$ are observed for the squared pressure control as shown in Fig. 10(a) [cf. Fig. 9(a)], suggesting that near field error sensing is not suitable for the squared pressure control under strong acoustic-panel coupling.

It can be seen from Figs. 9 and 10 that the attenuation of PE becomes insignificant at frequencies higher than $3\omega_{ac}$ for all the three control algorithms discussed, while that under the squared pressure control shows the tendency of amplification. However, the coexistence of ''quiet zones'' and ''amplification zones'' is possible within an enclosure under the active control. Sometimes, a large global increase of the sound pressure level may occur when the quiet zones are improperly forced by the control scheme. Also, the sound field inside an enclosure is expected to be nonuniform. Be-

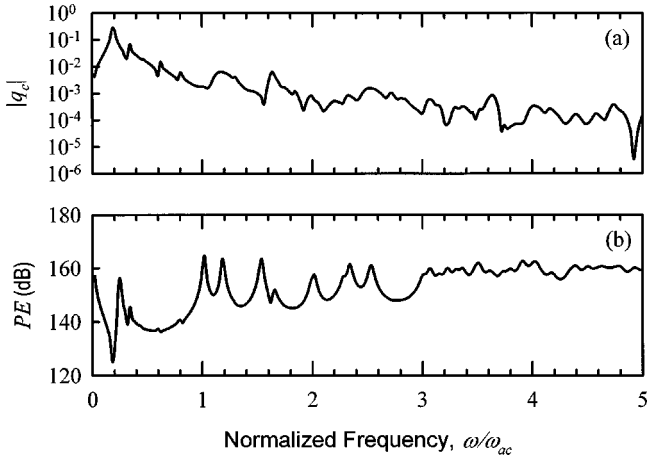

FIG. 11. (a) Secondary source strength of potential energy control for primary acoustic source at $\theta=\pi/6$, $\alpha=\pi/4$ and secondary source at (L_{x1},L_{x2},L_{x3}). (b) Total potential energy of acoustic source strength of unity at (L_{x1},L_{x2},L_{x3}). All data presented are in dB ref 10^{-12} Nm.

sides, the attenuation of sound pressure at all points inside an enclosed space is not necessary from the building services engineer's point of view, as only some portions of an enclosed space will be occupied by people. The creation of appropriate quiet zones is therefore more important. For example, it is desirable to produce quiet zones at noise-sensitive areas inside an enclosure, to reduce the impact of noise on workers in a plantroom. Also, the quiet zone in front of the walls will help to reduce the direct sound transmission. An understanding of the actual sound field under active control of sound transmission, especially at the low frequency range, is required for a detailed description of the effectiveness of the control algorithms.

V. VISUALIZATION OF SOUND ATTENUATION

As mentioned previously, the evaluation of a sound field under active control is of practical importance due to the limitation of the potential energy analysis. The visualization of a sound field inside the enclosure is decisive in the evaluation of the performance of the active control of sound, as it gives an idea of the distributions of the quiet and amplification zones, as well as the degree of their effects in the enclosure. In the present investigation, the numerical model is divided into $21\times21\times21$ uniform grid points throughout the enclosure, and the attenuation of the sound pressure level (SPL) is found from the difference between the calculated SPL before and after activating the acoustic secondary source by using Eq. (5).

Figure 12(a) shows the SPL attenuation at $\omega=0.3\omega_{ac}$ inside the enclosure with $\eta_c=0.01$ and $\varphi=1.04$ under the potential energy control. It can be observed that a high global reduction of SPL can be achieved at all points inside the enclosure. The peak quiet zone is located between the center of the enclosure and the flexible panel $(x2/L_{x2}=0)$. Such high global reductions of SPL are also found at even lower frequencies. At $\omega=0.7\omega_{ac}$, amplification zones appear near to the secondary source and on the $x1-x3$ wall on the side of the secondary source as shown in Fig. 12(b), though there is an attenuation of PE at this frequency (Fig. 9). The corresponding major quiet zone is found at the corner opposite to the acoustic control source. As the frequency increases beyond $0.7\omega_{ac}$, the quiet zones and the amplification zones are discretely distributed throughout the enclosure. At higher frequencies, the coexistence of quiet and amplification zones is observed, while the total potential energy attenuation is insignificant. An example is shown in Fig. 12(c), where $\omega=1.7\omega_{ac}$ (cf. Fig. 9). High global control of SPL can also be found at some eigenfrequencies [for instance, at $\omega=2.5\omega_{ac}$ as shown in Fig. 12(d)], but the quiet zones are observed at discretely confined areas inside the enclosure. Thus, the previous analysis of total potential energy can only effectively indicate the dominance of the quiet zones or the amplification zones. Figures 13(a) and (b) illustrate the sound pressure distributions at $\omega=1.7\omega_{ac}$ and $2.5\omega_{ac}$ without the active control, respectively. It can be observed that the amplification and the quiet zones under the active control do not col-

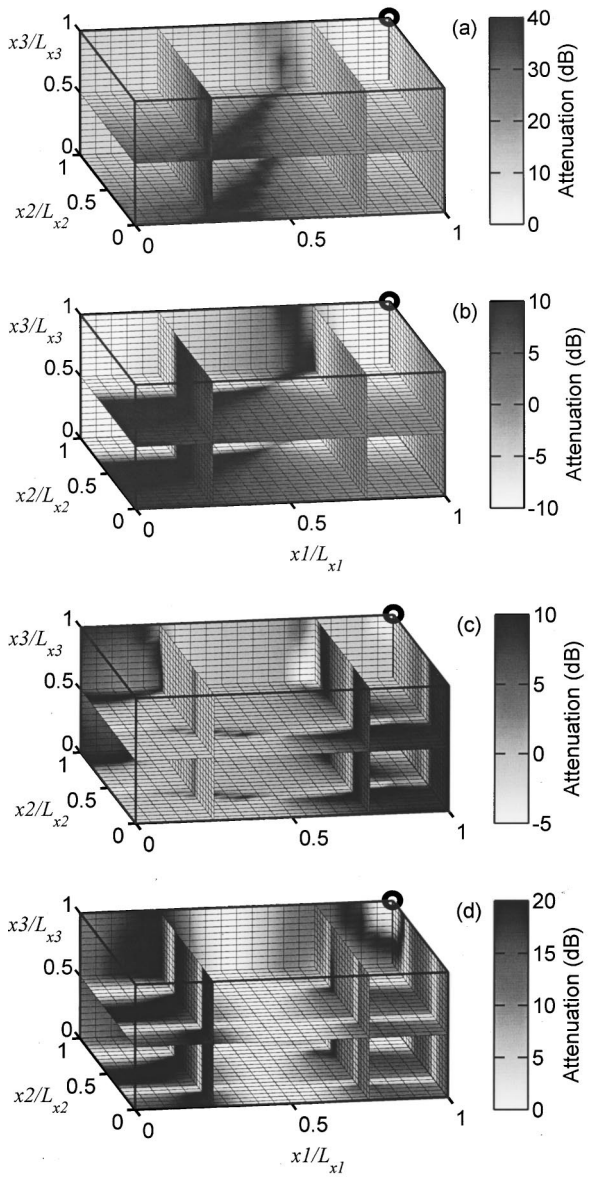

FIG. 12. Attenuation of SPL under potential energy control for primary source at $\theta=\pi/6$, $\alpha=\pi/4$ at different forcing frequencies. (a) $0.3\omega_{ac}$; (b) $0.7\omega_{ac}$; (c) $1.7\omega_{ac}$; (d) $2.5\omega_{ac}$. Secondary source at (L_x,L_y,L_z); $\eta_c=0.01$ and $\varphi=1.04$.

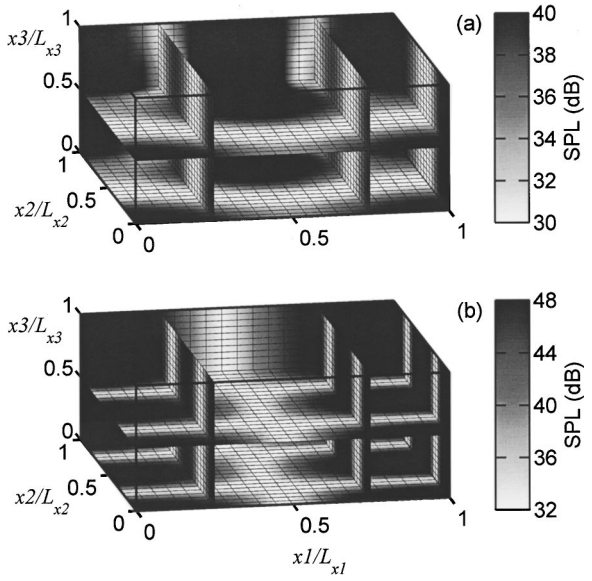

FIG. 13. SPL for primary source at $\theta=\pi/6$, $\alpha=\pi/4$ at different forcing frequencies. (a) $1.7\omega_{ac}$; (b) $2.5\omega_{ac}$. $\eta_c=0.01$ and $\varphi=1.04$. All data presented are in dB ref 2×10^{-5} N/m^2.

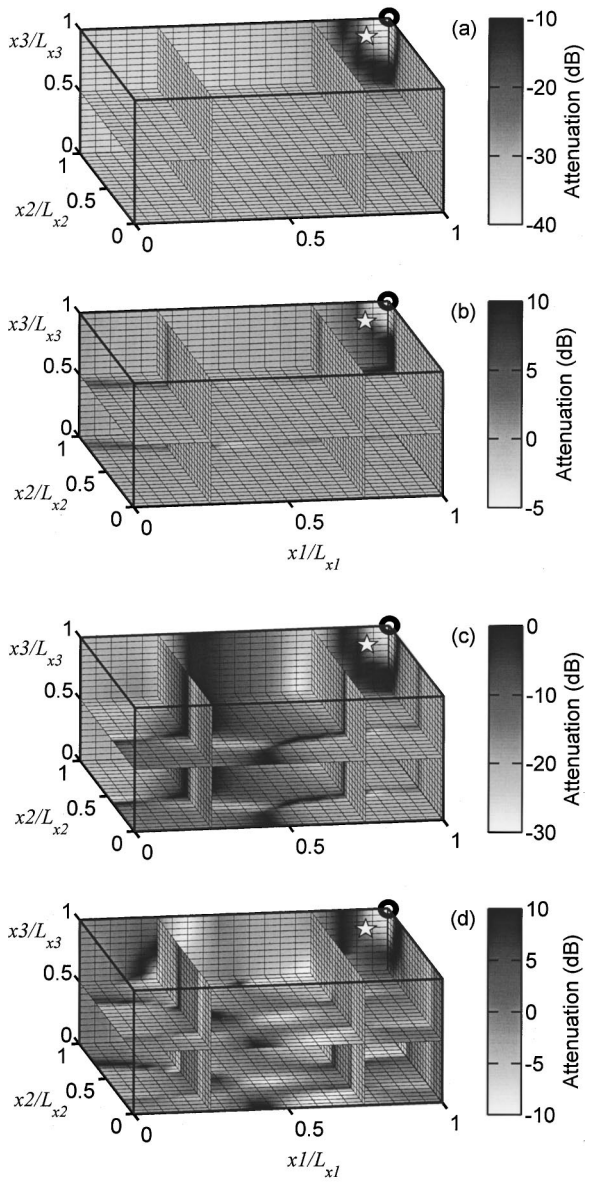

FIG. 14. Attenuation of SPL under squared pressure control for primary source at $\theta=\pi/6$, $\alpha=\pi/4$ at different forcing frequencies. (a) $0.3\omega_{ac}$; (b) $0.7\omega_{ac}$; (c) $1.7\omega_{ac}$; (d) $2.9\omega_{ac}$. Secondary source at (L_x,L_y,L_z); error sensor, ☆, at $(0.9L_x,0.9L_y,0.9L_z)$; $\eta_c=0.01$ and $\varphi=1.04$.

lapse with the nodal planes. No nodal plane is observed within the enclosure for $\omega<\omega_{ac}$. The magnitude of the sound field decreases at increased distance from the flexible panel wall.

Detrimental effects appear at some frequencies under the squared pressure control scheme as discussed before. This is due to the destructive interference of acoustic modes at the location of the error sensor.[14] A large increase of SPL throughout the enclosure can also be observed except at the location of the error sensor $(0.9L_{x1},0.9L_{x2},0.9L_{x3})$, as shown in Fig. 14(a) at $\omega=0.3\omega_{ac}$ [one of the detrimental effects shown in Fig. 9(a)]. Quiet zones reappear at $\omega=0.7\omega_{ac}$, as shown in Fig. 14(b). For increasing frequency beyond ω_{ac}, the quiet zones at the position of the error sensor quickly shrink in size, except at some acoustic mode frequencies as mentioned earlier. Detrimental effects are also observed at higher frequencies, resulting in a nearly global amplification [Fig. 14(c)]. In addition, discrete quiet zones and amplification zones occur as frequency increases beyond $2\omega_{ac}$. A typical example is shown in Fig. 14(d), with $\omega=2.9\omega_{ac}$.

The resultant SPL attenuation maps under the energy density control are similar to those under the squared pressure control, especially under remote error sensing. However, it is observed that the energy density control has the benefit of providing a more uniform SPL attenuation at most frequencies, and avoiding the occurrence of large localized attenuation in the expense of large sound amplifications at other locations. Since there is no significant attenuation produced by the energy density control due to small optimal secondary source strength for the error sensor near to the secondary source at frequency below $0.7\omega_{ac}$, the corresponding sound attenuation patterns are not discussed.

Figure 15 illustrates some examples of the SPL attenuation maps obtained under the energy density control with $\eta_c=0.01$ and $\varphi=1.04$. The error sensor is located at $(0.9L_{x1},0.9L_{x2},0.9L_{x3})$. It can be observed from Fig. 15(a) that the energy density control can provide SPL attenuation globally at $0.7\omega_{ac}$, while both the potential energy and the squared pressure controls produce amplification zones inside the enclosure [Figs. 12(b) and 14(b)]. The energy density control produce much less amplification of PE and SPL inside the enclosure at the frequencies of detrimental effects than the squared pressure control as shown in Fig. 15(b) $(\omega=1.7\omega_{ac})$. Again the amplification and the quiet zones do not collapse with the SPL nodal planes shown in Fig. 13.

For a stronger cavity-panel coupling system ($\eta_c=0.26$ and $\varphi=5.21$), though the attenuation of PE is small at $\omega=0.2\omega_{ac}$ (Fig. 10), global control of sound field and a quiet zone near to the secondary source under the potential energy control are still achievable as shown in Fig. 16(a). For frequencies below ω_{ac}, except for those near to $0.19\omega_{ac}$, wider quiet zone compared to that in Fig. 12(a) can be ob-

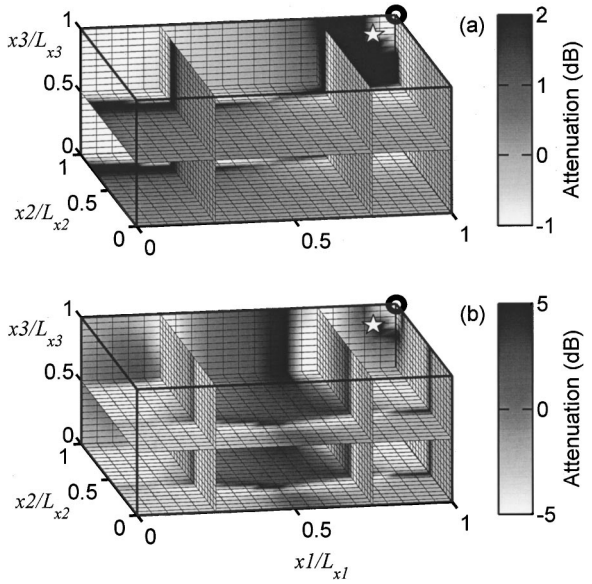

FIG. 15. Attenuation of SPL under energy density control for primary source at $\theta=\pi/6$, $\alpha=\pi/4$ at different forcing frequencies. (a) $0.7\omega_{ac}$; (b) $1.7\omega_{ac}$. Secondary source at (L_x, L_y, L_z); error sensor, ☆, at $(0.9L_x, 0.9L_y, 0.9L_z)$; $\eta_c=0.01$ and $\varphi=1.04$.

served with a stronger structural-acoustic coupled system as shown in Fig. 16(b) ($\omega=0.3\omega_{ac}$). The sound field pattern is similar to the previous system with $\eta_c=0.01$ and $\varphi=1.04$ as frequency increases, especially for $\omega>2\omega_{ac}$ (not shown here).

Figure 17(a) shows the SPL attenuation under the squared pressure control with near field error sensing at $(0.9L_{x1}, 0.9L_{x2}, 0.9L_{x3})$, with $\eta_c=0.26$, $\varphi=5.21$ and $\omega=0.3\omega_{ac}$ [one of the detrimental effects shown in Fig. 10(a)]. Amplification of SPL can be observed throughout the enclosure, except at the error sensor location, but it is much alleviated [cf. Fig. 14(a)] for the present stronger coupled system. For the remote error sensor at

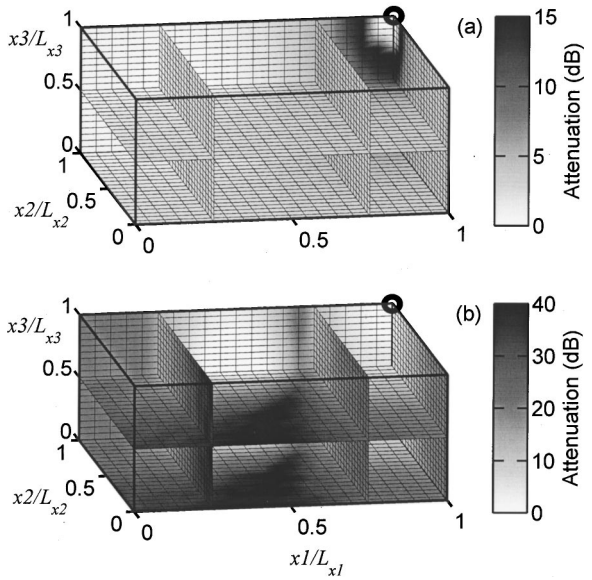

FIG. 16. Attenuation of SPL under potential energy control for primary source at $\theta=\pi/6$, $\alpha=\pi/4$ at different forcing frequencies. (a) $0.2\omega_{ac}$; (b) $0.3\omega_{ac}$. Secondary source at (L_x, L_y, L_z); $\eta_c=0.26$ and $\varphi=5.21$.

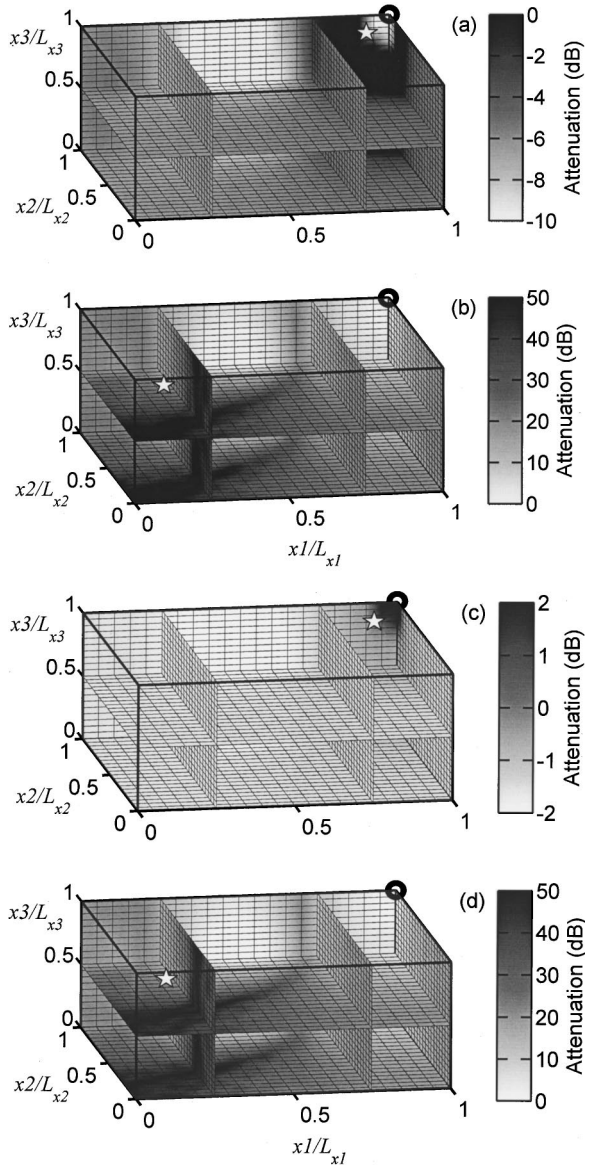

FIG. 17. Attenuation of SPL under squared pressure and energy density control algorithms for primary source at $\theta=\pi/6$, $\alpha=\pi/4$ at $0.3\omega_{ac}$. (a) Squared pressure control, error sensor at $(0.9L_x, 0.9L_y, 0.9L_z)$; (b) squared pressure control, error sensor at $(0.1L_x, 0.1L_y, 0.9L_z)$; (c) energy density control, error sensor at $(0.9L_x, 0.9L_y, 0.9L_z)$; (d) energy density control, error sensor at $(0.1L_x, 0.1L_y, 0.9L_z)$; secondary source at (L_x, L_y, L_z); $\eta_c=0.26$ and $\varphi=5.21$. ☆: error sensor location.

$(0.1L_{x1}, 0.1L_{x2}, 0.9L_{x3})$, higher SPL attenuation can be obtained at $0.3\omega_{ac}$ [as shown in Fig. 17(b)] under the squared pressure control compared with Fig. 17(a). Energy density control eliminates large amplification of sound pressures for near field error sensing at the frequencies of the detrimental effects, as shown in Fig. 17(c). In most cases studied, there is an inherent tendency for the squared pressure control to provide a high level of SPL attenuation at the error sensor locations, at the expense of SPL amplification at other areas, resulting in highly nonuniform noise attenuation, while the energy density control tends to minimize both potential (acoustic pressure) and kinetic (acoustic pressure gradient to a certain extent) energy density at error sensor locations and thus gives a more uniform control of sound field, especially at the frequency of detrimental effects as illustrated in Figs.

17(a) and (c). The resultant sound field under the energy density control with a remote error sensor is similar to that under the squared pressure control. Figure 17(d) gives a typical example of this phenomenon.

Snyder and Hansen[24] suggested that the optimum error microphone locations are the points of minimum sound pressure in the optimally controlled residual sound field created by a vibrating panel, while Ruckman and Fuller[25] proposed the locations to be at the antinodes of a vibrating cylindrical shell. Their studies evaluated the performance of active control in a free field. However, the problem becomes more complicated when the active sound transmission control inside an enclosure is concerned. Confusion exists between the nodal points and the points of minimum sound pressure under optimum control. In addition, different system performance may be found when the error sensing is done at the antinodes of sound pressure inside an enclosure (for example, see Figs. 9 and 10). Also, both the nodes and antinodes inside the enclosure cannot be easily predicted for frequencies other that the eigenfrequencies. For all the cases investigated in the present study, it is observed that forcing the quiet zone by the squared pressure control with error sensor located at the amplification zones or areas of low SPL attenuation under the potential energy control will increase SPL at other areas adversely. A typical example is shown in Fig. 17(a), where the error sensor is located near to the point of minimum SPL attenuation under the potential energy control [Fig. 16(b)]. In turn, placing the error sensor near to the peak quiet zones of potential energy control results in much better performance of global control effectiveness [Fig. 17(b)]. Though the present finding is obtained in an enclosure, it appears in line with those of free field control.[24] Similar results can be obtained for other combinations of θ and α.

In general, the acoustic energy density field is more uniform than the sound field inside the enclosure. Thus, the performance of the energy density control is less dependent on the error sensor locations than the squared pressure control. This has been proved by Parkins *et al.*[18] through an investigation of node structures. However, unsatisfactory energy density control and squared pressure control may still be found in some areas of nonuniform energy density field inside the enclosure, besides the nodal volumes.[14] Figure 18 shows the attenuation of the energy density inside the enclosure under the potential energy control at $0.7\omega_{ac}$ and $1.7\omega_{ac}$ with $\eta_c=0.01$ and $\varphi=1.04$. Large amplification of energy densities at the positions near to the secondary acoustic source can be observed for all cases in the present study, due to the secondary acoustic source.[14] While the energy density fields inside most areas in the enclosure are uniform (Fig. 19), the high energy density at $(0.9L_{x1},0.9L_{x2},0.9L_{x3})$ lowers the performance of the energy density control as shown previously in Figs. 9(a) and 10(a) if the error sensor is located there. Placing the error sensor, for instance, at $(0.1L_{x1},0.1L_{x2},0.9L_{x3})$, which is the location of high energy density attenuation under the potential energy control (Fig. 18), produces better PE attenuation [Figs. 9(e) and 10(e)] and sound field control [Fig. 17(d)] under the energy density error sensing scheme.

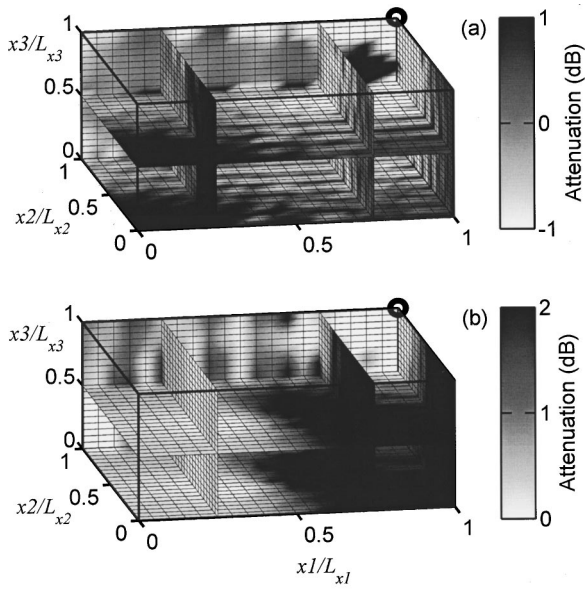

FIG. 18. Attenuation of energy density under potential energy control for primary source at $\theta=\pi/6$, $\alpha=\pi/4$ at different forcing frequencies. (a) $0.7\omega_{ac}$; (b) $1.7\omega_{ac}$. Secondary source at (L_x,L_y,L_z); $\eta_c=0.01$ and $\varphi=1.04$.

VI. CONCLUSIONS

This study investigates the effectiveness of active control of sound transmission into a slightly damped rectangular enclosed space. The performance of three different control algorithms, namely the potential energy control, the squared pressure control, and the energy density control, are investigated and compared in terms of the overall potential energy attenuation and the resultant sound pressure level attenuation patterns. A compact matrix formulation of the analytical steady-state solution under the energy density control is derived based on the application of the impedance-mobility

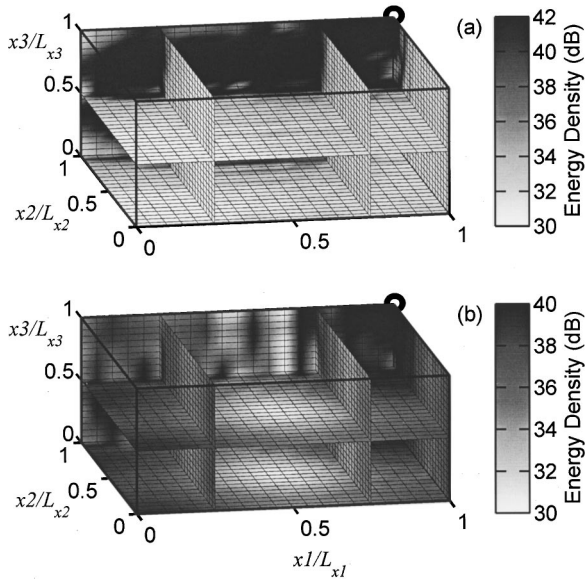

FIG. 19. Energy density under potential energy control for primary source at $\theta=\pi/6$, $\alpha=\pi/4$ at different forcing frequencies. (a) $0.7\omega_{ac}$; (b) $1.7\omega_{ac}$. Secondary source at (L_x,L_y,L_z); $\eta_c=0.01$ and $\varphi=1.04$. All data presented are in dB ref 10^{-12} N/m^2.

approach to a fully structural-acoustic coupled system. The frequency range in the present study extends to five times the first eigenfrequency of the enclosure.

Two control categories are classified in the potential energy analysis. One is for the case where the first eigenfrequency of the acoustic (cavity) mode is less than that of the structural (panel) mode, while the other is the opposite. For both categories, high potential energy attenuation under potential energy control can be achieved for driving frequency below the first resonance frequency of the structural mode, while for the latter, acoustic control source is also effective at the frequency beyond this structural mode frequency, but is ineffective at this frequency. Active vibration control is shown to be ineffective in the cavity-controlled modes.

It is shown that both quiet zones and amplification zones are created under all the control algorithms investigated, except at frequencies far below the first eigenfrequency of the cavity. High global reduction of the sound level can also be obtained at some acoustic eigenfrequencies under the potential energy control, but the quiet zones are discrete. In general, the potential energy control gives the best performance among the control algorithms studied, but it is difficult to implement.

Detrimental effects have been observed under the squared pressure control of sound transmission due to the inherent destructive modal interference at the position of the error sensor. At the frequencies of the detrimental effects, extremely localized sound attenuation with global amplification of the sound level is found. This adverse effect can be alleviated by remote error sensing or by applying the energy density control. The energy density control has the advantage of fewer detrimental effects than squared pressure control. It is ineffective for near field sensing due to nonuniform energy density near to the secondary source. However, the energy density control can eliminate the disadvantages of both detrimental effects and spillovers, and can provide a more uniform attenuation of sound pressures. For remote error sensing strategy, the squared pressure and the energy density controls give similar resultant sound fields.

Sound and energy density fields under the potential energy control give the preferential error sensor locations for the creation of quiet zones under the squared pressure and energy density controls, which cannot be found from the potential energy analysis of previous studies. Forcing the quiet zones of the squared pressure and energy density controls at the amplification zones of the potential energy control has adverse effects on the sound attenuation, resulting in ineffective active sound transmission control. Also, maximum performance of active control can be found when the error sensor is located at the peak quiet zones and peak energy density attenuation zones under the potential energy control for the squared pressure and the energy density controls respectively.

To conclude, the results obtained in the present study address some issues which, to the knowledge of the authors, are not fully addressed by the existing literature. They show clearly the inadequacy of the use of the total potential acoustic energy as a measure of three-dimensional active sound transmission control performance, especially when the driving frequency is higher than the first eigenfrequency of the enclosure. Large global increase of sound field is observed when localized quiet zones are improperly forced. This can hardly be indicated in the traditional potential energy attenuation plots. This paper also suggests an analysis of the global and local effectiveness of active sound transmission control using visualization of the sound field in conjunction with the total acoustic potential energy attenuation. Besides, it is shown that the optimal error sensor locations for the squared pressure and energy density controls can then be found from the resultant sound fields and energy density fields under the potential energy control scheme, respectively. Moreover, it is illustrated that the acoustic control source is worthwhile for practical use, especially for active sound transmission control. Finally, it is found that in general, for stronger structural-acoustic coupling systems, wider quiet zones and alleviated detrimental effects can be found compared with the weak structural-acoustic coupling systems. A more detailed investigation concerning the effects of the strength of structural-acoustic coupling on the performance of active control would be worthwhile.

ACKNOWLEDGMENTS

The financial support of the Hong Kong Polytechnic University and the Research Grant Council, HKSAR Government is gratefully acknowledged.

[1] P. Scuri, *Design of Enclosed Spaces* (Chapman and Hall, New York, 1995).
[2] C. R. Fuller and J. D. Jones, ''Experiments on reduction of propeller induced interior noise by active control of cylinder vibration,'' J. Sound Vib. **112**, 389–395 (1987).
[3] J. Pan, C. H. Hansen, and D. A. Bies, ''Active control of noise transmission through a panel into a cavity: I. Analytical study,'' J. Acoust. Soc. Am. **87**, 2098–2108 (1990).
[4] J. Pan and C. H. Hansen, ''Active control of noise transmission through a panel into a cavity: II. Experimental study,'' J. Acoust. Soc. Am. **90**, 1488–1492 (1991).
[5] J. Pan and C. H. Hansen, ''Active control of noise transmission through a panel into a cavity: III. Effect of the actuator location,'' J. Acoust. Soc. Am. **90**, 1493–1501 (1991).
[6] X. J. Qiu, J. Z. Sha, and J. Yang, ''Mechanisms of active control of noise transmission through a panel into a cavity using a point force actuator on the panel,'' J. Sound Vib. **182**, 167–170 (1995).
[7] B. S. Cazzolato and C. H. Hansen, ''Active control of sound transmission using structural error sensing,'' J. Acoust. Soc. Am. **104**, 2878–2889 (1998).
[8] S. D. Snyder and C. H. Hansen, ''The design of systems to control actively periodic sound transmission into enclosed spaces, part I: Analytical models,'' J. Sound Vib. **170**, 433–449 (1994).
[9] S. D. Snyder and C. H. Hansen, ''The design of systems to control actively periodic sound transmission into enclosed space, part II: Mechanisms and trends,'' J. Sound Vib. **170**, 451–472 (1994).
[10] S. M. Kim and M. J. Brennan, ''A comparative study of feedforward control of harmonic and random sound transmission into an acoustic enclosure,'' J. Sound Vib. **226**, 549–571 (1999).
[11] P. Joseph, S. J. Elliott, and P. A. Nelson, ''Near field zones of quiet,'' J. Sound Vib. **172**, 605–627 (1994).
[12] S. D. Sommerfeldt and P. J. Nashif, ''An adaptive filtered-x algorithm for energy-based active control,'' J. Acoust. Soc. Am. **96**, 300–306 (1994).
[13] Y. C. Park and S. D. Sommerfeldt, ''Global attenuation of broadband noise fields using energy density control,'' J. Acoust. Soc. Am. **101**, 350–359 (1997).
[14] S. K. Lau and S. K. Tang, ''Sound fields in a slightly damped rectangular enclosure under active control,'' J. Sound Vib. **238**, 637–660 (2000).
[15] A. Sampath and B. Balachandran, ''Studies on performance functions for interior noise control,'' Smart Mater. Struct. **6**, 315–332 (1997).

[16] B. S. Cazzolato, ''Sensing systems for active control of sound transmission into cavities,'' Ph.D. thesis, The University of Adelaide, Australia, 1999.
[17] S. M. Kim, ''Active control of sound in structural-acoustic coupled systems,'' Ph.D. thesis, University of Southampton, United Kingdom, 1998.
[18] J. W. Parkins, J. Tichy, and S. D. Sommerfeldt, ''A comparison of two active control methods through an investigation of node structures,'' Proc. ACTIVE 99 **2**, 729–740 (1999).
[19] P. Joseph, S. J. Elliott, and P. A. Nelson, ''Statistical aspects of active control in harmonic enclosed sound fields,'' J. Sound Vib. **172**, 629–655 (1994).
[20] P. A. Nelson and S. J. Elliott, *Active Control of Sound* (Academic, London, 1992).
[21] D. Roylance, *Mechanics of Materials* (Wiley, New York, 1996).
[22] S. M. Kim and M. J. Brennan, ''A compact matrix formulation using the impedance and mobility approach for the analysis of structural-acoustic system,'' J. Sound Vib. **223**, 97–113 (1999).
[23] A. J. Bullmore, P. A. Nelson, A. R. D. Curtis, and S. J. Elliott, ''The active minimization of harmonic enclosed sound field, part II: computer simulation,'' J. Sound Vib. **117**, 15–33 (1987).
[24] S. D. Snyder and C. H. Hansen, ''Using multiple regression to optimize active noise control system design,'' J. Sound Vib. **148**, 537–542 (1991).
[25] C. E. Ruckman and C. R. Fuller, ''Optimizing actuator locations in active noise control systems using subset selection,'' J. Sound Vib. **186**, 395–406 (1995).

General scales of community reaction to noise (dissatisfaction and perceived affectedness) are more reliable than scales of annoyance

R. F. S. Job[a] and J. Hatfield
Department of Psychology, University of Sydney, Sydney 2006, Australia

N. L. Carter and P. Peploe
National Acoustic Laboratories, Chatswood 2079, Australia

R. Taylor and S. Morrell
Department of Public Health, University of Sydney, Sydney 2006, Australia

(Received 21 March 2000; revised 29 November 2000; accepted 15 May 2001)

General measures of reaction to noise, which assess the respondent's perceived affectedness or dissatisfaction, appear to be more valid and internally consistent than more narrow measures, such as specific assessment of noise annoyance. However, the test–retest reliability of general and specific measures has yet to be compared. As a part of the large-scale Sydney Airport Health Study, 97 respondents participated in the same interview twice, several weeks apart. Test–retest reliabilities were found to be significant ($p<0.001$) for two general questions and three specific ''annoyance'' questions. The general measures were significantly more valid for four of the six correlations (with activity disturbance), and more stable than the annoyance scales for five of the six possible test–retest comparisons. Amongst 1015 respondents at Time 1, the questions regarding general reaction were more internally consistent than the questions regarding annoyance. Taken together, these data indicate that general measures of reaction to noise have superior psychometric properties (validity, internal consistency, and stability) compared with measures of specific reactions such as annoyance.
 [DOI: 10.1121/1.1385178]

PACS numbers: 43.50.Sr, 43.50.Qp, 43.50.Lj [MRS]

I. INTRODUCTION

Socioacoustic investigations aim to further understanding of negative reaction (which may include dissatisfaction, annoyance, anger, frustration, disappointment, and/or distress: see Job, 1993) by examining the relationships of various measures of reaction with noise exposure, and with other noise-related attitudes and effects, among people exposed to noise. Typically, one or more of the following purposes are served:

(1) Establishing which noise exposure index best predicts reaction, such that this index may be most appropriately employed for regulatory purposes (e.g., Bradley and Johan, 1979: compared 25 indices; Bullen *et al.*, 1991: 9 indices; Fields and Walker, 1982: 44 indices; and Job *et al.*, 1991: considered 88 indices).
(2) Plotting the relationship between noise exposure and negative reaction, in order to judge ''acceptable'' noise levels (for reviews see: Fidell *et al.*, 1991; Fields, 1994; Miedema and Vos, 1998; Schultz, 1978).
(3) Evaluating the effects of noise exposure mitigation measures (e.g., Narang *et al.*, 1995), and of changes in exposure (Brown *et al.*, 1985; Griffiths and Raw, 1986; Raw and Griffiths, 1990), on reaction.
(4) Elucidating the moderating role of reaction on the health outcomes of exposure to noise (for discussion see: Job, 1995, 1996).
(5) Understanding the causal mechanisms underlying reaction (e.g., dissatisfaction, annoyance) and other potential outcomes of noise exposure (e.g., cardiovascular disease, sleep disturbance) (see Fields, 1992; Hatfield *et al.*, in press; Job, 1993, 1995; Raw and Griffiths, 1990).

In order to meet these challenges, accurate (valid and reliable) measures of negative noise reaction are required. With more accurate reaction measures, noise/reaction relationships become more distinguishable (for the same sample size). Further, the statistical power for detecting reaction change following various mitigation measures (including changes in noise exposure), and for detecting relationships with various moderating factors, increases. In addition, real underlying correlations between variables may be evaluated by employing corrections for the reliability of their measurement as long as reliability is known (see Job, 1988b for examples of such calculations).

Thus, the more valid and reliable a measure of reaction, the more useful it is. Validity refers to the degree to which the measure actually assesses the variable it is designed to assess, and is usually evaluated employing correlations with established measures of the same variable or with theoretically relevant outcomes. Reliability takes two distinct forms: internal consistency and stability (or test–retest reliability). Internal consistency refers to the extent to which the separate

[a]Author to whom correspondence should be addressed; electronic mail: soamesj@psychvax.psych.su.oz.au

TABLE I. Internal consistency (average interitem correlation) for measures of reaction to noise as reported in socioacoustic surveys; specific reaction (annoyance) and general reaction (affectedness, dissatisfaction, bother).

Study	Noise Source	Annoyance reaction		General Reaction	
		No. of questions	Average r	No. of questions	Average r
Hede and Bullen, 1982a	Aircraft	3	0.79	2	0.82
Hede and Bullen, 1982b	Rifle range	4	0.80	2	0.86
Bullen and Hede, 1984	Artillery	3	0.73	2	0.78
Bullen *et al.*, 1991					
Bullen *et al.*, 1985	Military	5	0.40	2	0.78
Job *et al.*, 1991	Aircraft				
Bullen *et al.*, 1986	Aircraft	4	0.77	2	0.82
Job and Bullen, 1987	Power	3	0.54	2	0.80
Job and Hede, 1989	Station				
Jonah *et al.*, 1981	Traffic	21	0.53		
Nivison and Endresen, 1993	General	3	0.49		
Langdon and Griffiths, 1982	Traffic			2	0.72
O'Laughlin *et al.*, 1986	Rifle range			2	0.80
Average (s.d.)			*0.58(0.21)*		*0.81 (.03)*

items of a measure assess the same variable. It is usually evaluated employing Cronbach's alpha, or more simply, correlations between responses to separate questions within the one interview session. Stability refers to the extent to which the measure assesses the same variable across a significant time span. It is usually evaluated employing correlations of responses from one interview session with responses from a later interview session.

Typically, socioacoustic surveys have assessed reaction with a specific question involving annoyance: e.g. ''how *annoyed* are you by the noise from ... [the source—airplanes, trains, etc.]'', and consequently regulatory policy is often based on annoyance reactions. This measure has been criticized on the grounds of its reduced validity (Berglund and Lindvall, 1995; Job, 1993; Guski, 1997) and reliability (Bullen and Hede, 1983; Job, 1988a, 1991) relative to more general measures of reaction, such as perceived affectedness by, or dissatisfaction with, the noise.

Questions that ask only about annoyance, fail to measure many possible and important reactions to noise. For example, people may react to noise with anxiety, distraction, exhaustion, anger, frustration, disappointment, and fear. Data indicate that a general scale of reaction, incorporating questions about affectedness by, and dissatisfaction with, the noise, better captures overall reaction to noise than do annoyance questions (Hede *et al.*, 1979, in Job, 1993, p. 50). Thus, these general questions appear to be more valid measures of reaction. The validity of a measure is also indicated by the extent of its association with measures of other constructs to which it should be related, such as activity disturbance.

Reaction indices comprised of questions about general reaction (perceived affectedness and dissatisfaction) are also more internally consistent than indices comprised of questions about annoyance. A range of socioacoustic surveys have reported internal consistency for specific and global measures of reaction to noise (see Table I). On average, interitem correlations for general questions ($r=0.81$) are substantially higher than for the annoyance questions ($r=0.58$). Furthermore, of the six studies in Table I which included both measures, thus allowing for direct comparison of internal consistencies within the same sample, all found the internal consistency of the general scale to be higher than the annoyance scale.

The stability of general and specific measures of reaction has not yet been compared. The stability of questions regarding affectedness/dissatisfaction has been strikingly consistent (see Table II) and the average test–retest correlation of $r=0.60$ is adequate. Despite the frequent use of questions specifically measuring annoyance, the issue of their stability has been relatively neglected.

The present study compared measures of general reaction to noise (dissatisfaction and perceived affectedness) with specific measures of annoyance with the noise directly, in terms of stability (test–retest correlation), internal consistency (Cronbach's alpha, and interitem correlations), as well as validity (correlations with activity disturbance).

The importance of reaction. Negative reaction is one of the undisputed consequences of exposure to noise (for reviews see Fields, 1994; Job, 1988a; Job and Hatfield, 1998; Schultz, 1978), and understanding noise reaction is critical for several reasons. First, negative reaction itself constitutes a negative health factor within the World Health Organization's definition of health (as well-being, not just the absence of disease). People who are dissatisfied and annoyed, and

TABLE II. Stability (test–retest correlation) for measures of reaction to noise as reported in socioacoustic surveys; general reaction (affectedness, dissatisfaction, bother).

Study	Noise source	No. of questions	Interval	Stability
McKennell, 1963, 1978	Aircraft	1	Not known	0.63
Griffiths and Delazaun, 1976	Traffic	1	2 months	0.61
Langdon, 1978	Traffic	1	3 months	0.61
Griffiths *et al.*, 1980	Traffic		1 year	
dissatisfied		1		0.64
bothered		1		0.63
Hall and Taylor, 1982	Traffic	1	1 year	0.58
	Aircraft			0.53
Average (s.d.)				*0.60(0.04)*

who suffer disturbance to their daily activities (e.g., conversation, listening to music, watching television, reading, sleeping), clearly have reduced quality of life. Second, negative reaction to noise may contribute to other noise-induced health problems, such as self-reported symptoms (Graeven, 1974; Lercher, 1992; Tarnopolsky *et al.*, 1980; van Kamp, 1990) and objective measures of health (e.g., hypertension: Bluhm and Berglind, 1998; Cohen *et al.*, 1980; Melamed *et al.*, 1999; nervous stomach: Ohrstrom, 1989; allergies: Lercher, 1996a; use of medication: Lercher, 1996b; Knipschild and Oudschoorn, 1977; mental health problems: Kryter, 1990; Stansfeld, 1992). Further, several studies suggest that reaction to noise is a better predictor of several noise-related health effects than is noise exposure itself (e.g., antihypertensive treatment: Neus *et al.*, 1983; psychosocial well-being: Ohrstrom, 1989; nervous stomach: Ohrstrom, 1989; general health ratings: Lercher and Widmann, 1993). Although these studies were observational and so do not provide compelling evidence for causality, theoretical and empirical considerations suggest that reaction plays a causal role (for a review see Job, 1996).

II. METHOD

A. Subjects and sample selection

1015 respondents (51% female) over the age of 18 were included in the final sample, after 13.8% of residents who were initially approached refused to participate. Many Census Collection Districts were selected on the basis of noise exposure and location relative to Sydney (Kingsford Smith) Airport to produce a 2×2 design; current noise exposure was (1) ''high'' (mean exposure of 26.72 ANL, s.d.=6.75) or (2) ''low'' (mean exposure of 26.72 ANL, s.d.=2.52) and noise exposure was projected to either (1) decrease or increase (respectively), or (2) remain unchanged due to flight-path changes with the opening of the third runway and reduced operation of one of the existing runways (see Carter *et al.*, 1996). Random sampling procedures were employed and the four noise change areas produced by the design—''high to high'' (HH), ''high to low'' (HL), ''low to low′'' (LL), ''low to high'' (LH)—were approximately equally represented.

Of 1015 respondents, approximately 100 (25 in each noise change area) were randomly selected to be re-interviewed. This ''reliability sample'' comprised the 60 females and 37 males who were re-interviewed at Time 2.

B. Materials

A structured interview (based on previous socioacoustic survey questionnaires—see Bullen *et al.*, 1986; Job *et al.*, 1991; Langdon, 1976—and revised on the basis of the results of a pilot study) assessed reactions to noise, attitudes to the noise source, sensitivity to noise, noise-induced activity disturbance. Questions on physical and mental health were added.

Two questions assessed general reaction to aircraft noise: (i) ''Would you please...estimate how much you personally, are affected overall by aircraft noise?'' (ii) ''How dissatisfied are you with aircraft noise in this neighborhood? Please...estimate how much dissatisfaction you feel overall.''

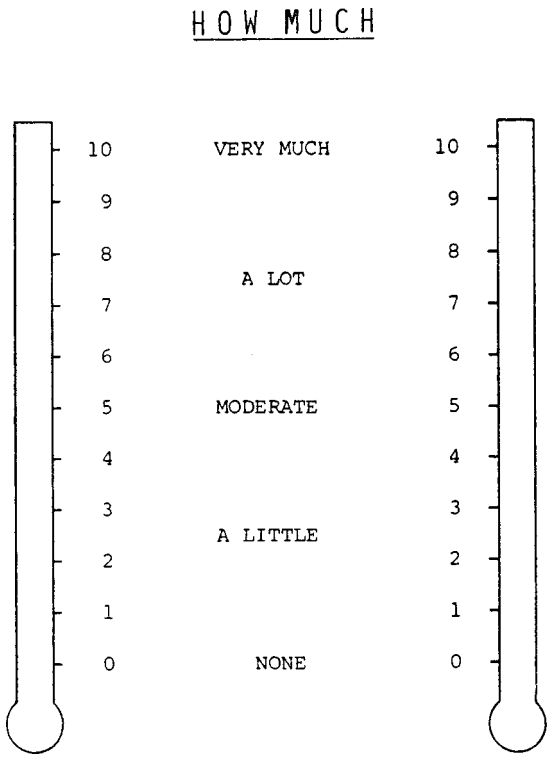

FIG. 1. ''Opinion thermometer'' with which responses to ANN1, ANN2, and general reaction (affectedness, dissatisfaction, bother) were made, in the Sydney Airport Health Study.

Three questions assessed annoyance with aircraft noise specifically: (i) ''How much annoyance do you feel when you hear a jet plane passing overhead?'' (ANN1); (ii) ''How much annoyance do you feel about aircraft noise?'' (ANN2); (iii) ''How would you describe your general feelings about the aircraft noise in this neighborhood?'' (ANN3). Response choices for this final question were ''highly,'' ''considerably,'' ''moderately,'' ''slightly,'' or ''not at all'' annoyed. For the remaining questions, subjects responded using an ''opinion thermometer''—a card depicting a thermometer marked with numbers from 1 to 10 and with an associated five-point verbal scale (2=''a little,'' 5=''moderate,'' 7=''a lot,'' 10=''very much''). [See Fig. 1]

These questions were placed individually through the questionnaire, and the first was asked before the survey had been identified as relating to noise. Thus, participants first responded to items relating to general neighborhood features. They were then asked to rate the extent to which they were annoyed by several everyday things: a list of noise situations of which ''a jet plane passing overhead'' was the third (ANN1). Only if subjects stated that the had *heard* ''aircraft noise'' in the next question, were they asked to rate their annoyance with this noise (ANN2). Only then were subjects told that ''this survey is particularly interested in how people in residential areas are affected by the noise from aircraft'' and asked to rate their affectedness by noise. Respondents giving a zero rating were not asked further questions on reaction. [It seems reasonable to assume that subjects who are annoyed by the noise would report being affected by it, so that subjects who do not report being affected at all can be assumed not to be annoyed. Thus, although ANN3 may be

slightly underestimated given that subject's reporting may not be consistent (see Fields *et al.*, 1997), this effect is probably not substantial.] Otherwise, several questions later respondents were asked ANN3, and then, after several further questions, rated their dissatisfaction.

Subjects were also asked to indicate whether local aircraft noise disturbs or interferes with 12 activities (e.g., conversation, watching TV, relaxing, household activities, entertaining). An activity disturbance index was computed by summing affirmative responses.

After being interviewed, subjects completed the Grossarth-Maticek health risk personality questionnaire (70 items) (Grossarth-Maticek and Eysenck, 1990) and the profile of mood states depression-dejection, tension-anxiety, and anger-hostility scales (19 items).

C. Procedure

Before the changes to the configuration of Sydney (Kingsford Smith) Airport, two interviews were conducted by trained interviewers at each subject's home.

1. Time 1

From a random starting point within each census collection district, every seventh residence along a predetermined path was approached. Further selections, e.g., of every eleventh residence, were made if the number of successful approaches within any census district did not reach the quota.

First, a letter was sent to every selected residence announcing the investigation. Second, interviewers door-knocked at selected residences and asked to speak to the person over 18 living at the residence who had last had a birthday. If this person had an inadequate command of English, was infirm, or was not a usual resident at the home, the residence was classified as ''out of range'' and no other person there interviewed. If the relevant person refused to participate no other resident was interviewed but one follow up call was made to the home in an attempt to obtain an interview with the initial respondent. If the relevant person was not present on any occasion the residence was classified as ''noncontact'' and up to five calls were made.

When a suitable individual agreed to participate, the structured interview was conducted and questionnaires given to the subject to complete while the interviewer waited (or returned at an agreed time).

2. Time 2

Six to twelve weeks after their initial interview, but still before runway configuration changes, selected Time 1 respondents were sent a letter announcing the intention to re-interview them and offering payment for participation.

Interviewers then knocked on the doors at these respondents' residences. Respondents who agreed to be re-interviewed participated in the structured interview and completed questionnaires in their homes.

D. Noise exposure measures

During the time interviews were being conducted (before the airport reconfiguration) aircraft noise was measured at numerous residential sites near flight paths in the vicinity of Sydney Airport. Mathematical noise models for aircraft arrivals and departures were developed from these measurements. These models allowed verification of the Integrated Noise Model (INM) program developed by the US Federal Aviation Administration when applied to Sydney Airport operations. The INM was then employed to produce aircraft noise exposure data (ANEI) for the sample areas and sample periods (see Peploe, 1996 for further details). ANEI paralleles NEF with a modified evening penalty (based on Australian reaction data, Bullen and Hede, 1983) of 6 dB between 7 pm and 7 am. Further, it is a measure of what has occurred rather than being a forecast. These noise data were geocoded to each participating residential address using Geographic Information System software.

TABLE III. Mean scores for measures of reaction to noise; specific reaction (annoyance: ANN1, ANN2, ANN3) and general reaction (affectedness, dissatisfaction), at Time 1 (whole sample, and reliability sample) and at Time 2, in the Sydney Airport Health Study.

	Time 1; whole sample	Time 1; reliability sample	Time 2; reliability sample
ANN1	5.86 (3.16)	6.11 (2.75)	6.23 (2.98)
ANN2	5.88 (3.36)	5.99 (3.18)	6.23 (3.08)
ANN3	2.85 (1.43)	2.79 (1.55)	2.74 (1.59)
Affected	5.60 (3.37)	5.49 (3.23)	5.52 (3.30)
Dissatisfied	4.99 (3.54)	5.02 (3.56)	5.15 (3.63)

III. RESULTS

A. Mean reaction scores

Means for ANN1, ANN2, ANN3, and the two general reaction questions at Time 1 (full sample, and reliability sample), and at Time 2, are reported in Table III.

Perceived affectedness, dissatisfaction, ANN1, and ANN2, are all measured on a ten-point scale where a higher score indicates more negative reaction. For ANN3, responses were made on a five-point scale.

Means and standard deviations were not appreciably different across the samples, particularly for the reliability sample at Time 1 compared to Time 2. In order to assess whether knowing the purpose of the survey influenced responses to ANN1, the mean at Time 1 was compared to the mean at Time 2, employing a repeated measures t-test. The means were not significantly different ($t_{192}=0.28$, $p=0.783$).

B. Construct validity (correlations with activity disturbance)

Employing the whole sample ($n=1015$), correlation coefficients of the activity disturbance index with each of the three annoyance questions, and with the two general reaction questions (assessing perceived affectedness and dissatisfaction) were compared (see Table IV). All five correlations were significant ($p<0.001$).

TABLE IV. Validity (correlations with activity disturbance) and stability (test–retest correlation) for measures of reaction to noise; specific reaction (annoyance: ANN1, ANN2, ANN3) and general reaction (affectedness, dissatisfaction), in the Sydney Airport Health Study.

Scale	Validity	Stability
ANN1	0.55	0.66
ANN2	0.64	0.72
ANN3	0.74	0.61
Affected	0.69	0.85
Dissatisfied	0.70	0.78

C. Comparison of correlations with activity disturbance for general versus specific measures

The correlation with activity disturbance of measures which assess annoyance about noise was compared with that (e.g. of measures which assess more general reactions to noise perceived affectedness), employing a two-tailed *z*-test.

Perceived affectedness had significantly higher construct validity than ANN1 ($z=4.65$, $p<0.001$) and ANN2 ($z=1.81$, $p<0.001$) but not ANN3 (means in a direction inconsistent with prediction). Dissatisfaction was significantly more valid than ANN1 ($z=6.59$, $p<0.001$) and ANN2 ($z=4.74$, $p<0.001$) but not ANN3 (means in a direction inconsistent with prediction).

Thus, overall, measures of general reaction to noise appear to be more valid than reaction measures phrased more specifically in terms of annoyance.

D. Stability (test–retest correlations)

Employing the ''reliability sample'' ($n=97$), correlation coefficients between Time 1 and Time 2 responses were calculated for each of the three annoyance questions, and the two general reaction questions (assessing perceived affectedness and dissatisfaction) (see Table IV). All five test–retest correlations were significant ($p<0.001$).

E. Comparison of test–retest correlations for general versus specific measures

The test–retest reliability (stability) of measures which assess annoyance about noise was compared with that of measures which assess more general reactions to noise (e.g. perceived affectedness), employing a two-tailed *z*-test.

Perceived affectedness was significantly more stable than each annoyance measure (ANN1: $z=3.17$, $p<0.001$; ANN2: $z=2.39$, $p<0.001$; ANN3: $z=3.75$, $p<0.000$). Dissatisfaction was significantly more stable than ANN1 ($z=1.73$, $p=0.042$) and ANN3 ($z=2.30$, $p=0.011$), but not ANN2 ($z=0.94$, $p=0.174$).

Thus, measures of general reaction to noise appear to be more stable than reaction measures phrased more specifically in terms of annoyance.

F. Internal consistency (Cronbach's alpha and interitem correlations

Internal consistency was assessed for the two general reaction questions (assessing perceived affectedness and dissatisfaction) and for the three specific annoyance questions, employing the Time 1 responses of the total sample ($N=1015$).

For the two general reaction questions Cronbach's alpha was 0.92, and the interitem correlation was 0.85. For the three specific annoyance questions Cronbach's alpha was 0.85 and the average interitem correlation was 0.75.

G. Comparison of interitem correlations for annoyance with aircraft noise versus aircraft overflight

People may be very annoyed when a jet aircraft passes overhead, without being annoyed with aircraft noise generally. Thus, the annoyance question which asks about overflight (ANN1) may not correlate as well with each of the other annoyance questions as they correlate with one another.

The correlation of ANN1 with ANN2 and with ANN3 ($r=0.79$, $r=0.67$, respectively) was compared with the correlation of ANN2 with ANN3 ($r=0.77$), employing a one-tailed *z*-test.

The correlation between ANN2 and ANN3 was significantly greater than the correlation between ANN1 and ANN3 ($z=4.50$,$p<0.001$), but did not differ significantly from the correlation between ANN1 and ANN2 (difference in the direction opposite to the prediction that the correlations involving ANN1 would be smaller).

H. Comparison of interitem correlations for general versus specific measures

The average interitem correlation (internal consistency) of the three specific annoyance questions was compared with the interitem correlation of the two general reaction questions, employing a two-tailed *z*-test. Internal consistency was significantly greater for the two general reaction questions than for the three specific annoyance questions ($z=6.61$, $p<0.001$).

In view of the results of the preceding section we also compared the interitem correlation of the two general reaction questions with the correlation between ANN2 and ANN3. Internal consistency as significantly greater for the two general reaction questions than for the three specific annoyance questions ($z=3.42$, $p<0.001$).

IV. DISCUSSION

The present study demonstrated that measures of general reaction to aircraft noise are more valid and reliable (stable and internally consistent) than more specific measures of annoyance with aircraft noise.

It was argued earlier that measures of reaction to noise which are phrased in general terms are likely to be more valid indicators of overall reaction than those which refer specifically to only a single aspect of potential reaction. Consistent with this claim, in the present study, measures of perceived affectedness by, and dissatisfaction with, aircraft noise demonstrated high correlations with activity disturbance, which lends support to their construct validity. Correlations were generally significantly higher for the measures of general reaction than for annoyance measures. However,

ANN3 demonstrated the highest correlations with activity disturbance. Interestingly, in this question respondents rate their ''general feelings'' about aircraft noise, and annoyance is referred to only in the responses scale.

Measures of perceived affectedness by and dissatisfaction with aircraft noise also demonstrated high test–retest correlations. The test–retest correlations for these general measures were significantly higher than were the test–retest correlations for each of three questions assessing annoyance with noise.

Of course changes in reaction may occur (possibly in response to changes in noise levels), such that test–retest correlations less than 1.00 do not imply errors in measurement. However, substantial systematic changes in noise levels are unlikely to have occurred between Time 1 and Time 2 measurements, both of which occurred before runway reconfiguration. Further, we might reasonably expect people to consider a more extended period of time (e.g., 1 year) when forming their answer, so that minor changes in the 6- to 12-week interval should have little effect. Finally, true change in reaction ought not to influence specific and general questions differentially. Thus, the higher test–retest correlations for general rather than for specific measures, is appropriately attributable to their greater reliability.

The conclusion that general reaction measures are also more internally consistent than measures of annoyance alone (see Table I), was replicated in the present study. The interitem correlation for two general reaction questions was significantly higher than the average interitem correlation for three specific annoyance questions, despite the tendency for a greater number of items to increase reliability. The internal consistency of both reaction measures was high.

Although test–retest and interitem correlations are likely to be inflated by the wide variance in noise exposure across the sample (Hall and Taylor, 1982), specific and general measures of reaction are likely to have been equally affected. Thus, the observed superiority of the general measure in terms of stability and internal consistency is likely to be genuine.

Several methodological considerations are relevant to the validity of these findings. First, there is a greater proportion of females in the reliability sample than in the larger sample, and so the reliability sample may not be representative of the general population. However, gender has a limited influence on reaction (Fields, 1992; Hatfield *et al.*, 1998), and in the present study levels of reaction do not appear to be substantially different for the reliability sample, compared to the whole sample. Second, the fact that respondents could have been aware of the purpose of the survey when they responded to ANN1 for the second, but not the first, time, may have influenced the reliability findings. Again, responses to ANN1 did not differ significantly from Time 1 to Time 2, and responses on the two occasions were highly correlated (see ''stability'' findings). Thus, the present findings should be valid and general.

The present study considered only reactions to aircraft noise. However, the higher internal consistency of general measures has been demonstrated in relation to several noise sources (see Table I). Plausibly, general reaction measures should also be more stable than specific measures, because they are likely to be less susceptible to momentary changes in any one aspect of reaction to noise than are measures which focus on only one aspect. This prediction is supported by the present examination. Furthermore, when the coefficient of determination is calculated from the relevant correlations (yielding the percentage of variance which is genuine variance rather than error) the differences between the general reaction and annoyance scales are of practical significance. For example, the mean test–retest reliability for the annoyance scale produces a substantially lower percentage of genuine variance than for the general scale ($r^2=0.440$ vs $r^2=0.664$). Thus, 22 percentage points more of the variance in the general scale is genuine variance.

The present data on the reliability of these measures may also be used to evaluate real underlying correlations between variables. For example, the extent to which the true variance of activity disturbance is related to reaction may be calculated using the following formula:

$$r_{\infty r}=r_{nr}/\sqrt{r_{nn}},$$

where $r_{\infty r}$ is the correlation between the activity disturbance and reaction with correction for the reliability of activity disturbance, r_{nr} is the obtained correlation between activity disturbance and reaction, and r_{nn} is the reliability coefficient of the activity disturbance index (adapted from Guilford, 1954, pp. 400–401). Thus, the lowest correlation between reaction and activity disturbance ($r=0.55$) reflects a true correlation of 0.81, when the stability of the activity disturbance index ($r=0.46$) is taken into account.

In sum, measures of general reaction (e.g., dissatisfaction and perceived affectedness) appear to be more stable, internally consistent, and valid than measures which assess only a single component of the potential reaction to noise (such as annoyance). General measures should thus allow a more accurate evaluation of dose–response relationships, a more accurate prediction of the behavioral and health outcomes of exposure to noise, and a more accurate assessment of noise mitigation tactics. Socioacoustic studies of reaction to noise should therefore incorporate measures of general reaction to noise as well as, or instead of, measures of annoyance.

ACKNOWLEDGMENT

This research was supported by funds from the Federal Airports Corporation (of Australia).

Berglund, B., and Lindvall, T. (**1995**). *Community Noise* (Archives of the Center for Sensory Research, Stockholm).

Bluhm, G., and Berglind, N. (**1998**). ''Traffic noise and health effects,'' in *Noise Effects. Proceedings of the Seventh International Congress on Noise as a Public Health Problem*, edited by N. L. Carter and R. F. S. Job (Noise Effects, Inc., Sydney, Australia), pp. 247–250.

Bradley, J. S., and Jonah, B. A. (**1979**). ''The effects of site selected variables on human response to traffic noise. 1. Type of housing by traffic noise level,'' J. Sound Vib. **66**, 589–604.

Brown, A. L., Hall, A., and Kyle-Little, J. (**1985**). ''Response to a reduction in traffic noise exposure,'' J. Sound Vib. **98**, 235–246.

Bullen, R. B., and Hede, A. J. (**1983**). ''Reliability and validity of reaction variables in community noise research,'' *Proceedings of the Fourth International Congress of Noise as a Public Health Problem*, pp. 1105–1114.

Bullen, R. B., and Hede, A. J. (**1984**). ''Community response to impulsive noise: A survey around Holdsworthy Army range,'' National Acoustic Laboratories Commissioned Report No. 3 (Australian Government Publishing Service, Canberra).
Bullen, R. B., Hede, A. J., and Job, R. F. S. (**1991**). ''Community reaction to noise from an artillery range,'' Noise Control Eng. J. **37**, 115–128.
Bullen, R. B., Hede, A. J., and Kyriacos, E., (**1986**). ''Reaction to aircraft noise in residential areas around Australian airports,'' J. Sound Vib. **108**, 199–225.
Bullen, R. B., Job, R. F. S., and Burgess, D. H. (**1985**). ''Reaction to Aircraft Noise on RAAF Bases,'' National Acoustic Laboratories Commissioned Report No. 7 (Australian Government Publishing Service, Canberra).
Carter, N. L., Job, R. F. S., Peploe, P., and Morrell, S. (**1996**). ''Response to major changes in runway configuration, operating procedures, and aircraft noise at Sydney Airport,'' edited by F. A. Hill and R. Lawrence, in *Proceedings of InterNoise 96, Liverpool* (Institute of Acoustics, St. Albans, UK), pp. 2311–2316.
Cohen, S., Evans, G. W., Krantz, D. S., and Stokols, D. (**1980**). ''Physiological, motivational, and cognitive effects of aircraft noise on children: Moving from the laboratory to the field,'' Am. Psychol. **35**, 231–243.
Fidell, S., Barber, D. S., and Schultz, T. J. (**1991**). ''Updating a dosage-effect relationship for the prevalence of annoyance due to general transportation noise,'' J. Acoust. Soc. Am. **89**, 221–233.
Fields, J. M. (**1992**). ''Effect of personal and situational variables on noise annoyance: With special reference to en route noise,'' NASA CR-189670, Hampton, VA.
Fields, J. M. (**1994**). ''A review of an updated synthesis of noise/annoyance relationships,'' NASA CR-194950, Hampton, VA.
Fields, J. M. *et al.* (**1997**). ''Guidelines for reporting core information from community noise reaction surveys,'' J. Sound Vib. **206**, 685–695.
Fields, J. M., and Walker, J. G. (**1982**). ''The response to railway noise in residential areas in Great Britain,'' J. Sound Vib. **8**, 177–255.
Graeven, D. B. (**1974**). ''The effects of airplane noise on health: An examination of three hypotheses,'' J. Health Soc. Behav. **15**, 336–343.
Griffiths, I. D., and Delazaun, F. R. (**1976**). ''Individual differences in sensitivity to traffic noise: An empirical study,'' J. Sound Vib. **55**, 93–107.
Griffiths, I. D., Landgon, F. J., and Swan, M. A. (**1980**). ''Subjective effects of traffic noise exposure: Reliability and seasonal effects,'' J. Sound Vib. **71**, 227–240.
Griffiths, I. D., and Raw, G. J. (**1986**). ''Community and individual response to changes in traffic noise exposure,'' J. Sound Vib. **111**, 209–217.
Grossarth-Maticek, R., and Eysenck, H. J. (**1990**). ''Personality, stress and disease: Description and validation of a new inventory,'' Psychol. Rep. **66**, 355–373.
Guilford, J. P. (**1954**). *Psychometric Methods* (Tata McGraw–Hill, Bombay).
Guski, R. (**1997**). ''Conceptual, methodological, and dose-response problems related to annoyance and disturbance,'' *Proceedings of Inter-Noise 97* (OPAKFI, Budapest), pp. 1077–1082.
Hall, F. L., and Taylor, S. M. (**1982**). ''Stability of social survey data on noise effects,'' J. Acoust. Soc. Am. **72**, 1212–1221.
Hatfield, J., Job, R. F. S., Carter, N. L., Peploe, P., Taylor, R., and Morrell, S. (**in press**). ''The influence of psychological factors on self-reported physiological effects of noise,'' Noise and Health.
Hatfield, J., Job, R. F. S., Peploe, P., Carter, N. L., Taylor, R., and Morrell, S. (**1998**). ''Demographic variables may have a greater modifying effect on reaction to noise when noise exposure changes,'' edited by N. L. Carter and R. F. S. Job, in *Noise Effects '98: Proceedings of the Seventh International Congress on Noise as a Public Health Problem, Sydney, Australia, November, 1998*, pp. 527–530.
Hede, A. J., Bullen, R. B., and Rose, J. A. (**1979**). ''A social study of the nature of subjective reaction to aircraft noise,'' National Acoustics Laboratories Report No. 79 (Australian Government Publishing Service, Canberra).
Hede, A. J., and Bullen, R. B. (**1982a**). ''Aircraft noise in Australia: A survey of community reaction,'' National Acoustic Laboratories Report No. 88 (Australian Government Publishing Service, Canberra, ACT).
Hede, A. J., and Bullen, R. B. (**1982b**). ''Community reaction to noise from a suburban rifle range,'' J. Sound Vib. **82**, 39–49.
Job, R. F. S. (**1988a**). ''Community response to noise: A review of factors influencing the relationship between noise exposure and reaction,'' J. Acoust. Soc. Am. **83**, 991–1001.
Job, R. F. S. (**1988b**). ''Over-reaction to changes in noise exposure: The possible effect of attitude,'' J. Sound Vib. **126**, 550–552.
Job, R. F. S. (**1991**). ''Internal consistency and stability of measurements of community reaction to noise'', Transportation Research Record, 1312 (Australian Government Publishing Service, Canberra, ACT).
Job, R. F. S., Bullen, R. B., and Burgess, D. H. (**1991**). ''Noise induced reaction in a work community adjacent to aircraft runways: The Royal Australian Airforce,'' edited by A. Lawrence, in *Proceedings of InterNoise 91: The Cost of Noise* (Noise Control Foundation, Poughkeepsie, NY), pp. 895–898.
Job, R. F. S. (**1993**). ''The role of psychological factors of community reaction to noise,'' edited by M. Vallet, in *Proceedings of the Sixth International Congress on Noise as a Public Health Problem* (INRETS, Arcueil Cedex, France), pp. 469–472.
Job, R. F. S. (**1995**). ''Measuring annoyance and other personal reactions to noise,'' edited by M. Newman, in *Proceedings of the 15th International Congress on Acoustics, Trondheim* (Acoustical Society of Norway, Trondheim, Norway), pp. 287–290.
Job, R. F. S. (**1996**). ''The influence of subjective reactions to noise on health effects of the noise,'' Environ. Int. **22**, 93–104.
Job, R. F. S., and Bullen, R. B. (**1987**). ''The effects of a face to face interview versus a group administered questionnaire in determining reaction to noise in the workplace,'' J. Sound Vib. **116**, 161–168.
Job, R. F. S., Bullen, R. B., and Burgess, D. H. (**1991**). ''Noise induced reaction in a work community adjacent to aircraft runways: The Royal Australian Airforce,'' edited by A. Lawrence, in *Proceedings of InterNoise 91: The Cost of Noise* (Noise Control Foundation, Poughkeepsie, NY), pp. 895–898.
Job, R. F. S., and Hatfield, J. (**1998**). ''Community reaction to noise,'' Acoust. Australia **26**, 35–39.
Job, R. F. S., and Hede, A. J. (**1989**). ''Community reaction to noise from power stations,'' edited by G. C. Maling, Jr., in *Proceedings of Inter-Noise 89* (Noise Control Foundation, New York), pp. 865–868.
Jonah, B. A., Bradley, J. S., and Dawson, N. E. (**1981**). ''Predicting individual subjective responses to traffic noise,'' J. Appl. Psychol. **66**, 490–501.
Knipschild, P. V., and Oudshoorn, N. (**1977**). ''Medical effects of aircraft noise: Drug survey,'' Int. Arch. Occup. Environ. Health **40**, 197–200.
Kryter, K. D. (**1990**). ''Aircraft noise and social factors in psychiatric hospital admission rates: A re-examination of some data,'' Psychol. Med. **20**, 395–411.
Langdon, F. J. (**1976**). ''Noise nuisance caused by road traffic in residential areas,'' J. Sound Vib. **47**, 243–282.
Langdon, F. J. (**1978**). ''Reliability of estimates of annoyance with road traffic noise,'' in *Proceedings of the Third International Congress on Noise as a Public Health Problem, Feiburg, West Germany,* pp. 567–570.
Langdon, F. J., and Griffiths, I. D. (**1982**). ''Subjective effects of traffic noise exposure. II. Comparisons of noise indices, response scales, and the effects of changes in noise levels,'' J. Sound Vib. **83**, 171–180.
Lercher, P. (**1992**). ''Auswirkung des Strassenverkehrs auf Lebensqualitaet und Gesundheit'' (Amt der Tiroler Landesregierung, Innsbruck).
Lercher, P. (**1996a**). ''Environmental noise and health: An integrated research perspective,'' Environ. Int. **22**, 117–129.
Lercher, P. (**1996b**). ''Road traffic noise, self medication, and prescriptions: A community study,'' edited by F. A. Hill and R. Lawrence, in *Proceedings of InterNoise 96, Liverpool* (Institute of Acoustics, St. Albans, UK), pp. 2171–2176.
Lercher, P. and Widmann, U. (**1993**). ''Factors determining community response to road traffic noise,'' edited by M. Vallet, in *Proceedings of the Sixth International Congress on Noise as a Public Health Problem* (INRETS, Arcueil Cedex, France), pp. 201–204.
McKennell, A. C. (**1963**). ''Aircraft noise annoyance around London (Heathrow) Airport,'' UK Govt. Survey Report No. S5337.
McKennell, A. C. (**1978**). ''Annoyance from Concorde flights around Heathrow,'' in *Proceedings of Third International Congress of Noise as a Public Health Problem,* pp. 562–566.
Melamed, S., Kristal-Boneh, E., and Froom, P. (**1999**). ''Industrial noise exposure and risk factors for cardiovascular disease: Findings from the CORDIS Study,'' Environ. Int. **4**, 49–56.
Miedema, H., and Vos, H. (**1998**). ''Exposure-respnose relationships for transportation noise,'' J. Acoust. Soc. Am. **104**, 3432–3445.
Narang, P. P., Butler, K. R., Schull, J. L., and Job, R. F. S. (**1995**). ''Sound insulation of residences exposed to aircraft noise,'' Report to the Department of Transport, Canberra (Australian Government Publishing Service, Sydney).

Neus, H., von Eiff, A.-W., Ruddel, H., and Schulte, W. (**1983**). ''Traffic noise and hypertension. The Bonn traffic noise study,'' edited by G. Rossi, in *Proceedings of the Fourth International Congress on Noise as a Public Health Problem* (Centro Richerche E. Studi Amplifon, Milano, Italy), pp. 694–698.
Nivison, M. E., and Endresen, I. M. (**1993**). ''An analysis of the relationships among environmental noise, annoyance and sensitivity to noise and the consequences for health and sleep,'' J. Behav. Med. **16**, 257–276.
Ohrstrom, E. (**1989**). ''Sleep disturbance, psycho-social and medical symptoms: A pilot survey among persons exposed to high levels of road traffic noise,'' J. Sound Vib. **133**, 117–128.
O'Laughlin, B. J., Bullen, R. B., Hede, A. J., and Burgess, D. H. (**1986**). ''Community reaction to noise from Williamstown rifle range,'' National Acoustic Laboratories Commissioned Report No. 9 (Australian Government Publishing Service, Canberra, ACT).
Peploe, P. (**1996**). ''Sydney Airport Health Study—Assessment and Calculation of Aircraft Noise Exposure,'' National Acoustics Laboratories Commissioned Report No. 133 (National Acoustic Laboratories, Sydney).
Raw, G. J., and Griffiths, I. D. (**1990**). ''Subjective response to changes in road traffic noise: A model,'' J. Sound Vib. **141**, 43–54.
Schultz, T. J. (**1978**). ''Synthesis of social surveys on noise annoyance,'' J. Acoust. Soc. Am. **64**, 377–405.
Stansfeld, S. A. (**1992**). ''Noise, noise sensitivity and psychiatric disorder: Epidemiological and psychophysical studies,'' Psychol. Med., Monograph Suppl. 22.
Tarnopolsky, A., Hand, D. J., Barker, S. M., and Jenkins, L. M. (**1980**). ''Aircraft noise, annoyance, and mental health: A psychiatric viewpoint,'' edited by J. V. Tobias, G. Jansen, and W. D. Ward, *Proceedings of Noise as a Public Health Problem* (ASHA, Rockville, MD), Report 10, pp. 588–594.
Van Kamp, I. (**1990**). *Coping with Noise and its Health Consequences* (Styx and PP Publications, Groningen).

Spatial fluctuations in measures for spaciousness

Diemer de Vries, Edo M. Hulsebos, and Jan Baan
Laboratory of Acoustic Imaging and Sound Control, Department of Applied Physics, Faculty of Applied Sciences, Delft University of Technology, P. O. B. 5046, 2600 GA Delft, The Netherlands

(Received 31 May 2000; revised 13 March 2001; accepted 4 April 2001)

In room acoustics, several measures have been defined that are supposed to quantify the apparent source width (ASW) in a hall, being one of the perceptual cues related to spaciousness. The most common ones are the lateral energy fraction (LF), i.e., the ratio between lateral and omnidirectional early energy, and the interaural cross correlation coefficient (IACC), all to be calculated from measured or simulated impulse responses. [Several versions of the LF are known in literature, having different names, generalized here as lateral energy fraction.] According to a method proposed by Berkhout *et al.* [J. Acoust. Soc. Am. **102**, 2757–2770 (1997)], for a fixed source position impulse responses have been measured along an array of closely spaced microphone positions in several halls. The above measures, when calculated from these impulse responses, show large fluctuations with small variations in microphone position due to interference of the different components of the wave field to which the human ear is apparently insensitive. A revision of the measures is discussed, which contributes to the suppression of the interference effects. In order to assess their perceptual significance, the fluctuations have to be related to just-noticeable differences (jnd's) in ASW. Since very different jnd values are given in the literature, the authors advise that new experiments should be conducted on this point.
[DOI: 10.1121/1.1377634]

PACS numbers: 43.55.Gx, 43.55.Hy, 43.55.Br [JDQ]

I. INTRODUCTION

Many authors[1–7] have reported that the common room acoustics measures show significant variations with small spatial displacements of source or microphone. Bradley *et al.*,[1] and also Pelorson,[2] found that for all measures considered, in all halls investigated, a 30-cm displacement leads to significant variations. Nielsen *et al.*[4] find 1.4–3.2-dB differences for clarity index C80 values measured at eight points inside a single seat. Based on such results, most workers choose to determine the measures at numerous positions scattered over a hall, and calculate hall averages and standard deviations of the measures to describe the hall's acoustic quality. It then appears[2] that discrimination between halls with quite different geometrical characteristics—and probably quite different acoustic quality—is difficult and sometimes even not possible with these measures.

Apparent source width (ASW), together with envelopment determining the perception of spaciousness, is recognized as one of the most important subjective measures for estimating the acoustic quality of a concert hall or opera house. The interaural cross-correlation coefficient (IACC) and the lateral energy fraction (LF) have been devised as objective measures to quantify ASW. Recently, Okano *et al.*[6] determined specific versions of IACC and LF in several concert halls, including the Amsterdam Concertgebouw. They found that the variations in these measures over individual positions within one hall are of equal or larger order than the variations of average values between different halls.

In the publications referred to above, the measure variations are only described and discussed in a statistical way. This gives very little insight into the physical causes of these variations, except that it must have something to do with interference. Berkhout *et al.*[8] introduced multichannel array technology in room acoustical analysis: impulse responses are measured along a hall-wide closely spaced (0.05-m) array of microphone positions, along which one microphone is mechanically moved. It appears that observation of all measured responses in one display reveals their spatial coherence and gives ample insight into the wave structure of the sound field (see Fig. 3 of Ref. 8). Besides, calculation of room acoustic measures for each array position enables deterministic investigation of their spatial variations.

Okano *et al.* end their paper[6] with the remark that ''they welcome the results of further research on the strengths and weaknesses of LFs as an acoustic measure of real halls.'' Inspired by this quote, the authors decided to investigate, using array measurements and simulations, the spatial behavior of LF and also of the other ASW measures that Okano *et al.* discuss in their paper. The starting point was a multichannel response measured in the Amsterdam Concertgebouw.

II. OKANO *ET AL.*'s ASW MEASURES IN THE CONCERTGEBOUW

The authors measured 555 impulse responses in the Amsterdam Concertgebouw along an array of microphone positions with 0.05-m intervals over almost the full hall width (27.7 m), with an omnidirectional loudspeaker placed center-front stage. From all these impulse responses, the same ASW measures have been calculated as discussed by Okano *et al.*[6] First, there is the early lateral energy fraction LF_E as defined by Hidaka *et al.*[3] as

$$LF_E = \frac{\int_{0.005}^{0.080} p_8^2(t)\,dt}{\int_0^{0.080} p^2(t)} = \frac{\int_{0.005}^{0.080} p^2(t)\cos^2\phi\,dt}{\int_0^{0.080} p^2(t)}, \qquad (1)$$

where $p_8(t)$ is the sound pressure measured by a figure-8 microphone with the null axis pointed to the source, and $p(t)$ the sound pressure measured by an omnidirectional microphone at the same position. Note that the figure-8 microphone weighs the squared pressure—being a measure of sound energy—with $\cos^2\phi$, where ϕ is the azimuthal angle between the direction of incidence of a sound wave and the line through the microphone axis. The early lateral energy fraction as originally proposed by Barron and Marshall[9] contains a weighting factor $\cos\phi$ for the energy. For reasons of measurement simplicity, LF_E according to Eq. (1) is usually applied instead. Following Okano *et al.*, from each impulse response LF_E has been calculated for the octave bands of 125, 250, 500, and 1000 Hz, respectively. Also, the average of these four values (denoted by Okano *et al.* as LF_{E4}) has been determined, as well as the broadband value LF_{bb} calculated over the full four-octave signal bandwidth. [The authors measured the multichannel impulse response with a Soundfield SPS 422 microphone, which not only records the sound pressure, but also the three components of the particle velocity vector. This enables the synthesis of the figure-8 microphone necessary to calculate the numerator of LF_E during data processing.] Figure 1 shows the results as a function of microphone offset, i.e., the lateral coordinate with respect to the array center. It should be noted that one seat encompasses about ten data points. It is seen that, for the octave band values, the fluctuations show an almost-periodicity with offset, resembling an amplitude-modulated carrier wave. The ''carrier period'' decreases with frequency. In the band-averaged and broadband versions, this ''carrier wave look'' disappears.

The fluctuating behavior of the measures can be deterministically related to the wave field measured along the array. To this end, the first 80 ms *re* first arrival of each impulse response is Fourier transformed to the frequency domain. Figure 2 shows the ''acoustic fingerprint'' that results when the ''early amplitude spectra'' of all traces are displayed as a function of microphone offset. It is seen that for each frequency the data show a small-scale periodicity due to interference; the spatial wavelength slowly but monotonically decreases with increasing frequency, as expected. Within one octave band, the spatial wavelength variation is so small that the periodicity of the wave field, and of the energy-based acoustic measures derived from it, is maintained. When averaging over a broad frequency band, the fluctuations tend to cancel out.

The average values over the array do not strongly deviate from the hall-averaged values given in Ref. 6, Table III. Numerous seats can be found where the LF_E octave band values show fluctuations of about 0.15 around an average between 0.10 and 0.25. For the band-averaged and the broadband versions, the fluctuations per seat decrease to about 0.10 around averages between 0.20 and 0.30. For offsets around zero, fluctuations are much higher for all bands and bandwidths. This is to be expected, since in this area the strong specular side-wall reflections interfere. If one wants to avoid this area, one should place the microphone at least 2 m off the center line for the low-frequency bands, which is significantly less than the 5 m mentioned by Okano *et al.* For

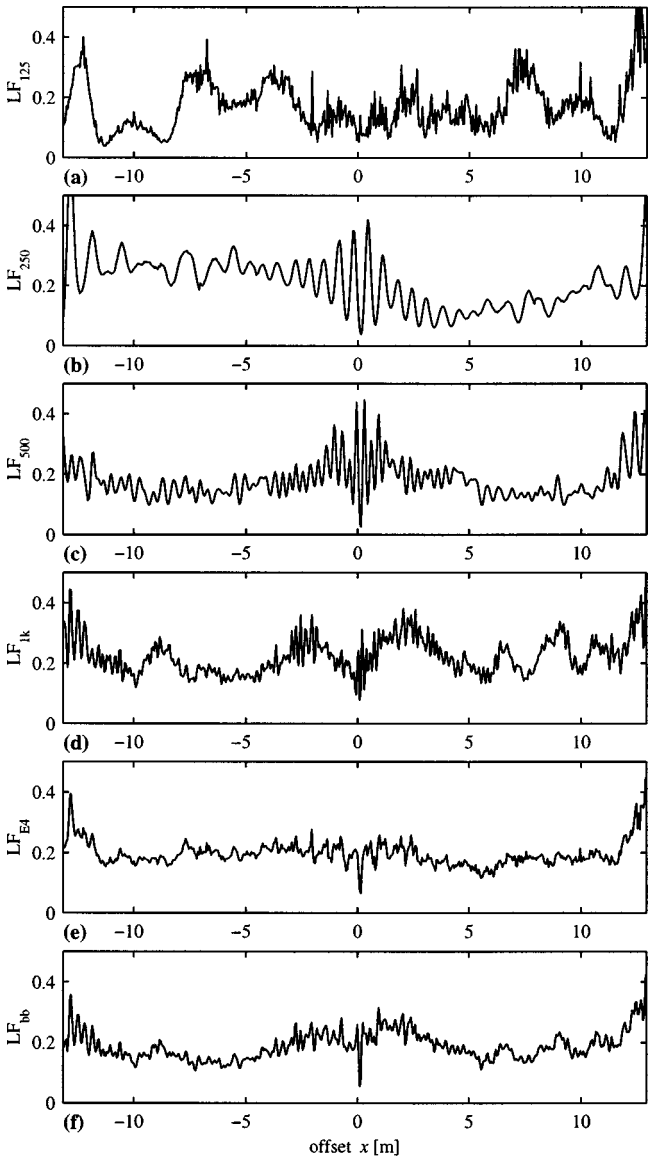

FIG. 1. Early lateral energy fractions calculated from the impulse responses measured in the Amsterdam Concertgebouw. From top to bottom, the values for the octave bands of 125, 250, 500, and 1000 Hz, the average value LF_{E4}, and the value for the full bandwidth are displayed as a function of microphone offset.

the band-averaged and the broadband versions, the behaviors of which show high similarity, an offset as small as 1 m is sufficient.

The second measure considered is the interaural cross-correlation coefficient IACC, introduced by Schroeder[10] and Ando[11] as the maximum within the delay time interval $|\tau| \leqslant 1$ ms of the crosscorrelation function $\rho_{lr}(\tau)$ between the pressures $p_l(t)$ and $p_r(t)$ at the left and right ear, respectively, of a real or dummy head, calculated over a time window $t_2 - t_1$

$$\rho_{lr}(\tau) = \frac{\int_{t_1}^{t_2} p_l(t)\, p_r(t+\tau)\, dt}{\sqrt{\int_{t_1}^{t_2} p_l^2(t)\, dt \int_{t_1}^{t_2} p_r^2(t)\, dt}}. \tag{2}$$

IACC has been calculated from binaural impulse responses measured with a KEMAR dummy head, being moved along the 555 array positions specified above. Fol-

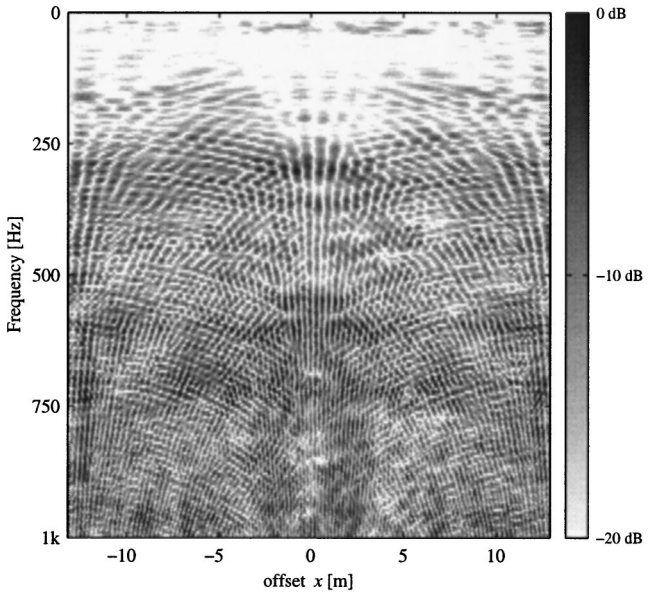

FIG. 2. The early amplitude spectra of the impulse responses measured in the Amsterdam Concertgebouw, obtained after Fourier transformation of the data between 0 and 80 ms *re* first arrival, as a function of microphone offset.

lowing again Okano *et al.*, the ''early'' 1-IACC between 0 and 80 ms (denoted by Okano *et al.* as 1-$IACC_E$) was calculated for the octave bands of 500, 1000, and 2000 Hz, respectively; the results are displayed as a function of dummy head offset in Fig. 3. Also, the average of the three octave band values is shown (denoted by Okano *et al.* as 1-$IACC_{E3}$), as well as the broadband version 1-$IACC_{bb}$ calculated over the full three-octave source bandwidth. As for LF_E, the values averaged over the array do not strongly deviate from the hall-averaged values given in Ref. 6, Table III. The fluctuations over a seat width are of the order 0.1, for all bands and bandwidths, around averages which strongly depend on frequency and bandwidth. As expected from the response pattern, also here the fluctuations are larger for the offsets around zero. To avoid this area, the microphone should be placed no less than 1 m off-center; this corresponds to the prescription given by Okano *et al.* There is a high similarity between the behavior of the band-averaged and the broadband version.

The results of this section confirm that there are large variations in the values of common measures for ASW, not only between seats in the same hall, but also at different positions at one and the same seat. [In deviation from the definition given in Eq. (1), the synthesized figure-8 microphone was always oriented in parallel with the array instead of with its null towards the source. This, however, does not affect the general conclusions following.] Octave band versions of LF_E and 1-$IACC_E$ fluctuate so strongly that their predictive value for ASW is highly questionable; band-averaged or broadband versions are preferred. But, the fluctuations in these versions also give rise to further questions. Given the fact that a listener in a concert hall will, in general, not perceive any change in ASW when he moves his head over a few centimeters, the difference limen in LF of 0.07, as indicated by Barron and Marshall[9] apparently does not hold in this situation. It seems that the measures considered are

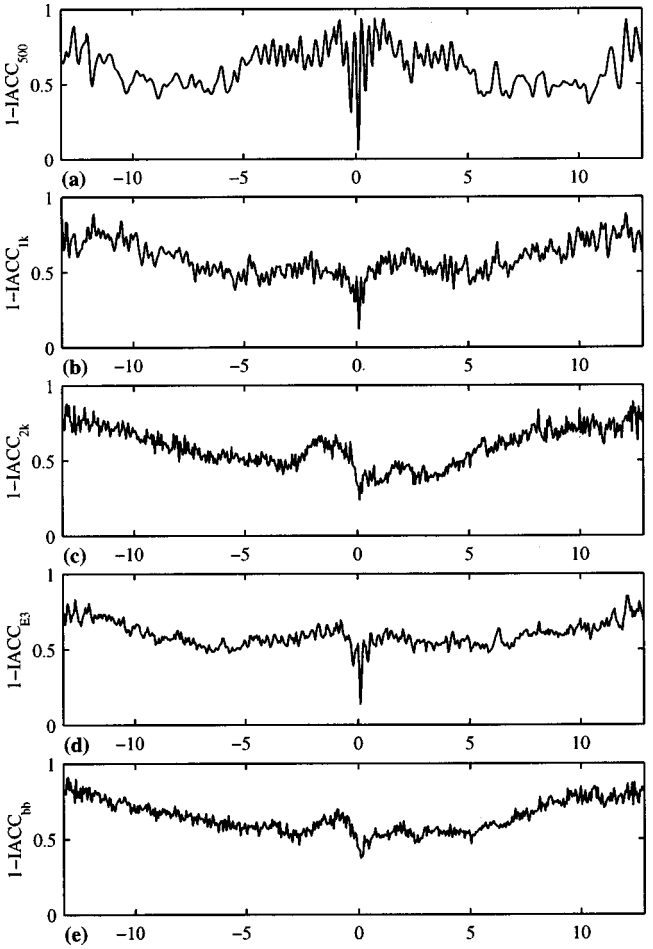

FIG. 3. 1-IACC calculated from binaural impulse responses measured in the Amsterdam Concertgebouw. From top to bottom, the values for the octave bands of 500, 1000, and 2000 Hz, the average value 1-$IACC_{E3}$, and the value for the full bandwidth are displayed as a function of dummy-head offset.

sensitive to local interference phenomena, where listeners are not, which suggests the formulation of new versions of these measures. This will be worked out in the following sections.

III. WEIGHTED BROADBAND VERSIONS OF ASW MEASURES

The strict time window boundary of 80 ms used in the early measures discussed above causes a discontinuity in the results: strong early reflections may suddenly disappear from the dataset when moving the microphone to the next array position. Therefore, in the following a smoothing time window $w(t)$ will be applied

$$w(t)=\begin{cases}1 & \text{for } 0<t<60 \text{ ms} \\ \cos^2 \pi(t-60)/80 & \text{for } 60<t<100 \text{ ms.}\end{cases} \tag{3}$$

In the previous section it was shown that determination of ASW measures after octave band filtering of impulse responses leads to large fluctuation of the resulting values. This fluctuation is smaller for broadband versions. Therefore, in the following only broadband measures will be considered, i.e., calculated over the full frequency range which is dominant for ASW perception. Potter *et al.*[12] showed that the dominant cues for spatial impression are found in the 500-Hz

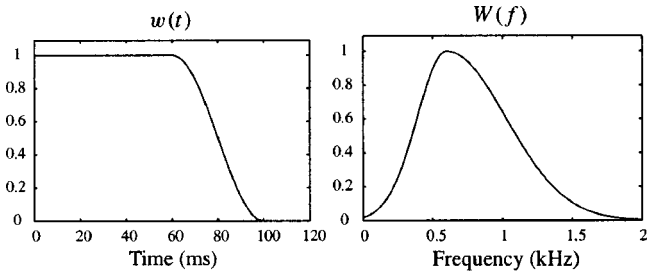

FIG. 4. Time and frequency windows applied to impulse responses when calculating ASW measures.

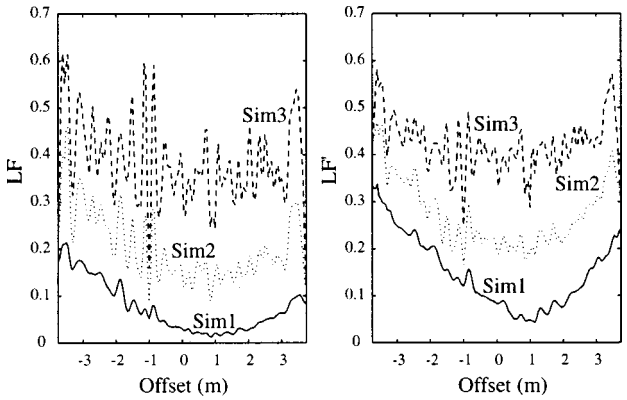

FIG. 5. LF and LF′ as a function of microphone offset, for sim1, sim2, and sim3.

octave band, corresponding with the dominance of frequencies around 600 Hz for lateralization earlier found by Raatgever[13] and specified by the following frequency window function:

$$W(f)=\begin{cases} e^{-(f/300-2)^2} & \text{for } f<600 \text{ Hz} \\ e^{-(f/600-1)^2} & \text{for } \geqslant 600 \text{ Hz}. \end{cases} \tag{4}$$

This window will be applied to all broadband measures treated in the remainder of this paper. Figure 4 depicts the two windows defined above. [When more low frequencies are included in the bandwidth, as suggested by Barron (Ref. 14), this will affect the fluctuating behavior of the measures. However, based on the results discussed in Sec. II, the order of fluctuation magnitude is expected to be the same.]

In order to discriminate the modified versions of the measures from those of Okano *et al.*, the subscript E will be dropped, although here the early part of the impulse responses is also considered. In further determinations of LF, the figure-8 microphone will be oriented, for each array position, with its null towards the source. Beside LF, the original version with the $\cos\phi$ weighting factor, to be denoted as LF′, will be calculated using velocity vector information. Also here, $\phi=\pi/2$ corresponds with the source direction for all array positions. Values of IACC are calculated from point simulations or measurements by applying a spatial filter based on the head-related transfer functions (HRTFs) of the KEMAR dummy head. This filter is described in the Appendix.

IV. SIMULATIONS AND MEASUREMENTS OF LF, LF′, AND 1-IACC

A. Simulations

Impulse responses were simulated for a rectangular room with dimensions $10\times7.5\times3$ m^3 using the mirror-image source model. The pressure reflection coefficient of front wall, rear wall (both 7.5×3 m^2), and floor is 0.8, that of the ceiling 0.5. The reflection coefficient of the left and right walls has been chosen as 0.2, 0.6, and 1.0 for the simulations sim1, sim2, and sim3, respectively. An omnidirectional source is positioned 3 m front, 1 m right, and 0.25 m below the room center. An array of pressure and velocity microphones with a 0.05-m spatial interval is situated 1.5 m above the floor, 2 m behind the room center over the full 7.5-m room width, thus encompassing 149 microphone positions. Figure 5 shows the values of LF and LF′ as a function of microphone offset. It is seen that for low side-wall reflectivity (sim1) the measures have low values, as expected. Local fluctuations are small in an absolute sense (<0.05), but relatively large (order 50%). Minimum values of the average curves are found for minimum distance between source and detector. From there, they monotonically increase towards the side walls. This can be understood as follows. When placed opposite the source, the synthesized figure-8 microphone has its sensitivity lobes perpendicular to the side walls, from which direction no specular reflections are incident: for the given configuration, the angle of incidence of the side-wall reflections on the array is about 45°. When moving towards the side walls, the figure-8 microphone facing the source with its null more and more turns its lobes into the directions of incidence of the reflections from the nearest side wall as well as from the front and rear walls. This yields an increase of the numerators of LF and LF′, whereas there is no argument in assuming that the common denominator shows this tendency as well. For increasing side-wall reflectivity (sim2, sim3), the average LF and LF′ curves shift upward, preserving their global shapes. The local fluctuations increase in an absolute sense (order 0.1 for sim2, order 0.2 for sim3), staying of order 50% in a relative sense.

Earlier, it had been stated that the fluctuations are caused by interference effects. This will now be considered in more detail. Figure 6(a) shows the offset-travel time representation of p and $p\cos\phi$ (the latter being proportional to the lateral velocity component) of two equal plane waves incident on the array under angles ϕ_0 and $\pi-\phi_0$, respectively—to be considered as an approximation of two reflections from opposite side walls—which cross each other at zero offset. Note that, due to the counterphase of the two lobes of the figure-8 microphone, $p\cos\phi$ has opposite sign for the two waves, yielding value zero at zero offset. Figure 6(b) shows offset-travel time representations of $p^2\cos^2\phi$ (the numerator integrand of LF), $p^2\cos\phi$ (the numerator integrand of LF′), and p^2 (the denominator integrand of both LF and LF′), together with their integrated values as a function of offset. It is seen that local minima of LF and LF′ are found at the interference point. In case of two waves in counterphase, local maxima are found. In general, it can be concluded that interference of waves gives rise to fluctuations.

The equivalent of Fig. 6(b) for the simulated wave field of sim2 is shown in Fig. 7. Again, interference of waves

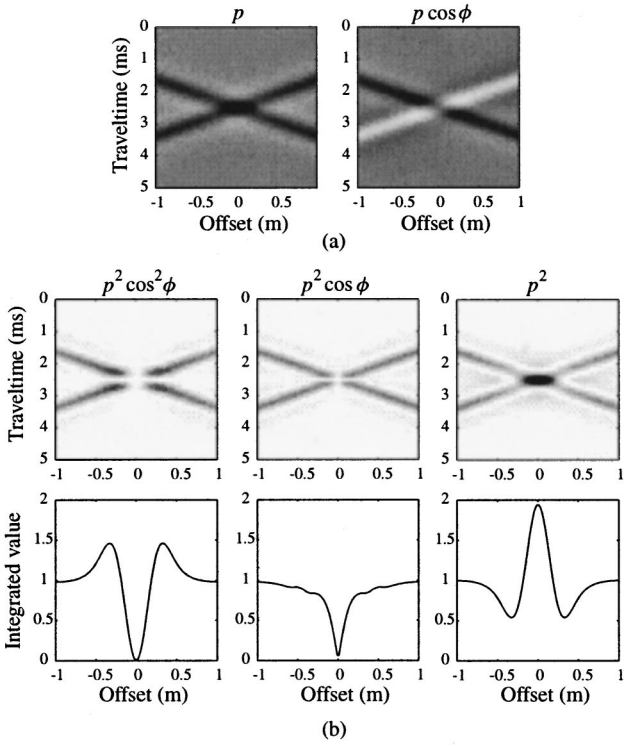

FIG. 6. (a) p and $p\cos\phi$ for two interfering identical plane waves, and (b) the offset-travel time representations of $p^2\cos^2\phi$, $p^2\cos\phi$, and p^2, together with their integrated values.

gives rise to strong fluctuations in both the numerators and the denominator of LF and LF′. Note that the numerator curves confirm the tendency of increase towards the side walls, in contrast to the denominator, which on the average remains constant.

Figure 8 shows the values of 1-IACC as a function of microphone offset for sim1, sim2, and sim3. The global

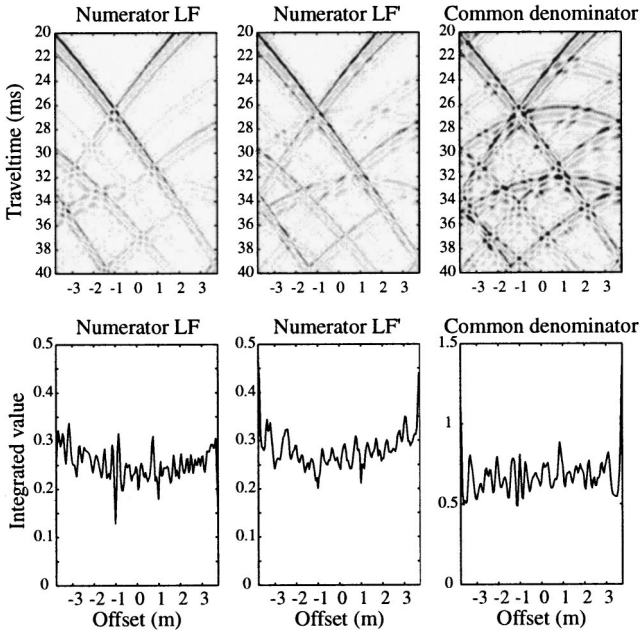

FIG. 7. Offset-travel time representations of the numerator integrands of LF and LF′ and their common denominator integrand, together with their integrated values.

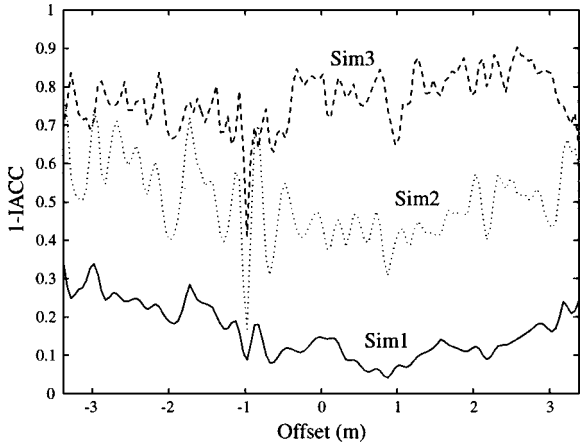

FIG. 8. 1-IACC as a function of microphone offset, for sim1, sim2, and sim3.

shapes of the curves are similar to those of LF and LF′; again, a global minimum is found (not convincingly in sim3) for minimum distance between source and microphone. When the dummy head faces the source, the signals at both ears are similar and thus the correlation is high. When moving towards the side walls, KEMAR increasingly shields and distorts the signal to the ear turned away from the source such that the interaural cross correlation decreases and 1-IACC increases. Also here, large local fluctuations occur, of the order 0.1 (50%) for sim1, 0.2 (40%) for sim2, and 0.2 (25%) for sim3. Here, the fluctuations decrease in a relative sense with increasing reflectivity. Since the numerator of the cross-correlation function [Eq. (2)], being a cross-energy density, has the same character as $p^2\cos\phi$, and the denominator is determined by two squared pressures, the fluctuations can be assigned to interference in a similar way as for LF and LF′.

B. Measurements

In the same way as earlier in the Amsterdam Concertgebouw, multichannel impulse response measurements have been done in the concert hall ''De Doelen'' in Rotterdam. The source was placed center-front stage, 12 m in front of an array of microphone positions over almost the full width (25 m) of the hall's main floor—a highly symmetric configuration. Figure 9 displays the values of LF and LF′ as a function of microphone offset. Here, the strong dip at zero offset is

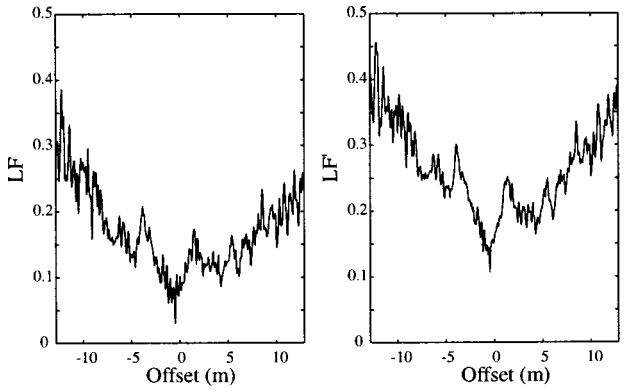

FIG. 9. LF and LF′ as a function of microphone offset, calculated from impulse responses measured in De Doelen, Rotterdam.

not so much caused by the synthesized figure-8 microphone looking perpendicular to the side walls—De Doelen has a hexagonal floorplan—as well by the strong interference between the two first-order side-wall reflections. Figure 10 shows the values of 1-IACC as a function of dummy-head offset. Again, the global shape is in good agreement with those of LF and LF′.

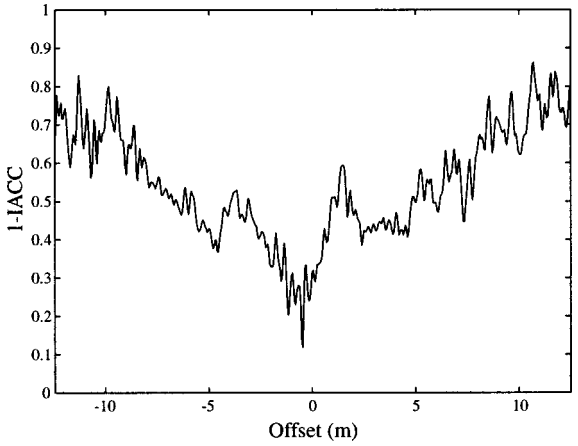

FIG. 10. 1-IACC as a function of dummy-head offset, calculated from impulse responses measured in De Doelen, Rotterdam.

V. THE LATERAL FRACTIONS REVISITED

In the previous section it was shown how the ASW measures fluctuate due to interference of wave-field components. Since ASW perception generally does not fluctuate correspondingly, it seems that the human auditory system is insensitive to these interference phenomena. Therefore, it is proposed to defined ASW measures of the same type as LF and LF′, but now based on the energies of the noninterfering wave-field components. This could be done by decomposing the wave field into plane waves by a double, i.e., temporal and spatial, Fourier transformation or a Radon transformation[8] of the offset-travel time dataset to the wave-number–frequency domain or the ray parameter–intercept time domain, respectively. This method, however, is not very accurate because of smearing effects due to the finite array length. Therefore, as an alternative method of decomposition, the wave field is separated by the nine spatial beam filters $\rho_n(x,t)$, $n=0,1,...,8$, as described in the Appendix. For each array microphone position x_m, the data are convolved in time with the corresponding trace $\rho_n(x_m,t)$ of the beam filter and the results are added for all microphone positions. Beam filter $\rho_0(x,t)$ is designed such that its directivity pattern $S0$ is given by

$$S0=\begin{cases}\cos(8\phi) & \text{for } -\pi/8<\phi<\pi/8\\ 0 & \text{for all other } \phi.\end{cases} \tag{5}$$

The other filters are chosen such that the corresponding directivity patterns are angle-shifted versions of $S0$, as illustrated in Fig. 11. A cosine shape has been chosen since in this case the sum of the squares of the overlapping filters equals 1 in all directions. This means that a mirror-image source gives the same contribution to the total energy as without beam filtering, but now without interference. For each beam, we calculate the lateral and the omnidirectional energy contributions and add these contributions to calculated the beam-filtered early lateral energy fractions BLF and BLF′ defined as

$$\mathrm{BLF}=\frac{\int_{0.005}^{0.080}\Sigma_{n=0}^{8}(\Sigma_m\rho_n(x_m,t)*p(x_m,t)\cos\phi)^2dt}{\int_{0.005}^{0.080}\Sigma_{n=0}^{8}(\Sigma_m\rho_n(x_m,t)*p(x_m,t))^2dt}, \tag{6a}$$

and

$$\mathrm{BLF}'=\frac{\int_{0.005}^{0.080}\Sigma_{n=0}^{8}(\Sigma_m|\rho_n(x_m,t)*p(x_m,t)\cos\phi||\rho_n(x_m,t)*p(x_m,t)|)dt}{\int_{0.005}^{0.080}\Sigma_{n=0}^{8}(\Sigma_m\rho_n(x_m,t)*p(x_m,t))^2dt}. \tag{6b}$$

The values of BLF and BLF′ as a function of microphone offset are given in Fig. 12, for the central parts of the simulated datasets sim1, sim2, and sim3, together with the values of LF and LF′ earlier shown in Fig. 5. It is seen that in the curves for the beam-split measure versions the strong local fluctuations are highly reduced, as expected. Figure 13 shows similar data for the impulse responses measured in De Doelen, with similar results.

VI. PERCEPTUAL RELEVANCE OF ASW MEASURE FLUCTUATIONS

Before the acoustical community decides to adopt new ASW measure versions, as proposed in the previous section, the perceptual relevance of the local fluctuations in the existing measures must be fully clarified. If it appears that these fluctuations do not correspond with perceptual differences—a result that is suggested by practical experience—and that the variations of the proposed new measures correspond with noticeable changes in ASW—which has to be investigated by new listening tests—it is worthwhile to consider the application of these new measures. Another smoothing operation is spatial averaging of the fluctuating values such that the ''carrier peridoicity'' is eliminated and the ''amplitude modulation'' remains. Again, the perceptual significance of the resulting variations has to be assessed by listening tests. A twofold conclusion can already be drawn: (1) the acoustic quality of a seat, or a group of neighboring seats, in terms of ASW cannot be quantified by one local measurement or calculation of the present measures LF, LF′, or IACC, which means that (2) there is no fixed local value of these measures that can form a criterion for ''good'' ASW.

In the literature, no unambiguous data on the percepti-

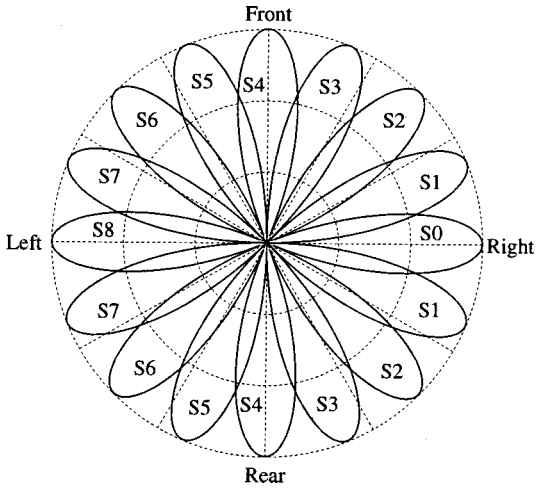

FIG. 11. Beam filters for plane-wave decomposition of multichannel impulse responses according to Eq. (5).

bility of ASW changes are found. Early results by Pollack *et al.*[15] on just-noticeable perceptual differences (jnd's) between binaural white-noise stimuli with different IACC values suggest that the jnd increases with decreasing IACC, just as the fluctuations in IACC reported in this paper. Based on the similar spatial behavior of LF, LF′, and 1-IACC, the jnd's for LF and LF′ are expected to increase with increasing values of the measures, just as the fluctuations in these measures. It is not certain that the jnd values found by Pollack *et al.* are also valid for musical signals heard in a concert hall, and that the noticed differences can be specified in terms of ASW. de Vries *et al.*[16] showed that, if this should be the case, the fluctuations hardly appear to be relevant from a perceptual point of view. However, using artificial impulse responses in an anechoic room convolved with music, Reichardt and Schmidt[17] found jnd's between 0.06 and 0.09 for LF′ varying from 0.2 to over 0.4; from a minimum value of LF′ around 0.3, the jnd increases for lower as well as higher LF′ values (Fig. 8 of Ref. 17). These jnd's are much lower then those estimated from the results of Pollack *et al.* (order 0.2 for LF′ around 0.3), but correspond with the difference limen of 0.07 that Barron[11] mentions. Cox *et al.*[18] find, for a simulated sound field in an anechoic room convolved with music, a jnd of 0.075 for IACC=0.33, which is much lower

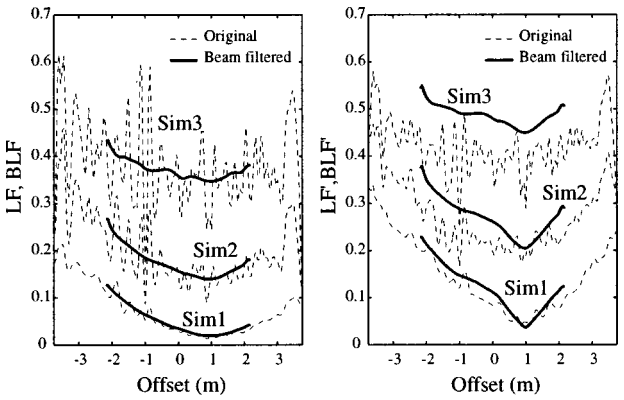

FIG. 12. LF and LF′ as a function of microphone offset for sim1, sim2, and sim3 (as in Fig. 5), together with their beam-filtered versions BLF and BLF′.

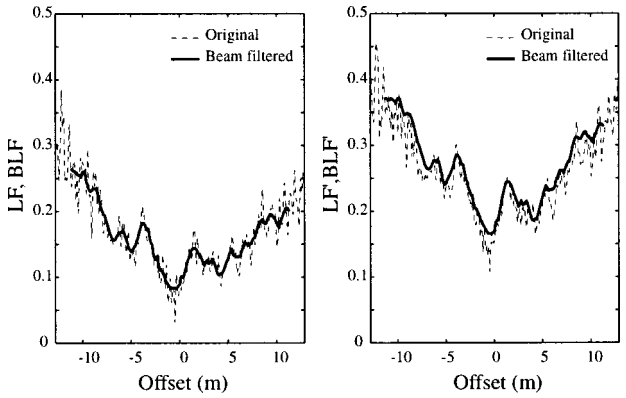

FIG. 13. LF and LF′ as a function of microphone offset calculated from impulse responses measured in De Doelen, Rotterdam (as in Fig. 9), together with their beam-filtered versions BLF and BLF′.

than the jnd of 0.38 indicated by Pollack *et al.* for the same IACC value.

Evidently, the question on the perceptual relevance of the fluctuations cannot be unambiguously answered using the literature data. New perceptual experiments should be carried out, preferably as a kind of ''round robin'' executed by institutes active in the field. The authors are readily prepared to make their array measurements available for this purpose.

VII. CONCLUSIONS

(i) Array measurements and simulations of impulse responses in halls reveal that the traditional ASW measures (LF, LF′, IACC) show large fluctuations on small spatial intervals (e.g., in front of one and the same seat) where no changes in ASW are perceived.

(ii) This means that a certain value of the traditional ASW measures does not correspond with a certain ASW; specification of ASW requirements in terms of local values of LF, LF′, or IACC is therefore useless.

(iii) Using the technique of beamforming, new versions of the existing ASW measures are proposed which—just as apparently the human auditory system—are insensitive to sound wave interference.

(iv) Based on the data from literature, the question of the perceptual relevance of the reported fluctuations cannot be unambiguously answered; new perceptual experiments should be carried out, preferably as a round robin.

APPENDIX: BEAM FILTERING

In order to reconstruct dummy-head measurements from microphone measurements (Sec. II), as well as for plane-wave decomposition of multichannel impulse responses (Sec. V), beam filters have been applied. The characteristics and the design of such filters are discussed in this Appendix.

Consider a linear array of M omnidirectional microphones at positions x_m $(m=1,...,M)$, a beam filter $\rho(x_m,t)$ and a pressure field $p(x_m,t)$ along the array. The output $z(t)$ of the beam filter is

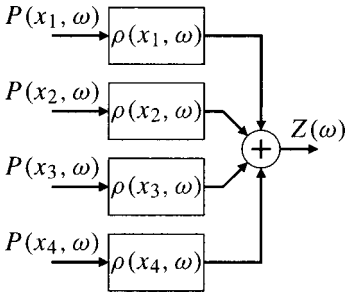

FIG. A1. Block diagram representation of Eq. (A2).

$$z(t)=\sum_{m=1}^{M}\rho(x_m,t)*p(x_m,t)$$

$$=\sum_{m=1}^{M}\int_{-\infty}^{\infty}\rho(x_m,t)p(x_m,t-\tau)d\tau. \tag{A1}$$

In practical situations only casual filters can be used, so that the lower limit of the integral in Eq. (A1) can be replaced by 0. In the frequency domain the convolution of Eq. (A1) becomes a multiplication

$$Z(\omega)=\sum_{m=1}^{M}\hat{\rho}(x_m,\omega)P(x_m,\omega). \tag{A2}$$

The output signal of a beam filter is thus obtained by filtering the signal at each microphone and adding all results, as illustrated in Fig. A1.

The directivity pattern of a beam filter $S(\omega,\phi)$ is defined as the response of the filter to plane waves with different angles of incidence. For the array of omnidirectional microphones considered here, the response only depends on the azimuth angle ϕ. In the frequency domain, the pressure along the array caused by a plane wave incident under this angle reads

$$P(x_m,\omega)=e^{j(\omega/c)x_m\cos\phi}. \tag{A3}$$

Substitution in Eq. (A2) yields for the directivity pattern

$$S(\omega,\phi)=\sum_{m=1}^{M}\rho(x_m,\omega)e^{j(\omega/c)x_m\cos\phi}. \tag{A4}$$

Note that the pattern is even in ϕ: waves incident on the array from front and rear under the same azimuthal angle cannot be discriminated.

A beam filter $\rho(x_m,t)$ that optimally approximates a specified directivity pattern can be designed by least-squares inversion, as shown in the following. The azimuthal angle is sampled as ϕ_n $(n=1,...,N)$. For each frequency component, Eq. (A4) can now be rewritten as a matrix equation

$$\mathbf{S}_n=\sum_{m=1}^{M}\mathbf{M}_{nm}\mathbf{P}_m, \tag{A5a}$$

with $\mathbf{S}_n=S(\omega,\phi)$, $\mathbf{P}_m=\hat{\rho}(x_m,\omega)$ and $\mathbf{M}_{nm}=e^{j(\omega/c)x_m\cos\phi}$, or in short

$$\mathbf{S}=\mathbf{MP}. \tag{A5b}$$

In order to obtain an optimal solution for $\mathbf{P}$ we apply a stabilized least-squares inversion to Eq. (A5b)

$$\mathbf{P}=(\mathbf{M}^*\mathbf{M}+c\mathbf{I})^{-1}\mathbf{M}^*\mathbf{S}, \tag{A6}$$

where c is a stabilization constant, $\mathbf{I}$ denotes the identity matrix, and $(.)^*$ means complex conjugation. Note that this inversion has to be carried out for each frequency component. For low values of c the matrix $\mathbf{M}^*\mathbf{M}+c\mathbf{I}$ becomes nearly singular and its inverse yields large eigenvalues, such that the filter may be very sensitive to noise. On the other hand, using a high value for c will result in a poor approximation of the desired directivity pattern. In general, the value $c=0.01$ yields a good compromise.

[1] J. S. Bradley and R. E. Halliwell, "Accuracy and reproducibility of auditorium acoustics measures," Proc. Inst. of Acoustics **10**, 399–406 (1988); J. S. Bradley, "Comparison of concert hall measurements of spatial impression," J. Acoust. Soc. Am. **96**, 3525–3535 (1994).

[2] X. Pelorson, J.-P. Vian, and J-D. Polack, "On the variability of room acoustical parameters: Reproducibility and statistical validity," Appl. Acoust. **37**, 175–198 (1992).

[3] T. Hidaka, L. L. Beranek, and T. Okano, "Interaural cross-correlation, lateral fraction, and low- and high-frequency sound levels as measures of acoustical quality in concert halls," J. Acoust. Soc. Am. **98**, 988–1007 (1995).

[4] J. L. Nielsen, M. M. Halstead, and A. H. Marshall, "On spatial validity of room acoustics measures," Proceedings of the 15th ICA Seattle, 2141–2142 (1998).

[5] K. Sekiguchi and T. Hanyu, "Study on acoustic index variations due to small changes in the observation point," Proceedings of the 15th ICA Seattle, 2121–2122 (1998).

[6] T. Okano, L. L. Beranek, and T. Hidaka, "Relations among interaural cross-correlation coefficient ($IACC_E$), lateral fraction (LF_E), and apparent source width (ASW) in concert halls," J. Acoust. Soc. Am. **104**, 255–265 (1988).

[7] D. de Vries and J. Baan, "Fluctuation of roomacoustical parameters on small spatial intervals," Collected Papers of the Forum Acusticum Berlin (CDROM), 5pAA3 (1999).

[8] A. J. Berkhout, D. de Vries and J. J. Sonke, "Array technology for acoustic wave field analysis in enclosures," J. Acoust. Soc. Am. **102**, 2757–2770 (1997).

[9] M. Barron and A. H. Marshall, "Spatial impression due to early lateral reflections in concert halls: The derivation of a physical measure," J. Sound Vib. **77**, 211–232 (1981).

[10] M. R. Schroeder, D. Gottlob, and K. F. Siebrasse, "Comparative study of European concert halls: Correlation of subjective preference with geometric and acoustic parameters," J. Acoust. Soc. Am. **56**, 1195–1201 (1974).

[11] Y. Ando, *Concert Hall Acoustics* (Springer, Berlin, 1985).

[12] J. M. Potter, F. A. Bilsen, and J. Raatgever, "Frequency dependence of spaciousness," Acta Acust. **3**, 417–427 (1995).

[13] J. Raatgever, "On the binaural proessing of stimuli with different interaural phase relations," Ph.D. thesis, Delft University of Technology (1980).

[14] M. Barron, "Measured early lateral energy fluctuations in concert halls and opera houses," J. Sound Vib. **232**, 79–100 (2000).

[15] J. Pollack and W. J. Trittipoe, "Binaural listening and interaural noise cross correlation," J. Acoust. Soc. Am. **31**, 1250–1252 (1959).

[16] D. de Vries, E. M. Hulsebos, and J. Baan, "Spatial fluctuation of spaciousness measures in auditoria," preprint 5147, 108th AES Convention (2000).

[17] W. Reichardt and W. Schmidt, "Die hörbaren Stufen des Raumeindruckes bei Musik," Acustica **17**, 175–179 (1966).

[18] T. J. Cox, W. J. Davies, and Y. W. Lam, "The sensitivity of listeners to early sound field changes in auditoria," Acustica **79**, 27–41 (1993).

Array element localization for towed marine seismic arrays[a)]

Stan E. Dosso[b)] and Michael Riedel
School of Earth and Ocean Sciences, University of Victoria, Victoria, British Columbia V8W 3P6, Canada

(Received 25 August 2000; revised 2 April 2001; accepted 27 April 2001)

This paper presents an approach to array element localization (AEL) for towed marine seismic arrays based on regularized inversion of direct and bottom-reflected acoustic ray travel times picked from recorded seismic sections. Depth-sensor measurements at a number of points along the array are included as *a priori* estimates (with uncertainties) in the inversion. The smoothest array shape consistent with the acoustic data and prior estimates is determined by minimizing the array curvature or roughness. A smooth array shape is physically reasonable; in addition, minimizing curvature provides *a priori* information about the correlation between hydrophone positions that allows the estimation of both the offset and depth of hydrophones that record only one (or even no) acoustic arrival due to the shadowing effects of water-column refraction or reflection from arbitrary bathymetry. The AEL inversion is applied to a 102-sensor, 1.2-km towed array to correct receiver positions in the seismic velocity analysis of a seabed gas hydrate survey. © *2001 Acoustical Society of America.* [DOI: 10.1121/1.1382618]

PACS numbers: 43.60.Pt, 43.30.Xm [DLB]

I. INTRODUCTION

Marine seismic reflection methods make use of a ship-towed array of hydrophones and an impulsive source (e.g., a compressed-air gun) to record seismo-acoustic arrivals that have reflected from sub-bottom layers.[1] The timing of these arrivals is then used to estimate the seismic-velocity structure of the sub-bottom on spatial scales from meters to kilometers, depending on the frequency and penetration depth of the source and the geometry of the array. Determining accurate locations for the individual hydrophones of a towed array is an important problem in marine seismology and in other towed array applications such as sonar signal processing. Hydrophone location affects the timing of acoustic arrivals, and, in seismic applications, localization errors manifest themselves in the velocity analysis applied to determine seabed lithology.

A variety of approaches have been developed for the problem of array element localization (AEL) for towed arrays. Advanced array systems employed in the petroleum exploration industry make use of GPS and high-frequency acoustic subsystems for precise localization; however, such technology is beyond the reach of many marine seismic research applications. More typically, towed arrays may include depth and heading sensors distributed at intervals along the array. The hydrophone locations can then be obtained by hydrodynamic modeling, which attempts to account for the dynamic behavior of the array under towing conditions.[2,3] Hydrodynamic modeling can be reasonably accurate, but requires detailed knowledge of the physical properties (weight, buoyancy, drag, etc.) of the array components, of the ship's speed and maneuvering characteristics, and of natural local disturbances (swell and currents), which may not be well known. More commonly, a simpler approach is employed which consists of applying a smooth interpolation between measurement points (e.g., a cubic spline) to estimate the intervening hydrophone positions, assuming known hydrophone offsets.[4] While it is physically reasonable to expect a smoothly-varying shape for a towed array, interpolation is obviously unable to resolve features of the array shape between measurement points. In addition, the actual offsets of the hydrophones and depth sensors during towing may not be well known. Acoustic approaches to AEL for towed arrays have also been developed. The sharpness method[5–7] is based on determining the parameters of an assumed sinusoidal array shape by optimizing a measure of the beamformer output for one or more far-field sources. The dual-shot method[8,9] solves for each hydrophone position individually (i.e., no assumptions about the array shape are made) based on inverting the travel times of acoustic arrivals from sources deployed by two consort ships maintaining station with the tow ship. In addition, a number of acoustic approaches to AEL for bottom-moored horizontal arrays have been developed which make use of multiple sources deployed around the array.[10–14]

Much of the AEL work referenced above was developed for sonar applications. Marine seismic applications are potentially simpler in two respects. First, although determining hydrophone positions while the tow ship maneuvers is of obvious importance in tactical sonar scenarios, marine seismic surveys can generally be designed with ship turns well outside of the region of interest. Thus, it is often justified to assume that the array streams directly behind the ship, which reduces AEL to a two-dimensional (2D) problem for the offset x (horizontal position relative to the source) and depth z for each hydrophone. Second, the impulsive seismic source can also be used for acoustic AEL.[15] In particular, the water-borne acoustic arrivals along direct and bottom-reflected paths provide useful positioning information that is often overlooked. These paths are illustrated by acoustic rays in

[a)]Portions of this work were presented in "Acoustic array element localization for marine seismology," in Proceedings of the 5th European Conference on Underwater Acoustics, Lyon, France, July 2000.

[b)]Electronic mail: sdosso@uvic.ca

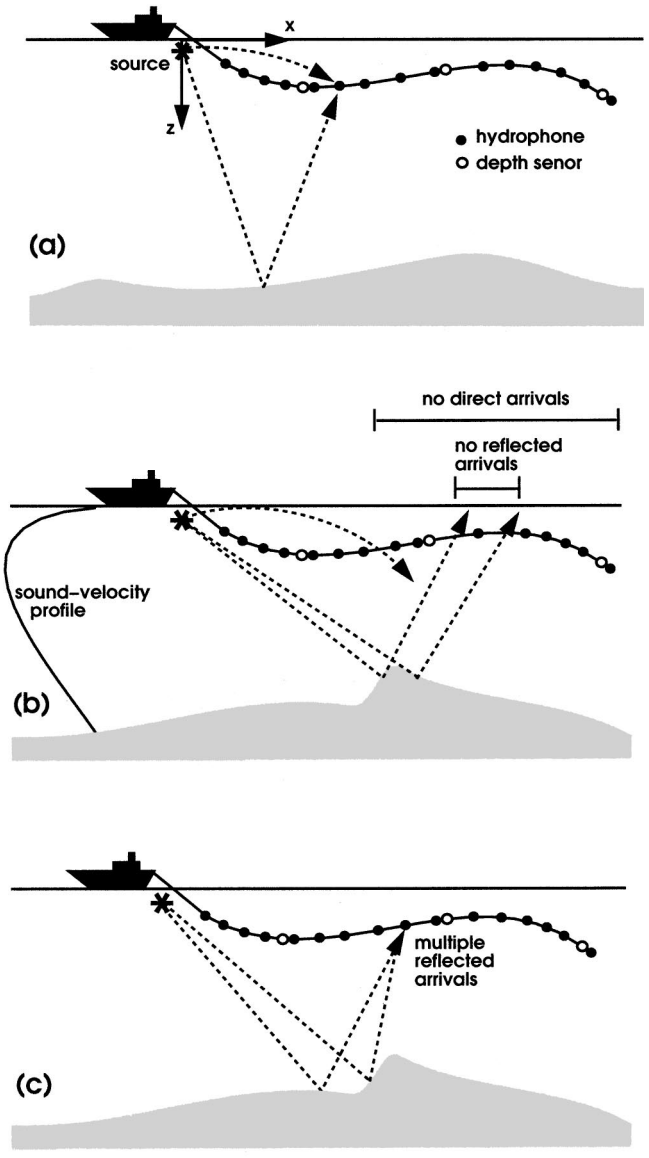

FIG. 1. Geometry of the AEL inverse problem is illustrated in (a). Shadow zones for direct and reflected arrivals are illustrated in (b). Convergent zones for reflected arrivals are illustrated in (c).

Fig. 1(a). Although the equation for travel time along a ray-path is nonlinear, it is readily linearized (Sec. II A), and hence the two equations (for direct and reflected rays) in two unknowns (hydrophone depth and offset) should provide a well-determined solution for hydrophone location. The difficulty with this approach is that these two arrivals are not necessarily present at all hydrophones, as illustrated in Fig. 1(b). For a source and array towed at relatively shallow depths, the negative sound-velocity gradient in the upper waters refracts acoustic rays downward so that no direct arrivals are recorded beyond a maximum offset determined by the ray that turns at the sea surface. In addition, the change in ray angle upon reflection at a seafloor with variable bathymetry can result in shadow zones at the array where no reflected arrivals are present. In measured seismograms, nonspecular reflections at the seafloor can result in weak arrivals within these shadow zones; however, these arrivals cannot be modeled using standard ray theory and therefore cannot be used in localization (the use of Gaussian beams might extend the applicability of ray theory within shadow zones, but this has not been addressed in the present paper). A further complication, illustrated in Fig. 1(c), is that variable bathymetry can result in two or more reflected arrivals at a given hydrophone (i.e., a convergence zone). These multiple arrivals do not represent useful independent information, since only the first arrival instant can be picked reliably on a seismogram. However, the ray path corresponding to the earliest arrival must be correctly identified if reflected rays are to be used to constrain hydrophone positions.

To date, acoustic AEL methods have been based on using arrivals from one or more sources such that the number of data (arrivals) exceed the number of unknowns (hydrophone and possibly source locations). However, for the marine seismic geometry illustrated in Fig. 1, shadow zones for direct and reflected arrivals result in an under-determined inverse problem. For instance, in the case of N_h hydrophones and M missing ray arrivals, inversion for the hydrophone offsets and depths and for source depth consists of solving $2N_h - M$ equations for $2N_h + 1$ unknowns. For a meaningful inversion, additional physical information regarding the solution, referred to as *a priori* information, must be included. Several forms of *a priori* information are available. First, depth sensors along the array can provide point depth estimates and the nominal source depth can be estimated from cable length and angle. Second, the assumption that the array is expected to be smooth provides *a priori* information about the array shape. A well-posed inversion that combines the acoustic data and *a priori* information can be formulated using the method of regularization.[12]

This paper presents an AEL inversion for marine seismic arrays based on a regularized inversion of ray travel times. Depth-sensor measurements and the nominal source depth are included as *a priori* information (with uncertainty estimates) in the inversion. The smoothest array shape consistent with the acoustic data and prior depth estimates is determined by minimizing the array roughness or curvature in two dimensions. Minimizing array roughness provides *a priori* information about the correlation between hydrophone positions which allows inversion for both the offset and depth of hydrophones that record only one (or even no) acoustic arrival. It is interesting to note that computing the smoothest model using only prior point estimates is equivalent to cubic spline interpolation;[16] hence, including acoustic data as well as prior estimates in the smoothest-model inversion should provide a significant improvement to the standard interpolation approach to AEL. Minimizing roughness also produces the simplest array shape consistent with the AEL data. Deviations in the solution from a straight array are required by the data, and are not simply artifacts of the inversion algorithm. A preliminary report on this work has been presented elsewhere.[17]

The general approach to AEL inversion developed here is applied to the COAMS (Canadian Ocean Acoustic Measurement System) array. Section II of this paper describes this array and the data collected during seismic survey COAMS '99.[18] Section III describes the AEL inversion algorithm, including the requisite inverse theory, ray theory

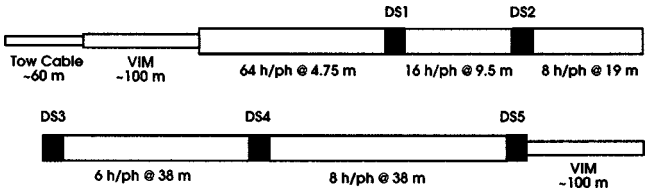

FIG. 2. Configuration of the COAMS array. Number of hydrophones (h/ph) and hydrophone spacings are indicated. DS stands for depth sensor (dark squares); VIM for vibration isolation module.

implementation, and a synthetic example. Section IV applies the AEL inversion to the COAMS array, including uncertainty analysis and an example of the improved seismic velocity results obtained with accurate hydrophone localization. Finally, Sec. V provides a summary and discussion.

II. COAMS MARINE SEISMIC ARRAY

The AEL inversion in this paper was developed for the COAMS marine seismic array, which is comprised of a total of 102 hydrophones and five depth sensors, with an acoustic aperture of approximately 1140 m. The configuration of the COAMS array is illustrated in Fig. 2. From the leading end (front of the array), the array consists of 64 hydrophones spaced at increments of 4.75 m, 16 hydrophones spaced at 9.5 m, 8 hydrophones spaced at 19 m, and 14 hydrophones spaced at 38 m. Depth sensors, calibrated to an accuracy of 0.5 m, are located at approximately 305, 457, 610, 838, and 1142 m. The array is towed on a 60 m cable, with a 100 m vibration isolation module (VIM) between the array and tow cable to reduce acoustic tow noise and the effects of sea–surface motion; a second VIM is located at the trailing end of the array. The tow cable, consisting of electrical conductors and a strength member enclosed in a steel sheath, is heavier than water and depresses the array at its leading end. The array itself is housed in an oil-filled plastic hose, and is lighter than water. To counteract the tendency for the array to float to the surface, small amounts lead sheeting were attached to the exterior of the array every 25 m beyond the third depth sensor. The air-gun source is towed independently of the array. Because of this, as well as the elasticity of the VIM and variability in the array dimensions, the precise source-to-receiver offsets are not known when towing, and only nominal values are available prior to AEL.

The data considered in this paper were collected during the COAMS '99 cruise,[18] which was designed to study methane gas hydrate deposits in continental-shelf sediments off the west coast of Vancouver Island, Canada (water depth ~1300 m). For this study, the array was operated at a nominal depth of 20 m, with a 40 cubic-in. (0.65 l) air-gun source towed approximately 20 m behind the ship at 2 m depth. The source was discharged every 20 m the ship traveled along predetermined survey lines. The seismic data were transmitted to the ship in analog form, where they were digitized at a sampling rate of 700 Hz and recorded on Exabyte tapes (an example of the recorded data is given in Sec. III). The ocean sound-velocity profile at the survey site was measured using a velocimeter cast. The bathymetry along the survey lines was measured using a 12 kHz echo-sounder. The echo-sounder recordings were subsequently digitized and corrected using the measured sound-velocity profile.

III. AEL INVERSION ALGORITHM

A. Inverse theory

This section briefly presents the inverse theory that forms the basis for the AEL inversion algorithm; more complete treatments of the field can be found in Refs. 12 and 19–23. The set of acoustic travel times **t** measured in an AEL survey can be written in general vector form as

$$\mathbf{t}=\mathbf{t}(\mathbf{m})+\mathbf{n}. \tag{1}$$

In Eq. (1), the model **m** of unknown parameters is taken to consist of the hydrophone offsets and depths $\{x_j, z_j, j=1,N_h\}$ and the source depth z_s. The forward mapping $\mathbf{t}(\mathbf{m})$ represents the acoustic travel times along direct and bottom-reflected ray paths between source and receivers (described in the Appendix). Finally, **n** represents the data errors (noise). The inverse problem of determining **m** from **t** is functionally nonlinear; however, a local linearization is obtained by expanding $\mathbf{t}(\mathbf{m})=\mathbf{t}(\mathbf{m}_0+\delta\mathbf{m})$ in a Taylor series to first order about an arbitrary starting model $\mathbf{m}_0$ to yield

$$\mathbf{t}=\mathbf{t}(\mathbf{m_0})+\mathbf{J}\delta\mathbf{m}, \tag{2}$$

where $\delta\mathbf{m}$ represents an unknown model perturbation and **J** is the Jacobian matrix consisting of the partial derivatives of the data functionals with respect to the model parameters,

$$J_{ij}=\partial t_i(\mathbf{m_0})/\partial m_j \tag{3}$$

(partial differentiation of the ray travel time is considered in the Appendix). Substituting $\delta\mathbf{m}=\mathbf{m}-\mathbf{m}_0$, the expansion can be written

$$\mathbf{Jm}=\mathbf{t}-\mathbf{t}(\mathbf{m_0})+\mathbf{Jm_0}\equiv\mathbf{d}. \tag{4}$$

Equation (4) defines a linear inverse problem for **m** in terms of known quantities (defined as modified data **d**), which can be solved using methods of linear inverse theory. Note that the uncertainties inherent in **d** are identical to those in the measured data **t**; however, since nonlinear terms are neglected in Eq. (4), the equations are not exact and the solution **m** may not adequately reproduce the measured data via the nonlinear forward problem. In this case, the starting model is updated, $\mathbf{m}_0\leftarrow\mathbf{m}$, and the inversion repeated iteratively until an acceptable solution is obtained (i.e., the linearization error becomes negligible). Note that since Eq. (4) is formulated in terms of the model **m**, rather than the perturbation $\delta\mathbf{m}$, *a priori* information regarding the model can be applied directly to the inversion, which is vital for the present application.

Under the standard assumptions that the error n_i on datum t_i is due to an independent, Gaussian-distributed random process with zero mean and standard deviation σ_i, the maximum-likelihood solution of the linearized system of Eq. (4) is obtained by minimizing the χ^2 data misfit,

$$\chi^2=|\mathbf{G}(\mathbf{Jm}-\mathbf{d})|^2, \tag{5}$$

where $\mathbf{G}=\mathrm{diag}[1/\sigma_i]$ weights the data according to their uncertainties. However, this least-squares approach is not ap-

plicable to underdetermined problems, such as the AEL inversion at hand. The method of regularization provides a particularly useful approach to underdetermined inversions based on explicitly including physical *a priori* information regarding the solution in the inversion. This is accomplished by minimizing an objective function ϕ which combines the χ^2 misfit with a regularizing term that imposes the *a priori* expectation that the model $\mathbf{m}$ resembles a prior estimate $\hat{\mathbf{m}}$,

$$\phi = |\mathbf{G}(\mathbf{Jm}-\mathbf{d})|^2 + \mu|\mathbf{H}(\mathbf{m}-\hat{\mathbf{m}})|^2, \tag{6}$$

where $\mathbf{H}$ is the regularization matrix (described below), and μ is a trade-off parameter controlling the relative importance assigned to the data misfit and the *a priori* expectation in the minimization. Minimizing ϕ with respect to $\mathbf{m}$, the regularized solution is

$$\mathbf{m} = \hat{\mathbf{m}} + [\mathbf{J}^T\mathbf{G}^T\mathbf{GJ} + \mu\mathbf{H}^T\mathbf{H}]^{-1}[\mathbf{J}^T\mathbf{G}^T\mathbf{Gd} - \mathbf{J}\hat{\mathbf{m}}]. \tag{7}$$

The regularization matrix $\mathbf{H}$ in Eqs. (6) and (7) controls the form of the *a priori* information applied in the inversion. For instance, if prior model parameter estimates $\hat{\mathbf{m}}$ are available, an appropriate regularization is given by

$$\mathbf{H} = \mathrm{diag}[1/\xi_j], \tag{8}$$

where ξ_j represents the uncertainty for the jth parameter estimate $\hat{m}_j$. An alternative form of regularization is to apply *a priori* information to derivatives of the model parameters. For instance, if the *a priori* expectation is that the parameters in $\mathbf{m}$ are well approximated by a smooth function of an independent variable u [with $m_j = m(u_j)$], then an appropriate choice is $\hat{\mathbf{m}} = \mathbf{0}$ and $\mathbf{H}$ consisting of the tridiagonal matrix with nonzero entries on the jth row given by

$$\mathbf{H} = \mathrm{tridiag}\left[\frac{-1}{(u_{j+1}-u_j)^2}, \quad \frac{u_{j+2}-u_j}{(u_{j+2}-u_{j+1})(u_{j+1}-u_j)^2}, \quad \frac{-1}{(u_{j+2}-u_{j+1})(u_{j+1}-u_j)}\right]. \tag{9}$$

Each row of $\mathbf{H}$ in Eq. (9) represents a discrete approximation to the second derivative operator $\partial^2/\partial u^2$. Hence, $|\mathbf{Hm}|^2$ provides a measure of the total curvature or roughness of the model. Applying this regularization minimizes the model roughness, producing the smoothest model. For either form of regularization, the trade-off parameter μ is chosen so that the χ^2 data misfit achieves its expected value of $\langle\chi^2\rangle = N$ for N data, thereby applying the *a priori* information subject to ensuring that the data are fit to a statistically appropriate level.

The AEL inversion formulated here for marine seismic arrays applies both types of *a priori* information described above. In particular, prior parameter estimates are available for the source depth and for the depth of the hydrophones adjacent to the depth sensors. The expectation that the towed array shape is smooth can be applied by minimizing the 2D curvature. To apply simultaneously two different types of *a priori* information, an augmented objective function can be formed which includes two regularization terms,

$$\phi = |\mathbf{G}(\mathbf{Jm}-\mathbf{d})|^2 + \mu_1|\mathbf{H}_1(\mathbf{m}-\hat{\mathbf{m}}_1)|^2 + \mu_2|\mathbf{H}_2(\mathbf{m}-\hat{\mathbf{m}}_2)|^2. \tag{10}$$

In Eq. (10), the first regularization term is taken to represent the *a priori* parameter estimates for the depth of the source and hydrophones at the depth sensors. Hence, $\hat{\mathbf{m}}_1$ consists of the prior estimates for these parameters, with zeros for the remaining parameters. The regularization matrix $\mathbf{H}_1$ is of the form of Eq. (8) with diagonal elements consisting of the reciprocal of the estimated uncertainty for parameters with prior estimates, and zeros for the remaining parameters. The second regularization term is taken to represent the *a priori* expectation of a smooth array shape. Hence, $\hat{\mathbf{m}}_2$ is taken to be zero, and $\mathbf{H}_2$ is of the form of Eq. (9) for the hydrophone position parameters, with the independent variable u in Eq. (9) taken to be the nominal hydrophone offsets. Rows of zeros are included in $\mathbf{H}_2$ at appropriate locations to separate the measures of curvature in x and z. In this case, minimizing Eq. (10) leads to

$$\mathbf{m} = \hat{\mathbf{m}}_1 + [\mathbf{J}^T\mathbf{G}^T\mathbf{GJ} + \mu_1\mathbf{H}_1^T\mathbf{H}_1 + \mu_2\mathbf{H}_2^T\mathbf{H}_2]^{-1} \times [\mathbf{J}^T\mathbf{G}^T\mathbf{Gd} - \mathbf{J}\hat{\mathbf{m}}_1]. \tag{11}$$

The AEL inversion algorithm consists of an iterative application of Eq. (11), initiated from an arbitrary starting model. Convergence of the algorithm is based on (i) obtaining a misfit to the measured data of $\chi^2 = N$, and (ii) obtaining a stable solution such that the rms (root-mean-square) change in the sensor positions between iterations is less than 0.1 m. Regarding the first criterion, note that although Eq. (11) is derived based on the χ^2 misfit for the linear inverse problem (4) that approximates the nonlinear problem (1) at each iteration, the convergence of the inversion algorithm must be judged in terms of the nonlinear misfit

$$\chi^2 = |\mathbf{G}(\mathbf{t}(\mathbf{m}) - \mathbf{t})|^2. \tag{12}$$

The most subtle aspect of implementing the inversion involves assigning values to the two trade-off parameters, μ_1 and μ_2, which control the balance between the data misfit and the two forms of *a priori* information. An effective procedure[12] is to set

$$\mu_2 = \beta\mu_1 \tag{13}$$

for a fixed value of β, and determine the value of μ_1 at each iteration which yields the desired χ^2 misfit. The parameter β provides a relative weighting between fitting the prior estimates (emphasized with small β) and achieving a smooth model (emphasized with large β). The final model obtained from this procedure can then be examined to ascertain whether the value of β was appropriate based on the parameter misfit associated with the *a priori* estimates, defined by

$$\hat{\chi}^2 = |\mathbf{H}_1(\mathbf{m}-\hat{\mathbf{m}}_1)|^2. \tag{14}$$

To fit the prior estimates to a statistically meaningful level requires $\hat{\chi}^2 \approx \hat{N}$, where $\hat{N}$ is the number of model parameters with *a priori* estimates. If $\hat{\chi}^2 \ll \hat{N}$ for a model $\mathbf{m}$ constructed according to Eq. (11), then the prior information is fit more closely than is reasonable statistically, and a larger value of β is required to reduce the relative weighting of the prior information. Conversely, if $\hat{\chi}^2 \gg \hat{N}$, the prior information is not fit closely enough, and a smaller value of β is required to increase the weighting of the prior information. The inver-

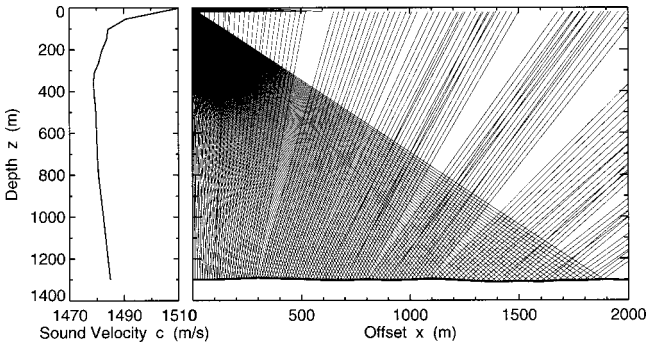

FIG. 3. Sound-velocity profile and representative direct and reflected ray paths for the synthetic inversion example with nominal source and receiver depths of 2 and 20 m, respectively.

sion can be repeated with a new value of β until $\hat{\chi}^2 \approx \hat{N}$ is achieved. In practice, determining an appropriate value for β is a straightforward procedure, typically requiring two or three trial inversions for a particular problem. The value of β usually remains constant when inverting successive data sets with similar uncertainties; hence, the algorithm is appropriate for batch processing.

The above procedure reduces the problem of determining two trade-off parameters to a 1D search for the parameter μ_1. The parameter μ_1 is chosen so that χ^2 is reduced by a controlled amount (e.g., a factor of 5) at each iteration until $\chi^2 = N$ is achieved. Controlling the reduction in χ^2 limits the change in the model at each iteration, which helps ensure that the linearization is valid and stabilizes the convergence. In practice, it is straightforward to determine the value of μ_1 which produces the desired χ^2 at a given iteration since χ^2 increases monotonically with μ_1 [this is evident from the minimization of Eq. (10) in which μ_1 weights the prior information at the expense of the χ^2 misfit; alternatively, it can be proved that $\partial\chi^2/\partial\mu_1$ is inherently positive[24]]. At early iterations an approximate value for μ_1 is sufficient, and a bisection algorithm is employed. Near convergence Newton's method is used for greater precision.

B. Ray theory implementation

The AEL inversion algorithm described in the preceding section assumes that the forward mapping (i.e., the ray tracing algorithm) correctly treats shadow and convergence zones at the array in an efficient, automated mode. This section briefly describes the approach devised to carry this out. The approach is perhaps best described by considering a specific example, such as that shown in Fig. 3. In this example, the ocean sound-velocity profile was measured during the COAMS '99 marine seismic survey, and the bathymetry is representative of the experiment site. Figure 3 illustrates the direct and bottom-reflected acoustic rays traced from a nominal source depth of 2 m to a nominal receiver depth of 20 m. Due to the negative sound-velocity gradient in the near-surface waters, the direct rays are refracted downward and do not intersect the receiver depth at offsets beyond approximately 600 m, producing a direct-ray shadow zone. The bottom-reflected rays are strongly influenced by the bathymetry, and exhibit shadow zones (e.g., at offsets of approximately 520–640 m) and convergence zones (e.g., 1200–1400 m offset) at the nominal receiver depth.

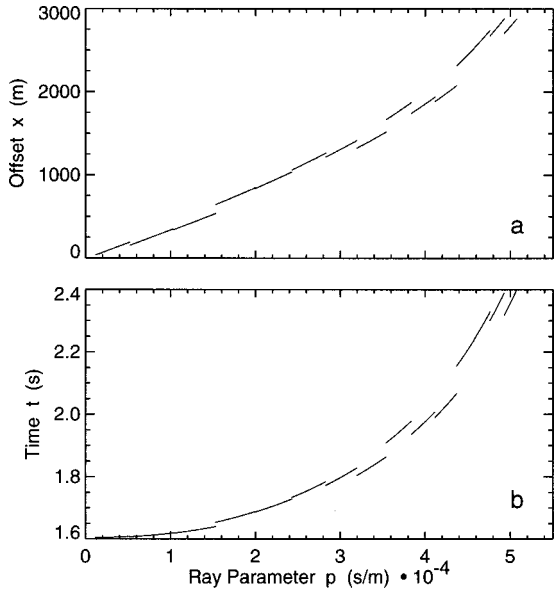

FIG. 4. Reflected ray offset x and travel time t as a function of ray parameter p for the synthetic inversion example.

An efficient identification of ray arrivals can be accomplished by precomputing look-up tables of the offset x and travel time t associated with all possible ray parameters p, which define the ray take-off angle (see the Appendix). Figure 4 illustrates these tables for the bottom-reflected rays. In Fig. 4(a), shadow zones result in vertical discontinuities in the offset plot, i.e., offsets which are not reached for any value of p (e.g., 520–640 m offset). Convergence zones result in overlapping segments in the offset plot, i.e., offsets that are reached for more than one p value (e.g., 1200–1400 m offset). To determine the eigenray connecting source and receiver for a given offset, the table represented by Fig. 4(a) can be consulted to find an appropriate starting value for p. The ray parameter is then refined for the actual source and receiver depths using Newton's method, as described in the Appendix. If the table indicates the particular offset is within a shadow zone, no eigenray exists. If the table indicates that the offset corresponds to a convergence zone, the traveltime table [Fig. 4(b)] is consulted to determine which of the possible values of p produces the shortest travel time. Look-up tables need be computed only once at the start of the inversion procedure, and are applicable provided the actual source and receiver depths are within approximately 30–50 m of the nominal depths. If the variability in receiver depths is greater than this, multiple look-up tables can be computed.

C. Synthetic inversion example

This section illustrates AEL inversion for marine seismic arrays with a realistic synthetic example; the following section considers inversion of data measured during the COAMS '99 survey. The number and spacing of the hydrophones and depth sensors used in the synthetic example is identical to that of the COAMS array, shown in Fig. 2. The true array shape is shown by the dotted line in Fig. 5(a); the source depth was taken to be 3 m. The sound-velocity pro-

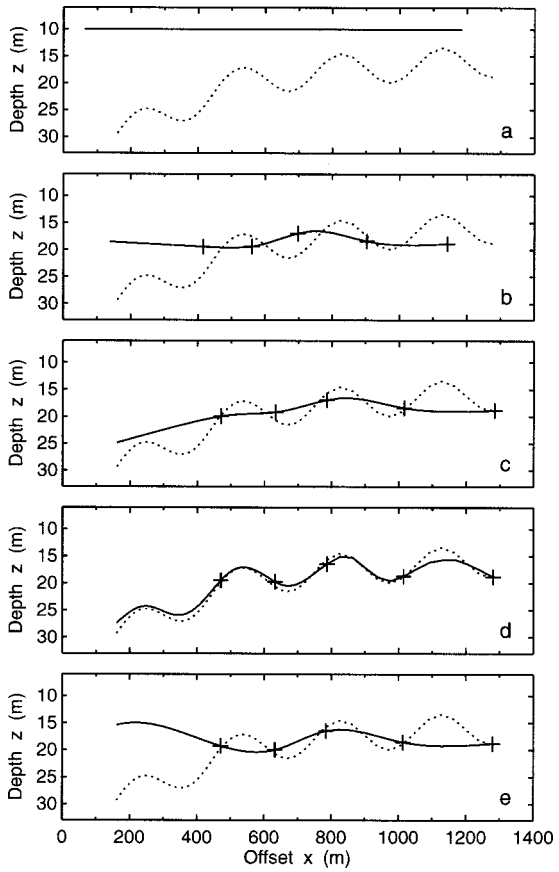

FIG. 5. Models obtained at iterations 0 (starting model), 1, 5, and 7 (final model) of the synthetic inversion example are given by solid lines in (a)–(d), respectively. Dotted lines indicate the true array shape, and crosses indicate depth-sensor positions. For comparison, the results of a cubic spline interpolation of the depth-sensor points is shown in (e).

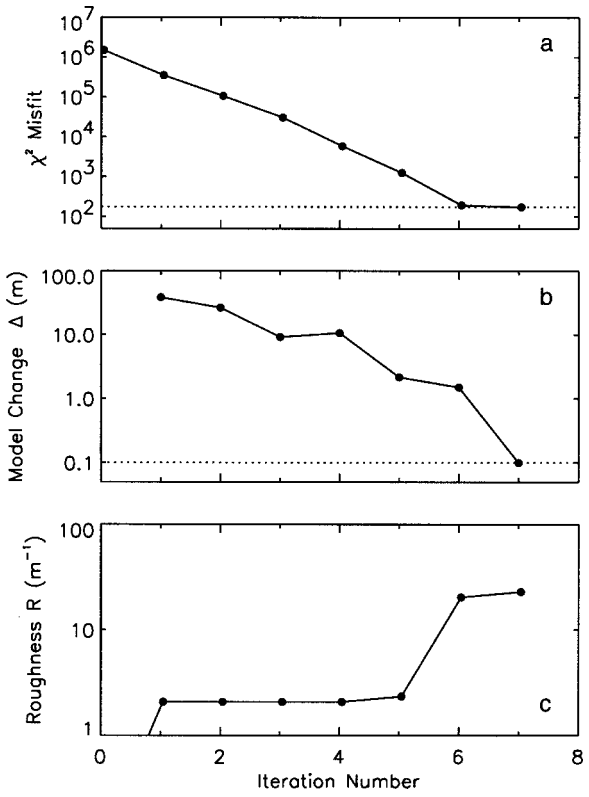

FIG. 6. Convergence properties for the synthetic inversion example. (a) shows the χ^2 data misfit, (b) shows the rms model change between iterations Δ, and (c) shows the model roughness R as function of iteration number. Dotted lines indicate the threshold values for χ^2 and Δ that must be achieved for convergence.

file, bathymetry and nominal ray paths are shown in Fig. 3, and the ray-parameter look-up tables in Fig. 4. For this environment, there are a total of 32 missing ray arrivals consisting of 21 direct arrivals (all hydrophones beyond 650 m offset) and 11 reflected arrivals (ten at hydrophones between 537–632 m, one at 1052 m). For the inversion, the synthetic travel-time data included Gaussian-distributed random errors with a standard deviation of 0.5 ms, the five depth-sensor measurements included errors of standard deviation 0.5 m, and the source depth estimate was in error by 1 m.

The starting model for the inversion, shown by the solid line in Fig. 5(a), was taken to be a straight array at 10 m depth, with both a uniform error (shift) of -100 m and random errors of standard deviation 10 m in the hydrophone offsets. This poor starting model is designed to illustrate the convergence of the inversion algorithm. The algorithm required 7 iterations to converge: the model produced at iterations 1, 5, and 7 (final model) are shown in Figs. 5(b)–(d). The convergence properties of the inversion are illustrated in Fig. 6, which shows the χ^2 data misfit, the rms model change between iterations Δ, and the model roughness $R=|\mathbf{H}_2\mathbf{m}|$ as a function of iteration number. The χ^2 misfit [Fig. 6(a)] decreases from a high initial value of 1.2×10^6 for the starting model (iteration 0) to the desired value of $\chi^2=173$ (the number of measured data) by iteration 7, at which point Δ has reached its threshold of 0.1 m for convergence [Fig. 6(b)]. As the data are more accurately fit, the structure of the array is resolved, and the roughness R increases from an initial zero value to a final value of 23 m^{-1} [Fig. 6(c)].

The final inversion result, shown in Fig. 5(d), is in excellent agreement with the true array shape. Note in particular that the array shape is well determined even at ranges beyond 537 m where there is never more than one arrival per hydrophone (and in some cases, no arrivals). The inversion result is clearly sensitive to the true array shape between depth sensors, providing good estimates of the hydrophone offsets and ranges, although the agreement gradually degrades with offset. The inversion result exhibits less structure (curvature) than the true array, providing a somewhat conservative estimate of the array shape. The rather complicated shape of the true model in this example was chosen to illustrate the ability of the AEL inversion to discern array shape with less than two arrivals; for a smoother true model, even better agreement would be expected. The complete inversion required about 3 min computation time on a 450 MHz PC running Interactive Data Language (IDL). For a better choice of starting model, the computation time is reduced by one-half or more. A virtually identical result was obtained by initiating the algorithm from a wide range of starting models, indicating the inversion is essentially insensitive to the choice of $\mathbf{m}_0$. Finally, for comparison, Fig. 5(e) shows the result of applying a cubic spline interpolation for the array shape, using the true hydrophone offsets (not generally known) and the depth sensor measurements. The array shape

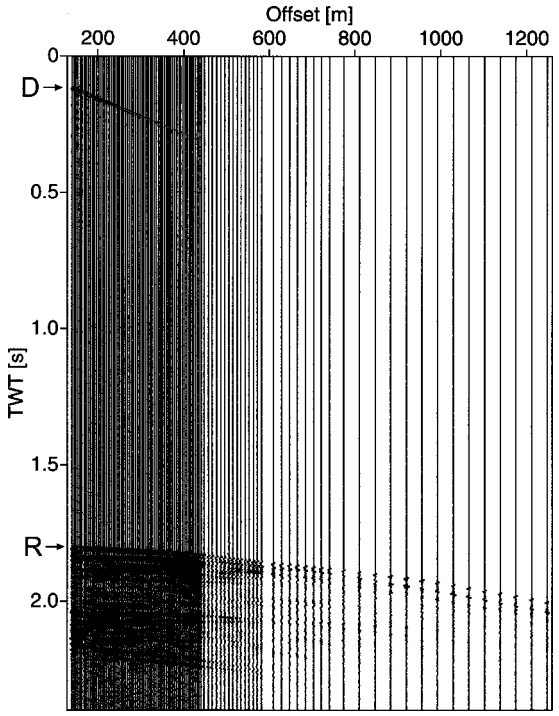

FIG. 7. Seismic section recorded using the COAMS array, showing the two-way travel time (TWT) of acoustic arrivals as a function of the nominal offset. Direct and bottom-reflected acoustic arrivals are indicated as D and R.

between depth sensors is not meaningful, leading to substantial positioning errors, particularly at the (unconstrained) leading end of the array.

IV. APPLICATION TO COAMS '99 DATA

A. Inversion of AEL data

In this section, the AEL inversion algorithm developed in Sec. III is applied to data from the COAMS '99 marine seismic survey, described in Sec. II. An example of the raw seismic data sections recorded during this survey is given in Fig. 7. The direct and bottom-reflected acoustic arrivals are identified on this section, and coherent sub-bottom reflections are also evident. The first-break travel times for the direct and reflected arrivals were picked using an automated matched-filter approach applied within prescribed time windows, with an estimated uncertainty of 1 ms (approximately the sampling interval). Note that direct arrival attenuates with offset due to refraction effects. It is difficult to identify this arrival beyond approximately 450 m in Fig. 7, and it cannot be picked reliably beyond 600 m.

The result of the AEL inversion for the COAMS array is shown in Fig. 8(a). The array shape smoothly fits the five depth-sensor estimates (large crosses). The observed shape is easily explained since the array itself is positively buoyant, but was weighed down by the heavy tow-cable at the leading end, and by sheet lead ballast attached to the array every 25 m beyond the third depth sensor (~800 m offset in Fig. 8), as described in Sec. I.

Although the array shape in Fig. 8(a) appears to be relatively simple, it represents a substantial improvement over a spline fit to the depth-sensor estimates, shown in Fig. 8(b). In

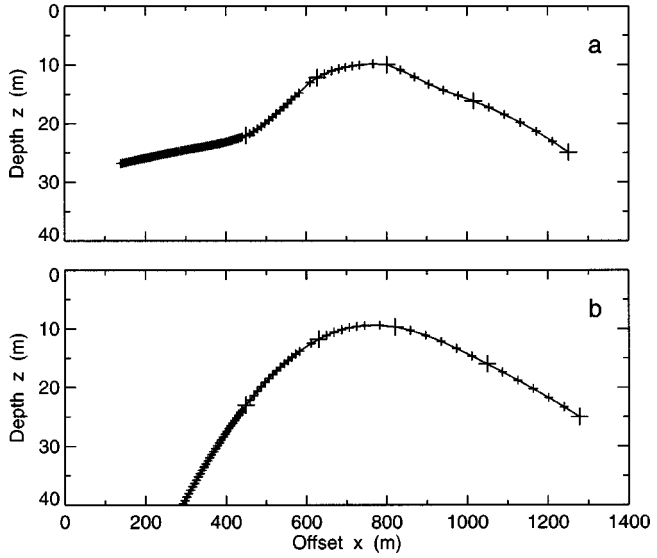

FIG. 8. COAMS array shape. Individual hydrophone positions are indicated by crosses, with large crosses indicating hydrophones co-located with depth sensors. (a) shows the result of AEL inversion for hydrophone depths and offsets; (b) shows the result of cubic spline interpolation for hydrophone depths at nominal offsets.

particular, the hydrophone positions determined from the spline fit are in poor agreement with the measured acoustic travel times. While the data misfit for the hydrophone positions determined via AEL inversion achieved the expected value of $\chi^2 = 184$ (the number of direct and reflected acoustic arrivals), the misfit computed for the hydrophone positions determined by the spline fit is $\chi^2 = 13\,315$, more than 70 times the expected value. The travel-time data predicted for the hydrophone positions computed via AEL inversion and spline fit are compared to the observed data in Fig. 9. In particular, the reflected arrivals [Fig. 9(b)] show substantial differences between the measured travel times and those computed for the spline fit at both short and long offsets.

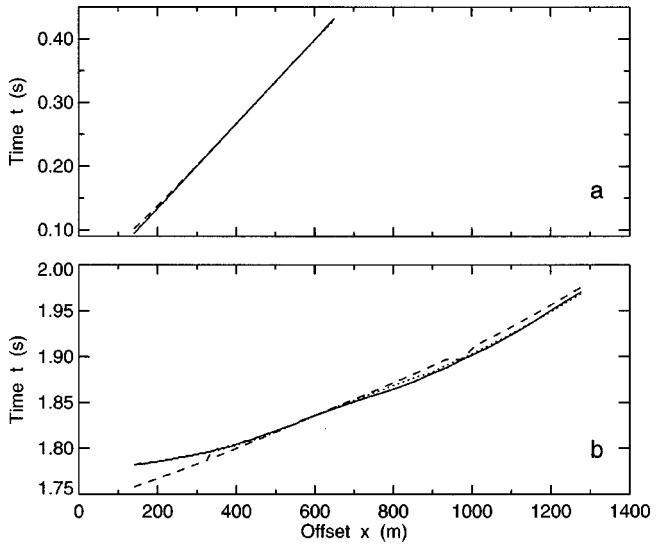

FIG. 9. Comparison of measured travel times (solid lines) with those computed for hydrophone/source positions as determined by the AEL inversion (dotted lines) and spline interpolation (dashed lines). Travel times are shown in (a) for the direct arrival, and in (b) for the reflected arrival. The horizontal axis represents the true hydrophone offsets.

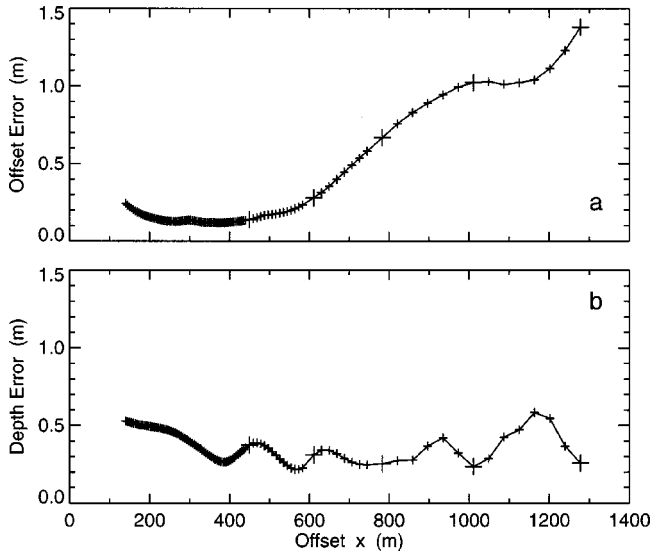

FIG. 10. Uncertainty estimates from Monte Carlo appraisal. The standard deviations of the hydrophone offsets and depths are shown in (a) and (b), respectively. The large crosses indicate hydrophones co-located with depth sensors.

To estimate the uncertainties associated with the AEL hydrophone localization, a Monte Carlo appraisal[23] was carried out. In this appraisal, the ''true'' hydrophone positions and source depth were taken to be those determined by the AEL inversion of the COAMS data [Fig. 8(a)], and simulated travel-time data were computed for this configuration. Each realization of the Monte Carlo process consisted of adding random errors to the simulated data, assigning *a priori* depth-sensor and source-depth estimates based on adding random errors to the true values, and subsequently applying the inversion algorithm initialized from a random starting model. The data errors were drawn from a Gaussian distribution with zero mean and standard deviation of 1 ms; the prior-estimates errors were Gaussian-distributed with a standard deviation 0.5 m for the depth-sensor measurements and 1 m for the source depth (these errors are identical to those assumed for the measured data, as described previously). In total, 60 inversion were carried out and the standard deviation (relative to the true value) of each hydrophone position was computed from the set of solutions. The resulting standard deviations are shown in Fig. 10. The hydrophone offset errors, shown in Fig. 10(a), are small ($\sim$0.2 m) out to offsets of approximately 600 m where two acoustic arrivals are usually present. Beyond this, the errors increase steadily to approximately 1.4 m at the maximum offset. The depth errors, shown in Fig. 10(b), are $\lesssim$0.5 m at all offsets. Beyond about 600 m, the depth errors exhibit minima at the locations of the depth sensors; however, at shorter offsets this is not the case. The results of a Monte Carlo appraisal such as this should generally be treated as an optimistic estimate of the actual uncertainty. The AEL appraisal neglects any errors due to the parameterization of the model as a 2D array, the assumption of Gaussian data and prior-estimate errors, and the use of 1D ray-tracing with specular reflection as the forward mapping.

B. Seismic velocity analysis

This section illustrates the importance of accurate AEL in marine seismic processing using data from the COAMS '99 survey. A primary goal of marine seismology is to determine a seabed seismic velocity model, which can be used to identify and classify sub-bottom lithology. Velocity estimation from multi-channel seismic data is generally performed by generating a velocity spectrum using semblance techniques.[1,25] This is an automated approach which calculates the semblance (a measure of coherency) for the normal moveout of multichannel data as a function of travel time and moveout velocity. Peaks in a contour plot of the semblance vs travel time and velocity (known as the velocity spectrum) correspond to reflected arrivals, and can be used to identify the seismic velocity profile and zero-offset travel times.

Seismic velocity analysis requires a good knowledge of the source and receiver positions (offset and depth). A basic assumption of the semblance technique is that the source and receivers are collinear and are located at the same depth. Corrections for nonuniform hydrophone depths can be made by adding appropriate time shifts to the seismic traces, which is equivalent to a vertical shift in position. The time shift is generally calculated based on the average sound velocity in the water column, assuming straight-line acoustic propagation (for the relatively small corrections in position, the error in neglecting ray curvature is negligible).

Prior to applying velocity analysis to the COAMS seismic data, the following standard processing steps were carried out:[1,25] (i) bandpass filtering to remove low-frequency noise; (ii) predictive deconvolution to suppress water-column multiples and the effects of source bubble oscillations; (iii) f-k (frequency-wave-number) filtering to suppress towing noise; (iv) slant-stack filtering to enhance the signal to noise ratio; and (v) sorting into the common midpoint (CMP) domain and generating super-CMP stacks by combining six adjacent CMPs to increase the stack fold (i.e., the number of reflections sampling the CMP).

Semblance plots were calculated for the COAMS data assuming three different array geometries (Fig. 11) to illustrate the importance of accurate AEL on the velocity analysis. Figure 11(a) shows the velocity spectrum calculated after correcting for the estimated receiver positions based on the results of the AEL inversion [Fig. 8(a)]. The velocity estimate for the seafloor reflection at 1.8 s two-way travel time (TWT) is about 1500 m/s, which is in good agreement with the harmonic-mean sound velocity of 1485 m/s for the measured sound-velocity profile. In addition, the velocity spectrum is generally sharp and well-resolved, and the maxima representing individual sub-bottom reflectors can be easily identified. These features are consistent with correct hydrophone positions. The continuous velocity profile estimated from the peak of the velocity spectrum is indicated by the solid line.

Figure 11(b) shows the velocity spectrum calculated using the nominal offsets and a constant hydrophone depth of 15 m below the source depth. The maximum associated with the seafloor reflection in this velocity spectrum is located at approximately 1300 m/s, which is $\sim$200 m/s too small. In-

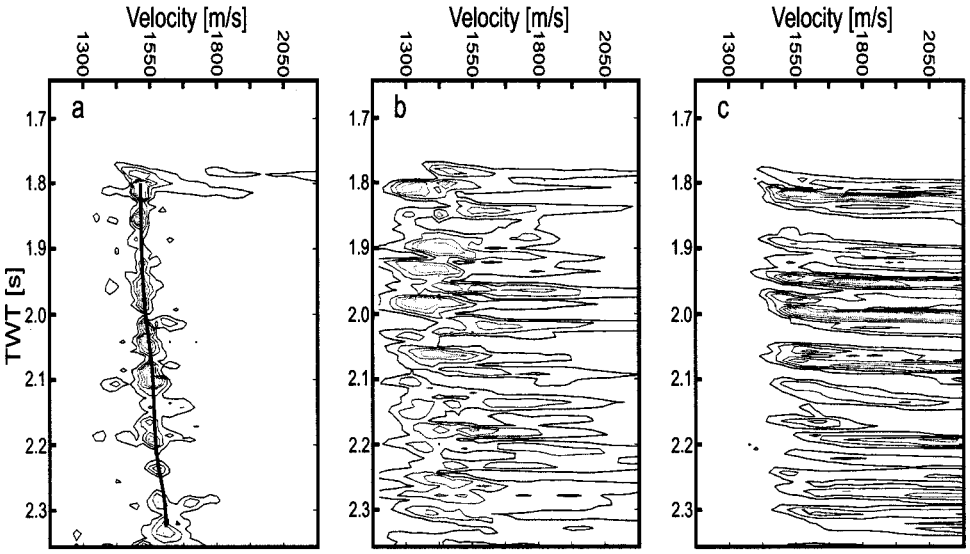

FIG. 11. Seismic velocity analysis of COAMS data using (a) hydrophone positions determined by AEL inversion, (b) nominal hydrophone offsets and depths 15 m below source, and (c) nominal hydrophone offsets and depths determined from cubic spline interpolation of depth-sensor measurements. Solid line in (a) represents the estimated velocity profile.

dividual local maxima corresponding to deeper reflections can still be identified, but the spectrum is not sharply resolved, and the velocities associated with reflections are generally too small. Figure 11(c) shows the velocity spectrum computed using the nominal hydrophone offsets and the spline-interpolation results for the hydrophone depths [Fig. 8(b)]. Velocities cannot be identified accurately from this spectrum as the individual maxima are smeared over much of the velocity range. The maximum associated with the seafloor reflection is split into two isolated peaks of nearly identical magnitude covering a velocity range from approximately 1450–1900 m/s, precluding a unique identification of velocity. The examples in Fig. 11 clearly show the improvement in velocity analysis obtained using accurate AEL inversion.

V. SUMMARY AND DISCUSSION

This paper developed an efficient inversion algorithm for the 2D localization of hydrophones of a towed marine seismic array. The inversion combines information from direct and bottom-reflected acoustic arrivals from the seismic source together with depth measurements made at intervals along the array and the physical assumption that the array shape is smooth. Hydrophone positions and source depth are obtained via regularized inversion of ray travel times for the smoothest array shape that is consistent statistically with the acoustic data and prior depth estimates. The smoothest shape is determined by minimizing array roughness (curvature). Determining the smoothest solution applies a prior model for the correlation between hydrophone positions that allows 2D localization for hydrophones that measure less than two arrivals due to water column-refraction or bottom-reflection effects (i.e., an under-determined inverse problem). For the shallow towing geometry considered here, this amounts to approximately half of the array by length. Minimizing roughness also produces the simplest array shape consistent with the data; features in the solution are definitely required by the data, and are not simply artifacts of the inversion algorithm or starting model. The common AEL approach of applying a cubic spline interpolation to prior position estimates is equivalent to inversion for the smoothest shape with no acoustic data; including acoustic data in the inversion provides strong additional constraints on hydrophone positions.

The inversion algorithm was applied to localize the elements of the 102-hydrophone, 1.2-km COAMS array during a marine seismic survey of sediment gas hydrate deposits off western Canada. The array shape determined was in good agreement with the known weight-buoyancy distribution along the array. A Monte Carlo simulation of the inversion indicated errors of 0.2–1.5 m in offset and $\lesssim$0.5 m in depth. The hydrophone locations determined by AEL inversion were shown to produce a substantial improvement in seismic velocity analysis compared to locations determined by a spline fit to the depth-sensor measurements and compared to a uniform-depth approximation. Finally, the approach developed here to treat underdetermined AEL for a towed array is generally applicable to other settings where either hydrophones or sources are expected to be distributed smoothly in space or to move along smooth tracks.

ACKNOWLEDGMENTS

This work was supported by an NSERC operating grant and a University of Victoria Graduate Student Fellowship. We thank Nicole Collison for an initial implementation of the ray tracing algorithm.

APPENDIX: RAY TRAVEL TIMES AND DERIVATIVES

The AEL inversion algorithm requires the computation of ray travel times and partial derivatives with respect to source and receiver coordinates. Expressions for these quantities for direct arrivals (including turning rays) and reflections from flat boundaries are given in Ref. 9. This Appendix derives travel-time derivatives for the case of reflections at a seafloor with arbitrary bathymetry. Some effort is expended here in deriving analytic expressions for the derivatives since numerical finite-difference approximations are generally inferior in inversion algorithms due to their inefficiency and to the difficulty in automating adaptive methods for determining the step size required for stable results.

Let the sound velocity profile be given by $c(z)$, the hydrophone and source positions be (x_h, z_h) and $(0, z_s)$, respectively, and the depth and bottom slope at the reflection point be z_b and α. The horizontal offset x and travel time t along a reflected acoustic ray are given by[1]

$$x = \int_{z_s}^{z_b} \frac{p_1 c(z)\,dz}{[1-p_1^2 c^2(z)]^{1/2}} - \int_{z_b}^{z_h} \frac{p_2 c(z)\,dz}{[1-p_2^2 c^2(z)]^{1/2}}, \tag{A1}$$

$$t = \int_{z_s}^{z_b} \frac{dz}{c(z)[1-p_1^2 c^2(z)]^{1/2}} - \int_{z_b}^{z_h} \frac{dz}{c(z)[1-p_2^2 c^2(z)]^{1/2}}. \tag{A2}$$

In Eqs. (A1) and (A2), $p_1 = \cos\theta_1(z)/c(z)$ and $p_2 = \cos\theta_2(z)/c(z)$ represent the ray parameters (constant along a ray path) of the downward- and upward-traveling rays, where $\theta_1(z)$ and $\theta_2(z)$ are the ray grazing angles at depth z. The difference between the reflected and incident ray parameters is due to the change in ray angle upon reflection at the bottom; this can be shown to lead to the relationship,

$$p_2 = p_1 \cos\alpha + \sin\alpha[1-p_1^2 c^2(z_b)]^{1/2}/c(z_b). \tag{A3}$$

The eigenray connecting source to receiver is determined by searching for a ray parameter value that produces the correct receiver offset $x = x_h$ (to a specified tolerance) using Eqs. (A1) and (A3). We have implemented an efficient procedure of determining p_1 using Newton's method. As described in Sec. II B, an initial estimate p_0 is obtained from a look-up table, such as illustrated in Fig. 4. An improved estimate is obtained by expanding x in a Taylor's series about p_0 and neglecting higher-order terms to yield

$$p_1 = p_0 + \left[\frac{\partial x(p_0)}{\partial p_1}\right]^{-1} (x_h - x(p_0)). \tag{A4}$$

If $x(p_1)$ computed from Eq. (A4) is within the tolerance of the desired offset x_h, the procedure is complete. If not, the starting value is updated, $p_0 \leftarrow p_1$, and the procedure repeated iteratively until a satisfactory value is obtained. Since Newton's method converges quadratically near the solution, this is an efficient procedure to determine eigenrays to high precision. The partial derivative in Eq. (A4) can be obtained by differentiating Eq. (A1) according to Leibntiz's rule,

$$\frac{\partial x}{\partial p_1} = \int_{z_s}^{z_b} \frac{c(z)\,dz}{[1-p_1^2 c^2(z)]^{3/2}} - \int_{z_b}^{z_h} \frac{c(z)\,dz}{[1-p_2^2 c^2(z)]^{3/2}} \frac{\partial p_2}{\partial p_1} + \left[\frac{p_1 c(z_b)}{[1-p_1^2 c^2(z_b)]^{1/2}} + \frac{p_2 c(z_b)}{[1-p_2^2 c^2(z_b)]^{1/2}}\right] \frac{\partial z_b}{\partial p_1}. \tag{A5}$$

Computation of Eq. (A5) requires expressions for $\partial p_2/\partial p_1$ and $\partial z_b/\partial p_1$. The former can be obtained by differentiating Eq. (A3) to yield

$$\frac{\partial p_2}{\partial p_1} = \cos\alpha - \frac{\sin\alpha}{[-p_1^2 c^2(z_b)]^{1/2}} \times \left[p_1 c(z_b) + \frac{1}{c^2(z_b)} \frac{\partial c(z_b)}{\partial p_1}\right]. \tag{A6}$$

In Eq. (A6), $\partial c(z_b)/\partial p_1$ is given by

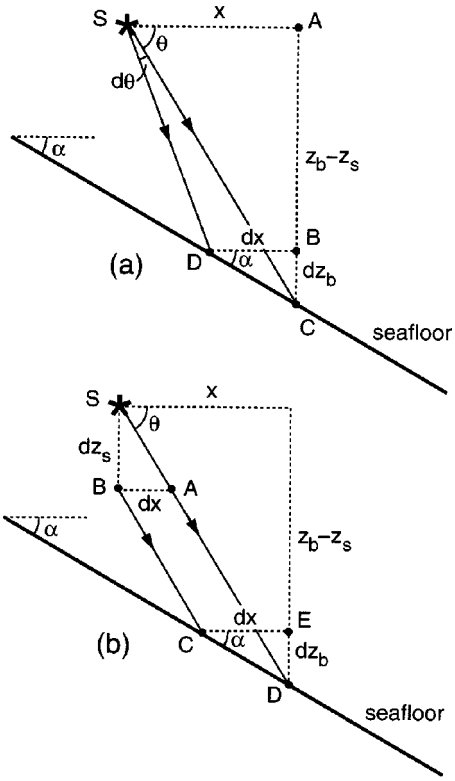

FIG. A1. Geometric constructions used to calculate (a) $\partial z_b/\partial p_1$, and (b) $\partial z_b/\partial z_s$.

$$\frac{\partial c(z_b)}{\partial p_1} = \frac{\partial c(z_b)}{\partial z_b} \frac{\partial z_b}{\partial p_1}, \tag{A7}$$

where $\partial c(z_b)/\partial z_b$ is the sound-velocity gradient at depth z_b. To derive an expression for $\partial z_b/\partial p_1$, assume that ray curvature is negligible. Then,

$$\frac{\partial z_b}{\partial p_1} = \frac{\partial z_b}{\partial(\cos\theta/c)} = -\frac{c}{\sin\theta} \frac{\partial z_b}{\partial\theta}. \tag{A8}$$

The relationship between dz_b and $d\theta$ is illustrated in Fig. A1(a). From this figure, triangle *SAC* leads to

$$dx = \cot\theta\, dz_b - (z_b - z_s)/\sin^2\theta\, d\theta, \tag{A9}$$

and triangle *BCD* leads to

$$dx = \cot\alpha\, dz_b. \tag{A10}$$

Solving Eqs. (A8)–(A10) leads to the desired expression,

$$\frac{\partial z_b}{\partial p_1} = \frac{c(z_b)(z_b - z_s)\sin\alpha}{\sin^2\theta \sin(\theta-\alpha)}. \tag{A11}$$

Although Eq. (A11) was derived neglecting ray curvature, comparisons of $\partial x/\partial p_1$ computed via Eqs. (A5)–(A7) and (A11) with carefully-applied numerical derivatives (including ray curvature) generally agreed to four significant digits, and were more accurate than expressions derived ignoring all effects of ray curvature [i.e., replacing $c(z)$ by a constant c].

Once a suitable ray parameter is determined, the travel time along the ray path is computed using Eq. (A2). In addition to travel times, the inversion algorithm requires partial

derivatives of the travel time with respect to receiver and source coordinates. Consider first the travel-time derivative with respect to the hydrophone offset x_h,

$$\frac{\partial t}{\partial x_h} = \frac{\partial t}{\partial p_1}\frac{\partial p_1}{\partial x}\frac{\partial x}{\partial x_h}. \tag{A12}$$

Noting that $\partial x/\partial x_h = 1$ for an eigenray,

$$\frac{\partial t}{\partial x_h} = \frac{\partial t}{\partial p_1} \Big/ \frac{\partial x}{\partial p_1}. \tag{A13}$$

In Eq. (A13), $\partial x/\partial p_1$ is given by Eq. (A5), and $\partial t/\partial p_1$ is obtained by differentiating Eq. (A2),

$$\frac{\partial t}{\partial p_1} = \int_{z_s}^{z_b} \frac{p_1 c(z)dz}{[1-p_1^2c^2(z)]^{3/2}} - \int_{z_b}^{z_h} \frac{p_2 c(z)dz}{[1-p_2^2c^2(z)]^{3/2}}\frac{\partial p_2}{\partial p_1} + \left[\frac{1}{c(z_b)[1-p_1^2c^2(z_b)]^{1/2}} + \frac{1}{c(z_b)[1-p_2^2c^2(z_b)]^{1/2}}\right]\frac{\partial z_b}{\partial p_1}, \tag{A14}$$

where $\partial p_2/\partial p_1$ and $\partial z_b/\partial p_1$ are given by Eqs. (A6), (A7), and (A11).

Next, consider differentiating Eq. (A2) with respect to hydrophone depth z_h,

$$\frac{\partial t}{\partial z_h} = \left[\int_{z_s}^{z_b} \frac{p_1 c(z)dz}{[1-p_1^2c^2(z)]^{3/2}} - \int_{z_b}^{z_h} \frac{p_2 c(z)dz}{[1-p_2^2c^2(z)]^{3/2}}\frac{\partial p_2}{\partial p_1}\right]\frac{\partial p_1}{\partial z_h} - \frac{1}{c(z_h)[1-p_1^2c^2(z_h)]^{1/2}}. \tag{A15}$$

In Eq. (A15), an expression is required for $\partial p_2/\partial z_h$. To obtain this, note that since x and z_h are independent coordinates, $\partial x/\partial z_h = 0$, which leads to

$$\frac{\partial x}{\partial z_h} = 0 = \int_{z_s}^{z_b} \frac{c(z)dz}{[1-p_1^2c^2(z)]^{3/2}}\frac{\partial p_1}{\partial z_h} - \int_{z_b}^{z_h} \frac{c(z)dz}{[1-p_2^2c^2(z)]^{3/2}}\frac{\partial p_2}{\partial p_1}\frac{\partial p_1}{\partial z_h} - \frac{p_2 c(z_h)}{[1-p_2^2c^2(z)]^{1/2}}. \tag{A16}$$

Solving Eq. (A16) for $\partial p_1/\partial z_h$ yields

$$\frac{\partial p_1}{\partial z_h} = \left[\frac{p_2 c(z_h)}{[1-p_2^2c^2(z_1)]^{1/2}}\right]\left[\int_{z_b}^{z_h} \frac{c(z)dz}{[1-p_2^2c^2(z)]^{3/2}}\frac{\partial p_2}{\partial p_1} - \int_{z_s}^{z_b} \frac{c(z)dz}{[1-p_1^2c^2(z)]^{3/2}}\right]^{-1}. \tag{A17}$$

The final partial derivative required is $\partial t/\partial z_s$; differentiating Eq. (A2) leads to

$$\frac{\partial t}{\partial z_s} = \frac{-1}{c(z_b)[1-p_1^2c^2(z_b)]^{1/2}} + \left[\int_{z_s}^{z_b} \frac{p_1 c(z)dz}{[1-p_1^2c^2(z)]^{3/2}} - \int_{z_b}^{z_h} \frac{p_2 c(z)dz}{[1-p_2^2c^2(z)]^{3/2}}\frac{\partial p_2}{\partial p_1}\right]\frac{\partial p_1}{\partial z_s} + \frac{1}{c(z_b)} \times [[1-p_1^2c^2(z_b)]^{-1/2} + [1-p_2^2c^2(z_b)]^{-1/2}]\frac{\partial z_b}{\partial z_s}. \tag{A18}$$

Evaluating Eq. (A18) requires expressions for $\partial p_1/\partial z_s$ and $\partial z_b/\partial z_s$. Noting $\partial x/\partial z_s = 0$ leads to

$$\frac{\partial p_1}{\partial z_s} = \left\{\frac{p_1 c(z_s)}{[1-p_1^2c^2(z_1)]^{1/2}} + \left[\frac{p_1}{[1-p_1^2c^2(z_b)]^{1/2}} + \frac{p_2}{[1-p_2^2c^2(z_b)]^{1/2}}\right]\frac{\partial z_b}{\partial z_s}c(z_b)\right\} \times \left\{\int_{z_s}^{z_b} \frac{c(z)dz}{[1-p_1^2c^2(z)]^{3/2}} - \int_{z_s}^{z_b} \frac{c(z)dz}{[1-p_2^2c^2(z)]^{3/2}}\frac{\partial p_2}{\partial p_1}\right\}^{-1}. \tag{A19}$$

The relationship between dz_b and dz_s is illustrated in Fig. A1(b), neglecting ray curvature. Triangle *SAB* leads to $dx = \cos\theta dz_s$ and triangle *CDE* leads to $dx = \cot\alpha dz_b$; combining these results yields

$$\frac{\partial z_b}{\partial z_s} = \frac{\tan\alpha}{\tan\theta}. \tag{A20}$$

The integrals involved in the above equations can be solved analytically if the sound-velocity profile is represented by a series of layers with a linear sound-velocity gradient in each layer. Let z_k and c_k represent the depth and sound velocity at the top of the kth layer and c_k' be the gradient in this layer. The three integral forms required may be evaluated as follows, where it is assumed $z_j > z_i$ and $w_k \equiv [1-p^2c_k^2]^{1/2}$,

$$\int_{z_i}^{z_j} \frac{pc(z)dz}{[1-p^2c^2(z)]^{1/2}} = \sum_{k=i}^{j-1} \frac{w_k - w_{k+1}}{pc_k'}, \tag{A21}$$

$$\int_{z_i}^{z_j} \frac{dz}{c(z)[1-p^2c^2(z)]^{1/2}} = \sum_{k=i}^{j-1} \frac{1}{c_k'}\left[\log_e \frac{c_{k+1}(1+w_k)}{c_k(1+w_{k+1})}\right], \tag{A22}$$

$$\int_{z_i}^{z_j} \frac{c(z)dz}{[1-p^2c^2(z)]^{3/2}} = \sum_{k=i}^{j-1} \frac{w_k - w_{k+1}}{p^2c_k'w_kw_{k+1}}. \tag{A23}$$

[1] W. M. Telford, L. P. Geldart, R. E. Sheriff, and D. A. Keys, *Applied Geophysics* (Cambridge University Press, New York, 1976), Chap. 4.

[2] E. Y. T. Kuo, "The dynamic response of a cable section in a towed three-dimensional array system," NUSC TR7481, Naval Underwater System Center, New London, CT, 1987.

[3] F. Milinazzo, M. Wilkie, and S. A. Latchman, "An effective algorithm for simulating the dynamics of towed cable systems," IEEE J. Ocean Eng. **14**, 513–526 (1987).

[4] E. Y. T. Kuo and M. J. Casati, "Physical splines, application to towed array dynamics," Naval Underwater System Center, New London, CT, 1990.

[5] H. P. Bucker, ''Beamforming a towed line array of unknown shape,'' J. Acoust. Soc. Am. **63**, 1451–1454 (1978).
[6] B. G. Ferguson, ''Sharpness applied to the adaptive beamforming of acoustic data from a towed array of unknown shape,'' J. Acoust. Soc. Am. **88**, 2695–2701 (1990).
[7] J. L. Riley, D. A. Gray, and B. G. Ferguson, ''Estimating the shape of a towed array of hydrophones using both acoustic and nonacoustic sensor techniques,'' in *Acoustic Signal Processing for Ocean Exploration*, edited by J. M. F. Moura and I. M. G. Lourtie (Kluwer, The Netherlands, 1993), pp. 225–230.
[8] E. C. van Ballegooijen, G. W. van Mierlo, S. van Schooneveld, P. M. van der Zalm, A. T. Parsons, and N. H. Field, ''Measurement of towed array position, shape and attitude,'' IEEE J. Ocean Eng. **14**, 375–383 (1989).
[9] S. E. Dosso and N. E. Collison, ''Regularized inversion for towed array shape estimation,'' in *Inverse Problems in Underwater Acoustics*, edited by M. I. Taroudakis and G. N. Makrakis (Springer-Verlag, Berlin, in press), p. 28.
[10] W. S. Hodgkiss, ''Shape determination of a shallow-water bottomed array,'' in *Proc. Oceans '89*, MTS/IEEE, 1199–1204 (1989).
[11] B. J. Sotirin and J. A. Hildebrand, ''Acoustic navigation of a large-aperture array,'' J. Acoust. Soc. Am. **87**, 154–167 (1990).
[12] S. E. Dosso, M. R. Fallat, B. J. Sotirin, and J. L. Newton, ''Array element localization for horizontal arrays via Occam's inversion,'' J. Acoust. Soc. Am. **104**, 846–859 (1998).
[13] S. E. Dosso and B. J. Sotirin, ''Optimal array element localization,'' J. Acoust. Soc. Am. **106**, 3445–3459 (1999).
[14] M. V. Greening, ''Array element localization of rapidly deployable systems,'' Can. Acoust. **28**, 7–13 (2000).
[15] R. Walia and D. Hannay, ''Source and receiver geometry corrections for deep towed multichannel seismic data,'' Geophys. Res. Lett. **26**, 1993–1996 (1999).
[16] D. R. Aldridge, S. E. Dosso, A. L. Endres, and D. W. Oldenburg, ''New methods for constructing flattest and smoothest models,'' Inverse Probl. **7**, 499–514 (1991).
[17] S. E. Dosso and M. Riedel, ''Acoustic Array Element Localization for Marine Seismology,'' in *Proceedings of the 5th European Conference on Underwater Acoustics* (European Communities, Luxembourg, 2000), pp. 595–600.
[18] M. Riedel, N. R. Chapman, R. D. Hyndman, G. D. Spence, and S. E. Dosso, ''A pseudo-3D seismic survey at a gas-hydrate field offshore Vancouver Island,'' EOS Trans. Am. Geophys. Union **80**, 481 (1999).
[19] D. W. Oldenburg, ''Funnel functions in linear and nonlinear appraisal,'' J. Geophys. Res., [Space Phys.] **88**, 7387–7398 (1983).
[20] S. C. Constable, R. L. Parker, and C. G. Constable, ''Occam's inversion: A practical algorithm for generating smooth models from electromagnetic sounding data,'' Geophysics **52**, 289–300 (1987).
[21] C. van Schooneveld, ''Inverse problems: A tutorial survey,'' in *Underwater Acoustic Data Processing*, edited by Y. T. Chan (Kluwer, The Netherlands, 1989), pp. 393–411.
[22] J. A. Scales, P. Docherty, and A. Gersztenkorn, ''Regularization of nonlinear inverse problems: Imaging the near-surface weathering layer,'' Inverse Probl. **6**, 115–131 (1990).
[23] W. H. Press, B. P. Flannery, S. A. Teukolsky, and W. T. Vetterling, *Numerical Recipes* (Cambridge University Press, New York, 1992).
[24] N. E. Collison and S. E. Dosso, ''Regularized matched-mode processing for source localization,'' J. Acoust. Soc. Am. **107**, 3089–3100 (2000).
[25] O. Yilmaz, *Seismic Data Processing: Investigations in Geophysics No. 2* (Society of Exploration Geophysicists, Tulsa, 1987).

Acoustic echo detection and arrival-time estimation using spectral tail energy

Phillip L. Ainsleigh
Naval Undersea Warfare Center, 1176 Howell Street, Newport, Rhode Island 02841

(Received 19 December 1995; revised 23 March 2001; accepted 26 April 2001)

An algorithm is introduced for detecting signal and echo onsets and estimating their arrival times in multipath acoustic data. The algorithm accommodates superimposed narrow-band signals with continuous onsets, unknown envelopes, and arrival-time separations of less than one cycle at the dominant tonal frequency. It does not require the multipath components to be shifted and weighted replicas of each other or of a template signal. The separation of closely spaced signals is enabled by applying a prefilter that isolates spectral ''tail'' energy in which the onsets are discernible, and by operating on the filtered data using a matched-subspace detector that is conditioned on previously detected onsets. This algorithm has particular value for laboratory measurements, as it utilizes the high signal-to-noise ratios available in a laboratory to solve a previously intractable detection and estimation problem. © *2001 Acoustical Society of America.* [DOI: 10.1121/1.1381027]

PACS numbers: 43.60.Qv, 43.60.Cg, 43.58.Vb [JCB]

I. INTRODUCTION

When a periodic signal is multiplied by a time gate with finite or semi-infinite extent, the result is a smearing of the signal's spectrum due to its being convolved with the spectrum of the gating function. The convolved spectrum has magnitude peaks occurring at the frequencies associated with the periodicities, with decaying ''tails'' on either side of the spectral peaks. This paper presents a spectral tail energy matched-subspace (STEMS) algorithm that makes use of this tail energy to estimate the number of multipath components and the onset time of each component in single-sensor multipath acoustical data. The algorithm accommodates superimposed signals with narrow bandwidths, long duration, unknown envelopes, distorted echoes, and onset time separations of less than a cycle at the lowest tonal frequency.

The STEMS algorithm comprises two major components: a prefilter and an iterative detection/estimation algorithm. The prefilter isolates spectral tail energy in which signal onsets are more discernible than in the received data. This tail energy is significantly smaller than the total signal energy, so the method requires a high signal-to-noise ratio (SNR). The algorithm is intended for use in repeatable laboratory experiments, where the observed data can be averaged over multiple experiments to increase SNR to a suitably high level. The iterative detection/estimation algorithm operates on the filtered data. During each iteration, a single multipath component is detected and its arrival time is estimated. A matched-subspace test statistic is calculated for each candidate arrival time using an oblique projection operator that suppresses energy due to previously detected onsets. If any values of the test statistic exceed the detection threshold, the location of the maximum is chosen as an arrival time. The algorithm stops iterating when no values exceed the threshold.

Echo detection and arrival-time estimation in multipath data have received a great deal of attention in radar, active sonar, array signal processing, and seismology.[1] Previous methods, however, depend on signal structure that is not available in the signals of interest here. For example, multipath components are sometimes assumed to be delayed replicas of each other.[2] Alternatively, the components are assumed to be delayed and scaled replicas of a transient that is either known or has a known parametric form.[3] Homomorphic deconvolution methods[4] circumvent the need for delayed replicas, but these methods require the signal components to have finite time duration, large bandwidth (B), and arrival separations greater than $1/B$. The STEMS algorithm is unique because it accommodates signals that do not satisfy the structure required by existing algorithms.

The motivation for this work is calibration testing of sonar transducers whose transfer functions are sensitive to temperature and pressure. Because of this sensitivity, testing must be performed in water-filled tanks whose temperature and pressure are varied in a controlled way. In a typical test, a transducer's unknown transfer function is characterized by measuring its steady-state response to a gated sinusoid at discrete frequencies across a band of interest, a process known as ''stepped-sine'' testing.[5] A difficult test scenario involves high-power acoustic projectors with low-frequency resonances and transient-response durations exceeding the echo-free response time of the measurement tank. In such cases, the echo-free steady-state response is estimated from echo-contaminated data using a previously developed multipath modeling algorithm.[6] That algorithm encounters numerical difficulties when attempting to simultaneously estimate the arrival times and other parameters for signals with closely spaced arrivals, and it requires knowledge of the number of echoes. Since irregular structures such as protruding lids and absorptive wedges make geometrical time-of-flight calculations for echoes infeasible, the need exists for an algorithm that estimates the number of significant echoes and their arrival times. These estimates are then used as fixed inputs for subsequent processing by multipath modeling algorithms.

II. STEMS ALGORITHM

The received multipath signal is sampled into the N-dimensional vector $\mathbf{y}$, which is modeled as

$$\mathbf{y}=\mathbf{s}+\mathbf{w}, \tag{1}$$

where $\mathbf{s}$ is the deterministic multipath signal and $\mathbf{w}$ is white Gaussian noise. For periodic or almost-periodic signals, the spectrum contains sharp peaks at the "tonal frequencies." For example, the tonal frequencies in a transducer's response to a stepped sinusoid include the driving frequency and the device's resonance frequencies. The tail energy is located on either side of these tonal peaks. In the example presented in Sec. III, the tail energy is extracted from the high-frequency side of the single tonal peak since the high-frequency tail energy provides better temporal resolution than does the low-frequency tail. In this case, the passband of the tail-energy filter is placed between the tonal frequency and the frequency at which the noise spectral energy exceeds the tail energy of the signal. For signals with multiple tonal frequencies, the filter passband is placed between tonal frequencies.

When designing the tail-energy filter, frequency sidelobes are a critical issue since tonal energy falling within the sidelobes could easily be significant relative to the tail energy. To avoid this issue, the time-domain tail component is generated by taking a fast Fourier transform (FFT), multiplying by a compactly supported frequency-shaping function, and taking an inverse FFT. The frequency-shaping function used here is a raised-cosine (Hamming) function with manually chosen center placement and width.

For the sake of the theoretical analysis to follow, it is convenient to represent the tail component (i.e., the bandpass-filtered data) as

$$\mathbf{g}=\mathbf{W}\mathbf{y}, \tag{2}$$

where $\mathbf{W}$ is the symmetric real $N\times N$ bandpass operator matrix, which can be written as

$$\mathbf{W}=\mathbf{F}^{*}\mathbf{D}\mathbf{F}. \tag{3}$$

Here, $\mathbf{F}$ denotes the complex symmetric $N\times N$ Fourier matrix,[7] whose pqth element is

$$F_{pq}=\frac{1}{\sqrt{N}}\omega^{(p-1)(q-1)}, \tag{4}$$

where $\omega=\exp(-j2\pi/N)$. The $N\times N$ diagonal matrix $\mathbf{D}$ contains samples of the filter's frequency-shaping function along its main diagonal, and $\mathbf{F}^{*}$ denotes the complex conjugate of $\mathbf{F}$. Premultiplying $\mathbf{y}$ by $\mathbf{F}$ corresponds to taking an FFT. Premultiplying the product $\mathbf{F}\mathbf{y}$ by $\mathbf{D}$ corresponds to weighting the data's spectral coefficients with the frequency-shaping function, which has two nonzero regions corresponding to the filter passband: one in the positive frequency range and its mirror image in the negative frequency range. Finally, premultiplying the product $\mathbf{DF}\mathbf{y}$ by $\mathbf{F}^{*}$ corresponds to taking an inverse FFT, which generates the bandpass-filtered time-domain signal.

Letting $\mathcal{N}(\mathbf{y};\mu,\mathbf{\Sigma})$ denote the normal density for vector $\mathbf{y}$ with mean vector μ and covariance matrix $\mathbf{\Sigma}$, the probability density for the received data, as modeled by Eq. (1), is

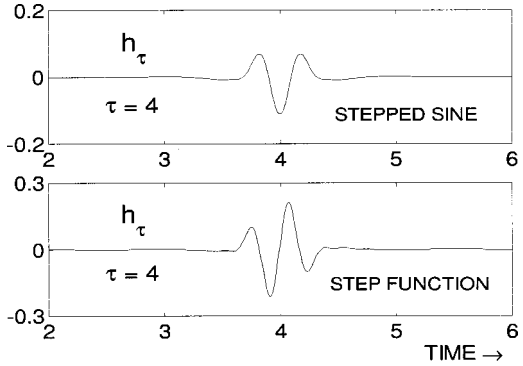

FIG. 1. Onset models for stepped-sine function (top) and step function (bottom).

$$p(\mathbf{y})=\mathcal{N}(\mathbf{y};\mathbf{s},\sigma^{2}\mathbf{I}_{N}), \tag{5}$$

where $\mathbf{I}_{N}$ is an $N\times N$ identity matrix and σ^{2} is the noise variance, which is estimated using the noise-only segment prior to the onset of the directly arriving signal. Since $\mathbf{g}$ is a linear function of the Gaussian variable $\mathbf{y}$, its density model is

$$p(\mathbf{g})=\mathcal{N}(\mathbf{g};\mathbf{W}\mathbf{s},\sigma^{2}\mathbf{W}^{2}). \tag{6}$$

The deterministic portion of the model takes the form

$$s=\sum_{k=1}^{N_{\tau}}\gamma_{\mathbf{k}}\mathbf{x}_{\mathbf{k}}, \tag{7}$$

where N_{τ} is the number of multipath components, each $\mathbf{x}_{\mathbf{k}}$ is a multipath component with arrival time $\tau_{\mathbf{k}}$, and each $\gamma_{\mathbf{k}}$ is a non-negative weighting coefficient. The tail component of each individual onset is modeled as

$$\mathbf{W}\mathbf{x}_{\mathbf{k}}\approx\tilde{\gamma}\mathbf{W}\mathbf{m}_{\tau_{\mathbf{k}}}=\tilde{\gamma}\mathbf{h}_{\tau_{\mathbf{k}}}, \tag{8}$$

where $\tilde{\gamma}$ is an unknown scale constant, $\mathbf{h}_{\tau_{\mathbf{k}}}=\mathbf{W}\mathbf{m}_{\tau_{\mathbf{k}}}$, and $\mathbf{m}_{\tau_{\mathbf{k}}}$ is template function such as a unit sinusoid or unit step function with start time $\tau_{\mathbf{k}}$.

Tail components are very similar for signals with the same continuity properties at the onset. Figure 1 shows the tail component of a unit stepped-sine function and a unit step function, each starting at time $t=4$. The stepped-sine function has a continuous onset since it turns on at the start of a cycle. To within a weighting constant, the tail component of the stepped sine is representative of tail components for signals with continuous onsets, such as stepped sines with different frequencies or ramp functions that turn on at zero. The step-function model is representative of signals with discontinuous onsets.

For closely spaced onsets, the tail energy overlaps to some extent even in the tail energy. To account for this, the model is extended to include previously detected onsets. The algorithm is then iterative, and a single onset is detected in each iteration. The model distribution for the ith iteration is

$$p_{\mathbf{i}}(\mathbf{g}|\,\tau_{\mathbf{i}},\gamma_{\mathbf{i}})=\mathcal{N}(\mathbf{g};\gamma_{\mathbf{i}}\mathbf{h}_{\tau_{\mathbf{i}}}+\tilde{\mathbf{H}}_{\mathbf{i}-1}\tilde{\mathbf{a}}_{\mathbf{i}-1},\sigma^{2}\mathbf{W}^{2}), \tag{9}$$

where $\tilde{\mathbf{H}}_{\mathbf{i}-1}=[\mathbf{h}_{\hat{\tau}_1},\mathbf{h}_{\hat{\tau}_2},\ldots,\mathbf{h}_{\hat{\tau}_{\mathbf{i}-1}}]$. Here, each vector $\mathbf{h}_{\hat{\tau}_{\mathbf{m}}}$ is the tail-energy model for the onset whose arrival time $\hat{\tau}_{\mathbf{m}}$ is estimated during the mth iteration, and $\tilde{\mathbf{a}}_{\mathbf{i}-1}$ is a nuisance

vector of unknown weighting coefficients. The unknown scale constants $\tilde{\gamma}$ from Eq. (8) have been absorbed into weight $\gamma_{\mathbf{i}}$ for the present candidate arrival time and into the weights in $\tilde{\mathbf{a}}_{\mathbf{i}-1}$ for the previously detected arrivals. In the first iteration, $\tilde{\mathbf{H}}_{\mathbf{0}}=\mathbf{0}$ if there is no *a priori* information. If there is prior knowledge (e.g., in a laboratory setting, the onset time of the directly arriving signal is determined from the emitter–receiver separation and sound speed), then models for known onsets are included in $\tilde{\mathbf{H}}_{\mathbf{0}}$.

Because of the similarity of the tail components for large classes of signals, a single template $\mathbf{h}_{\tau}$ can represent a wide range of signals. In some cases, however, the data may simultaneously contain a mixture of different signal classes (e.g., the classes of continuous-onset and discontinuous-onset signals). To accommodate such cases, the tail-component model is generalized as a linear combination of different onset models, that is, as

$$\mathbf{h}_{\tau_{\mathbf{i}}}=\mathbf{H}_{\tau_{\mathbf{i}}}\mathbf{a}_{\tau_{\mathbf{i}}}, \tag{10}$$

where the $N\times p$ matrix $\mathbf{H}_{\tau_{\mathbf{i}}}$ contains onset models for the different classes and $\mathbf{a}_{\tau_{\mathbf{i}}}$ is a p-dimensional nuisance vector of unknown weights. This leads to the model density

$$p_{\mathbf{i}}(\mathbf{g}|\,\tau_{\mathbf{i}},\gamma_{\mathbf{i}})=\mathcal{N}(\mathbf{g};\gamma_{\mathbf{i}}\mathbf{H}_{\tau_{\mathbf{i}}}\mathbf{a}_{\tau_{\mathbf{i}}}+\tilde{\mathbf{H}}_{\mathbf{i}-1}\tilde{\mathbf{a}}_{\mathbf{i}-1},\sigma^2\mathbf{W}^2). \tag{11}$$

The unknown weighting vectors $\tilde{\mathbf{a}}_{\mathbf{i}-1}$ and $\mathbf{a}_{\tau_{\mathbf{i}}}$ need not be estimated since the detector and arrival-time estimator are based on subspace projection techniques. In such methods, a symmetric projection operator, $\mathbf{P}_{\mathbf{A}}$, is used to project a vector onto a subspace $\langle\mathbf{A}\rangle$, the range space of a matrix $\mathbf{A}$. This operator satisfies the condition $\mathbf{P}_{\mathbf{A}}^2=\mathbf{P}_{\mathbf{A}}$ and its eigenvalues take only the values zero and one. The associated operator $\mathbf{P}_{\mathbf{A}}^{\perp}=\mathbf{I}-\mathbf{P}_{\mathbf{A}}$ projects a vector onto the orthogonal complement of $\langle\mathbf{A}\rangle$.

An existing matched-subspace detection method[8] for the model in Eq. (11) requires the covariance matrix to be a projection operator. Since the covariance matrix $\sigma^2\mathbf{W}^2$ in Eq. (11) is not a projector, a statistical approximation must be introduced to use the matched-subspace detector. To analyze the properties of the covariance matrix, the definition of the bandpass operator $\mathbf{W}$ in Eq. (3) and the finite support of the frequency-shaping function are noted to obtain the partitioned form of $\mathbf{W}^2$ given by

$$\mathbf{W}^2=[\mathbf{F}_L^*\mathbf{F}_B^*\mathbf{F}_H^*]\begin{bmatrix}\mathbf{0}&\mathbf{0}&\mathbf{0}\\ \mathbf{0}&\mathbf{B}^2&\mathbf{0}\\ \mathbf{0}&\mathbf{0}&\mathbf{0}\end{bmatrix}\begin{bmatrix}\mathbf{F}_L^T\\ \mathbf{F}_B^T\\ \mathbf{F}_H^T\end{bmatrix}=\mathbf{F}_B^*\mathbf{B}^2\mathbf{F}_B^T, \tag{12}$$

where $\mathbf{F}_L$, $\mathbf{F}_B$, and $\mathbf{F}_H$ contain the columns of $\mathbf{F}$ corresponding to the frequencies in the filter's lower stopband, passband, and upper stopband, respectively. The superscript T denotes transposition. The diagonal matrix $\mathbf{B}$ contains the nonzero values of the filter's frequency-shaping function. This shaping function is tapered so that the filter's impulse response decays rapidly, which helps to eliminate interference between the tail components of well-separated onsets. Matrix $\mathbf{W}^2$ is not a projection operator since the tapering introduces eigenvalues whose magnitudes are between zero and one. In order to apply the subspace detector, $\mathbf{B}$ is approximated with an identity matrix in the covariance term, which leads to the approximate model density

$$p_{\mathbf{i}}(\mathbf{g}|\,\tau_{\mathbf{i}},\gamma_{\mathbf{i}})=\mathcal{N}(\mathbf{g};\gamma_{\mathbf{i}}\mathbf{H}_{\tau_{\mathbf{i}}}\mathbf{a}_{\tau_{\mathbf{i}}}+\tilde{\mathbf{H}}_{\mathbf{i}-1}\tilde{\mathbf{a}}_{\mathbf{i}-1},\sigma^2\mathbf{P}_{\mathbf{F}_B}). \tag{13}$$

Here, $\mathbf{P}_{\mathbf{F}_B}=\mathbf{F}_B^*\mathbf{F}_B^T$ is a projection matrix due to the properties of $\mathbf{F}_B$. A maximal invariant statistic for testing $\mathcal{H}_0:\gamma_{\mathbf{i}}=0$ vs $\mathcal{H}_1:\gamma_{\mathbf{i}}>0$ in models of the form of Eq. (13) is given by[8]

$$\eta(\tau_{\mathbf{i}})=\mathbf{g}^T\mathbf{P}_{\mathbf{G}_{\tau_{\mathbf{i}}}}\mathbf{g}, \tag{14}$$

where

$$\mathbf{G}_{\tau_{\mathbf{i}}}=\mathbf{P}_{\mathbf{H}_{\mathbf{i}-1}}^{\perp}\mathbf{H}_{\tau_{\mathbf{i}}}. \tag{15}$$

Given the model in Eq. (13), the normalized statistic $\eta(\tau_{\mathbf{i}})/\sigma^2$ is noncentral χ^2-distributed with p degrees of freedom and noncentrality parameter $\lambda^2=\gamma_{\mathbf{i}}^2\mathbf{a}_{\tau_{\mathbf{i}}}^T\mathbf{H}_{\tau_{\mathbf{i}}}^T\mathbf{H}_{\tau_{\mathbf{i}}}\mathbf{a}_{\tau_{\mathbf{i}}}/\sigma^2$, and the uniformly most powerful (UMP) invariant test for detecting an onset is[9]

$$\eta(\tau_{\mathbf{i}})\underset{\mathcal{H}_0}{\overset{\mathcal{H}_1}{\gtrless}}\sigma^2\xi, \tag{16}$$

where ξ is a threshold that is set to obtain a desired false-alarm probability

$$P_{\mathrm{FA}}=1-\Pr\{\chi_p^2(0)\leqslant\xi\}. \tag{17}$$

If an onset is detected in the ith iteration, it is assigned an arrival time estimate given by

$$\hat{\tau}_{\mathbf{i}}=\arg\max_{\tau_{\mathbf{i}}}\,\eta(\tau_{\mathbf{i}}). \tag{18}$$

This estimated arrival time is most likely to have produced the observed data in the region near the onset.

A small mismatch between the tail components of the model and data can sometimes lead to constructive interference and elevated energy levels in regions removed from the onset. To avoid triggering false alarms, the threshold is inflated by an amount proportional to the largest difference between the test statistic and the threshold in all previous iterations. For example, in the first iteration, the threshold is $\sigma^2\xi$ since no echoes have been previously detected. If the maximum value of the detection statistic in the first iteration is $\eta_{\max}$, then the threshold in the second iteration is set to $\sigma^2\xi+\zeta\{\eta_{\max}-\sigma^2\xi\}$ for some small constant ζ. A value $\zeta=0.1$ is used in the simulation experiments presented in the next section.

III. SIMULATION EXPERIMENTS

The multipath test signal shown at the top of Fig. 2 is representative, to within a frequency scaling, of signals obtained in stepped-sine transducer measurements in a small tank. Noisy versions of this signal are used to demonstrate the algorithm's operation and to evaluate its performance.

Also shown in Fig. 2 are the three components that sum to produce the multipath signal. The second signal shown is the directly arriving signal with arrival time τ_0. This component is the stepped-sine response of the two-pole resonant system

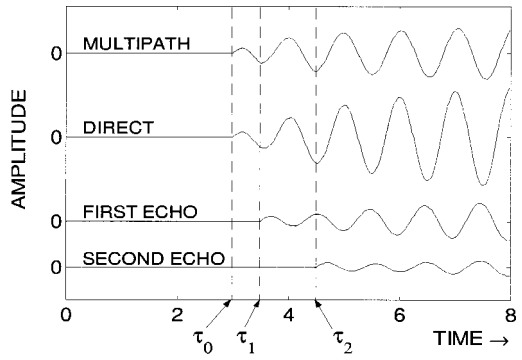

FIG. 2. Multipath test signal and component arrivals.

$$H(s)=\frac{s^2}{s^2+(\beta/Q)s+\beta^2}, \tag{19}$$

with $Q=8$ and $\beta=2\pi$. The corresponding resonance frequency is $f_c=1$ Hz. The system's natural response has the damping factor $\alpha_1=-0.3927$ and frequency $f_1=0.9980$ Hz. The frequency of the stepped-sine drive function is $f_0=1$ Hz. Normalized drive and resonance frequencies are used so that all time values are in fractions of a cycle. The at-resonance drive frequency is used because it is usually the most important frequency in the transfer-function measurement. The directly arriving component in Fig. 2 grows instead of decays because the system's natural response opposes the forced response until it dies out. The form of Eq. (19) also forces the direct component to have a continuous onset. The last two signals shown in Fig. 2 are echoes with arrival times τ_1 and τ_2, respectively. The echoes are amplitude- and phase-distorted versions of the directly arriving signal. The distortion is introduced by adding independent random amplitude scalings and phase shifts to the forced- and the natural-response components, subject to a constraint that imposes continuity in the arrival onsets. This constraint is employed to represent real-world boundary reflections. The continuous nature of the echo onsets makes them very difficult to detect, even in noiseless data.

The example signal is defined by

$$y(t)=\sum_{k=0}^{2} x_{\mathbf{k}}(t-\tau_{\mathbf{k}})\mu(t-\tau_{\mathbf{k}})+n(t), \tag{20}$$

where the $\tau_{\mathbf{k}}$ are the arrival times $\mu(t)$ is the unit step function, and $n(t)$ is white Gaussian noise. The multipath components are

$$x_{\mathbf{k}}(t)=A_{\mathbf{k},0}\cos\{2\pi f_0 t+\phi_{\mathbf{k},0}\} + A_{\mathbf{k},1}e^{-\alpha_1(t)}\cos\{2\pi f_1 t+\phi_{\mathbf{k},1}\}. \tag{21}$$

The amplitudes and phases of the forced- and natural-response portions of each multipath component are

$$A_{k,0}=\{8.0,8.0,8.0\},$$

$$\phi_{k,0}=\{1.5708,1.9635,2.0944\},$$

$$A_{k,1}=\{8.0157,8.8719,10.4730\},$$

$$\phi_{k,1}=\{-1.5083,-0.9847,-0.7229\}.$$

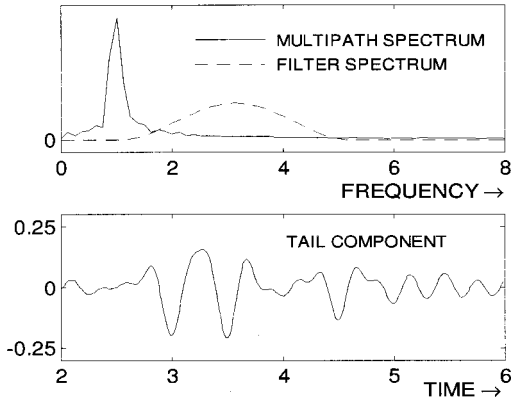

FIG. 3. Positive-frequency portion of the spectrum of the noisy test signal (SNR=18 dB) overlaid with the filter frequency-shaping function (top), and time-domain tail component (bottom).

The values inside braces for each variable are for onset indices $k=0,1,2$, respectively. All phase angles are in radians. The example signal is generated with a sampling rate $f_s=64$ Hz over a period of 8 s, yielding a sample size $N=512$ and a Nyquist frequency of 32 Hz. The arrival times are 3, 3.5, and 4.5 s for the direct signal, first echo, and second echo, respectively. The first echo arrives one-half of a cycle after the directly arriving signal.

The tail-energy filter and tail component are shown in Fig. 3. Because the multipath signal does not die down to zero during the observation time, the tail component exhibits edge effects from the discontinuity at the end of the observation gate. In laboratory testing, the observation time and the pretrigger delay for the excitation are controllable parameters, so problems from edge effects are avoided by extending the observation gate on either end to include buffer regions that the algorithm disregards when performing onset detection. The buffer regions used in the present example are 2 s (i.e., two cycles of the driving signal) in duration.

To obtain a repeatable measure of algorithm performance for different echoes, the multipath components in the test signal are scaled so that the heights of the first half-cycle are equal in all arriving components as depicted in Fig. 2. The signal-energy calculation is based on the root-mean-square energy in this first half-cycle. The noise energy is calculated from the portion of the received signal occurring before the onset of the direct signal.

The template function used in this example is $m_\tau(t)=\sin\{2\pi f_0(t-\tau)\}\mu(t-\tau)$, where f_0 is the known drive frequency. Algorithm iterations are demonstrated in Fig. 4, which shows the detection statistic and the modified detection threshold from each of four algorithm iterations. Peaks occur in the first iteration at the true onset times (3, 3.5, and 4.5 s), but the onsets cannot be separated. The maximum in this iteration corresponds to $\tau=3.5$ s, which is chosen as the estimate from the first iteration. The second iteration employs a detector which nulls the energy due to this onset. The maximum is again chosen, which this time picks up the onset at $\tau=3$ s. The process is repeated until no values exceed the threshold in the fourth iteration.

Algorithm performance is evaluated using 1000-trial Monte Carlo analysis across a range of SNR and probability

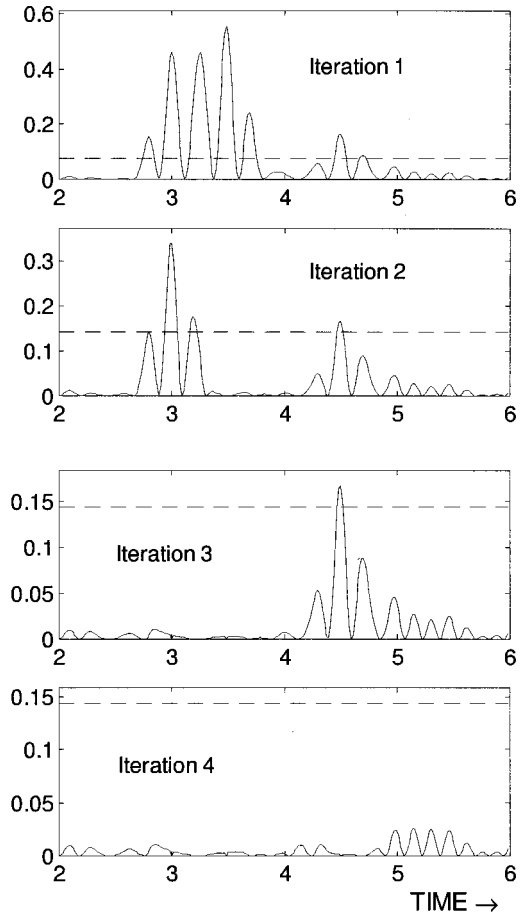

FIG. 4. Detection statistic (solid) and modified detection threshold (dashed) from four algorithm iterations (SNR=18 dB).

of false alarm (P_{FA}). The onset time for the direct signal is incorporated in these trials as prior information, so the focus here is on the echoes. Arrival-time estimates are assigned to the closest true arrival time. Figure 5 shows the observed detection probability P_D vs SNR for three different values of P_{FA}. Detection probabilities exceeding 99% are achieved at SNRs of 20 dB and higher for all values of P_{FA}. Perfect performance ($P_D=1$) is achieved at 22 dB and higher. Arrival-time estimation performance is judged by the bias and mean-squared error (MSE) of the estimates from all trials in which onsets are detected. Results are shown in Fig. 6

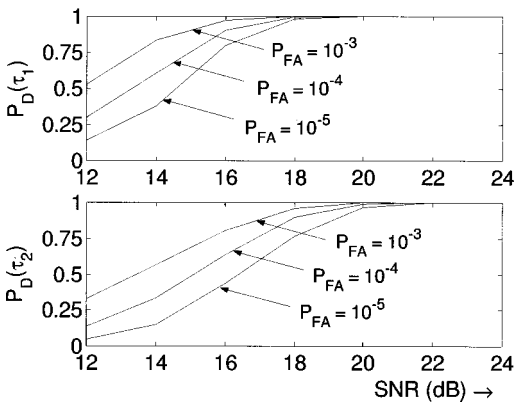

FIG. 5. ROC curves for detection of τ_1 (top) and τ_2 (bottom).

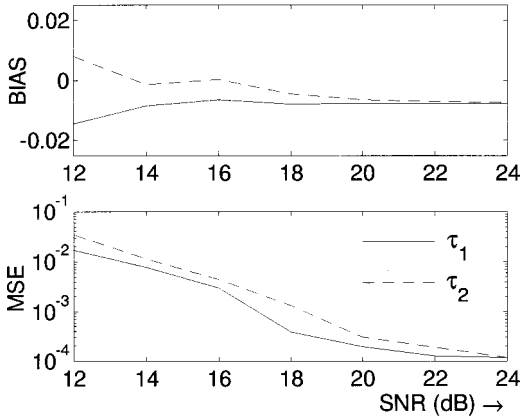

FIG. 6. Bias (top) and MSE (bottom) for estimation of τ_1 and τ_2.

for $P_{\mathrm{FA}}=10^{-3}$ since this gave the largest number of detections. While the estimates are slightly biased, the bias is less that 2% of a drive cycle at all SNR and it contributes very little to the MSEs, which are on the order of 1/1000th of a drive cycle at SNRs of 18 dB and higher.

IV. SUMMARY AND CONCLUSIONS

The STEMS algorithm is an effective approach for detecting signal onsets in multipath acoustic data and for estimating their arrival times. The algorithm processes high-frequency spectral tail energy using a matched-subspace filter that is conditioned on previously detected onsets. The algorithm was applied to a multipath signal having long-duration periodic components with small time separations between arrivals, a previously intractable problem. When applied to the test signal defined in Sec. III, the method provided detection probabilities exceeding 99%, and arrival-time MSEs on the order of 1/1000th of a cycle or less at the drive frequency, when the SNR is 20 dB and higher. Due to the very low noise floor and the ability to average over multiple test repetitions, SNRs of 40 to 60 dB are routinely obtained in Navy calibration facilities. The SNR requirements for method are thus well within the operating characteristics of these facilities.

The algorithm given here assumes that the noise variance is known from a noise-only segment prior to the start of the signal. Constant false-alarm rate (CFAR) matched-subspace detectors[8,9] can be used if the noise variance is not known.

ACKNOWLEDGMENTS

The author is indebted to Cliff Carter, Steve Forsythe, Stephen Greineder, and Roy Streit (all of NUWC, Division Newport) for valuable discussions and manuscript reviews, and to the Office of Naval Research (Code No. ONR-321SS, Transducer Technology Project, Acoustic Measurements Methodology Project) for funding.

[1] *Coherence and Time Delay Estimation: An Applied Tutorial for Research, Development, Test, and Evaluation Engineers*, edited by G. C. Carter (IEEE, New York, 1993).
[2] S.-K. Chow and P. M. Schultheiss, "Delay estimation using narrowband

processes,'' IEEE Trans. Acoust., Speech, Signal Process. **29**, 478–484 (1981).
[3] R. J. Vaccaro, C. S. Ramalingam, D. W. Tufts, and R. L. Field, ''Least-squares time-delay estimation for transient signals in a multipath environment,'' J. Acoust. Soc. Am. **92**, 210–218 (1992).
[4] J. C. Hassab, *Underwater Signal and Data Processing* (CRC Press, Boca Raton, 1989).
[5] R. J. Bobber, *Underwater Electroacoustic Measurements* (U.S. Government Printing Office, Washington, DC, 1970).
[6] P. L. Ainsleigh and J. D. George, ''Signal modeling in reverberant environments with application to underwater electroacoustic transducer calibration,'' J. Acoust. Soc. Am. **98**, 270–279 (1995).
[7] F. A. Graybill, *Matrices with Applications in Statistics*, 2nd ed. (Wadsworth, Pacific Grove, CA, 1983).
[8] L. L. Scharf and B. Friedlander, ''Matched subspace detectors,'' IEEE Trans. Signal Process. **42**, 2146–2157 (1994).
[9] L. L. Scharf, *Statistical Signal Processing: Detection, Estimation, and Time-Series Analysis* (Addison-Wesley, Reading, MA, 1991).

The behavior of evoked otoacoustic emissions during and after postural changes

Emile de Kleine[a] and Hero P. Wit
Department of Otorhinolaryngology, University Hospital Groningen, P.O. Box 30.001, 9700 RB Groningen, The Netherlands

Paul Avan
Biophysics Department, Faculty of Medicine, P.O. Box 38, 63001 Clermont-Ferrand, France

Pim van Dijk
Department of Otorhinolaryngology and Head & Neck Surgery, University Hospital Maastricht, P.O. Box 5800, 6202 AZ Maastricht, The Netherlands

(Received 24 January 2001; revised 18 April 2001; accepted 23 April 2001)

Click-evoked and stimulus frequency otoacoustic emissions (CEOAEs and SFOAEs, respectively) were studied in humans during and after postural changes. The subjects were tilted from upright to a recumbent position (head down 30 deg) and upright again. Due to the downward posture change, CEOAEs showed a phase increase (80 deg at 1 kHz) and a level decrease (0.5 at 1 kHz), especially for frequency components below 2 kHz. For SFOAEs, the typical ripple pattern showed a positive shift along the frequency axis, which can be interpreted as a phase shift of the inner-ear component of the microphone signal (90 deg at 1 kHz). This also occurred mainly for frequencies below 2 kHz. The altered posture is thought to cause an increase of the intracranial pressure, and consequently of the intracochlear fluid pressure, which results in an increased stiffness of the stapes system. The observed emission changes are in agreement with predictions from a model in which the stiffness of the cochlear windows was altered. For CEOAEs, the time to regain stability after a downward turn was of the order of 30 s, while this took about 20 s after an upward turn. For SFOAEs, this asymmetry was not found to be present (about 11 s, both for up- and downward turns). [DOI: 10.1121/1.1381025]

PACS numbers: 43.64.Jb, 43.64.Bt, 43.64.Kc [BLM]

I. INTRODUCTION

Otoacoustic emissions (OAEs) are sounds generated in the inner ear, which are measurable in the ear canal. They can be divided into two categories: spontaneous and evoked otoacoustic emissions (SOAEs and EOAEs, respectively). Within the category of evoked OAEs one can discern OAEs elicited in different manners, like click-evoked, stimulus frequency, distortion product, and noise-evoked OAEs (see Probst *et al.*, 1991; Maat *et al.*, 2000). Since the prevalence of OAEs is related to hearing loss, to date, OAE measurements are widely used to probe cochlear functioning.

Posture affects different aspects of hearing. First, posture has been shown to affect the audiogram fine structure, which is related to OAEs (Wilson, 1980). In addition, the effects of posture have been studied for various OAE types like SOAEs (de Kleine *et al.*, 2000), different kinds of transient evoked OAEs (e.g., Antonelli and Grandori, 1986; Büki *et al.*, 1996), and distortion product OAEs (Büki *et al.*, 2000). Hitherto, posture effects on stimulus frequency OAEs (SFOAEs) have not been studied.

Commonly, postural effects on hearing are attributed to changes in the static inner-ear pressure, which are thought to alter the transmission of the OAE from the inner ear to the ear canal. Posture is known to affect the intracranial pressure (ICP), probably mainly by gravity (Chapman *et al.*, 1990; see also Fig. 10 of de Kleine *et al.*, 2000). Since the cochlear aqueduct connects the intracranial space to the inner ear, their respective pressures are closely related. The properties of the cochlear aqueduct patency, however, are not fully clear. Therefore, the exact relation between ICP and inner-ear pressure is not trivial, especially during pressure manipulations (Gopen *et al.*, 1997; Thalen *et al.*, 1998). Postural experiments might give additional information on the aqueduct patency. Furthermore, this patency might play a role in the disturbed fluid regulation, which is hypothesized to be connected to Menière's disease (for a review, see Horner, 1993).

The present report describes the behavior of click-evoked and stimulus frequency OAEs before, during, and after controlled postural changes. For both these emission types, we first focused on the stationary (i.e., long-term) changes of the emission. Second, we studied the time course of the alterations, that is, the dynamic behavior of the changing OAE after a postural change.

II. MATERIALS AND METHODS

A. Materials

Click-evoked otoacoustic emissions (CEOAEs) and stimulus frequency otoacoustic emissions were recorded. For all recordings, an ER-10C microphone system from Etymotic Research was used with 40-dB gain. The microphone was connected to the subject's ear canal with a foam eartip.

[a]Electronic mail: E.de.Kleine@med.rug.nl

The microphone system was calibrated in a Zwislocki coupler. All recordings were performed in a soundproofed chamber. Subjects were aged 19–35 years; 9 male and 19 female; all subjects had no known hearing loss. Only one subject was used in both experiments. Over 50% of the subjects showed one or more SOAEs, of which only one was analyzed in previous research (de Kleine *et al.*, 2000).

Click stimuli were generated using a Stanford Research Systems DS345 function generator, which was connected to one speaker of the ER-10C microphone system. The—electrical—clicks consisted of 25-μs-wide rectangular pulses with a 50-Hz repetition rate, according to a commonly used nonlinear paradigm (one positive pulse was followed by three negative pulses, with an amplitude of one-third). The microphone signal was filtered and amplified with a Krohn-Hite 3550 filter (0.7–10-kHz bandpass) and a Stanford Research Systems SR560 preamplifier (300-Hz high-pass and 20-dB gain). The timing was controlled by a personal computer and a CED 1401plus intelligent interface (suitable for generating and receiving waveform, digital, and timing signals). The speaker and microphone signal were simultaneously stored on a Denon DAT recorder with a 48-kHz sampling rate. Off-line, the recorded signals were digitally transferred to a computer disk using a Singular Solutions A/D64x connected to a NeXT computer. The CEOAEs were computed by averaging an integer multiple of four click responses (henceforth to be called a ''block''), yielding the nonlinear part of the response.

Stimulus frequency OAEs were measured with an EG&G 5206 lock-in amplifier in (r,θ) mode, with a 300-ms time constant. The output of a Brüel & Kjær 1051 sine generator was fed to the reference channel of the lock-in amplifier and was delivered to one speaker of the ER-10C microphone system. The microphone signal was filtered and amplified with the preamplifier described above and returned to the signal channel of the lock-in amplifier. The r- and θ outputs of the lock-in amplifier (amplitude and phase) were sampled by the CED interface described above, with a 6-Hz sampling rate. After the experiment, the data were transferred to a personal computer.

B. Methods

Click-evoked and stimulus frequency OAEs were measured from normal-hearing subjects in upright and supine (−30 deg) position. For both emission types, stationary as well as dynamic aspects of the changes were studied.

The CEOAE experiments were carried out as follows. The subject was positioned on a reclinable bed, standing upright [Fig. 1(a)]. The eartip was inserted in the external ear canal and measurement was begun. After 1 min, the subject was tilted, within 3 s, to a head-down position, face up [−30 deg with respect to the horizontal plane; Fig. 1(b)]. About 2.5 min later, the reverse procedure was carried out (subject standing upright again). After an intervening 2.5-min interval, the recording was stopped, resulting in a total recording of 6 min.

The SFOAE measurements were carried out in two ways. In the first place, for three subjects, a tone sweep (10 Hz/s) of constant voltage was used as stimulus. This measurement was performed in the upright as well as the supine position (−30 deg), with an intermediate period of 2.5 min. Second, in studying the dynamics, a tone of constant amplitude *and* frequency was used as a stimulus, for a 5.5-min period. During these 5.5 min, the subject's posture was manipulated as in the case of the CEOAE experiment above (upright–supine–upright). Referring to this measurement as an SFOAE measurement is disputable, since the frequency of the tone was not swept; the method of measurement is nevertheless identical. Note that this measurement is equivalent to an impedance measurement, as performed in standard audiological practice, and therefore could be called accordingly. Results of this second type of SFOAE measurement were fitted with an exponential curve

$$f(t)=a(1-e^{-\alpha(t-t_0)})+c, \tag{1}$$

which satisfies the conditions

$$\begin{aligned} t&=t_0 \qquad f(t)=c \\ t&\to\infty \qquad f(t)\to a+c, \end{aligned} \tag{2}$$

where $\tau=\alpha^{-1}$ is the related time constant. Here, $f(t)$ is either amplitude or phase. The fitting was done by a least-squares algorithm.

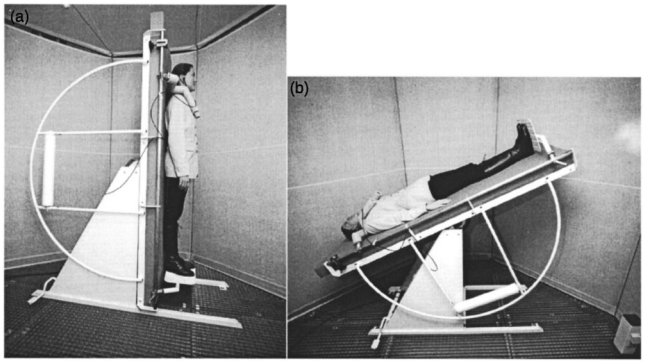

FIG. 1. The experimental setup with the subject (a) in upright position (+90 deg) and (b) in supine position (−30 deg).

III. RESULTS

A. Click-evoked otoacoustic emissions

Click-evoked otoacoustic emissions were measured continuously during a 6-min period, as described in the Materials and Methods sections. This experiment was performed on 16 ears. Figure 2(a) shows a typical example of two broadband-filtered CEOAEs from one ear; the two traces correspond to the upright and supine body position, as indicated. Emissions were computed by averaging the responses of two separate periods of about 57 s (i.e., 700 blocks) of one recording: the final stages of the first (upright: 3–60 s) and second part (supine; 153–210 s) of the experiment. The averaged signal was filtered by a broadband eighth-order Butterworth filter (0.5–10-kHz bandpass). The two traces differ clearly: mainly by phase, but also by amplitude. For all measurements, the CEOAEs related to the two positions could be distinguished easily. That is, the differences between the two

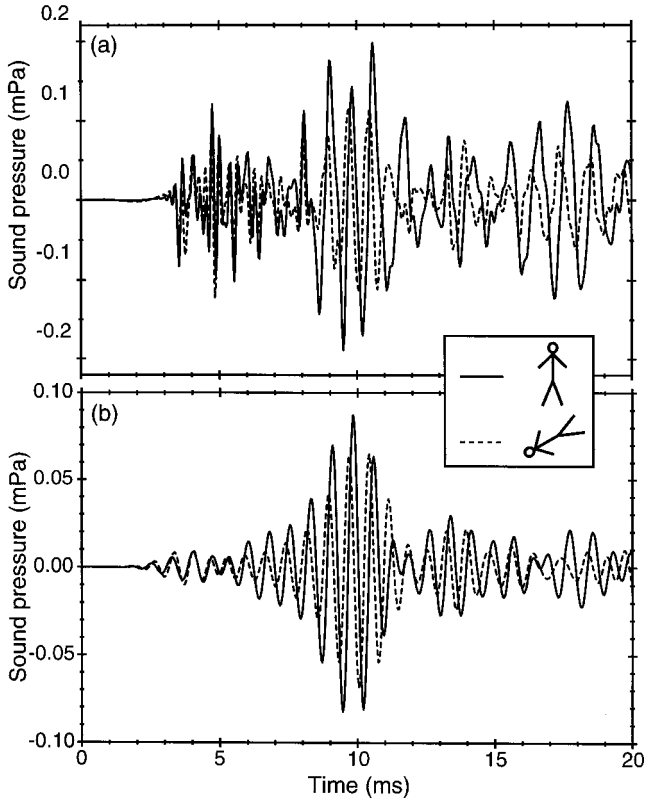

FIG. 2. A click-evoked otoacoustic emission in upright and supine position (+90 and −30 deg, respectively); (a) after a broadband filtering (500–5000 Hz), and (b) after a narrow-band filtering (1300–1600 Hz). Solid lines: upright (+90 deg), dashed lines: supine position (−30 deg). All signals represent an average of a stationary period of 57 s.

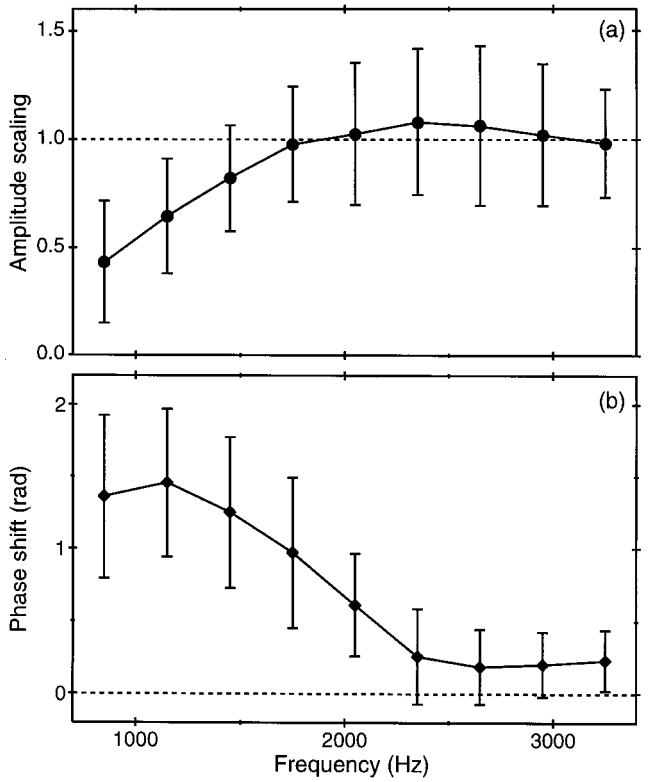

FIG. 3. The averaged amplitude and phase changes of CEOAEs, due to a postural change from upright to supine (+90 and −30 deg, respectively). (a) Amplitude scaling for nine adjacent frequency bands 300 Hz wide (from 700 to 3400 Hz). (b) Same data, for the phase shift. Error bars indicate the standard deviation around the average, implying a large variability. The shapes of the individual measurements were similar. The average values represent 16 ears.

CEOAEs in upright position were much smaller than the differences of each of these with the CEOAE in supine position.

In order to examine the frequency dependence of the changes in the CEOAEs, we filtered the emission responses with an eighth-order Butterworth bandpass filter with a 300-Hz bandwidth. This filtering was carried out for nine adjacent frequency bands, with center frequencies from 850 to 3250 Hz. For these nine frequency bands, we compared the stable (averaged) response in upright and supine body position [cf. Fig. 2(b)]. This comparison was made by fitting the CEOAE in upright position $[f_{\text{upright}}(t)]$ to the CEOAE in supine position $[f_{\text{supine}}(t)]$, where only a change in amplitude and a shift in time were permitted: $f_{\text{supine}}(a,dt;t) = a f_{\text{upright}}(t+dt)$. In other words, the fitting procedure yielded a gain factor a and a time shift dt which optimally transformed the upright response $f_{\text{upright}}(t)$ into the supine response $f_{\text{supine}}(t)$. Thus, for each frequency band two parameters were obtained to describe the CEOAE changes due to the postural change: (1) an amplitude scaling a, and (2) a time shift dt.

Following Büki *et al.* (1996), we calculated the phase change $d\phi$ from the time shift dt by the relation $d\phi = 2\pi f_c dt$, where f_c is the center frequency of the band filter. Figure 3 shows the averaged changes in amplitude and phase for all 16 experiments. In panel (a) the amplitude scaling, and in panel (b) the phase shift was plotted versus the center frequency of the band filter. Altogether, the postural change resulted in a decrease of the amplitude, and a positive phase shift. These influences were observed mainly for lower frequencies ($f<2$ kHz). The interindividual results showed great variability and therefore resulted in a huge deviation around the average. However, for individual subjects measurements showed behavior similar to the average. A spectral analysis of the CEOAE alterations did not yield additional information. Due to the short duration of the signal (20 ms), the frequency resolution was only 50 Hz, which is insufficient to probe subtle phase changes.

The time course of the changes in the CEOAEs was studied also. Since multiple responses (about 100 blocks) are needed to gain an averaged CEOAE, we reduced the time between stimulus pulses to be minimal, that is, 20 ms. Thus, one block took 80 ms and, consequently, 100 blocks could be averaged in 8.2 s. Figure 4 shows an example of a band-filtered CEOAE (1100–1400 Hz), for separate periods within the 6-min experiment: the solid lines denote the steady CEOAEs for the upright and supine position, whereas the dashed lines denote CEOAEs from the transitional period after the upright-to-supine rotation. In this case, the transition of the CEOAE after the downward change of position took approximately 1 min. After the upward rotation (at $t = 210$ s), it took about 20 s to regain a stable emission signal. In our experiments, the transition after the downward turn always lasted longer than after the upward turn, except for one. For the downward turn the average time to regain sta-

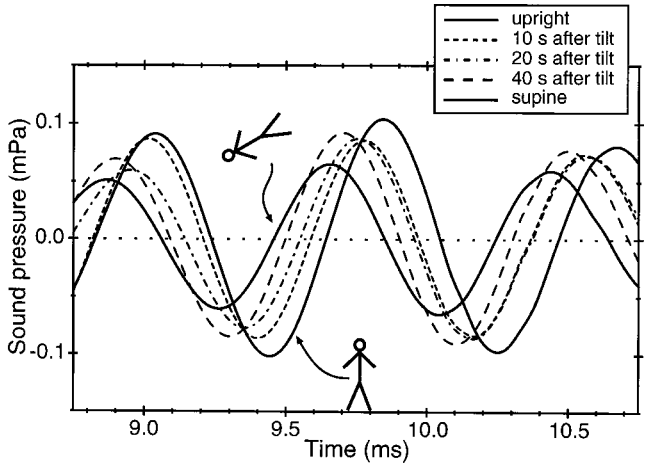

FIG. 4. A detail of the process of change of one CEOAE after a postural change from upright to supine position (+90 and −30 deg, respectively). The solid lines denote the (stationary) CEOAEs in upright and supine position, as indicated. The dashed lines denote the CEOAEs for the transitional period after the upright-to-supine rotation. Signals were averaged for subsequent periods of 10 s.

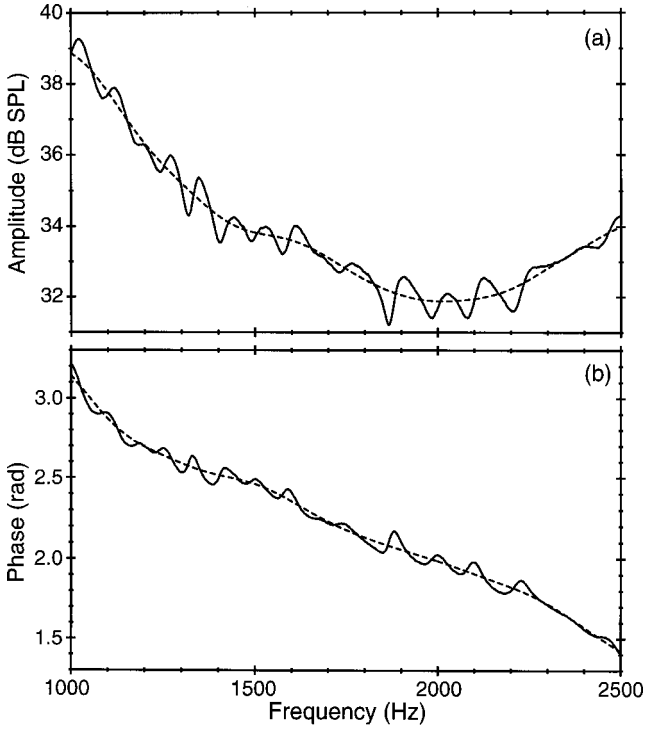

FIG. 5. (a) The amplitude and (b) the phase of one stimulus frequency OAE measurement, with the subject in upright position. The solid lines designate the characteristics of the microphone signal during a frequency sweep, as measured by a lock-in amplifier. The dashed lines were obtained by smoothing the solid lines with a Fourier interpolation method.

bility was 30 s; for the upward turn it was 20 s, where the accuracy for separate measurements was only one period of averaging, that is, 8.2 s. It should be noted that excessive noise from the subject could also be responsible for delaying the stability of the signal.

B. Stimulus frequency otoacoustic emissions

In three ears, we measured stimulus frequency otoacoustic emissions in the two distinct positions (upright and supine, −30 deg). For each position, the measurement lasted 150 s, in which the stimulus frequency was swept from 1000 to 2500 Hz. Before the measurement in supine position, an intermediate 2.5-min period of rest was taken, after which we assumed the emission response to be stable again. Figure 5 shows a typical example of such an SFOAE measurement: the amplitude and phase of the microphone signal, where the phase is relative to the electrical stimulus signal. The dashed lines denote the smoothed background of the actual signal (solid lines), obtained by a Fourier interpolation method. Figure 6 compares the amplitudes of the SFOAE measurements in upright and supine position [cf. Fig. 5(a)]. In panel (a) the amplitudes are plotted; the traces corresponding to the supine position were shifted by 2.5 dB. The differences between the actual trace and the background (the ripples, usually considered to be the nonlinear part of the SFOAE) were plotted in panel (b), for both postures. Here, the dashed line represents the SFOAE in supine position and the solid one the SFOAE in upright position. The two SFOAEs show a great resemblance, but differences can be observed clearly. The dashed line appears as a horizontally shifted version of the solid one. This shift along the frequency axis is of the order of magnitude of 10 Hz (a least-squares fit with $af+b$ gave $a=-0.021$ and $b=54\,\mathrm{Hz}$, corresponding to a shift of 33 Hz at 1000 Hz, down to 1.5 Hz at 2500 Hz).

Rippled magnitude patterns, such as the ones in Figs. 5 and 6, are obtained as a result of interference between two vectors (see the lower inset of Fig. 7): a large one, p_S corresponding to the external stimulus as it is delivered to the ear, with a smooth frequency dependence, and a smaller one, p_{OAE} corresponding to the emission, whose phase φ_{OAE} rapidly rotates, when frequency f is increased. The peaks in the rippled pattern appear at frequencies where the two vectors happen to have the same phase and reinforce each other, while the dips correspond to negative interference. Figure 7 shows the emission phase φ_{OAE} as a function of the stimulus frequency f, for each posture. The data were derived from the amplitude and phase data as shown in Figs. 5 and 6, where the stimulus sound pressure p_s was taken as the smooth (dashed) background. The phase difference between supine and upright posture could reasonably be described by a phase shift with linear frequency dependence (a least-squares fit with $af+b$ gave $a=-3.4\cdot10^{-4}\pi/\mathrm{Hz}$ and $b=0.86\pi$; in effect a shift of 0.52 π at 1 kHz, down to 0.07 π at 2.3 kHz).

Since SFOAE measurements take a considerable amount of time (in our case 2.5 min), the time course of the alterations is difficult to study. Therefore, we performed SFOAE measurements in which the subject's posture was altered, while a fixed frequency stimulus tone, with $f=1210\,\mathrm{Hz}$, was presented (i.e., as mentioned, an impedance measurement). This experiment was performed on 35 ears from 25 subjects. During these experiments, a vast majority of the measurements showed clear alterations in the microphone signal. As the phase appeared to be more sensitive to postural changes than the amplitude, we focused on the phase of the microphone signal. More specifically, the amplitude did not always return to its initial value, and changes sometimes were very small. Also, both positive and negative amplitude changes

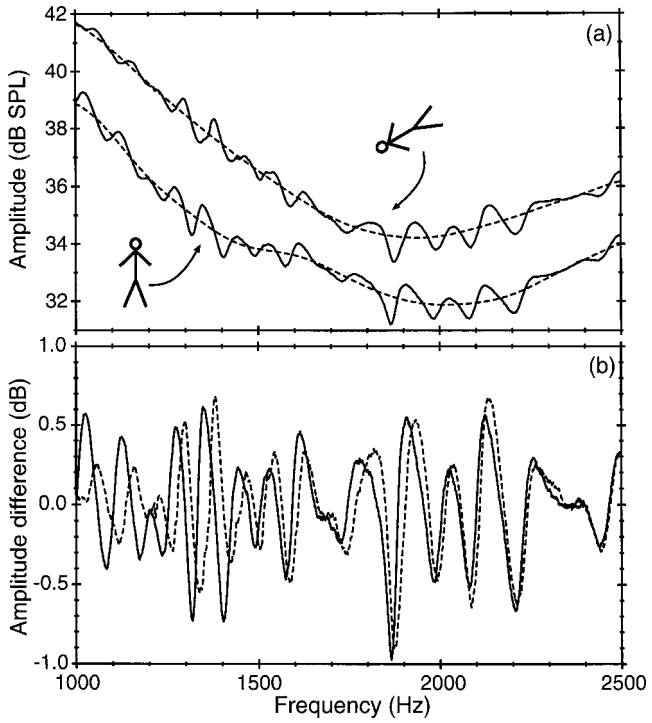

FIG. 6. (a) The amplitude of an SFOAE measurement for upright (+90 deg: lower traces) and supine position (−30 deg; upper traces, shifted by 2.5 dB). The solid lines designate the amplitude of the microphone signal during a frequency sweep, measured by a lock-in amplifier. The dashed lines were obtained by smoothing the solid lines with a Fourier interpolation method. (b) The fine structure of the amplitude of an SFOAE measurement, derived from panel (a) by subtracting the smooth from the rippled traces. Solid line: upright (+90 deg), dashed line: supine position (−30 deg). The pattern was shifted by about 30 Hz down to 1 Hz. Calculations on the phase gave similar results; see also Fig. 7.

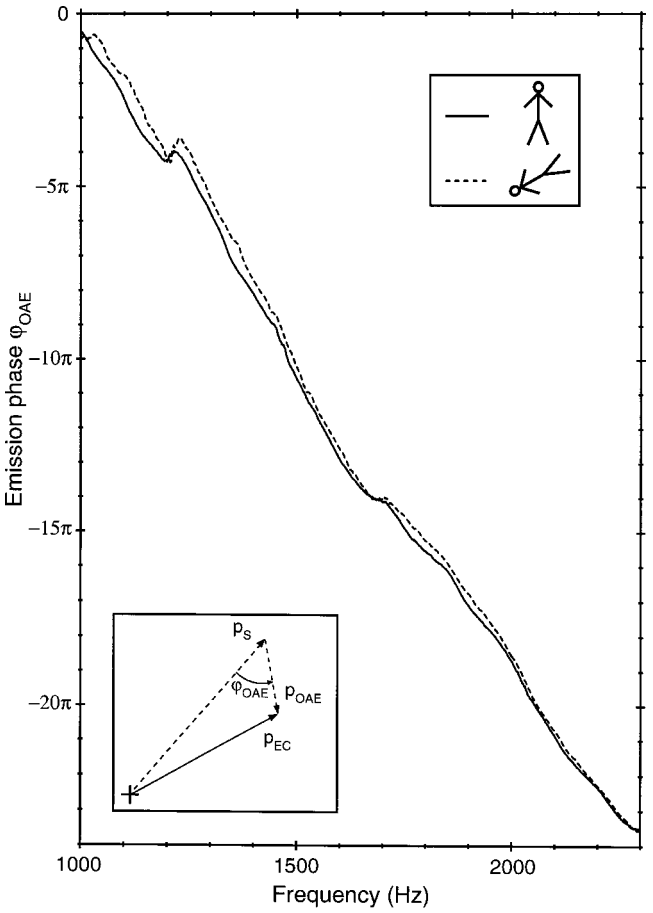

FIG. 7. The phase φ_{OAE} of the SFOAE as a function of the stimulus frequency, for two postures. This phase was derived from the measurements presented in Figs. 5 and 6. Solid line: upright (+90 deg), dashed line: supine position (−30 deg). The phase difference between supine and upright posture could reasonably be described by a phase shift with linear frequency dependence; from 0.52π at 1 kHz, down to 0.07π at 2.3 kHz (a least-squares fit with $af+b$ gave $a=-3.4\cdot10^{-4}\ \pi$/Hz and $b=0.86\pi$) Lower inset: the sound pressures of the stimulus tone p_S and of the emission p_{OAE} add up to the sound pressure in the ear canal p_{EC}.

were observed (ranging from −4 to +2 dB), where 57% showed an amplitude increase, in supine position. Figure 8 shows a typical example of the phase throughout one experiment. During the 5.5-min experiment the subject's posture was altered twice, as indicated in the graph. After each postural changes a gradual change in the phase was observed. The phase differences between both upright positions were much smaller than the phase difference between upright and supine position. The phase behavior was quantified by fitting it with a simple exponential function, yielding an amplitude a and a time constant τ for each postural change [see Eq. (1)]. In 26 of the 35 experiments, the phase behavior was comparable to Fig. 8, in three cases no evident phase change could be observed, and in six cases the phase behavior was different from Fig. 8, and thus could not be fitted with the exponential curve from Eq. (1). So, from 26 experiments, 52 time constants were obtained (one from the up- and one from the downward turn). Figure 9 shows a histogram of all the values of these time constants. The time constants of the downward change of position were shaded. The average of all time constants equaled 11.4 s, with a standard deviation of 6.1 s. For the up- and downward postural changes the averages were 11.1 s (s.d.=6.4) and 11.7 s (s.d.=5.6), respectively. The difference between these averages was not statistically significant.

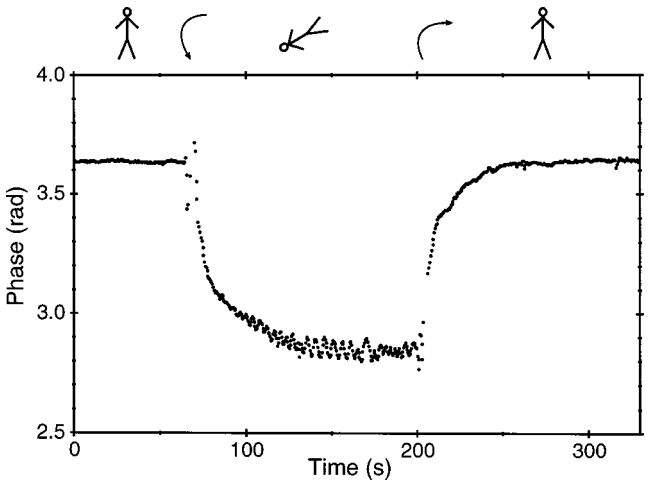

FIG. 8. A typical example of the phase of an SFOAE—of constant frequency—during an experiment in which the subject's posture was altered at about $t=60$ s and $t=200$ s, as indicated. Such measurements could be described by a simple exponential function [Eq. (1)]. For supine position, the phase shows a 4-Hz fluctuation, probably caused by breathing.

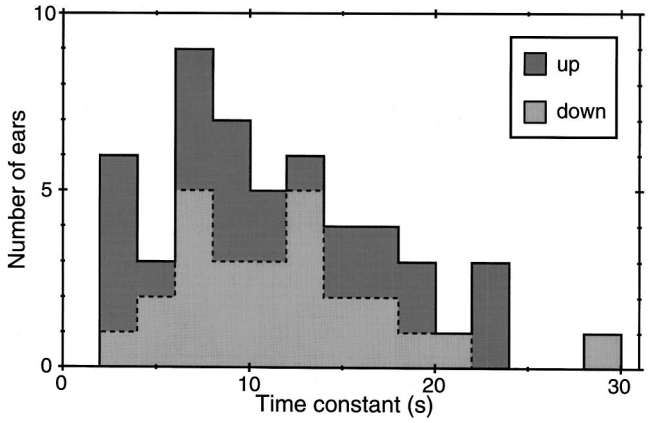

FIG. 9. Histogram of all 52 time constants of 26 SFOAE tilting experiments, with 2-s-wide bins. Dark and light gray parts of the histogram identify the time constants of the up- and downward postural changes, respectively, with average time constants of 11.1 s (s.d.=6.4) and 11.7 s (s.d. =5.6), respectively. The average of all time constants was 11.4 s (s.d. =6.1).

IV. DISCUSSION

The effects of posture on hearing have been investigated in various ways. In this report, we studied the effects of postural changes on click-evoked and stimulus frequency otoacoustic emissions. Due to a downward posture change, CEOAEs showed a phase increase and an amplitude decrease, especially for frequency components below 2 kHz (see Fig. 3), confirming previous findings of Büki *et al.* (1996). Changes of stimulus frequency OAEs after a downward posture change could be described by a positive phase shift of the inner-ear component, also mainly for low frequencies (Fig. 7). The time for both these OAE types to regain stability after a postural change, however, gave deviant results (Figs. 4 and 9). Test–retest differences for these transition times were not examined, and need further research. Previously, posture has already been shown to affect the auditory threshold (Wilson, 1980), acoustic impedance (Macrae, 1972; Magnano *et al.*, 1994), tympanic membrane displacement measurements (Phillips and Farrell, 1992), and different kinds of otoacoustic emissions (Büki *et al.*, 1996, 2000; de Kleine *et al.*, 2000). The exact origin of these changes has not been elucidated yet. Specifically, the question whether these changes stem from inner- or middle-ear alterations is still not clarified. It is, however, generally assumed that changes of the hydrostatic intracochlear pressure play an elemental role (e.g., Büki *et al.*, 2000; de Kleine *et al.*, 2000).

Intracochlear pressure is tightly related to intracranial pressure, the connections between the corresponding fluid systems being major factors in describing this relation. The patency of the cochlear aqueduct, the main connection between the cochlear and the cerebrospinal fluid (CSF) compartment, has been examined in several studies (e.g., Carlborg *et al.*, 1982). Recent histological studies have indicated that most cochlear aqueducts are rather narrow (about 0.1 mm) and filled with loose connective tissue, and thus likely to transmit low-frequency pressure waves from CSF to cochlear compartments (Gopen *et al.*, 1997). Because the aqueduct is connected to the scale tympani, such pressure waves will alter the perilymphatic pressure. Since no—substantial—pressure difference can endure between the perilymphatic and the endolymphatic compartment (Andrews *et al.*, 1991; Wit *et al.*, 2000), any pressure waves from the CSF will affect the intracochlear pressure throughout the cochlea in a uniform fashion.

The mechanisms governing the OAE alterations due to posture changes are still not clear. Since a downward posture change induces an increase of the inner-ear pressure, most authors assume that this results in a slight outward bulge in the cochlear windows, which increases their stiffness. In experiments with human temporal bones, Ivarsson and Pedersen (1977) have shown this stiffness to be variable. The increased stiffness is thought to alter properties of the ear, which alter the OAE characteristics (Wilson, 1980; Büki *et al.*, 1996). Calculations from a middle-ear model with variable stiffness of the stapes system do confirm these ideas for CEOAEs and DPOAEs, yielding phase changes (and to a lesser extent also amplitude changes) mainly at frequencies below 2 kHz (Avan *et al.*, 2000; Büki *et al.*, 2000). This middle-ear model consequently only includes transmission changes; no intracochlear mechanisms are taken into account. Interpretation of experimental results from spontaneous OAEs (SOAEs) are complex, but seem in agreement with these computations (de Kleine *et al.*, 2000).

At first sight, the changes of the steady state of SFOAEs showed a certain resemblance to the SOAE and auditory threshold changes: an upward frequency shift of the fine structure, mainly at low frequencies (<2 kHz). However, when regarding the SFOAE as the sum of two vectors (Dallmayr, 1987), the changes in the inner-ear part of the signal could be described as a phase shift with linear frequency dependence (Fig. 7). This is in agreement with findings on CEOAEs and DPOAEs and the middle-ear model mentioned earlier. Experiments on cadaver ears in cat (Lynch *et al.*, 1982) and cattle (Kringlebotn, 2000b) showed static pressure variations in the inner ear to affect sound transmission. Kringlebotn (2000b) notes, however, that with an intact ossicular chain these influences are only minor. Since in evoked OAE measurements the cochlear windows are passed twice, we expect that transmission changes cannot be disregarded. Altogether, an alteration of the stiffness of the stapes system is likely to be a factor of importance in our postural experiments.

In accordance with these ideas on the stiffness of the stapes system, variations of middle- and outer-ear pressure affect OAEs in a manner similar to the way postural experiments affect OAEs. In general, both positive and negative pressure induce a decrease of amplitude (for CEOAEs and DPOAEs), a phase shift (for CEOAEs and DPOAEs), or an increase of center frequency (for SOAEs); all effects are predominantly at frequencies below 2 kHz (e.g., Schloth and Zwicker, 1983; Naeve *et al.*, 1992; Hauser *et al.*, 1993; Büki *et al.*, 1996; Avan *et al.*, 2000). No data of effects of middle-ear pressure on SFOAEs are known to the authors. For the auditory threshold, Wilson (1980) reported posture and middle-ear pressure changes to give similar results, namely an interchange of the peaks and valleys in it. In cadaver ears of humans, Voss *et al.* (2000) have shown the impedance

measured in the ear canal to be dominated by compliance (i.e., stiffness). Also, in cattle cadaver ears the acoustic input impedance at the oval window was shown to be stiffness controlled up to 1 kHz; this impedance is determined mainly by the stiffness of the annular ligament at low frequencies, and by the cochlear input impedance at higher frequencies (Kringlebotn, 2000a). Static pressure differences at the footplate were shown to affect the amplitude and phase of the impedance; at higher frequencies (above 5 kHz) it was hardly affected. Thus, besides transmission alterations, we consider alterations of the middle-ear and cochlear window impedances to play an important role in the phenomena observed in our experiments.

The dynamics of the observed OAEs after the postural changes showed some noticeable phenomena. Most authors, though, did not investigate the time courses of the changes. For CEOAEs, the time to regain stability after a downward turn was about 30 s, and about 20 s after an upward turn (see also Fig. 4). As mentioned, these times are not very precise due to the measurement protocol. Faster measuring techniques might improve accuracy here (see Ferguson *et al.*, 1998). de Kleine *et al.* (2000) have shown comparable results for SOAEs: 1 min for the downward and less than 10 s for the upward turn. For DPOAEs, Büki *et al.* (2000) have observed a slow change (~25 s) after the downward postural change (their Fig. 5); they do not mention the time after the upward turn (their protocol was not symmetrical). From a personal communication with the authors, we know that after an upward turn the rate of change was always very fast, so that a stable phase was reached within 4 s. For SFOAEs—or the impedance—we found the two time constants of the up- and downward turn to be of same magnitude: approximately 11 s (see Figs. 8 and 9). Since all OAEs are assumed to arise by common mechanisms (e.g., Zwicker and Schloth, 1984; Shera and Guinan, 1999), this difference was not expected. It could be speculated that in the latter case (SFOAE) transmission changes are relatively of smaller importance than impedance changes and that these two alter at different rates. So, SOAEs, CEOAEs, as well as DPOAEs show slow alterations after a downward turn, and fast alterations after an upward turn. The impedance, however, showed equal time courses for both maneuvers.

Noninvasive measurements directly associated with intracochlear pressure are of potential interest for intracranial pressure monitoring. For this purpose, Marchbanks (1984) developed a method for measuring the tympanic membrane displacements during stapedius reflex contraction. This technique was used in different circumstances of altered ICP, such as hydrocephalus and posture (e.g., Reid *et al.*, 1990; Phillips and Farrell, 1992), and to study pressure regulation in patients with Menière's disease (Rosingh *et al.*, 1998). Alternatively, impedance or OAE measurements could also be useful in detecting ICP differences (Magnano *et al.*, 1994; Büki *et al.*, 1996, 2000; de Kleine *et al.*, 2000). One should, however, realize that the relation between the ICP and the inner-ear pressure is not trivial, especially in dynamic situations (Thalen *et al.*, 1998). Then, as mentioned before, the dynamical properties of the cochlear aqueduct come into play. Impedance changes during jugular compression, probably due to pressure changes of the CSF transmitted via the cochlear aqueduct to the perilymph, were shown to occur within a few seconds (Magnano *et al.*, 1994). Moreover, we observed the time courses of different OAE measurements having discordant properties (see the previous paragraph). Given the complexity of these pressure regulations, it is not certain whether ICP is reflected by such audiological measurements. Further, Magnæs (1978) reported the pressure changes of the ventricular CSF (i.e., ICP) as having a rapid (~2 s) and a slow secondary component (after ~10 s), for both sitting up and lying down. Nevertheless, we think that OAEs could well form a suitable tool for monitoring changes of the intracranial—and intracochlear—pressure, especially when the time of interest exceeds 10 s.

In conclusion, we observed changes of click-evoked OAEs after a posture change, mainly characterized by a phase shift, confirming previous findings. For stimulus frequency OAEs, we observed a positive frequency shift of the fine structure due to a postural change. The changes for both OAE types mainly occurred at the lower frequencies. These findings are consistent with a model in which posture affects cochlear window impedance due to modification of the intracochlear fluid pressure. The time courses of OAEs after the posture changes require a closer examination.

ACKNOWLEDGMENTS

This work was supported by the Netherlands Council for Earth and Life Sciences (ALW), part of the Netherlands Organization for Scientific Research (NWO). This study was also supported by the Heinsius Houbolt Foundation and is part of the research program of our department: Communication through Hearing and Speech. The program is incorporated in the Sensory Systems Group of the Groningen Graduate School for Behavioral and Cognitive Neurosciences (BCN).

Andrews, J. C., Böhmer, A., and Hoffman, L. F. (**1991**). ''The measurement and manipulation of endolymphatic pressure in experimental endolymphatic hydrops,'' Laryngoscope **101**, 661–668.

Antonelli, A., and Grandori, F. (**1986**). ''Long term stability, influence of the head position and modelling considerations for evoked otoacoustic emissions,'' Scand. Audiol. Suppl. **25**, 97–108.

Avan, P., Büki, B., Maat, B., Dordain, M., and Wit, H. P. (**2000**). ''Middle ear influence on otoacoustic emissions. I. Noninvasive investigation of the human transmission apparatus and comparison with model results,'' Hear. Res. **140**, 189–201.

Büki, B., Avan, P., Lemaire, J. J., Dordain, M., Chazal, J., and Ribári, O. (**1996**). ''Otoacoustic emissions: A new tool for monitoring intracranial pressure changes through stapes displacements,'' Hear. Res. **94**, 125–139.

Büki, B., Chomicki, A., Dordain, M., Lemaire, J.-J., Wit, H. P., Chazal, J., and Avan, P. (**2000**). ''Middle-ear influence on otoacoustic emissions. II. Contributions of posture and intracranial pressure,'' Hear. Res. **140**, 202–211.

Carlborg, B., Densert, B., and Densert, O. (**1982**). ''Functional patency of the cochlear aqueduct,'' Ann. Otol. Rhinol. Laryngol. **91**, 209–215.

Chapman, P. H., Cosman, E. R., and Arnold, M. A. (**1990**). ''The relationship between ventricular fluid pressure and body position in normal subjects and subjects with shunts: A telemetric study,'' Neurosurgery **26**, 181–189.

Dallmayr, C. (**1987**). ''Stationary and dynamical properties of simultaneous evoked otoacoustic emissions (SEOAE),'' Acustica **63**, 243–255.

de Kleine, E., Wit, H. P., Van Dijk, P., and Avan, P. (**2000**). ''The behavior of spontaneous otoacoustic emissions during and after postural changes,'' J. Acoust. Soc. Am. **107**, 3308–3316.

Ferguson, M. A., Davis, A. C., and Lovell, E. A. (**1998**). ''CSF and posture effects on transient evoked otoacoustic emissions—pilot study,'' in *Intracranial and Inner Ear Physiology and Pathophysiology*, edited by A. Reid, R. J. Marchbanks, and A. Ernst (Whurr, London), pp. 35–43.

Gopen, Q., Rosowski, J. J., and Merchant, S. N. (**1997**). ''Anatomy of the normal human aqueduct with functional implications,'' Hear. Res. **107**, 9–22.

Hauser, R., Probst, R., and Harris, F. P. (**1993**). ''Effects of atmospheric pressure variation on spontaneous, transiently evoked, and distortion product otoacoustic emissions in normal human ears,'' Hear. Res. **69**, 133–145.

Horner, K. C. (**1993**). ''Functional changes associated with experimentally induced endolymphatic hydrops,'' Hear. Res. **68**, 1–18.

Ivarsson, A., and Pedersen, K. (**1977**). ''Volume-pressure properties of round and oval windows,'' Acta Oto-Laryngol. **84**, 38–43.

Kringlebotn, M. (**2000a**). ''Acoustic impedances at the oval window, and sound pressure transformation of the middle ear in Norwegian cattle,'' J. Acoust. Soc. Am. **108**, 1094–1104.

Kringlebotn, M. (**2000b**). ''Frequency characteristics of sound transmission in middle ears from Norwegian cattle, and the effect of static pressure differences across the tympanic membrane and the footplate,'' J. Acoust. Soc. Am. **107**, 1442–1450.

Lynch III, T. J., Nedzelnitsky, V., and Peake, W. T. (**1982**). ''Input impedance of the cochlea in cat,'' J. Acoust. Soc. Am. **72**, 108–130.

Maat, B., Wit, H. P., and Van Dijk, P. (**2000**). ''Noise-evoked otoacoustic emissions in humans,'' J. Acoust. Soc. Am. **108**, 2272–2280.

Macrae, J. H. (**1972**). ''Effects of body position on the auditory system,'' J. Speech Hear. Res. **15**, 330–339.

Magnæs, B. (**1978**). ''Movement of cerebrospinal fluid within the craniospinal space when sitting up and lying down,'' Surg. Neurol. **10**, 45–49.

Magnano, M., Albera, R., Lacilla, M., Gabini, A., Naddeo, M., and Bruno, D. (**1994**). ''Impedance measurement as a noninvasive technique for the monitoring of intracranial pressure variations,'' Audiology **33**, 237–243.

Marchbanks, R. J. (**1984**). ''Measurement of tympanic membrane displacement arising from aural cardiovascular activity, swallowing, and intraaural muscle reflex,'' Acta Oto-Laryngol. **98**, 119–129.

Naeve, S. L., Margolis, R. H., Levine, S. C., and Fournier, E. M. (**1992**). ''Effect of ear-canal air pressure on evoked otoacoustic emissions,'' J. Acoust. Soc. Am. **91**, 2091–2095.

Phillips, A. J., and Farrell, G. (**1992**). ''The effect of posture on three objective audiological measures,'' Br. J. Audiol. **26**, 339–345.

Probst, R., Lonsbury-Martin, B. L., and Martin, G. K. (**1991**). ''A review of otoacoustic emissions,'' J. Acoust. Soc. Am. **89**, 2027–2067.

Reid, A., Marchbanks, R. J., Burge, D. M., Martin, A. M., Bateman, D. E., Pickard, J. D., and Brightwell, A. P. (**1990**). ''The relationship between intracranial pressure and tympanic membrane displacement,'' Br. J. Audiol. **24**, 123–129.

Rosingh, H. J., Wit, H. P., and Albers, F. W. J. (**1998**). ''Perilymphatic pressure dynamics following posture change in patients with Meniere's disease and in normal hearing subjects,'' Acta Oto-Laryngol. **118**, 1–5.

Schloth, E., and Zwicker, E. (**1983**). ''Mechanical and acoustical influences on spontaneous oto-acoustic emissions,'' Hear. Res. **11**, 285–293.

Shera, C. A., and Guinan, J. J. (**1999**). ''Evoked otoacoustic emissions arise by two fundamentally different mechanisms: A taxonomy for mammalian OAEs,'' J. Acoust. Soc. Am. **105**, 782–798.

Thalen, E. O., Wit, H. P., Segenhout, J. M., and Albers, F. W. J. (**1998**). ''Dynamics of inner ear pressure change caused by cerebrospinal fluid pressure manipulation in guinea pigs,'' in *Intracranial and Inner Ear Physiology and Pathophysiology*, edited by A. Reid, R. J. Marchbanks, and A. Ernst (Whurr, London), pp. 29–34.

Voss, S. E., Rosowski, J. J., Merchant, S. N., and Peake, W. T. (**2000**). ''Acoustic responses of the human middle ear,'' Hear. Res. **150**, 43–69.

Wilson, J. P. (**1980**). ''Evidence for a cochlear origin for acoustic reemissions, threshold fine-structure and tonal tinnitus,'' Hear. Res. **2**, 233–252.

Wit, H. P., Warmerdam, T. J., and Albers, F. W. J. (**2000**). ''Measurement of the mechanical compliance of the endolymphatic compartments in the guinea pig,'' Hear. Res. **145**, 82–90.

Zwicker, E., and Schloth, E. (**1984**). ''Interrelation of different oto-acoustic emissions,'' J. Acoust. Soc. Am. **75**, 1148–1154.

Basilar-membrane response to multicomponent stimuli in chinchilla

William S. Rhode[a] and Alberto Recio
Department of Physiology, University of Wisconsin, 1300 University Avenue, Madison, Wisconsin 53706

(Received 28 November 2000; accepted for publication 11 April 2001)

The response of chinchilla basilar membrane in the basal region of the cochlea to multicomponent (1, 3, 5, 6, or 7) stimuli was studied using a laser interferometer. Three-component stimuli were amplitude-modulated signals with modulation depths that varied from 25% to 200% and the modulation frequency varied from 100 to 2000 Hz while the carrier frequency was set to the characteristic frequency of the region under study (~6.3 to 9 kHz). Results indicate that, for certain modulation frequencies and depths, there is enhancement of the response. Responses to five equal-amplitude sine wave stimuli indicated the occurrence of nonlinear phenomena such as spectral edge enhancement, present when the frequency spacing was less than 200 Hz, and mutual suppression. For five-component stimuli, the first, third, or fifth component was placed at the characteristic frequency and the component frequency separation was varied over a 2-kHz range. Responses to seven component stimuli were similar to those of five-component stimuli. Six-component stimuli were generated by leaving out the center component of the seven-component stimuli. In the latter case, the center component was restored in the basilar-membrane response as a result of distortion-product generation in the nonlinear cochlea. [DOI: 10.1121/1.1377050]

PACS numbers: 43.64.Kc [LHC]

I. INTRODUCTION

The operation of the cochlea has principally been studied using tones and/or clicks (e.g., von Békésy, 1960; Robles *et al.*, 1976, 1986; Sellick *et al.*, 1982). This has provided an enormous amount of information about the complicated nonlinear cochlear system. However, since the cochlea is nonlinear (e.g., Rhode, 1971; Sellick *et al.*, 1982; Robles *et al.*, 1986), one cannot predict the response to a novel stimulus in a straightforward manner. Hence, until accurate models are developed, it is necessary to present each stimulus of interest in order to determine the cochlear response.

It is of interest to determine which response properties of the auditory nerve express cochlear mechanical filtering and which are due to later stages of signal processing by the inner hair cells and rectification that occurs at the hair cell–auditory nerve synapse. Commonly used stimuli for the study of auditory-nerve fiber (ANF) responses include amplitude-modulated (AM) signals, harmonic complexes, and clicks (e.g., Javel, 1980; Joris and Yin, 1992; Pfeiffer and Kim, 1972). These signals are important as they approximate signals encountered in the everyday environment and also communication signals such as speech. Nerve responses to AM signals indicate an enhancement of the response as measured by the modulation gain over a range of frequencies and intensities. That is, phase-locked firings of the ANF at the modulation frequency are greater than would be expected based on the modulation of the signal. The present study indicates that a portion of this enhancement is present in basilar-membrane (BM) vibration.

A common characteristic of all the stimuli used in this study is that they produce a pitch percept at the difference frequency between the individual components. The temporal discharge patterns of auditory-nerve fibers have been shown to contain information about the frequency content of a stimulus through both spatial and temporal patterns (Evans, 1978; Kiang *et al.*, 1965; Rose *et al.*, 1967). Early studies showed that the interspike intervals in response to two harmonically related tones corresponded to the fundamental frequency (Rose *et al.*, 1969). Other studies found interspike intervals corresponding to perceived pitches when amplitude-modulated stimuli were presented (Evans, 1978; Javel, 1980; Rhode, 1995), two-tone complexes (Greenberg and Rhode, 1987), and synthetic speech sounds (Delgutte, 1980; Miller and Sachs, 1984; Palmer *et al.*, 1986). In an extensive series of auditory nerve (AN) studies, Cariani and Delgutte (1996a, b) provided strong support for the hypothesis that the dominant interspike intervals are capable of explaining pitch perception for a variety of complex stimuli similar to those used in psychophysical experiments.

Horst *et al.* (1986, 1990) studied the representation of multicomponent ($N=4$ to 64) octave band stimuli centered at the characteristic frequency of an auditory-nerve fiber in cat. They observed that the edges of the stimulus spectrum were dominant in the response with increasing N and that the center component was reduced under these conditions. Here, we report that similar behavior is observed at the level of basilar-membrane mechanics for N as low as 3 and it appears that the frequency spacing of the stimulus components is the most important factor.

In order to explore a portion of the stimulus space used in auditory nerve studies, 1-, 3-, 5-, 6-, and 7- component stimuli were used to study basilar-membrane vibratory re-

[a]Author to whom correspondence should be addressed. Electronic mail: rhode@physiology.wisc.edu

sponses. Varying the frequency spacing between the components recapitulates studies of pitch coding in the auditory nerve.

II. METHODS

Methods are essentially those detailed in Cooper and Rhode (1992). Eight chinchilla cochleas were studied at approximately 3.5 mm from the basal end of the basilar membrane [characteristic frequency (CF) = 6.3–9 kHz]. All procedures were approved by the Animal Care and Use Committee of the University of Wisconsin.

Each animal was anesthetized with pentobarbital using a dose rate of 75 mg/kg. Additional doses were administered to maintain the animal in a deeply areflexive state. All anesthetics were administered intraperitoneally. A tracheotomy was performed to ensure an open airway and to place the animal on a respirator if necessary, though one was never used. After the ear was surgically removed, four screws were implanted in the skull and cemented in with dental cement in order to form a rigid base. A bolt was then cemented to the base to provide a stable fixation of the skull to a head holder with six degrees of freedom for the purpose of positioning the cochlea under the microscope.

The bulla was opened widely and a silver ball electrode was positioned so as to touch the edge of the round window for the purpose of recording the compound action potential (CAP) of the auditory nerve in response to short-duration tones (16 ms) for each animal. Since we recorded only in the high-frequency region of the cochlea, the stimulus was stepped in 2-kHz increments from 2 to 20 kHz. At each frequency a visual detection threshold for CAP was determined by viewing an average of 20 repetitions as the stimulus level was varied in 1-dB steps. If the thresholds were above our best threshold curve by more than 30 dB, no data were collected, as high CAP thresholds equated to little or no compression in the hook region (Sellick *et al.*, 1982). CAPs were not typically recorded after mechanical measurements were initiated except to verify they had increased whenever mechanical sensitivity decreased.

The overlying cochlear bone in a region with CFs between 6 and 10 kHz was shaved down using a microchisel until the remaining tissue and /or bone debris could be removed with a pick fabricated out of a microelectrode. Gold-coated polystyrene beads 25 μm in diameter served as retroreflectors. They were placed in the perilymph and allowed to sink to the basilar membrane. They have a specific gravity of 1.05 that is near that of water (1.0), and therefore any loading of the basilar membrane by the bead should be minimal. A glass cover slip was placed over the cochlear opening with no hydromechanical seal. The cover glass served to avoid the problem of an unstable air–fluid interface.

An opening in the bony ear canal, immediately over the tympanic membrane, was made so that an acoustically calibrated probe tube to which a $\frac{1}{2}$-in. Bruel & Kjaer condenser microphone is adjoined could be visualized as it was positioned parallel to the tympanic membrane within 1 mm of the tip of the malleus. The opening was sealed with a glass cover after a 45-μm bead was placed on the tympanic membrane at the tip of the malleus (or umbo). The bead was used as a retroreflector for the interferometer and allowed the measurement of the transfer function of the malleus. The sound source was a RadioShack supertweeter dynamic phone or a condenser microphone.

A. AM stimuli

Signals were synthesized and presented using a TDT system (Tucker-Davis Technologies ®) system. The formula for an AM signal is provided in Eq. (1)

$$S(t) = (1 + m \cdot \sin(2\pi f_{\text{mod}} t)) \sin(2\pi f_{\text{carr}} t). \tag{1a}$$

This can be expanded as a sum of three sinusoids

$$\begin{aligned} S(t) &= m/2 \cdot \cos(2\pi t(f_{\text{carr}} - f_{\text{mod}})) + \sin(2\pi f_{\text{carr}} t) \\ &\quad - m/2 \cdot \cos(2\pi t(f_{\text{carr}} + f_{\text{mod}})) \\ &= f_{\text{lsb}} + f_{\text{carr}} + f_{\text{usb}}. \end{aligned} \tag{1b}$$

where lsb=lower sideband, carr=carrier, and usb=upper sideband.

The carrier frequency, f_{carr}, was set equal to the characteristic frequency of the basilar membrane. The modulation frequency, f_{mod}, was varied in 100-Hz steps from 100 to 1000 Hz, and was set to 1250, 1500, and 2000 Hz beyond 1 kHz. The modulation coefficient or depth, m, was set to 0.25, 0.5, 1, or 2. When $m = 2$ the signal consists of three equal-amplitude tones and is also described as a 200% modulated signal. The stimulus level was varied from 0 to 90 dB SPL in 5-dB steps. Stimuli were 30 ms in duration, repeated 8 times at a rate of 10 per second.

The response was passed through a zero-phase high-pass filter to remove low-frequency noise (function filtfilt in MATLAB™, filter corner frequency = $f_{\text{mod}}/2$) before the envelope of the AM signal was recovered through the use of the Hilbert transform (Bennett, 1970). The envelope was then filtered using a fifth-order zero-phase Butterworth filter (corner frequency = $5 \cdot f_{\text{mod}}$). The minimum (min) and maximum (max) of the resulting envelope were determined by the use of a phase-locked loop technique that computes dc and the Fourier component (sine wave fit, abbreviated sinfit) at f_{mod}. When $m < 1$, modulation was then computed by the relation

$$\text{BM}_{\text{mod}} = (\max - \min)/(\max + \min) = a/\text{dc}, \tag{2}$$

where a = amplitude of the first Fourier component.

Gain for AM coding was defined as

$$\text{gain} = 20 \log_{10}(\text{BM}_{\text{mod}}/m). \tag{3}$$

A difficulty in determining modulation depth arises whenever $m > 1$ as this implies there will be a phase reversal in the envelope that can easily be missed upon visual inspection of the response. One solution used when $m = 2$ was to determine the ratio of the smaller peak/largest peak of the envelope whenever two distinct peaks per modulation period were present (e.g., Fig. 3). A curve was generated for this relation for $1 < m < 5$ that was used to determine the modulation based on the measured ratio (e.g., Fig. 4). This method broke down for modulation frequencies > 400 Hz, at which point it became difficult to ascertain that there were two distinct peaks in the envelope. Modulation gain was also measured by determining the ratio between the two largest spec-

tral components, ''two-component analysis,'' in the response (usually the carrier and the lower sideband). For example, regardless of which component was largest, a ratio of 0.5 was considered an indication of $m=1$ based on Eq. (1). This procedure was done as a check on the waveform analysis technique. The two-component situation arises because the cochlear filter often eliminates the upper sideband component, especially as f_{mod} increases. The two-component analysis generally resulted in modulation gain usually greater than the waveform technique and often resulted in a bandpass temporal modulation transfer function (tMTF=gain as a function of modulation frequency). A resolution of the difference between these approaches to estimate modulation gain was not obtained. It was decided that the waveform technique was most similar to methods previously employed to estimate modulation depth in auditory-nerve studies which rarely found bandpass tMTFs (e.g., Joris and Yin, 1992).

B. Multicomponent stimuli

A subset of these stimuli consisted of five equal-amplitude sinewaves with the first, third, or the fifth component frequency set equal to the CF of the basilar membrane location under study. The separation of the harmonics was varied in steps of 100 Hz up to 1 kHz and set to 1250, 1500, and 2000 Hz above 1 kHz. $F_{\mathrm{mod}}>2000$ Hz was not explored since ANFs do not show any AM coding for this condition. The stimulus level was varied from 0 to 90 dB SPL in 5-dB steps. Stimuli were 30 ms in duration, repeated 8 times at a rate of 10 per s. Analysis consisted of determining the amplitude of nine response components around CF using the sinfit procedure described above. The amplitude at the frequency difference was also determined but was insignificant or buried in the noise except for high levels and large frequency separations.

Also used were seven-component stimuli that consisted of seven equal-amplitude sine waves and six-component stimuli that consisted of the same complex with the center component deleted. The center component (i.e., the fourth) was always centered at CF. These stimuli had the same parameters as the five-component stimuli and were analyzed in the same manner except that 11 components were analyzed using the sinfit technique.

The amplitude of each component of all the stimuli used (AM, 5-, 6-, and 7-component stimuli) was compensated by the acoustic calibration. The starting phase of all the terms in Eq. (1b) as well as all the terms in the multicomponent stimuli was zero.

C. Single-tone basilar-membrane and middle-ear vibration measurements

Basilar membrane input–output (I/O) functions were determined using 30-ms tone bursts with 1-ms raised cosine rise and fall times and presented every 100 ms. The stimulus level covered a 100-dB SPL range in 5-dB SPL steps. A minimum of eight basilar-membrane and four middle-ear responses was averaged for each stimulus condition. Analysis consisted of Fourier decomposition of the steady-state portion of the averaged response at the stimulus frequency.

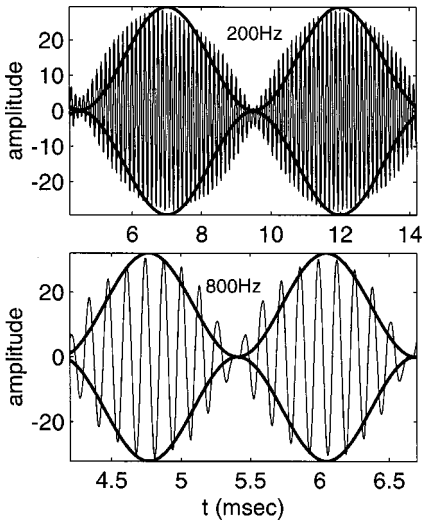

FIG. 1. Basilar-membrane response to an AM signal where the carrier=CF=8000 Hz with 100% modulation. The modulating frequency is listed alongside each panel. The time axis is adjusted so that approximately 2 cycles of the modulation are shown. The thick solid line is the envelope for ideal sinusoidal modulation of the carrier. Chinchilla ct07.

Measurements of the basilar-membrane I/O function at CF were made throughout the experiment to monitor the preparation's stability. Vibration of the ossicles was measured at the tip of the manubrium (umbo) or at the incudo-stapedial joint or both locations either before or after (sometimes both before and after) the basilar-membrane measurements.

D. Recording system

Mechanical responses were measured using a custom-built, displacement-sensitive heterodyne laser interferometer (Cooper and Rhode, 1992). The laser was coupled to the preparation using a long working distance lens (Nikon SLWD 5X, NA 0.1). The laser was focused to an area of $\sim$5-μm diameter on the reflective beads. The interferometer was not sensitive enough to measure basilar-membrane vibration without the gold-coated beads. Instantaneous phase was measured using two single-cycle phasemeters that worked in quadrature. The phasemeter outputs were sampled at 250 kHz and the phase was unwrapped using software. Response amplitudes were corrected for the frequency response of the recording system. The noise floor was <5 pm/$\sqrt{\mathrm{Hz}}$.

III. RESULTS

A. AM response variation with modulation frequency

A portion of the basilar membrane response to an AM signal ($m=1$) is shown in Fig. 1. At $f_{\mathrm{mod}}=200$ Hz, the modulation of the vibration is nearly 100%, while with increasing f_{mod} the modulation depth of basilar-membrane motion decreased systematically to 0.58 for $f_{\mathrm{mod}}=800$ Hz. The relation between modulation depth and modulation frequency is portrayed in the tMTF [Fig. 2(A)]. The modulation depth of basilar-membrane vibration is $>80\%$ up to 400 Hz with a reduction in the modulation depth that is a complicated function of frequency and stimulus level for f_{mod}

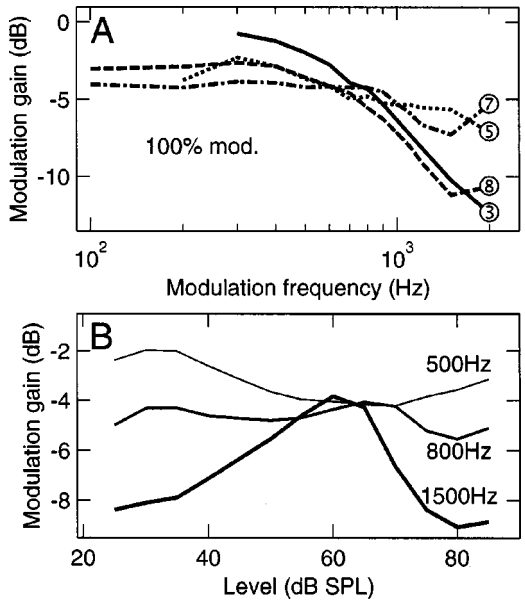

FIG. 2. (A) Basilar-membrane temporal modulation transfer functions (tMTFs) when $f_{carr}=8000$ Hz, f_{mod} is varied from 100 to 2000 Hz, and m $=1$. The symbols attached to the four curves correspond to stimulus level divided by 10 (e.g., symbol ③ refers to 30 dB SPL stimulus level. This labeling is used throughout). (B) Gain I/O functions at the three modulation frequencies indicated. Increasing line width corresponds to increasing modulation frequency. Ct07.

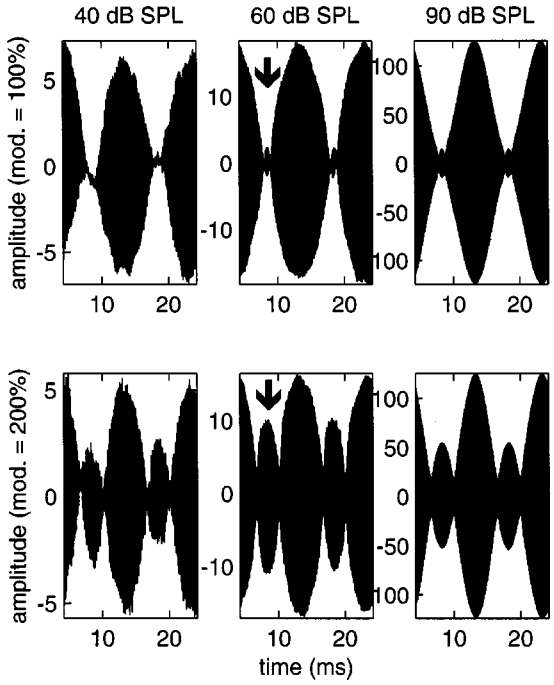

FIG. 3. Basilar-membrane response to AM when the carrier is set equal to CF$=8000$ Hz with the modulation frequency$=100$ Hz. The modulation depth is 100% for row 1 and 200 % for row 2. The level of the stimulus was varied from 40 to 90 dB as indicated above each column. The data were part of those collected over a 90-dB SPL range in 5-dB steps.

>400 Hz. Similar behavior was observed in data from seven other cochleae. The gain-level curve for $f_{mod}=500$ Hz increases at low levels, peaks near 25 dB SPL, and then decreases slightly [Fig. 2(B), thinnest dashed line]. However, the gain-level curve for $f_{mod}=1500$ Hz first increases, then reaches a peak at 60 dB SPL before it rapidly decreases as 80 dB SPL is approached.

For $f_{mod}=100$ Hz or lower, the motion of the basilar membrane is overmodulated as evidenced by a secondary peak in the BM response that is not present in the stimulus waveform (indicated by the arrow in Fig. 3, top row, center panel, $m=1$). Overmodualtion also occurs when 200% modulated AM signals are presented ($m=2$, row 2 of Fig. 3). The ratio of the secondary-to-primary peak in the stimulus waveform is 0.34 for a 200% modulated signal, while it is 0.64 at 60 dB SPL in the BM response (Fig. 3, second row, middle panel). This represents a gain of $\sim$7 dB in the BM response. The amount of BM overmodulation (and thus gain) is highest at midrange levels ($\sim$60 dB SPL), as is apparent in the gain-level curves for four low-modulation frequencies in Fig. 4, all of which exhibit similar level-dependent behavior.

The tMTFs for 25% and 50% modulation are similar in form (Fig. 5) to each other but differ from those for higher modulation depths in their frequency and level dependence. For lower modulation stimuli, tMTFs vary in a systematic way from low pass to high pass with increasing stimulus level. Modulation gain is near 0 dB for low-modulation frequencies but increases to 10 dB at high f_{mod} [Fig. 5(A)]. The gain-level functions increase monotonically when f_{mod} >700 Hz (panels A and B). This pattern deviates from the nonmonotonic gain-level function in the AN where the gain decreases as level increases beyond 10–15 dB SPL above neural threshold (Joris and Yin, 1992). Of course, the AN will discharge at all modulation phases with equal probability as the stimulus level is raised sufficiently, resulting in no modulation of the firing. In contrast, the mechanical modulation gain increases for all $f_{mod}>100$ Hz for levels >50 dB SPL.

The tMTFs for 200% modulation in Fig. 6, as well as results shown in Fig. 2, raise an interesting issue: how should the modulation gain be measured? Below 500 Hz the gain was recovered by measuring the height of the two peaks in a modulation period and determining what modulation is nec-

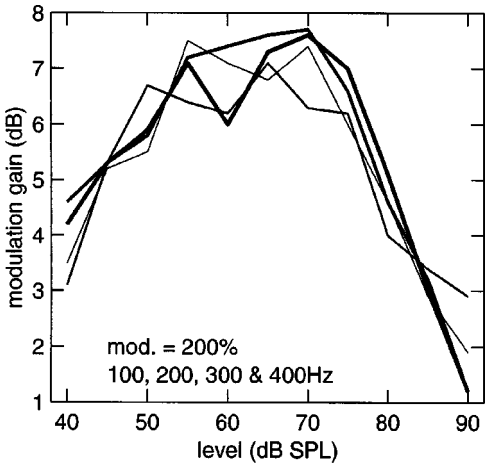

FIG. 4. Modulation gain-level functions for 100 to 400 Hz, $m=2$. The curves were obtained by determining what the modulation depth corresponds to the ratio of primary-to-secondary peak ratio observed in the basilar-membrane response. Increasing line thickness corresponds to increasing modulation frequency. Ct07.

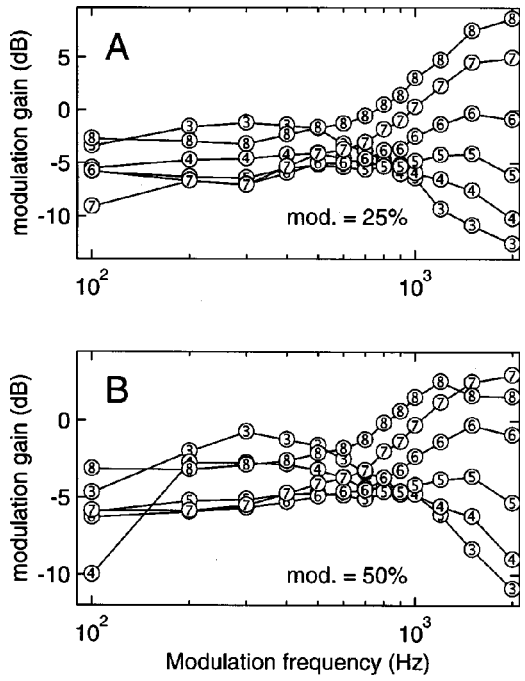

FIG. 5. Basilar-membrane temporal modulation transfer functions (tMTFs) when $f_{carr}=8000$ Hz, f_{mod} is varied from 100 to 2000 Hz, and $m=0.25$ and 0.5 in panel A and B, respectively. Numeric labeling of the curves is explained in Fig. 2.

essary to produce two peaks with this amplitude ratio (e.g., see Fig. 3, row 2). As f_{mod} is increased beyond 400 Hz, two peaks per modulation cycle are no longer distinct and the standard technique for determining gain was used. A gain of $\sim$5 dB for low f_{mod} transitions to a gain of <-8 dB for higher f_{mod}. However, the tMTF discontinuity is obvious and an abrupt transition of this nature is unlikely and suggests that the gain obtained could be an underestimate. The gain-level functions in the higher f_{mod} region are monotonic decreasing with increasing level, indicating that the BM is having increasing difficulty following the envelope. This is opposite the improved envelope following expected, given

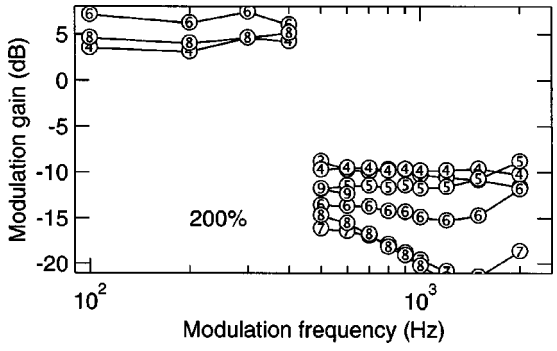

FIG. 6. tMTFs when $m=2$. The discontinuous set of curves results from using two different methods to determine the gain. When there are two distinct peaks per period, the gain is determined by measuring the height of the primary and secondary peaks (usually the modulation frequency is less than 500 Hz). The modulation gain that produces that ratio is then determined. The second method employed the Hilbert transform to obtain the envelope and thereby estimate the gain based on the ratio of the minimum to maximum values. Beyond 500 Hz it is difficult to tell if there are two peaks per modulation period, therefore, the assumption is that the modulation is less than 100%. Ct07.

that at high levels (usually >85 dB SPL) the basilar-membrane filter is broadened and becomes increasingly linear. A possible explanation may lie in an increase in two-tone suppression resulting from the use of equal-amplitude components. In contrast, at lower modulation depths of 25% and 50%, the gain did increase with level.

Similar tMTFs were obtained in seven other experiments. In all instances, the amplitude of the carrier in the basilar-membrane response did not vary significantly as a function of modulation frequency.

B. AM I/O functions

The I/O functions for a subset of the AM conditions studied show that when the carrier frequency is dominant ($m<2$), the response to it remains the largest component (symbol=○) at all levels except when $f_{mod}>600$ Hz and the stimulus level is >70 dB SPL (e.g., Fig. 7, column 1, $f_{mod}=1000$ Hz). This latter result is probably a consequence of broadening of BM filter and lowering of ''CF'' of the filter, whereby the lower sideband (①) becomes the largest component in the basilar-membrane response. The upper sideband (❶) does not play a role in the response when $f_{mod}>600$ Hz since it is usually smaller than the largest response component by 30 dB or more, having been reduced by the cochlear mechanical filter and suppressed by the lower frequency components.

When the modulation depth is 200%, the case of three equal components, the carrier is suppressed by the sidebands (column 2, Figs. 7 and 8, $f_{mod}=100$ Hz). That is, the carrier amplitude is lower than the sideband amplitudes by about 1 dB. As f_{mod} increases, the lower sideband becomes dominant at $\sim$50 dB SPL and at the same time the upper sideband is at least 20 dB smaller than the largest response component. When f_{mod} is increased to 2000 Hz, the carrier is dominant up to 55 dB SPL, at which level compression at f_{carr} and suppression by the lower sideband results in the lower sideband response component being larger than the carrier component.

Three distortion products above and three below the sideband frequencies were analyzed. For $f_{mod}>500$ Hz, the only distortion component of significant level (>-30 dB *re* the largest component) was $=f_{carr}-2f_{mod}$. This component (symbol=②) has been referred to as the cubic difference tone (CDT, Goldstein, 1967) and is $=2f_{1sb}-f_{carr}=f_{carr}-2f_{mod}$ and is the most prominent distortion component perceived psychophysically. The CDT is largest for small f_{mod} and large modulation depths, a result likely due to the stimulus frequencies being located within the nonlinear region of the cochlear filter. When the three AM-response components are nearly the same amplitude, the CDT can be within 6–10 dB of the carrier amplitude [Fig. 7(D) ②]. Distortion on the high-frequency side of the carrier can also be of similar amplitude under these conditions (panels A and D, curve for $f_{carr}+2f_{mod}$, ❷).

The amplitudes of nine response components for each of the conditions in Fig. 7 are superimposed on the isolevel-single-tone curves in Fig. 8 (note the differing frequency scales). In each instance of complex signals, it is the level of the center component that is specified). The frequency loca-

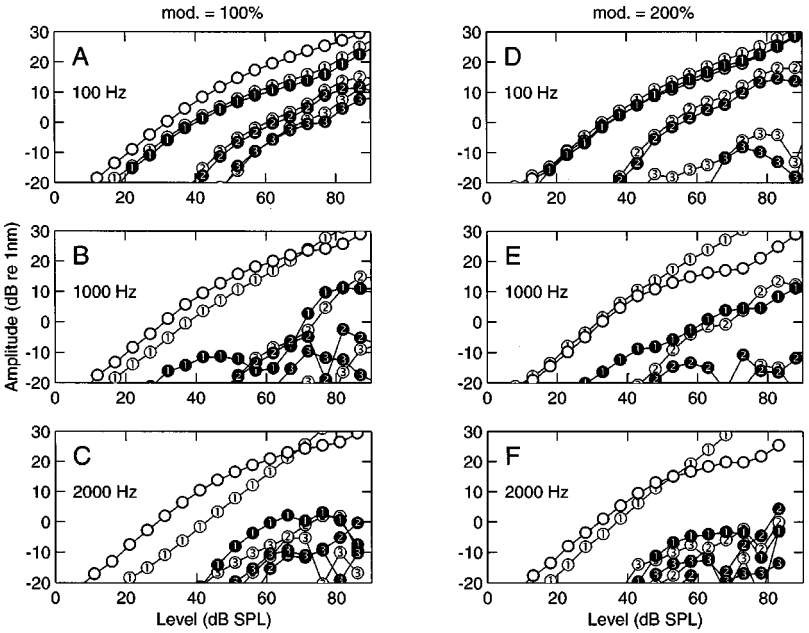

FIG. 7. Column 1: I/O curves for an AM signal with $m=1$ and the indicated modulation frequencies. Column 2: Same as row 1 except that $m=2$. The individual components are indicated by numbers: ① $=f_{carr}-f_{mod}$, ② $=f_{carr}-2\,f_{mod}$, ③ $=f_{carr}-3f_{mod}$,etc. ○ $=f_{carr}$, ❶ $=f_{carr}+f_{mod}$, ❷ $=f_{carr}+2\,f_{mod}$, ❸ $=f_{carr}+3f_{mod}$, etc. Ten components were analyzed: the three frequencies of the AM signal, three distortion frequencies on either side of the AM signal, and the modulation frequency. The response at the modulation frequency was always in the system noise and hence is not shown. Components that were deemed in the noise were removed from the display. Any data for levels <20 dB SPL or amplitudes <-20 dB *re* 1 nm are not shown. The modulation frequency is indicated in each panel. The modulation depth was 100% for the left column and 200% for the right column. Ct07.

tions of the stimulus components are indicated by the symbols along the top axis of the graph, with a triangle marking the location of the carrier frequency. For small f_{mod}, AM-response amplitudes are lower than for the single-tone response (indicated by the dashed lines with the tone levels marked by numbered symbols). This result is likely due to mutual suppression effects. Sideband amplitudes for 200% modulation are larger than for the carrier, as noted above [Fig. 8(D)]. Notice the large distortion components indicated by arrows at $f_{carr}\pm 4f_{mod}$, larger than the adjacent distortion components at $f_{carr}\pm 3f_{mod}$, a result that is opposite from the 100% modulation case [Fig. 8(A)]. The large difference between the components at $f_{carr}\pm 3f_{mod}$ between the 100% and 200% cases suggests that there may be cancellation of distortion products arising from several locations. Magnitudes of the distortion products decrease as f_{mod} increases for both 100% and 200% modulation. As the I/O functions for the lower sideband become linear, the lower sideband amplitude increases faster than the carrier's amplitude, resulting in suppression of the carrier at levels >50 dB SPL. The lower component tracks the single-tone-isolevel curves, while the carrier and upper sideband components increasingly deviate from the isolevel curves with increasing level. At the lower levels, the carrier amplitude tracks the single-tone curves, but by 60 dB the lower sideband suppresses the carrier by 10–20 dB (panels E and F, 200%). The amplitude of the lower sideband tracks the single-tone data better as f_{mod} is

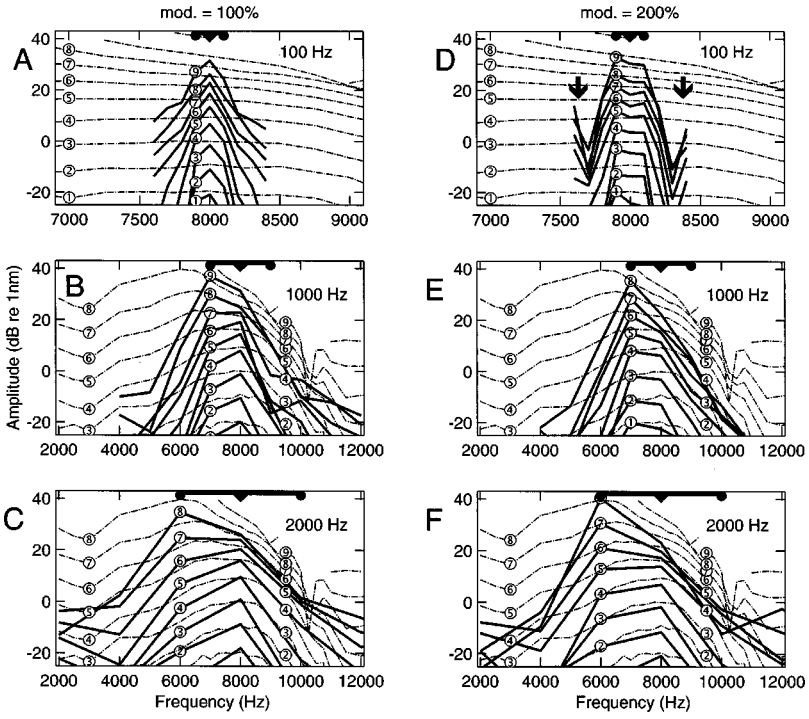

FIG. 8. The I/O data of Fig. 5 presented along the frequency axis (solid lines) with the isolevel BM data superimposed (dash-dot lines). Column 1: $m=1$. Column 2: $m=2$. Data below -25 dB *re* 1 nm were omitted. The use of the symbols is the same as in Fig. 7. The locations of the stimulus frequencies are indicated by solid circle symbols at the top of each panel and a diamond symbol indicates the CF frequency. This same method of indicating the stimulus components is used in all subsequent similar illustrations.

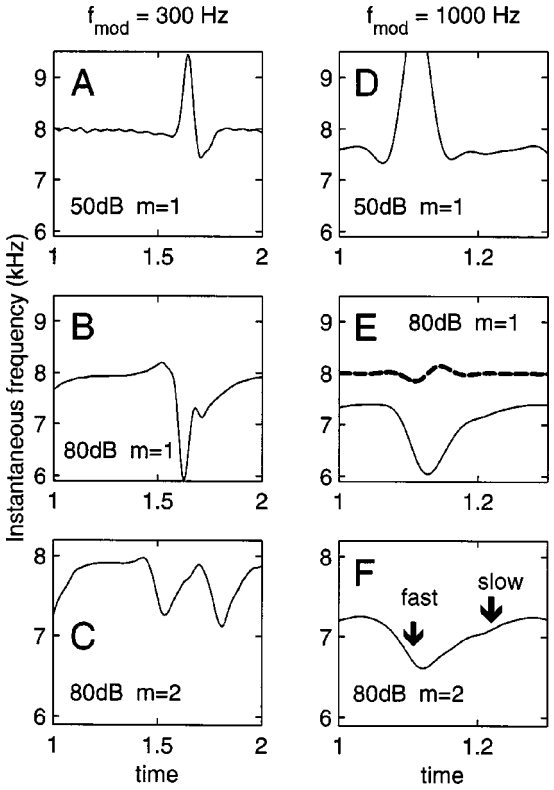

FIG. 9. Hilbert transform instantaneous frequency (IF) analysis of an AM signal recorded on the basilar membrane. Column 1: 300-Hz modulation; column 2: 1000-Hz modulation. Stimulus level and modulation depth specified in each panel. E. Dashed line is a superposition of an IF analysis on an AM signal passed through an isolevel basilar-membrane curve. F. Asymmetry of the IF around the envelope minimum indicated with arrows. Ct07.

increased (panel F) since it is positioned in the linear portion of the basilar-membrane response.

C. Envelope distortion in AM signals

Visual examination of the envelope of the waveforms, especially at high levels, shows the presence of distortion by virtue of the deviation of the actual response envelope for the ideal envelope indicated by the thick solid line in Fig. 1. Fourier analysis (results not shown) performed on the envelopes of both waveforms reveals the presence of a second-order harmonic whose level is about 11 dB below that of the fundamental frequency. The amount of distortion increases with level until it reaches a maximum value, then decreases for higher levels of stimulation, a nonmonotonic relation. Similar distortions were found in the waveforms used in the results shown in Fig. 5.

There is an asymmetry between the rise and fall of the AM envelope that may be related to the envelope distortion. This asymmetry was best observed by using the Hilbert transform to calculate the time derivative of phase of the analytic signal representation of the waveform (Bennett, 1970), which is defined as the instantaneous frequency (IF) of the AM signal. For low f_{mod}, the IF is near the carrier frequency for most of the modulation period, except in the low-amplitude portion where for low levels the IF moves in the direction of the upper sideband frequency [Figs. 9(A), (D)]. For higher levels the IF drops to a frequency lower than the lower sideband frequency [Figs. 9(B), (E)]. This occurs for both 100% and 200% modulation. As f_{mod} is increased, there is an increasing asymmetry in IF as a function of envelope phase; it appears to take longer times for IF to attain its final frequency [see the arrows in Fig. 9(F) fast decrease and slow increase in IF]. Further, for $f_{\mathrm{mod}} > 1000$ Hz the maximum frequency attained is never close to the carrier frequency with IF lower for 200% than 100% modulation. Zero-crossing analysis results in the same outcome, only with fewer sample points per period. A direct analysis of waveforms obtained by passing AM signals through a gammatone filter led to similar results without the asymmetry in the IF at the envelope minimum. Passing the AM signal through a filter that consisted of the isolevel amplitude and phase curves for the basilar membrane showed that the change in IF is much smaller than observed on the basilar membrane and was symmetric about the envelope minimum [dashed line, Fig. 9(E)]. IF also decreased with increasing levels for all f_{mod}.

IF asymmetry versus envelope phase is reminiscent of the ''glide'' that has been described for both AN-and BM responses to clicks (e.g., de Boer and Nuttall, 1997; Carney *et al.*, 1999). In the present instance, it appears that cochlear nonlinearity is necessary for the asymmetry and may be related to asymmetry in the envelope of the AM response.

D. Multicomponent stimuli

In a linear system, the presentation of five equal-amplitude sinusoids would result in a sample of the mechanical transfer function at the five stimulus frequencies. The component frequency separation or f_{diff} was varied in 100-Hz steps between 100 and 1000 Hz, while above 1000 Hz, frequency separations of 1250, 1500, and 2000 Hz were typically used. These stimuli are similar to the N-component octave band stimuli used by Horst *et al.* (1990) in studies of the auditory nerve. The frequency of the first, third, or the fifth component was set equal to the CF of the location of the basilar membrane under study since natural stimuli are not normally centered on a particular auditory unit's CF. The analysis was the same as employed for AM stimuli.

The response to varying frequency separation between components is illustrated in Figs. 10(A)–(C) along with waveforms (D)–(E). There is only a small component amplitude variation for $f_{\mathrm{diff}} = 100$ Hz. However, as in the AM case, the central component is reduced relative to the edge frequency components. In fact, the three central components are all reduced relative to the edge frequency components for levels between 20 and 80 dB SPL. A similar effect occurs at $f_{\mathrm{diff}} = 200$ Hz (results not shown), while at $f_{\mathrm{diff}} = 300$ Hz there is a reduction of the central components only at 70 dB SPL (panel B). As the frequency separation is increased, the high-frequency components are attenuated by the cochlear mechanical filter, while the low-frequency components located in the ''tail'' region of the filter, grow at a linear rate, hence faster than the center component. Initially, the CF component grows at the same rate as the single-tone response did up to 40 dB SPL, but its growth slows beyond that as a result of suppression by the lower-frequency components. At 70 dB SPL, the CF component is 20 dB below the single-tone

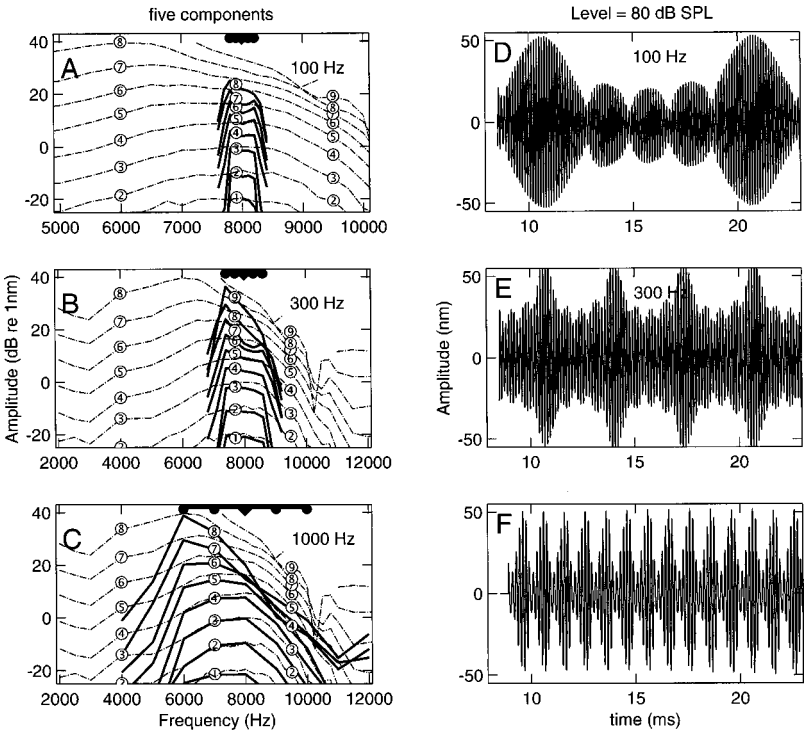

FIG. 10. Frequency analysis of the response of five-component stimuli for three frequency differences (f_{diff}=100, 300, and 1000 Hz) is illustrated. The third component frequency was set to CF. Dotted lines correspond to the single-tone-isolevel amplitude transfer function for this basilar-membrane location. Ct07.

amplitude, while all the lower-frequency components are at the single-tone level. The CF component is also ~20 dB lower than the 6-kHz component. When the frequency separation is >1000 Hz (not shown), high-frequency components extend beyond the compressive region of the basilar-membrane filter and are not suppressed by lower-frequency components. Figures 10(D)–(F) shows a portion of the BM response waveforms to the five-component stimuli (at 80 dB SPL) with f_{diff} equal to that in the panels immediately to the left.

An effect of varying which component frequency is set to CF when f_{diff}=1000 Hz is illustrated in Fig. 11. When the first component=CF, several of the components are beyond the cochlear filter and hence don't appear in the response. The component at CF is dominant and its amplitude closely tracks the single-tone amplitude [Fig. 11(A)]. Higher-frequency components that are within the passband of the cochlear filter are suppressed in this instance. When the third component=CF, the lower-frequency components respond to level increases with linear growth and suppress the CF and higher components [Fig. 11(B)]. At 70 dB SPL the CF component is suppressed over 20 dB relative to the single-tone response. With the fifth component at CF, the CF component is suppressed ~10 dB at 70 dB SPL. This is about 10 dB less suppression than in the previous case, suggesting that components on both sides of CF are required to achieve maximum suppression of the CF component. At low levels, all five components track the single-tone response (panel C).

The I/O functions corresponding to the data in Fig. 10 show the growth of the five individual components along with two upper- and two lower-frequency distortion components (Fig. 12). The distortion components nearest in frequency to the stimulus frequencies [③, ❸ where CF=8000

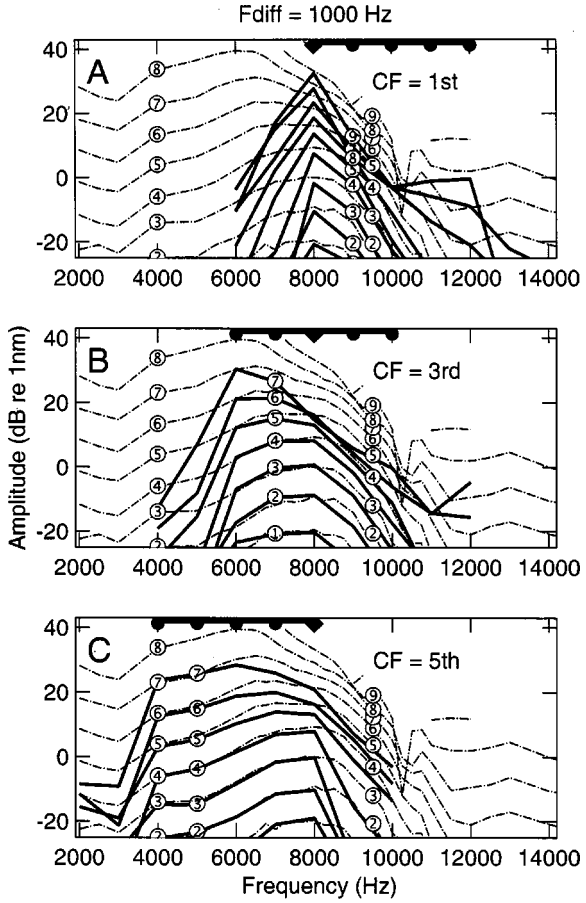

FIG. 11. The first, third, and fifth components of the five-component stimulus were set to CF (A, B, and C, respectively). Data shown for the case where f_{diff}=100 Hz. Single-tone-isolevel functions indicated with dash-dot lines. Level in SPL indicated by a numbered symbol (level=10* symbol number). Ct07.

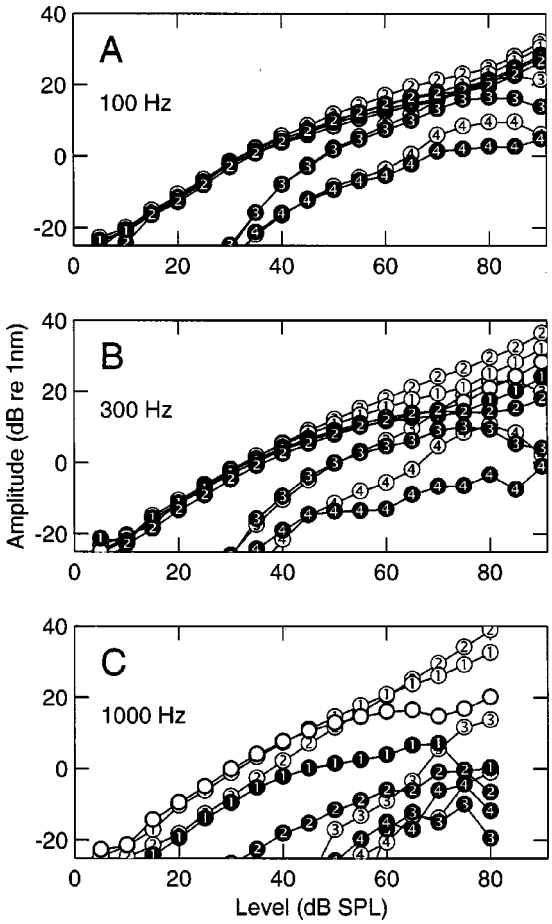

FIG. 12. I/O functions corresponding to the five-component data shown in Fig. 10. (A) $f_{diff}=100$ Hz. The five I/O curves are largely superimposed. (B) $f_{diff}=300$ Hz. (C) $f_{diff}=1000$ Hz. Third component frequency (○)=CF = 8000 Hz. Symbols are as indicated in Fig. 7. Ct07.

Hz, Figs. 12(A), (B)] are the largest distortion products and can equal or exceed the amplitude of the stimulus components [best seen in Fig. 13(B). ③]. The distortion tone, likely the cubic difference tone generated by the two lowest-frequency components, is normally the largest distortion component and attains maximum amplitude for small frequency differences. For $f_{diff}>1000$ Hz, only the distortion component labeled ③ is present in the response at a significant amplitude and only at higher levels (panel C). All other distortion components are relatively small.

The response to seven-tone stimuli was similar to that of five-component stimuli (Fig. 13). For small f_{diff} there is a reduction in the amplitude of the center components relative to the stimulus edge frequencies of 5900 and 6600 Hz for levels >20 dB SPL [Fig. 13(B)]. There is substantial mutual suppression of each component that decreases as f_{diff} increases (not shown). When the center component is omitted the response at that center frequency is negligible at low stimulus levels and reaches parity with the other components at midlevels [○ in Fig. 13(C) and the diamond symbol along the top of the panel in Fig. 13(D)].

To verify that level-dependent behavior observed in Fig. 13(D) wasn't present in the stimulus, i.e., a stimulus artifact, responses to multicomponent stimuli were measured in the vibration of the umbo. The umbo I/O curves were linear [Fig. 14(A)] and the amplitude distribution shows that the missing center component remains so at all stimulus levels [Fig. 14(B)]. Other tests of either AM stimuli or the five-component stimuli verified that component interaction and suppression is only present in the cochlea.

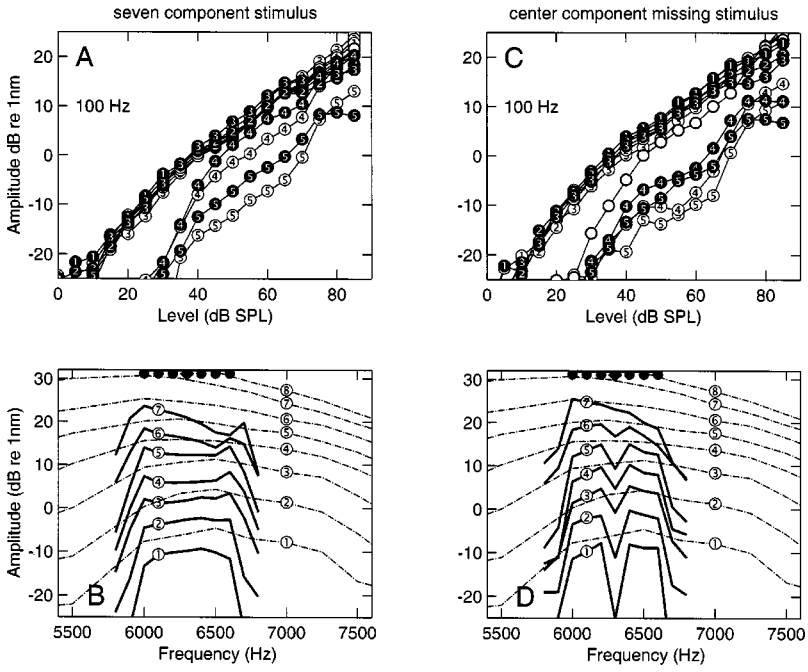

FIG. 13. Example of the basilar-membrane response to the seven-component stimulus where CF=6300 Hz. (A) I/O functions for $f_{diff}=100$ Hz for 11 response components: 5700 to 6800 Hz in 100-Hz steps. Stimulus frequencies: 5900 to 6600 Hz. (B) Isolevel responses for the complex versus single-tone curves. Example of the basilar-membrane response to the seven-component stimulus with the center component stimulus deleted (C and D). (C) I/O functions for $f_{diff}=100$ Hz for nine response components with the center component stimulus deleted. (D) Isolevel responses for the complex versus single-tone curves with the center component stimulus deleted. Symbols are as indicated in Fig. 7. Ct26.

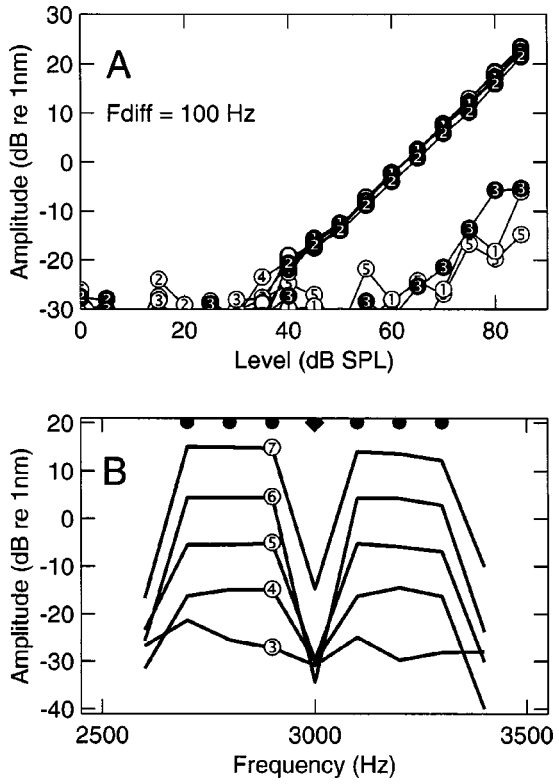

FIG. 14. Examples of the umbo responses to the seven-component stimulus with the center component stimulus deleted. CF=3000 Hz and f_{diff} =100 Hz. (Ct26, same animal as used for Fig. 13). Components labeled as in Fig. 13.

E. Phase versus level for multicomponent stimuli

There are well-known phase versus level effects in basilar-membrane mechanics (e.g., Geisler and Rhode, 1982) that are similar to those initially demonstrated in the auditory nerve; phase lags with increasing level for frequencies below CF and phase leads for frequencies above CF (Anderson *et al.*, 1971). However, for the mechanical results this is somewhat of a simplification since above 70–80 dB SPL there is a phase lag with increasing level for all frequencies (Ruggero *et al.*, 1997; Rhode and Recio, 2000).

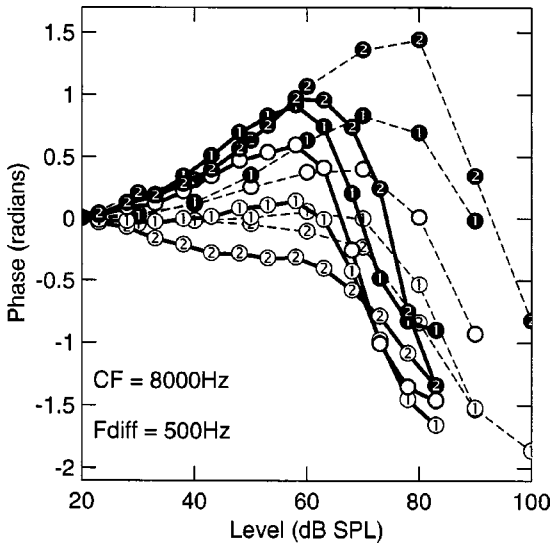

FIG. 16. Phase versus level curves (solid lines). Frequency difference is 500 Hz. Single-tone phase relations are superimposed (dashed lines). Same symbol assignment for both sets of curves as in Fig. 7. Ct17.

The relative phase versus level behavior for five-component stimuli at four difference frequencies largely recapitulates the behavior of the single-tone stimuli (Fig. 15). The smallest level (<70 dB SPL)-dependent phase changes occur for small f_{diff} [=100 Hz, Fig. 15(A)], which is similar to the neural results where there is relatively little phase change at CF. By f_{diff}=600 Hz, there are phase changes as large as 180° between 60 and 80 dB SPL (panel C). For larger f_{diff} there is almost no phase change with level for components lower than CF [Fig. 15(D), ① and ②]. The lower-frequency components have smaller phase changes that likely are due to their being in the linear part of the basilar-membrane response. The phase-level pattern is fairly consistent regardless of the difference frequency. There is a phase lead up to ~60 dB SPL and a phase lag from there to 90 dB SPL that approaches $\pi/2$ radians (90°).

By superimposing the single-tone phase relations on the multitone phase data, it is apparent that there is an effect of

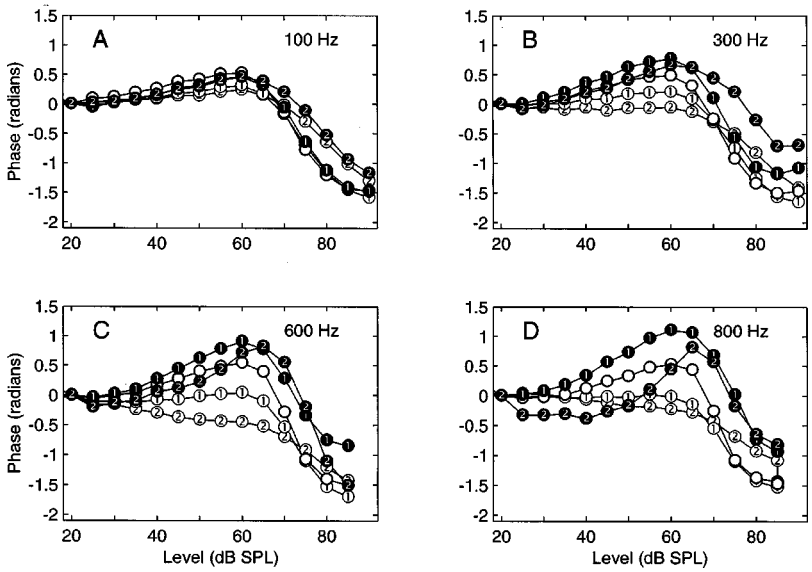

FIG. 15. Response phase-level functions for a set of five-component stimuli where the frequency separation is listed in each panel. CF=8000 Hz (○). The phase data were normalized by subtracting an average of the data points for the 15–25-dB SPL data so that both relative and level-dependent phase changes were easier to see. Same symbol assignment as in Fig. 7. Ct17.

multiple tones simultaneously being presented on the phase (Fig. 16, multitone data—solid lines; single-tone data—dashed lines). The principal effect of multiple tones is a faster rate of phase lag accumulation with increasing level except for the lowest-frequency component (7000 Hz, ②). For the two components above CF, there is nearly a π radians (180°) phase lag that occurs for a 20-dB level change (60–80 dB SPL). In addition, the level at which the phase lag begins appears to be about 10 dB lower than for the single-tone data.

The principal effect of inducing separate amounts of phase change in the individual components is to alter the waveform; the individual components are no longer in sine wave phase, and hence the peak of the waveform would be reduced. This effect likely contributes to the reduction in modulation gain for AM stimuli with increasing modulation frequency.

IV. DISCUSSION

A. AM

There has been relatively little in the literature as to the response of the basilar membrane to complex stimuli (cf. Schroeder maskers, Recio, and Rhode, 2000). However, the response of the auditory nerve to AM stimuli has been well documented (Javel, 1980; Smith and Brachman, 1980; Joris and Yin, 1992). Interpreting the relation between neural and mechanical behavior is complicated, since the inner hair cell's membrane properties and its synapse with the auditory nerve are interposed and limit the bandwidth of the transduction of mechanical motion to the neural domain (Kidd and Weiss, 1990). Rectification at the synapse primarily introduces even-order nonlinearities (Kiang *et al.*, 1965; Pfeiffer and Kim, 1972; Horst *et al.*, 1986) into the process that adds to the distortion resulting from cochlear mechanics that is primarily third order (cubic), although recent evidence indicates the presence of second-order harmonics in BM responses to single tones (Cooper, 1998).

The high-frequency component makes the smallest contribution to the basilar-membrane response because its response is reduced by the cochlear filter as the modulation frequency and stimulus level increase. The spectrum of the BM response is then reminiscent of a single sideband-modulated signal (Schwartz, 1959). It is noteworthy that there is no AM coding theory that applies to cochlear mechanical response since the sidebands are not of equal amplitude. The remaining two components vary in a predictable manner based on the properties of the cochlear filter and nonlinear compression (a simulation was also run using a gammatone filter with the stimulus set that yielded similar results). As the level is increased, the lowest-frequency component is the least compressed by the cochlear nonlinearity; therefore, it increases faster with increasing level than the other components. Therefore, for modulation depths less than 200%, modulation gain increases as the lower component amplitude approaches the amplitude of the carrier component. The maximum gain occurs when the two are equal in amplitude (assumes that the upper sideband component is significantly smaller than the carrier). The exception to the latter situation occurs for small f_{mod}, when all three components are relatively unfiltered and are similarly affected by the cochlear nonlinearity. In this latter instance there is edge enhancement of the spectrum; that is, both sideband components are larger than the carrier. This is reminiscent of Mach bands, where the edge of the band is enhanced relative to the center component (Carterette *et al.*, 1969) and the AN responses to the multicomponent stimuli of Horst *et al.* (1990). Edge enhancement also implies that the modulation gain is >0 dB. Edge component enhancement was also found in response to five- and seven-component stimuli.

Modulation gain in the AN-neural representation of AM signals varies with level but in a manner that is different than the mechanical gain relation to level. The neural gain reaches a maximum within 10–20 dB of the neural threshold and then decreases with increasing levels (Khanna and Teich, 1989; Joris and Yin, 1992). Mechanical modulation gain-level curves increase at low levels but do not show the same decrease with increasing levels as the neural curves [Fig. 2(B), $f_{\mathrm{mod}}=500$ Hz]. In fact, for modulation depths <1, gain continues to increase with level for $f_{\mathrm{mod}}>800$ Hz (Fig. 5). It appears that the mechanical tMTFs can be largely explained by the individual level curves for the three components. That is, the upper sideband's influence on the basilar-membrane vibration decreases with increasing f_{mod} so that the lower sideband and carrier are left to interact to produce the modulation. At low levels the carrier is usually larger (Fig. 7). Maximum gain occurs when the two lower-frequency components are equal in amplitude, which is analogous to 200% modulation. Therefore, if $m<2$, the gain is >0 dB. The lower sideband grows faster with level than the carrier ($=$CF), resulting in it becoming the largest component at high levels and also suppressing the carrier (and the higher-frequency component) at high levels. While there are instances of mechanical modulation gain-level curves with a nonmonotonic shape similar to the neural curves, there are also differences (Figs. 2 and 4). Their peak values occur between 60–70 dB SPL, substantially higher than those for the neural curves and for higher modulation depths than were typically used for the AN studies. A related study of neural coding of 200% modulated signals in primarylike units in the cochlear nucleus showed the peak in the modulation gain occurred between 25–40 dB SPL (Rhode, 1994). While there is a species difference between the neural and mechanical studies, it is likely that the primary determinant of any decrease in neural modulation gain with level results from auditory-nerve fibers being driven to saturation throughout the entire modulation period.

Comparison of a neural tMTF for a cat-AN fiber (CF $=6.9$ kHz, at the best modulation level for the unit, Joris and Yin, 1992) with several mechanical tMTFs (CF$=8$ kHz) shows they are similar (Fig. 17). Mechanical tMTFs are low pass at low levels (e.g., Fig. 2), as are neural tMTFs. The neural I/O curves are nonmonotonic, peaking between 20 and 40 dB SPL and decreasing rapidly with increasing levels. The decrease is due to the nerve discharging throughout the modulation period and the resulting decrease in firing synchronized to f_{mod}. Mechanical modulation gain (modulation depth$=1$) varies relatively little for low f_{mod}

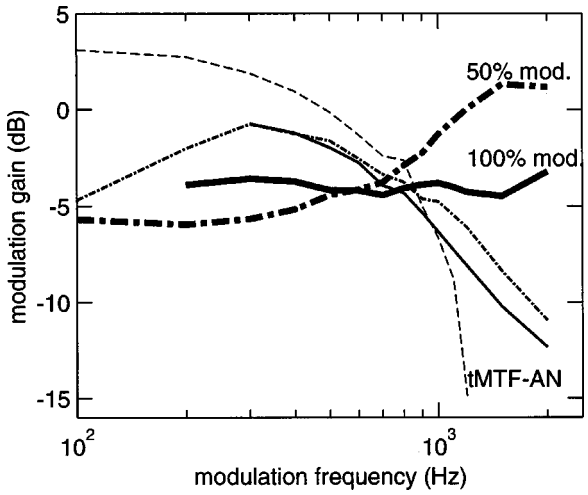

FIG. 17. Superposition of mechanical and neural tMTFs. The neural curve (dashed line) is adapted from Joris and Yin (1992) that they describe as taken at the best modulation level (usually 20–40 dB SPL). Mechanical tMTFs are for $m=0.5$ (dash-dot line) and $m=1$ (solid line) from the same experiment as shown in Figs. 2(A) and 5(B) but at levels of 30 and 65 dB SPL (indicated by a thin and thick line, respectively, Ct07).

while for higher f_{mod}'s they have a nonmonotonic shape similar to the neural curves but with the maximum value at higher levels.

Corner frequencies of the neural tMTFs decrease with decreasing CF and can vary nearly an octave with a mean value ~900 Hz at 10 kHz. For a 6.9-kHz fiber, the cutoff frequency was 400–500 Hz and around 1 kHz for higher CFs (Joris and Yin, 1992). In comparing BM tMTFs with neural tMTFs, the former have higher cutoff frequencies, suggesting that the neural frequency limit is a result of the filtering properties of hair cells (Fig. 17).

Joris and Yin found that the modulation of neural discharges increased as modulation depth increased while the average rate and phase remained nearly constant. In contrast, the BM response phase varies with level, both increasing and decreasing in various experiments. Little phase change in AN firing occurs with level changes for stimulus frequencies=CF; this suggests that the carrier frequency may not have been set to the exact CF of the basilar membrane (Fig. 16). Neural phase at CF is known to vary little but does so off CF (Anderson *et al.*, 1971). For modulation depths <1, modulation gain was generally >1. For modulation depths <1 and $f_{\mathrm{mod}}<800$ Hz, mechanical gain ranged between -2 and $+2$ dB, which is near that found for the AN response. However, for 100% modulation the gain was never >1, implying that there are other factors involved in determining the neural tMTF. An exception occurs for low f_{mod} ($=100$ Hz or less) where the occurrence of a second peak in the envelope implies modulation >100% (Fig. 3, top row).

Mechanical modulation gain decreases 2–8 dB for f_{mod} >1000 Hz depending on stimulus level and modulation depth. Regardless of modulation depth and stimulus level, the mechanical tMTFs are relatively flat in comparison to the neural tMTFs. The gains of mechanical tMTFs bracket the neural gain if one compares the $m=0.5$ functions at 20 and 50 dB SPL. However, with the same modulation used for the neural curve and mechanical tMTFs (solid lines) in Fig. 17, the mechanical gain is less than the neural. Therefore, some of the neural gain is likely due to hair cell and hair cell synapse properties. However, neural modulation gains also vary considerably and overlap the mechanical gains.

Some neural tMTFs can have a high-pass slope, as can mechanical tMTFs for low modulation depths. However, the corner frequency of neural tMTFs does not increase for CFs>10 kHz, which is likely due to low-pass filtering in the hair cells plus other mechanisms (Kidd and Weiss, 1990). The effect of adaptation may contribute to producing modulation gains >1 since faster stimuli will result in a larger transient response than that due to stimuli with slower rise times. These features suggests that neural effects modify the mechanical tMTFs and are necessary to fully account for the AN response to AM stimuli.

The amount of distortion in the envelope of responses to AM stimuli ($m\leqslant 1$) was unexpected (Figs. 1 and 3). It is not a consequence of distortion in the stimuli, as this was verified. Perhaps more surprising is that Fourier analysis of the envelope showed second-order harmonic distortion (≈10 dB below fundamental) is larger than the distortion measured, in the same animal, in responses to single tones (≈20 dB below fundamental). Envelope distortion occurs mostly when two of the spectral components of the AM stimulus (usually the carrier and the lower sideband) dominate the BM response. This is similar to the spectrum of a single-sideband AM stimulus. Computer simulations showed that the envelope of a single-sideband AM stimulus (even in the case of a linear system) is distorted. Coherent demodulation of the waveform (i.e., multiplying by a sinusoidal whose frequency equals the frequency of the modulation frequency) yields a waveform with less distortion. It is, however, unlikely that the auditory system performs this type of analysis.

B. Multicomponent stimuli

Horst *et al.* (1990) identified the short-term spectral content of the acoustic signal and instantaneous amplitude as being most important to acoustic coding. At low stimulus levels the response of the auditory nerve directly reflects a linear encoding of the stimulus. As the level is increased, nonlinear effects occur that can alter a component, such as decreasing or even eliminating the center frequency component of a harmonic complex. When a center component of the harmonic complex was left out, it was found restored in the output of the AN by the generation of distortion components due to the cochlear nonlinearity.

Present results indicate that basilar-membrane mechanics underlie much of the observed response of the AN to complex stimuli. The suppression of the center component for small f_{diff} is especially prominent. This effect is independent of the signal bandwidth and/or the number of stimulus components since it was observed for AM, five- and seven-component stimuli. The principal factor appears to be small $f_{\mathrm{diff}}(<300$ Hz), at least in the frequency region that was studied here. Generation of distortion components is also greatest at low f_{diff} and decreases rapidly with increasing f_{diff}.

Distortion component generation likely explains the restoration of a missing center component that could be a result

of the superposition of distortion products generated by both lower- and higher-frequency components. The missing component can be generated by combination two consecutive stimulus components interacting; that is, if the missing component is the center component, then CF=2❶−❷, 2①−②, 3❷−2❸, and 2②−③ for the seven-component stimulus (the symbols correspond to the stimulus components as used in Figure 13, e.g., the first distortion component=$2f_1-f_2$ =2❶−❷, when $f1$ and $f2$ are the first two stimulus components immediately above CF). A distortion component at CF could also be generated by the components below CF. In addition, one could consider whether the distortion products that are generated can themselves interact with all other components present in the cochlea. Apparently restoring the missing component is a result of distortion product generation due to the nonlinear nature of the cochlea.

The interactions of components in the cochlea are dependent on: (1) the compressive nonlinearity of the cochlea and (2) filtering in the cochlea. The first was demonstrated by showing that the center component is not restored when the experiment was performed on the umbo. Filtering of the stimulus waveform by a filter constructed from the isointensity functions shown in Fig. 13 also produced a waveform without any spectral component at the frequency of the missing component. This indicates that the occurrence of a response at the frequency of the missing component is due to a distortion in the cochlea, as it could not be generated using a linear filter. The filtering of the cochlea removes the higher-frequency components when the component spacing increases, thereby eliminating two-tone interactions with the high-frequency component. Before the signal is transmitted via the AN there is additional filtering due to the hair cell membrane properties and the effect of neural refractoriness. As the number of components (that are harmonically related) increases, the crest factor of the signal increases. The high-amplitude portion (the signal becomes an impulse train as the number of components approaches infinity) has a broad-spectrum composition, while the low-amplitude portion is dominated by components near the low- and high-frequency cutoffs of the signal. It follows that at low levels the broadband response will be encoded and that with increasing level the peak will be compressed more relative to the low-amplitude portion by the cochlear nonlinearity. It follows that edge frequencies contained in the low-amplitude portion of the signal will be better represented at high levels.

There are, of course, other factors that affect the output of the AN such as half-wave rectification, refractoriness, filtering due to hair cell membrane properties, and synaptic properties. A major contributing factor is two-tone suppression that is largely explained at the level of basilar-membrane mechanics (e.g., Ruggero *et al.*, 1992). However, suppression seen in AN fibers using low-frequency suppressors has never been completely explained and may involve nonmechanical processes (e.g., Hill *et al.*, 1989; Cooper, 1996; Geisler and Nuttall, 1997). Horst *et al.* found significant differences between the encoding by low- and high-spontaneously active AN fibers and suggested either a center clipping nonlinearity or an expansive nonlinearity as possible explanations for this behavior. Neither of these latter phenomena has been observed in basilar-membrane mechanics.

Use of multiple component signals was motivated by their similarity to many common communication signals including speech and the fact that they result in the perception of a pitch. Signals generated by a pulsatile source and subsequently filtered have a spectrum consisting of a series of harmonically related signals. Formants in speech consist of a maximum peak in the spectrum surrounded by several components separated by the pulse frequency, often 80 to 500 Hz. The signals used here are an approximation of these signals. The responses to them indicate that there are complex interactions that largely depend on the nonlinearity of the cochlea as to how the final signal spectrum is shaped. The bandwidth separation of the components and amplitude all are major factors in determining the final representation of the signal spectrum in the cochlea. Suppression is one of the most important factors in determining the contribution that each component makes in exciting the auditory nerve. There is clearly mutual suppression of closely spaced components combined with distortion product generation that determines the response to a complex signal. Mutual suppression could play a role in limiting cochlear damage at CF due to complex stimuli.

ACKNOWLEDGMENTS

This work was supported by the National Institute of Deafness and Communications Disorders, Grant No. R01 DC 01910. Special thanks to C. Dan Geisler for reading an earlier version of this manuscript and the journal reviewers of this article, Wiebe Horst and an anonymous reviewer.

Anderson, D. J., Rose, J. E., Hind, J. E., and Brugge, J. F. (**1971**). ''Temporal position of discharges in single auditory-nerve fibers within the cycle of a sine-wave stimulus: Frequency and intensity effects,'' J. Acoust. Soc. Am. **49**, 1131–1139.

Bennett, W. R. (**1970**). *Introduction to Signal Transmission* (McGraw-Hill, New York).

Cariani, P. A., and Delgutte, B. (**1996a**). ''Neural correlates of the pitch of complex tones. I. Pitch and pitch salience,'' J. Neurophysiol. **76**, 1698–1716.

Cariani, P. A., and Delgutte, B. (**1996b**). ''Neural correlates of the pitch of complex tones. II. Pitch shift, pitch ambiguity, phase invariance, pitch circularity, rate pitch, and the dominance region for pitch,'' J. Neurophysiol. **76**, 1717–1734.

Carney, L. H., Mc Duffy, M. J., and Shekter, I. (**1999**). ''Frequency glides in the impulse responses of auditory-nerve fibers,'' J. Acoust. Soc. Am. **105**, 2384–2391.

Carterette, E., Friedman, M. P., and Lovell, J. D. (**1969**). ''Mach bands in hearing,'' J. Acoust. Soc. Am. **45**, 986–998.

Cooper, N. P. (**1996**). ''Two-tone suppression in cochlear mechanics,'' J. Acoust. Soc. Am. **99**, 3087–3098.

Cooper, N. P. (**1998**). ''Harmonic distortion on the basilar membrane in the basal turn of the guinea-pig cochlea,'' J. Physiol. (London) **509**, 277–288.

Cooper, N. P., and Rhode, W. S. (**1992**). ''Basilar membrane mechanics in the hook region of the cat and guinea pig cochlea,'' Hear. Res. **63**, 163–190.

de Boer, E., and Nuttall, A. L. (**1997**). ''The mechanical waveform of the basilar membrane. I. Frequency modulations (glides) in impulse responses and cross-correlation functions,'' J. Acoust. Soc. Am. **101**, 3583–3592.

Delgutte, B. (**1980**). ''Representation of speech-like sounds in the discharge patterns of auditory-nerve fibers,'' J. Acoust. Soc. Am. **68**, 843–857.

Evans, E. F. (**1978**). ''Place and time coding in the peripheral auditory system: Some physiological pros and cons,'' Audiology **17**, 369–420.

Geisler, C. D., and Nuttall, A. L. (**1997**). ''Two-tone suppression of basilar membrane vibrations in the base of the guinea pig cochlea using low-side suppressors,'' J. Acoust. Soc. Am. **102**, 430–440.

Geisler, C. D., and Rhode, W. S. (**1982**). ''The phases of basilar-membrane vibration,'' J. Acoust. Soc. Am. **71**, 1201–1203.
Goldstein, J. (**1967**). ''Auditory nonlinearity,'' J. Acoust. Soc. Am. **41**, 676–689.
Greenberg, S., and Rhode, W. S. **(1987)**. ''Periodicity coding in the auditory nerve and ventral cochlear nucleus,'' in *Auditory Processing of Complex Sounds*, edited by W. A. Yost and C. S. Watson (Erlbaum, Hillsdale, NJ).
Hill, K. G., Strange, G., Gummer, A. W., and Mo, J. (**1989**). ''A model proposing synaptic and extra-synaptic influences on the responses of cochlear nerve fibers,'' Hear. Res. **39**, 75–90.
Horst, J. W., Javel, E., and Farley, G. R. (**1986**). ''Coding of fine spectral structure in the auditory nerve. I. Fourier analysis of period and interspike interval histograms,'' J. Acoust. Soc. Am. **79**, 398–416.
Horst, J. W., Javel, E., and Farley, G. R. (**1990**). ''Coding of fine spectral structure in the auditory nerve. II. Level-dependent nonlinear responses,'' J. Acoust. Soc. Am. **88**, 2656–2681.
Javel, E. (**1980**). ''Coding of AM tones in chinchilla auditory nerve: Implications for the pitch of complex tones,'' J. Acoust. Soc. Am. **68**, 133–146.
Joris, P. X., and Yin, T. C. T. (**1992**). ''Responses to amplitude-modulated tones in the auditory nerve,'' J. Acoust. Soc. Am. **91**, 215–232.
Khanna, S. M., and Teich, M. C. (**1989**). ''Spectral characteristics of the primary auditory-nerve fibers to amplitude-modulated signals,'' Hear. Res. **39**, 143–158.
Kiang, N. Y. S., Watanabe, T., Thomas, E. C., and Clark, L. F. **(1965)**. *Discharge Patterns of Single Fibers in the Cat's Auditory Nerve* (MIT, Cambridge, MA).
Kidd, R. C., and Weiss, T. F. (**1990**). ''Mechanisms that degrade timing information in the cochlea,'' Hear. Res. **49**, 181–208.
Miller, M. I., and Sachs, M. B. (**1984**). ''Representation of voice pitch in discharge patterns of auditory-nerve fibers,'' Hear. Res. **14**, 257–279.
Palmer, A. R., Winter, I. M., and Darwin, C. J. (**1986**). ''The representation of steady-state vowel sounds in the temporal discharge patterns of the guinea pig cochlear nerve and primarylike cochlear nucleus neurons,'' J. Acoust. Soc. Am. **79**, 100–113.
Pfeiffer, R. R., and Kim, D. O. (**1972**). ''Response patterns of cochlear nerve fibers to click stimuli: Descriptions for cat,'' J. Acoust. Soc. Am. **53**, 1669–1677.
Recio, A., and Rhode, W. S. (**2000**). ''Basilar membrane responses to broadband stimuli,'' J. Acoust. Soc. Am. **108**, 2281–2298.
Rhode, W. S. (**1971**). ''Observations of the vibration of the basilar membrane in squirrel monkey using the Mössbauer technique,'' J. Acoust. Soc. Am. **49**, 1218–1231.
Rhode, W. S. (**1994**). ''Temporal coding of 200% amplitude modulated signals in the ventral cochlear nucleus of cat,'' Hear. Res. **77**, 43–68.
Rhode, W. S. (**1995**). ''Interspike intervals as a correlate of periodicity pitch in cat cochlear nucleus,'' J. Acoust. Soc. Am. **97**, 2414–2429.
Rhode, W. S., and Recio, A. (**2000**). ''Study of mechanical motions in the basal region of the chinchilla cochlea,'' J. Acoust. Soc. Am. **107**, 3317–3332.
Robles, L., Rhode, W. S., and Geisler, C. G. (**1976**). ''Transient response of the basilar membrane measured in squirrel monkeys using the Mössbauer effect,'' J. Acoust. Soc. Am. **59**, 926–939.
Robles, L., Ruggero, M. A., and Rich, N. C. (**1986**). ''Basilar membrane mechanics at the base of the chinchilla cochlea. I. Input–output functions, tuning curves, and response phases,'' J. Acoust. Soc. Am. **80**, 1364–137.
Rose, J. E., Brugge, J. F., Anderson, D. J., and Hind, J. E. (**1967**). ''Phase-locked response to low-frequency tones in single auditory nerve fibers of the squirrel monkey,'' J. Neurophysiol. **30**, 769–793.
Rose, J. E., Brugge, J. F., Anderson, D. J., and Hind, J. E. (**1969**). ''Some possible neural correlates of combination tones,'' J. Neurophysiol. **32**, 402–423.
Ruggero, M. A., Rich, N. C., Recio, A., Narayan, S. S., and Robles, L. (**1997**). ''Basilar membrane responses to tones at the base of the chinchilla cochlea,'' J. Acoust. Soc. Am. **101**, 2151–2163.
Ruggero, M. A., Robles, L., and Rich, A. (**1992**). ''Two-tone suppression in the basilar membrane of the cochlea: Mechanical basis of auditory-nerve rate suppression,'' J. Neurophysiol. **68**, 1087–1099.
Schwartz, M. **(1959)**. *Information Transmission, Modulation, and Noise* (McGraw-Hill, New York).
Sellick, P. M., Patuzzi, R., and Johnstone, B. M. (**1982**). ''Measurement of basilar membrane motion in the guinea pig using the Mössbauer technique,'' J. Acoust. Soc. Am. **72**, 131–141.
Smith, R. L., and Brachman, M. L. (**1980**). ''Response modulation of auditory-nerve fibers by AM stimuli: Effects of average intensity,'' Hear. Res. **2**, 123–133.
Von Békésy, G. (**1960**). *Experiments in Hearing*, edited by E. G. Wever (McGraw-Hill, New York).

Frequency specificity of the human auditory brainstem and middle latency responses using notched noise masking[a)]

Peggy A. Oates[b)] and Suzanne C. Purdy[c)]
Discipline of Audiology, The University of Auckland, Private Bag 92-019, Auckland, New Zealand

(Received 4 January 2001; accepted for publication 22 May 2001)

This study investigated the frequency specificity of the auditory brainstem and middle latency responses to 80 and 90 dB ppe SPL 500-Hz and 90 dB ppe SPL 2000-Hz tonebursts. The stimuli were brief (2-1-2 cycle) linear-gated tonebursts. ABR/MLRs were recorded using two electrode montages: (1) Cz-nape of neck and (2) Cz-ipsilateral earlobe. Cochlear contributions to ABR wave V-Na and MLR waves Na-Pa and Pa-Nb were assessed by plotting notched noise tuning curves which showed amplitudes and latencies as a function of center frequency of the noise masker [Abdala and Folsom, J. Acoust. Soc. Am. **97**, 2394 (1995); *ibid.* **98**, 921 (1995)]. Maxima in the response amplitude profiles for the ABR and MLR to 80 dB ppe SPL tonebursts occurred within one-half octave of the nominal stimulus frequency, with minimal contributions to the responses from frequencies greater than one octave away. At 90 dB ppe SPL, contributions came from a slightly broader frequency region for both stimulus frequencies. Thus, the ABR/MLR to 80 dB ppe SPL tonebursts shows good frequency specificity which decreases at 90 dB ppe SPL. No significant differences exist in frequency specificity of: (1) ABR wave V-Na *versus* MLR waves Na-Pa and Pa-Nb at either stimulus frequency or intensity; and (2) ABR/MLRs recorded using the two electrode montages. [DOI: 10.1121/1.1385901]

PACS numbers: 43.64.Qh, 43.64.Ri, 43.66.Dc [LHC]

I. INTRODUCTION

The Auditory Brainstem (ABR) and Middle Latency Response (MLR) to tonebursts have been utilized as clinical tools for estimating the pure-tone behavioral audiogram in infants and difficult-to-test populations. The accuracy of threshold estimation is dependent upon the frequency and place specificity of the ABR and MLR to toneburst stimuli (Stapells *et al.*, 1994, 1985; Starr and Don, 1988).

During the last decade, several investigators have demonstrated that ABRs recorded to air-conducted toneburst stimuli in either quiet or notched noise masking provide reasonably accurate estimates of pure-tone behavioral thresholds in infants, young children and adults with normal hearing sensitivity or peripheral sensorineural hearing impairments (Beattie *et al.*, 1996; Munnerley *et al.*, 1991; Sininger and Abdala, 1996; Sininger *et al.*, 1997, 1998; Stapells *et al.*, 1995, 1990; Werner *et al.*, 1993). These behavioral threshold estimations are equally accurate for 500- through 4000-Hz tonebursts and are not affected by the audiometric configuration of the loss or the age at which ABR testing is conducted. Thus, ABRs to tonebursts recorded with ipsilateral notched noise masking have good frequency and place specificity.

There are some clinical populations in which the MLR is needed to estimate hearing sensitivity. Because the MLR to toneburst stimuli is not as critically dependent upon neuronal synchronization as the ABR, it plays an important role in estimating hearing thresholds for neurologically impaired individuals who have absent or abnormal ABRs (Kraus *et al.*, 1985b; Worthington and Peters, 1980). In addition, the MLR has been successfully used to estimate behavioral thresholds in individuals with sensorineural hearing losses (Kraus and McGee, 1990; McFarland *et al.*, 1977; Musiek and Donnelly, 1983) and pseudohypacusis (Musiek, 1982; Musiek and Donnelly, 1983). The majority of these studies, however, have been limited to single case reports and thus generalizing the accuracy of these behavioral threshold estimations to the hearing-impaired population is difficult.

MLRs to click and toneburst stimuli can be reliably recorded down to threshold levels in adults with normal hearing sensitivity (Kileny and Shea, 1986; McFarland *et al.*, 1977; Musiek and Donnelly, 1983; Musiek and Geurkink, 1981; Ozdamar and Kraus, 1983; Thornton *et al.*, 1977; Zerlin and Naunton, 1974). However, the existence of MLRs in infants and young children has been the subject of considerable debate. Several studies report that MLRs can be reliably obtained in neonates and young children during natural sleep (Frye-Osier *et al.*, 1982; Kavanagh *et al.*, 1988; McRandle *et al.*, 1974; Mendel *et al.*, 1977; Mendelson and Salamy, 1981; Suzuki and Hirabayashi, 1987; Suzuki *et al.*, 1983; Tucker and Ruth, 1996; Wolf and Goldstein, 1978, 1980). In contrast, others report that MLRs are unstable or absent when young children are in natural or pharmacologically induced sleep (Davis *et al.*, 1983; Engel, 1971; Hirabayshi, 1979; Kraus and McGee, 1993; Kraus *et al.*, 1989, 1985a; Okitsu, 1984; Skinner and Glattke, 1977; Stapells *et al.*, 1988). A number of pediatric MLR studies have identified

[a)]Portions presented at XVI Biennial Symposium of the International Evoked Response Audiometry Study Group, Tromso, Norway, June 3, 1999.

[b)]Author to whom correspondence should be addressed; electronic mail: PeggyOSwim369@aol.com. Current affiliation: Department of Communication Sciences and Disorders, Towson University, 8000 York Road, Towson, MA 21252.

[c)]Current affiliation: National Acoustics Laboratory, 126 Greville Street, Chatswood, New South Wales 2067, Australia.

stimulus and recording parameters as well as subject factors which likely account for these discrepancies.

It has been suggested that the MLR may provide a more frequency specific index of low frequency hearing sensitivity in comparison to the ABR (Kavanagh *et al.*, 1984; Kileny and Shea, 1986; Palaskas *et al.*, 1989; Scherg and Volk, 1983). This suggestion has been based upon two factors: (1) the MLR is larger in comparison to the ABR to 500-Hz tonebursts, leading to enhanced detectability of the response, especially close to threshold (Scherg and Volk, 1983; Wu and Stapells, 1994), and (2) several researchers have suggested that the MLR is less dependent on neural synchrony than the ABR, and thus the MLR may integrate longer portions of the stimulus (e.g., Kileny and Shea, 1986; Kraus and McGee, 1990; McFarland *et al.*, 1977; Scherg and Volk, 1983; Thornton *et al.*, 1977). Investigations of stimulus rise time effects on evoked potentials, however, have demonstrated that when rise times exceed 5 ms, significant decreases in the amplitudes of both the ABR and MLR occur (Beiter and Hogan, 1973; Lichtenstein and Stapells, 1997; Stapells and Picton, 1981; Vivion *et al.*, 1980). These findings suggest that the ABR and MLR integrate stimulus energy in a similar fashion.

At present, only four studies have directly compared the frequency specificity of the human ABR and MLR to 500- and 2000-Hz air-conducted tonebursts (Mackersie *et al.*, 1993; Oates and Stapells, 1997a,b; Wu and Stapells, 1994). These studies showed no differences in the frequency specificity of the ABR and MLR to low- and moderate-intensity (60 and 80 dB ppe SPL) tonebursts in normal hearing adults. The levels of 60 and 80 dB ppe SPL for 500- and 2000-Hz air-conducted brief tonebursts used in these studies are equivalent to approximately 35 and 55 dB HL depending upon the transducer employed, the rate of stimulation and the temporal characteristics (rise and fall times and duration of the plateau) of the stimuli (Stapells, 1989). No published research has addressed the question of how frequency specific the MLR is to higher intensity ($\geqslant$90 dB ppe SPL) tonebursts. Further research is needed to investigate the frequency and place specificity of the MLR at these higher stimulus intensities in order to realize its full clinical potential.

The notched noise masking technique has been successfully used to investigate the frequency specificity of the ABR to tonebursts in normal hearing adults (Beattie and Boyd, 1985; Beattie and Kennedy, 1992; Beattie *et al.*, 1994; Picton *et al.*, 1979; Stapells, 1984; Stapells and Picton, 1981). These investigations did not determine which specific frequencies contributed to the nonmasked response since the center frequency of the notch was fixed at the nominal stimulus frequency. Folsom and colleagues modified the original notched noise paradigm by varying the location of the notch surrounding the stimulus frequency (Abdala and Folsom, 1995a,b; Folsom and Wynne, 1986), allowing cochlear contributions to the evoked potentials from discrete frequency regions to be measured directly. Cochlear contributions to the ABR and MLR can be determined by plotting tuning curves which show response amplitudes and/or latencies as a function of the center frequency of the notched noise (Abdala and Folsom, 1995a,b).

An important consideration in comparing amplitude and latency measures across test conditions and subjects is the signal-to-noise (S/N) ratio of each averaged waveform. The S/N ratio is determined by the relative amplitude of the evoked potential peaks, the level of the residual background noise, and the amount of averaging which is conducted (Don and Elberling, 1994). The S/N ratio also depends, in part, upon the placement of the two electrodes used for the differential recording. Numerous investigators have demonstrated that using a vertical electrode recording montage (Cz to nape of the neck) results in significant enhancement of ABR wave V and MLR wave Pa amplitudes in comparison to the conventional (Cz/forehead to ipsilateral earlobe/mastoid) montage when recording these evoked potentials to nonmasked click stimuli in normal hearing adults (e.g., Beattie *et al.*, 1986; Hughes *et al.*, 1981; Kadoya *et al.*, 1988; King and Sininger, 1992; Kraus and McGee, 1988; McPherson *et al.*, 1985; Polyakov and Pratt, 1994). There is a paucity of literature, however, regarding the effects of nape of the neck as the reference electrode position when recording ABRs and MLRs to toneburst stimuli presented in either quiet or noise masked conditions.

Two recording techniques were employed in the current study in order to maximize the S/N ratio and ensure a similar quality of responses across conditions and subjects: (1) averaging was stopped when a certain residual averaged background noise level was reached as suggested by Don and Elberling (1996); and (2) the evoked potentials were recorded using both conventional (Cz to ipsilateral earlobe) and vertical (Cz to nape of the neck) electrode montages.

Using the notched noise technique, the aims of the present study were to assess: (1) cochlear contributions to the ABR and MLR to 80 and 90 dB ppe SPL 500-Hz and 90 dB ppe SPL 2000-Hz tonebursts, (2) the differences, if any, in the frequency and place specificity of the ABR *versus* the MLR, and (3) if the use of a noncephalic reference electrode located at the nape of the neck enhances the amplitude of ABR (wave V-Na) and/or MLR (waves Na-Pa and Pa-Nb) recorded with ipsilateral noise masking.

II. METHODS

A. Subjects

Ten normal-hearing adults (five males and five females) ranging in age from 23 to 42 years (mean=29.5 years, s.d. =6.92) participated in the study. All subjects had pure-tone behavioral thresholds of 15 dB HL (ANSI, 1996) or better at octave frequencies of 250–8000 Hz in the test ear with no significant otologic or neurologic histories. All subjects had type A tympanograms and a present ipsilateral reflex to a 90 dB HL 1000-Hz tone.

B. Stimuli

The stimuli were 500- and 2000-Hz (2-1-2 cycle) linear-gated tonebursts (see Fig. 1) generated by the NeuroScan STIM™ system. The stimuli were of alternating-onset polarity and were delivered using Etymotic Research ER-3A in-

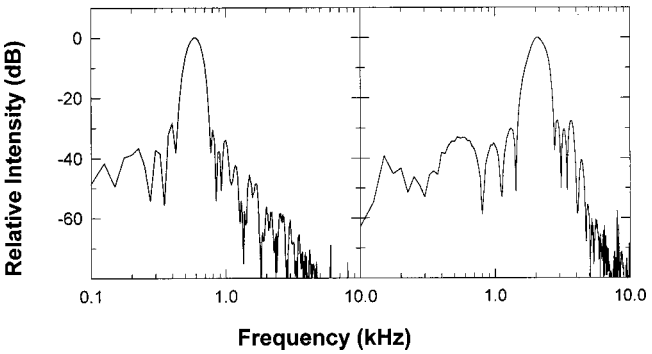

FIG. 1. Acoustic spectra for the linear-gated 500- and 2000-Hz tonebursts. The spectra were obtained by coupling the ER-3A insert earphone to a Brüel and Kjaer 2-cc adapter and a 4152 coupler, a 1-in. condenser microphone (type 4144), and a 2235 sound level meter. The ac output of the sound level meter was routed to the "SCAN" system of the Neuroscan. The spectra were obtained by taking averages of 200 fixed polarity stimulus presentations in the time domain using a uniform window and then performing an FFT. The stimuli were presented at a sampling rate of 25 600 Hz over an analysis time of 20 ms, with the stimulus waveform centered in this window.

sert earphones at a rate of 9.4/s. The 500- and 2000-Hz stimuli were presented at 90 dB ppe SPL to one ear per subject which was selected at random. The 500-Hz toneburst was also presented at 80 dB ppe SPL. The stimuli were calibrated daily using a Brüel and Kjaer DB0138 2-cc adaptor and 4152 coupler, 1 in. condenser microphone (type 4144) and sound-level meter (type 2235). The 90 dB ppe SPL values correspond to levels of 67 and 66 dB nHL for the 500- and 2000-Hz tonebursts, respectively. The behavioral nHL values were determined from a pilot study of ten adults with normal hearing sensitivity.

C. Broadband and notched noise masking

The broadband white noise was generated by a custom designed system. The band rejected or notched noise was produced by passing the noise through a Wavetek Brickwall filter (model 753A). The output of the filter was amplified and mixed by a custom designed ComSec system. White noise was selected for the masking stimulus rather than pink noise because effective masking (behavioral and electrophysiologic masking) for the 500- and 2000-Hz tonebursts could be achieved at a slightly lower intensity level using white noise (Oates, 1996).

The nominal center frequencies of the notch were: 500, 707, 1000, 1410, 2000, 2830, 4000 and 8000 Hz for both stimulus frequencies. Notches in the white noise were also centered around 125, 250 and 354 Hz for the 500-Hz stimuli and 5660 Hz for the 2000-Hz stimuli. The acoustic spectra of the notched noise conditions as measured by the Stanford Research System FFT spectrum analyzer (model SR760) showed that the mean depth of the notch was 40 dB with average rejection rates of 91.3 dB/octave for the low pass (LP) filter and 104.5 dB/octave for the high pass (HP) filter. The width of the notch was approximately 1.5 octaves (limitations of the Brickwall filter did not permit the use of a narrower notch width).

In the present study, the white noise needed to achieve effective masking for the 90 dB ppe SPL 500-Hz tonebursts had an overall intensity of 92.5 dB SPL and a bandwidth of 4000 Hz. Thus, the spectrum level of the white noise was $92.5-10\times\log 4000=56.5$ dB SPL. If the 1.5-octave-wide notch is centered around 500 Hz, it has a bandwidth of 544 Hz (297–841 Hz), and the overall bandwidth of the noise would be $4000-544=3456$ Hz. Therefore, the overall dB SPL of the notched noise centered around 500 Hz would be $56.5+10\times\log 3456=91.9$ dB SPL. The dB SPL of the notched noise thus varies as a function of the frequency at which the notch is centered.

D. Masker level

Pilot studies were conducted in order to determine the level of noise masking which would provide the most frequency specific isolation of cochlear regions and ensure reasonable safety limits of noise exposure for the subjects. In the first pilot study, we assessed whether the ABR and MLR to 90 dB ppe SPL 500- and 2000-Hz tonebursts could be effectively masked (behaviorally and electrophysiologically) using broadband white noise presented at S/N ratios of -10 dB or less in 10 subjects with normal hearing sensitivity. Broadband noise was presented at 90 dB SPL and increased in 1 dB steps until the ABR and MLR were judged to be completely masked or until a maximum noise intensity of 100 dB SPL (i.e., -10 dB S/N ratio) was reached. This maximum noise level was selected (1) to stay within reasonable safety limits and acceptable comfort levels for the subject, and (2) broadband noise presented at mean S/N ratios of between -1 and -5.5 dB has been found to effectively mask ABRs to 85 dB ppe SPL 500–4000 Hz tonebursts (Purdy *et al.*, 1989). S/N ratios of -5 to -10 dB effectively masked the ABR and MLR for 80% and 30% of the subjects, respectively. Behavioral masking was achieved for all subjects at S/N ratios of -5 to -10 dB. Based on these findings, it was decided that an effective masking approach could not be safely employed due to the extremely high noise intensities needed to ensure complete electrophysiologic masking of both the ABR and MLR for all subjects.

Because the level of broadband noise needed to achieve electrophysiologic masking varied over a range of at least 5 dB across subjects, each subject's effective masking level (EML) was used as the reference rather than a fixed S/N ratio. The broadband white noise level was set at the subject's effective masking level minus 6 dB. Effective masking could not be achieved for the MLR in most subjects, so the EML was determined based on electrophysiologic masking of the ABR. This resulted in mean S/N ratios of -2.5 dB (range: $+1$ to -4.5 dB) for the 500-Hz stimuli and $+0.7$ dB (range: $+7$ to -2 dB) for the 2000-Hz stimuli.

Employing this formula for determining the level of broadband white noise, the maximum noise exposure is 94.5 dB SPL. This value is in close agreement with the intensity levels of pink noise safely employed in a previous study (Oates and Stapells, 1997a,b).

The ABR and MLR responses to the 90 dB ppe SPL tonebursts may have been undermasked. Thus, these electrophysiologic responses likely received some cochlear contributions from the frequency region of the toneburst, rather than receiving contributions solely from the frequency region

of the notch. This issue is addressed later in the manuscript and evidence is presented suggesting that undermasking did not have a negative influence upon the results.

E. Evoked potential recordings

Recordings and waveform analyses were carried out using the Neuroscan SCAN™ system. The ABR and MLR were simultaneously recorded on two channels using gold-plated electrodes. The noninverting electrode was placed on the vertex (Cz) for both channels with the inverting electrode located on the ipsilateral earlobe (A1 or A2) for channel one and cervical vertebra 2 (Cv2) for channel two. A forehead electrode (Fpz) served as ground for both channels. Interelectrode impedances were 2000 Ohms or less. The electroencephalographic (EEG) signals were amplified (gain $=100\,000$) and analog filtered (10–1000 Hz, 6 dB/octave, Grass Neurodata Acquisition System model 12). The EEG signals were digitized (12-bit converter) using a sampling rate of 6168 Hz (512 points) over an analysis time of 83 ms (-3 to 80 ms) and stored as single-trial epochs. Eight thousand epoched trials were acquired for the quiet and each noise condition. Artifact rejection was set to $\pm 100\ \mu$V, which corresponds to the clipping level of the analog-to-digital convertor (Don and Elberling, 1994).

F. Data analysis

1. Digital filtering

The data for each subject consisted of 8000 sweeps recorded on two channels. Each epoch was digitally re-filtered with a HP filter setting of 20 Hz (24 dB/octave). The 20-Hz filter setting was selected because it decreases the variability in adult ABRs (Suzuki *et al.*, 1983) and is recommended as the optimal HP setting for estimating the signal-to-noise characteristics of the MLR (Gould *et al.*, 1992).

2. Estimate of residual background noise level and averaging

An estimate of the residual noise associated with each average was obtained using the Fsp technique. The variance of the voltage at a single point within the average was calculated over a block consisting of 256 sweeps, with the single point placed at 30 ms. The analysis window used in the Fsp calculation was from 4 to 74 ms. The digitally filtered set of 8000 sweeps for each recording condition was averaged off-line in two ways: (1) averaging continued until a residual background noise criterion of 60 nV was reached, and (2) four mutually exclusive averages were created, each meeting a residual noise level (RNL) criterion of 120 nV. The 60 nV criterion was chosen by calculating the ABR and MLR peak amplitudes corrected for residual noise as described by Don and Elberling (1996); see the Appendix. If a subject's RNL following 8000 sweeps exceeded 60 nV, then their set of ABR/MLR waveforms for that particular noise condition consisted of a grand average of the total 8000 single trials and either two or three replicate average waveforms each having a RNL of 120 nV. The majority of the subjects' grand average waveforms reached the 60 nV RNL criterion for the quiet and noise masked conditions (i.e., 89% and 77% for the 500- and 2000-Hz responses, respectively).

G. Procedure

All testing was performed in a double-walled sound attenuating booth. Subjects were seated in a reclining chair and watched subtitled videos during testing. Subjects were instructed to remain awake and their EEG was monitored on an oscilloscope. All subjects were tested with the 90 dB ppe SPL 500- and 2000-Hz linear-gated tonebursts in quiet and in the presence of notched noise masking. Nine of these subjects were also tested with the lower intensity (80 dB ppe SPL) 500-Hz toneburst. For the higher stimulus intensity, testing took place over two sessions with the order of the notched noise conditions randomized. For the lower stimulus intensity, the subjects could choose one or two recording sessions. Each subject's pure-tone behavioral thresholds (250–8000 Hz) and transient evoked otoacoustic emissions (OAE) were assessed at the beginning and end of each test session to ensure that no change in hearing sensitivity or OAE had occurred due to exposure to the noise stimuli.

Only nine subjects were tested for the 80 dB ppe SPL 500-Hz condition because the tenth individual reported a slight feeling of aural fullness prior to her final test session. She had no behavioral threshold shifts, changes in OAEs or tinnitus following her previous test sessions.

H. Response identification

The decision regarding the presence or absence of ABR wave V and MLR waves Na, Pa and Nb was made by combining the ratings of two experienced judges. Both judges had knowledge of the intensity of the stimulus but were blind to the center frequency of the notched noise.

Both raters assigned a score of "1" to "4" to ABR wave V and MLR waves Na, Pa and Nb in the grand average for the various notched noise conditions. Raters were instructed to rate each peak separately and therefore might have assigned different scores for specific peaks in the waveform. These ratings were based on the latency, morphology and replicability of the waveforms. A score of "4" indicated a "definite response," a "3" indicated a "probable response," a "2" indicated a "probable no response" and a "1" indicated a "definite no response." The ratings were then averaged and mean ratings of 2.5 or higher were considered "response present" (Stapells, 1984; Stapells *et al.*, 1990).

I. Response measurements

Peak-to-peak amplitudes of ABR wave V-Na and MLR waves Na-Pa and Pa-Nb were obtained for each subject from the grand average waveforms which were judged to contain a replicable response. Peaks which were judged as no response were assigned an amplitude value equal to the RNL present in the grand average tracing calculated by the Fsp technique. The peak-to-peak amplitude of wave V-Na for the ABR was measured rather than the conventional wave V-V′ because wave V′ was difficult to identify in a few subjects due to the presence of the post-auricular muscle reflex (PAMR). This was especially true when the ipsilateral earlobe was the ref-

erence electrode. Although PAMR interfered with wave V′ identification in these few cases, the latencies of waves V and Na were clearly visible.

Wave V was defined as the maximum vertex positive peak occurring between 6 and 20 ms or, if several peaks of equal amplitude occurred, the peak immediately preceding the largest negative shift was selected. Wave Na was defined as the most negative replicable trough immediately preceding wave Pa occurring in at least of three out of four replications between 10 and 30 ms. Wave Pa was the maximum vertex-positive peak immediately following Na between 20 and 50 ms. If wave Pa consisted of a single peak, the amplitude was measured at the point of the largest amplitude and latency was measured at the center of the peak. If wave Pa had multiple peaks, the largest amplitude was taken and the latency was measured at the mid point between waves Na and Nb. Wave Nb was defined as the largest vertex-negative peak following Pa and occurring between 40 and 75 ms. Latency values were corrected for the 0.92 ms delay introduced by the insert earphones.

J. Statistical analyses

Peak-to-peak amplitudes and latencies were analyzed using descriptive statistics and repeated measures analyses of variance (ANOVAs) using a linear mixed model design (Littell *et al.*, 1996). Satterthwaite's corrections for degrees of freedom for repeated measures were employed when appropriate (Satterthwaite, 1946). Results were considered statistically significant if $p<0.01$.

For the amplitude analyses, there were no missing data cells because an amplitude value equal to the RNL present in the grand average tracing was assigned. For the latency analyses, there were some missing data cells depending upon the notched noise condition. However, the analyses of variance were only conducted on the notched noise center frequency conditions where at least 80% of the subjects had responses.

In the SAS procedure for mixed model designs, individuals are not dropped if they have missing data (Brown and Prescott, 1999). Provided there is not a strong relationship between treatments and missing data, the theory on which the mixed model is based still holds for unbalanced or missing data. It is quite robust even when data are not missing entirely at random. In these mixed models, the specification of covariance means that each point influences the estimates of treatment effects at every other point. Thus, patients whose observations are limited will still contribute to the estimates at all points.

When significant results were found in the ANOVAs, Tukey *post hoc* tests were performed in order to investigate the pattern of these significant differences. Tukey *post hoc* testing is a method of adjusting for multiple *post hoc* comparisons, similar to the Bonferoni adjustment (SAS Online Document, Version 8, 1999; Snedecor and Cochran, 1978). Results of the *post hoc* analyses were considered significant if $p<0.05$.

III. RESULTS

A. Nonmasked responses

The waveforms located at the top of Figs. 2 and 3 are the nonmasked ABR and MLR recorded to 80 and 90 dB ppe SPL 500-Hz (Fig. 2) and 90 dB ppe SPL 2000-Hz (Fig. 3) tonebursts from the same subject. Responses recorded using the conventional (Cz-earlobe) and vertical (Cz-Cv2) electrode montages are displayed.

Table I contains the mean peak-to-peak amplitude values and absolute latencies for the nonmasked results at both stimulus frequencies. A two way repeated measures ANOVA (wave $\times$ electrode) for the amplitude results was calculated separately for each stimulus frequency and each intensity. The 500-Hz results revealed no significant differences in the peak-to-peak amplitudes of waves V-Na, Na-Pa and Pa-Nb at 80 and at 90 dB ppe SPL. The 2000-Hz results revealed a significant difference in the amplitudes of waves V-Na, Na-Pa and Pa-Nb [$p<0.001$]. Tukey *post hoc* analyses showed that peak-to-peak amplitude of MLR wave Pa-Nb was significantly smaller than ABR wave V-Na and MLR wave Na-Pa.

The mean peak-to-peak amplitudes of the responses for the 500- and 2000-Hz tonebursts recorded using the noncephalic electrode montage (Cz-Cv2) were slightly larger than those recorded using the conventional (Cz-earlobe) electrode montage, however, these differences did not reach statistical significance at either frequency or intensity [$p=0.012-0.024$]. The wave by electrode interaction did not reach statistical significance for any of the three stimulus conditions.

A two way repeated measures ANOVA (wave $\times$ electrode) of the nonmasked latency values revealed no statistically significant differences between the latencies recorded using the conventional and vertical electrode montages. The wave by electrode interaction was not significant at either stimulus frequency or intensity.

B. Waveforms recorded in notched noise masking

Below the nonmasked waveforms displayed in Fig. 2 are the same subject's waveforms recorded to the 80 and 90 dB ppe SPL 500-Hz tonebursts for the 11 notched noise conditions. In response to the 80 dB ppe SPL tonebursts, the largest ABRs and MLRs were present in the 354-, 500- and 707-Hz center frequency bands for this individual. For the responses to the 90 dB ppe SPL tonebursts, the largest peak-to-peak ABR and MLR amplitudes occurred in the 354- to 1000-Hz center frequency bands. Figure 3 displays the same subject's waveforms recorded to the 90 dB ppe SPL 2000-Hz tonebursts for the nine notched noise conditions. The largest peak-to-peak ABR and MLR amplitudes occurred in the 1410- to 2830-Hz center frequency bands. When the center frequency of the notch was located one to two octaves away from each of the nominal stimulus frequencies, the ABRs and MLRs were substantially reduced in amplitude or absent. This subject's waveforms are representative of the responses recorded from the remaining subjects.

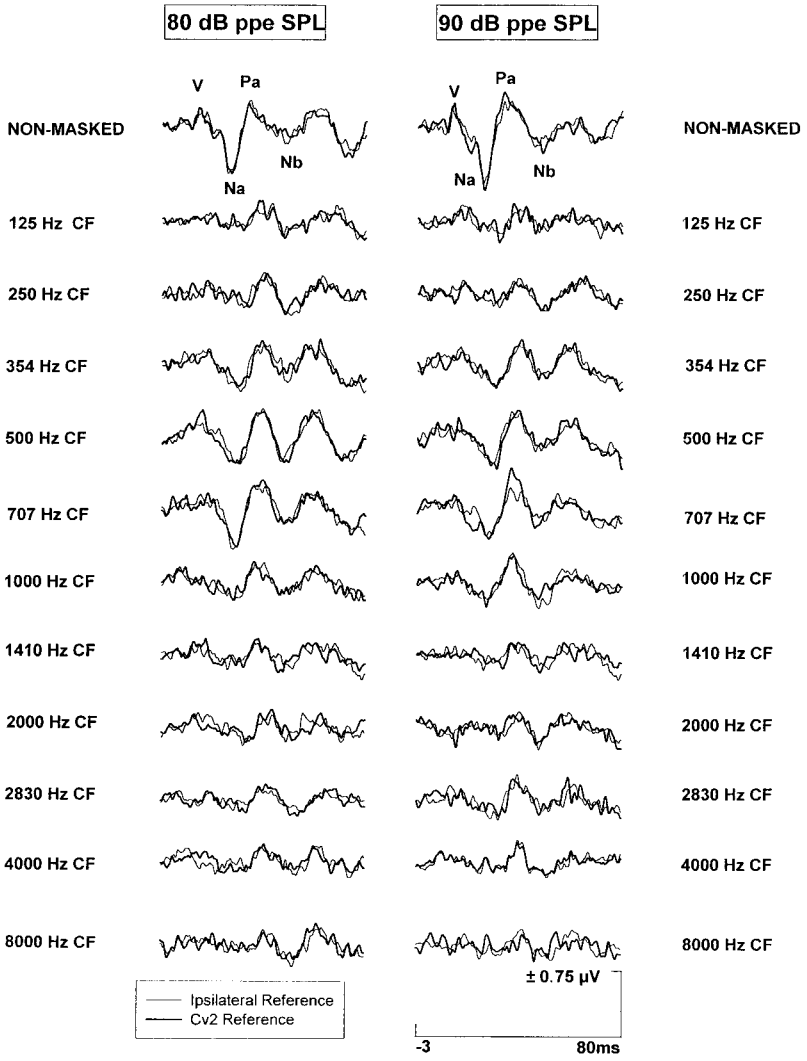

FIG. 2. Waveforms recorded from one subject to 80 and 90 dB ppe SPL 500-Hz tonebursts in the nonmasked condition and the 11 notched noise conditions. ABR wave V and MLR waves Na, Pa and Nb are labeled.

C. Notched noise response amplitude profiles

Peak-to-peak amplitudes of ABR wave V-Na and MLR waves Na-Pa and Pa-Nb were measured for each subject for all notched noise conditions. The amplitudes were then normalized to a percentage of the subject's amplitudes recorded in the nonmasked condition. Mean relative amplitudes for waves V-Na, Na-Pa and Pa-Nb to the 500- and 2000-Hz tonebursts are plotted in Figs. 4 and 5, respectively, as a function of the center frequency of the notched noise for each stimulus intensity and each electrode montage.

For the 80 dB ppe SPL 500-Hz tonebursts, the maxima in the mean ABR and MLR amplitude profiles occurred at 354, 500 and 707 Hz for both electrode montages. These frequency regions contribute almost equally to the response, especially for waves V-Na and Na-Pa. The peak in the mean amplitude profile for the 90 dB ppe SPL 500-Hz tonebursts occurred at 707 Hz for ABR wave V-Na for both electrode montages. For MLR waves Na-Pa and Pa-Nb, the peak in the mean amplitude profiles occurred at 500 Hz.

The mean ABR and MLR amplitude profiles for the 2000-Hz responses peaked at 1410 and 2000 Hz for both electrode montages. The 1000- and 2830-Hz frequency regions also contributed substantially to these higher frequency responses. The individual ABR and MLR response amplitude profiles for both stimulus frequencies showed maximum amplitudes within a half-octave of the nominal stimulus frequency for at least 80% of the subjects, irrespective of electrode montage or stimulus level.

Three way repeated measures ANOVAs (wave × electrode × notched noise center frequency) were calculated for each of the 500- and 2000-Hz response amplitude profiles. The results, displayed in Table II, showed an expected significant main effect for center frequency of the notched noise for the responses to the 500- and 2000-Hz tonebursts. In order to further investigate the pattern of these significant differences, Tukey *post hoc* analyses of the amplitude profiles were conducted for each stimulus frequency and intensity separately. For each stimulus condition (e.g., 500 Hz at 80 dB ppe SPL), independent *post hoc* tests of the amplitude profiles were conducted for each of the three waves (i.e., V-Na, Na-Pa and Pa-Nb). The *post hoc* tests for each wave compared the response amplitudes at one notch condition with the response amplitudes at each of the adjacent notch conditions. The notched noise center frequencies evaluated for the 500-Hz profiles were 125–8000 Hz, while the center frequencies evaluated for the 2000-Hz profiles were 500–8000 Hz.

The *post hoc* analyses for the 500-Hz profiles showed

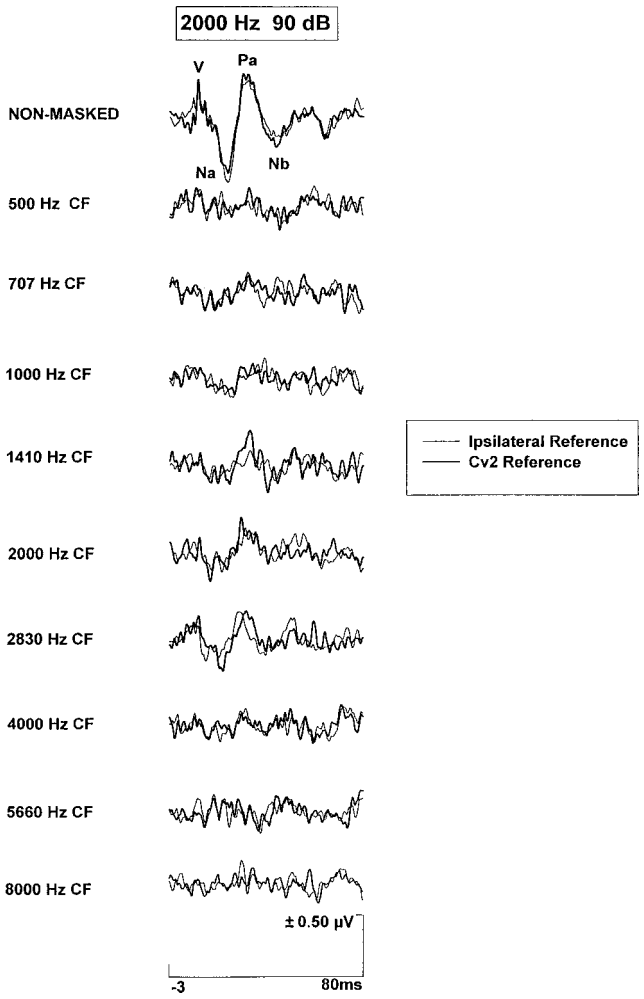

FIG. 3. Waveforms recorded from the same subject to 90 dB ppe SPL 2000-Hz tonebursts in the nonmasked condition and the nine notched noise conditions. ABR wave V and MLR waves Na, Pa and Nb are labeled.

that the amplitudes of waves V-Na, Na-Pa and Pa-Nb recorded when the center frequency of the notch was located between 354 and 707 Hz for the 80 dB SPL stimuli and between 354 and 1000 Hz for the 90 dB SPL stimuli were significantly higher [$p<0.01$] than when the center frequency of the notch occurred at lower (125–250 Hz) and higher (1410–8000 Hz) frequencies. Similarly, *post hoc* analyses of the 2000-Hz profiles revealed that the amplitudes of the ABR and MLR waves recorded when the notch was centered around 1000–2830 Hz were significantly higher [$p<0.01$] than when the center frequency was located at lower (500–707 Hz) and higher (4000–8000 Hz) frequencies.

The ANOVA results showed a significant main effect for wave for the responses to the 80 and 90 dB ppe SPL 500-Hz tonebursts. The main effect for wave, evident in Fig. 4, shows that the amplitude of MLR wave Pa-Nb is larger than the amplitudes of waves V-Na and Na-Pa.

The ANOVA results generally revealed no significant differences between the two electrode montages at either stimulus frequency nor any significant interactions. The only exceptions were that the wave by electrode and the electrode by notched noise CF interactions did reach statistical significance for the higher intensity 500-Hz responses.

D. Notched noise latency profiles

Mean absolute latency values are plotted in Fig. 6 as a function of the center frequency of the notched noise for each stimulus intensity and electrode montage. The latency profiles only include points where a minimum of 80% of the subjects had responses.

For the responses recorded to the 80 dB ppe SPL 500-Hz tonebursts, the minimum point in the latency profiles for the ABR and MLR occurred at 707 Hz for both recording montages. When the notch was centered at 707 Hz, the mean latencies (across electrode montage) of 11.48 and 33.53 ms for waves V and Pa, respectively, were in close agreement with the nonmasked wave V and Pa latencies displayed in Table I, implying that the primary contributions to the nonmasked latencies for the 80 dB ppe SPL responses come from the 707-Hz frequency region.

For the 90 dB ppe SPL 500-Hz tonebursts, the minima in the latency profiles occurred at 707 Hz for ABR wave V and at 1000 Hz for MLR wave Pa. When the notch in the broadband noise was located at 707 Hz, the mean latency of

TABLE I. Mean peak-to-peak amplitudes (μV) and absolute latencies (ms) for ABR/MLR to 80 and 90 dB ppe SPL 500-Hz and 90 dB ppe SPL 2000-Hz nonmasked linear-gated tonebursts.

		500 Hz				2000 Hz	
		80 dB ppe SPL		90 dB ppe SPL		90 dB ppe SPL	
		Cz-A1	Cz-Cv2	Cz-A1	Cz-Cv2	Cz-A1	Cz-Cv2
Amplitude:	ABR V-Na	0.47	0.57	0.59	0.68	0.68	0.74
	SD	0.18	0.19	0.22	0.24	0.12	0.12
	MLR Na-Pa	0.54	0.63	0.60	0.74	0.57	0.65
	SD	0.14	0.11	0.23	0.24	0.13	0.10
	MLR Pa-Nb	0.49	0.49	0.51	0.61	0.42	0.51
	SD	0.15	0.15	0.19	0.17	0.10	0.17
Latency:[a]	ABR wave V	11.42	11.17	10.44	10.61	7.45	7.50
	SD	0.80	0.97	0.75	0.77	0.32	0.27
	MLR wave Pa	33.20	32.21	31.71	31.03	28.03	28.43
	SD	1.63	1.50	2.03	1.37	1.78	1.54

[a]Absolute latency values have been corrected for ER-3A insert earphone delay.

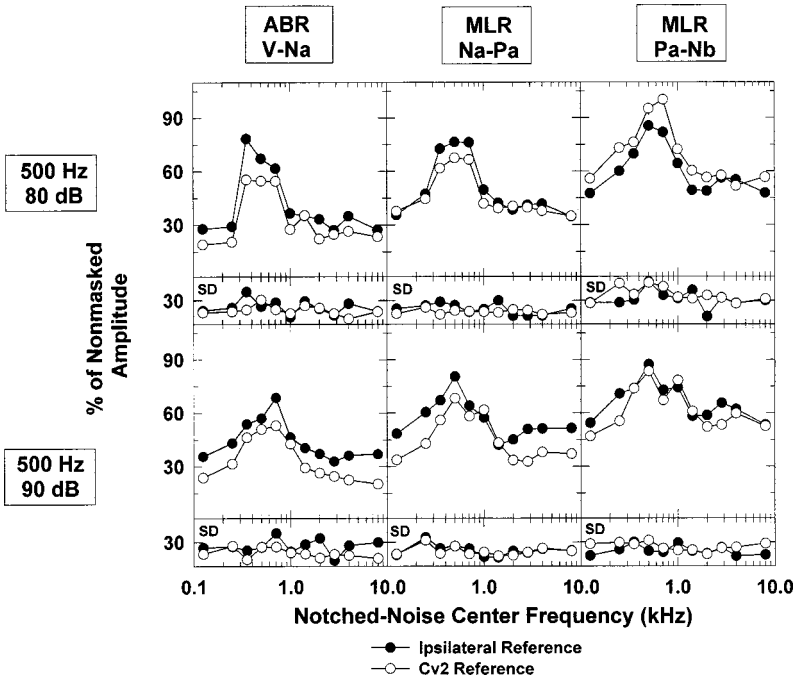

FIG. 4. Mean and standard deviation (s.d.) amplitude profiles for ABR wave V-Na and MLR waves Na-Pa and Pa-Nb to 80 and 90 dB ppe SPL 500-Hz tonebursts as a function of the nominal center frequency of the notched noise. Responses recorded with conventional and vertical electrode montages are in closed and open circles, respectively.

wave V was 10.98 ms, in close agreement with the nonmasked latency. Similarly when the notch occurred at 1000 Hz, the mean latency of wave Pa was 31.95 ms which agrees well with the nonmasked latency. These findings suggest that the nonmasked latencies of waves V and Pa to 90 dB SPL 500-Hz tonebursts are primarily determined by contributions from the 707 to 1000 Hz regions.

The minimum point in the latency profiles for the 2000-Hz responses occurred at 2830 Hz for the ABR and 1410–2000 Hz for the MLR. When the notch was centered at 2830 Hz, the mean wave V latency of 7.96 ms was in close agreement with the nonmasked wave V latencies. Similarly, when the notch was centered at either 1410 or 2000 Hz, the mean latencies of 28.69 and 28.49, ms respectively, were in good agreement with the nonmasked latencies for wave Pa.

Separate three way repeated measures ANOVAs were calculated for each of the 500- and 2000-Hz latency profiles.

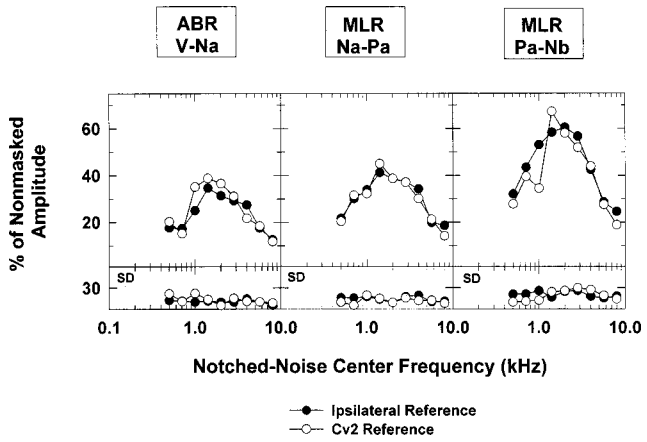

FIG. 5. Mean and standard deviation (s.d.) amplitude profiles for ABR wave V-Na and MLR waves Na-Pa and Pa-Nb to 90 dB ppe SPL 2000-Hz tonebursts as a function of the nominal center frequency of the notched noise. Responses recorded with conventional and vertical electrode montages are in closed and open circles, respectively.

Only notched noise center frequencies that produced responses from at least 80% of the subjects were included. The center frequencies analyzed were: (1) 354–1000 Hz for the 80 dB ppe SPL 500-Hz responses, (2) 125–4000 Hz for the 90 dB ppe SPL 500-Hz responses, and (3) 1000–4000 Hz for the 90 dB ppe SPL 2000-Hz responses.

A significant main effect for the CF of the notched noise occurred only for the 500-Hz responses and was present at each stimulus intensity. Tukey *post hoc* analyses of the latency profiles at 80 dB ppe SPL indicated that the latencies of waves V and Pa remained essentially unchanged as the center frequency of the notch was varied between 500 and 1000 Hz and increased significantly only when the notched noise was centered at 354 Hz ($p<0.001$). In contrast, *post hoc* comparisons for the 90 dB ppe SPL latency profiles showed that the latencies of waves V and Pa recorded when the center frequency of the notched noise was located at 500, 707 or 1000 Hz were significantly shorter ($p<0.05$) than those recorded when the center frequency of the notch occurred at lower (125–354 Hz) and higher (1410–4000 Hz) frequencies.

There were no statistically significant differences between the latencies of the responses recorded using the two electrode montages at either stimulus frequency. No interactions reached statistical significance for either the 500- or 2000-Hz responses.

E. Influence of electrode montage on RNL present in the averages

Table III presents descriptive statistics for the number of sweeps needed to reach a residual noise level criterion of 60 nV as a function of electrode montage. In general, a greater number of sweeps was required to reach this criterion for the responses recorded using the vertical electrode montage in comparison to the conventional montage (i.e., 11%–22% greater for the 500-Hz responses and 6%–20% greater for

TABLE II. Results of three-way repeated measures analyses of variance for 500- and 2000-Hz amplitude and latency profiles.

	Amplitude[a]			Latency		
	500 Hz 80 dB SPL	500 Hz 90 dB SPL	2000 Hz 90 dB SPL	500 Hz 80 dB SPL	500 Hz 90 dB SPL	2000 Hz 90 dB SPL
Wave	$p<0.001$	$p<0.001$	NS	$p<0.001$	$p<0.001$	$p<0.01$
Electrode	NS	NS	NS	NS	NS	NS
Notched noise						
Center frequency (Hz)	$p<0.001$	$p<0.001$	$p<0.001$	$p<0.001$	$p<0.001$	NS
Wave × Electrode	NS	$p<0.01$	NS	NS	NS	NS
Wave × Noise	NS	NS	NS	NS	NS	NS
Noise × Electrode	NS	$p<0.01$	NS	NS	NS	NS
Wave × Electrode × Noise	NS	NS	NS	NS	NS	NS

[a]ANOVAs for amplitude profiles were based on percent of the nonmasked amplitudes.

the 2000-Hz responses). There was also greater variability in the responses recorded using the vertical electrode montage as reflected in the higher standard deviation values for this recording channel.

IV. DISCUSSION

A. Frequency specificity of the ABR and MLR to 500- and 2000-Hz tonebursts

The results of this study suggest that ABR (wave V-Na) and MLR (waves Na-Pa and Pa-Nb) show good frequency specificity to 500-Hz tonebursts presented at 80 dB ppe SPL, as demonstrated by the maxima in the mean response amplitude profiles occurring at the nominal stimulus frequency or within a half-octave of this frequency. The ABR and MLR amplitudes drop off sharply on the low and high frequency sides of the profile peak, indicating that there is little cochlear contribution to these evoked potentials from frequency regions one or more octaves away from the probe frequency. The latency profiles for the 80 dB ppe SPL responses are centered at the nominal stimulus frequency or within a relatively narrow range (i.e., one octave) of this frequency, also indicating that the responses are frequency specific. At 90 dB ppe SPL, the amplitude and latency profiles are wider in comparison to the 80 dB ppe SPL profiles, reflecting an increased spread of cochlear excitation at the higher stimulus intensity.

It was not possible to safely achieve effective masking (behavioral and electrophysiologic masking) of the ABR and MLR for all subjects in the present study, especially for the responses to the 90 dB ppe SPL 500-Hz tonebursts. Therefore, contributions to the responses which occurred when the notch was centered at distant apical and basal locations (e.g., 250 or 4000 Hz) are likely due to subtotal masking of the energy present in the toneburst. This possibility was investigated by comparing the amplitude and latency of each subject's response to the 90 dB ppe SPL 500-Hz toneburst in the broadband noise (no notch) condition to their responses obtained in the various notched conditions. For at least 70% of the subjects, the amplitudes of ABR wave V-Na and MLR waves Na-Pa and Pa-Nb in the no notch condition were similar to those obtained when the notch was centered at least 2 octaves away from the toneburst frequency (i.e., the differences between these two conditions ranged from 0.01 to 0.04 μV for the ABR and 0.02 to 0.07 μV for the MLR). Similarly, for 75%–80% of the subjects, the latencies of ABR wave V and MLR wave Pa recorded in the no notch condition were in close agreement (0.03–0.39 ms for wave V and 0.15–0.63 ms for wave Pa) to those obtained when the notch was centered at least 2 octaves away from the toneburst frequency. This suggests that the small responses occurring when the notch was centered at distant locations are likely due to direct ipsilateral masking occurring at the nominal

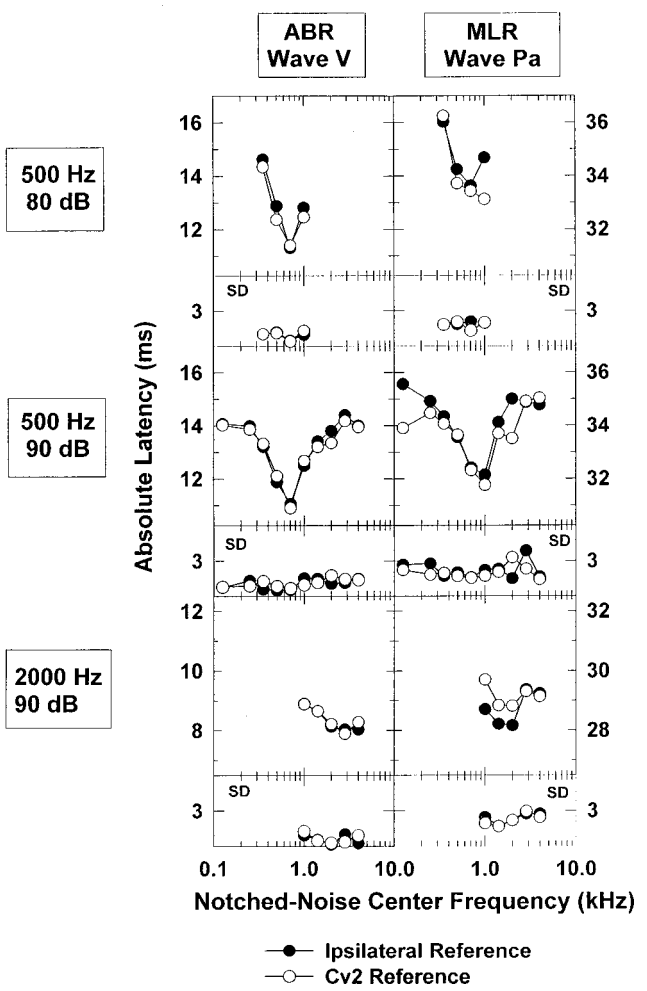

FIG. 6. Mean and standard deviation (s.d.) latency profiles for ABR wave V and MLR wave Pa to 80 and 90 dB ppe SPL 500-Hz (top and middle sections) and 90 dB ppe SPL 2000-Hz (lower section) tonebursts as a function of the nominal center frequency of the notched noise. Each symbol represents a minimum of eight subjects at each stimulus intensity.

TABLE III. Descriptive statistics for the number of sweeps needed to reach a residual noise level criterion of 60 nV as a function of electrode montage in the nonmasked and masked conditions for the 500-Hz and 2000-Hz tonebursts.

	500 Hz				2000 Hz	
	80 dB ppe SPL		90 dB ppe SPL		90 dB ppe SPL	
	Cz-A1	Cz-Cv2	Cz-A1	Cz-Cv2	Cz-A1	Cz-A2
Nonmasked Responses						
Mean	4608	4472	4230	5370	4531	5645
S.D.	1109	1830	1492	2229	1889	2288
Median	4864	4608	4096	5504	3840	6400
Range	2304–5888	2304–8000	2816–8000	2304–8000	2304–7680	2048–8000
Masked Responses Collapsed Across Notched Noise Conditions						
Mean	4748	5345	4727	5328	5054	5267
S.D.	1730	2084	1973	2164	1417	1216
Median	4352	5376	3136	5248	4740	5010
Range	2304–8000	1280–8000	1536–8000	1280–8000	2304–8000	1536–8000

stimulus frequency rather than responses reflecting the cochlear location of the notch.

The findings in the present study are in agreement with studies which have used various masking paradigms to investigate the frequency specificity of the ABR and MLR to nonmasked low and high frequency toneburst stimuli in normal hearing adults (Abdala and Folsom, 1995b; Burkard and Hecox, 1983; Folsom, 1984, 1985; Folsom and Wynne, 1987; Klein, 1983; Mackersie *et al.*, 1993; Oates and Stapells, 1997b; Picton *et al.*, 1979; Stapells and Picton, 1981; Wu and Stapells, 1994). These studies have shown that ABRs and MLRs to moderate intensity (i.e., 60–80 dB ppe SPL) nonmasked 500–4000 Hz tones are best tuned to the nominal stimulus frequency or a narrow range surrounding the probe frequency, and thus exhibit good frequency specificity. As stimulus intensity is increased (>80 dB ppe SPL) there is a reduction in the frequency specificity of the ABR, due to greater contributions to the evoked potentials from frequencies outside the nominal stimulus frequency as well as the increased effects of stimulus spectral splatter.

B. Determining cochlear site of response generation

The cochlear site of response generation (i.e., place specificity of the response) may be estimated from the amplitude and latency profiles. There has been some controversy, however, regarding how to determine the ''effective cochlear region'' within a derived band or a notched noise frequency band which determines the nonmasked amplitude and latency of the response (see Oates and Stapells, 1997b, for a further discusssion). The effective cochlear region is dependent upon a number of factors including the masking technique, steepness of filter slope, width of the derived or notched band, and frequency and intensity of the toneburst and noise stimuli (Stapells and So, 1999). These factors likely account for some of the disagreements present in the literature.

The results of the amplitude analyses in the current study suggest that the regions primarily contributing to the 500-Hz responses are the 354–707 Hz bands for the 80 dB ppe SPL responses and the 354–1000 Hz bands for the 90 dB ppe SPL responses. Similarly, the amplitude analyses suggest that the dominant cochlear place contributing to the 2000-Hz responses is a narrow frequency region surrounding the nominal stimulus frequency (i.e., 1000–2830 Hz bands).

Another approach that can be used to describe the cochlear regions contributing to the nonmasked response amplitude is to calculate the frequency range of the entire band (e.g., 0.75 octaves below 354 Hz and 0.75 octaves above 707 Hz for the 80 dB ppe SPL 500-Hz responses). Applying these calculations to the present data would suggest that the cochlear frequency regions contributing to nonmasked waves V and Pa amplitudes could be as wide as 210–1189 Hz and 210–1682 Hz for the 80 and 90 dB ppe SPL 500-Hz tonebursts, respectively, and 595–4759 Hz for the 90 dB ppe SPL 2000-Hz responses.

The results of our latency analyses suggest that the primary cochlear contributions to the nonmasked latencies for waves V and Pa come from the nominal stimulus frequency or within a narrow range ($\leqslant$ one octave) of the stimulus frequency for the 500- and 2000-Hz responses. However, if we assume that the responses of higher frequency regions of the cochlea within the notched band determine response latency (Oates and Stapells, 1997b), then the primary areas of the basilar membrane contributing to the nonmasked ABR and MLR latencies may also be estimated by considering the upper frequency edge of the 1.5-octave-wide notch. Using this approach, the frequency regions contributing to the nonmasked latencies of wave V and wave Pa for the 80 and 90 dB ppe SPL 500-Hz responses would be 1189 Hz ($707 \times 2^{0.75}$) and 1682 Hz ($1000 \times 2^{0.75}$), respectively, and would be 4759 Hz ($2830 \times 2^{0.75}$) for wave V and 2371–3364 Hz ($1410 \times 2^{0.75} - 2000 \times 2^{0.75}$) for wave Pa to the 90 dB ppe SPL 2000-Hz responses.

The uncertainty regarding cochlear place of response generation cannot be fully resolved, however, previous studies using a variety of masking techniques (HP/DR, pure-tone and notched noise masking) indicate that the cochlear region contributing to the nonmasked amplitudes and latencies of ABR wave V and MLR wave Pa to 60–80 dB ppe SPL tonebursts is within one octave of the nominal stimulus frequency (Abdala and Folsom, 1995b; Folsom and Wynne,

1987; Klein, 1983; Mackersie *et al.*, 1993; Oates and Stapells, 1997a,b; Wu and Stapells, 1994).

C. Frequency specificity of the ABR *versus* the MLR

The response amplitude and latency profiles in the current study demonstrate that there are no significant differences in the frequency specificity of ABR wave V-Na *versus* MLR waves Na-Pa and Pa-Nb to the 500- or 2000-Hz tonebursts at either stimulus intensity. This result is consistent with earlier studies employing pure-tone masking paradigms (Mackersie *et al.* 1993; Wu and Stapells, 1994) and the HP/DR technique (Oates and Stapells, 1997a,b) which showed that the ABR and MLR are equally frequency specific to 60 and 80 dB ppe SPL 500- and 2000-Hz tonebursts.

D. Effects of electrode montage

Electrode montage did not have a significant effect on the nonmasked peak-to-peak amplitudes of waves V-Na, Na-Pa or Pa-Nb at either stimulus frequency or intensity. This finding is not consistent with several studies which have reported larger amplitudes for waves V and Pa when the inverting electrode was at the nape of the neck compared to the ipsilateral earlobe/mastoid (Beattie *et al.*, 1986; Hughes *et al.*, 1981; Kadoya *et al.*, 1988; Katbamna *et al.*, 1996; King and Sininger, 1992; Kraus and McGee, 1988; McPherson *et al.*, 1985; Polyakov and Pratt, 1994). However, the lack of significant differences for the nonmasked ABR wave V and MLR wave Pa latencies between the conventional and noncephalic electrode montages is in agreement with previous studies (Beattie *et al.*, 1986; Hughes *et al.*, 1981; Kadoya *et al.*, 1988; McPherson *et al.*, 1985).

One possible explanation for the significant amplitude differences reported in previous studies for responses recorded with a vertical electrode montage *versus* a conventional montage might be differences in the levels of residual noise contributing to the waveform averages. In the present study, when residual noise levels (RNLs) contributing to the waveform averages were rigorously controlled by the Fsp technique, no significant differences in amplitudes existed between the evoked potentials recorded using the vertical and conventional electrode montages. The responses recorded using the vertical montage generally required a greater number of sweeps than the conventional montage to reach the 60 nV RNL criterion at both stimulus frequencies (see Table III). Therefore, if investigators do not control for the RNLs contributing to the waveform averages, it is likely that the RNLs would be higher for responses recorded using a vertical (Cz-nape of the neck) electrode montage in comparison to a conventional (Cz-earlobe/mastoid) montage. This potential difference in S/N ratios across recording channels could lead to differences in amplitude values across montages.

Although not significant, there was a trend for the responses recorded using the vertical montage to be larger than the conventional montage even when RNLs were controlled for. This finding suggests that differences in residual noise levels do not completely account for the amplitude differences reported in the earlier studies. Although wave V is dominated by activity at the vertex electrode, a reduced amplitude wave V can also be recorded using an electrode site near the ear (e.g., Barratt, 1980; Hall, 1992). Therefore, the conventional (Cz-earlobe/mastoid) electrode montage should result in some reduction of wave V amplitude which does not occur with the vertical (Cz-nape of the neck) electrode montage because the nape of the neck is essentially neutral for the ABR response (Hall, 1992).

The choice of cervical vertebra 2 as the site for the inverting electrode is in contrast with most previous studies which have used cervical vertebra 7 (Beattie *et al.*, 1986; Hughes *et al.*, 1981; Kadoya *et al.*, 1988; King and Sininger, 1992; Kraus and McGee, 1988; McPherson *et al.*, 1985; Polyakov and Pratt, 1994). Thus, the results of the present study may not be directly comparable to these earlier studies. However, Wolpaw and Woods (1982) demonstrated that the spatial and temporal voltage gradients are minimal over a relatively broad region (approximately 15 cm) of the inferior neck, implying that similar responses would be obtained from electrodes located at either Cv2 or Cv7.

E. Response changes seen with the introduction of notched noise masking and possible physiological correlates

The evoked potentials recorded in the presence of notched noise masking were smaller in amplitude and longer in latency than the nonmasked responses at both stimulus frequencies and intensities. The response changes likely occurred because of: (1) the removal of contributions to the response from frequencies outside of the rejection band of the notched noise (Stapells and Picton, 1981), and (2) the spread of masking into the notch from the low frequency edge of the notched band (Beattie *et al.*, 1992, 1994; Picton *et al.*, 1979). This second masking effect is more prominent at high noise intensities ($>$70 dB SPL) and results in a reduced area of the notch which is capable of responding to the toneburst.

The response changes which occurred with the introduction of noise masking likely reflect masking effects which occur in the peripheral and central auditory systems. There are at least two physiological mechanisms of masking which occur in the peripheral auditory system during a simultaneous masking paradigm such as that employed in the present study. According to traditional theory, simultaneous masking of a tonal signal by a masker with a different center frequency is thought to be due to the spread of neural excitation produced by the masker to the place along the basilar membrane corresponding to the signal frequency (Fletcher, 1940; Wegel and Lane, 1924; Zwicker, 1970). A second explanation is that simultaneous masking may be due to suppression of the neural responses to the signal by the masker, even if the masker does not excite the neurons tuned to the frequency of the tone (e.g., Arthur *et al.*, 1971; Dallos and Cheatham, 1977; Delgutte, 1990; Javel *et al.*, 1983; Pickles, 1984; Weber, 1983).

Excitatory and/or neural adaptation mechanisms of masking also occur in the auditory cortex during simultaneous noise masking paradigms (Phillips, 1985, 1990; Phillips and Cynader, 1985; Phillips *et al.*, 1985). In contrast to

auditory nerve fibers, some cortical neurons have reduced firing rates to high intensity noise stimuli or are completely unresponsive to broadband noise presented at any sound pressure level. Phillips and co-workers hypothesized that the response areas for these nonmonotonic cortical neurons are flanked by inhibitory areas which suppress spontaneous discharges.

Given the high intensities of broadband noise ($\geqslant$83 dB SPL) and the range of center frequencies of the notched noise (125–8000 Hz) employed in the present study, it is likely that both excitatory and suppressive mechanisms of masking in the auditory periphery and central auditory systems contributed to the changes in the evoked potentials which occurred with the noise masking.

F. Differential effects of noise masking on ABRs and MLRs to 500- *versus* 2000-Hz tonebursts

An intriguing finding in the present study was that noise masking had a greater impact on the amplitudes of the ABR and MLR recorded to 90 dB ppe SPL 2000-Hz tones compared to those recorded to the same intensity 500-Hz tones. Specifically, there was a 35%–61% reduction in the normalized amplitudes for the 2000-Hz responses compared to a 13%–44% reduction for the 500-Hz responses. This is consistent with Burkard and Hecox's 1983 study which reported that the effects of broadband noise masking within a derived band on wave V latencies and amplitudes to click stimuli were greater for responses from higher *versus* lower frequency derived bands.

The most likely physiologic explanation for the greater reduction in the normalized amplitudes of the higher frequency responses is the variation in the width of the critical band across frequency. Early psychoacoustic studies (Greenwood, 1961; Hawkins and Stevens, 1950; Scharf, 1970) have demonstrated that estimates of the critical bandwidth (in linear Hz) are approximately three times wider when a 2000-Hz pure tone is located at the center of the passband of noise compared to when a 500-Hz tone is at the center of the passband. This difference in critical band width would imply that greater or more intense masking would occur within the passband for the 2000-Hz responses in comparison to the same intensity 500-Hz responses.

Another possible explanation for these differential frequency effects may be that masking noise produces a desynchronization of the ABR which could be dependent, in part, upon the rise time of the stimuli. Responses coming from the low frequency regions of the basilar membrane are less synchronized compared to responses from the higher frequencies due to the longer rise time of the cochlear filter in the apical *versus* basal regions of the cochlea (Don *et al.*, 1998). Therefore, it is possible that the responses to the 500-Hz tonebursts may be less affected by the desynchronization effects of the masking noise. The differential effect of masking across stimulus frequency may have been more prominent in the present study because the tonebursts used had a constant number of cycles (2-1-2 cycles), resulting in a 1 ms rise time for the 2000-Hz stimuli and a 4 ms risetime for the 500-Hz stimuli. The results of the current study suggest that within-band masking effects may be more pronounced for stimuli with rapid rise times.

Two additional physiologic mechanisms which may have contributed to the differential amplitudes of the masked 500- *versus* 2000-Hz responses are: (1) differences in the density of afferent neurons in the apical *versus* basal regions of the cochlea, and (2) the asymmetrical excitation patterns along the basilar membrane (i.e., upward spread of masking) produced by noise maskers presented at intensities $>$70 dB SPL. Nadol (1988) demonstrated that humans with normal hearing sensitivity have their greatest density of spiral ganglion cells in the mid frequency regions (approximately 1000–6000 Hz) of the cochlea. If the degree of masking that occurs within the central auditory nervous system is proportional to the number of peripheral neurons being activated by the masker, then one might expect broader masker excitation and suppression patterns in this mid frequency region and thus greater masking effectiveness.

In summary, the differential response changes which occurred with masking for low *versus* high frequency tonebursts may be due to one or more of the following factors: (1) differences in critical bandwidths (in linear Hz) across frequencies, (2) differences in the effects of masking noise on the synchronous discharge of auditory nerve fibers in the apical *versus* basal regions for brief duration stimuli, (3) differences in density of afferent neurons in the apical *versus* basal regions of cochlea, and (4) the effects of upward spread of masking.

G. Implications

The results of this study demonstrate that ABR wave V-Na and MLR waves Na-Pa and Pa-Nb to 80 dB ppe SPL 500-Hz tones are frequency and place specific. When stimulus intensity is increased to 90 dB ppe SPL, there is a decrease in the frequency and place specificity of the responses, with greater cochlear contributions from the higher frequencies. Therefore, masking techniques such as notched noise masking (Stapells *et al.*, 1994, 1985) are required to ensure the frequency specificity of responses to 500- and 2000-Hz tonebursts presented at 90 dB ppe SPL or higher.

There are no significant differences in the frequency specificity of: (1) ABR wave V-Na *versus* MLR waves Na-Pa and Pa-Nb at either stimulus frequency or intensity, and (2) these evoked potentials recorded using the conventional (Cz-earlobe) electrode montage in comparison to the vertical (Cz-Cv2) montage.

MLRs to low and high frequency toneburst stimuli may be used as an adjunct to the ABR in estimating pure-tone behavioral thresholds in difficult-to-test adult populations. The MLR may also hold promise as a clinical tool for assessing hearing sensitivity in young children as long as appropriate technical factors are addressed and sleep state is carefully monitored.

ACKNOWLEDGMENTS

This research was funded by a research grant from The Deafness Research Foundation of New Zealand to the first author. We would like to express our special thanks to Drs.

Peter Thorne and Don Robertson for their valuable feedback on earlier drafts of this manuscript. The authors would also like to express their appreciation to Dr. David R. Stapells for his technical advice and Elizabeth Robinson for her statistical advice regarding this project. Lastly, we would like to express our appreciation to Dr. Bob Burkard and our other reviewer for their helpful suggestions on earlier drafts of this manuscript.

APPENDIX

Don and Elberling's (1996) formula for calculating the peak-to-peak amplitudes corrected for residual noise is $EP_{(p\text{-}p)} = \sqrt{[\mathrm{ABR}^2_{(p\text{-}p)} - (\mathrm{ratio} \times BN_{(\mathrm{rms})})^2]}$, where $EP_{(p\text{-}p)}$ is the estimate of the corrected or true evoked potential peak-to-peak amplitude, $\mathrm{ABR}_{(p\text{-}p)}$ is the measured amplitude of wave V from the peak to the succeeding trough in the averaged ABR, the ratio term is 3.07, and the $BN_{(\mathrm{rms})}$ is the estimate of the residual noise obtained using the single point variance of the Fsp. In a previous study (Oates and Stapells, 1997a), the mean peak-to-peak amplitudes of ABR wave V-V′ and MLR wave Na-Pa to 80 dB ppe SPL 500-Hz linear gated tones presented in various high pass noise masked conditions were 250 nV and 465 nV, respectively. If the measured peak-to-peak ABR and MLR amplitudes in the present study were similar, then the corrected peak-to-peak ABR and MLR amplitudes would be 169 nV and 427 nV, respectively. If these corrected amplitude values are normalized to a percentage of the peak-to-peak amplitude values, approximately 70% of the peak-to-peak ABR amplitude and 92% of the MLR amplitude could be reliably attributed to the EP if the residual averaged background noise was 60 nV or less. A pilot study conducted on five normal hearing adults showed that between 3500 to 6750 single sweeps were required to reach a residual noise criteria of 60 nV when the ABR and MLR were simultaneously recorded to 90 dB ppe SPL 500- and 2000-Hz tones using the recording parameters described in the present study. Therefore we chose to record 8000 single epochs per condition.

Abdala, C., and Folsom, R. C. (**1995a**). ''Frequency contribution to the click-evoked auditory brain-stem response in human adults and infants,'' J. Acoust. Soc. Am. **97**, 2394–2404.

Abdala, C., and Folsom, R. C. (**1995b**). ''The development of frequency resolution in humans as revealed by the auditory brain-stem response recorded with notched noise masking,'' J. Acoust. Soc. Am. **98**, 921–930.

ANSI (**1996**). ANSI S3.6-1996, ''Specification for audiometers'' (American National Standards Institute, New York).

Arthur, R. M., Pfeiffer, R. R., and Suga, N. (**1971**). ''Properties of ''two-tone inhibition'' in primary auditory neurones,'' J. Physiol. (London) **212**, 593–609.

Barratt, H. (**1980**). ''Investigation of the mastoid electrode contribution to the brain stem auditory evoked response,'' Scand. Audiol. **9**, 203–211.

Beattie, R. C., and Boyd, R. L. (**1985**). ''Early/middle evoked potentials to tone bursts in quiet, white noise and notched noise,'' Audiology **24**, 406–419.

Beattie, R. C., and Kennedy, K. M. (**1992**). ''Auditory brainstem response to tone bursts in quiet, notch noise, highpass noise, and broadband noise,'' J. Am. Acad. Audiol **3**, 349–360.

Beattie, R. C., Johnson, A., and Garcia, E. (**1996**). ''Frequency-specific auditory brainstem responses in adults with normal hearing,'' Aust. J. Audiol. **18**, 1–11.

Beattie, R. C., Thielen, K. M., and Franzone, D. L. (**1994**). ''Effects of signal-to-noise ratio on the auditory brainstem response to tone bursts in notch noise and broadband noise,'' Scand. Audiol. **23**, 47–56.

Beattie, R. C., Beguwala, F. E., Mills, D. M., and Boyd, R. L. (**1986**). ''Latency and amplitude effects of electrode placement on the early auditory evoked response,'' Journal of Speech and Hearing Disorders **51**, 63–70.

Beiter, R. C., and Hogan, D. D. (**1973**). ''Effects of variations in stimulus rise-decay time upon the early components of the auditory evoked response,'' Electroencephalogr. Clin. Neurophysiol. **34**, 203–206.

Brown, H., and Prescott, R. (**1999**). *Applied Mixed Models in Medicine* (Wiley, West Sussex, England).

Burkard, R., and Hecox, K. (**1983**). ''The effect of broadband noise on the human auditory evoked response. II. Frequency specificity,'' J. Acoust. Soc. Am. **74**, 1214–1223.

Dallos, P., and Cheatham, M. A. (**1977**). ''Analog of two-tone suppression in whole nerve responses,'' J. Acoust. Soc. Am. **62**, 1048–1051.

Davis, H., Hirsh, S. K., and Turpin, L. L. (**1983**). ''Possible utility of middle latency responses in electric response audiometry,'' Adv. Oto-Rhino-Laryngol. **31**, 208–216.

Delgutte, B. (**1990**). ''Physiological mechanisms of psychophysical masking: Observations from auditory-nerve fibers,'' J. Acoust. Soc. Am. **87**, 791–809.

Don, M., and Eberling, C. (**1994**). ''Evaluating residual background noise in human auditory brainstem responses,'' J. Acoust. Soc. Am. **96**, 2746–2757.

Don, M., and Eberling, C. (**1996**). ''Use of quantitative measures of auditory brain-stem response peak amplitude and residual background noise in the decision to stop averaging,'' J. Acoust. Soc. Am. **99**, 491–499.

Don, M., Ponton, C. W., Eggermont, J. J., and Kwong, B. (**1998**). ''The effects of sensory hearing loss on cochlear filter times estimated from auditory brainstem response latencies,'' J. Acoust. Soc. Am. **104**, 2280–2289.

Engel, R. (**1971**). ''Early waves of the electroencephalic auditory responses in neonates,'' Neuropaediatrie **3**, 147–154.

Fletcher, H. (**1940**). ''Auditory patterns,'' Rev. Mod. Phys. **12**, 47–65.

Folsom, R. C. (**1984**). ''Frequency specificity of human auditory brainstem responses as revealed by pure-tone masking profiles,'' J. Acoust. Soc. Am. **75**, 919–924.

Folsom, R. C. (**1985**). ''Auditory brain stem responses from human infants: Pure-tone masking profiles for clicks and filtered clicks,'' J. Acoust. Soc. Am. **78**, 555–562.

Folsom, R., and Wynne, M. (**1986**). ''Auditory brain-stem responses from human adults and infants: Restriction of frequency contribution by notched-noise masking,'' J. Acoust. Soc. Am. **80**, 1057–1064.

Folsom, R. C., and Wynne, M. K. (**1987**). ''Auditory brain stem responses from human adults and infants: Wave V tuning curves,'' J. Acoust. Soc. Am. **81**, 412–417.

Frye-Osier, H. A., Goldstein, R., Hirsch, J. E., and Weber, K. (**1982**). ''Early and middle AER components to clicks as response indices for neonatal hearing screening,'' Ann. Otol. Rhinol. Laryngol. **91**, 147–150.

Gould, H. J., Crawford, M. R., Mendel, M. I., and Dodson, S. L. (**1992**). ''Quantification technique for the middle latency response,'' J. Am. Acad. Audiol. **3**, 153–158.

Greenwood, D. D. (**1961**). ''Auditory masking and the critical band,'' J. Acoust. Soc. Am. **33**, 484–502.

Hall, J. W. (**1992**). *Handbook of Auditory Evoked Response* (Allyn and Bacon, Needham Heights).

Hawkins, J. E. and Stevens, S. S. (**1950**). ''The masking of pure tones and of speech by white noise,'' J. Acoust. Soc. Am. **22**, 6–13.

Hirabayashi, M. (**1979**). ''The middle components of the auditory electric responses (1) On their variation by age,'' Journal of Otolaryngology of Japan **82**, 449–456.

Hughes, J. R., Fino, J., and Gagnon, L. (**1981**). ''The importance of phase of stimulus and the reference recording electrode in brain stem auditory evoked potentials,'' Electroencephalogr. Clin. Neurophysiol. **51**, 611–623.

Javel, E., McGee, J., Walsh, E. J., Farley, G. R., and Gorga, M. P. (**1983**). ''Suppression of auditory nerve responses. II. Suppression threshold and growth, iso-suppression contours,'' J. Acoust. Soc. Am. **74**, 801–813.

Kadoya, C., Wada, S., and Matsuoka, S. (**1988**). ''Clinico-experimental studies on auditory evoked middle latency response (AEMLR) with specific reference to generation and auditory dominancy,'' Sangyo Ika Daigaku Zasshi **10**, 11–30.

Katbamna, B., Metz, D. A., Bennett, S., and Dokler, P. A. (**1996**). ''Effects of electrode montage on the spectral composition of the infant auditory brainstem response,'' J. Am. Acad. Audiol. **7**, 269–273.

Kavanagh, K. T., Crews, P. L., Domico, W. D., and McCormick, V. A.

(**1988**). ''Comparison of the intrasubject repeatability of auditory brain stem and middle latency responses elicited in young children,'' Ann. Otol. Rhinol. Laryngol. **97**, 264–271.
Kavanagh, K. T., Harker, L. A., and Tyler, R. S. (**1984**). ''Auditory brainstem and middle latency responses. II. Threshold responses to a 500-Hz tone pip,'' Ann. Otol. Rhinol. Laryngol. **93**, 8–12.
Kileny, P., and Shea, S. L. (**1986**). ''Middle-latency and 40-Hz auditory evoked responses in normal-hearing subjects: click and 500-Hz thresholds,'' J. Speech Hear. Res. **29**, 20–28.
King, A. J., and Sininger, Y. S. (**1992**). ''Electrode configuration for auditory brainstem response audiometry,'' American Journal of Audiology **1**, 63–67.
Klein, A. J. (**1983**). ''Properties of the brain-stem response slow-wave component. II. Frequency specificity,'' Arch. Otolaryngol. **109**, 74–78.
Kraus, N., and McGee, T. (**1988**). ''Color imaging of the human middle latency response,'' Ear Hear. **9**, 159–167.
Kraus, N., and McGee, T. (**1990**). ''Clinical applications of the middle latency response,'' J. Am. Acad. Audiol **1**, 130–133.
Kraus, N., and McGee, T. (**1993**). ''Clinical implications of primary and nonprimary pathway contributions to the middle latency response generating system,'' Ear Hear. **14**, 37–47.
Kraus, N., McGee, T., and Comperatore, C. (**1989**). ''MLRs in children are consistently present during wakefulness, stage 1, and REM sleep,'' Ear Hear. **10**, 339–345.
Kraus, N., Smith, D. I., Reed, N. L., Stein, L. K., and Cartee, C. (**1985a**). ''Auditory middle latency responses in children: Effects of age and diagnostic category,'' Electroencephalogr. Clin. Neurophysiol. **62**, 343–351.
Kraus, N., Smith, D. I., Reed, N. L., Stein, L. K., and Cartee, C. (**1985b**). ''Absent auditory brainstem response: Peripheral hearing loss or brainstem dysfunction?'' Laryngoscope **94**, 400–406.
Lichtenstein, V., and Stapells, D. R. (**1997**). ''Effective duration of stimuli for the auditory brainstem and middle latency response (ABR/MLR),'' Abstracts of the Fifteenth International Evoked Response Audiometry Study Group, 2.
Littell, R., Milliken, G., Stroup, W., and Wolfinger, W. (**1996**). ''SAS system for mixed models,'' SAS Technical Report P-229, SAS Institute Inc., North Carolina.
Mackersie, C., Down, K. E., and Stapells, D. R. (**1993**). ''Pure-tone masking profiles for human auditory brainstem and middle latency responses,'' Hear. Res. **65**, 61–68.
McFarland, W. H., Vivion, M. C., and Goldstein, R. (**1977**). ''Middle components of the AER to tone-pips in normal-hearing and hearing-impaired subjects,'' J. Speech Hear. Res. **20**, 781–798.
McPherson, D. L., Hirasugi, Y., and Starr, A. (**1985**). ''Auditory brain stem potentials recorded at different scalp locations in neonates and adults,'' Ann. Otol. Rhinol. Laryngol. **94**, 236–243.
McRandle, C. C., Smith, M. A., and Goldstein, R. (**1974**). ''Early averaged electroencephalic responses to clicks in neonates,'' Ann. Otolaryngol. **83**, 695–701.
Mendel, M. I., Adkinson, C. D., and Harker, L. A. (**1977**). ''Middle components of the auditory evoked potentials in infants,'' Ann. Otolaryngol. **86**, 293–299.
Mendelson, T., and Salamy, A. (**1981**). ''Maturational effects on the middle components of the averaged electroencephalic response,'' J. Speech Hear. Res. **46**, 140–144.
Munnerley, G. M., Greville, K. A., Purdy, S. C., and Keith, W. J. (**1991**). ''Frequency-specific auditory brainstem responses: Relationship to behavioral thresholds in cochlear-impaired adults,'' Audiology **30**, 25–32.
Musiek, F. E. (**1982**). ''An application of the auditory middle latency response: A case of pseudohypacusis,'' Nicolet Potentials **1**, 13–14.
Musiek, F. E., and Donnelly, K. (**1983**). ''Clinical applications of the (auditory) middle latency response—An overview,'' Seminars in Hearing **4**, 391–401.
Musiek, F. E., and Geurkink, N. A. (**1981**). ''Auditory brainstem and middle latency evoked response sensitivity near threshold,'' Ann. Otol. Rhinol. Laryngol. **90**, 236–240.
Nadol, J. B. (**1988**). ''Quantification of human spiral ganglion cells by serial section reconstruction and segmental density estimates,'' Am. J. Otolaryngol. **9**, 47–51.
Oates, M. A. (**1996**). ''Frequency specificity of the auditory brainstem and the middle latency responses,'' Doctoral Dissertation, Graduate Center City University of New York, New York.
Oates, P. A., and Stapells, D. R. (**1997a**). ''Frequency specificity of the human auditory brainstem and middle latency responses to brief tones. I. High-pass noise masking,'' J. Acoust. Soc. Am. **102**, 3597–3608.
Oates, P. A., and Stapells, D. R. (**1997b**). ''Frequency specificity of the human auditory brainstem and middle latency responses to brief tones. II. Derived response analyses,'' J. Acoust. Soc. Am. **102**, 3609–3619.
Okitsu, T. (**1984**). ''Middle components of the auditory evoked response in young children,'' Scand. Audiol. **13**, 83–86.
Ozdamar, O., and Kraus, N. (**1983**). ''Auditory middle-latency responses in humans,'' Audiology **22**, 34–49.
Palaskas, C. W., Wilson, M. J., and Dobie, R. A. (**1989**). ''Electrophysiologic assessment of low-frequency hearing: Sedation effects,'' Otolaryngol.-Head Neck Surg. **101**, 434–441.
Phillips, D. P. (**1985**). ''Temporal response features of cat auditory cortex neurons contributing to sensitivity to tones delivered in the presence of continuous noise,'' Hear. Res. **19**, 253–268.
Phillips, D. P. (**1990**). ''Neural representation of sound amplitude in the auditory cortex: Effects of noise masking,'' Behav. Brain Res. **37**, 197–214.
Phillips, D. P., and Cynader, M. S. (**1985**). ''Some neural mechanisms in the cat's auditory cortex underlying sensitivity to combined tones and wide-spectrum noise stimuli,'' Hear. Res. **18**, 87–102.
Phillips, D. P., Orman, S. S., Musicant, A. D., and Wilson, G. F. (**1985**). ''Neurons in the cat's primary auditory cortex distinguished by their responses to tones and wide-spectrum noise,'' Hear. Res. **18**, 73–86.
Pickles, J. O. (**1984**). ''Frequency threshold curves and simultaneous masking functions in single fibres of the guinea pig auditory nerve,'' Hear. Res. **14**, 245–256.
Picton, T. W., Ouellette, J., Hamel, G., and Smith, A. D. (**1979**). ''Brainstem evoked potentials to tonepips in notched noise,'' J. Otolaryngol. **8**, 289–314.
Polyakov, A., and Pratt, H. (**1994**). ''Three-channel Lissajous' trajectory of human middle latency auditory evoked potentials,'' Ear Hear. **15**, 390–399.
Purdy, S. C., Houghton, J. M., Keith, W. J., and Greville, K. A. (**1989**). ''Frequency-specific auditory brainstem responses. Effective masking levels and relationship to behavioral thresholds in normal hearing adults,'' Audiology **28**, 82–91.
SAS Technical Reports. (**1999**). SAS [On-line serial] Version 8. Available: http://www.sas.techsup.com.
Satterthwaite, F. E. (**1946**). ''An approximate distribution of estimates of variance components,'' Biometrics Bulletin **2**, 110–114.
Scharf, B. (**1970**), ''Critical bands,'' *Foundations of Modern Auditory Theory*, edited by J. V. Tobias (Academic, New York), Vol. 1, pp. 159–202.
Scherg, M., and Volk, S. A. (**1983**). ''Frequency specificity of simultaneously recorded early and middle latency auditory evoked potentials,'' Electroencephalogr. Clin. Neurophysiol. **56**, 443–452.
Sininger, Y. S., and Abdala, C. (**1996**). ''Hearing threshold as measured by auditory brain stem response in human neonates,'' Ear Hear. **17**, 395–401.
Sininger, Y. S., Abdala, C., and Cone-Wesson, B. (**1997**). ''Auditory threshold sensitivity of the human neonate as measured by the auditory brainstem response,'' Hear. Res. **104**, 27–38.
Sininger, Y. S., Cone-Wesson, B., and Abdala, C. (**1998**). ''Gender distinctions and lateral asymmetry in the low-level auditory brainstem response of the human neonate,'' Hear. Res. **126**, 58–66.
Skinner, P., and Glattke, T. J. (**1977**). ''Electrophysiologic responses and audiometry: State of the art,'' Journal of Speech and Hearing Disorders **42**, 179–198.
Snedecor, G., and Cochran, W. G. (**1978**). *Statistical Methods*, 6th ed. (Iowa State University Press, Ames, IA).
Stapells, D. R. (**1984**). ''Studies in evoked potential audiometry,'' Doctoral Dissertation, University of Ottawa, Ontario, Canada.
Stapells, D. R. (**1989**). ''Auditory brainstem response assessment of infants and children,'' Seminars in Hearing **10**, 229–251.
Stapells, D. R., and Picton, T. W. (**1981**). ''Technical aspects of brainstem evoked potential audiometry using tones,'' Ear Hear. **2**, 20–29.
Stapells, D. R., and So, M. R. (**1999**). ''High-pass noise masked/derived-band auditory brainstem responses: Cochlear contributions determined by narrowband maskers,'' Abstracts of the XVI International Evoked Response Audiometry Study Group, 2.
Stapells, D. R., Gravel, J. S., and Martin, B. A. (**1995**). ''Thresholds for auditory brain stem responses to tones in notched noise from infants and young children with normal hearing or sensorineural hearing loss,'' Ear Hear. **16**, 361–371.
Stapells, D. R., Picton, T. W., and Durieux-Smith, A. (**1994**). ''Electrophysi-

ologic measures of frequency-specific auditory function,'' in *Principles and Applications in Auditory Evoked Potentials*, edited by J. T. Jacobson (Allyn and Bacon, Needham Heights), pp. 251–283.
Stapells, D. R., Galambos, R., Costello, J., and Makeig, S. (**1988**). ''Inconsistency of the auditory middle latency response and steady-state responses in infants,'' Electroencephalogr. Clin. Neurophysiol. **71**, 289–295.
Stapells, D. R., Picton, T. W., Durieux-Smith, A., Edwards, C. G., and Moran, L. M. (**1990**). ''Thresholds for short-latency auditory-evoked potentials to tones in notched noise in normal-hearing and hearing-impaired subjects,'' Audiology **29**, 262–274.
Stapells, D. R., Picton, T. W., Pérez-Abalo, M., Read, D., and Smith, A. (**1985**). ''Frequency specificity in evoked potential audiometry,'' in *The Auditory Brainstem Response*, edited by J. T. Jacobson (College-Hill Press, San Diego), pp. 147–177.
Starr, A., and Don, M. (**1988**). ''Brain potentials evoked by acoustic stimuli,'' in *Human Event-Related Potentials, EEG Handbook*, edited by T. W. Picton (Elsevier, Amsterdam), pp. 97–157.
Suzuki, T., and Hirabayashi, M. (**1987**). ''Age-related morphological changes in auditory middle-latency response,'' Audiology **26**, 312–320.
Suzuki, T., Hirabayashi, M., and Kobayashi, K. (**1983**). ''Auditory middle responses in young children,'' Br. J. Audiol. **17**, 5–9.
Thornton, A. R., Mendel, M. I., and Anderson, C. V. (**1977**). ''Effects of stimulus frequency and intensity on the middle components of the averaged auditory electroencephalic response,'' J. Speech Hear. Res. **20**, 81–94.
Tucker, D., and Ruth, R. A. (**1996**). ''Effect of age, signal level, and signal rate on the auditory middle latency response,'' J. Am. Acad. Audiol. **7**, 83–91.
Vivion, M. C., Hirsch, J. E., Frye-Osier, J. L., and Goldstein, R. (**1980**). ''Effects of stimulus rise-fall time and equivalent duration on middle components of AER,'' Scand. Audiol. **9**, 223–232.
Weber, D. L. (**1983**). ''Do off-frequency simultaneous maskers suppress the signal?'' J. Acoust. Soc. Am. **73**, 887–893.
Wegel, R. L., and Lane, C. E. (**1924**). ''The auditory masking of one sound by another and its probable relation to the dynamics of the inner ear,'' Physiol. Rev. **23**, 266–285.
Werner, L. A., Folsom, R. C., and Mancl, L. R. (**1993**). ''The relationship between auditory brainstem response and behavioral thresholds in normal hearing infants and adults,'' Hear. Res. **68**, 131–141.
Wolf, K. E., and Goldstein, R. (**1978**). ''Middle component averaged electroencephalic responses to tonal stimuli from normal neonates. Initial report, Arch. Otolaryngol. **104**, 508–513.
Wolf, K. E., and Goldstein, R. (**1980**). ''Middle component AERs from neonates to low-level tonal stimuli,'' J. Speech Hear. Res. **23**, 185–201.
Wolpaw, J. R., and Wood, C. C. (**1982**). ''Scalp distribution of human auditory evoked potentials. I. Evaluation of reference electrode sites,'' Electroencephalogr. Clin. Neurophysiol. **54**, 15–24.
Worthington, D. W., and Peters, J. F. (**1980**). ''Quantifiable hearing and no ABR: Paradox or error?'' Ear Hear. **5**, 281–285.
Wu, C-Y., and Stapells, D. R. (**1994**). ''Pure-tone masking profiles for human auditory brainstem and middle latency responses to 500-Hz tones,'' Hear. Res. **78**, 169–174.
Zerlin, S., and Naunton, R. F. (**1974**). ''Early and late averaged electroencephalic responses at low sensation levels,'' Audiology **13**, 366–378.
Zwicker, E. (**1970**). ''Masking and psychological excitation as consequences of the ear's frequency analysis,'' in *Frequency Analysis and Periodicity Detection in Hearing*, edited by R. Plomp and G. F. Smoorenburg (Sijthoff, Leiden).

Auditory detection of hollowness

Robert A. Lutfi[a)]
Department of Communicative Disorders and Waisman Center, University of Wisconsin, Madison, Wisconsin 53706

(Received 6 June 2000; revised 13 November 2000; accepted 15 May 2001)

The airborne sounds produced by freely vibrating hollow and solid bars were synthesized according to the equations of bar motion from theoretical acoustics, and were presented to listeners over headphones. In a two-interval, forced-choice task, listeners were asked to distinguish between the hollow and solid bar sounds as bar length was varied at random from one presentation to the next. All other physical properties of the bar were held constant across trials. Listener decision strategies for detecting hollowness in iron, aluminum, and wood bars were determined from regression weights describing the relation between the listener's response and the frequency, intensity, and decay modulus of the individual partials comprising these sounds. The obtained weights were compared to those of a hypothetical listener that bases judgments on the acoustic relations intrinsic to hollowness, as determined from the equations for motion. Results indicate that listeners adopt roughly one of two decision strategies, either basing judgments on the appropriate acoustic relations, or basing judgments predominantly on frequency alone. The decision strategy of some listeners also changed from one type to the other with a change in bar material or upon replication of the same condition. The results are interpreted in terms of the vulnerability of the intrinsic acoustic relations to small perturbations in acoustic parameters, as would be associated with listener internal noise. They demonstrate that basic limits of human sensitivity can have a profound effect on the identification of rudimentary source attributes from sound, even in conditions where acoustic variation is largely dictated by physical variation in the source. [DOI: 10.1121/1.1385903]

PACS numbers: 43.66.Ba, 43.66.Fe [DWG]

I. INTRODUCTION

Everyday experience suggests that the ear is quite good at inferring basic attributes of objects from sound. The ''ping'' of the wine glass identifies the glass as fine crystal, the ''clunk'' of the table struck with your knuckle indicates that the table is hollow and made of wood. Such simple examples represent in principle how we use sound to gain information about our surroundings, but even in regard to these simple examples we understand very little of the process. What are the limits of our ability to determine physical attributes of the source in these cases, and what information in the sound is used to make such determinations? These are the questions that motivate the present experiments.

In earlier papers, we described a method for measuring precisely how a listener's judgments regarding the physical attributes of an object are influenced by specific acoustic parameters and their relations (Lutfi, 1995; Lutfi and Oh, 1994, 1995, 1997). The relative influence, in each case, is estimated from correlations of the listener's judgments with small, experimentally introduced perturbations in the values of acoustic parameters from trial to trial. Importantly, the perturbations are introduced in such a way so as not to violate the lawful relations governing the motion of the object, i.e., the sounds, in some sense, remain real. To do this, the sounds are synthesized digitally using a resonant source for which the equations for motion are known. In this study, as in the previous studies, we chose as our resonant source the struck, clamped bar. This is the preferred choice inasmuch as the equations for motion are relatively simple, yet they apply to a large class of common, freely vibrating objects. Many familiar musical instruments, for example, fall into the category of struck, clamped bars (triangle, tuning fork, wood block, and xylophone).

Our first experiments employed a standard, two-interval, forced-choice procedure to investigate the discrimination of differences in the material composition of bars (Lutfi and Oh, 1997). The goal was to measure the best possible performance under the most favorable listening conditions. Hence, all physical attributes of the bar were held constant except for material, and all listeners were given extensive training in the task before data collection. To provide a standard for evaluating listener performance, the equations for motion were analyzed to yield a maximum-likelihood test for the task, that is, a decision rule that would maximize percent correct. For each material discrimination, the test amounted to a specific weighting of the frequency, amplitude, and decay of individual partials in the sound. Listener decision weights, computed from the response correlations with these parameters, generally followed the maximum-likelihood weights, but were in all cases unduly biased toward frequency. In the most severe cases, the frequency bias resulted in as much as an 80% reduction in performance efficiency. The results suggest that, even under the best circumstances, a listener's ability to discriminate material is far from ideal.

In the present study we investigate yet another basic discrimination, the discrimination of hollow from solid bars.

[a)]Electronic mail: lutfi@waisman.wisc.edu

 0001-4966/2001/110(2)/1010/10/$18.00

The study is a natural outgrowth of the earlier study on material discrimination involving merely different relations among the same acoustic cues. However, in the present study we employ a different procedure for introducing perturbations in these cues. In the earlier procedure acoustic variation was introduced by perturbing bar material, the physical attribute to be discriminated. In the present procedure acoustic variation is introduced by perturbing a physical attribute of the bar unrelated to the discrimination. In the discrimination of solid from hollow bars we perturb bar length. We adopt this new procedure for two reasons. First, as a practical matter, we wished to readdress a specific issue regarding the methodology used in our previous study. In that study, the bars varied continuously along the physical dimension to be discriminated. Hence, the nominal discrimination between silver and iron, for example, was really more akin to choosing between two alloys having different relative concentrations of silver and iron. In the present study we investigate a task where there is no ambiguity regarding the two classes to be discriminated. In this case, the bar is either hollow or solid, and the only ambiguity is regarding the unrelated physical attribute, bar length.

The second reason for adopting this procedure is theoretical and has to do with the larger problem of how listeners determine source attributes from sound. The acoustic information intrinsic to different source attributes is necessarily confounded in the single pressure wave form arriving at the ear. How then might a listener determine from sound that a class of resonant objects is, say, hollow or is made of metal despite differences in the size or shape of individual exemplars or the manner in which they are driven to vibrate? Gibson (1966) has suggested that listeners ''pick up'' the requisite information identifying such general classes of objects or events in the form of higher order acoustic relations that are invariant within a class. While he did not go beyond a general description of these relations, others have since offered analytic treatments that identify the intrinsic acoustic information necessary to distinguish among certain general classes of resonant objects given few physical constraints (Wildes and Richards, 1988; Kac, 1966; Lutfi, 2000). One such case is the distinction between hollow and solid bars. It can be shown, for example, that specific relations among acoustic parameters that are intrinsic to freely vibrating hollow bars remain constant despite variation in bar size, shape, or material composition (Lutfi, 2000). In this particular case, at least, such relations seem likely candidates for the type of information Gibson had in mind. Will listener judgments of hollowness be based on these relations? The answer might depend on whether they provide a significant detection advantage. An analysis of the intrinsic acoustic relations associated with various bar attributes suggests that these relations can be subtle (Lutfi, 2000). Basic limits in auditory sensitivity might, therefore, exert a greater influence on the listener's selection of cues than the intrinsic acoustic relations that serve to disambiguate source attributes. We test the possibility in the present experiments. In particular, we compare the decision weights of listeners to those of a hypothetical listener that bases judgments on acoustic relations intrinsic to hollowness as determined from the equations for motion of the freely vibrating bar.

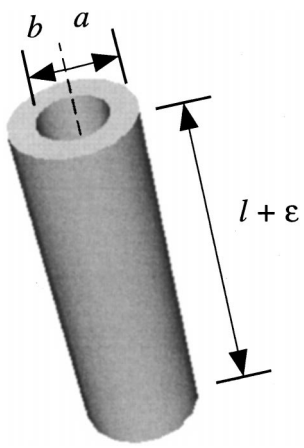

FIG. 1. Representation of bar geometry used in the study. The outer radius a was fixed at 2.0 cm in all conditions. The length l of the bar was either 10 or 25 cm in different conditions and was randomly perturbed for each presentation of a sound, $\varepsilon \in N(l, 0.5\ \text{cm})$. The hollow inner radius b was chosen for each listener to yield discrimination performance levels in the range of 70%–90% correct when compared to the solid bar, $b=0$.

II. METHODS

A. Stimuli

The procedure for synthesizing stimuli was identical to that described in Lutfi and Oh (1997) and is briefly reviewed here. The airborne sound of a cylindrical bar rigidly clamped at one end and struck at the other was synthesized over headphones using the theoretical equations describing the motion of the bar. The resultant sound-pressure wave form is a sum of exponentially damped sinusoids whose individual frequencies (ν_n,Hz), amplitudes (C_n,dyn/cm^2), and decay moduli (τ_n,s) are uniquely determined by the specific material and geometry of the bar, as well as the manner in which the bar is struck,

$$y=\sum_n C_n e^{-t/\tau_n}\sin(2\pi\nu_n t). \tag{1}$$

Altogether five bar parameters were incorporated in the stimulus synthesis. Related to bar geometry were bar length l, outer radius a, and inner radius b (hollowness), see Fig. 1. Related to bar material were elasticity Q and mass density ρ. The specific values used for the different conditions of the experiment are given in Table I. These values were chosen to represent different resonant sources that might realistically be encountered in everyday listening. The values of b ranged from 0.5 to 1.2 cm and were chosen individually for each listener and condition to yield average performance levels between 70% and 90% correct. Past experience has dictated that performance levels much above or below this range yield unreliable estimates of listener decision weights. The equations relating these physical parameters to the acoustic parameters of Eq. (1) are reviewed by Morse and Ingard (1968, pp. 175–191, 222). For a total force P of an impulse applied to the free end of the bar,

TABLE I. Physical and acoustic parameters associated with different clamped bars used in the study. Entries for acoustic parameters pertain to the first partial. Bar length l was perturbed from one presentation to the next, all other physical properties of the bars were held constant within a block of trials. Values of b are nominal as they were selected for each condition and listener to yield performance levels between 70% and 90% correct. Values of density and elasticity for different materials are taken from Kinsler and Frey (1962). Elasticity values for wood are contained in parentheses as they vary widely depending on factors related to the properties of the wood.

	Physical parameters			Acoustic parameters		
Bar type	Geom, l, a, b (cm)	Density, ρ (g/cm^3)	Elasticity, Q ($dyn/cm^2 \times 10^{11}$)	Frequency, ν (Hz)	Amp. $\lvert C \rvert$ (dB SPL)	Decay, τ (s)
Solid iron	10, 2.0, 0.0	7.7	10.5	2067	68.5	1.09
Hollow iron	10, 2.0, 1.0	7.7	10.5	2311	70.0	0.63
Solid wood	25, 2.0, 0.0	0.72	(60.0)	2586	69.1	0.05
Hollow wood	25, 2.0, 0.8	0.72	(60.0)	2785	70.0	0.04
Solid aluminum	10, 2.0, 0.0	2.7	7.1	2871	68.5	0.14
Hollow aluminum	10, 2.0, 1.0	2.7	7.1	3210	70.0	0.08

$$\nu_n = \frac{\pi}{2l^2}\sqrt{\frac{Q\kappa^2}{\rho}}\beta_n^2, \tag{2a}$$

$$C_n = (-1)^{n-1}\frac{lU}{\pi^2\beta_n^2}\sqrt{\frac{8\rho}{Q\kappa^2}}, \tag{2b}$$

$$\tau_n = 16\times 10^8(\pi\rho/4\kappa^2\nu_n^3), \tag{2c}$$

where $\beta_1 = 0.597$, $\beta_2 = 1.494$, and $\beta_{n>2} = n - \frac{1}{2}$ determine the frequency ratio of successive partials, $\kappa = \frac{1}{2}\sqrt{a^2+b^2}$ is the radius of gyration of the bar, and the gain term $U = P/[\rho\pi(a^2-b^2)]$. The value of P was chosen to fix the sound intensity for hollow bars at 70 dB SPL. Only the first three partials ($n = 1-3$) were synthesized as the higher partials were well beyond the range of audibility. Further details regarding the stimulus synthesis can be found in Lutfi and Oh (1997). Also, examples of these sounds can be heard at http://abrl.waisman.wisc.edu/.

As practical matter, a 5 ms cosine-squared ramp was used to truncate signals after 1 s. This kept trials at a reasonable length, while allowing adequate time for the second and third partials of the sounds to decay to inaudibility. Note that in the previous study signals were less than half this duration (400 ms). The longer duration is intended to ensure that the sounds are not too brief to allow for normal identification of bar attributes. All signals were played over a 16 bit, Crystal Audio 4237B DAC at a 40 kHz sampling rate. The output of the DAC was low-pass filtered with rapid rolloff above 16 kHz, asymptoting to a maximum 60 dB of attenuation at 22 kHz. Sounds were delivered to the right ear of listeners over Sennheiser Model 520 II headphones, and were calibrated using a loudness matching procedure. All signals were presented to individual listeners seated in a double-walled, IAC sound-attenuation chamber.

B. Procedure

For each presentation of a signal, a different perturbation in acoustic parameters was imposed without violating the lawful relations governing the values of these parameters. This was achieved by adding a random increment or decrement ϵ on each presentation to bar length, a physical attribute of the bar unrelated to hollowness.[1] All other physical attributes of the bar were held constant within trial blocks. In each condition, bar length was chosen at random from normal distributions to synthesize a set of 100 wave forms each for the hollow and solid bars. As indicated in Table I, the mean value of bar length l was 25 cm for the wood bars, whereas it was 10 cm for aluminum and iron bars. The longer length for wood bars was necessary to maintain the frequencies of the partials within the audible range. The standard deviation of bar length was fixed for all conditions at 0.5 cm. The exact value chosen is somewhat arbitrary, and is expected to affect the estimates of listener weights only to the extent that it causes performance to fall outside the acceptable range of 70%–90% correct.

Conditions were run in separate blocks of trials with replications across days. A two-interval, forced-choice procedure was used with sounds separated by 500 ms. On each trial one exemplar was chosen at random from the set of solid and hollow bar sounds for presentation. Each sound had equal probability of occurring in the first or second interval of the trial. The listener's task was to indicate by button press which of the two intervals contained the sound corresponding to the hollow bar. Correct feedback was given after each trial. Trials were run in blocks of 50 with short breaks between blocks taken at the discretion of the listener. Listeners practiced conditions for several hundred trials prior to data collection. After practice a total of 400 trials was run for each listener for each condition with at least one 400-trial replication of each condition made on a separate day. The listeners were seven students at the University of Wisconsin–Madison ranging in age from 20 to 38 years. Subject protocol required that listeners be allowed to terminate participation in a study at any time at their discretion. Hence, not all listeners participated in all conditions. Two of these listeners had participated in the earlier study on the discrimination of bar material. All listeners had normal hearing by standard audiometric tests, and all were paid at an hourly rate for their participation. Listeners were instructed that on each trial they would hear the sound of a hollow and a solid bar struck at one end and clamped at other, that the bars were struck with constant force, and that the bars were

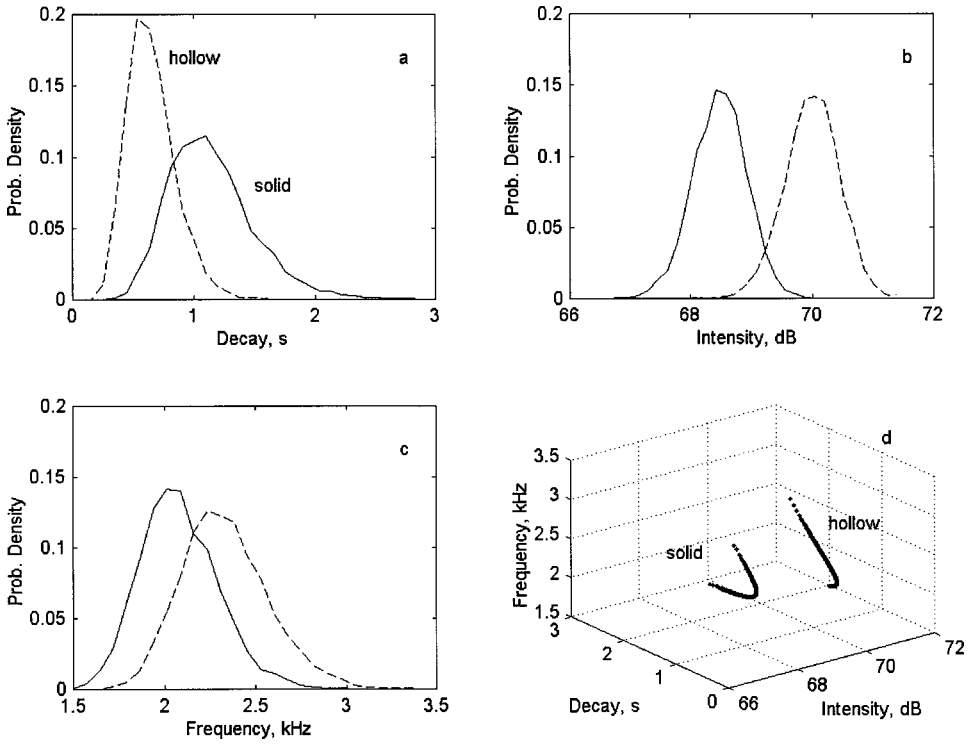

FIG. 2. Distribution of values of acoustic parameters (first partial) for the iron bar. (a)–(c) Values of each parameter for hollow (dashed curves) and solid (continuous curve) bars as bar length varies from one presentation to the next. A judgment of hollowness based on any one acoustic parameter in isolation would be prone to error inasmuch as the distributions overlap. (d) The distribution of parameter values from (a)–(c) are plotted relative to one another so as to reveal the intrinsic relations among the parameters that allow the bar to be identified as hollow or solid without error.

identical in all other respects except for length. They were instructed that the length would vary from one presentation to the next, but that in every case their goal was to identify the sound corresponding to the hollow bar. Before each block of trials the listeners were told the material of the bar, and were shown an example of a real bar having the geometric dimensions corresponding to those used to synthesize the sounds they heard.

C. Analysis of decision weights

Before we can properly analyze listener decision weights it is necessary to identify the relevant information for the detection of hollowness given the particulars of the task. The problem amounts to finding an analytic solution for hollowness using Eqs. (2a)–(2c). The derivation is straightforward. Note first that the information in successive partials is redundant—the frequency ν_n, amplitude C_n, and decay τ_n of the nth partial are merely scaled in each case by the constant factor β_n raised to some power. This means that for the conditions of the present experiments, where bar length l is perturbed, the problem of detecting hollowness reduces analytically to that of solving two equations for two unknowns. The two equations are any two of the equations (2a)–(2c) for any given n. The two unknowns are the inner radius of the bar b ($=0$ solid, >0 hollow) and bar length l. The value of b must be solved anew on each presentation given the observed values of ν_n, C_n, and τ_n, but there is always a unique solution on each presentation. Figure 2 demonstrates this result. Figures 2(a)–(c) show the distribution of values for each acoustic parameter (first partial) of the iron bar, both hollow (dashed curves) and solid (continuous curve), as length varies from one presentation to the next. Note that a judgment of hollowness based on any one acoustic parameter in isolation would be prone to error inasmuch as the distributions overlap. Figure 2(d) shows the same data, but now plotted in a way so as to reveal the relations among parameter values. Here it can be seen that there are unique combinations of ν_n, C_n, and τ_n that allow the bar to be identified as hollow or solid without error. (Note that it is the possibility of error-free performance that distinguishes the present task from that of our earlier study involving the discrimination of bar material.)

Having identified ν_n, C_n, and τ_n for any partial as containing the relevant information for hollowness, we next derive the maximum-likelihood decision rule. There are actually three such rules corresponding to the solutions obtained for each pair of the equations (2a)–(2c). The derivation proceeds identically in each case. Note first that when the outer radius a is constrained to have a single value, as it is in the present experiments, the inner radius b is monotonically related to the radius of gyration κ (or U/κ) as in the case of Eq. (2b). From Eqs. (2a)–(2c), moreover, we see that κ (and U/κ) is proportional to the product of parameter pairs raised to different powers. This means that each optimal decision rule can be expressed in terms of a weighted sum of the log of parameter pairs, where the weights are the corresponding powers. Consider, for example, optimal decisions based on ν_n and τ_n. From Eq. (2c), we see that κ is proportional to $\tau_n^{-1/2}\nu_n^{-3/2}$. A maximum-likelihood decision rule, therefore, is of the form,

$$R=1 \text{ iff } \mathrm{Dif}(-\tfrac{1}{2}\log\tau_n-\tfrac{3}{2}\log\nu_n)<0 \quad \text{else } R=2, \tag{3}$$

where R is the response, Dif is the difference between the second and first (i.e., second-first) interval of the forced-choice trial, and $-\frac{1}{2}$ and $-\frac{3}{2}$ are the optimal decision weights for the two acoustic parameters. Optimal decision weights for the other parameter pairs are analyzed in like fashion; for the combination of C_n and ν_n they are, respectively, 1 and

$\frac{1}{2}$, and for the combination of C_n and τ_n they are, respectively, 6 and -1.

The next step is to determine whether listeners make use of any one of the three optimal decision rules. This can be done using standard multiple regression (Winkler and Hays, 1975). Again, take rule (3) as an example. Since the combination of log-parameter values is linear, responses strictly based on Eq. (3) will correlate perfectly with interval differences between $\log \tau_n$ or $\log \nu_n$ once the relation between τ_n and ν_n is taken into account. That is, the partial correlation of the response with the differences in $\log \tau_n$ and $\log \nu_n$ will be -1 in each case. In fact, we do not expect listener responses to strictly follow Eq. (3) since we have selected conditions (i.e., perturbations in l and values of b) to produce errors in the response. A more realistic regression model is therefore

$$R=1 \text{ iff } \mathrm{Dif}(w_1 \log \tau_n = w_2 \log \nu_n) + \xi > 0 \quad \text{else } R=2, \tag{4}$$

where w_1 and w_2 are the regression weights for interval differences in $\log \tau_n$ and $\log \nu_n$, and ξ is listener error. The values of w_1 and w_2 for each listener can then be computed from the relation of listener's response and the interval differences in $\log \tau_n$ and $\log \nu_n$ on each trial using standard multiple regression analysis.[2] Now, if listener responses are based on Eq. (3) and the error ξ is unbiased, then the regression weights in Eq. (4) should bear the same relation as the optimal decision weights given in Eq. (3). In particular, w_1 and w_2 should both be negative and have a ratio of one to three. All three of the optimal decision rules can be evaluated in this way, the only difference being differences in the optimal decision weights for each rule.

III. RESULTS

A. Analysis of listener decision weights

Figures 3–5 give the computed regression weights for each listener for the three different bar materials. To facilitate comparisons the regression weights for each decision rule have been normalized so that their unsigned values sum to one. Different listeners are represented by different symbol types with repeated symbols representing replications, some taken several months apart. The end points of the three lines drawn in the top panel of each figure give the decision weights for the three optimal decision rules corresponding to each parameter pair. The end points of the three lines drawn in the bottom panel of each figure give the decision weights of a hypothetical listener that bases decisions on frequency ν_n alone. Listeners appear to fall into two distinct groups, one choosing to base decisions on the optimal combination of ν_n and τ_n (top panel), the other choosing not to apply any of the optimal decision rules, but rather choosing to base decisions largely on frequency alone (bottom panel). Listener membership in either group varies both within and across conditions of bar material. Note that the occasional appearance of the same symbol in both panels shows that some listeners chose to switch from one listening strategy to the other upon replication of the same condition. With the exception of these cases, however, test–retest reliability for individual estimates is good, even for those estimates taken several months apart. Inclusion of the practice trials, moreover, did not change the agreement between estimates. When questioned, listeners in the second group reported without exception that they were choosing as hollow the sound having the higher frequency or pitch. Indeed, Fig. 2(c) shows that better than chance performance can be achieved by basing decisions on frequency alone. Also, for a few listeners in the first group it is unclear as to whether the listening strategy involved an optimal weighting of frequency and decay or of intensity and decay (note for example the squares in Fig. 3). Performance levels in these instances, though within the acceptable range of the experiment, were apparently too high for the regression weights to distinguish among the different optimal decision rules.

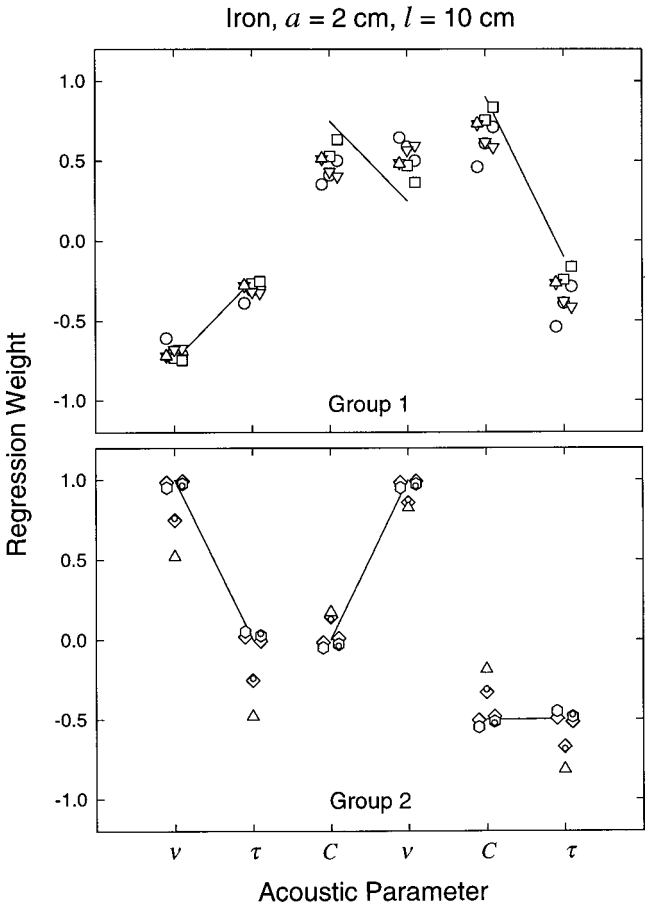

FIG. 3. Regression weights are plotted giving the relation of the listener's response to the pair of acoustic parameters underlying each optimal decision rule. Data are for the iron bar, $a=2$ cm, $l=10$ cm. The raw regression weights for each decision rule have been normalized so that their unsigned values sum to one. Different symbol types represent the regression weights for different listeners, and repeated symbols represent replications of conditions. The end points of the three lines drawn in the top panel give the decision weights for the three optimal decision rules corresponding to each parameter pair. Reading from left to right the parameter pairs are ν_n and τ_n, C_n and ν_n, and τ_n, and C_n. The end points of the three lines drawn in the bottom panel give the decision weights of a hypothetical listener that bases decisions on frequency ν_n alone. Listeners' data are plotted in one or the other panel depending on which decision rule most closely agreed with their regression weights. Note, in the bottom panel, that nonzero regression weights for the combination of τ_n and C_n are possible because each parameter covaries with ν_n, which is not included in the regression for τ_n and C_n.

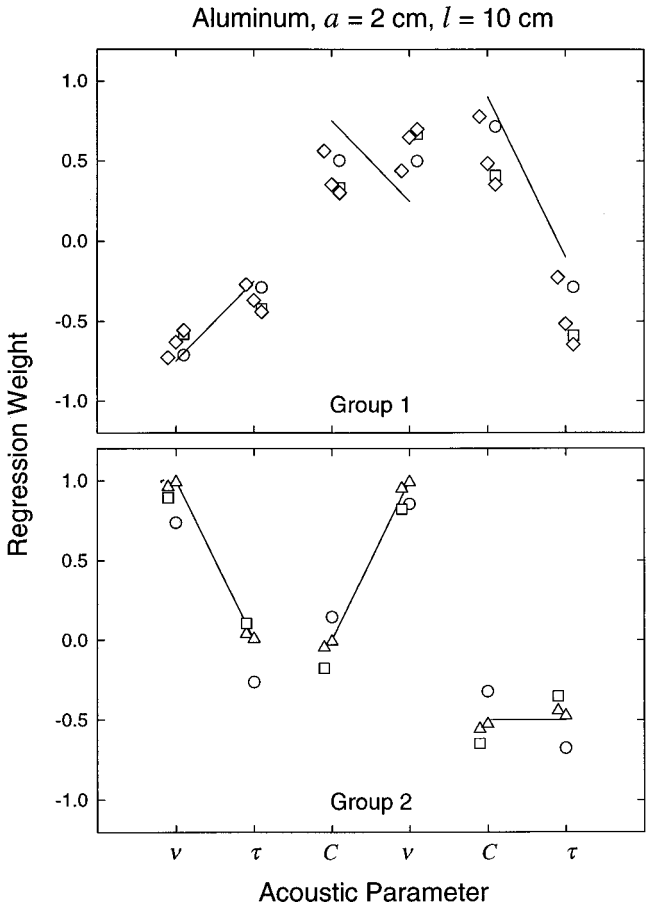

FIG. 4. Same as Fig. 3, except that data are for the aluminum bar, $a = 2$ cm, $l = 10$ cm. Except where a new listener's data are added, individual listeners maintain the same symbol type as in Fig. 3.

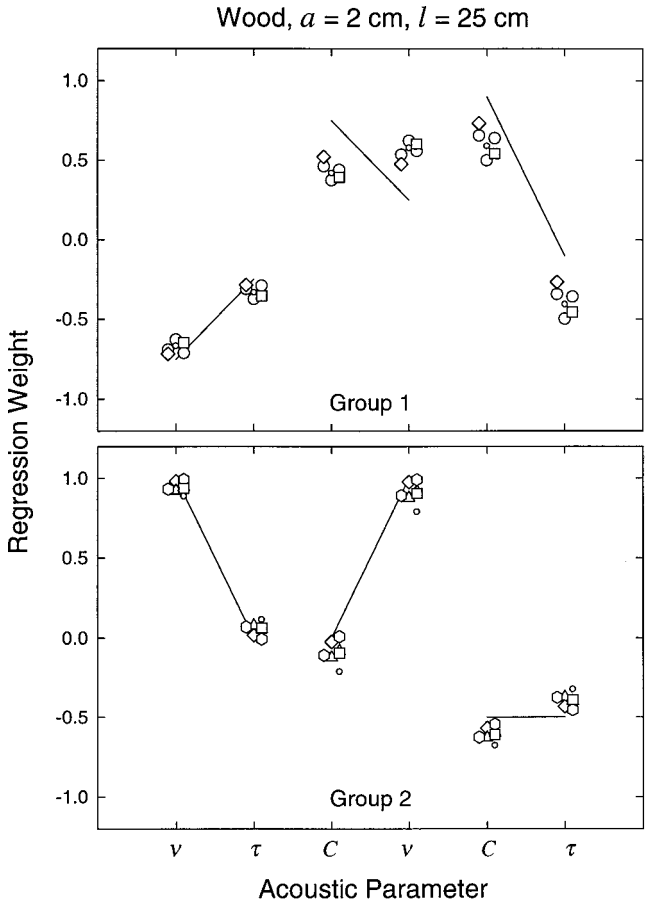

FIG. 5. Same as Fig. 3, except that data are for the wood bar, $a = 2$ cm, $l = 25$ cm. Except where a new listener's data are added, individual listeners maintain the same symbol type as in Fig. 3.

B. Effect of limited resolution on discrimination performance

For those listeners who appear to adopt an optimal decision rule it is of interest to consider what factors might have caused their performance to be less than perfect. One obvious factor is limited sensory resolution—that is, the inability on some trials to discriminate small differences in the frequency, amplitude, and decay of the individual partials of these sounds. Note, for example, in Table I, that the difference in mean intensity between the sounds for hollow and solid bars in these conditions is 0.9–1.5 dB. The normal intensity difference limen at these moderate sound levels is at best 0.7 dB (Jesteadt *et al.*, 1977). With the added perturbation in intensity the difference in intensity would have been difficult or impossible to discriminate on some proportion of trials. Table II gives an indication of the relative extent to which limited resolution affected discriminability of the individual acoustic parameters in these experiments. Table II lists, for three listeners, the d' values for the individual parameters expressed relative to those of an ideal observer (an observer with unlimited resolution). The d' values were obtained simply by rerunning conditions with the hollowness parameter b fixed at zero for all but one of the three relevant parameters. If limited resolution were to have no impact on performance in these conditions all values in Table II should equal 1.0. For the discrimination of frequency the values are, indeed, equal to or very nearly equal to 1.0. However, for the discrimination of intensity, and for the discrimination of decay for the iron bar, the values are significantly less than 1.0. These data suggest, not surprisingly, that limited sensory resolution is likely responsible for less than perfect performance of listeners who appeared to adopt an optimal decision rule. The data do not, however, necessarily imply that limited sensory resolution would significantly affect the selection of decision weights. This is because the analytic solution for hollowness depends on the *relation* among the values of acoustic parameters (cf. Fig. 3), not the value of any single parameter. Consequently, intensity (or decay) by its relation to frequency can convey information

TABLE II. Obtained d' values for the discrimination of individual acoustic parameters. The values are expressed relative to those of an ideal observer with no limit in sensory resolution.

Material	Listener symbol	d'/d'_{ideal}		
		Frequency	Intensity	Decay
Iron	Large-circle	0.92	0.36	0.31
	Up-triangle	0.95	0.38	0.29
	Diamond	1.00	0.38	0.42
Wood	Up-triangle	1.00	0.25	0.84
	Diamond	0.98	0.30	0.85

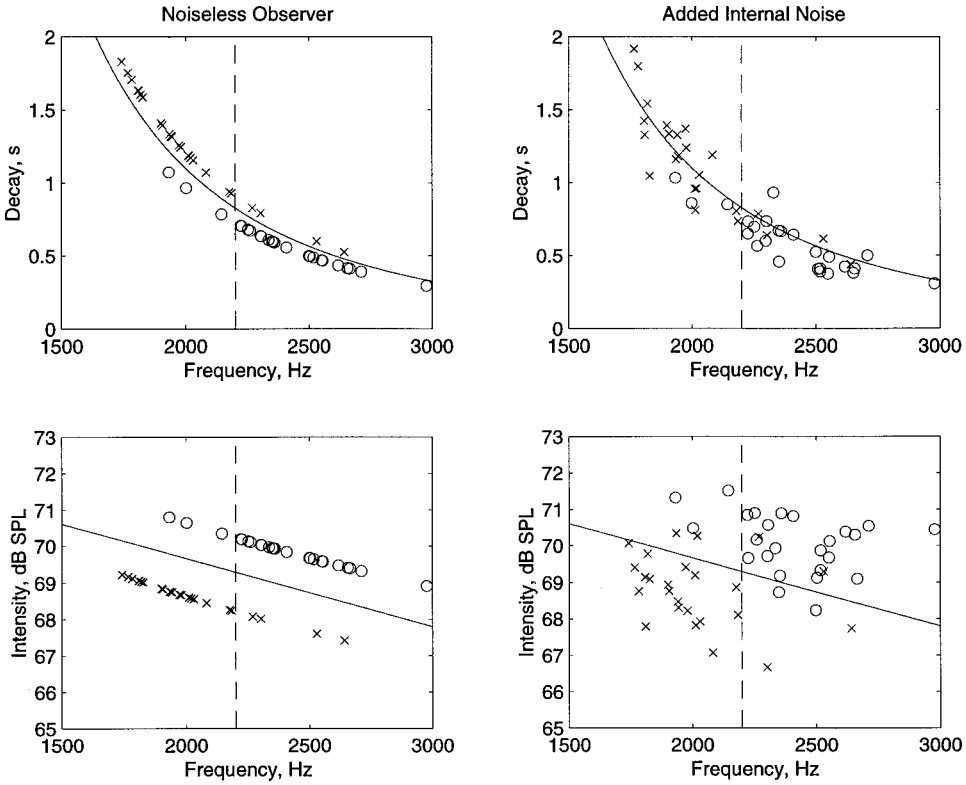

FIG. 6. Simulated effect of listener internal noise for iron bar with hollowness radius $b=1.0$. Circles and crosses represent, respectively, the parameter values for hollow and solid bars. Right and left panels represent, respectively, parameter values with and without internal noise jitter. The decision border corresponding to the optimal decision rule is given by the continuous curves. The decision border for an observer that bases judgments on frequency alone is given by the dashed curve. See the text for specific details.

regarding hollowness even on trials in which the difference in intensity (or decay) is too small to be detected.

Could limited resolution have affected the listener's selection of decision weights? To evaluate this question we generated expectations for listener performance in these experiments using a standard internal noise model (cf. Durlach *et al.*, 1986). Figure 6 shows the results of independently adding a small amount of jitter to each acoustic parameter so as to simulate the effect of internal noise. For frequency, intensity, and decay the percentage of jitter is, respectively, 0.2, 17, and 25. These values represent the current best empirical estimates of the difference limens for these parameters, for normal-hearing adults (Wier *et al.*, 1977; Jesteadt *et al.*, 1977; Van Heuven and Van Den Broecke, 1979).[3] The data shown in Fig. 6 are for the iron bar with hollowness radius $b=1.0$; similar results, however, were obtained for the aluminum and wood bars. The parameter values with (right) and without (left) jitter are designated separately for the hollow (circles) and solid (crosses) bars. The continuous curve in each panel is the decision border corresponding to the optimal combination of the designated acoustic parameters. The dashed curve is the decision border for an observer that bases judgments on frequency alone. The effect of adding internal noise in each case is to increase the number of crossings of the decision border that would yield an incorrect judgment. Importantly, however, the increase in crossings is much greater for the optimal decision rule than it is for the judgments based on frequency alone. This results in the two decision models producing more similar performance levels than would be anticipated based on the parameter values without internal noise.

Figure 7 shows the expected effect of the internal noise on the psychometric function. Here the dashed and continuous curves represent, respectively, performance based on the optimal weighting of frequency and decay, and performance-based differences in frequency alone. The data of individual listeners (symbols) are plotted for comparison. Note that for the iron bar (upper panel) there is only a small performance advantage for the optimal decision rule over the judgments based on frequency alone. In the range of $b=1.0-1.3$ cm where most of the listeners' data fall the advantage is less than 5%. For the wood bar (lower panel) the optimal decision rule actually yields poorer performance than for the judgments based on frequency alone. This can be understood from the distribution of the values of frequency and decay in Fig. 6 (upper panels), which are for iron, but show a similar pattern for wood. Here the values skirt the decision border of the optimal rule so closely that even a small amount of perturbation can force performance to be near chance.

The analysis of internal noise suggests a likely explanation for the specific pattern of listeners' decision weights. With limited resolution an optimal listening strategy, as would be associated with an analytic solution for hollowness, yields at best a small performance advantage in some conditions over judgments based on frequency alone. Also, since frequency is the most salient single cue, varying over many more just-noticeable differences than either decay or intensity (cf. Wier *et al.*, 1977; Jesteadt *et al.*, 1977; Van Heuven and Van Den Broecke, 1979), there is good reason to expect that listeners would often chose to base decisions on frequency alone in lieu of an optimal combination of acoustic parameters. The fact that performance levels of listeners generally fall within the bounds predicted by the optimal listening strategy and one based on frequency alone lends additional support to this analysis.

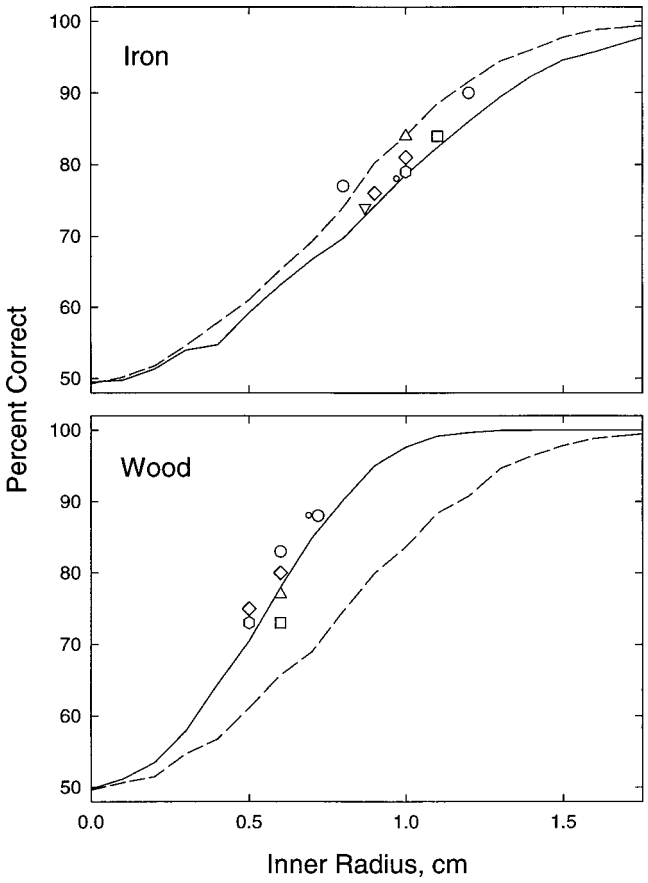

FIG. 7. Psychometric functions for internal noise simulation. Dashed curves are the functions resulting from optimal weighting of frequency and decay [as given by Eq. (3)]. The continuous curve is the function resulting from judgments based on frequency alone. The data of individual listeners are given different symbols consistent with those of Figs. 3–5.

IV. DISCUSSION

The results of these experiments reveal clear individual differences in the decision strategies that listeners use when judging hollowness from the synthesized sound of a struck, clamped bar. Listeners tend to fall into two groups in terms of their cue preference: those giving weight to frequency and decay consistent with an analytic solution for hollowness, and those giving predominant weight to frequency. The results also indicate, for some listeners, a change from one decision strategy to the other with changes in the material composition of the bar or with replication of a condition.

The general pattern of results is consistent with that obtained in the companion to this study involving the discrimination of bar material. There, too, significant individual differences were observed combined with a bias for frequency for many listeners. Apart from the difference in task, that study differed fundamentally from the present study in that the material discrimination was to some degree ambiguous. Unlike the present study, in which the bar was unequivocally hollow or solid, the companion study required, in effect, a decision between two bars of the same material in different relative concentrations. This ambiguity was suspected to have played a role in the outcome of the earlier experiments. However, the similarity in the pattern of results to those of the present study suggests that the earlier results were not specifically related to this ambiguity.

Several studies in the literature offer similar comparisons to the present study, though they used real or recorded sound sources. Kunkler-Peck and Turvey (2000) challenged listeners to determine from sound the height and width of a rectangular steel plate suspended by a loose support and struck in its center by a hard mallet. While listener judgments consistently underestimated the true values, the ratio of height to width was recovered with reliable accuracy, despite variations in plate material. Kunkler-Peck and Turvey offer both theoretical and acoustical analyses to show that there is sufficient information for the task in the separate modal frequencies associated with height and width. They imply a similar account of their listeners' ability to reliably identify the shape of plates (circle, triangle, or square) of different material. The ability to recover height–width ratios from sound has also been demonstrated for loosely suspended, struck bars made of metal and wood (Lakatos *et al.*, 1997). Acoustical analyses by these authors revealed that for metal bars the frequencies of both torsional and transverse bending modes correlated highly with height–width ratio and with listener judgments, suggesting that these modes may have served as potential cues. For wood bars the role of these modes was less clear as they were often weak or absent. Other physical attributes of objects or events that listeners have been shown to reliably judge from sound include the length of rods dropped on a hard surface (Carello *et al.*, 1998), the hardness of mallets striking metal pans (Freed, 1990), the breaking or bouncing of glass (Warren and Verbrugge, 1984), the position of hands clapping (Repp, 1987), and the gender of walkers (Li *et al.*, 1991). In each of these cases, specific features of the acoustic wave form or spectra have been correlated with the object or event and listener judgments to identify potential cues underlying the listeners' ability to perform the task.

Taken together, the past studies show that there is sufficient information in sound to allow identification of complex source attributes, and moreover, that listeners are capable of such identifications with limited variation in other source attributes. One might ask, therefore, what new information is provided by the present results? The answer lies in the approach to identifying potential acoustic cues. There are two important differences between the past and present studies in this regard. First, it should be noted that a strong correlation of a listener's judgments with a particular cue, as has been demonstrated in past studies, is not a sufficient condition to implicate that cue. Such a result does not rule out the possibility that the listener may use a very different cue that happens to be highly correlated with the one analyzed by the experimenter. Indeed, considering the complexity of the real acoustic events that listeners were asked to judge in past studies, it is almost certain that alternative cues were available in some cases.[4] The advantage in the present study of using synthesized sounds rather than real sound sources is that *all* relevant information for the specific task is contained in the equations for motion. This allows precise measurement of the independent and relative contribution of each potential source of information to the listener's response,

without lingering questions regarding the possibility of alternative acoustic cues. A second issue pertaining to the measurement of listener cues has to do with the performance levels of listeners in past studies. In many of these studies the focus has been on whether or not the listener is capable of accurately identifying a particular acoustic event, hence, conditions have often been selected where few or no identification errors are made. While high performance levels are to some extent informative regarding the capabilities of listeners in these tasks, they are much less informative regarding the possible cues used by listeners. Consider, for example, the outcome of the present study if inner radius values were selected to yield perfect performance. The correlation of the listener's response with an optimal decision rule would necessarily be one, but, because there are three such rules, it would not be possible to distinguish among them. Indeed, it might not even be possible conclude that the listener used any one of these rules. If the values of the inner radius were chosen such that individual parameter distributions did not overlap (cf. Fig. 2), listeners could achieve perfect performance by basing decisions on a single acoustic parameter alone. This is why it is essential that listeners make errors when using regression analyses to evaluate listener cues, and why we have chosen the conditions of the present study to yield performance levels between 70% and 90% correct.

Returning to the original motivation for the study, we can evaluate the conjecture that listener judgments would correlate highly with the invariant relations among acoustic parameters that are unique to hollowness. The results appear to provide only partial support. Although many listeners do, indeed, appear to base decisions on such relations, a nearly equal number appear to base decisions on simple differences in frequency. Moreover, there are differences in the way listeners approach the task that depend on the material of the bar, and that change with replication of the same condition. Generally speaking, therefore, the results do not provide clear support for the use of intrinsic cues for hollowness.

One must question how this outcome might have been influenced by the sound synthesis used in this study. Real bars, after all, come in many shapes, sizes, and materials, they are not perfectly symmetric or homogeneous, and they are not typically struck at exactly the same point with exactly the same force. Might such differences prove advantageous for detecting hollowness, and might the synthesized sounds be perceived differently for this reason? We do not rule out the possibility, but we think it unlikely for both analytic and empirical reasons. First, we have specifically chosen conditions of the experiment to maximize the likelihood that listeners would detect the acoustic information intrinsic to hollowness. These choices were based on extensive performance simulations of the type described in Sec. III B, involving a wide range of bar materials and geometries and known listener sensitivity (see Lutfi, 2000). A fixed impulse was used as the driving force because it is generally most diagnostic regarding bar properties. And, all bar properties, except for length, were fixed so that no acoustic variation, other than that resulting from changing length, could serve to confound the change intrinsic to hollowness. We have also considered the related question as to whether our synthesized sounds can be reliably discriminated from real bar sounds. Preliminary experiments involving direct comparisons by listeners suggest not (Lutfi and Oh, 1997); however, stronger evidence comes from experiments showing that listeners are insensitive to acoustic differences from real bar sounds far greater than those of our synthesized sounds (Lutfi and Oh, 1994).

While the possibility of more advantageous conditions for detection cannot be ruled out, it is instructive to consider why some listeners did not make better use of the information that was available to them in these conditions. Some insight is obtained by considering the effect of limited sensory resolution on judgments. The effect is potentially complex since it must depend on the listener's decision weights as well as the acoustic variation resulting from variation in bar parameters. We have relied, therefore, on an internal noise model to evaluate the potential interaction among these factors. An important outcome of this analysis is that the analytic solution for hollowness is highly vulnerable to the small perturbations in the acoustic parameters that would be associated with listener internal noise. The result is that judgments following the analytic solution yield no large performance advantage over judgments based on differences in frequency alone, indeed, in some cases they yield worst performance. This outcome appears to provide an explanation for both the overall performance levels of our listeners and their specific pattern of decision weights.

That such small perturbations in the acoustic signal, as would be associated with internal noise, could have such profound effects on listener judgments may seem surprising; certainly in the context of the large variation associated with changes in bar length and whether the bar is hollow or solid. Such effects are possible, however, because the intrinsic acoustic relations that would serve to disambiguate hollow from solid bars are subtle and so often do not yield a significant detection advantage over simple differences in individual acoustic parameters (cf. Figs. 6 and 7). The effect is comparable to an analysis of variance where the interaction effects (the intrinsic relations) are small compared to the main effects of variables (the simple differences in individual acoustic parameters). The results underscore the importance of limited sensitivity as a factor in source identification, and raise the question as to whether there are other conditions where limited sensitivity for acoustic relations may similarly play a role. Few studies have specifically addressed the question. Moreover, while analytic treatments have identified the intrinsic acoustic information associated with specific source attributes, they have not generally indicated conditions where, based on known limits of human sensitivity, this information might offer a significant categorical advantage over simple statistical differences in individual acoustic parameters (Jenison, 1997; Kac, 1966; Wildes and Richards, 1988). For the present case, at least, some relevant data are provided by the results of simulations we have used to select stimulus conditions for our experiments (see Lutfi, 2000). These simulations indicate that the results of the present study are not atypical of what would be expected for the discrimination of other rudimentary bar attributes such as

shape, size, or material. In such cases, judgments based on the intrinsic acoustic relations are rarely expected to offer a detection advantage over simple differences in individual acoustic parameters when limited sensitivity is taken into account. For the discrimination of material and hollowness, the results of these simulations are corroborated by data from human listeners (Lutfi and Oh, 1997).

Clearly, many factors can be expected to influence how a listener recovers a particular source attribute from sound, not the least of which are the dynamics of the source, how it is excited, and how it might vary along other physical dimensions. But while the acoustic effect of these factors can be profound, it is often the small changes in the relation among acoustic parameters that serve to disambiguate sources. In such cases, as in the present study, basic limits in human sensitivity can affect not only what a listener hears, but also how they listen.

ACKNOWLEDGMENTS

I would like to thank Dr. Claudia Carello and especially Dr. Daniel J. Freed, and Dr. D. Wesley Grantham for helpful comments on an earlier version of the manuscript. This research was supported by a grant from the NIDCD (No. R01 CD01262-10).

[1]We had also experimented with perturbations in parameters related to the material of the bar (density and elasticity). For these parameters, however, the resultant variation among acoustic parameters was too highly correlated to permit reliable estimates of listener decision weights.

[2]Specifically, the two regression weights in each case are given by the two-element vector $\mathbf{w}=(\mathbf{X}^T\mathbf{X})^{-1}\mathbf{X}^T\mathbf{y}$, where $\mathbf{y}$ is a column vector giving the listener's response on each trial, $\mathbf{X}$ has two columns corresponding to the interval differences for $\log \tau_n$ and $\log \upsilon_n$ on each trial, and $\mathbf{X}^T$ denotes the transposition of $\mathbf{X}$.

[3]These values may be underestimates as they come from conditions where there is minimal uncertainty regarding the values of stimulus parameters from trial to trial. The possible influence of stimulus uncertainty for conditions most similar to those of the present study is discussed in Lutfi and Oh (1997).

[4]By way of example, the spectral acoustic cues analyzed by Kunkler-Peck and Turvey (2000) almost certainly were correlated with spatial acoustic cues afforded by large suspended plates.

Carello, C., Anderson, K. A., and Kunkler-Peck, A. J. (**1998**). ''Perception of object length by sound,'' Psychological Science **9**, 211–214.

Durlach, N. I., Braida, L. D., and Ito, Y. (**1986**). ''Towards a model for discrimination of broadband signals,'' J. Acoust. Soc. Am. **80**, 63–72.

Freed, D. J. (**1990**). ''Auditory correlates of perceived mallet hardness for a set of recorded percussive sound events,'' J. Acoust. Soc. Am. **87**, 311–322.

Gibson, J. J. (**1966**). *The Senses Considered as Perceptual Systems* (Houghton–Mifflin, Boston).

Jenison, R. L. (**1997**). ''On acoustic information for motion,'' Ecological Psychol. **9**, 131–151.

Jesteadt, W., Wier, C. C., and Green, D. M. (**1977**). ''Intensity discrimination as a function of frequency and sensation level,'' J. Acoust. Soc. Am. **61**, 169–177.

Kac, M. (**1966**). ''Can one hear the shape of a drum?,'' Mathematics Monthly **13**, 21–23.

Kinsler, L. E., and Frey, A. R. (**1962**). *Fundamentals of Acoustics* (Wiley, New York), pp. 55–78.

Kunkler-Peck, A. J., and Turvey, M. T. (**2000**). ''Hearing shape,'' J. Exp. Psychol. **26**, 279–294.

Lakatos, S., McAdams, S., and Causse, R. (**1997**). ''The representation of auditory source characteristics: Simple geometric form,'' Percept. Psychophys. **59**, 1180–1190.

Li, X., Logan, R. J., and Pastore, R. E. (**1991**). ''Perception of acoustic source characteristics: Walking sounds,'' J. Acoust. Soc. Am. **90**, 3036–3049.

Lutfi, R. A. (**1995**). ''Correlation coefficients and correlation ratios as estimates of observer weights in multiple-observation tasks,'' J. Acoust. Soc. Am. **97**, 1333–1334.

Lutfi, R. A. (**2000**). ''Source uncertainty, decision weights, and internal noise as factors in auditory identification of a simple resonant source,'' Abstracts of the Association for Research in Otolaryngology **23**, 171.

Lutfi, R. A., and Oh, E. (**1994**). ''Auditory discrimination based on the physical dynamics of a tuning fork,'' J. Acoust. Soc. Am. **95**, 2967.

Lutfi, R. A., and Oh, E. (**1995**). ''Auditory detection of changes in mass density and elasticity of a tuning fork,'' J. Acoust. Soc. Am. **97**, 3330.

Lutfi, R. A., and Oh, E. (**1997**). ''Auditory discrimination of material changes in a struck-clamped bar,'' J. Acoust. Soc. Am. **102**, 3647–3656.

Morse, P. M., and Ingard, K. U. (**1968**). *Theoretical Acoustics* (Princeton University Press, Princeton, NJ), pp. 175–191.

Repp, B. H. (**1987**). ''The sound of two hands clapping: An exploratory study,'' J. Acoust. Soc. Am. **81**, 1100–1109.

Van Heuven, V. J., and Van Den Broecke, M. P. R. (**1979**). ''Auditory discrimination of rise and decay times in tone and noise bursts,'' J. Acoust. Soc. Am. **66**, 1308–1315.

Warren, W. H., and Verbrugge, R. R. (**1984**). ''Auditory perception of breaking and bouncing events: A case study in ecological acoustics,'' J. Exp. Psychol. **10**, 704–712.

Wier, C. C., Jesteadt, W., and Green, D. M. (**1977**). ''Frequency discrimination as a function of frequency and sensation level,'' J. Acoust. Soc. Am. **61**, 178–184.

Wildes, R., and Richards, W. (**1988**). ''Recovering material properties from sound,'' in *Natural Computation*, edited by W. Richards (MIT, Cambridge, MA), pp. 356–363.

Winkler, R. L., and Hays, W. L. (**1975**). *Statistics: Probability, Inference, and Decision* (Holt, Rinehart, and Winston, New York), pp. 683–695.

Interaural correlation sensitivity

John F. Culling,[a] H. Steven Colburn, and Matthew Spurchise
Department of Biomedical Engineering, Boston University, 44 Cummington Street, Boston, Massachusetts 02215

(Received 30 June 2000; revised 8 December 2000; accepted 3 May 2001)

Sensitivity to differences in interaural correlation was measured for 1.3-ERB-wide bands of noise using a 2IFC task at six frequencies: 250, 500, 750, 1000, 1250, and 1500 Hz. The sensitivity index, d', was measured for discriminations between a number of fixed pairs of correlation values. Cumulative d' functions were derived for each frequency and condition. The d' for discriminating any two values of correlation may be recovered from the cumulative d' function by the difference between cumulative d''s for these values. Two conditions were employed: the noisebands were either presented in isolation (narrow-band condition) or in the context of broad, contiguous flanking bands of correlated noise (fringed condition). The cumulative d' functions showed greater sensitivity to differences in correlation close to 1 than close to 0 at low frequencies, but this difference was less pronounced in the fringed condition. Also, a more linear relationship was observed when cumulative d' was plotted as a function of the equivalent signal-to-noise ratio (SNR) in dB for each correlation value, rather than directly against correlation. The equivalent SNR was the SNR at which the interaural correlation in an NoSπ stimulus would equal the interaural correlation of the noise used in the experiment. The maximum cumulative d' declined above 750 Hz. This decline was steeper for the fringed than for the narrow-band condition. For the narrow-band condition, the total cumulative d' was variable across listeners. All cumulative d' functions were closely fitted using a simple two-parameter function. The complete data sets, averaged across listeners, from the fringed and narrow-band conditions were fitted using functions to describe the changes in these parameters over frequency, in order to produce an interpolated family of curves that describe sensitivity at frequencies between those tested. These curves predict the spectra recovered by the binaural system when complex sounds, such as speech, are masked by noise. [DOI: 10.1121/1.1383296]

PACS numbers: 43.66.Ba, 43.66.Dc, 43.66.Pn [DWG]

I. INTRODUCTION

Several theories of binaural unmasking have emphasized the role of interaural correlation (Gabriel and Colburn, 1981; Durlach *et al.*, 1986; Koehnke *et al.*, 1986; Jain *et al.*, 1991; Culling and Summerfield, 1995; Bernstein and Trahiotis, 1992, 1996a, b). These authors have suggested that when an out-of-phase signal is added to a more intense, in-phase noise (NoSπ) the interaural correlation of the stimulus is reduced at the signal frequency, and this reduction is detected by the listener and heard as a faint tone, or, if the noise is sufficiently narrow band, as a broadening of the sound image. As pointed out by Jain *et al.*, provided the signal is less intense than the masker, the reduction in correlation is monotonically related to the strength of the signal; the more intense the signal, the less the interaural correlation. This fact raises the possibility that listeners may be able to use interaural decorrelation as a reliable index of the signal intensity, as well as just for signal detection. Discrimination of the intensities of different components of a complex signal is often important in sound identification. In particular, speech recognition requires accurate estimation of the first formant frequency, which is vital for the identification of many speech sounds. The estimation process is thought to be dependent upon the relative intensities of the group of peripherally-resolved harmonics in that frequency region, so an ability to discriminate different degrees of decorrelation would go some way towards explaining the binaural intelligibility level difference (Licklider, 1948; Carhart *et al.*, 1969a, b; Levitt and Rabiner, 1967a, b; Bronkhorst and Plomp, 1988).

Despite the importance of correlation discrimination, only a few papers have investigated listeners' ability to discriminate correlations (Pollack and Trittipoe, 1959a, b; Gabriel and Colburn, 1981; Grantham, 1982; Koehnke *et al.*, 1986; Jain *et al.*, 1991; Akeroyd and Summerfield, 1999), and all but one of these investigations reported discrimination for a reference correlation of 1.0 (and occasionally 0.0). The single exception is Pollack and Trittipoe's pair of articles, which measured correlation difference limens against seven reference values.[1] In their first article, these authors studied sensitivity to decorrelation for broadband sounds. They found that the difference limen was considerably smaller for correlations close to unity than for those close to zero. In their second article, they low- and high-pass filtered their stimuli in order to determine the role of different frequency regions. The latter study concluded that the most important frequency region was in the vicinity of 850 Hz for

[a]Author to whom correspondence should be addressed. Correspondence address: School of Psychology, Cardiff University, P.O. Box 901, Cardiff CF10 3YG, U.K. Electronic mail: cullingj@cardiff.ac.uk

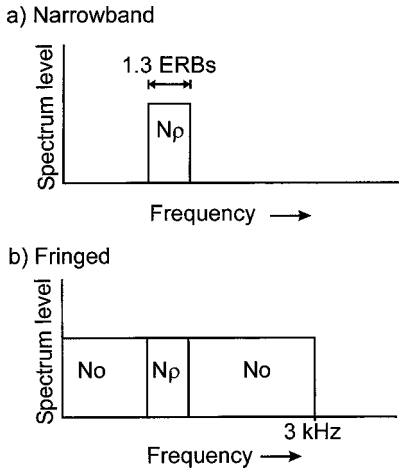

FIG. 1. Schematic illustration of the stimuli used in the two conditions.

a reference correlation of 0.0, but was 1700 Hz for a reference correlation of 0.5.

The present article aims to provide some primary data on interaural correlation sensitivity as a function of reference correlation and to encapsulate it into a simple usable form, so that it may be employed in predictions of the intensity difference limens of binaurally unmasked signals, binaural intelligibility level differences, dichotic-pitch percepts, and so forth. To this end, we have employed d' as a more flexible sensitivity measure than the difference limen and produced cumulative d' functions at each frequency. In an approach similar to that used by Baker *et al.* (1998) to describe the changing shape of auditory filters as a function of signal level and frequency, the data have been fitted with an eight-parameter function that controls the size and shape of the cumulative d' curve as a function of frequency.

II. EXPERIMENT

A. Stimuli

For each presentation interval, the 409.6-ms stimulus was generated immediately prior to its presentation using a TDT System 2 array processor at a 20-kHz sampling rate. Filtering was performed in the frequency domain, giving steep ''brick-wall'' cutoffs. All stimuli contained a target band that was 1.3 ERBs wide (Moore and Glasberg, 1983). The target band was centered at 250, 500, 750, 1000, 1250, or 1500 Hz. The corresponding bandwidths were, therefore, 68, 100, 133, 167, 202, and 238 Hz, respectively. The interaural correlation of the target band of noise was precisely controlled by mixing two orthogonal noises in appropriate ratios. Orthogonalization was achieved using the Gram–Schmidt procedure (Wozencraft and Jacobs, 1965), in which the correlated vector of two noises is subtracted from one of them and the waveform rescaled to the original amplitude (see the Appendix). Note that this contrasts with previous experiments in which randomly chosen samples of noise were combined; in those experiments the resulting correlation values in individual trials were randomly distributed about a chosen mean.

Two different conditions were investigated (see Fig. 1). In the narrow-band condition, the target band was presented in isolation. In the fringed condition, the target band was between spectrally contiguous flanking bands of noise (of the same spectrum level) which were also freshly generated for each trial. The flanking bands extended the spectrum of the stimulus and resulted in a flat spectrum between 0 and 3 kHz. The flanking bands had an interaural correlation of 1.0. The interaural correlations of the target bands depended on the condition. For each condition, a set of 15 pairs of correlation values were compared (Table I). In the narrow-band condition the values were clustered more closely than in the fringed condition at correlations close to 1.0. The differences in correlation were chosen (after pilot testing) to keep most of the d' values in the 0.5–2 range, which can be measured accurately without a very large number of trials. The interstimulus interval was determined by the processing time of the AP2. For the broadband condition, this was 1.2 s, while for the narrow-band condition it was 600 ms.

The sounds were presented to listeners in an IAC sound-attenuating chamber via a TDT System 2 rig (DD1 analog-to-digital converter; FT5-9 reconstruction filters; twin PA4 programmable attenuators; HB5 headphone amplifier) and Sennheiser HD414 headphones at an overall sound level of 87 dB(A) in the fringed condition. Sound levels were calibrated using a B&K artificial ear (type 4152), without flat-plate adapter, a B&K 1-in. microphone (type 4131) and B&K sound level meter (type 2203).

B. Procedure

Nine listeners took part in the study. Eight listeners, including the third author, completed both wideband and narrow-band conditions. Since five of these eight performed

TABLE I. The values of correlation, ρ, that listeners were required to discriminate in the fringed conditions and in the narrow-band condition.

Fringed							Narrow band						
	Higher correlation							Higher correlation					
Lower correlation	0.3	0.5	0.65	0.8	0.9	1.0	Lower correlation	0.5	0.7	0.8	0.9	0.95	1.0
0.0	√	√	√				0.0	√	√	√			
0.3		√	√	√			0.5		√	√	√		
0.5			√	√	√		0.7			√	√	√	
0.65				√	√	√	0.8				√	√	√
0.8					√	√	0.9					√	√
0.9						√	0.95						√

relatively poorly in the narrow-band condition, the first author also contributed data in this condition. The listeners were advised at the start of the experiment to attend to different cues in different conditions and to use the cue resulting in best performance. In the case of narrow-band stimuli, listeners were advised to listen for changes in the breadth of the sound image within their heads. This advice was given because the narrow-band condition was similar to a narrow-band binaural unmasking experiment, in which the width of image is well known to be the optimal cue (Colburn, 1996, p. 344). In the fringed condition, they were advised to listen for a whistling sound (like a tone in a broadband binaural unmasking experiment) within the background noise which would be louder in one interval than in the other. In addition to this advice, listeners received trial-by-trial feedback throughout the experiment and during up to 20 h of practice prior to data collection.

Each d' value was measured for a given pair of correlation values (ρ_1 and ρ_2) by presenting listeners with a 55-trial series of 2I-FC comparisons. The results of the first five trials in each series were discarded. Each two-interval trial consisted of freshly generated examples of each of the two correlations under test. Since the fringed conditions required listeners to focus on a particular frequency region, the listeners were supplied with cueing sounds which directed their attention. These sounds were narrow-band stimuli at the same frequency with $\rho=1.0$ and they were presented once at the beginning of a series, then after the first five (discarded) trials and then every ten trials thereafter. During a 40- to 60-min session listeners completed all 15 series of comparisons for a given frequency and condition. The first five or six sessions in the fringed and narrow-band conditions were treated as practice for those conditions. Two sets of d' values were collected for each listener at each frequency and in each condition. In the first session for a given frequency and condition, the pairs of correlations used in each run had values that increased from one run to the next (from upper left to bottom right in Table I), while in the second session the sequence of runs was reversed. Each pair of $d'_{(\rho_1,\rho_2)}$ values was then averaged.

C. Results

1. Summarizing the data

Due to the large quantity of data collected, two different methods of summarizing data were developed. One method involved fitting values and the other functions to the raw d' data. Both used the ''simplex'' multi-parameter fitting procedure (Press *et al.*, 1988, Chap. 10.4) in order to fit cumulative d' values or functions directly to the raw d' measurements. Each fit assumed that listeners made use of a unidimensional decision axis for detecting correlation differences. Given this assumption (and equal variance), measured values of d' should be additive:

$$d'_{(\rho_1,\rho_3)}=d'_{(\rho_1,\rho_2)}+d'_{(\rho_2,\rho_3)} \tag{1}$$

where $\rho_1\leqslant\rho_2\leqslant\rho_3$.

The reader will note from Table I that, assuming that d' is cumulative as expected, there is some redundancy in the data collected. For instance, we collected $d'_{(0.3,0.5)}$, $d'_{(0.5,0.65)}$ and $d'_{(0.3,0.65)}$. If d' is cumulative, the last of these should approximate the sum of the first two. When the simplex procedure was used to fit the data, the fitted values and functions were those most consistent with all the available data. The procedure works by postulating values for a set of parameters, such as the parameters of a fitted function or specific $d'_{(\rho,1)}$ values, predicting the data based on these parameters, and then comparing the predicted with the observed data. The sum-of-squared errors, SS, between the predicted and observed data are used to evaluate the settings of the parameters. The parameter values are then permuted and the evaluation repeated. This cycle continues until SS has been minimized. It is the method of parameter permutation which makes the simplex procedure an efficient multi-parameter fitting algorithm (for further details, see Press *et al.*, 1988, Chap. 10.4).

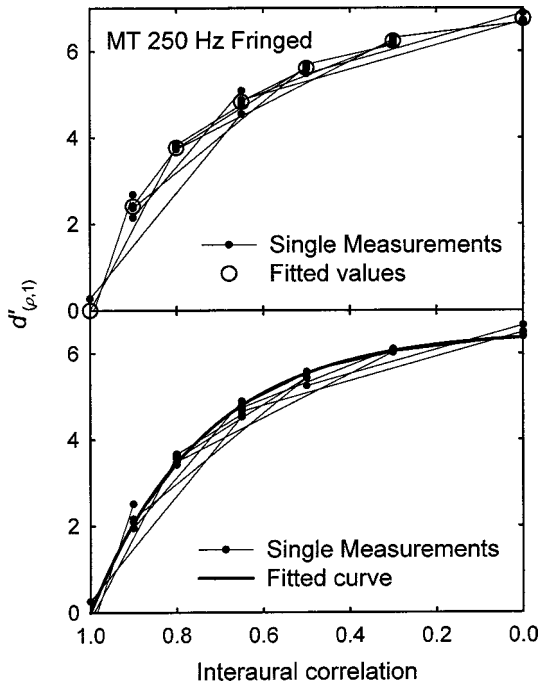

FIG. 2. Cumulative d' ($d'_{(\rho,1)}$) as a function of interaural correlation, ρ, for listener MT in the 250-Hz, fringed condition. The fitted $d'_{(\rho,1)}$ values are shown with large open circles (upper panel). The fitted function, created using Eq. (4), is shown with a thick line (lower panel). The individual measurements of d' taken from listener MT are shown on each panel using thin lines terminating in filled circles.

2. Cumulative sensitivity values

The first fitting procedure was used to fit six cumulative d' values, $d'_{(\rho,1)}$, to each set of 15 measured $d'_{(\rho_1,\rho_2)}$ values collected from a given listener, in a given condition (fringed/narrow band) and at a given frequency. $d'_{(\rho,1)}$ was evaluated for each nonunity value of ρ (e.g., 0.0, 0.3, 0.5, 0.65, 0.8, and 0.9). The results of this fitting procedure are illustrated by the large open circles in Figs. 2 and 3. Ideally, the individually measured values of $d'_{(\rho_1,\rho_2)}$ and the values of $d'_{(\rho,1)}$ derived from the fitting process should all observe Eq. (2):

$$d'_{(\rho_1,\rho_2)}=d'_{(\rho_1,1)}-d'_{(\rho_2,1)}. \tag{2}$$

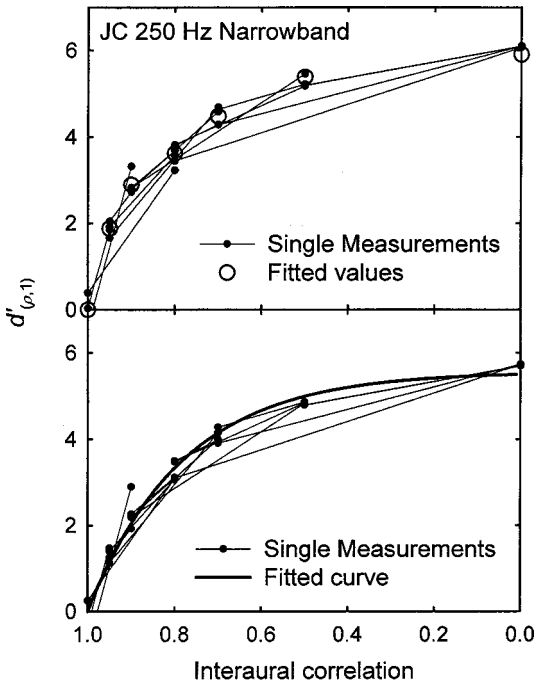

FIG. 3. As in Fig. 2, but for listener JC in the 250-Hz, narrow-band condition.

Deviation from this equivalence was assumed to represent a combination of measurement noise and suboptimal fitting of $d'_{(\rho,1)}$ values. Such deviation was therefore squared and summed across the 15 measured values of $d'_{(\rho_1,\rho_2)}$ to give the error term, SS, to be minimized by the fitting program.

The results of this fitting process can be seen in the large open symbols on the upper panels of Figs. 2 and 3. The thin lines terminated with filled circles represent the 15 $d'_{(\rho_1,\rho_2)}$ values to which the fit was made in each case. These lines are plotted between the appropriate correlation values on the abscissa, and their vertical extents correspond to the observed $d'_{(\rho_1,\rho_2)}$ values. Their vertical position minimizes the deviation between the filled symbols at each end and the corresponding open symbols. The total squared deviation across all these symbols therefore represents SS.

3. Correlation sensitivity as a function of correlation

The second fitting procedure was used to generate a summary of the form that appears in the thick curves on Figs. 2 and 3. These fits turned the same sets of 15 $d'_{(\rho_1,\rho_2)}$ values into curves describing cumulative d' as continuous functions. Continuous cumulative d' functions were fitted to the measured $d'_{(\rho_1,\rho_2)}$ values using the base equation:

$$d'_{(0,\rho)} = e^{(k\rho+n)} - e^{n}, \tag{3}$$

where k and n are fitted parameters. This equation was chosen because it always evaluates to zero at $\rho=0$, while the two parameters (in combination) control the rate of change of curvature and the value at $\rho=1$. Henceforth, an equivalent expression will be used for the change in correlation from $\rho=1$:

$$d'_{(\rho,1)} = e^{(k+n)} - e^{(k\rho+n)}. \tag{4}$$

The lower panels of Figs. 2 and 3 illustrate the quality of fit that is achieved using Eq. (4) for the fringed and narrow-band conditions, respectively. The thick lines are the fitted cumulative d' functions. Again, the fit minimized the squared errors between the observed $d'_{(\rho_1,\rho_2)}$ values and the differences between the $d'_{(\rho_1,1)}$ and $d'_{(\rho_2,1)}$ values from the fitted curve. The lower panels include the same thin lines terminated by filled symbols as the upper panels, but adjusted in vertical position, so that they reflect the quality fit achieved by the fitted functions.

As can be seen from Figs. 2 and 3, the quality of the fitted curve is acceptable. For the fit in Fig. 2, SS=1.90, slightly above the average value across all 17 data sets (1.51). In Fig. 3, an example of one of the poorest fits, SS =5.19. The high error is largely attributable to one unusually large d' measurement for the discrimination of correlations 0.9 and 1.0. Since the principle source of errors in the fits appeared to be noise in the measurements, Eq. (4) was adopted as a suitable fitting function to be used in the larger-scale fitting process to follow.

The functions in Figs. 2 and 3 are typical results for the dependence of $d'_{(\rho,1)}$ on 1-ρ, the reduction in correlation from unity. These results show the characteristically higher sensitivity to changes in ρ near unity correlation and the reduction in sensitivity near zero correlation. Performance in the fringed and narrow-band conditions are similar at 250 Hz in these examples. However, there are substantial variations across frequencies, between these two conditions and across listeners.

4. Correlation sensitivity at different frequencies

The thick curves in Figs. 4 and 5 show further functions fitted [using Eq. (4)] to the data at a single frequency for listeners RM and MS at each frequency tested. The symbols in Figs. 4 and 5 show the results of the first fitting procedure. These symbols show $d'_{(\rho,1)}$ at each of the correlation values used in the experiments.

Note that listener RM in Fig. 4 performed poorly in the narrow-band condition compared to the fringed condition while for listener MS in Fig. 5 the reverse occurred. Cumulative d' values between $\rho=0$ and $\rho=1$ ($d'_{(0,1)}$) are provided for each listener at each frequency in both conditions in Table II. Since the first five listeners in the table seemed to perform worse than the last four in the narrow-band condition, we chose to characterize their data separately in subsequent analyses (the ordering of the listeners in Table II does not reflect the order in which they participated in the experiment).

In general, performance decreases above 750 Hz. In addition, for most cases (and for 20 of 24 comparisons at the three lowest frequencies), the fringed stimuli have higher $d'_{(0,1)}$ values than the equivalent narrow-band conditions. This difference is remarkable because the fringes carry no additional information and could be considered simply as masking the information in the target band. However, as discussed below, the task is subjectively easier for most listeners with the fringe present.

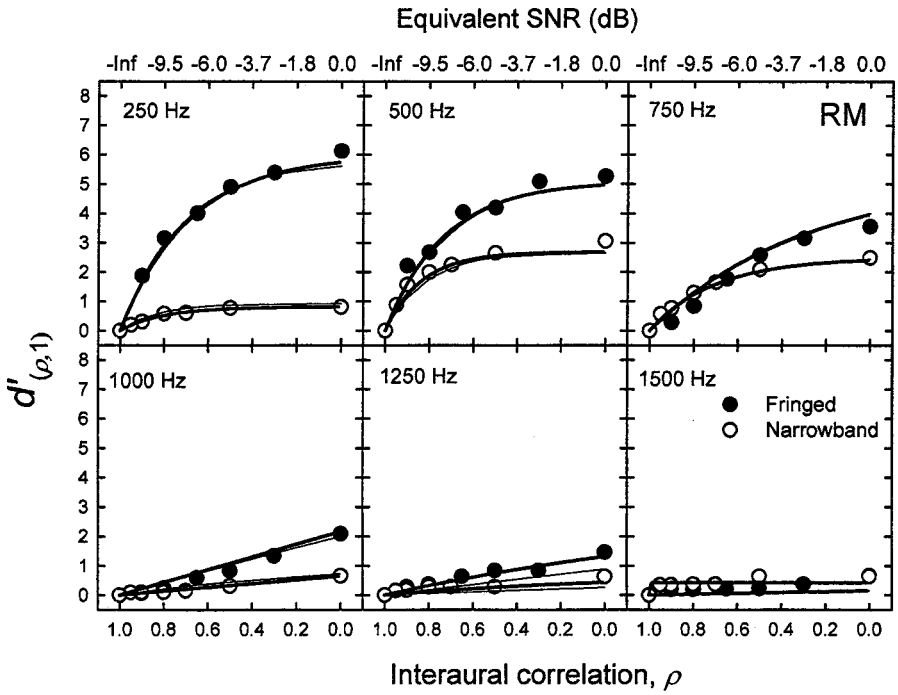

FIG. 4. Cumulative $d'(d'_{(\rho,1)})$ as a function of interaural correlation, ρ, at six frequencies for listener RM. The symbols are $d'_{(\rho,1)}$ values fitted to the raw data at each frequency. The thick lines are $d'_{(\rho,1)}$ functions fitted to the raw data at each frequency using Eq. (4). The thin lines are $d'_{(\rho,1)}$ functions fitted using the across-frequency fitting method based on Eqs. (5) and (6). The open circles and intersecting lines are for the narrow-band condition. The filled circles and intersecting lines are for the fringed condition. The top abscissa is marked with the signal-to-noise ratios that would produce the corresponding correlation values from the bottom abscissa if signal and noise were added in the NoSπ binaural configuration.

5. Correlation sensitivity as a function of correlation and frequency

Having established that Eq. (4) is well suited to represent the growth of cumulative d', it was also used to fit the data across different frequencies. Here, the parameters n and k were not fitted separately for each frequency. Instead, the data from all frequencies were fitted simultaneously using functions [Eqs. (5) and (6)] that related n and k to frequency,[2] f:

$$k = \frac{r_k}{1 + e^{s_k(f - t_k)}} + a_k, \tag{5}$$

$$n = \frac{r_n}{1 + e^{s_n(f - t_n)}} + a_n. \tag{6}$$

These functions are both logistic curves providing a sigmoidal transition between two asymptotic values. The parameters r, s, t, and a are free parameters of the fit: r controls the absolute range of the parameter, s controls the steepness of the transition in its value as a function of f, t controls the frequency of the transition, and a controls the asymptotic value as $f \to \infty$. The choice of logistic functions was motivated by the reduction in the binaural masking level difference (BMLD) and in correlation sensitivity at high frequen-

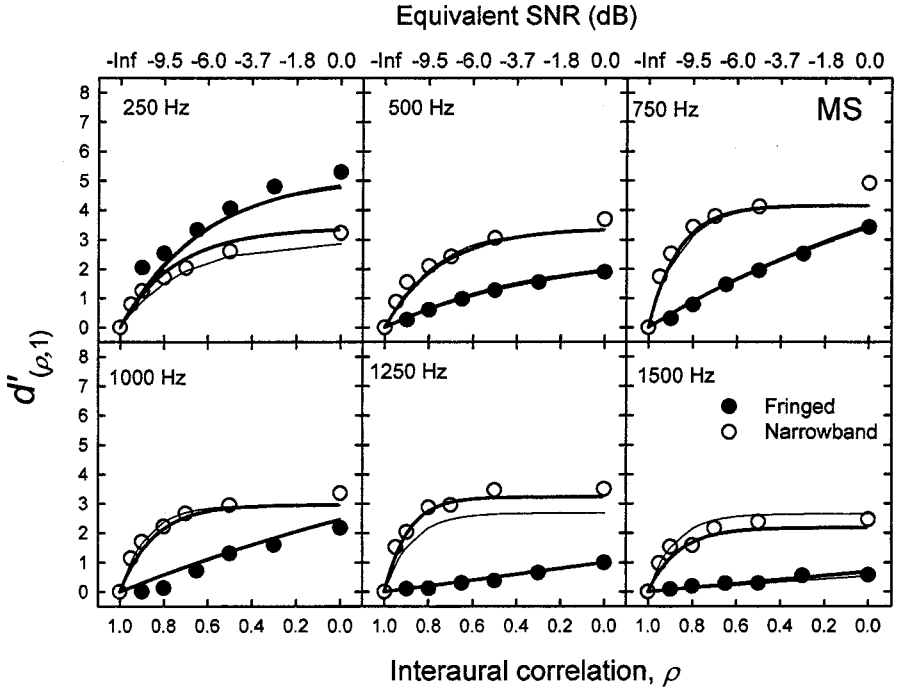

FIG. 5. As in Fig. 4, but for listener MS.

TABLE II. $d'_{(0,1)}$ for each listener in each condition and at each center frequency, fitted separately to the raw data for each listener, condition, and frequency using Eq. (4).

	Fringed center frequency (Hz)						Narrow-band center frequency (Hz)					
Listener	250	500	750	1000	1250	1500	250	500	750	1000	1250	1500
HF	1.26	2.96	2.13	1.43	0.88	0.35	0.75	1.62	1.46	0.51	1.25	0.65
KL	4.09	5.48	3.97	3.68	3.01	1.02	1.46	1.37	1.07	1.16	0.45	0.70
KV	3.26	4.48	3.30	1.92	0.80	0.54	1.51	1.45	2.94	2.43	2.03	1.62
RM	6.11	5.26	3.55	2.09	1.46	0.68	0.81	3.06	2.49	0.66	0.46	0.64
SH	3.38	3.84	3.87	5.14	0.94	0.24	1.43	2.30	3.38	1.37	1.48	1.71
AM	4.22	4.35	2.90	2.45	2.18	1.17	4.65	5.09	3.13	2.65	2.58	1.39
JC							6.26	6.26	6.71	4.78	3.15	3.17
MS	5.29	1.89	3.42	2.17	0.99	0.57	3.22	3.68	4.92	3.35	3.49	2.46
MT	6.75	7.72	8.07	5.81	4.21	2.99	4.94	4.58	3.68	2.82	3.22	2.93
$\bar{x}$	4.30	4.50	3.90	3.09	1.81	0.95	2.78	3.26	3.31	2.19	2.01	1.70
σ	1.75	1.75	1.78	1.62	1.24	0.88	2.05	1.76	1.71	1.40	1.17	0.97

cies (Durlach and Colburn, 1978, p. 431). Since the BMLD for broadband maskers asymptotes to around 3 dB at high frequencies, it was thought advisable to use a function which could produce the same sort of behavior. In the event, it was found that these two logistic functions could, in combination, produce a very wide range of surfaces, including surfaces with nonmonotonic changes over frequency (e.g., Fig. 8).

Figures 4 and 5 show fits to $d'_{(\rho_1,\rho_2)}$ values from individual listeners, while Figs. 6–8 show fits to averaged $d'_{(\rho_1,\rho_2)}$ values. These fits turned 90 data points (15 discriminations×6 frequencies) into a surface representing $d'_{(\rho,1)}$ as a continuous function of correlation and frequency. For the fringed data (Fig. 6), the pattern of results was similar across listeners, so the $d'_{(\rho_1,\rho_2)}$ values were averaged across all listeners before making a fit. For the narrow-band data, however, four listeners performed markedly better than the other five. These two groups were averaged and fitted separately (Figs. 7 and 8). The thin curves in Figs. 4 and 5 come from fits to the data from the individual listeners concerned. It can be seen that the fit closely approximates the $d'_{(\rho,1)}$ curves derived at individual frequencies (thick curves).

Table III shows the parameters that were fitted to the three averaged data sets. Figures 6–8 show surface plots for the growth in $d'_{(\rho,1)}$ as functions of both frequency and the signal-to-noise ratio required to produce the appropriate correlation when a signal is added to noise in the NoSπ configuration. The ''equivalent signal-to-noise ratio'' was calculated using Eq. (7), adapted from Jain *et al.* [1991, Eq. (1)]. Figure 6 shows this function for the averaged data from the fringed condition. Figure 7 show the function for the four more sensitive listeners in the narrowband condition. Figure 8 shows the same function for the five less sensitive listeners:

$$\mathrm{SNR} = 10\log_{10}\left(\frac{1-\rho}{1+\rho}\right). \tag{7}$$

III. DISCUSSION

The principal interest of the study was to find out how well listeners can discriminate different degrees of interaural correlation across a range of different correlations, rather than just at correlations close to one. The motivation for the study was to further the understanding of binaural masking

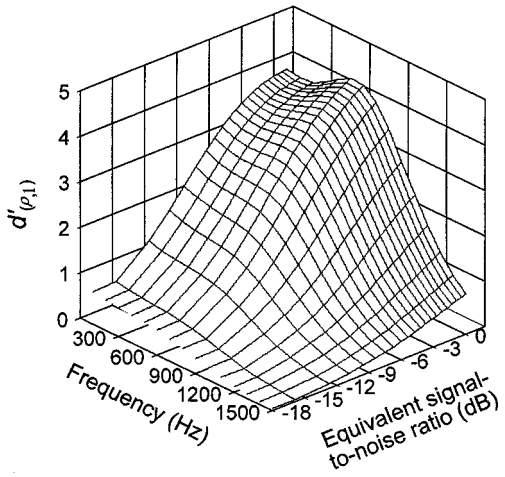

FIG. 6. Surface plot of the growth of $d'_{(\rho,1)}$ as a function of equivalent SNR and frequency for the *fringed* data. Surface lines are drawn at intervals of 100 Hz in the frequency dimension and 0.05 in the correlation dimension.

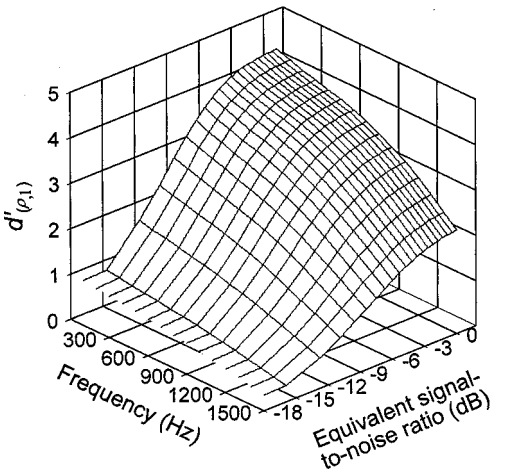

FIG. 7. As in Fig. 6, but plotted for the four *more sensitive* listeners in the *narrow-band* condition.

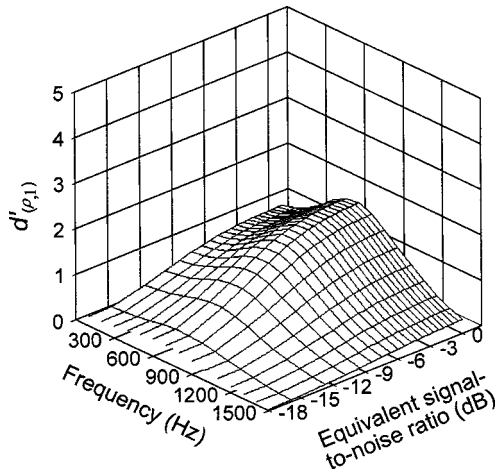

FIG. 8. As in Fig. 7, but plotted for the four *less sensitive* listeners in the *narrow-band* condition.

release and its application to speech recognition. The two main conditions of the experiment were consequently modeled upon the two most common types of BMLD experiment, in which a tonal signal is presented interaurally out-of-phase against either a diotic broadband noise or a diotic narrow-band noise.

A. Relationship to previous discrimination and BMLD experiments

If, as a number of authors have argued, binaural masking release is mediated by the detection of interaural decorrelation, the present stimuli should provide similar cues to the corresponding BMLD stimuli, since the tone in a BMLD stimulus usually acts to decorrelate the noise in its immediate frequency region. The fringed condition, in which listeners discriminated different interaural correlations of a target band of noise embedded within a broadband diotic noise, corresponds to BMLD conditions with a broadband masker. The narrow-band condition, in which only the target band was present, corresponds to BMLD conditions with a narrow-band masker. Consistent with these ideas, the listeners' experience of the task was quite different in the two conditions and closely resembled the experience of listening to the corresponding BMLD stimuli.

TABLE III. The fitted logistic parameters that control the values of n and k across frequency to produce an optimum fit with the 90 raw data points in each condition (15 measurements at six frequencies). These parameters determine the surfaces plotted in Figs. 6–8.

	Logistic parameter			
$d'_{(\rho,1)}$ parameter	r	s	t	a
Fringed (mean data)				
k	4.68	0.0027	666	0.023
n	3.17	−0.0047	560	−2.75
Narrow band (4 more sensitive listeners)				
k	6.67	0.0010	1500	0.010
n	2.25	−0.0020	708	−4.37
Narrow band (5 less sensitive listeners)				
k	5.97	0.0021	1500	0.018
n	1.81	−0.0062	423	−5.92

For the broadband stimuli, listeners heard a ''warbling tone'' or ''whistling noise'' standing out from the background in much the same way as listeners hear the target tone standing out form the noise in a broadband-BMLD stimulus. The whistling sound was louder the less correlated the target band was. For the narrow-band stimuli, listeners heard a broadening of the sound image for stimuli of lower correlation, just as listeners perceive a broadened sound image when a tone is added out-of-phase to a diotic narrow-band noise. The image was broader the less correlated the noise band was. Jain *et al.* (1991) performed a similar experiment, although with narrower target bands and only with correlations close to one. They compared the just-noticeable-differences (jnd's) in correlation (from one) of their 10-Hz-wide target bands with the differences in correlation at detection threshold for corresponding BMLD stimuli. They found these values to be very similar, indicating that detection of the decorrelation was sufficient to explain listeners' ability to detect the tones in the $\mathrm{No}S\pi$ condition of a BMLD experiment.

Taking threshold as $d'_{(\rho,1)}=1$, and rearranging Eq. (4), one obtains the following equation for the jnd from unity correlation where n and k are the fitting parameters discussed earlier:

$$\mathrm{jnd}_1=\frac{-\ln(1-e^{-(k+n)})}{k}. \tag{8}$$

From this equation, jnd's at 500 Hz are calculated to be 0.09 for the fringed condition, 0.06 for the four more sensitive listeners in the narrow-band condition, and 0.13 for the five less sensitive listeners in the narrow-band condition. These thresholds are substantially higher than those reported previously (Pollack and Trittipoe, 1959a, b; Gabriel and Colburn, 1981; Durlach *et al.*, 1986; Koehnke *et al.*, 1986; Jain *et al.*, 1991; Bernstein and Trahiotis, 1992, 1996a, b). It is difficult to determine the reasons for the poorer sensitivity observed here, since there are a large number of differences between the current experimental design and the methods used by other authors. The listeners were probably less well trained and had to contend with stimuli within a session which varied much more widely in correlation than in experiments that only measured jnd's close to a correlation of 1.0. Another factor is the use of batteries of 50 stimulus pairs with a fixed pair of correlation values. Such batteries may be relatively difficult for listeners to optimize their performance on since they may become disheartened when contending with a battery they find difficult, and may find it hard to maintain concentration on a battery they find very easy. The design of our experiments attempted to minimize such effects by testing pairs of correlation values that yielded values of d' in the 0.5–2 area for most listeners; nonetheless our experiments appear to underestimate sensitivity when the results are compared to measurements using other methods.

The present experiment measured sensitivity to differences in correlation as a function of reference correlation, rather than just at a correlation of one. The only published

precedents for this approach are the experiments of Pollack and Trittipoe (1959a, b), who decorrelated broadband, high-pass, or low-pass noise. Although they showed that listeners were sensitive to differences in correlation across a range of correlation values, their stimuli were not similar to those used in BMLD experiments. When the entire spectrum of a noise is decorrelated, listeners tend to hear a broadening of the sound image (as with narrow-band stimuli). Nonetheless, their results were similar to those observed here, in that listeners were found to be very sensitive to differences in correlation close to one and less sensitive at discriminating lower values of correlation. It is interesting to note that while listeners varied widely in their ability to discriminate the correlations of narrow-band stimuli, they all gave very similar patterns for the fringed stimuli. This difference in listener variability also seems to correspond with BMLD data; Bernstein *et al.* (1998) found that some listeners were much better than others at narrow-band BMLD experiments, while performance in broadband noise was relatively consistent across listeners.

B. Relationship to the binaural intelligibility level difference

The binaural intelligibility level difference is very similar to the BMLD, except that listeners are required to identify speech sounds and words, rather than to detect tones. However, a distinguishing feature of this task is that speech sounds are broadband and, when added in the NoSπ configuration to noise, they decorrelate all frequency channels to some extent. In order for listeners to make good use of their binaural systems, therefore, it is important that the encoding of embedded signals is graded. That is to say, that the perceptual salience of a speech component, recovered from noise by the binaural system, needs to grow progressively as the speech component becomes more intense. If this were not the case, the system might detect the presence of the speech, but be unable to discern its spectral profile.

The data of Pollack and Trittipoe show that listeners are far more sensitive to changes in correlation near to a correlation of unity than to changes at lower levels of correlation—a highly nonlinear relationship. The narrow-band conditions of the present experiment gave data that were consistent with this finding. However, in the fringed condition, we investigated listeners' ability to make such discriminations in a situation more similar to the understanding of speech in noise, where each subband will display a different interaural correlation. When listeners were required to discriminate different levels of correlation in one subband of a broadband sound, they not only heard the decorrelation in a different way (as a separate sound) but they were more sensitive to changes in correlation at low reference values, than when, as in the narrow-band condition, the whole stimulus was decorrelated. A novel finding is that, while the cumulative d' function in the narrow-band condition is curved at low frequencies, indicating greater sensitivity close to a correlation of one, the function straightens out to give a near-linear relationship at 1 kHz between interaural correlation and cumulative d' (Figs. 4 and 5). Further, when correlation is reexpressed as the equivalent SNR in dB, the relationship between $d'_{(\rho,1)}$ and SNR is quite linear for equivalent signal-to-noise ratios between about -18 and -6 dB even at low frequencies and in both the fringed and narrow-band conditions (Figs. 6 and 7). Thus, a fixed increment in d' corresponds to a fixed increment in dB (equivalent SNR) over a range of masked-signal intensities. In other words, where the levels of embedded signals are discriminated by virtue of the different degrees of decorrelation they generate, Weber's law appears to hold, at least approximately.

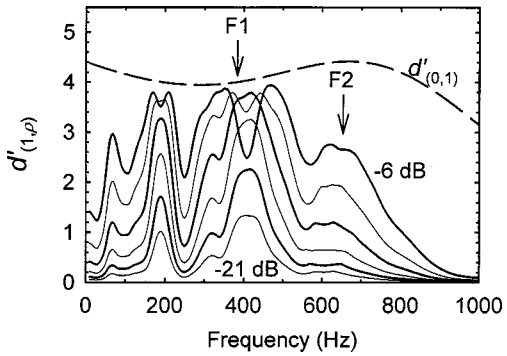

FIG. 9. Perceptually scaled spectra predicted to be recovered by the binaural system for the synthesized vowel /ɔ/ as in "bored" (British English) at overall SNRs from -6 to -21 dB in 3-dB steps. The vowel was synthesized by a Klatt (1980) cascade formant synthesizer ($F1=385$ Hz, $F2=657$ Hz) and added to speech-shaped noise in the NoSπ configuration. Frequency selectivity was modeled using the Patterson *et al.* (1987, 1988) gammatone filterbank. Corresponding frequency channels from the left- and right-hand channels were cross correlated in the range ± 2 ms. The maximum product-moment correlation was converted into $d'_{(\rho,1)}$ using Eqs. (4)–(6) and the parameters derived from the fringed stimuli in Table III. The dashed line shows the maximum cumulative sensitivity $d'_{(0,1)}$ as a function of frequency derived from Eqs. (4)–(6).

The results of the fringed condition therefore support the idea that listeners may be able to use the spectral profile of interaural correlation as an index of the intensity of otherwise masked components of speech. Figure 9 illustrates the implications of these data for the internal representation of speech, as provided by the binaural system. The figure shows a recovered spectrum for the synthesized vowel /ɔ/ (as in "bored") embedded in speech-shaped masking noise in the NoSπ binaural configuration. The vowel was synthesized with the Klatt (1980) cascade vowel synthesizer at a fundamental frequency of 100 Hz and with first and second formants at 385 and 657 Hz, respectively. This vowel was selected for its low second formant; the second formants of many vowels would be outside the range of frequencies for which the binaural system is most effective. Interaural coherence (the maximum interaural cross correlation calculated in the range ± 2 ms) was measured in corresponding frequency channels of a stereo pair of gammatone filterbanks (Patterson *et al.*, 1987, 1988), and these values were converted to $d'_{(\rho,1)}$, using Eqs. (4)–(6). The parameters employed (Table III) were from fitting the pooled results of the fringed condition.

Figure 9 shows a roughly linear growth of peaks in $d'_{(\rho,1)}$ corresponding to spectral features with increasing SNR. Spectral peaks attributable to both harmonics and formant peaks are visible at a succession of SNRs. The most promi-

nent peak, especially at the lower SNRs, is for the fourth harmonic, just above $F1$.

C. Relationship to dichotic pitches and other binaural phenomena

The parameters for fringed stimuli in Table III can be used in combination with Eqs. (4)–(6) in order to generate predictions of the binaurally recovered spectrum for any binaural stimulus. For instance, these parameters and equations were used by Culling (2000) in order to generate the perceptually-scaled binaurally-recovered spectra for various Fourcin-pitch stimuli in his ''revised'' mE-C model (Culling, 2000, Figs. 6 and 7). This method of prediction can be applied to any dichotic pitch stimulus in order to determine whether the correct pitch can be predicted from the pattern of interaural coherence across frequency.

IV. CONCLUSION

The results of the present experiment indicate that listeners can discriminate different levels of interaural correlation, especially in the context of a broadband (fringed) stimulus. It is possible that the information provided by spectral variation in correlation may account for listeners' improved understanding of the speech when listening to the NoSπ binaural configuration compared to the NoSo configuration.

ACKNOWLEDGMENTS

This work was supported by the MRC and NIDCD Grant No. DC00100.

APPENDIX: THE GRAM–SCHMIDT PROCEDURE

The Gram–Schmidt procedure allows one to start with one set of functions and to generate a second set of functions that are pairwise orthogonal (uncorrelated with each other) and normalized to have equal energy. This new set of functions is useful in several ways: all the original functions can be written as linear combinations of the new functions; all of the new functions have the same energy; all the new functions are uncorrelated.

The following procedure is simplified here to the case with only two waveforms in the set, because that is all we need. The procedure can be generalized to any number of waveforms. Also, we present the case of discrete-time (sampled) waveforms. In Wozencraft and Jacobs (1965), the case of continuous-time waveforms is presented.

Assume two N-sample nonzero waveforms a and b, that are not perfectly correlated with each other, such as two independent samples of noise. Represent them as $\{a_i\}$ and $\{b_i\}$ for $i=1,...,N$. There are four steps, outlined next, that result in two orthogonal waveforms $\{a_i\}$ and $\{b_i'\}$, where $\{b_i'\}$ has identical rms power to, and zero correlation with, $\{a_i\}$. Following this orthogonalization procedure, a and b' can be mixed according to Eq. (A1), to give a precise correlation, ρ, between a and the mixture m:

$$m_i=\rho a_i+\sqrt{1-\rho^2}b_i' \quad \text{for } i=1,...,N. \tag{A1}$$

The Gram–Schmidt orthogonalization procedure has four steps as follows:

(1) Calculate the rms power of a and b:

$$a_{\text{rms}}=\sqrt{\frac{\Sigma_{i=1}^{N}a_i^2}{N}}, \tag{A2}$$

$$b_{\text{rms}}=\sqrt{\frac{\Sigma_{i=1}^{N}b_i^2}{N}}. \tag{A3}$$

(2) Calculate the correlation, ρ_{ab}, between a and b:

$$\rho_{ab}=\frac{\Sigma_{i=1}^{N}a_ib_i}{a_{\text{rms}}b_{\text{rms}}}. \tag{A4}$$

(3) Subtract the correlated component of a from a scaled version of b. This subtraction yields c, which has zero correlation with a:

$$c_i=\frac{a_{\text{rms}}}{b_{\text{rms}}}b_i-\rho_{ab}a_i \quad \text{for } i=1,...,N. \tag{A5}$$

(4) Scale c to get b' which has zero correlation with, and equal power to, a:

$$b_i'=\frac{c_i}{\sqrt{1-\rho_{ab}^2}}. \tag{A6}$$

The entire process of generating b' may be summarized as

$$b_i'=\frac{a_{\text{rms}}}{b_{\text{rms}}\sqrt{1-\rho_{ab}^2}}b_i-\frac{\rho_{ab}}{\sqrt{1-\rho_{ab}^2}}a_i \quad \text{for } i=1,...,N. \tag{A7}$$

[1]Caution should be observed in reading Pollack and Trittipoe's paper, since the authors did not calculate their correlation values correctly (Jeffress and Robinson, 1962). A corrected version of some of their data may be found in Durlach *et al.* (1986, Table II).

[2]When fits were made for all frequencies simultaneously, the search space was found to contain many local minima, often producing similar surfaces by using quite different parameter sets. It was, therefore, found necessary to restart the ''simplex'' search algorithm repeatedly with randomly perturbed starting parameters in order to guarantee an optimal fit.

Akeroyd, M. A., and Summerfield, A. Q. (**1999**). ''A binaural analog of gap detection,'' J. Acoust. Soc. Am. **105**, 2807–2820.

Baker, R. J., Rosen, S., and Darling, A. M. (**1998**). ''An efficient characterisation of human auditory filtering across level and frequency that is also physiologically reasonable,'' in *Psychological and Physiological Advances in Hearing*, edited by A. R. Palmer, A. Rees, A. Q. Summerfield, and R. Meddis (Whurr, London), pp. 81–88.

Bernstein, L. R., and Trahiotis, C. (**1992**). ''Discrimination of interaural envelope correlation and its relation to binaural unmasking at high frequencies,'' J. Acoust. Soc. Am. **91**, 306–316.

Bernstein, L. R., and Trahiotis, C. (**1996a**). ''On the use of the normalized correlation as an index of interaural envelope correlation,'' J. Acoust. Soc. Am. **100**, 1754–1763.

Bernstein, L. R., and Trahiotis, C. (**1996b**). ''The normalized correlation: Accounting for binaural detection across center frequency,'' J. Acoust. Soc. Am. **100**, 306–316.

Bernstein, L. R., Trahiotis, C., and Hyde, E. L. (**1998**). ''Inter-individual differences in binaural detection of low-frequency of high-frequency tonal signals masked by narrow-band or broadband noise,'' J. Acoust. Soc. Am. **103**, 2069–2078.

Bronkhorst, A. W., and Plomp, R. (**1988**). ''The effect of head-induced interaural time and level differences on speech intelligibility in noise,'' J. Acoust. Soc. Am. **83**, 1508–1516.

Carhart, R., Tillman, T. W., and Greetis, K. R. (**1969a**). ''Release from multiple maskers: Effects of interaural time disparities,'' J. Acoust. Soc. Am. **45**, 411–418.
Carhart, R., Tillman, T. W., and Greetis, K. R. (**1969b**). ''Perceptual masking in multiple sound backgrounds,'' J. Acoust. Soc. Am. **45**, 694–703.
Colburn, H. S. (**1996**). ''Computational models of binaural processing,'' in *Auditory Computation*, edited by H. Hawkins, T. McMullen, A. Popper, and R. Fay (Springer, New York).
Culling, J. F., and Summerfield, Q. (**1995**). ''Perceptual segregation of concurrent speech sounds: Absence of across-frequency grouping by common interaural delay,'' J. Acoust. Soc. Am. **98**, 785–797.
Culling, J. F. (**2000**). ''Dichotic pitches as illusions of binaural unmasking. III. The existence regions of the Fourcin pitch,'' J. Acoust. Soc. Am. **107**, 2201–2208.
Durlach, N. I., and Colburn, H. S. (**1978**). ''Binaural phenomena,'' in *Handbook of Perception*, edited by E. C. Carterette and M. P. Friedman (Academic, New York), Vol. IV.
Durlach, N. I., Gabriel, K. J., Colburn, H. S., and Trahiotis, C. (**1986**). ''Interaural correlation discrimination. II. Relation to binaural unmasking,'' J. Acoust. Soc. Am. **79**, 1548–1557.
Gabriel, K. J., and Colburn, H. S. (**1981**). ''Interaural correlation discrimination. I. Bandwidth and level dependence,'' J. Acoust. Soc. Am. **69**, 1394–1401.
Grantham, D. W. (**1982**). ''Detectability of time-varying interaural correlation in narrow-band noise stimuli,'' J. Acoust. Soc. Am. **72**, 1178–1184.
Jain, M., Gallagher, D. T., Koehnke, J., and Colburn, H. S. (**1991**). ''Fringed correlation discrimination and binaural detection,'' J. Acoust. Soc. Am. **90**, 1918–1926.
Jeffress, L. A., and Robinson, D. E. (**1962**). ''Formulas for the coefficient of correlation for noise,'' J. Acoust. Soc. Am. **34**, 1658–1659.
Klatt, D. H. (**1980**). ''Software for a cascade/parallel formant synthesizer,'' J. Acoust. Soc. Am. **67**, 838–844.
Koehnke, J., Colburn, H. S., and Durlach, N. I. (**1986**). ''Performance in several binaural-interaction experiments,'' J. Acoust. Soc. Am. **79**, 1558–1562.
Levitt, H., and Rabiner, L. R. (**1967a**). ''Binaural release from masking for speech and gain in intelligibility,'' J. Acoust. Soc. Am. **42**, 601–608.
Levitt, H., and Rabiner, L. R. (**1967b**). ''Predicting binaural gain in intelligibility and release from masking for speech,'' J. Acoust. Soc. Am. **42**, 820–829.
Licklider, J. C. R. (**1948**). ''The influence of interaural phase relations upon the masking of speech by white noise,'' J. Acoust. Soc. Am. **20**, 150–159.
Moore, B. C. J., and Glasberg, B. R. (**1983**). ''Suggested formulae for calculating auditory-filter bandwidths and excitation patterns,'' J. Acoust. Soc. Am. **74**, 750–753.
Patterson, R. D., Nimmo-Smith, I., Holdsworth, J., and Rice, P. (**1987**). ''An efficient auditory filterbank based on the gammatone function,'' paper presented to the IOC speech group on auditory modelling at the Royal Signal Research Establishment, 14–15 Dec.
Patterson, R. D., Nimmo-Smith, I., Holdsworth, J., and Rice, P. (**1988**). ''Spiral vos final report, Part A: The auditory filter bank,'' Cambridge Electronic Design, Contract Report (APU 2341).
Pollack, I., and Trittipoe, W. J. (**1959a**). ''Binaural listening and interaural noise cross correlation,'' J. Acoust. Soc. Am. **31**, 1250–1252.
Pollack, I., and Trittipoe, W. J. (**1959b**). ''Interaural noise correlation: Examination of variables,'' J. Acoust. Soc. Am. **31**, 1616–1618.
Press, W. H., Flannery, B. P., Teukolsky, S. A., and Vetterling, W. T. (**1988**). *Numerical Recipes in C* (Cambridge U. P., Cambridge).
Wozencraft, J. M., and Jacobs, I. M. (**1965**). *Principles of Communication Engineering* (Wiley, New York).

Second-order temporal modulation transfer functions

Christian Lorenzi,[a] Catherine Soares, and Thomas Vonner
Laboratoire de Psychologie Expérimentale, UMR CNRS 8581, Institut de Psychologie, Université René Descartes Paris V, 71, Av. Edouard Vaillant, 92774 Boulogne-Billancourt, France

(Received 3 October 2000; revised 15 February 2001; accepted 3 May 2001)

Detection thresholds were measured for a sinusoidal modulation applied to the modulation depth of a sinusoidally amplitude-modulated (SAM) white noise carrier as a function of the frequency of the modulation applied to the modulation depth (referred to as f'_m). The SAM noise acted therefore as a ''carrier'' stimulus of frequency f_m, and sinusoidal modulation of the SAM-noise modulation depth generated two additional components in the modulation spectrum: $f_m - f'_m$ and $f_m + f'_m$. The tracking variable was the modulation depth of the sinusoidal variation applied to the ''carrier'' modulation depth. The resulting ''second-order'' temporal modulation transfer functions (TMTFs) measured on four listeners for ''carrier'' modulation frequencies f_m of 16, 64, and 256 Hz display a low-pass segment followed by a plateau. This indicates that sensitivity to fluctuations in the strength of amplitude modulation is best for fluctuation rates f'_m below about 2–4 Hz when using broadband noise carriers. Measurements of masked modulation detection thresholds for the lower and upper modulation sideband suggest that this capacity is possibly related to the detection of a beat in the sound's temporal envelope. The results appear qualitatively consistent with the predictions of an envelope detector model consisting of a low-pass filtering stage followed by a decision stage. Unlike listeners' performance, a modulation filterbank model using Q values $\geqslant 2$ should predict that second-order modulation detection thresholds should decrease at high values of f'_m due to the spectral resolution of the modulation sidebands (in the modulation domain). This suggests that, if such modulation filters do exist, their selectivity is poor. In the latter case, the Q value of modulation filters would have to be less than 2. This estimate of modulation filter selectivity is consistent with the results of a previous study using a modulation-masking paradigm [S. D. Ewert and T. Dau, J. Acoust. Soc. Am. **108**, 1181–1196 (2000)]. © *2001 Acoustical Society of America.* [DOI: 10.1121/1.1383295]

PACS numbers: 43.66.Ba, 43.66.Dc, 43.66.Mk [SPB]

I. INTRODUCTION

The characteristics of the temporal envelope of acoustic stimuli may play a crucial role in sound identification. Sensitivity to the temporal envelope is traditionally assessed by measuring a temporal modulation transfer function (TMTF), which displays the ability of listeners to detect sinusoidal amplitude modulation (SAM) as a function of the frequency of that modulation (Viemeister, 1977, 1979). Empirically, TMTFs are obtained by measuring the modulation depth, *m*, necessary to just detect the modulation of a SAM carrier as a function of the modulation frequency, f_m. Usually, TMTFs are measured with broadband noise carriers so as to preclude the use of spectral cues, since the modulation of broadband noise does not affect its (flat) long-term power spectrum. Such TMTFs are generally low pass in shape: Sensitivity to SAM is relatively independent of modulation frequency up to 50–60 Hz, and decreases progressively at higher modulation frequencies (e.g., Rodenburg, 1977; Viemeister, 1977, 1979; Bacon and Viemeister, 1985).

A traditional model used to account for the characteristics of these TMTFs is the ''linear envelope detector model.'' This model assumes that the temporal envelope of the stimuli is smoothed by a single (first-order) low-pass filter operating at a central (postcochlear) level (Viemeister, 1979; Forrest and Green, 1987; Strickland and Viemeister, 1996; Lorenzi *et al.*, 1999). Amplitude fluctuations faster than the cutoff frequency of this low-pass filter (estimated to be about 60–150 Hz) are attenuated, and this may explain why SAM detection thresholds increase at high modulation frequencies. The results of adaptation and masking experiments performed with amplitude-modulated sounds (e.g., Kay and Matthews, 1972; Green, 1976; Green and Kay, 1974; Tansley and Suffield, 1983; Houtgast, 1989; Bacon and Grantham, 1989; Yost *et al.*, 1989; Dau *et al.*, 1997a, b, 1999) have, however, suggested an alternative model, the so-called ''modulation filterbank,'' in which modulation filters, each tuned to a given modulation frequency, decompose the temporal envelope of sounds at a central level. In this approach, modulation at a given frequency is assumed to be detected by monitoring the output of a modulation filter tuned close to that frequency (e.g., Lorenzi *et al.*, 1995). In recent implementations of the modulation filterbank (Dau *et al.*, 1997a, b, 1999; Ewert and Dau, 2000), the bandwidth of modulation filters is assumed to increase with increasing center modulation frequency. The Q value of such filters was initially assumed to be equal to 2 for center modulation frequencies above 10 Hz (Dau *et al.*, 1997a, b, 1999). However, in a more recent implementation of the modulation filterbank, the Q value of such filters is assumed to be equal to 1 for center modulation frequencies up to 64 Hz (Ewert and Dau, 2000).

[a]Electronic mail: christian.lorenzi@psycho.univ-paris5.fr

 0001-4966/2001/110(2)/1030/9/$18.00

For a broadband noise carrier, the power of the intrinsic random fluctuations in the noise carrier appearing at the output of a modulation filter will therefore increase with increasing filter bandwidth (that is, with increasing filter center modulation frequency). The masking effect produced by these intrinsic random fluctuations will increase at high modulation frequencies, and this may explain why SAM detection thresholds degrade at high modulation frequencies (Dau *et al.*, 1997a, b, 1999). To date, the controversy regarding the nature of the temporal processor (a modulation filterbank or a linear envelope detector) still persists.

TMTFs measured with pure-tone carriers are quite different in shape (e.g., Zwicker, 1952; Viemeister, 1979; Fassel, 1994; Dau, 1996; Kohlrausch *et al.*, 2000). For a 5-kHz pure-tone carrier, SAM detection thresholds are constant between about 10–100 Hz. They increase in the range 100–400 Hz at a rate of 3–4 dB/oct. Finally, detection thresholds decrease abruptly above about 400 Hz (Dau, 1996; Kohlrausch *et al.*, 2000). The modulation frequency at which this rolloff occurs increases with the carrier frequency (Fassel and Püschel, 1993; Fassel, 1994; Dau, 1996; Kohlrausch *et al.*, 2000). The high-frequency region of these TMTFs can be understood easily on the basis of the auditory filter bank model (Fletcher, 1940; Patterson, 1976): (1) At high modulation frequencies, the sidebands of the modulated signal are spectrally resolved. Instead of basing decisions on the amplitude fluctuations, subjects listen to additional tones. (2) Tone-on-tone experiments (Dau, 1996; Kohlrausch *et al.*, 2000) also show that, at high modulation frequencies, SAM detection thresholds are determined by the masked threshold of the spectrally resolved lower sideband. (3) Finally, the progressive broadening of auditory filter bandwidths at high (audio) frequencies explains why the modulation frequency at which the rolloff occurs increases with the carrier frequency.

Thus, the characteristics of TMTFs measured with pure-tone carriers indirectly support the existence of a limited spectral decomposition of complex sounds within a bank of channels (the auditory filterbank). With this idea in mind, we suggest to test the existence of filters in the modulation domain by measuring ''second-order'' amplitude modulation detection thresholds, that is detection thresholds of a sinusoidal modulation applied to the modulation depth of a SAM white noise carrier (instead of unmodulated white noise or pure-tone carriers). The tracking variable would be the modulation depth of the sinusoidal variation applied to the modulation depth of the SAM noise. The effects of applying sinusoidal modulation to the depth of a SAM noise are illustrated in Fig. 1. In the top panel, the left signal corresponds to the waveform of a white noise sinusoidally amplitude modulated at a modulation frequency f_m of 16 Hz, with a constant modulation depth *m* of 50%. The right signal also corresponds to the waveform of a white noise sinusoidally amplitude modulated at $f_m = 16$ Hz; however, sinusoidal modulation has been applied to its modulation depth *m* at a frequency f'_m of 8 Hz, with a modulation depth m' of 50%. The cyclic variation in modulation depth produces a beat in its temporal envelope at a slow rate equal to f'_m. The bottom panel of Fig. 1 shows the modulation spectra of the noise

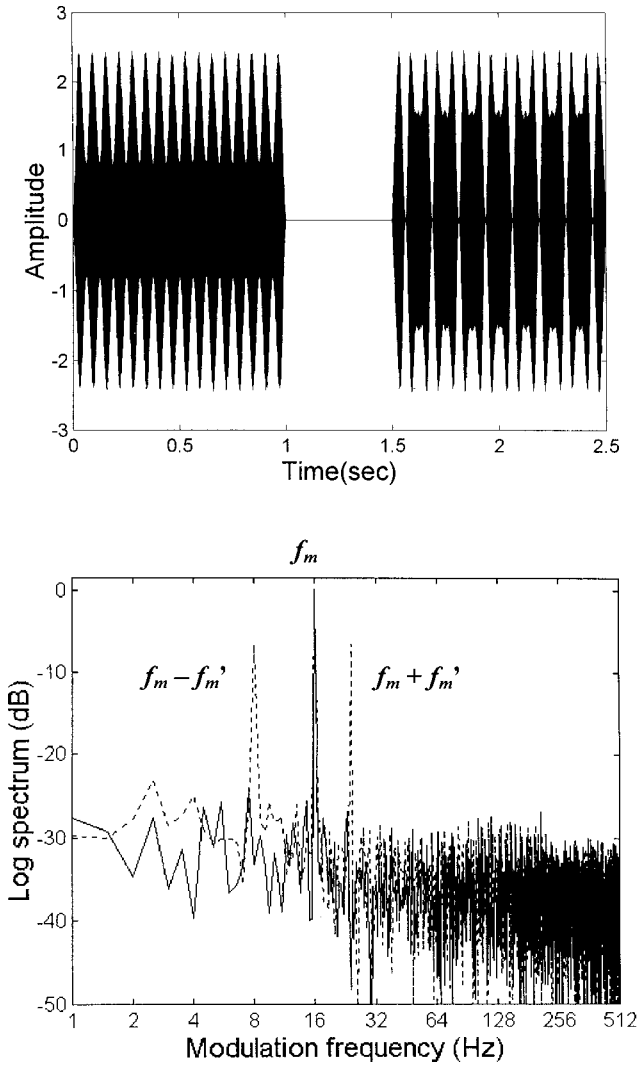

FIG. 1. Top panel, left signal: Waveform of a white noise with first-order SAM ($f_m = 16$ Hz, $m = 0.5$). Top panel, right signal: Waveform of a white noise with second-order SAM ($f_m = 16$ Hz, $f'_m = 8$ Hz, $m = m' = 0.5$). Bottom panel: Modulation spectra of the noises with first-order (continuous line) and second-order (dotted line) SAM.

with first-order (solid line) and second-order (dotted line) SAM (the modulation spectra are calculated for only one realization of the noise carrier). As expected, sinusoidal modulation applied to the modulation depth of a SAM noise carrier generates sidebands at $f_m - f'_m$ and $f_m + f'_m$ in the modulation spectrum of the ''second-order'' SAM noise.

By analogy with the results obtained with TMTFs measured with pure-tone carriers, the modulation filterbank model should therefore predict the following. (1) Second-order SAM detection thresholds should decrease at high second-order modulation frequencies f'_m (because modulation sidebands should be spectrally resolved at high second-order modulation frequencies if modulation filters are *narrowly* tuned). (2) Knowing that low SAM components are better detected than high ones (as a consequence of better modulation tuning to low modulation center frequencies), second-order SAM detection thresholds should be determined by the masked threshold of the resolved lower modulation sideband [masking being considered in the modulation domain, since previous studies (e.g., Bacon and Grantham,

1989; Houtgast, 1989) have shown that the detectability of SAM is generally degraded when a masking SAM is added]. (3) The second-order modulation frequency at which the rolloff should occur in the second-order TMTF should increase with increasing ''carrier'' modulation frequency, f_m (because of the progressive broadening of modulation filters at high center modulation frequencies). By contrast, the linear envelope detector model—a sluggish mechanism that smoothes fast fluctuations—should predict that detectability of second-order SAM should degrade at high second-order modulation frequencies. A very similar method was used by Rees and Kay (1985) to test the hypothesis of selective channels in the frequency-modulation domain.

The present study reports second-order TMTFs measured at various ''carrier'' modulation frequencies in normal-hearing listeners. First-order TMTFs and masked modulation detection thresholds were also collected to evaluate the extent to which second-order modulation sensitivity relates to first-order modulation sensitivity, modulation masking, and envelope beat detection. The empirical results are finally discussed in light of the modulation filterbank and linear envelope detector models.

II. METHOD

A. Listeners

Four listeners with normal hearing (mean age=20 years; s.d.=1 year), CS, TV, SA, and SR, participated in the experiments.

B. Stimuli and procedures

All psychophysical experiments were controlled by a PC-compatible computer. All stimuli were generated using a 16-bit D/A converter at a sampling frequency of 44.1 kHz, and were delivered binaurally (i.e., diotically) via Sennheiser HD 565 earphones. Statistically independent realizations of the white noise were used in all experiments (i.e., within and between trials). Listeners were tested individually in a soundproof booth. In each task, the standard and target stimuli were presented at 75 dB SPL. Both the standard and target stimuli had a 2-s duration including 25-ms rise/fall times shaped using a raised-cosine function. The interstimulus interval was 1 s.

1. First-order TMTFs

The listener's task was to detect the presence of a SAM applied to a white noise carrier. On each trial, a standard and a target stimulus were successively presented in random order to the listener. The standard, $S(t)$, consisted of a white noise $n(t)$. The target, $T(t)$, consisted of a white noise carrier sinusoidally amplitude modulated at a given modulation frequency. The expression describing the target was

$$T(t)=c[1+m\sin(2\pi f_m t+\phi_m)]n(t), \tag{1}$$

where m is the modulation depth ($0\leqslant m\leqslant 1$), f_m is the modulation frequency (f_m was 4, 8, 16, 32, 64, 128, or 256 Hz), and ϕ_m is the starting phase of the modulation, randomized on each interval. The term c is a multiplicative compensation term (Viemeister, 1979) set such that the overall power was the same in all intervals. The expression for c is given as follows:

$$c=[1+m^2/2]^{-0.5}. \tag{2}$$

The SAM detection thresholds were obtained using an adaptive two-interval, two-alternative forced-choice (2I, 2AFC) procedure with a two-down, one-up stepping rule that estimates the modulation depth, m, necessary for 70.7% correct detection. The listener's task was to identify the interval containing the modulation. Visual feedback about the correct interval was given after each trial. The step size of m variation corresponded initially to a factor of 1.585 [4 dB in decibels ($20\log m$)]; it was reduced to 1.26 (2 dB) after the first two reversals. The mean of the last 10 reversals in a block of 16 reversals was taken as the threshold estimate for that block (in %). For each listener and each modulation frequency, thresholds presented here are based upon three estimates. The worst threshold that can be measured corresponds to a modulation depth of 1 (100% modulated noise). The closer to 0 the value of m, the better the detection threshold.

2. Second-order TMTFs

The listener's task was to detect the presence of a sinusoidal modulation applied to the modulation depth of a SAM white noise carrier. On each trial, a standard and a target stimulus were successively presented in random order to the listener. The standard, $S(t)$, consisted of a white noise $n(t)$ sinusoidally amplitude modulated at a given modulation frequency f_m, with a fixed modulation depth m of 50% ($m=0.5$). The expression describing the standard was

$$S(t)=[1+m\sin(2\pi f_m t+\phi_m)]n(t) \tag{3}$$

where ϕ_m represents the starting phase of the modulation, randomized on each interval. The target, $T(t)$, consisted of a white noise sinusoidally amplitude modulated at a given modulation frequency f_m. Modulation depth was sinusoidally amplitude modulated at a given modulation frequency f'_m. The expression describing the target was

$$T(t)=[1+[0.5+m'\sin(2\pi f'_m t+\phi'_m)]\times\sin(2\pi f_m t+\phi'_m)]n(t), \tag{4}$$

where m' is the modulation depth of modulation-depth variation ($0\leqslant m'\leqslant 0.5$), f'_m is the frequency of modulation depth variation, and ϕ'_m represents the starting phase of modulations, randomized on each interval. The overall power was the same in all intervals. f_m (the ''carrier'' modulation frequency) was 16, 64, or 256 Hz. f'_m (the ''second-order'' modulation frequency) was 1, 2, 3, 4, 5, 6, 7, 8, or 11 Hz when f_m was 16 Hz; 3, 4, 6, 8, 11, 16, 23, 32, or 45 Hz when f_m was 64 Hz; and 3, 8, 23, 32, 45, 64, 90, 128, or 181 Hz when f_m was 256 Hz.

Second-order SAM detection thresholds were obtained using an adaptive 2I, 2AFC procedure with a two-down, one-up stepping rule that estimates the second-order modulation depth, m', necessary for 70.7% correct detection. The listener's task was to identify the interval containing the *modulation of modulation*. Visual feedback about the correct interval was given after each trial. The step size of m' varia-

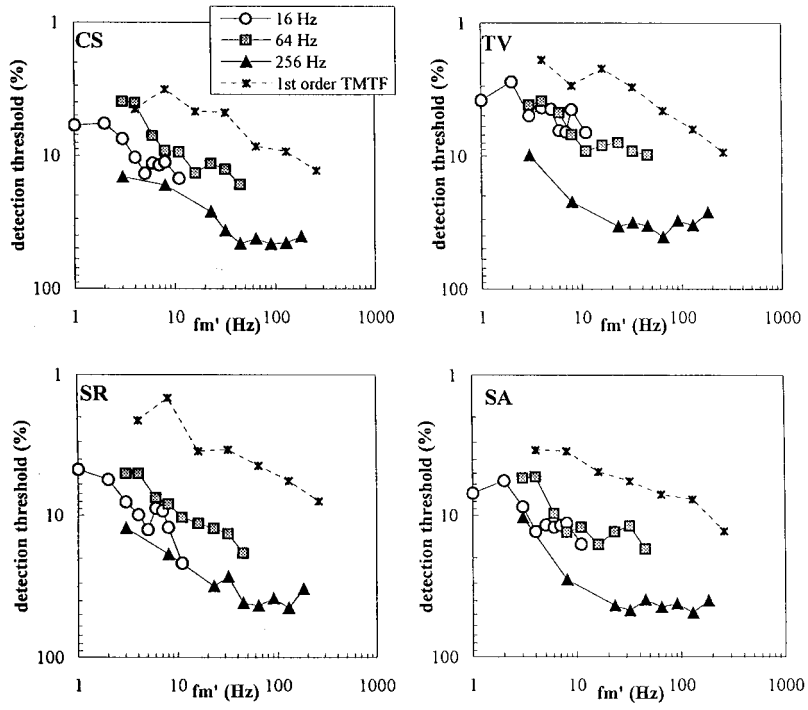

FIG. 2. Individual data for the four listeners. In each panel, the second-order TMTFs measured for $f_m = 16$ Hz (solid lines with unfilled circles), $f_m = 64$ Hz (solid lines with gray squares), and $f_m = 256$ Hz (solid lines with black triangles) are plotted along with the first-order TMTF (dotted lines with stars). In the case of second-order TMTFs, the ordinate indicates second-order modulation depth at threshold m', and the abscissa represents f'_m; in the case of first-order TMTFs, the ordinate indicates first-order modulation depth at threshold m, and the abscissa represents f_m. In both cases, modulation depth at threshold is expressed in linear units, and plotted on a logarithmic scale.

tion corresponded initially to a factor of 1.585 [4 dB in decibels ($20 \log m'$)]; this factor was reduced to 1.26 (2 dB) after the first two reversals. The mean of the last 10 reversals in a block of 16 reversals was taken as the threshold estimate for that block (in %). For each listener and experimental condition, thresholds presented here are based upon three estimates. The worst threshold that can be measured corresponds to a modulation depth m' of 0.5. The closer to 0 the value of m', the better the detection threshold.

3. Masked modulation detection thresholds

The third task was based on a classical "modulation masking" paradigm. On each trial, a standard and a target stimulus were successively presented in random order to the listener. The standard consisted of a white noise $n(t)$ sinusoidally amplitude modulated at the masker frequency. The expression describing the standard (i.e., the masker alone) was

$$S(t) = c[1 + m_{\text{mask}} \cos(2\pi f_{\text{mask}} t)]n(t), \tag{5}$$

where m_{mask} is the modulation depth of the masker, fixed at 0.5, f_{mask} is the masker modulation frequency, and c is a multiplicative compensation term defined below. f_{mask} was fixed at 64 Hz. The target consisted of white noise carrier $n(t)$ amplitude modulated by the sum of two sinusoidal modulators, the signal and the masker modulators. The expression describing the target (i.e., the signal-plus-masker waveform) was

$$T(t) = c[1 + m_{\text{mask}} \cos(2\pi f_{\text{mask}} t) + m_{\text{sig}} \cos(2\pi f_{\text{sig}} t)]n(t), \tag{6}$$

where m_{sig} is the modulation depth of the signal and f_{sig} is the signal modulation frequency. The masker and signal were in phase. The frequency f_{sig} was 32, 56, 61, 67, 72, or 96 Hz (the absolute spectral distance between signal and masker modulations was therefore of 3, 8, or 32 Hz, the signal modulation frequency being either below or above the masker modulation frequency). The term c is a compensation factor (Bacon and Grantham, 1989) set such that the overall power was the same in all intervals. The expression for c is given as follows:

$$c = [1 + (m_{\text{mask}}^2 + m_{\text{sig}}^2 + 2m_{\text{mask}} m_{\text{sig}})/2]^{-0.5}. \tag{7}$$

Masked modulation detection thresholds were obtained using an adaptive 2I, 2AFC procedure with a two-down, one-up stepping rule that estimates the signal modulation depth, m_{sig}, necessary for 70.7% correct detection. The listener's task was to choose the interval containing the signal modulation. Visual feedback as to the correct interval was given after each trial. The step size of m_{sig} variation corresponded initially to a factor of 1.585 (4 dB); this factor was reduced to 1.26 (2 dB) after the first two reversals. The mean of the last 10 reversals in a block of 16 reversals was taken as the threshold estimate for that block (in %). For each listener and experimental condition, thresholds presented here are based upon three estimates. The worst threshold that can be measured corresponds to a modulation depth of 0.5. The closer to 0 the value of m_{sig}, the better the detection threshold.

III. RESULTS

A. First- and second-order TMTFs

Individual and mean data for the four listeners are shown in Figs. 2 and 3, respectively. In each figure and each panel, the second-order TMTFs measured for $f_m = 16$ Hz (solid lines with unfilled circles), $f_m = 64$ Hz (solid lines with gray squares), and $f_m = 256$ Hz (solid lines with black triangles) are plotted along with the first-order TMTF (dotted lines with stars). In the case of second-order TMTFs, the

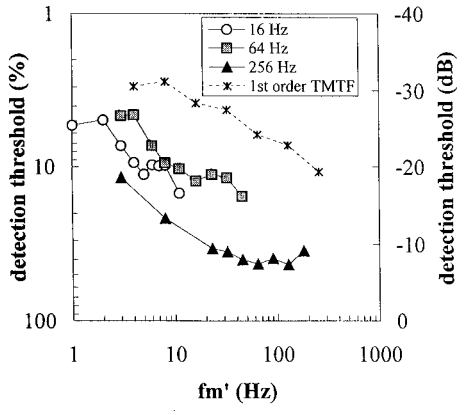

FIG. 3. Mean data for the four listeners. See Fig. 2 for legend details. The left ordinate shows modulation depth at threshold expressed in linear units ($100 \cdot m$), and plotted on a logarithmic scale. The right ordinate shows modulation depth at threshold expressed on a decibel scale ($20 \log m$).

ordinate indicates second-order modulation depth at threshold m', and the abscissa represents f'_m; in the case of first-order TMTFs, the ordinate indicates first-order modulation depth at threshold m, and the abscissa represents f_m. In Figs. 2 and 3, the left ordinate shows detection thresholds expressed in linear units ($100 \cdot m$) and plotted on a logarithmic scale; in Fig. 3 (mean data), the right ordinate shows detection thresholds expressed on a decibel scale ($20 \log m$), frequently used in previous studies. In agreement with previous studies (e.g., Viemeister, 1979; Bacon and Viemeister, 1985), first-order TMTFs display a typical low-pass characteristic (Fig. 3). Sensitivity is reduced by about 3 dB (in $20 \log m$) at $f_m = 64$ Hz; from this frequency, sensitivity decreases at a rate of about 3 dB/oct. For each "carrier" modulation frequency f_m, second-order TMTFs display a low-pass segment: For the lowest second-order modulation frequencies f'_m, sensitivity to second-order modulation remains constant up to 2 Hz when $f_m = 16$ Hz, and up to 4 Hz when $f_m = 64$ Hz; from these frequencies, sensitivity decreases with increasing f'_m. When $f_m = 256$ Hz, sensitivity decreases from 3 Hz (the lowest value of f'_m tested for this "carrier" modulation frequency). The rate of decrease estimated on the low-pass segment of the second-order TMTFs decreases when the "carrier" modulation frequency f_m increases: It is about 6 dB (in $20 \log m'$) per octave when $f_m = 16$ Hz, 4 dB/oct when $f_m = 64$ Hz, and 3 dB/oct when $f_m = 256$ Hz. Overall, the low-pass segment seems to be followed by a plateau: Above a given value of f'_m (of about $f_m/3$ or $f_m/4$), sensitivity remains relatively constant. However, individual second-order TMTFs (e.g., listeners CS and SR) show a noticeable notch (i.e., a loss of sensitivity) when f'_m is slightly below $f_m/2$ (this is especially noticeable when $f_m = 16$ Hz). Figures 2 and 3 also show that sensitivity measured for second-order modulation frequencies between 3–6 Hz increases when f_m increases from 16 to 64 Hz. However, overall sensitivity to second-order modulation degrades considerably for $f_m = 256$ Hz. First-order TMTFs show that modulation detection at 256 Hz is reduced by 9 dB compared to modulation detection at 16 Hz, and by 5 dB compared to modulation detection at 64 Hz. Nevertheless, the "carrier" modulation remains highly audible for $f_m = 256$ Hz, the detection threshold being about 10%. This suggests that the audibility of the "carrier" modulation is not responsible for the overall drop in sensitivity to second-order modulation when $f_m = 256$ Hz.

To assess the statistical significance of the differences in second-order modulation detection thresholds, a repeated measure analysis of variance (ANOVA) was conducted with factors f_m and f'_m. The analysis showed significant main effects of f_m [$F(2,6) = 262.8$, $p < 0.000\,01$] and f'_m [$F(8,24) = 23.3$, $p < 0.000\,01$], and significant interaction between f_m and f'_m [$F(16,48) = 9.6$, $p < 0.000\,01$]. *Post-hoc* tests (LSD) showed that, when $f_m = 16$ Hz, second-order modulation detection thresholds measured at $f'_m = 2$ Hz were not significantly different from those measured at $f'_m = 1$ Hz ($p = 0.84$), but they were significantly lower than those measured at $f'_m = 5$ Hz ($p < 0.05$); the analysis also showed that thresholds measured for $f'_m = 5$, 6, 7, 8, and 11 Hz were not significantly different from each other ($p > 0.60$). Similar patterns of results were obtained for $f_m = 64$ and 256 Hz, indicating that sensitivity degraded from $f'_m = 4$ Hz when $f_m = 64$ Hz, and from $f'_m = 3$ Hz when $f_m = 256$ Hz. *Post-hoc* tests also showed that second-order modulation detection thresholds measured for $f'_m = 4$ Hz were significantly lower when $f_m = 64$ Hz than when $f_m = 16$ Hz ($p < 0.05$); however, detection thresholds measured for $f'_m = 3$ or 6 Hz were not significantly different when $f_m = 16$ or 64 Hz. Finally, the analysis showed that detection thresholds measured for $f'_m = 3$ or 8 Hz were significantly higher when $f_m = 256$ Hz than when $f_m = 16$ or 64 Hz ($p < 0.05$).

B. Masked modulation detection thresholds

A modulation masking experiment was performed to investigate the extent to which each modulation sideband (of frequency $f_m - f'_m$ and $f_m + f'_m$) contributes to the second-order modulation detection threshold. This experimental paradigm corresponds to a transposition of that used by Kohlrausch *et al.* (2000) to the temporal-envelope domain. The masked modulation detection thresholds of the lower and the upper modulation sideband were measured separately in the presence of the "carrier" modulation acting as masker. Here, masker modulation frequency was fixed at 64 Hz. Measurement was performed as a function of the absolute spectral distance Δf (in the modulation spectrum) between the sideband and the carrier ($\Delta f = |f_{\text{mask}} - f_{\text{sig}}|$; Δf was 3, 8, or 32 Hz). Figure 4 shows the individual masked modulation detection thresholds plotted along with second-order modulation detection thresholds measured for a "carrier" modulation frequency f_m of 64 Hz. In the case of second-order TMTFs, the left and right ordinates indicate second-order modulation depth at threshold m', and the abscissa represents f'_m; in the case of masked modulation thresholds, the left and right ordinates indicate signal modulation depth at threshold m_{sig}, and the abscissa represents the absolute spectral distance between signal and masker modulation frequencies, Δf. The left ordinate shows detection thresholds expressed in linear units ($100 \cdot m_{\text{sig}}$ or $100 \cdot m'$) and plotted on a logarithmic scale, while the right ordinate

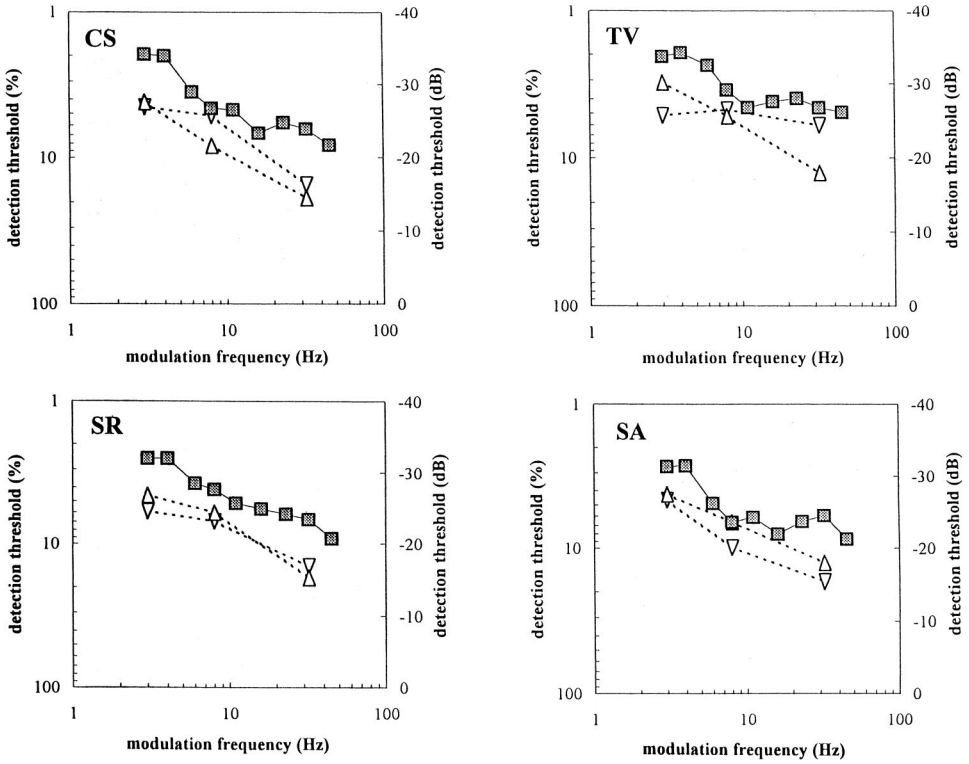

FIG. 4. Individual masked modulation detection thresholds (dotted lines with unfilled triangles) plotted along with second-order modulation detection thresholds measured for $f_m = 64$ Hz (solid lines with gray squares). In the case of second-order modulation thresholds, modulation depth at threshold (m') was transformed into modulation depth per sideband relative to the ''modulation'' carrier depth by subtracting 6 dB from $20 \log m'$. Triangles and inverted triangles represent masked detection thresholds for the upper and lower modulation sideband, respectively.

shows detection thresholds expressed on a decibel scale ($20 \log m_{\text{sig}}$ or $20 \log m'$). Triangles and inverted triangles represent masked detection thresholds for the upper and lower modulation sideband, respectively.

For a fully amplitude-modulated tone, the two sidebands are 6 dB attenuated relative to the carrier level. Therefore, in the case of second-order modulation thresholds, the depth of the modulation sidebands relative to the ''modulation'' carrier depth can be derived by dividing m' by a factor of 2 (or by subtracting 6 dB from $20 \log m'$). In Fig. 4, modulation depth at threshold (m') was therefore transformed into modulation depth per sideband relative to the ''modulation'' carrier depth, which implies a -6-dB vertical shift of the second-order modulation detection data relative to the values shown in Figs. 2 and 3.

For all listeners, masked modulation thresholds increase as the sideband modulation frequency is moved above or below the ''carrier'' modulation frequency f_m. This contrasts with previously reported modulation masking patterns, showing that modulation masking generally decreases as the modulation frequency is moved above or below the masker modulation frequency (e.g., Bacon and Grantham, 1989; Houtgast, 1989; Lorenzi *et al.*, 1997). However, the spectral distances Δf used in the present study are much smaller than what was used in these classical modulation masking studies. This inverse pattern of masking suggests that listeners are able to detect ''beats'' in the temporal envelope, which consists of a cyclic variation in the modulation depth at a slow rate f'_m. Similar effects have been reported by Strickland and Viemeister (1996), Sheft and Yost (1997), and Moore *et al.* (1999).

In order to reach the same modulation depth in a second-order modulation and a single modulation-sideband stimulus, the modulation depth per sideband for the latter has to be 6 dB higher than for the second-order modulation stimulus. The observed threshold difference of nearly 6 dB between these two conditions at small spectral distances can therefore be taken as strong evidence that envelope beat was the detection cue.

IV. GENERAL DISCUSSION

In summary, the data show the following.

(1) For each ''carrier'' modulation frequency, second-order modulation detection thresholds measured with a broadband noise carrier are lowest for (second-order) modulation frequencies below about 2–4 Hz; above 2–4 Hz, they generally increase with second-order modulation frequency up to a given second-order modulation frequency; above this frequency, second-order modulation thresholds remain roughly constant.
(2) Second-order modulation detection thresholds measured for low second-order modulation frequencies decrease when the ''carrier'' modulation increases from 16 to 64 Hz. However, they increase when the ''carrier'' modulation frequency increases to 256 Hz.
(3) Second-order modulation detection thresholds mirror the masked modulation detection thresholds of the lower and the upper modulation sidebands.

In the present experiments, the relative phase of second-order and ''carrier'' modulations was fixed [cf. Eq. (4)] because changes in relative phase affect modulation detectability (*i*) when modulations are harmonically related (e.g., Strickland and Viemeister, 1996; Lorenzi *et al.*, 1999), and (*ii*) when modulation depths are high (i.e., when modula-

tions are highly detectable; Moore and Sek, 2000). This may explain why noticeable notches or rebounds were observed in the second-order TMTFs when f'_m was close to $f_m/2$. (This was especially noticeable when $f_m = 16$ Hz.) Such local changes in detection threshold may therefore be due to the choice of a specific phase relationship between carrier and sidebands modulations. Further investigation of phase effects may help to clarify this issue.

At first sight, the results appear qualitatively (*i*) consistent with theoretical predictions of a linear envelope detector model consisting of a low-pass filtering stage and a decision stage, and (*ii*) inconsistent with predictions of a modulation filterbank model using narrowly tuned filters. Nevertheless, the current results seem consistent with predictions of a modulation filterbank model using *broadly* tuned filters. The latter point was studied by implementing a simplified version of the modulation filterbank model described by Dau *et al.* (1999) and Ewert and Dau (2000) consisting of three successive processing stages: (1) a half-wave rectifier, (2) a low-pass filter (first-order Butterworth) with a 3-dB cutoff frequency of 500 Hz, and (3) an array of overlapping linear bandpass filters (Dau *et al.*, 1996, 1997a, b) whose center frequencies range between 2 and 512 Hz. Center frequencies are spaced on a logarithmic scale from 2 to 512 Hz, and filters' density is set to 5 filters/oct. Filter bandwidths increase logarithmically over the whole range of center frequencies with constant Q values of 1, 2, or 4. The *change* produced by second-order modulation in the output of the modulation filter tuned to the lower sideband modulation frequency was calculated by subtracting the excitation evoked by the target to that evoked by the standard in this filter (i.e., the filter tuned to $f_m - f'_m$). Figure 5 shows the change in the output of this modulation filter as a function of f'_m. Simulations were performed for $f_m = 16$ Hz (left panel), 64 Hz (middle panel), and 256 Hz (right panel). Each panel shows the results of simulations for constant Q values of 1 (circles), 2 (squares), and 4 (triangles). Modulation depths of the ''carrier'' and second-order modulation (i.e., m and m', respectively) were both fixed at 50%. Figure 5 clearly shows that a modulation filter with a Q value of 1 would hardly signal the presence of second-order modulation whatever the value of f'_m (output change <1 dB); on the other hand, modulation filters with $Q \geqslant 2$ would easily signal the presence of second-order modulation (output change $\in [1-15$ dB$]$), but the pattern of change at the output of such filters predicts that detectability should *increase* with second-order modulation frequency. The present results clearly argue against a model based on finely tuned modulation bandpass filters [e.g., for $Q \geqslant 2$; Dau *et al.* (1997a, b, 1999)]. This suggests that, if such modulation filters do exist, their selectivity is poor. In the latter case, the Q value of modulation filters would have to be less than 2. This is more in line with the implementation of the modulation filterbank model proposed by Ewert and Dau (2000), in which the Q value of such filters is assumed to be equal to 1 for center modulation frequencies up to 64 Hz.

The present results also show that sensitivity to second-order modulation degrades considerably when the ''carrier'' modulation frequency increases from 64 to 256 Hz. First-order TMTFs indicate that the ''carrier'' modulation remains highly audible when $f_m = 256$ Hz, detection threshold being about 10%. This suggests that the audibility of the ''carrier'' modulation is not responsible for this overall loss in sensitivity to second-order modulation. Dau (1996) has shown that the deleterious effects of the intrinsic fluctuations of the noise carrier are greater at high modulation frequencies. Such statistical fluctuations might have affected the modulation sidebands generated by the second-order modulation, these deleterious effects being certainly strongest for the upper modulation sideband ($f_m + f'_m$). However, the way modulation sidebands might have been disrupted remains currently unexplained.

The experiment on modulation masking reveals that second-order modulation detection thresholds mirror the masked modulation detection thresholds of the lower and the upper modulation sidebands. Therefore, in contrast to the ''classical'' modulation masking patterns (e.g., Bacon and Grantham, 1989; Houtgast, 1989; Lorenzi *et al.*, 1997), the ability to detect modulation sidebands improves when sidebands and carrier modulations get closer. As for spectral masking in the audio-frequency domain, this result suggests (without demonstrating it) that the task is performed by listening to low envelope beat cues produced by the interaction

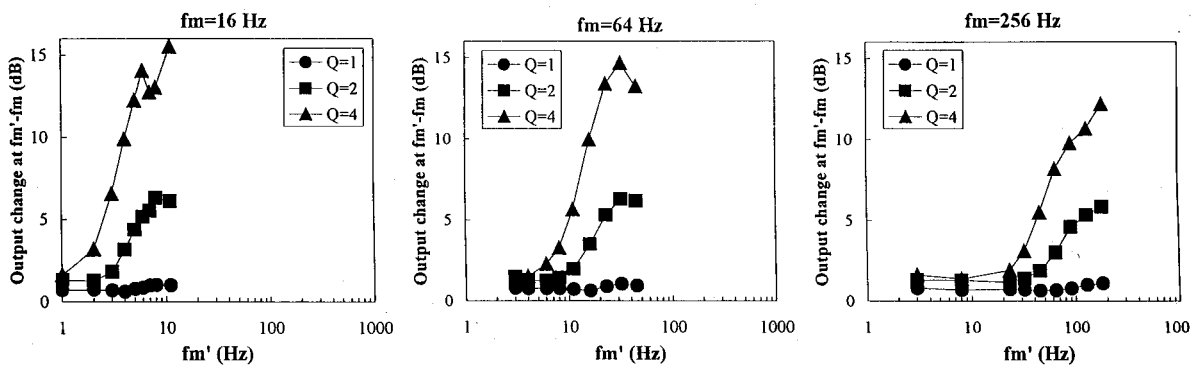

FIG. 5. Change produced by second-order modulation in the output of the modulation filter tuned to the lower sideband modulation frequency as a function of f'_m. Simulations were performed for $f_m = 16$ Hz (left panel), 64 Hz (middle panel), and 256 Hz (right panel). Each panel shows the results of simulations for constant Q values of 1 (circles), 2 (squares), and 4 (triangles). In each case, $m = m' = 0.5$.

between carrier and sideband modulation components. This is consistent with the subjective experience of subjects when listening to second-order modulation: A slow, cyclic variation in amplitude at f_m' is heard. At first sight, it appears difficult to account for this effect in terms of modulation filters, since there is no spectral energy at the envelope beat frequency in the modulation spectrum of the stimuli (see Fig. 1). However, applying a compressive nonlinearity before envelope extraction yields such a component in the modulation spectrum of stimuli with second-order SAM. This compressive nonlinearity may correspond to the fast acting compression performed by active mechanisms within the cochlea (e.g., Ruggero *et al.*, 1997; Moore and Oxenham, 1998) or to the transduction from basilar membrane vibration to neural activity (e.g., Yates, 1990; Regan and Regan, 1993). The idea that nonlinearities within the auditory system introduce distortion in the internal representation of the temporal envelope of sounds is also supported by previous electrophysiological and psychoacoustical studies using two-component modulators (Shofner *et al.*, 1996; Sheft and Yost, 1997; Moore *et al.*, 1999). For instance, the decrease in sensitivity to second-order modulation above 2–4 Hz is consistent with the results of Sheft and Yost (1997), who showed that the ''interference'' effect (i.e., the deleterious effect) of a beating two-component modulator on the detection of a probe modulator at the beat rate was greater for a 4-Hz beat rate than for a 10-Hz rate. The origin of this effect remains unclear, and further work is now needed to assess whether or not a modulation filterbank model including such nonlinearities may account for it. If detection of second-order modulation is actually based on the detection of spectral energy at the envelope beat frequency, second-order TMTFs may then be viewed as quantitative descriptions of the attenuation characteristics of low distortion components in the amplitude-modulation domain.

While sensitivity to first-order modulation is related to some aspects of *tempo* perception (for $f_m < \approx 30$ Hz), sensitivity to second-order modulation appears to be related to some aspects of *rhythm* perception, in that the sinusoidal increase and decrease in the modulation depth of SAM produce complex temporal patterns in which series of cycles of modulated noise alternate with segments of unmodulated noise at a low rate f_m'. Indeed, listeners reported performing the second-order modulation detection task by determining the interval evoking a rhythm percept instead of a regular tempo percept. Second-order TMTFs may therefore provide an interesting framework to study how perception transforms gradually from tempo to rhythm. In the same spirit, second-order TMTFs may also be of relevance to speech perception, in that our ability to detect patterns of periodicity (such as patterns of voicing) appears to be a major cue to consonant identity (e.g., Faulkner and Rosen, 1999).

ACKNOWLEDGMENTS

We thank Daniel Pressnitzer for helping us in running the modulation filterbank model and Laurent Demany, Gary Green, Tim Griffiths, Adrian Rees, Rebecca Millman, Michael Simpson, and William Woods for helpful and stimulating discussions. We also thank Sid P. Bacon, Torsten Dau, and an anonymous reviewer for helpful comments on an earlier version of this manuscript. This work was funded from the Cognitique program (MENRT).

Bacon, S. P., and Grantham, D. W. (**1989**). ''Modulation masking patterns: Effects of modulation frequency, depth and phase,'' J. Acoust. Soc. Am. **85**, 2575–2580.

Bacon, S. P., and Viemeister, N. F. (**1985**). ''Temporal modulation transfer functions in normal-hearing and hearing-impaired subjects,'' Audiology **24**, 117–134.

Dau, T. (**1996**). ''Modeling auditory processing of amplitude modulation,'' Ph.D. dissertation, Oldenburg.

Dau, T., Kollmeier, B., and Kohlrausch, A. (**1997a**). ''Modeling auditory processing of amplitude modulation. I. Modulation detection and masking with narrow-band carriers,'' J. Acoust. Soc. Am. **102**, 2892–2905.

Dau, T., Kollmeier, B., and Kohlrausch, A. (**1997b**). ''Modeling auditory processing of amplitude modulation. II. Spectral and temporal integration in modulation detection,'' J. Acoust. Soc. Am. **102**, 2906–2919.

Dau, T., Verhey, J., and Kohlrausch, A. (**1999**). ''Intrinsic envelope fluctuations and modulation-detection thresholds for narrow-band carriers,'' J. Acoust. Soc. Am. **106**, 2752–2760.

Ewert, S. D., and Dau, T. (**2000**). ''Characterizing frequency selectivity for envelope fluctuations,'' J. Acoust. Soc. Am. **108**, 1181–1196.

Fassel, R. (**1994**). ''Experimente und simulationsrechnungen zur wahrnehmung von amplitudenmodulationen im menschlichen gehör,'' Ph.D. dissertation, University of Göttingen.

Fassel, R., and Püschel, D. (**1993**). ''Modulation detection and masking using deterministic and random maskers,'' in *Contributions to Psychological Acoustics* (BIS, Oldenburg, Germany), pp. 419–429.

Faulkner, A., and Rosen, S. (**1999**). ''Contributions of temporal encodings of voicing, voicelessness, fundamental frequency, and amplitude variation to audio-visual and auditory speech perception,'' J. Acoust. Soc. Am. **106**, 2063–2073.

Fletcher, H. F. (**1940**). ''Auditory patterns,'' Rev. Mod. Phys. **12**, 47–65.

Forrest, T. G., and Green, D. M. (**1987**). ''Detection of partially filled gaps in noise and the temporal modulation transfer function,'' J. Acoust. Soc. Am. **82**, 1933–1943.

Green, G. G. R. (**1976**). ''Temporal aspects of audition,'' Ph.D. dissertation, Oxford.

Green, G. G. R., and Kay, R. H. (**1974**). ''Channels in the human auditory system concerned with the waveform of the modulation present in amplitude- and frequency-modulated tones,'' J. Physiol. (London) **241**, 29–30P.

Houtgast, T. (**1989**). ''Frequency selectivity in amplitude-modulation detection,'' J. Acoust. Soc. Am. **85**, 1676–1680.

Kay, R. H., and Matthews, D. R. (**1972**). ''On the existence in human auditory pathways of channels selectively tuned to the modulation present in frequency-modulated tones,'' J. Physiol. (London) **225**, 657–677.

Kohlrausch, A., Fassel, R., and Dau, T. (**2000**). ''The influence of carrier level and frequency on modulation and beat-detection thresholds for sinusoidal carriers,'' J. Acoust. Soc. Am. **108**, 723–734.

Lorenzi, C., Berthommier, F., and Demany, L. (**1999**). ''Discrimination of amplitude-modulation phase spectrum,'' J. Acoust. Soc. Am. **105**, 2987–2990.

Lorenzi, C., Micheyl, C., and Berthommier, F. (**1995**). ''Neuronal correlates of perceptual amplitude-modulation detection,'' Hear. Res. **90**, 219–227.

Lorenzi, C., Micheyl, C., Berthommier, F., and Portalier, S. (**1997**). ''Modulation masking in listeners with sensorineural hearing loss,'' J. Speech Lang. Hear. Res. **40**, 200–207.

Moore, B. C. J., and Oxenham, A. J. (**1998**). ''Psychoacoustic consequences of compression in the peripheral auditory system,'' Psychol. Rev. **105**, 108–124.

Moore, B. C. J., and Sek, A. (**2000**). ''Effects of relative phase and frequency spacing on the detection of three-component amplitude modulation,'' J. Acoust. Soc. Am. **108**, 2337–2344.

Moore, B. C. J., Sek, A., and Glasberg, B. R. (**1999**). ''Modulation masking produced by beating modulators,'' J. Acoust. Soc. Am. **106**, 908–918.

Patterson, R. D. (**1976**). ''Auditory filter shapes derived with noise stimuli,'' J. Acoust. Soc. Am. **59**, 640–654.

Rees, A., and Kay, R. H. (**1985**). ''Delineation of FM rate channels in man

by detectability of a three-component modulation waveform,'' Hear. Res. **18**, 211–221.
Regan, M. P., and Regan, D. (**1993**). ''Non linear terms produced by passing amplitude-modulated sinusoids through a hair cell transducer function,'' Biol. Cybern. **69**, 439–446.
Rodenburg, M. (**1977**). ''Investigation of temporal effects with amplitude modulated signals,'' in *Psychophysics and Physiology of Hearing* (Academic, London), pp. 429–437.
Ruggero, M. A., Rich, N. C., Recio, A., Narayan, S. S., and Robles, L. (**1997**). ''Basilar-membrane responses to tones at the base of the chinchilla cochlea,'' J. Acoust. Soc. Am. **101**, 2151–2163.
Sheft, S., and Yost, W. A. (**1997**). ''Modulation detection interference with two-component masker modulators,'' J. Acoust. Soc. Am. **102**, 1106–1112.
Shofner, W. P., Sheft, S., and Guzman, S. J. (**1996**). ''Responses of ventral cochlear nucleus units in the chinchilla to amplitude modulation by low-frequency, two-tone complexes,'' J. Acoust. Soc. Am. **99**, 3592–3605.
Strickland, E. A., and Viemeister, N. F. (**1996**). ''Cues for discrimination of envelopes,'' J. Acoust. Soc. Am. **99**, 3638–3646.
Tansley, B. W., and Suffield, J. B. (**1983**). ''Time-course of adaptation and recovery of channels selectively sensitive to frequency and amplitude modulation,'' J. Acoust. Soc. Am. **74**, 765–775.
Veimeister, N. F. (**1977**). ''Temporal factors in audition: A system analysis approach,'' in *Psychophysics and Physiology of Hearing* (Academic, London), pp. 419–428.
Viemeister, N. F. (**1979**). ''Temporal modulation transfer functions based upon modulation thresholds,'' J. Acoust. Soc. Am. **66**, 1364–1380.
Yates, G. K. (**1990**). ''Basilar membrane nonlinearity and its influence on auditory nerve rate-intensity functions,'' Hear. Res. **50**, 145–162.
Yost, W. A., Sheft, S., and Opie, J. (**1989**). ''Modulation interference in detection and discrimination of amplitude-modulation,'' J. Acoust. Soc. Am. **86**, 2138–2147.
Zwicker, E. (**1952**). ''Die grenzen der hörbarkeit der amplitudenmodulation und der frequenzmodulation eines tones,'' Acustica **2**, 125–133.

Exploring the temporal mechanism involved in the pitch of unresolved harmonics

Christian Kaernbach[a] and Christian Bering
Institut für Allgemeine Psychologie, Universität Leipzig, Seeburgstr. 14-20, 04103 Leipzig, Germany

(Received 3 September 1999; accepted for publication 2 May 2001)

This paper continues a line of research initiated by Kaernbach and Demany [J. Acoust. Soc. Am. **104**, 2298–2306 (1998)], who employed filtered click sequences to explore the temporal mechanism involved in the pitch of unresolved harmonics. In a first experiment, the just noticeable difference (jnd) for the fundamental frequency ($F0$) of high-pass filtered and low-pass masked click trains was measured, with $F0$ (100 to 250 Hz) and the cut frequency (0.5 to 6 kHz) being varied orthogonally. The data confirm the result of Houtsma and Smurzynski [J. Acoust. Soc. Am. **87**, 304–310 (1990)] that a pitch mechanism working on the temporal structure of the signal is responsible for analyzing frequencies higher than ten times the fundamental. Using high-pass filtered click trains, however, the jnd for the temporal analysis is at 1.2% as compared to 2%–3% found in studies using band-pass filtered stimuli. Two further experiments provide evidence that the pitch of this stimulus can convey musical information. A fourth experiment replicates the finding of Kaernbach and Demany on first- and second-order regularities with a cut frequency of 2 kHz and extends the paradigm to binaural aperiodic click sequences. The result suggests that listeners can detect first-order temporal regularities in monaural click streams as well as in binaurally fused click streams. [DOI: 10.1121/1.1381535]

PACS numbers: 43.66.Ba, 43.66.Hg, 43.66.Mk [RVS]

I. INTRODUCTION

A temporal mechanism involved in the perception of pitch has been suspected since the days of Ohm and Seebeck. In 1940, Schouten had suggested the existence of a mechanism which derives the pitch of unresolved harmonics through an analysis of the periodicity of the waveform (Schouten, 1940, 1970). In discrimination tasks with band-pass filtered pulse trains, Hoekstra (1979) measured a pitch jnd of below 0.1% for stimuli which contained harmonics below the 10th, while obtaining a jnd of 2% for harmonic orders above 20. In between, he found a transition. He argued that these levels reflect two different mechanisms of pitch analysis, one working for stimuli with spectrally resolvable components, and one working entirely on the temporal structure of the stimulus. His results were replicated by Houtsma and Smurzynski (1990) who showed that pitch discrimination for complex tones comprising high harmonics added in sine phase functions on two levels of performance. While the jnd is around 0.5% for complex tones containing harmonics below the 7th, it rises above 2.5% when the lowest harmonic in the signal is the 13th or higher. Furthermore, Houtsma and Smurzynski demonstrated that the two levels of performance differ with regard to their sensitivity to the phase relations of the harmonics. When the harmonics are added in Schröder phase, one obtains a stimulus with the same spectral information, but with a temporally less differentiated structure. In this condition, the jnd remains the same for stimuli with lower harmonics, but it increases to 4%–5% when only higher harmonics are included. These results were backed by Shackleton and Carlyon (1994) and by Carlyon and Shackleton (1994). They defined the resolvability of a harmonic complex in terms of the number of harmonics interacting within the same auditory filter as given by its 10-dB-down bandwidth, and they found that pitch matching for bandpass filtered harmonic complexes is not sensitive to phase relations of the harmonics when fewer than two harmonics interact (these are then said to be resolvable), while being sensitive to changes in phase relations when the number of interacting harmonics exceeds 3.25 (i.e., they are not resolvable). This would support the idea of two different pitch mechanisms working on resolvable and unresolvable harmonics, respectively. The latter mechanism would have to draw upon temporal regularities in the signal, while the former could also exploit spectral cues.

Psychophysical research on the ''temporal'' mechanism for the pitch of unresolved harmonics has mainly focused on the proof of its existence and on its dependence on the phase relations of the harmonics. Modeling of the temporal mechanism generally assumes some kind of autocorrelation algorithm to be at work. Kaernbach and Demany (1998) have demonstrated that first- and second-order temporal regularities are of quite different perceptual importance. This cannot easily be explained with any mechanism akin to an autocorrelation. However, due to the high cut frequency applied in their study (6 kHz), this conclusion may be limited to high-frequency regions. Furthermore, this high cut frequency entailed a degradation of the stimuli that let Kaernbach and Demany speak of ''rattle'' pitch rather than ''musical'' pitch. This constitutes an important drawback of their study as musicality is often considered a primary feature of pitch. It was the purpose of the present study to replicate and extend their

[a]Author to whom correspondence should be addressed. Electronic mail: christian@kaernbach.de

results at a lower cut frequency, and to test these sequences for their musicality.

Investigations into the temporal aspect of pitch perception have made use of a range of different stimuli. Apart from sinusoid complexes (e.g., Houtsma and Smurzynski, 1990), many experiments in psychoacoustics (e.g., Burns and Viemeister, 1981; Cariani and Delgutte, 1996a, b) and in physiology (see, e.g., Langner *et al.*, 1997) have applied sinusoidally amplitude-modulated (SAM) signals. Yost *et al.* (1998) investigated the temporal mechanisms involved in the analysis of iterated rippled noise (IRN, see also Yost, 1996). Kaernbach and Demany (1998) conducted their experiments with sequences of high-pass filtered clicks that were mixed with low-pass filtered noise. Periodic sequences of filtered clicks are equivalent to harmonic complexes added in cosine phase. This yields a temporally well-defined stimulus with a high peak factor and a low duty cycle. While the envelope of a SAM signal is higher than half of the maximum during 50% of a cycle, the temporal precision of a click train is only limited by the bandpass filtering done by the cochlea. Depending on the fundamental frequency of the train, one can obtain stimuli where, after cochlear filtering, the signal is higher than half of the maximum in less than 10% of a cycle. Furthermore, the interpretation of this stimulus as a series of filtered clicks admits aperiodic extensions of the paradigm where the stimulus conveys certain types of temporal regularities and excludes others. The experiments in the present article make use of these outlined advantages in different ways.

The first experiment reported in the present article is a variation of experiment III by Houtsma and Smurzynski (1990), using sequences of high-pass filtered clicks presented together with low-pass filtered noise. The jnd's reported by Houtsma and Smurzynski for complex tones with unresolvable harmonics and by Hoekstra (1979) for pulse trains are much larger than those they found for resolvable stimuli. Both studies used stimuli which cover only a small part of the cochlea. High-pass filtered clicks can offer more temporal information, i.e., on a larger part of the cochlea. Furthermore, there is no need to embed the sequences in pink noise which will disturb the signal portion of the stimulus. It should be sufficient to present low-pass filtered noise masking the region of possible distortion products. The aim of our experiment was to determine whether this optimized stimulus would have a lower jnd when containing only unresolvable harmonics, while still exhibiting the two-plateau jnd function. We would then be able to identify stimuli containing a maximum of temporal information but no resolvable harmonics, and use such stimuli to test further qualities of the elicited temporal pitch.

The next two experiments tested the musicality of these optimized temporal click sequences. Kaernbach and Demany reported informally that their stimuli did not convey musical information. However, this was not tested for systematically. One reason for the lack of musical quality might be that the cut frequency applied by Kaernbach and Demany (6 kHz) was much higher than necessary to exclude resolvable information. On the basis of the data found in the first experiment, we test the ability to discriminate and classify musical intervals constructed with periodic click sequences which are optimized with regard to their temporal properties.

Finally, a fourth experiment devised aperiodic click sequences that were similar to those applied by Kaernbach and Demany (1998). While their results could be argued to have validity only for frequency regions above 6 kHz, and that different mechanisms might be at work for frequencies which admit phase locking (i.e., below 4 kHz; see Rose *et al.*, 1967), the present study employs a cut frequency of 2 kHz that is well below this border. Once the applicability of their findings for these lower frequency regions was asserted, further conditions of the experiment using monaural and binaurally distributed irregular click sequences were devised to learn about the influences of such variations on the pitch percept.

II. EXPERIMENT 1: TWO LEVELS OF PITCH ANALYSIS

The jnd levels for temporal pitch analysis of 2% found by Hoekstra (1979) and of 2.5% reported by Houtsma and Smurzynski (1990) show that the temporal mechanism for unresolved harmonics is much less accurate than the mechanism for resolved harmonics. It should be noted that this performance was found for the isolated temporal mechanism, whereas the better performance for lower harmonics could be due to the cooperation of spectral and temporal mechanisms. It would nevertheless be highly interesting to find temporally defined stimuli that admit smaller jnd's.

In order to employ a temporally very accurate signal, periodic sequences of high-pass filtered clicks were devised which had characteristics similar to the sine-tone stimuli employed by Houtsma and Smurzynski or to the filtered click sequences used by Hoekstra. In contrast to those, however, they were not limited to a restricted frequency region either by a band-pass filter (Hoekstra) or by taking only a limited number of harmonics (Houtsma and Smurzynski) but contained all temporal information available up to the Nyquist frequency. It was anticipated that this would improve temporal pitch analysis. Furthermore, a different masker was used for the power spectrum below the signal. While Houtsma and Smurzynski had employed pink noise which has a certain intensity at the spectral location of the relevant signal components, in the present study white noise was used which was low-pass filtered such that its spectrum did not interfere with the signal, whereby a better signal-to-noise-ratio was obtained.

A. Stimuli and procedure

Periodic click sequences like those used in this experiment have a fundamental frequency equal to the number of clicks per second, and they contain all harmonics of the fundamental frequency with equal amplitude. In order to vary the lowest harmonic of the sequence, a high-pass filter was applied. The filter transition followed a logistic function containing several harmonics to avoid enhanced discriminability due to the appearance or disappearance of single harmonics at the cut frequency. The width was set to $\frac{1}{3}$ octave centered on the filter frequency, within which the amplitude increased from 10% to 90%. In order to ensure that the auditory power

spectrum would not contain resolved lower-order components arising from cochlear nonlinearity (Plomp, 1976), the signal was mixed with white noise. The noise was low-pass filtered at the same filter frequency as the sequence, using the inverted filter function such that the entire signal had a flat spectrum.

In the experiments, stimuli with fundamental frequencies of 100, 150, and 250 Hz were used. For each of these, the jnd was measured in 11 conditions, i.e., at eight different filter frequencies for filtered sequences mixed with noise as described above, at two filter frequencies for sequences without added noise, and for a pure tone of the fundamental frequency. The filter frequencies in the noise conditions were 500 Hz and 1, 1.5, 2, 2.5, 3, 4.5, and 6 kHz. In the two no-noise conditions, the sequences were filtered at 1 and 4.5 kHz, yielding signals with harmonics above the 10th and 45th, respectively, for a base frequency of 100 Hz, above the 6th and 30th for 150 Hz, and above the 4th and the 18th, for the base frequency of 250 Hz.

The experimental paradigm was an unforced weighted up–down adaptive procedure as described by Kaernbach (2001). On each trial, the subject was presented with a pair of stimuli A, B, which were presented twice sequentially in random order, i.e., either ABAB or BABA. The repetition aimed at eliminating the influence of previous trials. The task of the subject was to indicate via keyboard whether the last stimulus of the trial was the higher or the lower one, or whether he/she was not sure. Subjects were allowed to have a trial be repeated to them once. The subject had infinite time to answer and was given visual feedback on the correctness of his/her response, whereupon the next trial began.

Of the stimuli presented in a trial, one was constructed at a frequency f randomized with equal probability within $\pm 5\%$ of the base frequency f_0, while the other had a frequency of $(1+p)f$, where p was varied adaptively. For convenience, a logarithmic scale was used for the adaptive procedure. A given difference level of d dB on this scale translates into p according to $p=10^{d/10}$. The initial difference level d_0 for the runs was set to $d_0=-12$ dB (approx. 6.3% of the base frequency). The initial step size was $\Delta d=2$ dB. On a correct answer, the difference level was decreased by one step. If the answer was ''unsure,'' the difference level was increased by one step. After a wrong answer, it was increased by three steps. This leads to the point of 75% correct answers (Kaernbach, 2001). The maximum difference level admitted was -6 dB. The step size was halved after the third and after the fifth reversals. A run continued until the 16th reversal was reached, and the 75% threshold was then determined as the mean of all differences after the fourth reversal.

The experiment was run in a sound-proof both. The stimuli were digitally generated at 44.1 kHz and presented via electrostatic headphones at 60 dB SPL. The stimuli were presented diotically, with a length of 700 ms and a gap of 240 ms between each two. Where it was added, the noise started 240 ms before the first sequence and ended 240 ms after the fourth, including a linear on- and offset ramp of 150 ms. The pure tone stimuli had a ramp of 50 ms.

The experiment was divided into blocks comprising 11 runs, one run of each condition. The conditions were presented alternately ordered per block, either in the order ''mask,'' ''no mask,'' ''sine,'' or vice versa. The order of the two ''no mask'' conditions as well as of the eight ''mask'' conditions was randomized. Ten subjects between 19 and 26 years of age took part, all of whom were students either majoring in music or having at least amateur musical experience of some years standing. For all but one, the jnd was measured six times in each condition; for one subject, the experiment was run three times. One subject was the second author; the other subjects were paid for their participation.

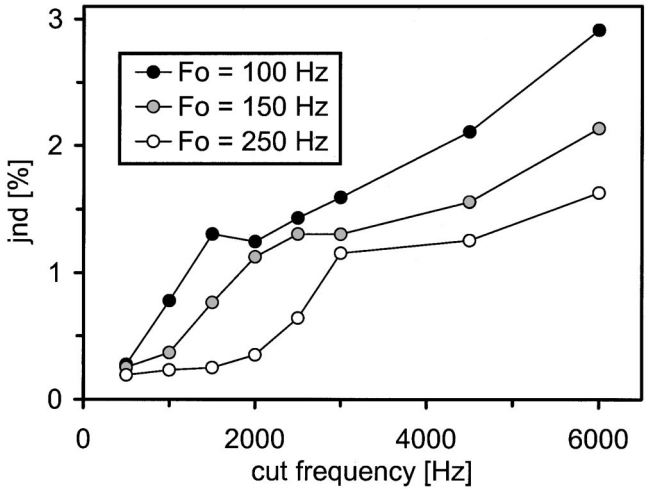

FIG. 1. Average jnd for the pitch of periodic click sequences in percent of the base frequency as a function of the filter frequency for three different fundamental frequencies. The two-plateau type of the jnd functions is clearly visible for all three functions, yet the exact position of the transition depends on the fundamental frequency.

B. Results and discussion

Figure 1 shows the resulting mean jnd of the noise conditions in percent of the base frequency as a function of the filter frequency. Notably, the curves of the three base frequencies start at a similar jnd of below 0.3%, namely 0.19% for 250 Hz, 0.25% for 200 Hz, and 0.27% for 100 Hz, with standard deviations of means between 0.02 and 0.03. The three functions then climb with different slopes and level off at a similar jnd of just around 1.25%. The 100-Hz function does so at the filter frequency of 1.5 kHz with a jnd of 1.3%, the 150-Hz function at a filter frequency of 2 kHz with a jnd of 1.1%, and the 250-Hz curve levels off at a filter frequency of 3 kHz with a jnd of 1.15%. Similarly, the standard deviations of means rise to values around 0.1 to 0.2, with the exception of 0.3 for 100 Hz at a cut frequency of 6 kHz. When plotting the jnd as a function of the lowest harmonic rather than the absolute filter frequency, the jnd rises concurrently for all three base frequencies around the lowest harmonic of 10 (see Fig. 2). This verifies the dependence of the transition on the lowest harmonic contained in the signal.

The results for stimuli with resolvable harmonics are compatible with those reported by Houtsman and Smurzynski, who had found a jnd of 0.4 Hz for the base frequency of 200 Hz, which equals 0.2%. Also, their jnd function sloped between the lowest harmonic of 7 up to 13. A major difference between the results is the level at which the curves

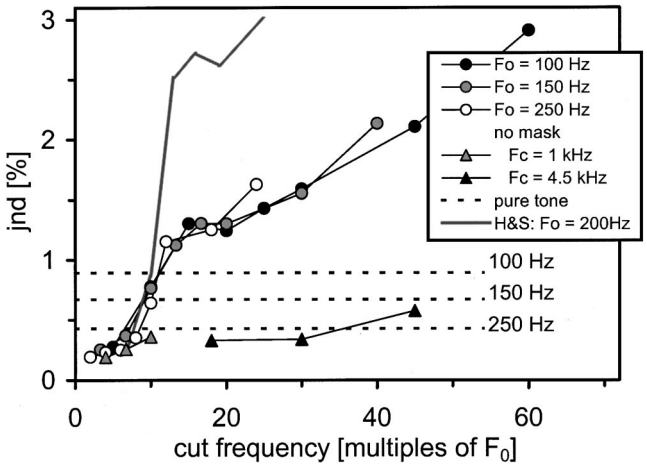

FIG. 2. Average jnd for the pitch of periodic click sequences in percent of the base frequency as a function of the lowest harmonic of the stimulus. As a function of harmonic number, the three jnd functions coincide. For comparison: jnd for complex tones of 11 harmonics of 200 Hz in sine phase as reported by Houtsma and Smurzynski (''H&S''). Also shown are the average jnd for single pure tones at the base frequencies (''pure''; from top to bottom: 100, 150, and 250 Hz) and the jnd for regular click sequences without masking noise (''no mask''; the three left-hand entries arise from the cut frequency of 1 kHz, the right-hand entries from 4.5 kHz).

saturate, as can be seen in Fig. 2. The jnd for the click sequences is considerably lower, which can be read as a direct indicator for the high temporal quality of the signal.

Figure 2 also depicts the jnd obtained for the ''no mask'' conditions and for the sine tones. Without masking noise, the jnd did not exceed 0.5% (with standard deviations of means ranging from 0.02 to 0.04), and there is no indication of a significant drop in performance between the two filter frequencies tested other than can be attributed to the decrease in signal. This emphasizes the importance of masking the lower part of the spectrum and reinforces the notion that the nonlinear ascent of the curves in the noise condition is not attributable to the degradation of the signal, but to a qualitative change in processing. Without masking, the spectrally resolvable distortion products prevent this transition from occurring.

The jnd for the pure tone conditions are almost uniformly higher than those for the click sequences without noise, and they are also higher than the jnd for the lowest filter frequencies in the noise condition. The lowest pure tone jnd measured was 0.43% for 250 Hz, the others lay at 0.67% for 150 Hz and 0.89% for 100 Hz (with a standard deviation of means of 0.04, 0.09, and 0.07, respectively). This result comes as no surprise, since pure tones do not contain as much information as complex tones and, consequently, as click sequences conveying information within the dominant region of pitch perception (Ritsma, 1967).

An important detail to remark about the plateau in Fig. 2 is that it does not have a zero slope, but does slowly increase in a manner not unlike an exponential curve. Cullen and Long (1986) had similarly found a rate jnd increment from 4.5% up to 15% for a lowest harmonic of $N=13$ to $N=100$ (equivalent to a cutoff frequency of 10 kHz for a base frequency of 100 Hz). Since in experiment 1 the click sequences were not bandpass filtered, all harmonics up to the Nyquist frequency were contained in the signal. Consequently, the number of harmonics gradually decreased as the filter frequency went up. However, the jnd cannot merely be a function of the number of harmonics, as Fig. 1 shows the jnd to depend on the fundamental frequency in exactly the opposite way, with 100 Hz showing the highest jnd, even though the stimulus contains the most harmonics when compared to the other two at a fixed filter frequency. Another hypothesis is that it could depend on the size of the cochlear region that is stimulated by the signal. In that case, all three curves should feature the same jnd for a fixed filter frequency, independent of the fundamental frequency. This does seem to be the case for 100 and 150 Hz at filter frequencies from 2 up to 3 kHz, but a separate explanation would have to be provided for the divergent progression of the jnds above 3 kHz.

Evidence that the two levels of performance do arise from two different mechanisms is revealed by examining the correlations of individual performances within and across the levels of the noise conditions. When correlating individual performances for any two noise conditions which both include harmonics below the 10th, we find an average value of 0.8, with a standard deviation of 0.12. Likewise, we find an average correlation of 0.69, with a standard deviation of 0.18, when pairwise correlating individual performances for conditions which include harmonics only above the 10th. This means that the ''rankings'' of the subjects are quite consistent within each of the two levels. In contrast, correlating performances across the transition yields an average correlation of 0.35, with a standard deviation of 0.2, i.e, the rankings are not stable between the two levels. This is a strong indication that the mechanisms involved in pitch analysis of stimuli with and of those without spectrally resolvable components differ.

III. EXPERIMENTS 2a AND b: THE MUSICALITY OF TEMPORAL PITCH

Musicality is an important feature of pitch perception. Several auditory stimuli convey a perception of ''high'' and ''low'' which does, however, not compare to pitch. It is often suggested that the identification of musical intervals may serve as a criterion for pitch perception. We wanted to test how far the stimuli used in the first experiment can convey musical information. It is obvious that by eliminating the resolvable harmonic information, one reduces the quality of pitch of the stimuli which are applied. This does not degrade the importance of temporal cues, as with natural stimuli in general both spectral and temporal analysis are possible and will probably both contribute to the perception of a high-quality and musical pitch. It would nevertheless be interesting to see whether to some degree musical quality remains within a purely temporal signal, or whether the resulting stimuli convey but a ''rattle pitch'' (Plomp, 1976, Chap. 7). Perhaps musicality does not constitute an all-or-none phenomenon but a quality with all kinds of gradations that depend on the amount of information left in the stimulus. A critical test for this view would be that those subjects that

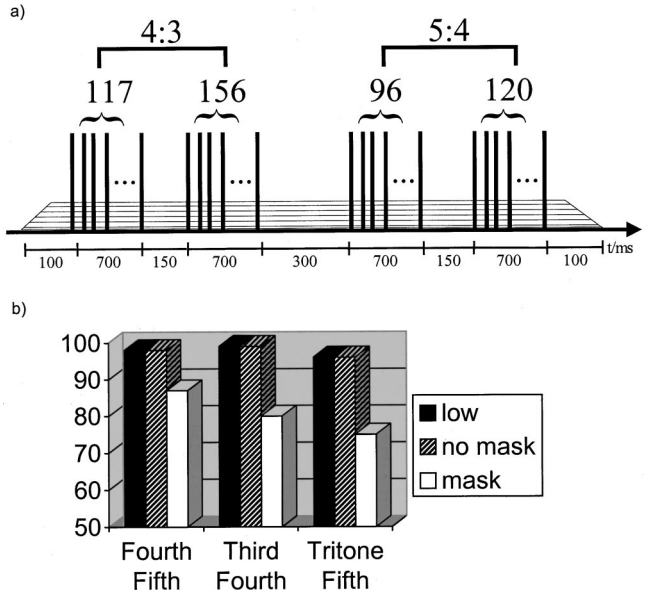

FIG. 3. (a) Schematic example of an interval discrimination trial. It consists of four click sequences embedded in noise. The first two sequences have a frequency ratio of 156 clicks to 117 clicks, equaling $\frac{4}{3}$ or a fourth, and the following two form a major third. (b) Average performance on musical interval discrimination for complexes comprising low harmonics (''low''), high-pass filtered click sequences without noise masker (''no mask'') and with noise masker (''mask''). For each stimulus, discrimination was tested for a major third against a fourth, a fourth against a fifth, and a fourth against a tritone. Performance is shown in percent of total trials.

show superior pitch processing for unresolvable harmonics in terms of their jnd will also have superior musical interval recognition.

A. Experiment 2a: Stimuli and procedure

In this experiment, discrimination tasks were run for three pairs of intervals: For a major third (frequency ratio of $\frac{5}{4}$) versus a fourth (frequency ratio of $\frac{4}{3}$), fourth against fifth (frequency ratio of $\frac{3}{2}$), and a tritone (frequency ratio of $\frac{45}{32}$) versus fifth. The target interval was the smaller one of both in all three cases. The discrimination of a fourth against a fifth was assumed to be the easiest. The ratio of the two frequency ratios is $\frac{8}{9}$, that is, the difference between the two intervals is one full tone. The other two discrimination tasks are nominally of the same difficulty, since in both cases the ratio of the frequency ratios is $\frac{15}{16}$, i.e., the difference between the intervals is a semitone in both cases. Yet, the last comparison (tritone versus fifth) should be more difficult, for two reasons. First, following Weber's law, it should be easier to judge a certain interval difference for smaller intervals than for larger ones. Second, while the comparison of a major third to a fourth comprises intervals that are quite familiar in normal musical contexts, the tritone represents an interval that will be not equally familiar to the subjects.

Each pair of intervals was tested for in three stimulus conditions: first, for periodic click sequences with low-pass filtered noise, second, for click sequences without a noise masker, and finally, for complex tones comprising the fundamental frequency itself as well as the next five harmonics (i.e., 1f,...,6f) added in sine phase. Figure 3(b) shows an example trial for click sequences with noise.

On each trial, two intervals were sequentially presented in random order, the lower tone preceding the higher one in each interval. Each tone was 700 ms long (the complex tones including a linear on-and offset ramp of 50 ms), with gaps of 150 ms between each two tones belonging to the same interval and a gap of 300 ms between the two intervals. In the noise condition, the noise started 100 ms before the first tone and ended 100 ms after the last, including a linear on- and offset ramp of 50 ms. Trials were grouped into blocks of 50 which were presented in random order in sets containing one block of each condition.

The frequency of the higher tone of each interval was randomized with equal probability within the range from 150 to 200 Hz; the lower tones were then computed accordingly. In order to guarantee that the signal was only temporally resolvable, the lowest harmonic was set to 15 in accordance with the results described in Sec. II. Given the maximum of 200 Hz for the base frequency, this condition equals a filter frequency of 3 kHz. Condition was made that the higher and the lower tones of two intervals tested for in one trial had to differ by 5% to ensure that subjects could not deduce the correct interval by comparison of either the higher or lower notes of the intervals.

Six subjects participated in the experiment, all of whom had also taken part in the experiment described in Sec. II. One subject accomplished five sets of blocks, all other subjects accomplished six sets. For each subject, the first set was discarded.

B. Experiment 2a: Results and discussion

Figure 3(b) shows the average discrimination rates for the three conditions and the three discrimination tasks. As predicted, performance is best for the fourth/fifth discrimination, and is lowest for the tritone/fifth discrimination. This holds for all three conditions. The two conditions without a noise masker (low partials versus high partials) practically yield the same results, i.e., 99% for the fourth/fifth discrimination (with a standard deviation of means of 0.3), 98% for discrimination of a third versus a fourth (with a standard deviation of means of 0.7 for low partials and 0.4 for high partials), and 96% for the tritone/fifth discrimination (with a standard deviation of 1.0). Although performance degrades for the noise conditions, performance clearly remains above chance level. Discrimination is 80% for fourth/fifth (with a standard deviation of means of 2.3), 87% for third/fourth (standard deviation of means: 1.8), and 75% for tritone/fifth (standard deviation of means: 1.7). Introspection indicates actual musical interval identification: Some subjects report singing the intervals in order to discriminate between them.

As subjects were matched, it was possible to correlate levels of performance between the jnd of temporal pitch and the interval discrimination. Figure 4 shows the interval discrimination performance for the tritone/fifth discrimination as a function of the corresponding jnd from experiment 1. There is a clear correlation of -0.75 to the effect that interval discrimination is worse the higher the jnd. This reinforces the view that for our stimuli the musicality of pitch is a gradual function of the reliability of recognition.

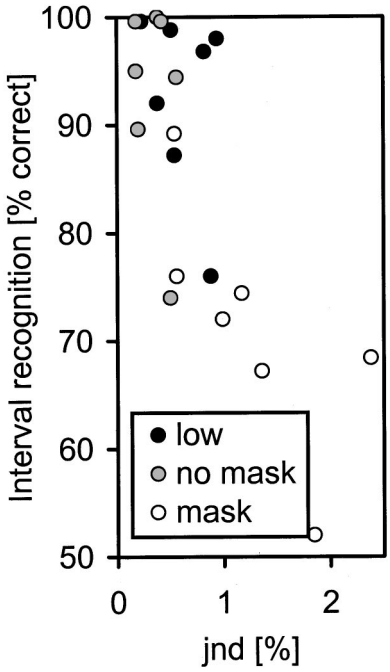

FIG. 4. Performance for musical interval discrimination of individual subjects (experiment 2) plotted against the jnd of pitch analysis (experiment 1). The labels ''low,'' ''no mask,'' and ''mask'' refer to the same conditions as in Fig. 3. The individual performance on interval discrimination shows to be correlated with the jnd, especially in the ''mask'' condition.

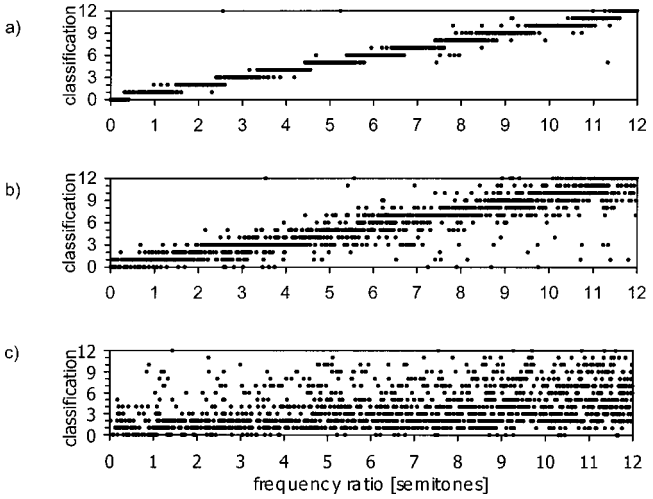

FIG. 5. Classifications as a function of the actual stimuli frequency ratio. (a) Musical condition. The classifications cluster tightly around the main diagonal. (b) Temporal condition. There is some scatter, but the clustering is still recognizable. (c) Infra-pitch condition. The classifications retain little structure.

C. Experiment 2b: Stimuli and procedure

Even though introspection indicates that in experiment 2a judgments were based on the musical identification of the intervals, the decisions could theoretically have merely been based on a comparison of the interval sizes. To eliminate this possibility, in the second musicality experiment, subjects had to classify intervals directly. On each trial, they were presented with two stimuli, which had an evenly randomized frequency ratio between 1.0 and 2.0. They had to classify the interval realized by the two stimuli by choosing the most adequate musical interval on a labeled computer keyboard. The task involved having to classify ambiguous intervals, as the actual frequency ratio of the stimuli could lie anywhere between two consecutive musical intervals. Consequently, the subjects received no feedback on the accuracy of their classification. The stimuli could be replayed at leisure via two keys on a computer keyboard, and subjects were encouraged to take as much time as they thought necessary to arrive at the best possible classification.

Three conditions were devised: In a ''musical'' control condition, the stimuli were unfiltered periodic click sequences in the octave from 80 to 160 Hz. These sequences include all harmonics of the base frequency, resolvable as well as unresolvable. The ''temporal'' condition used sequences constructed within the same octave, but containing only unresolvable harmonics. As in the previous experiment, this meant eliminating all spectral components below the 15th harmonic. Both stimuli of a trial were high-pass filtered at the adequate filter frequency for the higher of the two base frequencies, i.e., between 1.2 and 2.4 kHz, and had low-pass filtered white noise added. The ''infra-pitch'' condition was explicitly designed not to be musical. It used infra-pitch click sequences in the range from 8 to 16 Hz (Pressnitzer *et al.*, 1999), i.e., containing between eight and 16 evenly spaced clicks per second.

Due to the continuous range of the stimulus frequency ratios, a ''perfect'' classification was not possible. The best classification would map onto each musical interval the range of frequency ratios closest to this respective interval. It was anticipated that, for the first two conditions, subjects would get close to this level of performance, while basically having to guess in the third condition.

For each trial, a frequency ratio between 1.0 and 2.0 was randomly chosen. The lower frequency was then randomly set within the octave of possible frequencies (80 to 160 Hz, or 8 to 16 Hz) with the restriction that the higher frequency would also lie within the octave. This entailed that a trial with a frequency ratio of 2.0 would always be made up of the lower and the upper boundary of the respective octave.

For the first two conditions, each stimulus had a length of 1 s. In the filtered condition, the actual sequence was just 900 m long with a noise on- and offset of 50 ms each. In third condition, the length of the stimuli was randomized to have a length between 1 and 1.4 s in order to make sure that the classification would not rely on counting the number of clicks in the stimuli. All stimuli had linear on- and offset amplitude ramps of 150 m.

Three subjects with professional musical background took part in the experiment. Two of them completed 15 blocks in each condition, one completed 5 blocks. Each block comprised 50 trials. The first block of each condition and subject was discarded.

D. Experiment 2b: Results

As expected, classification was reported to be easy for the musical condition, more difficult, yet readily performable, for the temporal condition, and impossible for the infra-pitch condition. This qualitative impression was matched by the data. Figures 5(a)–(c) plots the classification as a func-

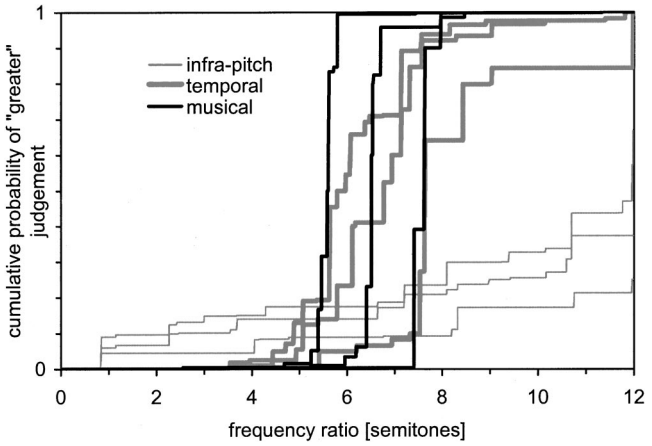

FIG. 6. The cumulative psychometric function for the judgment that the frequency ratio is higher than six, seven, and eight semitones, respectively, plotted for all three conditions. While there is a visible transition for the control condition as well as the temporal condition, the curve fails to reach 50% in the infra-pitch condition.

tion of the actual frequency ratio. Classification for the musical condition is nearly ideal, the correlation between actual frequency ratio and answer being 0.99. The classifications for the temporal condition group around the main diagonal in a similar manner. Even though there is visibly more scatter, the correlation is still 0.89. This is obviously in contrast to the result of the infra-pitch condition, in which classifications are widely spread. Here, the correlation is as low as 0.4.

A more accurate picture can be drawn by looking at the transitions of judgment between consecutive semitones. This is shown in Fig. 6, which plots the cumulative judgment transitions from 5th to 6th, from 6th to 7th, and from 7th to 8th, for all three conditions, as obtained using a pool-adjacent-violators algorithm. While the musical condition as well as the temporal condition both show a clear shift in judgment, the infra-pitch condition remains below 50% until the end of the abscissa. In the musical condition, the transitions were found to lie almost perfectly in the middle between semitones. For the temporal condition, there was an overall bias of the mean towards the higher semitone, i.e., the subject would tend to prefer the lower one. For the infra-pitch condition, transitions as such cannot be observed.

In conclusion, the three conditions reflect a gradual degradation of the ability of the subjects to classify the intervals in the order musical condition, temporal condition, and infra-pitch condition. However, the performance for the temporal condition is noticeably closer to that for the musical condition than to the performance for the infra-pitch condition. Consequently, if musicality were rigidly to be thought of as a quality either present or not in a pitch percept, instead of as a quality which can deteriorate gradually, the boundary would have to be set between the musical and the temporal conditions on the one side, and the infra-pitch condition on the other.

IV. EXPERIMENT 3: FINDING TEMPORAL REGULARITIES IN APERIODIC CLICK SEQUENCES

One of the major advantages of using sequences of filtered clicks instead of complexes of harmonically related components is the possibility to construct sequences that are not periodic but show some more complex kind of temporal regularity. Using such aperiodic sequences, Kaernbach and Demany (1998) demonstrated that the temporal mechanism involved in the pitch of unresolved harmonics can deal significantly better with first-order regularities (i.e., relating to the distances between a click and its direct successor) than with second-order regularities (relating to the distance between nonsuccessive clicks). A problem of their study was the rather high cut frequency of 6 kHz. Apart from yielding conceptually poor stimuli which reportedly contained but a ''rattle pitch,'' this frequency is beyond what generally is believed to be the limit to phase locking in auditory nerves (e.g., see Rose *et al.*, 1967). It is not certain how far this should be an important limit to a temporal mechanism that is supposed to operate on envelopes rather than on the fine structure of the signal. However, in order to obtain results that can be considered to be relevant to all kinds of temporal processing, it would be favorable to choose the filter frequency below 4 kHz.

Therefore, it was the aim of this experiment to replicate the results of Kaernbach and Demany at a cut frequency of 2 kHz. Furthermore, the approach of Kaernbach and Demany was taken a step further by splitting click sequences onto both ears, whereby a dichotic stimulus was obtained which had binaurally integrated interclick interval (ICI) statistics different from the ICI statistics for its two single, monaural parts. It was then possible to examine whether subjects would deal with these stimuli mainly according to the monaural characteristics or whether the statistics of the binaurally integrated stream would prevail.

A. Stimuli and procedure

In the first two conditions [''complete'' sequences, see Fig. 7(a)], which mainly aimed at verifying the results obtained by Kaernbach and Demany, subjects had to discriminate diotic *kxx*- and *abx*-sequences from random (x-) sequences. Since it was also the purpose of these control conditions to see whether the results would be confirmed for a filter frequency considerably below 4 kHz, the spacing of the sequences had to be chosen differently: k was set to 7.5 ms, and $a+b$ was set to 15 ms. Accordingly, x was randomized within [0, 15] ms. This equals an average of approximately 133 clicks per second, or a fundamental frequency of 133 Hz for the sequence, thereby admitting a filter frequency of 2 kHz. Filtering and masking with filtered white noise were done in the same manner as has been described in Sec. II A. The same noise was used in all three conditions. For the random sequences, a restriction devised by Kaernbach and Demany was adopted which ensured that the maximum of consecutive intervals either all within the higher or all within in the lower half of the interval distribution would be comparable to the target sequence. For a *kxx*-sequence this number cannot exceed 2, and for *abx* the limit is 3 (see Kaernbach and Demany, 1998).

In the following two conditions [''semi'' sequences, see Fig. 7(b)] the stimuli were generated according to the same rules as before, with the difference that every second click was left out. The semi-sequences show complementary char-

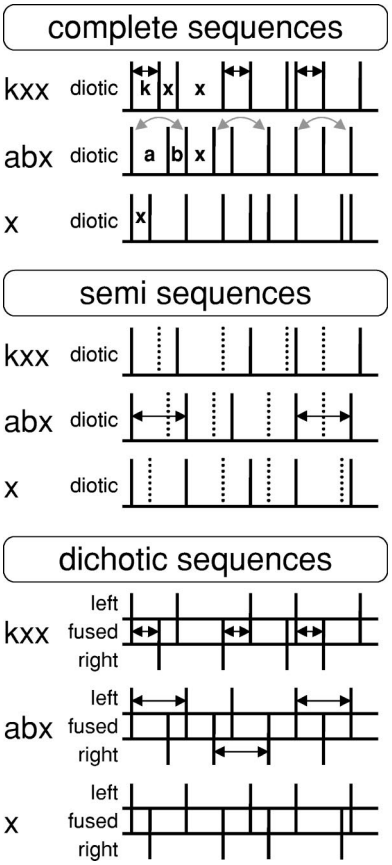

FIG. 7. (a) Schematic representation of *kxx*, *abx*, and random (*x*) click sequences as devised by Kaernbach and Demany (1998). The abscissa denotes course of time, vertical lines represent clicks. In a *kxx* sequence, the first (''*k*'') of each three intervals between two clicks is set to a constant time $k=7.5$ ms, while the following two (''*x*'') are randomized within [0, 15] ms. An *abx* sequence is constructed such that the first (''*a*'') of each three intervals is taken randomly from a uniform distribution [0, 15] ms, and the second interval (''*b*'') such that $a+b$ add up to a second-order interval of constant time of 15 ms with a click in between inserted at a random position. The third interval (''*x*'') is randomly chosen from [0, 15] ms. A random sequence contains intervals that are randomized within [0, 15] ms. (b) Diagram of the modified ''semi''-click sequences. In these sequences, every second click is left out. These are represented by the dotted lines. As can be seen, it is now with *abx* sequences that first-order intervals occur. If perception is based on first-order intervals, *abx* should now be easier to detect than *kxx*. (c) Dichotic *kxx*, *abx*, and random click sequences. The clicks are presented alternately to the left and to the right ear. Listening to one of the monaural streams would admit the detection of first-order intervals in *abx*, while listening to the binaurally fused stream would help to detect the first-order intervals in *kxx*.

acteristics to the complete sequences: While the *abx* semi sequences have a distinct first-order ICI peak at $a+b$ ms, the first-order ICI statistics of the *kxx* semi sequences is comparable to that of the random sequences. As a consequence, exactly the opposite discrimination performance was expected in these conditions.

Finally, in a fifth and sixth condition [''dichotic'' sequences, see Fig. 7(c)], the stimuli were each split into two complementary semi sequences, which were presented dichotically, one to the left ear and one to the right. In other words, the clicks are presented to the ears alternately. Looking at each monaural stream by itself, the stimuli cannot be distinguished from the semi-sequences [Fig. 7(b)], whereas the integrated stream of both ears reveals just an original,

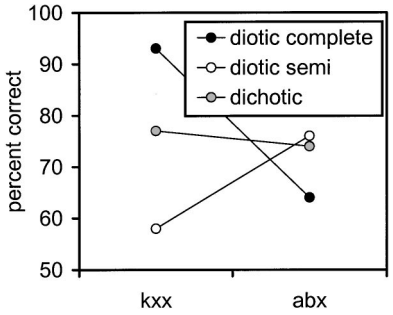

FIG. 8. Average performance for discrimination of *kxx* and *abx* against random sequences. The sequences were either presented diotically (''complete''), diotically with every second click left out (''semi''), or alternated between both ears (''dichotic''). Results are plotted as percentage correct of total of trials. While *kxx* can be discriminated perfectly in the complete condition and *abx* cannot, an inverse performance pattern at a somewhat lower overall performance level is to be observed for the semi condition. In the dichotic condition, *abx* can be discriminated as in the semi condition, while *kxx* can be discriminated at a level somewhat below the complete condition, but significantly above the semi condition.

''complete'' sequence [Fig. 7(a)]. So if the discrimination was accomplished by means of the binaurally integrated stream, the outcome should resemble the results from the ''complete'' conditions. If, on the other hand, the separate monaural streams were the basis for the discrimination, the results should be similar to those of the ''semi'' conditions.

Each trial consisted of a target sequence and an adequate (i.e., complete, semi or dichotic) random sequence, which were presented sequentially in random order for a duration of 750 ms each, with a gap of 250 ms in between. The low-pass filtered noise began 250 ms before the first sequence and ended 250 ms after the second, including a linear on- and offset of 100 ms. The subject was allowed to have the trial repeated once. He/she was to indicate via keyboard whether the target sequence had been the first or the second sequence. There was no time limit imposed. Upon answer, visual feedback was given. If the answer was incorrect, the subject was allowed to have the trial played once more. Then the next trial began.

Trials were grouped into blocks of 80, of which the first 40 were declared to be test trials and were excluded from evaluation. The blocks for the different conditions were presented in random order. A set of six blocks, one block for each condition, had to be completed before a new set began. The subjects were given information about which condition the current block belonged to, the conditions being neutrally named ''A,'' ''B'' to ''F'' condition. Five subjects took part in the experiment, all being students between 20 to 24 years of age. None had previous experience with psychoacoustic tasks. All subjects accomplished 18 sets of blocks of which the first 3 were excluded from evaluation.

B. Results and discussion

The results for the discrimination in the six different conditions are shown in Fig. 8. Performance for the complete conditions is comparable to what Kaernbach and Demany had found: The *kxx* sequences were discriminated nearly perfectly, while the *abx* sequences were discriminated with an average chance of 64%.

For the semi sequences, an inverted performance pattern is observed, as had been anticipated. The overall lower performance as compared to the complete condition is most likely due to the lower number of ICIs in these stimuli, i.e., it merely reflects a quantitative difference of the temporal information contained in the two types of sequences, not a qualitative difference.

Finally, for the dichotic sequences, the result is twofold: On the one hand, discrimination of *abx* can be done with the same performance as for the *abx* semi sequences. This necessarily implies that the task can be solved by means of the monaurally separated streams. It appears that only one of these streams was evaluated at each trial, as the performance is very close to that of a single semi sequence. On the other hand, the performance for the dichotic *kxx* sequences remains significantly above that for the semi *kxx* sequences and below that for the complete *kxx* sequences. This entails that the subjects were able to draw upon cues from the binaural stream, but could not to fuse the streams completely and obtain the performance level of the first condition. It would seem that the mechanism underlying discrimination is not exclusively committed to either binaural or monaural processing. However, the degradation of performance for the dichotic *kxx* sequences as compared to the complete *kxx* sequences suggests that monaural processing is more robust than binaural processing. Assuming binaural processing to be more robust, one would have expected such a degradation to occur for the dichotic *abx* sequences. Similarly, a prevalence of monaural processing has recently been reported by Carlyon *et al.* (2001), who found no binaural processing in streams with monaural regularities. Presumably, binaural processing will only work on streams with very weak or no monaural cues, as in the present experiment with the dichotic *kxx* sequences. It remains to be seen in future studies how far this prevalence might be influenced by attentional mechanisms (e.g., by directing the subject's attention towards monaural or binaural listening).

To control for the possibility of physical interaural cross-talk being the cause of the high performance on dichotic *kxx* sequences, these sequences were recorded with an artificial head. Cross-talk was found to occur at 24 dB below presentation level. The monaural halves of the recorded dichotic *kxx* sequences could not be discriminated above chance from random sequences. If there had been additional information provided by cross-talk of clicks, this performance should have been comparable to that for dichotic *kxx* sequences.

V. CONCLUSIONS

High-pass filtered and low-pass masked click sequences are an excellent tool to investigate the temporal mechanisms involved in auditory pitch perception. Their high temporal definition produces behavioral performances that are superior to those achieved with other stimuli (see experiment 1). At the same time, the difference between the performance for low and high harmonics remains sufficiently distinct to tell clearly where the domain of purely temporal pitch processing begins. The latter should not be considered as a separate phenomenon but as a mechanism that contributes to pitch perception over the entire region of the spectrum and can be sounded in isolation only for unresolved harmonics. It is obvious that the performance is lower for signals that sound this isolated temporal mechanism than for signals where it can be seconded by spectral cues. The classification of intervals constructed with unresolvable stimuli functions at a level comparable to that reached for fully musical stimuli (see experiment 2b). Subjects with a low temporal pitch jnd discriminate musical intervals constructed with spectrally unresolvable stimuli better than subjects with a higher temporal jnd (experiment 2a). This supports the notion of a unified pitch percept that draws from several mechanisms, one of them being the temporal mechanism under study.

A subject matter of interest is the nonzero slope of the right-hand part of the two-plateau jnd functions, i.e., the jnd for the unresolved harmonics (Fig. 2). It would be highly elucidating if one could find a variation of the experiment which would yield really flat plateau functions. Experiment 1 leaves open the question whether this could be achieved at least for a certain range of fundamental frequencies and of filter frequencies by covarying the upper limit of bandpass filtered clicks with the lower limit. It would be most interesting to find that with a constant ratio of upper and lower cut frequency (i.e., with the signal directed to a basilar membrane segment of constant length) one would find a constant jnd independent of the lower cut frequency, i.e., of the spectral region. This would support the idea that the temporal mechanism does operate on the envelope of the excitation of the basilar membrane for specific frequency ranges, as the envelope for unresolvable complex tones does not depend on the harmonic number of the carrier frequency.

Beside their high temporal definition, filtered click sequences tackle the temporal mechanism involved in pitch perception in a very direct and straightforward way, as they ''speak the language of the auditory nerve.'' Therefore, experiments can be designed that test specific hypotheses about this mechanism very directly. Experiment 3 is an example of the flexibility that is inherent to this kind of stimulation. The results for the ''complete'' sequences replicate those of experiment 3 of Kaernabach and Demany with a lower cut frequency. There seems to be no essential difference of temporal processing of first- and second-order regularities for spectral regions above and below 4 kHz. This supports the idea of an envelope analysis process that does not depend on the phase locking to the fine structure of the carrier. This mechanism operates more easily on first-order than on second-order temporal regularities, a fact that should be considered seriously by theoretical modelers of this temporal mechanism. The binaural condition of experiment 3 reveals that both monaural and binaural processing of temporal pitch is possible. This parallels similar results from spectral pitch according to which it seems possible to integrate the spectra of both ears before applying a spectral pattern algorithm (Houtsma and Goldstein, 1972). This could be an indication for the existence of early interaction between temporal and spectral pitch mechanisms.

ACKNOWLEDGMENTS

The authors would like to thank Laurent Demany, Peter Cariani, and an anonymous reviewer for their helpful comments on earlier drafts of the manuscript. This research was supported by the DFG Grant No. KA 824/5-1.

Burns, E. M., and Viemeister, N. F. (**1981**). ''Played-again SAM: Further observations on the pitch of amplitude-modulated noise,'' J. Acoust. Soc. Am. **70**, 1655–1660.

Cariani, P. A., and Delgutte, B. (**1996a**). ''Neural correlates of the pitch of complex tones. I. Pitch and pitch salience,'' J. Neurophysiol. **76**, 1698–1716.

Cariani, P. A., and Delgutte, B. (**1996b**). ''Neural correlates of the pitch of complex tones. II. Pitch shift, pitch ambiguity, phase-invariance, pitch circularity, rate-pitch, and the dominance region of pitch,'' J. Neurophysiol. **76**, 1698–1716.

Carlyon, R. P., and Shackleton, T. M. (**1994**). ''Comparing the fundamental frequencies of resolved and unresolved harmonics: Evidence for two pitch mechanisms?'' J. Acoust. Soc. Am. **95**, 3541–3554.

Carlyon, R. P., Demany, L., and Deeks, J. (**2001**). ''Temporal pitch perception and the binaural system,'' (to appear).

Cullen, Jr., J. K., and Long, G. (**1986**). ''Rate discrimination of high-pass-filtered pulse trains,'' J. Acoust. Soc. Am. **79**, 114–119.

Hoekstra, A. (**1979**). ''Frequency discrimination and frequency analysis in hearing,'' unpublished Ph.D. thesis, University of Groningen.

Houtsma, A., and Goldstein, J. L. (**1972**). ''The central origin of the pitch of complex tones: evidence from musical interval recognition,'' J. Acoust. Soc. Am. **51**, 520–529.

Houtsma, A., and Smurzynski, J. (**1990**). ''Pitch identification and discrimination for complex tones with many harmonics,'' J. Acoust. Soc. Am. **87**, 304–310.

Kaernbach, C. (**2001**). ''Adaptive threshold estimation with unforced-choice tasks,'' Percept. Psychophys. **63**(8) (in press).

Kaernbach, C., and Demany, L. (**1998**). ''Psychophysical evidence against the autocorrelation theory of auditory temporal processing,'' J. Acoust. Soc. Am. **104**, 2298–2306.

Langner, G., Sams, M., Heil, P., and Schulze, H. (**1997**). Frequency and periodicity are represented in orthogonal maps in the human auditory cortex: evidence from magnetoencephalography.'' J. Comp. Physiol., A **181**, 665–676.

Plomp, R. (**1976**). *Aspects of Tone Sensation* (Academic, London).

Pressnitzer, D., Patterson, R. D., and Krumbholz, K. (**1999**). ''The lower limit of melodic pitch for filtered harmonic complexes,'' J. Acoust. Soc. Am. **105**, 1152.

Ritsma, R. J. (**1967**). ''Frequencies dominant in the perception of the pitch of complex sounds,'' J. Acoust. Soc. Am. **42**, 191–198.

Rose, J. E., Brugge, J. F., Anderson, D. J., and Hind, J. E. (**1967**). ''Phase-locking responses to low-frequency tones in single auditory-nerve fibers of the squirrel monkey,'' J. Neurophysiol. **30**, 769–793.

Schouten, J. F. (**1940**). ''The residue and the mechanism of hearing,'' Proc. K. Ned. Akad. Wet. **43**, 991–999.

Schouten, J. F. (**1970**). ''The residue revisited,'' in *Frequency Analysis and Periodicity Detection in Hearing*, edited by R. Plomp and G. F. Smoorenburg (Sijthoff, Leiden), pp. 41–54.

Shackleton, T. M., and Carlyon, R. P. (**1994**). ''The role of resolved and unresolved harmonics in pitch perception and frequency modulation discrimination,'' J. Acoust. Soc. Am. **95**, 3529–3540.

Yost, W. A. (**1996**). ''Pitch of iterated rippled noise,'' J. Acoust. Soc. Am. **100**, 511–518.

Yost, W. A., Patterson, R., and Sheft, S. (**1998**). ''The role of the envelope in processing iterated rippled noise,'' J. Acoust. Soc. Am. **104**, 2349–2361.

Forward- and simultaneous-masked thresholds in bandlimited maskers in subjects with normal hearing and cochlear hearing loss

Judy R. Dubno[a] and Jayne B. Ahlstrom
Department of Otolaryngology–Head and Neck Surgery, Medical University of South Carolina, 39 Sabin Street, P.O. Box 250150, Charleston, South Carolina 29425

(Received 4 January 2000; revised 7 March 2001; accepted 23 April 2001)

Forward- and simultaneous-masked thresholds were measured at 0.5 and 2.0 kHz in bandpass maskers as a function of masker bandwidth and in a broadband masker with the goal of estimating psychophysical suppression. Suppression was operationally defined in two ways: (1) as a change in forward-masked threshold as a function of masker bandwidth, and (2) as a change in effective masker level with increased masker bandwidth, taking into account the nonlinear growth of forward masking. Subjects were younger adults with normal hearing and older adults with cochlear hearing loss. Thresholds decreased as a function of masker bandwidth in forward masking, which was attributed to effects of suppression; thresholds remained constant or increased slightly with increasing masker bandwidth in simultaneous masking. For subjects with normal hearing, slightly larger estimates of suppression were obtained at 2.0 kHz rather than at 0.5 kHz. For hearing-impaired subjects, suppression was reduced in regions of hearing loss. The magnitude of suppression was strongly correlated with the absolute threshold at the signal frequency, but did not vary with thresholds at frequencies remote from the signal. The results suggest that measuring forward-masked thresholds in bandlimited and broadband maskers may be an efficient psychophysical method for estimating suppression. [DOI: 10.1121/1.1381023]

PACS numbers: 43.66.Dc, 43.66.Ba, 43.66.Sr [SPB]

I. INTRODUCTION

Suppression, whereby strong activity at one frequency suppresses weaker activity at adjacent frequencies, has been demonstrated in psychophysical experiments for many years (e.g., Houtgast, 1974; Shannon, 1976; Terry and Moore, 1977; Weber and Green, 1978), but the relative contributions of suppression and spread of excitation in masking remain unclear (e.g., Delgutte, 1990; Moore and Vickers, 1997; Oxenham and Plack, 1998). Psychophysical measures of suppression in subjects with cochlear hearing loss have been obtained in relatively few studies. Direct estimates of suppression (using forward-masking procedures similar to those described by Shannon, 1976) suggested normal suppression when the suppressing tone was in a region of normal hearing, but reduced suppression when the suppressing tone was in a region of hearing loss (e.g.,Wightman *et al.*, 1977; Penner, 1980; Mills and Schmiedt, 1983; Thibodeau, 1991; Hicks and Bacon, 1999). Results of Mills (1982) demonstrated that dramatic changes in suppression areas surrounding low-frequency or high-frequency skirts of psychophysical tuning curves could result from noise exposures that did not elevate thresholds, suggesting that psychophysical measures of suppression may be particularly sensitive estimates of cochlear function.

The experiment reported here is the first of a series whose long-term goal was to relate suppression to speech recognition in noise for subjects with normal hearing and cochlear hearing loss. Given that suppression may reduce the effective masker level and improve the signal-to-noise ratio, as well as enhance spectral contrasts of certain speech features, suppression may provide an important benefit to understanding speech, especially in degraded listening conditions. Moreover, if individuals with cochlear hearing loss have reduced or absent suppression, they may not fully benefit from the improved signal-to-noise ratio or enhanced spectral contrasts provided by suppression, which contributes to their relatively poor speech recognition in noise.

Prior to initiating studies relating suppression and speech recognition, it was necessary to select and evaluate a psychophysical suppression metric that would be suitable to studies of speech recognition. A primary consideration was that the same maskers and suppressors be incorporated in both suppression and speech-recognition measures. As such, noise maskers and suppressors were preferred over tonal maskers and suppressors, for the following reasons. Bandwidths of noise maskers and suppressors can be selected to cover a relatively broad spectral region (similar to the broadband speech signal); in contrast, tonal maskers and suppressors are necessarily limited to very narrow regions, requiring measurements at several signal frequencies to sample spectral regions corresponding to speech stimuli. Noise maskers and suppressors also yield larger estimates of suppression than tonal maskers, perhaps due to the larger number of components serving as suppressors (Lee and Bacon, 1998). The larger effect size makes it easier to detect significant differences between experimental conditions or subject groups. Finally, tonal-suppression tasks may be particularly difficult

[a]Electronic mail: dubnojr@musc.edu

and time consuming for subjects who are untrained in psychophysical procedures, are hearing impaired, or are older. For these reasons, a suppression metric was selected wherein forward-masked thresholds were measured in bandpass maskers as a function of masker bandwidth. Results using this ''bandlimiting'' procedure have been evaluated in numerous studies of subjects with normal hearing (e.g., Houtgast, 1974; Weber, 1978; Moore and Glasberg, 1983, 1985).

The bandlimiting method was originally modeled on the neurophysiological findings that the firing rate of single neurons in the auditory nerve (Ruggero, 1973; Gilbert and Pickles, 1980) and cochlear nucleus (Greenwood and Goldberg, 1970) first increased in response to a noise of increasing bandwidth (but constant spectrum level) and then decreased as the noise bandwidth increased beyond the critical band. The decrease in response was attributed to the effects of noise components moving into neighboring suppression regions and suppressing the excitatory response. This general pattern was observed psychophysically by Houtgast (1974) and Weber (1978) using nonsimultaneous-masking paradigms (pulsation threshold and forward masking, respectively). In these psychophysical bandlimiting experiments, masked thresholds increased until the masker bandwidth reached the critical bandwidth, and then they decreased. Decreases in thresholds were not observed in simultaneous masking (also see Fletcher, 1940), which was attributed to both the signal and the masker being suppressed without resulting in an improved signal-to-noise ratio. The bandlimiting paradigm was applied to two subjects with hearing loss by Leshowitz and Lindstrom (1977), who observed no decrease in threshold in the region of threshold elevation with increasing bandwidth. This result was interpreted as demonstrating reduced suppression associated with subjects' cochlear pathology, consistent with physiological evidence of reduced two-tone rate suppression following noise exposure or other trauma (e.g., Schmiedt *et al.*, 1980; Salvi *et al.*, 1982; Schmiedt *et al.*, 1990). Thus the main goal of the first experiment in the series was to confirm and extend the early results of Leshowitz and Lindstrom (1977) to larger groups of subjects with normal hearing and cochlear hearing loss, to estimate suppression at a low and high signal frequency, and to assess associations between suppression and absolute thresholds.

Although the psychophysical results followed the general pattern of the neurophysiological findings and were consistent with assumptions of the effects of hearing impairment on suppression, alternative explanations have been proposed that were independent of suppression. One alternative explanation (Moore and Glasberg, 1986) argues that when a forward masker and a signal have similar spectral characteristics, the listener may have difficulty determining when the masker ended and the signal began. As the masker's bandwidth was increased, the quality of the masker became increasingly different from the signal, which reduced the listener's confusion and decreased the threshold. Forward-masked thresholds may not decrease for listeners with hearing loss because (1) these individuals were not able to make use of the quality-difference ''cue,'' and/or (2) the additional noise components were positioned in regions where thresholds were elevated. The potential confounding effects of confusion have been studied extensively (e.g., Moore and Glasberg, 1982, 1985; Neff, 1985, 1986). Moore and Glasberg (1983) concluded that if appropriate stimuli and procedures were used, the influence of ''cuing'' or confusion may be minimized (see Sec. II).

In this experiment, simultaneous- and forward-masked thresholds were measured at 0.5 and 2.0 kHz in bandpass maskers as a function of masker bandwidth. Subjects were younger adults with normal hearing and older adults with cochlear hearing loss. Suppression was estimated in two ways. Under the assumption that suppression was responsible for the reduction in threshold at the signal frequency as masker bandwidth increased, the magnitude of suppression was operationally defined as the change in forward-masked threshold as a function of masker bandwidth (or, more simply, as the difference in thresholds measured in a narrowband masker and in a broadband masker). Alternatively, given that the effect of suppression was to reduce the effective level of the masker, suppression was also quantified as a change in effective masker level with increasing masker bandwidth. Changes in masker level associated with suppression effects must take into account the nonlinear growth of forward masking (i.e., growth-of-masking slopes less than 1 dB/dB). As such, masked thresholds at the two signal frequencies were also measured as a function of broadband masker level, in order to estimate slopes of the growth-of-masking functions. Although suppression could affect growth-of-masking slopes when measured with a broadband masker, this masker was selected to avoid problems associated with the use of narrowband maskers (see Moore and Glasberg, 1983).

II. METHODS

A. Subjects

There were two subject groups: (1) eight younger adults with normal hearing (mean age: 21.3 years; range: 19–26); and (2) eight older adults with mild-to-moderate, bilaterally symmetrical hearing loss of cochlear origin (mean age: 68.3 years; range: 62–79). Seven of the eight normal-hearing subjects and five of the eight hearing-impaired subjects were available for measurements of growth of masking. Absolute thresholds for normal-hearing subjects were better than 15 dB HL (ANSI, 1989) at octave frequencies from 0.25 to 8.0 kHz and immittance measures were within normal limits. Hearing-impaired subjects were selected from among patients with adult-onset cochlear hearing loss (specific etiology unknown), absolute thresholds within specific ranges, and normal immittance measures. Thresholds of hearing-impaired subjects were restricted to ensure that (1) as the masker bandwidth increased, noise bands would not be introduced into areas of severe hearing loss or into areas where thresholds were changing abruptly with frequency, and (2) subjects' thresholds in the bandpass maskers were higher than their absolute thresholds. One ear of each subject was selected for testing. Subjects did not have experience with the psychophysical tasks used in this study. As such, subjects received approximately 2 h of practice with simultaneous

masking and 2 h of practice with forward masking prior to the start of data collection. Data collection was completed in four, 2-h sessions; an additional session was required for growth-of-masking measurements. Subjects were paid an hourly rate for their participation.

B. Apparatus and stimuli

Tonal signals were digitally generated (TDT DD1) pure tones, sampled at 50.0 kHz and low-pass filtered at 8.5 kHz. Signals were either 350 ms or 20 ms in duration, including 5-ms raised-cosine rise/fall ramps. Bandpass maskers were created by online digital filtering of a broadband noise (filter slopes >100 dB/oct). The bandpass maskers were centered at one of the two signal frequencies (0.5 or 2.0 kHz). For each signal, there were five or six bandpass maskers with varying bandwidths; bandwidths ranged from 0.2 to 1.0 kHz (for the 0.5-kHz signal) and from 0.4 to 2.0 kHz (for the 2.0-kHz signal). Bandwidths were increased from narrowest to widest by adding noise bands above and below the signal. A broadband masker was also included (low-pass cutoff set to 8.0 kHz). Cutoff frequencies were placed such that the bandwidths were symmetrical in linear frequency. Masker duration was 350 ms, including 5-ms raised-cosine rise/fall ramps. In simultaneous masking, the signal followed masker onset by 5 ms.[1] In forward masking, the duration between the masker and the signal was 0 ms (at the 0-voltage points).

The amplitudes of the signals and maskers were controlled individually using programmable and manual attenuators (TDT PA4). For the main experiment, bandpass-masker level was fixed at a spectrum level of 45 dB and signal level was varied adaptively. For growth-of-masking measures, the spectrum level of the broadband masker ranged from 25 to 50 dB. The signal was added to the masker (TDT SM3) and delivered through one of a pair of TDH-49 earphones mounted in supra-aural cushions. Spectral characteristics of all signals were verified using an acoustic coupler and a signal analyzer (Stanford Research model SR 760).

C. Procedures

For each subject, the following thresholds were measured: (1) absolute thresholds for 350-ms pure tones at selected one-third-octave frequencies ranging from 0.25 to 6.3 kHz; (2) absolute thresholds for 20-ms tones at one-third-octave frequencies ranging from 0.25 to 6.3 kHz; (3) simultaneous- and forward-masked thresholds for 20-ms tones at 0.5 and 2.0 kHz in bandpass maskers as a function of masker bandwidth, and in a broadband masker, with masker spectrum level fixed at 45 dB; and, for a subset of subjects, (4) simultaneous- and forward-masked thresholds for 20-ms tones at 0.5 and 2.0 kHz in a broadband masker as a function of masker level, with spectrum levels ranging from 25 to 50 dB. Quiet thresholds were measured first for all subjects; growth of masking was measured last. The order of signal frequency (0.5 kHz, 2.0 kHz) and masking condition (simultaneous, forward) was counterbalanced and, within these conditions, masker bandwidth (or masker level) was randomized.

Thresholds were measured using a single-interval (yes–no) maximum-likelihood psychophysical procedure, similar to that described by Green (1993) and discussed in detail in Leek *et al.* (2000). Each threshold was determined from 24 trials, 4 of which were catch trials. A monochrome monitor displayed the listen and vote periods. Subjects responded by clicking one of two mouse buttons corresponding to the responses ''yes, I heard the tone'' and ''no, I did not hear the tone.'' In this single-interval procedure, no feedback could be provided. Subjects were tested individually in a sound-treated room.

As discussed earlier, it has been suggested that forward-masked thresholds may be affected by confusion if stimulus conditions made it difficult to distinguish the signal from the masker and if the ability to distinguish the signal from the masker changed with masker bandwidth. As such, in this experiment, stimuli and procedures were selected to minimize these effects (Moore and Glasberg, 1985, 1986), including: (1) a relatively short signal duration of 20 ms, but long enough so that the signal had a tonal quality which was different from the ''noisy'' quality of the masker; (2) bandpass masker bandwidths which were not narrower than 20% of the signal frequency, thus avoiding very narrow bandwidths which may lack a ''noisy'' quality and have undesirable envelope fluctuations; and (3) practice periods which emphasized the quality differences between the masker and the signal and incorporated delays longer than 0 ms between the masker and signal. Although long-term learning effects were not measured parametrically in this experiment, thresholds were carefully monitored; none of the subjects displayed any systematic change in their forward-masked thresholds during the course of data collection. Despite these controls, it is impossible to rule out completely a possible influence of confusion effects with some of the forward-masked thresholds.[2]

III. RESULTS AND DISCUSSION

A. Quiet thresholds

Mean thresholds (in dB SPL) measured in quiet for normal-hearing and hearing-impaired subjects are shown in the upper panel of Fig. 1 for the 350-ms signals and in the lower panel of Fig. 1 for the 20-ms signals. Hearing-impaired subjects had a mild-to-moderate hearing loss with greater loss in the higher frequencies. Although not a goal of the experiment, it was of interest to assess duration-related differences in thresholds (350 vs. 20 ms) for the two subject groups. Across frequency, thresholds for the longer tone averaged 12.9 dB lower than those for the shorter tone for normal-hearing subjects (corresponding to −3.1 dB/doubling of duration, nearly equal to the expected −3 dB/doubling); the comparable value was only 5.4 dB (−1.3 dB/doubling of duration) for hearing-impaired subjects. Differences in thresholds between the longer and shorter signals decreased as signal frequency increased, especially for the hearing-impaired subjects, suggesting that the time constants of temporal integration were decreasing at higher frequencies (Plomp and Bowman, 1959) and with hearing loss (e.g., Hall and Fernandes, 1983; Florentine *et al.*, 1988).

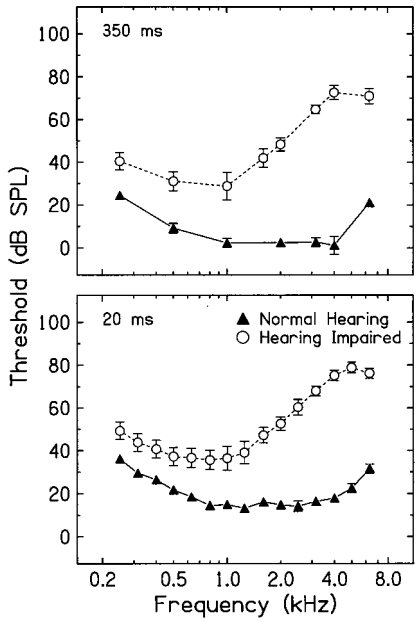

FIG. 1. Mean thresholds (in dB SPL) measured in quiet for normal-hearing subjects (filled triangles) and hearing-impaired subjects (open circles) for 350-ms signals (upper panel) and 20-ms signals (lower panel). Error bars indicate ±1 standard error of the mean (SE).

B. Simultaneous-masked thresholds

Figure 2 shows mean thresholds (in dB SPL) at 0.5 and 2.0 kHz measured in simultaneous masking (triangles) and forward masking (circles) as a function of masker bandwidth for normal-hearing subjects (filled) and hearing-impaired subjects (open). Thresholds in simultaneous masking will be discussed in this section; forward-masked thresholds will be discussed in the next section. Simultaneous-masked thresholds remained essentially constant as masker bandwidth increased for the 0.5-kHz signal, but increased with masker bandwidth for the 2.0-kHz signal. For the 2.0-kHz signal, masked thresholds for normal-hearing subjects increased from 81.1 dB SPL in the 0.4-kHz masker bandwidth to 84.7 dB SPL in the 2.0-kHz masker bandwidth, or about 1.4 dB/oct. Assuming a critical bandwidth at 2.0 kHz of 320 Hz (Scharf, 1970), thresholds should have remained constant for these ''super-critical'' bandwidths (Fletcher, 1940). Nevertheless, the trend of slightly increasing thresholds was similar to the simultaneous-masked thresholds at 2.0 kHz reported by Weber (1978; Fig. 4, p. 143).

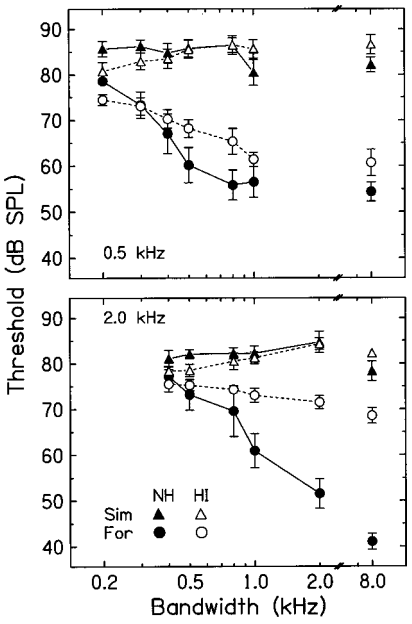

FIG. 2. Mean thresholds (±1 SE) for 20-ms signals measured in simultaneous masking (triangles) and forward masking (circles) as a function of masker bandwidth for normal-hearing subjects (NH, filled symbols) and hearing-impaired subjects (HI, open symbols). Thresholds for the 0.5-kHz signal are in the upper panel and thresholds for the 2.0-kHz signal are in the lower panel.

Recall that in the current experiment, for simultaneous masking, the 20-ms signal was temporally located near the beginning of the 350-ms masker (signal onset followed masker onset by 5 ms). As such, the slope of the functions relating simultaneous-masked thresholds to masker bandwidth may have been influenced by the effect known as overshoot. Overshoot refers to the observation that detection of a short signal may be poorer when the signal is located near the onset of a noise masker than when located near the middle or end of the masker (e.g., Zwicker, 1965a). Overshoot is most commonly attributed to short-term adaptation of auditory-nerve fibers tuned near and around the signal frequency, with perhaps a greater contribution from the higher frequency region (Bacon and Smith, 1991), although the precise mechanism is not yet known. For bandlimited maskers, overshoot was limited to maskers wider than a critical band (Zwicker, 1965b), and increased with masker bandwidth (Wright, 1997). That is, thresholds for signals near the temporal center of the masker remained constant with increasing masker bandwidth, whereas thresholds for signals near the onset of the masker (as in the current experiment) increased with masker bandwidth (Bacon and Smith, 1991). Moreover, overshoot was generally observed for frequencies >1.0 kHz; in the current experiment, thresholds increased with masker bandwidth for the 2.0-kHz signal but remained essentially constant for the 0.5-kHz signal.

For hearing-impaired subjects, simultaneous-masked thresholds at 2.0 kHz increased from 78.4 dB SPL in the 0.4-kHz masker bandwidth to 84.3 dB SPL in the 2.0-kHz masker bandwidth, or about 2.6 dB/oct. Similar increases in masked thresholds with bandwidth were observed for the 0.5-kHz signal. This slope approached the 3 dB/oct increase in threshold predicted for bandwidths within the critical band. Thus the greater increase in thresholds observed for hearing-impaired subjects may be related to wider critical bandwidths secondary to their cochlear hearing loss.

The greater increase in thresholds with bandwidth for hearing-impaired than for normal-hearing subjects was brought about by differences in thresholds between the groups in the two narrowest maskers, where thresholds of hearing-impaired subjects were *better* than those of normal-hearing subjects (see Fig. 2, triangles). This paradoxical result may also be attributed to overshoot. Overshoot has been shown to be reduced in subjects with temporary (McFadden and Champlin, 1990) or permanent hearing loss (Bacon and Takahashi, 1992). For subjects in those studies, overshoot was smaller because thresholds for signals near the masker

onset were *better* than those of normal-hearing subjects whereas thresholds for signals occurring later in the masker were equivalent to normal. Thus in the current experiment, better thresholds for hearing-impaired subjects in the two narrowest maskers were consistent with a reduction of overshoot for these subjects.[3] Poorer masked thresholds for hearing-impaired subjects than normal-hearing subjects in the broadband masker were not consistent with an overshoot explanation, given that overshoot increases with masker bandwidth (Wright, 1997).

C. Forward-masked thresholds

1. Suppression as a change in signal threshold with masker bandwidth

Figure 2 also shows forward-masked thresholds at 0.5 and 2.0 kHz measured as a function of masker bandwidth for normal-hearing subjects (filled circles) and hearing-impaired subjects (open circles). In contrast to the simultaneous-masked thresholds, forward-masked thresholds decreased as a function of masker bandwidth. From the narrowest to the widest masker (not including broadband), mean forward-masked thresholds of normal-hearing subjects decreased by 22.0 dB for the 0.5-kHz signal (slope $= -9.4$ dB/oct) and by 25.7 dB for the 2.0-kHz signal (slope $= -10.7$ dB/oct). For a 1.0-kHz signal and comparable maskers, similar effects of bandwidth were observed by Leshowitz and Lindstrom (1977) using forward masking, and by Houtgast (1974) using the pulsation-threshold technique (see also review of suppression magnitudes in Oxenham and Plack, 1998). For a 2.0-kHz signal and comparable maskers, changes in threshold as a function of masker bandwidth were larger than observed by Weber (1978), who reported that thresholds decreased at the rate of 4–5 dB/oct. Lee and Bacon (1998) estimated suppression as the difference in forward-masked thresholds for a 20-ms signal between an equivalent-rectangular-bandwidth (ERB) masker and a broadband masker. They observed about 12 dB of suppression at 0.5 kHz and about 18 dB of suppression at 2.0 kHz, with a 20-ms delay introduced between the masker and the signal to reduce confusion effects; ERB maskers were much narrower in bandwidth than the maskers used in the current experiment.

The pattern of threshold change as noise components were added around the signal frequency was notable. For example, thresholds at 0.5 kHz decreased until reaching a plateau beyond which no further decreases were observed (see upper panel of Fig. 2, filled circles). These results are consistent with physiological findings demonstrating that components added to the high-frequency side of a fiber's characteristic frequency will serve as suppressors only if they are within about one octave of the frequency to be suppressed (Arthur *et al.*, 1971). For the 0.5-kHz signal, the upper cutoff frequency of the masker with the widest bandwidth was just at the one-octave range; as such, an additional decrease in threshold for this masker was not expected. At 2.0 kHz, however, the upper cutoff frequency of the widest masker was 3.0 kHz, which was within one octave of the center frequency; forward-masked thresholds would be expected to decrease to approach those in the broadband masker.

For hearing-impaired subjects, threshold changes with masker bandwidth were smaller, especially at 2.0 kHz. For the 0.5-kHz signal, mean forward-masked thresholds decreased by 13.0 dB as a function of masker bandwidth (slope $= -5.4$ dB/oct). For the 2.0-kHz signal, thresholds decreased by only 4.0 dB (slope $= -1.7$ dB/oct). Thus for these subjects with cochlear hearing loss, suppression was reduced at both low and high frequencies relative to that observed for younger subjects with normal hearing, and was reduced to a greater extent in the region of greater hearing loss.

Although results of the current experiment suggested that suppression may be greater in the high frequencies, direct comparisons were not straightforward because of differences in relative masker bandwidths for the two signals. For both signals, masker bandwidths varied from narrowest to widest by 2.32 octaves. However, at 0.5 kHz, the narrowest bandwidth was 40% of the signal frequency, whereas at 2.0 kHz, the narrowest bandwidth was 20% of the signal frequency (but still greater than the critical bandwidth); the widest masker bandwidths (not considering broadband) were also necessarily different. For a more direct comparison of suppression for the two signal frequencies, differences between thresholds in a narrowband masker and the broadband masker were computed. Here, the narrowband maskers were those whose bandwidths were each 40% of the signal frequency (0.2 kHz for the 0.5-kHz signal and 0.8 kHz for the 2.0-kHz signal); the broadband masker was the same for the two signals. For normal-hearing subjects, mean differences in thresholds measured in narrowband and broadband maskers were 24.2 dB at 0.5 kHz and 28.5 dB at 2.0 kHz, which were consistent with frequency differences in suppression measured with similar procedures by Lee and Bacon (1998) and with those measured with pure tones by Hicks and Bacon (1999). (These results are shown in the upper panel of Fig. 4, which will be discussed later.) Larger amounts of suppression at the higher signal frequency were also consistent with greater nonlinear processing in the basal than apical regions of the cochlea (e.g., Rhode and Cooper, 1993; Cooper and Rhode, 1995), and greater nonlinearity for higher frequency than lower frequency auditory nerve fibers (e.g., Schmiedt *et al.*, 1980; Cai and Geisler, 1996). For hearing-impaired subjects, mean differences in thresholds between the narrowband maskers of equal relative bandwidth and the broadband masker were 13.8 dB at 0.5 kHz and 5.7 dB at 2.0 kHz, which was consistent with the finding of a greater reduction in suppression in the region of greater hearing loss.

It is important to emphasize that forward-masked thresholds were not limited by these subjects' absolute thresholds at the signal frequency. For the hearing-impaired subjects, mean absolute threshold for the 20-ms signal was 37.2 dB SPL at 0.5 kHz, which is substantially lower than the lowest forward-masked threshold for hearing-impaired subjects. Forward-masked thresholds for hearing-impaired subjects were, on average, at least 24 dB higher than their absolute

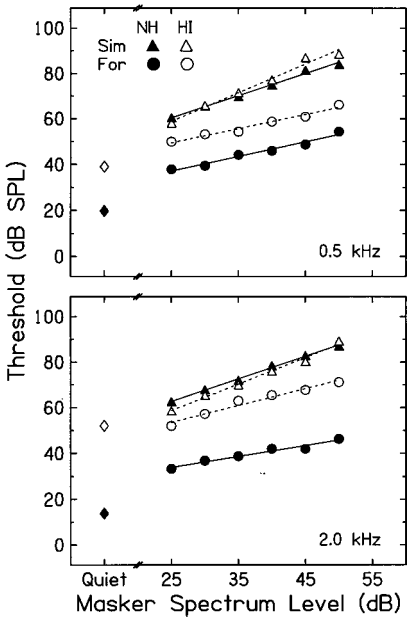

FIG. 3. Mean simultaneous-masked thresholds (triangles) and forward-masked thresholds (circles) for 20-ms signals as a function of the spectrum level of the broadband masker for normal-hearing subjects (NH, filled symbols) and hearing-impaired subjects (HI, open symbols). Mean thresholds in quiet are shown by the diamonds. Thresholds for the 0.5-kHz signal are in the upper panel and thresholds for the 2.0-kHz signal are in the lower panel. Regression lines were fitted to mean thresholds for normal-hearing subjects (solid lines) and hearing-impaired subjects (broken lines) derived using the least-squares procedure.

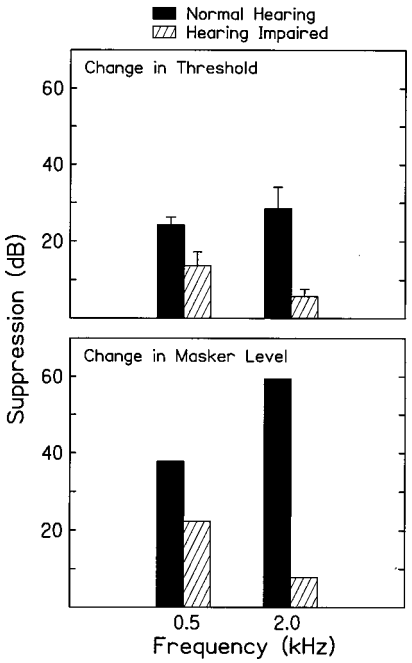

FIG. 4. Mean suppression (±1 SE) at 0.5 and 2.0 kHz for normal-hearing subjects (filled bars) and hearing-impaired subjects (striped bars). Suppression was defined as the difference in forward-masked thresholds measured in the narrowest and widest bandpass maskers (upper panel) and as the difference in effective masker level in the narrowest and widest bandpass maskers (lower panel). See text for description.

thresholds. For the subject with the highest absolute threshold, the best forward-masked threshold exceeded the absolute threshold by 12 dB. At 2.0 kHz, mean absolute threshold was 52.4 dB SPL for the hearing-impaired subjects; on average, forward-masked thresholds were at least 16–20 dB higher than their absolute thresholds. For the subject with the highest absolute threshold, the best forward-masked threshold exceeded the absolute threshold by 11 dB.

The finding that hearing-impaired subjects' masked thresholds improved much less for the 2.0-kHz signal than for the 0.5-kHz signal (suggesting much less suppression at 2.0 kHz than at 0.5 kHz) may be related to their higher absolute thresholds at 2.0 kHz than at 0.5 kHz, or to their generally higher thresholds in the higher frequencies. For the 0.5-kHz signal, the upper cutoff frequency of the widest bandpass masker was 1.0 kHz, which was within the region of only mild hearing loss for many hearing-impaired subjects. However, for the 2.0-kHz signal, the masker's upper cutoff frequency of the widest bandpass masker was 3.0 kHz, which was in the range where subjects' hearing loss was greater. The question of suppression's relationship to absolute thresholds will be addressed further in a later section.

2. Suppression as a change in effective masker level with bandwidth

Figure 3 shows mean forward-masked thresholds for 20-ms signals at 0.5 kHz (upper panel) and 2.0 kHz (lower panel) as a function of the spectrum level of the broadband masker. The solid and broken lines are regression lines fitted to mean thresholds for normal-hearing and hearing-impaired subjects, respectively, derived using the least-squares procedure. Masked thresholds of individual subjects were not included in the mean if they were within 5 dB of the absolute threshold; this rule excluded thresholds in the 25-dB and 30-dB maskers for two hearing-impaired subjects at 2.0 kHz. For comparison, growth-of-masking functions for simultaneous masking are also shown, for which the slopes were 0.98 and 0.99 for normal-hearing subjects for 0.5 and 2.0 kHz, respectively, and were higher for hearing-impaired subjects (1.27, 1.17).

For forward masking, the slopes of the growth-of-masking functions for the 0.5-kHz signal were 0.64 and 0.62 for the normal-hearing and hearing-impaired subjects, respectively. Comparable values for the 2.0-kHz signal were 0.48 and 0.74. These were somewhat steeper than reported by Lee and Bacon (1998) for ERB maskers and a longer signal delay, but similar to those found by Hicks and Bacon (1999) for tonal maskers. Suppression at 0.5 and 2.0 kHz estimated as a change in effective masker level is shown in the lower panel of Fig. 4. For each signal frequency, suppression was computed by taking the difference between the threshold in the narrowband masker of equal relative bandwidth and the broadband masker and dividing by the slope of the growth-of-masking function. Shown in the upper panel of Fig. 4 is suppression estimated as the difference in threshold at the signal frequency measured in narrowband and broadband maskers (described earlier). Suppression defined as a change in effective masker level was larger, but the pattern of results for the two signal frequencies and two subject groups remained about the same regardless of how suppression was defined. At the higher signal frequency, estimating

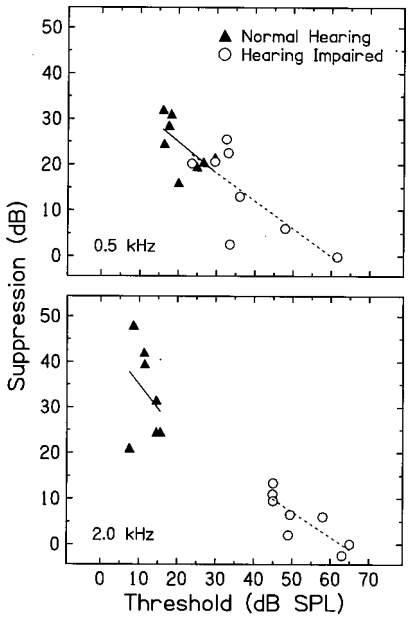

FIG. 5. Suppression for normal-hearing subjects (filled triangles) and hearing-impaired subjects (open circles) plotted against each subject's absolute threshold for the 20-ms tone at the signal frequency. Solid lines (normal-hearing subjects) and broken lines (hearing-impaired subjects) are linear regression functions fitted to individual data derived using the least-squares procedure. Suppression and thresholds at 0.5 kHz are in the upper panel and those at 2.0 kHz are in the lower panel. Suppression was defined as the difference in forward-masked thresholds measured in the narrowest and widest bandpass maskers.

suppression as a reduction in effective masker level tended to magnify the penalty of hearing loss on suppression. This resulted from the less steep growth-of-masking function for normal-hearing than for hearing-impaired subjects at 2.0 kHz.

3. Associations between suppression and absolute thresholds

Figure 5 plots suppression for normal-hearing and hearing-impaired subjects against each subject's absolute threshold for the 20-ms signal at the signal frequency. Suppression was defined as the difference in threshold at the signal frequency measured in narrowband and broadband maskers. Consider first the results for the 0.5-kHz signal (upper panel). Suppression generally decreased in the same manner for all subjects as the absolute threshold at the signal frequency increased. Overall, for every dB increase in threshold at the signal frequency, suppression decreased by about 0.6–0.7 dB. Suppression was strongly correlated with the 0.5-kHz threshold for hearing-impaired subjects ($r=-0.74$, $p<0.05$). Nevertheless, there was some intersubject variance in the suppression measurement, notably in the range of mild hearing loss (~25–30 dB) where suppression ranged from 2.5 to 25.5 dB. The correlation of suppression and threshold for normal-hearing subjects was only -0.61 ($p>0.05$); the weaker correlation was likely due to the truncated range of thresholds for the normal-hearing subjects. Where thresholds for the two groups overlapped, suppression for the two groups also overlapped.

For hearing-impaired subjects only, suppression at 0.5 kHz was also significantly correlated with thresholds at frequencies adjacent to 0.5 kHz, although these thresholds strongly co-varied. As such, partial correlations were computed to determine the association between suppression at 0.5 kHz and thresholds at adjacent frequencies while controlling for the correlations among thresholds at 0.25, 0.5, and 1.0 kHz. The results revealed that while 56% of the variance in suppression at 0.5 kHz was accounted for by the absolute threshold at 0.5 kHz, only 8.5% was accounted for by the threshold at 0.25 kHz, and only 1.5% by the threshold at 1.0 kHz. No statistically significant correlations were observed between suppression at 0.5 kHz and thresholds at frequencies other than 0.5 kHz. Thus effects of elevated thresholds on suppression appeared to be limited to the signal frequency.

Consider next the results for the 2.0-kHz signal (lower panel) where thresholds were substantially more elevated for the hearing-impaired subjects. Suppression generally decreased for all subjects as the threshold at the signal frequency increased. Suppression for subjects with normal hearing varied substantially over a very small range of thresholds ($r=-0.33$, $p>0.05$). This was likely a byproduct of the particular narrowband-masked threshold used in the suppression computation (i.e., 0.8-kHz masker), which was selected so that relative masker bandwidths for the two signal frequencies were equal. The intersubject variance for thresholds in that masker was notably larger than for other maskers, perhaps because masked thresholds improved somewhat differently with bandwidth among subjects; this resulted in increased variance in the suppression measure. No statistically significant correlations were observed between suppression at 2.0 kHz and thresholds at any signal frequency, which could be attributed to the truncated range of thresholds for the normal-hearing subjects.

For hearing-impaired subjects, suppression decreased with increasing threshold in a manner similar to that observed at 0.5 kHz. That is, for every dB increase in threshold at 2.0 kHz, suppression decreased by about 0.6 dB. The correlation between suppression at 2.0 kHz and the 2.0-kHz threshold for the hearing-impaired subjects was -0.84 ($p<0.01$); that is, 71% of the variance in suppression at 2.0 kHz was accounted for by the absolute threshold at 2.0 kHz. No other statistically significant correlations were observed between suppression at 2.0 kHz and thresholds at frequencies other than 2.0 kHz. Therefore, as noted for 0.5 kHz, effects of elevated thresholds on suppression appeared to be limited to the signal frequency. Moreover, these results suggested that the magnitude of suppression may not have been influenced by the introduction of noise components in regions where thresholds were elevated. There are several possible explanations for this result. First, the spectrum level of the masker was relatively high (45 dB) and was sufficient to elevate the absolute thresholds of hearing-impaired subjects (although the sensation level was reduced, of course). Second, the influence of thresholds other than at the signal frequency may be obscured by the fact that masker bandwidths were increased by adding noise bands above *and* below the signal frequency. Thus while noise was introduced in higher frequency regions where hearing loss was greatest, which

could result in a reduction in suppression, noise was also added in lower frequency regions where hearing was better. To address this question, in the next experiment of the series (Dubno and Ahlstrom, 2001a), bandwidths of bandpass maskers were increased by introducing noise components above and/or below the signal frequency.

Although fairly strong associations of suppression and signal–frequency threshold were observed in the current experiment, there remained considerable variance in suppression that could not be explained. One factor that was not controlled was subject age, as individuals with hearing loss were substantially older than those with normal hearing. Normal two-tone rate suppression has been observed in quiet-aged gerbils with significant age-related hearing loss, whereas suppression was absent in older gerbils exposed to noise (Schmiedt *et al.*, 1990). This suggests that, in the absence of acoustic injury, normal suppression should be observed in older subjects. However, auditory-filter bandwidth changes in older human subjects have been interpreted as reflecting age-related changes in suppression (Sommers and Gehr, 1998). These unresolved questions related to age and suppression are addressed more directly in the next experiment (Dubno and Ahlstrom, 2001a) by including a group of older subjects with normal hearing.

IV. SUMMARY AND CONCLUSIONS

Forward- and simultaneous-masked thresholds at 0.5 and 2.0 kHz were measured in bandpass maskers as a function of masker bandwidth for subjects with normal hearing and cochlear hearing loss. Suppression was defined as a reduction in forward-masked threshold as masker bandwidth was increased, and as a change in effective masker level as masker bandwidth was increased, taking into account nonlinear growth of forward masking estimated from growth-of-masking functions. Results may be summarized as follows.

(1) For subjects with normal hearing, slightly larger estimates of suppression were obtained at 2.0 kHz than at 0.5 kHz, regardless of whether suppression was defined as a change in threshold or a change in effective masker level. This is consistent with greater nonlinear processing at higher than at lower frequencies.
(2) For subjects with cochlear hearing loss, suppression was reduced substantially relative to that observed for subjects with normal hearing, and was reduced to a greater extent at 2.0 kHz, where hearing loss was greater, than at 0.5 kHz.
(3) Suppression was strongly correlated with the absolute threshold at the signal frequency, but was not related to thresholds at frequencies remote from the signal frequency.
(4) Simultaneous-masked thresholds stayed relatively constant (0.5 kHz) or increased slightly (2.0 kHz) as a function of masker bandwidth for normal-hearing subjects, and increased more for hearing-impaired subjects. These results may show evidence of the effects of overshoot, given that the signal was located near the onset of the masker, or may be related to hearing-impaired subjects' wider critical bandwidths.
(5) With appropriate selection of signals and maskers and stimulus conditions, forward-masked thresholds measured in bandlimited and broadband maskers may be an efficient psychophysical method for estimating suppression in subjects with normal hearing and cochlear hearing loss.

ACKNOWLEDGMENTS

This work was supported (in part) by Grants Nos. R01 DC00184 and P50 DC00422 from NIH/NIDCD. The authors thank Chris Ahlstrom for computer and signal-processing support, Fu-Shing Lee for advice on data analysis, and Amy R. Horwitz, John H. Mills, and Richard A. Schmiedt for editorial comments. We also thank Associate Editor Sid P. Bacon who provided helpful advice for improving the manuscript.

[1]The signal was temporally located near the beginning of the masker to correspond to the location of consonants in consonant–vowel syllables presented in the same maskers. These results are not reported here.

[2]In two subsequent experiments using the same masker bandwidths as in the current experiment, two forms of evidence suggest that confusion effects were not influencing forward-masked thresholds. First, in Dubno and Ahlstrom (2001a, b), masker bandwidths were increased by adding noise bands below and above the signal (as in the current experiment) and also by adding noise bands below the signal only and above the signal only. The decline in forward-masked thresholds with increasing masker bandwidth differed for the various band-widening methods. Second, in Dubno and Ahlstrom (2001b), forward-masked thresholds as a function of masker bandwidth were measured in three masker levels. Slopes of growth-of-masking functions were <1.0 regardless of masker bandwidth, arguing against the influence of confusion effects (Neff, 1985).

[3]Additional evidence for the contribution of overshoot to simultaneous-masked thresholds, and specifically for the greater importance of masker energy above the signal frequency, may be found in results from a subsequent experiment wherein simultaneous-masked thresholds were measured at 2.0 kHz in bandpass maskers as a function of masker bandwidth (Dubno and Ahlstrom, 2001a). The signal onset followed masker onset by 5 ms. Here, bandwidth was increased from narrowest to widest in three ways: by adding noise components below and above the signal frequency (as in the current experiment), and also by adding noise bands below the signal frequency only and above the signal frequency only. Subjects were younger and older adults with normal hearing. As was observed in the current experiment, simultaneous-masked thresholds increased with masker bandwidth for younger subjects with normal hearing. Moreover, thresholds increased to a greater extent (suggesting larger overshoot) when noise bands were added above the signal frequency than when noise was added below the signal frequency. No changes in simultaneous-masked thresholds with bandwidth were observed for older subjects with normal hearing, regardless of the masker location.

ANSI (**1989**). ANSI S3.6-1989, "Specifications for audiometers" (American National Standards Institute, New York).

Arthur, R. M., Pfeiffer, R. R., and Suga, N. (**1971**). "Properties of two-tone inhibition in primary auditory neurones," J. Physiol. (London) **212**, 593–609.

Bacon, S. P., and Smith, M. A. (**1991**). "Spectral, intensive, and temporal factors influencing overshoot," Q. J. Exp. Psych. **43A**, 373–399.

Bacon, S. P., and Takahashi, G. A. (**1992**). "Overshoot in normal-hearing and hearing-impaired subjects," J. Acoust. Soc. Am. **91**, 2865–2871.

Cai, Y., and Geisler, C. D. (**1996**). "Suppression in auditory-nerve fibers of cats using low-side suppressors. I. Temporal aspects," Hear. Res. **96**, 94–112.

Cooper, N. P., and Rhode, W. S. (**1995**). "Nonlinear mechanics at the apex of the guinea-pig cochlea," Hear Res. **82**, 225–243.

Delgutte, B. (**1990**). "Physiological mechanisms of psychophysical masking: Observations from auditory-nerve fibers," J. Acoust. Soc. Am. **87**, 791–809.

Dubno, J. R., and Ahlstrom, J. B. (**2001a**). ''Psychophysical suppression measured with bandlimited noise extended below and/or above the signal: Effects of age and hearing loss,'' J. Acoust. Soc. Am. **110**, 1058–1066.
Dubno, J. R., and Ahlstrom, J. B. (**2001b**). ''Psychophysical suppression effects for tonal and speech signals,'' J. Acoust. Soc. Am. (submitted).
Fletcher, H. (**1940**). ''Auditory patterns,'' Rev. Mod. Phys. **12**, 47–65.
Florentine, M., Fastl, H., and Buus, S. (**1988**). ''Temporal integration in normal hearing, cochlear impairment, and impairment simulated by masking,'' J. Acoust. Soc. Am. **84**, 195–203.
Gilbert, A. G., and Pickles, J. O. (**1980**). ''Responses of auditory nerve fibres to noise bands of different widths,'' Hear. Res. **2**, 327–333.
Green, D. M. (**1993**). ''A maximum-likelihood method for estimating thresholds in a yes–no task,'' J. Acoust. Soc. Am. **93**, 2096–2105.
Greenwood, D. D., and Goldberg, J. M. (**1970**). ''Responses of neurons in the cochlear nuclei to variations in noise bandwidth and to tone-noise combinations,'' J. Acoust. Soc. Am. **47**, 1022–1040.
Hall, J. W., and Fernandes, M. A. (**1983**). ''Temporal integration, frequency resolution, and off-frequency listening in normal-hearing and cochlear-impaired listeners,'' J. Acoust. Soc. Am. **74**, 1172–1177.
Hicks, M. L., and Bacon, S. P. (**1999**). ''Effects of aspirin on psychophysical measures of frequency selectivity, two-tone suppression, and growth of masking,'' J. Acoust. Soc. Am. **106**, 1436–1451.
Houtgast, T. (**1974**). ''Lateral suppression in hearing: A psychophysical study on the ear's capability to preserve and enhance spectral contrasts,'' Ph.D. dissertation (Academische Pers B. V, Amsterdam).
Lee, J., and Bacon, S. P. (**1998**). ''Psychophysical suppression as a function of signal frequency: Noise and tonal maskers,'' J. Acoust. Soc. Am. **104**, 1013–1022.
Leek, M. R., Dubno, J. R., He, N-j., and Ahlstrom, J. B. (**2000**). ''Experience with a yes–no single-interval maximum-likelihood procedure,'' J. Acoust. Soc. Am. **107**, 2674–2684.
Leshowitz, B., and Lindstrom, R. (**1977**). ''Measurement of nonlinearities in listeners with sensorineural hearing loss,'' in *Psychophysics and Physiology of Hearing*, edited by E. F. Evans and J. P. Wilson (Academic, London), pp. 283–292.
McFadden, D., and Champlin, C. A. (**1990**). ''Reductions in overshoot during aspirin use,'' J. Acoust. Soc. Am. **87**, 2634–2642.
Mills, J. H. (**1982**). ''Effects of noise on auditory sensitivity, psychophysical tuning curves, and suppression,'' in *New Perspectives on Noise-Induced Hearing Loss*, edited by R. Hamernik, D. Henderson, and R. Salvi (Raven, New York).
Mills, J. H., and Schmiedt, R. A. (**1983**). ''Frequency selectivity: Physiological and psychophysical tuning curves and suppression,'' in *Hearing Research and Theory*, edited by J. V. Tobias and E. D. Schubert (Academic, New York), Vol. 2.
Moore, B. C. J., and Glasberg, B. R. (**1982**). ''Contralateral and ipsilateral cueing in forward masking,'' J. Acoust. Soc. Am. **71**, 942–945.
Moore, B. C. J., and Glasberg, B. R. (**1983**). ''Growth of forward masking for sinusoidal and noise maskers as a function of signal delay; implications for suppression in noise,'' J. Acoust. Soc. Am. **73**, 1249–1259.
Moore, B. C. J., and Glasberg, B. R. (**1985**). ''The danger of using narrow-band noise maskers to measure 'suppression','' J. Acoust. Soc. Am. **77**, 2137–2141.
Moore, B. C. J., and Glasberg, B. R. (**1986**). ''Comparisons of frequency selectivity in simultaneous and forward masking for subjects with unilateral cochlear impairments,'' J. Acoust. Soc. Am. **80**, 93–107.
Moore, B. C. J., and Vickers, D. A. (**1997**). ''The role of spread of excitation and suppression in simultaneous masking,'' J. Acoust. Soc. Am. **102**, 2284–2290.
Neff, D. L. (**1985**). ''Stimulus parameters governing confusion effects in forward masking,'' J. Acoust. Soc. Am. **78**, 1966–1976.
Neff, D. L. (**1986**). ''Confusion effects with sinusoidal and narrow-band noise forward maskers,'' J. Acoust. Soc. Am. **79**, 1519–1529.
Oxenham, A. J., and Plack, C. J. (**1998**). ''Suppression and the upward spread of masking,'' J. Acoust. Soc. Am. **104**, 3500–3510.
Penner, M. (**1980**). ''Two-tone forward masking patterns and tinnitus,'' J. Speech Hear. Res. **23**, 779–786.
Plomp, R., and Bowman, M. A. (**1959**). ''Relation between hearing threshold and duration for tone pulses,'' J. Acoust. Soc. Am. **31**, 749–758.
Rhode, W. S., and Cooper, N. P. (**1993**). ''Two-tone suppression and distortion products on the basilar membrane in the hook region of cat and guinea pig cochleae,'' Hear. Res. **66**, 31–45.
Ruggero, M. A. (**1973**). ''Response to noise of auditory nerve fibers in the squirrel monkey,'' J. Neurophysiol. **36**, 569–587.
Salvi, R. J., Perry, J., Hamernik, R. P., and Henderson, D. (**1982**). ''Relationship between cochlear pathologies and auditory nerve and behavioral responses following acoustic trauma,'' in *New Perspectives on Noise-Induced Hearing Loss*, edited by R. Hamernik, D. Henderson, and R. Salvi (Raven, New York), pp. 165–188.
Scharf, B. (**1970**). ''Critical bands,'' in *Foundations of Modern Auditory Theory, Vol. I*, edited by J. V. Tobias (Academic, New York), pp. 159–202.
Schmiedt, R. A., Zwislocki, J. J., and Hamernik, R. P. (**1980**). ''Effects of hair cell lesions on responses of cochlear nerve fibers. I. Lesions, tuning curves, two-tone inhibition, and responses to trapezoidal-wave patterns,'' J. Neurophysiol. **43**, 1367–1389.
Schmiedt, R. A., Mills, J. H., and Adams, J. C. (**1990**). ''Tuning and suppression in auditory nerve fibers of aged gerbils raised in quiet or noise,'' Hear. Res. **45**, 221–236.
Shannon, R. V. (**1976**). ''Two-tone unmasking and suppression in a forward-masking situation,'' J. Acoust. Soc. Am. **59**, 1460–1470.
Sommers, M. S., and Gehr, S. E. (**1998**). ''Auditory suppression and frequency selectivity in older and younger adults,'' J. Acoust. Soc. Am. **103**, 1067–1074.
Terry, M., and Moore, B. C. J. (**1977**). '''Suppression' effects in forward masking,'' J. Acoust. Soc. Am. **62**, 781–784.
Thibodeau, L. M. (**1991**). ''Performance of hearing-impaired persons on auditory enhancement tasks,'' J. Acoust. Soc. Am. **89**, 2843–2850.
Weber, D. L. (**1978**). ''Suppression and critical bands in band-limiting experiments,'' J. Acoust. Soc. Am. **64**, 141–150.
Weber, D. L., and Green, D. M. (**1978**). ''Temporal factors and suppression effects in backward and forward masking,'' J. Acoust. Soc. Am. **64**, 1392–1399.
Wightman, F., McGee, T., and Kramer, M. (**1977**). ''Factors influencing frequency selectivity in normal and hearing-impaired listeners,'' in *Psychophysics and Physiology of Hearing*, edited by E. F. Evans and J. P. Wilson (Academic, London), pp. 295–306.
Wright, B. A. (**1997**). ''Detectability of simultaneously masked signals as a function of masker bandwidth and configuration for different signal delays,'' J. Acoust. Soc. Am. **101**, 420–429.
Zwicker, E. (**1965a**). ''Temporal effects in simultaneous masking by white noise bursts,'' J. Acoust. Soc. Am. **37**, 653–663.
Zwicker, E. (**1965b**). ''Temporal effects in simultaneous masking and loudness,'' J. Acoust. Soc. Am. **38**, 132–141.

Psychophysical suppression measured with bandlimited noise extended below and/or above the signal: Effects of age and hearing loss

Judy R. Dubno[a] and Jayne B. Ahlstrom
Department of Otolaryngology–Head and Neck Surgery, Medical University of South Carolina, 39 Sabin Street, P.O. Box 250150, Charleston, South Carolina 29425

(Received 4 January 2000; revised 7 March 2001; accepted 23 April 2001)

The objectives of this study were to measure suppression with bandlimited noise extended below and above the signal, at lower and higher signal frequencies, between younger and older subjects, and between subjects with normal hearing and cochlear hearing loss. Psychophysical suppression was assessed by measuring forward-masked thresholds at 0.8 and 2.0 kHz in bandlimited maskers as a function of masker bandwidth. Bandpass-masker bandwidth was increased by introducing noise components below and above the signal frequency while keeping the noise centered on the signal frequency, and also by adding noise below the signal only, and above the signal only. Subjects were younger and older adults with normal hearing and older adults with cochlear hearing loss. For all subjects, suppression was larger when noise was added below the signal than when noise was added above the signal, consistent with some physiological evidence of stronger suppression below a fiber's characteristic frequency than above. For subjects with normal hearing, suppression was greater at higher than at lower frequencies. For older subjects with hearing loss, suppression was reduced to a greater extent above the signal than below and where thresholds were elevated. Suppression for older subjects with normal hearing was poorer than would be predicted from their absolute thresholds, suggesting that age may have contributed to reduced suppression or that suppression was sensitive to changes in cochlear function that did not result in significant threshold elevation. [DOI: 10.1121/1.1381024]

PACS numbers: 43.66.Dc, 43.66.Ba, 43.66.Sr [SPB]

I. INTRODUCTION

There has been renewed interest in psychophysical measures of suppression as a result of questions regarding the role of suppression and spread of excitation in masking (Delgutte, 1990a; Beveridge and Carlyon, 1996; Moore and Vickers, 1997; Oxenham and Plack, 1998). Suppression has also received attention as a result of developments in cochlear mechanics, specifically, that active mechanical processes occur in the cochlea (see Yates, 1995, for a review). It has been proposed that an active cochlear mechanism is responsible for the sharp tips and narrow tuning observed in neural and psychophysical tuning curves. Furthermore, even small disruptions of the active process may produce relatively large changes in sensitivity and tuning (and, presumably, suppression). Consistent with this assumption, psychophysical measures of suppression in subjects with cochlear hearing loss have generally revealed reduced suppression in regions of impaired hearing (e.g., Wightman *et al.*, 1977; Mills and Schmiedt, 1983; Moore and Glasberg, 1986; Thibodeau, 1991), even in subjects with relatively mild threshold elevation (Hicks and Bacon, 1999).

In the first of a series of experiments whose long-term goal was to relate suppression to speech recognition in noise (Dubno and Ahlstrom, 2001a), psychophysical suppression for younger subjects with normal hearing and older subjects with cochlear hearing loss was estimated from forward-masked thresholds measured in bandlimited maskers as a function of masker bandwidth.[1] Slightly larger estimates of suppression were obtained at 2.0 kHz rather than at 0.5 kHz. For older subjects with cochlear hearing loss, suppression was reduced relative to normal in regions of elevated thresholds; suppression was correlated with absolute thresholds only at the signal frequency. In that study, however, the influence of thresholds other than at the signal frequency may have been obscured by the fact that masker bandwidths were increased from narrowest to widest by introducing noise bands above *and* below the signal frequency. Thus noise was introduced in higher-frequency regions where hearing loss was greatest and in lower-frequency regions where hearing was better.

In many neurophysiological bandlimiting experiments, bandwidths of bandpass noise were increased by introducing noise components above and below the edges of the noise while keeping the noise centered on the signal frequency. Other experiments introduced noise or tonal suppressors above or below the characteristic frequency (CF) to assess the complex manner in which suppression varies with the frequency of the suppressor. Using this technique, the results of Schalk and Sachs (1980) suggested that suppression may be greater with suppressors added above rather than below the CF. Other physiological evidence supports stronger suppression below the CF than above (Fahey and Allen, 1985; Delgutte, 1990b), although these results may have been influenced by using a relatively low-frequency noise (Delgutte, 1990b). The outcome clearly depended on how suppression

[a]Electronic mail: dubnojr@musc.edu

 0001-4966/2001/110(2)/1058/9/$18.00

was defined and measured. For example, *suppression thresholds* of auditory-nerve fibers were lower when the suppressor frequency was above the CF than below the CF (Sachs and Kiang, 1968). However, the *growth of suppression* with suppressor level was greater when the suppressor was below the CF than above the CF (Kiang and Moxon, 1974; Delgutte, 1990b), suggesting that suppression may be greater below the signal frequency than above for levels of speech and noise typically encountered in the environment. Given the long-term goal of relating suppression to speech recognition in noise, one purpose of the current experiment was to address the question of how psychophysical suppression varies with the frequency of the suppressor. In the current experiment, bandpass-masker bandwidths were varied with respect to the signal frequency in three ways. Bandwidth was increased by introducing noise components below and above the signal frequency while keeping the noise centered on the signal frequency, and also by adding noise bands below the signal frequency only, and above the signal frequency only. Adding noise components in this way also makes it possible to isolate the effects on suppression of hearing loss in lower- and higher-frequency regions.

An additional benefit of varying the masker bandwidth in three different ways was that threshold differences observed among these maskers may help rule out the influence of listener confusion, wherein subjects have difficulty differentiating the signal from the masker under certain conditions. The potential confounding effect of confusion on forward-masked thresholds in bandlimited maskers has been studied extensively (e.g., Moore and Glasberg, 1985; Neff, 1985, 1986). Although the effect of confusion can be substantial, Moore and Glasberg (1983) suggested that its influence may be minimized with appropriate stimuli and procedures (see Sec. II).

In the earlier study (Dubno and Ahlstrom, 2001a), subjects with hearing loss were older than subjects with normal hearing. Therefore, it was not possible to determine if differences in suppression observed between younger subjects with normal hearing and older subjects with cochlear hearing loss were due solely to threshold-related differences or if subjects' age also contributed to the results. Changes in auditory-filter bandwidth in older subjects with normal hearing have been attributed to changes in suppression with age (Sommers and Gehr, 1998). However, physiological evidence suggests that there is little correlation between magnitude of age-related hearing loss and two-tone rate suppression. For example, in gerbils raised in a quiet environment, normal two-tone suppression was observed in animals with significant age-related threshold elevation (Schmiedt *et al.*, 1990). However, two-tone rate suppression was absent in the region of the threshold elevation in older gerbils exposed to noise. Based on these results, in the absence of noise exposure, suppression would be expected to be independent of subjects' age. To address more directly the relationship between age and suppression, subjects in the current experiment included younger and older adults with normal hearing and older adults with cochlear hearing loss.

II. METHODS

A. Subjects

There were three subject groups: (1) ten younger adults with normal hearing (mean age: 28.2 years; range: 19–39); (2) five older adults with normal hearing (mean age: 69.2 years; range: 65–74); and (3) ten older adults with mild-to-moderate, bilaterally symmetrical cochlear hearing loss (mean age: 63.7 years; range: 56–74). Absolute thresholds of younger and older subjects with normal hearing were <20 dB HL (ANSI, 1989) at octave frequencies from 0.25 to 4.0 kHz and immittance measures were within normal limits. Hearing-impaired subjects had adult-onset cochlear hearing loss (specific etiology unknown), absolute thresholds within specific ranges, and normal immittance measures. Criteria for selection of hearing-impaired subjects was the same as in Dubno and Ahlstrom (2001a). One ear of each subject was selected for testing. Subjects received approximately 2 h of practice with forward masking prior to the start of data collection. Data collection was completed in three, 2-h sessions. Subjects were paid for their participation.

B. Apparatus and stimuli

Signals for quiet thresholds were 350-ms tones (with 5-ms raised-cosine rise/fall ramps) at selected one-third-octave frequencies ranging from 0.25 to 6.3 kHz. Signals for forward masking were 20-ms tones (with 5-ms raised-cosine rise/fall ramps) at 0.8 and 2.0 kHz. Tonal signals were digitally generated pure tones (TDT DD1), sampled at 50.0 kHz and low-pass filtered at 8.5 kHz. Bandpass maskers were created by digitally filtering a broadband noise (filter slopes >100 dB/oct). For each signal, there were five to seven bandpass maskers with varying bandwidths. Bandwidths ranged from 0.2 to 1.5 kHz (for the 0.8-kHz signal) and from 0.4 to 2.0 kHz (for the 2.0-kHz signal). The narrowest bandpass maskers were centered at the signal frequency. Bandwidths were increased from narrowest to widest in three ways. Bandwidths of ''Center Frequency Fixed'' maskers were increased by adding noise bands above and below the signal frequency (same as Dubno and Ahlstrom, 2001a). Bandwidths of ''Low-Frequency Edge Fixed'' maskers were increased by adding noise bands above the signal frequency (that is, fixing the low-frequency edge and varying the high-frequency cutoff). Bandwidths of ''High-Frequency Edge Fixed'' maskers were increased by adding noise bands below the signal frequency (that is, fixing the high-frequency edge and varying the low-frequency cutoff). A broadband masker was also included (low-pass cutoff set to 8.0 kHz). Masker duration was 350 ms, including 5-ms raised-cosine rise/fall ramps. The duration between the masker and the signal was 0 ms (at the 0-voltage points).

The amplitudes of the signals and maskers were controlled individually using programmable and manual attenuators (TDT PA4). The masker level was fixed at a spectrum level of 45 dB and the signal level was varied adaptively. The signal was mixed with the masker (TDT SM3) and delivered through one of a pair of TDH-49 earphones mounted in supra-aural cushions. Spectral characteristics of all signals

were verified using an acoustic coupler and a signal analyzer (Stanford Research model SR 760).

C. Procedures

Procedures were similar to those in Dubno and Ahlstrom (2001a) and are briefly reviewed here. Thresholds were measured using a single-interval (yes–no) maximum-likelihood psychophysical procedure with 24 trials, 4 of which were catch trials (Green, 1993; Leek *et al.*, 2000). Thresholds in quiet were measured for 350-ms tones at selected one-third-octave frequencies and for 20-ms tones at 0.8 and 2.0 kHz. Forward-masked thresholds were measured for the 20-ms tones at 0.8 and 2.0 kHz in bandpass maskers as a function of masker bandwidth and in a broadband masker. Quiet thresholds were measured first for all subjects. The order of band-widening method (Center Frequency Fixed, Low-Frequency Edge Fixed, High-Frequency Edge Fixed) was selected randomly for each subject; all thresholds for one band-widening method were measured before going on to another method. Within each band-widening method, the order of signal frequency (0.8 kHz, 2.0 kHz) and then masker bandwidth was randomized. Two threshold measurements were obtained in each condition; if these differed by more than 5 dB, a third measurement was obtained. Each data point was the average of the two closest threshold measurements.

Stimuli and procedures for forward masking were selected to minimize the effects of confusion between the masker and the signal (Moore and Glasberg, 1985, 1986), including: (1) a 20-ms signal, which was long enough to have a tonal quality to differentiate it from the masker's ''noisy'' quality; (2) bandpass masker bandwidths which were $\geqslant$20% of the signal frequency (very narrow masker bandwidths have envelope fluctuations which are similar to those of the signal); and (3) practice sessions wherein subjects were trained to differentiate the quality differences between the masker and the signal, using masker-signal delays $>$0 ms. None of the subjects displayed systematic changes in their forward-masked thresholds during the course of data collection. As noted earlier, different results for the various band-widening conditions provide evidence against the influence of confusion, although it is difficult to rule its effects out entirely.[2]

III. RESULTS AND DISCUSSION

A. Quiet thresholds

Mean thresholds (in dB SPL) for the three groups of subjects are shown in Fig. 1 for 350-ms signals (top) and for 20-ms signals (bottom). Thresholds for the older subjects with normal hearing were slightly higher than those of younger subjects, although all subjects in these two groups met the criterion of ''normal hearing.'' Hearing-impaired subjects had a mild-to-moderate hearing loss which was greater in the higher frequencies than in the lower frequencies. Duration-related differences in thresholds (350 vs. 20 ms) at 0.8 and 2.0 kHz for the three subject groups were also assessed. Across frequency, thresholds for the longer tone averaged 10.4 dB lower than those for the shorter tone for younger subjects (corresponding to -2.5 dB/doubling of duration, similar to the expected -3 dB/doubling). Threshold differences (350 vs. 20 ms) were only 6.8 dB (-1.6 dB/doubling) and 5.7 dB (-1.4 dB/doubling) for older subjects with normal hearing and hearing loss, respectively, suggesting that the time constants for temporal integration were decreasing for older subjects, even those with relatively normal hearing.

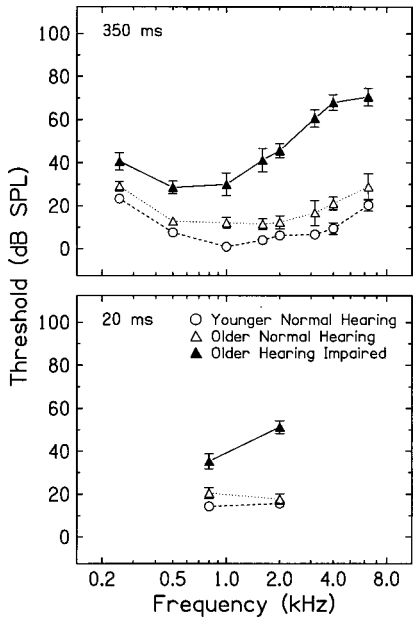

FIG. 1. Mean thresholds (in dB SPL) measured in quiet for younger subjects with normal hearing (open circles), older subjects with normal hearing (open triangles), and older subjects with cochlear hearing loss (filled triangles) for 350-ms signals (top panel) and 20-ms signals (bottom panel). Error bars indicate ± 1 standard error of the mean (SE).

B. Psychophysical suppression in younger subjects with normal hearing

1. Masked thresholds and suppression

Figures 2 and 3 show mean thresholds at 0.8 and 2.0 kHz, respectively, measured in forward masking as a function of masker bandwidth for three subject groups. In each panel, the parameter is band-widening method. The magnitude of suppression was defined as the difference in forward-masked thresholds measured in the narrowest and widest bandpass maskers (not including broadband). Mean suppression values are shown in Fig. 4 for the two signal frequencies, three band-widening methods, and three subject groups. At the 0.8-kHz signal frequency, the widest bandwidth that could be achieved was narrower for the High-Frequency Edge Fixed masker than for the other maskers. Relative masker bandwidths (i.e., bandwidth as a percentage of the signal frequency) were also somewhat different for the two signal frequencies. Therefore, to compare threshold changes as a function of masker bandwidth for each of the three band-widening methods and two signals, the slope of the function relating threshold to bandwidth (in dB/oct) was also determined for each condition by linear regression on the individual data. The following section considers results for the younger subjects with normal hearing (top panels of Figs.

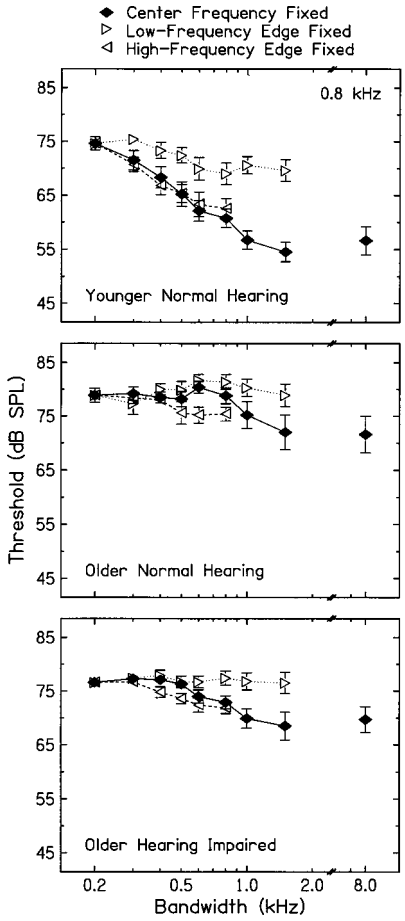

FIG. 2. Mean thresholds (±1 SE) for 20-ms signals at 0.8 kHz measured in forward masking as a function of masker bandwidth and in a broadband masker for younger subjects with normal hearing (top panel), older subjects with normal hearing (middle panel), and older subjects with cochlear hearing loss (bottom panel). In each panel, the parameter is band-widening method. With *Center Frequency Fixed* maskers, bandwidth was increased from narrowest to widest by adding noise below and above the signal frequency. With *Low-Frequency Edge Fixed* maskers, noise was added above the signal by increasing the upper cutoff frequency. With *High-Frequency Edge Fixed* maskers, noise was added below the signal by decreasing the lower cutoff frequency.

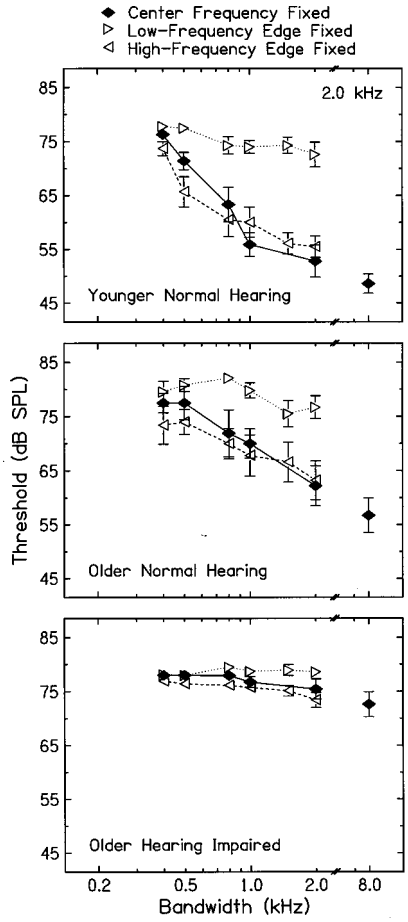

FIG. 3. Same as Fig. 2, but for the 2.0-kHz signal frequency.

2, 3, and 4). Results for the older subjects with normal hearing and cochlear hearing loss will be considered in a later section.

From the narrowest to the widest masker bandwidth, forward-masked thresholds at 0.8 kHz of younger subjects with normal hearing decreased most for center frequency fixed maskers (slope = −6.9 dB/oct), slightly less when the masker's high-frequency edge was fixed (−6.0 dB/oct), and least when the masker's low-frequency edge was fixed (−1.9 dB/oct). Thus suppression was larger when noise was introduced below the signal than when noise was introduced above the signal. The same pattern was observed for the 2.0-kHz signal, although suppression estimates were generally larger. Slopes of functions relating 2.0-kHz thresholds to masker bandwidth were −9.4, −6.6, and −2.0 dB/oct, for noise above and below the signal frequency, noise below only, and noise above only, respectively. The finding of greater suppression at higher than lower signal frequencies was consistent with frequency differences in suppression observed by Lee and Bacon (1998) and Hicks and Bacon (1999), and was similar to differences in suppression found between 0.5 and 2.0 kHz in our earlier study (Dubno and Ahlstrom, 2001a).[3]

One of the most consistent findings of the current study was that less suppression was observed when suppressors were introduced above rather than below the signal frequency. Moreover, there were clear differences in how thresholds changed as noise components were added above or below the signal frequency (compare functions with ◁ and ▷ symbols in top panels of Figs. 2 and 3). When noise was introduced above the signal frequency, thresholds decreased slightly as the masker's upper cutoff frequency was raised, until reaching a plateau beyond which no further decreases in thresholds were observed. In contrast, when noise was introduced below the signal frequency, thresholds decreased more and continued to decrease as the masker's lower cutoff frequency was lowered.

2. Physiological correlates

The effects of signal and suppressor frequency on psychophysical suppression for younger subjects with normal hearing may be explained by the unique shapes of suppression regions on the low- and high-frequency sides of tuning curves. The area of the suppression band that flanks the steep high-frequency side of the tuning curve is typically smaller and more vertical than the area of the band that surrounds the broad low-frequency tail of the tuning curve, especially for

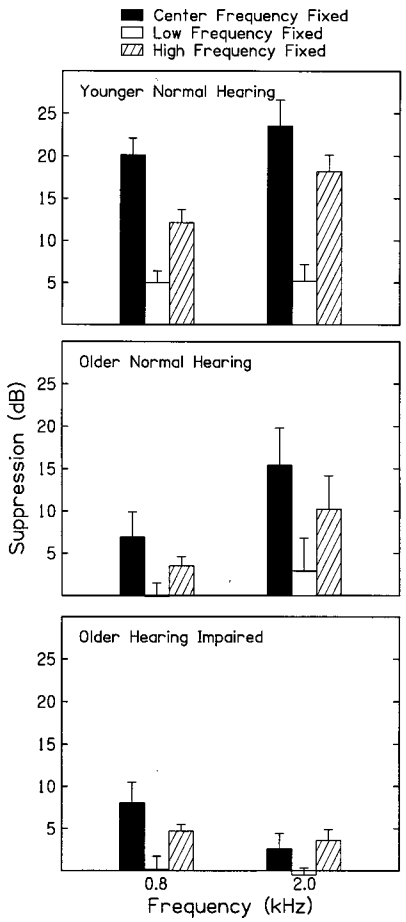

FIG. 4. Mean suppression (±1 SE) at 0.8 and 2.0 kHz for younger subjects with normal hearing (top panel), older subjects with normal hearing (middle panel), and older subjects with cochlear hearing loss (bottom panel). In each panel, the parameter is band-widening method, as described in the caption for Fig. 2 and in the text. Suppression was defined as the difference in forward-masked thresholds measured in the narrowest and widest bandpass maskers.

higher-frequency fibers (e.g., Harris, 1979; Schmiedt, 1982). Thus when noise bands were introduced above the signal frequency, thresholds decreased as noise impinged on the narrow high-frequency suppression area. Increasing the upper cutoff frequency of the masker placed noise components in regions beyond the suppression band which were neither excitatory nor suppressive. Therefore, no further improvement in threshold would be expected. These assumptions are also consistent with physiological findings demonstrating that components added to the high-frequency side of the CF serve as suppressors only if they are within about one octave of the frequency to be suppressed (Arthur *et al.*, 1971). For the 0.8-kHz signal in the current experiment, the upper cutoff frequency of maskers with the two widest bandwidths approached or exceeded the one-octave range; as such, additional decreases in threshold for these maskers would not be expected. This pattern of thresholds as a function of masker bandwidth was also observed at 2.0 kHz, although the wider bandpass maskers were less than one octave from the signal frequency.

Suppression areas on the high-frequency side of physiological tuning curves are relatively larger for lower-frequency fibers than for higher-frequency fibers (e.g., Schmiedt, 1982). This frequency difference is also consistent with results of the current experiment, shown in the top panels of Figs. 2 and 3 (▷ symbols for younger subjects with normal hearing). When noise components were added above the signal frequency (impinging on the high-frequency suppression area), thresholds decreased more for the lower-frequency signal than for the higher-frequency signal before both reached their plateau.

Given the larger area of the suppression band flanking the broad low-frequency tail of the tuning curve, especially for higher-frequency fibers, larger decreases in thresholds would be expected as noise was introduced below the signal frequency, especially for higher-frequency signals. Moreover, thresholds should continue to improve as the masker's low-frequency cutoff was decreased. This is consistent with the current results wherein masked thresholds decreased more and continued to decrease with low-frequency cutoff when noise was introduced below the signal frequency. This effect was greater for the higher-frequency signal than for the lower-frequency signal. Larger amounts of suppression at the higher-frequency signal were also consistent with greater nonlinear processing in the basal than apical regions of the cochlea, and greater nonlinearity for higher frequency than lower frequency auditory-nerve fibers (e.g., Schmiedt *et al.*, 1980; Rhode and Cooper, 1993; Cooper and Rhode, 1995; Cai and Geisler, 1996).

C. Psychophysical suppression in older subjects with normal hearing and cochlear hearing loss

1. Masked thresholds and suppression

Forward-masked thresholds as a function of masker bandwidth for older subjects with normal hearing and older subjects with cochlear hearing loss are shown in the middle and bottom panels of Figs. 2 and 3, for 0.8 and 2.0 kHz, respectively; mean suppression values for these two groups are shown in the middle and bottom panels of Fig. 4 for the two signal frequencies and three band-widening methods.

For the two groups of older subjects, differences among the three band-widening methods were similar to those observed for younger subjects, but threshold changes were much smaller, especially for subjects with hearing loss. Consider first the results for older subjects with normal hearing (middle panels of Figs. 2, 3, and 4). The slope of the function relating forward-masked thresholds at 0.8 kHz to masker bandwidth was −2.5 dB/oct when noise was added above and below the signal frequency and −2.1 dB/oct when noise was added below only. In contrast to the generally monotonic functions for the younger subjects, for these conditions, thresholds remained relatively constant for the narrower bandwidths, and then decreased (or increased and decreased) for the wider bandwidths only. Forward-masked thresholds remained constant when noise was added above the signal, suggesting very little, if any, suppression. The same pattern was observed for the 2.0-kHz signal, but estimates of suppression were slightly larger, though not as large as those of younger subjects. Slopes of functions relating forward-masked thresholds to masker bandwidth were −6.7, −4.5,

and −2.2 dB/oct, for noise above and below the signal frequency, noise below only, and noise above only, respectively.[4]

Consider next the results for older subjects with cochlear hearing loss (bottom panels of Figs. 2, 3, and 4). The patterns of threshold change with bandwidth and magnitude of suppression were similar at 0.8 kHz to those of the older subjects with normal hearing; that is, thresholds remained relatively constant for the narrower bandwidths and decreased in wider bandwidth maskers. Slopes were −3.5 dB/oct when noise was added above and below the signal and −2.5 dB/oct when noise was added below the signal only. Thresholds remained constant when noise was added above the signal only. Almost no improvement in threshold with bandwidth was observed for the 2.0-kHz signal, suggesting little suppression. Comparable slopes were −1.2, −1.4, and 0.2 dB/oct for noise above and below the signal frequency, noise below only, and noise above only, respectively.

Forward-masked thresholds were not limited by hearing-impaired subjects' absolute thresholds at the signal frequency. Mean threshold for the 20-ms signal at 0.8 kHz was 35.3 dB SPL, which was substantially lower than the lowest forward-masked threshold for the hearing-impaired subjects. Absolute thresholds of subjects with hearing loss were, on average, at least 33 dB better than their forward-masked thresholds. For the subject with the highest absolute threshold, the best forward-masked threshold exceeded the absolute threshold by 22 dB. Mean absolute threshold for the 20-ms signal at 2.0 kHz was 51.3 dB SPL, which was, on average, at least 21 dB better than the mean forward-masked thresholds. For the subject with the highest absolute threshold, the best forward-masked threshold exceeded the absolute threshold by 11 dB.

2. Associations between suppression and absolute thresholds

There were notable differences in how suppression varied with subject age and hearing loss. For example, differences in suppression among the three subject groups varied somewhat with signal frequency, as summarized in Fig. 4. At both signal frequencies, less suppression was observed for older than for younger subjects with normal hearing, but age-related differences in magnitude of suppression were larger at 0.8 kHz than at 2.0 kHz. Mean absolute threshold for the 20-ms signal at 0.8 kHz for the older subjects with normal hearing was slightly higher than that of the younger group, whereas thresholds at 2.0 kHz were nearly identical to those of the younger subjects. Suppression for older subjects with cochlear hearing loss was reduced more at 2.0 kHz than at 0.8 kHz, which was consistent with these subjects' higher absolute thresholds for higher frequency signals.

The relation between suppression and absolute thresholds is examined in Fig. 5, which plots suppression for younger subjects with normal hearing, older subjects with normal hearing, and older subjects with cochlear hearing loss against each subject's absolute threshold at the signal frequency. Suppression is shown for the condition wherein noise was added above and below the signal frequency.[5] Suppression generally decreased as the absolute threshold at the signal frequency increased, as shown by the slopes of the regression lines for subjects with cochlear hearing loss. For these subjects, for every dB increase in threshold at the signal frequency, suppression decreased by about 0.4–0.5 dB. For subjects with hearing loss, suppression at 2.0 kHz was strongly correlated with their 2.0-kHz threshold ($r=-0.82$, $p<0.01$); the comparable relationship for 0.8 kHz was similar but not statistically significant ($r=0.59$, $p>0.05$). At both frequencies, older subjects with the poorest thresholds consistently showed little suppression. However, there was substantial variance in the results for older subjects whose thresholds were in the range of normal hearing or mild hearing loss at 0.8 kHz (~20–30 dB SPL); suppression for these subjects ranged from 0 to 23 dB. Thus suppression for some older subjects with better thresholds was within the range of the younger subjects, especially at 2.0 kHz. At 0.8 kHz, suppression for some older subjects with normal hearing was poorer than would be predicted from their absolute thresholds. No statistically significant correlations were observed between suppression at 0.8 or 2.0 kHz and thresholds at frequencies lower or higher than the signal frequencies. Thus effects of elevated thresholds on suppression may not extend beyond the signal frequency.

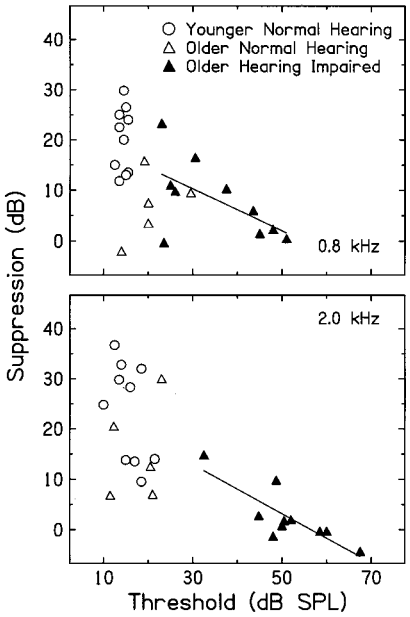

FIG. 5. Suppression for younger subjects with normal hearing (open circles), older subjects with normal hearing (open triangles), and older subjects with cochlear hearing loss (filled triangles) plotted against each subject's absolute threshold for the 20-ms tone at the signal frequency. The solid lines are linear regression functions fit to individual data for older subjects with hearing loss, derived using the least-squares procedure. Suppression and thresholds at 0.8 kHz are in the top panel and those at 2.0 kHz are in the bottom panel. Suppression was defined as the difference in forward-masked thresholds measured in the narrowest and widest bandpass maskers.

The association between suppression and absolute thresholds for the younger subjects was more difficult to detect, owing to the truncated range of thresholds for this group. Nevertheless, there was a trend for less suppression to be observed in younger subjects with higher absolute thresholds at and around the signal frequency. Indeed, a statistically significant correlation was observed between suppres-

sion at 2.0 kHz and the 2.0-kHz threshold ($r=-0.76$, $p<0.05$). The individual differences observed in the current experiment (with excellent intrasubject reliability) were consistent with that reported for other psychophysical suppression measures (e.g., Wright, 1996).

3. Physiological correlates

Many of the current findings for older subjects with cochlear hearing loss were consistent with effects of cochlear pathology on two-tone rate suppression (e.g., Salvi *et al.*, 1982) and with changes in tuning and two-tone rate suppression in auditory-nerve fibers of older gerbils exposed to noise at an early age (Schmiedt *et al.*, 1990). For older gerbils, early noise exposure resulted in increased thresholds at the CF, decreased slopes of the high-frequency side of tuning curves, and reduced or absent two-tone rate suppression especially above the CF. Below the CF, thresholds of remaining suppression areas were elevated. The survivability of suppression areas below and above the CF was relatively independent and was not strongly dependent on the threshold at the CF. For older subjects with cochlear hearing loss in the current experiment, suppression was virtually absent when maskers were introduced above either signal frequency. Some suppression was observed when noise was introduced below the signal frequency, suggesting that suppression above and below the signal frequency was independent. Indeed, no statistically significant correlations were observed between suppression measures below and above either signal frequency, consistent with evidence of separate mechanisms underlying suppression on the low-frequency and high-frequency sides of tuning curves (e.g., Cheatham and Dallos, 1990; Schmiedt *et al.*, 1990).

The magnitude of suppression measured with noise components below the signal was reduced for subjects with hearing loss, especially at 2.0 kHz. If suppression areas were present in these subjects but suppression thresholds were elevated (as shown in some noise-aged gerbils in Schmiedt *et al.*, 1990), reduced suppression with noise components below the signal may be attributed to the reduced sensation level of the masker. That is, larger threshold changes with bandwidth (and more normal suppression) may have been revealed in these subjects by using higher level maskers which would more likely impinge on elevated suppression areas.

Results for the older subjects with normal hearing from the current experiment differed from those observed by Schmiedt *et al.* (1990) for older gerbils raised in quiet. These authors observed normal two-tone rate suppression above and below the CF for gerbils with age-related threshold shifts of as much as 40 dB, with increases in the tips but not the tails of tuning curves. For older subjects with normal hearing in the current experiment, suppression was present but less than observed for younger subjects. It was notable that when noise was introduced below the signal, the function relating threshold to masker bandwidth reached a plateau for the younger but not the older subjects (compare $\triangleleft$ symbols in top and middle panels of Fig. 3), suggesting that suppression areas may have extended into lower-frequency regions for the older subjects with normal hearing. Thus greater suppression may have been revealed in these older subjects had the masker's lower-frequency cutoff been decreased further. This was not the case for the 0.8-kHz signal (middle panel of Fig. 2), where suppression was poorer than would be predicted from these subjects' relatively normal absolute thresholds.

Thus suppression for the older subjects with normal hearing was poorer than observed by Schmiedt *et al.* (1990) for older gerbils raised in quiet. Of course, in addition to effects of age, these older human subjects were likely exposed to a variety of exogenous factors during their lifetime, including noise and pharmacologic agents, that did not significantly elevate their thresholds (although their thresholds were slightly elevated relative to the younger subjects). Reduced suppression in these subjects, therefore, may represent evidence of changes in cochlear state that did not result in significant threshold elevation.

IV. SUMMARY AND CONCLUSIONS

Suppression was assessed psychophysically by measuring forward-masked thresholds at 0.8 and 2.0 kHz in bandpass maskers as a function of masker bandwidth and in a broadband masker. Masker bandwidths were varied with respect to the signal frequency by introducing noise components above and/or below the signal. Subjects were younger and older adults with normal hearing and older adults with hearing loss. Results may be summarized as follows.

(1) Forward-masked thresholds decreased as a function of masker bandwidth, which was attributed to the effects of suppression. For all subjects, thresholds decreased with increasing masker bandwidth more when noise was added below the signal than when noise was added above the signal. These results were consistent with some physiological evidence of stronger suppression for a suppressor below a fiber's CF than above and with the unique areas and shapes of suppression regions on the low- and high-frequency sides of neural tuning curves.
(2) For younger subjects with normal hearing, suppression was greater at 2.0 kHz than at 0.8 kHz. This was consistent with an assumption of greater nonlinear processing at higher than at lower frequencies. The largest difference in suppression as a function of frequency was observed when noise was introduced below the signal. This was consistent with differences in shapes of suppression regions of lower frequency and higher frequency auditory-nerve fibers.
(3) For older subjects with cochlear hearing loss, suppression was reduced substantially relative to that observed for younger subjects with normal hearing, and was reduced to a greater extent at 2.0 kHz, where hearing loss was greater, than at 0.8 kHz. For both signal frequencies, suppression was virtually absent when noise was extended above the signal. Reductions in suppression when noise was extended below the signal may be attributed to elevated suppression thresholds and reduced masker sensation levels, or to reduced suppression.
(4) Suppression at 0.8 kHz and 2.0 kHz for older subjects with normal hearing was reduced relative to that of younger subjects. Age-related differences in magnitude

of suppression were larger at 0.8 kHz than at 2.0 kHz. Thus suppression for some older subjects with normal hearing was poorer than would be predicted from their absolute thresholds. These results suggested that age contributed to a reduction of suppression, or that suppression measures were sensitive to changes in cochlear function that did not result in significant threshold elevation.

(5) Given the presumed benefits of suppression for improving signal-to-noise ratios and spectral contrasts, reduced suppression for older subjects with and without hearing loss may contribute to these subjects' difficulties understanding speech in noisy environments. Accordingly, a goal of the next experiment of the series (Dubno and Ahlstrom, 2001b) was to assess the functional benefits of suppression for speech recognition in noise.

ACKNOWLEDGMENTS

This work was supported (in part) by Grants Nos. R01 DC00184 and P50 DC00422 from NIH/NIDCD. The authors thank Chris Ahlstrom for computer and signal-processing support, Fu-Shing Lee for advice on data analysis, and Amy R. Horwitz, John H. Mills, and Richard A. Schmiedt for editorial comments. We also thank Associate Editor Sid P. Bacon who provided helpful advice for improving the manuscript.

[1]Background and rationale for the ''band-limiting'' procedure are provided in detail in Dubno and Ahlstrom (2001a).

[2]In a subsequent experiment using the same masker bandwidths as in the current experiment (Dubno and Ahlstrom, 2001b), forward-masked thresholds were measured as a function of masker bandwidth for three masker levels. Growth of masking slopes were <1.0 regardless of masker bandwidth. These results provide evidence that confusion effects were not influencing forward-masked thresholds (Neff, 1985).

[3]Although results suggested that suppression was greater at higher than lower frequencies, differences in relative masker bandwidths for the two signals could have affected this comparison. For example, masker bandwidths varied from narrowest to widest by 2.91 octaves for the 0.8-kHz signal but by only 2.32 octaves for the 2.0-kHz signal. In addition, at 0.8 kHz, the narrowest bandwidth was 25% of the signal frequency, whereas at 2.0 kHz, the narrowest bandwidth was 20% of the signal frequency. The widest masker bandwidths (not considering broadband) were also necessarily different for the two signal frequencies. To determine if these factors affected the interpretation of frequency-related differences in suppression, suppression was also defined as the difference between thresholds in a narrow-band masker and the broadband masker. Here, the narrow-band maskers were those whose bandwidths were each 25% of the signal frequency (0.2 kHz for the 0.8-kHz signal and 0.5 kHz for the 2.0-kHz signal); the broadband masker was the same for the two signal frequencies. Whereas the magnitude of suppression defined in this manner was slightly larger or smaller in some conditions than shown in Fig. 4, the general pattern of the results for the two signal frequencies and the three band-widening methods remained the same. That is, greater suppression was observed at 2.0 kHz than at 0.8 kHz.

[4]When suppression was defined as the difference between thresholds in the narrowband maskers with equal relative bandwidths and the broadband masker (see Footnote 1), mean suppression at 2.0 kHz for the older subjects with normal hearing was larger. This was attributed to the older subjects' lower thresholds in the broadband masker than in the next narrowest bandwidth.

[5]The general relationships among subject groups and suppression observed in Fig. 5 for noise introduced above and below the signal frequency were maintained when noise was added below the signal only. An exception was that suppression at 0.8 kHz varied less with threshold. Little suppression was observed when noise was added above the signal; as such, associations of suppression and thresholds for these conditions were weak.

ANSI (**1989**). ANSI S3.6-1989, ''Specifications for Audiometers'' (American National Standards Institute, New York).

Arthur, R. M., Pfeiffer, R. R., and Suga, N. (**1971**). ''Properties of two-tone inhibition in primary auditory neurones,'' J. Physiol. (London) **212**, 593–609.

Beveridge, H. A., and Carlyon, R. P. (**1996**). ''Effects of aspirin on human psychophysical tuning curves in forward and simultaneous masking,'' Hear. Res. **99**, 110–118.

Cai, Y., and Geisler, C. D. (**1996**). ''Suppression in auditory-nerve fibers of cats using low-side suppressors. I. Temporal aspects,'' Hear. Res. **96**, 94–112.

Cheatham, M. A., and Dallos, P. (**1990**). ''Comparison of low- and high-side two-tone suppression in inner hair cell and organ of Corti responses,'' Hear. Res. **50**, 193–210.

Cooper, N. P., and Rhode, W. S. (**1995**). ''Nonlinear mechanics at the apex of the guinea-pig cochlea,'' Hear. Res. **82**, 225–243.

Delgutte, B. (**1990a**). ''Physiological mechanisms of psychophysical masking: Observations from auditory-nerve fibers,'' J. Acoust. Soc. Am. **87**, 791–809.

Delgutte, B. (**1990b**). ''Two-tone rate suppression in auditory-nerve fibers: Dependence on suppressor frequency and level,'' Hear. Res. **49**, 225–246.

Dubno, J. R., and Ahlstrom, J. B. (**2001a**). ''Forward- and simultaneous-masked thresholds in bandlimited maskers in subjects with normal hearing and cochlear hearing loss,'' J. Acoust. Soc. Am. **110**, 1049–1057.

Dubno, J. R., and Ahlstrom, J. B. (**2001b**). ''Psychophysical suppression effects for tonal and speech signals,'' J. Acoust. Soc. Am. **110**, 1058–1066.

Fahey, P. F., and Allen, J. B. (**1985**). ''Nonlinear phenomena as observed in the ear canal and at the auditory nerve,'' J. Acoust. Soc. Am. **77**, 599–612.

Green, D. M. (**1993**). ''A maximum-likelihood method for estimating thresholds in a yes–no task,'' J. Acoust. Soc. Am. **93**, 2096–2105.

Harris, D. M. (**1979**). ''Action potential suppression, tuning curves and thresholds: Comparison with single-fiber data,'' Hear. Res. **1**, 133–154.

Hicks, M. L., and Bacon, S. P. (**1999**). ''Effects of aspirin on psychophysical measures of frequency selectivity, two-tone suppression, and growth of masking,'' J. Acoust. Soc. Am. **106**, 1436–1451.

Kiang, N. Y. S., and Moxon, E. C. (**1974**). ''Tails of tuning curves of auditory-nerve fibers,'' J. Acoust. Soc. Am. **55**, 620–630.

Lee, J., and Bacon, S. P. (**1998**). ''Psychophysical suppression as a function of signal frequency: Noise and tonal maskers,'' J. Acoust. Soc. Am. **104**, 1013–1022.

Leek, M. R., Dubno, J. R., He, N.-j., and Ahlstrom, J. B. (**2000**). ''Experience with a yes–no single-interval maximum-likelihood procedure,'' J. Acoust. Soc. Am. **107**, 2674–2684.

Mills, J. H., and Schmiedt, R. A. (**1983**). ''Frequency selectivity: Physiological and psychophysical tuning curves and suppression,'' in *Hearing Research and Theory*, edited by J. V. Tobias and E. D. Schubert (Academic, New York), Vol. 2.

Moore, B. C. J., and Glasberg, B. R. (**1983**). ''Growth of forward masking for sinusoidal and noise maskers as a function of signal delay: Implications for suppression in noise,'' J. Acoust. Soc. Am. **73**, 1249–1259.

Moore, B. C. J., and Glasberg, B. R. (**1985**). ''The danger of using narrow-band noise maskers to measure ''suppression'','' J. Acoust. Soc. Am. **77**, 2137–2141.

Moore, B. C. J., and Glasberg, B. R. (**1986**). ''Comparisons of frequency selectivity in simultaneous and forward masking for subjects with unilateral cochlear impairments,'' J. Acoust. Soc. Am. **80**, 93–107.

Moore, B. C. J., and Vickers, D. A. (**1997**). ''The role of spread of excitation and suppression in simultaneous masking,'' J. Acoust. Soc. Am. **102**, 2284–2290.

Neff, D. L. (**1985**). ''Stimulus parameters governing confusion effects in forward masking,'' J. Acoust. Soc. Am. **78**, 1966–1976.

Neff, D. L. (**1986**). ''Confusion effects with sinusoidal and narrow-band noise forward maskers,'' J. Acoust. Soc. Am. **79**, 1519–1529.

Oxenham, A. J., and Plack, C. J. (**1998**). ''Suppression and the upward spread of masking,'' J. Acoust. Soc. Am. **104**, 3500–3510.

Rhode, W. S., and Cooper, N. P. (**1993**). ''Two-tone suppression and distortion products on the basilar membrane in the hook region of cat and guinea pig cochleae,'' Hear. Res. **66**, 31–45.

Sachs, M. B., and Kiang, N. Y. S. (**1968**). ''Two-tone inhibition in auditory-nerve fibers,'' J. Acoust. Soc. Am. **43**, 1120–1128.

Salvi, R. J., Perry, J., Hamernik, R. P., and Henderson, D. (**1982**). ''Relationship between cochlear pathologies and auditory nerve and behavioral

responses following acoustic trauma,'' in *New Perspectives on Noise-Induced Hearing Loss*, edited by R. Hamernik, D. Henderson, and R. Salvi (Raven, New York), pp. 165–188.
Schalk, T. B., and Sachs, M. B. (**1980**). ''Nonlinearities in auditory-nerve fiber responses to bandlimited noise,'' J. Acoust. Soc. Am. **67**, 903–913.
Schmiedt, R. A. (**1982**). ''Boundaries of two-tone rate suppression of cochlear-nerve activity,'' Hear. Res. **7**, 335–351.
Schmiedt, R. A., Zwislocki, J. J., and Hamernik, R. P. (**1980**). ''Effects of hair cell lesions on responses of cochlear nerve fibers. I. Lesions, tuning curves, two-tone inhibition, and responses to trapezoidal-wave patterns,'' J. Neurophysiol. **43**, 1367–1389.
Schmiedt, R. A., Mills, J. H., and Adams, J. C. (**1990**). ''Tuning and suppression in auditory nerve fibers of aged gerbils raised in quiet or noise,'' Hear. Res. **45**, 221–236.
Sommers, M. S., and Gehr, S. E. (**1998**). ''Auditory suppression and frequency selectivity in older and younger adults,'' J. Acoust. Soc. Am. **103**, 1067–1074.
Thibodeau, L. M. (**1991**). ''Performance of hearing-impaired persons on auditory enhancement tasks,'' J. Acoust. Soc. Am. **89**, 2843–2850.
Wightman, F., McGee, T., and Kramer, M. (**1977**). ''Factors influencing frequency selectivity in normal and hearing-impaired listeners,'' in *Psychophysics and Physiology of Hearing*, edited by E. F. Evans and J. P. Wilson (Academic, London), pp. 295–306.
Wright, B. A. (**1996**). ''Correlated individual differences in conditions used to measure psychophysical suppression and signal enhancement,'' J. Acoust. Soc. Am. **100**, 3295–3303.
Yates, G. K. (**1995**). ''Cochlear structure and function,'' in *Hearing*, edited by B. C. J. Moore (Academic, San Diego).

Temporal modulation transfer functions obtained using sinusoidal carriers with normally hearing and hearing-impaired listeners

Brian C. J. Moore[a] and Brian R. Glasberg
Department of Experimental Psychology, University of Cambridge, Downing Street, Cambridge CB2 3EB, United Kingdom

(Received 3 May 2001; revised 15 May 2001; accepted 17 May 2001)

Temporal modulation transfer functions were obtained using sinusoidal carriers for four normally hearing subjects and three subjects with mild to moderate cochlear hearing loss. Carrier frequencies were 1000, 2000 and 5000 Hz, and modulation frequencies ranged from 10 to 640 Hz in one-octave steps. The normally hearing subjects were tested using levels of 30 and 80 dB SPL. For the higher level, modulation detection thresholds varied only slightly with modulation frequency for frequencies up to 80 Hz, but decreased for high modulation frequencies. The decrease can be attributed to the detection of spectral sidebands. For the lower level, thresholds varied little with modulation frequency for all three carrier frequencies. The absence of a decrease in the threshold for large modulation frequencies can be explained by the low sensation level of the spectral sidebands. The hearing-impaired subjects were tested at 80 dB SPL, except for two cases where the absolute threshold at the carrier frequency was greater than 70 dB SPL; in these cases a level of 90 dB was used. The results were consistent with the idea that spectral sidebands were less detectable for the hearing-impaired than for the normally hearing subjects. For the two lower carrier frequencies, there were no large decreases in threshold with increasing modulation frequency, and where decreases did occur, this happened only between 320 and 640 Hz. For the 5000-Hz carrier, thresholds were roughly constant for modulation frequencies from 10 to 80 or 160 Hz, and then increased monotonically, becoming unmeasurable at 640 Hz. The results for this carrier may reflect ''pure'' effects of temporal resolution, without any influence from the detection of spectral sidebands. The results suggest that temporal resolution for deterministic stimuli is similar for normally hearing and hearing-impaired listeners. [DOI: 10.1121/1.1385177]

PACS numbers: 43.66.Mk, 43.66.Dc, 43.66.Sr [SPB]

I. INTRODUCTION

One way of characterizing the temporal resolution of the auditory system is to measure the threshold for detecting changes in the amplitude of a sound as a function of the rapidity of the changes. In the simplest case, white noise is sinusoidally amplitude modulated, and the threshold for detecting the modulation is determined as a function of modulation frequency (Rodenburg, 1977; Viemeister, 1977, 1979). The function relating threshold to modulation frequency is known as a temporal modulation transfer function (TMTF). Modulation of white noise does not change its long-term magnitude spectrum, so one can be reasonably confident that the pattern of results depends on temporal resolution *per se*. TMTFs obtained in this way generally show a reasonably flat section for low modulation frequencies. Performance for this section is presumably determined mainly by the amplitude resolution of the auditory system. For modulation frequencies above about 50 Hz, sensitivity declines (Rodenburg, 1977; Viemeister, 1977, 1979; Bacon and Viemeister, 1985; Formby and Muir, 1988; Strickland and Viemeister, 1997). The decline is usually interpreted as a measure of the limited ability of the auditory system to follow rapid amplitude fluctuations.

TMTFs have also been measured using sinusoidal carriers (Zwicker, 1952; Viemeister, 1979; Sek, 1994; Fassel and Kohlrausch, 1995; Dau *et al.*, 1997a; Strickland and Viemeister, 1997; Kohlrausch *et al.*, 2000). In this case, the interpretation of the results is complicated by the fact that the modulation introduces spectral sidebands, which may be detected as separate components if they are sufficiently far in frequency from the carrier frequency (Sek and Moore, 1994; Kohlrausch *et al.*, 2000). Even when the sidebands are not detectable, the results may be influenced by ''off-frequency listening,'' i.e., the use of the output of an auditory filter that is not centered at the carrier frequency. This can happen in two ways. First, the effective modulation depth at the outputs of the auditory filters might be greater for a filter centered close to the frequency of one of the sidebands than for a filter centered at the carrier frequency. Subjects may be able to select the filter with the highest modulation at its output. The extent of the difference between the on-frequency and off-frequency filters would vary with the frequency separation of the carrier and sidebands, and hence with modulation frequency (Dau, 1996), so this form of off-frequency listening would influence the shape of the TMTF. Second, even when the frequency separation of the carrier and sidebands is very

[a]Author to whom correspondence should be addressed; electronic mail: bcjm@cus.cam.ac.uk

small, subjects may make use of the outputs of auditory filters tuned well above the signal frequency (the high-frequency side of the excitation pattern), for which there is less compression than for filters tuned close to the signal frequency (Zwicker, 1956, 1970; Robles *et al.*, 1986; Nelson and Schroder, 1997; Moore and Oxenham, 1998); the effective modulation depth would be greater on the high-frequency side of the excitation pattern. However, since the compression appears to be very fast-acting (Robles *et al.*, 1986; Recio *et al.*, 1998), this form of off-frequency listening would not be expected to influence the shape of the TMTF, at least for the range of modulation frequencies where sidebands are not detectable.

When the carrier frequency is high, the effects of resolution of sidebands and off-frequency listening of the first type are likely to be small for modulation frequencies up to a few hundred Hertz. For example, for a carrier frequency of 5000 Hz, the equivalent rectangular bandwidth (ERB) of the auditory filter is about 560 Hz (Glasberg and Moore, 1990), and the ''edge'' components in complex tones need to be separated by more than about 0.75 ERB from neighboring components to be ''heard out'' as separate tones, even when all components have equal amplitude (Moore and Ohgushi, 1993). Thus, the results obtained for low modulation frequencies are likely to reflect temporal resolution rather than spectral resolution or off-frequency listening. Consistent with this, TMTFs for high carrier frequencies generally show an initial flat portion (sensitivity independent of modulation frequency), a portion where sensitivity decreases with increasing modulation frequency, presumably reflecting the limits of temporal resolution, and then a portion where sensitivity increases again, presumably reflecting the detection of spectral sidebands (Kohlrausch *et al.*, 2000). The ''transition'' modulation frequency, at which sensitivity is worst, increases with increasing carrier frequency, and typically is about 5%–6% of the carrier frequency (about 0.5 ERB) (Kohlrausch *et al.*, 2000).

The initial flat portion of the TMTF extends to about 100–120 Hz for sinusoidal carriers, but only to 50 or 60 Hz for a broadband noise carrier. It has been suggested that the discrepancy occurs because of the inherent amplitude fluctuations in a noise carrier, which limit the detectability of the imposed modulation (Fleischer, 1982; Dau, 1996; Dau *et al.*, 1997a, 1997b, 1999). The effect of the inherent fluctuations depends upon their similarity to the imposed modulation. When a narrowband noise carrier is used, which has relatively slow inherent amplitude fluctuations, TMTFs show the poorest sensitivity for low modulation frequencies (Fleischer, 1982; Dau *et al.*, 1997a). In principle, then, TMTFs obtained using sinusoidal carriers provide a better measure of the inherent temporal resolution of the auditory system than TMTFs obtained using noise carriers, provided that the modulation frequency is within the range where spectral resolution does not play a major role.

The present study compares TMTFs obtained using sinusoidal carriers for normally hearing subjects and for subjects with cochlear hearing loss. The latter have reduced frequency selectivity (Pick *et al.*, 1977; Glasberg and Moore, 1986; for a review, see Moore, 1998) and so the modulation frequency at which spectral resolution starts to play a role should be higher than for normally hearing subjects. Thus, for subjects with cochlear hearing loss, TMTFs for sinusoidal carriers should be influenced mainly by temporal resolution over a relatively wide range of modulation frequencies.

Several previous studies measuring TMTFs for hearing-impaired subjects have used broadband noise carriers. These studies showed that hearing-impaired listeners were generally less sensitive to high frequencies of modulation than normal listeners (Formby, 1982; Lamore *et al.*, 1984; Bacon and Viemeister, 1985). However, this may have been largely a consequence of the fact that high frequencies were inaudible to the impaired listeners (Bacon and Viemeister, 1985); most of the subjects used had greater hearing losses at high frequencies than at low. Bacon and Gleitman (1992) measured TMTFs for broadband noise using subjects with relatively flat hearing losses. They found that at equal (high) SPLs performance was similar for hearing-impaired and normally hearing subjects. At equal (low) SLs, the hearing-impaired subjects tended to perform better than the normally hearing subjects. Moore *et al.* (1992) controlled for the effects of listening bandwidth by measuring TMTFs for an octave-wide noise band centered at 2 kHz, using subjects with unilateral and bilateral cochlear hearing loss. Over the frequency range covered by the noise, the subjects had reasonably constant thresholds as a function of frequency, both in their normal and their impaired ears. This ensured that there were no differences between subjects or ears in terms of the range of audible frequencies in the noise. To ensure that subjects were not making use of information from frequencies outside the nominal passband of the noise, the modulated carrier was presented in an unmodulated broadband noise background. For the subjects with unilateral impairments, performance was similar for the normal and impaired ears, both at equal SPL and equal SL.

The present study was intended to provide more information about temporal resolution for listeners with cochlear hearing loss, using carriers without inherent fluctuations, i.e., sinusoids. This is important since the inherent fluctuations in a noise carrier may have different effects for normally hearing and hearing-impaired subjects. For example, loudness recruitment appears to have the effect of magnifying the perceived fluctuation of a modulated sound (Moore *et al.*, 1996), and this may have adverse effects on temporal resolution, at least for the task of gap detection (Moore and Glasberg, 1988; Glasberg and Moore, 1992; Moore *et al.*, 2001); see, however, Hall *et al.* (1998). In addition, we wished to clarify the role of spectral sidebands in modulation detection by hearing-impaired subjects. We anticipated that the reduced frequency selectivity of listeners with cochlear hearing loss would lead to poorer resolution of spectral sidebands, allowing temporal resolution *per se* to be measured over a relatively wide range of modulation frequencies.

TABLE I. Absolute thresholds for the test ears of the hearing-impaired subjects, measured in two ways: (1) using conventional manual audiometry, and expressed in dB HL; (2) using a three-alternative forced-choice procedure, and in dB SPL.

Subject		Frequency (Hz) 250	500	1000	2000	4000	5000	8000
GW	HL	40	50	60	55	65		70
	SPL			66.5	65.5		74.9	
TT	HL	40	35	35	50	60		65
	SPL			44.9	65.3		77.2	
AR	HL	30	35	40	45	50		50
	SPL			51.1	65.2		61.2	

II. THE EXPERIMENT: TMTFs FOR SINUSOIDAL CARRIERS

A. Procedure

Thresholds for the detection of sinusoidal amplitude modulation (AM) of a sinusoidal carrier were measured using a three-alternative forced-choice three-down one-up procedure tracking the 79.4% point on the psychometric function. The carrier was gated, and it was unmodulated in two of the intervals and modulated in the other; subjects had to indicate the interval containing the modulated carrier. Observation intervals were marked by lights on the response box and feedback was provided after each trial by a light indicating the correct interval. Twelve turnpoints were obtained in a given run, and the threshold estimate for that run was taken as the mean value of $20 \log m$ at the last eight turnpoints (where m is the modulation index). The step size (defined in terms of $20 \log m$) was 5 dB up to the first four turnpoints, and 2 dB thereafter. At least three runs were obtained for each condition.

B. Stimuli

The carrier frequency was 1000, 2000, or 5000 Hz. The modulation frequency was 10, 20, 40, 80, 160, 320, or 640 Hz. Each carrier burst lasted 540 ms, including 20 ms raised-cosine rise/fall ramps. The interval between bursts within a trial was 500 ms. The overall level of the modulated and unmodulated stimuli was the same, regardless of modulation depth. The normally hearing subjects were tested using levels of 30 and 80 dB SPL. The hearing-impaired subjects were, in most cases, tested only using a level of 80 dB SPL. For two subjects, GW and TT, the absolute thresholds at 5000 Hz were above 70 dB SPL, and a level of 90 dB was used for this frequency. At the levels used, the sensation levels were in a similar range to those for the normally hearing subjects tested at 30 dB SPL, i.e., 15–30 dB SL.

Stimuli were digitally generated using a Tucker–Davis Technologies (TDT) system with a 16-bit digital-to-analog converter (DD1, 50-kHz sampling rate), lowpass filtered at 20 kHz (Kemo VBF8, mark 4), attenuated (TDT PA4), passed through a headphone buffer (TDT HB6), and delivered to a double-walled sound attenuating booth. Stimuli were delivered to one earpiece of a Sennheiser HD580 headphone via a final manual attenuator (Hatfield 2125). Sound levels are specified as levels close to the eardrum; the frequency response of the HD580 at the eardrum was estimated using a KEMAR manikin (Burkhard and Sachs, 1975), averaging the results for the large and small ears.

C. Subjects

Four normally hearing subjects were tested, with ages ranging from 23 to 54 years. One was author BG. All had absolute thresholds better than 15 dB HL at all audiometric frequencies in the ear tested. Three subjects with symmetrical mild to moderate cochlear hearing loss were tested. Their ages in years were 84 (GW), 80 (TT), and 70 (AR). Their absolute thresholds for the test ear, measured using manual audiometry (Grason–Stadler GSI-16 audiometer) are given in Table I. Table I also gives thresholds in dB SPL at the test frequencies, estimated using a three-alternative forced-choice, three-down one-up procedure. Impedance audiometry revealed normal middle-ear function. All subjects were trained until their performance appeared to be stable. This took only a few hours. All subjects except BG were paid for their services.

III. RESULTS

Individual results for the normally hearing subjects are shown in Fig. 1. Note that the results are plotted with worst performance at the top of the y axis, opposite to the way in which TMTFs are often plotted. To avoid clutter, error bars are not shown. The standard deviation of the three threshold estimates for a given subject and condition was typically about 1 dB. The pattern of results was similar across subjects, and mean data are shown in Fig. 2. Performance was better for the higher carrier level (open symbols), than for the lower level, which is consistent with earlier work (Riesz, 1928; Zwicker, 1952; Kohlrausch *et al.*, 2000). The effect of level for low modulation frequencies can be attributed to two factors. First, at high levels the excitation pattern spreads over a greater range of center frequencies. Subjects can probably combine information from different parts of the pattern (i.e., across auditory filters) in order to improve performance (Florentine and Buus, 1981; Moore and Sek, 1994). Second, as noted earlier, at high levels subjects can use information from the high-frequency side of the excitation pattern, for which there is less compression than at the peak of the pattern (Zwicker, 1956; Zwicker, 1970; Nelson and Schroder, 1997; Moore and Oxenham, 1998).

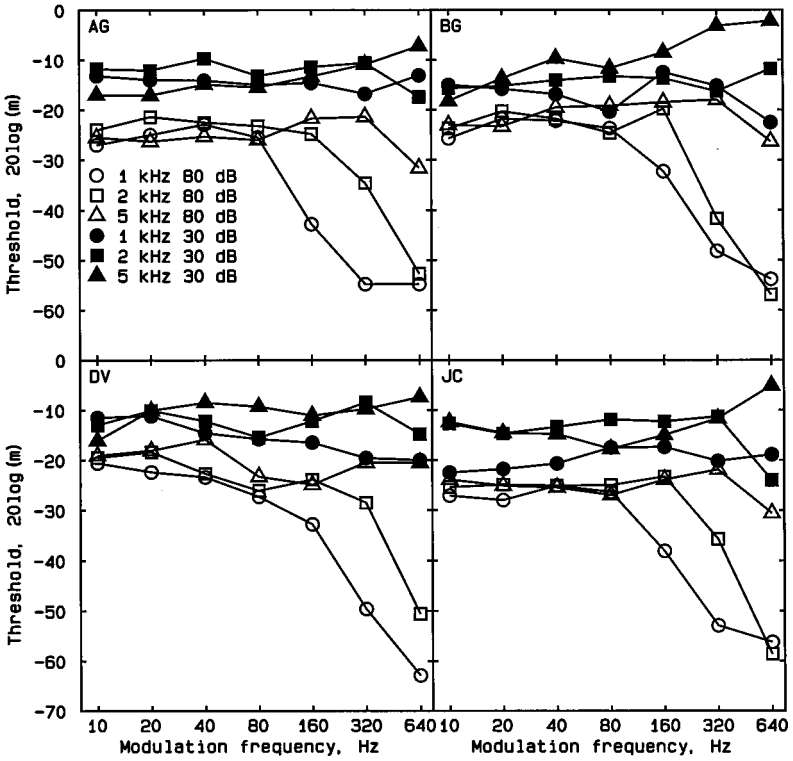

FIG. 1. Individual results for the four normally hearing subjects. The modulation detection threshold (20 log *m*) is plotted as a function of modulation frequency. The parameters are level and carrier frequency, as indicated in the key. Each panel shows results for one subject.

For high modulation frequencies, performance at the high level improved markedly for the two lower carrier frequencies, and the improvement started at a lower modulation frequency for the 1000-Hz carrier (circles) than for the 2000-Hz carrier (squares). For the 5000-Hz carrier frequency (triangles), performance tended to worsen slightly as the modulation frequency was increased from 80 to 320 Hz, and then improved slightly for the highest modulation frequency. The improvement in performance with increasing modulation frequency almost certainly reflects the detection of spectral sidebands. For the 1000-Hz carrier, these appear to be clearly detectable for the modulation frequency of 160 Hz, while for the 2000-Hz carrier they are detectable for the modulation frequency of 320 Hz.

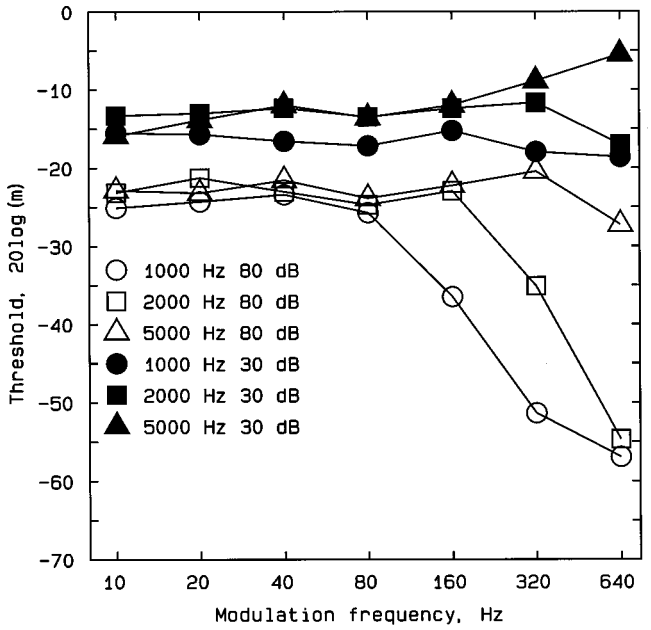

FIG. 2. Mean results for the four normally hearing subjects. Otherwise as in Fig. 1.

For the lower carrier level, thresholds did not vary markedly with modulation frequency, except at 640 Hz, where there was a small increase in threshold for the 5000-Hz carrier and a small decrease for the 2000-Hz carrier. Mean performance was slightly better for the 1000-Hz carrier than for the other two carriers, probably reflecting the fact that the average SL was slightly higher at 1000 Hz (26 dB SL) than at 2000 Hz (19 dB SL) or 5000 Hz (19 dB SL). Even though thresholds did not vary markedly with modulation frequency, the mechanism underlying modulation detection presumably did change. The failure of thresholds to decrease for the large modulation frequencies presumably reflects the low SL of the stimuli. The value of $20 \log m$ at threshold was typically around -16 dB for the 1000-Hz carrier, which means that each sideband had a level 22 dB below the carrier level. Thus, each sideband had a level of about 8 dB SPL, which was just above the mean absolute threshold of 4 dB SPL (at 1000 Hz). For the 2000- and 4000-Hz carriers, the sideband level was about 12 dB SPL, again, just above the mean absolute threshold of 11 dB SPL. Modulation detection thresholds for the highest modulation frequencies were presumably mediated by sideband detection for the two lower carrier frequencies, but the low overall level of the stimuli did not allow thresholds to fall below about -12 to -16 dB.

The small rise in threshold for the 5000-Hz carrier for the 640-Hz modulation frequency probably occurred because temporal resolution was relatively poor at that frequency, but the spectral sidebands were not sufficiently separated from the carrier to be easily detectable. Consistent with this, cal-

culations based on the excitation-pattern program published by Glasberg and Moore (1990) indicate that the excitation level produced by a 30-dB SPL 5000-Hz tone is only about 10 dB down from the peak excitation level for frequencies 640 Hz on either side of 5000 Hz. To be detectable, each sideband would have to have a level comparable to the excitation level of the carrier, which would require a value of $20 \log m$ of about -4. This is close to the observed threshold values.

The individual results for the hearing-impaired subjects are shown in Fig. 3. Symbols with up-pointing arrows indicate cases where thresholds could not be measured, as even $m = 1$ (100% modulation) did not lead to sufficient detectability. For low modulation frequencies, the thresholds are similar to those for the normally hearing subjects with the carrier level of 80 dB SPL, and are generally lower (better) than the thresholds obtained for the carrier level of 30 dB SPL. Since the SLs of the stimuli for the hearing-impaired subjects were similar to those for the normally hearing subjects for the 30-dB carrier level, the results indicate that the hearing-impaired subjects were better than the normally hearing subjects at AM detection when the stimuli were at similar SLs. This is consistent with previous research indicating that at equal low SLs amplitude resolution can be better for subjects with cochlear hearing loss than for normally hearing subjects (Jerger *et al.*, 1959; Buus *et al.*, 1982a, 1982b; Moore, 1995).

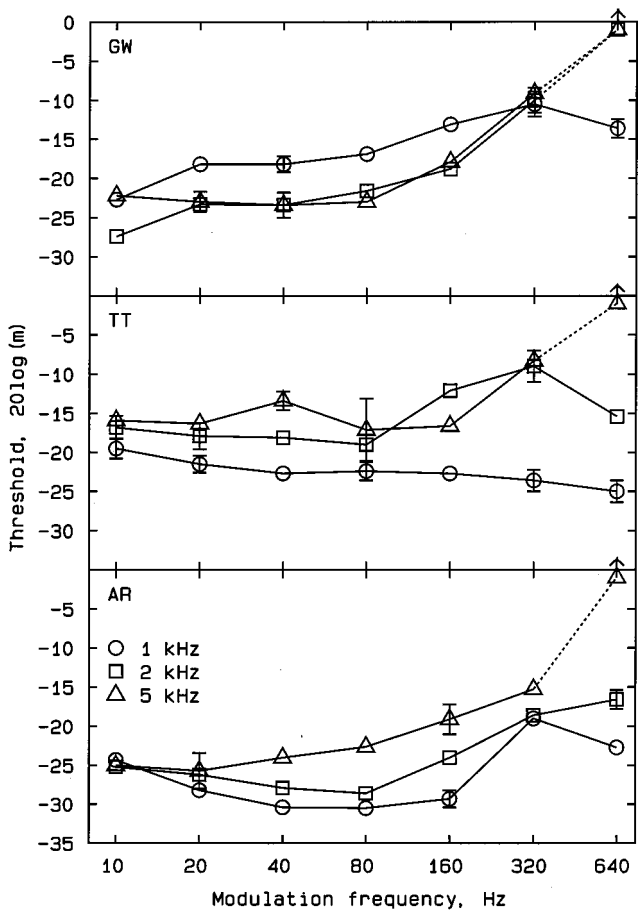

FIG. 3. Individual results for the hearing-impaired subjects. The modulation detection threshold ($20 \log m$) is plotted as a function of modulation frequency. The parameter is carrier frequency, as indicated in the key. The level was 80 dB SPL, except for the 5000-Hz carrier for subjects GW and TT, where the level was 90 dB SPL. Error bars indicate ± one standard deviation. They are omitted when they would be smaller than the size of the symbol used to represent a given point.

Consider first the results for the 1000-Hz carrier. For TT, who had the smallest hearing loss at this frequency (see Table I), the pattern of results resembles that found for the normally hearing listeners at the 30-dB SPL carrier level; the thresholds varied only slightly with modulation frequency. For subject AR, who has a slightly greater hearing loss at this frequency, the thresholds decreased by about 5 dB as the modulation frequency was increased from 10 to 40 Hz, remained constant up to 160 Hz, increased at 320 Hz, and then decreased by about 4 dB at 640 Hz. The increase at 320 Hz presumably reflects the effects of temporal resolution, while the decrease at 640 Hz reflects detection of a spectral sideband; probably it was the lower sideband that was detected, as AR had only a mild hearing loss for frequencies below 1000 Hz. For the modulation frequency of 160 Hz, it is very unlikely that spectral sidebands were detectable; at the modulation detection threshold, each sideband would have had a level of 44 dB SPL, which would have been below the absolute threshold. Thus, the results for AR indicate that temporal resolution is as good for a modulation frequency of 160 Hz as it is for lower modulation frequencies. The thresholds for GW for the 1000-Hz carrier rose slightly as the modulation frequency was increased from 10 to 20 Hz, remained roughly constant for frequencies from 20 to 80 Hz, increased slightly as the frequency increased to 160 and 320 Hz, and then decreased slightly at 640 Hz. The decrease at 640 Hz presumably reflects detection of a spectral sideband; the level of each sideband was 61 dB SPL, which would have been just above the absolute threshold at 360 Hz (but below the absolute threshold at 1640 Hz). Again, the results suggest relatively good temporal resolution for modulation frequencies up to 160 Hz.

Consider next the results for the 2000-Hz carrier (squares). For all three subjects, thresholds were roughly constant for modulation frequencies up to 80 Hz, and increased with increasing modulation frequency from 80 to 320 Hz. This increase probably reflects the effects of temporal resolution. For the modulation frequency of 640 Hz, threshold was unmeasurable for GW. She was probably unable to detect the AM *per se* at this modulation frequency, while at the same time she was unable to detect the spectral sidebands, either because of poor frequency selectivity, or because the sidebands were too close to absolute threshold, or both. For subject AR, the threshold for the modulation frequency of 640 Hz was only slightly higher than that for the frequency of 320 Hz. Probably, the threshold for the 640-Hz frequency was determined by detection of the spectral sideband at 1360 Hz, whose level of 57 dB would have been just above the absolute threshold. For subject TT, the threshold for the modulation frequency of 640 Hz was slightly lower than that for the frequency of 320 Hz, presumably reflecting his ability to detect the spectral sideband at 1360 Hz, whose level of 59 dB would again have been somewhat above the absolute threshold.

Finally, consider the results for the 5000-Hz carrier (triangles). Recall that for this carrier, GW and TT were tested at a level of 90 dB SPL. The pattern of results was similar for all three subjects. Thresholds were roughly independent of modulation frequency for frequencies up to 80 Hz (GW and AR) or 160 Hz (TT), and increased for modulation frequencies above that. Threshold could not be determined for any subject for the 640-Hz modulation frequency. The results for the 5000-Hz carrier probably reflect ''pure'' effects of temporal resolution, free from any influence of the detection of spectral sidebands.

IV. DISCUSSION

The results are consistent with the idea that, for high modulation rates, spectral sidebands were less detectable for the hearing-impaired than for the normally hearing subjects. Indeed, for the 5000-Hz carrier, it appears that spectral sidebands were not detectable at all for the hearing-impaired subjects. It is noteworthy that, for this carrier frequency, the hearing-impaired subjects could not detect the modulation for the 640-Hz modulation frequency. However, this may partly reflect the relatively low SL of the stimuli, since performance on several measures of temporal resolution worsens at very low SLs. These measures include TMTFs (Bacon and Viemeister, 1985; Kohlrausch *et al.*, 2000), gap detection (Plomp, 1964; Shailer and Moore, 1983), and the rate of recovery from forward masking (Glasberg *et al.* 1987). Hearing-impaired subjects might be able to detect 640-Hz AM at higher overall levels. Bacon and Gleitman (1992) have presented data consistent with this idea. They measured TMTFs with a broadband noise carrier, using normally hearing subjects and subjects with relatively flat hearing losses. When the SL of the carrier was about 20 dB, the normally hearing subjects could not detect AM at frequencies above 256 Hz, whereas when the SL was increased to 30 dB they could detect AM at frequencies up to 1024 Hz. The results for their hearing-impaired subjects showed individual variability, but also tended to improve with increasing SL. At the SL of 20 dB, the modulation thresholds for the hearing-impaired subjects were often lower (better) than for the normally hearing subjects, which is consistent with our own results. It should be noted that the *shapes* of TMTFs for noise carriers do not vary markedly with level. Sensation level seems mainly to affect amplitude resolution, as reflected in the asymptotic modulation detection threshold for low modulation frequencies.

We have interpreted the results for the normally hearing subjects as resulting from the combined effects of detection of the modulation *per se* and detection of spectral sidebands at large modulation rates. However, it is also possible that, for the 80-dB carrier level, the normally hearing subjects detected a distortion component at the modulation frequency. Evidence for the existence of such a distortion product, when bandpass noise carriers are used, has been provided by Wiegrebe and Patterson (1999). For a bandpass filtered noise carrier with a level per ERB (Glasberg and Moore, 1990) of about 72 dB SPL, modulated with $m=1$ ($20\log m=0$ dB), they estimated the level of the distortion product to be about 20 dB SPL, i.e., about 52 dB below the effective level of the carrier. The modulation thresholds measured in our experiment for the normally hearing subjects for the 80-dB carrier were mostly below -20 dB for modulation frequencies of 160 Hz and below, corresponding to $m=0.1$; for higher modulation frequencies the thresholds were even lower. At these reduced modulation depths, we would expect the relative level of the distortion product at the modulation frequency to be at least 20 dB lower, i.e., 72 dB or more below the carrier level. Thus, the effective level of the distortion product at the modulation frequency is expected to be 8 dB SPL or less. Since the absolute thresholds of our subjects at low frequencies (160 Hz and below) were well above 8 dB SPL, it seems unlikely that our results were influenced by detection of a distortion product at the modulation frequency.

Temporal resolution measured using TMTFs is often characterized by a time constant, τ, defined as $1/(2\pi f_c)$, where f_c is the frequency at which sensitivity has declined by 3 dB relative to that measured for low modulation frequencies. Such a measure cannot be applied to the data for our normally hearing subjects, as, in most cases, there was not a 3-dB decline in sensitivity at any modulation frequency. The failure to find a decline presumably reflects the ability of the subjects to detect spectral sidebands at high modulation frequencies. However, TMTFs obtained using sinusoidal carriers do sometimes show a region of decreased sensitivity for normally hearing subjects, especially when a very high carrier frequency is used (Kohlrausch *et al.*, 2000); sensitivity at first decreases and then increases again for very large modulation frequencies. The value of f_c in such cases is typically about 150 to 200 Hz, giving a value of τ of about 1.1 to 0.8 ms. For the mean data of our hearing-impaired subjects obtained with the 5000-Hz carrier, the value of f_c was 155 Hz ($\tau\approx 1$ ms). Thus, there is no indication of reduced temporal resolution in our hearing-impaired subjects.

V. CONCLUSIONS

(1) The TMTFs obtained using sinusoidal carriers with normally hearing subjects resemble those found by previous researchers. Modulation detection thresholds for low modulation rates reflect the effects of both amplitude resolution and temporal resolution. Modulation detection thresholds for high modulation rates reflect the detection of spectral sidebands. The modulation rate at which the spectral sidebands first become detectable increases with increasing carrier frequency. Performance was better for a carrier level of 80 dB SPL than for a carrier level of 30 dB SPL, especially at high modulation rates.

(2) For low modulation rates, modulation detection thresholds for the hearing-impaired subjects tested at 80 dB SPL were similar to those for the normally hearing subjects at 80 dB SPL, and lower (better) than for the normally hearing subjects at 30 dB SPL. This indicates that, at similar SLs, hearing-impaired subjects perform better than normally hearing subjects.

(3) For high modulation rates, thresholds for the hearing-impaired subjects usually did not decline with increasing modulation rate, and when they did, the decreased was small. This suggests that spectral sidebands were less detectable for the hearing-impaired than for the normally

hearing subjects. For the 5000-Hz carrier, it appears that spectral sidebands were not detectable at all, as performance worsened monotonically with increasing modulation rate.

(4) For the 5000-Hz carrier, the cutoff frequency of the TMTF was about 155 Hz, corresponding to a time constant of about 1 ms. These values are similar to those for normally hearing subjects. Thus, the results suggest that temporal resolution for deterministic stimuli is similar for hearing-impaired and for normally hearing subjects.

ACKNOWLEDGMENTS

This work was supported by the MRC (U.K.). We thank Joanna Czwartos for gathering some of the data reported in this paper. We also thank Sid Bacon and an anonymous reviewer for helpful comments on an earlier version of this paper.

Bacon, S. P., and Gleitman, R. M. (**1992**). ''Modulation detection in subjects with relatively flat hearing losses,'' J. Speech Hear. Res. **35**, 642–653.

Bacon, S. P., and Viemeister, N. F. (**1985**). ''Temporal modulation transfer functions in normal-hearing and hearing-impaired subjects,'' Audiology **24**, 117–134.

Burkhard, M. D., and Sachs, R. M. (**1975**). ''Anthropometric manikin for acoustic research,'' J. Acoust. Soc. Am. **58**, 214–222.

Buus, S., Florentine, M., and Redden, R. B. (**1982a**). ''The SISI test: A review. Part I,'' Audiology **21**, 273–293.

Buus, S., Florentine, M., and Redden, R. B. (**1982b**). ''The SISI test: A review. Part II,'' Audiology **21**, 365–385.

Dau, T. (**1996**). ''Modeling auditory processing of amplitude modulation,'' Ph.D. thesis, University of Oldenburg.

Dau, T., Kollmeier, B., and Kohlrausch, A. (**1997a**). ''Modeling auditory processing of amplitude modulation. I. Detection and masking with narrowband carriers,'' J. Acoust. Soc. Am. **102**, 2892–2905.

Dau, T., Kollmeier, B., and Kohlrausch, A. (**1997b**). ''Modeling auditory processing of amplitude modulation. II. Spectral and temporal integration,'' J. Acoust. Soc. Am. **102**, 2906–2919.

Dau, T., Verhey, J. L., and Kohlrausch, A. (**1999**). ''Intrinsic envelope fluctuations and modulation-detection thresholds for narrow-band noise carriers,'' J. Acoust. Soc. Am. **106**, 2752–2760.

Fassel, R., and Kohlrausch, A. (**1995**). ''Modulation detection as a function of carrier frequency and level,'' in *IPO Annual Progress Report 30*, edited by M. D. Brouwer-Janse, D. J. Hermes, W. M. C. J. van Overveld, and H. de Ridder (IPO, Eindhoven).

Fleischer, H. (**1982**). ''Modulationsschwellen von Schmalbandrauschen,'' Acustica **51**, 154–161.

Florentine, M., and Buus, S. (**1981**). ''An excitation-pattern model for intensity discrimination,'' J. Acoust. Soc. Am. **70**, 1646–1654.

Formby, C. (**1982**). ''Differential sensitivity to tonal frequency and to the rate of amplitude modulation of broad-band noise by hearing-impaired listeners,'' Ph.D. thesis, Washington University, St. Louis.

Formby, C., and Muir, K. (**1988**). ''Modulation and gap detection for broadband and filtered noise signals,'' J. Acoust. Soc. Am. **84**, 545–550.

Glasberg, B. R., and Moore, B. C. J. (**1986**). ''Auditory filter shapes in subjects with unilateral and bilateral cochlear impairments,'' J. Acoust. Soc. Am. **79**, 1020–1033.

Glasberg, B. R., and Moore, B. C. J. (**1990**). ''Derivation of auditory filter shapes from notched-noise data,'' Hear. Res. **47**, 103–138.

Glasberg, B. R., and Moore, B. C. J. (**1992**). ''Effects of envelope fluctuations on gap detection,'' Hear. Res. **64**, 81–92.

Glasberg, B. R., Moore, B. C. J., and Bacon, S. P. (**1987**). ''Gap detection and masking in hearing-impaired and normal-hearing subjects,'' J. Acoust. Soc. Am. **81**, 1546–1556.

Hall, J. W., Grose, J. H., Buss, E., and Hatch, D. R. (**1998**). ''Temporal analysis and stimulus fluctuation in listeners with normal and impaired hearing,'' J. Speech Lang Hear Res. **41**, 340–354.

Jerger, J., Shedd, J., and Harford, E. (**1959**). ''On the detection of extremely small changes in sound intensity,'' Arch. Otolaryngol. **69**, 200–211.

Kohlrausch, A., Fassel, R., and Dau, T. (**2000**). ''The influence of carrier level and frequency on modulation and beat-detection thresholds for sinusoidal carriers,'' J. Acoust. Soc. Am. **108**, 723–734.

Lamore, P. J. J., Verweij, C., and Brocaar, M. P. (**1984**). ''Reliability of auditory function tests in severely hearing-impaired and deaf subjects,'' Audiology **23**, 453–466.

Moore, B. C. J. (**1995**). *Perceptual Consequences of Cochlear Damage* (Oxford University Press, Oxford).

Moore, B. C. J. (**1998**). *Cochlear Hearing Loss* (Whurr, London).

Moore, B. C. J., and Glasberg, B. R. (**1988**). ''Gap detection with sinusoids and noise in normal, impaired and electrically stimulated ears,'' J. Acoust. Soc. Am. **83**, 1093–1101.

Moore, B. C. J., Glasberg, B. R., Alcántara, J. I., Launer, S., and Kuehnel, V. (**2001**). ''Effects of slow- and fast-acting compression on the detection of gaps in narrow bands of noise,'' Br. J. Audiol. (submitted).

Moore, B. C. J., and Ohgushi, K. (**1993**). ''Audibility of partials in inharmonic complex tones,'' J. Acoust. Soc. Am. **93**, 452–461.

Moore, B. C. J., and Oxenham, A. J. (**1998**). ''Psychoacoustic consequences of compression in the peripheral auditory system,'' Psychol. Rev. **105**, 108–124.

Moore, B. C. J., and Sek, A. (**1994**). ''Effects of carrier frequency and background noise on the detection of mixed modulation,'' J. Acoust. Soc. Am. **96**, 741–751.

Moore, B. C. J., Shailer, M. J., and Schooneveldt, G. P. (**1992**). ''Temporal modulation transfer functions for band-limited noise in subjects with cochlear hearing loss,'' Br. J. Audiol. **26**, 229–237.

Moore, B. C. J., Wojtczak, M., and Vickers, D. A. (**1996**). ''Effect of loudness recruitment on the perception of amplitude modulation,'' J. Acoust. Soc. Am. **100**, 481–489.

Nelson, D. A., and Schroder, A. C. (**1997**). ''Linearized response growth inferred from growth-of-masking slopes in ears with cochlear hearing loss,'' J. Acoust. Soc. Am. **101**, 2186–2201.

Pick, G., Evans, E. F., and Wilson, J. P. (**1977**). ''Frequency resolution in patients with hearing loss of cochlear origin,'' in *Psychophysics and Physiology of Hearing*, edited by E. F. Evans and J. P. Wilson (Academic, London).

Plomp, R. (**1964**). ''The rate of decay of auditory sensation,'' J. Acoust. Soc. Am. **36**, 277–282.

Recio, A., Rich, N. C., Narayan, S. S., and Rugero, M. A. (**1998**). ''Basilar-membrane responses to clicks at the base of the chinchilla cochlea,'' J. Acoust. Soc. Am. **103**, 1972–1989.

Riesz, R. R. (**1928**). ''Differential intensity sensitivity of the ear for pure tones,'' Phys. Rev. **31**, 867–875.

Robles, L., Ruggero, M. A., and Rich, N. C. (**1986**). ''Basilar membrane mechanics at the base of the chinchilla cochlea. I. Input-output functions, tuning curves, and response phases,'' J. Acoust. Soc. Am. **80**, 1364–1374.

Rodenburg, M. (**1977**). ''Investigation of temporal effects with amplitude modulated signals,'' in *Psychophysics and Physiology of Hearing*, edited by E. F. Evans and J. P. Wilson (Academic, London).

Sek, A. (**1994**). ''Modulation thresholds and critical modulation frequency based on random amplitude and frequency changes,'' J. Acoust. Soc. Jpn. (E) **15**, 67–75.

Sek, A., and Moore, B. C. J. (**1994**). ''The critical modulation frequency and its relationship to auditory filtering at low frequencies,'' J. Acoust. Soc. Am. **95**, 2606–2615.

Shailer, M. J., and Moore, B. C. J. (**1983**). ''Gap detection as a function of frequency, bandwidth and level,'' J. Acoust. Soc. Am. **74**, 467–473.

Strickland, E. A., and Viemeister, N. F. (**1997**). ''The effects of frequency region and bandwidth on the temporal modulation transfer function,'' J. Acoust. Soc. Am. **102**, 1799–1810.

Viemeister, N. F. (**1977**). ''Temporal factors in audition: A system analysis approach,'' in *Psychophysics and Physiology of Hearing*, edited by E. F. Evans and J. P. Wilson (Academic, London).

Viemeister, N. F. (**1979**). ''Temporal modulation transfer functions based on modulation thresholds,'' J. Acoust. Soc. Am. **66**, 1364–1380.

Wiegrebe, L., and Patterson, R. D. (**1999**). ''Quantifying the distortion products generated by amplitude-modulated noise,'' J. Acoust. Soc. Am. **106**, 2709–2718.

Zwicker, E. (**1952**). ''Die Grenzen der Hörbarkeit der amplitudenmodulation und der frequenzmodulation eines tones,'' Acustica **2**, 125–133.

Zwicker, E. (**1956**). ''Die elementaren grundlagen zur bestimmung der informationskapazität des Gehörs,'' Acustica **6**, 356–381.

Zwicker, E. (**1970**). ''Masking and psychological excitation as consequences of the ear's frequency analysis,'' in *Freqeuncy Analysis and Periodicity Detection in Hearing*, edited by R. Plomp and G. F. Smoorenburg (Sijthoff, Leiden).

Binaural processing model based on contralateral inhibition. I. Model structure

Jeroen Breebaart[a)]
IPO, Center for User–System Interaction, P.O. Box 513, NL-5600 MB Eindhoven, The Netherlands

Steven van de Par and Armin Kohlrausch
IPO, Center for User–System Interaction, P.O. Box 513, NL-5600 MB Eindhoven, The Netherlands and Philips Research Laboratories Eindhoven, Prof. Holstlaan 4, NL-5656 AA Eindhoven, The Netherlands

(Received 23 May 2000; revised 18 December 2000; accepted 3 May 2001)

This article presents a quantitative binaural signal detection model which extends the monaural model described by Dau *et al.* [J. Acoust. Soc. Am. **99**, 3615–3622 (1996)]. The model is divided into three stages. The first stage comprises peripheral preprocessing in the right and left monaural channels. The second stage is a binaural processor which produces a time-dependent internal representation of the binaurally presented stimuli. This stage is based on the Jeffress delay line extended with tapped attenuator lines. Through this extension, the internal representation codes both interaural time and intensity differences. In contrast to most present-day models, which are based on excitatory–excitatory interaction, the binaural interaction in the present model is based on contralateral inhibition of ipsilateral signals. The last stage, a central processor, extracts a decision variable that can be used to detect the presence of a signal in a detection task, but could also derive information about the position and the compactness of a sound source. In two accompanying articles, the model predictions are compared with data obtained with human observers in a great variety of experimental conditions.
[DOI: 10.1121/1.1383297]

PACS numbers: 43.66.Pn, 43.66.Ba, 43.66.Dc [DWG]

I. INTRODUCTION

Over the past decades many models of binaural processing have emerged that address various aspects of binaural hearing. Among other things, these models are able to predict the intracranial locus of a binaural sound (Lindemann, 1985; Raatgever and Bilsen, 1986; Stern *et al.*, 1988; Shackleton *et al.*, 1992; Gaik, 1993) or account for binaural masking level differences (Durlach, 1963; Green, 1966; Colburn, 1977; Stern and Shear, 1996; Bernstein and Trahiotis, 1996), as well as for binaural pitch phenomena (Bilsen and Goldstein, 1974; Bilsen, 1977; Raatgever and Bilsen, 1986; Raatgever and van Keulen, 1992; Culling *et al.*, 1996). The majority of these models rely on the coincidence counter hypothesis following an internal delay line as suggested by Jeffress (1948). The physiological basis for such coincidence counters are the so-called excitation–excitation (EE)-type cells (Rose *et al.*, 1966; Goldberg and Brown, 1969; Yin and Chan, 1990; Joris and Yin, 1995; Joris, 1996; Batra *et al.*, 1997a, b). These cells are found in the medial superior olive. Their discharge rate in response to binaural stimulation depends on the interaural time difference (ITD) and, at favorable ITDs, i.e., when exhibiting maximum response, typically exceeds the sum of the responses for either ear alone (Goldberg and Brown, 1969). This favorable ITD is referred to as the cell's *best delay*. If a given neuron is activated by different frequencies, the different periodic discharge curves appear to reach a maximum amplitude for the same interaural delay of the stimulus. This delay is referred to as the cell's *characteristic delay* and provides an estimate of the difference in travel time from each ear to the coincidence detector.

In models based on an array of EE-type cells with a range of characteristic delays, the neural discharge rate resulting from the EE interaction is usually modeled as an interaural cross-correlation function. The intracranial locus of a sound presented with a certain interaural time difference is usually assumed to be based on the locus of the largest neural activity or on the centroid computed along the internal delay line. For a signal without any interaural time disparity, the interaural cross-correlation function is maximum at an internal delay of zero. An interaural time difference results in a shift of the cross-correlation function along the delay axis and hence leads to a predicted lateralization.

Some of these models also allow for the prediction of binaural masking level differences (BMLD). When a broadband noise is presented in phase to both ears, and pure tones are presented out of phase to each ear simultaneously (NoSπ condition), the masked threshold is generally lower than when both the noise and the tone are presented in phase (NoSo condition) (Hirsh, 1948a; Hafter and Carrier, 1970; Zurek and Durlach, 1987). Within the framework of these models, the detection of the Sπ signal is based on the reduction of the cross-correlation value for NoSπ due to the addition of the test signal (Colburn, 1973, 1977; Colburn and Latimer, 1978; Durlach *et al.*, 1986; van de Par and Kohlrausch, 1995; Bernstein and Trahiotis, 1996; Stern and Shear, 1996).

Another important theory of binaural hearing is the equalization–cancellation (EC) theory (Durlach, 1963, 1972). The basic idea of the EC theory is that the auditory

[a)]Now at: Philips Research Laboratories Eindhoven, Prof. Holstlaan 4, NL-5656 AA Eindhoven, The Netherlands. Electronic mail: jeroen.breebaart@philips.com

system attempts to eliminate masking components by first transforming the stimuli presented to the two ears in order to equalize the two masking components (E-process). Possible equalization transformations are interaural level adjustments and internal time delays, but also internal phase shifts have been suggested as part of the transformation repertoire. It is assumed that this E-process is performed imperfectly due to internal errors. Consequently, if the stimulus in one ear is subtracted from the stimulus in the other ear (C-process), part of the energy of the masker cannot be canceled. For many binaural masking conditions, this operation leads to an improvement in the signal-to-masker ratio and hence to the prediction of a BMLD. The EC theory proposed by Durlach is purely analytical. More recently, time-domain EC models have emerged which besides BMLDs (cf. Culling and Summerfield, 1995; Zerbs, 2000) also account for binaural pitch phenomena (Culling and Summerfield, 1998).

There is some support from physiological data that an EC-like process exists in the mammalian auditory system. A subgroup of cells in the lateral superior olive (LSO) and a subgroup of cells in the inferior colliculus (IC) are excited by the signals from one ear and inhibited by the signals from the other ear (Rose *et al.*, 1966; Boudreau and Tsuchitani, 1968; Kuwada *et al.*, 1984; Joris and Yin, 1995; Batra *et al.*, 1997a, b; Palmer *et al.*, 1997; McAlpine *et al.*, 1998). The cells in the LSO are typically excited by the ipsilateral ear and inhibited by the contralateral ear and are therefore classified as EI-type (excitation–inhibition) cells. For neurons situated in the IC the excitatory and inhibitory channels are typically reversed and these cells are classified as IE-type cells. The opposite influence of the two ears makes these cells sensitive to interaural intensity differences (IIDs). With increasing inhibitory level, the neuron's activity decreases up to a certain level where its activity is completely inhibited. The IID necessary to completely inhibit the cell's response varies across neurons (Park *et al.*, 1997; Tsuchitani, 1997; Park, 1998). We refer to the minimum interaural intensity difference needed to completely inhibit the activity as the neuron's *characteristic IID*. Within a phenomenological context we may think of the whole population of EI-type neurons with different characteristic IIDs as multiple ''taps'' wherein differences in level between channels are processed in parallel, very similar to the ITD sensitivity for EE-type neurons. There are some suggestive data for the LSO (Park *et al.*, 1997; Tsuchitani, 1997) and for the IC (Irvine and Gago, 1990) that the IID sensitivity of EI-type neurons reflects the differences in threshold between the excitatory and inhibitory inputs that innervate each EI-type cell. In addition to IID sensitivity, EI-type cells have been reported to exhibit ITD sensitivity as well (Joris and Yin, 1995; Joris, 1996; Park, 1998). These results suggest that both ITD and IID sensitivity may be understood by considering the outcome of a subtractive mechanism for EI-type neurons with a characteristic IID *and* ITD.

Despite this apparent similarity between EI-type cell properties and the basic mechanism of the EC theory, it is uncertain to what extent EI-type neurons contribute to binaural hearing phenomena in humans. In experimental animals, ITD-sensitive IE units only comprise 12% of low-frequency units in the IC (Palmer *et al.*, 1997). Furthermore, anatomical studies revealed that the LSO in humans is much less well developed than in experimental animals (Moore, 1987). Hence the physiological basis for a human binaural processing model based on EI-type neurons is uncertain.

Although the two binaural mechanisms previously described are different in their phenomenological properties, this does not necessarily mean that these processes differ in terms of their predictive scope. In fact, Domnitz and Colburn (1976) argued that for an interaurally out-of-phase tonal signal masked by a diotic Gaussian noise, a model based on the interaural correlation and a model based on the distribution of the interaural differences will predict essentially the same thresholds. Furthermore, Colburn and Durlach (1978) and Green (1992) stated that the decision variables based on the correlation and on an EC mechanism are linear functions of one another, hence resulting in equivalent predictions. Consequently, as written in Colburn and Durlach (1978), the effect of interaural parameters of both the masker and signal can be accounted for independently of whether the decision variable is identified with the interaural correlation or with the interaural differences.

Recently, however, it has been shown that in certain other conditions, differences exist between these models. For example, Breebaart *et al.* (1999) showed that $\mathrm{NoS}\pi$ conditions with non-Gaussian noise result in different predictions for the two theories. It was argued that an EC-like model may be favored over a model based on the cross correlation in that it describes thresholds for static and dynamically varying ITDs and IIDs more satisfactorily: it provides a way to describe sensitivity to IIDs and ITDs, as well as binaural detection data with one single parameter. Second, Breebaart and Kohlrausch (2001) demonstrated that uncertainty in the binaural parameters is treated differently by models based on the correlation compared to models based on an EC-like mechanism. A third difference between the two binaural mechanisms is related to the temporal processing. More specifically, the effect of signal and masker duration in an $\mathrm{NoS}\pi$ condition is difficult to understand in terms of the cross correlation (see Sec. V). A fourth difference is related to stimulus-level variability. The EC-type detection process is not vulnerable to stimulus level variability. Cross-correlation-based models, on the other hand, require specific accommodations to reduce the detrimental effects of stimulus level variability on detection performance in narrow-band noise conditions (see van de Par *et al.*, 2001; Colburn and Isabelle, 2001).

In summary, for many binaural detection conditions, models based on the EC theory and models based on the cross correlation are expected to give very similar predictions. In conditions where these predictions are not similar, however, a model based on an EC mechanism may be favored over a cross-correlation model because of its wider predictive scope and the fact that less specific assumptions have to be made. We therefore have chosen to base the binaural interaction in our model on an EI-like interaction. This choice will be further motivated in Sec. VII.

II. MODEL PHILOSOPHY

Two different approaches can be pursued when developing a model. An important category of models is purely analytical. This means that the model and its predictions heavily rely on stimulus statistics rather than on explicit waveforms. This class of models provides a powerful means to understand many aspects of data in the literature, independent of details of realization. At the same time the analytical nature presents us with the limitation that it is very difficult to obtain predictions for arbitrary stimulus configurations, like for frozen-noise tokens. This drawback conflicts with the most important objective in our modeling efforts: to develop a model that can simulate a wide variety of binaural detection data *without any restrictions with respect to the stimuli*. In this respect, we followed the philosophy of Dau *et al.* (1996a) to make the model applicable to binaural conditions with stochastic as well as deterministic stimuli, such as frozen noise. Therefore, the model must be able to deal with actual time signals and each processing stage of the model must be described accordingly. The advantage of this approach is that the model can be used as an artificial observer, for example, in a three-interval, forced-choice procedure with adaptive signal adjustment or for measuring psychometric functions. We tried to combine this philosophy with the requirements of binaural models that were discussed by Colburn and Durlach (1978), who stated that all published models were deficient in at least one of the following areas:

(1) Providing a complete quantitative description of how the stimulus waveforms are processed and of how this processing is corrupted by internal noise.
(2) Having a sufficiently small number of free parameters in the model to prevent the model from becoming merely a transformation of coordinates or an elaborate curve-fit.
(3) Taking account of general perceptual principles in modeling the higher-level, more central portions of the system for which there are no adequate systematic physiological results available.
(4) Deriving all the predictions that follow from the assumptions of the model and comparing these predictions to all the relevant data.
(5) Relating the assumptions and parameters of the model in a serious manner to known physiological results.

With respect to the first two points, we decided to expand the monaural detection model developed by Dau *et al.* (1996a). This model provides a detailed description of the processing of stimulus waveforms and the extension of this model to a binaural model requires only a few extra model parameters. This extension has the advantage that the large predictive scope of the original monaural model is inherited by the current model. A detailed description of the complete model and its various stages are given in Secs. III–VI.

As noted by Colburn and Durlach (1978) in their third point, it is presently not possible to base the central decision process on systematic physiological data. The analysis stage of the current model is therefore based on mathematical principles rather than physiological knowledge. In particular, an adaptive template-matching procedure was incorporated. The idea of template matching has been used before in modeling monaural auditory perception (cf. Dau, 1992; Dau *et al.*, 1996a) and also for binaural perception (Holube *et al.*, 1995). A new feature that was added is the adaptive nature of the template-matching procedure: if the signal level is changed during a run in a forced-choice detection task with adaptive signal-level adjustment, the model adapts its internal templates accordingly. The advantage of this approach is that the model does not need to ''learn'' the stimulus and available detection cues beforehand and hence simulations can start on the fly (as real subjects do).

With respect to the fourth and fifth points raised by Colburn and Durlach (1978), we refer to the two accompanying articles, which focus on simulations of various detection experiments. In particular, Breebaart *et al.* (2001a) focuses on spectral and interaural parameters of the stimuli, and Breebaart *et al.* (2001b) deals with temporal stimulus properties.

III. MODEL OVERVIEW

The model is divided into three stages as shown in Fig. 1. The first stage comprises peripheral preprocessing, including the spectral filtering and hair cell transduction in the cochlea. In the second stage, the binaural processor, the signals from one ear are compared to the corresponding signals from the other ear by means of EI interactions as a function of the internal characteristic IID and ITD. The third stage is a central processor. This stage can decide whether a signal is present in a masker, but in principle could also extract localization information from the EI-type activity pattern. This central stage receives both the outputs of the binaural processor as well as the direct outputs of the peripheral preprocessor. Each box within the three stages of Fig. 1 represents a building block which is a functional or phenomenological model of physiological stages in the mammalian auditory system. Each stage and its building blocks will be specified separately in the following sections.

IV. PERIPHERAL PROCESSING STAGE

The first stage of the model simulates the effective signal processing of the peripheral auditory system resulting from the outer, middle, and inner ear and the auditory nerve. This stage is very similar to the implementation described by Dau *et al.* (1996a). The processing blocks have the following properties:

(1) The combined outer and middle ear transfer function is modeled by a time-invariant bandpass filter with a rolloff of 6 dB/oct below 1 kHz and −6 dB/oct above 4 kHz. This filter is sufficient to simulate headphone data. For simulations with directional sound, additional convolution with a corresponding head-related transfer function (HRTF) would be necessary. Since we only simulate headphone experiments in this article and the two subsequent articles, HRTF filtering is not included.
(2) The cochlea including the basilar membrane is modeled by a third-order gammatone filterbank (Johannesma, 1972; Patterson *et al.*, 1988), using filters with a bandwidth corresponding to the equivalent rectangular bandwidth (ERB) (Glasberg and Moore, 1990). The spectral

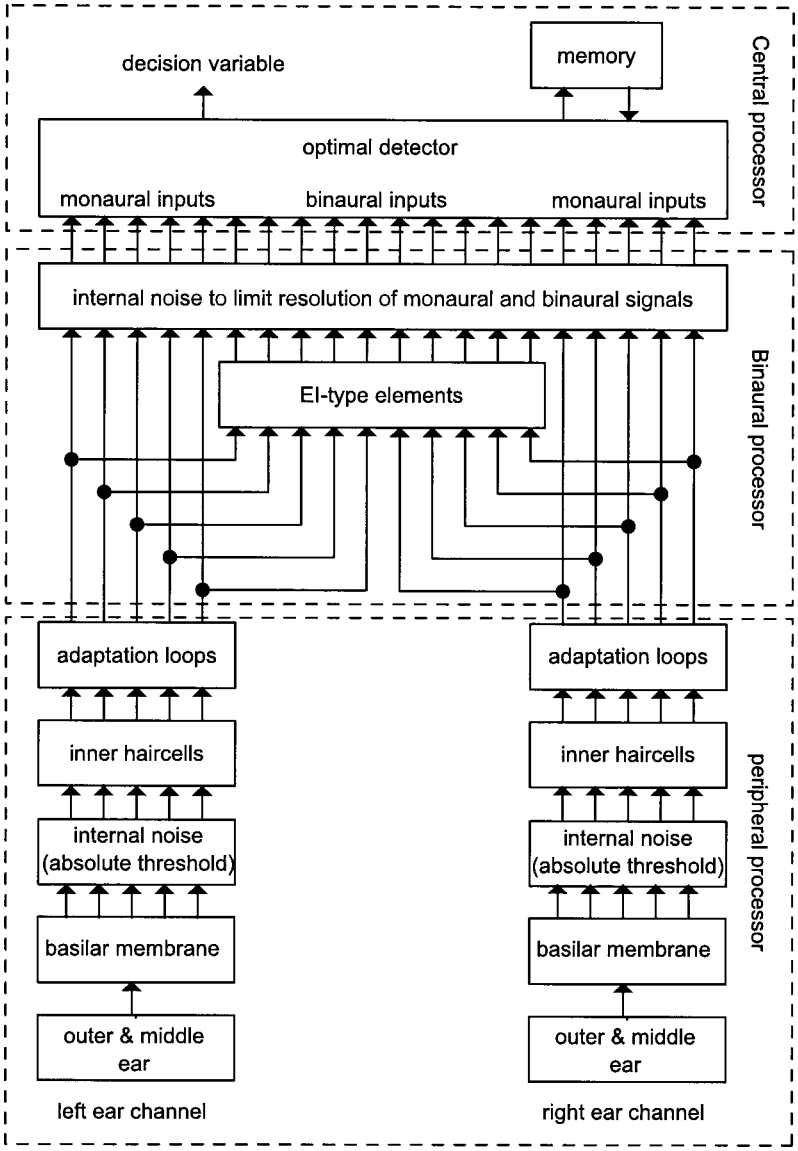

FIG. 1. Successive stages of the model. The signals arriving from both ears are processed by a peripheral preprocessing stage (outer and middle ear transfer function, linear basilar membrane model, additive internal noise, inner hair cell stage, and adaptation loops), followed by a binaural processor. The signals from the monaural channels and the binaural channels are processed by a central processor, which extracts one decision variable. Internally represented input signals are corrupted by internal noise and are compared to templates stored in memory. This comparison results in a single decision variable.

spacing is two filters per ERB. Because of the linear behavior of the gammatone filterbank, basilar membrane nonlinearities such as compression are not included in this stage.

(3) To incorporate an absolute threshold (i.e., a noise floor), an independent Gaussian noise is added to each signal originating from the filterbank. The noise is statistically independent for each frequency channel and has a level which corresponds to a sound pressure level of 60 μPa (i.e., 9.4 dB SPL). This value is chosen such that the absolute threshold of a 2-kHz input signal with a level of 5 dB SPL results in a level increase of about 1 dB. In combination with the effect of stage 1, the model thus has a frequency-dependent absolute threshold. For long-duration sinusoidal signals, this threshold is about 5 dB SPL between 1 and 4 kHz.

(4) The effective signal processing of the inner hair cells is modeled by a half-wave rectifier, followed by a fifth-order low-pass filter with a cutoff frequency (-3 dB point) of 770 Hz. For frequencies below about 770 Hz, the low-pass filter has (almost) no effect on the output. Hence only the negative phase of the waveform is lost and therefore the timing information in the fine structure of the waveform is preserved at the output. For frequencies above 2000 Hz, (nearly) all phase information is lost after the low-pass filter and only the envelope of the incoming signals is present at the output of this stage. For frequencies in between, a gradual loss of phase information is observed. In this way, the model effectively simulates the decrease of phase locking with increasing frequency observed in the auditory nerve (Kiang, 1975; Johnson, 1980; Weis and Rose, 1988; Bernstein and Trahiotis, 1996).

(5) To include the influence of adaptation with various time constants, a chain of five adaptation loops was included (Dau *et al.*, 1996a, b). For a signal with a flat temporal envelope, the input–output characteristic of this chain in steady state is almost logarithmic. The output of these adaptation loops is expressed in model units (MU). These units are scaled in such a way that input levels which correspond to a sound pressure level of 0 and 100 dB are scaled to 0 and 100 MU, respectively. Fast dynamic changes in the envelope are not compressed by the adaptation loops but are processed almost linearly.

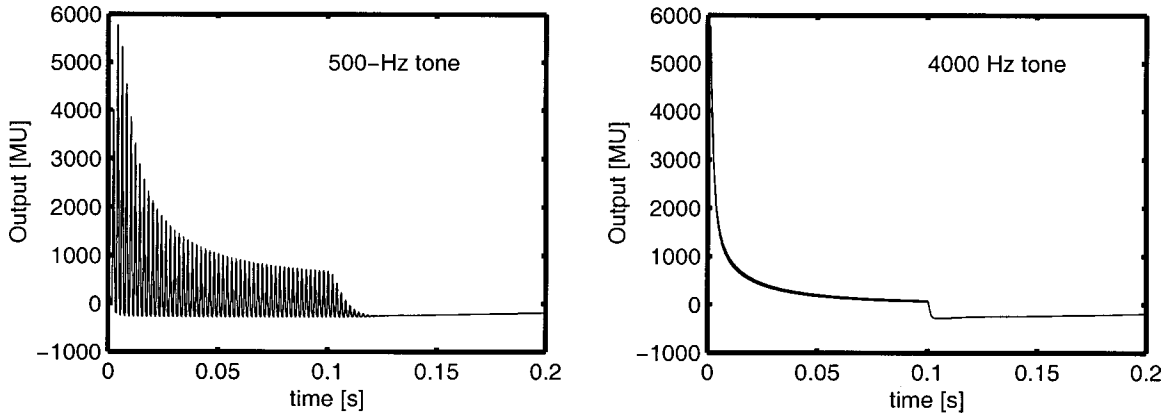

FIG. 2. Output of the peripheral preprocessor for a 500-Hz tone (left panel) and a 4000-Hz tone (right panel) of 100-ms duration. The output was calculated for a filter tuned to the frequency of the tone.

These adaptation loops are included at this stage of the model for the following reason. In the first place, the adaptation loops have been successful in predicting detection performance in monaural nonsimultaneous masking conditions (Dau *et al.*, 1996b, 1997). Therefore, the current model has the same capabilities of predicting monaural thresholds, including specific masker waveform dependence and forward and backward masking. Furthermore, Kohlrausch and Fassel (1997) concluded that adaptation has to *precede* the binaural interaction stage in order to account for binaural forward masking data.

Second, it has been shown frequently that for both monaural and binaural detection of signals added to a wideband masker with a variable level, the threshold *signal-to-masker* ratio is approximately constant, as long as the masker level is well above the absolute threshold (cf. McFadden, 1968; Hall and Harvey, 1984). If it is assumed that a certain constant *change* at the output of the adaptation loops is needed to detect a signal, the signal must be equal to a certain *fraction* of the masker level due to the logarithmic compression. Hence the signal-to-masker ratio will be approximately constant at threshold. Thus, by compressing the input signals logarithmically combined with the assumption that a fixed change in the output is necessary for detection, the model can account for the constant signal-to-masker ratio. Hence the adaptation loops work as an automatic gain control exhibiting a monotonic relation between steady-state input and output levels. To be more explicit, the output waveform is not a simple linearly scaled version of the input signal. This has implications for binaural conditions with an overall IID, which are discussed in Breebaart *et al.* (2001a).

An example of the output of the peripheral preprocessing stage is given in Fig. 2. The left panel shows the output for a 500-Hz tone with a duration of 100 ms in the auditory channel tuned to the frequency of the tone, while the right panel shows the same for a 4000-Hz tone, both at a level of 70 dB SPL. In this example, it is clear that for high frequencies the fine structure of the input waveform is lost. Furthermore, effects of peripheral filtering (longer ringing for the 500-Hz signal) and adaptation are clearly visible. Because of the amplitude scaling of the output of the adaptation loops, the fine structure waveform of the output can in principle go negative, to ensure that the *average* steady-state output approximates the rms input in dB SPL. This has no effect on the performance of the model.

V. BINAURAL PROCESSING STAGE

A. Structure

In the binaural processor, signals from corresponding auditory channels are compared by EI-type elements. Each EI-type element is described by a characteristic ITD and a characteristic IID. We can think of such a characterization as being the result of an orthogonal combination of the Jeffress' delay line (Jeffress, 1948) with the multiple IID taps of Reed and Blum (1990). This combination is depicted in Fig. 3.

The upper and lower horizontal lines carry the time signals from corresponding auditory channels from the right and left ears. The tapped delays (denoted by triangles) combined with the opposite transfer directions of the signals result in a relative interaural delay that varies with the *horizontal* position within the matrix. At the left side, the right-ear signal is delayed compared to the left-ear signal and vice versa. Our extension lies in the fact that each tap of the delay line is connected to a chain of attenuators (depicted by the blocks). The EI-type elements (circles) are connected to these tapped attenuator lines. In a similar way as for the delay line, a relative attenuation occurs which varies with the *vertical* position within the matrix. In this way, the two-parameter characterization of each element, which is included for each frequency band, results in a three-dimensional time-varying activity pattern if auditory stimuli are presented to the model.

B. Time-domain description

In principle, two different EI-type elements can be assigned to each auditory filter: one which is excited by the left ear and inhibited by the right ear and a second one with interaurally reversed interaction. The output E_L of the EI-type elements which are excited by the left ear and inhibited by the right ear is defined as

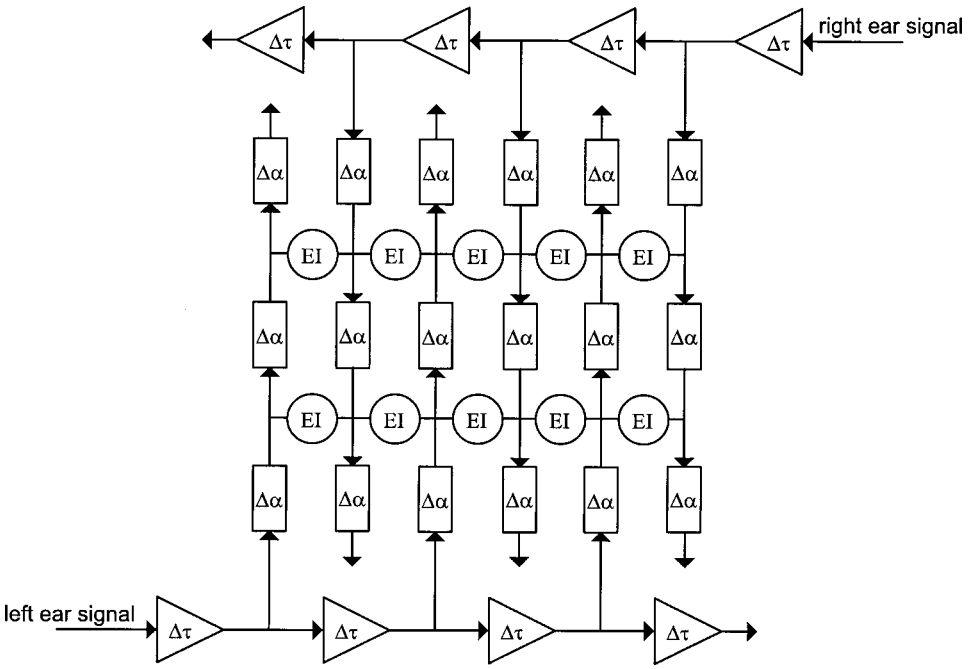

FIG. 3. Structure of the binaural processor. The triangles denote delays ($\Delta\tau$), the blocks are attenuators ($\Delta\alpha$), and the circles denote EI-type elements.

$$E_L(i,t,\tau,\alpha)=\lceil 10^{\alpha/40}L_i(t+\tau/2)-10^{-\alpha/40}R_i(t-\tau/2)\rceil^2, \tag{1}$$

while the output of the EI elements excited by the right ear and inhibited by the left ear, E_R, is given by

$$E_R(i,t,\tau,\alpha)=\lceil 10^{-\alpha/40}R_i(t-\tau/2)-10^{\alpha/40}L_i(t+\tau/2)\rceil^2. \tag{2}$$

Here, $L_i(t)$ denotes the time-domain output from the left-ear peripheral preprocessor at filter *i*, $R_i(t)$ the output from the right-ear peripheral preprocessor at filter *i* and the subscript *i* refers to auditory channel *i*. The characteristic IID in dB is denoted by α, the characteristic ITD in seconds by τ. The ceiling brackets ($\lceil\cdot\rceil$) denote a half-wave rectifier: if the inhibitory signal is stronger than the excitatory signal, the output is zero. The fact that the output is squared is explained later. From Eqs. (1) and (2) we can see that the left and right ear signals undergo a relative delay of τ and a relative level adjustment of α dB. Different values of τ and α correspond to different EI-type elements, resulting in a *population* of elements in the (τ,α) space. It is assumed that all possible combinations of τ and α that may occur in real-life listening conditions are represented by an EI-type element, but that some elements are able to deal with even larger values of τ and α. In the model, internal delays of up to 5 ms and internal intensity differences of $\alpha=10$ dB are realized.[1]

We found that it is very convenient to reduce the number of EI-type elements by combining the outputs E_L and E_R given in Eqs. (1) and (2). It can be shown that summation of these signals results in an output E given by

$$E(i,t,\tau,\alpha)=(10^{\alpha/40}L_i(t+\tau/2)-10^{-\alpha/40}R_i(t-\tau/2))^2. \tag{3}$$

An important consequence of the above summation is that the EI-type element described in Eq. (3) does not have a monotonic dependence on the externally presented IID but it shows a *minimum* in its activity if the inputs match the characteristic IID of the element. From this point on, the term EI-type element will refer to the combined elements as described in Eq. (3). To incorporate a finite binaural temporal resolution, the EI-activity E is processed by a sliding temporal integrator $w(t)$. This integrator is based on results from Kollmeier and Gilkey (1990) and Holube *et al.* (1998) and consists of a double-sided exponential window $w(t)$ with a time constant c of 30 ms:

$$E'(i,t,\tau,\alpha)=\int_{-\infty}^{\infty}E(i,(t+t_{\text{int}}),\tau,\alpha)w(t_{\text{int}})\,dt_{\text{int}}, \tag{4}$$

with

$$w(t)=\frac{\exp(-|t|/c)}{2c}. \tag{5}$$

Finally, a compressive function is applied to the output of the integrator to model saturation effects in the EI cells:

$$E''(i,t,\tau,\alpha)=ap(\tau)\ \log\ (bE'(i,t,\tau,\alpha)+1)+n(i,t,\tau,\alpha). \tag{6}$$

An internal noise $n(i,t,\tau,\alpha)$ limits the accuracy of internal binaural processing.[2] It is assumed that the rms level of this Gaussian-noise source is constant and equals 1 MU, and that the noise is independent of time *t*, auditory channel *i*, and is the same for different EI-type elements. The scalars *a* and *b* are constants. These constants describe the sensitivity to interaural differences and are fixed and equal for all EI-type elements. By adjusting *a* and *b*, the output of the EI-type elements is scaled relative to the internal noise and hence the sensitivity for binaural differences can be adjusted.

The weighting function $p(\tau)$ refers to the fact that cells with larger characteristic interaural delays are less frequent than cells with smaller characteristic delays (Batra *et al.*, 1997a). This corresponds to Jeffress' (1948) statement that for coincidence counter neurons, ''cells are less dense away from the median plane.'' In our approach, fewer cells means less accurate precision in processing and hence more internal

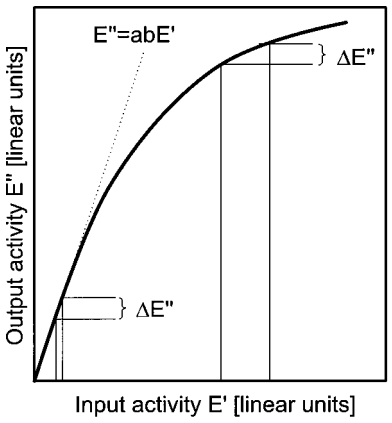

FIG. 4. Input–output characteristic of the EI-type element. The dotted line represents the line $E''=abE'$ (see text).

noise. To include this relative increase in the internal noise, the EI-type element is scaled by a weighting function which *decreases* with internal delay. The weighting function is described as follows:

$$p(\tau)=10^{-|\tau|/5}, \tag{7}$$

where the internal delay τ is expressed in ms. This formula resulted from data with $(\mathrm{NoS}\pi)_\tau$ stimuli which are presented in Appendix A. Such a distribution along internal delays has also been included in several other binaural detection and localization models (Colburn, 1977; Stern and Colburn, 1978; Stern *et al.*, 1988; Shackleton *et al.*, 1992; Stern and Shear, 1996).

A graphical representation of Eq. (6), leaving out the internal noise, is shown in Fig. 4. For small values of E', the input–output function is linear. For higher values of E', the curve converges to a logarithmic function.

The rationale for including the logarithmic transformation in Eq. (6) is as follows. Egan *et al.* (1969) measured psychometric functions for $\mathrm{NoS}\pi$ stimuli as a function of the signal power. They found that the sensitivity index d' was linearly related to the signal power $\langle S^2\rangle$:

$$d'=m\langle S^2\rangle/\langle N^2\rangle. \tag{8}$$

Here, $\langle N^2\rangle$ denotes the masker power and m is a constant. We will now show that this experimental finding matches our EI-type element input–output function for low signal-to-masker ratios. For an No masker alone, there is no activity E'' for an EI-type element with $\tau=0$ and $\alpha=0$ (if the internal errors are neglected), since the masker is completely canceled. When an $\mathrm{S}\pi$ signal is added to the masker, the quadratic input–output characteristic of the EI-type elements results in an output which is related linearly to the *power* of the difference signal between the left and right ear signals. Hence for an interaurally out-of-phase signal, the result of Eq. (3) (i.e., E) is linearly related to the signal power $\langle S^2\rangle$. The temporal integrator in Eq. (4) does not alter this property. Since for the measurement of psychometric functions the signal level is low (i.e., near threshold), the result of Eq. (6) can be described in a first-order approximation by

$$E''(i,t,0,0)\approx abp(\tau)E'(i,t,0,0)+n(i,t,0,0). \tag{9}$$

This relation, without incorporation of the internal noise n, is shown by the dotted line in Fig. 4. Thus, the change at the output of the EI-type element near threshold as a function of the input can be described by a linear relation, as given in Eq. (9). If E'' is used as a decision variable in the $\mathrm{NoS}\pi$ detection paradigm, d' is related linearly to the signal power $\langle S^2\rangle$ as found by Egan *et al.* (1969). The fact that the *power* of the signal is used as a decision variable in $\mathrm{NoS}\pi$ paradigms is also supported by the results of Breebaart *et al.* (1999). They proposed the power of the difference signal as a detection variable for stimuli which comprise combinations of static and dynamically varying ITDs and IIDs. The slope relating signal power to d' in the model is represented by the product ab. Therefore, this product represents the model's sensitivity to binaural stimuli with a reference correlation near $+1$.

For maskers which are not perfectly correlated, for example, in an $\mathrm{N}\rho\mathrm{S}\pi$ condition with $\rho<0.95$, the approximation from Eq. (9) does not hold. For such stimuli, E'' can be approximated by

$$E''(i,t,0,0)\approx ap(\tau)\ \log\ bE'(i,t,0,0)+n(i,t,0,0). \tag{10}$$

Thus, the input–output relation of this curve is logarithmic. If it is assumed that a certain constant change in E'' is needed to detect a signal (this assumption is reflected in the additive noise with a constant rms value), the change in E' must be equal to a certain *fraction* of E'. Thus, for an additive noise n, we need a constant Weber fraction in E' for equal detectability. This Weber fraction is also shown in Fig. 4. At higher input levels, the change in the input (E') necessary to produce a fixed change in the output $(\Delta E'')$ is larger than at low input levels. This is in essence similar to the EC theory (Durlach, 1963). Durlach assumed a fixed signal-to-masker ratio after a (partial) cancellation of the masker. Since Durlach's theory is very successful in predicting BMLDs for wideband $\mathrm{N}\rho\mathrm{S}\pi$ conditions, it is expected that our model has similar prediction performance for these stimuli. As can be observed from Eq. (10), the Weber fraction necessary at threshold is determined by the constant a. Thus, a represents the model's sensitivity for binaural signals at reference correlations smaller than $+1$.

In the following, some basic aspects of the binaural processing stage will be demonstrated. For all examples, the sample rate of the processed stimuli was 32 kHz. The model parameters a and b were set to 0.1 and 0.000 02, respectively. These values resulted from the calibration procedure as described in Breebaart *et al.* (2001a). All output examples given in this section are shown without the incorporation of the internal noise $n(i,t,\tau,\alpha)$ and with $p(\tau)=1$ for all delays to show the properties at hand more clearly.[3]

C. Static ITDs and IIDs

If a 500-Hz pure tone at a level of 70 dB is presented to the model, an activity pattern in the binaural processor occurs as shown in the upper panel of Fig. 5. Here, the idealized [i.e., no internal noise and $p(\tau)=1$] activity of EI units (E'') at 500-Hz center frequency is shown as a function of the characteristic ITD and IID of each element. This activity

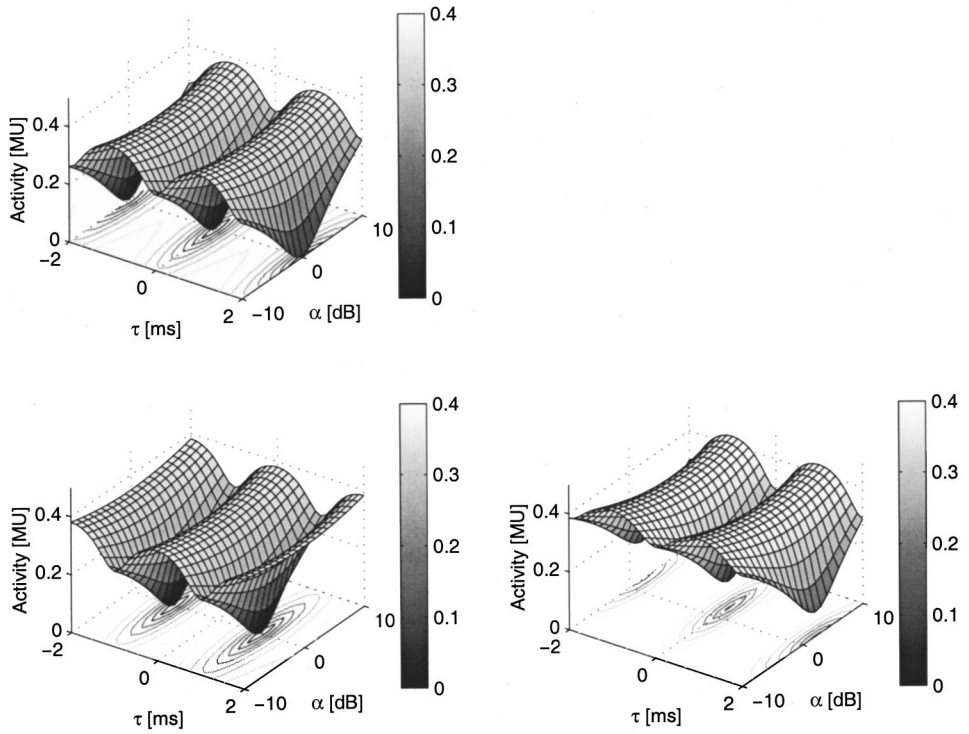

FIG. 5. Idealized [no internal noise, $p(\tau)=1$] EI-activity patterns for a 500-Hz sinusoid as a function of the characteristic IID and ITD of each unit. The upper panel corresponds to a diotic signal (i.e., no external IID or ITD). The signal in the lower-left panel has an ITD of 1 ms and no IID; the signal in the lower-right panel has an IID of 20 dB and no ITD.

was computed from the stationary part of the response; it covers the range from 250 to 500 ms after the onset of the tone.

The pattern is periodic along the characteristic ITD axis (τ) and shows a sharp minimum along the characteristic IID axis (α). At the minimum ($\tau=\alpha=0$) the signals are perfectly matched and thus are fully cancelled. For other characteristic values within the EI array, only partial cancellation occurs, resulting in a remaining activity for these units. Due to the periodic nature of the 500-Hz signal, minimum activity will occur at delays of integer amounts of the signal period. If we apply an external interaural time difference of 1 ms to a 500-Hz tone, an activity pattern occurs as shown in the lower-left panel of Fig. 5. Basically, the pattern is the same as the pattern shown in the upper panel of Fig. 5 except for a shift along the characteristic ITD axis. Thus, externally presented ITDs result in a shift of the pattern along the internal ITD axis. By scanning the minimum in the pattern, the externally presented ITD can be extracted in a similar way as in models based on cross correlation.

If a sound is presented with a certain external IID, a similar shift along the internal characteristic IID axis occurs. This is shown in the lower-right panel of Fig. 5. The externally presented IID was 20 dB. The pattern is shifted towards positive characteristic IIDs. A noteworthy effect is that the activity in the minimum is no longer equal to zero, indicating that the waveforms from the left and right sides cannot be canceled completely. This incomplete cancellation results from the nonlinear processing in the peripheral processor: due to the different input levels at both sides the waveforms cannot be equalized perfectly by applying an internal characteristic IID. Since incomplete cancellation corresponds to a reduced correlation, and this is typically associated with a less compact auditory image, our model's output corresponds to the observation that applying IIDs to a diotic stimulus results in a less compact perceived image (Blauert, 1997, p. 170).

Thus, by determining the position of the minimum in the activity pattern, both the externally presented ITD and IID can be extracted. For wideband stimuli the ambiguity of which delay is the delay that corresponds to the location of a sound source can be obtained by combining information across frequency bands (for example, a straightness measure) as demonstrated by Stern *et al.* (1988) and Shackleton *et al.* (1992). For narrow-band stimuli and pure tones, the ITD can usually be resolved by the headwidth constraint: in daily-life listening conditions the interaural delay is limited to about 0.7 ms by the size of the head.

The ITDs and IIDs are very important when the location of a sound source must be estimated (especially the azimuth). Studies have shown that the perceived locus of a sound source depends on both the IID and the ITD (Sayers, 1964; Yost, 1981; Schiano *et al.*, 1986). For stimuli presented through headphones, the ITD and IID can be manipulated in such a way that their contributions to the laterality of the perceptual image tend to cancel or reinforce each other. ''Time-intensity tradeability'' refers to the extent to which the intracranial locus of a binaural sound depends only on the combined effect of these time and intensity differences, as opposed to the magnitude of these differences considered individually. This trading effect is, however, not perfect. Hafter and Carrier (1972) and Ruotolo *et al.* (1979) found that subjects can discriminate between images that are perceived with the same lateralization but were created by different combinations of IIDs and ITDs. This implies incomplete trading of these interaural parameters. The current model can, in principle, account for this phenomenon, because IID and ITD estimates of the presented sound source

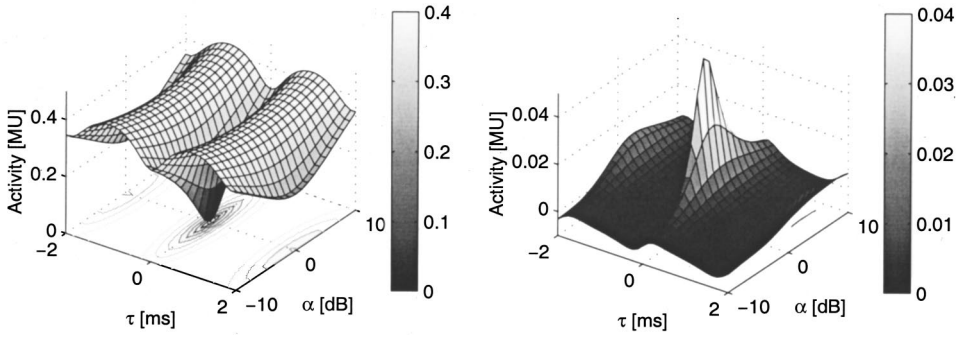

FIG. 6. Left panel: Idealized EI-activity for a wideband diotic noise (0–4000 Hz) with an overall level of 70 dB SPL for an auditory filter centered at 500 Hz. Right panel: change in the activity pattern of the left panel if a 500-Hz interaurally out-of-phase signal ($S\pi$) is added with a level of 50 dB.

can be extracted independently from the activity pattern and can be combined into one lateralization estimate, for example by weighted addition (e.g., Hafter, 1971).

D. Time-varying ITDs

In order to analyze the effect of time-varying interaural parameters, consider the internal representation for binaural beats (cf. Perrott and Nelson, 1969; Perrott and Musicant, 1977). The presentation of two identical tones, one to each ear, results in a single fused image centered in the listener's head. If a small interaural frequency difference is introduced (up to 2 Hz), apparent motion is reported. For intermediate frequency differences (i.e., up to 40 Hz), roughness (fast beats) is heard and for large frequency differences, two separate images are perceived. In the model, two tones with the same frequency result in an EI activity pattern as shown in the upper panel of Fig. 5. If the fine-structure waveforms are compared on a short time scale, a *small* interaural frequency difference is equivalent to an interaural phase difference that increases linearly with time. Since this phase difference increases with time, an ongoing shift of the minimum along the characteristic delay axis occurs, and the perceived locus of the sound moves along the line connecting both ears. If the interaural frequency difference is increased (e.g., 10 Hz), the limited temporal resolution of the model becomes increasingly important. During the time span defined by the temporal window, the interaural phase differences will now change considerably. Therefore there is no EI-type element which can cancel the signal completely, resulting in an increase of the EI activity in the valley and a lowering of the maximum activity. Consequently, there is no sharp minimum within the pattern, indicating that there is no well-defined audible locus. Thus, in accordance with psychophysical data, such fast motion is not represented within the binaural display.

E. Binaural detection

Human observers are very sensitive to changes in the interaural correlation of binaural signals. This sensitivity reveals itself in the phenomenon of binaural masking level differences (BMLDs). If an interaurally out-of-phase signal is added to an interaurally in-phase noise, the threshold for detecting the signal is up to 25 dB lower than for an in-phase signal (Hirsh, 1948b; Hafter and Carrier, 1970; Zurek and Durlach, 1987). In our modeling framework, the addition of the $S\pi$ signal results in a specific change in the EI activity pattern. To demonstrate this, the left panel of Fig. 6 shows the idealized EI activity for a diotic wideband noise (0–4 kHz, 70 dB overall level) for an auditory filter centered at 500 Hz.

If a 500-Hz out-of-phase signal with a level of 50 dB SPL is added, the activity pattern changes. The difference between the pattern for the No noise alone and the $NoS\pi$ stimulus is shown in the right panel of Fig. 6 (note the different scale on the activity axis). Clearly, for a characteristic IID and ITD of zero, there is a substantial change in activity while for other characteristic values, the change is much less. This change in activity can be used as a basis for a decision process in a detection task as will be described in the next section.

VI. CENTRAL PROCESSOR

The central processor receives both binaural (from the binaural processor) and monaural (directly from the adaptation loops) information. For signal detection purposes, the model can be used as an ''artificial observer,'' for example in a three-interval, forced-choice (3-IFC) procedure with feedback. The feedback is used by the artificial observer to learn what features of the stimuli have to be used for successful detection. In the 3-IFC procedure, two intervals contain only the masker, while the third interval contains the masker plus signal. The model's task is to identify which interval contains the test signal. This task is implemented in the following way. We assume that a template, $\bar{E}(i,t,\tau,\alpha)$, is stored in memory, consisting of the mean internal representation of several masker-alone realizations. The ability of listeners to use such a template for detection purposes was suggested before by Dau (1992) and Dau *et al.* (1996a), and for binaural detection by Holube *et al.* (1995) and by Breebaart and Kohlrausch (2001). In our simulations, such a template can be derived in the beginning of a simulated adaptive track, where the large difference between masker-alone and masker-plus-signal intervals allows an easy automatic identification of the masker-alone and the signal intervals. Also the feedback from the simulated adaptive track provides identification of the masker-alone intervals. The task for the detection algorithm is to determine which interval induces an internal representation that differs most from this template. In principle, the differences for all EI-type elements (i.e., as a function of the channel i, time t, characteristic delay τ, and characteristic intensity difference α) could be used. However, this results in a considerable complexity due to the large number of dimensions which causes the computing

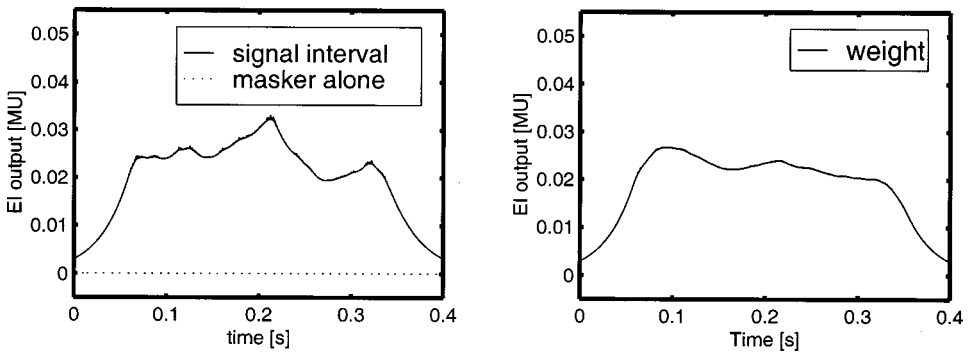

FIG. 7. NoSπ EI-activity as a function of time for the EI-type element with $\alpha=\tau=0$ without incorporation of internal noise. The left panel shows the output for a single signal interval (solid line) and for a masker alone (dotted line). The right panel shows the average difference between masker alone and masker-plus-signal. The masker had a duration of 400 ms. The 300-ms signal was temporally centered in the masker. Both signal and masker were gated with 50-ms Hanning windows.

power necessary to compute the output for all relevant EI-type elements to be enormous. We found that for the conditions described in the two accompanying articles it is sufficient to reduce this multidimensional space to only two dimensions, namely time and auditory frequency channel. For each detection experiment, the optimal combination of τ and α is determined for the on-frequency channel. These values are kept constant during that specific experiment for all channels. For example, in a wideband NoSπ condition, we already showed that for this specific condition, a maximum change in activity occurs for $\alpha=\tau=0$ (see Fig. 6, right panel), while for other values of α and τ, a much smaller effect is observed. It is therefore reasonable to only analyze the position corresponding to minimum activity (which is not necessarily $\alpha=\tau=0$), knowing that not too much information is lost. Conceptually, this would mean that listeners only pay attention to *one* position in space.

The idealized output for one token of an No masker alone as a function of time for the EI-type element with $\tau=\alpha=0$ is shown by the dotted line in the left panel of Fig. 7. The masker had a duration of 400 ms, and the 300-ms signal was temporally centered in the masker. Since there is no internal noise and the masker is completely canceled, the output is zero. This result is independent of specific masker realizations, and therefore the template for the masker alone consists also of a zero line. If a signal is added to the masker (with the same parameters as for Fig. 6), the output increases. This is shown by the solid line in the left panel of Fig. 7 for one realization of an NoSπ condition. The peaks and valleys in the output are the result of the adaptation loops in the peripheral preprocessing. If at a certain moment the noise masker has a relatively large amplitude, the adaptation loops will react to this large amplitude and compress the incoming signals more heavily. The result is that the sinusoidal signal, which has a constant envelope, is reduced in level at the output of the adaptation loops and hence the EI output decreases. Similarly, if a valley occurs in the masker envelope, the EI output increases. The occurrence of valleys and peaks in the noise masker occurs completely at random; the expected value of the masker amplitude is constant over time. Hence the expected output of the EI-type element in an NoSπ condition is also constant over time. This is demonstrated in the right panel of Fig. 7. The solid line (labeled ''weight'') represents the mean output for an NoSπ condition averaged over ten stimulus realizations. These weights inform the model about where in time and frequency the cues for the detection process are present (e.g., the integration window). As expected, the weight is nearly constant, except for the on- and offset of the signal.

An idealized example that has a nonzero output for a masker alone is given in Fig. 8. Here the masker and signal have the same properties as in the previous example, except for the fact that the interaural masker correlation was reduced to 0.5 (i.e., an NρSπ condition with $\rho=0.5$) and the signal level was increased to 60 dB. As in the left panel of Fig. 7, the solid line represents the output for a single masker-plus-signal interval, the dotted line represents the mean output for ten masker-alone intervals (i.e., the template). At the interval between 100 and 350 ms, the signal interval (solid line) results in a larger output than the template (dotted line). This is the cue that the model must detect. In contrast, during the interval from 0 to 100 ms the signal interval actually results in a smaller output than the averaged masker alone. This is the result of the specific fine structure waveform of the current masker realization and is not related to the presence or absence of the signal. This demonstrates the necessity of the weights[4] shown in the right panel of Fig. 8. As in Fig. 7, the weights consist of the average difference

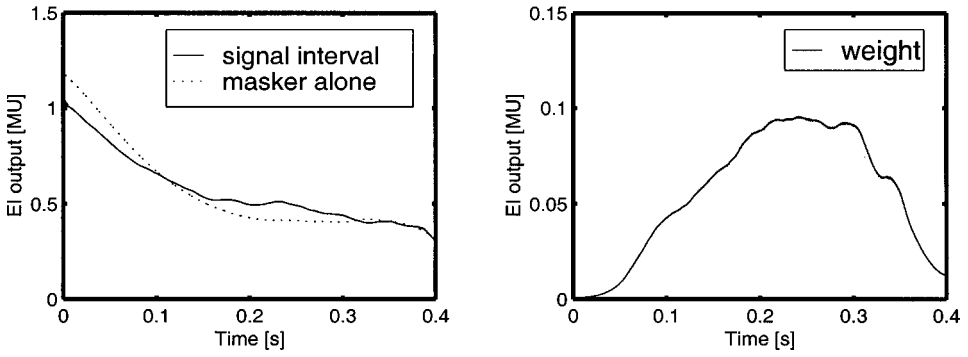

FIG. 8. Same as in Fig. 7, only for an NρSπ condition with $\rho=0.5$.

between the masker-alone intervals and the masker-plus-signal intervals. Since the weights are relatively low during the first 100 ms, the model ''knows'' that in this time interval, differences between template and actual stimulus are no reliable cue for the presence of the signal.

To facilitate monaural detection, the output of the adaptation loops is included after being low-pass filtered by a double-sided exponential window with time constants of 10 ms. These low-pass-filtered outputs are multiplied by a constant factor which denotes the monaural sensitivity of the model. The resulting signals are treated as an extra set of signals $E''(i,t)$ which enter the optimal detector. This detector compares the presented stimulus with the average internal representation of the masker-alone stimulus. This average internal representation is referred to as the *template*. All differences across frequency channels and time between the actual stimulus and the template are weighted according to weight functions as shown in, e.g., the right panels of Figs. 7 and 8 and subsequently combined into one distance measure. This process is described in detail in Appendix B.

VII. MOTIVATION FOR EI-BASED BINAURAL PROCESSING

As described in the Introduction, basically two binaural interaction processes have been used extensively in binaural models during the last decades. One is based on the interaural cross correlation, the other on the EC theory. These mechanisms are supported by so-called EE and EI units, respectively, as found in the neurophysiological pathway. In terms of their predictive scope, these mechanisms are very similar (Domnitz and Colburn, 1976; Colburn and Durlach, 1978; Green, 1992). For several reasons it is almost impossible to validate all these models with the same data which have been used for the current model. First, a substantial part of the models have not been specified as time-domain models which makes comparisons impossible without additional assumptions. Second, it is difficult to analyze and simulate all of these models including all variations and suggestions for improvements that have been suggested because of the enormous amount of work involved. Third, by describing the current model it is not our intention to demonstrate failures of other models but to show the predictive scope of a time-domain model based on EI interaction. For many of the conditions simulated in the accompanying articles (Breebaart *et al.*, 2001a, b), predictions would be similar if the binaural interaction was based on an EE(correlation)-type interaction instead of an EI-type interaction. There are, however, some conditions where we think that the interaural correlation and EC-based models do *not* give similar results or require different assumptions.

(1) A first difference concerns the effect of changes in the duration of the signal and the masker in an NoSπ condition. In principle, two approaches can be applied when using the interaural cross correlation. The first is to assume that the (normalized) correlation is calculated from the complete duration of the stimulus. The normalized interaural cross correlation (ρ) for an NoSπ condition is then given by

$$\rho = \frac{\langle N^2 \rangle - \langle S^2 \rangle}{\langle N^2 \rangle + \langle S^2 \rangle}. \tag{11}$$

Here, $\langle N^2 \rangle$ denotes the masker energy and $\langle S^2 \rangle$ denotes the signal energy in the interval over which the correlation is computed, i.e., the duration of the masker burst. For a masker alone, the interaural correlation is 1, because $\langle S^2 \rangle$ equals zero. The addition of an interaurally out-of-phase signal results in a decrease in the cross correlation. If the *signal* duration is changed within the interval from which the cross correlation is computed, a constant signal *energy* will lead to a constant decrease in the cross correlation. Thus, a doubling in the signal duration can be compensated by a decrease of the signal power by a factor of 2 and vice versa. This inverse relation between signal duration and binaural masked thresholds is indeed close to experimental data, which show an effect of 4.5 dB/doubling and 1.5 dB/doubling of signal duration for signal durations below and beyond 60 ms, respectively (cf. Zwicker and Zwicker, 1984; Yost, 1985; Wilson and Fowler, 1986; Wilson and Fugleberg, 1987). According to such a scheme, a doubling in *masker* duration while having a constant short signal duration should lead to a 3-dB increase in threshold. This does not, however, correspond to psychophysical results: NoSπ thresholds for a signal of fixed duration are hardly influenced by the masker duration (McFadden, 1966; Trahiotis *et al.*, 1972; Robinson and Trahiotis, 1972; Kohlrausch, 1986).

Alternatively, the correlation can be computed only from the stimulus part that contains the signal. In this case, the interaural correlation would be *independent* of the duration of both signal and masker (as long as the masker duration is at least as long as the signal duration) and hence thresholds would not be influenced by either signal or masker duration, which, again, is in contrast with the experimental results.

The performance of a cross-correlation model could be improved by assuming that an internal noise source is present which accumulates over the signal interval. If the model computes the cross correlation only from the signal portion of the presented stimulus, both the signal energy and internal noise energy increase equally with signal duration. However, the *variability* of the accumulated internal noise energy *decreases* with signal duration because the number of independent noise samples increases. Since this variability is the limiting factor in the detection process, thresholds are expected to decrease by 1.5 dB/doubling of signal duration. Although this is an improvement of such a model, it still predicts a much shallower slope than found experimentally (see Breebaart *et al.*, 2001b). In the current model, the output of the EI elements that cancel the masker completely is independent of the masker duration, while an increase of the signal duration results in lower thresholds because the change in the internal activity pattern will be present for a longer period. The third article in this series (Breebaart *et al.*, 2001b) demonstrates that the model can quantitatively account for the effect of signal duration in an NoSπ detection task.

(2) The interaural cross correlation is insensitive to static interaural intensity differences. If the relative intensities of the signals arriving at both ears are changed, the nor-

malized cross correlation remains unchanged. Since it is well known that both ITDs and IIDs result in a lateralization of the perceived locus of a sound source (Sayers, 1964), the cross-correlation approach needs additional assumptions to incorporate the processing of IIDs. Some suggestions have been made to incorporate the processing of IIDs, which are based on the incorporation of inhibition of secondary peaks in the cross-correlation function (cf. Lindemann, 1986) or a separate evaluation of the IIDs which is superimposed on the interaural cross correlation (Stern and Colburn, 1978). Hence it is certainly possible to incorporate IID sensitivity in a cross-correlation-based model. However, we think that the integral IID and ITD sensitivity for static and dynamically varying interaural differences in the current model is a strong point. The common treatment of ITDs and IIDs is a rather restrictive aspect of the model. The internal errors in binaural processing of IIDs and ITDs are characterized by one variable only, the amount of internal noise. In addition, the internal averaging of the binaurally processed stimuli occurs with one temporal window. Thus, the same (internal) temporal resolution is applied to IIDs, ITDs, and binaural detection experiments with tones in noise.

(3) A third point concerns normalization of the interaural cross correlation. Several models that have been published are essentially based on the unnormalized cross correlation, i.e., on the product of the (peripherally filtered) waveforms. However, Breebaart *et al*. (1998) and van de Par *et al.* (2001) noted that unnormalized cross-correlation models cannot account for binaural detection data with narrow-band noise maskers because of their inability to cope with fluctuations in the overall masker energy. They argued that the uncertainty in the excitation of the simulated neural activity (i.e., the unnormalized cross correlation) resulting from a diotic narrow-band masker is much larger than the reduction in the excitation due to the addition of an interaurally phase-reversed sinusoid (i.e., NoSπ). This leads to the prediction of very poor binaural performance. Hence cross-correlation-based models require specific accommodations to reduce the detrimental effects of stimulus level variability (see van de Par *et al*., 2001; Colburn and Isabelle, 2001). An often-proposed solution is to normalize the inputs to the cross correlator. However, the accuracy of this normalization must be better than we think is physiologically plausible. Therefore, van de Par *et al.* (2001) suggested that an equalization–cancellation (EC) mechanism may be favored over models based on cross correlation since this approach is insensitive to overall fluctuations in the masker energy.

VIII. SUMMARY AND CONCLUSIONS

A binaural signal detection model was described that transforms arbitrary stimuli into a three-dimensional internal representation with a minimum of free parameters. This representation is based on Durlach's EC theory instead of the common cross-correlation approach. It was explained that for many experimental conditions, models based on the EC theory or the cross correlation give similar predictions, but that in conditions where predictions differ, an EC-like mechanism may be favored over the cross-correlation. The internal representation is analyzed by a template-matching procedure which extracts information about the presence or absence of a signal added to a masker. The two accompanying articles (Breebaart *et al.*, 2001a, b) provide quantitative predictions for a wide range of binaural signal detection conditions derived with the model described in this article. In particular, Breebaart *et al.* (2001a) discusses the influence of spectral masker and signal parameters on detection thresholds, while Breebaart *et al.* (2001b) deals with temporal stimulus parameters.

ACKNOWLEDGMENTS

The investigations were supported by the Research Council for Earth and Life-sciences (ALW) with financial aid from the Netherlands Organization for Scientific Research (NWO). We want to thank the Associate Editor Wesley Grantham, Steve Colburn, and two anonymous reviewers for their very valuable comments and suggestions for improving the original manuscript.

APPENDIX A: EXPERIMENTAL DETERMINATION OF $P(\tau)$

A simple experiment was performed to determine the effect of internal delays upon binaural detection. In particular, an interaural delay was superimposed on an NoSπ stimulus. The task was to detect a signal within an interaurally delayed masker. The signal had a reversed interaural phase plus the same additional delay that was applied to the masker. We refer to this stimulus as $(\mathrm{NoS}\pi)_\tau$. The rationale for this paradigm is that if the binaural system can compensate for the external delay which is present in both masker and signal, the stimulus effectively corresponds to NoSπ and a large BMLD should be observed. It is expected, however, that with increasing delays, this compensation results in more internal errors and thresholds will increase. The distribution of errors as a function of τ needed to model these data correctly can be captured in the $p(\tau)$ function.

Our data were obtained for one subject only using a three-interval, forced-choice procedure with adaptive signal-level adjustment. A 400-ms narrow-band masker (10 Hz wide) with center frequencies of 125 and 500 Hz was presented at a level of 65 dB SPL. The 300-ms signal was temporally centered in the masker and had a frequency which was equal to the center frequency of the noise. Both masker and signal were gated with 50-ms Hanning windows. Delays up to half the period of the center frequency were used. The results are shown in Fig. A1. The triangles correspond to a center frequency of 500 Hz, the squares to 125 Hz. The diamonds represent data from a similar experiment performed by Colburn and Latimer (1978). They measured $(\mathrm{NoS}\pi)_\tau$ thresholds for a 500-Hz signal added to a wideband (20–1000 Hz) Gaussian-noise masker with an overall level of 75 dB SPL.

As expected, the thresholds increase with increasing delay. The slope of this increase is about 2 dB/ms, which is indicated by the dashed line. The delay dependence of the thresholds is close to linear if the thresholds are expressed in dB. To incorporate a similar threshold dependence in our model, the weighting function must have an exponential de-

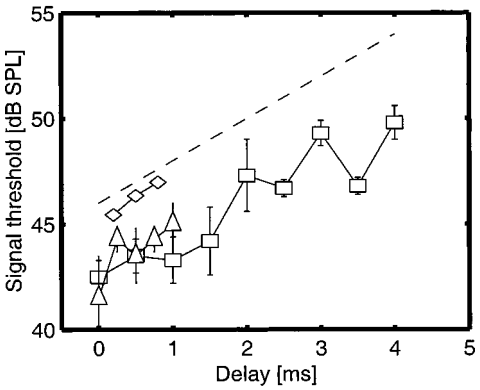

FIG. A1. $(\mathrm{NoS}\pi)_\tau$ thresholds as a function of the interaural delay τ. The triangles correspond to a center frequency of 500 Hz, the squares to 125 Hz. The diamonds are data adapted from Colburn and Latimer (1978). The error bars denote the standard error of the mean. The dashed line indicates a slope of 2 dB/ms.

cay. A slope of 2 dB/ms means that every 3 ms the signal amplitude is doubled at threshold, which corresponds to a factor of 4 in the EI-type element output. Therefore, the $p(\tau)$ function must decrease by a factor of 4 every 3 ms, which results in the formulation given in Eq. (7).

APPENDIX B: OPTIMAL DETECTOR

A set of channels E'' consisting of binaural and monaural signals (one for each frequency channel) is presented at the input of the optimal detector. Since further processing of the monaural and binaural channels is exactly equal, we will refer to the complete set of channels $E''(i,t)$ as the input of the optimal detector rather than using binaural and monaural channels separately.

For the channel i, the distance $U(i,t)$ between a template $\bar{E}(i,t)$ and the actual output $E''(i,t)$ is given by

$$U(i,t)=E''(i,t)-\bar{E}(i,t). \tag{B1}$$

The variance of $U(i,t)$ resulting from internal noise and masker uncertainty is denoted by $\sigma^2(i,t)$, while the mean difference between masker plus test signal and masker alone near threshold level is denoted by $\mu(i,t)$. A single number which describes the total difference between stimulus and template is assigned to each interval. This difference value, U, is computed by integrating the temporally weighted difference signal $U(i,t)$:

$$U=\int_i\int_{t=0}^{t=T}\frac{\mu(i,t)}{\sigma^2(i,t)}U(i,t)di\,dt, \tag{B2}$$

where T denotes the interval duration. Thus, integration is performed over both time and auditory channels. The weighting function $(\mu(i,t)/\sigma^2(i,t))$ ensures that the model only takes differences between template and actual signal into account at positions where differences are expected. Furthermore, if at a certain position, the difference has a large amount of variability (i.e., a large value of σ), this uncertain output has a smaller weight compared to positions with smaller uncertainty. The weighting function is optimal when the variability represented by σ is Gaussian, an assumption which does not always hold for the internal representation. Still it seems the most reasonable choice to use this weighting function. In a detection task decisions will be based on the value of U. The higher U, the greater the likelihood that a signal is present. Thus, in a 3-IFC procedure the model will choose the interval with the highest value of U. After each trial, the model receives feedback. By storing the internal representations of the three stimuli in memory (i.e., two masker-alone realizations and one masker-plus-signal realization), the model can update its estimate of $\bar{E}(i,t)$, $\sigma^2(i,t)$, and $\mu(i,t)$. $\bar{E}(i,t)$ is updated by averaging the output $E(i,t)$ of all presented masker realisations. In a similar way, the average value of all internal signal representations is computed. Then $\mu(i,t)$ is obtained by subtracting the mean internal representation of masker-alone intervals and of masker-plus-signal intervals. Finally, $\sigma^2(i,t)$ is obtained by computing the variance in the internal masker-alone representations.

[1]If the sound pressure at the ear drums is considered, much larger interaural intensity differences may occur than 10 dB. However, these differences in the acoustic signals are severely reduced by the compression in the adaptation loops. We found that the limit for α of 10 dB is appropriate for all conditions that we tested. The range for the internal delays was chosen such that at very low frequencies (i.e., 100 Hz), a delay of half the period of that frequency (e.g., 5 ms) is available.

[2]In Sec. IV, an additive noise was described to implement the absolute threshold of hearing. This is a different noise source from the noise mentioned here which is added at the level of the EI-type elements. The EI-type element noise limits the detection of interaural differences which are present in stimuli with a level above the absolute threshold.

[3]The effect of internal noise was not included in the graphs because all pictures consist of a *snapshot* of the EI activity at a certain moment in time. The amount of internal noise for such a snapshot is of the same order of magnitude as the output and hence the model properties that are demonstrated would be impossible to see. The fact that the model does not suffer from this internal noise in the same way as the visual observer does is due to the fact that the optimal detector which is present in the central processor (see Sec. VI for details) is able to strongly reduce the internal noise by temporal integration.

[4]It should be noted that in these examples, the variability in the EI output due to internal noise or due to stimulus uncertainty was not taken into account. As shown in Appendix B, the weight that is actually applied by the model consists of the average difference in EI output between masker alone and masker plus signal, *divided* by the variance in the output for a masker alone.

Batra, R., Kuwada, S., and Fitzpatrick, D. C. (**1997a**). ''Sensitivity to interaural temporal disparities of low- and high-frequency neurons in the superior olivary complex. I. Heterogenity of responses,'' J. Neurophysiol. **78**, 1222–1236.

Batra, R., Kuwada, S., and Fitzpatrick, D. C. (**1997b**). ''Sensitivity to interaural temporal disparities of low- and high-frequency neurons in the superior olivary complex. II. Coincidence detection,'' J. Neurophysiol. **78**, 1237–1247.

Bernstein, L. R., and Trahiotis, C. (**1996**). ''The normalized correlation: accounting for binaural detection across center frequency,'' J. Acoust. Soc. Am. **100**, 3774–3787.

Bilsen, F. A. (**1977**). ''Pitch of noise signals: Evidence for a 'central spectrum,' '' J. Acoust. Soc. Am. **61**, 150–161.

Bilsen, F. A., and Goldstein, J. L. (**1974**). ''Pitch of dichotically delayed noise and its possible spectral basis,'' J. Acoust. Soc. Am. **55**, 292–296.

Blauert, J. (**1997**). *Spatial Hearing: The Psychophysics of Human Sound Localization* (MIT, Cambridge, MA).

Boudreau, J. C., and Tsuchitani, C. (**1968**). ''Binaural interaction in the cat superior olive S segment,'' J. Neurophysiol. **31**, 442–454.

Breebaart, J., and Kohlrausch, A. (**2001**). ''The influence of interaural stimulus uncertainty on binaural signal detection,'' J. Acoust. Soc. Am. **109**, 331–345.

Breebaart, J., van de Par, S., and Kohlrausch, A. (**1998**). ''Binaural signal detection with phase-shifted and time-delayed noise maskers,'' J. Acoust. Soc. Am. **103**, 2079–2083.
Breebaart, J., van de Par, S., and Kohlrausch, A. (**1999**). ''The contribution of static and dynamically varying ITDs and IIDs to binaural detection,'' J. Acoust. Soc. Am. **106**, 979–992.
Breebaart, J., van de Par, S., and Kohlrausch, A. (**2001a**). ''Binaural processing model based on contralateral inhibition. II. Dependence on spectral parameters,'' J. Acoust. Soc. Am. **110**, 1089–1104.
Breebaart, J., van de Par, S., and Kohlrausch, A. (**2001b**). ''Binaural processing model based on contralateral inhibition. III. Dependence on temporal parameters,'' J. Acoust. Soc. Am. **110**, 1105–1117.
Colburn, H. S. (**1973**). ''Theory of binaural interaction based on auditory-nerve data: I. General strategy and preliminary results on interaural discrimination,'' J. Acoust. Soc. Am. **54**, 1458–1470.
Colburn, H. S. (**1977**). ''Theory of binaural interaction based on auditory-nerve data. II. Detection of tones in noise,'' J. Acoust. Soc. Am. **61**, 525–533.
Colburn, H. S., and Durlach, N. I. (**1978**). ''Models of binaural interaction,'' in *Handbook of Perception*, edited by E. Carterette and M. Friedman (Academic, New York), Vol. IV, pp. 467–518.
Colburn, H. S., and Isabelle, S. K. (**2001**). ''Physiologically based models of binaural detection,'' in *Physiological and Psychophysical Bases of Auditory Function*, edited by D. J. Breebaart, A. J. M. Houtsma, A. Kohlrausch, V. Prijs, and R. Schoonhoven (Shaker Publishing BV, Maastricht), pp. 161–168.
Colburn, H. S., and Latimer, J. S. (**1978**). ''Theory of binaural interaction based on auditory nerve data. III. Joint dependence on interaural time and amplitude differences in discrimination and detection,'' J. Acoust. Soc. Am. **64**, 95–106.
Culling, J. F., and Summerfield, Q. (**1995**). ''Perceptual separation of concurrent speech sounds: absence of across-frequency grouping by common interaural delay,'' J. Acoust. Soc. Am. **98**, 785–797.
Culling, J. F., and Summerfield, Q. (**1998**). ''Measurements of the binaural temporal window using a detection task,'' J. Acoust. Soc. Am. **103**, 3540–3553.
Culling, J. F., Summerfield, Q., and Marshall, D. H. (**1996**). ''Dichotic pitches as illusions of binaural unmasking,'' J. Acoust. Soc. Am. **99**, 2515–2529.
Dau, T. (**1992**). ''Der optimale Detektor in einem Computermodell zur Simulation von psychoakustischen Experimenten,'' Master's thesis, Universität Göttingen, Göttingen.
Dau, T., Kollmeier, B., and Kohlrausch, A. (**1997**). ''Modeling auditory processing of amplitude modulation: II. Spectral and temporal integration,'' J. Acoust. Soc. Am. **102**, 2906–2919.
Dau, T., Püschel, D., and Kohlrausch, A. (**1996a**). ''A quantitative model of the 'effective' signal processing in the auditory system: I. Model structure,'' J. Acoust. Soc. Am. **99**, 3615–3622.
Dau, T., Püschel, D., and Kohlrausch, A. (**1996b**). ''A quantitative model of the 'effective' signal processing in the auditory system: II. Simulations and measurements,'' J. Acoust. Soc. Am. **99**, 3623–3631.
Domnitz, R. H., and Colburn, H. S. (**1976**). ''Analysis of binaural detection models for dependence on interaural target parameters,'' J. Acoust. Soc. Am. **59**, 598–601.
Durlach, N. I. (**1963**). ''Equalization and cancellation theory of binaural masking-level differences,'' J. Acoust. Soc. Am. **35**, 1206–1218.
Durlach, N. I. (**1972**). ''Binaural signal detection: Equalization and cancellation theory,'' in *Foundations of Modern Auditory Theory*, edited by J. Tobias (Academic, New York), Vol. II, pp. 369–462.
Durlach, N. I., Gabriel, K. J., Colburn, H. S., and Trahiotis, C. (**1986**). ''Interaural correlation discrimination: II. Relation to binaural unmasking,'' J. Acoust. Soc. Am. **79**, 1548–1557.
Egan, J. P., Lindner, W. A., and McFadden, D. (**1969**). ''Masking-level differences and the form of the psychometric function,'' Percept. Psychophys. **6**, 209–215.
Gaik, W. (**1993**). ''Combined evaluation of interaural time and intensity differences: Psychoacoustic results and computer modeling,'' J. Acoust. Soc. Am. **94**, 98–110.
Glasberg, B. R., and Moore, B. C. J. (**1990**). ''Derivation of auditory filter shapes from notched-noise data,'' Hear. Res. **47**, 103–138.
Goldberg, J. M., and Brown, P. B. (**1969**). ''Response of binaural neurons of dog superior olivary complex to dichotic tonal stimuli: Some physiological mechanisms of sound localization,'' J. Neurophysiol. **32**, 613–636.
Green, D. (**1992**). ''On the similarity of two theories of comodulation masking release,'' J. Acoust. Soc. Am. **91**, 1769.
Green, D. M. (**1966**). ''Signal-detection analysis of equalization and cancellation model,'' J. Acoust. Soc. Am. **40**, 833–838.
Hafter, E. R. (**1971**). ''Quantitative evaluation of a lateralization model of masking-level differences,'' J. Acoust. Soc. Am. **50**, 1116–1122.
Hafter, E. R., and Carrier, S. C. (**1970**). ''Masking-level differences obtained with pulsed tonal maskers,'' J. Acoust. Soc. Am. **47**, 1041–1047.
Hafter, E. R., and Carrier, S. C. (**1972**). ''Binaural interaction in low-frequency stimuli: the inability to trade time and intensity completely,'' J. Acoust. Soc. Am. **51**, 1852–1862.
Hall, J. W., and Harvey, A. D. G. (**1984**). ''NoSo and NoSπ thresholds as a function of masker level for narrow-band and wideband masking noise,'' J. Acoust. Soc. Am. **76**, 1699–1703.
Hirsh, I. (**1948a**). ''Binaural summation and interaural inhibition as a function of the level of masking noise,'' Am. J. Psychol. **61**, 205–213.
Hirsh, I. (**1948b**). ''The influence of interaural phase on interaural summation and inhibition,'' J. Acoust. Soc. Am. **20**, 536–544.
Holube, I., Colburn, H. S., van de Par, S., and Kohlrausch, A. (**1995**). ''Model simulations of masked thresholds for tones in dichotic noise maskers,'' J. Acoust. Soc. Am. **97**, 3411–3412.
Holube, I., Kinkel, M., and Kollmeier, B. (**1998**). ''Binaural and monaural auditory filter bandwidths and time constants in probe tone detection experiments,'' J. Acoust. Soc. Am. **104**, 2412–2425.
Irvine, D. R. F., and Gago, G. (**1990**). ''Binaural interaction in high-frequency neurons in inferior colliculus of the cat: Effects of variations in sound pressure level on sensitivity to interaural intensity differences,'' J. Neurophysiol. **63**, 570–591.
Jeffress, L. A. (**1948**). ''A place theory of sound localization,'' J. Comp. Physiol. Psychol. **41**, 35–39.
Johannesma, P. I. M. (**1972**). ''The pre-response stimulus ensemble of neurons in the cochlear nucleus,'' in *Proceedings of the Symposium of Hearing Theory* (IPO, Eindhoven, The Netherlands).
Johnson, D. H. (**1980**). ''The relationship between spike rate and synchrony in responses of auditory-nerve fibers to single tones,'' J. Acoust. Soc. Am. **68**, 1115–1122.
Joris, P. X. (**1996**). ''Envelope coding in the lateral superior olive. II. Characteristic delays and comparison with responses in the medial superior olive,'' J. Neurophysiol. **76**, 2137–2156.
Joris, P. X., and Yin, T. C. T. (**1995**). ''Envelope coding in the lateral superior olive. I. Sensitivity to interaural time differences,'' J. Neurophysiol. **73**, 1043–1062.
Kiang, N. Y. S. (**1975**). ''Stimulus representation in the discharge patterns of auditory neurons,'' in *The Nervous System* (Raven, New York), Vol. 3.
Kohlrausch, A. (**1986**). ''The influence of signal duration, signal frequency and masker duration on binaural masking level differences,'' Hear. Res. **23**, 267–273.
Kohlrausch, A., and Fassel, R. (**1997**). ''Binaural masking level differences in nonsimultaneous masking,'' in *Binaural and Spatial Hearing in Real and Virtual Environments*, edited by R. H. Gilkey and T. Anderson (Lawrence Erlbaum Assoc., Mahwah, NJ), Chap. 9, pp. 169–190.
Kollmeier, B., and Gilkey, R. H. (**1990**). ''Binaural forward and backward masking: Evidence for sluggishness in binaural detection,'' J. Acoust. Soc. Am. **87**, 1709–1719.
Kuwada, S., Yin, T. C. T., Syka, J., Buunen, T. J. F., and Wickesberg, R. E. (**1984**). ''Binaural interaction in low-frequency neurons in inferior colliculus of the cat. IV. Comparison of monaural and binaural response properties,'' J. Neurophysiol. **51**, 1306–1325.
Lindemann, W. (**1985**). ''Die Erweiterung eines Kreuzkorrelationsmodells der binauralen Signalverarbeitung durch kontralaterale Inhibitionsmechanismen,'' Ph.D. thesis, Ruhr-Universität Bochum, Bochum.
Lindemann, W. (**1986**). ''Extension of a binaural cross-correlation model by contralateral inhibition. I. Simulation of lateralization for stationary signals,'' J. Acoust. Soc. Am. **80**, 1608–1622.
McAlpine, D., Jiang, D., Shackleton, T. M., and Palmer, A. R. (**1998**). ''Convergent input from brainstem coincidence detectors onto delay-sensitive neurons in the inferior colliculus,'' J. Neurosci. **18**, 6026–6039.
McFadden, D. (**1966**). ''Masking-level differences with continuous and with burst masking noise,'' J. Acoust. Soc. Am. **40**, 1414–1419.
McFadden, D. (**1968**). ''Masking-level differences determined with and without interaural disparities in masker intensity,'' J. Acoust. Soc. Am. **44**, 212–223.
Moore, J. K. (**1987**). ''The human auditory brain stem: A comparative view,'' Hear. Res. **29**, 1–32.

Palmer, A. R., McAlpine, D., and Jiang, D. (**1997**). ''Processing of interaural delay in the inferior colliculus,'' in *Acoustical Signal Processing in the Central Auditory System*, edited by J. Syka (Plenum, New York), pp. 353–364.
Park, T. J. (**1998**). ''IID sensitivity differs between two principal centers in the interaural intensity difference pathway: the LSO and the IC,'' J. Neurophysiol. **79**, 2416–2431.
Park, T. J., Monsivais, P., and Pollak, G. D. (**1997**). ''Processing of interaural intensity differences in the LSO: role of interaural threshold differences,'' J. Neurophysiol. **77**, 2863–2878.
Patterson, R. D., Holdsworth, J., Nimmo-Smith, I., and Rice, P. (**1988**). ''Svos final report: The auditory filterbank,'' Tech. Rep. APU report 2341.
Perrott, D., and Nelson, M. (**1969**). ''Limits for the detection of binaural beats,'' J. Acoust. Soc. Am. **46**, 1477–1480.
Perrott, D. R., and Musicant, A. D. (**1977**). ''Minimum auditory movement angle: Binaural localization of moving sound sources,'' J. Acoust. Soc. Am. **62**, 1463–1466.
Raatgever, J., and Bilsen, F. (**1986**). ''A central spectrum theory of binaural processing. Evidence from dichotic pitch,'' J. Acoust. Soc. Am. **80**, 429–441.
Raatgever, J., and van Keulen, W. (**1992**). ''Binaural time processing at high frequencies: The central spectrum model extended,'' in *Proceedings of the 14th International Congress on Acoustics*, pp. H6-3.
Reed, M. C., and Blum, J. J. (**1990**). ''A model for the computation and encoding of azimuthal information by the lateral superior olive,'' J. Acoust. Soc. Am. **88**, 1442–1453.
Robinson, D. E., and Trahiotis, C. (**1972**). ''Effects of signal duration and masker duration on detectability under diotic and dichotic listening conditions,'' Percept. Psychophys. **12**, 333–334.
Rose, J. E., Gross, N. B., Geisler, C. D., and Hind, J. E. (**1966**). ''Some neural mechanisms in the inferior colliculus of cat which may be relevant to localization of a sound source,'' J. Neurophysiol. **29**, 288–314.
Ruotolo, B. R., Stern, R. M., and Colburn, H. S. (**1979**). ''Discrimination of symmetric time-intensity traded binaural stimuli,'' J. Acoust. Soc. Am. **66**, 1733–1737.
Sayers, B. M. (**1964**). ''Acoustic image lateralization judgments with binaural tones,'' J. Acoust. Soc. Am. **36**, 923–926.
Schiano, J. L., Trahiotis, C., and Bernstein, L. R. (**1986**). ''Lateralization of low-frequency tones and narrow bands of noise,'' J. Acoust. Soc. Am. **79**, 1563–1570.
Shackleton, T., Meddis, R., and Hewitt, M. (**1992**). ''Across frequency integration in a model of lateralization,'' J. Acoust. Soc. Am. **91**, 2276–2279.
Stern, R. M., and Shear, G. D. (**1996**). ''Lateralization and detection of low-frequency binaural stimuli: Effects of distribution of internal delay,'' J. Acoust. Soc. Am. **100**, 2278–2288.
Stern, R. M., Zeiberg, A. S., and Trahiotis, C. (**1988**). ''Lateralization of complex binaural stimuli: A weighted-image model,'' J. Acoust. Soc. Am. **84**, 156–165.
Stern, R. M. J., and Colburn, H. S. (**1978**). ''Theory of binaural interaction based on auditory-nerve data. IV. A model for subjective lateral position,'' J. Acoust. Soc. Am. **64**, 127–140.
Trahiotis, C., Dolan, T. R., and Miller, T. H. (**1972**). ''Effect of backward masker fringe on the detectability of pulsed diotic and dichotic tonal signals,'' Percept. Psychophys. **12**, 335–338.
Tsuchitani, C. (**1997**). ''Input from the medial nucleus of trapezoid body to an interaural level detector,'' Hear. Res. **105**, 211–224.
van de Par, S., and Kohlrausch, A. (**1995**). ''Analytical expressions for the envelope correlation of certain narrow-band stimuli,'' J. Acoust. Soc. Am. **98**, 3157–3169.
van de Par, S., Trahiotis, C., and Bernstein, L. R. (**2001**). ''A consideration of the normalization that is typically included in correlation-based models of binaural detection,'' J. Acoust. Soc. Am. **109**, 830–833.
Weis, T. F., and Rose, C. (**1988**). ''A comparison of synchronization filters in different auditory receptor organs,'' Hear. Res. **33**, 175–180.
Wilson, R., and Fowler, C. (**1986**). ''Effects of signal duration on the 500-Hz masking-level difference,'' Scand. Audiol. **15**, 209–215.
Wilson, R., and Fugleberg, R. (**1987**). ''Influence of signal duration on the masking-level difference,'' J. Speech Hear. Res. **30**, 330–334.
Yin, T. C. T., and Chan, J. C. K. (**1990**). ''Interaural time sensitivity in medial superior olive of cat,'' J. Neurophysiol. **64**, 465–488.
Yost, W. A. (**1981**). ''Lateral position of sinusoids presented with interaural intensive and temporal differences,'' J. Acoust. Soc. Am. **70**, 397–409.
Yost, W. A. (**1985**). ''Prior stimulation and the masking-level difference,'' J. Acoust. Soc. Am. **78**, 901–906.
Zerbs, C. (**2000**). ''Modeling the effective binaural signal processing in the auditory system,'' Ph.D. thesis, Oldenburg University, Germany.
Zurek, P. M., and Durlach, N. I. (**1987**). ''Masker-bandwidth dependence in homophasic and antiphasic tone detection,'' J. Acoust. Soc. Am. **81**, 459–464.
Zwicker, U. T., and Zwicker, E. (**1984**). ''Binaural masking-level difference as a function of masker and test-signal duration,'' Hear. Res. **13**, 215–220.

Binaural processing model based on contralateral inhibition. II. Dependence on spectral parameters

Jeroen Breebaart[a)]
IPO, Center for User–System Interaction, P.O. Box 513, NL-5600 MB Eindhoven, The Netherlands

Steven van de Par and Armin Kohlrausch
IPO, Center for User–System Interaction, P.O. Box 513, NL-5600 MB Eindhoven, The Netherlands and Philips Research Laboratories Eindhoven, Prof. Holstlaan 4, NL-5656 AA Eindhoven, The Netherlands

(Received 23 May 2000; revised 18 December 2000; accepted 3 May 2001)

This and two accompanying articles [Breebaart *et al.*, J. Acoust. Soc. Am. **110**, 1074–1088 (2001); **110**, 1105–1117 (2001)] describe a computational model for the signal processing in the binaural auditory system. The model consists of several stages of monaural and binaural preprocessing combined with an optimal detector. In the present article the model is tested and validated by comparing its predictions with experimental data for binaural discrimination and masking conditions as a function of the spectral parameters of both masker and signal. For this purpose, the model is used as an artificial observer in a three-interval, forced-choice adaptive procedure. All model parameters were kept constant for all simulations described in this and the subsequent article. The effects of the following experimental parameters were investigated: center frequency of both masker and target, bandwidth of masker and target, the interaural phase relations of masker and target, and the level of the masker. Several phenomena that occur in binaural listening conditions can be accounted for. These include the wider effective binaural critical bandwidth observed in band-widening NoSπ conditions, the different masker-level dependence of binaural detection thresholds for narrow- and for wide-band maskers, the unification of IID and ITD sensitivity with binaural detection data, and the dependence of binaural thresholds on frequency. [DOI: 10.1121/1.1383298]

PACS numbers: 43.66.Pn, 43.66.Ba, 43.66.Dc [DWG]

I. INTRODUCTION

This article describes and discusses simulations of binaural detection tasks with a binaural processing model which is described in detail in the preceding article (Breebaart *et al.*, 2001a). This model basically consists of three stages. The first stage simulates the effective signal processing of the basilar membrane and the inner haircells and includes adaptation by means of adaptation loops (Dau *et al.*, 1996a). Binaural interaction is modeled in the second stage by means of a contralateral inhibition mechanism: the model computes the squared difference signal between the left and right ears as a function of time, frequency channel, internal interaural delay (τ in seconds), and internal interaural level adjustment (α in dB). These binaural signals are corrupted by internal noise and subsequently analyzed by the third stage in the model, the central processor. The model is used as an artificial observer in a three-interval, forced-choice procedure, in which the central processor matches the representations of the presented stimuli to templates (derived during previous presentations), and on this basis the model indicates which interval contains the signal.

The scope of the simulations of this article is restricted to binaurally ''stationary'' stimuli. For these cases, the spectral parameters and the interaural phase relations of the stimuli were not varied as a function of time, and the stimuli had a duration which was long in comparison to the temporal resolution of the auditory system. First, the ability of the model to capture some basic properties of binaural hearing is demonstrated. These include interaural intensity difference (IID) and interaural time difference (ITD) sensitivity and binaural detection performance of tones in noise as a function of the bandwidth, center frequency, and interaural phase relationships of the stimuli.

The second and major focus of this article is on the apparently wider critical bandwidth in binaural conditions that has been found in a number of studies. If an interaurally out-of-phase signal (Sπ) must be detected against an No masker of variable bandwidth, the estimate of the critical bandwidth is two to three times the estimate which is found in monaural experiments (Sever and Small, 1979; Zurek and Durlach, 1987; van de Par and Kohlrausch, 1999). Hall *et al.* (1983) found that this descrepancy between monaural and binaural estimates is largest at high masker levels. Furthermore, the wider effective bandwidth is only observed if the interaural cross correlation of the masker is very close to +1 (van der Heijden and Trahiotis, 1998). On the other hand, experiments that use a masker with frequency-dependent interaural phase relations reveal a critical band estimate that basically agrees with the monaural estimate (Sondhi and Guttman, 1966; Kohlrausch, 1988; Kollmeier and Holube, 1992; Holube *et al.*, 1998). Furthermore, data that were obtained as a function of the bandwidth of the *signal* also show a monaural bandwidth behavior (Langhans and Kohlrausch,

a)Now at: Philips Research Laboratories Eindhoven, Prof. Holstlaan 4, NL-5656 AA Eindhoven, The Netherlands. Electronic mail: jeroen.breebaart@philips.com

1992; Breebaart *et al.*, 1999). In this article, it is demonstrated that the current model, which includes peripheral filters with a bandwidth based on monaural estimates, can account for all observations described earlier. Depending on the experimental paradigm, the model shows different bandwidth dependencies. It is also explained that the wider effective critical bandwidth does not result from a poorer spectral resolution of the binaural auditory system compared to the monaural system, but is related to the ability of the model to *integrate* information across filters.

In a third article (Breebaart *et al.*, 2001b), temporal properties of the model are discussed, which include the effect of signal and masker duration, phase transitions in the time domain, and forward masking.

II. METHOD

A. Relevant stages of the model

In the Introduction, a coarse description of the general model setup was given. In this section, the stages of the model that are relevant for the simulations described in this article (i.e., spectral behavior) are discussed in more detail. For a detailed description of the complete model, see Breebaart *et al.* (2001a).

(i) Filtering of the gammatone filterbank. The filterbank present in the peripheral processing stage determines the spectral resolution of the model, in line with the ERB estimates published by Glasberg and Moore (1990).

(ii) Inner hair cell model. This stage consists of a half-wave rectifier followed by a fifth-order low-pass filter with a cutoff frequency (-3 dB) of 770 Hz. Hence below 1000 Hz, both the ITDs and IIDs are preserved at the output of this stage. However, above 2 kHz, the output approximates the envelope of the incoming signals and hence only IIDs and ITDs present in the envelope are preserved. Between 1 and 2 kHz, the ITD in the fine structure waveforms is gradually lost.

(iii) Adaptation loops. The chain of adaptation loops in the peripheral processor has an almost logarithmic input–output characteristic in steady state and is a nonlinear device. These properties have two consequences. First of all, it has been shown frequently that for both monaural and binaural detection of signals added to a wideband masker with a variable level, the threshold *signal-to-masker* ratio is approximately constant, as long as the masker level is well above the absolute threshold (cf. McFadden, 1968; Hall and Harvey, 1984). If it is assumed that a certain constant *change* at the output of the adaptation loops is needed to detect a signal, the signal must be equal to a certain *fraction* of the masker level due to the logarithmic compression. Hence the signal-to-masker ratio will be approximately constant at threshold. Second, due to the nonlinear behavior, large interaural intensity differences at the input cannot be canceled completely by a linear level adjustment at the output.

(iv) Compressive input–output characteristic of EI-type elements. The temporally smoothed difference signal of the EI-type elements is compressed logarithmically. In combination with an additive internal noise, this stage results in thresholds of interaural differences that depend on the interaural cross correlation of the reference stimuli.

(v) Weighting as a function of the internal delay. The model includes a weighting function that decreases with the internal delay of the EI-type elements. Consequently, the relative amount of internal noise increases with internal delay.

(vi) Optimal detector in the central processor. The EI-type element outputs are corrupted by an additive internal noise. Subsequently, the internal representations of the external stimuli are compared to a template that consists of the average masker-alone representation. The differences between the actual stimulus and the template are weighted and integrated both in the time and the frequency domain according to an optimal criterion. This enables the optimal detector to reduce the internal signal-to-noise ratio for stimuli that have a valuable detection cue in more than one auditory filter.

B. Procedure

Masked thresholds were simulated using an adaptive three-interval forced-choice (3IFC) procedure. The masker was presented in three consecutive intervals. One of the intervals contained the signal. The model's task was to indicate which interval contained the signal. The level of the signal was adjusted according to a two-down one-up algorithm (Levitt, 1971). The initial step size for adjusting the level was 8 dB. The step size was halved after every second track reversal until it reached 1 dB. The run was then continued for another eight reversals. The median level at these last eight reversals was used as the threshold value. At least five repetitions were performed for each parameter value. All thresholds are plotted as mean values of all repetitions, and the error bars denote the standard deviation of the repetitions.

C. Stimuli

All stimuli were generated digitally at a sampling frequency of 32 kHz. The maskers used in the different experiments had a duration of 400 ms unless stated differently. They were presented interaurally in-phase (No), interaurally out-of-phase ($N\pi$), or with a specific interaural correlation ($N\rho$) obtained by combining No and $N\pi$ noises (cf. Breebaart and Kohlrausch, 2001). The signals were presented interaurally in-phase (So), interaurally out-of-phase ($S\pi$), or to one ear only (Sm). Bandpass Gaussian noises were generated by computing the Fourier transform of white noise and setting the amplitude coefficients outside the desired frequency range to zero. After an inverse Fourier transform, the bandpass noise was obtained.

In all simulations, the level, bandwidth, on- and offset ramps, and onset delay of both the maskers and signals were set to the values used in the corresponding experiments with human subjects. If more data sets from various authors with different experimental settings were used, the experimental

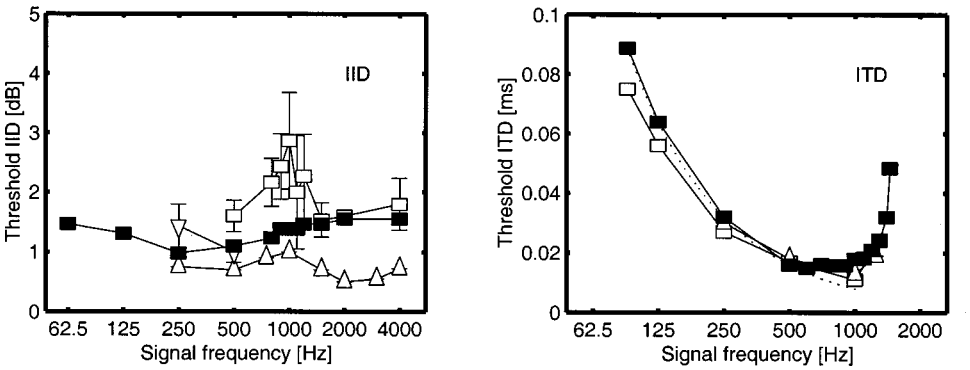

FIG. 1. IID thresholds (left panel) and ITD thresholds (right panel) for tones as a function of frequency. The open symbols denote data adapted from literature, the filled symbols are model predictions. The dotted line in the right panel denotes a constant interaural phase difference of 0.05 rad. Legend left panel: squares, Grantham (1984); upward triangles, Mills (1960); downward triangles, McFadden *et al.* (1971). Legend right panel: squares, Klumpp and Eady (1956); upward triangles, Zwislocki and Feldman (1956).

settings from one of these studies were used for determining the model simulations. Comparison with the other data sets was possible because in such conditions, the binaural masking level differences (BMLDs) were calculated or thresholds were expressed relative to the spectrum level of the masking noise.

D. Model calibration

As described in the preceding article (Breebaart *et al.*, 2001a), the model effectively calculates the difference signal between the left and right ears as a function of an internal delay and internal level adjustment. The subtraction is performed by so-called EI (excitation-inhibition) elements. The sensitivity to interaural differences of these EI-type elements is determined by two (fixed) model parameters *a* and *b*. By changing these parameters, the EI output is scaled relative to the internal noise which has a fixed level. These sensitivity parameters were determined as follows. Detection thresholds were simulated for a 500-Hz interaurally out-of-phase sinusoid in a Gaussian low-pass masker (cutoff frequency of 1 kHz) which had an interaural correlation of 0.64[1] and an overall level of 65 dB SPL. In this condition only the parameter *a* determines the detectability of the tone. This parameter was adjusted to reach a threshold of 46 dB SPL. Subsequently, the interaural correlation of the masker was set to $+1$ and the parameter *b* was adjusted in order to reach a threshold of 38 dB SPL. These thresholds were adapted from frozen-noise $N\rho S\pi$ data given by Breebaart and Kohlrausch (2001). The resulting values of *a* and *b* are 0.1 and 0.000 02, respectively. The monaural sensitivity of the model was adjusted such that the just noticeable difference in intensity of a 500-Hz, 400-ms sinusoid with a level of 65 dB SPL was 1 dB.

Note that during all simulations, all model parameters and procedures were kept constant. This restriction has the consequence that sometimes overall differences between model predictions and experimental data sets occur. However, similar differences exist between experimental data sets from different publications. For such conditions, much better predictions could have been obtained by calibrating the model's BMLD separately for each experiment. Nevertheless, all parameters were kept constant in order to demonstrate to what extent the current model can account for different experimental findings.

III. SIMULATIONS

A. Detection of static interaural differences

The first simulations comprised the detection of static interaural intensity and time differences. Hence in these experiments only pure tones were presented to the model in the absence of any noise masker. The pure tones had a duration of 400 ms and were gated with 50-ms Hanning ramps. The presentation level was 65 dB SPL. The reference stimuli were presented diotically and the target interval contained an IID in the first set of simulations and an ITD in the second set. The size of the ITD or IID was varied adaptively, similar to the procedure described in Sec. II A. For IID discrimination simulations, various frequencies between 62.5 and 4000 Hz were tested. For ITD discrimination simulations, frequencies with octave spacing were used below 500 Hz and a linear spacing of 100 Hz was used above 500 Hz. In the left panel of Fig. 1, the IID thresholds (filled symbols) of the model are presented as a function of the frequency of the tone together with experimental data (open symbols). The experimental data were adapted from literature: squares denote Grantham (1984), upward triangles Mills (1960), and downward triangles denote McFadden *et al.* (1971). The predicted IID thresholds do not depend systematically on the frequency and lie between 1 and 1.6 dB. This is well in the range of the experimental data. The remarkable bump at 1 kHz seen in one set of the experimental data is, however, lacking in the predictions.

The right panel of Fig. 1 shows ITD thresholds as a function of frequency. The open squares are data adapted from Klumpp and Eady (1956), the upward triangles from Zwislocki and Feldman (1956), and the filled symbols are model predictions. For frequencies up to 500 Hz, the ITD threshold decreases with increasing frequency. This ITD threshold curve can be characterized by a constant phase sensitivity, as shown by the dotted line. This line represents a constant phase difference of 0.05 rad. For frequencies above 1 kHz, the ITD threshold increases sharply due to the decrease of phase locking in the inner hair cell stage. Above 1.5 kHz, the model is not sensitive to static ITDs in the fine structure of the presented waveforms.

The predictions for IID thresholds and ITD thresholds below 1000 Hz only depend on the model parameters *a* and *b* which were derived from $N\rho S\pi$ and $NoS\pi$ detection experiments (see Sec. II D). In these experiments, both IIDs

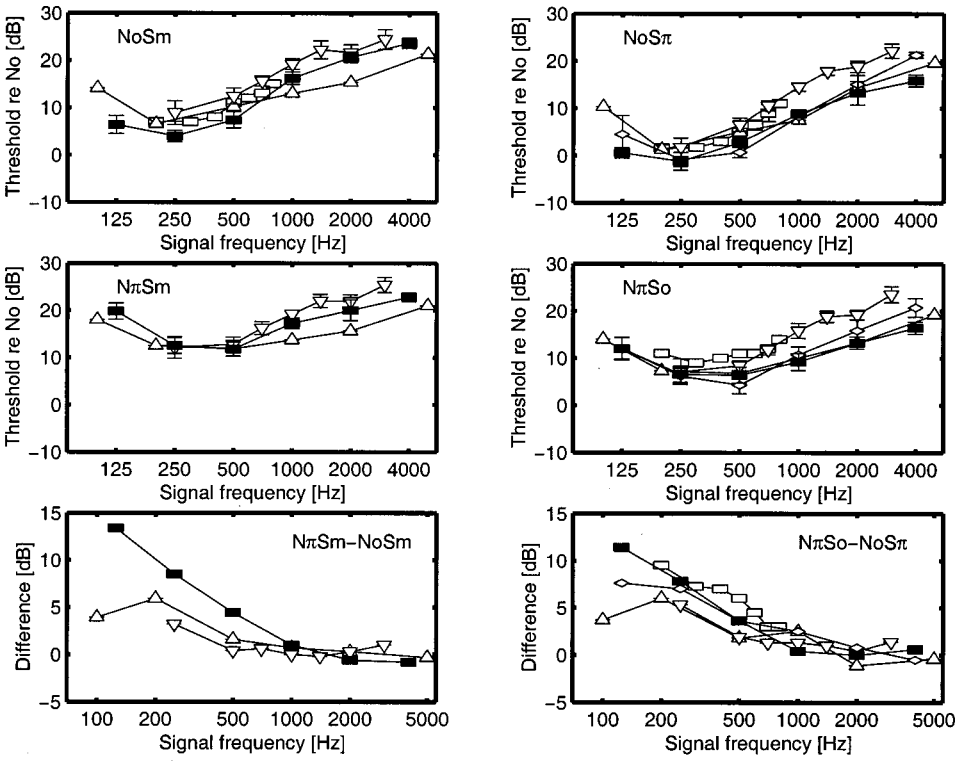

FIG. 2. Masked thresholds for wideband NoSm (upper left panel), NoSπ (upper right panel), NπSm (middle left panel), and NπSo (middle right panel) conditions as a function of the frequency of the signal. The lower left panel represents the difference in threshold between the NπSm and NoSm conditions, the lower right panel between NπSo and NoSπ. The open symbols denote experimental data adapted from literature, the filled symbols are model predictions: Squares, Kohlrausch (1988); upward triangles, Hirsh (1948); downward triangles, Hirsh and Burgeat (1958); diamonds, van de Par and Kohlrausch (1999).

and ITDs are present in the stimulus, which fluctuate as a function of time. In the simulations shown in Fig. 1, the stimuli contained only static IIDs or static ITDs. Thus, this model is able to unify IID and ITD sensitivity with binaural detection data. The use of a cancellation mechanism to achieve the correct sensitivity for both IIDs and ITDs was already suggested by Breebaart *et al.* (1999). They found that for their stimuli containing several different probability distributions of the IIDs or ITDs, a model based on subtraction may be favored over models based on the interaural cross correlation or models based on the direct evaluation of the interaural differences.

B. Dependence on frequency and interaural phase relationships in wideband detection conditions

A low-pass noise with a cutoff frequency of 8 kHz and a spectral level of 40 dB/Hz was used as masker. The following binaural conditions were tested: NoSπ, NπSo, NoSm, and NπSm. Thresholds were determined as a function of the frequency of the signal (125, 250, 500, 1000, 2000, and 4000 Hz). The upper and middle panels in Fig. 2 represent the results of the four different conditions that were tested. The open symbols are experimental data extracted from different studies (see figure caption for a description), and the filled symbols are the model predictions. The thresholds are plotted relative to the spectral level of the masker to compensate for differences in masker spectral level.

For the NoSm and the NoSπ conditions (upper panels), the thresholds decrease slightly with frequency between 125 and 500 Hz and they increase towards higher frequencies with a slope of 4 to 5 dB/oct. In the model, this slope partly results from the increased bandwidth of the auditory filters towards high frequencies because thresholds are expressed relative to the masker spectral level. This fact predicts a threshold increase by about 3 dB/oct.[2]

A second reason why thresholds increase above 1 kHz center frequency is related to the loss of phase locking in the inner hair-cell model. In the stimuli that are considered here, both interaural intensity and time differences are present (cf. Zurek, 1991). As described in Sec. II A, the model is insensitive to interaural time differences within the fine structure of the waveforms for frequencies above 1.4 kHz, because of the loss of phase locking in the inner haircell stage. Hence a part of the cues that are available at low frequencies are lost at high frequencies resulting in higher thresholds.

A third reason for a threshold increase with frequency results from peripheral compression. Above 1.4 kHz, only the envelope of the incoming waveforms is present at the output of the inner haircell stage. These envelopes are compressed by the nonlinear adaptation loops that follow the inner haircell stage. Such a compression results in a decrease of the stimulus IID (van de Par, 1998; van de Par and Kohlrausch, 1998). Furthermore, compression makes the model less sensitive to interaural time differences present in the envelopes, because the envelopes are flattened. Hence compression results in higher thresholds at frequencies above 1.4 kHz. Low-frequency detection is not affected much by compression because the model can use ITDs in the fine structure waveforms which are not affected by compression.

The major difference between the NoSπ and NoSm conditions is an overall difference of 6 dB. This difference can be understood by considering the fact that an Sπ signal results in twice as much increase in the EI-type element output compared to an Sm signal. To compensate for this difference, the Sm signal level must be raised by 6 dB.

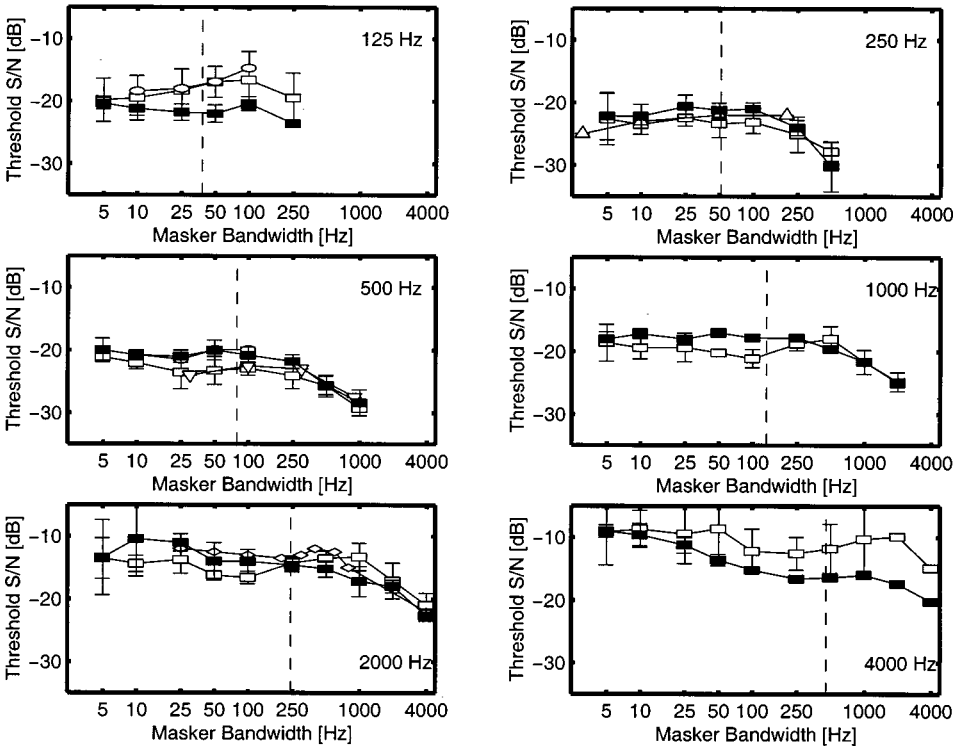

FIG. 3. NoSπ thresholds as a function of the masker bandwidth for a constant overall level of the masker. The six panels represent center frequencies of 125, 250, 500, 1000, 2000, and 4000 Hz, respectively. The dashed line indicates the ERB value at the signal frequency. The filled symbols are model predictions. The open symbols are data adapted from literature: squares, van de Par and Kohlrausch (1999); upward triangles, Wightman (1971); downward triangles, van der Heijden and Trahiotis (1998); diamonds, Sever and Small (1979); circles, Breebaart *et al.* (1998).

The NπSo and NπSm conditions show similar thresholds as the NoSπ and NoSm conditions for frequencies beyond 1 kHz, while for frequencies below 1 kHz, the interaurally out-of-phase maskers result in higher thresholds than the in-phase maskers. This difference is depicted in the lower panels of Fig. 2. The left panel shows the difference in thresholds between the NπSm and NoSm conditions, the right panel between NπSo and NoSπ. The model predictions in these two panels are very similar for the monaural and dichotic signal, having differences of 12 to 14 dB at 125 Hz center frequency which decreases to 0 dB around 1 or 2 kHz. These frequency effects are the result of two model properties which are included in most EC-like models (cf. Durlach, 1963; Rabiner *et al.*, 1966; Metz *et al.*, 1968) and in models based on coincidence detectors (Colburn, 1977; Stern and Shear, 1996). The first comprises a limited repertoire of internal delays. A lower center frequency corresponds to a larger internal delay necessary to compensate for the phase shift of the masking noise and hence less sensitivity to changes in the EI-type element output. The second is the fact that the phase shift can only be compensated by an internal delay, resulting in imperfect cancellation of the noise masker due to damping of the autocorrelation function of the noise.

C. NoSπ masker-bandwidth dependence

If an interaurally out-of-phase signal is masked by an interaurally in-phase noise of variable bandwidth, a remarkable phenomenon is observed which is usually referred to as the wider effective binaural critical bandwidth: the critical bandwidth estimate from binaural band-widening experiments is often a factor 2 to 3 higher than monaural estimates (cf. Bourbon and Jeffress, 1965; Sever and Small, 1979; Hall *et al.*, 1983; Zurek and Durlach, 1987; van de Par and Kohlrausch, 1999). In order to show that the model can account for this phenomenon, NoSπ thresholds were determined as a function of the bandwidth of the masker at center frequencies of 250, 500, 1000, 2000, and 4000 Hz. The bandwidth was varied between 5 Hz and twice the center frequency. The overall masker level was kept constant at 65 dB SPL. Both model predictions (filled symbols) and experimental data (open symbols) are shown in Fig. 3, where the 6 panels correspond to center frequencies of 125, 250, 500, 1000, 2000, and 4000 Hz, respectively. The data can be characterized as staying fairly constant up to a certain bandwidth and then declining with 3 dB/oct. The bandwidth at which this decline starts is much larger than what is expected from monaural notched-noise experiments (Glasberg and Moore, 1990), as shown by the dashed lines in Fig. 3. The estimated critical bandwidths of the model are also larger by a factor up to 2 or 3, in line with the experimental data.

At 4 kHz, the simulated thresholds decrease as a function of bandwidth for bandwidths between 10 and 250 Hz, an effect which is not observed in the experimental data. The threshold decrease with bandwidth at 4 kHz of the model can be understood by considering the properties of the adaptation loops in the peripheral processor. Due to the loss of phase locking at high frequencies, the outputs of the inner haircell model only contain IIDs and some ITD information present in the envelope of the waveforms. The IIDs are reduced in magnitude due to the compressive nature of the adaptation loops. The amount of compression depends on the bandwidth of the stimulus. If the bandwidth is small (i.e., 10 Hz), the envelope of the masker varies slowly with time. Hence the adaptation loops which adapt with certain time constants easily follow these envelope fluctuations. Consequently, the envelopes are compressed logarithmically. If the masker bandwidth is increased, the speed of fluctuation in the envelopes

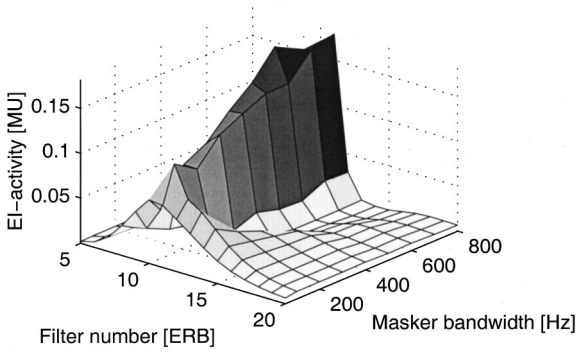

FIG. 4. EI activity without internal noise as a function of masker bandwidth and peripheral filter number for an NoSπ condition with a signal-to-masker ratio of -25 dB and a fixed masker level of 65 dB.

increases accordingly. As described in the preceding article (Breebaart *et al.*, 2001a), fast fluctuations are processed more linearly, while slow fluctuations in the envelope are processed logarithmically. Hence the magnitude of the IID after the adaptation loops depends on the bandwidth of the stimulus: a very large bandwidth results in larger IID after adaptation and hence lower NoSπ thresholds.[3]

At all center frequencies the increased effective bandwidth is captured by the model. The explanation for this result in this specific experimental paradigm relies on the across-frequency integration of information according to an optimal detector, as described by van de Par and Kohlrausch (1999). This spectral integration is an integral part of the central processor in this model (cf. Breebaart *et al.*, 2001a, Sec. VI). For a narrow-band masker (i.e., below the monaural critical bandwidth), the on-frequency filter has the largest stimulus power. For off-frequency channels, the entire stimulus resides at the skirts of the filters and is therefore reduced in its power. However, the relative amount of masker and signal energy is hardly changed. Since the signal-to-masker ratio within an auditory channel determines the detectability, information about the presence of the signal is not only available in the on-frequency channel, but also in several off-frequency channels. The only limitation for this extended availability is the absolute threshold: if the stimulus is attenuated too much it becomes undetectable in that channel. This extended availability of information is depicted in Fig. 4. In this figure, the output for a 500-Hz NoSπ stimulus of an EI-type element with $\alpha=\tau=0$ without internal noise is shown as a function of the masker bandwidth and of the auditory-filter number. The masker had a fixed level of 65 dB while the signal-to-masker ratio was -25 dB.

If a masker alone were presented, the output of these EI-type elements would be zero (neglecting the internal noise) since the masker can be canceled completely. Thus, any increase in the activity can be used as a cue for the presence of the signal. This increase by the presence of the Sπ signal is shown in Fig. 4. If the masker bandwidth is very small (10 Hz wide), a whole range of EI-type elements shows a considerable amount of activity. The fact that in this condition the cue for detection is available in several channels enables reduction of the internal error in the following way. The internal error which is added to the EI-type elements is *independent* across elements. Thus, individual noise sources add up by their intensities. On the other hand, the increase in the EI-type elements by the addition of the signal is available in several filters and is *correlated* and therefore adds up linearly. Thus, if the model uses the sum of activities across several elements instead of using the output of only one element, the internal signal-to-noise ratio is increased. This results in lower thresholds for narrow-band maskers.

For bandwidths that just exceed the critical bandwidth, the masker energy in the on-frequency channel starts to be reduced by the bandpass filter. This results in an increase in the signal-to-masker ratio in the on-frequency channel. This can be observed from Fig. 4 by the increasing EI activity with increasing bandwidth for filter 10. However, the signal-to-masker ratio in the *off-frequency* channels starts to be *reduced*. This is clearly visible for filters 13 to 20; the activity *decreases* with increasing masker bandwidth. Therefore, the ability of the model to reduce the internal error by integrating across filters is diminished. Both processes influence the internal error about equally but in opposite directions, resulting in constant thresholds for bandwidths between the critical bandwidth and two to three times that value. For even larger bandwidths, all off-frequency channels are masked. Only the on-frequency channel provides useful information and due to filtering thresholds decrease with 3 dB/oct of masker bandwidth. In summary, the wider critical bandwidth in the model is the result of an uncorrelated noise source in each auditory filter combined with an optimal detector. Other implementation issues are relatively unimportant, a notion which is supported by the results of Zerbs (2000). He developed a binaural signal detection model which is also based on an EC-like process but with a different implementation of the binaural processing stage. This model does account in a very similar way for the wider effective critical bandwidth.

Another set of data that can be explained by this across-channel integration hypothesis has been published by Hall *et al.* (1983), who also performed band-limiting NoSπ measurements. In their study, the spectral *energy* density of the masker was kept constant and they estimated the binaural critical bandwidth at three noise levels, namely, 10, 30, and 50 dB/Hz. Their critical-bandwidth estimate increased as the noise level increased. To test whether the model can account for this observation, the same experiment was simulated with masker bandwidths of 10, 50, 100, 200, 400, 600, and 800 Hz and a center frequency of 500 Hz. Both model predictions and data adapted from Hall *et al.* (1983) are shown in the left panel of Fig. 5.

The squares denote a spectral energy density of 10 dB/Hz, the upward triangles of 30 dB/Hz, and the downward triangles 50 dB/Hz. At bandwidths below the monaural critical bandwidth, the thresholds increase with increasing bandwidth. This is the result of the increasing amount of masker energy within the auditory filter. At a certain wider bandwidth the thresholds remain constant. Hall *et al.* used the bandwidth that corresponds to a threshold 3 dB below this constant threshold level as an estimate of the critical bandwidth. For the 10 dB/Hz condition, the estimate was 58 Hz, very close to the monaural estimate of 79 Hz at 500 Hz (Glasberg and Moore, 1990). At 50 dB/Hz, however, the estimate was 220 Hz, which was close to three times the mon-

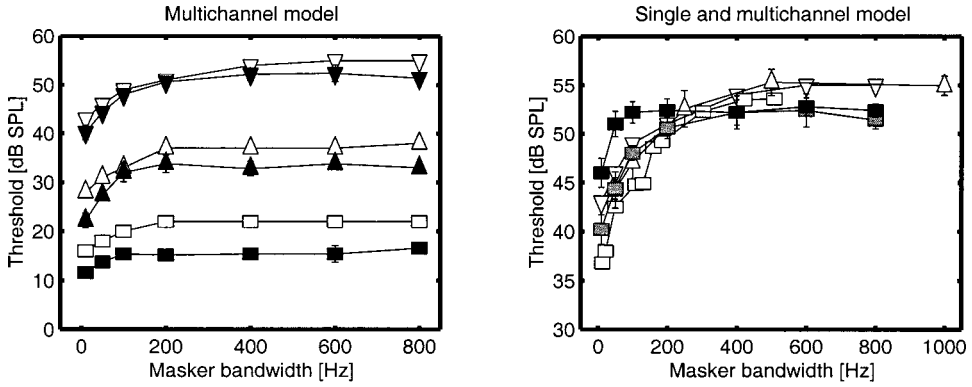

FIG. 5. NoSπ thresholds as a function of masker bandwidth. Left panel: predictions of a multichannel model. In all conditions, the spectral energy density of the masker was kept constant at 10 dB/Hz (squares), 30 dB/Hz (upward triangles), and 50 dB/Hz (downward triangles). The open symbols are data adapted from Hall *et al.* (1983), the filled symbols are model predictions. Right panel: similar to the left panel for a masker level of 50 dB/Hz. The squares denote data adapted from Bourbon (1966), the upward triangles denote Cokely and Hall (1991), and the downward triangles Hall *et al.* (1983). The gray symbols represent the multichannel model, the black symbols the single-channel model.

aural estimate. Our explanation for this level dependence of the critical band estimate also relies on across-frequency integration. Consider the experiment with a narrow-band masker with a spectral level of 10 dB/Hz. In this case, the excitation pattern across auditory channels is very narrow due to the low stimulus level. Off-frequency channels do not provide useful information since the stimulus level in these channels is below absolute threshold. Therefore, the bandwidth dependence of thresholds will depend only on processing of the on-frequency channel and consequently reflects the critical bandwidth of this on-frequency channel. For high stimulus levels (i.e., 50 dB/Hz) the same argument for the wider critical bandwidth can be given as described earlier.

The differences in predictions that are obtained between a model that uses across-frequency integration and a model with only single-channel processing are shown in the right panel of Fig. 5. Here, experimental data for a spectral level of 50 dB/Hz are shown (open symbols) combined with model simulations for a single-channel model (on-frequency channel only, filled symbols) and for the multi-channel model (gray symbols). Clearly, the bandwidth dependence of the single-channel model resembles monaural behavior instead of the wider binaural bandwidth. Furthermore, the multi-channel model has lower thresholds for bandwidths up to 400 Hz. The difference is as large as 6 dB. Thus, below a bandwidth of 400 Hz, the model can improve its detection performance by integrating information across filters. At larger bandwidths, all off-frequency channels are masked and the performance for both the single- and multi-channel models is equal. This demonstrates that in the model, the wider critical bandwidth results from across-frequency integration.

A general observation regarding the experiments from Hall *et al.* (1983) is that the model predictions are up to 5 dB lower than the experimental data. One reason for this difference may be the fact that the model used a two-down, one-up procedure to vary the signal level, while in the original experiment, a three-down, one-up procedure was used. Hence the thresholds for the experimental data are somewhat higher than for the model predictions.

In summary, critical aspects of the model necessary to explain the wider effective critical bandwidth are the uncorrelated internal noise in each auditory filter combined with an optimal integration of information across frequency.

D. NπSo masker-bandwidth dependence

In this section, interaurally out-of-phase maskers of variable bandwidth combined with a diotic signal (i.e., NπSo) are discussed. Thresholds for different center frequencies (125, 250, 500, and 1000 Hz) and bandwidths (from 5 Hz up to twice the center frequency) were simulated. The overall masker level was kept constant at 65 dB SPL. The experimental data for the four different center frequencies (adapted from van de Par and Kohlrausch, 1999) and model simulations are shown in Fig. 6.

If the NπSo thresholds are compared to the NoSπ thresholds shown in Fig. 3, one can see that at 125 and 250 Hz, the slope relating bandwidth to threshold at subcritical bandwidths is significantly different, while at higher center frequencies, no difference is observed. This observation holds for both model predictions and experimental data. In our model, the differences between the two experimental conditions are the result of the same model properties that were mentioned in Sec. III B: the fact that the interaural phase shift in the masker can only be compensated by an internal delay. Thus both a *lower* center frequency and a *wider* masker bandwidth result in more masker energy that cannot be canceled and a relative increase in the internal noise. In addition, the limited range of internal delays becomes more important for lower frequencies. This is supported by the data: the slope relating threshold to bandwidth is steeper at 125 Hz center frequency than at higher frequencies. Moreover, this slope is practically zero for the 500- and 1000-Hz conditions. At these frequencies, the effect of damping of the autocorrelation function of the noise is so small that the thresholds are not influenced by this effect. Hence the thresholds approach the NoSπ thresholds (see Fig. 3). Furthermore, overall differences in thresholds occur across center frequencies, which are most clearly visible at 125 and 250 Hz.

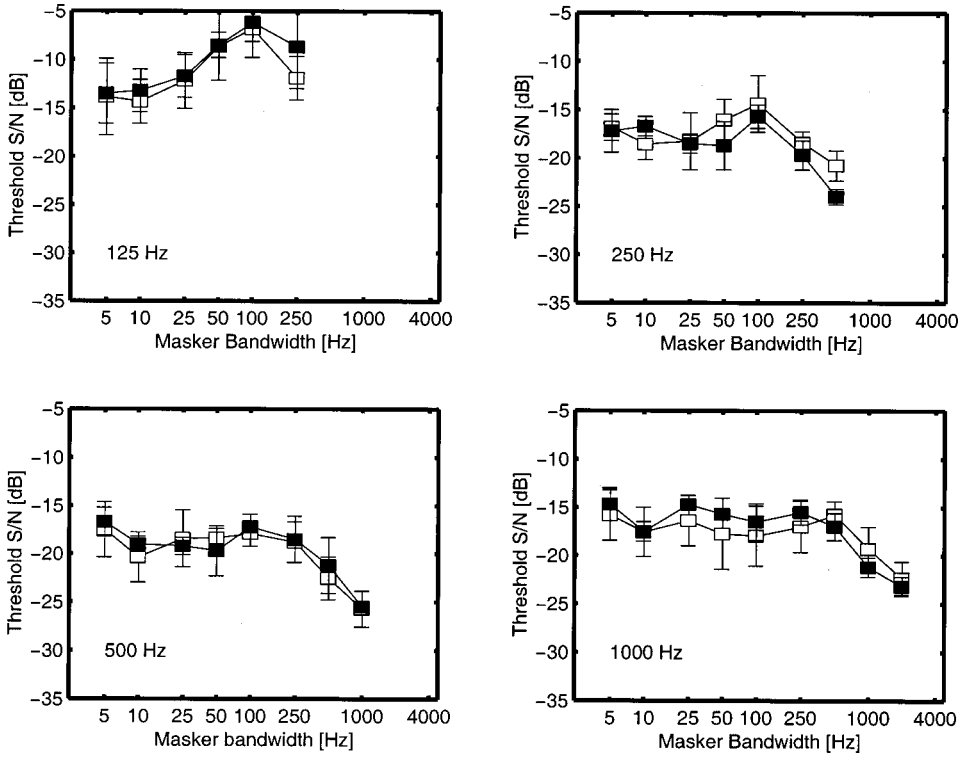

FIG. 6. NπSo thresholds as a function of masker bandwidth for 125-Hz (upper-left panel), 250-Hz (upper-right panel), 500-Hz (lower-left panel), and 1000-Hz center frequency (lower-right panel). The open symbols are data adapted from van de Par and Kohlrausch (1999), the filled symbols are model predictions. The masker had the same overall level at all bandwidths.

E. NρSπ masker-bandwidth dependence

NρSπ detection thresholds were measured as a function of the bandwidth of the masker by van der Heijden and Trahiotis (1998). The overall masker level was kept constant. They used several values of interaural correlation (ρ) ranging from -1 to $+1$. Their results show that the wider effective critical bandwidth is only observed for interaural masker correlations >0.97 and that for smaller correlations, the effective critical bandwidth is similar to the monaural estimate. Their results and the model simulations are shown in Fig. 7. The left panel shows the experimental data, the right panel shows model predictions.

The empirical curves for the largest interaural correlations (i.e., 1 and 0.997) show flat thresholds for masker bandwidths between 30 and 300 Hz, indicating a wider critical bandwidth. In these conditions, the *internal* noise limits the detection and an internal error reduction scheme is applied as described in the NoSπ band-widening condition (see Sec. III C). For an interaural masker correlation of -1, however, the thresholds are similar to the monaural thresholds since no binaural advantage is present in an NπSπ condition. These monaural thresholds show a bandwidth dependence well in line with the view that the decision variable that is used in the detection process has the same statistics as the energy at the output of an auditory filter. For bandwidths below the critical bandwidth, thresholds decrease with 1.5 dB per octave of masker bandwidth. This slope results from the sample-by-sample variability in the masker energy (Bos and de Boer, 1966). Thus, in these conditions, the *external stimulus variability* limits the detection of the tone instead of the internal noise. Since this external variability (or masker energy fluctuation) is highly correlated across auditory channels, the model *cannot reduce this variability* by combining information across frequency. Breebaart and Kohlrausch

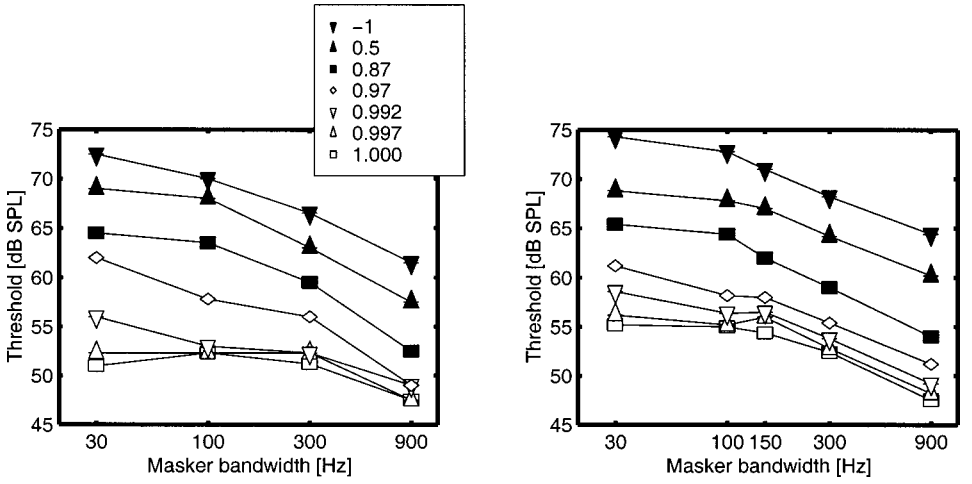

FIG. 7. NρSπ thresholds as a function of masker bandwidth for a constant overall level of the masker. The left panel shows experimental data adapted from van der Heijden and Trahiotis (1998); the right panel shows model predictions. Different curves denote different interaural masker correlations.

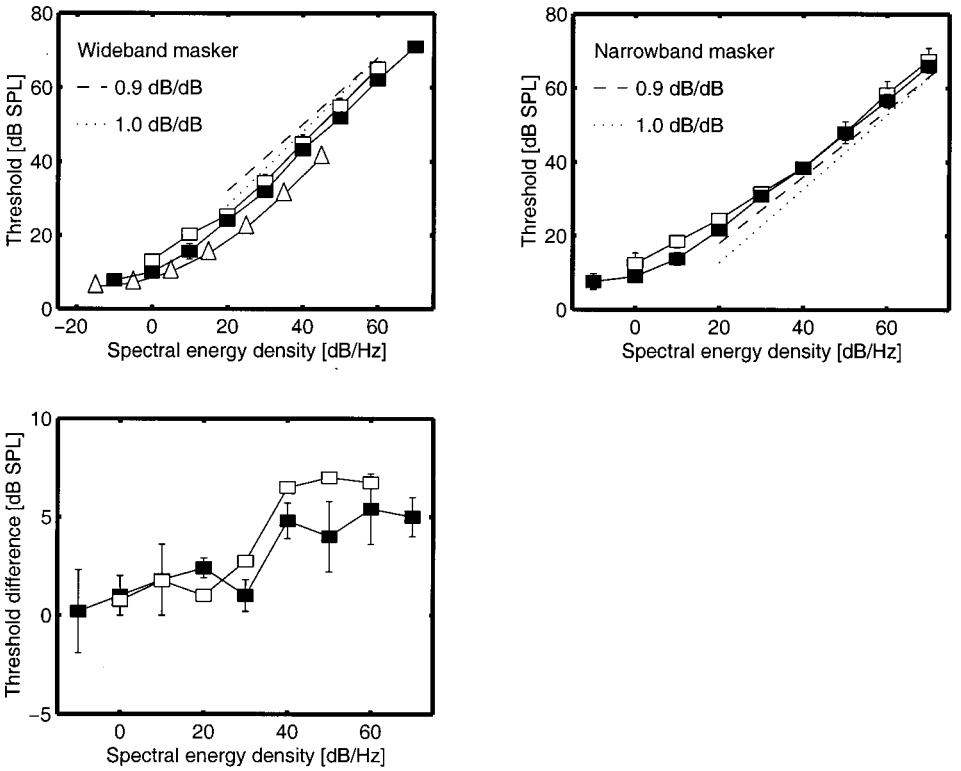

FIG. 8. NoSπ thresholds as a function of the spectral energy density of the masker for broadband noise (upper-left panel) and narrowband noise (upper-right panel). Open symbols are data adapted from literature: squares from Hall and Harvey (1984), upward triangles from McFadden (1968). The filled symbols are model predictions. The dashed lines have a slope of 0.9 dB/dB, the dotted lines have a slope of 1 dB/dB. The lower panel contains the difference in thresholds between broadband and narrow-band conditions in the same format as the upper panels.

(1999) suggested that a similar argument holds for NρSπ conditions. They measured NρSπ thresholds as a function of both the masker correlation and the masker bandwidth. They showed that variability of the interaural differences has a strong effect on the binaural performance and that reduction of this variability results in a decrease in thresholds. The current model supports this hypothesis in a qualitative way. For interaural correlations below 0.97, the fluctuations in the EI-element output are dominated by external stimulus fluctuations. The amount of fluctuation increases with masker correlation reduction or masker bandwidth reduction. This is also seen in the model predictions: the data decrease with both a bandwidth increase or a correlation increase. This experiment shows that our model can account both for external stimulus fluctuations and for internal errors as limitations for detection.

F. NoSπ masker-level dependence

If the across-frequency hypothesis as stated earlier is correct, different influences of masker level on NoSπ are expected for a narrow-band masker compared to a broadband masker. For a broadband masker, off-frequency channels cannot contribute to the detection of the signal because these channels are masked by the broadband noise. On the other hand, off-frequency channels can contribute in the case of a narrow-band masker as long as the stimulus level in these channels is above the absolute threshold. The number of off-frequency channels that can be used depends on the stimulus level: at a higher level the excitation pattern along the frequency axis is larger and hence more auditory filters can contribute to the reduction of the internal error. Thus, the increase in the NoSπ threshold with masker level should be shallower for a narrow-band masker than for a broadband masker.

For the broadband condition, a broadband (0–8000 Hz) Gaussian noise served as masker. Its spectral energy density varied between −15 and 70 dB/Hz. The signal was a 500-Hz interaurally out-of-phase tone. The upper-left panel of Fig. 8 shows the experimental data (open symbols) and the model predictions (filled symbols) as a function of the noise level.

For spectral levels below 0 dB/Hz, the thresholds are approximately constant. For these conditions, the masker energy within an auditory filter is too low to influence the detectability of the signal: the threshold is determined by the absolute hearing threshold. If the spectral level of the masker is increased, the amount of masker energy within the on-frequency auditory filter increases also, resulting in higher thresholds. The slope relating masker level and threshold equals 1 dB/dB (indicated by the dotted line) for masker spectral levels above about 20 dB/Hz.

The upper-right panel of Fig. 8 shows NoSπ thresholds for a narrow-band masker (50 Hz wide) spectrally centered around the signal. The data are very similar to the data for the wideband condition except for the fact that the slope relating signal threshold to spectral noise level is lower. This is indicated by the dashed line, which has a slope of 0.9 dB/dB. As expected, the availability of off-frequency channels in the narrow-band condition results in a shallower slope compared to the broadband condition where off-frequency channels do not provide useful information about the presence of the signal. The difference in thresholds between broadband and narrow-band conditions is depicted in the lower panel of Fig. 8, for both the experimental data (open symbols) and model predictions (filled symbols).

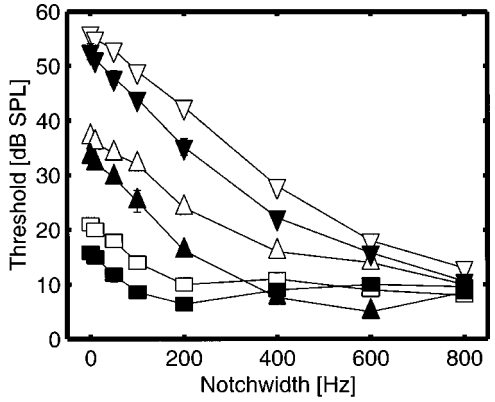

FIG. 9. NoSπ thresholds as a function of masker notchwidth. For each set of connected points, the spectral energy density of the masker was kept constant at 10 dB/Hz (squares), 30 dB/Hz (upward triangles), and 50 dB/Hz (downward triangles). The open symbols are data adapted from Hall *et al.* (1983), the filled symbols are model predictions.

G. NoSπ notchwidth dependence

In the context of across-frequency integration it is interesting to consider additional conditions where the use of off-frequency channels is disabled. Such a paradigm was presented by Hall *et al.* (1983). Instead of a band-limited masker, they used a notched noise and varied the notchwidth. The out-of-phase signal was spectrally centered in the gap. This experiment was performed at three spectral noise levels, 10, 30, and 50 dB/Hz. The data (open symbols) and the model predictions (filled symbols) are shown in Fig. 9. The data show a decrease with increasing notchwidth until the absolute threshold is reached. Hall *et al.* (1983) used the notchwidth corresponding to a 3-dB threshold improvement compared to thresholds at a notchwidth of 0 Hz as an estimate of the critical bandwidth. These estimates for the three masker levels were close to the monaural estimate and did not depend on the masker level. This finding is also supported by the model predictions. The slope relating threshold to notchwidth is very similar and hence the 3-dB estimates of the critical bandwidth are similar, too. Thus, as expected, the wider effective critical bandwidth is not observed for these stimuli. An overall difference of up to 5 dB between the model predictions and the experimental data adapted from Hall *et al.* (1983) is observed in Fig. 9. This difference was already discussed in Sec. III C, where for a different data set from the same study the same systematic difference was observed.

H. Maskers with phase transitions in the spectral domain

Another experimental paradigm to measure the spectral resolution of the binaural auditory system was used by Kohlrausch (1988). He measured the detectability of an interaurally out-of-phase signal in a masker which had a frequency-dependent phase difference: for frequencies below 500 Hz, the masker was in phase, while above 500 Hz the masker was interaurally out-of-phase. This condition is denoted NoπSπ. The spectral energy density of the masker was 43 dB/Hz. When the signal frequency was sufficiently below 500 Hz, the effective stimulus configuration was NoSπ and a large BMLD was observed. For frequencies well above 500 Hz, the stimulus corresponded to NπSπ, and no BMLD could be measured. For frequencies near 500 Hz, a gradual increase in thresholds was observed, indicating a limited spectral resolution of the auditory system. The data combined with model predictions are shown in the left panel of Fig. 10. The right panel shows thresholds for an NπoSπ condition, where the masker is interaurally out-of-phase below 500 Hz and in-phase above 500 Hz.

The gradual change in the thresholds near 500 Hz results from the limited spectral resolution of the filterbank. For example, if the signal has a frequency of 200 Hz in the NoπSπ condition, the channel tuned to 200 Hz effectively contains an NoSπ condition. The cue for detection is most salient for an EI-type element with $\alpha=\tau=0$. If the signal frequency is increased, an increasing amount of the antiphasic masker energy is present in a channel tuned to the signal frequency. This part of masker energy cannot be canceled by the EI-type element. Hence the input level of the EI-type element for a masker alone increases with increasing signal frequency. Therefore, a gradual increase of the thresholds is observed near the frequency of the masker phase transition. This gradual increase reflects the monaural critical bandwidth because spectral integration cannot occur.

A modified version of such a measurement of the spectral resolution of the auditory system uses a masker that has an inverted interaural phase relationship within a passband of the masker. Basically four conditions can be used in this way which are referred to as NoπoSπ, NπoπSπ, NoπoSo, and NπoπSo. The S denotes the interaural phase of the signal, the N denotes the frequency-dependent interaural phase relationship of the masker. Thus, an Noπo masker is interaurally in-phase except for a certain inner passband which is interaurally out-of-phase. This passband is centered around the

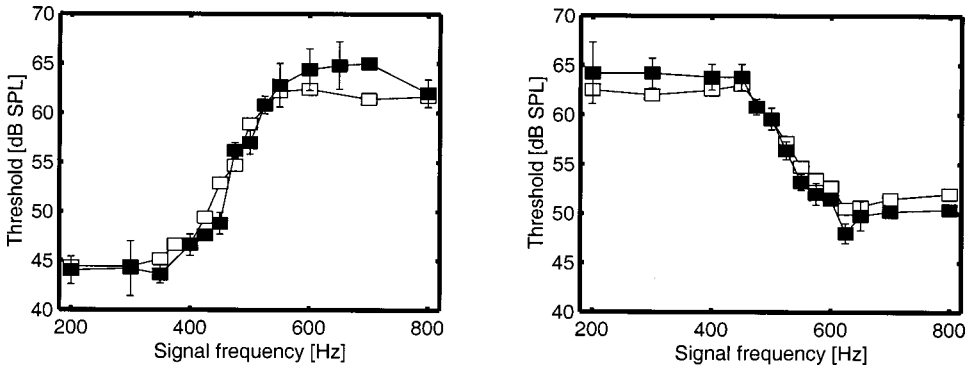

FIG. 10. Frequency dependence of Sπ thresholds for a masker with a frequency-dependent interaural phase difference. The left panel shows thresholds for an NoπSπ stimulus configuration (masker interaurally in-phase below 500 Hz and out-of-phase above 500 Hz), the right panel for NπoSπ (masker interaurally out-of-phase below 500 Hz and in-phase above 500 Hz). The open symbols are data adapted from Kohlrausch (1988), the filled symbols are model predictions.

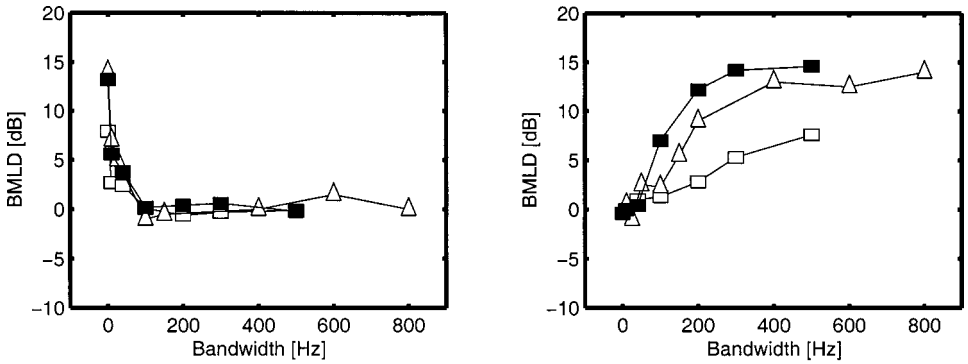

FIG. 11. NoπoSπ MLDs (left panel) and NπoπSπ MLDs (right panel) as a function of the bandwidth of the central band (see text for details). The open squares are experimental data adapted from Sondhi and Guttman (1966), the triangles are adapted from Holube *et al.* (1998). Filled symbols are model predictions.

signal. Thus, in case of NoπoSπ, the condition is effectively NπSπ if the passband is wider than the critical band, while it is NoSπ if the passband has a bandwidth of 0 Hz. By studying the bandwidth dependence of such conditions, the frequency resolution of the binaural auditory system can be estimated. Such an experiment was performed by Sondhi and Guttman (1966) and also by Holube *et al.* (1998). Their most striking result was that NoπoSπ and NπoπSπ thresholds reveal a completely different bandwidth dependence. This can be observed in Fig. 11. The left panel shows the BMLD as a function of the bandwidth of the inner band for the NoπoSπ condition, the right panel for NπoπSπ. The filled symbols are the model predictions, the open symbols are experimental data.

The NoπoSπ condition (left panel) has a BMLD which is large for a very small bandwidth but decreases quickly with bandwidth. This strong decrease in the BMLD is expected for the following reason. If the bandwidth of the out-of-phase passband is equal to half the equivalent rectangular bandwidth of the auditory filter, the amount of masker energy from the in-phase noise and the out-of-phase noise is approximately equal in the on-frequency filter.[4] Consequently, the effective interaural correlation of the masker in the on-frequency filter is about zero. For such a low correlation value, the BMLD is reduced to only 3 dB. Thus, if the bandwidth of the passband is 40 Hz, the BMLD should be significantly reduced. This is supported by the data in Fig. 11: for this bandwidth the BMLD is only a few dB.

In the NπoπSπ condition (right panel of Fig. 11), the bandwidth dependence of the thresholds is completely different. If the bandwidth of the passband is very large (i.e., 500 Hz), the condition is effectively NoSπ and a large BMLD is observed. If the bandwidth is decreased, the amount of masker energy in the on-frequency filter that is interaurally out-of-phase increases. Since these parts of the masker reside at the skirt of the filter, this masker energy is strongly attenuated. Consequently, the interaural masker correlation in the on-frequency channel decreases, but not very much. Only if the bandwidth is equal to about half the equivalent rectangular bandwidth,[4] the BMLD is reduced to about 3 dB for the same reason as in the NoπoSπ condition. Therefore, a much more gradual decrease in the BMLD is observed if the bandwidth of the passband is decreased. This is supported by both model predictions and experimental data. This interpretation is also supported by Fig. 12, which shows the BMLDs of the model as a function of the computed interaural cross correlation of the masker after peripheral filtering. The squares denote the NoπoSπ condition, the triangles the NπoπSπ condition. For both conditions, the BMLD for an interaural correlation of zero is very close to 3 dB. Furthermore, the BMLD as a function of the correlation is very similar for both conditions.

A substantial difference between the two data sets is observed in the maximum BMLD: the data of Sondhi and Guttman (1966) have a maximum BMLD of about 7 dB, while the data of Holube *et al.* (1998) show BMLDs of up to 14 dB. The reason for these differences is unclear, but the model could accommodate these differences by changing the parameters *a* and *b*.

I. NoSπ signal-bandwidth dependence

Langhans and Kohlrausch (1992) measured NoSπ thresholds for target signals of variable bandwidth. In this experiment, the masker consisted of a band-limited diotic noise (0–2 kHz, No=47 dB/Hz), while the signal consisted of harmonic complexes with a flat amplitude spectrum, a spectral spacing between the components of 10 Hz, and a center frequency of 400 Hz. The upper and lower frequency boundaries of the harmonics were varied in order to generate signals of different bandwidths. The total number of components in the complex was 1, 3, 5, 7, 9, 11, 15, 17, 19, or 41. The masked thresholds of the harmonic complex tones as a function of the number of components is shown in Fig. 13. The thresholds are expressed as level per component.

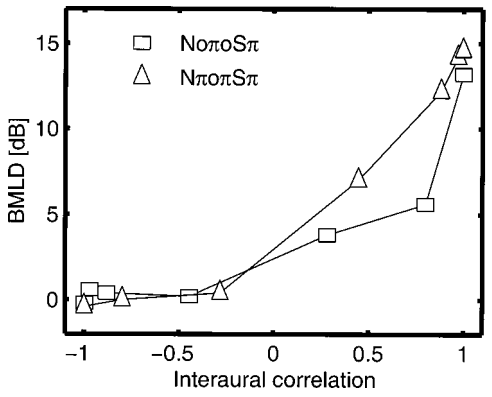

FIG. 12. BMLDs of the model as a function of the (computed) interaural correlation after peripheral filtering. The squares correspond to the NoπoSπ condition, the triangles to the NπoπSπ condition.

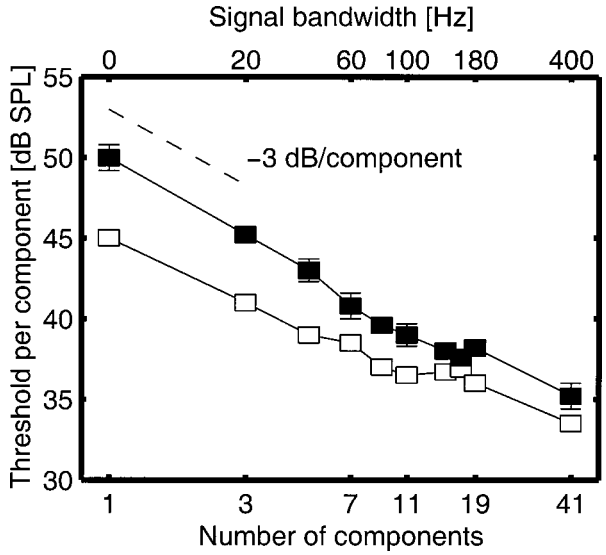

FIG. 13. Threshold level per component for an out-of-phase harmonic complex in an in-phase noise masker as a function of the number of signal components. The signal components had a spectral spacing of 10 Hz and were centered around 400 Hz. The open symbols are data adapted from Langhans and Kohlrausch (1992), the filled symbols are model predictions.

Figure 13 shows a decrease of the masked threshold with increasing number of components. This can be understood as follows. If the number of components is increased from one to three, the total signal level is 4.7 dB higher than the level of the individual components. The bandwidth of a signal which consists of three components equals 20 Hz, hence the signal has a smaller bandwidth than the auditory filter. Therefore, a threshold decrease of 4.7 dB per component is expected between one and three components in order to keep the signal power in the auditory filter constant. This is supported by the data and the model predictions. As long as the signal bandwidth is below the critical bandwidth, it is expected that an increase in the number of harmonics results in a decrease in the masked threshold level per component due to the increase in the total signal level. If the auditory filters had a rectangular shape (ideal bandpass filter), a doubling of the number of harmonics would result in a decrease of 3 dB in the level per component as long as the signal bandwidth is below the auditory filter bandwidth (nine harmonics). This is indicated by the dashed line. Of course, a rectangular filter is not a valid description of the auditory filters. Therefore, the decrease in threshold is a little bit less than 3 dB [see Langhans and Kohlrausch (1992) for a detailed analysis of the slope in their data]. A striking result is, however, that the thresholds still decrease for more than ten harmonics. In this case, the bandwidth of the signal exceeds the auditory filter bandwidth. To account for these results, it is necessary to include several filters in the detection process rather than only the center channel since the cue for detection is available in several filters. As described in Sec. III C, the availability of the cue for detection in several filters enables the improvement of the internal signal-to-noise ratio which results in lower signal thresholds for broadband signals. As can be observed from Fig. 13, the model accounts for this across-channel processing of binaural cues. However, the efficiency of this process in the model seems to be a little bit too high because the model predictions decrease stronger with increases in signal bandwidth than the experimental data.

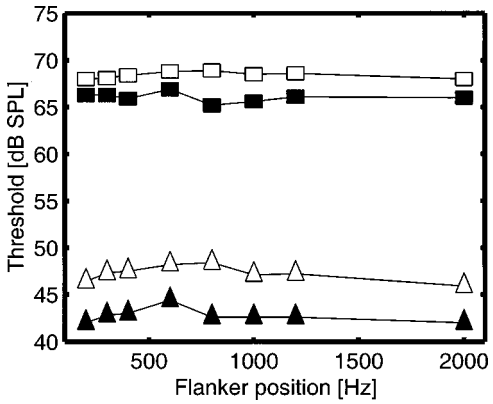

FIG. 14. Detection thresholds for a 500-Hz signal added to a 50-Hz-wide noise masker with a center frequency of 500 Hz as a function of the center frequency of a 30-Hz-wide flanking band. Squares correspond to thresholds for an interaurally in-phase signal, triangles to an out-of-phase signal. Open symbols are experimental data adapted from Cokely and Hall (1991), filled symbols are model predictions.

J. NoSπ including spectral flanking bands

Cokely and Hall (1991) measured narrow-band NoSo and NoSπ thresholds with a fixed-frequency masker (50 Hz wide centered around 500 Hz, No=50 dB/Hz) combined with an interaurally in-phase flanking noise band (30 Hz wide, No also 50 dB/Hz) of variable frequency. They found that for monaural detection (i.e., masker and signal both interaurally in phase), the flanking band had only a small effect on the masked thresholds if presented spectrally close to the signal (thresholds increased by less than 1 dB, which is expected on the basis of the increase in the masker energy in the on-frequency channel). For the NoSπ condition, however, a larger effect was observed (up to 2.5 dB), which is difficult to understand in terms of stimulus properties within the on-frequency channel. The experimental data combined with model predictions are given in Fig. 14, where the thresholds are shown as a function of the center frequency of the flanking band. The squares denote the monaural (NoSo) condition, the triangles refer to the binaural (NoSπ) condition. The open symbols are experimental data, the filled symbols are model predictions.

Although there is an overall difference of about 5 dB between experimental data and model predictions for the NoSπ condition, the effect of the flanking band is very similar. If the flanker has a center frequency that is close to the fixed-frequency masker, the thresholds of the model increase up to 2.4 dB. As described in Sec. III C, a narrow-band NoSπ condition allows the reduction of the internal error in the model. The addition of an additive noise band at a higher or lower frequency results in (partial) masking of the off-frequency channels. Therefore, the efficiency of internal error reduction is decreased and an increase in thresholds is observed. In the NoSo condition, this effect is not present, because in this condition, the sample-by-sample variability of noise energy limits the detection. As described in Sec.

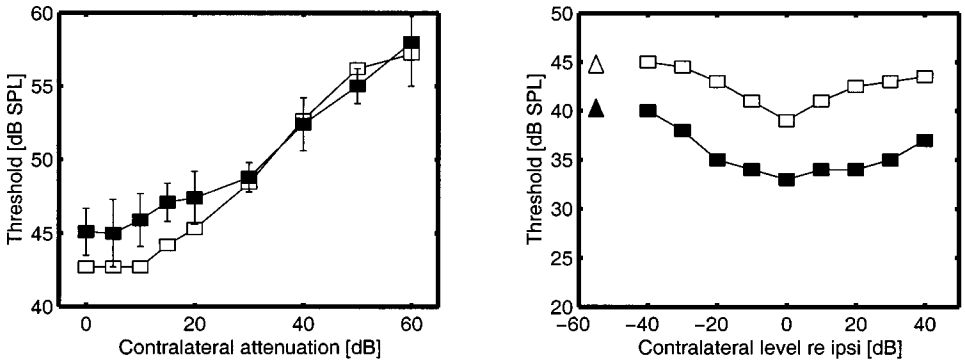

FIG. 15. Left panel: NoSπ thresholds as a function of the attenuation of the stimuli at one ear. The thresholds are expressed in terms of the level at the nonattenuated ear. The open symbols are data adapted from McFadden (1968), the filled symbols are model predictions. Right panel: NoSm thresholds as a function of the noise level in the nonsignal ear relative to the signal ear. The open symbols are adapted from Weston and Miller (1965), the filled symbols are model predictions. The squares denote the NoSm conditions, the triangles are the monaural NmSm reference conditions.

III E, this external variability is correlated across auditory channels and cannot be reduced by the model.

K. NoSπ with interaural disparities in stimulus intensity

In this experiment, performed by McFadden (1968), the masker consisted of an interaurally in-phase wideband noise with a spectral density of 45 dB/Hz; the signal was a 400-Hz interaurally out-of-phase tone. The total stimulus at one ear was attenuated by a variable amount (i.e., both masker and signal had an equal contralateral attenuation, hence the signal-to-masker ratio was the same in both ears). The results are shown in the left panel of Fig. 15. The abscissa shows the disparity in interaural stimulus intensity, the ordinate shows the signal threshold in terms of the level at the ear without attenuation.

Clearly, for a contralateral attenuation between 0 and 10 dB, the thresholds remain constant. In this region, the model can fully compensate for the externally presented IID. If the external IID is increased, however, the thresholds increase. This is the result of the nonlinear preprocessing stage. As described in the accompanying model paper, the adaptation loops which are present in the peripheral processor are highly nonlinear and show a compressive behavior. Therefore, the externally presented IID is reduced and the EI-type element that optimally compensates for the external IID has a characteristic IID that is much smaller than the external IID. Despite the availability of EI-type elements that can compensate for the *mean* level difference at the output of the adaptation loops, these cells cannot cancel the masker noise completely due to the nonlinear processing which results in different waveforms at the output of the adaptation loops from the left and right sides. Hence parts of the noise masker are present in the output of the EI-type element, resulting in increasing thresholds. Moreover, for an IID of 60 dB, the attenuated signal lies below the absolute threshold; the model cannot cancel any part of the masking noise. Hence the thresholds are determined by the monaural masker level in the nonattenuated ear.

A similar experiment was performed by Weston and Miller (1965). They measured NoSm detection thresholds at 500 Hz as a function of the noise level in the nonsignal ear. The noise level in the signal ear was 26 dB/Hz. Besides attenuating, Weston and Miller (1965) also increased the noise level in the nonsignal ear. Their results are shown in the right panel of Fig. 15 as a function of the relative noise level in the nonsignal ear compared to the signal ear. The open symbols denote their experimental data, the filled symbols are model predictions. The triangles refer to the monaural reference conditions. Interestingly, both for a decrease and an *increase* in the contralateral noise level, thresholds increase. This effect is also captured by the model. Both curves show an increase of 3 to 4 dB if the contralateral level is increased by 40 dB. In the model, this increase is caused by the nonlinear processing of the peripheral adaptation loops as described earlier.

The predictions and experimental data for NoSm differ by about 5 to 6 dB, the latter being higher. The maximum BMLD found by Weston and Miller (1965) is about 5.5 dB, while the model predicts a maximum BMLD of about 7 dB. These values are in line with other experimental data, showing BMLDs between 5 and 10 dB for NoSm (Hirsh, 1948; Hirsh and Burgeat, 1958; Kohlrausch, 1988).

L. NoSm as a function of the notchwidth and bandwidth in the nonsignal ear

Hall and Fernandes (1984) measured NoSm detection thresholds for stimuli with a variable masker bandwidth or notchwidth in the nonsignal ear. A 500-Hz pure-tone signal was presented with a 600-Hz-wide band of noise to the signal ear. Bands of noise ranging in width from 25 to 600 Hz, or notched noises (bandwidth also 600 Hz) ranging in notchwidth from 0 to 600 Hz, were presented to the nonsignal ear. The effects of varying the bandwidth were different from those of varying the notchwidth. If the bandwidth was varied, the thresholds decreased over a range of 400 Hz, while for the notched experiment, significant threshold changes only occurred for notchwidths between 0 and 50 Hz. These results are shown in Fig. 16. The left panel corresponds to thresholds as a function of the bandwidth of the masker in the nonsignal ear, the right panel to the notchwidth.

Both model and experimental data show a different behavior as a function of bandwidth for a notched or bandlimited masker. This can be understood as follows. If a

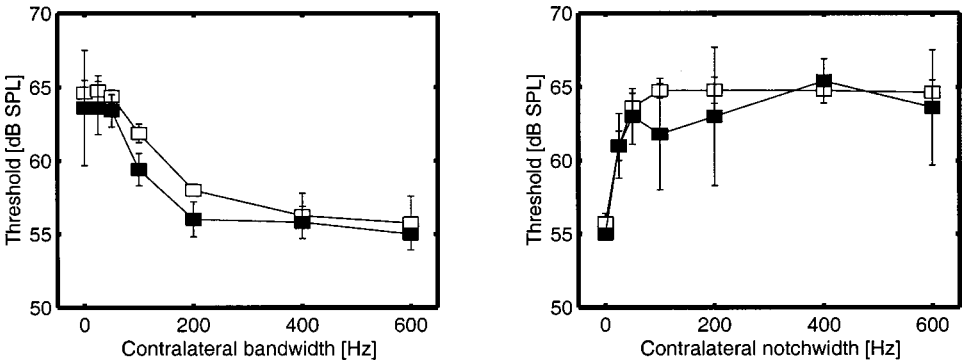

FIG. 16. NoSm thresholds as a function of the bandwidth in the nonsignal ear (left panel) and as a function of the notchwidth in the nonsignal ear (right panel). The open symbols are data adapted from Hall and Fernandes (1984), the filled symbols are model predictions.

narrow-band masker is presented in the nonsignal ear, the masker cannot be canceled by a simple subtraction, since the masker waveforms in both ears are completely different. In fact, for a bandwidth of 0 Hz, the stimulus corresponds to NmSm (i.e., masker and signal are presented to one ear only), and no binaural advantage can be achieved. If the bandwidth in the nonsignal ear is increased, the similarity (or cross correlation) between the maskers at both ears increases which enables the model to cancel the masker more efficiently. This efficiency increases even beyond the critical bandwidth. As a result of this, the signal thresholds decrease with increasing bandwidth, as observed in the data. For the notched noise, a similar process occurs. In the absence of a notch (i.e., a notchwidth of 0 Hz), the masker can be canceled completely and a large binaural advantage is observed. With increasing notchwidth, the cancellation of the masker is less successful and thresholds increase. The essential reason for the different slopes relating threshold to bandwidth or notchwidth lies in the fact that the masker cancellation is performed after peripheral filtering.

As described earlier, the nonsignal ear contains only *part* of the masker of the signal ear; some spectral components are removed. If more spectral components are removed, the amount of masker energy that remains after cancellation increases and hence the signal thresholds increase. Thus, the amount of masker energy *after peripheral filtering* that is present in the signal ear but *not* in the nonsignal ear determines the detection threshold. If the notchwidth is increased from 0 to 25 Hz, there exists a large difference between the maskers at both ears since this part of the masker is in the center of the auditory filter. Therefore, an increase in the notchwidth has a strong effect on the thresholds. Moreover, for notchwidths beyond 50 Hz, the thresholds are equal to the monaural thresholds, indicating that the binaural system cannot increase the detection performance.

In the band-limited case, however, this process is reversed. For a bandwidth of 600 Hz, the maskers in both ears are equal and a large binaural advantage is observed. If the bandwidth is decreased to 400 Hz, the thresholds do not increase since the parts of the masker that are removed in the nonsignal ear are filtered out by the bandpass filter of the inner ear. Only at a bandwidth of 300 Hz do the maskers at both ears become somewhat decorrelated after peripheral filtering and the thresholds show a slight increase. For smaller bandwidths, the correlation between the maskers after filtering decreases and thresholds show a gradual increase. Since the part of the masker that is removed in the nonsignal ear resides in the filter skirt, a reduction in the bandwidth has less effect than an increase in the notchwidth at the center of the filter.

IV. CONCLUSIONS

Predictions for binaural detection performance were shown as a function of the spectral parameters and interaural phase relationships of both maskers and signals. Although some overall differences exist between the model predictions and the experimental data, most of the experimental results can be accounted for with the present model. All stages that are included in the model contribute in some way to the exactness of the predictions. For example, the loss of phase locking in the inner haircells at frequencies above 770 Hz is necessary to account for the ITD thresholds shown in Fig. 1 and the increase of binaural thresholds above 1 kHz (see Fig. 2). For some simulations, almost all stages have to be taken into account to obtain a good fit. Examples are the experiments discussed in Sec. III E (i.e., NπSo as a function of the bandwidth and center frequency). The combined effect of peripheral filtering, compressive behavior of the EI-type elements, the distribution of internal delays, and the chain of adaptation loops in the peripheral preprocessing stage results in good predictions, which cannot be achieved if any of these elements is removed. The price one has to pay is a more complex model than those used and described so far.

In summary, the current model accounts for many binaural detection phenomena in a quantitative way. These include

(i) the wider effective critical bandwidth in bandwidening NoSπ conditions,
(ii) the unification of IID and ITD sensitivity with binaural detection data,
(iii) the level dependence of binaural thresholds,
(iv) the frequency dependence of binaural detection thresholds,
(v) the effect of frequency and bandwidth on the difference between NoSπ and NπSo thresholds,
(vi) the combination of both external stimulus fluctuations and internal errors into one decision variable, and
(vii) the influence of interaural level differences on binaural thresholds.

ACKNOWLEDGMENTS

The investigations were supported by the Research Council for Earth and Life-sciences (ALW) with financial aid from the Netherlands Organization for Scientific Research (NWO). We would like to thank the Associate Editor Wesley Grantham, Steve Colburn, and an anonymous reviewer for their very valuable contributions for improving the contents of the original manuscript.

[1]The value of 0.64 for the interaural correlation was chosen because this was the lowest correlation that was used in a recent study measuring NρSπ thresholds (Breebaart and Kohlrausch, 2001). Data from this study were used because these thresholds were obtained with *frozen* noise. The advantage of using frozen noise is that these thresholds are not influenced by stimulus uncertainty, but are only determined by internal noise.

[2]Note that in the peripheral preprocessing stage of the model, a chain of adaptation loops is included. For an input signal with a constant envelope, the input–output characteristic of the chain of adaptation loops is almost logarithmic. Due to this compression, the signal level must be a certain *fraction* of the masker level to produce a fixed change in an EI-type-element output which is necessary to exceed the internal noise level. Thus, if the masker energy within one auditory channel increases (which is the case towards higher frequencies), the thresholds increase by the same amount.

[3]This mismatch is another example of the same disadvantage caused by the strong overshoot of the adaptation loops [see Dau *et al.* (1996b) for a discussion]. Despite several years of simulations, neither we nor our colleagues in Oldenburg have so far found a satisfying solution for this problem which would reduce the overshoot and preserve the major advantage of this stage: its ability to predict nonsimultaneous masking.

[4]For the filter at 500 Hz in the model, a bandwidth of 42 Hz (i.e., 0.53 times the ERB) resulted in a correlation of zero.

Bos, C. E., and de Boer, E. (**1966**). ''Masking and discrimination,'' J. Acoust. Soc. Am. **39**, 708–715.

Bourbon, W. T. (**1966**). ''Effects of bandwidth and level of masking noise on detection of homophasic and antiphasic tonal signals,'' Ph.D. thesis, University of Texas, Austin, Texas.

Bourbon, W. T., and Jeffress, L. A. (**1965**). ''Effect of bandwidth of masking noise on detection of homophasic and antiphasic tonal signals,'' J. Acoust. Soc. Am. **37**, 1180–1181.

Breebaart, J., and Kohlrausch, A. (**1999**). ''Modeling the role of masker-correlation uncertainty in binaural masking experiments,'' J. Acoust. Soc. Am. **105**, 1391.

Breebaart, J., and Kohlrausch, A. (**2001**). ''The influence of interaural stimulus uncertainty on binaural signal detection,'' J. Acoust. Soc. Am. **109**, 331–345.

Breebaart, J., van de Par, S., and Kohlrausch, A. (**1998**). ''Binaural signal detection with phase-shifted and time-delayed noise maskers,'' J. Acoust. Soc. Am. **103**, 2079–2083.

Breebaart, J., van de Par, S., and Kohlrausch, A. (**1999**). ''The contribution of static and dynamically varying ITDs and IIDs to binaural detection,'' J. Acoust. Soc. Am. **106**, 979–992.

Breebaart, J., van de Par, S., and Kohlrausch, A. (**2001a**). ''Binaural processing model based on contralateral inhibition. I. Model setup,'' J. Acoust. Soc. Am. **110**, 1074–1088.

Breebaart, J., van de Par, S., and Kohlrausch, A. (**2001b**). ''Binaural processing model based on contralateral inhibition. III. Dependence on temporal parameters,'' J. Acoust. Soc. Am. **110**, 1105–1117.

Cokely, J. A., and Hall, J. W. (**1991**). ''Frequency resolution for diotic and dichotic listening conditions compared using the bandlimiting measure and a modified bandlimiting measure,'' J. Acoust. Soc. Am. **89**, 1331–1339.

Colburn, H. S. (**1977**). ''Theory of binaural interaction based on auditory-nerve data. II. Detection of tones in noise,'' J. Acoust. Soc. Am. **61**, 525–533.

Dau, T., Püschel, D., and Kohlrausch, A. (**1996a**). ''A quantitative model of the 'effective' signal processing in the auditory system: I. Model structure,'' J. Acoust. Soc. Am. **99**, 3615–3622.

Dau, T., Püschel, D., and Kohlrausch, A. (**1996b**). ''A quantitative model of the 'effective' signal processing in the auditory system: II. Simulations and measurements,'' J. Acoust. Soc. Am. **99**, 3623–3631.

Durlach, N. I. (**1963**). ''Equalization and cancellation theory of binaural masking-level differences,'' J. Acoust. Soc. Am. **35**, 1206–1218.

Glasberg, B. R., and Moore, B. C. J. (**1990**). ''Derivation of auditory filter shapes from notched-noise data,'' Hear. Res. **47**, 103–138.

Grantham, D. W. (**1984**). ''Interaural intensity discrimination: insensitivity at 1000 Hz,'' J. Acoust. Soc. Am. **75**, 1191–1194.

Hall, J. W., and Fernandes, M. A. (**1984**). ''The role of monaural frequency selectivity in binaural analysis,'' J. Acoust. Soc. Am. **76**, 435–439.

Hall, J. W., and Harvey, A. D. G. (**1984**). ''NoSo and NoSπ thresholds as a function of masker level for narrow-band and wideband masking noise,'' J. Acoust. Soc. Am. **76**, 1699–1703.

Hall, J. W., Tyler, R. S., and Fernandes, M. A. (**1983**). ''Monaural and binaural auditory frequency resolution measured using bandlimited noise and notched-noise masking,'' J. Acoust. Soc. Am. **73**, 894–898.

Hirsh, I. (**1948**). ''The influence of interaural phase on interaural summation and inhibition,'' J. Acoust. Soc. Am. **20**, 536–544.

Hirsh, I., and Burgeat, M. (**1958**). ''Binaural effects in remote masking,'' J. Acoust. Soc. Am. **30**, 827–832.

Holube, I., Kinkel, M., and Kollmeier, B. (**1998**). ''Binaural and monaural auditory filter bandwidths and time constants in probe tone detection experiments,'' J. Acoust. Soc. Am. **104**, 2412–2425.

Klumpp, R. G., and Eady, H. R. (**1956**). ''Some measurements of interaural time difference thresholds,'' J. Acoust. Soc. Am. **28**, 859–860.

Kohlrausch, A. (**1988**). ''Auditory filter shape derived from binaural masking experiments,'' J. Acoust. Soc. Am. **84**, 573–583.

Kollmeier, B., and Holube, I. (**1992**). ''Auditory filter bandwidths in binaural and monaural listening conditions,'' J. Acoust. Soc. Am. **92**, 1889–1901.

Langhans, A., and Kohlrausch, A. (**1992**). ''Spectral integration of broadband signals in diotic and dichotic masking experiments,'' J. Acoust. Soc. Am. **91**, 317–326.

Levitt, H. (**1971**). ''Transformed up–down methods in psychoacoustics,'' J. Acoust. Soc. Am. **49**, 467–477.

McFadden, D. (**1968**). ''Masking-level differences determined with and without interaural disparities in masker intensity,'' J. Acoust. Soc. Am. **44**, 212–223.

McFadden, D., Jeffress, L. A., and Ermey, H. L. (**1971**). ''Difference in interaural phase and level in detection and lateralization: 250 Hz,'' J. Acoust. Soc. Am. **50**, 1484–1493.

Metz, P., Bismarck, G., and Durlach, N. (**1968**). ''Further results on binaural unmasking and the EC model. II. Noise bandwidth and interaural phase,'' J. Acoust. Soc. Am. **43**, 1085–1091.

Mills, A. (**1960**). ''Lateralization of high-frequency tones,'' J. Acoust. Soc. Am. **32**, 132–134.

Rabiner, L., Laurence, C., and Durlach, N. (**1966**). ''Further results on binaural unmasking and the EC model,'' J. Acoust. Soc. Am. **40**, 62–70.

Sever, J., and Small, A. (**1979**). ''Binaural critical masking bands,'' J. Acoust. Soc. Am. **66**, 1343–1350.

Sondhi, M. M., and Guttman, N. (**1966**). ''Width of the spectrum effective in the binaural release of masking,'' J. Acoust. Soc. Am. **40**, 600–606.

Stern, R. M., and Shear, G. D. (**1996**). ''Lateralization and detection of low-frequency binaural stimuli: Effects of distribution of internal delay,'' J. Acoust. Soc. Am. **100**, 2278–2288.

van de Par, S. (**1998**). ''A comparison of binaural detection at low and high frequencies,'' Ph.D. thesis, Eindhoven University of Technology, Eindhoven.

van de Par, S., and Kohlrausch, A. (**1998**). ''Diotic and dichotic detection using multiplied-noise maskers,'' J. Acoust. Soc. Am. **103**, 2100–2110.

van de Par, S., and Kohlrausch, A. (**1999**). ''Dependence of binaural masking level differences on center frequency, masker bandwidth and interaural parameters,'' J. Acoust. Soc. Am. **106**, 1940–1947.

van der Heijden, M., and Trahiotis, C. (**1998**). ''Binaural detection as a function of interaural correlation and bandwidth of masking noise: Implications for estimates of spectral resolution,'' J. Acoust. Soc. Am. **103**, 1609–1614.

Weston, P., and Miller, J. (**1965**). ''Use of noise to eliminate one ear from masking experiments,'' J. Acoust. Soc. Am. **37**, 638–646.

Wightman, F. (**1971**). ''Detection of binaural tones as a function of masker bandwidth,'' J. Acoust. Soc. Am. **50**, 623–636.

Zerbs, C. (**2000**). ''Modeling the effective binaural signal processing in the auditory system,'' Ph.D. thesis, Oldenburg University, Germany.

Zurek, P. M. (**1991**). ''Probability distributions of interaural phase and level differences in binaural detection stimuli,'' J. Acoust. Soc. Am. **90**, 1927–1932.
Zurek, P. M., and Durlach, N. I. (**1987**). ''Masker-bandwidth dependence in homophasic and antiphasic tone detection,'' J. Acoust. Soc. Am. **81**, 459–464.
Zwislocki, J., and Feldman, R. S. (**1956**). ''Just noticeable differences in dichotic phase,'' J. Acoust. Soc. Am. **28**, 860–864.

Binaural processing model based on contralateral inhibition. III. Dependence on temporal parameters

Jeroen Breebaart[a)]
IPO, Center for User–System Interaction, P.O. Box 513, NL-5600 MB Eindhoven, The Netherlands

Steven van de Par and Armin Kohlrausch
IPO, Center for User–System Interaction, P.O. Box 513, NL-5600 MB Eindhoven, The Netherlands and Philips Research Laboratories Eindhoven, Prof. Holstlaan 4, NL-5656 AA Eindhoven, The Netherlands

(Received 23 May 2000; revised 18 December 2000; accepted 3 May 2001)

This paper and two accompanying papers [Breebaart *et al.*, J. Acoust. Soc. Am. **110**, 1074–1088 (2001); **110**, 1089–1104 (2001)] describe a computational model for the signal processing of the binaural auditory system. The model consists of several stages of monaural and binaural preprocessing combined with an optimal detector. Simulations of binaural masking experiments were performed as a function of temporal stimulus parameters and compared to psychophysical data adapted from literature. For this purpose, the model was used as an artificial observer in a three-interval, forced-choice procedure. All model parameters were kept constant for all simulations. Model predictions were obtained as a function of the interaural correlation of a masking noise and as a function of both masker and signal duration. Furthermore, maskers with a time-varying interaural correlation were used. Predictions were also obtained for stimuli with time-varying interaural time or intensity differences. Finally, binaural forward-masking conditions were simulated. The results show that the combination of a temporal integrator followed by an optimal detector in the time domain can account for all conditions that were tested, except for those using periodically varying interaural time differences (ITDs) and those measuring interaural correlation just-noticeable differences (jnd's) as a function of bandwidth. © *2001 Acoustical Society of America.* [DOI: 10.1121/1.1383299]

PACS numbers: 43.66.Pn, 43.66.Ba, 43.66.Dc [DWG]

I. INTRODUCTION

This is the third paper describing our binaural signal detection model and its ability to predict binaural detection thresholds in a great variety of experimental conditions. This model basically consists of three stages (Breebaart *et al.*, 2001a). The first stage simulates the effective signal processing of the basilar membrane and the inner hair cells and includes adaptation by means of adaptation loops (Dau *et al.*, 1996a). Binaural interaction is modeled in the second stage by means of a contralateral inhibition mechanism: the model computes the squared difference signal between the left and right ears as a function of time, frequency channel, internal interaural delay (τ in seconds), and internal interaural level adjustment (α in dB). These binaural signals are corrupted by internal noise and subsequently analyzed by the third stage in the model, the central processor. The model is used as an artificial observer in a three-interval, forced-choice procedure, and the central processor matches the representations of the presented stimuli to templates (derived during previous presentations); on this basis the model indicates which interval contains the signal.

In the second paper of this series (Breebaart *et al.*, 2001b), model predictions for binaural detection were discussed as a function of the spectral parameters of the stimuli, keeping the temporal parameters constant. All stimuli had a duration which was long compared to the temporal resolution of both the monaural and binaural stages of the model (i.e., 200 ms or longer). We demonstrated that the model is very successful in describing the threshold dependence on spectral stimulus parameters and that this success can, to a large extent, be attributed to an optimal combination of information across auditory channels.

In the current paper, we focus on the temporal properties of the stimuli, keeping the spectral parameters constant. Two important temporal properties are studied intensively. The first concerns temporal *integration*. It has been shown that the binaural system is able to integrate binaural cues temporally if such a process enhances a detection task. For example, an increase of the signal duration in an NoSπ condition results in a decrease of the signal threshold for signal durations up to 300 ms (Zwicker and Zwicker, 1984; Wilson and Fowler, 1986; Wilson and Fugleberg, 1987; Bernstein and Trahiotis, 1999). The second property is related to the temporal *resolution* of the binaural auditory system. Several studies have revealed that the auditory system is sluggish in its processing of interaural differences. For example, the minimum audible angle of a sound source strongly depends on its velocity (Perrott and Musicant, 1977). Experiments using time-varying interaural intensity differences (IIDs) revealed that IID detection shows a low-pass behavior with a cutoff frequency of about 20 Hz (Grantham, 1984). The detection of dynamic ITDs seems to be even worse; Grantham and Wightman (1978) showed that ITD detection has a low-

[a)]Now at: Philips Research Laboratories Eindhoven, Prof. Holstlaan 4, NL-5656 AA Eindhoven, The Netherlands. Electronic mail: jeroen.breebaart@philips.com

pass response with a cutoff frequency of 2 to 5 Hz. Detection experiments performed with a masker which has a time-varying interaural correlation show that the binaural auditory system has a time constant between 44 and 243 ms (Grantham and Wightman, 1979; Kollmeier and Gilkey, 1990; Culling and Summerfield, 1998; Akeroyd and Summerfield, 1999), which is rather high compared to the 4 to 44 ms for monaural processing (Kollmeier and Gilkey, 1990; Plack and Moore, 1990). The aim of the current study is to demonstrate that the model presented in Breebaart *et al.* (2001a) can also account for these temporal phenomena.

II. METHOD

A. Relevant stages of the model

In the Introduction, a coarse description of the general model setup was given. In this section, the stages of the model that are relevant for the simulations described in this paper (i.e., temporal behavior) are discussed in more detail. For a detailed description of the complete model, see Breebaart *et al.* (2001a).

(i) Filtering of the gammatone filterbank. The filterbank present in the peripheral processing stage determines the spectral resolution of the model, in line with the equivalent rectangular bandwidth (ERB) estimates published by Glasberg and Moore (1990). Due to the limited bandwidth of the filters in the gammatone filterbank, ringing occurs which influences forward-masking thresholds for very short signal delays.

(ii) A chain of five adaptation loops is included in the peripheral preprocessor. These adaptation loops limit the detectability of short low-level signals presented shortly after the offset of a high-level masker. Due to this limitation, the monaural detection model by Dau *et al.* (1996a) has been successful in predicting detection performance in monaural nonsimultaneous masking conditions (Dau *et al.*, 1996b, 1997). Because the current model includes the same stages as the model by Dau *et al.* (1996a), this predictive scope is inherited by our model. Furthermore, because the binaural interaction follows the peripheral adaptation (cf. Kohlrausch and Fassel, 1997), binaural forward masking will also be limited in its steepness through the presence of the adaptation loops.

(iii) Central temporal window. In the binaural processor, EI-type elements calculate the squared-difference signal between the outputs of the peripheral processor for each auditory filter. These difference signals are convolved with a double-sided exponential window with an equivalent rectangular duration (ERD) of 60 ms to account for a limited binaural temporal resolution. Because this window operates on the difference signal, the same window is used to analyze IIDs and ITDs as well as binaural detection data.

(iv) Compressive input–output characteristic of EI-type elements. The temporally smoothed difference signal of the EI-type elements is compressed logarithmically. In combination with an additive internal noise, this stage results in thresholds of interaural differences that depend on the interaural cross correlation of the reference stimuli.

(v) Optimal detector in the central processor. The EI-type element outputs are corrupted by an additive internal noise. Subsequently, the internal representations of the external stimuli are compared to a template that consists of the average masker-alone representation. The differences between the actual stimulus and the template are weighted and integrated both in the time- and the frequency domain according to an optimal criterion. This enables the optimal detector to reduce the influence of the internal noise, and to accumulate information about the signal by adapting its observation interval (matched temporal integrator).

B. Procedure and stimuli

The procedure, the method of generation of stimuli, and the model calibration were the same as those described in the spectral paper (Breebaart *et al.*, 2001b). In particular, all model parameters were kept fixed for all simulations described in this paper and were the same as in the previous paper. For details regarding the procedure and model calibration, refer to Breebaart *et al.* (2001b). In all simulations, the duration, level, on- and offset ramps, bandwidth, and onset delay of both the maskers and signals equaled the values used in the experiments with human subjects. If more data sets from various authors with different experimental settings were used, the experimental settings from one of these studies were used for determining the model simulations. Comparison with the other data sets was possible because in such conditions, we either calculated binaural masking level differences (BMLDs) or normalized the thresholds with the spectral level of the masking noise.

III. SIMULATIONS

A. NρSπ and NρSm correlation dependence for wideband noise

This section deals with the detection of a signal in the presence of a masker with various (fixed) values of the interaural correlation (ρ). Similar stimuli were discussed in the spectral paper (Breebaart *et al.*, 2001b, Sec. III E) focusing mainly on the bandwidth dependence of the masker. In this section, the nonstationary behavior of interaural differences in such conditions will be discussed. By ''nonstationary'' we mean that the expected values of the statistical properties, such as the interaural correlation, are constant, but that these properties evaluated on a short-time basis change as a function of time within each interval. It is therefore valuable to discuss NρSπ thresholds in the current paper, since these experiments reflect the detection of a change in the *distribution* of interaural differences rather than the detection of the *presence* of interaural cues.

Robinson and Jeffress (1963) measured thresholds for a wideband NρSπ condition. They used a 150-ms, 500-Hz tone as signal presented in a 150-ms noise masker. The masker had a spectral level of 50 dB/Hz. Their data are shown in the left panel of Fig. 1 (open symbols), together

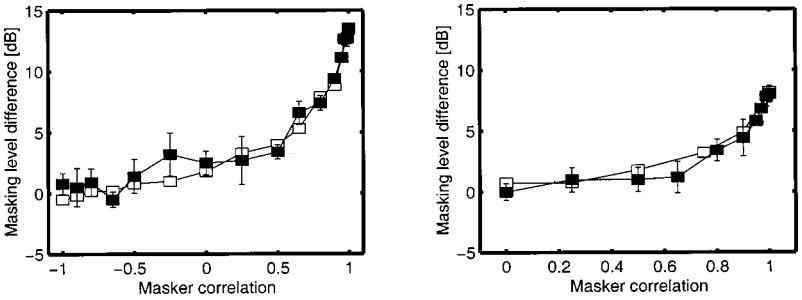

FIG. 1. NρSπ (left panel) and NρSm (right panel) BMLDs as a function of the interaural masker correlation. The white symbols are experimental data adapted from Robinson and Jeffress (1963) for NρSπ and from Wilbanks and Whitmore (1968) for NρSm. The black symbols are model predictions.

with the model predictions (filled symbols). The binaural masking level difference (BMLD) is shown as a function of the interaural masker correlation. For a correlation of $+1$, the condition corresponds to NoSπ and a large BMLD is observed, which decreases with decreasing correlation. If the masker is interaurally uncorrelated ($\rho=0$), a BMLD of only 2 to 3 dB is present, which completely disappears if the correlation is decreased further towards -1.

The right panel shows data for a monaural signal (i.e., NρSm), adapted from Wilbanks and Whitmore (1968). In this experiment, a 200-ms signal was used, also with a frequency of 500 Hz. The spectral masker level was 33 dB/Hz. The data show a similar curve as the NρSπ condition, with two important differences. First, the BMLD at $\rho=+1$ is 6 dB smaller for the NρSm condition. Second, almost no BMLD is observed in the NρSm condition with $\rho=0$, while the NρSπ condition still shows a BMLD of a few dB at this masker correlation.

To understand why the BMLDs decrease with a decrease in the masker correlation, it is useful to first have a closer look at the way these partially correlated maskers are generated. Usually, the Nρ masker is obtained by combining the waveforms of two or three independent noise sources. We will focus on the method using two noise sources, keeping in mind that the method using three noise sources is in principle similar (cf. van der Heijden and Trahiotis, 1997). If two independent noise sources having time-domain waveforms given by $N_1(t)$ and $N_2(t)$ are used to generate a noise with an interaural correlation of ρ, the left and right channels $\mathrm{L}(t)$ and $\mathrm{R}(t)$ consist of the following linear combination of these noises:

$$\begin{aligned}\mathrm{L}(t)&=\tfrac{1}{2}\sqrt{2}\sqrt{1+\rho}N_1(t)+\tfrac{1}{2}\sqrt{2}\sqrt{1-\rho}N_2(t),\\ \mathrm{R}(t)&=\tfrac{1}{2}\sqrt{2}\sqrt{1+\rho}N_1(t)-\tfrac{1}{2}\sqrt{2}\sqrt{1-\rho}N_2(t).\end{aligned}\tag{1}$$

If such a stimulus is presented to the model, and if we neglect the processing of the peripheral preprocessor, the waveforms $\mathrm{L}(t)$ and $\mathrm{R}(t)$ enter an EI-type element that optimally cancels the masker (no internal delay or level adjustment, i.e., $\tau=\alpha=0$). In our implementation (see Breebaart *et al.*, 2001a), the output (E) of the EI-type element is then given by

$$E(t)=(\mathrm{L}(t)-\mathrm{R}(t))^2.\tag{2}$$

Substitution of Eq. (1) into Eq. (2) results in

$$E(t)=(2-2\rho)N_2^2(t).\tag{3}$$

In a very similar way, it can be shown that the addition of an interaurally out-of-phase signal $[S_\pi(t)]$ to the same masker results in

$$E(t)=(2-2\rho)N_2^2(t)+4S_\pi^2(t).\tag{4}$$

The processes in the model that follow the EI-type element basically consist of time averaging resulting in a running average E of the energy of $(2-2\rho)N_2(t)$, followed by the logarithmic input–output relation of the EI-type elements. As can be observed from Eq. (3), a decreasing interaural correlation ρ results in an increasing amount of masker energy that cannot be canceled by the EI-type elements. As described in the first paper (Breebaart *et al.*, 2001a), this results in higher signal thresholds due to the logarithmic input–output behavior. The above explanation also holds for the NρSm condition, except for the fact that the amount of signal energy in Eq. (4) is decreased by a factor of 4. Thus, to achieve a similar change in E as for an Sπ signal, the signal level must be increased by 6 dB, an effect that is clearly found in the data for $\rho>0.7$. For lower correlation values, the signal level in the NρSm condition approaches the monaural threshold and hence thresholds remain constant if the correlation is reduced further.

B. NρSπ thresholds for narrow-band noise

Breebaart and Kohlrausch (2001) measured NρSπ thresholds as a function of both the correlation and the masker bandwidth. The masker duration was 300 ms. A 500-Hz sinusoid with a duration of 200 ms was used as the signal. Breebaart and Kohlrausch (2001) found that for a narrow-band masker with a bandwidth of 10 Hz, thresholds varied more with the interaural correlation than for a wideband masker. The narrow-band masker resulted in a much steeper curve for correlations between 0.8 and $+1$ compared to the wideband case. This is depicted in Fig. 2. Both the 10-Hz-wide (squares) and the 1000-Hz-wide (triangles) data are shown as a function of the masker correlation. The black symbols denote the model predictions; the white symbols are experimental data. The separation between the narrow-band and the broadband data is due to the choice of a constant overall masker level of 65 dB SPL, which gives a higher spectral level for the 10-Hz-wide masker.

Breebaart and Kohlrausch (2001) argued that the differences between the 10-Hz curve and the 1000-Hz curve are due to the fact that two different factors limit the detection process: internal errors and external variability. For the wideband masker, the thresholds are determined by the internal

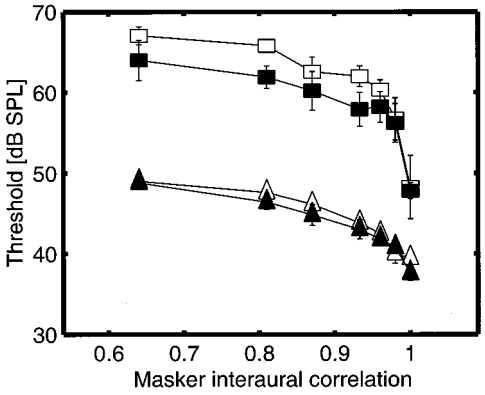

FIG. 2. Running-noise NρSπ thresholds for a masker bandwidth of 10 Hz (squares) and 1000 Hz (triangles). The overall masker level was 65 dB SPL for both bandwidths. The black symbols are model predictions; the white symbols are data adapted from Breebaart and Kohlrausch (2001).

errors. In our model, the specific relation between threshold and interaural correlation results from the logarithmic input–output curve present in the EI-type elements which was explained in Sec. II A.

For the narrow-band condition, other factors are important. The temporal sluggishness filter effectively calculates a running average of the output of Eq. (3) if a masker alone is present. This output increases if the signal is present. Because this output serves as a decision variable, the model must look for fluctuations in this variable that are attributable to the addition of the signal. Since the squared waveform of $N_2(t)$ is present in Eq. (3), a running average of $N_2(t)$ is obtained, multiplied with a scalar which depends on the interaural correlation. If the bandwidth of N_2 is very small, the energy estimate E shows large fluctuations due to the limited number of degrees of freedom in the noise. If the standard deviation of these fluctuations is larger than the *change* in E due to the addition of the signal with a certain level, it is very unlikely that the model is able to detect the signal because of the large amount of *stimulus variability*. This is exactly what happens in the narrow-band NρSπ condition. Instead of being limited by internal errors, the thresholds are limited by external stimulus fluctuations if $\rho<1$. Since the amount of E energy increases with decreasing correlation [as can be observed from Eq. (3)], the amount of fluctuations in E also increases with decreasing correlation, hence resulting in increasing thresholds. This property is not altered by the logarithmic input–output function of the EI-type elements, since both the fluctuations and the change in the output due to the signal are transformed by the same process. Thus, for the narrow-band condition with ρ at or below 0.98, thresholds are relatively high due to the ''external'' variability in E. Only when $\rho=1$ does external variability play no role, and thresholds are only determined by the internal error and are therefore relatively low.

C. Interaural cross-correlation discrimination

Gabriel and Colburn (1981) measured just-noticeable differences (jnd's) in interaural cross correlation from two reference correlations (0 and +1) at several bandwidths. The total noise level was kept constant at 75 dB SPL and the stimuli were spectrally centered at 500 Hz. At a reference correlation of +1, their results indicated that for bandwidths less than 115 Hz the correlation jnd was equal to about 0.004, while for larger bandwidths, the jnd increased monotonically with the noise bandwidth. On the other hand, at a reference correlation of 0, the jnd *decreased* with increasing bandwidth, having a value of 0.7 for narrow-band stimuli (3 Hz) and 0.3 for the broadband case (4500 Hz). Their results are summarized in Fig. 3. The left panel shows the correlation jnd's at a reference correlation of +1, the right panel at a reference correlation of 0. The white symbols are the experimental data for different subjects; the black symbols denote model predictions.

The model predictions for a reference correlation of +1 (left panel) show a completely different behavior from the experimental data: the experimental data increase with increasing bandwidth, while the model predictions show a monotonic decrease with increasing bandwidth. Only for the data at 40 and 115 Hz is there a close resemblance between model predictions and experimental data. The decrease in correlation jnd with increasing bandwidth for the model can be explained as follows. For all bandwidths, the reference condition has a correlation of +1. Consequently, the stimulus can be eliminated completely by the model. Thus, the reference intervals result in no internal activity for EI-type elements that are optimally tuned to this detection task. If the interaural correlation of the stimulus is reduced, the masker cannot be canceled completely, which results in some activity in the model. If the stimulus bandwidth is small (i.e., 3 to 10 Hz), this cue for detection is available in the on-frequency filter and in some adjacent filters due to spread of excitation. If the bandwidth is increased, the number of auditory filters that contains information about the change in the correlation increases since the change in the interaural correlation occurs

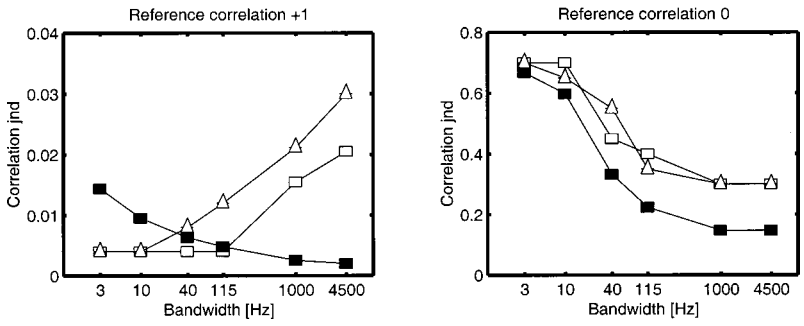

FIG. 3. Just-noticeable differences in the interaural correlation at a reference correlation of +1 (left panel) and 0 (right panel) as a function of the bandwidth of the stimulus. The white symbols are experimental data adapted from Gabriel and Colburn (1981) for two different subjects. The filled symbols are model predictions.

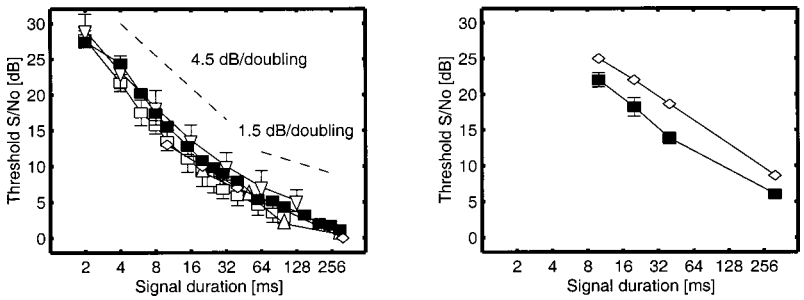

FIG. 4. NoSπ thresholds as a function of the signal duration. Data in the left panel are for a signal frequency of 500 Hz, in the right panel for a signal of 4 kHz. The white squares are data adapted from Wilson and Fugleberg (1987), the upward triangles from Yost (1985), the downward triangles from Wilson and Fowler (1986), and the diamonds from Bernstein and Trahiotis (1999). The black symbols are model predictions. Thresholds are given as signal level *re* masker spectrum level.

at the complete spectrum of the stimulus. This enables the model to integrate information across auditory filters, resulting in an effective reduction of the internal noise. This in turn results in lower thresholds, as observed in the model predictions. This effect is not observed in the experimental data, however.

The right panel of Fig. 3 shows data for the reference correlation of 0. Both model predictions and experimental data show a decrease in the correlation jnd with increasing bandwidth, although the model is more sensitive to changes in the correlation at bandwidths beyond 40 Hz. This decrease in the correlation jnd can be explained by considering stimulus uncertainty. If the bandwidth is very small (3 Hz), the fluctuations in the output of the EI-type elements are very large (see Sec. III B.). Increases in the bandwidth result in more degrees of freedom in the masker and hence less uncertainty in the output of the EI elements. This decreased uncertainty is reflected by the decrease in the correlation jnd. For bandwidths beyond 115 Hz, increases in the bandwidth have almost no effect on the stimulus uncertainty because these parts of the stimulus fall outside the auditory filter and hence thresholds remain constant.

D. NoSπ signal duration

An important property that has a very strong effect on thresholds in an NoSπ condition is the duration of the signal. The threshold behavior in this experimental paradigm basically reflects the ability of the binaural auditory system to *integrate* information over time. Several studies showed an increase in detection performance of up to 25 dB if the signal duration is increased from 2 to 250 ms (cf. Yost, 1985; Wilson and Fowler, 1986; Wilson and Fugleberg, 1987; Bernstein and Trahiotis, 1999). The results of these studies are shown in Fig. 4 (white symbols) for a center frequency of 500 Hz (left panel) and for 4 kHz (right panel). Since in these studies different noise levels were used ranging from 26.3 to 47 dB/Hz, we expressed thresholds as the ratio between signal level and spectral masker density. The thresholds decrease with a slope of 4.5 dB/oct for durations up to about 60 ms, while for longer durations, this slope is shallower (1.5 dB/oct). The model predictions are shown by the black symbols in Fig. 4. They were derived for a 500-ms wideband noise masker with a spectral energy density of 36.2 dB/Hz (similar to Wilson and Fugleberg, 1987).

The model predictions show a very similar signal-duration dependence to the experimental data. These results can be explained as follows. First, consider a signal of very short duration (2 ms). In this case, the signal interval contains interaural differences which are present within a short period of time compared to the duration of the binaural window (about 60 ms). As described in the first model paper (Breebaart *et al.*, 2001a), the output of each EI-type element is averaged over time by a temporal integrator. Consequently, the cue for detection at the *averaged* output of such a temporal window is strongly reduced for a very short signal. Therefore, the signal must have a relatively high level to elicit a change in the averaged output that can be detected by the model. If the duration of the signal is increased but does not exceed the duration of the temporal window, the average output of the temporal window increases and hence the signal level decreases at threshold. Since the output of the temporal averager is proportional to the signal energy, this process accounts for a decrease of 3 dB for each doubling of the of signal duration, as long as the signal duration does not exceed the time constant of the temporal averager. For durations exceeding 60 ms, this process does not influence the detection process.

An additional effect of 1.5 dB per duration doubling results from the reduction of the internal error with increasing signal duration by the optimal detector. A longer signal duration means that the average output is available for a longer time. This enables the model to reduce the internal error in the decision variable in a similar way as was described for spectral integration of information (see Breebaart *et al.*, 2001b, for details). After the temporal averager, an additive noise is combined with the output of the EI-type elements, followed by an optimal detector. If, after the temporal integrator, the cue for detection is available for a long time, the optimal detector can decrease the amount of noise in its decision variable by integrating the EI-element output over the total signal duration. In this way, a doubling in the signal duration results in a doubling in the overall difference in output between masker and masker plus signal, while the amount of noise increases with the square root of 2. Hence, the detectability of the signal is increased, which results in a lower threshold. Thresholds are expected to decrease with 1.5 dB per doubling of signal duration. Thus, the combined effect of the processes described above accounts for the 4.5 dB per doubling for signal durations below 60 ms and 1.5 dB beyond 60 ms.

The slope of 4.5 dB/doubling for signal durations below 60 ms and 1.5 dB/doubling beyond 60 ms is also present in the model simulations at 4 kHz (right panel of Fig. 4). Except for an overall difference of about 4 dB, these model predictions are very close to the experimental data, although

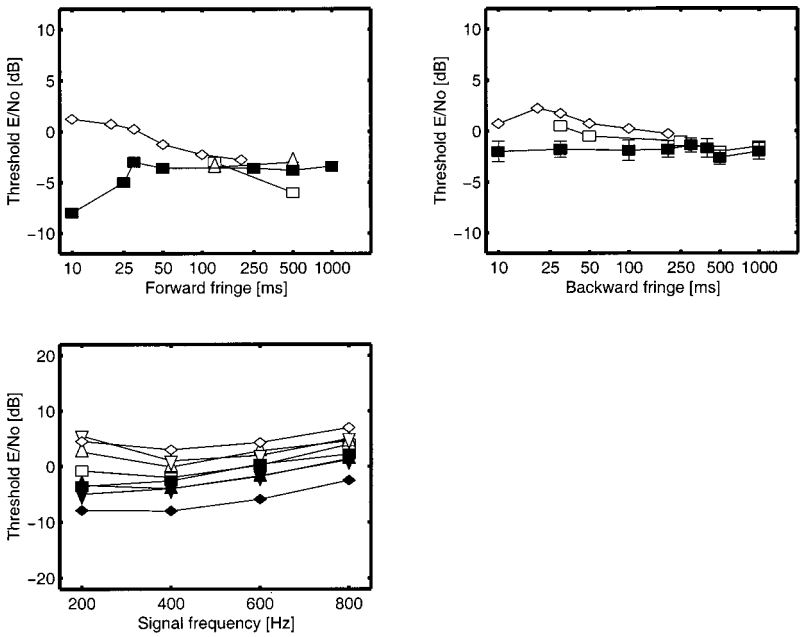

FIG. 5. NoSπ thresholds as a function of the masker duration. The upper-left panel denotes experimental data with a forward fringe, the upper-right panel with a backward fringe. The lower panel shows thresholds for a signal temporally centered in a masker for four different masker durations (squares denote 500 ms, upward triangles 100 ms, downward triangles 50 ms, and diamonds 25 ms) as a function of the center frequency. The white squares in the upper panels are experimental data for a 500-Hz, 32-ms signal adapted from Robinson and Trahiotis (1972), the upward triangles are from the same study with a 256-ms signal, the diamonds are adapted from Zwicker and Zwicker (1984) for a 400-Hz signal. The black symbols are model predictions for a 500-Hz, 20-ms signal.

the difference in slope below and beyond 60 ms cannot be deduced from the experimental data.

E. NoSπ masker duration

Besides reports on the duration of the signal, several studies have been published on the effect of the duration of the masker. Basically three configurations have been tested. The first uses a forward noise fringe of variable length (Robinson and Trahiotis, 1972; Zwicker and Zwicker, 1984; Yost, 1985), while in the second configuration, a backward noise fringe is used (Trahiotis *et al.*, 1972; Zwicker and Zwicker, 1984; Yost, 1985). A third condition includes a signal which is temporally centered in the masker (Kohlrausch, 1986). The duration of the fringe in these studies varied between 10 and 256 ms; the center frequency was always 500 Hz (except for Zwicker and Zwicker, 1984, using 400 Hz). Most experiments were performed with relatively short signals (10 to 32 ms). The experimental results are shown in Fig. 5. The upper-left panel shows data for a forward fringe, the upper-right panel for a backward fringe. The lower panel shows four different curves for four different masker durations (25, 50, 100, and 500 ms) as a function of center frequency. The white symbols are data from different data sets, the black symbols are the model predictions for a 20-ms, 500-Hz signal added to a broadband masker with a level of 50 dB/Hz (similar to Trahiotis *et al.*, 1972). Thresholds are expressed as the ratio between signal energy and spectral masker density to enable comparison between data sets.[1]

The predicted thresholds hardly change if the masker duration is varied. This is in contrast to what is observed if the *signal* duration is changed, as discussed in Sec. D. A maximum decrease of 5 dB is observed experimentally if the forward masker fringe is increased (top-left panel of Fig. 5). The model predictions show no effect of the masker duration at all, except for very short forward fringes. The absence of a distinct effect of masker duration is expected, since the output of an EI-type element optimally tuned for this condition has no activity for a masker alone and has some activity during the presence of the signal. Since this activity is used as a cue for the detection, and since it does not depend on the duration of the masker, the model's predictions do not, in principle, depend on the masker duration. The decrease in thresholds for very short forward fringes is a consequence of the monaural adaptation loops (Dau *et al.*, 1996a). These loops are not completely charged during the first 25 ms of the stimulus and a substantial overshoot in the output of the adaptation loops exists just after the onset. If interaural differences are presented within this short period of time, they will result in a stronger change at the output of EI-type elements than if they were presented with a longer forward masker fringe. Therefore, the thresholds are up to 5 dB lower during the first 25 ms. This effect is clearly visible in the upper-left panel of Fig. 5 for short forward fringes and in the lower panel (with the centered signal). In the latter case, simulated thresholds are more than 10 dB lower than the experimental data for a 25-ms masker (2.5-ms forward fringe). For masker durations of 50 ms and beyond, the model predicts nearly constant thresholds, while the experimental data show a slight decrease with increasing masker duration. On the other hand, the backward fringe has no influence on the state of the adaptation loops; hence, the thresholds do not depend on the duration of the backward fringe, as demonstrated in the right panel of Fig. 5.

F. Maskers with phase transitions in the time domain

The previous sections dealt with the ability of the binaural auditory system to *integrate* information over time. Besides integration, another very important temporal property that can be measured is the temporal *resolution* of the system. In analogy to the frequency-domain phase transition which we discussed in the accompanying paper (Breebaart *et al.*, 2001b), an interaural phase transition can be applied in the time domain. As the spectral phase transition enabled the estimation of the spectral resolution, the time-domain

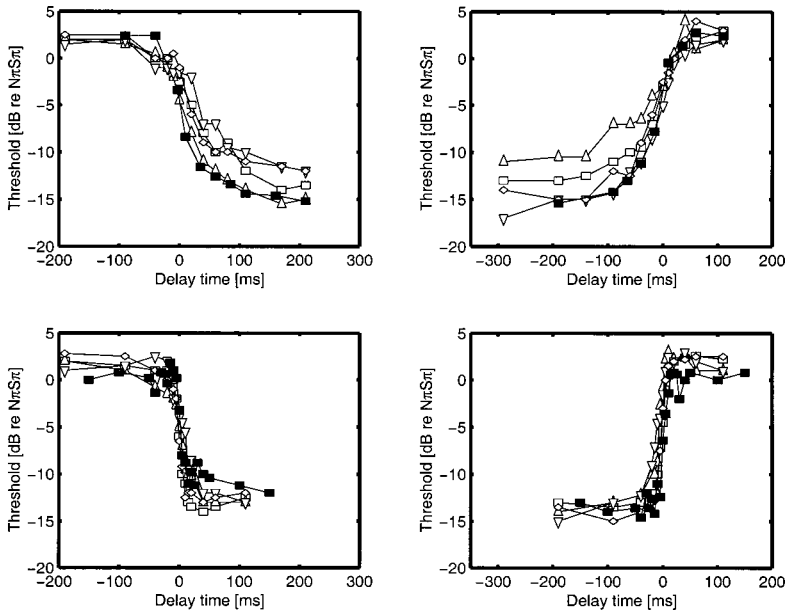

FIG. 6. $N\pi oS\pi$ (upper-left panel) and $No\pi S\pi$ (upper-right panel) thresholds as a function of the temporal position of the signal center relative to the masker–phase transition. The lower-left and lower-right panels correspond to the monaural $N\pi(-15dB)N\pi S\pi$ and $(-15dB)N\pi N\pi S\pi$ conditions, respectively (see the text). The 0-dB point on the ordinate denotes the nontransient $N\pi S\pi$ thresholds. White symbols are experimental data for different subjects adapted from Kollmeier and Gilkey (1990); the black symbols are model predictions.

equivalent enables estimation of the temporal resolution. One possible realization of such a phase transition is a masker which is first interaurally in phase and then interaurally out of phase. This condition is referred to as $No\pi S\pi$ if an interaurally out-of-phase signal is used. In a similar way, $N\pi oS\pi$ refers to a masker that is interaurally out of phase first, followed by an in-phase noise. If the signal is centered within the in-phase masker portion, the effective condition is $NoS\pi$ and a large BMLD is observed. On the other hand, if the signal is presented during the out-of-phase masker portion, no BMLD is expected. Experimental data have shown that for signal positions close to the masker phase transition, a gradual change of the threshold is observed (Kollmeier and Gilkey, 1990; Holube *et al.*, 1998). The experimental data of individual subjects from Kollmeier and Gilkey (1990) are shown in Fig. 6. These data were measured with a 500-Hz, 20-ms signal added to a broadband noise with a spectral energy density of 40 dB/Hz. The thresholds are plotted as a function of the signal center relative to the occurrence of the phase transition of the masker. The upper-left panel corresponds to an $N\pi oS\pi$ condition, the upper-right panel to $No\pi S\pi$. In both conditions, a gradual change in threshold is observed near the phase transition (0 ms). The model predictions (black symbols) have a similar gradual change in threshold as the experimental data and follow the lower bound of the four subjects.

The gradual change as observed in Fig. 6 is thought to reflect the *temporal resolution* of the binaural auditory system. In the model, this resolution is limited by the temporal averager at the output of all EI-type elements; the stepwise masker correlation change is heavily smoothed by the averager, and hence thresholds show a gradual change instead of a stepwise one.

The lower panels in Fig. 6 show data obtained for a corresponding ''monaural'' condition. Both the signal and the two masker portions were presented interaurally out of phase ($N\pi N\pi S\pi$), and one of the masker portions was decreased in level by 15 dB. The data in the lower-left panel were obtained for a masker that drops by 15 dB at the second half of the total stimulus [this condition is referred to as $N\pi(-15dB)N\pi S\pi$], while the data in the lower-right panel were obtained for a 15-dB increase at the stimulus center. The open symbols denote data from different subjects adapted from Kollmeier and Gilkey (1990); the filled symbols are model predictions. Clearly, the time constant for processing monaural cues is much shorter than for the processing of binaural cues. The ability of the present model to also predict monaural forward- and backward masking relies on a completely different process from that involved in predicting the binaural temporal resolution effects. The monaural data are predicted due to the presence of the adaptation loops prior to any binaural interaction. Since the model incorporates all the stages of the monaural model described by Dau *et al.* (1996a, b), it inherits the predictive power of that model for all cases where no binaural interaction is needed.

An extension of the experiment with one masker phase transition in the time domain is obtained by using two phase transitions. Culling and Summerfield (1998) measured detection thresholds of a 500-Hz 20-ms $S\pi$ signal which was added to a broadband in-phase noise masker (No) of variable duration, preceded and followed by 400 ms of interaurally uncorrelated noise. The spectral energy density of the noise was 40 dB/Hz. We refer to this condition as $NuouS\pi$. Culling and Summerfield (1998) found that thresholds decrease by up to 12 dB with increasing No duration from 20 to 960 ms. The data are shown in Fig. 7. The white symbols are data for three different subjects; the black symbols are model predictions.

For No durations between 20 and 400 ms, the modeled thresholds agree well with the subjects' data. For further increases in No duration there is a discrepancy, because the experimental data tend to decrease further, while the modeled thresholds remain constant. This indicates that the temporal *resolution* of the human binaural auditory system is very well represented by the model, but that some really long-term processes with a temporal extension of 500 ms and more are not covered by our present model structure.

Besides using stepwise correlation changes in the

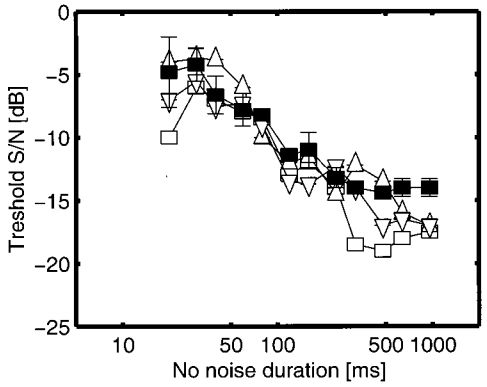

FIG. 7. NuouSπ detection thresholds as a function of the duration of the No noise. White symbols are experimental data for different subjects adapted from Culling and Summerfield (1998); black symbols are model predictions.

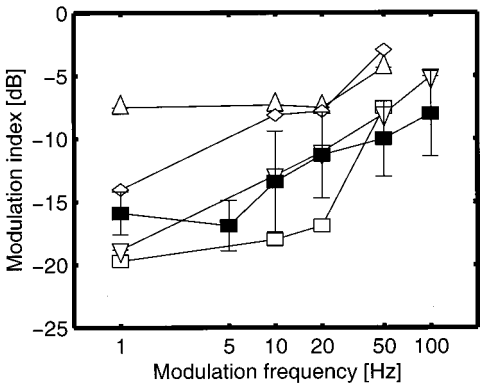

FIG. 9. Modulation depth (in dB) required for discrimination of interaural in-phase modulation from out-of-phase modulation as a function of the modulation frequency. The white symbols denote results for different subjects adapted from Grantham (1984); the black symbols are model predictions.

masker, experiments have also been performed with a sinusoidally changing interaural masker correlation. Holube *et al.* (1998) measured the detectability of a 500-Hz, 20-ms signal as a function of the correlation modulation period. The signal was always centered at a temporal position where either an No or Nπ noise was present. The masker duration was 2500 ms for the modulation periods of 2- and 1 s and 750 ms for shorter periods. A bandlimited masker (0.1 to 1 kHz) was used with an overall level of 75 dB SPL. The results (white symbols) combined with model predictions (black symbols) are shown in Fig. 8. The left panel corresponds to a signal presentation at a position where the noise was interaurally in phase, the right panel where it was out of phase. Thresholds are expressed relative to the monaural (NoSo) thresholds.

The thresholds for the signal presentation centered on No decrease with increasing modulation period. This is the result of the decreasing amount of Nπ noise at the input of the temporal window of the EI-type element during the presentation of the signal. A similar argument holds for the presentation during the Nπ masker phase. With decreasing period, an increasing amount of Nπ noise is present in the EI-type element during signal presentation, resulting in higher thresholds.

In contrast to earlier modeling approaches (Kollmeier and Gilkey, 1990; Holube *et al.*, 1998), our implementation does explain data for stepwise and sinusoidal correlation modulation with the *same* temporal window. We will come back to this observation in the General Discussion (Sec. IV).

G. Discrimination of dynamic interaural intensity differences

Grantham (1984) measured observers' ability to detect time-varying interaural intensity differences. The stimuli consisted of interaurally uncorrelated noises of which the envelopes were sinusoidally modulated. The task was to discriminate between a modulation which was interaurally in phase and a modulation which was interaurally out of phase, the latter resulting in interaural intensity differences. The noise used in this experiment had a bandwidth of 0.4 octaves centered at 500 Hz and had a level of 75 dB SPL. The stimulus duration was 1000 ms. The results of Grantham (1984) (open symbols) combined with the model predictions (filled symbols) are shown in Fig. 9.

As can be observed in Fig. 9, the thresholds increase with increasing modulation rate, indicating a low-pass modulation function of the binaural auditory system. Although the data show large variations across subjects, the model predictions are a good representation of the subject denoted by the downward triangles. The general trend is that of a low-pass filter; the modulation index required at threshold increases with increasing modulation frequency. In our model, this can be understood as follows. The unmodulated noise that was used had an interaural correlation of 0. If a sinusoidal modulation is superimposed on the noise waveform, the interaural correlation of the noise remains unchanged. Now, consider the output of an EI-type element centered at the stimulus center frequency and $\alpha=\tau=0$. For the interaurally in-phase

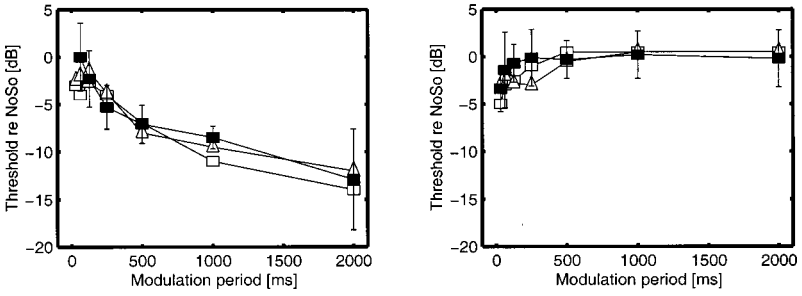

FIG. 8. Detection thresholds for an Sπ signal presented in a noise masker with a sinusoidally modulated interaural correlation. Thresholds are plotted relative to the monaural (NoSo) threshold. The left panel corresponds to a signal presentation at a point where the interaural masker correlation was +1, the right panel to a masker correlation of −1. The white symbols are data adapted from Holube *et al.* (1998); the black symbols are model predictions.

modulator (i.e., the reference stimuli), the output of the EI-type element has a similar pattern as the modulator: during positive modulator phases the masker energy is increased and hence the uncorrelated masker results in an increased amount of activity. On the other hand, a negative modulator phase results in a decrease in the EI activity. These modulations are, however, only present for low modulation frequencies (<10 Hz); for higher modulation frequencies the EI-output modulation depth decreases due to the temporal averaging. Thus, as long as the modulation period is beyond the time constant of the temporal averager of the EI-type elements, the externally presented monaural modulation is reflected by a modulation of the EI-type element output. The out-of-phase modulator results in hardly any modulation in the EI-type element output: every attenuation (i.e., negative modulator phase) of the left-ear signal is accompanied by an amplification of the right-ear signal (i.e., a positive modulator phase) and vice versa, resulting in only a very small effect on the EI activity. Thus, as long as the modulations in the EI-type output due to the in-phase modulator are clearly visible (i.e., slow modulations), the model shows a low modulation threshold which increases with increasing modulation frequency.

H. Discrimination of dynamic interaural time differences

Grantham and Wightman (1978) measured the detectability of sinusoidally time-varying interaural time differences present in a low-pass noise. The spectra of the noise stimuli were approximately flat between 10 and 3000 Hz. The presentation level was 70 dB SPL, the duration 440 ms. Grantham and Wightman (1978) found that the peak ITD required for detection strongly depends on the modulation frequency, having a value of about 30 μs at a modulation rate of 0 Hz, which increases to 90 μs at 20 Hz. Interestingly, the thresholds decrease again for higher modulation rates, reaching a value of about 30 μs at a modulation rate of 500 Hz. The results are shown in Fig. 10. The white symbols denote the experimental data; the black symbols are model predictions.

The bell-shaped curve which is seen in the experimental data is not observed in the model predictions. Considering the properties of the model, this is expected, since the average or peak interaural difference that occurs in this stimulus does not depend on the modulation rate. Therefore, the model predictions do not show a bell-shaped curve but decrease monotonically by a factor of about 2.5. This decrease

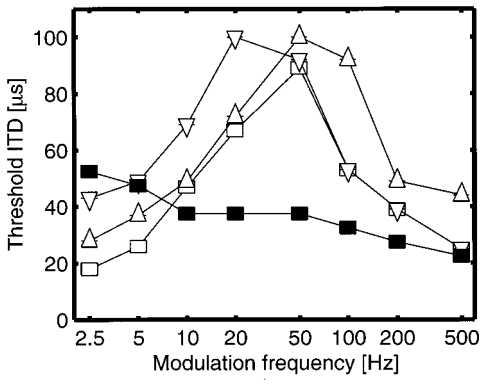

FIG. 10. Peak interaural time difference in microseconds at threshold as a function of the modulation frequency for the detection of sinusoidally varying interaural time differences. The open symbols are experimental data adapted from Grantham and Wightman (1978) representing different subjects; the black symbols are model predictions.

is related to the fact that the ITD at the onset of the signal is set to 0 and changes sinusoidally during the stimulus. If a modulation rate of 10 Hz is used, the first maximum in the ITD occurs 25 ms after the stimulus onset. At a modulation rate of 20 Hz, the maximum occurs at 12.5 ms, etc. As discussed in Sec. III E, interaural differences closer to the onset of the stimulus result in lower thresholds due to the overshoot in the peripheral adaptation loops. Therefore, the ITD thresholds shown in Fig. 10 decrease with increasing modulation rate.

I. Binaural forward masking

In the previous experiments, the signal was always presented simultaneously with the masker. If a short signal is presented *after* the masker, a phenomenon referred to as forward masking is observed. For signals that are presented at increasing delays with respect to the masker offset, the thresholds decrease gradually towards the absolute threshold instead of showing a stepwise change (cf. Punch and Carhart, 1973; Yama, 1992; Kohlrausch and Fassel, 1997). This elevation is observed for signal delays of up to 200 ms. Moreover, a binaural release of masking can be observed if the signal is presented interaurally out of phase compared to an in-phase signal. For example, Yama (1992) measured forward-masking thresholds for a 10-ms, 250-Hz signal combined with a low-pass (0–2.5 kHz, overall level of 70 dB SPL), 500-ms running noise. Linear ramps of 5-ms duration were used to gate both signal and masker. The results show a BMLD of about 14 dB for simultaneous masking, which

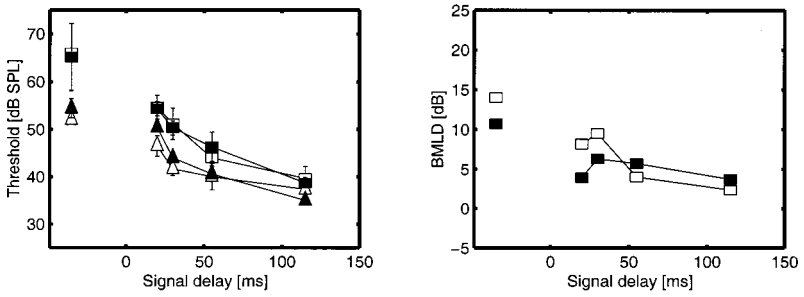

FIG. 11. Signal thresholds for NoSπ (triangles) and NoSo conditions (squares) as a function of the time difference between masker and signal offset (left panel) and corresponding BMLDs (right panel). White symbols are experimental data adapted from Yama (1992); black symbols are model predictions. The signal duration was 10 ms. The symbols at the left in both panels denote thresholds for simultaneous masking.

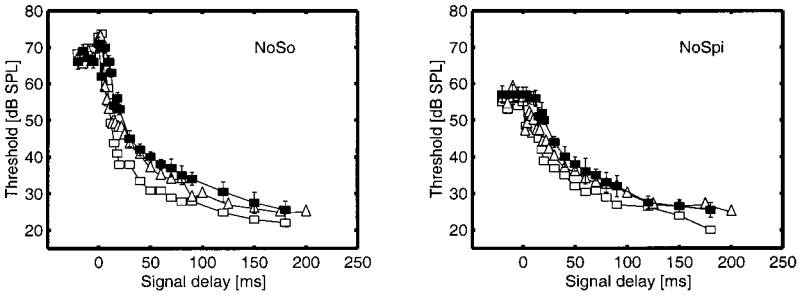

FIG. 12. Forward-masking thresholds for a 20-ms So signal (left panel) and an Sπ signal (right panel) as a function of the time difference between masker and signal offset. A 300-ms frozen-noise (No) served as the masker. The white symbols are experimental data adapted from Kohlrausch and Fassel (1997); the black symbols are model predictions.

decreases to a few dB for signal delays of 100 ms, as can be observed in the left panel of Fig. 11. Thresholds are shown as a function of the time difference between signal and masker offset. The squares denote monaural (i.e., NoSo) thresholds; the triangles denote binaural (NoSπ) thresholds. The right panel shows the corresponding BMLDs, for both the model and the experimental data.

As can be observed from Fig. 11, the model (black symbols) shows a similar threshold behavior as the experimental data. For simultaneous masking, a BMLD of 14 dB is observed in the experimental data and a few dB less for the model predictions. Both the binaural and monaural forward-masking thresholds show a decrease towards the absolute threshold, which is about 35 dB for both the So and Sπ signal. In the region of 0 to 100 ms, a substantial BMLD can be observed which is, however, smaller than the BMLD for simultaneous masking.

Results that seem to be in contradiction with those found by Yama (1992) were obtained by Kohlrausch and Fassel (1997). Their forward-masking experiments only showed BMLDs for signal delays up to 20 ms instead of the 100 ms found by Yama (1992). The data were obtained with a 300-ms frozen-noise masker which was spectrally flat between 20 and 1000 Hz. The overall masker level was 70 dB SPL. A 20-ms, 500-Hz signal was used. The same values were used to obtain the model predictions. However, the frozen-noise sample was different from the one used in the experiments. The results and model predictions are shown in Fig. 12. The left panel corresponds to monaural conditions (NoSo), the right panel to binaural conditions (NoSπ).

In the NoSo condition, thresholds start to decrease as soon as the offset of the signal occurs after the masker offset. In contrast, NoSπ thresholds remain constant for signal delays up to about 10 ms. For larger signal delays, the thresholds gradually decrease with signal delay towards the absolute threshold. This decrease is stronger for the monaural (NoSo) condition than the binaural (NoSπ) condition. Hence, a substantial BMLD is only found for signal delays up to 20 ms. Kohlrausch and Fassel (1997) also measured forward masking thresholds for a 20-ms masker. The waveform of this short masker was identical to the last 20 ms of the long masker. The results are shown in Fig. 13 in the same format as Fig. 12.

The main difference between the threshold behavior of 300-ms and 20-ms maskers is the slope of the forward-masking curve, which is steeper for the short masker. In the model, this steeper curve is the result of the fact that the adaptation loops which are part of the peripheral preprocessor are not completely ''charged'' if a masker of only 20 ms is used (Dau *et al.*, 1996b).

Also in this condition, the model shows BMLDs only for signal delays of up to 20 ms, perfectly in line with the experimental data. The difference in BMLD behavior between the conditions shown Fig. 11 on the one hand and in Figs. 12 and 13 on the other hand is related to the difference in signal duration that was used. Yama (1992) used a relatively short signal (10 ms), while Kohlrausch and Fassel (1997) used a 20-ms signal. If a short signal is presented to the model, the onset of the signal will result in an increase of the output of the peripheral adaptation loops compared to the output in the absence of the signal. On the other hand, if the signal is turned off, the adaptation loops are (at least partially) adapted to the (higher) input signal; hence, the signal offset results in a decrease of the output. Moreover, due to the adaptation of the system, the activity after the offset will be *less* than if *no signal* was present. An example of this property can be seen in the lower panel of Fig. 7 of Dau *et al.* (1996a): the presence of the signal results in both an overshoot at the signal onset and an undershoot at the signal offset. If the duration is sufficiently long compared to the temporal resolution of the monaural system, the model can use both the overshoot at the onset of the signal and the undershoot at the offset of the signal to detect the signal's presence. If a very short signal is used, however, the tempo-

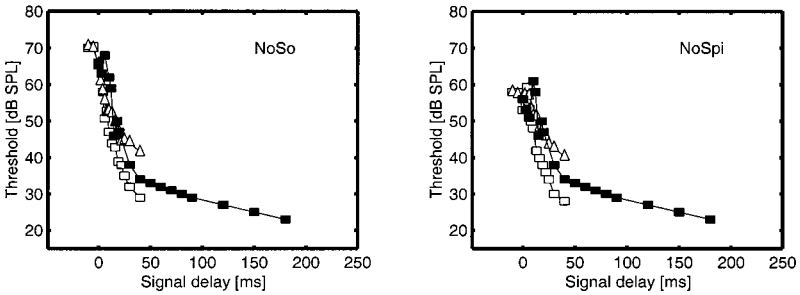

FIG. 13. Forward-masking thresholds for a 20-ms So signal (left panel) and an Sπ signal (right panel) as a function of the time difference between masker and signal offset. In this case, the masker had a duration of only 20 ms. The white symbols are experimental data adapted from Kohlrausch and Fassel (1997); the black symbols are model predictions.

ral averager at the output of the adaptation loops partially cancels the undershoot by the overshoot, resulting in a smaller overall effect at the output of the temporal averager. In the binaural case, the temporal window does not reduce the detectability of the signal because the window is applied *after* the computation of the *squared difference* between the left and right channels. Therefore, monaural thresholds are elevated more strongly if the signal duration is decreased from 20 to 10 ms than binaural thresholds. This is also observed in the model predictions. If a 20-ms signal is used (Figs. 12 and 13), both the monaural and binaural cues are about equally strong and no BMLD is observed for signal delays beyond 20 ms. When using a 10-ms signal, however, the monaural thresholds are elevated more than the binaural thresholds, resulting in a BMLD which is still present even for signal delays up to 100 ms.

IV. GENERAL DISCUSSION

We have shown that our binaural model is quite successful in describing the dependence of binaural detection thresholds on temporal stimulus properties. These properties include the effect of signal and masker duration, forward masking, and detection against stimuli with a time-varying interaural correlation. By means of a temporal integrator followed by an optimal detector in the time domain, the model accounts both for temporal resolution and for temporal integration properties within a single framework. It is interesting to note that a similar framework in the spectral domain is present in the model (i.e., a set of bandpass filters followed by an optimal detector in the frequency domain), also leading to very good predictions as a function of spectral stimulus parameters (see Breebaart *et al.*, 2001b).

Although many of the simulations shown in this paper and in the previous papers show a good fit between the data and the predictions, very similar results would probably be obtained if the basic EI interaction in the model was replaced by an EE (or cross-correlation) interaction. There are, however, some specific experimental conditions that may give rise to some modeling difficulties. In the first model paper (Breebaart *et al.*, 2001a), we expected that models based on the interaural cross correlation may not account for the effect of both signal and masker duration. Two methods of computing the interaural correlation were discussed. The first comprised computation over the complete stimulus (i.e., masker duration). We argued that this method would result in a strong increase of detection thresholds with an increase of masker duration, which is not found in experimental data. The second method comprised computation of the correlation only for the stimulus part that contains the signal. In this case, a maximum effect of 1.5 dB/oct of signal duration is expected, which is not in line with experimental results showing a stronger influence of signal duration for durations below about 60 ms. It is therefore difficult to explain the effects of both masker and signal duration with a model based on cross correlation. The simulation results in Sec. III D and III E show that a model based on EI-type interaction in combination with an optimal detector shows a performance which is more in line with the experimentally obtained results.

The simulations as a function of interaural correlation and bandwidth revealed that the detection performance of the model can in principle be limited by two sources of errors, namely stimulus uncertainty in the externally presented signals and errors in the internal accuracy (internal noise).

The data in Figs. 6 and 7 (stepwise correlation change in the time domain) revealed that a double-exponential window with time constants of 30 ms (equivalent rectangular duration, or ERD, of 60 ms) can account for the limited temporal resolution of the binaural system which is observed in different experiments, which often reveals different underlying temporal windows. The shape and ERD of the window were chosen to fit the experimental results of Kollmeier and Gilkey (1990). A somewhat larger value for the ERD of 100 ms was found by Culling and Summerfield (1998). Their estimate was based on a Gaussian window. They also fitted their data with a double-exponential window, resulting in ERDs between 48 and 117 ms, which is much closer to the temporal window we used throughout the whole paper. These results support the fact that the ERD itself is not a very valuable property to discuss without mentioning the window shape from which it is derived.

The data in Fig. 8 were obtained for a sinusoidally changing masker correlation. The ERD found by Holube *et al.* (1998) that fitted these data (using a double-exponential window) was 91 to 122 ms. A similar experiment by Grantham and Wightman (1979) revealed an ERD of 139 to 189 ms. Despite these rather large ERDs compared to the ERD of our model, the simulations give a good fit to the data. This suggests that not only the shape of the temporal window, but also the stimulus configuration has an influence on the ERD that is estimated from experimental data: experiments with stepwise correlation changes result in lower estimates of the time constants than sinusoidal correlation changes (Kollmeier and Gilkey, 1990; Holube *et al.*, 1998).

A possible explanation for these differences in the estimate of the ERD was given by Holube *et al.* (1998). They stated that ''the reason for this mismatch seems to be the different detection strategies employed for the various tasks that are affected by the consistency of binaural information across frequency and time.'' In their fitting procedure, Kollmeier and Gilkey (1990) and Holube *et al.* (1998) obtained the predicted thresholds by computing the weighted integration of the instantaneous interaural cross correlation *at the temporal center of the signal*. For the sinusoidal changes in the correlation, it is likely that this detection strategy results in the highest signal-to-masker ratio, given the fact that both the temporal window and the correlation modulation are symmetric around that moment. It is not obvious, however, that this strategy is also optimal for the stepwise correlation changes. In fact, an analysis of the optimal detector in our model revealed that within the framework of our model, the optimal position for detecting the signal is about 10 ms further away from the masker phase transition (i.e., off-time listening). Hence, by analyzing the correlation slightly away from the temporal center of the signal, lower thresholds are obtained. Consequently, the fitting procedure used by Kollmeier and Gilkey (1990) and Holube *et al.* (1998) for step-

wise correlation changes *underestimates* the time constants present in the system. This is perfectly in line with their experimental results: the time constants for stepwise correlation changes were about a factor of 2 lower than for the sinusoidal correlation changes.

One of the experimental findings that the present model could not account for is the bandwidth dependence of interaural correlation jnd's for a reference correlation of +1 (see Fig. 3). The experimental data show a substantial decrease in performance with bandwidth, while the model's performance increases. A possible explanation for this discrepancy is that the binaural auditory system can only integrate cues across frequency if these cues *are highly correlated* across auditory filters. Since the data show the strongest increase in the correlation jnd for bandwidths beyond the ERB of the auditory filters, it is likely that the increase in the thresholds results from across-frequency effects instead of within-filter stimulus properties. If a stimulus with a correlation of +1 is presented, the stimulus can be canceled completely. The reduction of the correlation can thus in the model be detected by an increase in the residual noise after optimal cancellation. If the noise is broadband, this residue is in principle independent across peripheral filters. Our model does not incorporate the correlation of cues across frequency. However, it could be possible that the binaural auditory system does.

Another experimental result that cannot be accounted for by the model is the low-pass characteristic that is obtained with dynamically varying ITDs (Fig. 10). A model that can account for these data is the position-variable model of Stern and Bachorski (1983). In their model, the intracranial locus of the stimulus is estimated by computing a weighted centroid of the running cross-correlation function. The running cross-correlation function is computed using an exponentially decaying averaging window with a fixed time constant. If the ITD is modulated with a period that is longer than the duration of the temporal averager, the peak of the running cross-correlation function follows the externally presented ITD. Consequently, the weighted centroid modulates similarly. If the ITD modulation frequency is increased, the low-pass characteristic of the running cross correlation averages the ITD over time. This results in a lower but wider peak of the cross-correlation function. Moreover, the maximum displacement of the peak decreases. Consequently, the amplitude of the time-varying centroid of the cross correlation *decreases*. Since this centroid is used as a decision variable, thresholds increase with increasing modulation rate. In fact, the model of Stern and Bachorski (1983) was very successful in predicting the data shown in Fig. 10 for the left side of the bell-shaped curve.

It would in principle be possible to modify our model in such a way that it does not use increases in the activity in the EI-type pattern but rather an estimate of the position of the sound source as a decision variable. This can be facilitated by scanning the position of the minimum within the EI-type element activity pattern. The reason that we did not base the model's decision process on a position variable is that such an approach has a detrimental effect on the fits of other data. For example, in our second paper (Breebaart *et al.*, 2001b), NoSπ thresholds were discussed as a function of the bandwidth of the masking noise. The predicted thresholds as well as the experimental data show approximately constant thresholds for bandwidths up to twice the ERB of the peripheral filters. We expect that a position-variable model, independently of whether the binaural interaction is based on EE or EI processing, cannot account for this result. The addition of an Sπ signal to a diotic masker results in the presence of dynamically varying IIDs and ITDs in the stimulus. The rate of fluctuation of these differences depends on the bandwidth; a larger bandwidth corresponds to faster fluctuations. Consequently, the NoSπ thresholds for a position-variable model are expected to increase with increasing bandwidth, which is not in line with the experimental data. In summary, we do not see how the absence of an effect of the ITD modulation rate in bandlimited NoSπ conditions and the clear effect of ITD modulation shown by Grantham and Wightman (1978) can be explained with the same detection mechanism.

Finally, the strong overshoot in the peripheral adaptation loops which results in lower detection thresholds for a binaural signal presented during the first 25 ms of the masker is an unwanted effect. In a certain way, we can end this series of binaural modeling papers with a remark similar to one made at the end of the discussion by Dau *et al.* (1996b). The temporal dynamics and nonlinear compression effects of the adaptation loops are useful in understanding a number of binaural effects like binaural forward masking and the influence of overall interaural level differences on binaural unmasking and on lateralization, while for some specific conditions, their temporal dynamic is too strong. Obviously, we so far have not found the optimal realization of this stage. Therefore, we will, together with our colleagues in Oldenburg, continue in our efforts to improve the understanding of this part of our monaural and binaural models.

ACKNOWLEDGMENTS

The investigations were supported by the Research Council for Earth and Life-sciences (ALW) with financial aid from the Netherlands Organization for Scientific Research (NWO). We would like to thank the Associate Editor Wesley Grantham, Richard Stern, and an anonymous reviewer for their valuable suggestions for improving the original manuscript.

[1]The data adapted from Zwicker and Zwicker (1984) were measured at 400-Hz center frequency instead of 500 Hz. In contrast to the other studies, their masking noise was not spectrally flat but had a spectral energy distribution that is referred to as *uniform masking noise*. The amplitude spectrum of this noise type is spectrally flat from 0 to 500 Hz and decreases with 10 dB/dec above 500 Hz. To be able to use their data, we calculated the spectral energy density of their masking noise at 400-Hz center frequency and used this value to plot the data.

Akeroyd, M. A., and Summerfield, A. Q. (**1999**). "A binaural analog of gap detection," J. Acoust. Soc. Am. **105**, 2807–2820.

Bernstein, L. R., and Trahiotis, C. (**1999**). "The effects of signal duration on NoSo and NoSπ thresholds at 500 Hz and 4 kHz," J. Acoust. Soc. Am. **105**, 1776–1783.

Breebaart, J., and Kohlrausch, A. (**2001**). "The influence of interaural stimulus uncertainty on binaural signal detection," J. Acoust. Soc. Am. **109**, 331–345.

Breebaart, J., van de Par, S., and Kohlrausch, A. (**2001a**). ''Binaural processing model based on contralateral inhibition. I. Model setup,'' J. Acoust. Soc. Am. **110**, 1074–1088.
Breebaart, J., van de Par, S., and Kohlrausch, A. (**2001b**). ''Binaural processing model based on contralateral inhibition. II. Dependence on spectral parameters,'' J. Acoust. Soc. Am. **110**, 1089–1104.
Culling, J. F., and Summerfield, Q. (**1998**). ''Measurements of the binaural temporal window using a detection task,'' J. Acoust. Soc. Am. **103**, 3540–3553.
Dau, T., Kollmeier, B., and Kohlrausch, A. (**1997**). ''Modeling auditory processing of amplitude modulation. II. Spectral and temporal integration,'' J. Acoust. Soc. Am. **102**, 2906–2919.
Dau, T., Püschel, D., and Kohlrausch, A. (**1996a**). ''A quantitative model of the 'effective' signal processing in the auditory system. I. Model structure,'' J. Acoust. Soc. Am. **99**, 3615–3622.
Dau, T., Püschel, D., and Kohlrausch, A. (**1996b**). ''A quantitative model of the 'effective' signal processing in the auditory system. II. Simulations and measurements,'' J. Acoust. Soc. Am. **99**, 3623–3631.
Gabriel, K. J., and Colburn, H. S. (**1981**). ''Interaural correlation discrimination. I. Bandwidth and level dependence,'' J. Acoust. Soc. Am. **69**, 1394–1401.
Glasberg, B. R., and Moore, B. C. J. (**1990**). ''Derivation of auditory filter shapes from notched-noise data,'' Hear. Res. **47**, 103–138.
Grantham, D. W. (**1984**). ''Discrimination of dynamic interaural intensity differences,'' J. Acoust. Soc. Am. **76**, 71–76.
Grantham, D. W., and Wightman, F. L. (**1978**). ''Detectability of varying interaural temporal differences,'' J. Acoust. Soc. Am. **63**, 511–523.
Grantham, D. W., and Wightman, F. L. (**1979**). ''Detectability of a pulsed tone in the presence of a masker with time-varying interaural correlation,'' J. Acoust. Soc. Am. **65**, 1509–1517.
Holube, I., Kinkel, M., and Kollmeier, B. (**1998**). ''Binaural and monaural auditory filter bandwidths and time constants in probe tone detection experiments,'' J. Acoust. Soc. Am. **104**, 2412–2425.
Kohlrausch, A. (**1986**). ''The influence of signal duration, signal frequency and masker duration on binaural masking level differences,'' Hear. Res. **23**, 267–273.
Kohlrausch, A., and Fassel, R. (**1997**). ''Binaural masking level differences in nonsimultaneous masking,'' in *Binaural and Spatial Hearing in Real and Virtual Environments*, edited by R. H. Gilkey and T. Anderson (Lawrence Erlbaum Assoc., Mahwah, NJ), Chap. 9, pp. 169–190.
Kollmeier, B., and Gilkey, R. H. (**1990**). ''Binaural forward and backward masking: evidence for sluggishness in binaural detection,'' J. Acoust. Soc. Am. **87**, 1709–1719.
Perrott, D. R., and Musicant, A. D. (**1977**). ''Minimum auditory movement angle: Binaural localization of moving sound sources,'' J. Acoust. Soc. Am. **62**, 1463–1466.
Plack, C. J., and Moore, B. C. J. (**1990**). ''Temporal window shape as a function of frequency and level,'' J. Acoust. Soc. Am. **87**, 2178–2187.
Punch, J., and Carhart, R. (**1973**). ''Influence of interaural phase on forward masking,'' J. Acoust. Soc. Am. **54**, 897–904.
Robinson, D., and Jeffress, L. (**1963**). ''Effect of varying the interaural noise correlation on the detectability of tonal signals,'' J. Acoust. Soc. Am. **35**, 1947–1952.
Robinson, D. E., and Trahiotis, C. (**1972**). ''Effects of signal duration and masker duration on detectability under diotic and dichotic listening conditions,'' Percept. Psychophys. **12**, 333–334.
Stern, R. M., and Bachorski, S. J. (**1983**). ''Dynamic cues in binaural perception,'' in *Hearing—Physiological Bases and Psychophysics*, edited by R. Klinke and R. Hartmann (Springer, Berlin), pp. 209–215.
Trahiotis, C., Dolan, T. R., and Miller, T. H. (**1972**). ''Effect of backward masker fringe on the detectability of pulsed diotic and dichotic tonal signals,'' Percept. Psychophys. **12**, 335–338.
van der Heijden, M., and Trahiotis, C. (**1997**). ''A new way to account for binaural detection as a function of interaural noise correlation,'' J. Acoust. Soc. Am. **101**, 1019–1022.
Wilbanks, W., and Whitmore, J. (**1968**). ''Detection of monaural signals as a function of interaural noise correlation and signal frequency,'' J. Acoust. Soc. Am. **43**, 785–797.
Wilson, R., and Fowler, C. (**1986**). ''Effects of signal duration on the 500-Hz masking-level difference,'' Scand. Audiol. **15**, 209–215.
Wilson, R., and Fugleberg, R. (**1987**). ''Influence of signal duration on the masking-level difference,'' J. Speech Hear. Res. **30**, 330–334.
Yama, M. (**1992**). ''Effects of temporal separation and masker level on binaural analysis in forward masking,'' J. Acoust. Soc. Am. **91**, 327–335.
Yost, W. A. (**1985**). ''Prior stimulation and the masking-level difference,'' J. Acoust. Soc. Am. **78**, 901–906.
Zwicker, U. T., and Zwicker, E. (**1984**). ''Binaural masking-level difference as a function of masker and test-signal duration,'' Hear. Res. **13**, 215–220.

Spatial unmasking of nearby speech sources in a simulated anechoic environment

Barbara G. Shinn-Cunningham[a)]
Boston University Hearing Research Center, Departments of Cognitive and Neural Systems and Biomedical Engineering, Boston University, 677 Beacon St., Room 311, Boston, Massachusetts 02215

Jason Schickler
Boston University Hearing Research Center, Department of Biomedical Engineering, Boston University, Boston, Massachusetts 02215

Norbert Kopčo
Boston University Hearing Research Center, Department of Cognitive and Neural Systems, Boston University, Boston, Massachusetts 02215

Ruth Litovsky
Boston University Hearing Research Center, Department of Biomedical Engineering, Boston University, Boston, Massachusetts 02215

(Received 18 August 2000; revised 24 May 2001; accepted 25 May 2001)

Spatial unmasking of speech has traditionally been studied with target and masker at the same, relatively large distance. The present study investigated spatial unmasking for configurations in which the simulated sources varied in azimuth and could be either near or far from the head. Target sentences and speech-shaped noise maskers were simulated over headphones using head-related transfer functions derived from a spherical-head model. Speech reception thresholds were measured adaptively, varying target level while keeping the masker level constant at the ''better'' ear. Results demonstrate that small positional changes can result in very large changes in speech intelligibility when sources are near the listener as a result of large changes in the overall level of the stimuli reaching the ears. In addition, the difference in the target-to-masker ratios at the two ears can be substantially larger for nearby sources than for relatively distant sources. Predictions from an existing model of binaural speech intelligibility are in good agreement with results from all conditions comparable to those that have been tested previously. However, small but important deviations between the measured and predicted results are observed for other spatial configurations, suggesting that current theories do not accurately account for speech intelligibility for some of the novel spatial configurations tested.
[DOI: 10.1121/1.1386633]

PACS numbers: 43.66.Pn, 43.66.Ba, 43.71.An, 43.66.Rq [LRB]

I. INTRODUCTION

When a target of interest (T) is heard concurrently with an interfering sound (a ''masker,'' M), the locations of both target and masker have a large effect on the ability to detect and perceive the target. Previous studies have examined how T and M locations affect performance in both detection (e.g., see the review in Durlach and Colburn, 1978 or, for example, recent work such as Good, Gilkey, and Ball, 1997) and speech intelligibility tasks (e.g., see the recent review by Bronkhorst, 2000). Generally speaking, when the T and M are located at the same position, the ability to detect or understand T is greatly affected by the presence of M; when either T or M is displaced, performance improves.

While there are many studies of spatial unmasking for speech (e.g., see Hirsh, 1950; Dirks and Wilson, 1969; MacKeith and Coles, 1971; Plomp and Mimpen, 1981; Bronkhorst and Plomp, 1988; Bronkhorst and Plomp, 1990; Peissig and Kollmeier, 1997; Hawley, Litovsky, and Colburn, 1999), all of the previous studies examined targets and maskers that were located far from the listener. These studies examined spatial unmasking as a function of angular separation of T and M without considering the effect of distance. One goal of the current study was to measure spatial unmasking for a speech reception task when a speech target and a speech-shaped noise masker are within 1 meter of the listener. In this situation, changes in source location can give rise to substantial changes in both the overall level and the binaural cues in the stimuli reaching the ears (e.g., see Duda and Martens, 1997; Brungart and Rabinowitz, 1999; Shinn-Cunningham, Santarelli, and Kopčo, 2000). Because the acoustics for nearby sources can differ dramatically from those of more distant sources, insights gleaned from previous studies may not apply in these situations. In addition, previous models (which do a reasonably good job of predicting performance on similar tasks; e.g., see Zurek, 1993) may not be able to predict what occurs when sources are close to the listener precisely because the acoustic cues at the ears are so different than those that arise for relatively distant sources.

For noise maskers that are statistically stationary (such

a)Electronic mail: shinn@cns.bu.edu

 0001-4966/2001/110(2)/1118/12/$18.00

as steady-state broadband noise in anechoic settings, but not, for instance, amplitude-modulated noise or speech maskers), spatial unmasking can be predicted from simple changes in the acoustic signals reaching the ears (e.g., see Bronkhorst and Plomp, 1988; Zurek, 1993). For T fixed directly in front of a listener, lateral displacement of M causes changes in (1) the relative level of the T and M at the ears (i.e., the target to masker level ratio, or TMR), which will differ at the two ears (a monaural effect) and (2) the interaural differences in T compared to M (a binaural effect, e.g., see Zurek, 1993). For relatively distant sources, the first effect arises because the level of the masker reaching the farther ear decreases (particularly at moderate and high frequencies) as the masker is displaced laterally (giving rise to the acoustic ''head shadow''). Thus, as M is displaced from T, one of the two ears will receive less energy from M, resulting in a ''better-ear advantage.'' Also, for relatively distant sources the most important binaural contribution to unmasking occurs when T and M give rise to different interaural time differences (ITDs), resulting in differences in interaural phase differences (IPDs) in T and M, at least at some frequencies (e.g., see Zurek, 1993). The overall size of the release from masking that can be obtained when T is located in front of the listener and a steady-state M is laterally displaced (and both are relatively distant from the listener) is on the order of 10 dB (e.g., see Plomp and Mimpen, 1981; Bronkhorst and Plomp, 1988; Peissig and Kollmeier, 1997; Bronkhorst, 2000). Of this 10 dB, roughly 2–3 dB can be attributed to binaural processing of IPDs, with the remainder resulting from head shadow effects (e.g., see Bronkhorst, 2000).

If one restricts the target and masker to be at least 1 meter from the listener, the only robust effect of distance on the stimuli at the ears is a change in overall level (e.g., see Brungart and Rabinowitz, 1999). Thus, for relatively distant sources, the effect of distance can be predicted simply from considering the dependence of overall target and masker level on distance; there are no changes in binaural cues, the better-ear-advantage, or the difference in the TMR at the better and worse ears.

There are important differences between how the acoustic stimuli reaching the ears change when a sound source is within a meter of and when a source is more than a meter from the listener (e.g, see Duda and Martens, 1997; Brungart and Rabinowitz, 1999; Shinn-Cunningham *et al.*, 2000). For instance, a small displacement of the source towards the listener can cause relatively large increases in the levels of the stimuli at the ears. In addition, for nearby sources, the interaural level difference (ILD) varies not only with frequency and laterality but also with source distance. Even at relatively low frequencies, for which naturally occurring ILDs are often assumed to be zero (i.e., for sources more than about a meter from the head), ILDs can be extremely large. In fact, these ILDs can be broken down into the traditional ''head shadow'' component, which varies with direction and frequency, and an additional component that is frequency independent and varies with source laterality and distance (Shinn-Cunningham *et al.*, 2000).

In the ''distant'' source configurations previously studied, the better ear is only affected by the relative laterality of T versus M; the only spatial unmasking that can arise for T and M in the same direction is a result of equal overall level changes in the stimuli at the two ears. Moving T closer than M will improve the SRT while moving T farther away will decrease performance, simply because the level of the target at both ears varies with distance (equivalently). In contrast, when a source is within a meter of the head, the relative level of the source at the two ears depends on distance. Changing the distance of T or M can lead not only to changes in overall energy, but changes in the amount of unmasking that can be attributed to binaural factors, the difference in the TMR at the two ears (as a function of frequency), and even which is the better ear. In addition, overall changes in the level at the ears can be very large, even for small absolute changes in distance. Although the distances for which these effects arise are small, in a real ''cocktail party'' it is not unusual for a listener to be within 1 meter of a target of interest (i.e., in the range for which these effects are evident).

We are aware of only one previous study of spatial unmasking for speech intelligibility in which large ILDs were present in both T and M (Bronkhorst and Plomp, 1988). In this study, the total signal to one ear was attenuated in order to simulate monaural hearing impairment. Unlike the Bronkhorst and Plomp study, the current study focuses on the spatial unmasking effects that occur when realistic combinations of IPD and ILD, consistent with sources within 1 m of the listener, are simulated for different T and M geometries.

II. EXPERIMENTAL APPROACH

A common measure used to assess spatial unmasking effects on speech tasks is the speech reception threshold (SRT), or the level at which the target must be presented in order for speech intelligibility to reach some predetermined threshold level. The amount of spatial unmasking can be summarized as the difference (in dB) between the SRT for the target/masker configuration of interest and the SRT when T and M are located at the same position.

In these experiments, SRT was measured for both ''nearby'' sources (15 cm from the center of the listener's head) and ''distant'' sources (1 m from the listener). Tested conditions included those in which (1) the speech target was in front of the listener and M was displaced in angle and distance; (2) M was in front of the listener and T displaced in angle and distance; and (3) T and M were both located on the side, but T and M distances were manipulated.

The goals of this study were to (1) measure how changes in spatial configuration of T and M affect SRT for sources near the listener; (2) explore how the interaural level differences that arise for nearby sources affect spatial unmasking; and (3) quantify the changes in the acoustic cues reaching the two ears when T and/or M are near the listener.

A. Subjects

Four healthy undergraduate students (ages ranging from 19–23 years) performed the tests. All subjects had normal hearing thresholds (within 15 dB HL) between 250 and 8000 Hz as verified by an audiometric screening. All subjects were native English speakers. One of the subjects was author JS

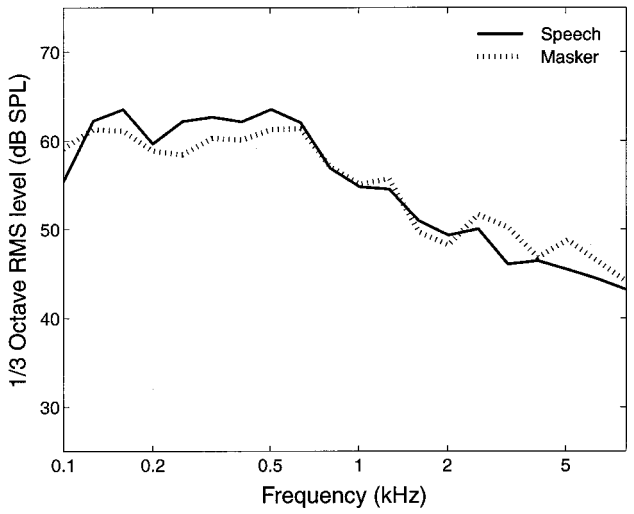

FIG. 1. Average spectral shape of speech-shaped noise masker and speech targets, prior to HRTF processing.

with relatively little experience in psychoacoustic experiments; the other three subjects were naive listeners with no prior experience.

B. Stimuli

1. Source characteristics

In the experiments, the target (T) consisted of a high-context sentence selected from the IEEE corpus (IEEE, 1969). Sentences were chosen from 720 recordings made by two different male speakers. These materials have been employed previously in similar speech intelligibility experiments (Hawley *et al.*, 1999). The recordings, ranging from 2.41–3.52 s in duration, were scaled to have the same rms pressure value in their ''raw'' (nonspatialized) forms. An example sentence is ''The DESK and BOTH CHAIRS were PAINTED TAN,'' with capitalized words representing ''key words'' that are scored in the experiment (see Sec. C).

The masker (M) was speech-shaped noise generated to have the same spectral shape as the average of the speech tokens used in the study. For each masker presentation, a random 3.57-s sample was taken from a long (24-s) sample of speech-shaped noise (this length guaranteed that all words in all sentences were masked by the noise). Figure 1 shows the rms pressure level in 1/3-octave bands (dB SPL) of the 24-s-long masking noise and the average of the spectra of the speech samples used in the study.

2. Stimulus generation

Raw digital stimuli (i.e., IEEE sentences and speech-shaped noise sampled at 20 kHz) were convolved with spherical-head head-related transfer functions (HRTFs) off-line (see below). T and M were then scaled (in software) to the appropriate level for the current configuration and trial. The resulting binaural T and M were then summed in software and sent to Tucker-Davis Technologies (TDT) hardware to be converted into acoustic stimuli (using the same equipment setup described in Hawley *et al.*, 1999). Digital signals were processed through left- and right-channel D/A converters (TDT DD3-8), low-pass filters (10-kHz cutoff; TDT FT5), and attenuators (TDT PA4). The resulting binaural analog signals were passed through a Tascam power amplifier (PA-20 MKII) connected to Sennheiser headphones (HD 520 II). No compensation for the headphone transfer function was performed. A personal computer (Gateway 2000 486DX) controlled all equipment and recorded results.

3. Spatial cues

In order to simulate sources at different positions around the listener, spherical-head HRTFs were generated for all the positions from which sources were to be simulated. These HRTFs were generated using a mathematical model of a spherical (9-cm-radius) head with diametrically opposed point receivers (ears; for more details about the model or traits of the resulting HRTFs see Rabinowitz *et al.*, 1993; Brungart and Rabinowitz, 1999; Shinn-Cunningham *et al.*, 2000). Source stimuli (T and M) were convolved to generate binaural signals similar to those that a listener would experience if the T and M were played from specific positions in anechoic space.

It should be noted that the spherical-head HRTFs are not particularly realistic. They contain no pinnae cues (i.e., contain no elevation information), are more symmetrical than true HRTFs, and are not tailored to the individual listener. As a result, sources simulated from these HRTFs are distinguishably different from sounds that would be heard in a real-world anechoic space. As a result, the sources simulated with these HRTFs may not have been particularly ''externalized,'' although they were generally localized at the simulated direction. There was no attempt to evaluate the realism, externalization, or localizability of the simulated sources using the spherical-head HRTFs. Nonetheless, the spherical-head HRTFs contain all the acoustic cues that are unique to sources within 1 m of the listener (i.e., large ILDs that depend on distance, direction, and frequency; changes in IPD with changes in distance), a result confirmed by comparisons with measurements of human subject and KEMAR HRTFs for sources within 1 m (see, for example, Brown, 2000; Shinn-Cunningham, 2000). Further, because the unique acoustic attributes that arise for free-field near sources are captured in these HRTFs, we believe that any unique behavioral consequences of listening to targets and maskers that are near the listener will be observed in these experiments.

4. Spatial configurations

In different conditions, the target and masker were simulated from any of six locations in the horizontal plane containing the ears; that is, at three azimuths (0°, 45°, and 90° to the right of midline) and two distances from the center of the head (15 cm and 1 m). The 15 spatial configurations investigated in this study are illustrated in Fig. 2. The three panels depict three different conditions: target location fixed at (0°, 1 m) [Fig. 2(a)], masker fixed at (0°, 1 m) [Fig. 2(b)] and target and masker both at 90° [Fig. 2(c)]. All subsequent graphs are arranged similarly. Note that the configuration in which T and M are both located at (0°, 1 m) appears in both panels (a) and (b) of Fig. 2; this spatial configuration was the (diotic) reference used in computing spatial masking effects.

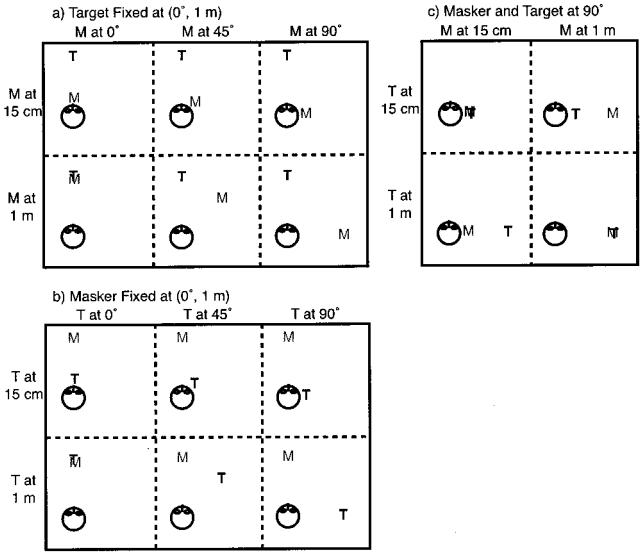

FIG. 2. Spatial configurations of target (T) and masker (M). Conditions: (a) T fixed (0°, 1 m); (b) M fixed (0°, 1 m); and (c) T and M at 90°.

5. Presentation level

If we had simulated a masking source emitting the same energy from different distances and directions, the level of the masker reaching the better ear would vary dramatically with the simulated position of M. In addition, depending on the location of M, the better ear can be either the ear nearer or farther from T. For instance, if T is located at (90°, 1 m) and M is located at (90°, 15 cm) [see Fig. 2(c), bottom left panel], T is nearer to the right ear, but the left ear will be the ''better ear.''

In order to roughly equate the masker energy *reaching the better ear* (as opposed to keeping constant the distal energy of the simulated masker), masker level was normalized so that the root-mean-square (rms) pressure of M at the better ear was always 72 dB SPL. With this choice, the masker was always clearly audible at the worse ear (even when the masker level was lower at the worse ear) and at a comfortable listening level at the worse ear (even when the masker level was higher at the worse ear). Of course, the worse-ear masker level varied with spatial configuration, and could either be greater or less than 72 dB SPL depending on the locations of T and M.

C. Experimental procedure

All experiments were performed in a double-walled sound-treated booth in the Binaural Hearing Laboratory of the Boston University Hearing Research Center.

An adaptive procedure was used to estimate the SRT for each spatial configuration of T and M. In each adaptive run, the T level was adaptively varied to estimate the SRT, which was defined as the level at which subjects correctly identified 50% of the T sentence key words.

For each configuration, at least three independent, adaptive-run threshold estimates were averaged to form the final threshold estimate. If the standard error in the repeated measures was greater than 1 dB, additional adaptive runs were performed until the standard error in this final average was equal to or less than 1 dB.

The T and M locations were not known *a priori* by the subject, but were held constant through a run, which consisted of ten trials. Runs were ordered randomly and broken into sessions consisting of approximately seven runs each.

Within a run, the first sentence of each block was repeated multiple times in order to set the T level for subsequent trials. The first sentence in each run was first played at 44 dB SPL in the better ear. The sentence was played repeatedly, with its intensity increased by 4 dB with each repetition, until the subject indicated (by subjective report) that he could hear the sentence. The level at which the listener reported understanding the initial sentence set the T level for the second trial in the run. On each subsequent trial, a new sentence was presented to the subject. The subject typed in the perceived sentence on a computer keyboard. The actual sentence was then displayed (along with the subject's typed response) on a computer monitor (visible to the subject) with five ''key words'' capitalized. The subject then counted up and entered into the computer the number of correct key words perceived. Scoring was strict, with incorrect suffixes scored as ''incorrect;'' however, homophones and misspellings were not penalized. Listeners heard only one presentation of each T sentence.

If the subject identified at least three of the five key words correctly, the level of the T was decreased by 2 dB on the subsequent trial. Otherwise (i.e., if the subject identified two or fewer key words), the level of the T was increased by 2 dB. Thus, if the subject performed at or above 60% correct, the task was made more difficult; if the subject performed at or below 40% correct, the task was made easier. This procedure (which, in the limit, will converge to the presentation level at which the subject will achieve 50% correct) was repeated until ten trials were scored. SRT was estimated as the average of the presentation levels of the T on the last eight (of ten) trials.

III. RESULTS

A. Target-to-masker levels at speech reception threshold

In order to visualize the changes in relative spectral levels of T and M with spatial configuration, the average TMR in third-octave spectral bands was computed as a function of center frequency at 50%-correct SRT and plotted in Fig. 3.

By construction (because T and M have the same spectral shape), the TMR is equal in both ears and independent of frequency for configurations in which T and M are located at the same position (i.e., for two diotic configurations and two configurations with T and M at 90°). However, in general, the overall spectral shape of both T and M depends on spatial configuration and the TMR varies with frequency.

In the diotic reference configuration, the TMR is −7.6 dB [e.g., see Fig. 3(a), bottom left panel]. In other words, when the diotic sentence is presented at a level 7.6 dB below the diotic speech-shaped noise, subjects achieve threshold performance in the reference configuration. This diotic reference TMR is plotted as a dashed horizontal line in all panels

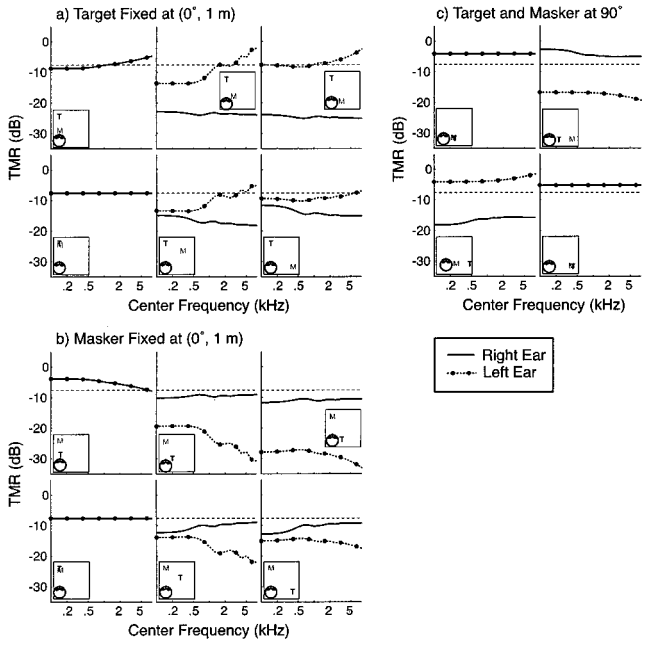

FIG. 3. Target-to-masker level ratio (TMR) in 1/3-octave frequency bands for left (dotted lines with symbols) and right (solid lines) ears as a function of center frequency at speech reception threshold. Conditions: (a) T fixed (0°, 1 m); (b) M fixed (0°, 1 m); and (c) T and M at 90°.

in order to make clear how the TMR varies with spatial configuration. When threshold TMR at the better ear is lower than the diotic reference TMR, the results indicate the presence of spatial masking effects that cannot be explained by overall level changes. In such cases, other factors, such as differences in binaural cues in T and M, are likely to be responsible for the improvements in SRT.

Figure 3(a) shows the results when T is fixed at (0°, 1 m). For these spatial configurations, the TMR at the better (left) ear (dotted line with symbols) is generally equal to or smaller than the reference TMR. TMR is lowest when M is located at (45°, 1 m) (bottom center panel); in this case, the TMR at low frequencies is as much as 14 dB below the diotic reference TMR (the TMR at higher frequencies is approximately equal to the diotic reference TMR). The worse-ear TMR (right ear; solid line) is often much smaller than that of the better ear, particularly when M is at 15 cm.

When the masker is fixed at the reference position (0°, 1 m) [Fig. 3(b)], the TMR at the better (right) ear (solid line) is below the reference TMR at all frequencies for all four cases in which T is laterally displaced. The magnitude of this improvement is roughly the same (2–3 dB) whether T is near or far, at 45° or 90°. In the diotic case for which T is at (0°, 1 m) and M is at (0°, 15 cm) [top-left panel in Fig. 3(b)], the TMR is roughly 4 dB larger than in the diotic reference configuration. This result indicates a small spatial *dis*-advantage in this diotic configuration compared to the ''typical'' diotic reference configuration when T and M are both distant after taking into account the overall level of M.

In all four configurations for which both T and M are located laterally [Fig. 3(c)], the TMR at the better ear is roughly 3–4 dB larger at all frequencies than the diotic reference TMR. In other words, listeners need a laterally located speech source to be presented at a relatively high level when it competes with a masker located in the same lateral direction. This is even true when M is at 1 m and T is at 15 cm [top right panel of Fig. 3(c)], despite the fact that the better- (right-) ear stimulus is at a substantially higher overall level than the worse- (left-) ear stimulus in this configuration.

B. Mean difference in monaural TMRs

The results in Fig. 3 show that the difference in the TMRs at the two ears can be very large when either T or M is near the listener (a direct consequence of the very large ILDs that arise for these sources). This difference is important for understanding and quantifying the advantage of having two ears, independent of any binaural processing advantage. For instance, if a monaurally impaired listener's intact ear is the acoustically worse ear, the impaired listener will be at a larger disadvantage for many of the tested configurations than when both T and M are distant. In order to quantify the magnitude of these acoustic effects, the absolute value of the mean of the difference in left- and right-ear TMR was calculated, averaged across frequencies up to 8000 Hz.

The leftmost data column in Table I gives the mean of $|\mathrm{TMR}_{\mathrm{right}}-\mathrm{TMR}_{\mathrm{left}}|$ at SRT, averaged across frequency. Because the TMRs change with frequency, this estimate cannot predict SRT directly; for instance, moderate frequencies (e.g., 2000–5000 Hz) convey substantially more speech information than lower frequencies. Nonetheless, these calculations give an objective, acoustic measure, weighting all frequencies equally, of differences in the better and worse ear signals.

From symmetry and because T and M have the same spectral shape, the difference in better- and worse-ear TMR is the same if M is held at (0°, 1 m) and T is moved or T is fixed and M is moved (see Table I, comparing top and center sections).

For configurations in which both T and M are far from the head, the acoustic difference in the TMRs at the two ears ranges from 5–10 dB, depending on the angular separation of T and M. If T remains fixed and a laterally located M is moved from 1 m to 15 cm (or vice versa), the difference between the better and worse ear TMR increases substantially. For instance, with T fixed at (0°, 1 m) and M at (90°, 15 cm), the difference in TMR is nearly 20 dB (third line in Table I). For spatial configurations in which one source is near the head but not in the median plane, part of this difference in better- and worse-ear TMR arises from ''normal'' head-shadow effects and part arises due to differences in the relative distance from the source to the two ears (Shinn-Cunningham *et al.*, 2000).

In the configurations for which both T and M are located at 90°, there is no difference in the TMR at the ears when T and M are at the same distance. When one source is near and one is far, the TMR at the ears differs by roughly 13 dB.

It should be noted that there are even more extreme spatial configurations than those tested here. For instance, with T at (−90°, 15 cm) and M at (+90°, 15 cm) the acoustic difference in the TMRs at the two ears would be on the order of 40 dB (i.e., twice the difference obtained when one

TABLE I. Spatial effects for different spatial configurations tested. Leftmost data column shows the mean of the absolute difference $|TMR_{right} - TMR_{left}|$ at SRT, averaged across frequencies up to 8000 Hz. The second data column gives the predicted magnitude of the difference in the monaural left- and right-ear SRTs from the Zurek model calculations. The third data column gives the binaural advantage calculated from Zurek model calculations (the difference in predicted SRT for binaural and monaural better-ear listening conditions).

			Left/right asymmetry (acoustic analysis) (dB)	Left/right asymmetry (Zurek predictions) (dB)	Binaural advantage (Zurek predictions) (dB)
T (0°, 1 m)	M (15 cm)	M (0°)	0	0	0
		M (45°)	17.5	14.6	2.0
		M (90°)	19.6	17.9	1.5
	M (1 m)	M (0°)	0	0	0
		M (45°)	9.8	7.5	2.4
		M (90°)	6.4	5.2	2.2
M (0°, 1 m)	T (15 cm)	T (0°)	0	0	0
		T (45°)	17.5	14.5	1.5
		T (90°)	19.6	17.2	1.5
	T (1 m)	T (0°)	0	0	0
		T (45°)	9.8	7.5	1.9
		T (90°)	6.4	5.2	2.2
T & M (90°)	T (15 cm)	M (15 cm)	0	0	0
		M (1 m)	13.2	12.6	0.8
	T (1 m)	M (15 cm)	13.2	12.6	0.9
		M (1 m)	0	0	0

source is diotic and one source is at 90°, 15 cm). This analysis demonstrates that one novel outcome of T and M being very close to the head is that the difference in the TMRs at the two ears can be dramatically larger than in previously tested configurations.

C. Spatial unmasking

Figure 4 plots the amount of spatial unmasking for each spatial configuration.[1] In the figure, the amount of ''spatial unmasking'' equals the decrease in the distal energy the target source must emit for subjects to correctly identify 50% of the target key words if the distal energy emitted by the masking source were held constant. This analysis includes changes in the overall level of T and M reaching the ears with changes in source position (and assumes that SRT depends only on TMR and is independent of the absolute level of the masker for the range of levels considered).

When T is fixed at (0°, 1 m) [Fig. 4(a)], the release from masking is largest when the 1-m M is at 45° and decreases slightly when M is at 90°. The dependence of the unmasking on M distance is roughly the same for all M directions: moving M from 1 m to 15 cm increases the required T level by roughly 13 dB for M in all tested directions (0°, 45°, and 90°).

When M is fixed ahead [Fig. 4(b)], moving the 1-m-distant T to either 45° or 90° results in the same unmasking. Moving the T close to the head (15 cm) results in a large amount of spatial unmasking, primarily due to increases in the level of T reaching the ears. For a given T direction, the effect of decreasing the distance of T increases with its lateral angle.

Figure 4(c) shows the spatial unmasking that arises when T and M are both located at 90°. When T and M are at the same distance [either at 15 cm, circles at left of Fig. 4(c); or at 1 m, squares at right of Fig. 4(c)], there is a 3-dB increase in the level the target source must emit compared to the reference configuration. When T and M are at different distances, spatial unmasking results are dominated by differences in the relative distances to the head.

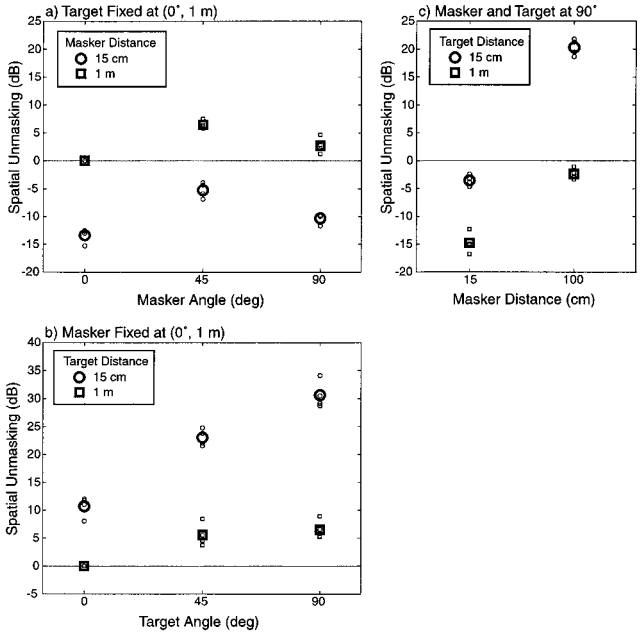

FIG. 4. Spatial advantage (energy a target emits at threshold for a constant-energy masker) relative to the diotic configuration. Positive values are decreases in emitted target energy. Large symbols give the across-subject mean; small symbols show individual subject results. Conditions: (a) T fixed (0°, 1 m); (b) M fixed (0°, 1 m); and (c) T and M at 90°.

D. Discussion

Our findings are generally consistent with previous results that show that speech intelligibility improves when T and M give rise to different IPDs, and that spatially separating a masker and target tends to reduce threshold TMR.

However, in some of the spatial configurations tested, the threshold TMR at the better ear is greater than the TMR in the diotic reference configuration. For instance, in all four spatial configurations with T and M at 90° [Fig. 3(c)], the better-ear TMR is roughly the same (independent of the relative levels of the better and worse ears) and elevated compared to the TMR in the diotic reference configuration. These results are inconsistent with predictions from previous models, which generally assume that binaural performance is always at least as good as would be observed if listeners were presented with the better-ear stimulus monaurally. Discrepancies between the current findings and predictions from an existing model (Zurek, 1993) are considered in detail in the next section.

For distant sources, changing the distance of T or M may change the overall level at the better ear, but it causes an essentially identical change at the worse ear. Thus, the difference between listening with the worse and the better ears is independent of T and M distance when T and M are at least 1 m from the listener. One of the novel effects that arises when either T or M is within 1 meter of the head is that the difference between the TMR at the better and worse ears can be dramatically larger than if both T and M are distant (see Table I). For the configurations tested, the difference in the TMRs at the two ears can be nearly double the difference that occurs when both T and M are at least a meter from the listener [e.g., 19.6 dB for a diotic T and M at (90°, 15 cm) versus 9.8 dB for diotic T and M at (90°, 1 m)].

Analysis of the spatial unmasking (Fig. 4) emphasizes the large changes in overall level that can arise with small displacements of a source near the listener. For the configurations tested, the change in the level that the target must emit to be intelligible against a constant level masker ranges from -31 to $+15$ dB (relative to the diotic reference configuration).

IV. MODEL PREDICTIONS

A. Zurek model of spatial unmasking of speech

Zurek (1993) developed a model based on the Articulation Index (AI,[2] Fletcher and Galt, 1950; ANSI, 1969; Pavlovic, 1987) to predict speech intelligibility as a function of target and masker location. AI is typically computed for a single-channel system as a weighted sum of target-to-masker ratios (TMRs) across third-octave frequency bands. In Zurek's model, the TMRs at both ears are considered, along with interaural differences in the T and M.

To compute the predicted intelligibility, Zurek's model first computes the actual TMR at each ear in each of 15 third-octave frequency bands (spaced logarithmically between 200 to 5000 Hz). The "effective TMR" (R_i) in each frequency band i is the sum of (1) the larger of the two true TMRs at the left and right ears and (2) an estimate of the "binaural advantage" in band i. The binaural advantage in each band, derived from a simplified version of Colburn's model of binaural interaction (Colburn, 1977a, b), depends jointly on center frequency and the relative IPD of target and masker at the center frequency of the band. The advantage in a particular frequency band equals the estimated binaural masking level difference (BMLD) for a "comparable" tone-in-noise detection task. Specifically, if the difference in the IPD of T and M at the center frequency of band i is equal to x rad, the binaural advantage in band i is estimated as the expected BMLD when detecting a tone at the band center frequency in the presence of a diotic masker when the tone has an IPD of x rad. The maximum binaural advantage in a band [taken directly from Zurek, 1993, Fig. 15.2, and shown in Fig. 5(a) as a function of frequency] occurs when, at the band center frequency, the IPD of T and M differ by π rad. When the difference in the T and M IPD at the band center frequency is less than π rad, the binaural advantage in the band is lower (in accord with the Colburn model). The amount of information (γ_i) in each band (the "band efficiency") is computed as

$$\gamma_i = \begin{cases} 0, & R_i < -12 \text{ dB} \\ R_i + 12, & -12 \text{ dB} < R_i < 18 \text{ dB}. \\ 30, & R_i > 18 \text{ dB} \end{cases} \quad (1)$$

This operation assumes that there is no incremental improvement in target audibility with increases in TMR above some asymptote (i.e., 18 dB) and no decrease in target audibility with additional decrements in TMR once the target is below masked threshold (i.e., -12 dB). The analysis implicitly assumes that the target is well above absolute threshold. Finally, the values of γ_i are multiplied by the frequency-dependent weights shown in Fig. 5(b) (which represent the relative importance of each frequency band for understanding speech) and summed to estimate the effective AI. The effective AI can take on values between 0.0 (if all R_i are less than or equal to 12 dB) and 1.0 (if all R_i are greater than or

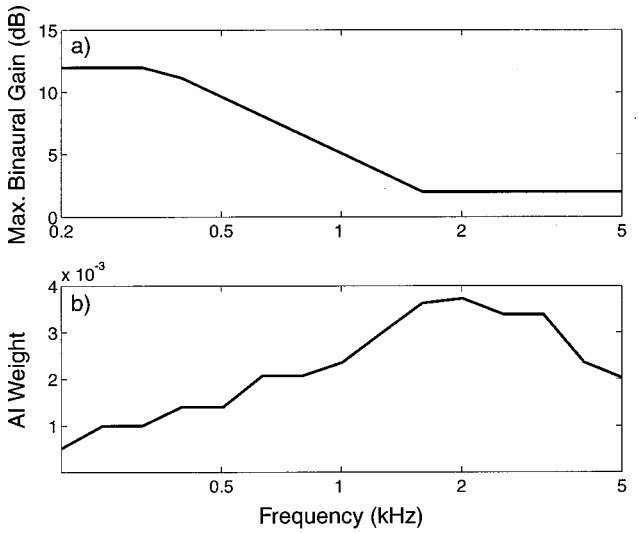

FIG. 5. Binaural AI model assumptions (Zurek, 1993). Panel (a) shows maximal binaural advantage (improvement in effective target-to-masker level ratio or TMR) as a function of frequency, which only arises when IPD of T and M differ by 180°. Panel (b) shows weighting of information at each frequency for speech intelligibility.

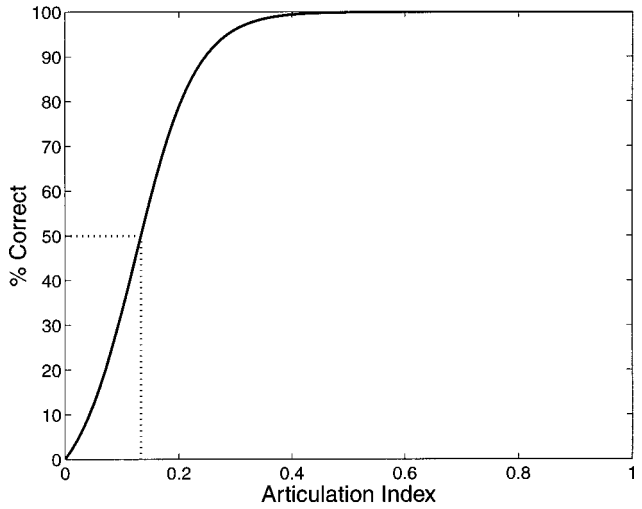

FIG. 6. Assumed relationship between AI and percent words correct assumed for high-context speech (as described in Hawley, 2000). Dashed lines show threshold level for the experiments reported herein.

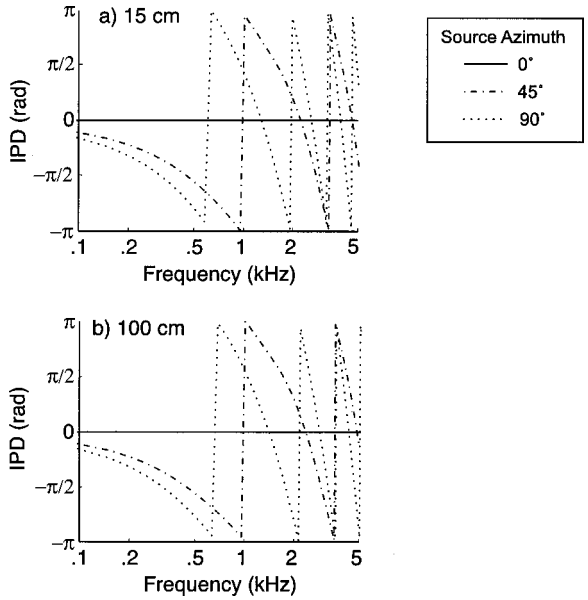

FIG. 7. Interaural phase differences as a function of frequency for the spherical-head HRTFs. (a) Near distance (15 cm) in top panel. (b) Far distance (1 m).

equal to 18 dB). For a given speech intelligibility task and a given set of speech materials, percent correct is a monotonic function of AI (e.g., see Kryter, 1962); for the high-context speech materials used in the present study, this correspondence, as derived by Hawley (2000), is shown in Fig. 6.

Using this model, Zurek (1993) was able to predict the spatial unmasking effects observed in a number of studies that used steady-state maskers (such as broadband noise) and positioned both T and M at a distance of at least 1 m from the subject (e.g., Dirks and Wilson, 1969; Plomp and Mimpen, 1981; Bronkhorst and Plomp, 1988, among others). In this paper, we apply this model to cases when the target and/or masker are close to the subject (i.e., 15 cm).

B. Predicted speech intelligibility at speech reception threshold

In order to calculate model predictions of the current results, the IPDs in the spherical-head HRTFs were analyzed. Figure 7, which plots the IPD in the HRTFs (as a function of frequency) for the positions used in the study, shows that IPD varies dramatically with source laterality and only slightly with distance (e.g., see Brungart and Rabinowitz, 1999; Shinn-Cunningham *et al.*, 2000). Using the left- and right-ear TMRs at the measured SRT (Fig. 3), the difference in T and M IPD was used to compute the effective TMR (the TMR at the better ear, adjusted for binaural gain) and the ''band efficiency'' in each frequency band. From these values, the AI was calculated and used to predict percentage correct key words using the mapping shown in Fig. 6.

We applied a similar analysis to the left and right ear stimuli in isolation (i.e., for a comparable configuration but with one of the ears ''turned off''). To generate these monaural predictions, the appropriate monaural TMR (Fig. 3) was used to compute the AI directly (excluding any binaural contributions). In this way, we predicted not only the percentage-correct words for binaural stimuli but also left- and right-ear monaural stimuli.

Figure 8 shows the predicted percentage correct on our high-context speech task when the T and M levels equaled those presented at SRT. Predictions are shown for binaural listeners (x's) as well as monaural-left and monaural-right listeners (triangles and circles, respectively). The relative levels of T and M used in the predictions are those at which subjects correctly identified approximately 50% of the sentence key words. Thus, the model correctly predicts an observed result when the prediction is close to 50%. For our purposes, predictions falling within the gray area in each panel (within 10% of the defined 50%-correct threshold) are considered to match measured performance.[3] Note that in the

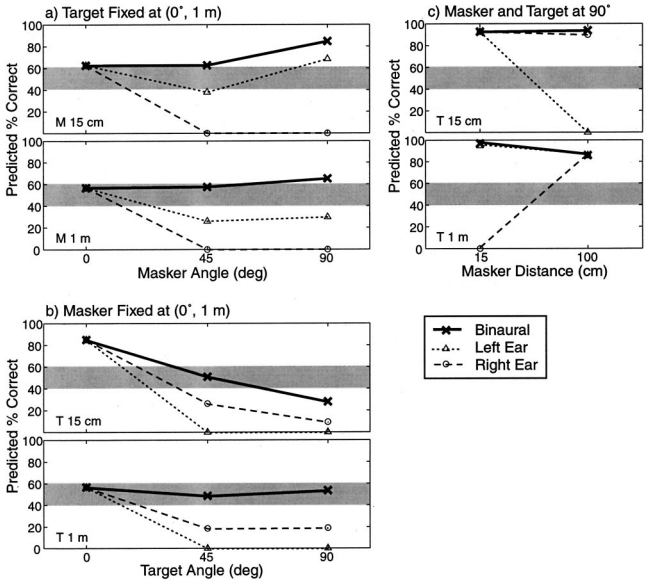

FIG. 8. Predicted percent-correct word scores from model using TMRs and binaural cues present at threshold (actual performance indicated by gray region). Bold exes show binaural model predictions; triangles and circles give monaural, left- and right-ear predictions, respectively. Conditions: (a) T fixed (0°, 1 m) and M at each of 6 locations; (b) M fixed (0°, 1 m) and T at each of 6 locations; and (c) T and M at 90° and 15 cm or 1 m.

model, predicted monaural performance (triangles or circles) is always less than or equal to binaural performance (exes), because any binaural processing will only increase the AI calculated from the better ear (and hence the predicted level of performance).

The one constant feature in Fig. 8 concerns the worse-ear monaural predictions. In every configuration for which the TMR differs in the two ears [four in Fig. 8(a) (circles), four in Fig. 8(b) (triangles), and two in Fig. 8(c) (rightmost triangle in top panel, leftmost circle in bottom panel)] the worse-ear, predicted percent correct is 0%.

Figure 8(a) shows predictions for T fixed ahead. For the diotic configurations [left side of Fig. 8(a)] both ears receive the same stimulus, left- and right-ear monaural predictions are identical, and there is no predicted benefit from listening binaurally. For all configurations in which M is at 1 m [lower panel, Fig. 8(a)], binaural predictions fall within or slightly above the expected range. Predictions for the better (left) ear are near 30% correct when the 1-m M is positioned laterally. When M is at 15 cm [upper panel in Fig. 8(a)], the binaural model predictions are generally higher than observed performance, but the error is only significant when M is at (90°, 15 cm) (binaural prediction near 90% correct). The monaural better-ear prediction is slightly below measured performance when M is at (45°, 15 cm) and substantially above measured performance when M is at (90°, 15 cm).

Figure 8(b) shows the predictions when M is fixed at (0°, 1 m). For this condition, the binaural predictions fit the data well for all configurations in which T is at the farther (1 m) distance [lower panel in Fig. 8(b)]. For the distant, laterally displaced T, better-ear predictions fall well below true binaural performance (19% correct for T at 45° and 90°). When T is at 15 cm, the binaural model predictions are less accurate, overestimating performance for T at 0° and underestimating performance for T at 90°.

In all four configurations in which T and M are positioned at 90° [Fig. 8(c)], the model predicts that both binaural performance and monaural better-ear performance should be much better than what was actually observed, with the predictions ranging from 86% to 95% correct.

C. Predicted spatial unmasking

The Zurek model (1993) was also used to predict the magnitude of the spatial unmasking in the various spatial configurations. To make these predictions, the mapping in Fig. 6 was used to predict the AI at which 50% of the key words are identified (see the dashed lines in Fig. 6). We then computed the level that T would have to emit in order to yield this threshold AI for each spatial configuration (assuming that the level emitted by M is fixed) and subtracted the level T would have to emit in the diotic reference configuration. Similar analysis was performed for left- and right-ear monaural signals in order to predict the impact of having only one functional ear.

Results of these predictions are shown in Fig. 9. In the figure, the large symbols show the mean unmasking found in the binaural experiments (presented previously in Fig. 4), while the lines with small symbols show the corresponding binaural (solid lines), left-ear (dashed lines), and right-ear

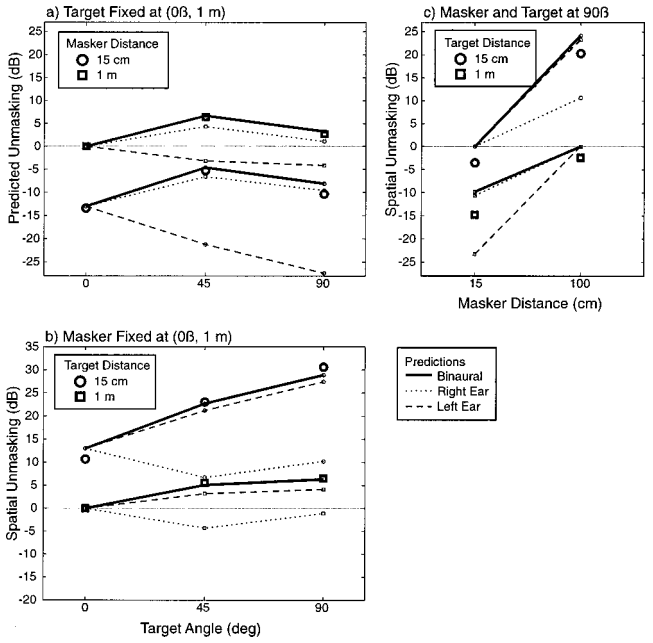

FIG. 9. Spatial advantage (energy a target emits at threshold for a constant-energy masker) and model predictions, relative to diotic reference. Symbols show across-subject means of measured spatial advantage, repeated from Fig. 4. Lines give model predictions: solid line for binaural model; dotted and dashed lines for left and right ears (without binaural processing), respectively. In any one configuration, the difference between the solid line and the better of the dotted or dashed lines gives the predicted binaural contribution to unmasking; the difference between the dotted and dashed lines yields the predicted better-ear advantage.

(dotted lines) predictions. To the extent that the model is accurate, the difference in binaural and better-ear predictions at each spatial configuration gives an estimate of the binaural contribution to spatial unmasking; the difference between the binaural and worse-ear predictions predicts how large the impact of listening with only one ear can be (i.e., if the acoustically better ear is nonfunctional).

The binaural predictions capture the main trends in the data, accounting for 99.05% of the variance in the measurements. The only binaural predictions that are not within the approximate 1-dB standard error in the measurements correspond to the same configurations for which the predicted percent-correct scores fail.

D. Difference between better- and worse-ear thresholds

The spatial unmasking analysis presented in Fig. 9 separately estimates binaural, monaural better-ear, and monaural worse-ear thresholds (in dB). From these values, we can predict the binaural advantage (i.e., the difference between the binaural and the better-ear threshold) and the difference between the better- and worse-ear thresholds (at least to the extend that the Zurek, 1993 model is accurate). These values are presented in Table I. The difference between the better- and worse-ear thresholds (second data column) is calculated as the absolute value of the difference (in dB) of the threshold T levels for left- and right-ear monaural predictions. This difference ranges from 5–18 dB for configurations in which T and M are not in the same location. Comparing these estimates (which weigh the TMR at each frequency according

to the AI calculation) to estimates made from the strict acoustic analysis (which weigh all frequencies up to 8000 Hz equally; first data column) shows (not unexpectedly) that the two methods yield very similar results. The predicted binaural advantage (third data column in Table I), defined as the difference between binaural and monaural better-ear model predictions for each configuration, is uniformly small, ranging from 0–2 dB.

E. Discussion

The Zurek model (1993) does a very good job of predicting the results for all spatial configurations similar to those that have been tested previously. In fact, the model fails only when T and/or M are near the head or when both T and M are located laterally.

Of the 15 independent spatial configurations tested, predicted performance is better than observed for six configurations, worse than observed for one configuration, and in agreement with the measurements in the remaining eight configurations. In six of the seven configurations for which the model prediction differs substantially from observed performance, T and/or M have ILDs that are larger than in previously tested configurations.

The Zurek model uses a simplified version of Colburn's model (1977a, b) of binaural unmasking to predict the binaural gain in each frequency channel, given the interaural differences in T and M. Colburn's original model accounts for the fact that binaural unmasking decreases with the magnitude of the ILD in M because the number of neurons contributing binaural information decreases with increasing ILD. The simplified version of the Colburn model used in Zurek's formulation does not take into account how the noise ILD affects binaural unmasking. If one were to use a more complex version of the Colburn binaural unmasking model, the predicted binaural gain would be smaller for spatial configurations in which there is a large ILD in the masker. Binaural predictions from such a corrected model would fall somewhere between the current binaural and better-ear predictions.

Unfortunately, such a correction will not improve the predictions. In particular, of the seven predictions that differ substantially from the measurements, there is only one case in which decreasing the binaural gain in the model prediction could substantially improve the model fit [T at (0°, 1 m) and M at (90°, 15 cm); see Fig. 9(a), circle at right side of panel]. In five of the remaining configurations in which the predictions fail [circle symbol at left of Fig. 9(b) and all four observations in Fig. 9(c)], even the better-ear model analysis predicts more spatial unmasking than is observed, and in the final configuration [e.g., circle symbol at right of Fig. 9(b)] both the binaural and better-ear analysis predict less unmasking than was observed. In fact, for this configuration, any decrement in the binaural contribution of the model will degrade rather than improve the binaural prediction fit.

The model assumes that binaural processing can only improve performance above what would be achieved if listening with the better ear alone. Current results suggest that this may not always be the case; we found that measured binaural performance is sometimes worse than the predicted performance using the better ear alone. We know of only one study that found a binaural *dis*-advantage for speech unmasking. Bronkhorst and Plomp (1988) manipulated the overall interaural level differences of the signals presented to the subjects in order to simulate monaural hearing loss. Subjects were tested with binaural, better-ear monaural, and worse-ear monaural stimuli as well as conditions in which the total signal to one of the ears was attenuated by 20 dB. In some cases, monaural performance using only the better-ear stimulus was near binaural performance; in these cases, attenuating the worse ear stimulus by 20 dB had a negligible impact on performance. If both ears had roughly the same TMR but the IPDs in T and M differed, binaural performance was best, performance for left- and right-ear monaural conditions was equal (and worse than binaural performance), and attenuating either ear's total stimulus caused a small (1–2 dB) degradation in SRT. Of most interest, in conditions for which there was a clear ''better ear'' (i.e., when the TMR was much larger in one ear than the other), performance with the better ear attenuated by 20 dB was worse than monaural performance for the better-ear stimulus, even though the better-ear stimulus was always audible. The researchers noted that this degradation in performance appears to be ''due to a ''disturbing'' effect of the relatively loud noise presented in the other ear'' (Bronkhorst and Plomp, 1988, p. 1514), because the better-ear stimulus played alone yielded better performance than the binaural stimulus. In the current experiment, some of the configurations for which the binaural predictions exceeded observed performance had a worse-ear signal that was substantially louder than the better-ear signal. However, when T was at (90°, 15 cm) and M was at (90°, 1 m), binaural performance was worse than predicted better-ear performance, even though the worse-ear signal was quieter than the better-ear signal. One possible explanation for these results is that large ILDs in the stimuli can sometimes degrade binaural performance below better-ear monaural performance, even if the worse-ear stimulus is quieter than the better-ear stimulus.

Finally, it should be pointed out that while the overall rms level of the stimuli was held constant at the better ear, the spectral content in T and M changed with spatial position as a result of the HRTF processing. It may be that some of the prediction errors arise from problems with the monaural, not binaural, processing in the model. Further experiments are needed to directly test whether binaural performance is worse than monaural better-ear performance in spatial configurations like those tested.

V. CONCLUSIONS

The results of these experiments demonstrate that the amount of spatial unmasking that can arise when T and/or M are within 1 m of a listener is dramatic. For a masker emitting a fixed-level noise, the level at which a speech target must be played to reach the same intelligibility varies over approximately 45 dB for the spatial configurations considered. Much of this effect is the result of simple changes in stimulus level with changes in source distance; however, other phenomena also influence these results.

It is well known that, on spatial unmasking tasks, monaural listeners are at a disadvantage compared to binaural listeners. In roughly half of the possible spatial configurations, the better-ear advantage is lost and any binaural processing gains are ineffective for these listeners (e.g., see Zurek, 1993). However, the current results suggest that when either T or M are close to the listener, monaural listeners can suffer from disadvantages (compared to normal-hearing listeners) that are as much as 13 dB greater observed for configurations in which T and M are at least 1 meter from the listener [i.e., from Table I, when T is at (0°, 1 m), the estimated left/right asymmetry is 19.6 dB for M at (90°, 15 cm) and only 6.4 for M at (90°, 1 m)]. Specifically, for the configurations tested, the worse-ear TMR can be nearly 20 dB lower than the better-ear TMR. While the current experiments did not measure performance of monaural listeners directly, this analysis supports the view that having two ears provides an enormous advantage to listeners in noisy environments, especially when the sources of interest are close to the listener. However, much of the benefit obtained from listening with two ears appears to derive from having two independent ''mixes'' of T and M, one of which often has a better TMR than the other. The specifically binaural processing advantages expected in the tested configurations are comparable to those observed in previous studies, on the order of 2 dB. Of course, even 2 dB of improvement in TMR can lead to vast improvements in speech intelligibility near SRT, leading to improvements in percent-correct word identification of over 20%.

The current experiments included a number of novel spatial configurations that have not previously been investigated. For many of these configurations, the Zurek model of spatial unmasking of speech fails to predict observed performance. The reasons underlying these failures (which all simulate either T or M very near the listener or have both T and M located at 90°) must be investigated further. One of the failed predictions may be partially corrected by considering a binaural unmasking model that takes into account the ILD in the masker [i.e., when M is at (90°, 15 cm) and T is at (0°, 1 m)]. However, such a correction will not improve the model predictions for any of the remaining configurations for which the model fails.

Analysis suggests that binaural processing of interaural phase decreases SRT by 1–2 dB for the configurations considered in the current study, similar to the gain observed for configurations in which T and M are both at least 1 meter from the listener (e.g., see Bronkhorst, 2000). However, for the configurations in which better-ear monaural predictions of SRT are lower than the SRTs observed with binaural presentations, there may actually be a disadvantage to listening with two ears (compared to listening with the better ear alone). Additional experiments using monaural control conditions must be performed in order to fully explore whether large ILDs degrade speech intelligibility or whether monaural better-ear performance is worse than predicted in these configurations.

ACKNOWLEDGMENTS

This work was supported in part by AFOSR Grant No. F49620-98-1-0108 to B.G.S.C. and NIDCD Grant No. DC02696 to R.Y.L. Portions of this work were presented at the Spring 2000 meeting of the Acoustical Society of America. Les Bernstein, Bob Gilkey, and an anonymous reviewer provided very helpful, constructive comments on earlier versions of this manuscript.

[1]Intersubject differences were relatively modest in these experiments, with an average sample standard deviation across the four subjects of 1.7 dB. These subject differences are shown in Fig. 4, but are left off of Figs. 3 and 4 for clarity.

[2]The AI has since been extended and renamed as the Speech Intelligibility Index or SII; see ANSI, 1997.

[3]On average, the standard error in the SRTs across the four subjects is 0.85 dB. From this, we can estimate the corresponding standard error in percent-correct estimates as follows. Near the 50%-correct point, the AI function is roughly linear. Assuming all frequency bands have TMRs between −12 and 18 dB, the AI is linear with TMR. Thus, under these assumptions (i.e., near the 50%-correct point with all frequency bands contributing to the AI and not saturated), percent correct is a linear function of TMR with a slope of roughly 12%/dB. Multiplying the standard error in the estimate of SRT times this slope yields a rough approximation of the standard error in the percentage correct of 0.85*12%=10.2%. Note that if some frequency bands are inaudible or saturated, the estimated error in percent correct will actually be less than 10.2%.

ANSI (**1969**). ANSI 53.5-1969, ''American National Standard Methods for the Calculation of the Articulation Index'' (American National Standards Institute, New York).

ANSI (**1997**). ANSI 53.5-1997, ''Methods for Calculation of the Speech Intelligibility Index'' (American National Standards Institute, New York).

Bronkhorst, A. W. (**2000**). ''The cocktail party phenomenon: A review of research on speech intelligibility in multiple-talker conditions,'' Acustica **86**, 117–128.

Bronkhorst, A. W., and Plomp, R. (**1988**). ''The effect of head-induced interaural time and level differences on speech intelligibility in noise,'' J. Acoust. Soc. Am. **83**, 1508–1516.

Bronkhorst, A. W., and Plomp, R. (**1990**). ''A clinical test for the assessment of binaural speech perception in noise,'' Audiology **29**, 275–285.

Brown, T. J. (**2000**). ''Characterization of Acoustic Head-Related Transfer Functions for Nearby Sources,'' M.Eng. thesis, Electrical Engineering and Computer Science, Massachusetts Institute of Technology.

Brungart, D. S., and Rabinowitz, W. M. (**1999**). ''Auditory localization of nearby sources. I. Head-related transfer functions,'' J. Acoust. Soc. Am. **106**, 1465–1479.

Colburn, H. S. (**1977a**). ''Theory of binaural interaction based on auditory-nerve data. II. Detection of tones in noise,'' J. Acoust. Soc. Am. **64**, 525–533.

Colburn, H. S. (**1977b**). ''Theory of binaural interaction based on auditory-nerve data. II. Detection of tones in noise,'' J. Acoust. Soc. Am. **61**, 525–533. See Aip Document No. E-PAPS JASMA-6-525-98.

Dirks, D. D., and Wilson, R. H. (**1969**). ''The effect of spatially separated sound sources on speech intelligibility,'' J. Speech Hear. Res. **12**, 5–38.

Duda, R. O., and Martens, W. L. (**1997**). ''Range-dependence of the HRTF for a spherical head,'' IEEE ASSP Workshop on Applications of DSP to Audio and Acoustics.

Durlach, N. I., and Colburn, H. S. (**1978**). ''Binaural phenomena,'' in *Handbook of Perception*, edited by E. C. Carterette and M. P. Friedman (Academic, New York), Vol. 4, pp. 365–466.

Fletcher, H., and Galt, R. H. (**1950**). ''The perception of speech and its relation to telephony,'' J. Acoust. Soc. Am. **22**, 89–151.

Good, M. D., Gilkey, R. H., and Ball, J. M. (**1997**). ''The relation between detection in noise and localization in noise in the free field,'' in *Binaural and Spatial Hearing in Real and Virtual Environments*, edited by R. Gilkey and T. Anderson (Erlbaum, New York), pp. 349–376.

Hawley, M. L. (**2000**). ''Speech Intelligibility, Localization and Binaural Hearing in Listeners with Normal and Impaired Hearing,'' Ph.D. dissertation, Biomedical Engineering, Boston University.

Hawley, M. L., Litovsky, R. Y., and Colburn, H. S. (**1999**). ''Speech intelligibility and localization in a multi-source environment,'' J. Acoust. Soc. Am. **105**, 3436–3448.
Hirsh, I. J. (**1950**). ''The relation between localization and intelligibility,'' J. Acoust. Soc. Am. **22**, 196–200.
IEEE (**1969**). ''IEEE recommended practice for speech quality measurements,'' IEEE Trans. Audio Electroacoust. **17**(3), 225–246.
Kryter, K. D. (**1962**). ''Methods for the calculations and use of the Articulation Index,'' J. Acoust. Soc. Am. **34**, 1689–1697.
MacKeith, N. W., and Coles, R. R. A. (**1971**). ''Binaural advantages in hearing of speech,'' J. Laryngol. Otol. **85**, 213–232.
Pavlovic, C. V. (**1987**). ''Derivation of primary parameters and procedures for use in speech intelligibility predictions,'' J. Acoust. Soc. Am. **82**, 413–422.
Peissig, J., and Kollmeier, B. (**1997**). ''Directivity of binaural noise reduction in spatial multiple noise-source arrangements for normal and impaired listeners,'' J. Acoust. Soc. Am. **101**, 1660–1670.
Plomp, R., and Mimpen, A. M. (**1981**). ''Effect of the orientation of the speaker's head and the azimuth on a noise source on the speech reception thresholds for sentences,'' Acustica **48**, 325–328.
Rabinowitz, W. R., Maxwell, J. Shao, Y., and Wei, M. (**1993**). ''Sound localization cues for a magnified head: Implications from sound diffraction about a rigid sphere,'' Presence **2**(2), 125–129.
Shinn-Cunningham, B. G. (**2000**). ''Distance cues for virtual auditory space,'' in Proceedings of the IEEE-PCM 2000, pp. 227–230, Sydney, Australia, 13–15 December.
Shinn-Cunningham, B. G., Santarelli, S., and Kopčo, N. (**2000**). ''Tori of confusion: Binaural localization cues for sources within reach of a listener,'' J. Acoust. Soc. Am. **107**, 1627–1636.
Zurek, P. M. (**1993**). ''Binaural advantages and directional effects in speech intelligibility,'' in *Acoustical Factors Affecting Hearing Aid Performance*, edited by G. Studebaker and I. Hochberg (College-Hill, Boston).

Consonant identification under maskers with sinusoidal modulation: Masking release or modulation interference?[a)]

Bom Jun Kwon[b)] and Christopher W. Turner
Department of Speech Pathology and Audiology, University of Iowa, Iowa City, Iowa 52242

(Received 25 October 2000; accepted for publication 12 May 2001)

The present study investigated the effect of envelope modulations in a background masker on consonant recognition by normal hearing listeners. It is well known that listeners understand speech better under a temporally modulated masker than under a steady masker at the same level, due to masking release. The possibility of an opposite phenomenon, modulation interference, whereby speech recognition could be degraded by a modulated masker due to interference with auditory processing of the speech envelope, was hypothesized and tested under various speech and masker conditions. It was of interest whether modulation interference for speech perception, if it were observed, could be predicted by modulation masking, as found in psychoacoustic studies using nonspeech stimuli. Results revealed that masking release measurably occurred under a variety of conditions, especially when the speech signal maintained a high degree of redundancy across several frequency bands. Modulation interference was also clearly observed under several circumstances when the speech signal did not contain a high redundancy. However, the effect of modulation interference did not follow the expected pattern from psychoacoustic modulation masking results. In conclusion, (1) both factors, modulation interference and masking release, should be accounted for whenever a background masker contains temporal fluctuations, and (2) caution needs to be taken when psychoacoustic theory on modulation masking is applied to speech recognition. [DOI: 10.1121/1.1384909]

PACS numbers: 43.71.Es, 43.66.Dc [KRK]

I. INTRODUCTION

A number of investigations have demonstrated that listeners reach higher levels of speech understanding under a temporally fluctuating noise background than a steady (unmodulated) noise background presented at the same level (Wilson and Carhart, 1969; Festen and Plomp, 1990; Bronkorst and Plomp, 1992; Howard-Jones and Rosen, 1993; Takahashi and Bacon, 1992; Eisenberg *et al.*, 1995; Bacon *et al.*, 1998). This is attributed to listeners' ability to detect speech cues at moments the instantaneous level of the masker is low. Because a modulated masker would not evenly mask the entire duration of a speech waveform as much as a masker without modulation would, this phenomenon has been referred to as a release from masking, or alternatively described as listening-in-the-valley (or -dip). The improvement of speech intelligibility in SRT (speech reception threshold) typically amounts to 6–10 dB for normal-hearing listeners. The present study tests for the possibility of an opposite scenario; speech intelligibility could also be reduced due to the interference of temporal modulations in a masker with the auditory processing of modulations in the speech envelope. Conservatively speaking, a fluctuating masker might have the effect of reducing speech intelligibility in a direction that counteracts the effect of masking release.

A. Modulation detection interference (MDI) and modulation masking (MM)

The above hypothesis originates from psychoacoustic experiments where listeners' sensitivity to amplitude modulation (AM) in a signal was measured under the presence of a modulated masker; listeners were less able to detect AM when there was competing modulation in a masker. This was demonstrated by both tonal carriers (Yost and Sheft, 1989, 1994; Yost *et al.*, 1989; Bacon and Konrad, 1993; Bacon and Moore, 1993; Bacon *et al.*, 1995; Strickland and Viemeister, 1996) and broadband noise carriers (Houtgast, 1989; Bacon and Grantham, 1989). Conventionally, the former is usually referred to as modulation detection interference (MDI), and the latter is referred to as modulation masking (MM).[1] Both MDI and MM are highly dependent upon the modulation rates of the signal and masker; the effect is greatest when two modulation rates are the same, and it decreases as the difference between them increases. In other words, MDI (or MM) exhibits selectivity in the modulation frequency domain as an analogue to the selectivity in tone-on-tone masking. The concept of ''modulation tuning'' has been quantitatively established with a modulation filterbank theory by Dau and his colleagues (1997)

B. Modulations in speech

Envelope modulations in the speech waveform are known to play a significant role in speech intelligibility. Information from amplitude modulation of the speech envelope is particularly critical when speech is represented at limited spectral resolution (e.g., van Tasell *et al.*, 1987; Shannon

[a)]Portions of this paper were presented at 139th meeting of Acoustical Society of America, Atlanta, Georgia, June 2000.

[b)]Author to whom correspondence should be addressed; electronic mail: bkwon@cochlear.com. Current address: Cochlear Corporation, 61 Inverness Drive East, Englewood, CO 80112.

 0001-4966/2001/110(2)/1130/11/$18.00

et al., 1995). In the concept of speech transmission index (STI), the amount of modulation in the speech waveform is quantitatively related to speech intelligibility (Houtgast and Steeneken, 1985). In addition, it was found that modulations in the speech waveform between about 4 and 16 Hz play a critical role in speech perception; filtering out (or reducing) very fast/slow envelope fluctuations in the waveform did not degrade sentence intelligibility as long as modulations remained in the above range (Drullman *et al.*, 1994a, 1994b).

C. Specific goals and overview in experiments

From the above, it is reasonable to hypothesize that modulation interference might occur in speech perception under the background of a modulated masker. Modulations in a masker would reduce sensitivity to detect modulations in the speech envelope (according to MDI or MM; section A above); that is, modulations in a masker would reduce the amount of speech modulations perceptually available to a listener. With less available modulation information, as a result, speech intelligibility could be reduced (according to studies on reducing modulations; see section B). Nevertheless, most previous studies have reported data supporting masking release. The present study primarily attempts to resolve the apparent paradox between two contradictory concepts: masking release and modulation interference. Would modulation interference ever be observed in speech perception?[2] If so, will it follow the same pattern as seen in psychoacoustic MM/MDI results? Which of the two phenomena would be observed under what conditions?

Two groups of experiments were performed in the present study: one group with wide-band stimuli, the other with bandlimited stimuli. Each of these adopted the experimental paradigm used in parallel psychoacoustic MM/MDI studies. Experiment 1 tested the selectivity of modulation interference (if any) in the modulation frequency domain using wide-band stimuli. Experiment 2 tested the effect of separation of carrier frequencies using bandlimited stimuli. In experiments 3 and 4, wide-band and bandlimited stimuli were tested, in the same experimental settings as experiments 1 and 2, respectively; but the speech stimuli contained reduced information in the spectral and temporal domains, in order to test the same hypotheses under conditions where speech cues are more limited and less redundant.

II. GENERAL METHODOLOGY

A. Subjects, equipment, stimuli, and task

Six normal-hearing listeners (pure-tone thresholds better than 20 dB HL) between the ages of 21 and 29 participated in the present study. They were compensated for their participation. Sufficient practice sessions were given to each subject prior to data collection to ensure stable performance. Each subject, seated in a sound-attenuated booth, listened to speech samples in /aCa/ context through Senheiser HD 25SP1 headphones. The 16 consonants tested were as follows: /b, d, g, p, t, k, z, s, m, n, f, v, θ, ð, ʒ, ʃ/. The frequency range of speech stimuli used in the experiments was 100–8000 Hz. Speech stimuli were recorded by four speakers (two for each gender) and were digitized at a sampling rate of 22 050 Hz. The duration of each speech stimulus ranged from 0.8 to 1.3 s. MATLAB programs processed the stimuli and controlled the experiments at a Macintosh PowerPC 9500. The sound card, Audiomedia III, of the computer had a proper anti-aliasing filter at the output of the D/A converter. Listeners responded by pressing a button on a response box connected to the computer. Percent-correct scores of consonant identification were measured. Calibration was referenced to a 6-cc coupler measurement: the full, calibrated amplitude was attenuated to keep the output at the headphone at 70 dB SPL throughout the experiments.

B. Assessment of modulation interference

Throughout the current study, the amount of modulation interference was taken as a difference in percent-correct scores (the score under an unmodulated masker minus the score under a modulated masker). This measure will be abbreviated as MI in this paper. If this amount is negative, it would then indicate that masking release was observed.

III. EXPERIMENT 1—MODULATION FREQUENCY DOMAIN

A. Rationale

In experiment 1, it was examined whether selectivity of modulation masking in the modulation frequency domain would be observed. Envelope modulations in speech were restricted by low-pass filtering the envelope (temporal smearing, Drullman *et al.*, 1994a), so that the range of the speech modulations available to listeners was limited. Specific questions addressed were (1) ''will masking release or modulation interference be observed?'' (i.e., is the recognition score under a modulated masker higher or lower than under an unmodulated masker?), (2) ''does the pattern of modulation interference, if any, follow the modulation-frequency selectivity pattern seen in MM/MDI results?'' If the underlying mechanisms of MM/MDI are still effective in speech recognition, we could expect more interference when the rate of modulation of the masker lies within the range of speech modulations than when it falls outside of the speech modulations. Figure 1 displays schematic plots of the expected MI pattern if the results follow that observed in psychoacoustic MM/MDI research.

B. Stimulus processing

1. Speech processing—Noiseband modulation processing

In view of the fact that the present study involved temporal (envelope) processing in the auditory system, it was preferable to use speech with reduced spectral resolution to maximize the importance of temporal cues. Recognition of speech with reduced spectral resolution has been extensively studied by a number of investigators for listeners with normal-hearing and impaired-hearing (Shannon *et al.*, 1995; Dorman *et al.*, 1997; Fu *et al.*, 1998; Turner *et al.*, 1995, 1999). The processing to achieve such reduction in spectral resolution generally involves the following steps: (1) the whole frequency range of speech is partitioned by bandpass

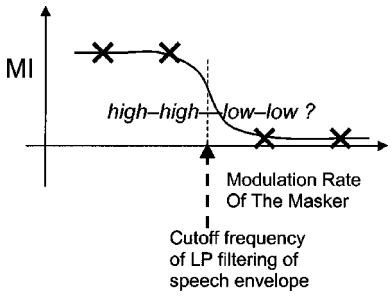

FIG. 1. A schematic plot for expected pattern of MI. Positive or negative MI represents modulation interference or masking release, respectively. According to the MM/MDI principles, with low-pass filtering of the speech envelope, the MI curve should show the pattern of *high-high-low-low*. (It is high when the masker modulation is in the region of speech modulations, otherwise it is low.)

filters into separate frequency bands, (2) the envelope of each band is extracted (in the present study, the envelope was extracted by the Hilbert transform) and is used to modulate a bandlimited random noise in the same frequency band, (3) these modulated noise bands are summed across all bands with proper adjustments of levels to restore the general long-term spectrum of the original signal. This processing strategy, which has also been used as a simulation of a cochlear implant, will be referred to as ''noiseband modulation'' processing in this paper. In experiment 1, the number of processing bands was chosen to be 12,[3] and the division of frequency bands was logarithmic, which made each band roughly 1.4-octave wide. FIR filters for the filterbank were designed to have 1 dB of passband ripple, and 40 dB of stopband attenuation and to be approximately of the 200th order. The slopes of the filter skirt characteristics exceeded 70 dB/oct except for the lowest band.

2. Speech envelope conditions

There were three conditions of speech stimuli, based upon conditions of envelope processing: (1) low pass at 4 Hz (LP4), (2) low pass at 16 Hz (LP 16), (3) no envelope-processing (REF; control condition). The low-pass filtering

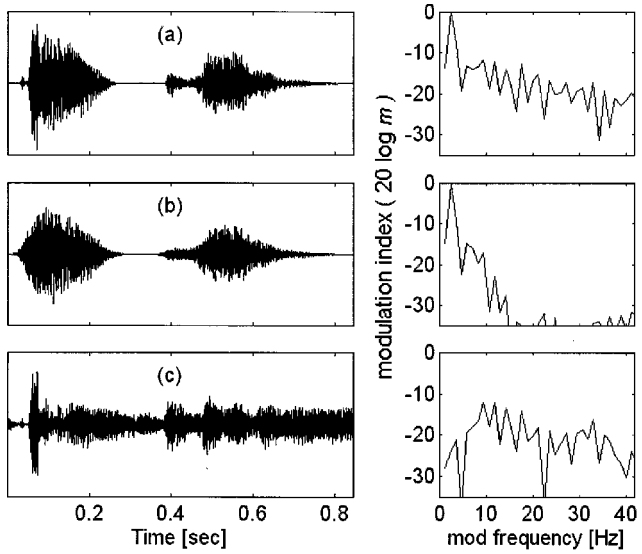

FIG. 3. Waveforms and corresponding modulation spectra of /aka/ spoken by a male speaker; (a) REF, (b) LP4, (c) HP8 (cf. experiment 3). Visit http://www.geocities.com/bomjunkwon/sounds/kwonturner01.htm to play sound samples.

of the envelope was accomplished in the same manner as in the study by Drullman *et al.* (1994a) except for minor differences. Figure 2 displays a block diagram of the signal processing for experiment 1. Figure 3 illustrates some of the speech waveforms and modulation spectra to demonstrate the effect of the envelope filtering.

3. Masker conditions

The masker was wide-band random noise with a uniform distribution and was either unmodulated or subjected to sinusoidal modulation (modulation depth: 100%) at one of the following rates: 1.5, 3, 9, 25, or 40 Hz. The starting phase of the sinusoidal modulation was random on each trial. After pilot experiments, the signal-to-noise ratio (SNR) was chosen to be 5 dB in all of the conditions (except for condition REF of 2 dB)[4] in order to obtain recognition scores avoiding

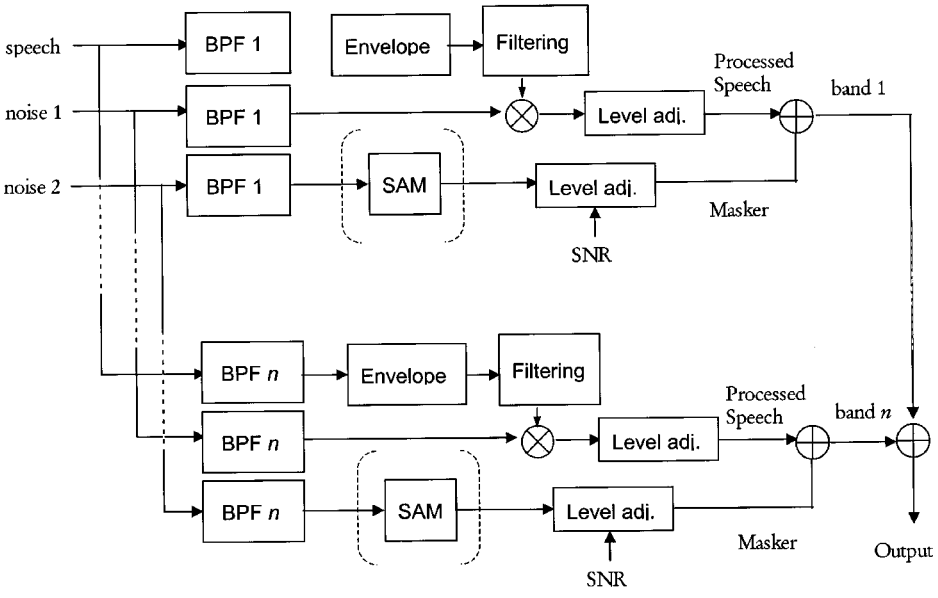

FIG. 2. A block diagram of the signal processing for experiment 1 (and 3). This processing is basically a combination of noiseband modulation (Shannon *et al.*, 1995) and envelope filtering (Drullman *et al.*, 1994a, b). Noise1 is used for the processing of noiseband modulation, and noise2 is used for the masker. Both noise1 and noise2 are not correlated with each other. For simplicity, only the first and last bands are displayed.

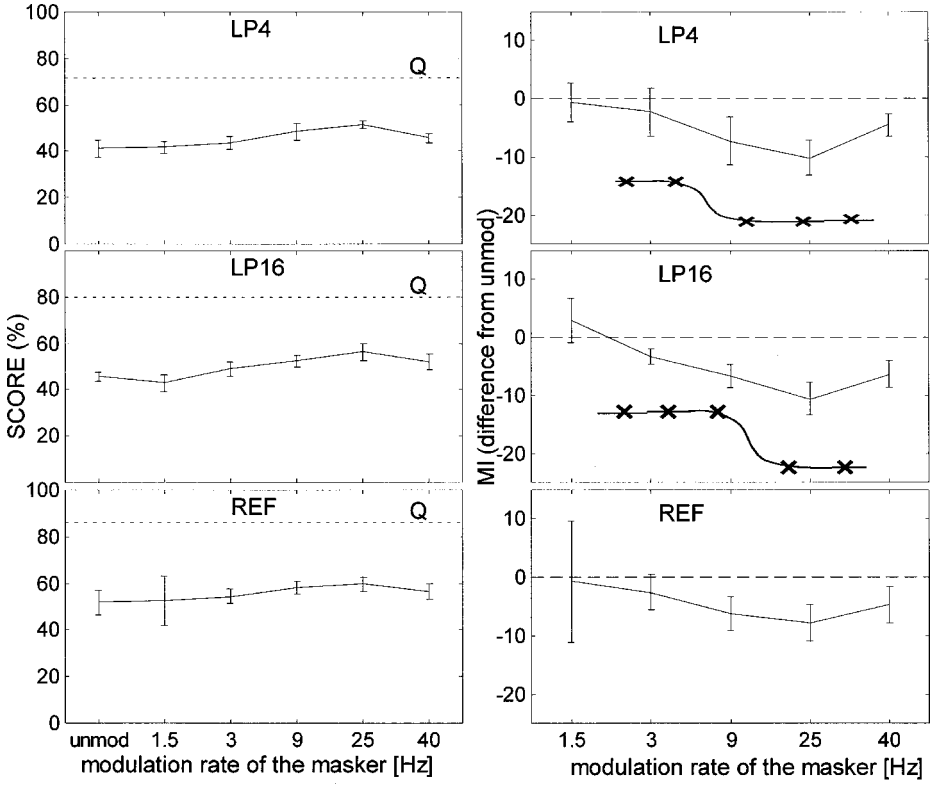

FIG. 4. Result of experiment 1. Wideband speech was processed by twelve-channel noiseband modulation processing. Three conditions of speech stimuli were tested, LP4, LP16, and REF, according to the low-pass cutoff frequency in the speech envelope. Signal-to-noise ratio was 5 dB (except that it was 2 dB in REF). (Left) Percent scores of consonant recognition as a function of modulation rate of the masker for speech conditions. "unmod" indicates a steady (unmodulated) masker. Dotted line with a mark *Q* in each panel indicates the score measured without the masker. (Right) The pattern of MI, the amount of modulation interference, i.e., the difference from the score under the unmodulated masker. Free-hand schematic drawings in LP4 and LP16 represent the shape of the MI curve that would have been obtained if the selectivity in modulation masking was in effect (cf. Fig. 1).

a ceiling (or floor) effect. The long-term spectral shape of the masker was matched with the speech spectrum.

C. Procedure

Initially, the score for each speech condition was measured without a masker to obtain a reference score level. Next, a masker was added to the speech at the chosen SNR with either no modulation or a selected modulation rate. Each speech×masker session consisted of 64 trials. All blocks of conditions were tested in a randomized order to avoid an order effect. Subjects were provided with feedback on each trial.

D. Results and discussion

The left panels of Fig. 4 display group mean recognition scores as a function of modulation rate of the masker for each speech condition (LP4, LP16, REF). Scores from the quiet condition (without a masker) are also indicated by a dotted line (with a mark *Q*) in each graph. The "*Q*" score in condition REF is 85.9%, which is somewhat lower than some previous studies where almost perfect scores were measured with eight-channel processing.[5] The amount of modulation interference, MI, i.e., the difference in scores between conditions with the unmodulated masker and the modulated masker is plotted in the right panels of Fig. 4. In most of the speech×masker conditions, MIs are negative, i.e., masking release was prevalent over modulation interference. A one sample *t*-test rejected the hypothesis that the gross mean of MI was zero ($p<0.05$). Neither an effect of modulation rate [$F(4,60)=2.07$, $p=0.096$] nor an effect of speech condition [$F(2,60)=0.09$, $p=0.91$] was significant in a repeated measure of ANOVA. It is quite obvious that the MI curves in Fig. 4 do not follow the expected pattern from MM/MDI, as in the schematic drawings in Fig. 4.

Does the effect of modulation interference exist in speech recognition? Even though the results suggest that masking release was the predominant effect, the possibility still remains that modulation interference (even without a specific modulation-frequency selectivity) contributed to the measurements, thus the MI curves in Fig. 4 might reflect the "net" effect of both phenomena, masking release and modulation interference. It is worthwhile to note that three MI curves in Fig. 4 even appear to be parallel, which is confirmed by nonsignificant interaction between two factors, modulation rates and speech condition [$F(8,60)=1.03$, $p=0.43$]. Because the modulations in the speech stimuli in condition REF are not restricted, the effect of modulation interference in this condition was not expected to exhibit modulation-frequency selectivity[6] as would be seen in the other two conditions. The similar shape in all the MI curves indicates that the restriction in speech envelope modulations did not make a noticeable difference in present measurements. Thus the psychoacoustic phenomenon of MM/MDI is not applicable to speech recognition (at least in the modulation frequency domain).

IV. EXPERIMENT 2—CARRIER FREQUENCY DOMAIN

A. Rationale, stimulus conditions, and procedures

In experiment 2, the effect of carrier frequency on modulation interference was examined using bandlimited speech and noise. Seven frequency bands, each roughly 2.5-octave wide, were selected in the frequency region 100–

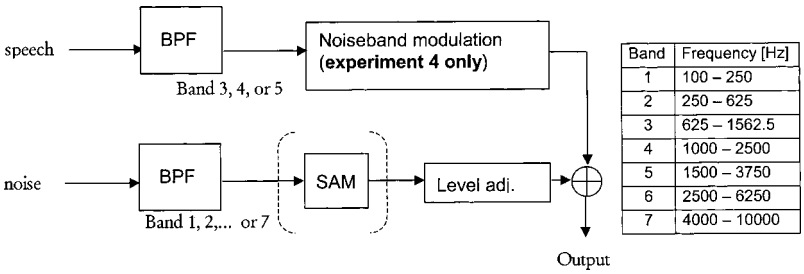

Band	Frequency [Hz]
1	100 – 250
2	250 – 625
3	625 – 1562.5
4	1000 – 2500
5	1500 – 3750
6	2500 – 6250
7	4000 – 10000

FIG. 5. A block diagram of the signal processing for experiment 2 (and 4). Speech and noise are bandpass filtered, and noise is either sinusoidally modulated at 8 Hz or unmodulated. The rms was matched before they were mixed. Frequencies of each band are displayed in the table. Additionally, bandlimited speech was processed for experiment 4 through the noiseband modulation (3-ch or 2-ch).

8000 Hz (refer to Fig. 5 for frequencies of each band). Seven FIR bandpass filters were designed for each band, with filter slopes of at least 80 dB/oct.

The maskers were random noise, filtered through a bandpass filter corresponding to each of the bands (band 1 through band 7). The same set of /aCa/ speech stimuli was used as in experiment 1. Three speech conditions were tested: speech at band 3, at band 4, and at band 5. The rms levels of speech and masker were matched before they were combined. Therefore, the ''nominal'' signal-to-noise ratio was always 0 dB.

For each of the three speech conditions, scores without a masker were initially obtained for a baseline reference. The masker, in each of the seven bands, was either unmodulated or sinusoidally modulated at 8 Hz (modulation depth: 100%). For each condition of speech (band 3, 4, or 5), masker band (band 1, 2,..., or 7), and masker modulation type (unmodulated or modulated), 64 trials were run to obtain the score for each subject.

B. Results and discussion

Group mean scores are plotted in the left panels of Fig. 6 for each speech condition as a function of the masker band. Bars marked by *Q* indicate scores for the quiet condition (without a masker). The general pattern of recognition scores as a function of carrier band of the masker reflects the degree of spectral masking; the score is lowest when the speech and masker are in the same carrier frequency band, and it increases as the carrier band of the masker is further away from the speech band. The *Q* scores are 60%–70%. These scores decrease by as much as 30%–40% when a masker at the same band as speech is added. The scores with the unmodulated masker, when the masker is more than two bands away from the speech, are not different from the *Q* scores. This indicates that the bandlimited noise masker without modulations at this level, located more than two or three octaves away from the speech, does not have a substantial influence upon speech recognition.

MI curves in the right panels in Fig. 6 show that there was a significant amount of interference when the masker band was spectrally remote from the speech band (especially when the masker band was higher in frequency than the speech band). This large degree of interference decreases as the speech and masker bands are closer. Furthermore, when the two bands are the same, the MI becomes negative; that is, masking release is observed. The effect of the masker band was significant [$F(6,119)=5.0$, $p<0.001$]. This pattern makes an interesting contrast with previous MDI results; MDI as a function of carrier frequency separation is flat (Yost and Sheft, 1994) or often increases as the carrier frequencies are close due to within-channel processing (Bacon and Konrad, 1993; Bacon and Moore, 1993). This may be

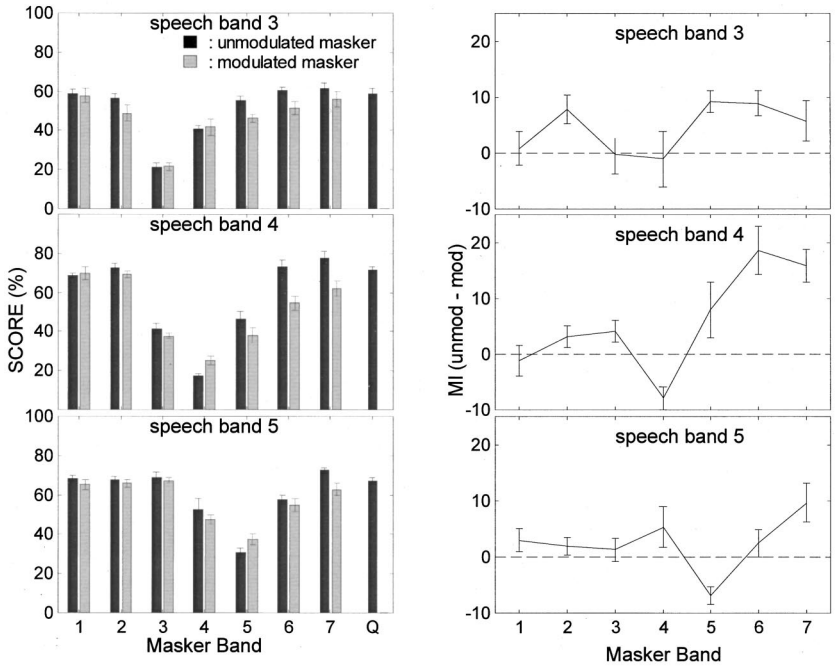

FIG. 6. Result of experiment 2. Speech was bandlimited in either band 3, 4, or 5. (Left) Percent-correct of consonant recognition scores as a function of the frequency band of a masker. Left and right bar in each condition represent the score under the unmodulated and modulated masker, respectively. The condition with a mark *Q* in each panel represents the score without a masker. (Right) MI plots for each condition, the difference in scores (score under the modulated masker minus score under the unmodulated masker).

attributed to the combined contribution from masking release and modulation interference. When the speech and masker were far from each other (especially when the masker was at a high frequency band), the effect of modulation interference was dominant, and this was in part because the masker did not have a strong effect of peripheral masking, i.e., no room for a release to occur. As the masker moved closer to the speech band, the effect of masking release became stronger, and the contribution from modulation interference relatively decreased. Masking release was the main factor that made the present trend different from MDI results. In psychoacoustics within-channel processing somewhat increased MDI; in the present experiment within-channel processing increased masking release.

Unlike experiment 1, where masking release was prevalent, clear evidence of modulation interference (i.e., positive MI) was demonstrated under certain conditions in experiment 2. Why is the effect of modulation interference more visible in experiment 2? It is conceivable that a greater effect of masking release would be measured when the speech target has rich information as in experiment 1. In other words, masking release would occur when a speech waveform has a high degree of redundancy across frequency so that listeners can identify phonemes from a ''partially'' masked speech waveform. It is not difficult to imagine that such a process would be less effective when the speech contains less redundancy. For this reason, in experiment 2, where bandlimited speech was the target stimulus, relatively more effect of modulation interference was measured. Therefore, we further hypothesized that modulation interference might be most visible when the speech waveform did not provide a sufficient degree of redundancy that would facilitate masking release. This was tested in experiments 3 and 4.

V. EXPERIMENT 3 AND 4

A. Rationale, stimulus, and procedures

Masking release was conspicuous with wide-band speech stimuli (experiment 1), and modulation interference was observable under several conditions with bandlimited speech stimuli (experiment 2). Therefore, it seems that, while both masking release and modulation interference are possibly playing a role in speech perception under a modulated masker, the effect of modulation interference might be enhanced (or the effect of masking release is lessened) when speech stimuli do not contain a high degree of redundant information. To test this hypothesis, speech conditions with less redundancy were tested in experiments 3 and 4. Two more conditions were tested in experiment 3 as an extension of experiment 1: speech with poorer spectral resolution and speech without amplitude fluctuations at syllabic rates. In experiment 4, which is an extension of experiment 2, three more conditions with limited spectral resolution within the narrow band were tested (note that spectral resolution was intact in experiment 2). The experimental procedures and participants in experiment 3 and 4 were the same as experiments 1 and 2.

Specific speech processing conditions tested in experiment 3 are as follows: (1) four-channel noiseband modulation with the envelope low-pass filtered at 16 Hz (LP16-4ch), (2) twelve-channel noiseband modulation with the envelope high-pass filtered at 8 Hz (HP8). Speech with four-channel noiseband processing was used to test the effect of reduced spectral resolution, or the effect of less speech information available to listeners. With the same rationale as in experiment 1, the envelope was low-pass filtered to determine whether selectivity of modulation masking would be observed. In the second condition, the spectral resolution was twelve-channel, the same as in experiment 1, but the envelope was high-pass filtered. As a counterpart to ''envelope-smearing'' in the low-pass envelope, speech with the high-pass envelope does not allow slow amplitude fluctuations, which may be considered as ''syllable-deprived'' speech [cf. Fig. 3(c)]. For this case, the selectivity of modulation masking was tested by seeing if high MI was observed under the maskers with high modulation rates (the opposite of Fig. 1). The level of the masker was adjusted to yield 5 dB of SNR for both of the conditions. The signal processing procedure in experiment 3 was the same as in experiment 1, except for a different number of channels for LP16-4ch, and the high-pass filtering stage of the envelope for HP8. The processing for high-pass filtering of the envelope followed the steps adopted by Drullman *et al.* (1994b).

In experiment 4, the speech conditions were as follows: (1) speech at band 4, three-channel processing; (2) speech at band 4, two-channel processing; and (3) speech at band 5, three-channel processing. The scheme for the band division was logarithmic. Because each bandwidth is approximately 2.5-octave, a logarithmic partition of three- or two-channel noiseband modulation processing makes individual bands approximately 0.8-octave wide, or 1.25-octave wide, respectively. The same level and type of the masker was used as experiment 2: 0 dB SNR, and either unmodulated or sinusoidally modulated at 8 Hz.

B. Results and discussion—Experiment 3

Percent-correct scores and Ml for condition LP16-4ch are plotted in the top panels of Fig. 7. The mean score for four-channel processing without a masker is 50.9%. The amounts of modulation interference, as seen in the right top panel, are close to zero and are not statistically significant ($p = 0.06$). This result differs from experiment 1 in that the effect of masking release is now reduced, as expected, due to the poor spectral resolution, and yet the effect of modulation interference is not significantly increased either. In the lower panels of Fig. 7, results for condition HP8 are plotted. Significant Mls are noticeable in this condition: consonant identification was more difficult under a modulated masker than under an unmodulated masker. Comparison between the Ml curves and the schematic drawings indicates that the selectivity representing psychoacoustic MM/MDl is not found, consistent with experiment 1. To summarize, reducing spectral resolution resulted in a decrease in masking release, although it stopped short of substantially enhancing the effect of modulation interference. On the other hand, ''syllable-deprived'' speech was highly susceptible to modulation interference and listeners were not able to take advantage of ''listening-in-the-valley.''

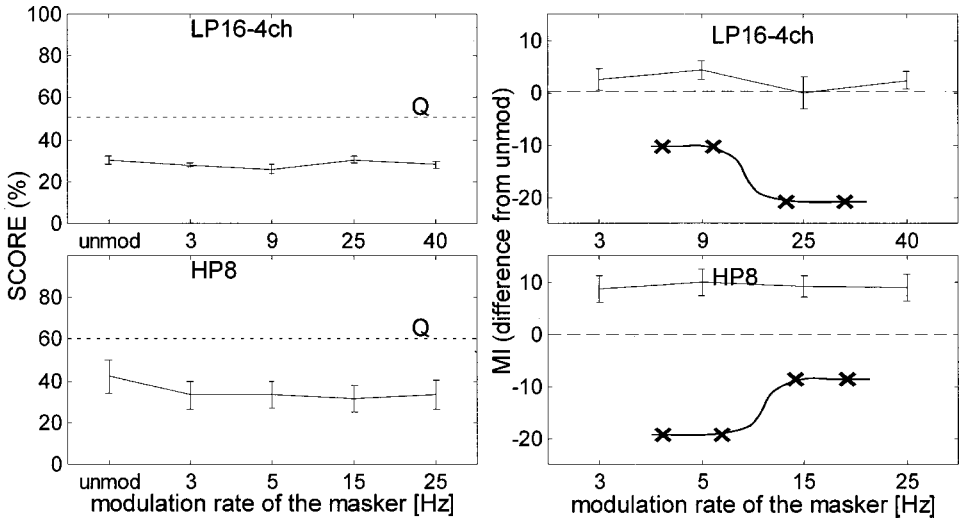

FIG. 7. Result of experiment 3, in the same format Fig. 4, for conditions LP16-4ch (four-channel noiseband modulation with low-pass envelope with the cutoff frequency 16 Hz) and HP8 (twelve-channel noiseband modulation with high-pass envelope with the cutoff frequency 8 Hz). The signal-to-noise ratio was 5 dB. (Left) Percent-scores and MI plots for conditions LP16-4ch and HP8. (Right) MI plots for each condition. Schematic drawings are also accompanied; see the caption for Fig. 4 for details.

C. Results and discussion—Experiment 4

In Fig. 8, percent-scores and Ml from experiment 4 are plotted. In comparison with experiment 2, the percent-scores in Fig. 8 are generally lower than those in Fig. 6, as expected, due to the poorer spectral resolution of the speech target. The general characteristic in the Ml patterns in experiment 4 (the right column of Fig. 8) is still similar to what was seen in experiment 2: the Ml is lowest when the speech and the masker are in the same band, and it increases as the masker band moves away from the speech band. It should be noted that Mls in experiment 4 (Fig. 8) are generally higher than in experiment 2. A contrast analysis reveals that Mls in experiment 4 are significantly higher than Mls in experiment 2 ($p=0.002$), which confirms the hypothesis that speech with less redundancy would induce more modulation interference.

VI. GENERAL DISCUSSION

A. Masking release or modulation interference?

The primary interest in the present study was to investigate the effect of temporal fluctuations (modulation) of a masker upon speech recognition. The data in the present study suggest that two effects, masking release and modulation interference, ought to be taken into account. It is likely that both factors are potentially involved in the speech masking process whenever a masker contains temporal fluctuations. Although under some instances one may be more dominant than the other, there is no evidence to exclude ei-

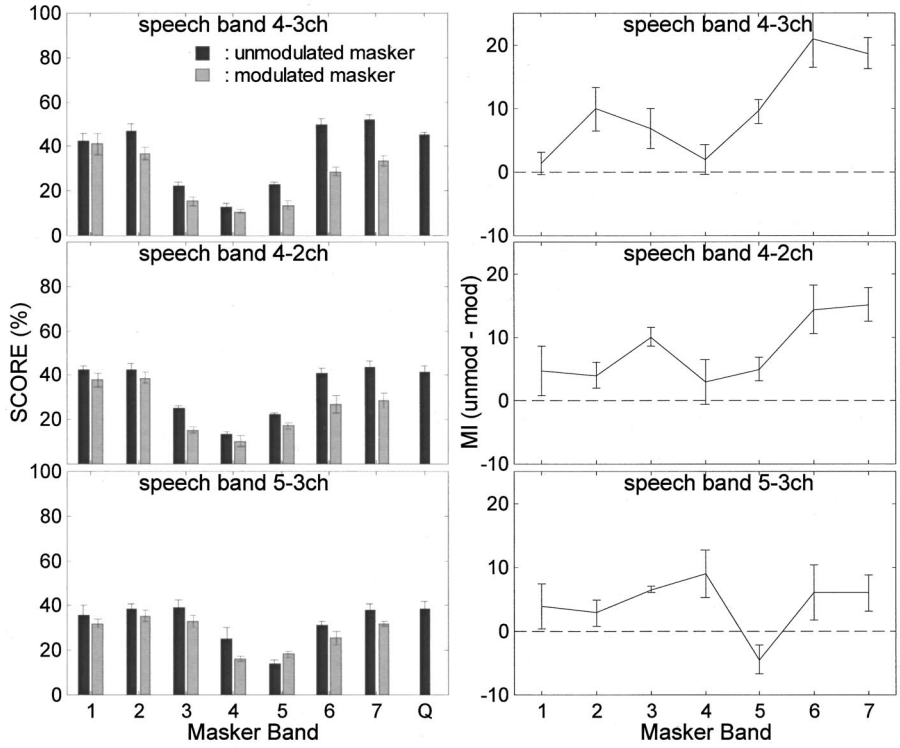

FIG. 8. Result of experiment 4 in the same format as Fig. 6. (Left) Percent-correct scores as a function of the masker band for speech condition band 4-3ch, band 4-2ch, and band 5-3ch. (Right) MI plots for each condition.

ther factor. Therefore, it is sensible to regard the Ml measurement as the net result from the two counteracting effects.

1. Masking release

Masking release is a phenomenon in which listeners presumably take advantage of temporal ''dips'' in a masker, when listening to speech under the presence of a masker. In many studies the ability of ''dip-listening'' has been discussed in relation with listeners' temporal resolution (e.g., Zwicker and Schorn, 1982; Buus, 1985); it was suggested that listeners with sensorineural hearing loss would have poorer temporal resolution because they enjoy the dip-listening to a much lesser degree than listeners with normal hearing (Festen and Plomp, 1990; Bronkorst and Plomp, 1992; Bacon *et al.*, 1998). In this concept, it may be thought that the greater the portion of speech stimulus physically exposed through a dip, the greater chance that the amount of masking release is observed. For example, the effect of masking release would be higher with an interrupted noise (square wave modulated noise) than with sinusoidally modulated noise (Bacon *et al.*, 1998). Also the higher modulation depth in the masker would result in a greater effect of masking release; for a speech-babble masker, the number of talkers needs to be small (less than four) to maximize the effect, as more distinct temporal fluctuations are produced in such a masker (Pollack and Pickett, 1958). Another factor bound to the masking release for speech-listening is ''top-down'' processing; it is well known that the human auditory system is capable of restoring missing phonemes by proper use of context (cf. Warren, 1970). Although linguistic context was not available in the present experiments, in which nonsense syllables were used as stimuli, missing portions of the speech waveform could be largely reconstructed by their neighborhood context (such as formant transitions) as long as the masker did not cover the entire duration of the stimulus. It is highly likely that this ''information-rich'' nature of speech stimuli enhanced masking release observed in the present experiments. The close relation between the degree of ''information-rich'' or redundancy in speech stimuli and masking release was demonstrated in the present experiments; in experiments 3 and 4 the effect of masking release is reduced or even lost under conditions with less information available in the speech stimulus.

a. Relation with comodulation masking release. Despite of the proximity in terminology, comodulation masking release (CMR) has been discussed in a little different context from masking release observed in speech experiments. CMR usually refers to the improvement in (nonspeech) signal detection when the background noise is modulated coherently (co-modulation) across frequency in comparison with the condition where such comodulation in noise does not exist. CMR has generally been investigated with respect to across-channel processing of the auditory system (e.g., Hall *et al.*, 1984, 1988; Carlyon *et al.*, 1989). However, a few studies have demonstrated considerable contribution from within-channel processing (Schooneveldt and Moore, 1987; Richards *et al.*, 1997; Verhey *et al.*, 1999), in which temporal beats in the masker waveform due to the within-channel interactions among stimuli might be attributed to the detection improvement. Perhaps at least part of masking release for speech has a common theoretical ground with this within-channel effect of CMR—''listening-in-the-valley.'' It might not be coincidental that, in experiment 2, masking release occurred when the speech and masker were at the same band—the within-channel masking condition.

2. Modulation interference

In the present study, modulation interference predominantly occurred in condition HP8 (''syllable-deprived speech'') in experiment 3, and in several conditions of experiments 2 and 4, when the effect of traditional masking was minimal. It may be worthwhile to look into individual cases to understand the nature of modulation interference in speech. For condition HP8 in experiment 3, the auditory processing of speech envelope was hindered by modulations in a masker by means of modulation interference. Although the speech stimulus did not have syllabic fluctuations in the envelope [cf. Fig. 3(c)], listeners were still able to track and recover the (lost) syllabic distinction and to identify the medial consonant under the quiet and unmodulated masker. Once the masker was modulated, however, their ''syllable-portion-tracking'' ability degenerated, which reduced the scores by around 10% from the score under an unmodulated masker.

The deterioration of speech intelligibility due to modulation of a masker may be explained by selective attention of auditory objects discussed by Bergman (1990). In experiments 2 and 4, when the noise band was spectrally remote from the speech band, especially at a high frequency, as discussed earlier, the unmodulated noise did not have a masking effect: listeners did not experience a noticeable difficulty segregating the unmodulated noise from the speech. Once the high frequency noise band was modulated, however, the noise band caused a perceptual illusion: it was processed as if it were a part of speech band. Even though the noiseband did not have the spectral characteristic of the speech target, listeners were inadvertently attending to high frequency noiseband due to its amplitude modulation, which resulted in a decrease in the score under the modulated masker. These instances of modulation interference, including those in condition HP8 (experiment 3), indicate that modulation of a masker may induce an illusory attention which would cause phonemic confusion that would not normally occur under an unmodulated masker.

One might wonder why only one factor, masking release, has been a major focus of investigation in speech experiments, if the other factor, modulation interference, always coexisted. This is probably because most of the previous experiments have focused on the robustness of human speech recognition to take advantage of redundant speech information. There are many sources of redundancy available at each level of speech recognition. Most studies have used sentence materials in their experiments, which allowed the listeners to take advantage of the context. For some studies with nonsense syllable tests (e.g., Howard-Jones and Rosen, 1993), the experiments were devised in favor of masking release, for example, using square wave modulation. The contribution of modulation interference was

most likely hidden in those studies, therefore, the existence of modulation interference might have been largely ignored. As found in the present study, modulation interference does occur under certain circumstances and is suspected to have some effect even when masking release was predominantly observed. The possibility exists that listeners with sensorineural hearing loss or cochlear implant users, who may not receive the full redundancy of speech, may be even more vulnerable to the effects of modulation interference than the normal-hearing listeners of the present study.

B. Relevancy of a psychoacoustic MDI (or MM) to speech experiments

Finally, it is worth speculating on one of the most interesting findings in the present study—lack of selectivity of modulation interference in the modulation frequency domain (experiments 1 and 3). This is at odds with apparent selectivity of MM/MDI in the modulation frequency domain, which have allowed us to regard MM/MDI pattern as ''modulation tuning.'' Discussion on this issue might be particularly insightful considering the growing interest among recent investigators in describing the temporal properties of a signal in the modulation frequency domain by means of modulation spectrum (e.g., Dau *et al.*, 1997; Schreiner and Langner, 1996), analogous to conventional spectrum analysis. If a modulation filterbank exists and speech modulations are processed in such a frame, the interference due to modulation naturally should exhibit a characteristic of modulation masking. What happened to this process?

First, the discrepancy may be attributed to the difference in the listener's task. In traditional MM/MDI studies, listeners had only to detect whether or not there was modulation. In the present study, listeners were told to identify phonemes, i.e., detecting modulations in a stimulus was not the only goal in the task, all of the other aspects of speech cues beyond amplitude modulation could be utilized to perform the identification task. The difference in the task—detection and identification—might have caused a different degree of the involvement of cognitive factors. Perhaps an identification experiment with nonspeech or synthetic speech stimuli under similar experimental conditions could yield some findings that bridge the gap between the present study and previous MM/MDI studies.

Second, a difference in the nature of modulations between the masker and the speech target is another factor that contributed to the discrepancy. Modulations in a speech waveform are characterized by their transiency (except for syllabic rate of modulation), which is contrasted with periodicity in the masker modulation. For example, modulations in a stimulus /ata/ that carry the relevant cues for the phoneme /t/ reside only in a limited time range. Applying a masker with periodic modulation to ''mask'' the ''time-limited modulation'' in the target would not be successful in this sense, and it is not surprising that the results did not follow the usual pattern of masking, i.e., frequency selectivity. Instead of being governed by the rules of modulation ''tuning,'' modulation interference in speech was subject to perceptual grouping of auditory objects, where modulation of the masker may result in a misleading cue for recognition.

It should be noted that, as Moore points out (1997, pp. 166–168), the concept of modulation tuning is still controversial: this tuning is, at best, very broad and often quite shallow. Moreover, there have been several studies reporting results hard to interpret by means of a modulation filterbank (Sheft and Yost, 1997; Kwon and Shannon, 2001). Although early MM/MDI studies have spawned the concept of modulation tuning, MM/MDI may alternatively be better associated with the concepts unrelated to modulation masking, such as auditory grouping (e.g., Hall and Grose, 1991; Yost, 1992). If one wants to construct a masker that would induce a high degree of modulation interference in speech perception, one should make the condition facilitate auditory grouping; for example, modulation in the masker needs to roughly resemble the speech modulations and also to be synchronized to cause perceptual fusion. Nevertheless, we still feel hesitant to discard the concept of a modulation filterbank. The modulation filterbank model has been successfully employed to interpret several auditory processes related to envelope processing (for example, Dau *et al.*, 1999; Verhey *et al.*, 1999; Derleth and Dau, 2000). Another reason to give consideration to the model would be that the model is based upon well-developed quantitative analyses, which the alternative theory—auditory grouping—lacks for the most part. A thorough investigation would resolve this issue. At least, we can conclude from the present results that the masking paradigm in the modulation frequency domain is not compatible with the situation of speech recognition.

VII. SUMMARY AND CONCLUSION

(1) Both masking release and modulation interference are believed to occur whenever a background masker contains temporal fluctuations. Neither effect should be ignored to better understand the nature of masking with temporal fluctuations. The former effect is especially distinct when the speech stimuli provide a high degree of redundant speech information so that listeners can identify phonemes by only partial portions of speech exposed between modulation peaks in a masker. The latter effect is observed when modulation in a masker interferes with speech envelope processing in the auditory system in such a way as to hinder listeners' syllable processing, or by pretending to be a part of modulating speech bands, which is not ordinarily possible by a noise without modulations.

(2) Even though the modulation interference is believed to be effective, it seems to operate in a far more complex way than psychoacoustic MM/MDI. The general trend of psychoacoustic modulation masking no longer appears in speech recognition; the modulation rates of a speech target and a masker do not predict the amount of modulation interference, and the amount of modulation interference decreases as carrier frequencies of a speech target and a masker get closer. This advises us that caution is necessary when a psychoacoustic principle, usually obtained from nonspeech stimuli, is applied to speech recognition. The process of speech recognition, as in the identification of phonemes or words, is far more complex than a simple task such as detection or discrimination along in a single stimulus dimen-

sion. Therefore, previous findings on the modulation frequency domain, such as a modulation filterbank and modulation spectrum of speech, require more thorough investigation before they can be applied to speech perception.

ACKNOWLEDGMENTS

This work was supported in part by NIDCD R01 grant awarded to the second author. The publication of this paper was also supported in part by Bob Shannon. This paper is partially based on first author's Ph.D. dissertation submitted to the University of Iowa. We are grateful to the following individuals for providing constructive feedback during the early stages in this study and/or insightful criticisms on the early version of this manuscript: Paul Abbas, Richard Hurtig, Gregg Oden, Rochelle Newman (at the University of Iowa), Bob Shannon, Qian-Jie Fu, Monita Chatterjee, Mark E. Robert, John Galvin, III (at House Ear Institute, Los Angeles, California), Keith Kluender, Torsten Dau, and an anonymous reviewer. In addition, Sid Bacon and the anonymous reviewer helped the authors use the terms, MM and MDI, correctly.

[1]Researchers often use the term MDI to denote across-channel modulation masking without the strict requirement that carriers be tonal.

[2]To our knowledge, there are two studies in the literature reporting data that may be interpreted as modulation interference (Danhauer and Leppler, 1979; Souza and Turner, 1994). However, the theoretical basis for this phenomenon was not discussed until van der Horst and Dreschler (1998) attempted to mask the speech envelope by modulated maskers: unfortunately, they did not find the effect of modulation masking for speech and did not provide any further explanation.

[3]The choice of 12 was made on the consideration that fine structure of speech should be destroyed to some extent, and the score in quiet background should not be at a ceiling.

[4]We tested a few other conditions of SNR and found that the effect of SNR was minimal or inconclusive (Kwon, 2000). The general pattern of results was similar to what is reported here.

[5]This might be attributed to the selection of consonants in this study; frequent confusion usually occurs in noise-modulation processing between the pairs /f, θ/, /v, ð/, and /ð, ʒ/, and not all of these consonants were selected in the previous studies. Also the division of frequency bands in this study might have contributed to the lower performance; it was found that the ''optimal'' performance was observed when the bands were divided linearly at low frequency and logarithmically at high frequency (Fu, 1997). Therefore, it is possible the listeners performed sub-optimally in this study with the logarithmic frequency division in the whole band.

[6]In fact, we do not rule out the selectivity in condition REF, because the modulation spectrum of speech has its own shape, and some sort of selectivity could result from the shape. However, it is not clearly known what role the modulation spectrum plays in the selectivity of modulation interference, as masking release also intervenes in the present measurements. Thus although MI pattern in condition REF might have its own ''shape,'' we simply argue that it should not exhibit the same selectivity that could be found in condition LP4 and LP16 if psychoacoustic MM/MDI was effective.

Bacon, S. P., and Grantham, D. W. (**1989**). ''Modulation masking: Effects of modulation frequency, depth, and phase,'' J. Acoust. Soc. Am. **85**, 2575–2580.

Bacon, S. P., and Konrad, D. L. (**1993**). ''Modulation detection interference under conditions favoring within- or across-channel processing,'' J. Acoust. Soc. Am. **93**, 1012–1022.

Bacon, S. P., and Moore, B. C. J. (**1993**). ''Modulation detection interference: Some spectral effects,'' J. Acoust. Soc. Am. **93**, 3442–3453.

Bacon, S. P., Opie, J. M., and Montoya, D. Y. (**1998**). ''The effects of hearing loss and noise masking on the masking release for speech in temporally complex backgrounds,'' J. Speech Lang. Hear. Res. **41**, 549–563.

Bregman, A. S. (**1990**). *Auditory Scene Analysis* (The MIT Press, Cambridge, MA).

Bronkhorst, A. W., and Plomp, R. (**1992**). ''Effect of multiple speechlike maskers on binaural speech recognition in normal and impaired hearing,'' J. Acoust. Soc. Am. **92**, 3132–3139.

Buus, S. (**1985**). ''Release from masking caused by envelope fluctuations,'' J. Acoust. Soc. Am. **78**, 1958–1965.

Carlyon, R. P., Buus, S., and Florentine, M. (**1989**). ''Comodulation Masking Release for three types of modulator as a function of modulation rate,'' Hear. Res. **42**, 37–46.

Danhauer, J. L., and Leppler, J. G. (**1979**). ''Effects of four noise competitors on the California Consonant Test,'' J. Speech Hear Disord. **44**, 354–362.

Dau, T., Kollmeier, B., and Kohlrausch, A. (**1997**). ''Modeling auditory processing of amplitude modulation. I. Detection and masking with narrow-band carriers,'' J. Acoust. Soc. Am. **102**, 2892–2905.

Dau, T., Verhey, J., and Kohlrausch, A. (**1999**). ''Intrinsic envelope fluctuations and modulation-detection thresholds for narrow band noise carriers,'' J. Acoust. Soc. Am. **102**, 2892–2905.

Derleth, R. P., and Dau, T. (**2000**). ''On the role of envelope fluctuation processing in spectral masking,'' J. Acoust. Soc. Am. **108**, 285–296.

Dorman, M. F., Loizou, P., and Rainey, D. (**1997**). ''Speech intelligibility as a function of the number of channels of stimulation for signal processors using sine-wave and noise-band outputs,'' J. Acoust. Soc. Am. **102**, 2403–2411.

Drullman, R., Festen, J. M., and Plomp, R. (**1994a**). ''Effect of temporal envelope smearing on speech perception,'' J. Acoust. Soc. Am. **95**, 1053–1064.

Drullman, R., Festen, J. M., and Plomp, R. (**1994b**). ''Effect of reducing slow temporal modulations on speech reception,'' J. Acoust. Soc. Am. **95**, 2670–2680.

Eisenberg, L. S., Dirks, D., and Bell, T. S. (**1995**). ''Speech recognition in amplitude-modulated noise of listeners with normal and listeners with impaired hearing,'' J. Speech Hear. Res. **38**, 222–233.

Festen, J. M., and Plomp, R. (**1990**). ''Effects of fluctuating noise and interfering speech on the speech-reception threshold for impaired and normal hearing,'' J. Acoust. Soc. Am. **88**, 1725–1736.

Fu, Q.-J. (**1997**). ''Speech perception in acoustic and electric hearing,'' Ph.D. dissertation, University of Southern California, Los Angeles.

Fu, Q.-J., Shannon, R. V., and Wang, X. (**1998**). ''Effects of noise and spectral resolution on vowel and consonant recognition: Acoustic and electric hearing,'' J. Acoust. Soc. Am. **104**, 3586–3596.

Hall, J. W., and Grose, J. H. (**1991**). ''Some effects of auditory grouping factors on modulation detection interference (MDI),'' J. Acoust. Soc. Am. **90**, 3028–3035.

Hall, J. W., Grose, J. H., and Haggard, M. P. (**1988**). ''Comodulation masking release for multicomponent signals,'' J. Acoust. Soc. Am. **83**, 677–686.

Hall, J. W., Haggard, M. P., and Fernandez, M. A. (**1984**). ''Comodulation masking release as a function of bandwidth and test frequency,'' J. Acoust. Soc. Am. **88**, 113–118.

Houtgast, T. (**1989**). ''Frequency selectivity in amplitude-modulation detection,'' J. Acoust. Soc. Am. **85**, 1676–1680.

Houtgast, T., and Steeneken, H. J. M. (**1985**). ''A review of the MFT concept in room acoustics and its use for estimating speech intelligibility in auditoria,'' J. Acoust. Soc. Am. **77**, 1069–1077.

Howard-Jones, P. A., and Rosen, S. (**1993**). ''The perception of speech in fluctuation noise,'' Acustica **78**, 258–272.

Kwon, B. J. (**2000**). ''Speech perception under maskers with temporal fluctuations: interference or release?'' Ph.D. thesis, University of Iowa, Iowa City.

Kwon, B., and Shannon, R. V. (**2001**). ''Is modulation masking due to a modulation filterbank or simply temporal interference?'' Abs. of 24th Annual Midwinter Research Meeting of Assoc. Res. Otol. Vol. 24, p. 247.

Moore, B. C. J. (**1997**). *An Introduction to the Psychology of Hearing*, 4th ed. (Academic, San Diego, CA).

Pollack, I., and Pickett, J. M. (**1958**). ''Stereophonic listening and speech intelligibility against voice babble,'' J. Acoust. Soc. Am. **30**, 131–133.

Richards, V. M., Buss, E., and Tian, L. (**1997**). ''Effects of modulator phase for comodulation masking release and modulation detection interference,'' J. Acoust. Soc. Am. **102**, 468–476.

Schooneveldt, G. P., and Moore, B. C. J. (**1987**). ''Comodulation masking release (CMR): Effects of signal frequency, flanking band frequency, masker bandwidth, flanking band level, and monotic versus dichotic pre-

sentation of flanking band,'' J. Acoust. Soc. Am. **82**, 1944–1956.
Schreiner, C. E., and Raggio, M. W. (**1996**). ''Neuronal response in cat primary auditory cortex to electrical stimulation: II. Repetition coding,'' J. Neurophysiol. **75**, 1283–1300.
Shannon, R. V., Zeng, F.-G., Kamath, V., Wygonski, J., and Ekelid, M. (**1995**). ''Speech recognition with primarily temporal cues,'' Science **270**, 303–304.
Sheft, S., and Yost, W. A. (**1997**). ''Modulation detection interference with two-component masker modulators,'' J. Acoust. Soc. Am. **102**, 1106–1112.
Souza, P. E., and Turner, C. W. (**1994**). ''Masking of speech in young and elderly listeners with hearing loss,'' J. Speech Hear. Res. **37**, 655–661.
Strickland, E. A., and Viemeister, N. F. (**1996**). ''Cues for discrimination of envelopes,'' J. Acoust. Soc. Am. **99**, 3638–3646.
Takahashi, G. A., and Bacon, S. P. (**1992**). ''Modulation detection, modulation masking, and speech understanding in noise in the elderly,'' J. Speech Hear. Res. **35**, 1410–1421.
Turner, C. W., Chi, S.- L., and Flock, S. (**1999**). ''Limiting spectral resolution in speech for listeners with sensorineural hearing loss,'' J. Speech Hear. Res. **42**, 773–784.
Turner, C. W., Souza, P. E., and Forget, L. N. (**1995**). ''Use of temporal envelope cues in speech recognition by normal and hearing-impaired listeners,'' J. Acoust. Soc. Am. **97**, 2568–2576.
Van der Horst, R., and Dreschler, W. A. (**1998**). ''Modulation masking in a speech recognition task for hearing impaired subjects,'' *Proceedings of the International Congress on Acoustics, ICA/ASA-98, Seattle*, 1979–1980.
Van Tassell, D. J., Soli, S. D., Kirby, V. M., and Widen, G. P. (**1981**). ''Speech waveform envelope cues for consonant recognition,'' J. Acoust. Soc. Am. **82**, 1152–1161.
Verhey, J. L., Dau, T., and Kollmeier, B. (**1999**). ''Within-channel cues in comodulation masking release (CMR): Experiments and model predictions using a modulation-filterbank model,'' J. Acoust. Soc. Am. **106**, 2733–2745.
Warren, R. M. (**1970**). ''Perceptual restoration of missing speech sounds,'' Science **167**, 392–393.
Wilson, R. H., and Carhart, R. (**1969**). ''Influence of pulsed masking on the threshold for spondees,'' J. Acoust. Soc. Am. **46**, 998–1010.
Yost, W. A. (**1992**). ''Auditory image perception and amplitude modulation: Frequency and intensity discrimination of individual components for amplitude-modulated two-tone complexes,'' in *Auditory Physiology and Perception*, edited by Y. Cazals, L. Demany, and K. Horner (Pergamon, Oxford), pp. 487–493.
Yost, W. A., and Sheft, S. (**1989**). ''Across critical band processing of amplitude modulated tones,'' J. Acoust. Soc. Am. **85**, 848–857.
Yost, W. A., and Sheft, S. (**1994**). ''Modulation detection interference: Across frequency processing and auditory grouping,'' Hear. Res. **79**, 48–58.
Yost, W. A., Sheft, S., and Opie, J. (**1989**). ''Modulation interference in detection and discrimination of amplitude modulation,'' J. Acoust. Soc. Am. **86**, 2138–2147.
Zwicker, E., and Schorn, K. (**1982**). ''Temporal resolution in hard-of-hearing patients,'' Audiology **21**, 474–492.

On the effectiveness of whole spectral shape for vowel perception

Masashi Ito[a)]
Wako Research Center, Honda R & D Co., Ltd., 1-4-1 Chuo, Wako-shi, Saitama 351-0193, Japan

Jun Tsuchida and Masafumi Yano
Research Institute of Electrical Communication, Tohoku University, 2-1-1 Katahira, Aobaku, Sendai 980-8577, Japan

(Received 5 January 2001; accepted for publication 14 May 2001)

The formant hypothesis of vowel perception, where the lowest two or three formant frequencies are essential cues for vowel quality perception, is widely accepted. There has, however, been some controversy suggesting that formant frequencies are not sufficient and that the whole spectral shape is necessary for perception. Three psychophysical experiments were performed to study this question. In the first experiment, the first or second formant peak of stimuli was suppressed as much as possible while still maintaining the original spectral shape. The responses to these stimuli were not radically different from the ones for the unsuppressed control. In the second experiment, $F2$-suppressed stimuli, whose amplitude ratios of high- to low-frequency components were systemically changed, were used. The results indicate that the ratio changes can affect perceived vowel quality, especially its place of articulation. In the third experiment, the full-formant stimuli, whose amplitude ratios were changed from the original and whose $F2$'s were kept constant, were used. The results suggest that the amplitude ratio is equal to or more effective than $F2$ as a cue for place of articulation. We conclude that formant frequencies are not exclusive cues and that the whole spectral shape can be crucial for vowel perception. © *2001 Acoustical Society of America.*
[DOI: 10.1121/1.1384908]

PACS numbers: 43.71.Es, 43.71.An [CWT]

I. INTRODUCTION

Since the classic study of Peterson and Barney (1952), it has been recognized that vowels are perceived based on spectral resonances called formants and that the lower two or three formant frequencies are the essential cues for vowel perception. Klatt (1982) suggested that formant frequency changes could cause a change in phonetic quality while changing other parameters such as formant bandwidth or spectral tilt would not induce a change in phonetic quality, but be perceived as a change of speaker or transmission channel. The target model of vowel perception explains that vowels are represented as these formant frequencies and are perceived as a result of a comparison between inputs and targets. This formant hypothesis is now widely accepted, the primary reason being that the concept of formant can unify vowel characteristics among articulatory, acoustic, and perceptual aspects (Strange, 1989). However there has been some concern raised against a formant hypothesis being regarded as providing exclusive cues for vowel perception. We will now discuss these problems in detail.

The first problem is the difficulty in extracting formant frequencies. Although auditory systems have a ''harmonics sieve'' mechanism, which can extract harmonics of a certain fundamental frequency ($F0$) and suppress other components (Darwin and Gardner, 1986; Culling and Darwin, 1994), little is known about the mechanism of extracting formant frequencies from harmonics. The simplest model of the extraction could be a local peak picking of the spectrum, which was implicitly assumed in several studies (e.g., Lea and Summerfield, 1994). de Cheveigne and Kawahara (1999) clearly pointed out that a harmonic representation does not contain all the information about a spectral envelope which directly reflects vocal tract shape. There must be lack of information by nature. The peak-picking extraction thus cannot work accurately when $F0$ is high such as in a women's voice, or when adjacent formant frequencies are close such as with first and second formant frequencies ($F1$,$F2$) of a back vowel or $F2$ and third formant frequency ($F3$) of a front vowel. All of these situations are observed frequently in natural speech.

The second problem of the formant hypothesis is that some cues other than formant frequency can also affect vowel perception. Chistovich and Lublinskaja (1979) found that a change in the relative amplitude of adjacent formants could induce a change in the perceived vowel quality when the formant-frequency separation was less than 3–3.5 bark. The spectral averaging process named ''center of gravity (COG)'' was proposed to explain this phenomenon. Assmann (1991) examined the COG effect on back vowels by using multiformant synthesized speech and also found that some amplitude changes could affect the perceived vowel quality when $F0$ of the stimulus was high (250 Hz). Contrary to the COG hypothesis, the shifts of phoneme boundary were larger when the formant-frequency separation was greater than 3.5 bark. Beddor and Hawkins (1990) investigated the effect of spectral prominence on vowel perception with synthesized vowel stimuli whose first formant bandwidths were manipu-

a)Electronic mail: masashi.itou@f.rd.honda.co.jp

lated. They concluded that spectral peak frequency was primary and spectral shape was secondary as cues for vowel perception when the prominence of the peak was sufficient, and that the entire spectral shape of the peak was the most important cue when the prominence was not sufficient. These results indicate that in some limited situations the spectral shape can affect a perceived vowel quality even if formant frequencies are constant.

Taking a position against the formant hypothesis, several studies suggested that the whole spectral shape is required to perceive vowels. Bladon (1982) raised three objections against the formant hypothesis. The first was a reduction objection, pointing out that there must be a lack of information in translating the spectrum into formant frequencies. The second was a determination objection concerned with the difficulty in extracting formant frequency similar to that discussed previously. The third was a perceptual adequacy objection because there are some inconsistencies between formant-frequency representation and perceptual distance. Based on these objections, Bladon and Lindblom (1981) proposed a ''whole-spectrum model'' that took no account of formant frequency. The model calculated a spectral representation of loudness density versus pitch for each stimulus and estimated perceptual quality distances between stimulus pairs. This model showed a high correlation with the results of psychophysical experiments. Further, Zahorian and Jagharghi (1993) compared formant frequency and spectral shape as a cue for vowel perception in automatic vowel classification experiments. Spectral shape was represented as the coefficients in a discrete cosine transform expansion (DCTCs) of a modified log amplitude spectrum with a bark frequency scale. The performance for DCTCs was higher than for formants even if fundamental frequency was added to the formants, while this representation has more parameters than formant representation. This result supports the whole-spectrum model. Zahorian and Jagharghi thus concluded that DCTCs are a more complete representation of vowels than are formants.

The purpose of this study is to verify the validity of formant frequencies as cues for vowel perception through psychophysical experiments. In particular, formant frequencies and spectral shape are compared. Based on the results, we will discuss the formant hypothesis and whole-spectrum model.

II. EXPERIMENT 1

In order to evaluate the effectiveness of formant frequencies for vowel perception as opposed to whole spectral shape, a psychophysical experiment was performed with three kinds of stimuli. The first stimuli were control stimuli generated by a cascade-type Klatt synthesizer (Klatt, 1980). The parameters of the stimuli were $F1$ and $F2$. The second stimuli were with $F1$ suppressed and these were made from the control by suppressing their first formant peaks while maintaining the original spectral shapes as much as possible. The frequencies of the suppressed formant peaks could not be detected by local peak picking. The third stimuli were with $F2$ suppressed, also generated in a manner similar to the $F1$-suppressed stimuli.

TABLE I. The control parameters for cascade-Klatt type synthesizer (Klatt, 1980) in experiment 1. $F1$ and $F2$ are variables whose minimum and maximum values are displayed, while other parameters are constant.

Symbol	Name	Value
$F0$	Fundamental frequency (Hz)	125
$F1$	First formant frequency (Hz)	250–1250
$F2$	Second formant frequency (Hz)	750–2250
$F3$	Third formant frequency (Hz)	2500
$F4$	Fourth formant frequency (Hz)	3500
$F5$	Fifth formant frequency (Hz)	4500
$B1$	First formant bandwidth (Hz)	62.5
$B2$	Second formant bandwidth (Hz)	62.5
$B3$	Third formant bandwidth (Hz)	125
$B4$	Fourth formant bandwidth (Hz)	125
$B5$	Fifth formant bandwidth (Hz)	125
FGP	Glottal resonator frequency (Hz)	0
BGP	Glottal resonator bandwidth (Hz)	100

A. Method

1. Stimuli

A spectral envelope of the control stimulus was synthesized by a cascade-type Klatt synthesizer. The parameters are listed in Table I. A total of 96 stimulus envelopes were synthesized. $F1$ and $F2$ were variable while all other parameters were constant. $F1$ was varied between 250 and 1250 Hz in 125-Hz steps and $F2$ was varied between 750 and 2250 Hz in 125-Hz steps. Of these 117 stimuli, 21, whose $F1-F2$ separation was less than 200 Hz, were rejected because such stimuli are unnatural (Klatt, 1980). Based on these spectral envelopes, harmonic complexes were generated with a fundamental of 125 Hz and in cosine phase. Each stimulus was 400 ms long and onset and offset were shaped with a 40-ms raised cosine. After generation, all stimuli were normalized to have identical values of rms amplitude. The sampling frequency for all stimuli was 10 kHz.

A spectral envelope of the $F1$-suppressed stimulus was made from a control envelope by suppressing the first formant peak. The process of suppression satisfied the following three criteria: (1) The spectral envelope in the suppressed region was linear on scales of ERB-rate (equivalent rectangular bandwidth) and logarithmic amplitude; (2) the envelope and its first difference were continuous at both edges of the suppressed region; (3) the suppressed region contained the first formant peak and was as narrow as possible while still satisfying the above two criteria. ERB rate was approximated by (Glasberg and Moore, 1990),

$$\text{ERB rate}(f) = 21.4 \log_{10}(4.37f + 1.0). \quad (1)$$

A total of 96 $F1$-suppressed envelopes were calculated from the control envelopes. Based on these envelopes, steady-state harmonic stimuli were generated in the same fashion as the control. Their amplitudes were also normalized in order to maintain an identical rms value.

The $F2$-suppressed stimuli were generated from the controls in the same manner as the $F1$-suppressed stimuli except for the suppressed peak. In this case, the second formant peak was suppressed and the first formant peak was unchanged. The amplitudes of the $F2$-suppressed stimuli were also normalized to the common rms value. Four panels

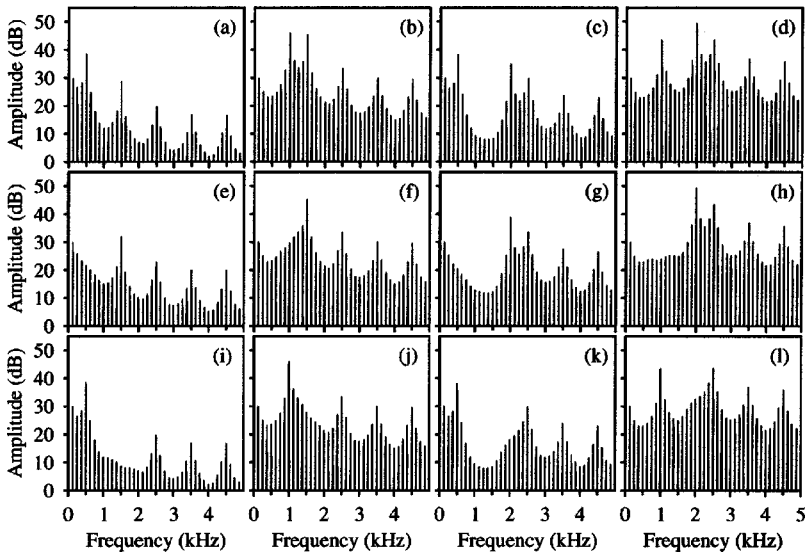

FIG. 1. Examples of amplitude spectra of 12 stimuli in experiment 1. Horizontal and vertical axes correspond to frequency (kHz) and amplitude (dB). (a)–(d) Control stimuli. (e)–(h) $F1$-suppressed stimuli. (i)–(l) $F2$-suppressed stimuli. (a), (e), (i) $F1=500$ Hz and $F2=1500$ Hz. (b), (f), (j) $F1=1000$ Hz and $F2=1500$ Hz. (c), (g), (k) $F1=500$ Hz and $F2=2000$ Hz. (d), (h), (l) $F1=1000$ Hz and $F2=2000$ Hz.

on the upper, middle, and bottom line of Fig. 1 show the examples of amplitude spectra of the control, $F1$-suppressed and $F2$-suppressed stimuli, respectively. The panels on each column originally have the same formant frequencies.

2. Procedure and subjects

Stimulus generation and data collection were controlled by a personal computer (IBM-PC). All of the stimuli were generated with 16-bit quantization and a 10-kHz sampling rate with terminal analog method. They were presented at about 75 dB SPL over headphones (LambdaNova CLASSIC, STAX) in a sound attenuated room. Subjects were required to respond with what vowel they heard, where the answers were restricted to one of five Japanese vowels, /a/, /i/, /u/, /e/ and /o/. We recorded the response via a keyboard. After the answer and a silence of more than 1 s, the next stimulus was presented. Stimuli were not repeated and subjects had to select one of the allowed five choices.

The experiments consisted of three sessions, the control, $F1$ suppression, and $F2$ suppression. All subjects served the three sessions successively. Each session was divided into four blocks and each block consisted of six trials. Each trial consisted of 96 stimuli and the order of presentation of stimuli was at random. Each subject performed one or two blocks a day to keep the concentration level properly high. The first trial of each block served as training and was not used for analysis.

Four student volunteers, aged 22–23 years, participated in the experiments. All of them were native Japanese speakers and had no hearing loss.

B. Results and discussion

For all of three types of stimuli, 20 responses of each subject were recorded. According to the responses, recognition rates of the five vowels were calculated at 96 lattice points in $F1-F2$ space. To obtain the phoneme boundaries of each vowel, the recognition rates were required for all points in $F1-F2$ space. So, we calculated the recognition rates at arbitrary points in $F1-F2$ space by linear interpolation of the rates of the surrounding four lattice points. Figure 2 shows these phoneme boundaries for control stimuli. Each panel corresponds to a subject. The horizontal axis indicates the first formant frequency ($F1$) of the stimuli and the vertical axis indicates the second formant frequency ($F2$). The thick and thin lines represent 50% and 90% phoneme boundaries, respectively. Although there was a little difference, the relative locations of the five vowels on the $F1-F2$ plane were quite similar for every subject. These locations resemble other studies that examined Japanese vowel perception (e.g., Ueda and Watanabe, 1987) and the study of Peterson and Barney (1952). The results for control stimuli support the formant hypothesis that vowels are represented and perceived by formant frequencies.

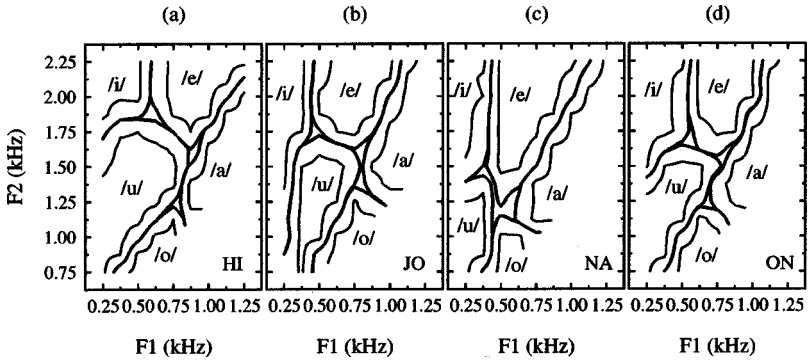

FIG. 2. Phoneme boundaries for the control stimuli in experiment 1: (a) subject HI, (b) subject JO, (c) subject NA, (d) subject ON. Horizontal axis and vertical axis correspond to first and second formant frequency of stimuli, respectively. Thick lines represent 50% phoneme boundaries for each vowel. Thin lines represent 90% phoneme boundaries. The open triangles located at the lower right in each panel correspond to the forbidden stimuli caused by the closed-formant criteria (see the text).

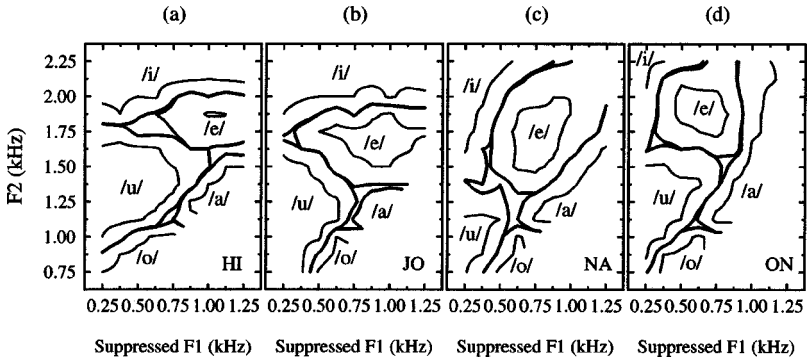

FIG. 3. Phoneme boundaries for $F1$-suppressed stimuli in experiment 1 in the same manner as in Fig. 2 except that the horizontal axis corresponds to suppressed first formant frequency.

Let us assume that vowels are recognized on the basis of $F1$ and $F2$, and that these formant frequencies are extracted by simple peak picking of the spectral envelope, in which extracted perceptual first and second formant frequencies are named $P1$ and $P2$, respectively. Since this model cannot extract the suppressed formant frequencies, it will interpret $F1$-suppressed stimulus as that $P1=F2$ and $P2=F3$. The vowel calculated by this model thus would not vary according to a suppressed $F1$, and would change only for $F2$ because all of the stimuli had constant $F3$ values. Further, the results for control stimuli predict that the vowels would vary from /i/ to /e/ to /a/ with an increase in $F2$.

The response for $F1$-suppressed stimuli however disagrees with this prediction. Figure 3 shows the phoneme boundaries for $F1$-suppressed stimuli. The horizontal axis corresponds to suppressed $F1$ and the vertical axis corresponds to $F2$. The thick and thin lines represent 50% and 90% phoneme boundaries, respectively. Contrary to the prediction, there were some changes of perceived vowel quality corresponding to suppressed $F1$. For example, the recognition rate of vowel /u/ decreased and the rate of /a/ increased with an increase in suppressed $F1$ at $F2=1125$ Hz for all subjects. Further, vowels /u/ and /o/ which did not appear as predictions of the simple model were perceived at an above 90% in recognition rate in response to the stimulus with suppressed $F1$. The pattern of phoneme boundaries for $F1$-suppressed stimuli was closer to control than predicted. The relative locations of the five vowels for $F1$-suppressed stimuli resembled the control for subjects NA [Figs. 2(c) and 3(c)] and ON [Figs. 2(d) and 3(d)]. For subjects HI [Figs. 2(a) and 3(a)] and JO [Figs. 2(b) and 3(b)], there were some discrepancies between the control and the $F1$ suppression especially in the region where $F2$ was high, where the prediction might explain the result.

Figure 4 shows the phoneme boundaries for $F2$-suppressed stimuli. The horizontal axis corresponds to $F1$ and the vertical axis corresponds to suppressed $F2$. The simple model mentioned previously also would not be able to extract suppressed $F2$ and would calculate that $P1=F1$ and $P2=F3$. The perceived vowel thus would not change according to suppressed $F2$ (vertical axis). This prediction was also incompatible with the result. For all subjects, changes of perceived vowel quality were observed corresponding to suppressed $F2$. For instance, the recognition rates for /u/ and /o/ were decreased and the rates for /i/ and /e/ were increased with an increase of suppressed $F2$. The results of experiment 1 cannot be explained by formant hypothesis based on the simple peak-picking mechanism and support the hypothesis that vowel quality is perceived by the whole spectral shape.

The phoneme boundaries for $F2$ suppression were quite similar to the control except around the region of $F1=600$ Hz and $F2=1200$ Hz. The similarity between $F2$ suppression and control was apparently larger than the ones between $F1$ suppression and control. This indicates that vowel quality, especially its place of articulation (front/back), can be perceived even if $F2$ information is not available. There would thus be other cues for place of articulation instead of the second formant frequency. The amplitude ratio of high- to low-frequency components of the spectrum might be a good candidate for one of these cues. Klatt (1980) pointed out that formant peak amplitude *An* would be increased with an increase in lower formant frequency Fm $(n>m)$ in the cascade-type synthesizer. Figure 5 shows the amplitude ratios of $A3$ to $A1$ of $F2$-suppressed stimuli which are identical to those of control stimuli. Apparently, the amplitude ratio almost linearly increases with the increase of suppressed $F2$. This amplitude ratio might be used as a cue for place of

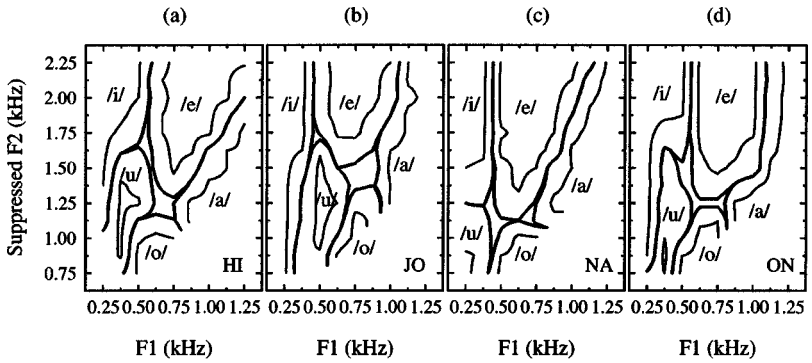

FIG. 4. Phoneme boundaries for the $F2$-suppressed stimuli in experiment 1 in the same manner as in Fig. 2 except that vertical axis corresponds to suppressed second formant frequency.

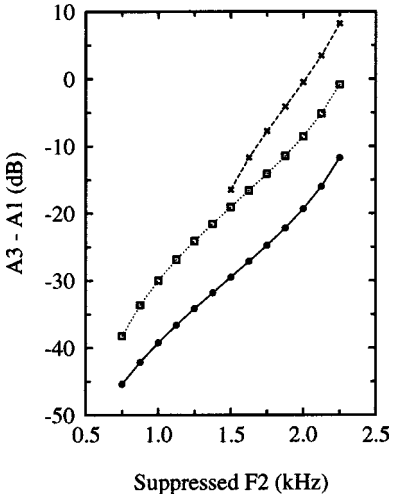

FIG. 5. The amplitude ratios of $A3$ to $A1$ for $F2$-suppressed stimuli as a function of suppressed $F2$. Horizontal axis and vertical axis correspond to suppressed $F2$ (kHz) and $A3-A1$ (dB), respectively. Closed circles (solid line) represent the stimuli of $F1=250$ Hz. Squares (dotted line) represent the stimuli of $F1=500$ Hz. Crosses (dashed line) represent the stimuli of $F1=1250$ Hz.

articulation instead of $F2$. This possibility was directly examined in the next experiment.

III. EXPERIMENT 2

Klatt (1982) suggested that only formant frequencies could affect perceived vowel quality while formant bandwidth and spectral tilt could not, and that changes in bandwidth and tilt were perceived as changes of speakers or transmission channel. The result of experiment 1 for $F2$-suppressed stimuli, however, implies that relative amplitudes of high- to low-frequency components of the spectrum can affect perceived vowel quality. The influence of this amplitude ratio to vowel perception will be examined here.

A. Method

1. Stimuli

In order to examine the perceptual effect of the amplitude ratio more clearly, it is useful to change the lower formant frequency and the higher formant amplitude of stimuli independently. So the simple synthesizer was used in this experiment instead of a cascade-Klatt synthesizer. The frequency response was $R(f)$ as described in the following:

$$R(f)=\max(10^{D_n(f)/20}), \quad n=1,...,N. \tag{2}$$

$$D_n(f)=A_n-\frac{6|f-F_n|}{B_n}, \tag{3}$$

where Fn, Bn, and An represented frequency, bandwidth, and peak amplitude of the nth formant, respectively. The number of formants, N, was four. Figure 6 shows amplitude spectra of stimuli synthesized by this filter. Every slope of the peaks had a linear correlation between frequency (Hz) and logarithmic amplitude (dB). A total of 81 envelopes were synthesized by varying $F1$ and $A1$. $F1$ was varied between 250 and 1250 Hz in 125-Hz steps. The relative amplitude $A1-A2$ was varied between 0 and 48 dB in 6-dB steps.

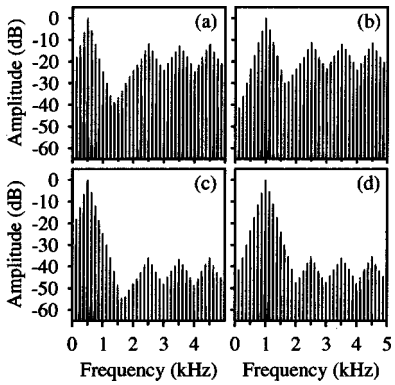

FIG. 6. Examples of amplitude spectra of the stimuli in experiment 2. The horizontal axis and vertical axis correspond to frequency (kHz) and amplitude (dB), respectively. (a) $F1=500$ Hz and $A2-A1=-12$ dB, (b) $F1=1000$ Hz and $A2-A1=-12$ dB, (c); $F1=500$ Hz and $A2-A1=-36$ dB, (d) $F1=1000$ Hz and $A2-A1=-36$ dB.

Formant amplitudes $A2$, $A3$, and $A4$ were the same and they changed in the same way. This amplitude change thus varies negatively with the change of amplitude ratio of high- to low-frequency components of the spectrum. The range of the relative amplitude involved the range of $A1-A3$ of all the control stimuli in experiment 1. Table II shows the parameters for the synthesizer. According to these envelopes, cosine-phase harmonic stimuli with a 125-Hz fundamental were generated in the same fashion as in experiment 1. Stimulus duration was 400 ms and rise/fall times were 40 ms with a half-length Hanning window. Amplitudes of all stimuli were normalized in order to maintain an identical rms value.

2. Procedure and subjects

The procedure of experiment 2 was the same as for experiment 1 except for the number of stimuli involved in a single trial. In experiment 2, a single trial consisted of 81 stimuli. Four blocks, consisting of six trials of stimuli, were performed on each subject. The subjects in experiment 2 were the same as in experiment 1.

B. Results and discussion

Figure 7 shows the phoneme boundaries of vowels in experiment 2. The four panels correspond to subjects. The horizontal axis indicates $F1$ (Hz) and the vertical axis indicates $A2-A1$ (dB). The thick and thin lines represent 50% and 90% phoneme boundaries, respectively. These boundaries were obtained by linear interpolation as in experiment 1. If the relative amplitude of the stimulus did not affect the

TABLE II. The control parameters for an envelope synthesizer in experiment 2 (see the text). $F1$ and $A1$ are variables whose minimum and maximum values are displayed, while other parameters are constant in the experiment.

Formant number N	Frequency Fn (Hz)	Bandwidth Bn (Hz)	Amplitude An (dB)
1	250–1250	62.5	0–48
2	2500	125	0
3	3500	125	0
4	4500	125	0

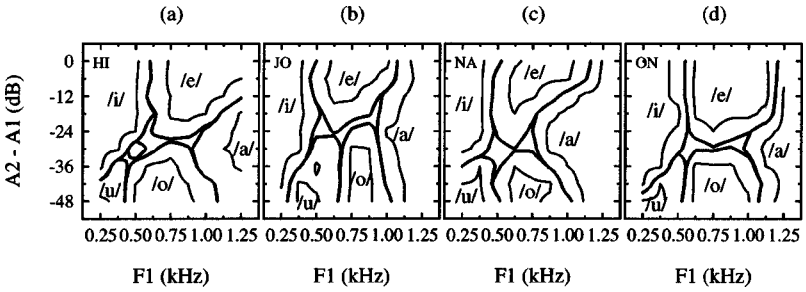

FIG. 7. Phoneme boundaries in experiment 2. Each panel corresponds to the result for an individual subject, the arrangement is in the same manner as in Fig. 2. The horizontal axis corresponds to $F1$ (kHz). Vertical axis corresponds to $A2-A1$. The thick line in (a) which surrounds an isolated region represents 50% phoneme boundary of vowel /u/.

perceived vowel, all of the phoneme boundaries would be parallel to the vertical axis. As shown in Fig. 7, the result was not compatible with this prediction. For example, the increase of $A2-A1$ induced the change of perceived vowel from /u/ to /i/ when $F1=375$ Hz, and /o/ to /e/ when $F1$ was near 750 Hz. In all subjects it was observed that the relative amplitude change could induce the change of perceived vowel quality even if all of the formant frequencies were constant. Since the closest separation of $F1$ and $F2$ was about 4.5 bark ($F1=1250$ Hz, $F2=2500$ Hz), the amplitude influence to vowel perception observed in this experiment could not be explained by COG in which 3.5 bark of frequency separation was critical to integrate the energy. The critical band value B was approximated by (Zwicker and Terhardt, 1980)

$$B=13\tan^{-1}(0.76f)+3.5\tan^{-1}\{(f/7.5)^2\}. \tag{4}$$

Furthermore, the result supports the hypothesis that the amplitude ratio of high- to low-frequency components of the spectrum is an essential cue for place of articulation of perceived vowel. Figure 7 indicates that stimuli whose $A2-A1$ were decreased, and the amplitudes of low-frequency components were sufficiently larger than high-frequency components, were perceived as back vowels, while the stimuli whose $A2-A1$ were near zero and with the entire spectral shape flat were perceived as front vowels. Comparing Fig. 4 with Fig. 7, the phoneme boundaries in experiment 2 had patterns similar to those for $F2$-suppressed stimuli in experiment 1. As shown in Fig. 5, the amplitude ratio was approximately linearly proportional to the suppressed $F2$. This implies that the vertical axis in Fig. 4 was compatible with that in Fig. 7 and the results in experiment 2 were consistent with those for $F2$ suppression in experiment 1.

Beddor and Hawkins (1990) suggested that spectral shape was the more important cue for vowel perception rather than formant frequencies or COG when the spectral prominence of the low-frequency region was not sufficient, and that spectral shape was a secondary cue when the prominence was sufficient. In experiment 2, stimuli had no spectral peak between 1250 and 2500 Hz where $F2$ peak often exists for natural speech. If this lack of $F2$ is interpreted as insufficient prominence of $F2$, it is possible that the amplitude influence of our experiment was only effective in limited situations such as those suggested by Beddor and Hawkins. This was examined in the next experiment.

IV. EXPERIMENT 3

In experiment 2 we found that the amplitude ratio of high- to low-frequency components of the spectrum could affect perceived vowel quality, especially its place of articulation. However, it was not clear whether this amplitude information was always effective even if every formant peak could be extracted by peak picking. To compare the influence of the amplitude ratio with formant frequencies, a psychophysical experiment was performed. The stimulus was five-formants synthesized vowels, in which $F2$ was constant and the amplitude ratios of $A1$ to $A3$, $A4$ and $A5$ were variable. Thus in this experiment the amplitude ratio competed with the second formant frequency.

A. Method

1. Stimuli

The envelopes $S(f)$ of stimuli in experiment 3 were almost the same as those of the controls in experiment 1 except for the second formants, which was fixed at 1500 Hz throughout this experiment. $S(f)$ was calculated by the convolution of $T(f)$ and $U(f)$ as follows. At first, the envelope $T(f)$ with five formants was synthesized by a cascade-Klatt model at the fixed $F2$, in which $F1$ was varied between 250 and 1250 Hz in 125-Hz steps and other parameters were given as in Table I. Since the amplitude ratio of high- to low-frequency components of the control increases with an increase of $F2$ (Fig. 5), this relationship was used in the stimuli in this experiment. $U(f)$ was utilized to manipulate amplitude ratios of stimuli with a parameter "nominal $F2$" and was defined by

$$U(f)=10^{V(f)/20}, \tag{5}$$

$$V(f)=\begin{cases} 0 & \text{for } f<F2 \\ \dfrac{\mathrm{ERB}(f)-18.8}{4.24}W & \text{for } F2\leqslant f<F3 \\ W & \text{for } f\geqslant F3, \end{cases} \tag{6}$$

$$W=R(F1,\ \text{nominal } F2)-R(F1,\ 1500), \tag{7}$$

where $R(a,b)$ indicates the amplitude ratio (dB) of $A3$ to $A1$ of the control stimuli, $F1=a$ and $F2=b$. The amplitude ratio of $A3$ to $A1$ of $S(f)$ was thus equal to $R(F1,$ nominal $F2)$, in which nominal $F2$ was varied between 750 and 2250 Hz in 125-Hz steps. Figure 8 shows amplitude spectra of the stimuli. For example, the stimulus in Fig. 8(a), $F1=500$ Hz and nominal $F2=2000$ Hz, has the same amplitude ratio of $A3$ to $A1$ as the control stimulus in Fig. 1(c),

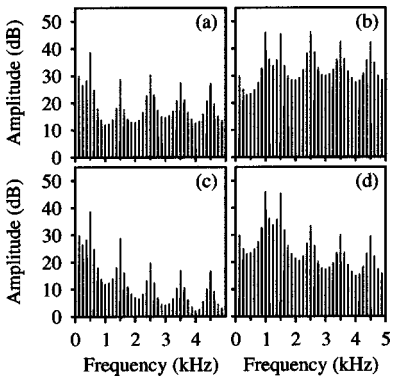

FIG. 8. Examples of amplitude spectra of the stimuli in experiment 3. The horizontal axis and vertical axis correspond to frequency (kHz) and amplitude (dB), respectively. (a) $F1=500$ Hz and nominal $F2=2000$ Hz, (b) $F1=1000$ Hz and nominal $F2=2000$ Hz, (c) $F1=500$ Hz and nominal $F2=1500$ Hz, (d) $F1=1000$ Hz and nominal $F2=1500$ Hz.

$F1=500$ Hz and $F2=2000$ Hz. A total of 96 envelopes were synthesized. Based on these envelopes, a cosine-phase harmonic complex with 125-Hz fundamental was generated in the same manner as in experiment 1. The duration was 400 ms and rise/fall times were 40 ms with half-length Hanning window. Amplitudes of all stimuli were normalized in order to have a common rms value.

2. Procedure and subjects

The procedure of experiment 3 was the same as in experiment 1 except for the number of stimuli types. There was only one type of stimuli in experiment 3 while there were three types of stimuli in experiment 1. Four blocks, consisting of six trials of 96 stimuli, were performed on each subject. The subjects were identical to those in experiment 1.

B. Results and discussion

Figure 9 shows the phoneme boundaries of each vowel in experiment 3. The horizontal axis corresponds to $F1$ and the vertical axis corresponds to nominal $F2$. The thick and thin lines represent 50% and 90% phoneme boundaries calculated by linear interpolation. Assuming formant frequencies to be exclusive cues for perception, all phoneme boundaries should be parallel to the vertical axis, and $F1$'s at boundaries should be predicted based on the results for control stimuli in experiment 1. For example, 50% boundary between /u/ and /a/ should occur at $F1=854$ Hz for subject HI [Fig. 9(a)], /i/–/u/ and /u/–/a/ boundaries should occur at $F1=317$ Hz and 799 Hz, respectively, for subject JO [Fig. 9(b)], /i/–/e/ and /e/–/a/ boundaries should occur at $F1=385$ Hz and 750 Hz, respectively, for subject NA [Fig. 9(c)], /i/–/u/ and /u/–/a/ boundaries should occur at $F1=315$ Hz and 786 Hz, respectively, for subject ON [Fig. 9(d)]. It was only in the region where nominal $F2=1500$ Hz that this prediction was compatible with the result. There were changes of perceptual vowel quality according to nominal $F2$ in all subjects. Specifically, we observed that three of four subjects perceived a vowel changed from /u/ to /i/ with an increase of nominal $F2$ when $F1$ was about 250 Hz, two of four subjects perceived a vowel changed from /o/ to /e/ when $F1$ was about 750 Hz, and all subjects perceived a vowel changed from /a/ to /e/ when $F1$ was from about 875 to 1000 Hz. These results indicate that the amplitude ratio can affect vowel perception even if all formant frequencies are available.

The shaded lines in Fig. 9 represent 50% phoneme boundaries for control stimuli in experiment 1. The boundaries in experiment 3 for subject NA [Fig. 9(c)] and ON [Fig. 9(d)] were quite similar to those found in experiment 1. For subject HI [Fig. 9(a)] and JO [Fig. 9(b)], there were no stimuli perceived as vowel /o/ above a 50% recognition rate in experiment 3. These were the major differences from experiment 1. The recognition rates of front vowel /e/ were however increased corresponding to nominal $F2$ for these subjects. We conclude that, in general, high nominal-$F2$ stimuli are perceived as front vowels and low nominal-$F2$ stimuli are perceived as back vowels. This result supports our hypothesis that amplitude ratio of spectrum is an essential cue for place of articulation. We might not conclude that the amplitude ratio is an exclusive cue compared with second formant frequency due to the differences among subjects. However, the results imply that the amplitude ratio is no less effective than $F2$ for place of articulation.

V. GENERAL DISCUSSION

Formants form a central concept in speech production that combines vocal tract shape with acoustical characteristics of pronounced vowels (Fant, 1960). For example, articulatory ''openness'' and ''advance (place of articulation)'' roughly corresponds to $F1$ and $F2$, respectively. Miller (1989) investigated natural utterances of American English vowels acoustically and showed that each of them was individually clustered in auditory perceptual space (APS) corresponding to formant frequencies and fundamental frequency.

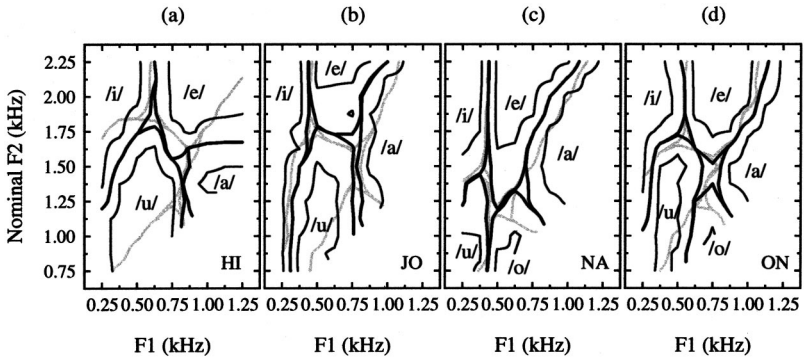

FIG. 9. Phoneme boundaries in experiment 3 in the same manner as in Fig. 2 except that the vertical axis corresponds to nominal $F2$. The thick line and thin line represent 50% and 90% phoneme boundaries in experiment 3. The shaded line represents 50% phoneme boundaries for control stimuli in experiment 1.

Further, he pointed out that vowels could be identified in this APS with extremely high accuracy. This implies that formant frequencies might be utilized as cues for vowel perception in our auditory system.

Klatt (1982) performed some psychophysical experiments with synthesized vowels to evaluate the influence of spectral-shape characteristics such as formant frequency, formant bandwidth, spectral tilt, and filtering passband/stopband on vowel perception. He concluded that the formant frequency was the most important cue for vowel perception, and that the other characteristics could not affect the perception of the vowel quality although they induced speaker individualities.

In our first experiment we examined the response for the stimuli with the first or second formant suppressed. If formant frequencies are exclusive cues for vowel quality perception, this suppression should inevitably change the perception of vowel quality. However, in contrast with this prediction, the response for the suppressed stimuli was not greatly changed from the control. These results cannot easily be explained by formant hypothesis based on the local peak-picking mechanism. It strongly implies to us that formant frequencies are not exclusive cues for vowel perception.

In opposition to the formant hypothesis, Bladon (1981) proposed a whole-spectrum model for vowel perception. However, it does not seem to be appropriate to view this model as opposed to the formant hypothesis because formant frequency is also involved in the ''whole-spectrum'' characteristics. In the automatic classification experiments using naturally spoken vowel stimuli, Zahorian (1993) compared the performances of two classification models, one based on the DCTCs represented by a whole spectral shape and the other based on the formant frequencies. The performance of the former was higher than the latter even if the latter were allowed to utilize the information of stimuli fundamental frequencies. Although this result might indicate that some information other than formant frequencies is useful for vowel perception, the model based on the DCTCs required more input parameters than those based on formant frequencies. The performance of the DCTCs model was worse than the formant model for the same number of input parameters. In other words, from the viewpoint of information compression, formant frequencies were more effective in vowel perception than the whole spectral shape. Consequently, the whole-spectrum model should not be viewed as the complete opposite of the formant hypothesis but it does suggest the incompleteness of formant representation.

In addition to formant frequencies, we demonstrated that the amplitude ratio of high- to low-frequency components might also be a crucial cue for vowel perception. The result of our second experiment showed that changes in this ratio could induce a change in perceived vowel quality, especially its place of articulation (front/back). This cannot be explained by COG theory because the frequency separation in our experiment was always greater than 3.5 bark. In speech production theory, place of articulation is nearly perceived depending on the frequencies of the second formant, in which high-$F2$ and low-$F2$ stimuli are perceived as front and back vowel, respectively. Since in the cascade-type speech production model, the changes in $F2$ inevitably accompany the changes in higher formant amplitudes (Klatt, 1980), the amplitude ratio might be regarded as only a secondary cue of formant frequency change. However, the amplitude ratio is easily perceived in our auditory system, while the formant frequencies are not always detected distinctly. It is reasonable to assume that this robust cue is utilized in our vowel perception system. In fact, Lienard and Benedetto (1999) found that the relative intensity of high- to low-frequency components of speech became stronger when a speaker intended to communicate with a listener in a remote location. Since a high-frequency tone is attenuated greater than a low-frequency one during propagation, this implies that this pre-emphasis mechanism might cancel the inequality of attenuation and the amplitude ratio is very important for vowel perception.

Beddor and Hawkins (1990) concluded that spectral shape was the primary cue for vowel perception only when the lower spectral prominence was weak, while it was secondary when the prominence was sufficient. In experiment 2, there was no prominent peak in the frequency region of the stimuli where $F2$ was expected to be in natural speech. This seems to agree well with the results in the limited conditions as pointed out by Beddor and Hawkins. The results of our third experiment, however, showed that the amplitude ratio was still effective for vowel perception even when the prominence of the $F2$ peak was sufficient. That is, the effect of the amplitude ratio on the perception of place of articulation was found to be equal to or greater than that of $F2$. For example, we observed in subjects that the increase of the amplitude ratio caused increases in the recognition rates for front vowels, while $F2$ was constant. For two of four subjects, the decrease of the amplitude ratio caused increases in the recognition rates for back vowels, while $F2$ was constant. The similarity of the phoneme boundary pattern between experiment 3 and the control of experiment 1 for these two subjects strongly supports the hypothesis that place of articulation is perceived by the amplitude ratio [Figs. 9(c) and (d)].

It should be noted that our hypothesis has at least three problems. The first is the definition of the amplitude ratio. It was defined as the relative amplitude of the higher to the first formant peak in experiment 2 while it was defined as the relative amplitude of the third formant to the first one in experiment 3. These definitions are similar, but there is no quantitative comparison between the two. So, if the amplitude ratio is essential for vowel perception, it is crucial to clarify how it is detected by our auditory system. It probably appears as an excitation pattern of the neural network (Moore and Glasberg, 1986). The second problem of the amplitude ratio hypothesis is that it cannot explain the relation between spectral shape and vowel height. For $F1$-suppressed stimuli in experiment 1, some recognition rates of vowels changed depending on the suppression of $F1$. Another cue other than the amplitude ratio seems to be required to explain this result. The third problem is a context effect. Since vowel perception is known to be context dependent, there is a possibility that subjects adapted their criteria to each type of stimuli in our experiments. We believe this influence might

be small because there are no significant differences in statistics among the responses of each block through all experiments. These questions remain for further study.

The results of our experiments indicate that vowels can be perceived by the whole spectral shape of stimuli even if their formant frequency is not available. The simplest model for these results is storing the spectral shapes of all of vowels as the templates, comparing input with them, and determining the output vowel based on the similarity between templates and input. This type of model has been adopted often in recent commercially available systems for speech perception. However, this is obviously not proper as a cognitive model for human beings because it cannot explain our excellent ability at speaker adaptation with limited storage capacity. This is the reason why an elegant compressed representation of whole spectrum shape is required. We propose the amplitude ratio as one of candidates for the compressed representation. This cannot be psychophysically verified using a cascade-type synthesizer, which was used in several studies (e.g., Fahey and Diehl, 1996), because the synthesizer cannot produce the formant frequencies and their amplitudes independently. This might be one of the reasons why the effect of amplitude ratio has not been clarified.

VI. CONCLUSIONS

(1) Formant frequencies are not exclusive cues for vowel perception. All three of our experiments support this conclusion. In experiment 1, a suppression of the first or second formant peak did not cause a great difference in distribution patterns of recognition rates when whole spectral shape was not largely changed (Figs. 2–4). In experiments 2 and 3, a modification of whole spectral shape did induce a change of perceived vowel even when all formant frequencies were constant (Figs. 7 and 9).

(2) The amplitude ratio of high- to low-frequency components is no less effective for place of articulation than the second formant frequency. Using a cascade-Klatt synthesizer, the changes in $F2$ inevitably accompany the changes in higher formant amplitudes (Fig. 5). As seen in experiment 2, this change of the amplitude ratio of high- to low-frequency components itself caused the change of perceived vowel in its place of articulation (Fig. 7). This effect was also verified in experiment 3, in which the amplitude ratio of high- to low-frequency components competed against the second formant frequency (Fig. 9).

ACKNOWLEDGMENTS

We would like to thank Dr. Hiroshi Tsujino for his encouragement and guidance throughout this project. We are also grateful to Dr. Tatsuya Hirahara for his useful suggestions in our preliminary experiments. This research was partially supported by a grant from Honda R&D Co., Ltd.

Assmann, P. F. (**1991**). ''The perception of back vowels: Centre of gravity hypothesis,'' Q. J. Exp. Psychol. **43**, 423–448.

Beddor, P. S., and Hawkins, S. (**1990**). ''The influence of spectral prominence on perceived vowel quality,'' J. Acoust. Soc. Am. **87**, 2684–2704.

Bladon, R. A. W., and Lindblom, B. (**1981**). ''Modeling the judgment of vowel quality differences,'' J. Acoust. Soc. Am. **69**, 1414–1422.

Bladon, R. A. W. (**1982**). ''Arguments against formants in the auditory representation of speech,'' in *The Representation of Speech in the Peripheral Auditory System*, edited by R. Carlson and B. Granstrom (Elsevier, Amsterdam), pp. 95–102.

Chistovich, L. A., and Lublinskaja, V. V. (**1979**). ''The center of gravity effect in vowel spectra and critical distance between the formants,'' Hear. Res. **1**, 185–195.

Culling, J. F., and Darwin, C. J. (**1994**). ''Perceptual and computational separation of simultaneous vowels: Cues arising from low-frequency beating,'' J. Acoust. Soc. Am. **95**, 1559–1569.

Darwin, C. J., and Gardner, R. B. (**1986**). ''Mistuning a harmonic of a vowel: Grouping and phase effects on vowel quality,'' J. Acoust. Soc. Am. **79**, 838–845.

de Cheveigne, A., and Kawahara, H., (**1999**). ''Missing-data model of vowel identification,'' J. Acoust. Soc. Am. **105**, 3497–3508.

Fahey, R. P., and Diehl, R. L. (**1996**). ''The missing fundamental in vowel height perception,'' Percept. Psychophys. **58**, 725–733.

Fant, G. (**1960**). *Acoustic Theory of Speech Production* (Mouton, Gravenhage, The Netherlands).

Glasberg, B. R., and Moore, B. C. J. (**1990**). ''Derivation of auditory filter shapes from notched-noise data,'' Hear. Res. **47**, 103–138.

Klatt, D. H. (**1980**). ''Software for a cascade/parallel formant synthesizer,'' J. Acoust. Soc. Am. **67**, 971–995.

Klatt, D. H. (**1982**). ''Speech processing strategies based on auditory models,'' in *The Representation of Speech in the Peripheral Auditory System*, edited by R. Carlson and B. Granstrom (Elsevier, Amsterdam), pp. 181–196.

Lea, A. P., and Summerfield, Q. (**1994**). ''Minimal spectral contrast of formant peaks for vowel recognition as a function of spectral slope,'' Percept. Psychophys. **56**, 379–391.

Lienard, J. S., and Benedetto, M. G. (**1999**). ''Effect of vocal effort on spectral properties of vowels,'' J. Acoust. Soc. Am. **106**, 411–422.

Miller, J. D. (**1989**). ''Auditory-perceptual interpretation of the vowel,'' J. Acoust. Soc. Am. **85**, 2114–2134.

Moore, B. C. J., and Glasberg, B. R. (**1986**). ''The role of frequency selectivity in the perception of loudness, pitch and time,'' in *Frequency Selectivity in Hearing*, edited by B. C. J. Moore (Academic, London), pp. 250–308.

Peterson, G. E., and Barney, H. L. (**1952**). ''Control methods used in a study of the vowels,'' J. Acoust. Soc. Am. **24**, 175–184.

Strange, W. (**1989**). ''Evolving theories of vowel perception,'' J. Acoust. Soc. Am. **85**, 2081–2087.

Ueda, Y., and Watanabe, A. (**1987**). ''Visible/tactile vowel information to be transmitted to the hearing impaired,'' J. Acoust. Soc. Jpn. **8**, 99–108.

Zahorian, S. A., and Jagharghi, A. J. (**1993**). ''Spectral-shape features versus formants as acoustic correlates for vowels,'' J. Acoust. Soc. Am. **94**, 1966–1982.

Zwicker, E., and Terhardt, E. (**1980**). ''Analytical expressions for critical-band rate and critical bandwidth as a function of frequency,'' J. Acoust. Soc. Am. **68**, 1523–1525.

Speech recognition in noise as a function of the number of spectral channels: Comparison of acoustic hearing and cochlear implants

Lendra M. Friesen,[a] Robert V. Shannon, Deniz Baskent, and Xiaosong Wang
Department of Auditory Implants and Perception, House Ear Institute, 2100 West Third Street, Los Angeles, California 90057

(Received 9 September 2000; accepted for publication 3 May 2001)

Speech recognition was measured as a function of spectral resolution (number of spectral channels) and speech-to-noise ratio in normal-hearing (NH) and cochlear-implant (CI) listeners. Vowel, consonant, word, and sentence recognition were measured in five normal-hearing listeners, ten listeners with the Nucleus-22 cochlear implant, and nine listeners with the Advanced Bionics Clarion cochlear implant. Recognition was measured as a function of the number of spectral channels (noise bands or electrodes) at signal-to-noise ratios of +15, +10, +5, 0 dB, and in quiet. Performance with three different speech processing strategies (SPEAK, CIS, and SAS) was similar across all conditions, and improved as the number of electrodes increased (up to seven or eight) for all conditions. For all noise levels, vowel and consonant recognition with the SPEAK speech processor did not improve with more than seven electrodes, while for normal-hearing listeners, performance continued to increase up to at least 20 channels. Speech recognition on more difficult speech materials (word and sentence recognition) showed a marginally significant increase in Nucleus-22 listeners from seven to ten electrodes. The average implant score on all processing strategies was poorer than scores of NH listeners with similar processing. However, the best CI scores were similar to the normal-hearing scores for that condition (up to seven channels). CI listeners with the highest performance level increased in performance as the number of electrodes increased up to seven, while CI listeners with low levels of speech recognition did not increase in performance as the number of electrodes was increased beyond four. These results quantify the effect of number of spectral channels on speech recognition in noise and demonstrate that most CI subjects are not able to fully utilize the spectral information provided by the number of electrodes used in their implant. [DOI: 10.1121/1.1381538]

PACS numbers: 43.71.Ky, 43.66.Sr, 43.66.Ts [CWT]

I. INTRODUCTION

Previous work with cochlear implants has demonstrated that speech recognition increases with increasing number of electrodes (Holmes *et al.*, 1987; Dorman *et al.*, 1989; Kileny *et al.*, 1992; Geier and Norton, 1992; Lawson *et al.*, 1993; Collins *et al.*, 1994; Lawson *et al.*, 1996; Fishman *et al.*, 1997; Eddington *et al.*, 1997). However, most of this work has been done in quiet listening conditions, while most everyday listening situations contain background noise, which reduces intelligibility even for individuals with normal hearing. In noisy listening conditions even normal-hearing (NH) listeners with 16 spectral channels do not achieve the same performance level as with full-spectrum speech (Fu *et al.*, 1998; Eddington *et al.*, 1997).

Studies with cochlear implants (Fishman *et al.*, 1997; Eddington *et al.*, 1997; Dorman and Loizou, 1997, 1998; Dorman *et al.*, 1997; Fu *et al.*, 1998) have demonstrated that speech recognition improves as the number of electrodes increases in quiet listening conditions, at least up to four to seven electrodes. Fu *et al.* (1998) measured recognition of vowels and consonants as a function of signal-to-noise ratio in three cochlear implant listeners and in four normal-hearing listeners in conditions simulating cochlear implants with both CIS and SPEAK-like strategies. Recognition scores for vowels and consonants decreased as the S/N level worsened in all conditions. Recognition of vowels and consonants was further measured in Nucleus-22 cochlear implant users with either their normal SPEAK speech processor or a custom processor with a four-channel CIS strategy. The best cochlear implant users showed similar performance with the CIS strategy in quiet and in noise to that of normal-hearing listeners when listening to correspondingly spectrally degraded speech, suggesting that the noise susceptibility of cochlear implant users is at least partly due to the loss of spectral resolution. Eddington *et al.* (1997) found that three implant listeners with the Ineraid device with six-channel CIS processors were recognizing consonants and sentences in both quiet and in noise at the same level as normal-hearing listeners with four to six channel noise processors.

Studies with acoustic hearing have demonstrated that speech recognition is reduced when the spectral resolution is degraded by spectral smearing or hearing impairment (Stelmachowicz *et al.*, 1985; Dubno and Dorman, 1987; Horst, 1987; ter Keurs *et al.*, 1992, 1993; Hill *et al.*, 1968; Baer and Moore, 1993, 1994; Turner *et al.*, 1999; Shannon *et al.*,

[a]Author to whom correspondence should be addressed. Electronic mail: lfriesen@hei.org

 0001-4966/2001/110(2)/1150/14/$18.00

TABLE I. General information on Nucleus-22 listeners (CI=cochlear implant, HL=hearing loss, C. Otosclerosis=Cochlear otosclerosis).

Listener	Speech processing strategy	Age (years)	Gender	CI ear	Etiology	Age of HL Onset		Age of profound HL onset		Hearing aid usage		Duration of CI use (years)
						L	R	L	R	L	R	
N3	SPEAK	56	M	R	Trauma	45	10	45	45	N	N	7
N4	SPEAK	40	M	R	Trauma	35	35	35	35	N	N	5
N6	SPEAK	65	F	R	Ototoxicity	54	54	54	54	Y	Y	7
N7	SPEAK	55	M	R	Unknown	20	20	47	44	Y	N	2
N9	SPEAK	55	F	L	Hereditary	8	8	38	38	Y	Y	7
N14	SPEAK	63	M	R	Unknown	37	37	47	61	N	Y	1
N15	SPEAK	70	F	L	C. Otosclerosis	62	62	75	75	Y	Y	2
N17	SPEAK	71	F	R	Unknown	41	41	68	68	Y	Y	1
N18	SPEAK	77	F	R	Otosclerosis	40	40	45	45	Y	Y	1
N19	SPEAK	70	M	L	Unknown	40	40	62	56	Y	N	1

1995; Boothroyd *et al.*, 1996; Dorman *et al.*, 1997; Dorman and Loizou, 1997, 1998; Nejime and Moore, 1997; Eddington *et al.*, 1997; Fu *et al.*, 1998). In general, these studies found that speech recognition in quiet listening conditions was highly resistant to spectral smearing, with significant decreases in performance occurring only when the spectrum was smeared over 1000 Hz, or reduced to less than four spectral channels. Speech recognition was more susceptible to spectral smearing in the presence of added noise (Fu *et al.*, 1998; Baer and Moore, 1993; Nejime and Moore, 1997; Eddington *et al.*, 1997).

In the present experiment, speech recognition was measured as a function of the number of electrodes in various levels of noise, for three processing strategies: SPEAK, CIS, and SAS. Speech recognition was also measured in normal-hearing listeners with noise-band processors (Shannon *et al.*, 1995) as a function of the number of bands and signal-to-noise ratio.

II. METHODS

A. Listeners

Ten adults (18 years and older) utilizing the Nucleus-22 cochlear implant with the SPEAK speech processing strategy and nine adults using the Clarion cochlear implant device, each having at least six months CI experience, participated in this study. Five of the Clarion patients used the continuous interleaved sampler (CIS) processor (Wilson *et al.*, 1991) and four used the simultaneous analog stimulation (SAS) processor. All were postlingually deafened and native speakers of American English. General demographic information for the 19 subjects is presented in Tables I and II. All Nucleus-22 listeners had 20 active electrodes available for use, while Clarion users had either seven or eight, depending on the speech processing strategy used: SAS users had seven available electrode pairs and CIS users had eight available electrode pairs. Five normal-hearing listeners, ranging in age from 18 to 53 years, were recruited as controls.

B. Speech materials

Speech perception tests used were all presented without lip-reading (sound only). The tests consisted of medial vowel and consonant discrimination, monosyllable word recognition, and sentence recognition.

Vowel stimuli were taken from materials recorded by Hillenbrand *et al.* (1995) and were presented to the listeners with custom software (Robert, 1998). Ten presentations (five

TABLE II. General information of Clarion listeners (CI=cochlear implant, HL=hearing loss, C. Otosclerosis=cochlear otosclerosis).

Listener	Speech processing strategy	Age (years)	Gender	CI ear	Etiology	Age of HL Onset		Age of profound HL onset		Hearing aid usage		Duration of CI use (years)
						L	R	L	R	L	R	
C1	CIS	66	F	L	Otosclerosis	32	32	45	45	Y	N	1
C3	CIS	56	M	R	Unknown	18	0	18	45	N	N	3
C4	CIS	51	F	L	Meningitis	1.5	1.5	47	47	Y	N	2
C5	CIS	38	M	L	Unknown	3	3	28	22	Y	Y	2.5
C9	CIS	46	F	R	Ototoxicity	43	43	45	45	Y	Y	0.5
C2	SAS	72	M	R	C. Otosclerosis	30	30	69	69	Y	N	2
C6	SAS	61	F	R	Menieres	22	33	57	57	Y	Y	1
C7	SAS	82	M	R	Unknown	15	15	63	63	N	Y	2
C8	SAS	76	M	R	Unknown	18	64	75	64	Y	N	0.5

male and five female talkers) each of 12 medial vowels (/i ɔ ɛ u ɪ ʊ ʌ æ ɝ o ɑ e/) were presented in a /h/-vowel-/d/ context (heed, hawed, head, who'd, hid, hood, hud, had, heard, hoed, hod, hayed). Chance level on this test was 8.33% correct and the 95% confidence level was 13.4% correct.

Consonant stimuli were taken from materials created by Turner *et al.* (1992, 1999) and Fu *et al.* (1998). Consonant confusion matrices were compiled from 12 presentations (2 repetitions of 3 male and 3 female talkers) of each of 14 medial consonants /b d g p t k m n f s ʃ v z θ/, presented in an /a/-consonant-/a/ context. Tokens were presented in random order by custom software (Robert, 1998; Shannon *et al.*, 1999) and the confusion matrices were analyzed for information received on the production-based categories of voicing, manner, and place of articulation (Miller and Nicely, 1995). Chance performance level for this test was 7.14% correct, and the 95% confidence level was 11.1% correct.

The CNC Word Test from the Minimum Speech Test Battery for Adult Cochlear Implant Users CD (House Ear Institute and Cochlear Corporation, 1996) was used to evaluate open-set phoneme and word recognition. The CD contains ten lists of 50 monosyllabic words containing 150 phonemes. Listener responses were scored separately for words and phonemes correctly identified. Because there were more test conditions (25) than lists of words (10), the word lists used in the conditions with the poorest scores were repeated.

Recognition of words in sentences was measured using the Hearing in Noise Test (HINT) sentences (Nilsson *et al.*, 1994) from the Minimum Speech Test Battery for Adult Cochlear Implant Users CD (House Ear Institute and Cochlear Corporation, 1996). For each condition, data was collected for ten sentences of varying lengths from each listener. The sentences were of easy-to-moderate difficulty, presented with no context and no feedback, and no sentences were repeated to an individual listener. Sentences were scored in terms of words correct.

C. Experimental speech processor conditions

Each listener was tested with five experimental speech processors immediately after receiving them (no practice). Each of the five experimental processors was tested in quiet and with four different signal-to-noise ratios (S/N) of +15, +10, +5, and 0 for a total of 25 conditions. The Nucleus-22 SPEAK processing strategy divides speech into 20 contiguous frequency bands and normally assigns the output of each band to one electrode pair. The listeners' original frequency band divisions were used. In the present experiment, processors were created with 2, 4, 7, 10, and 20 activated electrodes by assigning the output of more than one band to a single electrode pair. In the normal 20-electrode processor the output of analysis bands 1, 2, 3, 4, and 5 would normally be assigned to active electrodes 1, 2, 3, 4, and 5, respectively. In the present experiment a four-electrode experimental processor was created by assigning the outputs of all five bands to active electrode 3 only. In this case active electrodes 1, 2, 4, and 5 received no stimulation. When this assignment pattern was repeated along the entire electrode array the outputs of the 20 analysis filters were presented to only four active electrodes. In similar fashion, analysis filters were summed to create processors with ten, seven, four, and two active electrodes. In the seven-electrode condition the basal-most electrode pair was assigned only two frequency bands instead of three [see Fishman *et al.* (1997) for more details].

In the normal SPEAK processing strategy the acoustic signal is analyzed into 20 frequency bands and between six and ten frequency bands with the highest energy are selected for stimulation approximately every 4 ms (McDermott *et al.*, 1992a, b; Seligman and McDermott, 1995). The average pulse rate per electrode was higher in the experimental processors, because the activated electrodes received the output from more than one analysis filter band. For example, if an electrode pair was assigned to receive the output of three contiguous analysis bands (seven-electrode processor condition), then that electrode pair received a stimulation pulse if any of the three filter bands was selected for stimulation. If all three filter bands were selected for stimulation, the electrode pair would receive three pulses in that stimulus frame. Thus, as the number of electrodes was reduced, the effective stimulation pulse rate on each electrode pair was increased. ''Stimulus level'' coding was used, which changes the electrical stimulation level by changing both pulse amplitude and pulse phase duration (Cochlear Corp., 1995). At high stimulation levels the pulse duration is longer, which results in a lower overall pulse rate. All listeners were programmed in the bipolar-plus-one mode electrode pairing (BP+1) for both their normal processors and for all experimental conditions.

With the Clarion SAS and CIS speech processing strategies, the outputs of seven or eight frequency bands are normally directed to seven or eight electrode pairs assigned to those frequency bands (Clarion Reference Manual, 1998). With a reduction in the number of electrode pairs, the total frequency range remains the same, but the range for each electrode is broadened, with the exception of the two-electrode processor. With the two-channel processor only high- and low-frequency bands are transmitted, and the mid-frequency information is left out (Breeuwer and Plomp, 1984). Five electrode conditions were created where all seven or eight electrode pairs were utilized initially and then reduced to six, four, three, and two pairs. For the six-electrode condition electrodes 1, 2, 4, 5, 7, and 8 were used with the CIS processing strategy, while electrodes 1, 2, 3, 5, 6, and 7 were used with SAS processing. The four-electrode condition utilized electrodes 1, 3, 5, and 7; the three-electrode condition involved electrodes 1, 4, and 7; and the two-electrode condition involved electrodes 2 and 6. In the Clarion device the overall stimulation rate is held constant for the CIS processor. As the number of electrodes was reduced, the stimulation rate per electrode increased.

Normal-hearing listeners were tested using a noise band simulation of CIS-like processing (see Shannon *et al.*, 1995). Test conditions consisted of the five S/N ratios used for implant listeners, with up to four additional noise conditions: −2.5, −5, −7.5, and −10 dB S/N. Acoustic processors were designed with 20, 16, 12, 8, 6, 4, and 2 bands. For two, four, six, and eight band processors the same frequency divisions were used as the Clarion processor. For noise-band proces-

sors with more than eight bands, the entire frequency range from 100 Hz to 6 kHz was divided into equal parts in terms of cochlear distance in mm, using the cochlear tonotopic formula of Greenwood (1990). The envelope was extracted from each band by half-wave rectification and low-pass filtering at 160 Hz. This envelope signal was then used to modulate a wideband white noise, which was then bandpass filtered with the same filter set as was used on the original speech signal. The modulated noise bands were then summed and presented through a calibrated loudspeaker in a sound treated room (IAC). The speech-shaped masking noise was added to the speech signals at the desired speech-to-noise ratio prior to processing.

D. Procedure

During all testing the listener was seated 1 m in front of a loudspeaker (Grason-Stadler audio monitors) in a sound treated room (IAC). The presentation level was 65 dB SPL for all speech perception testing, as measured by a B&K 1-in microphone (Model #4144) at the location of the listener's head. All speech materials were recorded. A computer with a sound card (Turtle Beach Fiji), CD player, and a GSI audiometer (Model 16) were used to present the test items. The GSI 16 audiometer generated the speech-shaped noise used during the vowel, consonant, and word tests for the implant listeners. The CD utilized for presenting the HINT sentence materials provided the speech-shaped noise for that test.

Threshold (T) and comfort (C) or most comfortable (M) loudness levels were measured separately for each experimental condition. The five experimental processors were presented to each listener in random order. Within each of the five experimental processor conditions, the four noise conditions were presented in random order, following the condition in quiet. The condition in quiet was always presented first in order to further familiarize the listener with the task. The battery of speech tests was administered to each listener immediately after they were given the experimental processor (no practice). The listener's normal settings were restored to the speech processor after each testing session until the listener returned for the next experimental condition, typically one week later. After the T and C level adjustments, Nucleus-22 listeners' were told to set their sensitivity level to the most comfortable position with the function switch set to normal (N). This setting was used during all the test conditions for that particular processor.

For the Nucleus-22 device electrical thresholds (T) and maximum acceptable loudness (C) levels were obtained using the Nucleus diagnostic and programming system with a personal computer and a dual processor interface with Cochlear Corporation 6.100 software. For obtaining T and C levels the stimulus was a 250-Hz pulse train of 500-ms duration. Threshold levels were estimated by a standard clinical bracketing procedure. One to five pulse bursts were presented and the listener was instructed to count the number heard. The T level used in the processor was the level at which the listener counted the number of bursts correctly 100% of the time. To obtain C levels the experimenter increased the electrical level until the listener judged the loudness was at the maximum acceptable level. Adjacent electrodes were balanced for loudness at C level for each electrode.

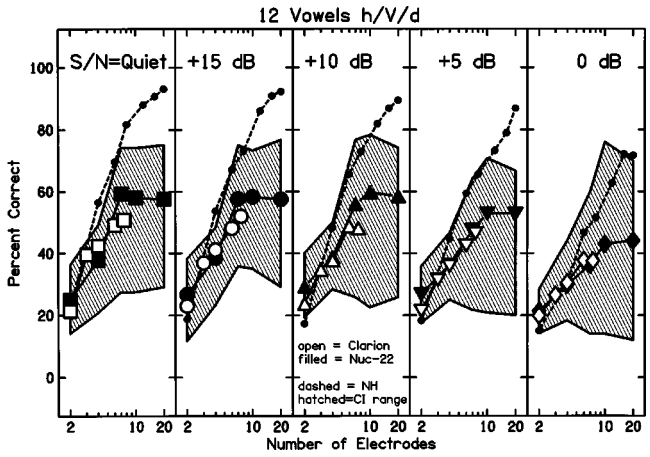

FIG. 1. Recognition of 12 medial vowels in a h/V/d context as a function of the number of spectral channels for normal-hearing listeners (dashed line with small filled symbols) or as a function of the number of electrodes used with Nucleus-22 cochlear implant listeners (filled symbols) and Clarion cochlear implant listeners (open symbols). The hatched area plots the range of performance across all 19 cochlear implant listeners. From left to right the panels present vowel recognition as a function of decreasing signal-to-noise ratio.

For the Clarion device electrical thresholds (T) and most comfortable loudness (M) levels were obtained using the SCLIN for Windows software, Clinician's Programming Interface (CPI), and power supply with a personal computer. The Input Dynamic Range was set to −60 dB SL for all conditions. All other parameters were set as in the listener's original processor. In the CIS processing strategy, threshold levels were estimated by a standard clinical bracketing procedure. Initially, all the electrodes were screened for threshold level and the patient was instructed to identify when they first heard the sound. Then, going back to the first electrode, one to five pulse bursts were presented and the listener was instructed to count the number heard. The T level used in the processor was the level at which the listener counted the number of bursts correctly 50% of the time. To obtain M levels the experimenter increased the electrical level until the listener judged the loudness was at the most comfortable loudness level (the level where they heard the sound at a normal conversational level and could listen to it for a long time without discomfort). Adjacent electrodes were balanced for loudness at M level for each electrode.

The SAS measurement procedures were identical to CIS except the measurement of T and M levels began with the most basal channel, whereas with CIS the measurements began with the most apical channel as per the Clarion device fitting manual (Clarion, 1998).

III. RESULTS

Figures 1–4 present the results for vowels, consonants, CNC words, and HINT sentences, respectively. Within each figure, the panels present recognition performance for quiet listening conditions and signal-to-noise levels of +15, +10, +5, and 0 dB, respectively, from left to right. In each panel

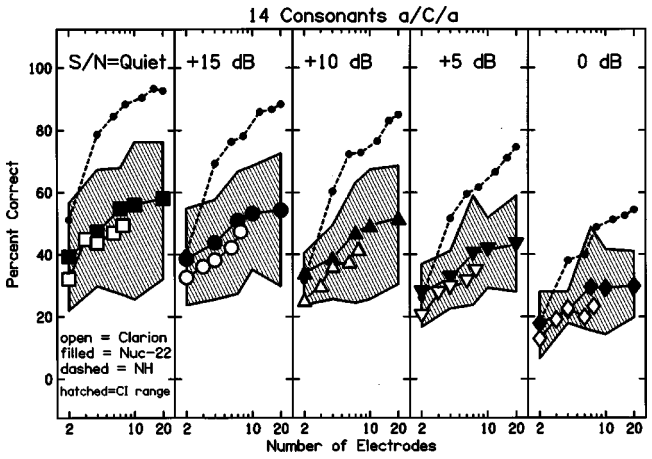

FIG. 2. Recognition of 14 medial consonants in an a/C/a context as a function of the number of spectral channels for normal-hearing listeners (dashed line with small filled symbols) or as a function of the number of electrodes used with Nucleus-22 cochlear implant listeners (filled symbols) and Clarion cochlear implant listeners (open symbols). The hatched area plots the range of performance across all 19 cochlear implant listeners. From left to right the panels present consonant recognition as a function of decreasing signal-to-noise ratio.

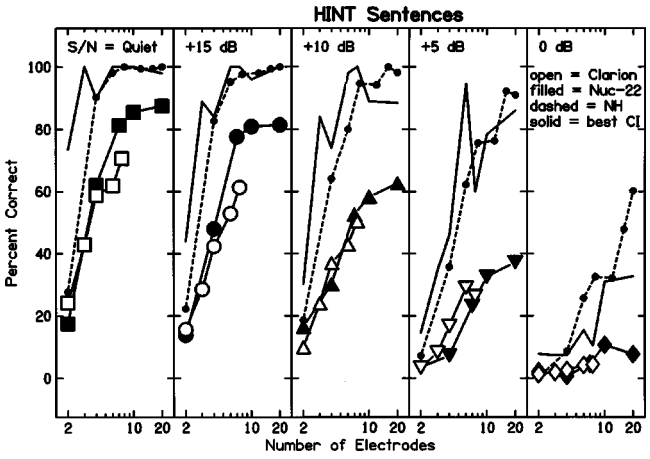

FIG. 4. Recognition of HINT sentences as a function of the number of spectral channels for normal-hearing listeners (dashed line with small filled symbols) or as a function of the number of electrodes used with Nucleus-22 cochlear implant listeners (filled symbols) and Clarion cochlear implant listeners (open symbols). The solid line plots the best performance level across all 19 cochlear implant listeners. From left to right the panels present consonant recognition as a function of decreasing signal-to-noise ratio.

the open symbols present data from subjects with the Clarion device, filled symbols present data from subjects with the Nucleus-22 device, and the dashed line with small filled symbols presents results from normal-hearing listeners with noise-band processors. Average standard deviations for the three types of listeners on the four sets of test materials are given in Table III. Note that the variability was similar for the two sets of implant listeners, while the standard deviation for normal-hearing listeners was generally about half that observed in the implant listeners. The hatched area in Figs. 1 and 2 outlines the entire range of performance across all 19 implant subjects. Tables IV and V present listener scores for all tests in quiet with their original processor.

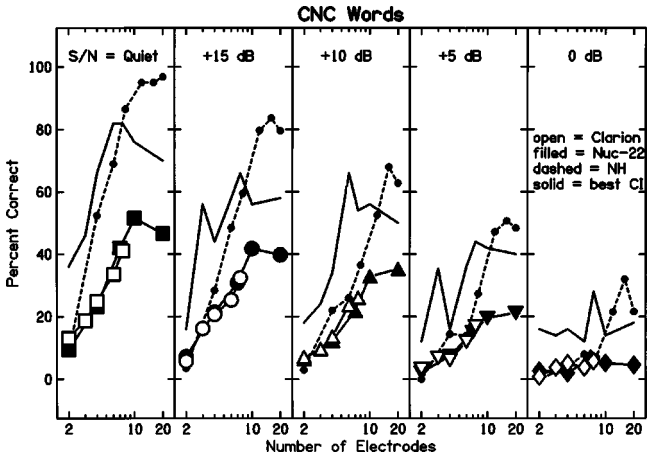

FIG. 3. Recognition of CNC words as a function of the number of spectral channels for normal-hearing listeners (dashed line with small filled symbols) or as a function of the number of electrodes used with Nucleus-22 cochlear implant listeners (filled symbols) and Clarion cochlear implant listeners (open symbols). The solid line plots the best performance level across all 19 cochlear implant listeners. From left to right the panels present consonant recognition as a function of decreasing signal-to-noise ratio.

A. Comparison of implants

For Clarion listeners, a repeated measures ANOVA revealed no difference in performance between the CIS and SAS patients (Table VI) for all numbers of electrodes and all noise levels. The two groups of Clarion listeners were then grouped together for comparison with Nucleus listeners. For this comparison the Nucleus results from 7, 10, and 20 electrodes were all grouped together and compared to Clarion results with 7 or 8 electrodes. In all other cases similar numbers of electrodes were compared across the two devices. A repeated measures ANOVA revealed no significant difference in performance for listeners with the two implants for all conditions (Table VI). Speech recognition with both the Clarion and Nucleus-22 processors improved as the number of electrodes increased (up to seven or eight) for all conditions. Even though more electrodes were available with the Nucleus-22 speech processor, performance was not significantly better than for seven or eight electrodes with the Clarion device. A repeated measures ANOVA was performed, comparing results for Nucleus CI listeners with 7, 10, and 20 electrodes (Table VII). While there was no significant difference in speech recognition for consonants or vowels, there was a marginally significant effect for words and sentences. *Post-hoc t*-tests revealed that there was a marginally significant difference between the seven- and ten-electrode results for word recognition in quiet and at +15 dB S/N ratio ($p<0.05$), but not at other noise levels. *Post-hoc*

TABLE III. Average standard deviations (%) for each test and listener type. Standard deviations were averaged across noise conditions and number of channels.

	Normal-hearing	Clarion	Nucleus-22
Vowels	4.87	11.50	10.95
Consonants	3.58	10.81	9.67
CNC words	7.50	11.86	10.32
HINT sentences	7.24	19.74	15.21

TABLE IV. Nucleus-22 listeners' scores (%) in quiet with original processor.

Listener	Strategy	Vowels	Consonants	CNC words	HINT sentences
N3	SPEAK	53	47	46	85
N4	SPEAK	68	71	70	100
N6	SPEAK	67	60	54	92
N7	SPEAK	57	58	46	92
N9	SPEAK	72	76	76	100
N14	SPEAK	29	32	12	58
N15	SPEAK	58	57	34	89
N17	SPEAK	37	51	28	81
N18	SPEAK	75	60	44	96
N19	SPEAK	58	55	66	94
Mean score		57	57	48	89

tests revealed no significant differences between seven and ten electrodes for sentences at any noise level.

B. Comparison of acoustic and electric hearing

The performance of NH listeners was significantly better than CI listeners for all noise conditions (Table VI). In addition, scores of the NH listeners continued to increase up to 20 channels with similar signal processing conditions. For consonant recognition (Fig. 1), NH listeners scored consistently higher than the best CI listeners for all numbers of electrodes/bands, particularly at high signal-to-noise levels. For vowel recognition (Fig. 2), performance by the best CI listeners (top edge of the hatched area) was similar to NH listeners, but only up to eight electrodes. As the number of electrodes was increased beyond eight, performance for the CI listeners remained relatively constant, while for NH listeners, performance continued to increase with the number of bands. For CNC word recognition (Fig. 3) and HINT sentence recognition (Fig. 4) only the best performance by CI patients is presented because the lowest performance level was near zero for all conditions. As with the phoneme results, the best performance level with cochlear implants was similar to that of NH listeners with the same processing, up to seven to eight channels/electrodes. As the number of channels/electrodes was increased above seven to eight, word and sentence recognition continued to increase in normal-hearing listeners. The line representing the best implant score is somewhat erratic because it represents a single score. With a small number of channels/electrodes and at high noise levels the best implant listeners appear to have higher scores than NH listeners for the same conditions. This might be due to the greater experience of implant listeners in such difficult listening conditions. In their everyday listening experience implant listeners must constantly reconstruct linguistic information from partially received phonemic fragments, whereas NH listeners only face such a challenging reconstruction problem infrequently.

TABLE V. Clarion listeners' scores (%) in quiet with original processor.

Listener	Strategy	Vowels	Consonants	CNC words	Hint sentences
C1	CIS	46	52	20	87
C3	CIS	57	60	64	89
C4	CIS	28	25	28	40
C5	CIS	78	75	82	100
C9	CIS	26	33	22	60
C2	SAS	58	65	48	91
C6	SAS	77	55	48	96
C7	SAS	45	36	24	40
C8	SAS	43	42	34	34
Mean score		51	49	41	75

TABLE VI. Repeated measures ANOVA F-values between subjects (df $=1$ for all F values).

Test	CIS-SAS	Nucleus-Clarion	NH-CI	Better-poorer listeners
Vowels	0.025	0.812	13.981[a]	71.579[a]
Consonants	0.003	1.748	32.840[a]	25.210[a]
Words	0.215	0.065	16.776[a]	28.252[a]
Sentences	0.419	0.165	25.598[a]	58.821[a]

[a] $p<0.05$.

C. Comparison of good and poor implant scores

One interesting feature of the results can be observed by comparing the top and bottom borders of the hatched area in Figs. 1 and 2. The hatched area represents the overall range of scores obtained from all 19 implant listeners. The top and bottom edges of the hatched area do not necessarily represent the scores from single implant listeners, although they are representative of the performance curves from the better and poorer implant listeners. The better-performing implanted listeners improved as the number of electrodes was increased up to seven, while the poorer-performing listeners showed little increase in performance as the number of electrodes was increased above four. This was particularly true in tests that rely more heavily on spectral cues (such as vowel recognition) and at low S/N ratios. A repeated measures ANOVA was performed between the two groups of performers, revealing a statistically significant difference for all tests (Table VI). This result suggests that implant listeners with better speech recognition are able to utilize more channels of spectral information than those with poor speech recognition. To test this hypothesis, consonant confusion matrices were analyzed for the two implant listeners with the best scores and the two implant listeners with the poorest scores.

Consonant recognition was analyzed into the traditional production-based categories of voicing, manner of articulation, and place of articulation (Miller and Nicely, 1955). The percent correct for each of these features is presented in Fig. 5 for the two best users and the two poorest users of each device and for NH listeners with similar processing. The results show that the better implant users were able to utilize all three categories of cues better than the poorer implant users. A repeated measures ANOVA was performed on the feature scores, revealing a statistically significant difference between the better and poorer hearing listeners (voicing: $F=33.728$, $p<0.001$, manner: $F=11.595$, $p<0.05$, and place: $F=14.279$, $p<0.01$). At high signal-to-noise ratios the number of electrodes did not affect the reception of voicing. However, at poor signal-to-noise ratios the percent correct on voicing increased with the number of electrodes up to four. This may be due to the noise interfering with the per-

TABLE VII. Repeated measures ANOVA *F*-values within subjects for Clarion, Nucleus-22 (all electrode combinations), Nucleus-22 (7-, 10-, and 20-electrode maps only), all cochlear implant listeners (Nucleus-22 and Clarion combined), and normal-hearing listeners.

Electrode factor	Clarion	Nucleus-22	Nucleus-22 (7-, 10-, 20-electrode maps only)	CI listeners	Normal-hearing listeners
Vowels	20.648[b]	41.633[b]	3.202	53.544[b]	159.768[b]
Consonants	15.543[b]	27.603[b]	1.147	59.438[b]	222.124[b]
Words	13.383[b]	38.270[b]	7.461[a]	45.854[b]	56.918[b]
Sentences	11.912[b]	59.982[b]	5.288[a]	56.632[b]	247.631[b]
Noise factor					
Vowels	21.966[b]	34.161[b]	40.066[b]	36.400[b]	4.448[b]
Consonants	62.346[b]	81.310[b]	60.389[b]	146.019[b]	4.184[b]
Words	17.487[b]	52.858[b]	54.645[b]	40.335[b]	13.531[b]
Sentences	36.937[b]	132.997[b]	141.768[b]	118.740[b]	6.825[b]
Electrode–noise interaction					
Vowels	2.355[a]	6.311[b]	1.965	9.428[b]	120.085[b]
Consonants	2.212[a]	0.791[a]	0.639	2.594[a]	673.979[b]
Words	4.924[b]	6.830[b]	1.681	9.637[b]	633.295[b]
Sentences	4.521[b]	12.693[b]	0.438	27.952[b]	364.443[b]

[a]$p<0.05$.
[b]$p<0.001$.

ception of the temporal cues for voicing, which should not require much spectral information. When temporal cues are masked by noise, voicing can be conveyed by spectral cues (e.g., the ratio of energy above and below 1500 Hz), but multiple electrodes are required to provide this spectral information. A similar pattern of performance was observed for the reception of manner cues. Percent correct on the place of articulation increased as the number of electrodes increased

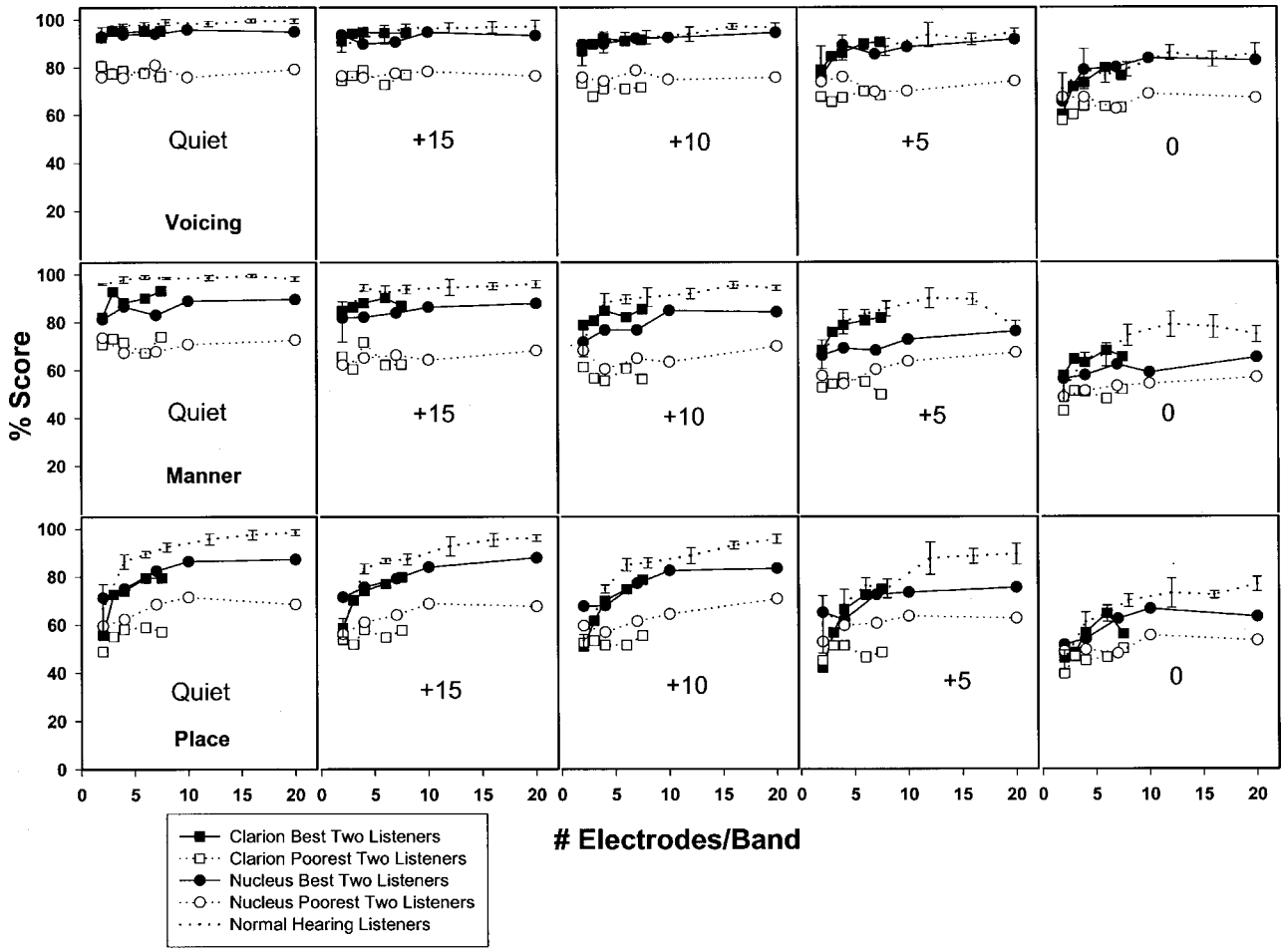

FIG. 5. Percent correct on the consonant features of voicing (top row), manner (middle row), and place of articulation (lower row) as a function of the number of electrodes or number of spectral bands. Dotted lines with error bars represent the range of results from normal-hearing listeners. Filled symbols present the average of the two best scores from CI listeners with each device, while open symbols present the average of the two poorest scores from CI listeners with each device.

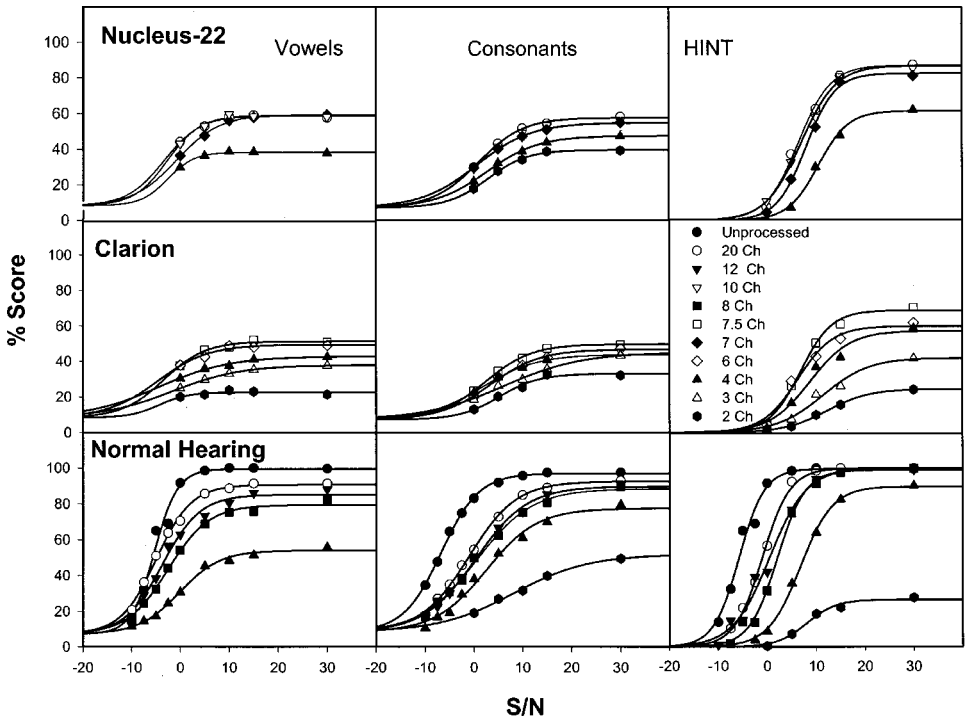

FIG. 6. Recognition functions as a function of signal-to-noise ratio for NH and CI listeners for consonant, vowel, and sentence recognition. Lines plot the fit of a sigmoidal model [Eq. (1)] to the data. Parameters of the model from these fits, as well as the rms error of each fit, are presented in Tables VIII–X.

at all noise levels (but only increased up to seven to ten electrodes for implant listeners).

In this study, the better listeners with the Nucleus-22 device were receiving similar amounts of information on voicing, manner, and place as the better listeners with the Clarion device (both CIS and SAS). In addition, scores for the best implant listeners were similar to that of the normal-hearing listeners with the same number of processing channels. Scores from poor-performing listeners with both implant devices were also similar to each other, indicating that the electrode design and speech processor strategy were not the primary factors affecting speech recognition or the pattern of performance across implant listeners. Note that the poorer-performing implant listeners were only receiving 80% correct on voicing and 70% correct on manner cues, regardless of the number of electrodes. This is an unusual result because voicing and manner cues are thought to be conveyed primarily by temporal information and should be easily available to implant listeners. The better-performing implant listeners and NH listeners received essentially 100% of the voicing and manner information with only two channels of spectral information. This is consistent with a previous result by Shannon *et al.* (1995). Yet the poorer-performing implant listeners never achieved this level of performance even with the maximum number of electrodes.

D. Performance-intensity functions

The vowel, consonant, and sentence recognition data from Figs. 1–4 are replotted in Fig. 6 as a function of SN ratio. Data from each condition was fit with a simple three-parameter sigmoidal model (Boothroyd *et al.*, 1996):

$$\%C = P_0 + (Q - P_0)/(1 + e^{-\beta(x - \mathrm{PRT})}), \quad (1)$$

where P_0 is the chance performance level, Q is the percent correct in quiet, β is related to the slope of the function, x is the level of the noise in dB, and PRT is the phoneme recognition threshold in dB, which is the S/N ratio at which the performance falls to 50% of the level in quiet. The values of Q, β, and PRT and the standard error of the fit are presented in Tables VIII–X for consonant, vowel, and sentence recognition, respectively. As can be seen in Fig. 6 and Tables VIII–X, this function provided excellent fits to all curves of performance as a function of signal-to-noise ratio. In general, as the number of spectral channels/electrodes decreased, the level of performance in quiet decreased, and the PRT increased. The slopes of the functions were relatively constant across conditions, decreasing slightly for the two-channel condition. The parameter values obtained for the NH listeners were similar to those obtained under similar conditions, but with different speech materials, by Fu *et al.* (1998).

Figure 7 plots the PRT as a function of the number of spectral channels (or number of electrodes) for consonant, vowel, and sentence recognition. The PRTs for NH listeners from the present study (filled squares) are comparable to PRTs from NH listeners in a previous study (Fu *et al.*, 1998). In both studies, the PRT decreased linearly as a function of the logarithm of the number of spectral channels. Regression slopes are presented in Table XI. Slopes of linear regression fits to the NH data are −2.57, −2.44, and −2.87 dB/doubling of the number of channels for consonants, vowels, and sentences, respectively (Table XI). In contrast, the PRT for CI listeners, except for the Clarion listeners with HINT sentences, changed little as the number of electrodes was increased.

IV. DISCUSSION

A. Comparison of implant devices and processing strategies

A key result in the present study is that there was no significant difference in speech recognition performance be-

TABLE VIII. Sigmoidal model parameters for consonant recognition. (PRT=phoneme recognition threshold, β=related to the slope of the function, and Q=percent correct in quiet.)

Listeners	Channels/Electrodes	PRT (dB)	Q (%)	β	Standard error of fit (%)
Nucleus-22	2	2.90±0.31	39.6±0.6	0.21±0.38	0.68
	4	2.70±0.31	47.5±0.7	0.20±0.36	0.64
	7	0.59±0.20	54.9±0.5	0.17±0.28	0.45
	10	0.90±0.09	56.0±0.2	0.20±0.16	0.24
	20	0.90±0.29	57.6±0.8	0.21±0.38	0.85
Clarion	2	5.23±1.04	33.0±1.7	0.24±0.95	1.75
	3	6.16±1.14	45.1±2.0	0.12±1.26	1.22
	4	1.75±0.34	43.9±0.6	0.17±0.44	0.61
	6	3.42±0.58	46.7±1.3	0.19±0.64	1.23
	7/8	2.33±0.29	49.7±0.7	0.42±0.35	0.71
NH	2	7.81±1.06	52.0±2.2	0.13±1.05	1.29
	4	2.30±0.73	77.7±2.6	0.18±0.53	2.78
	6	1.16±0.34	84.7±1.3	0.17±0.26	1.37
	8	0.30±0.45	88.6±1.8	0.17±0.37	1.92
	12	0.13±0.31	89.9±1.3	0.18±0.25	1.48
	16	−0.89±0.44	93.0±1.9	0.18±0.38	2.21
	20	−1.21±0.22	92.7±0.6	0.20±0.20	1.25
	Unprocessed	−6.86±0.12	96.9±0.6	0.26±0.14	1.06

tween Nucleus and Clarion implant systems either as a function of the signal-to-noise ratio or as the number of electrodes was varied. For each of these conditions the range of speech recognition performance was wide, but the range of performance and average scores were not different between Nucleus and Clarion devices, or between the SAS and CIS strategies in Clarion patients. Indeed, in our limited sample even the average scores of the two best implant listeners and the two poorest implant listeners were similar between the Nucleus and Clarion systems. In this sample of ten Nucleus and nine Clarion implant listeners there were no differences in performance in spite of the large differences between the systems tested (i.e., electrode design and placement, analog versus pulsatile stimulation, SPEAK versus SAS versus CIS, fast versus slow stimulation rate). In contrast, the number of electrodes had a large and significant effect on all devices and speech processing strategies.

B. Effect of S/N ratio

Figure 6 plots the speech recognition scores as a function of the S/N ratio for consonants, vowels, and sentences. Note that all curves are well fit by the three-parameter sigmoidal function of Eq. (1). The standard error of the fits is less than 3% for most curves (Tables VIII–X). The slopes of the normalized functions are similar for high numbers of channels, but are shallower when the number of channels is small, as has been documented previously (Boothroyd *et al.*, 1996; Fu *et al.*, 1998).

TABLE IX. Sigmoidal model parameters for vowel recognition. (PRT=phoneme recognition threshold, β=related to the slope of the function, and Q=percent correct in quiet.)

Listeners	Channels/Electrodes	PRT (dB)	Q (%)	β	Standard error of fit (%)
Nucleus-22	2	…	…	…	
	4	−2.50±0.70	38.4±0.5	0.36±0.69	0.67
	7	−2.06±0.39	59.6±0.8	0.21±0.50	0.88
	10	−2.60±1.03	58.9±1.3	0.29±1.09	1.45
	20	−3.30±1.11	58.7±1.1	0.26±1.08	1.75
Clarion	2	−4.33±7.17	22.5±0.9	0.33±4.92	1.32
	3	−1.63±0.04	37.9±0.0	0.14±0.06	0.04
	4	−4.39±1.24	42.8±1.0	0.14±1.54	0.87
	6	−4.64±2.01	49.2±1.4	0.19±1.95	1.56
	7/8	−3.30±1.25	51.3±1.2	0.23±1.30	1.45
NH	2	…	…	…	…
	4	0.02±0.43	53.7±1.1	0.25±0.35	1.57
	6	−1.95±0.29	68.8±0.9	0.22±0.27	1.33
	8	−2.39±0.29	79.8±1.2	0.24±0.27	1.76
	12	−3.56±0.47	84.9±2.2	0.26±0.46	2.35
	16	−4.81±0.55	88.6±2.6	0.26±0.58	4.38
	20	−4.86±0.27	90.6±1.4	0.28±0.28	2.35
	Unprocessed	−6.75±0.13	96.9±0.6	0.26±0.15	1.10

TABLE X. Sigmoidal model parameters for sentence recognition. (PRT=phoneme recognition threshold, β =related to the slope of the function, and Q=percent correct in quiet.)

Listeners	Channels/Electrodes	PRT (dB)	Q (%)	β	Standard error of fit (%)
Nucleus-22	2	...	...	...	...
	4	10.05±0.50	61.5±2.4	0.33±0.40	2.42
	7	8.05±0.37	82.6±2.3	0.33±0.30	2.51
	10	7.02±0.43	86.8±2.5	0.28±0.35	2.64
	20	6.47±0.53	87.1±3.2	0.30±0.44	3.55
Clarion	2	12.22±0.51	24.5±0.8	0.23±0.43	0.70
	3	11.42±1.55	42.0±4.0	0.21±1.30	3.39
	4	8.73±1.44	57.3±5.3	0.24±1.18	5.17
	6	6.27±1.17	59.9±4.6	0.28±1.00	5.04
	7/8	6.86±0.59	68.8±2.9	0.31±0.49	3.19
NH	2	8.01±0.95	26.6±1.8	0.11±0.76	2.05
	4	6.73±0.29	89.8±1.8	0.11±0.76	2.05
	6	3.52±0.46	96.6±2.82	0.31±0.33	3.65
	8	2.03±0.38	99.1±2.3	0.35±0.27	3.45
	12	0.46±0.61	100.0±3.5	0.26±0.48	4.87
	16	−0.62±0.67	100.0±4.3	0.31±0.57	6.51
	20	−1.01±0.19	100.0±1.2	0.35±0.17	2.06
	Unprocessed	−5.75±0.36	99.7±2.5	0.38±0.35	4.92

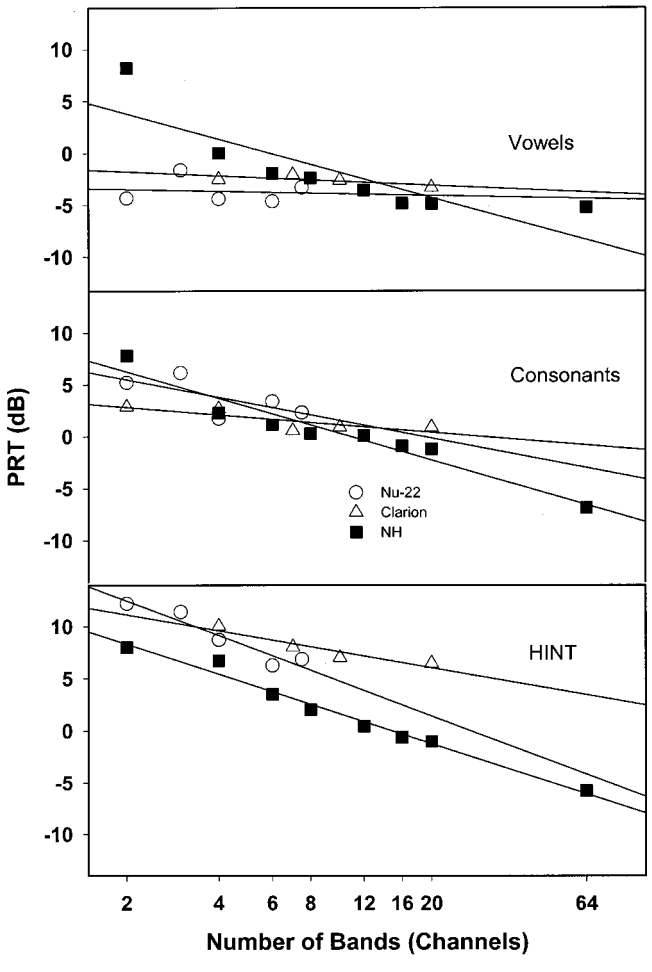

FIG. 7. Phoneme recognition threshold (PRT) as a function of the number of electrodes or bands for consonant (top), vowel (middle), or sentence (bottom) recognition. Filled symbols present data from NH listeners, while open symbols present data from CI listeners. Regression lines are fit to each set of data, with the parameters and fits listed in Table XI.

At high S/N ratios, sentence recognition is high for all number of channels greater than three. At low S/N ratios, however, a reduction in the number of channels is equivalent to reducing the S/N ratio. The best performing CI listeners need a 5–10 dB better S/N ratio to obtain performance equivalent to normal-hearing listeners using 20 channels, indicating that even the best CI listeners are using the equivalent of about 8 channels. One implication of this result is that implant listeners would be able to understand speech much better in noise if we could increase the number of spectral channels effectively used. Because the sentence recognition function has a slope of 6%–10%/dB, a 5-dB difference in S/N ratio could potentially produce a 30%–50% improvement in sentence recognition.

C. Effect of the number of electrodes

The results in quiet basically replicate the overall pattern of results of Fishman *et al.* (1997), who also found that speech recognition for Nucleus-22 listeners improved with the number of electrodes. However, Fishman *et al.* found no further improvement as the number of electrodes increased beyond four. The present results show a similar pattern of results, although speech recognition continued to improve up to seven electrodes for vowel and consonant recognition and up to ten electrodes in Nucleus listeners for word and sen-

TABLE XI. Slopes (dB/doubling of functions from Fig. 7) relating PRT and the log number of channels from the present study and Fu *et al.* (1998).

Listeners	Consonants Slope	Vowels Slope	Sentences Slope
Nucleus-22	−0.73	−0.40	−1.55
Clarion	−1.69	−0.17	−3.33
Normal-hearing	−2.57	−2.44	−2.87
Fu *et al.* (1988) (NH)	−2.90	−2.35	...

tence recognition. This improvement up to ten electrodes appeared to be more evident at medium noise levels (see Figs. 3 and 4).

In this study there did appear to be a slight difference in the pattern of performance between the better implant users and the poorer users. The poorer users did not improve in performance as the number of electrodes was increased beyond three or four. This result is different from the result observed by Fishman *et al.* (1997) where both good and poor implant users improved only up to four electrodes. A possible reason for this difference is that the poorer performers in this study had lower scores than those in the Fishman *et al.* study. The larger range of performance in the present study may have accentuated a real difference between good and poor implant users, with this study showing that poor performance was limited by the ability to use information from more than four electrodes. It is possible that the use of multiple electrodes was limited by electrode interactions.

Speech recognition with the Clarion device increased as the number of electrodes increased up to the maximum number available (eight for CIS, seven for SAS). It would be interesting to see if adding more channels to the Clarion strategies resulted in an increase in performance, or whether the performance would reach a plateau at seven or eight electrodes similar to the SPEAK results. The newest version of the Clarion implant (the C-II) will allow 16 independent channels of stimulation at high stimulation rates. The present experiment should be repeated with that new device to see if the performance level asymptotes at eight electrodes or not.

In listeners with the Nucleus-22 device utilizing the SPEAK processing strategy, speech recognition performance increased as the number of electrodes increased, but only up to seven to ten electrodes. There were no significant differences in performance for 7, 10, or 20 electrodes for vowel and consonant recognition, although there was a significant improvement from 7 to 10 electrodes for word and sentence recognition. Normal-hearing listeners, in contrast, continued to improve in speech recognition as the number of spectral bands was increased, at all noise levels.

One of the most puzzling aspects of the present data is that even the best CI performance appears to be limited to the equivalent of seven to ten spectral channels. In the Fishman *et al.* (1997) study, an asymptote in performance was observed with four electrodes for consonants and CUNY sentences and seven electrodes for the more difficult tests of vowels and NU6 words (although the increase in performance from four to seven electrodes did not achieve statistical significance). Our results showed an asymptote of seven electrodes for consonants and vowels and ten electrodes for words and sentences. One explanation for the difference may be due to the more difficult test materials used in this study for vowels and consonants (male and female multitalkers), compared to the Fishman *et al.* study (one male talker). However, this difference in test difficulty does not apply to words and sentences. Another possible reason for the difference is that in the present experiment the number of subjects and distribution of scores may have provided sufficient statistical power to show a significant improvement from four to seven electrodes for vowels and consonants and from seven to ten electrodes for words and sentences.

Let us consider three hypotheses to explain the differences between CI and NH performance, in particular what factors might limit performance in CI listeners to seven to ten channels.

D. Hypothesis 1: Stimulation rate is the primary factor limiting performance

Consider the hypothesis that the limitation of implant listeners to seven to ten channels of spectral information is due to the relatively low pulse rate/electrode in the SPEAK processing strategy. If this hypothesis is correct, then a SPEAK or CIS system with a faster pulse rate per electrode might show an improvement in performance as the number of electrodes is increased above seven. The CIS strategy implemented in the Nucleus-24 device allows stimulation of up to 12 electrodes at stimulation rates of up to 1200 pps/electrode. The ACE strategy, which is a hybrid of SPEAK and CIS strategies allows stimulation of up to 20 electrodes out of 22 at rates of up to 720 pps/electrode. These stimulation rates are considerably higher than rates allowed by the Nucleus-22 SPEAK processor. However, preliminary data (Arndt *et al.*, 1999) indicate no difference between the 22 and 24 systems in the average level of performance, even with the full number of electrodes and higher stimulation rates, so it is unlikely that patients with the 24 systems are improving in performance beyond seven electrodes. More data is needed to confirm this observation. If this preliminary result is confirmed, it would suggest that stimulation rate is not the primary factor limiting the number of usable channels of spectral information. Because of the high variability across CI listeners, this comparison should be done within subjects.

Several groups (Wilson *et al.*, 1988; Rubinstein *et al.*, 1999; Chatterjee and Robert, 2001) have recently suggested that very high stimulation rates (>4 kHz/electrode) might aid channel independence by producing stochastic neural firing on each electrode. The hypothesis is that synchronous firing across electrodes, as probably occurs with low-rate stimulation, can cause the entire pattern of firing to group together as a single ''auditory object.'' This grouping may not allow the information from each electrode to be usable independently. Stimulation rates high enough to introduce stochastic firing near each electrode may overcome this ''forced'' grouping and allow the information on each electrode to contribute independently. Special interfaces and implant devices are necessary to test this hypothesis.

E. Hypothesis 2: Electrode interaction is the primary factor limiting performance

It seems reasonable to assume that interaction between electrodes would reduce the effective tonotopic selectivity of a multichannel implant and thus could limit the listeners ability to understand speech. Cochlear current spread, producing interaction between electrodes, may limit spectral resolution in cochlear implants. Physically, electrical current spread should be greater at higher stimulation levels and for monopolar stimulation modes. However, some researchers have

noted better electrode discrimination at higher overall levels, indicating that increased current spread in the cochlea does not necessarily lead to poorer electrode discrimination (McKay *et al.,* 1999; Pfingst *et al.,* 1999). In addition, speech recognition performance may even improve with stimulation level (Skinner *et al.,* 1997). Several studies have shown that monopolar stimulation mode, which should produce a broad current distribution, can provide the same or better speech perception ability than bipolar stimulation modes (Kileny *et al.,* 1998; Zwolan *et al.,* 1996).

Three of the implant listeners in the present study (N3, N4, and N7) were also subjects in two previous psychophysical studies of electrode interaction (Chatterjee and Shannon, 1998; Hanekom and Shannon, 1998). Chatterjee and Shannon (1998) measured forward masking patterns across the electrode array as a measure of the spread of excitation in a cochlear implant. They observed that excitation patterns measured in cochlear implants were broader than similar measures in acoustic hearing, but saw no widening of the patterns with level. Hanekom and Shannon (1998) measured electrode interaction using gap detection, also with listeners N3, N4, and N7. In both studies, listener N3 had the most electrode interaction and poorest speech recognition and N4 had the least interaction and the highest speech recognition. Listener N3 also showed more changes in the pattern of electrode interaction as stimulation parameters were changed than N4 and N7. While there seems to be a rough association between electrode interaction and speech recognition, the relation is does not appear to be strong one. And it does not appear that electrode interaction is the limiting factor for listeners like N4, who show little electrode interaction yet show the same asymptote in speech recognition with seven electrodes as other listeners.

Observe the difference between the upper and lower edge of the hatched area in Figs. 1 and 2. The upper edge, which represents the best implant scores across all 19 listeners increases in performance up to seven or eight channels. The lower edge, representing the poorest scores across all implant listeners, does not increase substantially from 4 to 20 electrodes. Thus, consistent with the electrode interaction hypothesis, poor CI speech recognition is limited to three or four effective spectral channels, while good implant speech recognition improves with the number of electrodes, up to seven or eight.

Several other studies have shown a modest correlation between electrode interaction and speech recognition performance (Nelson *et al.,* 1995; Hanekom and Shannon, 1996; Throckmorton and Collins, 1999; Zwollan *et al.,* 1997; Collins *et al.,* 1997; Donaldson and Nelson, 2000; Henry *et al.,* 2000). In general, cochlear implant listeners with more electrode interaction contain lower speech recognition scores, but only a small portion of the variance is accounted for by the electrode interaction.

If electrode interactions are limiting performance on the top end of implant performance with seven to ten channels, then the poorer users may have an increased amount of electrode interaction that limits their performance even further—not allowing performance to improve beyond the three- to four-channel level, no matter how many electrodes are used. Inspection of the results in Figs. 1 and 2 shows that the implant listeners who are poor at speech recognition did not improve as the number of electrodes was increased above three or four. If this is the case, then it is of utmost importance to discover the cause of the electrode interactions and either correct this problem in the signal processing or with new electrode designs.

F. Hypothesis 3: Warping in the spectral-tonotopic mapping is the primary factor limiting performance

Another possible cause of the limitation in the use of all channels is the presence of distortion in the representation of the spectral information. Fu and Shannon (1999a) found that speech recognition was reduced when the spectral information was represented at cochlear locations that were shifted either apically or basally from their normal location. They found the same pattern of results for 4, 8, and 16 bands of spectral resolution, indicating that higher levels of spectral resolution did not mitigate the negative effects of a frequency-place shift. Shannon *et al.* (1998) found that speech recognition was reduced when the tonotopic distribution of spectral information was warped nonlinearly from its normal acoustic mapping. Both studies observed that a warping in the tonotopic distribution could not only result in a reduced number of effective channels of spectral information, but could also reduce the reception of what are thought to be primarily temporal cues in speech, like voicing and manner. Fu (1997) and Shannon *et al.* (1998) saw significant reductions in voicing, manner, and place information received on consonants when the tonotopic mapping was distorted. A similar pattern was observed in the poorer implant listeners in this study, i.e., their reception of voicing and manner were significantly poorer than in the implant users with better performance. In normal-hearing listeners nearly 100% of the voicing and manner information in consonants is received for all processors with two or more channels [Shannon *et al.* (1995) and Fig. 5]. Compare the reception of voicing and manner cues in Fig. 5 between the normal-hearing listeners and the two groups of implant listeners. The implant listeners with poor performance received less voicing and manner information with 20 electrodes than the NH and better-performing implant listeners received with only 2 electrodes. Thus, a reduction in the reception of voicing and manner cues indicates more than simply a loss of the number of effective channels of spectral information. The reduction in speech recognition due to frequency-place distortions appears to be independent of spectral resolution, and so would exacerbate the reduction due to a reduced number of channels of spectral information. Based on the Fu and Shannon (1999a) results on tonotopic shifting and the Fu (1997) and Shannon *et al.* (1998) results on frequency-place warping, we suggest that overall poor reception of voicing and manner cues could indicate the presence of a shift or warping in the frequency-place mapping in those patients.

V. CONCLUSIONS

Speech recognition was similar for the Clarion and Nucleus-22 cochlear implant listeners in this study both as a function of noise level and as function of number of electrodes. Speech recognition improved significantly as a function of the number of electrodes up to seven to ten electrodes. No improvement was observed in speech recognition as the number of electrodes was increased from 7 to 20 for vowels and consonant recognition and no improvement was observed as the number of electrodes was increased from 10 to 20 for word and sentence recognition. For the limited sample size of the present study, this pattern of results suggests that the number of electrodes is a more important factor in implant performance than the differences in design between the two implants. Comparison to normal-hearing listeners with similar processing suggests that some cochlear implant listeners can fully utilize the spectral information provided (up to eight electrodes), but others do not. The relatively small improvement for the poorer implant performers as the number of spectral channels was increased suggests that these individuals are not able to utilize the spectral information provided. Even the implant listeners with the best speech recognition appeared to be unable to utilize more than seven to ten channels of spectral information, no matter how many channels of information are presented. The reason for this limitation is not clear. We speculate that this limitation may be due to electrode interactions, and to possible tonotopic shifts and warping in the frequency-to-place mapping of spectral information.

ACKNOWLEDGMENTS

We thank the cochlear implant and normal-hearing listeners for their patience and persistence in these experiments. A special thanks goes to Dr. Qian-Jie Fu for his insight and to Mark Robert for his technical help. We also appreciate the helpful comments of two anonymous reviewers. Funding for this research was provided by NIH Grant No. R01-DC-01526 and NIH Contract No. N01-DC-92100.

Arndt, P., Staller, S., Arcaroli, J., Hines, A., and Ebinger, K. (**1999**). *Within subject comparison of advanced coding strategies in the Nucleus 24 cochlear implant* (Cochlear Corporation, Englewood, CO).

Baer, T., and Moore, B. C. J. (**1993**). ''Effects of spectral smearing on the intelligibility of sentences in noise,'' J. Acoust. Soc. Am. **94**, 1229–1241.

Baer, T., and Moore, B. C. J. (**1994**). ''Effects of spectral smearing on the intelligibility of sentences in the presence of interfering speech,'' J. Acoust. Soc. Am. **95**, 2277–2280.

Boothroyd, A., Mulhearn, B., Gong, J., and Ostroff, J. (**1996**). ''Effects of spectral smearing on phoneme and word recognition,'' J. Acoust. Soc. Am. **100**, 1807–1818.

Breeuwer, M., and Plomp, R. (**1984**). ''Speechreading supplemented with frequency-selective sound-pressure information,'' J. Acoust. Soc. Am. **76**, 686–691.

Chatterjee, M., and Robert, M. (**2001**). ''Noise enhances modulation sensitivity in cochlear implant listeners: Stochastic resonance in a prosthetic sensory system?,'' J. Assoc. Res. Otolaryngol. **2**(2) (in press).

Chatterjee, M., and Shannon, R. V. (**1998**). ''Forward masked excitation patterns in multielectrode cochlear implants,'' J. Acoust. Soc. Am. **103**, 2565–2572.

Clarion by Advanced Bionics (**1998**). ''SCLIN 98 for windows device fitting manual,'' Sylmar, California.

Cochlear Corporation (**1995**). *Audiologist Handbook* (Englewood, CO).

Collins, L. M., Zwolan, T. A., and Wakefield, G. H. (**1997**). ''Comparison of electrode discrimination pitch ranking, and pitch scaling data in postlingually deafened adult cochlear implant subjects,'' J. Acoust. Soc. Am. **101**, 440–455.

Collins, L., Zwolan, T., O'Neill, J., and Wakefield, G. (**1994**). ''Analysis of electrode pair confusions and implications for speech recognition in cochlear implant listeners,'' in *Abstracts of the Seventeenth Midwinter Meeting, Association for Research in Otolaryngology*, edited by D. Lim, p. 161.

Donaldson, G. S., and Nelson, D. A. (**2000**). ''Place-pitch sensitivity and its relation to consonant recognition by cochlear implant listeners using the MPEAK and SPEAK speech processing strategies,'' J. Acoust. Soc. Am. **107**, 1645–1658.

Dorman, M. F., and Loizou, P. C. (**1997**). ''Speech intelligibility as a function of the number of channels of stimulation for normal-hearing listeners and patients with cochlear implants,'' Am. J. Otol. Suppl. **18**, S113–S114.

Dorman, M. F., and Loizou, P. C. (**1998**). ''Identification of consonants and vowels by cochlear implant patients using a 6-channel continuous interleaved sampling processor and by normal-hearing subjects using simulations processors with two to nine channels,'' Ear Hear. **19**, 162–166.

Dorman, M. F., Loizou, P. C., and Rainey, D. (**1997**). ''Speech understanding as a function of the number of channels of stimulation for processors using sine-wave and noise-band outputs,'' J. Acoust. Soc. Am. **102**, 2403–2411.

Dorman, M. F., Dankowski, K., McCandless, G., and Smith, L. M. (**1989**). ''Consonant recognition as a function of the number of channels of stimulation by patients who use the Symbion cochlear implant,'' Ear Hear. **10**, 288–291.

Dubno, J. R., and Dorman, M. F. (**1987**). ''Effects of spectral flattening on vowel identification,'' J. Acoust. Soc. Am. **82**, 1503–1511.

Eddington, D. K., Rabinowitz, W. R., Tierney, J., Noel, V., and Whearty, M. (**1997**). ''Speech Processors for Auditory Prostheses,'' 8th Quarterly Progress Report, NIH Contract N01-DC-6-2100.

Fishman, K., Shannon, R. V., and Slattery, W. H. (**1997**). ''Speech recognition as a function of the number of electrodes used in the SPEAK cochlear implant speech processor,'' J. Speech Hear. Res. **40**, 1201–1215.

Fu, Q.-J. (**1997**). ''Speech Perception in Acoustic and Electric Hearing,'' doctoral dissertation, University of Southern California.

Fu, Q.-J., and Shannon, R. V. (**1999a**). ''Recognition of spectrally degraded and frequency-shifted vowels in acoustic and electric hearing,'' J. Acoust. Soc. Am. **105**, 1889–1900.

Fu, Q.-J., and Shannon, R. V. (**1999b**). ''Recognition of spectrally degraded speech in noise with nonlinear amplitude mapping,'' in *Proceedings of the 1999 IEEE Conference on Acoustics, Speech and Signal Processing*, Vol. 1, pp. 369–372.

Fu, Q. J., Shannon, R. V., and Wang, X. (**1998**). ''Effects of noise and spectral resolution on vowel and consonant recognition: Acoustic and electric hearing,'' J. Acoust. Soc. Am. **104**, 3586–3596.

Geier, L. V., and Norton, S. (**1992**). ''The effect of limiting the number of Nucleus 22 cochlear implant electrodes programmed on speech perception,'' Ear Hear. **13**, 340–348.

Greenwood, D. D. (**1990**). ''A cochlear frequency-position function for several species—29 years later,'' J. Acoust. Soc. Am. **87**, 2592–2605.

Hanekom, J. J., and Shannon, R. V. (**1996**). ''Place pitch discrimination and speech recognition in cochlear implant users,'' S. African J. Com. Dis. **43**, 27–40.

Hanekom, J. J., and Shannon, R. V. (**1998**). ''Gap detection as a measure of electrode interaction in cochlear implants,'' J. Acoust. Soc. Am. **104**, 2372–2384.

Henry, B. A., McKay, C. M., McDermott, H. J., and Clark, G. M. (**2000**). ''The relationship between speech perception and electrode discrimination in cochlear implantees,'' J. Acoust. Soc. Am. **108**, 1269–1280.

Hill, F. J., McRae, L. P., and McClellan, R. P. (**1968**). ''Speech recognition as a function of channel capacity in a discrete set of channels,'' J. Acoust. Soc. Am. **44**, 13–18.

Hillenbrand, J., Getty, L. A., Clark, M. J., and Wheeler, K. (**1995**). ''Acoustic characteristics of American English vowels,'' J. Acoust. Soc. Am. **97**, 3099–3111.

Holmes, A., Kemker, F. J., and Merwin, G. (**1987**). ''The effects of varying the number of cochlear implant electrodes on speech perception,'' Am. J. Otol. **8**, 240–246.

Horst, J. W. (**1987**). ''Frequency discrimination of complex signals, frequency selectivity, and speech perception in hearing-impaired subjects,'' J. Acoust. Soc. Am. **82**, 874–885.

House Ear Institute and Cochlear Corporation (**1996**). Minimum Speech Test Battery for Adult Cochlear Implant Users CD.
Kileny, P., Zimmerman-Phillips, S., Zwolan, T., and Kemink, J. (**1992**). ''Effects of channel number and place of stimulation on performance with the cochlear corporation multichannel implant,'' Am. J. Otol. **13**, 117–123.
Kileny, P. R., Zwolan, T. A., Telian, S. A., and Boerst, A. (**1998**). ''Performance with the 20+2L lateral wall cochlear implant,'' Am. J. Otol. **19**, 313–319.
Lawson, D., Wilson, B., and Finley, C. (**1993**). ''New processing strategies for multichannel cochlear prosthesis,'' Prog. Brain Res. **97**, 313–321.
Lawson, D., Wilson, B. S., Zerbi, M., and Finley, C. C. (**1996**). ''Speech Processors of auditory prostheses,'' Third Quarterly Progress Report, NIH Contract NO1-DC-5-2103.
McDermott, H. J., McKay, C. M., and Vandali, A. E. (**1992a**). ''A new portable sound processor for the University of Melbourne/Nucleus Limited Multichannel cochlear implant,'' J. Acoust. Soc. Am. **91**, 3367–3371.
McDermott, H. J., McKay, C. M., Vandali, A. E., and Clark, G. M. (**1992b**). ''A comparison of speech perception of cochlear implantees using the Spectral Maxima Sound Processor (SMSP) and the MSP (Multipeak) processor,'' Acta Otolaryngol. (Stockholm) **112**, 752–761.
McKay, C. M., O'Brien, A., and James, C. J. (**1999**). ''Effect of current level on electrode discrimination in electrical stimulation,'' Hear. Res. **136**, 159–164.
Miller, G., and Nicely, P. (**1955**). ''An analysis of perceptual confusions among some English consonants,'' J. Acoust. Soc. Am. **27**, 338–352.
Nejime, Y., and Moore, B. C. J. (**1997**). ''Simulation of the effect of threshold elevation and loudness recruitment combined with reduced frequency selectivity on the intelligibility of speech in noise,'' J. Acoust. Soc. Am. **102**, 603–615.
Nelson, D. A., VanTassell, D. J., Schroeder, A. C., Soli, S., and Levine, S. (**1995**). ''Electrode ranking of 'place pitch' and speech recognition in electric hearing,'' J. Acoust. Soc. Am. **98**, 1987–1999.
Nilsson, M., Soli, S., and Sullivan, J. A. (**1994**). ''Development of the Hearing in Noise Test for the measurement of speech reception thresholds in quiet and in noise,'' J. Acoust. Soc. Am. **95**, 1085–1099.
Pfingst, B. E., Holloway, L. A., Zwolan, T. A., and Collins, L. M. (**1999**). ''Effects of stimulus level on electrode-place discrimination in human subjects with cochlear implants,'' Hear. Res. **134**, 105–115.
Robert, M. E. (**1998**). ''CONDOR: Documentation for Identification Test Program,'' (House Ear Institute, Los Angeles).
Rubinstein, J. T., Wilson, B. S., Finley, C. C., and Abbas, P. J. (**1999**). ''Pseudospontaneous activity: Stochastic independence of auditory nerve fibers with electrical stimulation,'' Hear. Res. **127**, 108–118.
Seligman, P., and McDermott, H. (**1995**). ''Architecture of the Spectra 22 Speech Processor,'' Ann. Otol. Rhinol. Laryngol. Suppl. **104**, 139–141.
Shannon, R. V., Zeng, F.-G., and Wygonski, J. (**1998**). ''Speech recognition with altered spectral distribution of envelope cues,'' J. Acoust. Soc. Am. **104**, 2467–2476.
Shannon, R. V., Jensvold, A., Padilla, M., Robert, M., and Wang, X. (**1999**). ''Consonant recordings for speech testing,'' J. Acoust. Soc. Am. (ARLO) **106**, L71–L74.
Shannon, R. V., Zeng, F-G., Kamath, V., Wygonski, J., and Ekelid, M. (**1995**). ''Speech recognition with primarily temporal cues,'' Science **270**, 303–304.
Skinner, M. W., Holden, L. K., Holden, T. A., Demorest, M. E., and Fourakis, M. S. (**1997**). ''Speech recognition at simulated soft, conversational, and raised-to-loud vocal efforts by adults with cochlear implants,'' J. Acoust. Soc. Am. **101**, 3766–3782.
Stelmachowicz, P. G., Jesteadt, W., Gorga, M. P., and Mott, J. (**1985**). ''Speech perception ability and psychophysical tuning curves in hearing impaired listeners,'' J. Acoust. Soc. Am. **77**, 620–627.
ter Keurs, M., Festen, J. M., and Plomp, R. (**1992**). ''Effect of spectral envelope smearing on speech reception I,'' J. Acoust. Soc. Am. **91**, 2872–2880.
ter Keurs, M., Festen, J. M., and Plomp, R. (**1993**). ''Effect of spectral envelope smearing on speech reception. II,'' J. Acoust. Soc. Am. **93**, 1547–1552.
Throckmorton, C. S., and Collins, L. M. (**1999**). ''Investigation of the effects of temporal and spacial interactions on speech-recognition skills in cochlear-implant subjects,'' J. Acoust. Soc. Am. **105**, 861–873.
Turner, C. W., and Henn, C. C. (**1989**). ''The relation between vowel recognition and measures of frequency resolution,'' J. Speech Hear. Res. **32**, 49–58.
Turner, C. W., Chi, S.-L., and Flock, S. (**1999**). ''Limiting spectral resolution in speech for listeners with sensorineural hearing loss,'' J. Speech Hear. Res. **42**, 773–784.
Turner, C. W., Fabry, D. A., Barrett, S., and Horowitz, A. R. (**1992**). ''Detection and recognition of stop consonants by normal-hearing and hearing-impaired listeners,'' J. Speech Hear. Res. **35**, 942–949.
Wilson, B. S., Finley, C. C., Lawson, D. T., Wolford, R. D., Eddington, D. K., and Rabinowitz, W. M. (**1991**). ''New levels of speech recognition with cochlear implants,'' Nature (London) **352**, 236–238.
Wilson, B. S., Finley, C. C., Lawson, D., and Zerbi, M. (**1998**). ''Temporal representations with cochlear implants,'' Am. J. Otol. **18** (Suppl.), S30–S34.
Zwolan, T. A., Collins, L. M., and Wakefield, G. H. (**1997**). ''Electrode Discrimination and speech recognition in postlingually deafened adult cochlear implant subjects,'' J. Acoust. Soc. Am. **102**, 3673–3685.
Zwolan, T. A., Kileny, P. R., Ashbaugh, C., and Telian, S. A. (**1996**). ''Patient performance with the Cochlear Corporation 20+2 implant: bipolar versus monopolar activation,'' Am. J. Otol. **17**, 717–723.

Effects of low-pass filtering on the intelligibility of speech in quiet for people with and without dead regions at high frequencies[a)]

Deborah A. Vickers, Brian C. J. Moore,[b)] and Thomas Baer
Department of Experimental Psychology, University of Cambridge, Downing Street, Cambridge CB2 3EB, United Kingdom

(Received 2 January 2001; accepted for publication 26 April 2001)

A dead region is a region of the cochlea where there are no functioning inner hair cells (IHCs) and/or neurons; it can be characterized in terms of the characteristic frequencies of the IHCs bordering that region. We examined the effect of high-frequency amplification on speech perception for subjects with high-frequency hearing loss with and without dead regions. The limits of any dead regions were defined by measuring psychophysical tuning curves and were confirmed using the TEN test described in Moore *et al.* [Br. J. Audiol. **34**, 205–224 (2000)]. The speech stimuli were vowel–consonant–vowel (VCV) nonsense syllables, using one of three vowels (/i/, /a/, and /u/) and 21 different consonants. In a baseline condition, subjects were tested using broadband stimuli with a nominal input level of 65 dB SPL. Prior to presentation via Sennheiser HD580 earphones, the stimuli were subjected to the frequency-gain characteristic prescribed by the ''Cambridge'' formula, which is intended to give speech at 65 dB SPL the same overall loudness as for a normal listener, and to make the average loudness of the speech the same for each critical band over the frequency range important for speech intelligibility (in a listener without a dead region). The stimuli for all other conditions were initially subjected to this same frequency-gain characteristic. Then, the speech was low-pass filtered with various cutoff frequencies. For subjects without dead regions, performance generally improved progressively with increasing cutoff frequency. This indicates that they benefited from high-frequency information. For subjects with dead regions, two patterns of performance were observed. For most subjects, performance improved with increasing cutoff frequency until the cutoff frequency was somewhat above the estimated edge frequency of the dead region, but hardly changed with further increases. For a few subjects, performance initially improved with increasing cutoff frequency and then worsened with further increases, although the worsening was significant only for one subject. The results have important implications for the fitting of hearing aids. [DOI: 10.1121/1.1381534]

PACS numbers: 43.71.Ky, 43.66.Sr, 43.66.Ts [CWT]

I. INTRODUCTION

It has been known for many years that cochlear hearing loss is sometimes associated with complete destruction of the inner hair cells (IHCs) within the cochlea (Engström, 1983; Borg *et al.*, 1995). Sometimes the IHCs may still be present, but may be sufficiently abnormal that they no longer function. The IHCs are the transducers of the cochlea, responsible for converting the vibration patterns on the basilar membrane into action potentials in the auditory nerve (Yates, 1995). When the IHCs are nonfunctioning over a certain region of the cochlea, no transduction will occur in that region. For this reason, we refer to such a region as a *dead region* (Moore and Glasberg, 1997; Moore *et al.*, 2000).

One way of characterizing a dead region is in terms of the place in the cochlea that is dead. For example, one might refer to a basal dead region or an apical dead region. In the present article we define a dead region in terms of the characteristic frequencies (CFs) of the IHCs and/or neurons *immediately adjacent* to the dead region (Moore, 2001). For example, if there is a dead region at the basal end of the cochlea, and the CF of the IHCs/neurons immediately adjacent to the dead region is 2 kHz, we describe this as a dead region extending from 2 kHz upwards.

Recently, we have described a test for the identification of dead regions which is intended to be short and simple enough for use in clinical practice (Moore *et al.*, 2000). The test is based upon the detection of sinusoids in the presence of a broadband noise, designed to produce almost equal masked thresholds (in dB SPL) over a wide frequency range, for normally hearing listeners and for listeners with hearing impairment but without dead regions. This noise is called threshold equalizing noise (TEN). The detection threshold is approximately equal to the level of the noise in a one-ERB-wide band centered at 1 kHz; ERB stands for equivalent rectangular bandwidth of the auditory filter, and its normal value at 1000 Hz is about 132 Hz (Glasberg and Moore, 1990). For example, a noise level of 70 dB/ERB usually leads to a masked threshold of about 70 dB SPL. An abnormally high masked threshold at a particular frequency is taken to indicate a dead region (see later in this work).

[a)]Small portions of the data described in this article were presented in Vickers *et al.* (2001) and Moore *et al.* (2001).

[b)]Author to whom correspondence should be addressed. Electronic mail: bcjm@cus.cam.ac.uk

 0001-4966/2001/110(2)/1164/12/$18.00

To assess the validity of the TEN test, psychophysical tuning curves (PTCs) were measured using the same hearing-impaired listeners as tested with the TEN. It is commonly assumed that, when the tip of a PTC is shifted away from the signal frequency, this indicates that the signal frequency falls in a dead region (Thornton and Abbas, 1980; Florentine and Houtsma, 1983; Turner *et al.*, 1983; Moore, 1998; Moore *et al.*, 2000; Moore and Alcántara, 2001; Moore, 2001). In total, Moore *et al.* (2000) tested 20 ears of 14 subjects with sensorineural hearing loss. Generally, there was a very good correspondence between the results obtained using the TEN test and the PTCs; if, for a given signal frequency, the masked threshold in the TEN was 10 dB or more higher than normal (i.e., 10 dB or more above the noise level per ERB) *and* the TEN produced at least 10 dB of masking (i.e., the masked threshold was 10 dB or more above the absolute threshold), then the tip of the PTC determined using that signal frequency was shifted. If the masked threshold in the TEN was not 10 dB or more higher than normal, the tip of the PTC was not shifted. Hence, the following ''rule'' was formulated: if the threshold in the TEN is 10 dB or more above the TEN level/ERB, and the TEN produces at least 10 dB of masking, this is indicative of a dead region at the signal frequency.

The presence or absence of dead regions has important implications for the fitting of hearing aids, and for the benefit that may be expected from hearing aids. There have been reports over a period of many years suggesting that people with moderate-to-severe hearing loss at high frequencies often do not benefit from amplification of high frequencies, or even perform more poorly when high frequencies are amplified (Villchur, 1973; Moore *et al.*, 1985; Murray and Byrne, 1986; Turner and Cummings, 1999; Hogan and Turner, 1998; Ching *et al.*, 1998; Amos and Humes, 2001). In these studies, no definite explanation could be offered for the lack of benefit from amplification of high frequencies, although some authors speculated that IHC or neural dysfunction might be involved.

Murray and Byrne (1986) tested five subjects with near-normal hearing for frequencies up to 1 kHz, and losses of 65 to 80 dB between 4 and 8 kHz. Speech stimuli were initially amplified using the frequency-gain characteristic prescribed by the NAL(R) procedure (Byrne and Dillon, 1986); this was done separately for each subject. Then the stimuli were low-pass filtered with cutoff frequencies of 4.5, 3.5, 2.5, or 1.5 kHz. They presented running (continuous) speech in speech-shaped noise. The (input) noise level was fixed at 70 dBA, and subjects were asked to adjust the speech level until 50% of the speech could be understood. This speech level was called the speech reception threshold (SRT). Three of the subjects performed better (the SRT was lower) when the cutoff frequency was 2.5 or 3.5 kHz than when it was 4.5 kHz. For the other two subjects, there was little change in SRT as the cutoff frequency was decreased from 4.5 to 2.5 kHz. These results indicate that, for people with moderate-to-severe high-frequency hearing loss, amplification of the high frequencies in speech is not always beneficial, and may sometimes impair speech reception.

Hogan and Turner (1998) tested nine subjects with near-normal hearing at low frequencies and high-frequency hearing losses ranging from about 40 to 110 dB. Subjects were required to identify nonsense syllables using speech that had been given high-frequency emphasis (to restore audibility) and was then low-pass filtered with various cutoff frequencies. When the high-frequency loss was greater than 55 dB, increasing the high-frequency cutoff often was of little benefit, or made performance worse.

Turner and Cummings (1999) investigated the intelligibility of nonsense syllables in a group of ten subjects whose hearing loss at high frequencies (averaged for 4, 5, and 6.3 kHz) ranged from about 40 to 71 dB. Recognition was tested across a wide range of presentation levels. At high levels, scores reached an asymptote below 100%, i.e., performance was imperfect, but did not improve further with increasing audibility of the speech. Turner and Cummings calculated the audibility of different parts of the speech spectrum for speech at this asymptotic performance level, based on the audiogram of each subject. They found that providing audible speech at frequencies above 3 kHz tended to produce little or no improvement in recognition scores whenever the hearing loss exceeded 55 dB.

Overall, the studies described above clearly show that, when the hearing loss exceeds about 55 dB at high frequencies, amplification of high frequencies is often not beneficial. The authors of these studies have often interpreted their results in terms of damage to IHCs in the basal region of the cochlea. Specifically, it has been suggested that subjects who do not benefit from amplification have dead regions (or at least extensive damage to the IHCs) at high frequencies, while subjects who do benefit from amplification have surviving IHCs and neurons with high CFs. However, the studies all suffer from the drawback that there was no independent test for the existence of dead regions, and therefore the extent of any dead regions was unknown.

In the present article, we describe the results of a study of the effect of low-pass filtering on the intelligibility of speech, using subjects with high-frequency hearing loss. PTCs were measured for each subject to detect and define the limits of any dead region and the TEN test was used to confirm the diagnosis. Subjects both with and without dead regions were tested.

II. METHOD

A. Subjects

Ten subjects with high-frequency hearing loss were tested. The audiograms of the ears tested are given in Table I. The table also shows the ages of the subjects. The losses were diagnosed as being sensorineural (presumably cochlear) based on normal tympanometry and lack of an air-bone gap. The presence and extent of any dead regions were assessed by the measurement of PTCs, determined exactly as described in Moore *et al.* (2000), using Sennheiser HD580 earphones. When the frequency at the tip of the PTC was shifted away from the signal frequency, the frequency at the tip was taken to indicate the edge frequency of the dead region. The TEN test described earlier (Moore *et al.*, 2000) was used to confirm the presence and extent of the dead regions. The test

TABLE I. Audiometric (air conduction) thresholds of the test ears of the subjects, in dB HL. The * symbol indicates frequencies falling within the estimated dead region. The ↑ symbol indicates that audiometric thresholds were too high to be measured with the available audiometer. The age of each subject (years) is also shown.

			Frequency (kHz)									
Subject	Ear	Age	0.25	0.5	0.75	1.0	1.5	2.0	3.0	4.0	6.0	8.0
DT	L	76	25	15		15		45		45		50
DT	R		20	10		5		60		65	60	60
KC	L	65	10	10		10	40	65	70	75	70	65
KC	R		10	10		10	15	45	60	60	60	55
VW	L	73	50	60		70		60	70	60	65	
VW	R		40	55		70	75	65	75	85	75	90
LR	L	48	15	55		70	85*	100*	115*	120*	↑*	↑*
LR	R		10	55		65	80	90*	110*	95*	↑*	↑*
CA	L	55	25	30	45	65*	110*	↑*	↑*	↑*	↑*	↑*
CA	R		15	35	55	65*	110*	↑*	↑*	↑*	↑*	↑*
RC	L	71	15	10		5	60*	75*		105*		90*
DW	L	64	5	5		10	25	55		65		85*
NC	L	76	20	25	30	35	60*	70*	95*	110*	↑*	↑*
NC	R		25	25	55	70*	90*	95*	95*	110*	↑*	↑*
MW	L	60	30	55	60	65	85*	110*	110*	100*	↑*	↑*
MW	R		15	40		65*	75*	80*	105*	95*	110*	↑*
PJ	L	70	20	20		45	55	60	65	65*	80*	80*
PJ	R		10	10		35	60	60	70	70*	80*	80*

was administered exactly in the way described by Moore *et al.* (2000), using TEN levels of 30, 50, and 70 dB per ERB and TDH 49 earphones. However, the signal frequencies were more closely spaced than described in Moore *et al.* (2000), so as to define the edges of the dead regions more precisely. If, for a specific signal frequency, the threshold in the TEN was 10 dB or more above the TEN level/ERB, and the TEN produced at least 10 dB of masking for at least one masker level, this was taken as indicating a dead region at the signal frequency. There was always a good correspondence between the results of the TEN test and the measurements using PTCs. Examples of the PTCs and the results of the TEN test (for subjects KC, LR, RC, and PJ) are given in Moore *et al.* (2000).

Of the ten subjects, seven had high-frequency dead regions and three did not; generally, the subjects with dead regions had more severe high-frequency hearing losses than those without dead regions. The frequencies falling within the diagnosed dead regions are indicated by asterisks (*) in Table I. Edge frequencies of the dead regions, estimated from the PTC measurements, are given in the figures which will be presented later. For all of the subjects with dead regions, the dead region appeared to extend from the estimated edge frequency up to the highest frequency that was tested (10 kHz). Testing was done separately for each ear, but some subjects were tested using one ear only. In total, 12 ears with dead regions and 6 ears without dead regions were tested.

B. Stimuli and conditions

The speech stimuli were vowel–consonant–vowel (VCV) nonsense syllables, using one of three vowels (/i/,/a/ or /u/) and 21 different consonants. These were: /p, t, k, b, d, g, f, θ, s, ʃ, h, v, z, r, l, j, w, tʃ, dʒ, n, m/. The syllables were spoken by a female speaker with a British accent. The initial vowel was always the same as the final vowel. Each combination of vowel and consonant was presented once in each list in a randomized order, giving a total of 63 tokens per list. There were four different tokens of each VCV combination; the tokens used varied across lists. All lists were recorded on CDR and were replayed from the CDR for presentation to the subjects.

In a baseline condition, subjects were tested using broadband stimuli (bandwidth 7500 Hz) with a nominal input level of 65 dB SPL. Prior to presentation via Sennheiser HD580 earphones, the stimuli were subjected to the frequency-gain characteristic prescribed by the ''Cambridge'' formula (Moore and Glasberg, 1998). The formula is

$$\mathrm{IG}(f) = 0.48\mathrm{HL}(f) + \mathrm{INT}(f), \tag{1}$$

where $\mathrm{IG}(f)$ is the insertion gain in dB at frequency f, $\mathrm{HL}(f)$ is the hearing loss in dB at frequency f, and $\mathrm{INT}(f)$ is an intercept whose value depends on frequency. For frequencies of 1000 Hz and above, the value of INT is approximately 0 dB, so the insertion gain is approximately 0.48 times the hearing loss.

The Cambridge formula is intended to give speech at 65 dB SPL the same overall loudness as for a normal listener, and to make the average specific loudness [the loudness per ERB or per critical band; see Moore and Glasberg (1997)] of the speech the same for all frequencies over the range important for speech intelligibility, i.e., about 500 to 5000 Hz. Of course, this is only possible for a listener without a dead region in that frequency range. For a listener with a dead region, the specific loudness is zero for all critical bands falling within the dead region. In any case, the goal of the frequency-dependent amplification was to restore audibility as far as possible, while avoiding excessive loudness. The gain specified by the Cambridge formula was calculated and applied separately for each ear of each subject. The maximum insertion gain applied was 50 dB. If the Cambridge formula called for an insertion gain greater than 50 dB, then

the insertion gain was limited to 50 dB. In practice, this occurred when the hearing loss at high frequencies was 105 dB or more. The gain limit was reached in the following cases: LR, both ears for frequencies of 3000 Hz and above; CA, both ears for frequencies of 1500 Hz and above; NC, both ears for frequencies of 4000 Hz and above; MW, left ear for frequencies of 2000 Hz and above; and MW, right ear for frequencies of 6000 Hz and above.

The stimuli for all other conditions were initially subjected to this same frequency-gain characteristic. Then, the speech was low-pass filtered with various cutoff frequencies. The cutoff frequencies were chosen separately for each subject, to cover a range from slightly below to well above the estimated edge frequency of the dead region, when present. For subjects without a dead region, the cutoff frequencies were chosen to span the range 800 to 7500 Hz. The number of cutoff frequencies varied across subjects, depending on the amount of time that they were willing to be tested.

The HD580 earphones are intended to have a ''diffuse field'' response, i.e., they give a response at the eardrum similar to what would be obtained listening with an open ear in a diffuse sound field. If the response corresponded exactly to that intended, then the insertion gains called for by Eq. (1) could be specified in terms of electrical gains, without any compensation for the frequency response of the earphone. However, measurements using a KEMAR manikin (Burkhard and Sachs, 1975), averaging the responses obtained for the ''large'' and ''small'' ears, showed small deviations (± 3 dB over the range 250 to 5000 Hz) from the diffuse-field-to-eardrum transformation; this transformation was estimated from the mean of the results published in Killion *et al.* (1987), Kuhn (1979), and Shaw (1980). These deviations were compensated in the digital filter described later in this work, so that the resulting insertion gains corresponded as accurately as possible to the desired values.

A Tucker-Davis Technologies (TDT) PowerDAC with six digital signal processors was used to implement the Cambridge formula filter (Camfilter) and the low-pass filter for each condition and each subject. The Camfilter was implemented on one processor and the low-pass filter on the other five processors, to give maximum cutoff sharpness. The response of the filter typically fell by more than 50 dB when the frequency was increased from the nominal cutoff frequency to 0.25 oct above it. The Camfilters were designed using the FIR2 function in MATLAB. The low-pass filters were designed either with the Remez function or the FIR1 function.

C. Procedure

Subjects were given a list of the possible consonants, with examples of their pronunciation. They were asked to respond by writing down the consonant they heard for each token, ignoring the vowel. They were given 10 min of practice at the beginning of each session and the first test list was considered practice and was not scored. At least two lists were used for each condition. These were always presented in different test sessions. The order of testing of the different cutoff frequencies was randomized in the first test session. This order was reversed for the second session to balance the effects of practice and fatigue. In some cases, especially when the results appeared to be unusually variable, additional lists were used, up to a maximum of five. For the additional tests, a new random order was used for the different cutoff frequencies.

III. RESULTS

A. Overall percent correct

Figure 1 shows the percentage correct scores on the VCV test, plotted as a function of the lowpass filter cutoff frequency, for the six ears without dead regions. Error bars indicate $\pm$ one standard deviation. The scores generally improved monotonically with increasing cutoff frequency, although for DT the scores flattened off above 2000 Hz. These results are consistent with earlier results obtained using subjects with mild to moderate high-frequency hearing loss (Skinner and Miller, 1983), and they indicate that listeners without dead regions are able to make effective use of high-frequency information in speech. Asymptotic scores on this rather difficult task were between 70% and 87% correct.

To quantify the extent to which the subjects without dead regions were able to make use of high-frequency information, scores were compared for the broadband speech (7500 Hz bandwidth) and the speech low-pass filtered at 2000 Hz. The mean scores for these two conditions were 77.2% and 65.1%, respectively. A one-way within-subjects analysis of variance (ANOVA) of the scores for these two conditions showed a significant effect of cutoff frequency; $F(1,5) = 13.33$, $p = 0.015$.

Figures 2 and 3 show results for the 12 ears with dead regions. The estimated edge frequencies of the dead regions are given in each panel, and are also indicated by the arrows. Generally, performance improved somewhat as the cutoff frequency was increased from just below the estimated edge frequency of the dead region to a frequency up to 1 oct above it. When the cutoff frequency was increased still further, two different patterns were observed. For some subjects (LR both ears, DW left ear, NC both ears, MW both ears, PJ both ears), performance stayed roughly constant, or increased only very slightly. This indicates that these subjects gained little or no benefit from amplification of frequencies more than 50% to 100% above the estimated edge frequency of the dead region, but also that amplification of those frequencies did not impair performance. For subjects NC, MW, and LR, the limited benefit may have been partly due to the fact that the amplification called for by the Cambridge formula could not be applied at high frequencies; the highest frequency at which the required gain could be applied, called f_h, was 4000 Hz for NC (both ears), 2000 Hz for the left ear of MW, 6000 Hz for the right ear of MW, and 3000 Hz for LR (both ears). However, it is noteworthy that scores tended to approach asymptotic values for cutoff frequencies well below f_h.

For the remaining subjects (CA both ears, RC left ear), performance worsened when the cutoff frequency was more than 50% to 100% above the estimated edge frequency of the dead region. This indicates that amplification of high frequencies had a deleterious effect on performance, consistent

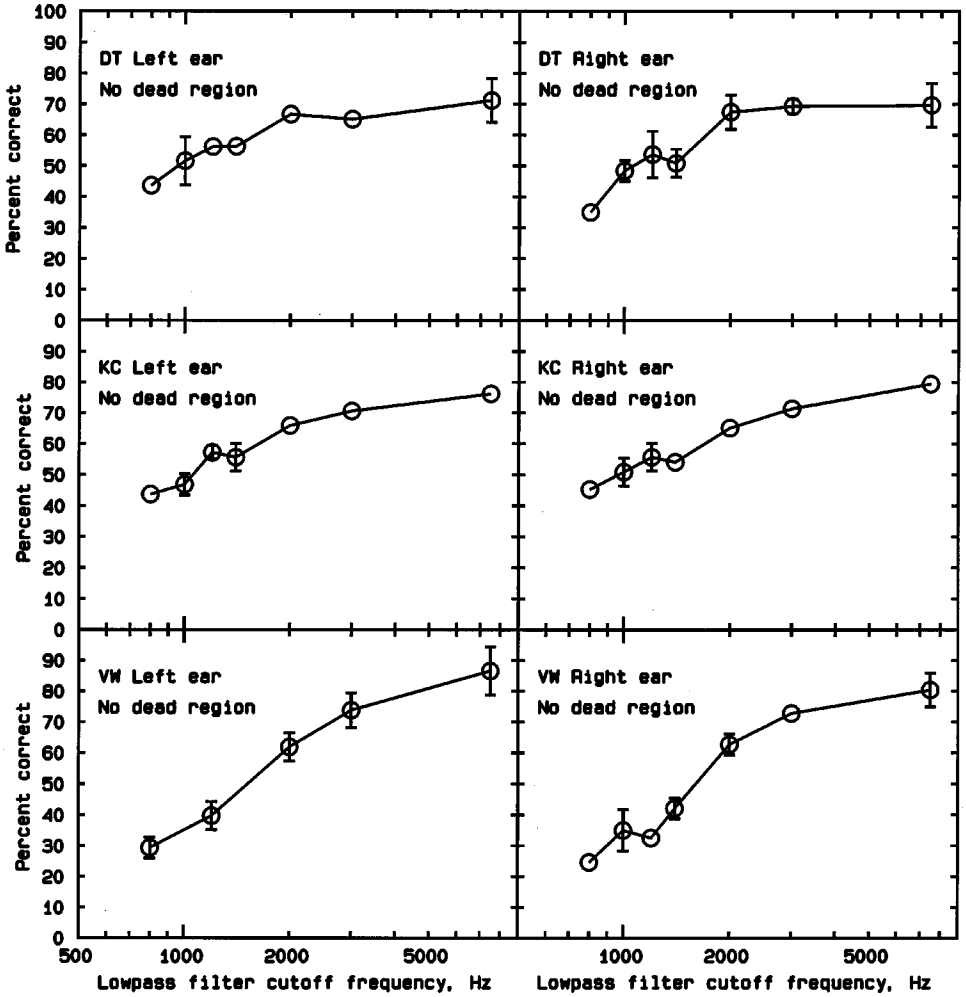

FIG. 1. Results for the six ears without dead regions. The percentage correct score on the VCV test is plotted as a function of the low-pass filter cutoff frequency. Error bars indicate ± one standard deviation.

with earlier results of Murray and Byrne (1986) and Hogan and Turner (1998). To assess the statistical significance of the worsening with increasing cutoff frequency, scores were compared for the cutoff frequency giving the highest score and the cutoff frequency of 7500 Hz. This was done using both *t*-tests and chi-square tests (under the null hypothesis that the expected scores were equal for the two cutoff frequencies). For CA, the decrease was not significant for either ear. For RC the decrease was significant on both tests at $p < 0.05$ (two-tailed). Given the number of such comparisons that could be made, the results do not provide convincing evidence for a decrease in performance with increasing cutoff frequency for any subject. However, CA and RC have both been tested in a subsequent experiment using VCV stimuli presented in background noise, and the general pattern of the results was similar to that found here; performance was best for an intermediate cutoff frequency. Therefore, we are inclined to believe that the decrease in performance with increasing cutoff frequency is ''real.''

To assess the overall extent to which the subjects with dead regions were able to make use of high-frequency information, scores were compared for the broadband speech (7500 Hz bandwidth) and the speech low-pass filtered at 2000 Hz. This analysis excluded the three ears for which the estimated edge frequency of the dead region lay above 2000 Hz (DW, left; PJ left and right). The mean scores for these two conditions were 48.5% and 47.1%, respectively. A one-way within-subjects ANOVA of scores for these two conditions showed no significant effect of cutoff frequency; $F(1,8) = 0.24$.

To give an overall impression of the pattern of results for the subjects having dead regions with edge frequencies below 2000 Hz, the cutoff frequencies used for each ear of each subject were expressed relative to the estimated edge frequency of the dead region for that ear and subject. The data for each ear (percent correct versus relative frequency) were fitted with a cubic spline function. The cubic spline functions were then averaged across ears. The result is shown in Fig. 4 (solid curve). For comparison, a similar analysis was applied to the results for the subjects without dead regions; these results are plotted in Fig. 4 as a function of absolute (not relative) frequency in kHz (dashed curve). The two frequency scales are roughly comparable, as a relative frequency of 1 corresponds, on average, to a frequency a little below 1 kHz; the geometric mean of the estimated edge frequencies of the dead regions was 942 Hz.

For the subjects with dead regions, the fitted function increases with increasing relative frequency up to about 1.7,

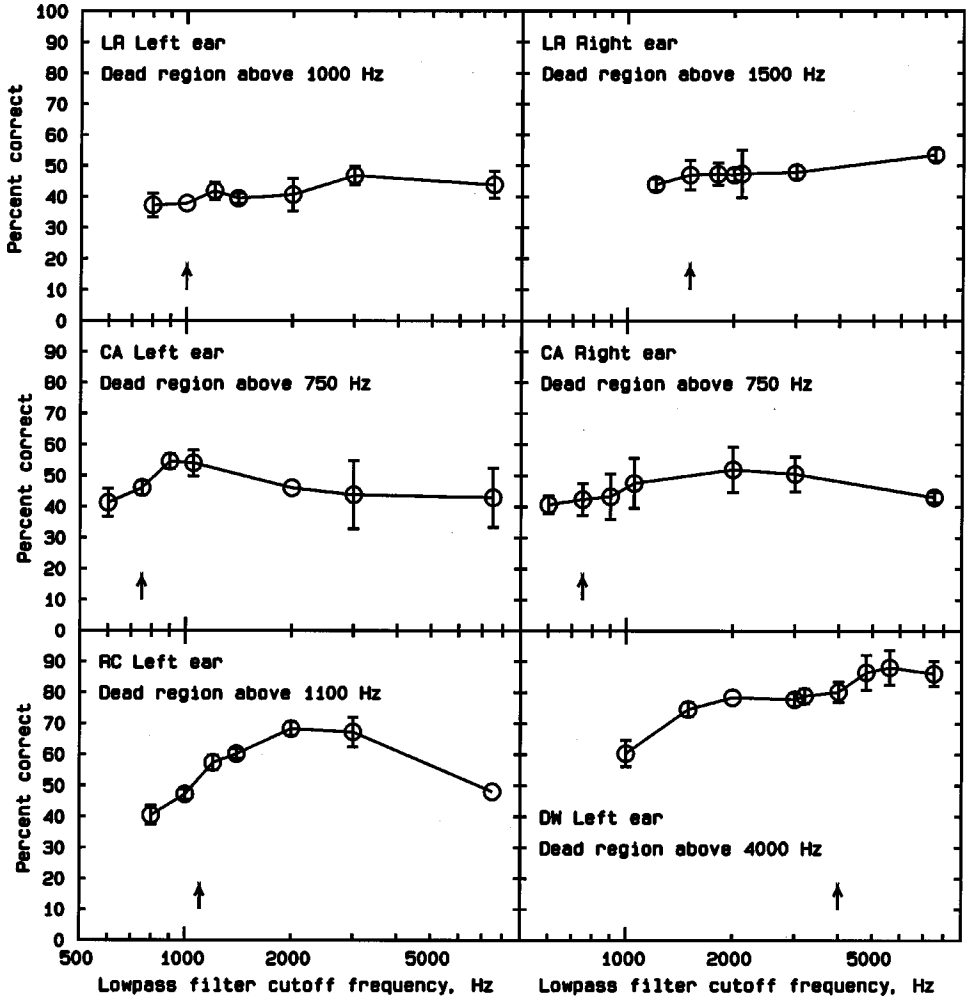

FIG. 2. Results for six ears with dead regions. Otherwise as in Fig. 1.

and then flattens off. This indicates that there is typically some benefit to intelligibility of amplifying frequencies up to about 70% above the estimated edge frequency of the dead region. For the subjects without dead regions, the fitted function increases progressively with increasing cutoff frequency, indicating that broadband amplification gives the best performance.

As another method for comparing the effect of changes in cutoff frequency for the two groups of subjects, we used the cubic-spline fits to determine the frequency at which the score was 0.9 times that measured for the broadband stimuli (7500-Hz bandwidth). For the mean cubic-spline fit to the data for subjects without dead regions, this value was 2.5 kHz. For the fits to the data for individual ears without dead regions, the value ranged from 1800 to 3700 Hz. For the fits to the data for individual ears with dead regions below 2000 Hz, the value ranged from 880 Hz (RC, left ear) to 3450 Hz (LR, right ear), but most values were below 1200 Hz. The arithmetic mean value was 1400 Hz, and the geometric mean value was 1100 Hz. For one subject (CA, left and right ears), the scores did not drop below 0.9 times those measured for the broadband stimuli even for the lowest cutoff frequency used (600 Hz). Thus, reducing the cutoff frequency had markedly smaller effects on performance for the subjects with dead regions than for the subjects without dead regions.

To assess the extent to which the subjects with dead regions were able to make use of information from frequencies just above the estimated edge frequency of the dead region, scores were compared for the low-pass filter cutoff frequency closest to the estimated edge frequency, and for the cutoff frequency closest to 1.7 times the estimated edge frequency. This analysis included all ears with dead regions. The mean scores for these two conditions were 50.6% and 55.9%, respectively. A one-way within-subjects ANOVA of scores for these two conditions showed a highly significant effect of cutoff frequency; $F(1,11)=33.7$, $p<0.001$. Thus, there was a significant benefit from amplifying frequencies up to 70% above the estimated edge frequencies of the dead regions.

For the cases where the dead region had an estimated edge frequency of 3000 Hz or more (PJ both ears, DW left ear), performance at the optimum cutoff frequency ranged from 75% to 87%. These scores are comparable to those obtained by the subjects without dead regions when listening to broadband speech. This is not surprising, as most of the important information in speech lies below 3000 Hz (Fletcher, 1953; ANSI, 1969; Pavlovic, 1987; ANSI, 1997). However, for cases where the dead region had a lower estimated edge frequency, performance at the optimum cutoff frequency was poorer, ranging from 48% to 68%. This is

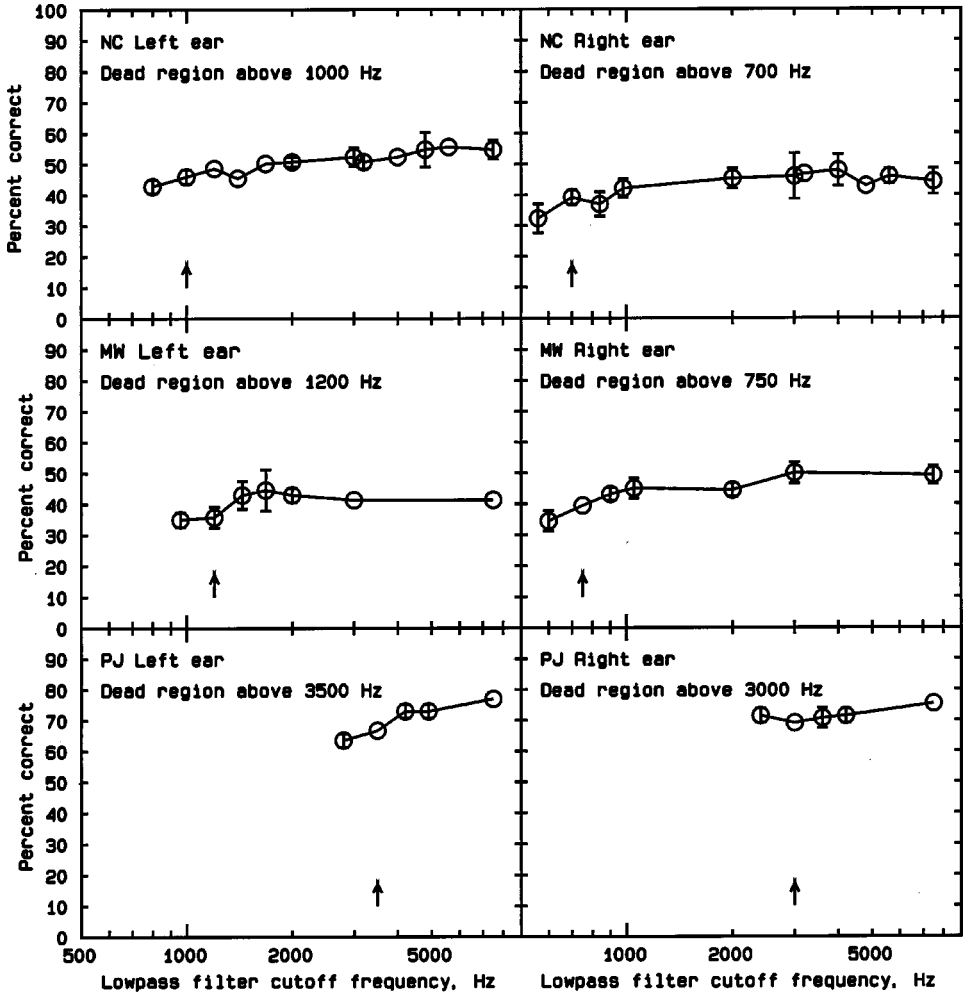

FIG. 3. Results for a further six ears with dead regions. Otherwise as in Fig. 1.

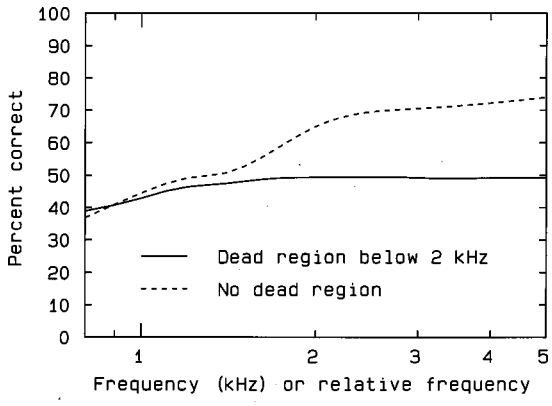

FIG. 4. Mean cubic spline functions fitted to the data for subjects without dead regions (dashed curve) and for subjects with dead regions starting below 2000 Hz (solid curve). For the group without dead regions, percent correct is plotted as a function of filter cutoff frequency in kHz. For the group with dead regions, frequency is expressed relative to the estimated edge frequency of the dead region.

consistent with the idea that the higher frequency components in the speech did not provide usable information, even though they were amplified by as much as 50 dB.

B. Transmission of phonetic features

It is of interest to determine which phonetic features are affected most by changes in bandwidth, and to determine whether the effect of bandwidth on transmission of phonetic features differs for subjects without and with dead regions. To examine these issues, the results for each ear of each subject were analyzed to determine the percentage information transmission for the phonetic features of voicing, place, and manner (Miller and Nicely, 1955) as a function of filter cutoff frequency. We used a method called sequential information analysis (SINFA) in which each feature is treated independently (Wang and Bilger, 1973). The first stage was to compile a stimulus-response matrix from the results for each ear and each filter cutoff frequency; data were combined across runs to do this. For each feature, the information transmitted (IT) from stimulus to response was computed. For the feature giving the maximum proportion of IT, the value of the IT computed in this way was taken as the final value. In the majority of cases, this feature was voicing.

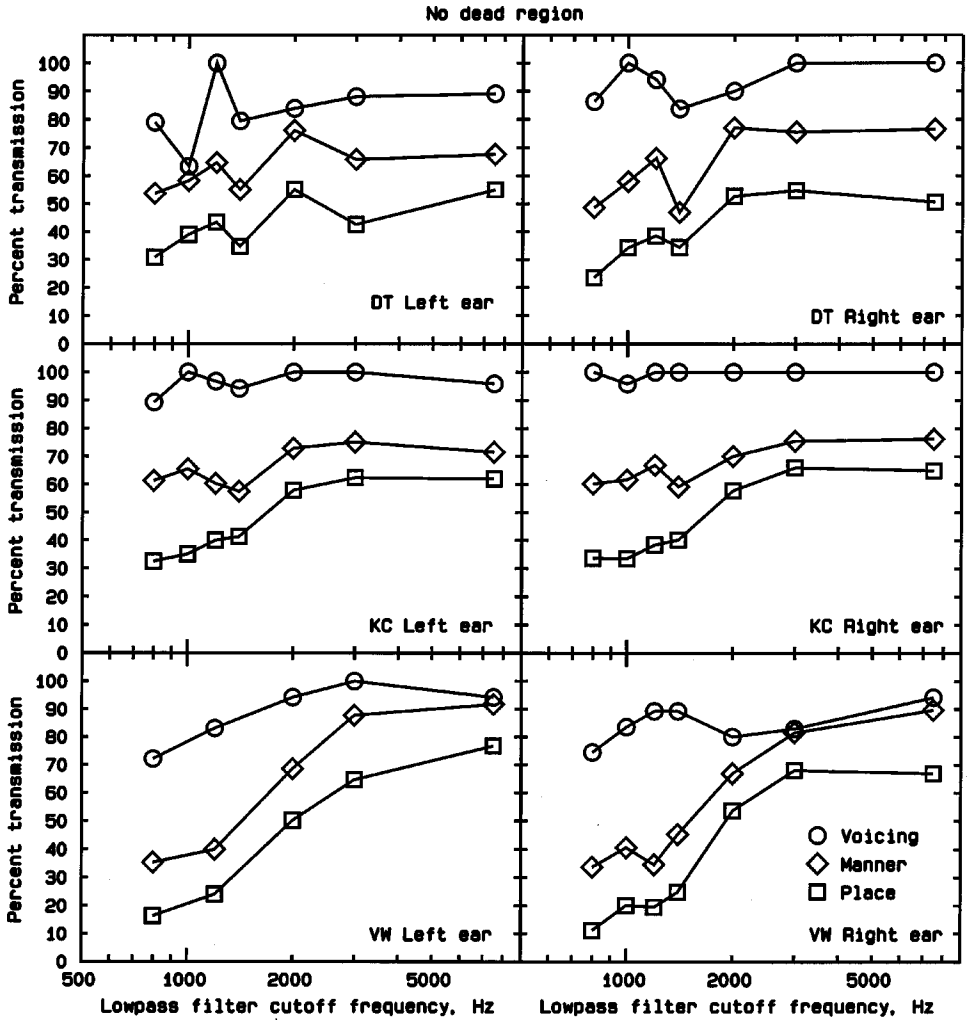

FIG. 5. Information transmission scores for the features of voicing (circles), manner (diamonds), and place (squares) plotted as a function of the low-pass filter cutoff frequency, for six ears without dead regions.

The analysis was then repeated with the selected (maximally transmitted) feature partialed out (held constant). The feature giving the next highest IT was selected, and the IT for that feature was taken as the final value. This feature was typically manner. Finally, the analysis was repeated with the first two selected features partialed out. This gave the IT for the remaining feature (always place). The analysis was conducted using a software package called ''FIX'' produced by Mike Johnson of the Department of Phonetics and Linguistics, University College, London; it is available from http://www.phon.ucl.ac.uk/resource.htm.

The results are shown in Figs. 5–7. In each panel, the percentage of transmitted information is plotted as a function of filter cutoff frequency for the features voicing, place, and manner. The percentage of information transmitted was nearly always highest for voicing and lowest for place. Scores for voicing remained above 70% even for cutoff frequencies as low as 800 Hz, indicating that information about voicing can be extracted effectively from low-frequency components of speech. For the subjects without dead regions (Fig. 5), scores for manner tended to increase with increasing cutoff frequency, and scores for place increased even more, at least for cutoff frequencies up to 3000 Hz. For the subjects with dead regions (Figs. 6 and 7), scores for manner and place tended to improve initially with increasing cutoff frequency, but did not improve once the cutoff frequency was more than 50% to 100% above the estimated edge frequency of the dead region. Generally, the pattern of the results for the transmission of place information was similar to that found for the overall scores. This makes sense, as errors in the overall scores were mainly associated with errors in identifying the place feature.

These results have possible implications for the design of future signal-processing hearing aids for people with high-frequency dead regions. Such aids might attempt to enhance specific speech cues, or to recode those cues into a more discriminable form. The SINFA analyses suggest that it will be more profitable to enhance cues related to the features of place and manner than to enhance cues related to voicing.

IV. DISCUSSION

Previous studies have shown that some hearing-impaired listeners benefit from amplification of high frequencies, while others do not (Villchur, 1973; Skinner and Miller, 1983; Moore *et al.*, 1985; Murray and Byrne, 1986; Turner

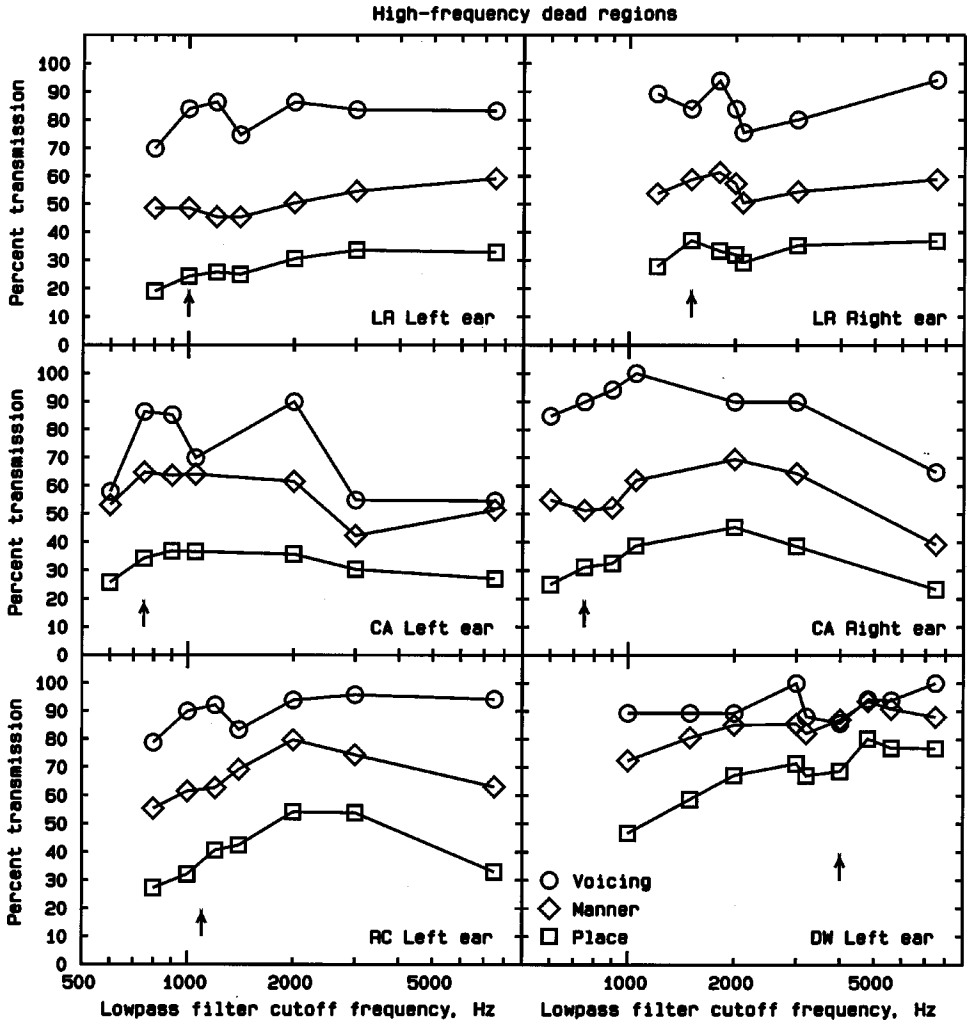

FIG. 6. Results for six ears with dead regions. Otherwise as in Fig. 4.

and Cummings, 1999; Hogan and Turner, 1998; Ching *et al.*, 1998; Amos and Humes, 2001). These studies have also shown a trend for larger hearing losses to be associated with reduced benefit (or negative benefit) from amplification. However, it does not seem possible to predict reliably from the audiogram which patients will benefit from amplification of high frequencies, and which patients will not. Our data suggest that the key factor is the presence or absence of a dead region at high frequencies. Patients without a dead region at high frequencies will generally benefit from amplification of high frequencies, whereas patients with a dead region will generally not benefit, except for frequencies that are a little (50% to 100%) above the estimated edge frequency of the dead region.

There are several theoretical reasons why people with dead regions might extract little or no information from frequency components of speech that fall within a dead region, even if those components are amplified sufficiently to make them audible. These reasons include the following.

(1) The frequency components are received through the ''wrong'' place in the cochlea. When there is a high-frequency dead region, amplified high-frequency components will be detected and analyzed via the frequency ''channels'' or places that are tuned to lower frequencies. This mismatch between frequency and place may lead to difficulty in interpreting the information derived from the high frequencies. There is some evidence supporting this idea from studies involving the simulation of hearing loss and/or of cochlear implant signal processing (Shannon *et al.*, 1998). However, extended learning with ''remapped'' stimuli may partially compensate for this problem (Rosen *et al.*, 1999).

(2) If the components falling in the dead region are amplified sufficiently to make them audible, they will be detected and analyzed via the same neural channels that are used for other frequencies, and this may impair the analysis of those other frequencies. For example, if there is a high-frequency dead region, the amplified high-frequency components will be detected and analyzed through the same neural channels as are used for the low and medium frequencies. Since speech is a broadband signal, usually containing components covering a wide frequency range, this may lead to some form of ''information overload'' in those channels.

(3) Information in speech, such as information about formant frequencies, may partly be coded in the time patterns of the neural impulses (phase locking) (Young and Sachs, 1979; Miller *et al.*, 1997; Baer *et al.*, 1993; Baer

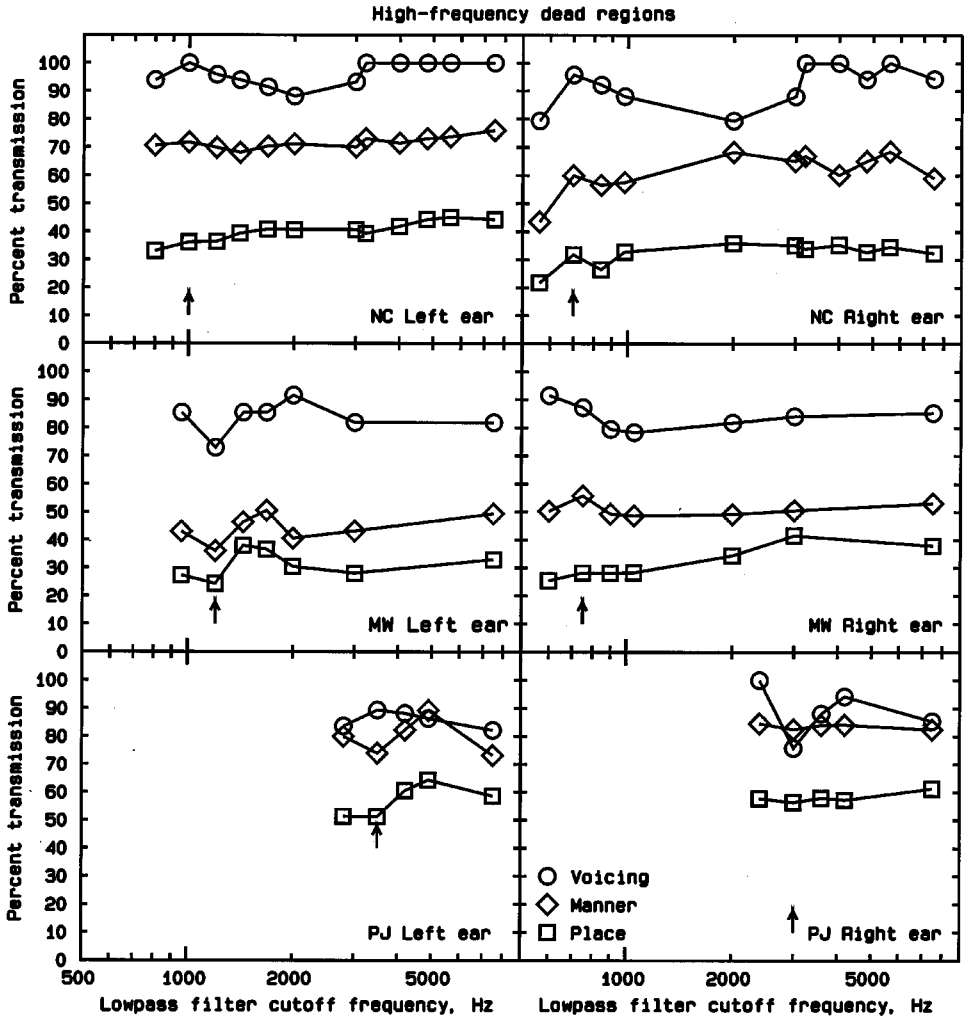

FIG. 7. Results for a further six ears with dead regions. Otherwise as in Fig. 4.

and Moore, 1997). The analysis of temporal information may normally be done on a place-specific basis. For example, the neural machinery required to ''decode'' temporal information from frequencies around 2000 Hz may be restricted to neural channels with CFs close to 2000 Hz (Loeb *et al.*, 1983; Srulovicz and Goldstein, 1983). This is the theoretical rationale behind the measure ''average localized synchronized rate'' (Young and Sachs, 1979; Miller *et al.*, 1997). When there is a mismatch between the frequencies of the speech components and the place where they are detected, the temporal decoding mechanisms required to analyze those speech components may not operate effectively.

The potential benefit of a hearing aid is sometimes assessed by calculation of the articulation index for speech amplified by that hearing aid (Pavlovic *et al.*, 1986; Fabry and Van Tasell, 1990; Rankovic, 1991; Humes and Riker, 1992; Moore and Glasberg, 1998). Our results suggest that this method needs to be treated with considerable caution. For people without dead regions, the articulation index may provide a valid indication of the audibility and intelligibility of speech. However, for people with dead regions, the articulation index may lead to overestimates of the intelligibility of speech. This may partly account for the finding that people with severe to profound hearing loss often show poorer speech intelligibility than predicted from the articulation index (Fletcher, 1952; Dugal *et al.*, 1978; Pavlovic, 1984; Pavlovic *et al.*, 1986; Smoorenburg, 1992).

Our results have important implications for the fitting of hearing aids to people with high-frequency dead regions. They suggest that there will be little or no benefit to speech perception from amplifying frequencies *well inside* a dead region. However, there may be some benefit in amplifying frequencies up to 50% to 100% above the estimated edge frequency of the dead region. Some caution is needed here, as the present results were obtained only using speech in quiet. The ''optimum'' cutoff frequency may be different for speech presented in background noise. We are currently conducting experiments to assess whether this is the case. Also, amplification of high frequencies might be of some benefit in providing awareness of environmental sounds.

It should be emphasized that, for patients *without* high-frequency dead regions, amplification of the high frequencies can be (and usually is) beneficial; see the results in Fig. 1 and in Skinner and Miller (1983). Hence, before deciding what form of amplification should be provided for a patient with high-frequency hearing loss, it is important to determine whether that patient has a high-frequency dead region, and, if

so, what its extent is. The TEN test is recommended for this purpose.

For a patient with a dead region at high frequencies, there may be several benefits of reducing the gain at high frequencies. First, it can sometimes lead to improved speech intelligibility, although further data are needed to assess the reliability of this effect and to assess the proportion of patients for whom it occurs. Second, it may reduce problems associated with acoustic feedback, which often occurs when trying to achieve the gains appropriate for a severe to profound loss. Third, it may reduce distortion in the hearing aid, especially intermodulation distortion. Such distortion can lead to reduced speech intelligibility (Crain and van Tasell, 1994). Finally, it allows the dispenser to concentrate efforts on providing appropriate amplification over the frequency range where there is useful residual hearing.

An alternative approach for people with extensive high-frequency dead regions is to use frequency transposition or frequency compression (Johansson, 1966; Velmans and Marcuson, 1983; Posen *et al.*, 1993; Parent *et al.*, 1997; McDermott *et al.*, 1999; Turner and Hurtig, 1999). Hearing aids incorporating frequency transposition and/or compression move high-frequency components to lower frequencies, where auditory function may be better. The results of trials of such aids have generally been disappointing and they have not found widespread acceptance. However, promising results have been found in some studies (Parent *et al.*, 1997; Turner and Hurtig, 1999). The limited benefit demonstrated so far may partly have occurred because the transposition/compression aids have been fitted to patients without clear knowledge of the extent of the dead regions. Hopefully, the availability of the TEN test will lead to more accurate diagnosis of dead regions, and hence to the possibility of better fitting. More research in this area is clearly needed.

V. CONCLUSIONS

For VCV syllables presented in quiet, the benefit of high-frequency amplification for subjects with high-frequency hearing loss differed according to whether or not there was a dead region at high frequencies. In the present study, dead regions and their limits were diagnosed using the TEN test and by measurement of PTCs. The stimuli were given frequency-dependent amplification according to the Cambridge formula before low-pass filtering with various cutoff frequencies. For subjects without dead regions, speech reception improved progressively with increasing low-pass filter cutoff frequency. For people with dead regions, speech reception improved with increasing cutoff frequency until the cutoff frequency was 50% to 100% above the estimated edge frequency of the dead region. With further increases in cutoff frequency, speech reception either remained constant or declined. The results indicate that people with dead regions at high frequencies do not benefit from amplification of frequencies more than 50% to 100% above the estimated edge frequency of the dead region.

When fitting hearing aids to people with high-frequency hearing loss, a test such as the TEN test should be applied to detect any dead regions and define their limits. When a dead region is not present, amplification should be applied over as wide a bandwidth as possible. When a dead region is present, and when problems with acoustic feedback are encountered, consideration should be given to applying amplification only for frequencies up to 50% to 100% above the estimated edge frequency of the dead region. Alternatively, or in addition, consideration should be given to provision of a hearing aid incorporating frequency transposition or frequency compression.

ACKNOWLEDGMENTS

This work was supported primarily by the MRC (UK) with additional support from Starkey (USA), Defeating Deafness (UK), and the RNID (UK). We thank José Alcántara, Brian Glasberg, Martina Huss, and Josephine Marriage for their contributions to this work. We also thank José Alcántara, Mary Florentine, and an anonymous reviewer for helpful comments on an earlier version of this article.

Amos, N. E., and Humes, L. E. (**2001**). ''The contribution of high frequencies to speech recognition in sensorineural hearing loss,'' in *Physiological and Psychophysical Bases of Auditory Function*, edited by D. J. Breebaart, A. J. M. Houtsma, A. Kohlrausch, V. F. Prijs, and R. Schoonhoven (Shaker, Maastricht).

ANSI (**1969**). ANSI S3.5, ''American national standard methods for the calculation of the articulation index'' (American National Standards Institute, New York).

ANSI (**1997**). ANSI S3.5-1997, ''American national standards methods for the calculation of the articulation index'' (American National Standards Institute, New York).

Baer, T., and Moore, B. C. J. (**1997**). ''Evaluation of a scheme to compensate for reduced frequency selectivity in hearing-impaired subjects,'' in *Modeling Sensorineural Hearing Loss*, edited by W. Jesteadt (Erlbaum, Hillsdale, NJ).

Baer, T., Moore, B. C. J., and Gatehouse, S. (**1993**). ''Spectral contrast enhancement of speech in noise for listeners with sensorineural hearing impairment: effects on intelligibility, quality and response times,'' J. Rehabil. Res. Dev. **30**, 49–72.

Borg, E., Canlon, B., and Engström, B. (**1995**). ''Noise-induced hearing loss-Literature review and experiments in rabbits,'' Scand. Audiol. **24**, Suppl. 40, 1–147.

Burkhard, M. D., and Sachs, R. M. (**1975**). ''Anthropometric manikin for acoustic research,'' J. Acoust. Soc. Am. **58**, 214–222.

Byrne, D., and Dillon, H. (**1986**). ''The National Acoustic Laboratories' (NAL) new procedure for selecting the gain and frequency response of a hearing aid,'' Ear Hear. **7**, 257–265.

Ching, T., Dillon, H., and Byrne, D. (**1998**). ''Speech recognition of hearing-impaired listeners: Predictions from audibility and the limited role of high-frequency amplification,'' J. Acoust. Soc. Am. **103**, 1128–1140.

Crain, T. R., and van Tasell, D. J. (**1994**). ''Effect of peak clipping on speech recognition threshold,'' Ear Hear. **15**, 443–453.

Dugal, R., Braida, L. D., and Durlach, N. I. (**1978**). ''Implications of previous research for the selection of frequency-gain characteristics,'' in *Acoustical Factors Affecting Hearing Aid Performance*, edited by G. A. Studebaker and I. Hochberg (University Park, Baltimore).

Engström, B. (**1983**). ''Stereocilia of sensory cells in normal and hearing impaired ears,'' Scand. Audiol. Suppl. **19**, 1–34.

Fabry, D. A., and Van Tasell, D. J. (**1990**). ''Evaluation of an articulation-index based model for predicting the effects of adaptive frequency response hearing aids,'' J. Speech Hear. Res. **33**, 676–689.

Fletcher, H. (**1952**). ''The perception of sounds by deafened persons,'' J. Acoust. Soc. Am. **24**, 490–497.

Fletcher, H. (**1953**). *Speech and Hearing in Communication* (Van Nostrand, New York).

Florentine, M., and Houtsma, A. J. M. (**1983**). ''Tuning curves and pitch matches in a listener with a unilateral, low-frequency hearing loss,'' J. Acoust. Soc. Am. **73**, 961–965.

Glasberg, B. R., and Moore, B. C. J. (**1990**). ''Derivation of auditory filter shapes from notched-noise data,'' Hear. Res. **47**, 103–138.

Hogan, C. A., and Turner, C. W. (**1998**). ''High-frequency audibility: Benefits for hearing-impaired listeners,'' J. Acoust. Soc. Am. **104**, 432–441.
Humes, L. E., and Riker, R. (**1992**). ''Evaluation of two clinical versions of the articulation index,'' Ear Hear. **13**, 406–409.
Johansson, B. (**1966**). ''The use of the transposer for the management of the deaf child,'' Int. Audiol. **5**, 362–372.
Killion, M. C., Berger, E. H., and Nuss, R. A. (**1987**). ''Diffuse field response of the ear,'' J. Acoust. Soc. Am. Suppl. 1 **81**, S75.
Kuhn, G. (**1979**). ''The pressure transformation from a diffuse field to the external ear and to the body and head surface,'' J. Acoust. Soc. Am. **65**, 991–1000.
Loeb, G. E., White, M. W., and Merzenich, M. M. (**1983**). ''Spatial cross correlation: A proposed mechanism for acoustic pitch perception,'' Biol. Cybern. **47**, 149–163.
McDermott, H. J., Dorkos, V. P., Dean, M. R., and Ching, T. Y. C. (**1999**). ''Improvements in speech perception with use of the AVR TranSonic frequency-transposing hearing aid,'' J. Speech. Lang. Hear. Res. **42**, 1323–1335.
Miller, G. A., and Nicely, P. E. (**1955**). ''An analysis of perceptual confusions among some English consonants,'' J. Acoust. Soc. Am. **27**, 338–352.
Miller, R. L., Schilling, J. R., Franck, K. R., and Young, E. D. (**1997**). ''Effects of acoustic trauma on the representation of the vowel /ε/ in cat auditory nerve fibers,'' J. Acoust. Soc. Am. **101**, 3602–3616.
Moore, B. C. J. (**1998**). *Cochlear Hearing Loss* (Whurr, London).
Moore, B. C. J. (**2001**). ''Dead regions in the cochlea: Diagnosis, perceptual consequences, and implications for the fitting of hearing aids,'' Trends Amplif. **5**, 1–34.
Moore, B. C. J., and Alcántara, J. I. (**2001**). ''The use of psychophysical tuning curves to explore dead regions in the cochlea,'' Ear Hear. (in press).
Moore, B. C. J., and Glasberg, B. R. (**1997**). ''A model of loudness perception applied to cochlear hearing loss,'' Aud. Neurosci. **3**, 289–311.
Moore, B. C. J., and Glasberg, B. R. (**1998**). ''Use of a loudness model for hearing aid fitting. I. Linear hearing aids,'' Br. J. Audiol. **32**, 301–319.
Moore, B. C. J., Huss, M., Vickers, D. A., and Baer, T. (**2001**). ''Psychoacoustics of dead regions,'' in *Physiological and Psychophysical Bases of Auditory Function*, edited by D. J. Breebaart, A. J. M. Houtsma, A. Kohlrausch, V. F. Prijs, and R. Schoonhoven (Shaker, Maastricht).
Moore, B. C. J., Huss, M., Vickers, D. A., Glasberg, B. R., and Alcántara, J. I. (**2000**). ''A test for the diagnosis of dead regions in the cochlea,'' Br. J. Audiol. **34**, 205–224.
Moore, B. C. J., Laurence, R. F., and Wright, D. (**1985**). ''Improvements in speech intelligibility in quiet and in noise produced by two-channel compression hearing aids,'' Br. J. Audiol. **19**, 175–187.
Murray, N., and Byrne, D. (**1986**). ''Performance of hearing-impaired and normal hearing listeners with various high-frequency cut-offs in hearing aids,'' Aust. J. Audiol. **8**, 21–28.
Parent, T. C., Chmiel, R., and Jerger, J. (**1997**). ''Comparison of performance with frequency transposition hearing aids and conventional hearing aids,'' J. Am. Acad. Aud. **8**, 355–365.
Pavlovic, C. (**1987**). ''Derivation of primary parameters and procedures for use in speech intelligibility predictions,'' J. Acoust. Soc. Am. **82**, 413–422.
Pavlovic, C., Studebaker, G., and Sherbecoe, R. (**1986**). ''An articulation index based procedure for predicting the speech recognition performance of hearing-impaired individuals,'' J. Acoust. Soc. Am. **80**, 50–57.
Pavlovic, C. V. (**1984**). ''Use of the articulation index for assessing residual auditory function in listeners with sensorineural hearing impairment,'' J. Acoust. Soc. Am. **75**, 1253–1258.
Posen, M. P., Reed, C. M., and Braida, L. D. (**1993**). ''Intelligibility of frequency-lowered speech produced by a channel vocoder,'' J. Rehabil. Res. Dev. **30**, 26–38.
Rankovic, C. M. (**1991**). ''An application of the articulation index to hearing aid fitting,'' J. Speech Hear. Res. **34**, 391–402.
Rosen, S., Faulkner, A., and Wilkinson, L. (**1999**). ''Adaptation by normal listeners to upward spectral shifts of speech: implications for cochlear implants,'' J. Acoust. Soc. Am. **106**, 3629–3636.
Shannon, R. V., Zeng, F.-G., and Wygonski, J. (**1998**). ''Speech recognition with altered spectral distribution of envelope cues,'' J. Acoust. Soc. Am. **104**, 2467–2476.
Shaw, E. A. G. (**1980**). ''The acoustics of the external ear,'' in *Acoustical Factors Affecting Hearing Aid Performance*, edited by G. A. Studebaker and I. Hochberg (University Park, Baltimore).
Skinner, M. W., and Miller, J. D. (**1983**). ''Amplification bandwidth and intelligibility of speech in quiet and noise for listeners with sensorineural hearing loss,'' Audiology **22**, 253–279.
Smoorenburg, G. F. (**1992**). ''Speech reception in quiet and in noisy conditions by individuals with noise-induced hearing loss in relation to their tone audiogram,'' J. Acoust. Soc. Am. **91**, 421–437.
Srulovicz, P., and Goldstein, J. L. (**1983**). ''A central spectrum model: a synthesis of auditory-nerve timing and place cues in monaural communication of frequency spectrum,'' J. Acoust. Soc. Am. **73**, 1266–1276.
Thornton, A. R., and Abbas, P. J. (**1980**). ''Low-frequency hearing loss: perception of filtered speech, psychophysical tuning curves, and masking,'' J. Acoust. Soc. Am. **67**, 638–643.
Turner, C. W., Burns, E. M., and Nelson, D. A. (**1983**). ''Pure tone pitch perception and low-frequency hearing loss,'' J. Acoust. Soc. Am. **73**, 966–975.
Turner, C. W., and Cummings, K. J. (**1999**). ''Speech audibility for listeners with high-frequency hearing loss,'' Am. J. Audiol. **8**, 47–56.
Turner, C. W., and Hurtig, R. R. (**1999**). ''Proportional frequency compression of speech for listeners with sensorineural hearing loss,'' J. Acoust. Soc. Am. **106**, 877–886.
Velmans, M., and Marcuson, M. (**1983**). ''The acceptability of spectrum-preserving and spectrum-destroying transposition to severely hearing-impaired listeners,'' Br. J. Audiol. **17**, 17–26.
Vickers, D. A., Baer, T., and Moore, B. C. J. (**2001**). ''Effects of lowpass filtering on speech intelligibility for listeners with dead regions at high frequencies,'' Br. J. Audiol. **35**, 148–149.
Villchur, E. (**1973**). ''Signal processing to improve speech intelligibility in perceptive deafness,'' J. Acoust. Soc. Am. **53**, 1646–1657.
Wang, M. D., and Bilger, R. C. (**1973**). ''Consonant confusions in noise: A study of perceptual features,'' J. Acoust. Soc. Am. **54**, 1248–1266.
Yates, G. K. (**1995**). ''Cochlear structure and function,'' in *Hearing*, edited by B. C. J. Moore (Academic, San Diego).
Young, E. D., and Sachs, M. B. (**1979**). ''Representation of steady-state vowels in the temporal aspects of the discharge patterns of populations of auditory-nerve fibres,'' J. Acoust. Soc. Am. **66**, 1381–1403.

A computational sensorimotor model of bat echolocation

Harry R. Erwin[a)]
Department of Computer Science, George Mason University, Fairfax, Virginia 22030

Willard W. Wilson[b)] and Cynthia F. Moss[c)]
Department of Psychology, Program in Neuroscience and Cognitive Science, University of Maryland, College Park, Maryland 20742

(Received 7 July 2000; revised 1 April 2001; accepted 24 April 2001)

A computational sensorimotor model of target capture behavior by the echolocating bat, *Eptesicus fuscus*, was developed to understand the detection, localization, tracking, and interception of insect prey in a biological sonar system. This model incorporated acoustics, target localization processes, flight aerodynamics, and target capture planning to produce model trajectories replicating those observed in behavioral insect capture trials. Estimates of target range were based on echo delay, azimuth on the relative intensity of the echo at the two ears, and elevation on the spectral pattern of the sonar return in a match/mismatch process. Flapping flight aerodynamics was used to produce realistic model trajectories. Localization in all three spatial dimensions proved necessary to control target tracking and interception for an adequate model of insect capture behavior by echolocating bats. Target capture using maneuvering flight was generally successful when the model's path was controlled by a planning process that made use of an anticipatory internal simulation, while simple homing was successful only for targets directly ahead of the model bat. [DOI: 10.1121/1.1381026]

PACS numbers: 43.80.Ka, 43.80.Lb, 43.58.Ta, 43.60.Cg, 43.60.Lq [WA]

I. INTRODUCTION

Bats use active sensing by echolocation for spatial orientation with acoustic signals. This involves the transmission, reception, and processing of ultrasound, and yields spatial acoustic information about the environment. Animal sonar systems operate with sensorimotor feedback control, in which spatial acoustic information carried by echoes guides behavior. In echolocating bats, echo-dependent motor behaviors include adjustments in the position of the head and pinnae, in the activity of the muscle groups controlling the flight path, and in the production patterns of sonar signals. The bat's motor responses (head, pinna, and body movements; sonar vocalizations) to spatial information carried by echoes, in turn, have a direct impact on the acoustic input to its sonar receiver (Valentine and Moss, 1998). Biological sonar thus requires the coordinated operation of auditory and motor systems, and a central goal of this modeling study is to deepen our understanding of these component systems and their interactions.

Acoustic information carried by sonar reflections allows the echolocating bat to determine the three-dimensional (3D) position of a target in space. The arrival time, intensity, and spectrum of echoes at the two ears encode the location of an object in azimuth and elevation. In terrestrial animals, azimuth can be estimated from interaural time- or intensity difference (ITD or IID) cues (Blauert, 1997; Grothe and Park, 1998; Harnischpfeger, Neuweiler, and Schlegel, 1985; Shimozawa *et al.*, 1974; Simmons *et al.*, 1983). However, Pollak (1988) has shown that time and intensity trade off in binaural auditory neurons, which supports the alternative view that ITDs are not useful cues for localization in bats since the maximum ITDs (no greater than 55 μs in *E. fuscus*; Koay *et al.*, 1998) are much smaller than the neural latency shifts introduced by head shadowing (several ms in Jen and Chen, 1988; discussed in Moss and Schnitzler, 1995; Pollak, 1988). Elevation can be estimated from interaural differences in the return spectra generated by the structure of the pinna and tragus (Grinnell and Grinnell, 1965; Lawrence and Simmons, 1982; Wotton, Haresign, and Simmons, 1995, 1996; Wotton and Simmons, 2000) or by asymmetric movements of the pinna (Mogdans, Ostwald, and Schnitzler, 1988; Walker, Peremans, and Hallam, 1998), as seen in *Rhinolophus ferrumequinum*. In *E. fuscus*, the elevation-dependent spectral profile of the echo appears to be important, as this species' pinnae do not have the mobility seen in *R. ferrumequinum*. The third dimension, the distance between the bat and a target, can be determined from the time delay between the outgoing sound and the returning echo (Hartridge, 1945; Simmons, 1973).

To capture prey successfully, the bat must control its flight path to arrive at a location within 2–3 cm of the insect (Trappe and Schnitzler, 1982; Webster and Griffin, 1962). Often the bat positions itself above the prey item to scoop it up with its tail membrane, requiring precise information about target azimuth, elevation, and distance. Webster and Brazier (1965) discuss the accuracy of this positioning, pointing out that in wingtip captures, ''the very tip of the wing is often bent over to form a catching shelf or groove about half an inch square.'' The bat's capture plan is ex-

[a)]Now at: Informatics Centre, University of Sunderland, Sunderland SR1 0DD, United Kingdom. Electronic mail: herwin@world.std.com
[b)]Now at: Tucker-Davis Technologies, 4637 NW 6th Street, Gainesville, FL 32609. Electronic mail: wwilson@tdt.com
[c)]Electronic mail: cmoss@psyc.umd.edu

pressed as adjustments in the flight path, changes in the call generation pattern, and the timing and coordination of the final capture maneuver with the wing or tail membrane. An important question is whether the bat controls this process by anticipating or predicting the future position of the target or using the current position estimate in a nonpredictive mode. This question can be fully addressed only when a moving target is present, but some insight can be derived from studies of stationary target capture, as some basic nonpredictive tactics such as simple homing are identifiable.

A second question concerns the directional components of the target's position that may be required by the bat's sonar system at various stages of insect capture. Range, azimuth, and elevation information characterize a target's position in 3D space, and can be used in any strategy. Azimuth and elevation without range can be used by simple nonpredictive strategies, such as lead pursuit (where the bat aims to fly ahead of the target), lag pursuit (where the bat aims behind the target), and simple homing (where the bat flies at the target). The bat can also triangulate a stationary target from a distance to fully localize it without using range. Azimuth and elevation need not be estimated simultaneously, but can be estimated over a series of sonar signals if the bat modulates the acoustic input to its two ears by rotating its head or flicking its ears, providing enough data to localize a nonmaneuvering target in both azimuth and elevation. This mechanism appears to be used by the bat, *R. ferrumequinum* (Mogdans *et al.*, 1988; Walker *et al.*, 1998). Whether the bat requires target range information to successfully intercept insect prey is important, as localization parameters provide the primary input to the bat's capture planning algorithm.

A third question involves the bat's control of its head aim when it pursues targets on the wing. In particular, where is the bat directing its sonar beam when it tracks and intercepts insect prey? The direction of the beam affects the values of the localization cues used by the bat to estimate azimuth and elevation and is an input to the algorithm by which those cues are extracted from the return. The bat's head aim is difficult to observe in wide-angle infrared video recordings of target capture in a laboratory flight room, but Webster and Brazier (1965) in high-speed photographic studies of insect pursuits on the wing and Masters *et al.* (1985) in a study of target tracking from a platform have reported that bats keep head aim locked to the target with an accuracy of about ± 5 deg. This question can be addressed indirectly by modeling the head aim process to determine whether the model bat must turn its head to face a target to produce the localization accuracy needed for successful insect capture.

Masters (1988) and Kuc (1994) have published computational models of the prey-capture process. Masters followed up on experimental work by Webster and Brazier (1965), who had reported that bats accustomed to catching *Drosophila* in the lab showed progressive changes in their behavior when presented with mealworms projected ballistically in the air over a series of trials. At first the bats attempted to catch the mealworms by flying above them, but later modified their flight paths to approach the insects from below. These observations suggested to them that the bats had learned the motion of the targets and were adjusting for it in their capture planning.

Masters modeled the bat's flight path as it followed three strategies: nonpredictive, predictive one sonar pulse ahead, and predictive to the path intersection. The target was modeled to follow a ballistic trajectory, and the bat's flight aerodynamics was modeled assuming a fixed minimum turning radius and a constant velocity. He showed that the curvature of the model bat's flight trajectories indicated the strategy used; he also demonstrated that a nonpredictive strategy was feasible, and observed that the bat's previous experience with the target trajectory was a potentially confounding variable.

Kuc (1994) developed his model to better understand the sensorimotor processes in prey capture by echolocating bats. He simulated a call consisting of a 25-kHz fundamental and a single 50-kHz overtone and used simple models of the beam pattern and the transfer characteristics of the bat's ear and head. The model did not perform complete localization; instead, range was used only to schedule the calls. Kuc's model controlled flight by using a simple homing strategy, zeroing the offset of the target from a center axis by measuring the difference between the return intensities at the two ears for azimuth and the difference between the intensity in the fundamental and overtone for elevation. The model homed on the target and collided with it. The model bat's reaction time was set equal to the intercall interval, which became unrealistically short during the terminal buzz. Aerodynamics was simplified, with the model bat flying at a constant speed, without banking, and with a unlimited turn rate.

Kuc's model bat captured targets using simple homing based on azimuth and elevation, and he showed that narrowband measurements of target intensity in each ear at 25 and 50 kHz were sufficient to support this. His model was successful for stationary targets, but his assumptions did not include the fine coordination of spatial acoustic information and orienting behavior that is observed in natural insect capture maneuvers by echolocating bats.

Our present paper reports the initial results from a two-phase study of bat sensorimotor integration. The first phase involved the development and calibration of a computational model of the prey-capture process and an investigation of the positional cues and motor behaviors likely to be required for the successful capture of a stationary target. This refined Kuc's approach by the inclusion of biologically realistic data on call acoustics, aerodynamics, and target localization, with the goal that the model would replicate the complex maneuvers seen during insect pursuit and capture. Empirical data were used to calibrate and validate the model, ruling out various alternative algorithms for target localization and capture planning. The second phase introduces moving targets to fully investigate whether the bat uses predictive or nonpredictive strategies to capture insect prey on the wing, and our findings from the second study will be reported in a subsequent publication.

II. METHODS

A. Behavioral calibration

Measurements of the flight and acoustic behavior of bats during capture of stationary targets (tethered mealworms,

Tenebrio molitor) in an open room were used to provide data for calibrating and validating the model. The methods used to collect and analyze these data are described in Wilson and Moss (2001) and are summarized below.

1. Animal subjects

The bats used in the behavioral trials were selected from a group maintained in the bat vivarium at the University of Maryland. These bats were collected (in July and August of 1997) from private homes in Maryland, housed two or three to a cage, exposed to a reversed 12:12-hour light–dark cycle, maintained at 12–16 grams body weight, and fed during experiments. Animal husbandry was carried out in accordance with guidelines established and overseen by the Institutional Animal Care and Use Committee at the University of Maryland.

2. Behavioral studies of echolocation behavior

Seven echolocating big brown bats (*E. fuscus*) were trained to capture tethered whole mealworms (*T. molitor*) in a large flight room ($6.4\times7.4\times2.6$ m) with the ceiling and walls lined with acoustical foam (Sonex™, Illbruck) and a carpeted floor. Insect capture data from two of the bats were used in the calibration trials, and data from the other five were used in the validation trials. Two genlocked (frame synchronized), high-speed video cameras (Kodak MotionCorder, 640×240 pixels, 240-Hz frame rate, and 1/240-s shutter speed) were positioned just below the ceiling in opposite corners of the flight room. A volume 2.2×2.2 (horizontal) $\times1.6$ m (vertical) within the region defined a calibrated space for reliable 3D reconstruction of the bats' flight path. A calibration frame (Peak Performance Technologies) was placed in the center of the flight room and videotaped by both cameras prior to each recording session.

Experiments were carried out using only long-wavelength (>650 nm) lighting (Plexiglas #2711, Reed Plastics, and Bogen Filter #182) to eliminate the use of vision by the bats (Hope and Bhatnagar, 1979). Mealworms were suspended at a height of about 1.0 m above the floor by monofilament line (Trilene Ultra Thin, 0.1-mm diameter) within a 5.3-m target area in the center of the room. Once each bat achieved a consistent capture rate of nearly 100%, audio and video recordings of its capture behavior began.

A small marker (Scotchlite™ reflective tape folded to present eight reflective surfaces from different angles) was glued to the bat's head and/or back where fur had been removed by depilatory cream (Nair®). This marker reflected IR back to the cameras as a bright spot that was used to help track the bat's position during subsequent reconstruction of its three-dimensional flight path.

A mealworm was suspended at a randomly selected location within the target area, and then the bat was released in a random direction to orient on the target area and find the mealworm. So that the bat would not memorize the target area, the mealworm was suspended outside the calibrated region of the room 50% of the time, and those trials were not video recorded.

The high-speed video cameras were used to record target position, bat flight path, and capture behavior. The resulting images were used in calculation of the three-dimensional positions of the bat, target, and microphones.

Echolocation signals were recorded using two ultrasonic transducers (Ultrasound Advice) placed within the calibrated space. Microphone output was amplified (Ultrasound Advice) and recorded on direct channels of a high-speed tape recorder (Racal Store-4 at 30 in. per s). An FM channel of the tape recorder was used to record TTL synch pulses corresponding to the start of each video frame and gated to the end of video acquisition.

B. Model description

1. Programming

The model was developed using the C++ programming language (ISO/IEC, 1998; Stroustrup, 1997) running on a Macintosh computer. The Metrowerks Codewarrior PRO 5.0 C++ programming environment was used.

The model was a combined continuous/discrete event simulation, with the system state elements that change continuously updated at each event. It was written using both object-oriented and generic programming techniques (Austern, 1998), making use of a time-ordered queue to sequence the scheduling and execution of events, and updating the continuous components of the system state from event to event using an adaptive 4th/5th-order Runge–Kutta integration algorithm (Press *et al.*, 1988). There was an event every 1/240th second synchronous with each video frame and additional events that were scheduled asynchronously.

2. Model design

The model consisted of five major functions, which ran asynchronously. The target position function was responsible for maintaining and updating the target position, which in this study was held fixed. The acoustics function was responsible for scheduling and generating the call, integrating its position through space to the single target and back, and triggering sensory processing after a specified reaction time delay. The sensory processing function then used the echolocation return data to generate a measurement of the relative position of the target for updating the target state estimate. The motor planning function used the target state to plan and control the motor actions of the model, and the motor response function finally maintained and updated the state of the model bat.

3. Acoustics

Acoustics was modeled using the sonar equation [Eq. (1), based on Camp, 1970; Møhl, 1988; Skolnik, 1980], with the SNR_{dB} being the signal to noise ratio of the return in decibels for each 1-kHz band. Target detection was assumed to occur if the total signal energy between 25 and 40 kHz exceeded an absolute detection threshold assumed to reflect both the internal noise of the bat's nervous system and sensitivity of its auditory receiver in that range of frequencies. The components of the echolocation return signal—signal level (SL), transmission losses (TL), and target strength

(TS)—were explicitly modeled. Of the noise components, noise spectral density (Nd) and noise bandwidth (BW)—the product of which is the noise power entering the receiver in the spectral frequencies to which it is sensitive—were assumed to be negligible relative to the detection threshold. The directivity of the pinnae (DI) was explicitly modeled. Model calibration indicated that a signal level corresponding to −1 dB was strong enough for the model bat to detect a simulated insect target at realistic ranges, and that figure was used in the study.

$$(\mathrm{SL}-2\mathrm{TL}+\mathrm{TS})-(\mathrm{No}+\mathrm{BW}-\mathrm{DI})=\mathrm{SNR}_{\mathrm{dB}}. \quad (1)$$

Calibration data for the individual components of the acoustics model were taken from the literature. A realistic call pattern based on Hartley and Suthers (1989) was used with a maximum sonar transmission level of 104 dB peak-to-peak sound-pressure level at 10 cm in the frequency range of 30–33 kHz (Kick, 1982). The model applied greater attenuation to high-frequency components of the call (Hartley, 1989) as an adjustment to the transmission loss computed from the spatial divergence of the signal. The target cross-section fluctuations were based on Griffin (1967, Fig. 6, p. 291) and were modeled statistically, assuming a uniform distribution of orientations. The mean target strength (TS) was taken from data reported by Webster and Brazier (1965, their Figs. II-6 and II-7). The transfer function of the bat's ear was based on data reported by Wotton (1994) and Wotton *et al.* (1995, 1997).

For computational feasibility, the bat's call was modeled as an impulse in time (rather than the bat's FM sweep) with a spectral intensity pattern that varied in azimuth and elevation. These patterns were stored in a table, and the model interpolated linearly between tabulated points. The ear-transfer functions were stored similarly in three-dimensional tables, indexed by azimuth, elevation, and frequency. The frequency range was from 20 to 80 kHz with an interval of 1 kHz, and the azimuth and elevation were indexed corresponding to 10-deg intervals between −70 to +70 deg.

Intercall intervals changed as a function of range and were estimated from the vocalization data of the calibration trials. The interval value at long range was 66 ms, and that figure was used when the target was unlocalized or for azimuths and elevations where the model bat was not facing the target. Otherwise, the scheduling of call emissions was based on the model bat's estimate of its range to the target.

The reaction time of the bat was modeled as a constant 100-ms delay between the reception of the sonar return and the resulting update to the target state and changes to the model's behavior. This was chosen as a representative value for auditory responses in bats (Casseday and Covey, 1996) and is consistent with the reaction times reported in behavioral studies (Cahlander, McCue, and Webster, 1964; Cahlander and Webster, 1960; Kalko, 1995). Reaction times of 50-, 200-, and 400-ms were also studied.

4. Sensory processing

Sensory processing was responsible for maintaining the target state estimate. Range was estimated from the round-trip acoustic travel time to the target and azimuth from the intensity difference of the returns in the two ears. This algorithm was designed to produce an accurate range estimate when the model bat was approaching the target. The time associated with each measurement was the time of return receipt, rather than the time the call was reflected by the target, so that the raw range measurement had to be adjusted for potential movement of the bat model towards the target between the call generation and echo detection times. As a result, when the model bat did not approach the target, the range estimate had negative bias.

Azimuth was estimated by comparing the measured IID with a set of standard values. These were produced based on the response of the model to a set of standard spherical targets (sized to produce a target strength change of −20 dB at 10 cm) arrayed in azimuth at 2-m distance and 0 elevation. The algorithm for elevation treated the wideband spectral measurements as vectors in a high-dimensional vector space (Apostol, 1967, Chap. 12) and computed the elevation estimate by comparing them to a set of standard spectra generated within the model for the standard targets positioned at 2 m, at 0 azimuth and at 10-deg elevation intervals. The elevation for the best matching spectrum was used as the elevation measurement.

The model performed a state update only if the target was detected in both ears. The algorithm for determining this integrated the return signal energy in each ear in the frequency range between 25 and 40 kHz and compared that to an absolute detection threshold. If the target was detected in a single ear, the model bat turned towards that ear to increase the target intensity in the other ear. If the target was detected in both ears, the positional cue measurements were used by the model to update the target state estimate.

The position and velocity of the target, of the model bat's body center of mass, and the model's estimate of the target position were stored in Cartesian coordinates, and the bank angle of the bat was stored in radians. In the sensory processing function, these were converted into range, azimuth, and elevation by translating to the head from the body-centered coordinates and using the current direction of the head and the current bank angle to define a head-centered coordinate system. The inverse transformation was similarly handled.

Alternative models of head aim behavior were explored in the model and controlled by an input parameter, with the bat either facing forward throughout the trial or facing the target whenever it was localized in the forward hemisphere.

5. Motor planning

The motor planning function maintained a simple scheme of action based on when the target had been detected, the target location estimate, and the state of the model bat. The final capture maneuver was handled by having the model level out and begin straight flight at a range of 0.28 m from the target during final approach. This distance was based on experimental data from the calibration trials showing the bat leveling out and extending its tail membrane to form a pouch to capture the mealworm at about that distance.

Both simple target homing and an anticipatory algorithm making use of a predictive internal simulation of the capture

process to control the flight to the target (Rosen, 1985) were investigated for the motor planning function. The simple target homing algorithm was similar to that used by Kuc (1994) and consisted of turning the flight vector of the model bat to face the target.

The anticipatory algorithm was developed after it was noted in the calibration trials that the real bat did not simply home on the target, but often flew past, looped around, and returned to capture the insect. In this algorithm, if an internal simulation of the capture predicted that the trajectory generated by a simple homing strategy would miss the target location, additional tactics were implemented. The model first attempted to tighten its turn by slowing. If that succeeded in setting up a capture, the model bat would follow a tight circle into the target, similar to the trajectories seen in some calibration trials. If that then also failed, the capture attempt was abandoned, with the model climbing away from the target and returning for a second attempt.

6. Motor response

The motor response function computed a thrust, lift, and bank angle to execute the commands provided by motor planning. Those values were then used to compute the current acceleration vector and the rate of change of bank as input to a Runge–Kutta integrator to update the model state.

A simple flapping-flight model (Rayner, 1979, 1987) was used to estimate the maximum lift and thrust combinations the real bat could generate at various airspeeds and angles of attack. This was based on data from Norberg (1987, 1990) and computed the lift, thrust, and drag of the model bat flight stroke in 1/240th s increments, assuming 13.5 wingbeats per second (Wilson and Moss, 2001). Each wingbeat was modeled in ten equal spanwise increments. The model bat was assumed to have a mass of 15 g, with a 30-cm wingspan and 0.015-m^2 wing area, corresponding to a slightly retracted wing. Stall angle used was 1/3 radian based on von Mises (1959). Velocity at the tip of the wing was 5 m/s. Bat speed was varied from 1.0 to 4.5 m/s and the resulting lift, thrust, and drag forces were computed for 0.1-radian increments of the stroke plane angle from 0.0 to 1.0 radians. The resulting values were then fitted with a second-order polynomial approximation ($r^2=0.99$) to give an equation that was used in the model.

Aerodynamic limits (preferred speed and maximum tolerated acceleration) were estimated from an aerodynamic analysis (von Mises, 1959) of the calibration trial data. Behavioral data from the calibration trials showed that the bats could decelerate as quickly as 4 m/s^2, which was in excess of the deceleration that drag alone would produce, so the model was designed to use reversed thrust to slow.

C. Data analysis

1. Video processing methods

A commercial motion analysis system (Peak Performance Technologies Motion Analysis System-Motus) was used to digitize both camera views using a Miro DC-30 Plus interface and to calculate the three-dimensional location of points marked in both camera views. Digitization was to 1/4-pixel resolution using magnification. The reflective marker placed on the bat's head and /or back was marked in each video frame where visible. The trajectory was extrapolated when the reflective marker was not visible over a segment of video frames (e.g., when concealed by a wing). The marker spanned several video pixels, and the center of the marker was estimated by eye and digitized.

The accuracy of the system was within $\pm 0.5\%$ over the calibrated volume. The three-dimensional space calibration frame provided 25 control points for direct linear transformation (DLT) calibration. The calibration procedure produced a mean residual error of 1.0 cm in each coordinate for the 25 control points.

The bat's velocity was estimated from the difference between position measurements separated by a time interval of 100 ms, producing a mean error of 0.245 m/s. Acceleration was estimated by measuring the change between two velocity estimates separated by a 200-m interval, resulting in a mean error of 1.73 m/s^2.

2. Audio processing methods

The model was calibrated to replicate the bat's intercall timing (onset to onset) as a function of range and orientation relative to the target. This timing was derived from recordings of the bat's sonar vocalizations processed from three channels of the Racal Store-4 reel-to-reel recorder. Sounds were played back at 1/4th the recording speed (7.5 in/s) and digitized using a National Instruments board (AT-MIO-16-1) with a sampling rate of 60 kHz per channel, resulting in an effective sampling rate of 240 kHz per channel. Custom software (LABVIEW) trimmed the digitized audio data to begin with the first and end with the last frame of video acquisition and output files were exported to a digital signal-processing program (SONA-PC, Waldmann). Using Sona-PC, a fast Fourier transform (FFT) was performed over 256 points per time step, with 16–20 points being replaced in each time step and displayed as time waveforms and spectrograms. The onset time, duration, and start- and end frequencies of the first harmonic of the emissions were marked with a cursor on the display and downloaded to a spreadsheet program (MICROSOFT EXCEL 97). Audio and video data were then merged in a single analysis file in order to associate vocal behavior with bat position at call onset.

3. Statistical analyses and hypothesis testing

Statistical analysis of the modeling runs was performed using the S-PLUS exploratory analysis tool (Statistical Sciences, 1995). Measurements were stored in a relational database (MICROSOFT FOXPRO), with each record containing the sample values for the independent variables, the specific group or case being studied, the time of the target capture, and a ''censoring'' variable indicating whether the model run was continued until capture occurred or terminated at 4 s. For comparative analysis of multiple modeling runs, these data were used as input for a statistical test consisting of a combination of the log-rank test and the Peto–Wilcoxon test

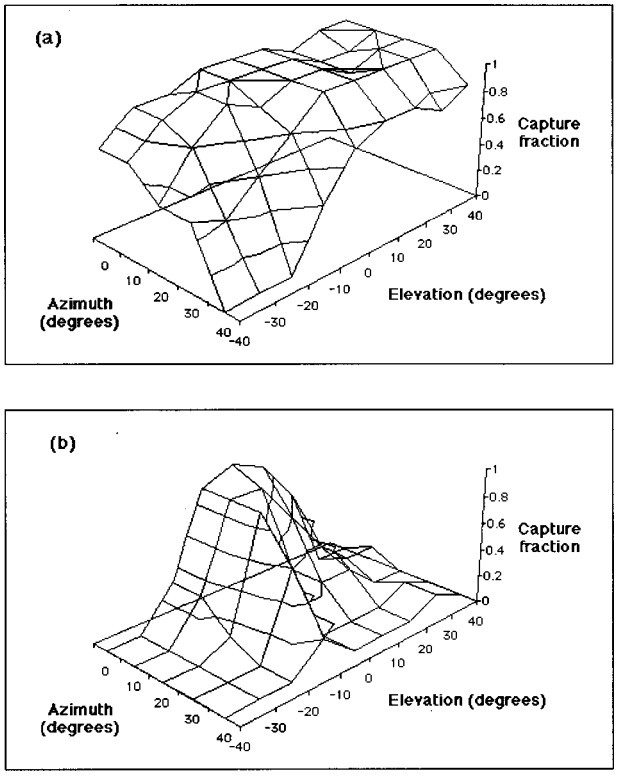

FIG. 1. Capture success fraction for (a) anticipatory and (b) simple homing strategies in the right frontal half hemisphere both for a grid of target locations initially 2 m from the model bat, ten samples per position.

with an estimator approximately distributed as a chi-squared statistic with one degree of freedom (see Harrington and Fleming, 1982).

III. RESULTS

A. Model calibration and validation

1. Calibration

The model was calibrated against the behavior seen in 16 empirical trials selected as representing typical target capture behavior in *E. Fuscus*. In these runs, the model bat was given the same initial state (body position and velocity) as the real bat and modeled in its approach to the target. (The initial state was estimated from the position of the bat at the beginning of the video recording and the velocity estimated from the positions at the beginning and 100 ms later.) The model was then calibrated by revising the algorithms of the model and input parameters incrementally until the observed behavior was replicated, much as a neural network is trained. It was then validated against an additional 15 empirical trials and finally run against a grid of standard spherical targets positioned at 2 m from the initial position of the model bat. The probability of capture of the standard targets using an anticipatory motor planning algorithm is presented in Fig. 1(a). Capture probabilities of 80% or higher were seen for initial elevations between 40 and −10 deg out to 30 deg azimuth, and for initial elevations between −20 and −30 deg out to 20 deg azimuth. Performance using the simple homing strategy was markedly poorer, with capture probabilities greater than 80% occurring only within a zone that was within 20 deg of the midline and between +10 and −10 deg elevation [see Fig. 1(b)].

TABLE I. Statistical sensitivity of the model to variation in the calibration data. The χ^2 statistic was computed using the log-rank test (Harrington and Fleming, 1982); df—degrees of freedom, p—probability.

Case	χ^2	df	p
Ear-transfer pattern	0.1	1	0.801
Call pattern	3.4	1	0.0345
Target fluctuation	0.2	1	0.653
Target spectral variation	1.2	1	0.274

2. Sensitivity

The sensitivity of the model to variation in the acoustical calibration data was investigated (see Table I). Only replacement of the realistic call pattern with an isotropic pattern (an unrealistic pattern with the same intensity spectrum at all azimuths and elevations) produced a statistically significant difference in the model's performance at the 5% level, with the isotropic pattern performing more poorly. The isotropic pattern eliminated information that could be used to estimate elevation, so this was unsurprising. Calibration data changes that did not affect model performance included statistical smoothing of the ear-transfer function (to smooth away local features that did not extend over more than 30% of the azimuth, elevation, or frequency range), elimination of target cross-section fluctuation (so that the target echo amplitude didn't flicker), and elimination of random target spectral intensity variation (which could have affected the elevation estimation algorithm).

The model was insensitive to maximum acceleration tolerated during maneuvering flight (a standard of 1.49 times the acceleration of gravity) and to maximum acceleration tolerated prior to target localization (a standard of 1.33 times the acceleration of gravity). It was also insensitive to preferred speed (3.32 m per second was the standard). Unrealistic performance was seen in turns when the model used steady-state aerodynamics, and it was also unrealistic when it used drag for deceleration. The model was realistic when the model used flapping-flight aerodynamics and reversed thrust for deceleration.

In those trials with an initially unlocalized target, model performance was very sensitive to the timing of when the model bat left its search pattern and began to approach the target. It was also sensitive to reaction time, detection threshold, and call timing as they affected this. The model performance when the reaction time was 200 ms or longer was particularly poor due to this sensitivity and also possibly due to lack of control.

Finally, although the exact trajectory produced in each model run was sensitive to the timing and values of the simulated sensory measurements, so that the choice of random number seed had a visible effect on the trajectory, the model was *statistically* insensitive to the choice of random number seed.

3. Validation

The criterion for successful replication was a capture time within 25% of the value seen in the behavioral trial requiring similar tactics. The first criterion was chosen based on the observed magnitude of the variation in bat velocity in the calibration trials at standard points—2.86 m/s with a standard deviation of 0.52 m/s at capture and of 2.70 m/s with a standard deviation of 0.59 m/s at a point 200 ms before capture. Limiting the second criterion to a similar choice of tactics was based on the observation that the tactics of the model were robust, but the exact trajectory followed by the model was dependent on the precise timing of the model's commitment to attempt capture of the target. The tactics seen in the calibration trials (produced by two bats) reappeared in the validation trials (produced by five other bats) along with some new tactics. Twelve of 15 validation trials were successfully replicated.

The most commonly observed tactic in the behavioral trials was a circling maneuver with the bat slowing to sharpen its turn while remaining near the target, a tactic the model used when it anticipated that simple homing would fail. If this tactic also failed, the model was programmed to abandon the pass and fly out to try again.

A few validation trials with novel tactics showed that the anticipatory motor planning algorithm generated simpler behavior than that actually observed. In one trial the model bat homed directly on the target in all modeling runs investigated, but the real bat flew above the target and turned and dove to capture it at the last moment. In other trials, the real bat delayed its capture of the target by 250–325 ms, usually by circling around it, while the model bat homed directly at the target. These trials—viewed in a context where the model consistently chose more direct flight paths than the real bat, even when successful—raised the question of whether the assumptions about the motor reaction time or initial target localization were in error. This led to a sensitivity study of these questions (Fig. 2) using a trial that began about 850 ms before contact. The behavior of the real bat (shown at the top) was consistent with capture using an anticipatory strategy, first slowing to sharpen its turn to compensate for a delayed start of 50–100 ms, and then homing on the target. The next four rows show various modeling runs, with different initial conditions (localized or unlocalized target), motor planning algorithms (anticipatory or simple homing), and motor reaction times (50, 100, 200, and 400 ms).

In Fig. 2, the observed bat's behavior was most similar to the pattern shown in the first row for the model, with motor reaction times of 50–200 ms. With the 400-ms reaction time, the model bat flew past the target and made a sharp turn to intercept it. The sharp turn illustrated for this model run resembled the real bat's behavior in some insect capture trials, where it performed a tight climbing turn to do a quick change of direction. The second and fourth rows show that a simple full-speed homing strategy initiated immediately after target localization would have been successful but did not match the observed trajectory. Since the real bat had probably localized the target before the start of the video recording, this suggests the bat had not *committed* to the capture at that point; otherwise, a similar trajectory would have been expected.

B. Localization cues and capture performance

The model computed range by measuring the echo delay between call and return time, dividing that by the speed of sound to estimate the round-trip distance, and adjusting the estimate to account for the model bat's motion towards (or away from) the target between the call emission and echo return times. This adjustment was designed to minimize the range error at the point where the model bat initiated its final capture maneuver (at a range of 0.28 m based on the distance measured in the calibration trials), and produced a systematically negative range error when the bat was not flying towards the target. The error in range varied smoothly with time for each individual trial, producing recognizable trajectories in the plots. Figure 3(a) shows the model's range localization error compared to the actual range for the validation runs, with anticipatory strategies and 100-ms reaction time. The mean value of the range localization error over 974 samples in the 15 validation runs was -1.3 mm with a standard deviation of 2.4 mm.

Errors in azimuth were produced by the linear interpolation used to estimate azimuth from the sound intensities in the two ears. Figure 3(b) shows the model's azimuth error as a function of range with a mean value of 0.2 deg and a standard deviation of 2.2 deg.

The model was designed to use spectral measurements consisting of 1-kHz narrow-band intensity samples between 20 to 80 kHz from each ear in a match/mismatch process for estimating elevation. The elevation error had two sources: a quantization error introduced by the 5-deg interval between the comparison spectra and any error in the choice of the best-matching comparison spectrum. Figure 3(c) shows the model's elevation error as a function of range with a mean value of 0.8 deg and a standard deviation of 2.0 deg. As the model bat neared the target, azimuth and elevation were able to change more rapidly, and the target was more likely to be out of the region where localization was most accurate. This produced higher angular error values when the model bat was near the target.

When the model used simple homing as its motor planning algorithm, only using range to schedule the capture maneuver, its overall capture performance was poorer than the anticipatory model for targets located off-axis. When the model used anticipatory motor planning, it functioned poorly if any of the three localization components (range, azimuth, and elevation) were missing. Azimuth and elevation were important at all stages of the model's capture process, and range was required in those trials with an anticipatory strategy where the model bat maneuvered.

The model was also modified so that the head would either aim in the direction of flight throughout the run or at the target once it was localized. In the latter case, the model bat circling a target would turn its head up to 90 deg toward the target. This had little effect when the underlying behavioral trial used a simple homing strategy, but when the model bat had to maneuver, successful interception occurred only when head aim at the target was enabled.

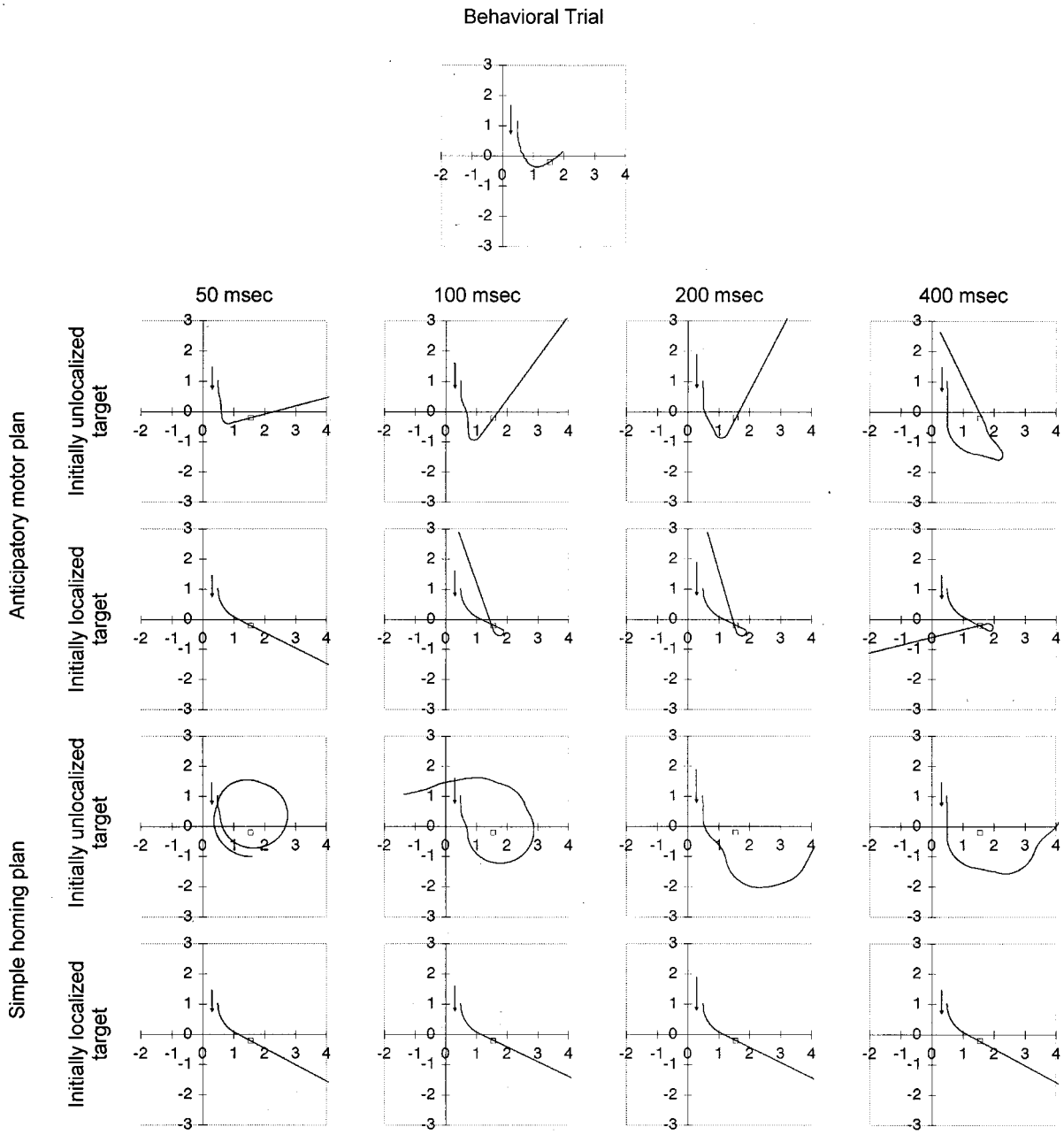

FIG. 2. Sensitivity study of a validation trial seen from above, with the reaction time and motor planning algorithm being varied. The columns show model runs with reaction times of 50, 100, 200, and 400 ms. The rows show the model bat approaching targets that were at an unknown (unlocalized) or known (localized) location at the beginning of the run, and with an anticipatory or a simple homing algorithm. Coordinates are in meters. Target location is shown by a box; bat trajectory by the line and the arrow shows direction of flight.

IV. DISCUSSION

Webster and Brazier (1965) studied the insect capture behavior of the echolocating bat, *Myotis lucifugus*, when pursuing moths in foliage. The moths used evasive maneuvers, changing their direction of flight up to 90 deg in 200 ms. The speed of the bats' reaction to the moth maneuvers, while simultaneously avoiding branches and twigs, suggests a relatively direct translation of sensory data into motor behavior. The modeling reported here begins to provide some insight into the important parameters for successful prey interception by echolocating bats. In particular, the results of the modeling suggest that the bat anticipates when and where the target will be at the point of interception and plans its motor behavior to position itself in 3D space to capture the prey at a specified location.

A. Model performance

Using anticipatory motor planning, the model showed realistic capture performance for initial target positions between the acoustic axes of the ears (at ± 30-deg azimuth) and with initial elevations between -10 and $+40$ deg. The model's spatial localization performance was about 0.8 cm at 15 cm (about the distance of a wingtip catch), which was better than the 1.5 cm estimated in three dimensions by Webster and Griffin (1962) and also better than the estimated 1.27 cm

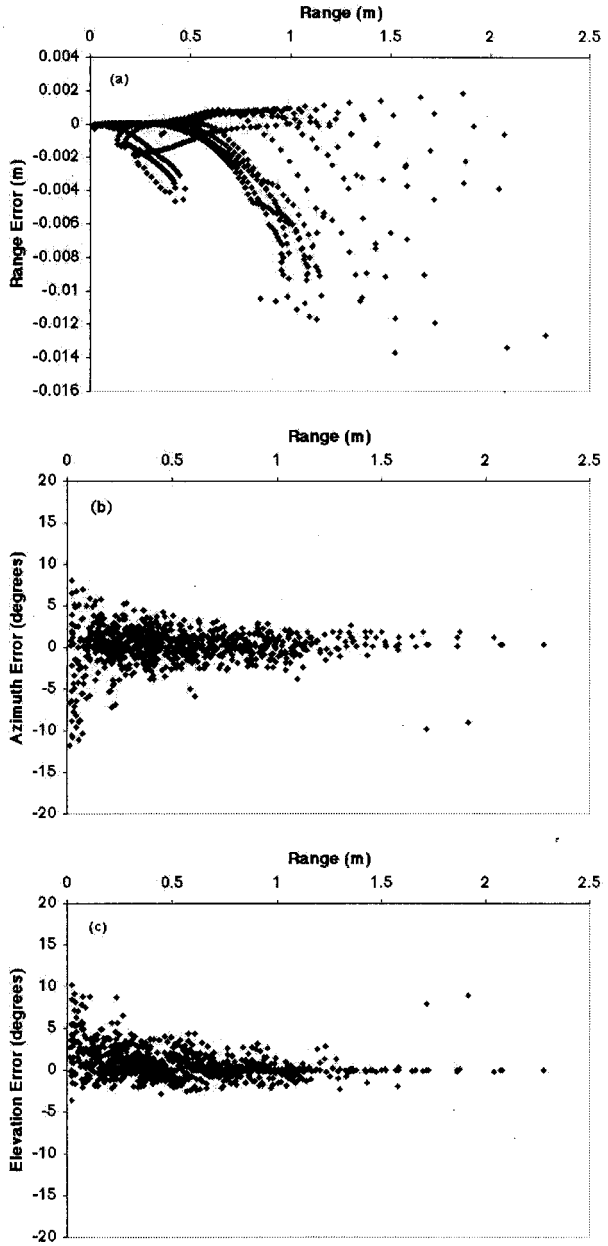

FIG. 3. (a) Range; (b) azimuth; and (c) elevation localization performance of the model during the validation runs. Each dot represents the error associated with a single call, plotted against range. There were 974 samples from 15 validation runs using anticipatory planning and 100-ms reaction time.

required for a wingtip catch reported by Webster and Brazier (1965). Standard deviations of localization accuracy were estimated to be 2.4 mm for range, 2.0 deg for azimuth, and 2.2 deg for elevation. The azimuthal localization performance was comparable with the 1.5-deg threshold for discriminating the azimuthal separations of thin rods, reported by Simmons *et al.* (1983) and was somewhat better than the 3.0 deg estimated for elevation by Lawrence and Simmons (1982). On the other hand, the model had markedly better performance than the minimum audible angle of about 14 deg reported in Koay *et al.* (1998) for passive localization in azimuth, which corresponds to about 3.5–4 cm at a 15-cm range, too large for the wingtip catch that *E. fuscus* is sometimes seen to make. Clearly the task demands of passive localization are distinct from those of active echolocation, which may explain the very different behavioral estimates of localization performance.

Figure 1 shows that the model failed to capture targets when they were outside a zone defined by the acoustic axes of the ears and the upper half of the frontal hemisphere when the model bat was initially facing forward. This is interesting, given the high capture rate observed in the laboratory insect capture experiments, and evidence from laboratory and field studies that vespertilionid bats use a search cone 150–180 deg wide (Griffin, Webster, and Michael, 1960; Kalko, 1995). The general pattern of tactics used by the model in its *successful* captures—simple homing at full speed for near-zero elevations, slower homing captures above that, and multiple target passes at very high and low elevations as the model anticipated that the first pass would fail—showed no sensitivity to initial target azimuth. This suggests that the poor model performance seen at large azimuths was not due to failure to select the correct tactics, but instead might be attributed to the model bat's failure to localize the target adequately.

This model performance is consistent with acoustic studies of the combined directional characteristics of the bat's sonar emission and receiver reported in Wotton, Jenison, and Hartley (1997), and suggests that the head of *E. fuscus* would shadow low-elevation targets from both ears and that interaural intensity differences (IIDs) should also be ambiguous at azimuths outside the acoustic axes of the two ears. Since this bat species can capture targets with about 90% reliability in behavioral trials and often uses ''pouncing'' tactics to capture targets from above, the modeling is incomplete in how it handles localization. To deal with the problem of shadowing low-elevation targets, *E. fuscus* may face slightly downward or use scanning motions to cover the lower half of the frontal hemisphere. Recordings of echolocation calls produced by *E. fuscus* in the field reveal alternations in signal intensity are consistent with the proposed head-scanning behavior by bats (Surlykke and Moss, 2000).

To localize targets at large azimuths, *E. fuscus* may use interaural time differences (Simmons *et al.*, 1995), to supplement intensity differences. There may also be cues hidden in the intensity spectrum, given the evidence that intensity and time differences trade off (Pollak, 1988). Alternatively, these bats may simply maneuver to bring candidate targets into the zone where they can be localized. These ideas will be explored in future modeling.

The model was used to investigate why the FM bat aims its head at the target with an estimated accuracy of about ± 5 deg (*M. lucifugus* in Webster and Brazier, 1965). As noted above, the localization performance of the model was best when the target was initially between the two ears and above the region shadowed for both ears. This is a 60- to 80-deg cone forward of the bat, and the behavioral trial data indicate that the bat frequently captured a target using maneuvers that would take it outside that forward cone if the bat did not aim its head at the target. The trajectories followed by the bats in the behavioral trials appear to be consistent with a body orientation that would allow them to keep the target in that cone with less than 90 deg of head rotation.

B. Comparison with other models

Kuc's (1994) model attempted to reduce to zero an elevation error signal at the two ears that was estimated as a linear combination of the target intensity in the fundamental and the overtone. The model presented here was initially designed to use that approach, but the complex pattern of biologically realistic target echoes was incompatible with the use of linear interpolation in this task. The model was therefore redesigned to compare simulated wideband spectral intensity measurements (taken every 1 kHz between 20 and 80 kHz in each ear) to calibrated standard spectra to find a nearest match. The elevation for the best-matching comparison spectrum was then used as the estimate of the elevation of the target. This approach is likely to be a simplified representation of the biological processing since it uses an impulse rather than an FM sweep as input, but it avoids having to explicitly identify an elevation-dependent notch (as discussed in Wotten *et al.*, 1996), and allows other elevation-dependent spectral cues to be used as well. This approach was successful in the model, but a realistic representation of what occurs in sonar localization by FM bats would require a fast match/mismatch in auditory processing. The modeling runs also suggest that a general change in shape of the intensity spectrum with elevation, rather than specific detection of a spectral notch, may be a robust elevation cue, since it would make more use of the information in the echo. The model showed how this approach might be calibrated to the environment, adapting to the humidity (Hartley, 1989) and the bat's current call pattern (Hartley and Suthers, 1989), which Griffin (1958, p. 184) notes can vary a great deal (see also Surlykke and Moss, 2000).

Both Masters (1988) and Kuc (1994) used simplified aerodynamics in their models. Masters assumed a fixed minimum turning radius and a fixed velocity of 5 m/s. Kuc assumed a fixed velocity of 3 m/s, no banking, and unlimited turn rate. Both sets of assumptions are inconsistent with the behavioral data, and produce flight trajectories that differ from those calculated from high-speed video recordings of insect captures by echolocating bats. Although the present model continues to use simplified aerodynamics, the banking and maneuvering it simulates interact with acoustics and motor planning in complex ways, for example, showing that target tracking requires an accurate estimate of the bat's own state, including bank, yaw, and pitch. Planning the target capture also needs this state estimate, since the bat's speed controls how quickly it can turn and what regions of the space around it can be easily accessed in an attempt to intercept the target. This suggests that further work in flight aerodynamics would provide valuable insight into the sensorimotor process underlying target capture by bats.

C. Target capture behavior

Finally, the present model shows that three-dimensional target localization is necessary to replicate the full set of insect capture behaviors exhibited by the echolocating FM bat. For simple homing strategies, range was not needed to produce the trajectories seen in the behavioral trials, but was still required to deploy the bat's tail membrane in the final capture maneuver at the appropriate time. Azimuth and elevation were needed for all trials, which is not surprising, given that flight maneuvers cause the bat to bank, translating azimuth to elevation and elevation to azimuth.

The behavior seen in the experimental trials fell into three primary categories: captures using a simple homing strategy, delayed captures (where the bat circled or flew past the target before turning for the capture), and two-pass maneuvers to gain a position from which a simple homing capture could then be staged. Similar tactics were previously noted by Griffin *et al.* (1960), Webster and Brazier (1965), Miller and Olesen (1979), Miller (1984), Kick and Simmons (1984), Schnitzler *et al.* (1988), and Kalko (1995), but the modeling of those trials now confirms that aerodynamics and acoustics constrain the bat by limiting the points in nearby space that it can easily fly to or sample using echolocation. Selection of the most direct path to target capture does not seem to be a central factor driving the bat's behavior. The real bats rarely homed along a fast straight trajectory to the target, preferring slower homing trajectories that curved into the target, and sometimes deferred a direct capture. This has also been seen in the field and possibly reflects a strategy to maximize capture success in view of the erratic and evasive flight behavior of some insect prey (Kalko, 1995; Surlykke, 1988).

Some of the maneuvers seen in the experimental trials can now be understood as implementing a simple plan to gain a position above and aiming at the target, from which a homing capture can be attempted. Other trials suggest that the bat localized the target before committing to capture it. Execution of many of these plans appears to involve anticipatory control, since they often required starting a maneuver at some specific position relative to an already localized target.

A likely explanation of some of these delayed captures is that the bat was carefully positioning itself in 3D space to maximize its probability of successful target capture. The capture maneuver involves tight coordination of the timing of the distance-dependent vocalization patterns and positioning of the tail or wing membrane with respect to the insect to successfully intercept the prey. The bat may need to approach the insect from a specific direction and with specific timing to perform this maneuver successfully, especially if the target is moving. Different behavior may be seen when the insect is free to evade the bat, and new experiments in the lab will provide insight into this area. Studies combining sensorimotor modeling with behavioral experiments using moving targets are underway to illuminate these questions.

The two motor planning algorithms investigated were not fully satisfactory. Simple homing was effective in only part of the forward hemisphere and could not handle targets to the side that were closer than the turn radius of the bat. The anticipatory motor planning algorithm used tended to produce sharper turns than those observed in the behavioral trials and resulted in straight rather than curved trajectories toward the insect. A third algorithm (''adaptable homing'') is now being explored. This estimates the maximum speed the model bat would have to fly to be able to pass through the target location using homing guidance, then adjusts to that

speed by climbing and using reverse thrust. This is expected to improve the performance of the model in future studies.

V. CONCLUSIONS

This new sensorimotor model melds a small repertoire of motor tactics with biologically realistic acoustics and aerodynamics to replicate the echolocating FM bat's target capture behavior from experimental trials. Kuc (1994) had proposed his model as a ''small step toward understanding the power of acoustic information processing employed in nature.'' Using Kuc's work as a starting point and taking the next step of adding biological realism in selected areas, this model has shown how the elevation span for capture can be increased from 20 to 50 deg, while maintaining the same azimuthal cone. Kuc's homing model, lacking memory and using only azimuth and elevation signals to collide with the target, did not fully model how bats capture insects. The present model incorporates the use of distance information, which is required for the bat to accurately time its range-dependent vocal production patterns and to position itself at the point of intercept to collect (not collide with) the prey item.

A model using a small number of narrow-band intensity samples from each ear to estimate elevation, such as that employed by Kuc (1994), encounters difficulties when presented with echoes with realistic intensity spectra. A model that collects a spectral intensity sample over a wide band seems to be robust against noise and performs well for targets within a 60-to-80-deg cone in front of the bat.

Realistic aerodynamics constrains the bat's behavior more than was suggested in Kuc's (1994) and Masters's (1988) models. The bat has to bank to turn and is limited in the maximum accelerations that it can generate, often forcing it to maneuver to perform the target capture. Further research into the aerodynamics of echolocating bats, such as *E. fuscus*, in maneuvering flight will be valuable for understanding the role of aerodynamic constraints in defining target capture behavior.

Rapid target capture does not appear to be the preferred strategy for the bat. There is evidence that the bat does not commit immediately to target capture, instead delaying capture beyond the time simply required to maneuver to a collision with the target. The purpose of those delays is unclear, but may include target classification or maneuvers to maximize the success of target capture with a potentially long response latency. The good performance of the model with a reaction time of 100 ms suggests that anticipatory planning of tightly timed behaviors can compensate for the delay between receipt of the sensory stimulus and the corresponding motor response.

The demonstration that the model can capture targets over a wide range of elevations and azimuths, despite a reaction time of 100 ms or more, also shows that target capture algorithms need not have millisecond responsiveness. Timing seems to be important when maneuvers have to be initiated, but with accurate 3D localization of a stationary target, those maneuvers can be scheduled hundreds of milliseconds in advance of their execution. Capture of evading insects is likely to be more difficult for the bat, but once the insect commits to an escape maneuver, it limits its future ability to turn or accelerate, so that a good prediction of the insect's motion path would still allow the bat to schedule maneuvers in advance. Hence, an accurate representation of the environment that takes into account the constraints on the behavior of the objects being modeled may allow the most economical control of behavior, whether the system is concerned with making or avoiding contact with objects.

ACKNOWLEDGMENTS

Peter Abrams, Myriam Tron, and Amy Kryjak assisted in the data collection and analysis of behavioral trials. Paul Kelley developed the custom software used to trim the digitized audio data. We thank two anonymous reviewers for their valuable comments on an earlier draft of this manuscript. This research was funded by a TRW Fellowship to H.R.E.; No. NIMH R01-MH56366; No. NSF IBN-9258255 and the Whitehall Foundation (No. S97-20) awards to C.F.M.: and training grant awards (Comparative and Evolutionary Biology of Hearing) No. 5 T32 DC-00046 from NIDCD, NIH, and National Research Service Award No. 1 F32 MH11489 from NIMH, NIH, to W.W.W.

Apostol, T. (**1967**). *Calculus* (Blaisdell, Waltham), Vol. 1.
Austern, M. (**1998**). *Generic Programming and the STL* (Addison-Wesley, Reading, MA).
Blauert, J. (**1997**). *Spatial Hearing: The Psychophysics of Human Sound Localization*, revised ed., translated by J. S. Allen (MIT Press, Cambridge, MA).
Cahlander, D. A., McCue, J. J. G., and Webster, F. A. (**1964**). ''The determination of distance by echolocation,'' Nature (London) **201**, 544–546.
Cahlander, D. A., and Webster, F. A. (**1960**). *The Bat's Reaction Time* (47G-0008): MIT Lincoln Laboratory.
Camp, L. (**1970**). *Underwater Acoustics* (Wiley-Interscience, New York).
Casseday, J. H., and Covey, E. (**1996**). ''A neuroethological theory of the operation of the inferior colliculus,'' Brain Behav. Evol. **47**, 311–336.
Griffin, D. R. (**1958**). *Listening in the Dark* (Comstock, Ithaca).
Griffin, D. R. (**1967**). ''Discriminative echolocation by bats,'' in *Animal Sonar Systems*, edited by R. G. Busnel (Laboratoire de Physiologie Acoustique, Jouy-en-Josas-78).
Griffin, D. R., Webster, F. A., and Michael, C. R. (**1960**). ''The echolocation of flying insects by bats,'' Anim. Behav. **8**, 141–154.
Grinnell, A. D., and Grinnell, V. S. (**1965**). ''Neural correlates of vertical localization by echolocating bats,'' J. Physiol. (London) **181**, 830–851.
Grothe, B., and Park, T. J. (**1998**). ''Sensitivity to interaural time differences in the medial superior olive of a small mammal, the Mexican free-tailed bat,'' J. Neurosci. **18**(16), 6608–6622.
Harnischpfeger, G., Neuweiler, G., and Schlegel, P. (**1985**). ''Interaural time and intensity coding in the superior olivary complex and inferior colliculus of the echolocating bat, *Molossus ater*,'' J. Neurophysiol. **53**, 89–109.
Harrington, D. P., and Fleming, T. R. (**1982**). ''A class of rank test procedures for censored survival data,'' Biometrika **69**, 554–566.
Hartley, D. J. (**1989**). ''The effect of atmospheric sound absorption on signal bandwidth and energy and some consequences for bat echolocation,'' J. Acoust. Soc. Am. **85**, 1338–1347.
Hartley, D. J., and Suthers, R. A. (**1989**). ''The sound emission of the echolocating bat, *Eptesicus fuscus*,'' J. Acoust. Soc. Am. **85**, 1348–1351.
Hartridge, H. (**1945**). ''Acoustic control in the flight of bats,'' Nature (London) **156**, 490–494, **156**, 692–693.
Hope, G. M., and Bhatnagar, K. P. (**1979**). ''Electrical response of bat retina to spectral stimulation: Comparison of four microchiropteran species,'' Experientia **35**, 1189.
ISO/IEC. (**1998**). *Standard for the* C++ *Programming Language, ISO/IEC 14882*: ITI.
Jen, P. H. S., and Chen, D. (**1988**). ''Directionality of sound pressure transformation at the pinna of echolocating bats,'' Hear. Res. **34**, 101–108.
Kalko, E. K. V. (**1995**). ''Insect pursuit, prey capture, and echolocation in pipistrelle bats (*Microchiroptera*),'' Anim. Behav. **50**, 861–880.

Kick, S. A. (**1982**). ''Target detection by the echolocating bat, *Eptesicus fuscus*,'' J. Comp. Physiol., A **145**, 431–435.
Kick, S. A., and Simmons, J. A. (**1984**). ''Automatic gain control in the bat's sonar receiver and the neurophysiology of echolocation,'' J. Neurosci. **4**, 2725–2737.
Koay, G., Kearns, D., Heffner, H. E., and Heffner, R. S. (**1998**). ''Passive sound-localization ability of the big brown bat (*Eptesicus fuscus*),'' Hear. Res. **119**, 37–48.
Kuc, R. (**1994**). ''Sensorimotor model of bat echolocation and prey capture,'' J. Acoust. Soc. Am. **96**, 1965–1978.
Lawrence, B. D., and Simmons, J. A. (**1982**). ''Measurements of atmospheric attenuation at ultrasonic frequencies and the significance for echolocation by bats,'' J. Acoust. Soc. Am. **71**, 585–590.
Masters, W. M. (**1988**). ''Prey Interception: Predictive and Nonpredictive Strategies,'' in *Animal Sonar: Processes and Performance*, edited by P. E. Nachtigall and P. W. Moore (Plenum, New York), pp. 467–470.
Masters, W. M., Moffat, A. J. M., and Simmons, J. A. (**1985**). ''Sonar tracking of horizontally moving targets by the big brown bat *Eptesicus fuscus*,'' Science **228**, 1331.
Miller, L. A. (**1984**). ''Hearing in Green Lacewings and their Responses to the Cries of Bats,'' in *Biology of Chrysopidae*, edited by M. Canard, Y. Semeria, and T. R. New (Dr. W. Junk, The Hague), Vol. 27, pp. 134–149.
Miller, L. A., and Olesen, J. (**1979**). ''Avoidance behavior on green lacewings I. Behavior of free flying green lacewings to hunting bats and ultrasound,'' J. Comp. Physiol., A **131**, 113–120.
Mogdans, J., Ostwald, J., and Schnitzler, H.-U. (**1988**). ''The role of pinna movement for the localization of vertical and horizontal wire obstacles in the greater horseshoe bat, *Rhinolophus ferrumequinum*,'' J. Acoust. Soc. Am. **84**, 1676–1679.
Møhl, B. (**1988**). ''Target Detection by Echolocating Bats,'' in *Animal Sonar: Processes and Performance*, edited by P. E. Nachtigall and P. W. Moore (Plenum, New York), pp. 435–450.
Moss, C. F., and Schnitzler, H.-U. (**1995**). ''Behavioral Studies of Auditory Information Processing,'' in *Hearing by Bats*, edited by A. N. Popper and R. R. Fay (Springer, New York), Vol. 5, pp. 87–145.
Norberg, U. M. (**1987**). ''Wing Form and Flight Mode in Bats,'' in *Recent Advances in the Study of Bats*, edited by M. B. Fenton, P. Racey, and J. M. V. Rayner (Cambridge University Press, Cambridge, MA), pp. 43–56.
Norberg, U. M. (**1990**). *Vertebrate Flight* (Springer, Berlin).
Pollak, G. D. (**1988**). ''Time is traded for intensity in the bat's auditory system,'' Hear. Res. **36**, 107–124.
Press, W. H., Flannery, B. P., Teukolsky, S. A., and Vetterling, W. T. (**1988**). *Numerical Recipes in C: the Art of Scientific Computing* (Cambridge University Press, Cambridge, MA).
Rayner, J. M. V. (**1979**). ''A new approach to animal flight mechanics,'' J. Exp. Biol. **80**, 17–54.
Rayner, J. M. V. (**1987**). ''The Mechanics of Flapping Flight in Bats,'' in *Recent Advances in the Study of Bats*, edited by M. B. Fenton, P. Racey, and J. M. V. Rayner (Cambridge University Press, Cambridge, MA), pp. 23–42.
Rosen, R. (**1985**). *Life Itself: A Comprehensive Inquiry Into the Nature, Origin, and Fabrication of Life* (Columbia University Press, New York).
Schnitzler, H.-U., Kalko, E., Miller, L., and Surlykke, A. (**1988**). ''How the Bat, *Pipistrellus kuhli*, hunts for insects,'' in *Animal Sonar: Processes and Performance*, edited by P. E. Nachtigall and P. W. Moore (Plenum, New York), pp. 619–624.
Shimozawa, T., Suga, N., Hendler, P., and Schuetze, S. (**1974**). ''Directional sensitivity of echolocating system in bats producing frequency modulated signals,'' J. Exp. Biol. **60**, 53–69.
Simmons, J. A. (**1973**). '' The resolution of target range by echolocating bats,'' J. Acoust. Soc. Am. **54**, 157–173.
Simmons, J. A., Ferragamo, M. J., Saillant, P. A., Haresign, T., Wotton, J. M., Dear, S. P., and Lee, D. N. (**1995**). ''Auditory Dimensions of Acoustic Images in Echolocation,'' in *Hearing by Bats*, edited by A. N. Popper and R. R. Fay (Springer, New York), Vol. 5, pp. 146–190.
Simmons, J. A., Kick, S. A., Lawrence, B. D., Hale, C., Bard, C., and Escudiè, B. (**1983**). ''Acuity of horizontal angle discrimination in the echolocating bat, *Eptesicus fuscus*,'' J. Comp. Physiol., A **153**, 321–330.
Skolnik, M. I. (**1980**). *Introduction to Radar Systems*, 2nd ed. (McGraw-Hill, New York).
Statistical Sciences (**1995**). S-PLUS Guide to Statistical and Mathematical Analysis, Version 3.3, Seattle.
Stroustrup, B. (**1997**). *The* C++ *Programming Language* (Addison-Wesley, Reading, MA).
Surlykke, A. (**1988**). ''Interaction between echolocating bats and their prey,'' in *Animal Sonar: Processes and Performance*, edited by P. E. Nachtigall and P. W. Moore (Plenum, New York).
Surlykke, A., and Moss, C. F. (**2000**). ''Echolocation behavior of the big brown bat, *Eptesicus fuscus*, in the field and the laboratory,'' J. Acoust. Soc. Am. **108**, 2419–2429.
Trappe, M., and Schnitzler, H.-U. (**1982**). ''Doppler-shift compensation in insect-catching horseshoe bats,'' Naturwissenschaften **69**, 193–196.
Valentine, D. E., and Moss, C. F. (**1998**). ''Sensorimotor Integration in Bat Sonar,'' in *Bat Biology and Conservation*, edited by T. H. Kunz and P. A. Racey (Smithsonian Institution, Washington and London), pp. 220–230.
von Mises, R. (**1959**). *Theory of Flight* (Dover, New York).
Walker, V. A., Peremans, H., and Hallam, J. C. T. (**1998**). ''One tone, two ears, three dimensions: A robotic investigation of pinnae movements used by rhinolophid and hipposiderid bats,'' J. Acoust. Soc. Am. **104**, 569–579.
Webster, F. A., and Brazier, O. G. (**1965**). *Experimental Studies on Target Detection, Evaluation and Interception by Echolocating Bats* (Wright-Patterson Air Force Base, Dayton, OH).
Webster, F. A., and Griffin, D. R. (**1962**). ''The role of the flight membrane in insect capture by bats,'' Anim. Behav. **10**, 332–340.
Wilson, W. W., and Moss, C. F. (**2001**). ''Sensory-motor Behavior of Free-flying FM Bats during Target Capture,'' in *Advances in the Study of Echolocation in Bats and Dolphins*, edited by J. Thomas, C. F. Moss, and M. Vater (University of Chicago Press, Chicago).
Wotton, J. M. (**1994**). ''The basis for vertical sound localization of the FM bat, *Eptesicus fuscus*: Acoustical cues and behavioral validation,'' unpublished doctoral dissertation, Brown University.
Wotton, J. M., Haresign, T., and Simmons, J. A. (**1995**). ''Spatially dependent acoustic cues generated by the external ear of the big brown bat, *Eptesicus fuscus*,'' J. Acoust. Soc. Am. **98**, 1423–1445.
Wotton, J. M., Haresign, T., and Simmons, J. A. (**1996**). ''Sound source elevation and external ear cues influence the discrimination of spectral notches by the big brown bat, *Eptesicus fuscus*,'' J. Acoust. Soc. Am. **100**, 1764.
Wotton, J. M., Jenison, R. L., and Hartley, D. J. (**1997**). ''The combination of echolocation emission and ear reception enhances directional spectral cues of the big brown bat, *Eptesicus fuscus*,'' J. Acoust. Soc. Am. **101**, 1723–1733.
Wotton, J. M., and Simmons, J. A. (**2000**). ''Spectral cues and perception of the vertical position of targets by the big brown bat, *Eptesicus fuscus*,'' J. Acoust. Soc. Am. **107**, 1034–1041.

LETTERS TO THE EDITOR

This Letters section is for publishing (a) brief acoustical research or applied acoustical reports, (b) comments on articles or letters previously published in this Journal, and (c) a reply by the article author to criticism by the Letter author in (b). Extensive reports should be submitted as articles, not in a letter series. Letters are peer-reviewed on the same basis as articles, but usually require less review time before acceptance. Letters cannot exceed four printed pages (approximately 3000–4000 words) including figures, tables, references, and a required abstract of about 100 words.

Comment on "Free vibration analysis of laminated piezoceramic hollow spheres" [J. Acoust. Soc. Am. 109, 41 (2001)]

George R. Buchanan[a] and Guillermo R. Ramirez
Department of Civil and Environmental Engineering, Tennessee Technological University, Cookeville, Tennessee 38505

(Received 19 February 2001; revised 5 April 2001; accepted 13 April 2001)

In a recent article, Chen [J. Acoust. Soc. Am. **109**, 41–50 (2001)] presented a three-dimensional analysis for piezoelectric hollow thick spheres. Results were presented for several configurations for shells of layered piezoelectric materials. The elastic material constants for PZT-4 that were used in the paper were in error and this letter is an attempt to justify and offer suggestions that can preserve the value of the analysis. © *2001 Acoustical Society of America.* [DOI: 10.1121/1.1379082]

PACS numbers: 43.20.Bi, 43.20.Ks [CBB]

The author[1] is to be commended for the detailed mathematical analysis and subsequent numerical results. The publication of frequencies of vibration for piezoelectric spheres is timely and welcome. In fact, it was anticipated that results reported in the paper could be used to verify a finite-element analysis that is currently being developed for piezoelectric thick-shell vibration.

The author was obviously unaware that some of the piezoelectric constants for PZT-4 are in error. The error can be traced to his Ref. 45.[1] Tang and Xu[2] took their data from Dieulesaint and Royer[3] and evidently copied the wrong data from Table 4.7,[3] page 151. The values for c_{13}, c_{33}, and c_{44} that were recorded by Tang and Xu[2] correspond to beryllium that are in the line above PZT-4 of Table 4.7.[3] It follows that the majority of the frequency results given in the paper will not correspond to a real material. However, the results can be useful to verify numerical studies.

The results given in Chen's Table I,[1] as well as a com-

TABLE I. Finite-element frequencies Ω for a transversely isotropic shell compared with Table I of Ref. 1.

Mode	1	2	3	4	5	6	7	8	
				Frequency of the first class					
Table I (Ref. 1)	2.392	3.556	3.697	⋯	4.873	5.997	⋯	⋯	
FE	2.392	3.556	3.698	4.695	4.880	5.985	6.017	6.524	
				Frequency of the second class					
Table I (Ref. 1)	1.782	2.496	3.104	3.393	3.673	⋯	⋯	⋯	5.151[a]
FE	1.783	2.502	3.120	3.394	3.707	4.089	4.280	4.617	5.152[a]

[a]The frequency corresponding to $n=0$ in Table I[1] is the 11th frequency when taken in numerical ascending order.

TABLE II. Finite-element frequencies Ω for a transversely isotropic shell using the elastic constants for PZT-4 (nonpiezoelectric).

Mode	1	2	3	4	5	6	7	8
First class	1.329	2.079	2.759	2.409	3.409	3.556	3.930	4.046
Second class	1.047	1.680	2.147	2.213	2.331	2.683	2.971	3.420

[a]Electronic mail: gbuchanan@tntech.edu

 0001-4966/2001/110(2)/1188/2/$18.00

panion paper,[4] for a homogeneous transversely isotropic sphere were verified using a finite-element analysis. Subsequently, the frequencies given in his Table II[1] using only the elastic constants were verified using the incorrect elastic constants. The correct elastic constants, $c_{11}=c_{22}=13.9$, $c_{33}=11.5$, $c_{12}=7.8$, $c_{13}=c_{23}=7.4$, $c_{44}=c_{55}=2.56$, and $c_{66}=3.06$ multiplied by $(10^{10}\ \mathrm{N/m^2})$, were used to compute the first few frequencies of the first and second kind. The finite-element results are given in our Tables I and II. The accuracy of the finite-element analysis is demonstrated in Table I by comparing with Chen's Table I.[1] The order in which the frequencies are computed using a finite-element solution will differ from the separation of variables solution technique. All frequencies, beginning with the lowest, are found when using the finite-element formulation. The first and second kinds of spherical motion can be separated, if desirable, by controlling the boundary conditions. Frequencies corresponding to Chen's Table II,[1] PZT-4(E), are given in our Table II using the elastic constants given above. Table II shows that the error caused by using the incorrect elastic constants is significant.

A definitive presentation of the finite-element analysis for thick piezoelectric spherical shells is planned for publication. The basic element and results for homogeneous isotropic thick shells has been submitted for possible publication.[5]

[1] W. Q. Chen, ''Free vibration analysis of laminated piezoceramic hollow spheres,'' J. Acoust. Soc. Am. **109**, 41–50 (2001).

[2] Y. Y. Tang and K. Xu, ''Exact solutions of piezoelectric materials with moving screw and edge dislocation,'' Int. J. Eng. Sci. **32**, 1579–1591 (1994).

[3] E. Dieulesaint and D. Royer, *Elastic Waves in Solids* (Wiley, New York, 1980).

[4] W. Q. Chen and H. J. Ding, ''Free vibration of multilayered spherically isotropic hollow spheres,'' Int. J. Mech. Sci. **43**, 667–680 (2001).

[5] G. R. Buchanan and B. S. Rich, ''Effect of boundary conditions on free vibration of thick spherical shells,'' J. Vib. Control (submitted).

Reply to "Comment on 'Free vibration analysis of laminated piezoceramic hollow spheres [J. Acoust. Soc. Am. 109, 41 (2001)]' "

W. Q. Chen[a)]
Department of Civil Engineering, Zhejiang University, Hangzhou 310027, People's Republic of China

(Received 19 March 2001; accepted for publication 13 April 2001)

We reply to the preceding Comment.
[DOI: 10.1121/1.1379083]

PACS numbers: 43.20.Bi, 43.20.Ks [CBB]

I am very grateful to Professor G. R. Buchanan and Professor G. R. Ramirez for their helpful comment[1] on my paper.[2] The three incorrect elastic constants that were directly cited from Tang and Xu[3] have not been carefully checked because I could not find the book of Dieulesaint and Royer[4] in the library of our university. Thus, when my paper was written and even before I read the comment,[1] I was completely unaware that some of the piezoelectric constants for PZT-4 are in error, as Professor G. R. Buchanan and Professor G. R. Ramirez pointed out in their Comment.[1]

The analytical method developed in my paper[2] is of particular value because it can be used as a benchmark to clarify various two-dimensional shell theories or numerical methods. It is also verified by Buchanan and Ramirez using the finite-element method.[1]

Finally, it should be noted here that in my paper only the lowest natural frequency for each mode is given, while Buchanan and Ramirez[1] give the natural frequencies beginning with the lowest. In other words, some natural frequencies given by Buchanan and Ramirez[1] may correspond to the same mode number *n*.

[a)]Electronic mail: caijb@ccea.zju.edu.cn

[1] G. R. Buchanan and G. R. Ramirez, "Comment on 'Free vibration analysis of laminated piezoceramic hollow spheres,' " J. Acoust. Soc. Am. **110**, 1188–1189 (2001).
[2] W. Q. Chen, "Free vibration analysis of laminated piezoceramic hollow spheres," J. Acoust. Soc. Am. **109**, 41–50 (2001).
[3] Y. Y. Tang and K. Xu, "Exact solutions of piezoelectric materials with moving screw and edge dislocation," Int. J. Eng. Sci. **32**, 1579–1591 (1994).
[4] E. Dieulesaint and D. Royer, *Elastic Waves in Solids* (Wiley, New York, 1980).

On reducing vibration transmission in a two-dimensional cantilever truss structure using geometric optimization and active vibration control techniques

D. K. Anthony and S. J. Elliott
Institute of Sound and Vibration Research, University of Southampton, Southampton SO17 1BJ, United Kingdom

(Received 8 May 2000; accepted for publication 12 April 2001)

Four optimization strategies were used to improve the average vibration isolation between the base and the end of a 10-m long two-dimensional (2D) cantilever truss structure. These were combinations of optimizing the structure geometry and the application of active vibration control (AVC) with optimal actuator positions. A power distribution analysis to investigate the mechanisms by which each strategy achieves reductions in the vibration transmission is reported. The trade-off is also explored between the freedom allowed in the size of the geometric changes and the number of actuators used in an AVC system to achieve a given level of vibration attenuation. © *2001 Acoustical Society of America.* [DOI: 10.1121/1.1381022]

PACS numbers: 43.40.Vn, 43.40.Tm, 43.40.Cw [PJR]

I. INTRODUCTION

Lightweight truss structures are commonly used in the aerospace industry, and there is considerable interest in the vibration transmission properties of such structures when excited by either acoustic or vibrational sources over frequency bandwidths of a few tens of hertz to tens of kilohertz.[1] The authors recently reported the optimization of a truss structure to minimize the average broadband vibration transmission using (i) the optimization of the structure geometry,[2] (ii) the application of active vibration control (AVC) with optimal actuator placement,[3] and (ii) the combined use of both strategies.[4] The consideration of robust optimization, which was an additional common theme in these references, is not reported here. The results pertinent to this letter are first briefly summarized in Secs. II, III, and IV. Then, a power analysis of the mechanisms by which the optimization has achieved its aim is reported, and last, the trade-off between geometric optimization and the use of AVC is demonstrated.

The specific aim of the optimization study was to minimize the average vibration transmission from the base to the end of a structure, whose unoptimized geometry is shown in Fig. 1(a), over the frequency range 150–250 Hz, realized in 21 frequency steps. The base excitation was modeled as a transverse force applied at midlength to the beam with ends at (0,0) and (0,1), and the reduction in vibration was measured at the beam with ends at (10,0) and (10,1) (subsequently denoted the end beam). The vibration of the end beam was quantified by the average vibrational energy level that arises due to the balance of energy supplied to the beam and the energy dissipated due the beam vibration (by virtue of beam damping). For simplicity, the presence of an AVC actuator on a structure beam was not considered to change its mechanical properties.

II. OPTIMAL ACTIVE VIBRATION CONTROL

One optimization strategy is to apply feedforward active control of vibration (AVC) to the original structure geometry, using double-acting axial actuators. Feedforward AVC can be used for the reduction of vibration in the low- and mid-frequency regions, provided a suitable reference signal exists.[5] The optimization task is to find the actuator positions that achieve the best average vibration reductions over the frequency band considered. Systems using one, two, and three actuators were considered, resulting in 39, 741, and 9139 possible actuator positions combinations, respectively (the end beam cannot accommodate an actuator). It is feasible to computationally evaluate all these actuator combinations, and thus, in this case, an exhaustive search offers the best optimization technique. Figure 1 shows the optimum positions for two actuators on the unoptimized structure geometry, which achieves a frequency-averaged attenuation of 31.1 dB. The attenuation at the individually controlled frequencies is also shown. The average values of attenuation achieved across the ten best-ranking actuator positions using one, two, and three actuators are shown in Table I as AVC(1), AVC(2), and AVC(3). The total control effort required by each control system is the sum of the squared moduli of the actuator forces at each frequency, and provides an indication of the electrical power required to drive an AVC system. It is shown normalized to the total control effort of primary input.[3]

III. GEOMETRIC OPTIMIZATION

An alternative optimization strategy is to redesign the geometry of the structure in order to inherently achieve a better performance. This was considered for the structure by allowing the midspan joints a freedom of ± 0.25 m. This optimization is fully described in Ref. 2, and the results discussed here refer to the broadband results in this reference, where the average energy level was evaluated over a bandwidth from 150 to 250 Hz.

The geometric redesign is a multimodal, highly combinatorial optimization problem that is often accomplished using so-called natural algorithms, such as Genetic algorithms.[6] These were used to solve this highly combinatorial optimization problem. The 36 joint coordinates were coded into binary string chromosomes, and optimized structure designs

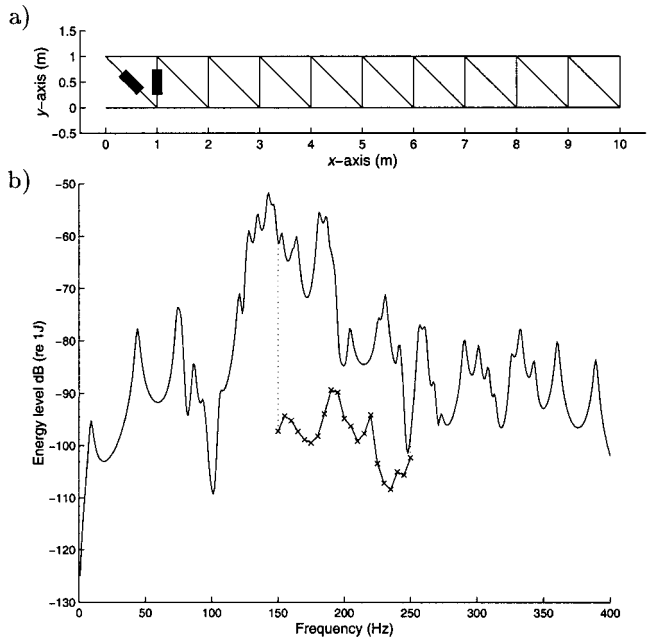

FIG. 1. Truss structure with unoptimized geometry. (a) Optimum actuator positions, (b) energy level of the end beam against frequency without AVC (—), with AVC at frequencies shown –×–×–.

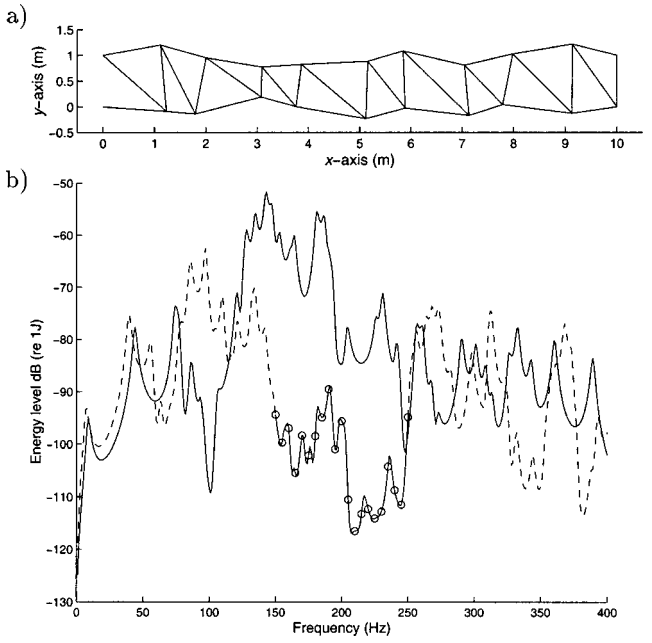

FIG. 2. Geometrically optimized truss structure. (a) Optimized geometry, (b) energy level of the end beam against frequency before optimization (—), after optimization (– – –). The objective function is the average value of the frequency region denoted –○–○–.

were taken to be the best solutions occurring after 15 generations, each of 300 chromosomes. Due to the stochastic nature of the algorithm, different optimized structures were produced using different initial random number seeds for the algorithm. In this study ten such structures were generated. All ten structures had different geometries but showed a similar level of performance. Figure 2 shows the best structure produced by such an optimization, and the changes in energy level in the end beam against frequency before and after optimization. The frequency-averaged reduction in the vibrational energy is 33.3 dB, which is similar to the attenuation achieved for AVC(2), as shown in Table I. Despite its irregular geometry, the structure is relatively easy to construct using modern methods and useful reductions in average vibrational energy have been obtained, by over a factor of 1000, using only geometric redesign. It provides an alternative *passive* solution to AVC, which does not suffer a significant reduction in static strength.[7]

TABLE I. Summary of results for the average performance and control effort for the structures resulting from all the optimization strategies considered. Optimization type key: Geometric, geometric optimization only; AVC, active vibration control only; PTA, passive-then-active optimization strategy; CO, combined optimization strategy.

Optimization type (No. actuators)	Geometric attenuation contribution (dB)	AVC attenuation contribution (dB)	Overall attenuation (dB)	AVC total control effort (normalized)
Geometric	32.6	···	32.6	···
AVC (1)	···	9.2	9.2	350
AVC (2)	···	27.7	27.7	1400
AVC (3)	···	45.9	45.9	2900
PTA (1)	32.6	11.2	43.2[a]	7.4
PTA (2)	32.6	32.2	63.6[a]	9.6
CO (1)	21.0	27.5	48.7[a]	4.3
CO (2)	16.7	60.3	78.4[a]	29

[a]As a consequence of the logarithmic scaling, the addition of the two average components of the overall attenuation does not result in the average overall attenuation.

IV. OPTIMAL COMBINED STRATEGIES

A sensible progression from the two individual optimization strategies reported in the previous sections is to combine them. The optimization of both the geometry and the AVC actuator positions have been previously reported for these frequencies in similar types of structures.[8–10] Reference 10 uses the addition of extra damping to a number of structural beams instead of geometric adjustment. The two combined strategies used were (i) to apply AVC with optimally placed actuator positions to structures whose geometries had previously been optimized (passive-then-active optimization, PTA), and (ii) to optimize the structure geometry and actuator positions simultaneously (combined optimization, CO).

Figure 3 shows the structure that resulted from the PTA optimization strategy; using an exhaustive search to locate the best two-actuator positions on the structure that had previously been geometrically optimized (shown in Fig. 2). (In fact, a slightly better overall performance was achieved using this strategy with another of the ten geometrically optimized structures discussed in Sec. III.) The energy levels in the end beam at the individual frequencies for which the AVC are applied are also shown in Fig. 3. The average overall attenuation for the ten structures, the average attenuation achieved due to the previous geometric optimization and due to the AVC, using one and two actuators, are shown in Table I as PTA(1) and PTA(2). For a two-actuator AVC system it is seen that the average attenuation achieved by geometric optimization and AVC is almost the same. The average attenu-

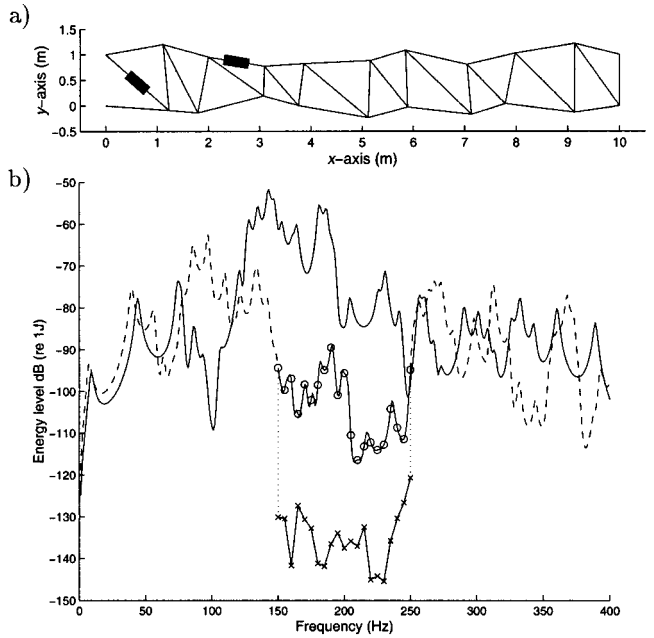

FIG. 3. Geometrically optimized truss structure from Fig. 2. (a) Optimum actuator positions; (b) energy level of the end beam against frequency: before optimization (—); after optimization outside the objective function frequency range (– – –); value of objective function without AVC, –○–○–; with AVC, –×–×–.

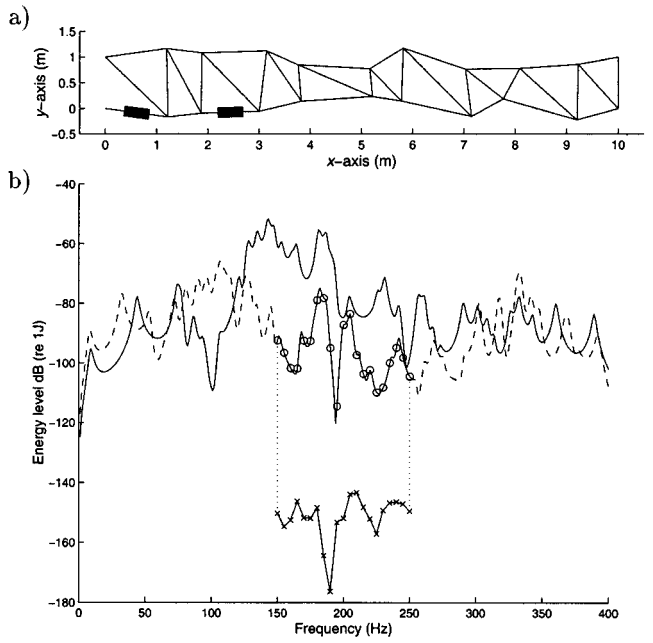

FIG. 4. Truss structure optimized using combined optimization strategy, CO. (a) Optimum geometry and actuator positions; (b) energy level of the end beam against frequency: before optimization (—); after optimization outside the objective function frequency range (– – –); value of objective function without AVC, –○–○–; with AVC, –×–×–.

ation in the vibration of the end beam using the AVC system on a geometrically optimized structure is of a similar level as that using the unoptimized structure. It is interesting to note that the overall attenuation is approximately equal to the sum of the values of attenuation achieved by optimizing the structure's geometry, and the application of AVC to the unoptimized structure.

The CO (combined optimization) strategy uses the same genetic algorithm optimization employed for the geometric redesign detailed in Sec. III. Again, a chromosome was used to represent the structure geometry, but extended to additionally represent the actuator positions. Ten such structures were designed, with AVC using one and two actuators. The best structure using two actuators is shown in Fig. 4 along with the energy level in the end beam against frequency, with the AVC system operational and nonoperational. The overall AVC attenuation is in excess of 60 dB and, in practice, is likely to be limited due to system noise. The average results across the ten best structures with one and two actuators are shown as CO(1) and CO(2) in Table I. Comparing the amount of reduction achieved by the geometrically optimized structure in Table I, a smaller geometric contribution is seen for the structures using the CO strategy. However, with the CO strategy, far greater reductions are achieved per actuator. It is also apparent from Table I that an AVC system is more efficient when applied to a structure which has also undergone geometric optimization, as the values of total control effort for both the average PTA optimization and the CO strategies are significantly less than for the average performance of the AVC strategy.[11] This is true either on a per-actuator or per-dB attenuation basis.

V. ANALYSIS OF POWER WITHIN OPTIMIZED STRUCTURES

The mechanisms by which the reductions in the energy level in the end beam have been achieved have been investigated by analyzing the energy flow (i.e., power) within the structure. Table II shows the change in input power (due to the change in the mechanical impedance presented to the input force) and the change in the distribution of the power dissipated within the structure between the end beam and the remainder of the structure. The power supplied or dissipated by the actuators, where applicable, were not significant compared with the components given and are ignored here for simplicity. For geometric optimization, the reduction in the energy level of the end beam has been achieved by a 10 dB reduction in the input power, but also by a 22 dB reduction in power redistribution. For the AVC system, the reductions are

TABLE II. Average power components of optimised structures, with and without AVC operational. Passive beams are those not containing an actuator. (Optimization type key the same as for Table I.)

Optimization type (No. actuators)	Primary input power reduction (dB)		Power redistribution between passive beams and the end beam (dB)	
	w/o AVC	with AVC	w/o AVC	with AVC
Geometric	10.7	⋯	22.3	⋯
AVC (1)	⋯	0.6	⋯	9.6
AVC (2)	⋯	0.9	⋯	28.0
AVC (3)	⋯	1.0	⋯	46.4
PTA (1)	10.7	10.7	22.3	32.9
PTA (2)	10.7	10.5	22.3	53.9
CO (1)	9.7	9.8	14.4	39.5
CO (2)	10.0	10.4	8.5	69.9

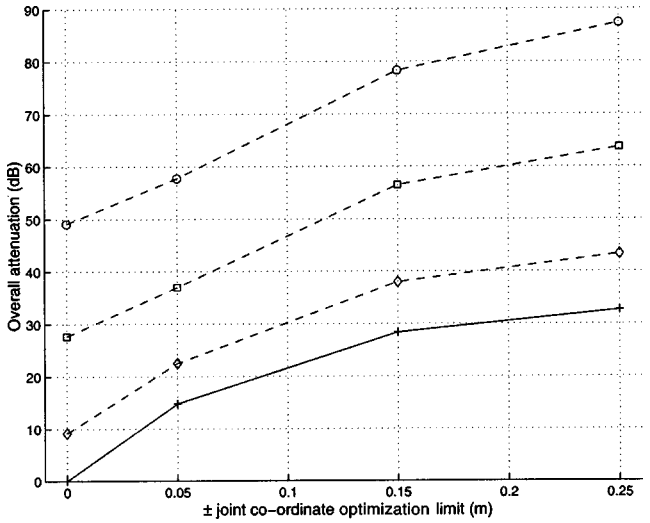

FIG. 5. Average overall attenuation achieved in the end beam against the joint coordinate limit used in the optimization. —, geometric optimization only, PTA (passive-then-active) optimization, with one actuator, ◇; two actuators, □; three actuators, ○.

seen to be chiefly from the power redistribution, with little effect on the input power. For the PTA optimization strategy, the application of AVC augments the gain achieved by redistribution of the preceding geometric optimization, but has no further effect on the reduction in input power. For the CO strategy, similar levels of reduction in input power are achieved as with the geometric optimization, however, a smaller level of power redistribution due to the geometry alone results. The CO strategy produces the most effective use of the AVC, as when operational the largest additional power redistribution results.

Thus, in general, geometric optimization works by reducing the input power to the structure, and also a varying degree of power redistribution. The application of optimal AVC in each case enhances the power redistribution, but is most effective when optimized simultaneously with the structure geometry. Fuller details are given in Ref. 7, where a study of the power in the individual beams is also given. For three optimally placed actuators, a strategy of blocking the flow of energy down the structure is clearly seen, suggesting that these solutions would be more robust to changes in mechanical impedance at the end beam (due to a change in the mass of the load, for example).

VI. TRADE-OFF BETWEEN PASSIVE AND ACTIVE METHODS

It is clear that more than one strategy may be used to provide similar reductions in vibration. When optimizing the geometry, allowing a greater freedom in the possible movement of the joint is expected to affect the attenuation in the vibration level achievable. Likewise, increasing the number of optimally placed actuators in an AVC system is expected to increase the attenuation achievable. This hypothesis was considered for the attenuation achievable using solely geometric redesign, and also the subsequent application of AVC using optimally placed actuator positions (the PTA strategy). The results are presented in Fig. 5, which shows the average overall attenuation achievable over ten structures optimized to reduce vibration in the end beam with different limits on the extent in the variation in the joint coordinates, initially using geometric redesign. The performance is then shown when subsequently applying AVC using one, two, and three optimally placed actuators. The additional attenuation provided by the AVC systems is, again, not significantly affected by the geometric optimization and so, to a first approximation, the two values of attenuation can simply be added. The levelling out of the attenuation as the joint coordinate limits increase indicates that not much more attenuation would result if these limits were increased (although to avoid joint-beam contact, greater freedom is not possible in this case).

Thus, to achieve a value of attenuation in the frequency-averaged vibration reduction of about 30 dB, three options are possible: (i) geometric redesign with a maximum joint coordinate freedom of about ± 0.2 m, (ii) geometric redesign of the geometry with a freedom of ± 0.1 m and the application of AVC with one optimally placed actuator, and (iii) the application of two optimally placed AVC actuators on an unoptimized structure. A trade-off thus exists between passive (geometric redesign) and active (AVC) optimization techniques.

ACKNOWLEDGMENTS

The first author acknowledges a studentship from the Faculty of Engineering and Applied and Science at the University of Southampton, UK. The authors wish to thank Professor A. J. Keane for his help with the reported work, which was undertaken in the Computational Engineering and Design Center, also at the University of Southampton.

[1] J. C. Forgave, K. F. Man, and J. M. Newell, ''Spacecraft acoustic and random vibration test optimization,'' Sound Vib. **33**(3), 28–31 (1999).
[2] D. K. Anthony, S. J. Elliott, and A. J. Keane, ''Robustness of optimal design solutions to reduce vibration transmission in a lightweight 2-D structure. Part I: Geometric redesign,'' J. Sound Vib. **229**, 505–528 (2000).
[3] D. K. Anthony and S. J. Elliott, ''Robustness of optimal design solutions to reduce vibration transmission in a lightweight 2-D structure. Part II: Application of active vibration control techniques,'' J. Sound Vib. **229**, 529–548 (2000).
[4] D. K. Anthony, ''Robustness of optimal design solutions to reduce vibration transmission in a lightweight 2-D structure. Part III: Using both geometric redesign and the application of active vibration control,'' accepted for publication in J. Sound Vib.
[5] C. R. Fuller, S. J. Elliott, and P. A. Nelson, *Active Control of Vibration* (Academic, London, 1996).
[6] M. Mitchell, *An Introduction to Genetic Algorithms* (MIT Press, Cambridge, MA, 1996).
[7] D. K. Anthony, ''Robust optimal design using passive and active methods of vibration control,'' Ph.D. thesis, University of Southampton, UK, 2000.
[8] X. Liu, D. W. Begg, and D. R. Matravers, ''Optimal topology/actuator placement design of structures using SA,'' J. Aerosp. Sci. **10**(3), 119–125 (1997).
[9] X. Liu, D. W. Begg, and R. J. Fishwick, ''Genetic approach to optimal topology/controller design of adaptive structures,'' Int. J. Numer. Methods Eng. **41**(5), 815–830 (1998).
[10] G. Chen, R. J. Bruno, and M. Salama, ''Optimal placement of active/passive members in truss structures using simulated annealing,'' AIAA J. **29**, 1327–1334 (1991).
[11] This comparison of average performance against average total control effort for each optimization strategy was given in a graphical format in Ref. 4.

On the performance of acoustic crosstalk cancellation in a reverberant environment

Darren B. Ward
Department of Electrical and Electronic Engineering, Imperial College of Science, Technology and Medicine, Exhibition Road, London SW7 2BT, United Kingdom

(Received 7 December 2000; revised 2 May 2001; accepted 22 May 2001)

Acoustic crosstalk cancellation systems create a virtual audio environment by using loudspeakers to deliver appropriate binaural signals to the listener. Typically, the system is designed to equalize the direct-path transfer functions between the loudspeakers and the ears. In this paper statistical room acoustics is used to derive a closed-form expression that predicts the performance of such a system when used in a reverberant environment, and the expression is verified through simulations. The results of this paper enable designers to undertake a preliminary analysis of how well a given crosstalk cancellation system will perform in a reverberant environment, without resorting to time-consuming measurements or image-model simulations. © *2001 Acoustical Society of America.*
[DOI: 10.1121/1.1386635]

PACS numbers: 43.60.−c, 43.60.Cg, 43.55.Br, 43.66.Pn [JCB]

I. INTRODUCTION

The aim of a crosstalk cancellation system (CCS) is to equalize the transfer functions (TFs) from one or more loudspeakers to a listener's ears, thereby providing the listener with an accurate binaural image of a virtual acoustic environment. A CCS is typically designed by assuming a model for the TFs with the head in a nominal position. It has been shown that robustness of the CCS to movement of the listener from the assumed design position is critically dependent on the loudspeaker geometry.[1,2]

Since most virtual audio systems will be used in reverberant rooms, it is important to also consider the effect that reverberation plays on the system performance. Although the CCS could theoretically be designed to equalize the complete reverberant-path TFs from loudspeakers to ears, this would require exact knowledge (or very accurate modeling) of these reverberant TFs. It has recently been shown that equalization in a reverberant environment is extremely nonrobust,[3] so it is reasonable to assume that any practical CCS system will be designed to equalize only the direct-path TFs.

In this paper, we determine the performance that can be expected in a reverberant environment for a CCS that only equalizes the direct-path TFs. A statistical approach is used to derive results for the mean-square ear response that one could expect to achieve in a reverberant room. The utility of these results is that a designer can quickly undertake a preliminary analysis of how well a CCS system will perform when used in a particular environment (e.g., in a room with a certain size and reverberation time). Different schemes (say, with different loudspeaker geometries) can also be compared without requiring multiple time-consuming measurements or image-model simulations.

II. NOTATION AND PRELIMINARIES

Consider a room with volume V, total wall surface area S, and an average absorption coefficient of α (defined as the ratio of the intensity of sound pressure absorbed by a wall surface to the intensity incident on the surface). The sound field at any point in the room can be considered as the superposition of an infinite number of plane waves arriving from all propagation directions.[4] This diffuse model of the reverberant sound field becomes valid above the Schroeder frequency,[5] $f_S = 2000\sqrt{T_{60}/V}$, where $T_{60} = 0.161V/(S\alpha)$ is the reverberation time, defined as the time taken for the sound-pressure level to decay by 60 dB once the source has stopped.

At an observation point $\mathbf{x}$ in the room, the sound pressure due to a source located at $\mathbf{y}$ can be written

$$p(\mathbf{y},\mathbf{x}) = p_d(\mathbf{y},\mathbf{x}) + p_r(\mathbf{y},\mathbf{x}), \tag{1}$$

where $p_d(\mathbf{y},\mathbf{x})$ is the pressure due to the direct sound, and $p_r(\mathbf{y},\mathbf{x})$ is the pressure due to the reverberant field (assumed to be diffuse).

Define the frequency response function (Green's function) between a source located at $\mathbf{y}$ and an observation point $\mathbf{x}$ as $g(\mathbf{y},\mathbf{x})$. It is related to the sound pressure by[3]

$$p(\mathbf{y},\mathbf{x}) = -jk\rho c\sigma_y g(\mathbf{y},\mathbf{x}), \tag{2}$$

where $k = 2\pi f/c$ is the wave number, c is the speed of sound propagation in air, ρ is the density of air, and σ_y is the source strength of the acoustic source at $\mathbf{y}$. From (1) and (2), the transfer function $g(\mathbf{y},\mathbf{x})$ can also be written as the sum of a direct-path TF $g_d(\mathbf{y},\mathbf{x})$, and a reverberant-path TF $g_r(\mathbf{y},\mathbf{x})$.

A. Theorem 1

The cross correlation between the reverberant-path TFs at a single point $\mathbf{x}$*, due to acoustic sources at* $\mathbf{y}_1$ *and* $\mathbf{y}_2$ *is*

$$\langle g_r^*(\mathbf{y}_1,\mathbf{x}) g_r(\mathbf{y}_2,\mathbf{x})\rangle = \left(\frac{1-\alpha}{\pi S\alpha}\right)\frac{\sin(k\|\mathbf{y}_1-\mathbf{y}_2\|)}{k\|\mathbf{y}_1-\mathbf{y}_2\|}, \tag{3}$$

where $\langle\cdot\rangle$ *denotes the expectation operator.*

1. Proof

The correlation between the reverberant acoustic pressure at two observation points $\mathbf{x}_1$ and $\mathbf{x}_2$ is given by the well-known relation[4]

$$\langle p_r^*(\mathbf{y},\mathbf{x}_1)p_r(\mathbf{y},\mathbf{x}_2)\rangle = \langle |p_r(\mathbf{y},\mathbf{x})|^2\rangle \frac{\sin(k\|\mathbf{x}_1-\mathbf{x}_2\|)}{k\|\mathbf{x}_1-\mathbf{x}_2\|}, \quad (4)$$

where the mean-square acoustic pressure of the reverberant field is given by[3]

$$\langle |p_r(\mathbf{y},\mathbf{x})|^2\rangle = 4\rho c W\left(\frac{1-\alpha}{S\alpha}\right), \quad (5)$$

with $W=\rho c k^2|\sigma_y|^2/(4\pi)$ the power of the acoustic source.[6] But from (2) we have

$$\langle p_r^*(\mathbf{y},\mathbf{x}_1)p_r(\mathbf{y},\mathbf{x}_2)\rangle = (\rho c k)^2|\sigma_y|^2\langle g_r^*(\mathbf{y},\mathbf{x}_1)g_r(\mathbf{y},\mathbf{x}_2)\rangle. \quad (6)$$

Substituting (5) into (4), and equating with (6) gives

$$\langle g_r^*(\mathbf{y},\mathbf{x}_1)g_r(\mathbf{y},\mathbf{x}_2)\rangle = \left(\frac{1-\alpha}{\pi S\alpha}\right)\frac{\sin(k\|\mathbf{x}_1-\mathbf{x}_2\|)}{k\|\mathbf{x}_1-\mathbf{x}_2\|}. \quad (7)$$

The result (3) follows immediately from the principle of reciprocity.[4]

This theorem will be used in the following section to analyze the expected ear responses when a CCS is used in a reverberant room.

III. ACOUSTIC CROSSTALK CANCELLATION

Consider the general N-loudspeaker CCS shown in Fig. 1, in which b_L and b_R are the binaural signals (that are to be delivered to the listener's ears), $\mathbf{l}_n$, $n=1,...,N$, is the location of the nth loudspeaker, $\mathbf{e}_L$ is the location of the listener's left ear (and similarly for $\mathbf{e}_R$ and the right ear), and $\hat{b}_L$ is the signal received at the left ear (and similarly for $\hat{b}_R$). At any frequency, this system is described by the linear equation

$$\begin{bmatrix}\hat{b}_L\\ \hat{b}_R\end{bmatrix} = \begin{bmatrix} g(\mathbf{l}_1,\mathbf{e}_L) & \cdots & g(\mathbf{l}_N,\mathbf{e}_L)\\ g(\mathbf{l}_1,\mathbf{e}_R) & \cdots & g(\mathbf{l}_N,\mathbf{e}_R)\end{bmatrix}\begin{bmatrix} h_1 & h_{N+1}\\ \vdots & \vdots\\ h_N & h_{2N}\end{bmatrix}\begin{bmatrix} b_L\\ b_R\end{bmatrix}$$

$$\hat{\mathbf{b}}=\mathbf{GHb}, \quad (8)$$

where $g(\cdot,\cdot)$ is the acoustic TF between the appropriate loudspeaker and ear. To simplify notation we have suppressed the explicit dependency on frequency.

Without loss of generality, consider reproduction of the left binaural channel only (similar results hold for the right channel). Denote the TFs between b_L (which we will hereafter refer to as the input) and each ear as $\hat{v}_L$ and $\hat{v}_R$, respectively. Thus

$$\begin{bmatrix}\hat{v}_L\\ \hat{v}_R\end{bmatrix} = \begin{bmatrix} g(\mathbf{l}_1,\mathbf{e}_L) & \cdots & g(\mathbf{l}_N,\mathbf{e}_L)\\ g(\mathbf{l}_1,\mathbf{e}_R) & \cdots & g(\mathbf{l}_N,\mathbf{e}_R)\end{bmatrix}\begin{bmatrix} h_1\\ \vdots\\ h_N\end{bmatrix}$$

$$\hat{\mathbf{v}}=\mathbf{Gh}. \quad (9)$$

Separate the acoustic TF matrix into the sum of direct-path and reverberant-path parts, i.e., $\mathbf{G}=\mathbf{G}_d+\mathbf{G}_r$. Further partition the direct-path TF matrix into left and right ear vectors, $\mathbf{G}_d=[\mathbf{d}_L,\mathbf{d}_R]^T$ where $\mathbf{d}_L=[g_d(\mathbf{l}_1,e_L),...,g_d(\mathbf{l}_N,\mathbf{e}_L)]^T$ and similarly for $\mathbf{d}_R$. Also partition the reverberant-path TF matrix as $\mathbf{G}_r=[\mathbf{r}_L,\mathbf{r}_R]^T$ where $\mathbf{r}_L=[g_r(\mathbf{l}_1,\mathbf{e}_L),...,g_r(\mathbf{l}_N,\mathbf{e}_L)]^T$ and similarly for $\mathbf{r}_R$.

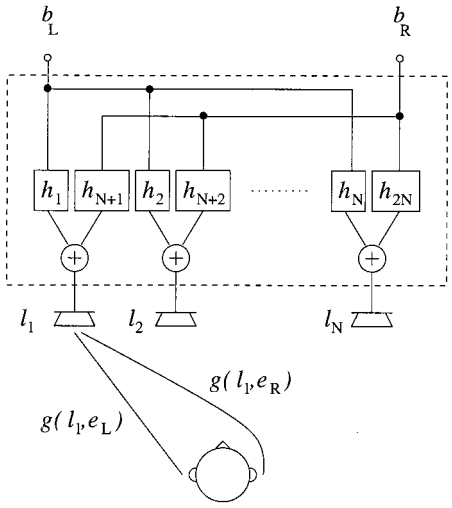

FIG. 1. General N-loudspeaker CCS system.

Assume the CCS filters are designed to equalize the direct-path TFs only, such that

$$\mathbf{v}=\mathbf{G}_d\mathbf{h}, \quad (10)$$

where $\mathbf{v}=[v_L,v_R]^T$ contains the desired TFs between the input and each ear. Thus, (9) becomes

$$\hat{\mathbf{v}}=\mathbf{v}+\mathbf{G}_r\mathbf{h}. \quad (11)$$

The actual ear responses are now given by

$$\hat{v}_L=v_L+\mathbf{r}_L^T\mathbf{h}, \quad (12a)$$

$$\hat{v}_R=v_R+\mathbf{r}_R^T\mathbf{h}. \quad (12b)$$

Consider the left-ear response. The expected mean-square response is

$$\langle|\hat{v}_L|^2\rangle = |v_L|^2+\langle\mathbf{h}^H\mathbf{r}_L^*\rangle+\langle\mathbf{r}_L^T\mathbf{h}\rangle+\langle\mathbf{h}^H\mathbf{r}_L^*\mathbf{r}_L^T\mathbf{h}\rangle. \quad (13)$$

Expectation here is taken with respect to the distribution of the loudspeaker and listener locations, assumed to be in a fixed geometry relative to each other, but with the complete system randomly oriented and placed within the room. In other words, the direct-path TFs remain unchanged for any position within the room, and expectation is therefore taken over the reverberant path.

From (10), $\mathbf{h}$ is a linear combination of the direct-path TFs, and since the direct and reverberant sound pressures at any point in the room are uncorrelated in a diffuse field, it follows that all cross terms in (13) are zero. Thus

$$\langle|\hat{v}_L|^2\rangle = |v_L|^2+\mathbf{h}^H\langle\mathbf{r}_L^*\mathbf{r}_L^T\rangle\mathbf{h}. \quad (14)$$

Substitution of (3) gives the following result.

A. Corollary 1

For the left binaural channel, let $\mathbf{h}$ *be the filter weights that equalize the direct-path TFs for a CCS designed to have ideal ear responses of* v_L *and* v_R. *If this CCS is located in a*

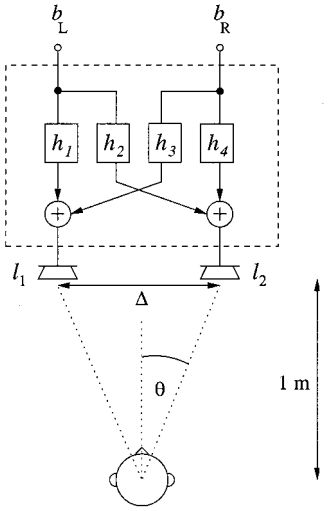

FIG. 2. Two-loudspeaker CCS geometry.

room with total wall surface area S and average absorption coefficient α, the actual mean-square ear responses for this channel are

$$\langle|\hat{v}_L|^2\rangle = |v_L|^2 + \varepsilon, \tag{15a}$$

$$\langle|\hat{v}_R|^2\rangle = |v_R|^2 + \varepsilon, \tag{15b}$$

where

$$\varepsilon = \left(\frac{1-\alpha}{\pi S\alpha}\right)\left[\mathbf{h}^H\mathbf{h} + \sum_{\substack{n=1\\ n\neq m}}^{N}\sum_{m=1}^{N} h_n^* h_m \frac{\sin(k\|\mathbf{l}_n - \mathbf{l}_m\|)}{k\|\mathbf{l}_n - \mathbf{l}_m\|}\right], \tag{16}$$

is the absolute error, and $\mathbf{l}_n$ *is the location of the n*th *loudspeaker*.

We make the following comments:

(1) The results are valid for any v_L and v_R, so that frequency shaping functions can be readily included in the desired ear-response functions. No assumptions about the structure of the direct-path acoustic TF matrix $\mathbf{G}_d$ in (10) have been made, and thus, head-related transfer function (HRTF) effects can also be readily included.

(2) For each ear the expected mean-square response is equal to the ideal mean-square response plus an error term (16), where this error is the same for both ear responses.

(3) The error term consists of two parts, with each part being scaled by a constant that is determined by the room parameters (and is directly proportional to the room reverberation time). One part is the L_2 norm of the loudspeaker weights, $\mathbf{h}^H\mathbf{h}$. The second part (consisting of the $\sin(\cdot)/(\cdot)$ terms) falls off rapidly with increasing frequency or with increasing loudspeaker spacing.

(4) One can interpret these results in terms of the directional response of the loudspeaker array. Substitution of (10) gives the ideal mean-square response at the left ear as $|v_L|^2 = \mathbf{h}^H\mathbf{d}_L^*\mathbf{d}_L^T\mathbf{h}$. This is the array response at a single direction (the left ear), whereas $\mathbf{h}^H\mathbf{h}$ is effectively the array response over all directions. If $\mathbf{h}^H\mathbf{h}$ is large, then although the ideal ear response $|v_L|^2$ is fixed [as it must be if the weights satisfy (10)], a large amount of power will be directed to positions away from the head. This would increase reverberation, thereby perturbing the CCS performance away from the ideal. We note from (10) that $\mathbf{h}^H\mathbf{h}$ will be large if the direct-path TF matrix $\mathbf{G}_d$ is poorly conditioned. Our conclusion is that the loudspeaker geometry (which determines the conditioning of $\mathbf{G}_d$) plays a critical role in the performance of a CCS in a reverberant environment.

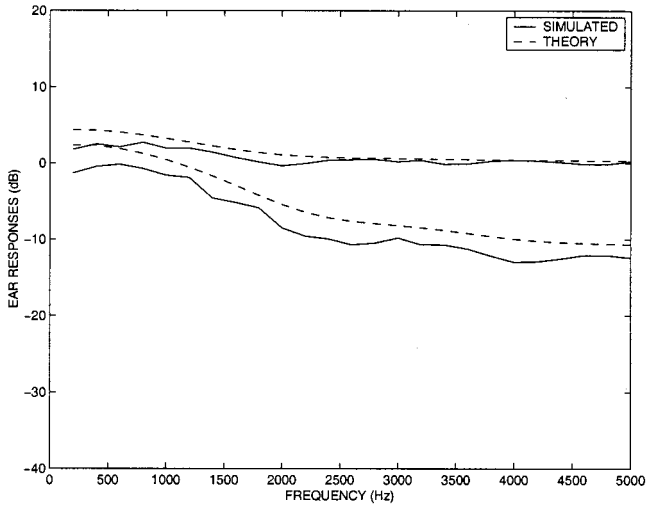

(a)

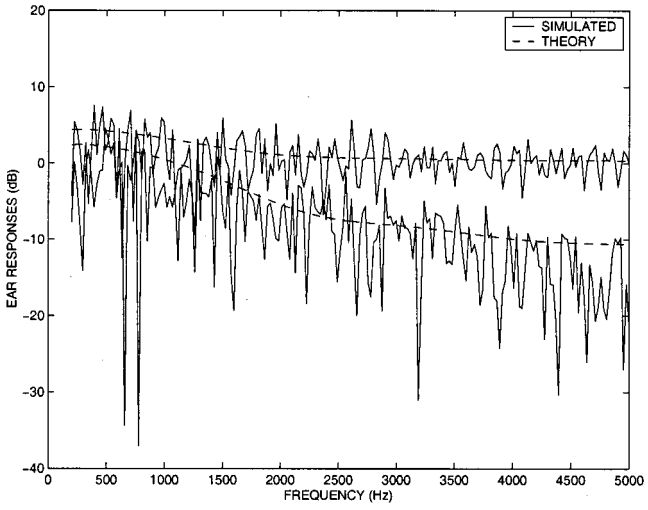

(b)

FIG. 3. Ear responses as a function of frequency: (a) spatially averaged responses; (b) responses for a single simulation run. Image model simulation of a room (6.4×5×4 meters) with $T_{60}=0.2$ s. Loudspeakers are located at $\theta=\pm 5°$. In each case the top two curves are the left-ear responses, the bottom two curves are the right-ear responses.

IV. TWO-LOUDSPEAKER CCS EXAMPLE

Consider the two-channel CCS shown in Fig. 2. For reproduction of the left binaural signal only, let the desired ear responses be

$$\mathbf{v}=\begin{bmatrix} e^{-j2\pi f\tau_0} \\ 0 \end{bmatrix}. \tag{17}$$

In other words, the left binaural signal is reproduced at the left ear with a delay of τ_0 seconds, and the right ear response is zero.

In this case (15) reduces to

$$\langle|\hat{v}_L|^2\rangle = 1+\varepsilon, \tag{18a}$$

$$\langle|\hat{v}_R|^2\rangle = \varepsilon, \tag{18b}$$

where

$$\varepsilon = \left(\frac{1-\alpha}{\pi S\alpha}\right)\left[\mathbf{h}^H\mathbf{h} + \frac{\sin(k\Delta)}{k\Delta}(h_1^*h_2 + h_1h_2^*)\right], \tag{19}$$

and $\Delta = \|\mathbf{l}_1 - \mathbf{l}_2\|$ is the distance between the loudspeakers.

To validate the theoretical results derived in this paper, we now present simulation results. A room with dimensions of $6.4\times5\times4$ meters, having a reverberation time of $T_{60} = 0.2$ s was simulated using the image method.[7] Referring to Fig. 2, the loudspeakers were separated by a distance of $\Delta = 0.175$ m, and the listener was located 1 m back along the line bisecting the loudspeakers. This corresponds to a loudspeaker angle of $\theta = 5°$. No HRTF effects were included (i.e., the ears were modeled as two point receivers at a distance of $r_H = 0.0875$ m either side of the head center). The CCS filters were designed according to (10), with the direct-path TF from the first loudspeaker to the left ear given by $g_d(\mathbf{l}_1, \mathbf{e}_L) = \exp(-jk\|\mathbf{l}_1 - \mathbf{e}_L\|)/(4\pi\|\mathbf{l}_1 - \mathbf{e}_L\|)$, and similarly for the other loudspeaker–ear pairs. For each simulation run, this overall geometry was placed randomly within the room (keeping the arrangement at least 1 m from any wall), and a total of 100 simulations was made.

The average mean-square ear responses (averaged over 100 locations within the room) are shown in Fig. 3(a), together with the predicted results (dashed line). The average results are in good agreement with what one calculates from (18). The frequency responses for a single run are shown in Fig. 3(b) for comparison. Ideally (that is, with no reverberation) the left-ear response should be unity, and the right-ear response should be zero.

V. CONCLUSIONS

Virtual audio systems that use acoustic crosstalk cancellation are invariably designed to equalize the direct-path TFs only. It has previously been shown by a number of authors that movement of the listener away from the design position results in reduced performance. In this paper, we have derived expressions for the reduction in performance that one can expect to obtain in a reverberant environment. As in previous studies, it was found that the conditioning of the direct-path TF matrix plays an important role in determining system performance. Finally, we note that the performance of the CCS in a reverberant environment has been quantified here by measuring the expected mean-square frequency responses at the listener's ears. Psychoacoustic phenomena such as the precedence effect[8] (by which sound localization is primarily determined by the first arriving sound), may mean that the subjective performance for a human listener is not as poor as one might predict from the results in this paper. This is supported to some degree by a recent experimental study,[9] but is open to further investigation.

[1] O. Kirkeby, P. Nelson, and H. Hamada, "The stereo dipole—A virtual source imaging system using two closely spaced loudspeakers," J. Audio Eng. Soc. **46**, 387–395 (1998).

[2] D. Ward and G. Elko, "Effect of loudspeaker position on the robustness of acoustic crosstalk cancellation," IEEE Signal Process. Lett. **6**, 106–108 (1999).

[3] B. Radlović, R. Williamson, and R. Kennedy, "Equalization in an acoustic reverberant environment: Robustness results," IEEE Trans. Speech Audio Process. **8**, 311–319 (2000).

[4] P. Nelson and S. Elliot, *Active Control of Sound* (Academic, London, 1992).

[5] M. Schroeder, "Statistical parameters of the frequency response curves of large rooms," J. Audio Eng. Soc. **35**, 299–305 (1987). Originally published in German in Acustica **4**, 594–600 (1954).

[6] P. Morse and K. Ingard, *Theoretical Acoustics* (McGraw-Hill, New York, 1968).

[7] J. Allen and D. Berkley, "Image method for efficiently simulating small-room acoustics," J. Acoust. Soc. Am. **65**, 943–950 (1979).

[8] J. Blauert, *Spatial Hearing: The Psychophysics of Human Sound Localization* (MIT Press, Cambridge, MA, 1983).

[9] T. Takeuchi, P. Nelson, O. Kirkeby, and H. Hamada, "The effects of reflections on the performance of virtual acoustic imaging systems," in Proceedings Active 97, Budapest, Hungary (August 1997).

k-omega beamforming on non-equally spaced line arrays

B. R. Breed
Signal Systems, Incorporated, 1715 South Capital of Texas Highway, Suite 102, Austin, Texas 78746-6552

(Received 20 September 2000; revised 28 April 2001; accepted 30 April 2001)

It is not generally known that *k*-omega beamforming can be applied to nonuniform line arrays. The concept is that each of the nonuniform array signals is deemed to come from the nearest array element on a fictitious uniform array spatially sampled at a high-enough density that location errors are negligible. The *k*-omega approach can mimic the time delay and sum approach to an arbitrary degree of accuracy. Interpolating weights are derived and applied to a center-tapered logarithmic array as an example. Benefits of this beamforming approach over the direct approach are discussed.
 [DOI: 10.1121/1.1383768]

PACS numbers: 43.60.Gk, 43.30.Wi, 43.30.Pc [JCB]

I. INTRODUCTION

The implementation of acoustic beamforming using frequency-domain array-sensor data has become somewhat standard in applications of sonar (acoustic) processing on equally spaced line arrays. Efficient methods are particularly important in underwater acoustics applications because of the large number of sensors involved. The frequency domain method has been termed *k-omega beamforming*. Maranda[1] describes the various techniques that are possible in this beamforming application. All these methods take advantage of an FFT applied across the sensors (as originally suggested by Williams[2] and Rudnick[3]). The method most often implemented is that originally developed by Demuth[4] and coworkers at IBM, Federal System Division, using, among others, frequency-sampling techniques developed on Proteus.[5,6] Because it uses common DSP operations such as the FFT and an interpolation, it is the implementation of choice on DSP cards. That the method can also be implemented on non-equally spaced arrays with little loss in efficiency is the purpose of this short note.

On an equally spaced (uniform) array, especially where the number of sensors is equal to the spatial-FFT size, the interpolation coefficients can be approximated using frequency-sampling principles.[6] They are the desired beam's response sampled and truncated at the wave numbers of the spatial FFT in the neighborhood of the desired beam's maximum response axis (MRA). In most situations it is easier to determine the coefficients somewhat differently. In this note a more general procedure is used to derive the interpolation weights. Depending on the application, some grooming of these coefficients is needed after the full (exact) interpolation set is truncated (see below).

In the following section the spatial-FFT method is applied to nonuniform arrays. A logarithmically spaced array is used to demonstrate the approach. Following this is a discussion of some of the advantages and of possible variants.

II. SPATIAL-FFT BEAMFORMING ON NONUNIFORM ARRAYS

The concept is to assign the signals received on the nonuniform array to adjacent sensors on a putative, dense, uniform array. Other sensors on the uniform array are zeroed. The uniform array is given a small-enough spacing that the difference in location of a particular sensor and the nearest location on the sparse array is negligible. Whether this difference is negligible or not at a particular sensor spacing depends on the requirements of the individual system. Figure 1 shows a 25-element logarithmic array with sensor locations marked by Xs. In this example, the array's spacing increases by a factor of 1.1 for each step away from the center. A 64-element uniform array (with an approximately equal total length) is shown adjacent to the nonuniform array. The set of arrows below this uniform array shows the locations of the sensors on the uniform array that are closest to the individual sensors on the nonuniform array. In the *k*-omega beamforming approach, each of these sensors is assigned the signal arriving on the sensor nearest it on that array. The remaining sensors are zeroed. This zeroing has no effect since these sensors are fictitious and are not assigned any of the signals arriving on the real array.

If the sensor data for frequency f are denoted x_n, the spatial-FFT at this frequency can be written

$$X_m = \sum_{n=0}^{N-1} x_n e^{-2\pi j(nm/N)}. \tag{1}$$

x_n is zero for the zeroed sensors. The kth time delay and sum beam can be written

$$b_k = \sum_{n=0}^{N-1} w_n x_n e^{-2\pi j(fndu_k/c)}, \tag{2}$$

where d is the uniform spacing, and u_k is the cosine of the kth beam's MRA angle from forward endfire. The w_n; $n=0,1,...,N-1$, are shading weights. These are assigned the value zero for the zeroed sensors on the uniform array. As always, the selection of the shading weights is at the option of the implementer. The *k*-omega beamformer expresses Eq. (2) in terms of Eq. (1), by substituting the expression for x_n in terms of the X_m; $m=0,...,N-1$

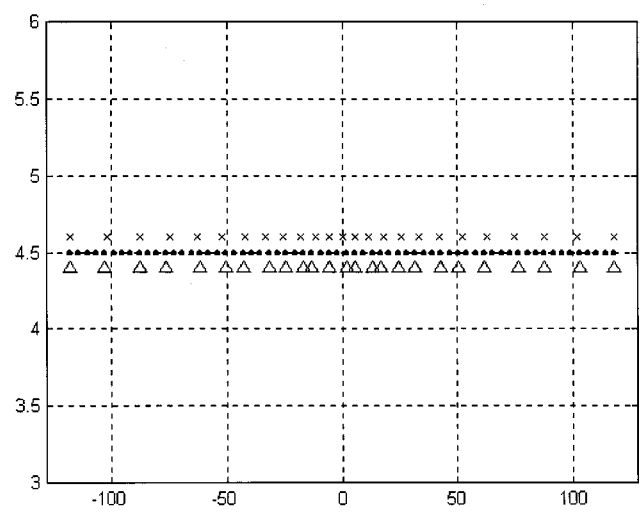

FIG. 1. A nonuniform array denoted by ×, with a uniform array denoted by +. The sensor locations nearest those on the nonuniform array are marked with △.

$$b_k=\frac{1}{N}\sum_{n=0}^{N-1} w_n \sum_{m=0}^{N-1} X_m e^{2\pi j(nm/N)} e^{-2\pi j(fndu_k/c)}$$
$$=\sum_{m=0}^{N-1} X_m \frac{1}{N}\sum_{n=0}^{N-1} w_n e^{-2\pi j(n/N)([fNdu_k/c]-m)}$$
$$=\sum_{m=0}^{N-1} X_m H_{mk}, \tag{3}$$

where H_{mk}, for m and $k=0,...,N-1$ is a set of interpolation weights that exactly interpolates the spatial-FFT outputs to the desired beams

$$H_{mk}=\frac{1}{N}\sum_{n=0}^{N-1} w_n e^{-2\pi jn/N([fNdu_k/c]-m)}. \tag{4}$$

The (computer throughput) advantage of the *k*-omega beamformer is that many fewer than N coefficients are needed to perform this interpolation function for each output beam. This results from H_{mk} being significantly large only for spatial-FFT numbers, m, near where

$$\left(\frac{fNdu_k}{c}-m\right)\cong 0. \tag{5}$$

The typical procedure to take advantage of this is to define an m number by means of

$$m_0(k)\equiv\left[\!\left[\frac{fNdu_k}{c}\right]\!\right], \tag{6}$$

where $[\![a]\!]$ denotes the integer part of a, and an s number defined by means of

$$s(k)\equiv\left[\!\left[\left(\frac{fNdu_k}{c}-m_0(k)\right)N_r+0.5\right]\!\right], \tag{7}$$

in terms of which Eq. (3) can be written

$$b_k\cong\sum_{m=0}^{N-1} X_m \frac{1}{N}\sum_{n=0}^{N-1} w_n e^{-2\pi j(n/N)(m_0(k)+s(k)/N_r-m)}. \tag{8}$$

Truncating to N_c, spatial-FFT beams centered about $m_0(k)$ gives us

$$b_k\cong\sum_{p=-(N_c-1)/2}^{(N_c-1)/2} X_{m_0(k)+p} W_{p,s(k)}, \tag{9}$$

where the interpolation coefficients are given by the N_r-rowed by N_c-columned matrix (table of coefficients)

$$W_{p,s}=\frac{1}{N}\sum_{n=0}^{N-1} w_n e^{-2\pi j(n/N)(p+s/N_r)}. \tag{10}$$

There have been two approximations in this derivation. First, by truncating to N_r rows in the coefficient table, the pointing direction of the interpolated beam is accurate only to

$$\Delta u=\pm\frac{c}{2fNdN_r} \tag{11}$$

in cosine of the pointing angle, but this is no real restriction since N_r can be made large. Second, truncating in Eq. (9) to N_c coefficients is an approximation. Had this truncation not been made, the interpolated beam would be the exact time delay and sum beam pointed in the particular quantized pointing direction. It is this truncation to a smaller number of coefficients that is important to the efficiency of *k*-omega beamforming.

In many applications to nonuniform arrays, there exists a common sensor spacing that evenly divides each of the spacings on the array. In these cases the selection of the spacing to be used for the putative uniform array is apparent. In many if not most of these applications, the table of coefficients derived using Eq. (10) is completely adequate. In the application presented here the shading weights of Eq. (2) were selected to be unity for those elements not zeroed. In this case the unmodified truncated coefficients caused sidelobe levels that differed more than desired from those of the time delay and sum beams. In such cases it is useful to find a perturbed coefficient set in which the rows of the coefficient matrix of Eq. (10) are individually modified using a directed search to reduce the squared error between the interpolated beam and the time delay and sum beam. There are many methods available to do this. A suitable method consists of defining a cost function such as

$$J(W_p;p=1,...,N_c)\equiv\int_{-1}^{1} w(u)\left|B(u,W)-B_d(u)\right|^2 du,$$

where $B(u,W)$ is the beam-pattern function obtained with the weight vector W and B_d is the desired function, in this case the exact time delay and sum pattern. The most direct method for finding a set of N_c weights that has a lower cost is to modify each coefficient, in turn, by a small amount in each of a sequence of steps. This is described using pseudo code as follows:

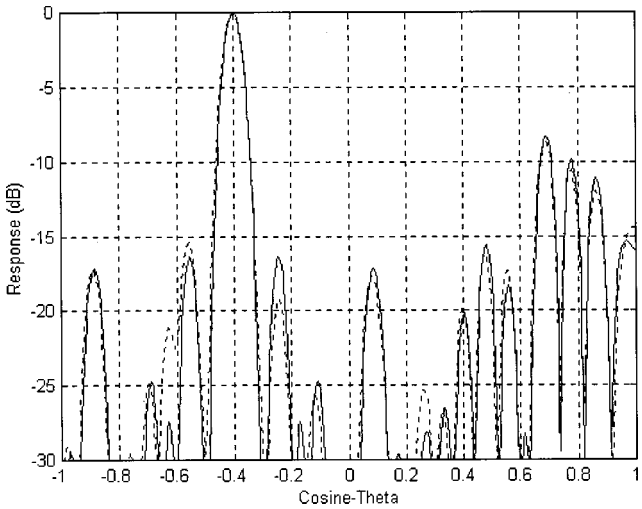

FIG. 2. Comparison of beam patterns. Time delay and sum beam steered to -0.4 on the nonuniform array, solid curve. *k*-omega beamformer response, dashed curve.

Let

Del$=a$ (a is a small scalar)

K=The initial value of J with the initial weighting vector

Then

While Del$>b$ (b is a small scalar controlling the degree of convergence)

For all $k<N_c+1$

For Δ assigned to each of $(1,-1,i,-i)$

If $J(W_k=W_k+\Delta\text{Del})<K$

$K=J(W_k+\Delta\text{Del})$, and $W_k=W_k+\Delta\text{Del}$

Endif

Endfor

Endfor

If a change has occurred in K, continue

Else Del=Del/2, continue

Endif

Endwhile

Exit.

Where the notation $J(W_k=W_k=\Delta\text{Del})$ denotes the value of J with the kth coefficient in the vector W changed by adding ΔDel. The new value of J is denoted $J(W_k+\Delta\text{Del})$. ΔDel is a positive or negative, real or imaginary, increment to a coefficient. When the cost function has more than one local minimum there is no guarantee that there will be convergence to the desired pattern using this particular code. If the initial delta, a, is small, it has been found to converge properly for the several tens of cases we have tried. There are of course many variations on this theme.

This algorithm was applied to generate the coefficients (or interpolation weights) that produce the results shown in Fig. 2. This figure compares the ''ideal,'' uniformly shaded, time delay and sum beam (solid curve) with the uniformly shaded *k*-omega beam (dashed curve) formed using only seven coefficients.

III. DISCUSSION

On a per-beam basis a time delay and sum beam (implemented with phase delays) requires M complex multiplications and additions, with M being the number of sensors on the nonuniform array. On the other hand, the *k*-omega beamformer requires N_c complex multiplications plus each beam's *pro rata* share of the cost of the spatial FFT. This share is proportional to $\log_2 N$ if N beams are formed. A simple calculation shows that, for the example considered in this note, the *k*-omega approach is significantly more efficient. That such efficiencies are available for *nonuniform* arrays is not generally known, and the arrays used in sonar (acoustical) processing are often of this type.

The table of interpolation coefficients is usually precomputed in applications of the method. A significant fact is that the same N_r by N_c set of coefficients can be used for all pointing directions and for all frequencies. The independence on pointing direction results from the translation invariance of beam patterns when expressed in terms of the cosine of the angle from endfire. This invariance is available on *all line arrays*. The frequency independence comes from the fact that the spatial-FFT beams' MRAs scale with frequency at exactly the same rate that a given beam's spatial response does.

We can relate the expression Eq. (10) for the coefficients to sampling in wave number (analogous to frequency sampling filter designs). For a plane wave from $u=\cos\theta$, the broadside beam response is

$$b(u)=\sum_{n=0}^{N-1} w_n e^{-2\pi j(fnd/c)u}. \tag{12}$$

Except for the $(1/N)$ factor, the coefficients are seen to be equal to the sampled beam response. Thus,

$$W_{p,s}=b\left(\frac{fc}{Nd}(p+s/Nr)\right). \tag{13}$$

The frequency sampling approach (to interpolation coefficient generation) works even for sparse line arrays.

A variant of the approach in this note is to use a better spatial interpolation than the ''nearest-neighbor'' method used above. This means that, rather than assigning the sensor signals to the closest uniform array location, the signals themselves can be interpolated to fit a sparser uniform array. A smaller value for N would result. Generally, however, the spatial interpolation costs more than what can be saved by reducing N.

ACKNOWLEDGMENTS

The first applications of *k*-omega beamforming to logarithmic arrays were performed at Hughes Aircraft Company, Fullerton, CA, with Ron Warren, Jim Mayer, and Jeff Strauss. Applications to extended apertures were performed with the assistance of Ted Posch.

[1] B. Maranda, ''Efficient digital beamforming in the frequency domain,'' J. Acoust. Soc. Am. **86**, 1813–1819 (1989).

[2] J. R. Williams, ''Fast beamforming algorithm,'' J. Acoust. Soc. Am. **44**, 1454–1455 (1968).

[3] P. Rudnick, ''Digital beamforming in the frequency domain,'' J. Acoust. Soc. Am. **46**, 1089–1090 (1969).
[4] G. Demuth, ''Frequency domain beamforming techniques,'' IEEE International Conference on Acoustics and Speech Signal Processing 713–715 (1977).
[5] B. R. Breed, ''A sampling theorem for periodic, band limited signals,'' Technical Memorandum, Radian Corporation, Austin, TX, August 1973, Revised May 1974.
[6] G. L. Demuth, ''A truncated convolution for beam interpolation and shaping at the output of a two-dimensional (space-time) FFT, Technical Memorandum, Federal Systems Division, IBM Corporation, Bethesda, MD, October 1975.

A method for studying variability in fricatives using dynamic measures of spectral mean

Benjamin Munson
Department of Communication Disorders, University of Minnesota, 115 Shevlin Hall, 164 Pillsbury Avenue, Minneapolis, Minnesota 55455

(Received 31 October 2000; accepted for publication 30 May 2001)

This paper presents a new method for studying within-speaker variability in fricative spectra. In this method, nonlinear regression is used to predict values of the spectral mean of a 10-ms window of frication noise from its position in the fricative. The resulting measure of model fit, R^2, is used as an index of within-speaker variability. This method was applied to a corpus of /s/ and /ʃ/ tokens spoken by three groups of participants: 3–4-year-old children, 7–8-year-old children, and adults. Results indicated that fricatives were more variable when produced before the stop consonant /p/ than before /t/. No difference in variability was noted between adults and children, although a nonsignificant trend of decreased variability in adults was noted. © *2001 Acoustical Society of America.* [DOI: 10.1121/1.1387093]

PACS numbers: 43.70.Fq [AL]

I. INTRODUCTION

A large literature has examined factors that influence within-speaker variability in speech production. For example, numerous studies have examined variability as a function of age and neuromotor function (e.g., Eguchi and Hirsch, 1969; Lee, Potamianos, and Narayanan, 1999; Weismer *et al.*, 1992; Wohlert and Smith, 1999). These studies have found that, for some spectral and temporal measures, children are more variable than adults, older adults are more variable than younger adults, and speakers with certain speech disorders are more variable than individuals without speech disorders. One common assumption underlying these studies is that trial-to-trial variability within speakers is an index of speech motor control. Speakers with greater variability are assumed to have poorer speech motor control than those with relatively less variability.

Studies have differed in both the speech sounds whose variability has been examined and in the measures of variability that have been used. A number of studies have measured variability in duration. There are many advantages to studying duration: the same measurement scale is used for different speech sound types (vowels, sonorant consonants, obstruent consonants); duration is assumed to directly reflect underlying timing mechanisms; and reliable duration measurements can easily be made from either acoustic or kinematic signals.

Relatively fewer studies have examined variability in spectral parameters. In general, these studies have focused on variability in vowel formants and fundamental frequency (e.g., Eguchi and Hirsch, 1969; Lee, Potamianos and Narayanan, 1999). Variability in the spectra of consonants has not been studied extensively, largely because there is no one acoustic parameter that reliably corresponds to different phonetic features of consonants in the way that formant frequency relates to the phonetic features of vowels. For example, a recent study by Jongman, Wayland, and Wong (2000) examined the acoustic characteristics of American English fricatives and found that many acoustic measures were needed to characterize the eight American English fricatives. One such measure is the first spectral moment, spectral mean (abbreviated m_1). Spectral mean is calculated by treating the frequency distribution in a power spectrum as a random distribution of numbers, and taking the mean of that distribution (Forrest *et al.*, 1988; Nittrouer, 1995). A number of studies have examined spectral mean in fricatives. Jongman *et al.* (2000) found that spectral mean of the center 40 ms of fricatives discriminates between the four places of articulation in English. The greatest difference was found between alveolar fricatives (/s/, /z/) and palatoalveolar fricatives (/ʃ/, /ʒ/): /s/ and /z/ are characterized by a higher spectral mean than /ʃ/ and /ʒ/.

The current study examines variability in the spectral mean of the fricatives /s/ and /ʃ/. There are a number of ways spectral mean could potentially be used to study variability in fricative production. One way would be to choose a portion of the fricative, calculate the mean for the spectrum of that portion, and examine trial-to-trial variability in this measure. A second way would be to calculate the mean for the spectrum of the entire fricative and examine trial-to-trial variability in this measure. These methods are potentially problematic in that fricatives whose spectral characteristics change over time would not necessarily be measured as more variable than those whose spectral characteristics are consistent across time. While previous research has not found that the spectral mean varies greatly throughout the course of the fricative (Behrens and Blumstein, 1988; Shadle and Mair, 1996), these investigations have been limited to fricatives in prevocalic or intervocalic position. There is reason to believe that spectral mean might vary over time in other contexts. The spectrum of fricatives is dependent on the size and shape of the cavity anterior to the noise source (Stevens, 1998). For example, if an /s/ were produced with rounded lips, the cavity would increase in size and the spectral mean would lower relative to the m_1 for /s/ produced with unrounded lips. If /s/ were produced in a phonetic context where it overlapped with an adjacent lip rounding or labial closure gesture, then

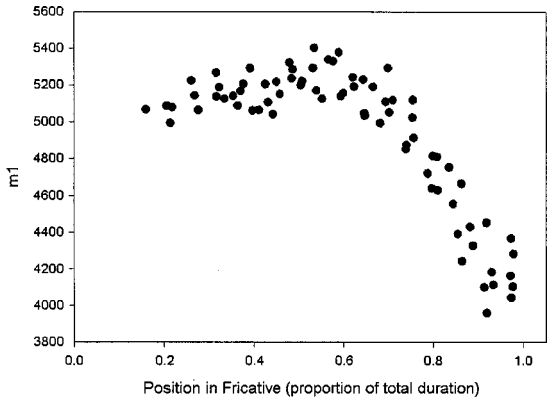

FIG. 1. Spectral moments for 10-ms windows of the fricative /s/ in five repetitions of the word *swing* produced by an adult female ($R^2=0.889$).

changes in spectral mean over the course of the fricative would occur.

This letter proposes a new mechanism for studying spectral variability in fricatives. This method examines changes in spectral mean throughout the time course of the fricative. For illustration, consider the fricative /s/ in the word *swing*. At fricative onset, m_1 is high. As the lips begin to round for the following /w/, the spectrum of the noise falls. Figure 1 is a plot of m_1 for each nonoverlapping 10-ms window in /s/ in five different productions of the word *swing* by an adult female speaker of English. Values for m_1 are plotted with respect to their position in the fricative, expressed as a proportion of the total duration of the fricative, rather than with respect to their absolute duration. This allows fricatives of different durations to be compared with one another. Figure 2 is a plot of m_1 for each nonoverlapping 10-ms window in /s/ in five different productions of the word *spike* by the same speaker of English. Informal observation of these plots shows that values for m_1 of the /s/ in *spike* are more widely scattered than those for the /s/ in *swing*, suggesting that the /s/ in *spike* is more variable than the /s/ in *swing*. An objective measure of scatter can be obtained by fitting a nonlinear regression equation to these data and examining the measure of model fit, R^2. When a nonlinear regression is fit to the data plotted in Figs. 1 and 2, we find that the R^2 for the /s/ in *spike* is 0.512 and the R^2 for the /s/ in *swing* is 0.889. Thus, the informal observations are validated: the /s/ in *swing* has a higher R^2 than the /s/ in *spike*, indicating less scatter around the regression line and less variability.

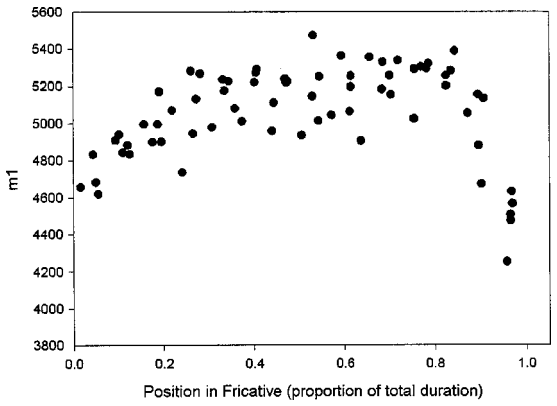

FIG. 2. Spectral moments for 10-ms windows of the fricative /s/ in five repetitions of the word *spike* produced by an adult female ($R^2=8.512$).

The proposed method for studying variability in fricative spectra does not have the problems associated with it that the other two approaches have. Because changes in the fricative spectrum across time are measured, fricatives with spectra that change over time are measured as more variable than those that are relatively steady across time.

The purpose of this letter is to illustrate this method of measuring variability in fricative spectra using time-dependent changes in spectral mean. The corpus chosen for analysis contains the fricatives /s/ and /ʃ/ spoken by three groups of participants: young children (3- to 4-year-olds), older children (7- to 8-year olds), and adults. These fricatives were produced in nonsense words preceding the stop consonants /p/ and /t/. Three effects are predicted. First, it is predicted that children will demonstrate greater variability than adults. This prediction is made based on the large body of research suggesting that other spectral features of children's speech, such as $F0$ and vowel formants, are more variable than those of adults' (e.g., Lee *et al.*, 1999). Second, it is predicted that the fricatives /s/ and /ʃ/ will be more variable before the sound /p/ than before the sound /t/. As the lips begin to close for the following /p/, the spectral mean of the fricatives will lower (as in Figs. 1 and 2). If speakers are inconsistent in the point during the course of the fricative at which they begin lip rounding, then greater variability will result. The articulatory movement associated with the sound /t/ has a much smaller effect on the size of the cavity anterior to the friction source, and it is predicted that it will have a much weaker influence on spectral characteristics of preceding fricatives. Finally, it is predicted that there will be an interaction between age group and following stop consonant. Previous research has demonstrated that children produce greater overlap between adjacent consonant and vowel articulatory gestures than adults (e.g., Nittrouer, Studdert-Kennedy, and Neely, 1996). Thus, we predict the influence of following consonant will be greatest for children, whose coordination of adjacent articulatory gestures is immature.

II. METHODS

a. Stimuli. Fricatives were elicited using prerecorded production prompts. This was done to insure that a consistent model would be provided to all participants. The two target fricatives were embedded in four nonsense word prompts, preceding the consonants /p/ and /t/. Each nonword had a CVCCVC syllable structure with a stressed initial syllable. The fricative-stop sequence was the medial CC. None of the words contained a stressed syllable that was a word that would be familiar to young children, as determined by its absence from Moe, Hopkins, and Rush's (1983) corpus. An adult male speaker of American English read the nonwords in the frame *an X* as part of a longer list of 26 nonwords. Words were digitized onto a 486 personal computer with a sound card while they were being produced. A sampling rate of 20 kHz and 16-bit quantization were used. Stimuli were filtered at 8.7 kHz and were normalized for amplitude.

The four nonwords were transferred to the hard drive of a Pentium II 450-MHz computer for presentation to adult participants. For presentation to children, stimuli were recorded onto an audio CD, so that they could be played from an ordinary portable CD player. This required their sampling rate to be converted to 22.05 kHz. A subjective assessment indicated no appreciable differences in sound quality between the two sampling rates.

b. Participants. Individuals from three age groups participated in the study. All participants had been recruited as part of a larger study examining factors influencing temporal and spectral properties of medial diphone sequences (Munson, 2000). The first group of participants ($n=9$) was recruited from a local day-care center. The mean age of the participants was 3;10 (years;months) with a standard deviation of 8.6 months. All participants were reported by their parents to be monolingual speakers of English. Two standardized tests were given to this group: A standardized test of speech sound production accuracy (The *Goldman-Fristoe Test of Articulation* [GFTA], Goldman and Fristoe, 1986) and a test of expressive vocabulary size (the *Expressive Vocabulary Test* [EVT], Williams, 1997). The mean percentile rank for the GFTA was 54 (s.d.=31). The mean standard score for the EVT was 112 (s.d.=12).

The second group of participants ($n=9$) was recruited from a local after-school program. The mean age of these participants was 8;4, with a standard deviation of 6.8 months. The mean percentile rank for the GFTA was 99 (s.d.=0). The mean standard score for the EVT was 101 (s.d.=7.2). All participants were reported by their parents to be monolingual speakers of English, and to have no history of speech, language, or hearing disorders.

The third group of participants ($n=10$) was recruited from the Department of Speech and Hearing Science at The Ohio State University. All participants were naive to the purposes of the study. The mean age of these participants was 27;5, with a standard deviation of 65.5 months. The GFTA and EVT were not administered to this group of participants. No participant reported a history of speech, language, or hearing disorders. All participants were native speakers of English. Details regarding individual participants can be found in Munson (2000).

c. Procedures. Testing procedures differed slightly for the three age groups. Adults were recorded in a sound-treated booth in a university laboratory. The booth contained a speaker (JBL Pro-III) connected to a Pentium II 450-MHz personal computer which played the production prompts. Participants wore a head-mounted microphone (AKG Micromic C420) connected to a DAT recorder (Sony DAT deck DTC-690) through a preamplifier. Four repetitions of the production prompt for each word were played to the participants (e.g., a [bɪspət], a [bɪspət], a [bɪspət], a [bɪspət]). Participants were instructed to repeat all four repetitions of the nonword prompt, matching rate of speech and intonation as closely as possible. When speakers made errors, the experimenter verbally corrected them, and then replayed the prompt. The four nonsense words were embedded in a longer list of nonsense words containing medial fricative–stop, nasal–stop, and stop–stop sequences.

A single experimenter tested the youngest group of participants in a quiet room in their preschool, during regular school hours. Production prompts were played from a portable CD player (Aiwa CSD-ES225). Participants wore a head-mounted microphone (AKG Micro-mic C420) connected to a portable DAT recorder (Sony DAT Walkman AVLS) through a power source (Rolls Phantom power adapter PB23). Production prompts were elicited by showing the participants small stuffed animals and telling them that they should repeat the CD player when it ''said'' the animal's name. When participants made repetition errors, the experimenter provided a correct model and then replayed the prompt. Each prompt was played until the experimenter judged that at least four noise-free, error-free productions of the target word had been uttered. The four nonwords were embedded in a longer list of nonsense words. In addition to the experimental task, participants completed the GFTA, the EVT, and a pure-tone hearing screening at 500, 1000, 2000, and 4000 Hz (ANSI, 1989). Following each session, children received stickers or prizes as a reward.

A single experimenter tested the school-aged participants in a quiet room in the school during an after-school program. Children were told that a CD player would play some words that were not real words of English, and that they should repeat exactly what they heard. Production prompts were played from a portable CD player (Aiwa CSD-ES225). Participants wore a head-mounted microphone (AKG Micro-mic C420) connected to a portable DAT recorder (Sony DAT Walkman AVLS) through a power source (Rolls Phantom power adapter PB23). When children made mistakes, the experimenter provided a correct verbal model and replayed the prompt. Prompts were replayed until the experimenter judged that the participant had uttered at least four noise-free, error-free tokens of each target nonword. These children completed a pure-tone hearing screening at 500, 1000, 2000, and 4000 Hz (ANSI, 1989). No standardized tests were administered to these children, as they had been given a battery of tests for a larger study in which they were participating within the last 2 months. Following each experimental session, children received stickers or small prizes as rewards.

d. Acoustic analysis. Data were digitized on a Pentium II 450-MHz computer using a 20-kHz sampling rate with 16-bit quantization, and were filtered at 8.7 kHz. Individual target words were segmented from the larger sound file and viewed using Entropics Systems' XWAVES signal-processing software running on a Pentium II 400-MHz computer using the Linux operating system. Tokens containing disfluencies, speech errors, or extraneous noise were removed from the analysis. The onset and offset of /s/ and /ʃ/ were identified based on the onset of high-frequency aperiodic noise. In cases where the onset of the fricative overlapped with the previous vowel (i.e., the fricative was partially voiced) the onset was marked as the onset of aperiodic noise in the high-frequency region. In cases where the offset of the previous vowel was devoiced, the onset of the fricative was marked as the point at which there ceased to be an obvious formant structure in the aperiodic noise.

Spectral moments were was calculated using the proce-

TABLE I. Mean R^2 for the fricatives /s/ and /ʃ/.

Fricative	Context	Younger children	Older children	Adults
/s/	*p*	0.052 (0.052)	0.111 (0.137)	0.104 (0.145)
	t	0.201 (0.207)	0.199 (0.250)	0.172 (0.137)
/ʃ/	*p*	0.087 (0.123)	0.089 (0.093)	0.095 (0.088)
	t	0.097 (0.103)	0.209 (0.151)	0.204 (0.103)

dure described in Forrest *et al.* (1988) with three differences. First, pre-emphasis was not applied before moments were calculated, as the target sounds were voiceless and would not be affected by the 6-dB per octave roll-off present in the glottal waveform. Second, a 500 Hz high-pass filter was applied to the spectrum before the moments were calculated, so that spectral mean for voiced (or partially voiced) fricatives would be comparable to the spectral mean of voiceless fricatives. Thus, spectral mean was calculated over the 500 to 8700 Hz spectral range. Finally, only the moments calculated from the linear (Hertz) scale were used.

III. RESULTS

a. Nonlinear regression. The first spectral moment for each 10-ms window was used as the dependent variable in a nonlinear regression with position in fricative, expressed as a proportion of the total duration of the fricative, as the dependent variable. Spectral moments from nonoverlapping 10-ms windows were used to satisfy the requirement that pairs of observations analyzed in a regression be independent. The data were fit to the nonlinear equation $y = ae^{bx}$. The measure of scatter around the regression line, R^2, was used as an index of within-speaker variability. The number of data points for each regression could not be controlled, as fricatives varied in duration and participants varied in the number of usable tokens that they produced.

b. Analysis of variance. The R^2 values derived from the nonlinear regression analyses were subjected to a 2 fricative (/s/ vs /ʃ/) × 2 following stop context (/p/ vs /t/) × 3 age group mixed measure analysis of variance with a Huynh–Felt correction for sphericity (Huynh and Felt, 1976). The η^2 statistic, a measure of effect size, is reported for all significant effects. Fricative and following stop consonant were within-subjects measures; age group was the between-subjects measure. No effect of fricative consonant was found, $F[1,25] = 0.204$, $p > 0.05$. A significant main effect of following stop consonant was found $F[1,25] = 5.602$, $p < 0.05$, $\eta^2 = 0.183$ [a medium effect size (Cohen, 1988)]. The influence of following stop consonant was in the predicted direction: fricatives were more variable before the consonant /p/ the before /t/. No effect of age group was found $F[2,25] = 1.175$, $p > 0.05$. A nonsignificant trend in the expected direction was found: adults were less variable that both groups of children. Finally, none of the interactions was significant, including the predicted interaction between age and following stop context ($F[2,25] = 1$, $p > 0.05$). Mean R^2 values can be found in Table I.

IV. DISCUSSION

This letter presented a method for examining variability in fricative spectra using time-dependent changes in spectral moments. This method is advantageous because it exploits time-varying changes in fricative spectra in assessing within-speaker variability. Using this method, it was shown that the fricatives /s/ and /ʃ/ were more variable before /p/ than before /t/, and that variability did not decrease across different age groups. Further research should use this method to examine whether variability in fricative spectra is influenced by the same factors that have been shown to affect variability in other temporal and spectral parameters, such as vowel formants, fundamental frequency, and phoneme duration.

ACKNOWLEDGMENTS

The author gratefully acknowledges Pauline Welby and Mary Beckman for providing help in writing the XWAVES scripts used to calculate spectral moments. This work was funded by NIH (Training Grant No. DC0051 to Robert A. Fox and Grant No. DC02932 to Jan Edwards), the Ohio State University Graduate School, and the University of Minnesota.

ANSI (**1989**). ''Specifications for Audiometers'' (American National Standards Institute, Washington, D.C.).
Behrens, S., and Blumstein, S. (**1988**). ''Acoustic characteristics of English voiceless fricatives: A descriptive analysis,'' J. Phonetics **18**, 51–63.
Cohen, J. (**1988**). *Statistical Power Analysis for the Behavioral Sciences* (Erlbaum, Hillsdale, NJ).
Eguchi, S., and Hirsh, I. (**1969**). ''Development of speech sounds in children,'' Acta Oto-Laryngol., Suppl. **257**.
Forrest, K., Weismer, G., Milenkovic, P., and Dougall, P. (**1988**). ''Statistical analysis of word-initial voiceless obstruents: Preliminary data,'' J. Acoust. Soc. Am. **84**, 115–123.
Goldman, R., and Fristoe, M. (**1986**). *The Goldman–Fristoe Test of Articulation* (Pro-Ed, Austin, TX).
Huynh, H., and Feldt, L. (**1976**). ''Estimation of the Box correction for degrees of freedom from sample data in randomized block and split-plot designs,'' J. Ed. Stat. **1**, 69–82.
Jongman, A., Wayland, R., and Wong, S. (**2000**). ''Acoustic characteristics of English fricatives,'' J. Acoust. Soc. Am. **108**, 1252–1263.
Lee, S., Potamianos, A., and Naryanan, S. (**1999**). ''Acoustics of children's speech: Developmental changes of temporal and spectral parameters,'' J. Acoust. Soc. Am. **105**, 1455–1468.
Moe, S., Hopkins, M., and Rush, L. (**1982**). *A Vocabulary of First-Grade Children* (Thomas, Springfield, IL).
Munson, B. (**2000**). ''Phonological Pattern Frequency and Speech Production in Children and Adults,'' Unpublished doctoral dissertation, The Ohio State University.
Nittrouer, S. (**1995**). ''Children learn separate aspects of speech production at different rates: Evidence from spectral moments,'' J. Acoust. Soc. Am. **97**, 520–530.
Nittrouer, S., Studdert-Kennedy, M., and Neely, S. (**1996**). ''How children learn to organize their speech gestures: Further evidence from fricative-vowel syllables,'' J. Speech Hear. Res. **39**, 379–389.
Shadle, C., and Mair, S. (**1996**). ''Quantifying spectral characteristics of fricatives,'' in Proceedings of the International Conference on Speech and Language Processing (ICSLP), 1521–1524.
Stevens, K. (**1998**). *Acoustic Phonetics* (MIT Press, Cambridge, MA).
Weismer, G., Martin, R., Kent, R., and Kent, J. (**1992**). ''Formant trajectory characteristics of males with ALS,'' J. Acoust. Soc. Am. **91**, 1085–1098.
Williams, K. (**1997**). *Expressive Vocabulary Test* (American Guidance Services, Circle Pines, MN).
Wohlert, A., and Smith, A. (**1998**). ''Spatiotemporal stability of lip movements in older adult speakers,'' J. Speech, Lang. Hear. Res. **41**, 41–50.